LEGIBILITY NOTICE

A major purpose of the Technical Information Center is to provide the broadest dissemination possible of information contained in DOE's Research and Development Reports to business, industry, the academic community, and federal, state and local governments.

Although a small portion of this report is not reproducible, it is being made available to expedite the availability of information on the research discussed herein.

1

Summary of Major Activities

at the 40- to 200-J level were completed. They supported completely our predictions in the military applications area, in particular with accurate physics measurements.

UCRL--50021-81

DE83 011875

Dr. 1428-1

UCRL-50021-81
Distribution Categories
UC-21, 22

1981 Laser Program Annual Report

Scientific Editor:
E. Victor George

Publication Editors:
John R. Strack
Gerald R. Grow

MS date:
August 1982

Lawrence Livermore National Laboratory

Available from: National Technical Information Service • U.S. Department of Commerce
5285 Port Royal Road • Springfield, VA 22161 • $28.00 per copy • (Microfiche $3.50)

Acknowledgments

Preparing a comprehensive technical report of this magnitude is a large effort that involves the work of literally hundreds of people. The overall content of this report is, of course, the result of the efforts of the entire staff of our Program. The names of authors and major contributors responsible for a particular piece of work appear generally at the end of the article describing that work. The authors had the added tasks of organizing and writing the material and patiently participating in the iterative editing, review, and proofreading processes necessary for final publication. The able and responsive assistance of the Section Editors in collecting and reviewing articles was an especially valuable contribution.

The process of preparing and publishing this report required the talents and participation of many members of the LLNL Technical Information Department. I am indebted to all of them for their help and support in this task: Elsa Pressentin, and then Louise Rufer, both editors, coordinated all aspects of production, keeping them under control and on schedule. Donald Cowden, William Fulmer, and Wilma Leon planned, guided, and coordinated the artwork and layout. Wilma Leon, in particular, deserves special mention for the prodigious commitment of her time and talent, seeing the effort through from its inception to final printing. William Fulmer, Group Leader of the Special Design Projects Team, and Rick Wooten brought considerable imagination and creativity to designing the general format and in preparing divider pages, section introductions, and covers. The tedious and exacting job of proofreading was capably done by Jill Silvers and Delores Mason. Composition and final page makeup of a difficult, demanding text was the work of Barbara Phillips, whose cheerful willingness to undertake last-minute revisions and corrections was a mainstay of the effort. Cathy Wood and Peter Link were especially helpful in developing typesetting-system formats for on-line final page makeup; Cathy also assisted Barbara in composition. Elaine Price ensured that composition resources remained available despite setbacks in the schedule. Final printing specification and review for format consistency were expertly handled by Margaret Sylvester. Mel Moura did his usual fine job of coordinating the printing and binding contracts and maintaining high standards of printing quality under an extremely tight schedule. Charles McCaleb, and later Howard Lentzner, oversaw the editorial support, while the job of editing complex technical articles was accomplished by Thomas Elkjer, Jerry Grow, Robert Hendrickson, Robert Kirvel, and John Strack. Thomas Elkjer deserves praise for his diligence in compiling the indexes for this report. Fernando Santos and his colleagues mounted a magnificent effort to prepare the final camera-ready pages of this report against a daunting schedule. Richard Pond of the Classification Office ensured that issues concerning the sensitivity of technical information were resolved quickly. Bert Weis of the Patent Office was responsible for the meticulous review and final clearance of this material for public use.

Olga Parker of the Laser Program Multimedia group devoted a great deal of time coordinating preparation of the original versions for most of the illustrations used in this report. The Program clerical staff and administrative assistants sustained the responsibility for preparing the original manuscripts, in addition to their normal workloads. Their contributions are greatly appreciated. To these people, and all the others we have not mentioned by name, I offer thanks for hard work.

Susan Simecka, my assistant in preparing this report, merits special thanks; her dedication was an essential ingredient in every aspect of the generation and production of this report. I am pleased also to acknowledge the superb editorial contribution made by Jerry Grow, who monitored and reviewed every article from initial rough draft to final camera-ready copy. Finally, I must reserve special praise for the work of John Strack. His role as TID project manager who set the agenda for this report, formulated realistic publications policies, advised contributors, oversaw production, and served as overall steersman for the effort cannot be overestimated. I feel that his orchestration of scientific input, editorial review, artistic production, administrative control, and final composition, typesetting, and layout, were critical to the successful delivery of the 1981 Annual. He has my thanks for a job well done.

E. V. George

Preface

This report presents the unclassified activities and accomplishments of the Laser Program at the Lawrence Livermore National Laboratory for the calendar year 1981. The classified work of the Program in 1981 is being reported separately. The Laser Program at LLNL, comprised of both Laser Fusion and Laser Isotope Separation efforts, is supported by the United States Department of Energy.

Our purpose in preparing these reports is to present our work in depth for the benefit of the inertial-confinement-fusion and isotope-separation communities. Accordingly, concepts, theoretical analyses, computational results, design and configuration of experiments, data, and results are presented in detail to allow critical technical evaluation and to make it possible to reproduce or extend any of the work presented here. In 1981, we realized significant scientific and engineering accomplishments in all areas of our Program, as summarized in Section 1.

This report is published in sections that correspond to the division of technical activity in the Program. Section 1 provides a Program Overview, presenting highlights of the technical accomplishments of the elements of the Program, a summary of activities carried out under the Glass Laser Experiments Lead Laboratory Program, as well as discussions of Program resources and facilities. Section 2 covers the work on solid-state Nd:glass lasers, including systems operations and Nova and Novette systems development. Section 3 reports on target-design activities, plasma theory and simulation, code development, and atomic theory. Section 4 presents the accomplishments of the Target Fabrication group, Section 5 contains the results of our diagnostics development, and Section 6 reports the results of laser-target experiments conducted during the year, along with supporting research and development activities. Section 7 presents the results from laser research and development, including solid-state R&D and the theoretical and experimental research on advanced lasers. Section 8 contains the results of studies in areas of energy and military applications, including those relating to electrical energy production by inertial-confinement fusion systems.

E. V. George

Contents

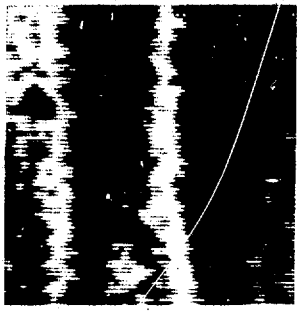

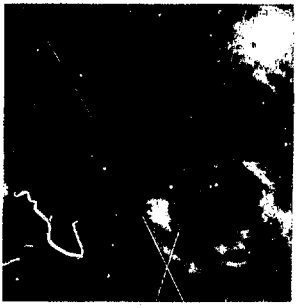

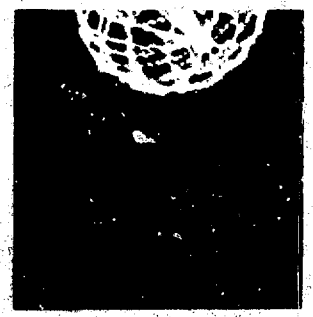

Subject and author indexes follow the last page of Section 8.

Laser Program Overview
Section 1

Laser Program Overview

Contents

Section Editor: E. V. George

Laser Program Overview

Introduction

J. L. Emmett

The principal components of the Laser Program at the Lawrence Livermore National Laboratory (LLNL) are Inertial Confinement Fusion (ICF) and Laser Isotope Separation (LIS). The goal of the ICF Program is to produce significant, well-diagnosed thermonuclear experiments with laboratory laser facilities. In the near term, these experiments are for military applications (for example, understanding material responses under very high temperatures and pressures, or studying processes that occur under extreme conditions experienced in nuclear weapons). With high-gain targets, simulations of nuclear explosion effects can also be obtained. The combination of high-gain targets, an efficient driver, and a reliable reactor system will make available the promise of unlimited fusion power for world energy requirements. This latter possibility offers tremendous economic payoff, but it also will require considerable technical and economic development.

During the last decade of ICF research, we have made significant progress toward achieving our goals. We now have a good understanding of the physical processes occurring with direct-illumination and hohlraum targets. We have been able to construct large, flexible laboratory laser drivers, and with them we have demonstrated control of laser beam-plasma interactions so as to obtain an environment around the fuel capsule suitable for symmetrical, high-density compression. We have achieved a diagnosed compression of deuterium–tritium (D–T) to 100× its liquid density. We have also begun, and will be conducting, a wide variety of experiments of significance to the Nuclear Weapons Program at LLNL using our Nd:glass laser facilities.

In 1981, we completed our 1-μm laser-target experimental program. We completed our experiments with Shiva in December 1981 and dismantled part of it for use in Novette and Nova. We disassembled the Argus laser in August 1981 to make room for the 10-kJ, 0.53-μm Novette laser. During 1981, we completed our measurements on direct-drive and radiation-driven targets using 2ω and 3ω light on Argus. In particular, from our hohlraum experiments, we found greatly improved target performance at the shorter wavelengths. With Shiva, we measured the production of hot electrons associated with the onset of Raman and $2\omega_{pe}$ instabilities in controlled scalelengths using disk targets. These data greatly improved our understanding of the interaction of light with long scalelengths in reactor-size targets. Another important series of experiments—conducted in collaboration with the Naval Research Laboratory (NRL)—were those in which we measured the ablation-induced acceleration of foils. The foil motion was diagnosed by using x-ray backlighting to illuminate the target and a unique x-ray microscope and x-ray streak camera to record the data. The results of these, and similar experiments on imploding fuel capsules, permitted us to measure the coupling efficiency of the laser drive to the target, the state of the moving material, and the uniformity of target motion, both in a planar and in a converging case.

Our work during the next decade of experimentation will be associated with detailed measurements of laser-target scaling and compressed fuel conditions. Novette and Nova scaling experiments will conclude with measurements of laser interaction of scalelengths appropriate to high-gain targets. On Novette, by

using cryogenic targets, we expect to measure 200–400× liquid D-T density compression and up to 1000× with Nova. Our emphasis will be quality of the convergence, the conditions of the fuel when it begins to burn, and the efficiency of implosions. As a result of taking these programmatic directions, we have begun studies of cryogenic target construction, high-resolution x-ray-imaging diagnostics, including a framing camera to obtain two-dimensional recording of the data and techniques to develop target layers or fuel additives for radiochemical analysis. The laser requirements will be met with the Nova laser. This laser is now specified to be a 10-beam system, with harmonic conversion to provide ~70 kJ of 0.53- or 0.35-μm light for a variety of target experiments. (The funding decisions and change of scope of the original 1-μm laser to accommodate the harmonic system were not finalized in 1981, the period of this report. We received DOE approval for the Nova Phase I 10-beam harmonic-conversion project in April 1982.)

We reorganized the Laser Program at LLNL in the summer of 1981 to reflect the growth of the LIS Program and the need to change priorities in ICF. In particular, the Fusion Laser Program was divided into the Laser Systems Program and the Laser R&D Program to reflect the fact that the Nova/Novette technologies were maturing and R&D resources had to be applied to developing a new driver. The remaining activities—Target Design, Target Fabrication, Fusion Experiments, and Systems Studies—remained substantially the same as before. Our lead laboratory responsibilities continue in the area of advanced driver development, but at a very reduced level, because there was insufficient funding for the KrF-scaling program developed last year. Our responsibility as lead laboratory for short-wavelength laser experiments continues. This activity has fostered continued interchange between the laboratories—LLNL, University of Rochester Laboratory for Laser Energetics, KMS Fusion, Inc., and the Naval Research Laboratory (NRL). In addition to our collaboration with NRL on the accelerated-foil experiment described above, we worked with KMS to obtain target-scaling information and target-fabrication technology, and we have collaborated with the University of Rochester on harmonic-conversion technology.

The goal of the Laser Isotope Separation Program is to develop laser isotope separation technology for both military and civilian applications. The atomic vapor laser isotope separation process (AVLIS), which we are developing for the production of enriched uranium fuel for light-water reactors, holds the promise for being more efficient, less expensive, and less energy-consuming than currently available technologies. During 1981, process designs for the applications of laser isotope separation to uranium and plutonium enrichment were completed. Detailed analysis on plant and development module design, science and technology base, and program plan for LIS deployment for uranium enrichment were presented to the Department of Energy's Process Evaluation Board (PEB). (In 1982, the PEB recommended the selection of our atomic vapor LIS Process—over Los Alamos National Laboratory's molecular LIS process, and TRW's plasma-separation process—for large-scale engineering development and demonstration.) In a departure from previous *Laser Program Annual Reports*, a review of the progress during 1981 for the Laser Isotope Separation Program is not included in this year's report.

Summary of Major Activities

In this report, we present the achievements and research accomplishments for calendar year 1981 for the Laser Program. These results represent the combined activities of more than 642 people, with a total operating budget of $87.2 million for the year. In the remainder of this section, we present a summary of the major technical activities of the inertial confinment fusion (ICF) program (along with some unclassified highlights of the laser isotope separation (LIS) program), followed by highlights of the Lead Laboratory Program and summaries of Program resources and physical facilities.

Fusion Lasers

The overall objective of the Fusion Laser Program is—through our in-house technical efforts state-of-the art to provide the short-wavelength laser system facilities required for the national ICF program. The Fusion Laser Program was reorganized in 1981; it presently consists of two technical disciplines: Solid State Laser Systems and Fusion Laser Research and Development. A brief synopsis of the major accomplishments for 1981 is given in the paragraphs that follow.

Solid State Laser Systems. The objective of the Solid State Laser Program is to design, construct, and operate the Nd:glass laser facilities required for inertial fusion research at LLNL. In 1981, we focused our efforts on three technical areas: Argus/Shiva operations, Novette, and Nova.

During the year, we concluded the series of fusion-target experiments using the Shiva laser system, finally shutting the entire facility down on December 23. Up to that time, a great deal of scaling information on fusion targets was obtained; a particular example of work conducted in 1981 was the measurement of the production of hot electrons associated with the onset of the Raman and $2\omega_{pe}$ instabilities in controlled-plasma-scalelength targets. With the Argus facility we completed a very successful series of measurements on direct-drive and hohlraum-drive targets using 2ω and 3ω radiation. Several physics and engineering experiments related to frequency conversion were also conducted with the Argus facility. In August 1981, the Argus Facility was shut down to prepare its building for installation of the Novette laser system.

The Novette laser system (shown in Fig. 1-1) was designed to provide >10 kJ of 2ω light for laser—plasma interaction experiments and to test the performance of the

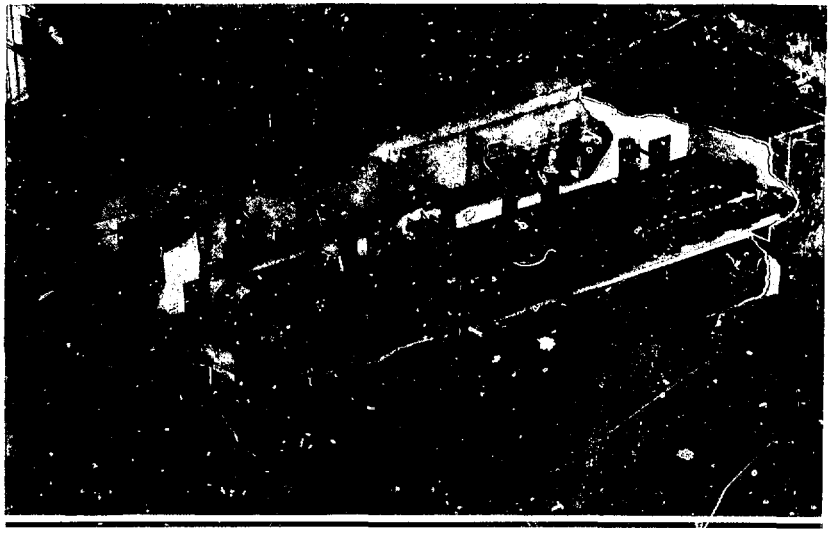

Fig. 1-1. Artist's conception of the Novette Laser System scheduled for completion in the fall of 1982.

large-aperture Nova laser components. It uses Shiva laser parts for the small-aperture component and the target system, Nova large-aperture laser components, and special support hardware, such as the support frame. In addition, it uses prototype harmonic generation and diagnostic systems for testing our Nova concepts. Installation of the system began in September 1981, with completion estimated for November 1982.

Progress on the Nova design continued, driven very strongly by the Novette schedule. The successful Argus short-wavelength target-interaction experiments and the successful laser harmonic-conversion modeling and experiments program led to a recommendation to DOE to change the scope of Nova to include 2ω and 3ω target-irradiation capability. The Nova harmonic system design (see Fig. 1-2) was completed and presented to DOE. It has the unique capability of generating either 2ω or 3ω (as well as using unconverted beams at 1.053 μm) by simply rotating a double crystal array from its 2ω position by 10° and tilting it by 0.25° to generate 3ω light with the same ~70% conversion efficiency experienced with 2ω. This system has extended the versatility of the Nova laser markedly, and led to formal DOE acceptance of the change in scope in April 1982.

Fusion Laser Research R&D. In 1981, Solid State Lasers R&D and Advanced Lasers were combined into one program. The goals of the program were to continue to support the research and development necessary for Nova, Novette, and the ongoing laser research programs; and to conduct research on advanced systems capable of being used for a single-pulse test facility or a high-repetition-rate reactor driver. The Solid State support included harmonic conversion, damage measurements at 1ω and its harmonics, and the development of Nova components, such as the plasma shutter. The advanced research activities center on developing new laser architectures and efficient solid state amplifier designs, new lasers (e.g., the free-electron laser), crystalline laser media, pulsed power sources (such as the compensated pulsed alternator), and innovations in rare-gas-halide design using Raman pulse compression techniques. In 1981, a poor spatial quality KrF laser was used as a pump source for a good spatial quality Stokes beam. We found that the good spatial quality of the Stokes beam was preserved after amplification, in agreement with theoretical expectations (see Fig. 1-3).

Target Design. The combined efforts of our plasma, code development, and design groups are required for the design of targets to achieve program goals. The demonstration of the compression of D–T to reactor-target densities, approaching 1000× liquid density is a principal program objective.

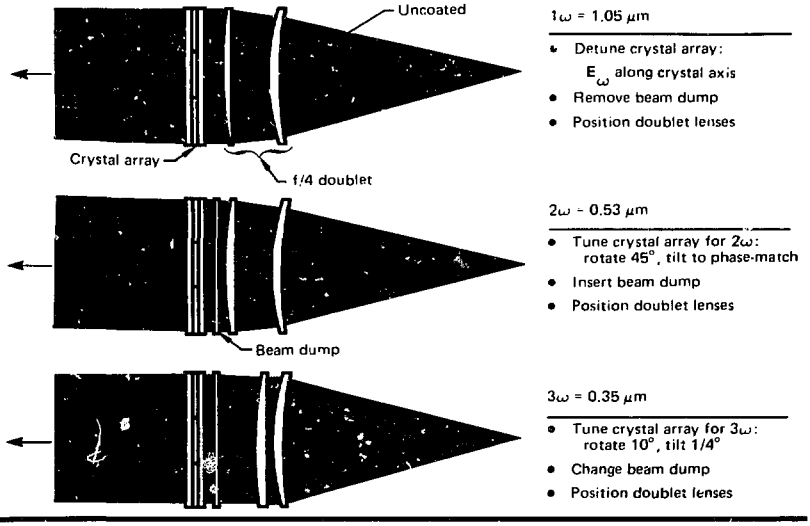

Fig. 1-2. The Nova harmonic-conversion system.

The Argus series of experiments on wavelength scaling was designed and analyzed in 1981. Using light of wavelengths 1.06, 0.53, and 0.35 μm, these experiments further confirmed our predictions of excellent laser–plasma coupling and reduction in hot electron production at short wavelengths. Novette experiments were planned for further tests of the coupling of intense laser light with larger-scale-length underdense plasmas. These high-density and plasma-scaling Novette experiments are a precursor to Nova scaling experiments in which we plan to implode scaled-down versions of our reactor targets to the same fuel densities as in the reactor-scale target designs.

A number of improvements were made to LASNEX. These include improved treatment of the transport of suprathermal electrons and x rays. In addition, our studies of ion-beam-driven targets have provided a clear outline of the parameter space for effective driving of ion-beam-reactor targets.

Target Fabrication. The target fabrication program continued to provide a wide variety of targets for the on-going Argus experimental series using 2ω and 3ω light, as well as a vigorous Shiva program designed to understand both suprathermal electron production and target-coupling effects. In addition to the ongoing experimental program, a great deal of effort is being expended on target developments for future activities. These activities are centered on producing targets capable of attaining highly compressed D–T fuel conditions on Novette, typically 200–400×, and 500–1000× on Nova. In addition, metal shells for the inner shell of a direct-drive two-shell target were developed. Finally, to diagnose final fuel conditions, tracer gases and tracer layers are desired in the fuel to permit the use of x-ray spectroscopic and radiochemistry techniques.

As a result of these new requirements, we began concentrating our advanced research on metal shell formation, on hole-drilling techniques using an ion drill developed by Hughes Research Laboratories that can drill 1-μm holes through more than 10 μm of material, and on radiographic measurements of opaque shells.

Fusion Experiments and Diagnostics. The Fusion Experiments program completed experiments on the harmonically converted Argus laser; a wide variety of target types were irradiated. Studies of absorption, energy transport, suprathermal electron production, and stimulated scattering processes at the 40- to 200-J level were completed. They supported completely our predictions

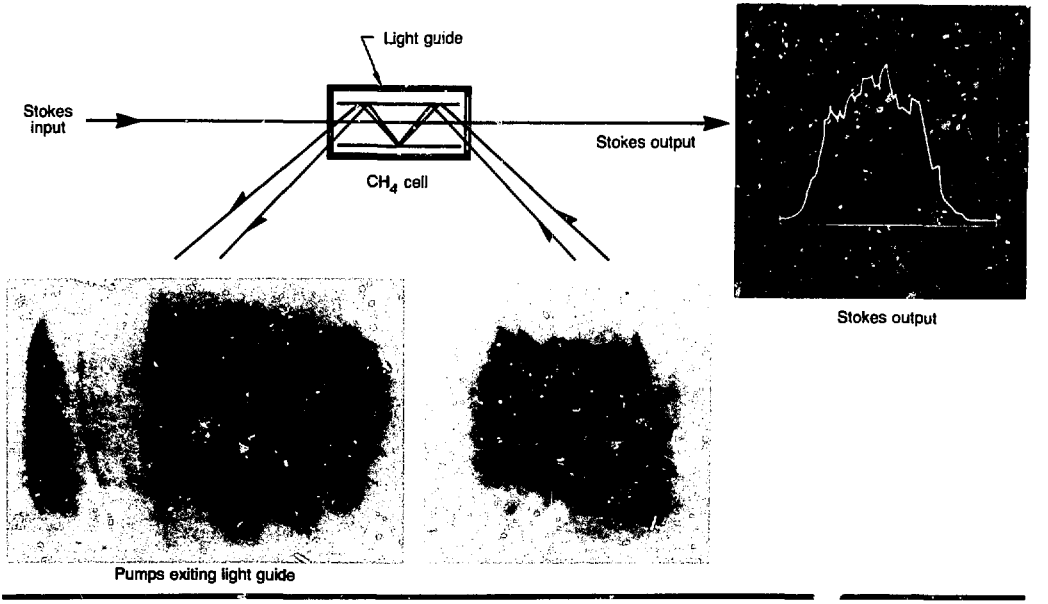

Fig. 1-3. Backward-wave Raman scattering in methane.

at the 40- to 200-J level were completed. They supported completely our predictions on the benefits of using submicrometer laser wavelengths in laser–plasma interaction. Figure 1-4 illustrates these results; for completeness, we show data from LLNL, l'Ecole Polytechnique, the University of Rochester, the Naval Research Laboratory, and Rutherford Laboratory.

Using the Shiva laser, we essentially finished our studies at the 10-kJ level using 1-μm light. These studies included the design of targets with acceptable levels of preheat. They also included x-ray backlighting techniques, which we used for accurate measurement of the coupling of laser light to spherical and planar targets. This technique enables us to measure the energy and power-transfer efficiency of the light-to-fuel-capsule process. To more completely understand the light-to-plasma-coupling process, we developed a sophisticated x-ray/optical-streak-camera diagnostic that has enabled us to measure the relationship between the onset of stimulated light scattering and the production of hot electrons. This work culminated an extremely successful and productive four years of experimentation on Shiva.

Energy and Military Applications. The first realized benefit of ICF research will lie in the military applications area, in particular with accurate physics measurements. The versatility of our Nd:glass research lasers regarding pulse duration and pulse shaping, harmonic-conversion capability, and independent beam targeting was demonstrated this year. The x-ray backlighting techniques demonstrated a technique for fluid-instability measurements and for shock-wave measurements. The ability to focus several beams on a common spot has provided us with a technique to obtain uniform drive for equation-of-state measurements. By shifting the laser wavelength, we can now control the level of target preheat for accurate materials studies. We began experiments, using several of the above techniques, by obtaining accurate non-LTE (local thermodynamic equilibrium) spectral measurements on the Shiva laser.

The ultimate benefit of ICF is the attainment of high-gain target performance. The output from these targets is potentially useful for nuclear-effects simulation; with efficient drivers and an automatic target factory, commercial ICF may be possible.

In the area of reactor design, we completed several studies on our liquid lithium wall HYLIFE (high-yield, lithium-injection, fusion energy) reactor concept. The most interesting results of these studies showed

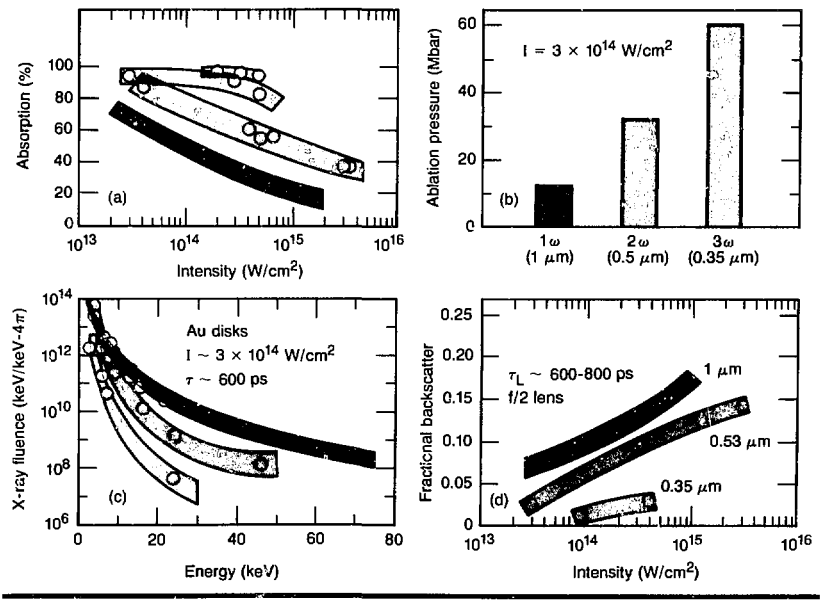

Fig. 1-4. A summary of work conducted with the harmonics of the Nd:glass laser.

withstand 30 years of pulsed operation without fatigue or radiation damage to the walls, and has a residual radioactivity, biological hazard potential, and thermal decay power that are all 10× lower than present fission reactors or planned fusion reactors. This reactor design provides us with an attractive baseline concept for ICF. To improve this design, we have investigated a wide range of other systems that are consistent with the ICF concept. They include higher-repetition-rate concepts, a higher-temperature concept, and a specialized hydrogen production system.

Authors: J. F. Holzrichter

Laser Isotope Separation

During 1981, process designs for the application of laser isotope separation (LIS) to uranium and plutonium enrichment were completed. In lieu of contributions of this *Annual Report* (as well as the counterpart classified LIS *Annual Report* produced in past years), documents describing the plant design, development module design, science and technology base, and program plan for LIS deployment for uranium enrichment were presented to the USDOE Process Evaluation Board (PEB). This thorough documentation is published in many classified volumes, under separate covers.

In early 1982, the PEB recommended the selection of our Atomic Vapor LIS (AVLIS) process for large-scale engineering development and demonstration over Los Alamos National Laboratory's Molecular LIS process and TRW's (Redondo Beach, Calif.) Plasma Separation process. A similar competition and selection among these three processes is anticipated later in 1982 for plutonium enrichment. Our analysis shows that—based on its state of development and economic potential—the AVLIS process is again more attractive than the competing processes. We are looking forward to the process selection.

The Special Isotope Separation Laboratory (SISL) and office complex (Building 482) are being built to support the LIS Program by providing the facilities for production-systems performance tests, component engineering, and long-term technology advances. The facility will include 85 000 ft^2 (7900 m^2) of laboratory space and additional office space for 175 people. This $25 million line-item project is currently proceeding within budget on an accelerated schedule toward laboratory occupancy in the second quarter of FY83.

Author: J. I. Davis

Lead Laboratory Program for 1.06-μm and Shorter-Wavelength Experiments

A Lead Laboratory Program was formalized in 1979 to coordinate the activities of participants involved in laser fusion with 1.06-μm and shorter wavelengths. LLNL has responsibility for technical oversight of the Program. Major contractors participating in the pursuit of National ICF goals and milestones are KMS Fusion, Inc. (KMSF), the University of Rochester's Laboratory for Laser Energetics (UR/LLE), and the Naval Research Laboratory (NRL). Additional funds and technical direction are also provided to specific efforts in both university and industrial research laboratories. The technical and fiscal organization, as well as the operating mode of the Lead Laboratory Program, were described in our *1980 Laser Program Annual Report.*

The objectives of the supporting programs, both at the major support laboratories and those activities of universities and industry also funded through the lead laboratory program, are to supplement the effort at LLNL in areas of critical importance, and to complement the efforts at LLNL by pursuing promising alternate approaches. Table 1-1 summarizes the Glass Laser Experiments Lead Laboratory Program supported university and industrial research contracts in place in 1981. Each support laboratory continues to have an identified technical area of concentration.

KMS Fusion

The KMSF program emphasizes both target fabrication technology and laser-target

interaction physics for both classified and unclassified portions of the program. KMS Fusion continued to support the National ICF Program by fabricating targets for use by the major program participants. Some of the polymeric and glass shells of various compositions reflect an extension of capabilities in areas such as shell dimensions and hydrogen permeation. Work on planar lithium foils for NRL experiments required acquiring expertise in processing and handling highly reactive lithium in order to maintain its purity.

Several types of hohlraum targets were fabricated in support of the KMSF classified target experiments program. The remaining unclassified work centered on producing planar targets of low density, low average-atomic-number foams. Fibrous foam targets with $\rho \sim 0.02$ g/cm^3 and mean fiber separations ~ 1 μm were produced. In addition multi-layered diagnostic targets for thermal and suprathermal transport experiments were also fabricated. Significant advances were made in obtaining uniform, smooth polymer and aluminum coatings on glass sphere targets.

The KMSF Chroma I laser, which produces up to 2 TW at 100 ps, with two 20-cm-diam beams, provides a capability of operating at 1.05, 0.53, and 0.35 μm. During 1981, KMSF engaged in four ICF target-irradiation campaigns:

- Long-scalelength, low-density gas-jet experiments,
- High-Z disk laser-plasma interaction experiments,
- Hohlraum experiments dedicated to investigating physics issues of indirect drive.
- The first phase of a direct-drive, uniform-illumination, cryogenic implosion experiment.

Gas-jet experiments were conducted during the spring of 1981 to study laser-plasma interactions in long-scalelength, underdense plasmas. Because of the long axial scale lengths, gas jet plasmas provide an interesting facility to study reactor-like laser-plasma interactions, which can be well characterized by interferometric techniques. Early results indicate that the dominant coupling mechanisms are inverse bremsstrahlung and stimulated Brillouin scattering (SBS).

High-Z disk experiments were performed at 1.05 and 0.53 μm to compare with similar spherical experiments performed earlier at KMSF, wherein CH-, Al- and Au-coated glass microspheres were irradiated at intensities from 1 to 5×10^{15} W/cm^2, and with high-Z disk experiments performed at LLNL. The series emphasized the study of nonlinear laser-plasma interaction effects by employing space and time-resolved optical diagnostics, and plasma profiles as determined by holographic interferometry. When a high-intensity focal region was created ahead of the disk target, stimulated Raman scattering was observed at a level consistent with the existence of low-density plasma conditions in the focal region. Time-resolved measurements of the 2ω emission show that if plasma generated at the disk surface participates in the emission

Table 1-1. 1981 university and industrial research supported by the ICF glass laser experiments lead laboratory program.

Institution	Principal *Investigator*	*Topic*
UC/San Diego	K. Brueckner	Heavy ion transport effects
U. Washington	A. Pietrzyk	Stimulated optical scattering experiments
NRL	J. Boris	Implosion stability physics
UCLA	F. Chen	Laser interactions with plasma small-scale turbulence
Westinghouse	E. Sucov	Dry-wall ICF reactors
MPB	M. Bachynski	Hot-electron transport theory
U. Arizona	R. Morse	Implosion dynamics and stability theory
U. Hawaii	B. Henke	X-ray measurements, reference laboratory
Math. Sci. NW	R. Crawford	Opacity measurements
U. Florida	C. Hooper	Evaluation of opacity effects in ICF experiments
UCLA	A. Wong	Two-dimensional, stimulated scattering experiments

occurring at the focal spot, it must be traveling at a velocity greater than 10^8 cm/s.

University of Rochester/Laboratory for Laser Energetics

The experimental and theoretical/calculational program at Rochester emphasizes studying the feasibility of the multibeam, short-wavelength (0.35 μm), direct-illumination approach to ICF. The two major facilities used for these studies are the symmetric 24-beam, 1.06-μm Omega laser, and the single-beam, frequency-tripled (0.35 μm) GDL laser.

Some of the major results obtained from experiments using the GDL 0.35-μm laser system on disk targets include

- Absorption measurements in the intensity regime of 10^{13} to 1.5×10^{15} W/cm^2 showed that inverse bremsstrahlung was the primary absorption mechanism. Absorption in excess of 70% at 10^{15} W/cm^2 was measured with high-Z targets.
- Energy-transport measurements using layered targets showed an enhanced ablation rate with 0.35-μm radiation, compared to longer-wavelength experiments.
- Preheat measurements showed considerably reduced fast electron induced preheat with 0.35-μm radiation, compared to longer-wavelength irradiation.
- Ablation-pressure measurements yielded results in the 80-Mbar range at an on-target intensity of 10^{15} W/cm^2.

The full Omega laser system was activated as a 1.06-μm target-irradiation facility. The following summarizes some of the achievements using this facility

- Operation of a 24-beam system, with all beams accurately pointed, focused, and syncronized, was demonstrated.
- In an initial experimental program performed with 100-ps pulses at power levels up to 7 TW, and simple D–T glass microballoon targets operating in the exploding-pusher mode, neutron yields of 1.3×10^{10} were obtained.
- The characteristics of the passive and active elements in the Omega beamline were measured to determine the near and equivalent plane intensity and phase distributions through the systems, and to use these data to normalize appropriate propagation codes. With 100-ps pulses and 200 GW/beam, a maximum peak-to-valley intensity variance was measured in the near field of ~20% and in the equivalent target plane of ~50%.
- A set of target experiments was performed using 700 ps pulses with 12 and 24 beams on spherical targets of nominal 400-μm diameter. Absorption values ranged from 70% at 10^{14} W/cm^2 for Ti spheres, to ~25% at 10^{15} W/cm^2 for CH spheres.
- The dependence of shell convergence symmetry on irradiation uniformity was investigated using 700-ps pulses in the low 10^{14} W/cm^2 range, irradiating 400-μm-diam targets having aspect ratios as high as 200. Preliminary results indicate these targets are sensitive to large-scalelength irradiation nonuniformities.
- Theoretical investigations were conducted of the optimal Omega focusing strategy for beams of realistic radial intensity profile and beam-to-beam energy imbalance. The calculated nonuniformity of irradiation was found to be approximately 6% for focal distances of +6R.
- Extensive numerical simulations of the nonlinear evolution of ablation-driven Rayleigh–Taylor instability were performed.

In addition, the UR/LLE facilities continue to be available for a wide variety of experiments proposed and conducted by outside users under the DOE-sponsored National Laser Users Facility (NLUF) Program.

Naval Research Laboratory

The program at NRL emphasizes the identification and elucidation of critical physics issues affecting the direct-laser-driven approach to high-gain ICF. NRL is conducting a program, which it initiated in 1978, to use long-pulse, low-intensity, near-infrared laser pulses (1 μm) to ablatively accelerate targets to as near ICF reactor conditions as possible, and to critically examine the physics requirements that most impact a high-gain pellet.

The output from the Pharos II Nd-Laser (500 J, 3 ns, 1.05 μm) is used to accelerate flat millimeter-diameter disk targets. The intensity uniformity across the millimeter focal spot is uniform to better than ±35%. Time-synchronized 200- to 500-ps laser

pulses are available for optical and x-ray diagnostics.

During 1981, considerable progress was made in the understanding of ablative acceleration of targets in the 10^{13} W/cm^2 regime. Some highlights of the 1981 program include

- Cold target velocities of 160 km/s were attained with: hydrodynamic efficiency $\simeq$15%; rear-surface temperatures of 7 eV; an ablation pressure of 5 Mbar; and target uniformity $\delta v/v = \pm 7\%$.
- The properties and structure of the high density portion of the accelerated targets were measured using the double-target method and x-ray backlighting.
- Illumination uniformity scaling was developed as a function of irradiance and perturbation wavelength. "Cloudy day" effect smoothing was observed.
- Structured targets have been used to begin experiments on Rayleigh–Taylor, Kelvin–Helmholtz, and associated hydrodynamic instabilities.
- A joint NRL–LLNL experiment at Shiva to extend some of the NRL results into the 10^{14} W/cm^2 range was planned and conducted.
- A tracer-dot diagnostic technique was invented and used to measure the ablated-plasma-flow properties.
- A study of the benefits of phase conjugation to improve pellet illumination uniformity was made. With 24 beams, a $\pm 2\%$ uniformity could be attained using phase conjunction.
- Wavelength-irradiance scaling of $I^{0.7}\lambda^{2.7}$ for symmetrization was found computationally and theoretically.

Author: L. W. Coleman

Program Resources

For FY81, resources in the Laser Program totaled $87.2 million in operating funds, $13.3 million in equipment funds, and $35.7 million for construction projects. Total internal program manpower, including the Nova construction project, was 642 employees. Table 1-2 and Fig. 1-5 show the history of funding and manpower for the last 10 years for the Laser Fusion and Laser Isotope Separation Programs.

Laser Fusion Program

Operating funds of $57.5 million represented a 10% increase in buying power over FY80. The start of the Novette project and other high-procurement-oriented activities resulted in a manpower reduction from last year. This reflects the Program's commitment to high industrial and academic participation in program activities. Procurement of Novette-related hardware, operating spares for Nova, and Nova prototypes resulted in higher proportional costs for the Glass Laser Development element of the program, compared with FY80. The distribution of costs by program element is shown in Table 1-3.

The Nova project was appropriated $25 million, bringing the total thus far to $104 million of the authorized $195 million. Construction of the office and laboratory building neared completion, and orders for laser components and materials were placed.

An additional $5.5 million was appropriated for the Fusion Target Development Facility, allowing building construction (due

Table 1-2. Resources of Laser Fusion and LIS programs for FY81 in comparison with those of prior years.

	Fiscal year										
	1972	1973	1974	1975	1976	1976T[a]	1977	1978	1979	1980	1981
Operating costs ($ million)											
Laser Fusion	9.5	13.5	18.4	19.9	22.2	7.0	30.8	40.4	40.6	48.0	57.5
Laser Isotope Separation	—	—	0.74	4.8	7.2	2.1	8.1	10.9	14.2	17.9	29.7
Manpower											
Laser Fusion	156	232	223	230	244	259	281	355	355	362	354
Laser Isotope Separation	—	—	23	70	90	92	94	116	131	151	190
Equipment ($ million)											
Laser Fusion	0.9	1.1	1.17	2.0	2.4	0.5	2.8	3.6	3.1	2.8	4.7
Laser Isotope Seperation	—	—	0.13	0.7	1.5	0.3	2.4	1.9	2.2	2.1	8.6

[a]Transition quarter.

for completion in early 1982) and procurement of components for the special facilities.

Equipment funding of $4.7 million represented a needed increase over previous years, allowing the procurement of necessary instruments and analytical tools required for advances in diagnostics, target fabrication, and laser research and development.

Laser Isotope Separation

In FY81, the operating budget for the Laser Isotope Separation Programs was $29.7 million, the equipment budget was $8.6 million, and the General Plant Projects (GPP) budget was $1.35 million. The manpower numbers reflect all LLNL personnel in direct support of the programs: scientific, technical, nontechnical, clerical, and craft. In addition to this in-house LLNL manpower, we use non-LLNL contract personnel for support of peak-program loads. This effort averaged approximately 50 "heads" for FY81. A breakout of the LIS Programs by FY81 budget category and manpower is given in Table 1-4.

Authors: L. P. Altbaum and J. P. Dow

Table 1-3. Laser fusion program – FY81 costs and manpower by budget category.

Budget category	Manpower	Cost ($ thousand)
Nd:glass laser development	46	11 402
New laser development	28	3 864
Fusion theory and experiments	268	40 503
Energy and military applications	10	1 584
Heavy-ion source development	2	172
	354	57 525

Budget category	Manpower	Cost ($ thousand)
Atomic-vapor process—uranium isotope separation	133	18 635
Atomic-vapor process—plutonium isotope separation	48	10 155
Deuterium ionic isotope separation	1	100
Plutonium gas centrifuge	4	540
Advanced lithium recovery	4	300
	190	29 730

Table 1-4. Laser Isotope Separation programs – FY81 operating costs and manpower by budget category.

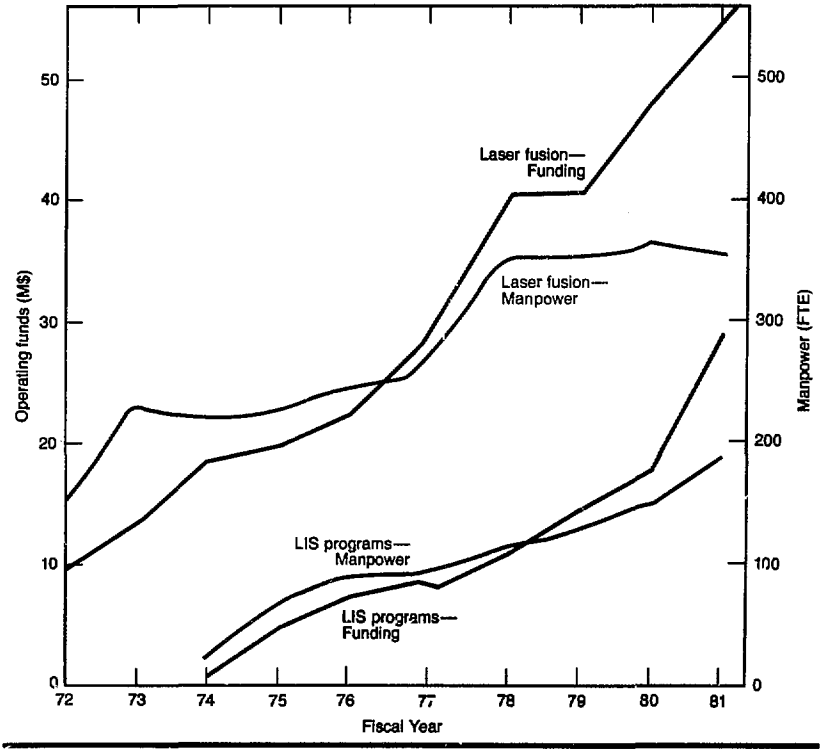

Fig. 1-5. Ten-year history of Laser Program operating funds and manpower.

Program Facilities

Introduction

Throughout the past year, the Laser Program has continued to experience significant growth. We have made important progress toward housing all of our people and experiments in permanent facilities, and we are now at work providing the program with an internal communication system. We have completed, or brought to near completion, several new office and laboratory buildings. Significant progress has been made toward the completion of the Nova Project, and the preparation for Novette has begun. Modification and modernization of many existing facilities have been carried out, and the initial planning and design for additional new facilities has been accomplished (see Fig. 1-6).

Major construction efforts for the ICF program centered on construction of the Fusion Target Development Facility, the dismantling of the Argus experiment for the start of Novette construction, and the start of work on a Program-wide information network.

Table 1-5 summarizes the comparative space distribution for the program for 1980 and 1981. The current total of 411 057 ft^2 represents an increase of 12.0% from 1980 and indicates the continuing expansion of office and laboratory space requirements.

Laser Fusion

Nova Office Building and Nova Laboratory. Building construction and physical progress continued throughout 1981 on both the 59 000-ft^2 Nova office building and the 115 000-ft^2 Nova laboratory addition. Completion of both facilities is expected in early 1982.

Novette. The completion of initial planning and the removal of the Argus experiment from the Building 381 high bay will allow for the upcoming assembly and installation of Novette in 1982. All facility modifications were accomplished within the initial cost and schedule guidelines.

Fusion Target Development Facility (FTDF). Construction of the building was

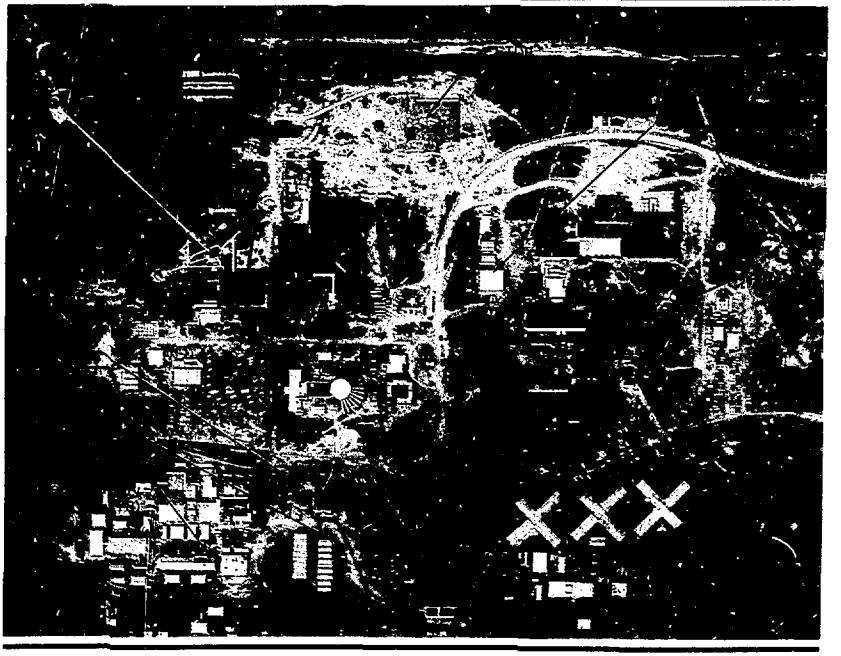

Fig. 1-6. Overall laser program locating new facilities.

90% complete in 1981, despite inclement weather and other delays. The new 47 500-ft^2 facility (shown in Fig. 1-7) will be ready for occupancy and activation in early 1982. Preparations are under way for this move, and activation should be done by April 1982.

FTDF is being constructed to meet the present and anticipated future needs of the ICF program. Since its earliest development, the Laser Target Fabrication effort has been scattered throughout the program in various laboratories and temporary trailers. This has produced cramped, often inadequate working conditions. The new FTDF building will provide the central laboratory capability necessary to fabricate the complex targets required for achieving major program milestones.

Construction on the entire $7.6 million line-item project, which began in December of 1980 and includes both conventional and special facilities, is scheduled to be completed by February 1982. One of the many noteworthy aspects of the project is the decision to employ the "design-construct" method for engineering and construction.

In recent years "design-construct" has become the predominant building technique for industrial interests in the San Francisco Bay Area. Most of the newer construction in the region of Santa Clara County popularly called "Silicon Valley" was accomplished using this the approach. Early in the planning phase for FTDF, several comparable facilities at a number of companies were visited and evaluated. Those major facilities, similar in design and application to structures at LLNL, have been completed in less than one-half the normal time and for less than 60% of the cost for previous methods.

The "design-construct" approach represents a major departure from building methods previously employed at LLNL. Past practice had always been to develop the criteria for building use and application, hire an architect/engineer (AE) firm to design the building, solicit construction bids, and award a contract based on detailed plans and specifications.

By contrast, in the "design-construct" approach, a single contractor is hired to design and build the facility, using only standardized methods of construction. These standardized methods are derived from a set of "performance specifications" established by LLNL. Matching the performance specifications with the applicable standardized construction method allows the contractor to determine a fixed-price bid. FTDF represents the first major project of its kind at LLNL and within the Department of Energy.

Laser Machine Shop. An important event in the progress of the Program's

Table 1-5. Laser program space distribution for 1980 and 1981.

Building space (ft^2)	1980	1981	% Change
Permanent Offices	50 930	50 930	0
Owned Office Trailers	74 007	74 007	0
Rental Office Trailers	11 329	28 365	150.4
Permanent Laboratories	191 956	207 806	8.3
Technician Support Areas	38 929	49 949	28.3
TOTAL	367 151	411 057	11.96

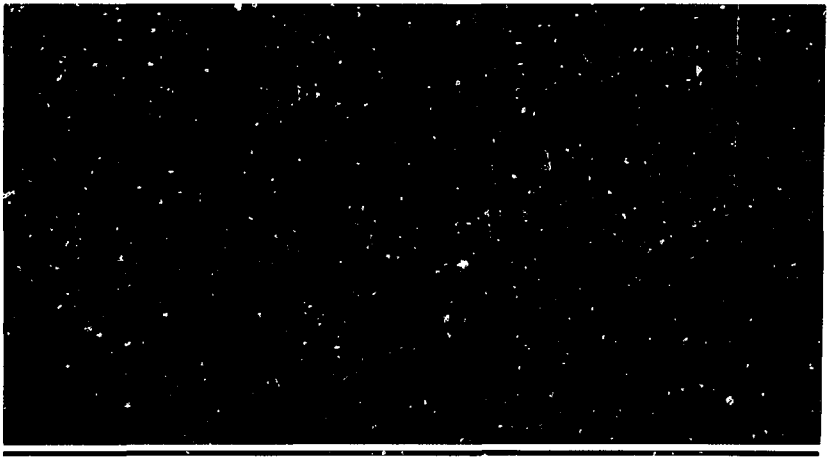

Fig. 1-7. Fusion target development facility (FTDF).

facility plans was the construction and activation of the 6700-ft^2 Laser Machine Shop. Relocation of the Machine Shop from the Building 381 basement was a vital first step for the installation of the Novette experiment. The new shop was finished on time and provides space for future growth.

Fusion Experiments Analysis Facility. The first phases of construction for the Fusion Experiments Analysis Facility (FEAF) began in September 1981. This 2500-ft^2 addition to Building 381 will contain the computer equipment for data analysis of Novette and Nova experimental results. The facility will be completed in mid 1982.

Building 381 Interior Upgrade. Planning and design work continued during 1981 on the interior upgrade of Building 381, the Laser Fusion Office Building. Work will include the optimization of office space, the determination of equipment locations, the establishment of conference room requirements, and the development of total upgrading needs.

LIDNET. As the Laser Program has continued to grow, the timely dissemination of information to program people has become increasingly more difficult. To help solve this problem, we are currently installing an internal communications system which will allow the real-time distribution of general information throughout the program.

Following an encouraging conceptual study, plans are now being implemented to provide a system called LIDNET (the Laser *I*nformation *D*istribution *NET*work), which will initially consist of about 18 color-television monitors strategically located around the Laser Program. These receivers will be interconnected to form a small closed-circuit television network. The system operator and central elements of LIDNET will be located in the new Fusion Experiments Analysis Facility.

The use of different television channels will allow us to place information on various channels for easy and quick access. The Lab's in-house channels will carry lecture broadcasts and educational materials. Laser Program information will include items such as meeting room availability, meeting announcements, the availability of new publications, as well as general information. Eventually, channels will allow program scientists to monitor experiment status in real time. The final system will significantly improve the flow of information within the Program.

Laser Isotope Separation

Beam Line-of-Sight Pipeline (LOS). The 2600-ft-long LOS pipeline was completed for the LIS program in October 1981 on schedule and well within our budget. This 20-in.-diam pipe was installed in two straight sections between Buildings 175 and 272 and Buildings 272 and 332 to provide a vacuum line-of-sight for experiments in the various facilities. The installation alignment variation was within ±1 in. for each

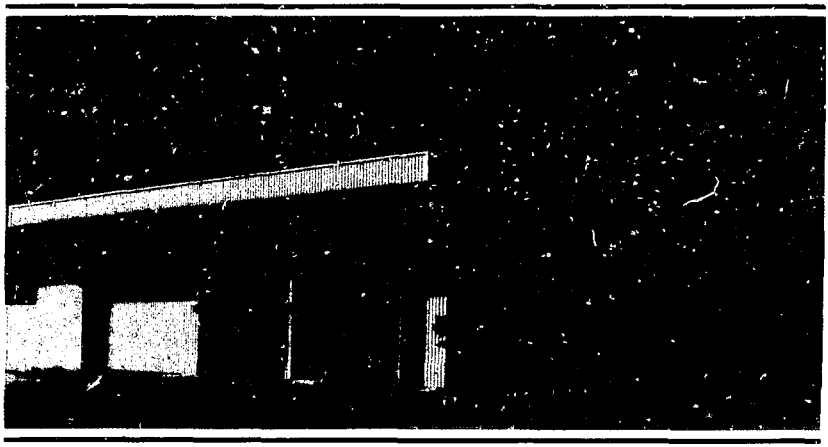

Fig. 1-8. Laser electro-optical facility (LEO-Building 272).

section. The vacuum integrity was verified at 20 μTorr. Project activation is under way.

Isotope Separation Collector Facility. The Isotope Separation Collector Facility, which provides 8000 ft^2 of highly versatile laboratory-quality floor space, was bid using the "design-construct" concept. The building shell was constructed by an outside contractor, while the interior was being designed in house. Installation of the interior, including ceilings, walls, lights, etc., was done by the LLNL craft labor contractor. Through this approach, we were able to award the contract in February 1981 and complete the facility in October. This facility completes the major development in the 170 block and is an integral portion of the Building 175–177 complex.

Laser Electro-Optical Facility (LEO). The 7850-ft^2 LEO building (shown in Fig. 1-8) provides permanent light laboratory space for high-power laser experiments in the laser isotope separation (LIS) program. Working in conjunction with the LOS pipeline, the new laser systems can be used with the existing Mars experiment, experiments in Building 332, and eventually within the new collector facility. Construction began in April and was completed in early November 1981.

Special Isotope Separation Laboratory. Construction began on the new Special Isotope Separation Laboratory (SISL) late in 1981. The $25 million project includes 60 000 ft^2 of office space and 85 000 ft^2 of laboratory to support the technology development effort of the LIS Program. Congressional appropriation of $14 million permits construction to continue in FY82 with project completion in 1983.

Long-Range Facilities Planning

The continued need for a long-range development plan for the Laser Program has resulted in the creation of formal documents to direct and detail the requirements of facilities planning. The successful completion of this effort was a major accomplishment of the Facilities Group during the past year. These plans will act as the fundamental criteria for subsequent development of program facilities.

Author: R. A. McCardle

Major Contributors: M. L. Atkinson, R. L. Hanks, S. Hisola, R. A. Jones, R. P. Rufer, J. M. Replogle, and J. F. Wengert

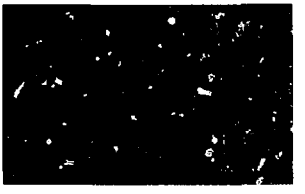

Solid-State Laser Systems
Section 2

Solid-State Laser Systems

Contents

Section Editor: E. Bliss

Solid-State Laser Systems

Introduction

R. O. Godwin

The major events of 1981 in the solid-state laser program are summarized in the following paragraphs. In the articles that follow, we give expanded descriptions of progress in the design and construction of our new laser systems, Novette and Nova. Activities during 1981 on the operating solid-state laser systems are covered in Section 6.

Argus. After five years of very successful experimentation, the Argus system was shut down in August to prepare its building for installation of the Novette laser system. Transforming Argus from an operating experimental facility to a completely empty laser bay was completed in only two weeks. During its last months of operation, Argus was used for several physics and engineering experiments related to frequency conversion, for a series of wavelength-scaling target experiments, and, finally, for high-power 2ω (frequency-doubled) target experiments. These activities are described in Section 6.

Shiva. During 1981, we employed the Shiva laser system to conduct fusion-target experiments for the LLNL Weapons Program, for the Laser Program, and for the Naval Research Laboratory (as described in Section 6). In the fall, 2 of the 20 Shiva beamlines were partially removed to free their hardware for use in the Novette laser system. The entire Shiva laser was finally shut down on December 23 to prepare for construction of the Nova laser system. Shiva had an operating lifetime of slightly more than four years.

Nova and Novette. Design and construction of the Nova laser system continued during the year. Meanwhile, because of uncertainties in the funding rate and scope of the Nova project, we directed a major effort toward designing and procuring the hardware necessary to demonstrate the first two beams of the Nova laser system in the form of the Novette laser. The firm objective of operating two Nova laser beams as Novette gave the Nova project group strong motivation to accomplish specific goals while the issue of Nova's funding rate and project scope was being resolved by the Department of Energy.

Shortly before midyear, the Laser Fusion Program was reorganized in preparation for the transition from Argus and Shiva to Novette and Nova. Since this change spelled a major shift in Laser Program priorities and facilities management, we decided to combine under common management the operation of Argus and Shiva and the task of designing and constructing Novette and Nova. The newly formed organization is called the Laser Systems and Operations Group, which consists of three functional groups: the systems operations group, the Nova project group, and the Novette project group.

Formation of the Laser Systems and Operations Group minimized the difficulty of scheduling and coordinating activities between the operating lasers and the newly constructed systems. For example, when the Argus laser system was shut down and removed in preparation for installation of Novette, the Argus personnel were easily transferred to either the Shiva operations team or the Nova project group. Similarly, when Shiva was shut down, its personnel were transferred to either the Novette or the Nova project group to provide required manpower.

The Novette project group, which will assemble and activate the laser, currently consists of a project office with matrix support from the Nova project group. When Novette becomes operational in late 1982, a Novette operations

group will be formed to operate and maintain the Novette laser system. Integrated management of laser activities is helping us make better use of both Laboratory and contract personnel.

Novette

Introduction

Even a cursory review of the inertial-confinement fusion (ICF) literature of three years ago reveals that opinion was divided concerning the wavelength at which lasers would best drive an ICF target.[1-3] Early simulations suggested that short-wavelength laser light ($\lambda < 1.0$ μm) would couple to target plasmas more efficiently than longer wavelengths ($\lambda > 1.0$ μm). Shorter-wavelength heating of higher electron-plasma densities would, it was thought, lead to laser-plasma interactions that were freer of "anomalous" absorption processes.[2,3] Meanwhile the Nova laser project, authorized by Congress to reach ICF ignition conditions, was well under way.[4,5]

It has now been established, through much small-scale experimental work at LLNL and other laboratories, that the above hypotheses concerning laser-plasma interaction at shorter wavelengths are substantially correct.[6-8] Data from these experiments made harmonic conversion of Nova highly attractive to target designers; it hardly seemed prudent to extrapolate 30-J Argus laser experiments to systems designed for operation at several hundred kilojoules. With this realization, experimenters and laser designers reviewed many alternatives for multikilojoule, short-wavelength laser–target interaction facilities.

Not surprisingly, the carefully cost-optimized Nova laser chain was the least expensive option analyzed. The Novette laser system, first reported in the *1980 Laser Program Annual Report*, is composed of Argus and Shiva parts, a special frame, and borrowed large-aperture Nova amplifiers[5]; Novette's construction costs have been significantly reduced by taking advantage of early Nova component deliveries. Figure 2-1 is an artist's rendering of Novette viewed from the southwest.

The Novette project has a number of missions. The first activity is testing the laser-design concepts that are critical to Nova. Our simulations of the pulsed gain, insertion losses, cumulative aberrations, and nonlinear propagation effects that dominate glass laser design will all be verified or improved with Novette experience. We will also be able to cope with operations issues, such as system maintenance, alignment, and target focusing, well before we must deal with these problems on Nova. This

Fig. 2-1. Novette viewed from the southwest.

opportunity alone may pay for the Novette project, but there are many other Novette missions of even greater importance. For example, Novette will advance laser-system engineering by providing a test bed for pulse shaping, which is considered essential for Nova ignition targets. Novette is also likely to be the first LLNL facility to irradiate cryogenic targets.

Roughly one-half of Novette's target-experiment time will be devoted to high-density implosion studies to support Nova target design. Another one quarter of the target-irradiation effort will go into scaling studies that, we hope, will make use of multikilojoule, short-wavelength laser light to verify and extend experiments conducted with Argus and Shiva. The final one-quarter of Novette's experimental time will be devoted to studying plasma physics in support of other divisions at LLNL. Novette was planned with these priorities in mind; the following 10 articles describe its state of development at the end of 1981.

Author: K. R. Manes

Novette Status Summary

The Novette laser fusion system, first described in the *1980 Laser Program Annual Report*,[9] is a two-beam irradiation system that will provide an early capability for performing high-power fusion experiments at 0.53 μm. As described last year, the system consists of

- Two Nd:phosphate-glass laser chains made up of parts from Shiva and borrowed parts from Nova.
- Appropriately designed master-oscillator and preamplifier stages.
- Large-aperture potassium dihydrogen phosphate (KDP) arrays for frequency-doubling.
- The Shiva target chamber, modified to accept two large-aperture beams.
- Target-diagnostic systems, consisting mainly of modified Shiva and Argus instruments.

During 1981, we finalized the laser design; nearly completed the detailed design of Novette's unique systems and components; ordered parts; and established a workable schedule for system activation. During the year, we also altered the system to improve performance or to address cost and schedule constraints. Major changes include

- Using a neutral-solution antireflection process[10] on spatial-filter lenses, apodizers, crystal-array windows, and focus lenses to reduce losses and improve damage thresholds.
- Reducing the glass thickness in the final-focusing train by using f/4 doublet focusing lenses, which also function as the diagnostic splitters and target-chamber vacuum windows.
- Moving the 50-mm rod amplifiers from the master oscillator room (MOR) to the preamplifier section on the center spaceframe.
- Locating local particulate filters within the spaceframe to provide a clean environment for intercomponent couplings in the laser chains.

Construction of Novette is well underway. To make room for Novette, the Argus laser was shut down on September 1, 1981; the Argus components were removed and modifications were undertaken. By year's end, workers had begun to install the laser and target spaceframes, the central VAX computer, and the MOR components. At the end of 1981, the Shiva facility was shut down to provide components and manpower for the completion of Novette.

Figure 2-2 shows the present activation schedule, which is designed to realize the first 0.53-μm target experiment by the end of 1982. Critical items in the schedule are the large-aperture, neutral-solution-processed optics; the KDP frequency-conversion arrays; and the large-aperture amplifiers. At present, we believe these items can be obtained in time to keep the proposed schedule.

Laser-System Configuration. The Nd:phosphate-glass amplifier chains[11] for Novette will be built from parts borrowed from the first two chains of Nova. The early assembly of these chains will allow Nova chain performance and beam quality to be assessed before assembly of the full Nova system. Novette will also provide us with an early 2ω target-irradiation capability. Figure 2-3 shows the layout of these chains in the west section of the Building 381 high bay; Fig. 2-4 shows the layout of the chain turning mirrors and diagnostics, the

Fig. 2-2. Activation schedule for Novette; the goal is to fire a 2ω target shot by the end of 1982.

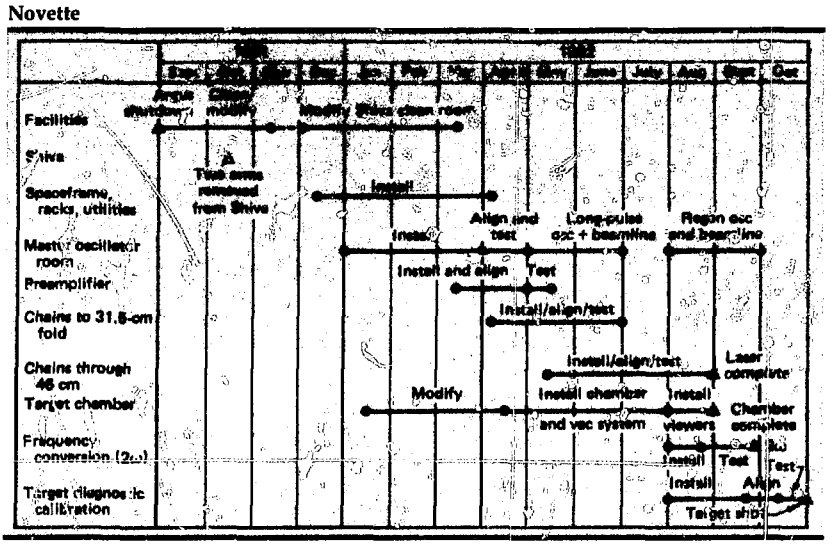

frequency-conversion optics, and the target chamber in the east section of the bay.

During 1981, the neutral-solution leaching process[10] evolved to the point that high-damage-threshold antireflective (AR) surfaces on BK-7 glass could be applied repeatably to large-aperture optics. The neutral-solution process thus became applicable to Novette optics and allowed us to replace the previously uncoated spatial-filter input lenses in our design with lenses having both low loss and a high damage threshold. In addition, there will be an increase in the damage resistance of the spatial-filter output lenses, the 46-cm apodizers, the crystal-array windows, and the target-focusing optics when thin-film AR surfaces are replaced with neutral-solution-processed surfaces.

Table 2-1 lists the optical components in the Novette chain, indicating their important optical properties and surface treatment. Figure 2-5 shows the damage threshold assumed for surfaces in assessing Novette system performance. Our latest experience indicates that the damage threshold of surfaces properly treated with the neutral-solution process equals or exceeds that of bare surfaces.[12]

Chain Performance at 1.05 μm. We have used the MALAPROP and SNOBALL system-simulation codes[13,14] to reexamine energy-output capabilities of the Novette chains, including the properties of neutral-solution-processed AR surfaces. The MALAPROP runs determined the output-energy limitations imposed by the damage threat to surfaces within the laser chain at various pulse lengths. The SNOBALL runs then gave detailed interstage energies and fluences and the nonlinear self-focusing growth (ΔB) accumulated between successive spatial-filter pinholes at the MALAPROP maximum energies. For these runs, we used the conservative amplified gains and other system parameters listed in Table 2-1 and the surface-damage thresholds shown in Fig. 2-5. To obtain conservative performance projections, we have chosen to use the nominal lower-limit amplifier-gain values, rather than the median values used in most Nova calculations. Thin-film AR coatings remain on the Faraday rotator disks, and we included these in the MALAPROP simulations. We increased the transmission level of the spatial-filter input lenses to 0.99 to account for the lower losses resulting from the AR processing.

Figures 2-6 and 2-7 show results of the MALAPROP calculations at 1 and 3 ns, respectively. At 1 ns, damage to the neutral-solution AR surface of the input lens to the 46-to-74-cm spatial filter limits the 1ω output to 8.9 kJ/beam on the target. The corresponding maximum drive energy to the frequency-conversion crystals is 9.4 kJ/beam. At 3 ns, damage to the thin-film AR surface of the 31.5-cm Faraday rotator disk limits the 1ω output to 13.6 kJ/beam on target. The corresponding

maximum drive energy to the KDP crystals is 14.5 kJ/beam.

The results of the SNOBALL calculations, summarized in Table 2-2, confirm that the maximum-energy projections given by MALAPROP are realistic. At 1 ns, the ΔB of 2.9 in the 46-cm stages is below the value of 3.5 thought to be the maximum permissible for satisfactory spatial-filter pinhole transmission.[15]

For pulse lengths between 0.1 and 1 ns, we believe the performance limit is imposed by ΔB instability growth in the 46-cm stages, resulting in a constant power output

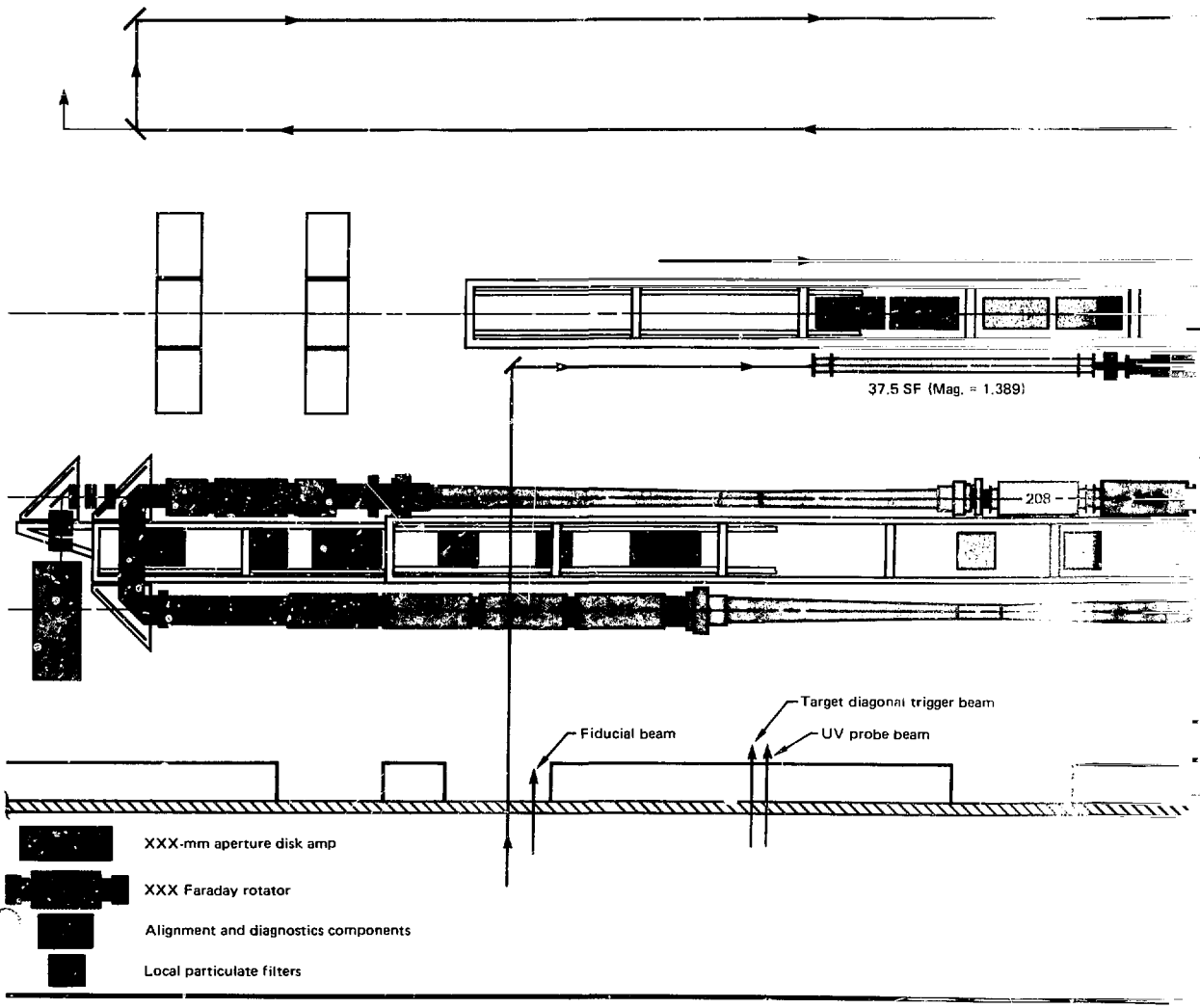

this range of pulse lengths. For pulse lengths between 3 and 5 ns, we have assumed a constant damage threshold, resulting in a constant maximum output energy over the range of pulse lengths. These assumptions, and a linear interpolation between 1 and 3 ns, lead to the 1.05-μm performance curves from 0.1 to 5 ns shown in Fig. 2-8.

Performance at 0.53 μm. The 74-cm-diam, 1.05-μm output from the Novette laser chains will be frequency-doubled in monolithic KDP crystal arrays located between the final turning mirror and the

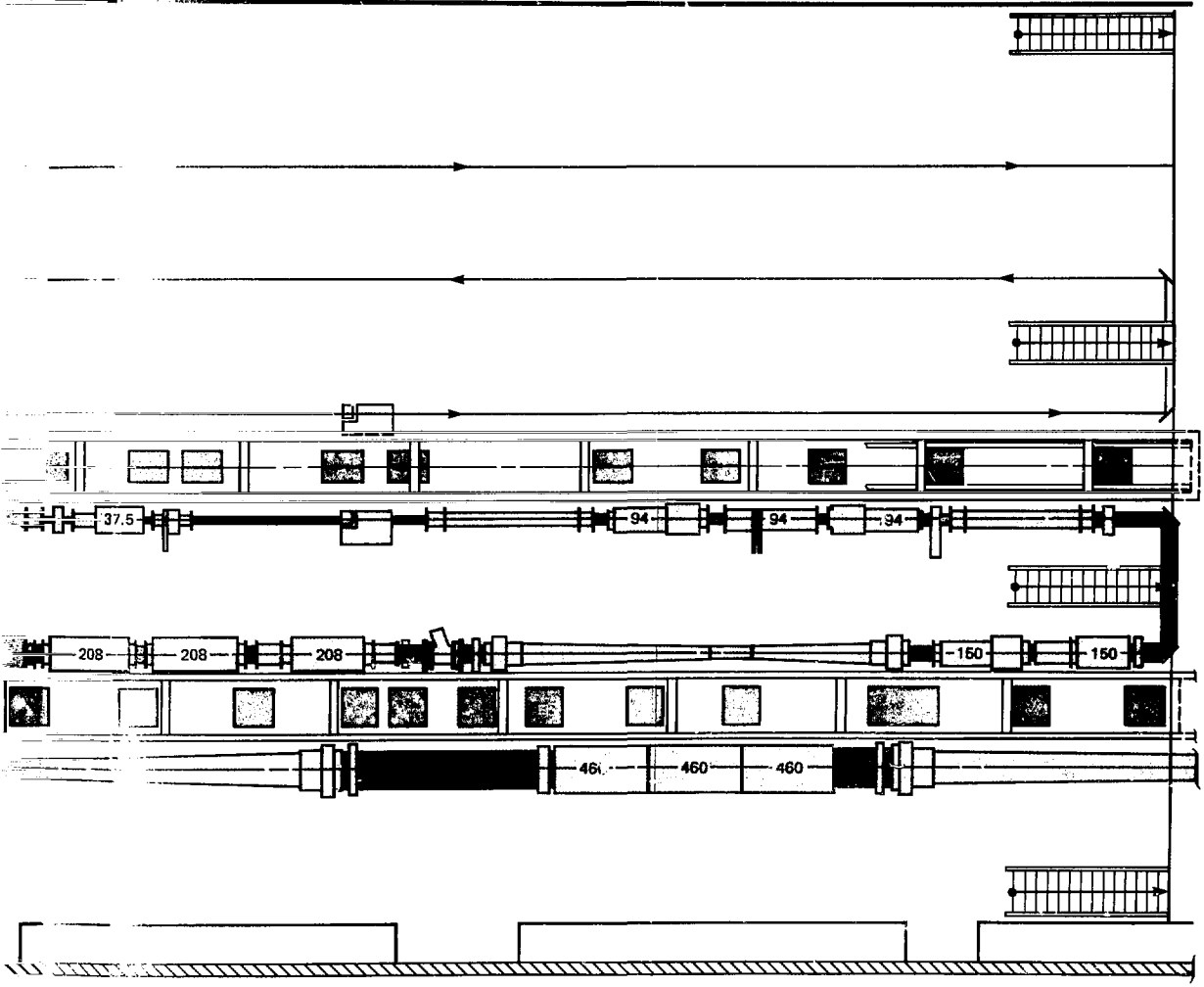

Fig. 2-3. One Novette laser-amplifier chain in the Building 381 high bay.

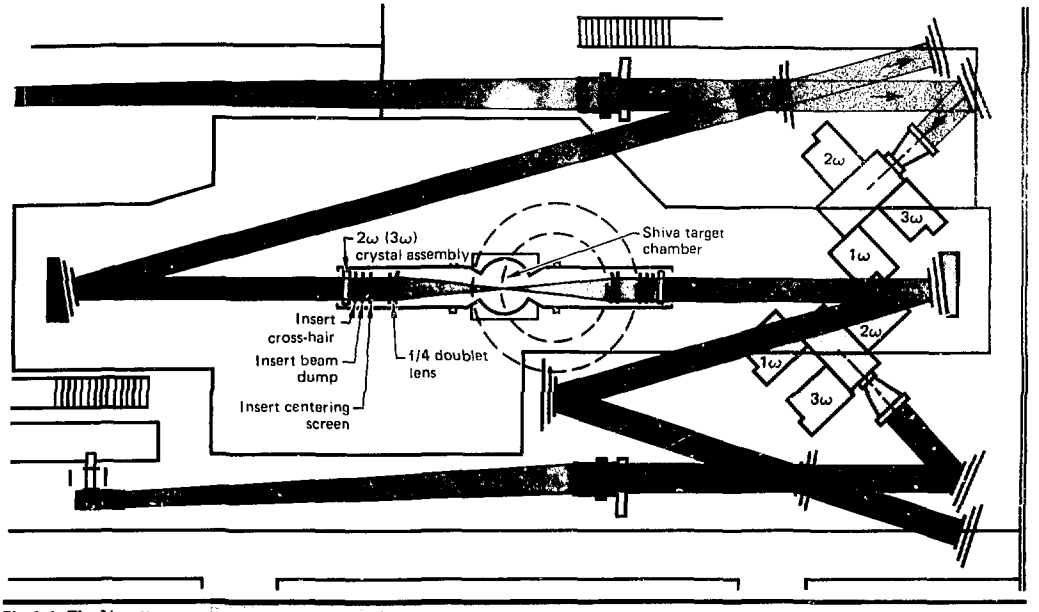

Fig. 2-4. The Novette output-beam transport, frequency-doubling, and target-focusing systems.

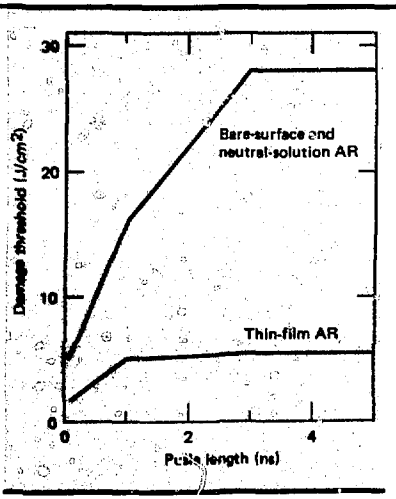

Fig. 2-5. Surface-damage thresholds assumed in assessing Novette amplifier-chain performance.

target-focusing lenses. The individual elements in the array are machined so that their faces are accurately oriented with the phase-matching angle to allow the array to be adjusted for optimum conversion as a single element. The individual KDP crystals are Type II; we chose a thickness of 18 mm to obtain conversion efficiencies greater than 70% for intensities between 0.8 and 5.0 GW/cm^2. Efficient conversion will be possible for pulse lengths up to 5 ns.

Present plans are to build one 5- × 5-crystal array of 15- × 15-cm crystals and one 3- × 3-crystal array of 27- × 27-cm crystals. The first large-aperture crystals will be harvested in mid-1982; however, the yield of good-quality large crystals may be insufficient to produce the 3- × 3-crystal array. If this is the case, and depending on the availability of material, we may build a second 5- × 5-crystal array for the initial activation of Novette. We see no serious obstacle to eventually obtaining large enough boules to build a 74-cm-aperture, 3- × 3-crystal array.

The constraints on 0.53-μm energy available to the target are imposed by

- Amount of 1.06-μm energy available from the laser to drive the crystals.
- The conversion efficiency of the crystal array.
- Nonlinear self-focusing growth in the frequency-conversion and focusing-optics trains.[16]

With the advent of neutral-solution AR surfaces, and with the low average-energy density at the crystal array resulting from expanding the beam to 74 cm, the damage threat to frequency-conversion and focusing optics appears not to be a serious constraint, except in intensity spikes that result from instability growth.

No.	Component description	Beam diameter (cm)	Glass thickness (cm)	No. and angle	Refraction index	Nonlinear index	Small-signal gain	Surface treatment[a]	Propagation distances (cm)
0	Preamp and alignment								
1	Apodizer	2.7	0	1	1	0	0.63	—	0
2	SF input	2.7	0.5	1	1.507	1.24	0.99	TF	5
3	Pinhole								
4	SF output	3.75	0.5	1	1.507	1.24	0.99	TF	523
5	Rod (50 mm)	3.75	40	1	1.523	1.05	20	TF	628
6	Pockels isolator	3.75	11	1	1.5	1	0.87	TF,P	763
7	Splitter	3.75	0.5	1	1.507	1.24	0.97		1 113
8	SF input	3.75	0.5	1	1.507	1.24	0.99	TF	1 233
9	Pinhole								
10	SF output	9.17	1	1	1.507	1.24	0.99	TF	1 528
11	Disk (94 mm)	9.17	2.4	−6	1.523	1.05	6.5	B	1 579
12	Faraday isolator	9.17	4.3	1	1.67	2.1	0.88	TF,P	1 852
13	Disk (94 mm)	9.17	2.4	−6	1.523	1.05	6.5	B	1 971
14	SF input	9.17	1.2	1	1.507	1.24	0.99	NS	2 176
15	Pinhole								
16	SF output	15	1.2	1	1.507	1.24	0.99	NS	2 433
17	Mirror	15	0	1			0.99	HR	2 685
18	Faraday isolator	15	2.5	1	1.67	2.1	0.92	TF,P	2 900
19	Disk (150 mm)	15	3	−4	1.523	1.05	3.6	B	3 045
20	SF input	15	1.4	1	1.507	1.24	0.99	NS	3 247
21	Pinhole								
22	SF output	20.8	1.9	1	1.507	1.24	0.99	NS	3 991
23	Splitter	20.8	2	1	1.507	1.24	0.97		4 058
24	Faraday isolator	20.8	2.9	1	1.67	2.1	0.89	TF,P	6 356
25	Disk (208 mm)	20.8	2.5	−3	1.523	1.05	2.1	B	4 465
26	Disk (208 mm)	20.8	2.5	−3	1.523	1.05	2.1	B	
27	Disk (208 mm)	20.8	2.5	−3	1.523	1.05	2.1	B	
28	SF input	20.8	1.8	1	1.507	1.24	0.99	NS	5 050
29	Pinhole								
30	SF output	31.5	2.8	1	1.507	1.24	0.99	NS	6 096
31	Faraday isolator	31.5	4.8	1	1.67	2.1	0.88	TF,P	6 356
32	Mirror	31.5	0	1			0.97	HR	6 669
33	Disk (315 mm)	31.5	4.3	−2	1.523	1.05	1.7	B	7 074
34	Disk (315 mm)	31.5	4.3	−2	1.523	1.05	1.7	B	
35	Disk (315 mm)	31.5	4.3	−2	1.523	1.05	1.7	B	
36	Disk (315 mm)	31.5	4.3	−2	1.523	1.05	1.7	B	
37	SF input	31.5	2.6	1	1.507	1.24	0.99	NS	7 822
38	Pinhole								
39	SF output	46	3.7	1	1.507	1.24	0.99	NS	9 100
40	Slit apodizer	46	3	1	1.507	1.24	0.99	NS	9 487
41	Disk (460 mm)	46	4.3	−2	1.523	1.05	2.85	B	9 558
42	Disk (460 mm)	46	4.3	−2	1.523	1.05	1.85	B	
43	Disk (460 mm)	46	4.3	−2	1.523	1.05	1.85	B	
44	SF input	46	3.7	1	1.507	1.24	0.99	NS	10 089
45	Pinhole								
46	SF output	74	5.7	1	1.507	1.24	0.99	NS	12 489
47	Focus optics	74	12.7	1	1.507	1.24	0.91	NS	15 803

[a]TF - thin-film AR.
NS - neutral-solution AR.
B - bare surface.
HR - thin-film, high reflection.
P - thin-film polarizer.

Table 2-1. Novette optical configuration.

The crystal thickness of 18 mm optimizes the 2ω conversion process over the intensity range of interest for Novette. The upper curve in Fig. 2-9 shows the calculated conversion efficiency for Gaussian temporal pulses in a single crystal with a misalignment of 100 μrad from the optimum phase-matching angle. Measured conversion data from single crystals in large-aperture beams ($D \approx 10$ cm) typically fit the calculations of $\Delta\theta = 100$ μrad (Ref. 17). The lower curve in Fig. 2-9 is a match to the experimental data obtained from the 15-cm-aperture, 3- × 3-crystal prototype array. We believe the departure from the calculated curve results from differences in the orientation of

Fig. 2-6. MALAPROP calculations of peak fluences at Novette spatial-filter lenses and focusing optics at a pulse length of 1 ns.

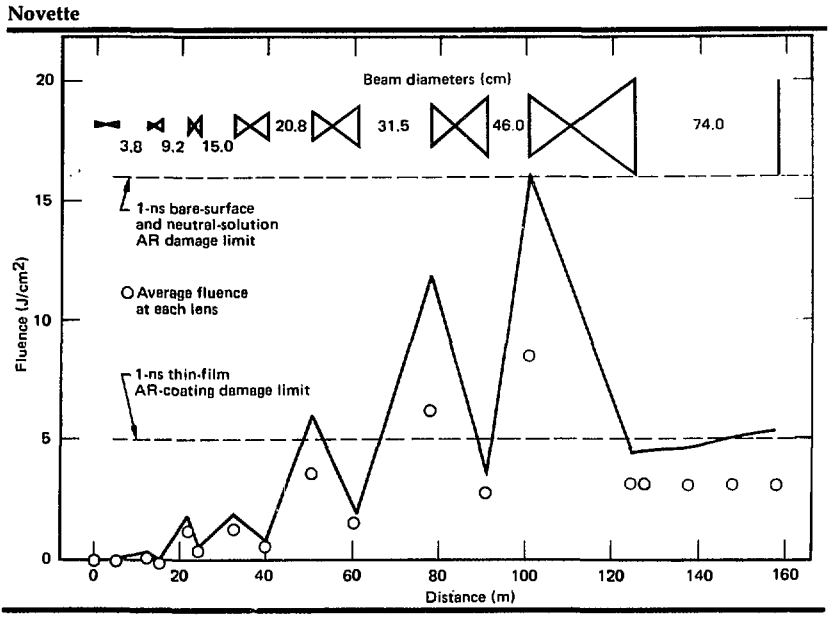

Fig. 2-7. MALAPROP calculations of peak fluences at Novette spatial-filter lenses and focusing optics at a pluse length of 3 ns.

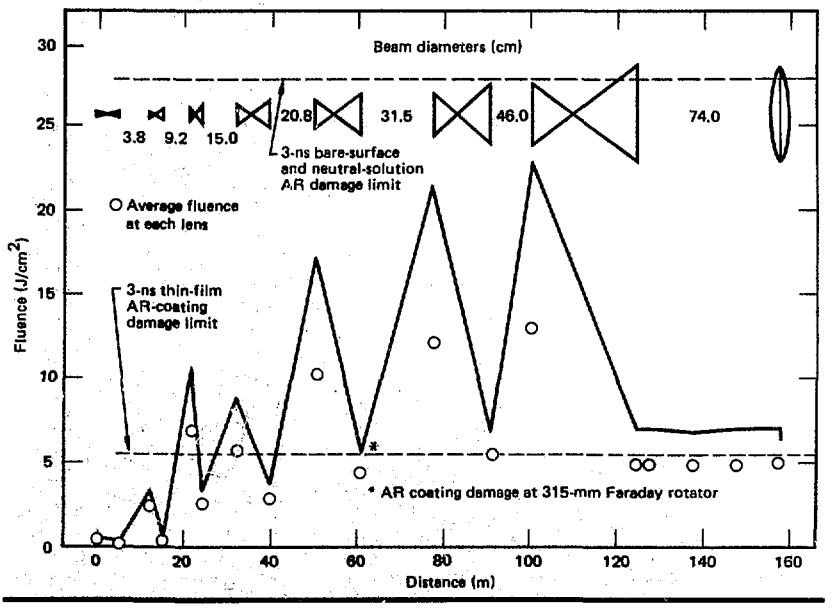

individual crystals in the array from the phase-matching angle (typically 100 μrad for this array).

The machining of the Novette arrays will profit from the experience gained with the prototype; we expect the Novette arrays to be closer to the optimum angle than the prototype, and conversion-efficiency values should approach the upper curve in Fig. 2-9. Additional losses will occur from residual reflection and scattering at surfaces and from apodizing the interstices between array elements. Because the design of the crystal and apodizer are not yet finalized,

No.	Component description	Small-signal gain	1 ns Saturation gain	1 ns Energy (J)	1 ns B-integral Added	1 ns B-integral Total	1 ns Fluence (J/cm²)	3 ns Saturation gain	3 ns Energy (J)	3 ns B-integral Added	3 ns B-integral Total	3 ns Fluence (J/cm²)
1	Apodizer	0.63	0.63	0.111	0	0	0.044	0.63	0.8525	0	0	0.3376
2	SF input	0.99	0.99	0.1099	0.0284	0.0284	0.0277	0.99	0.844	0.0726	0.0726	0.2127
3	Pinhole			0.1099		0.0284			0.844		0.0726	
4	SF output	0.99	0.99	0.1088	0.0146	0.0429	0.0142	0.99	0.8356	0.0373	0.110	0.1092
5	Rod (50 mm)	20	18.12	1.971	0.0567	0.0571	0.255	15.19	12.69	0.133	0.1341	1.641
6	Pockels isolator	0.87	0.87	1.715	0.0437	0.1008	0.255	0.87	11.04	0.0937	0.2278	1.641
7	Splitter	0.97	0.97	1.664	0.225	0.103	0.2218	0.97	10.71	0.482	0.2326	1.426
8	SF input	0.99	0.99	1.647	0.220	0.1052	0.2152	0.99	10.6	0.473	0.2373	1.385
9	Pinhole			1.647		0.105			10.6		0.2366	
10	SF output	0.99	0.99	1.631	0.0730	0.106	0.0356	0.99	10.49	0.157	0.2389	0.2293
11	Disk (94 mm)	6.5	6.014	9.805	0.0189	0.1248	0.2121	5.565	58.42	0.0389	0.2778	1.264
12	Faraday isolator	0.88	0.88	8.629	0.269	0.1517	0.2121	0.88	51.41	0.0535	0.3313	1.264
13	Disk (94 mm)	6.5	5.651	48.76	0.0968	0.2485	1.055	4.365	224.4	0.1697	0.5009	4.853
14	SF input	0.99	0.99	48.28	0.0259	0.2744	1.055	0.99	222.1	0.0398	0.5407	4.853
15	Pinhole			48.28		0.1692			222.1		0.3034	
16	SF output	0.99	0.99	47.79	0.959	0.284	0.3903	0.99	219.9	0.0147	0.5554	1.796
17	Mirror	0.99	0.99	47.32	0	0.284	0.3864	0.99	217.7	0	0.5554	1.778
18	Faraday isolator	0.92	0.92	43.53	0.0289	0.3129	0.3825	0.92	200.2	0.0443	0.5997	1.76
19	Disk (150 mm)	3.6	3.208	139.7	0.1072	0.4201	1.129	2.69	538.8	0.1519	0.7515	4.355
20	SF input	0.99	0.99	138.3	0.0324	0.4525	1.129	0.99	533.4	0.0416	0.7931	4.355
21	Pinhole			138.3		0.1781			533.4		0.2524	
22	SF output	0.99	0.99	136.9	0.0226	0.4751	0.5813	0.99	528	0.0291	0.8222	2.242
23	Splitter	0.97	0.97	132.8	0.0233	0.4984	0.5754	0.97	512.2	0.03	0.8522	2.22
24	Faraday isolator	0.89	0.89	118.2	0.0481	0.5465	0.5582	0.89	455.9	0.0618	0.914	2.153
25	Disk (208 mm)	2.1	1.95	230.4	0.0711	0.6176	0.9688	1.778	810.5	0.0881	1.002	3.408
26	Disk (208 mm)	2.1	1.884	434.1	0.1366	0.7541	1.825	1.658	1 344	0.1527	1.155	5.651
27	Disk (208 mm)	2.1	1.787	775.7	0.2521	1.006	3.261	1.536	2 064	0.2465	1.401	8.678
28	SF input	0.99	0.99	767.9	0.1202	1.126	3.261	0.99	2 044	0.1066	1.508	8.678
29	Pinhole			767.9		0.6739			2 044		0.7148	
30	SF output	0.99	0.99	760.2	0.0807	1.207	1.408	0.99	2 023	0.0716	1.58	3.746
31	Faraday isolator	0.88	0.88	669	0.1975	1.405	1.394	0.88	1 780	0.1752	1.755	3.709
32	Mirror	0.97	0.97	648.9	0	1.405	1.226	0.97	1 727	0	1.755	3.264
33	Disk (315 mm)	1.7	1.557	1010	0.1734	1.578	1.852	1.45	2 504	0.1505	1.905	4.591
34	Disk (315 mm)	1.7	1.516	1531	0.2675	1.845	2.807	1.396	3 496	0.216	2.121	6.409
35	Disk (315 mm)	1.7	1.466	2 245	0.4015	2.247	4.116	1.343	4 694	0.2983	2.42	8.605
36	Disk (315 mm)	1.7	1.413	3172	0.5828	2.83	5.814	1.293	6 071	0.3959	2.815	11.13
37	SF input	0.99	0.99	3140	0.3095	3.139	5.814	0.99	6 010	0.1975	3.013	11.13
38	Pinhole	0.9999		3140		2.013			6 010		1.505	
39	SF output	0.99	0.99	3108	0.2045	3.344	2.699	0.99	5 950	0.1305	3.143	5.166
40	Slit apodizer	0.96	0.96	2984	0.1616	3.505	2.672	0.96	5 712	0.1031	3.247	5.115
41	Disk (460 mm)	1.85	1.574	4697	0.3812	3.887	4.038	1.46	8 341	0.2376	3.484	7.17
42	Disk (460 mm)	1.85	1.497	7031	0.5907	4.477	6.044	1.386	11 560	0.3411	3.825	9.935
43	Disk (460 mm)	1.85	1.42	9982	0.8697	5.347	8.581	1.319	15 250	0.4641	4.289	13.11
44	SF input	0.99	0.99	9882	0.6501	5.997	8.581	0.99	15 100	0.331	4.62	13.11
45	Pinhole	0.9997		9870		2.858			15 100		1.608	
46	SF output	0.99	0.99	9780	0.383	6.38	3.281	0.99	14 950	0.1951	4.816	5.014
47	Focus optics	0.91	0.91	8900	0.8103	7.19	3.249	0.91	13 600	0.4127	5.228	4.964

Table 2-2. Calculated performance of the Novette chains at 1.05 μm for pulses of 1 and 3 ns (saturation fluence = 3.82 J/cm²).

we cannot assign a hard number, but we have estimated this loss at 4%.

Since the nonlinear self-focusing instability parameter, B, varies inversely with wavelength, the growth of beam spatial noise can become a serious problem for high-power, high-frequency beams. Including the dispersion in n_2, B at comparable intensities is approximately 2.5 larger at 0.53 μm than at 1.06 μm (Ref. 18). This factor caused us to examine closely the total glass thickness between the crystal array and the target, as well as the upper B limit that is tolerable in these assemblies.

The configuration that resulted from these examinations preserves the functions required, with considerable reduction in the glass thickness between the frequency-doubling crystals and the target (Fig. 2-10). The configuration shown in the figure consists of

- Windows on the frequency-doubling array with a 20:1 diameter-to-thickness ratio.
- A 2-cm-thick 1ω beam absorber.

- Focusing optics comprising an f/4 doublet of BK-7 glass.

The first element of the lens doublet serves as the vacuum barrier for the target chamber; an uncoated back surface on the second element provides a 4% reflection to the alignment/diagnostic packages, eliminating the need for separate vacuum windows and diagnostics beamsplitters. The f/4 lenses, while not optimal for a two-beam system, represent a compromise between speed and glass thickness that is reasonable until a faster reflective focusing system can be obtained.

We have used finely zoned MALAPROP code runs to assess the maximum ΔB that can be tolerated in the 2ω optical train between the crystal array and the target. Figure 2-11 summarizes the results, showing the peak intensity of self-focusing spikes plotted against the nonlinear self-focusing growth accumulated through the 2ω optical train. The self-focusing spikes, measured at the rear surface of the second lens element, were caused by small obscurations in the beam at the input to the crystal-array output window. The results shown in the figure are for modulation caused by a single round obscuration in the beam and for two obscurations close enough to form overlapping interference rings. Note the occurrence of intensity growth that is characteristic of an exponentially growing instability.

For the case of two interfering obscurations, the maximum permissible ΔB at which obscurations remain below the bare-surface damage threshold lies in the range from 2.0 to 2.5. This constraint limits the intensity of the 2ω beam, as Fig. 2-12 illustrates. The ordinate in this figure is the 1ω drive to the frequency-conversion crystal; the abscissa is the 2ω output intensity. The curve shows the upper limit of the transfer efficiency to 2ω for a Gaussian temporal pulse shape of maximum intensity shown on the 1ω axis. The maximum available 1ω drive at three pulse lengths is shown by the vertical red lines. The horizontal solid green lines are the 2ω intensities that correspond to $\Delta B = 2.0$ and 2.5. Clearly, with the present focusing-optic arrangement, the limit is always imposed by the 1ω drive from the laser; however, this situation would change with the addition of only a small amount of a nonlinear material into the 2ω beam path, or with a small increase in 1ω power available from the laser chains. Energies on the right side of the figure are the maximum credible 2ω energies available at each pulse length.

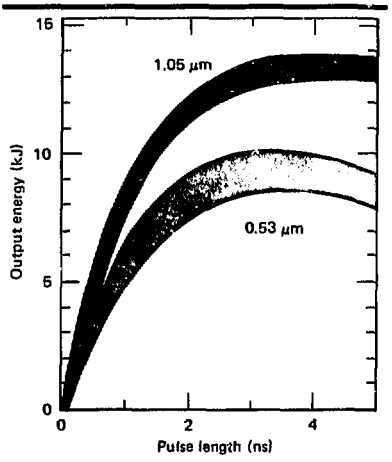

Fig. 2-8. Projected energy on target from a single Novette beam at 1.05 and 0.53 μm as a function of pulse length.

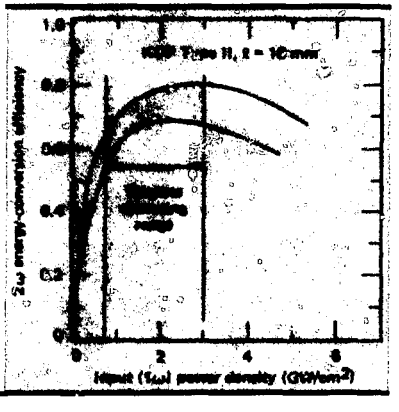

Fig. 2-9. The conversion efficiency of the Novette frequency-doubling array is expected to lie within the green band.

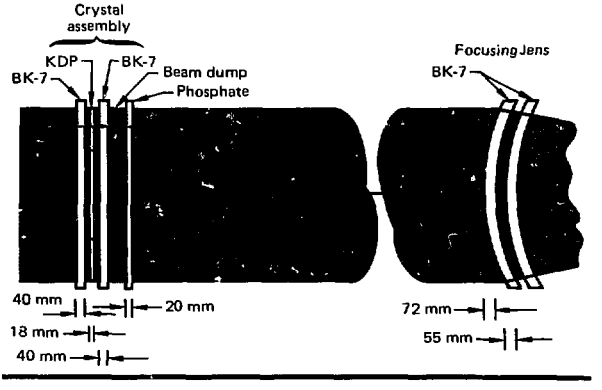

Fig. 2-10. Arrangement of Novette frequency-conversion and focusing optics.▼

Figure 2-8 summarizes the on-target energy capabilities of a single Novette beam. The upper red curve illustrates the maximum 1.05-μm output discussed above. The lower, green band represents our current best estimate of the 0.53-μm output capability. We expect Novette's performance to closely approach the upper limit derived from the single-crystal conversion-efficiency curve in Fig. 2-9, but performance typical of the prototype-array data (i.e., lower limit) cannot yet be excluded.

The limited availability of large-aperture UV-transmitting optics and of large-aperture KDP boules precludes frequency-tripling on Novette during its initial operating period. In 1982, we must address the problems of obtaining large-aperture, high-quality UV optics and high-quality KDP crystals. We expect that sufficient quantities will be available to frequency-triple Novette in one to two years. Frequency-tripling will be accomplished primarily by changing the KDP arrays to the quadrature arrangement described in the Nova portion of this section. It will also be necessary to change the present array output windows to fused silica; change the focusing lenses to fused silica, or substitute a reflective focusing system; and add the 3ω diagnostics and alignment packages. With these changes, energy capabilities typical of those described for Nova beamlines at 3ω should be possible.

Summary. The two-beam Novette laser will provide the capability for performing high-power target-irradiation experiments with frequency-doubled beams (0.53 μm) from large-aperture Nd:phosphate-glass amplifier chains beginning in late 1982. The system will be able to deliver up to 13 TW to fusion targets in 1-ns pulses, or up to 20 kJ in pulses of 3 to 5 ns. An option to frequency-triple (0.35 μm) is available for the future, when large-aperture UV optics become available and budget conditions permit.

Author: D. R. Speck

Major Contributors: J. T. Hunt, K. R. Manes, W. W. Simmons, and W. E. Warren

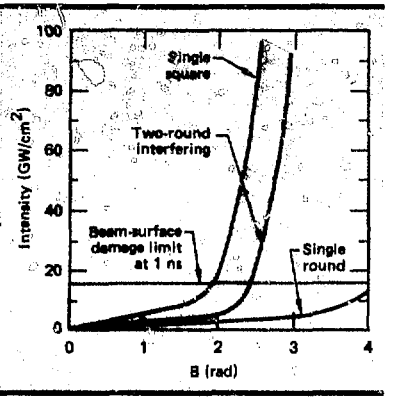

Fig. 2-11. Calculations of peak intensity at the output surface of the Novette focusing lenses resulting from nonlinear growth of modulation caused by obscurations on the input surface of the array output window.

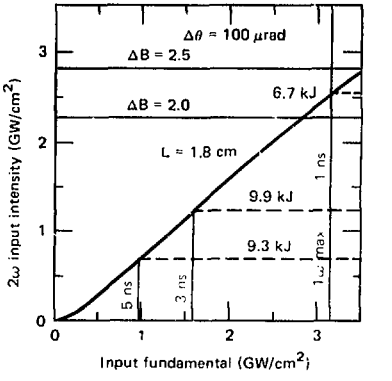

Fig. 2-12. Output 2ω power density vs the input fundamental for Gaussian pulses.

Novette Master Oscillator Room and Preamplifier Configuration

During 1981, we developed our early conceptual design of the Novette master oscillator room (MOR) and preamplifiers into the final design now being built. The requirements listed in the *1980 Laser Program Annual Report*[19] have not been significantly altered, but we have made several changes in the detailed implementation of the requirements.

The required pulse-width range for target irradiation is obtained from the two oscillators on the main table (lower right in Fig. 2-13). The short-pulse oscillator will generate pulses in the range from less than 100 ps to 1 ns, and the pulse slicer following the long-pulse oscillator will provide pulses from 1 to 5 ns, or longer. The operating

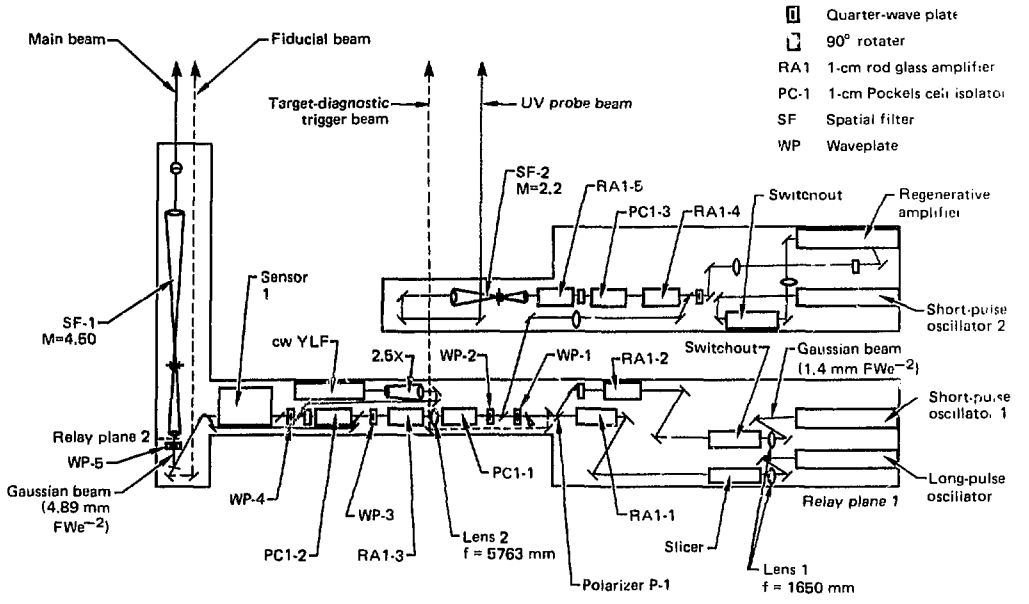

Fig. 2-13. Schematic of the Novette master oscillator room.

principle and synchronization of the Novette oscillators have already been described in detail.[20] The only new development is the use of Nd:YLF crystals having gain maxima at 1.05 μm to match the phosphate glass in the amplifier chains.

The switchout and slicer following the oscillators are two-stage, 10-mm-diam Pockels-cell devices giving prepulse attenuation of better than 10^7. The isolators (PC1-1 and PC1-2 in Fig. 2-13) are both single-stage Pockels cell devices, that use the same 10-mm-diam Pockels cells as in the switchout. These two isolators will give additional prepulse attenuation of 10^7.

The MOR amplifiers (RA1-1 through RA1-5) will all be 1-cm-diam, high-gain phosphate-glass amplifiers. In tests with less than 1 kJ of pump energy in a prototype amplifier, we observed small-signal gains in excess of 30. In these tests, we used a 15-cm-long Q-98 (Kigre) rod with 3% Nd doping in a double-ellipse pump cavity. We therefore designed the Novette amplifiers for 1-cm-diam glass rods with a 15-cm active length. For the required gain of 30, the pump energy will be less than 1 kJ; thus, we expect an operating lifetime of ~4 × 10^6 shots, equal to one year's operation, when the amplifiers are pulsed every 10 s.

We had previously planned to use Nd:YLF preamplifiers at a repetition rate up to 10 pps, but the uncertain availability of good-quality 1-cm-diam YLF and the cost of developing the necessary high-repetition rate power supplies led us to use glass preamplifiers. Consequently, we expect the repetition rate of the Novette preamplifiers to drop from about 10 pps with YLF to 0.1 pps with glass. As we describe below, this primarily affects the use of the preamplifiers to align the frequency-conversion crystal arrays.

Relay Design. The Novette laser beam is fully relayed from the oscillator into the aperture at the start of each laser chain. Each oscillator has a flat output mirror that establishes the input relay plane for the system. The calculated spot size from both oscillators is 1.40 mm (full width to e^{-2} intensity) for the Gaussian beams. Lenses Nos. 1 and 2 (shown in Fig. 2-13) then magnify the beam to fill the rod amplifier (RA1-3) and relay the beam from the oscillator to the input of the spatial filter (SF-1). Spatial filter SF-1 then relays the beam into the laser bay to relay plane 3 (Fig. 2-14). Spatial filter SF-3 relays the beam to the 6.36-mm-diam aperture at relay plane 4. The final spatial filter in the preamplifier (SF-4) relays the

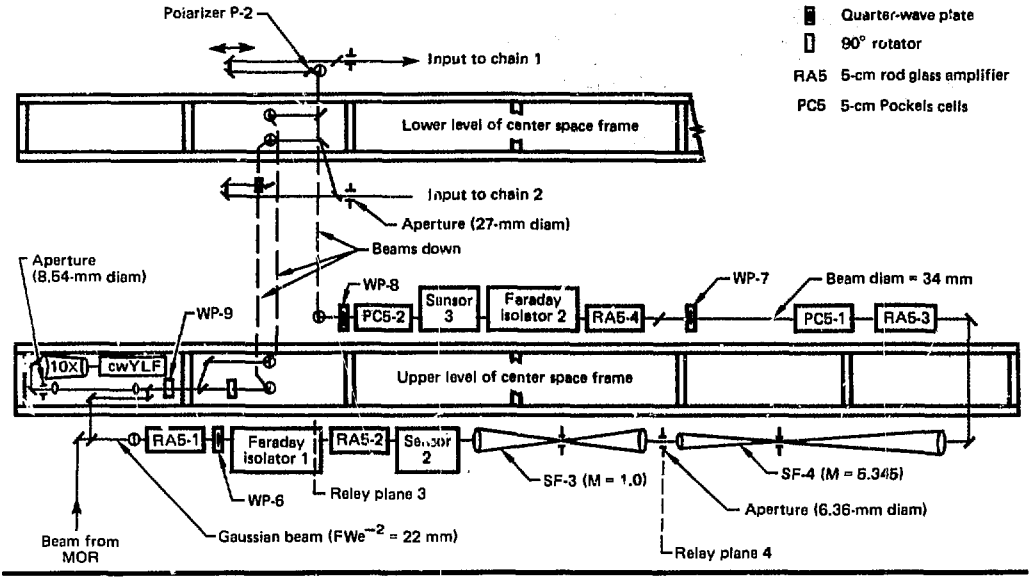

Fig. 2-14. Schematic of the Novette preamplifier section.

beam to the laser-arm input aperture of 27-mm diameter. The combined transmission of these two apertures is 10%, giving each arm a beam that is uniform to ±5% (neglecting diffraction effects in the system).

In conventional relays in a laser chain, the beam is focused between the relay lenses; these sections of the chain are evacuated and contain no components. We have departed from this practice on Novette, however. For the relay following the oscillators (formed by lenses Nos. 1 and 2), the input spot size from the oscillators is small, and the total relay distance is long enough (15 m) that the actual beam waist between the lenses is about the same as the spot size from the oscillators. This allows us to put components between the lenses.

We have chosen the positions and focal length of the two lenses to magnify the beam and fill the aperture of the final 1-cm rod amplifier (RA1-3 in Fig. 2-13) and to allow enough propagation distance from the oscillator to lens No. 1 to produce a sufficiently large spot size in the switchout following lens No. 1. The focal lengths of lenses Nos. 1 and 2 are 1650 and 5763 mm, respectively, placed 1634 and 9047 mm from the oscillator. The advantage of the Novette relay design is that we can fully relay the beam from the oscillator without requiring the use of long evacuated pipes that waste space on the oscillator table. We also obtain a beam waist of 1.57 mm in the section between the pulse shaper and the first turning mirror following the long-pulse oscillator. This section of the beam chain is a good location for a fast optical switch that can shape more complicated pulses from the long-pulse oscillator.

The beam shape remains Gaussian through the first two 5-cm rod amplifiers (RA5-1 and RA5-2 in Fig. 2-14); and it is then filtered (SF-3) to reduce spatial modulation on the beam as much as possible. The beam is next passed through a hard aperture and relayed to the chain-input aperture with relay SF-4.

If there is no pinhole in spatial filter SF-4, large diffraction rings result on the beam at the output of the filter. At the chain-input aperture, however, the beam is perfectly relayed without diffraction rings. By properly choosing the size of the pinhole, we can reduce the diffraction rings that follow the spatial filter, but we then introduce modulation on the beam at the chain-input aperture. We will select and employ the pinhole so that the diffraction rings at both locations are about the same. Calculations show that, under these circumstances, the modulation on the beam in the section between SF-4 and the chain-input aperture is about 10% for a beam diameter of 34 mm. In

practice, we will make the beam diameter in this section as large as possible without clipping the beam in the components (thereby reducing diffraction effects as much as possible).

X-ray Backlighting. We have designed the Novette MOR to provide for x-ray backlighting of the target. The short-pulse oscillator will generate pulses of 0.07 to 1 ns for target irradiation, and the long-pulse oscillator will be used for backlighting. The pulses from the two oscillators are combined with polarizer P-1 (Fig. 2-13); they are timed 20 ns apart, with the target-irradiation pulse first. The mix of these two pulses into the system is then selected by waveplate WP-1, and both pulses are amplified in a common beamline through the 5-cm amplifier RA5-4 (Fig. 2-14). Pockels cell PC5-2 will switch the polarization of the second (backlighting) pulse, and polarizer P-2 will then separate these pulses and send a different pulse down each chain. We will add a 20-ns delay to the target-irradiation chain so that the target-irradiation pulse and the backlighting pulse arrive at the target simultaneously.

We will also use the short-pulse oscillator in the MOR to align the 2ω-conversion crystals at this end of the beam chains. In this application, a 100-ps pulse from the short-pulse oscillator is amplified through the 1-cm rod amplifiers up to a repetition rate of 0.1 pps (the maximum for glass amplifiers). Waveplate WP-3 (Fig. 2-13) is adjusted to switch the polarization; the polarizer following WP-3 redirects the beam so that it bypasses Pockels cell isolator PC1-2 and sensor No. 1. The beam is then recombined into the main beamline with orthogonal polarization and relayed into the laser bay with spatial filter SF-1.

In the laser bay, the beam is once again redirected by a polarizer located upstream from the first 5-cm rod amplifier (Fig. 2-14). The beam then goes directly to the chain-input aperture, bypassing all the components in the preamplifier section. We estimate that ~100 mJ can be put through the chain-input aperture at a spot size of 22 mm (full width at e^{-2} intensity), which—at a spot size of 42 cm at the crystal array—will yield ~0.02 μJ of 2ω energy (sufficient for detection).

In the Novette MOR, we will also generate ~20-ps pulses for UV probing of the Novette target. As Fig. 2-13 shows, these short pulses are obtained by running a

Fig. 2-15. The Novette MOR at the end of 1981 (point of view corresponds to the upper right of Fig. 2-14).

second short-pulse oscillator synchronously with the primary oscillators for target irradiation and injecting a 100-ps pulse from the additional oscillator into a regenerative pulse compressor[21,22] to obtain a synchronous 20-ps pulse. This pulse is amplified by two 1-cm glass amplifiers to about 20 mJ and is sent to the laser, where the pulse is Raman-shifted and converted to the fourth harmonic for UV probing of the target.

There are two continuous-wave (cw) YLF alignment lasers in the front end of Novette. The first one is located in the MOR beamline just before sensor No. 1. This cw laser is used to align the preamplifier section and the laser chains. The second cw YLF laser is located on the laser spaceframe (lower left of Fig. 2-14); this alignment laser goes directly to the chain-input apertures to give its maximum power into either or both of Novette's arms.

The MOR is being built in a separate room adjacent to the laser high bay. We are using the existing Argus concrete tables in the MOR, with the addition of a 12-in.-high computer floor around the tables for wiring and other utilities. We have also built acrylic covers over the tables and installed blowers that circulate air into the covers through high-efficiency particulate (HEPA) filters. We expect these steps to provide the components on the tables with a class-100 clean environment. (Classes of cleanliness refer to the number of particles $<0.3\ \mu m$ in $1\ ft^3$.) Figure 2-15 shows the MOR under renovation at the end of 1981; in this photograph, facility modifications have been completed, and the tables are being readied for component installation.

All power conditioning for the oscillator and 1-cm amplifiers will be located on racks in the MOR. Power into the MOR is filtered through isolation transformers, and interaction with the rest of the Novette system is through fiber-optic cables. The lack of direct electrical connection to the laser bay or control room, and the single-point grounding system in the MOR, combine to provide good immunity from electrical noise.

Author: D. J. Kuizenga

Major Contributors: E. S. Bliss, J. E. Murray, and D. R. Speck

Novette Laboratory

The Novette target-irradiation system illustrated in Fig. 2-16 will occupy approximately 32 000 ft^2 in Building 381, where the Argus system was previously housed. Approximately 40% of this space is located on the first floor in the 28-ft-high main bay, which will contain the laser preamplifier, laser-driver sections, and the target chamber with its support equipment. Principal access to the main bay is through 18-ft-high doors in the west and north walls. An emergency exit in the east wall has also been added. Personnel can enter the support laboratory areas through the hallway access, the master oscillator room, the Novette operations center, or the target-staging laboratory.

The remainder of the first-floor space, approximately 7000 ft^2, is occupied by the major support laboratories required to operate Novette

- The target-staging lab is used to prepare and maintain equipment in the target area and to prepare targets for insertion into the target chamber.
- The diagnostics room provides a central location for acquisition of all target- and most laser-diagnostic data.
- The central computer room houses the minicomputer that supports Novette's centralized control facility.
- The control room houses the central operator consoles from which Novette's control and data-acquisition functions will be coordinated.
- The operations center is located centrally for the coordination of Novette construction and operation.
- The master oscillator room houses the four oscillators and supporting control equipment for the Novette laser. For the safety of personnel and equipment, the MOR and control rooms are electrically isolated (to 60 kV) from the rest of the facility.
- The electro-optics and calorimetry laboratory houses off-line electro-optics repair facilities and a calibration station.

The 12 000 ft^2 basement area immediately under the high bay houses the power conditioning equipment and target-diagnostics areas. The high-voltage capacitor banks will be separated from the rest of the basement by safety walls that will isolate the area in

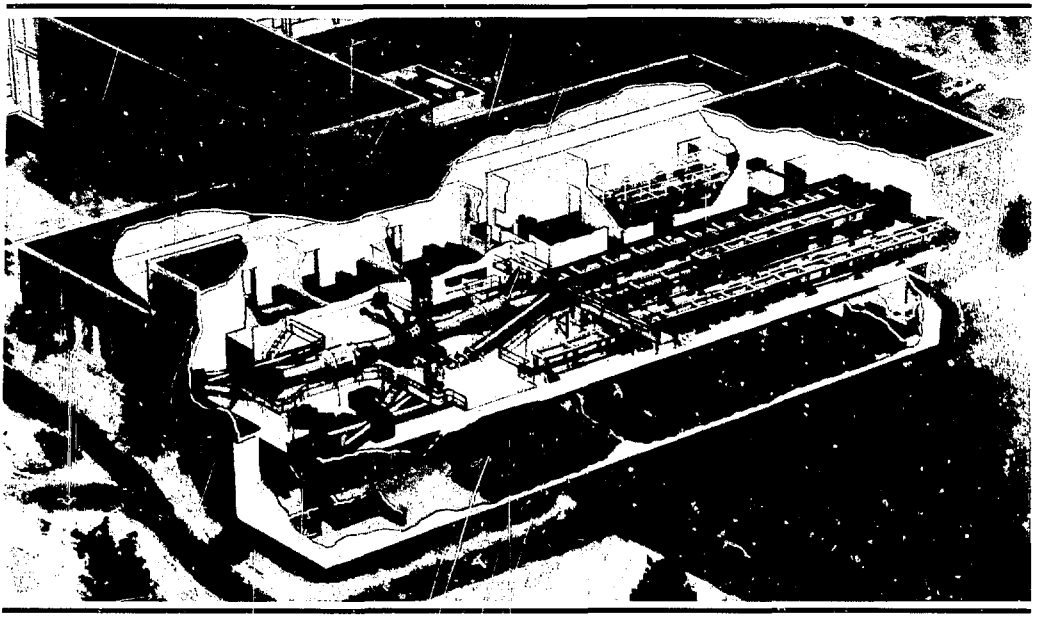

Fig. 2-16. Novette viewed from the northeast.

the event of capacitor failures and will prevent accidental access when the banks are being charged. The remaining area underneath the target chamber will be used for access to diagnostics instruments that protrude through the 4-ft concrete floor. This area will also house two special-purpose laboratories: one for optical spectrometer equipment, and the other for radiation-chemistry diagnostics. There will also be a curtained area for holographic reconstruction during backlighting experiments.

Although most of the Novette laser-system design closely parallels the design of the Nova system, a number of Novette subsystems differ; their configuration is dictated in part by particulars of the facility. The status of major Novette-specific activities is described in the following four articles.

Author: G. J. Suski

Cleanliness and Temperature Control. The Novette system in Building 381 does not have a temperature-control system comparable to that of the Nova system in Building 391. Nonetheless, temperature control in the Novette laser bay is certainly adequate: as measured at beam height over a period of three days, temperature deviations in the laser bay are $\pm 0.5°C$; in the MOR, temperature deviations are $\pm 2.5°C$.

For a system as large as Nova, a fully filtered, recirculating air-conditioning system is needed to meet required temperature and cleanliness standards. For the smaller Novette system, in which the components are arranged on a horizontal plane close to the floor, we can control air cleanliness by using smaller filter units in strategic locations.

In Novette's circulation system, air enters through the ceiling and exhausts at the base of the sidewalls. Filters located immediately downstream of the blowers filter 95% of all particles 5 μm or larger. These Novette filters are less effective than the Nova HEPA filters (located where air enters the room) that will filter all particles 0.3 μm or larger.

Novette's clean air will be provided by placing filter modules inside the space-frame; these modules will blow class-100 air horizontally across component interfaces that open for operational or maintenance reasons. From recent tests and previous experience, we know that this system can easily achieve class-1000 clean air locally near open components, and better than class-10 000 clean air generally. The filters recirculate room air and have a combined recirculation volume of 66 000 ft^3/min,

completely filtering room air every 5.5 min. To lower the airborne particle count in the Novette bay, we have covered the acoustical ceiling tiles with heat-shrinkable plastic wrap, painted the acoustic wall tiles with acrylic paint, and installed new floor covering.

The Novette clean-air modules are arranged inside the spaceframe with horizontal flow (rather than overhead with vertical flow) to allow convenient overhead crane access and to prevent supporting structures from interfering with laser operational space. The modules will not touch the frame; they are mounted on the floor with vibration-isolated mounts. The air-module motors will require approximately 15 kW for power; Building 381 can easily accommodate this additional load.[23]

Cleanliness of the MOR was achieved with an innovative approach. The optical tables were enclosed in large sliding covers with HEPA filter modules suspended in the top (see Fig. 2-4). This arrangement provides class-100 clean-air conditions, greatly reducing the contaminants on optical surfaces.

Authors: C. A. Hurley and H. G. Patton

Spaceframe. The Novette spaceframe serves as a stable support for all components in the laser system. There are four major frame units, three for the laser and one for the target area (Fig. 2-17). Their total weight is 50 tons. All frames are constructed using 6-in.-square (i.e., 6 × 6 in.) steel tubing for main column and beam members; diagonal bracing members are constructed of 4-in.-square steel tubing for ease of fabrication. The beams are tied to the building floor with strategically located seismic anchors and allowed to thermally expand from the anchor locations on roller-bearing supports. The supporting floor is a massive 1-m-thick monolithic reinforced concrete slab that sits on concrete columns. The spaceframe can move with respect to this slab because its thermal inertia differs from that of the slab.

The four frame units were designed to be dynamically stable, while accommodating convenient maintenance and utility access to components. We used computer analyses to establish the dynamic response of each frame both to ground vibrations measured at the site and to LLNL design-basis seismic loadings. Deformations resulting from ground vibrations were judged to be acceptable on the basis of laser-beam deflection. We used modal analyses of the frames to determine the influence of frame-member size and locations, as well as variations in support and anchor-restraint conditions.

Analysis of the Novette spaceframe is not complete. However, we checked the tallest laser frame and found it to be at least four times stiffer than the Nova frame. Based on this early analysis, we assume that the

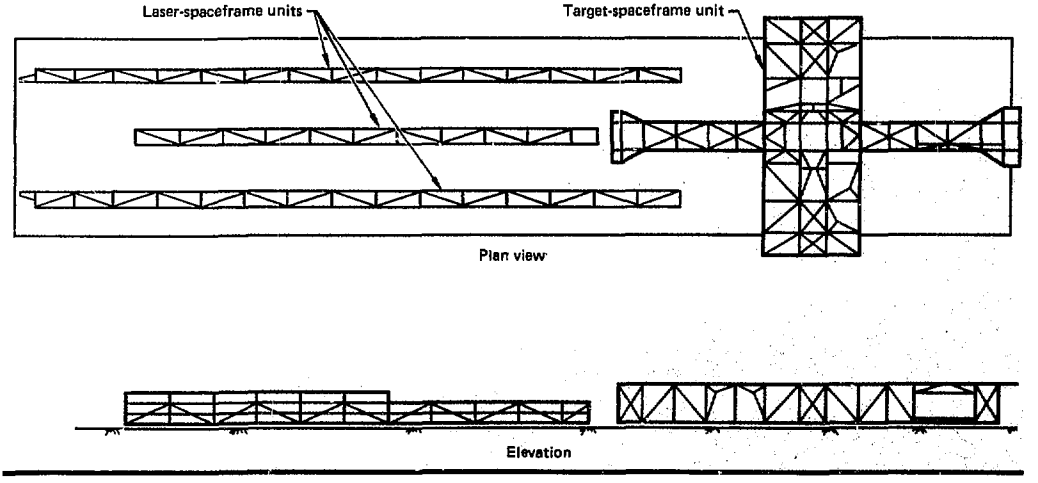

Fig. 2-17. Two views of the Novette spaceframe.

spaceframe design is sufficiently stable, and our knowledge of the Nova design gives us confidence that the Novette design is stable. We are, therefore, proceeding with fabrication.

The north and south laser frames are 154 ft long, 6 ft high, and 4 ft wide. The third laser-frame unit, which is located between the north and south frames, is 106 ft long and 4 ft wide. At one end, it has a section raised 8 ft 6 in. from the floor. The target spaceframe unit is shaped like a cross, 93 ft long and 54 ft wide; it has a platform measuring 21 by 54 ft at the center, surrounding the target chamber. This area is primarily for diagnostic support and access. The working level of the target frame is elevated 9 ft from the floor; the center of the target chamber is supported 12 ft from the floor. The target-chamber frame unit is accessed by a system of stairs and foot walks that are vibrationally isolated from the spaceframe. Space under the raised target frame is reserved for service and for diagnostics packages.

Author: C. A. Hurley

Novette Nitrogen-Cooling System. After firing, Novette laser components will be convectively cooled with a closed-loop, nitrogen-gas system similar to that planned for Nova. The nitrogen gas is distributed through a welded-aluminum piping system. The flow through a component is established by the pressure loss in the component filter; groups of amplifiers with a common filter are cooled in series to minimize the nitrogen flows required.

The nitrogen gas is recirculated by a "Roots-type" blower and thermally conditioned by a chiller unit. An additional chiller unit allows a further reduction in the gas temperature during the initial cooling phase to achieve a more rapid cooling of the laser components; at the design flow of 500 cfm per chain, cooling time is calculated to be less than two hours.[24,25] A liquid-nitrogen storage tank and vaporizer unit supplies nitrogen gas for purging and filling the closed-loop distribution system.

Author: H. L. Julien

Novette Power Conditioning

The Novette pulse-power system is a two-beam subset of the Nova pulse-power system. Differences between the two systems arise from differences between their buildings and from Novette's rapid construction schedule. The grounding of the Novette system, which has been arranged to be electrically similar to Nova and Shiva, was accomplished by arranging cables in the basement to substitute for the ground mat that exists in the newer systems. Because of the limited space available in the basement, high-density capacitors are used more extensively in Novette than in Nova. Pockels-cell pulsers for the Novette MOR have been taken from Shiva with little or no modification. We are working to improve the reliability of these units, and we anticipate a later upgrade.

Bank Staging and Layout. The Novette energy-storage layout is shown in Fig. 2-18. The rod bank is separately enclosed and interlocked (the left side of the figure), so that the rod amplifiers can be fired independently. Capacitor racks are run north to south, with circuits stacked six high. A 6-ft aisle runs along the south end of the racks for access by forklift and the capacitor-loading equipment module (CLEM). Along the south and east walls of the bank are the switches and switch-control racks that make up part of the wall structure. To the east of the storage area are the power supplies, fan-outs, and cross-connect racks. A personnel aisle runs along the far south wall outside the bank area. The dashed outlines in Fig. 2-18 indicate space allocated to capacitor banks, switch racks, and power supplies both for future additional 46-cm amplifiers and for a backlighting beam.

The Novette power-conditioning staging for the capacitor bank, power supplies, and switches is summarized in Table 2-3. The first column lists such major components as amplifiers, Faraday rotators, and the pulsed ionization lamp check (PILC) (The PILC is a subsystem used to check out the pulsed-power system in general and the flashlamps in particular; it is described in detail in "Power Systems and Energy Storage," later in this section.)

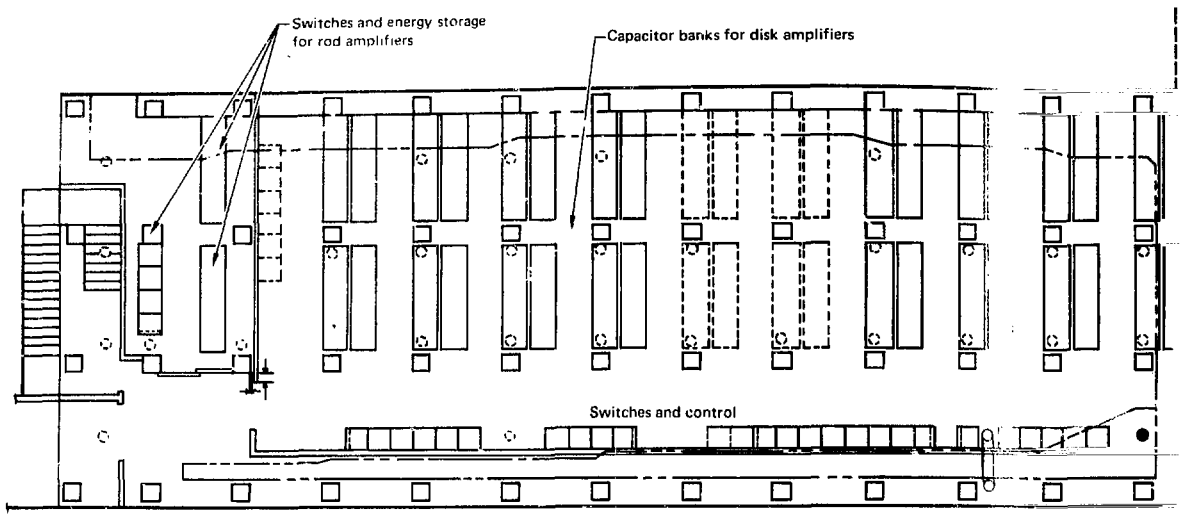

Controls. The Novette control system is a subset of the Nova control system (see "Control Systems," later in this section); it uses the same techniques and the same hardware. Figure 2-19 shows the organization of the two central operator consoles that control the four primary subsystems (power conditioning, alignment, laser diagnostics, and target diagnostics). Much of the power-conditioning control system hardware has been fabricated and tested as part of the 1-MJ test facility. Items controlled, synchronized, or monitored for Novette include the master oscillator, nine groups of ignitron switches, seven diagnostic devices, 16 high-voltage power supplies, and the safety interlock system. Some control-system segments have been installed in the Novette building; integration of these devices with the control computers will begin early in 1982.

Control-system operation of the laser is described in detail in "Sequencing, Synchronization, and Safety Systems," later in this section. With the command menus displayed, the shot director can execute selective tasks, request the display of system status, or request additional control options, thereafter inputting his commands to the control system via a touch panel monitored by the VAX computer. Status data are displayed to the operator via color graphic displays. Commands to hardware devices are relayed from the controlling VAX computer to the devices by a pair of microprocessors. These microprocessors constantly poll all devices for status information and signal status changes to the VAX.

Software for the control computers is scheduled to be completed in time for overall system activation. Much of the microprocessor software has been completed and tested as part of the Nova prototype system. We have also defined control and display software for the control-room consoles and have generated some sample displays.

Personnel-Safety Interlock System. The Novette personnel-safety interlock system is designed to protect personnel from electrical and optical hazards. Protection is accomplished by a logic system that monitors doors, runsafes, panic-interrupt boxes, beam shutters, and other interlock points and decides when laser oscillators and power supplies may generate optical and electrical hazards.

Interlock logic is implemented in a triple-redundant voting format in which there are

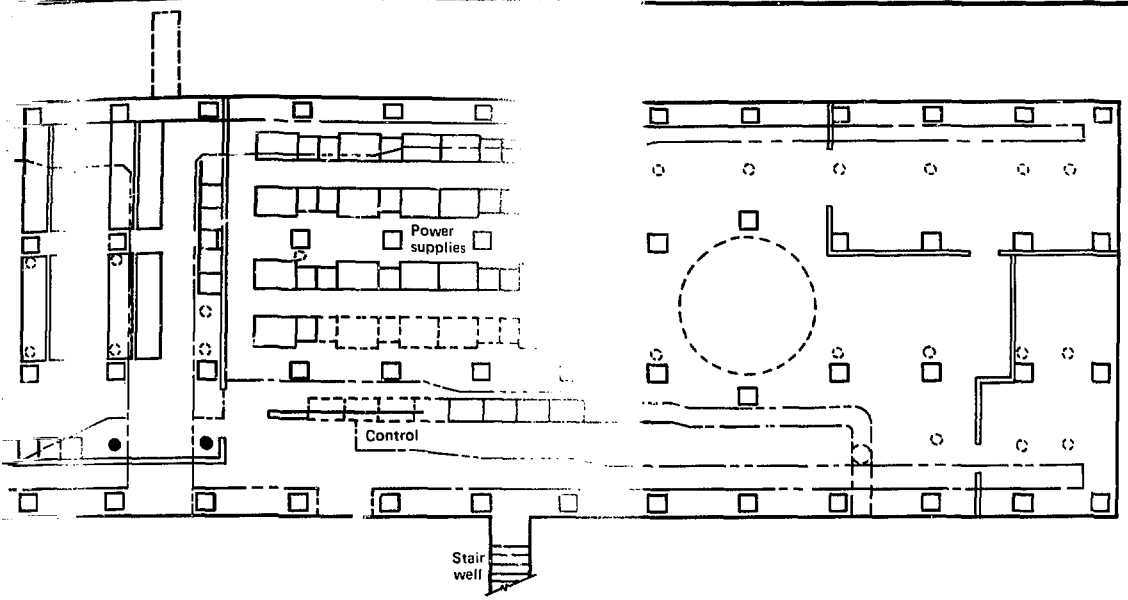

Fig. 2-18. Novette energy-storage layout.

Component	No.	Circuits	Energy	Lamps	Capacitance per circuit (μF)	Inductor size (μH)	Power supply	Switches
Faraday rotator (9.4 cm)	4	4	84–3 kJ[a]	—	101	—	1	1
Faraday rotator (15.0 cm)	2	8	192–3 kJ	—	116	—	1	1
Faraday rotator (20.8 cm)	2	10	400–5 kJ	—	200	—	1	1
Faraday rotator (31.5 cm)	2	10	400–5 kJ	—	200	—	1	1
Rod amplifiers	6	6	252–3 kJ	36–19 in[b]	203	450	1	2
Disk amplifier (9.4 cm)	4	32	576–3 kJ	64–44 in	87	450	1	2
Disk amplifier (15.0 cm)	2	24	432–3 kJ	48–44 in	87	450	—	2
Disk amplifier (20.8 cm)	6	48	1200–12.5 kJ	96–44 in	104	450	2	2
Disk amplifier (31.5 cm)	8	80	3000–12.5 kJ	160–44 in	156	650	4	4
Disk amplifier (46.0 cm)	6	96	3600–12.5 kJ	480–19 in	156	450	3	6
PILC	—	3	18–3 kJ	—	—	—	1	3
Total		321	7800–12.5 kJ	516–19 in	—	—	16	25
			800–5 kJ	368–44				
			1554–3 kJ					

[a]The 3-, 5-, and 12.5-kJ figures indicate the energy per capa
[b]The 19- and 44-in. figures indicate the size of the flashlam

Table 2-3. Novette power-conditioning staging.

three identical logic units that vote. The system takes the action specified by two of the three interlock logic units. The interlock logic units are implemented with solid-state logic, extensively filtered to prevent erroneous actions and damage due to electrical noise generated by the pulse-power system. The logic is programmed with a patch panel in the logic-unit chassis. This allows us to return to the current configuration, while evaluating changes in the system-interlock logic. The voting is implemented with mechanical relays, chosen because the typical failure mode is an open circuit (as opposed to a short circuit for solid-state devices).

Electrical isolation between (1) the interlock logic system and the devices inside the MOR and (2) the control room is accomplished with fiber optics. A dc fiber-optic signal transmits the state of the control-room and MOR keys to the logic units. Fiber-optic converters are used within the MOR in conjunction with voting circuitry. Fiber-optic signals from the interlock-logic units are converted to 120-V (ac) outputs as a result of a two-out-of-three vote of the fiber-optic converters. Contact closures within the MOR are converted to dc fiber-optic signals by the fiber-optic converters and sent to the interlock-logic units.

All inputs and outputs of the interlock-logic units, the fiber-optic converters, and the relays in the voting circuitry are monitored by the power-conditioning front-end processors. These data are available to the VAX computer through a multiport memory.

Oscillator Controls and Fast Timing. Novette will serve as the proving ground for the Nova oscillator controls, now under development, which are discussed in detail in "Nova Front End: Oscillator Subsystems," later in this section. Components and assemblies making up this prototype subsystem have been developed and tested at the unit level and have been installed in the Novette MOR. Integration into an operating subsystem will both support Novette and qualify the design for Nova. High manufacturing standards have been set for all assemblies, so that few changes will be needed to upgrade the Novette oscillator controls to the quality level and configuration required for Nova.

Authors: D. J. Christie, D. G. Gritton, B. T. Merritt, J. A. Oicles, and K. Whitham

Major Contributors: B. M. Carder, G. R. Dreifuerst, R. W. Holloway, J. W. Morton, and J. A. C. Smart

Novette Crystal Arrays for Harmonic Generation

During 1981, we continued to develop the techniques and components required for large-aperture frequency conversion. Various aspects of this development are reported in "Harmonic Conversion" in Section 7; the results of the prototype tests described there are encouraging; they provide valuable information for the design calculations and scaling of the first two large-aperture (74 cm) KDP crystal arrays, which are to be installed on the Novette system in late summer of 1982. The first of these arrays will utilize 15-cm-square crystal segments in a 5×5 matrix. This element size was chosen because of material availability and compatibility with the Novette activation schedule. Longer-range plans for Novette and Nova call for 27-cm-square segments in a 3×3 matrix (see "Frequency Conversion and Target Focus," later in this section).

By the end of 1981, we had received 34 15.5-cm KDP crystal blanks. These blanks are being processed through the same production cycle used for the prototype crystals (see "Harmonic Conversion" in Section 7). Figure 2-20 is a photograph of a 15-cm-square crystal blank mounted on the diamond-turning machine for a face-cutting operation. Pen marks on the crystal surface are used to visually monitor material removal. When finished, the crystals will be 15-cm-square by 1.8 cm thick and will be precisely oriented (to within ± 30 μrad) for Type-II phase matching from the 1.05-μm fundamental to the 0.53-μm second harmonic at 22°C.

Fabrication and installation of the 74-cm-aperture Novette harmonic-generation arrays during the coming year will provide early 2ω capability for Novette. We will also gain valuable large-array experience that can be applied to frequency conversion on Nova.

Authors: B. C. Johnson and J. D. Williams

Major Contributors: F. T. Marchi, B. W. Woods, and S. E. Stokowski

Novette Target Systems

The Novette target system consists of a mixture of Nova and Shiva hardware and software systems. We plan to use many of the Shiva diagnostics as well, supplementing them with new instruments for specialized measurements. The Novette control

Fig. 2-19. Novette control system.

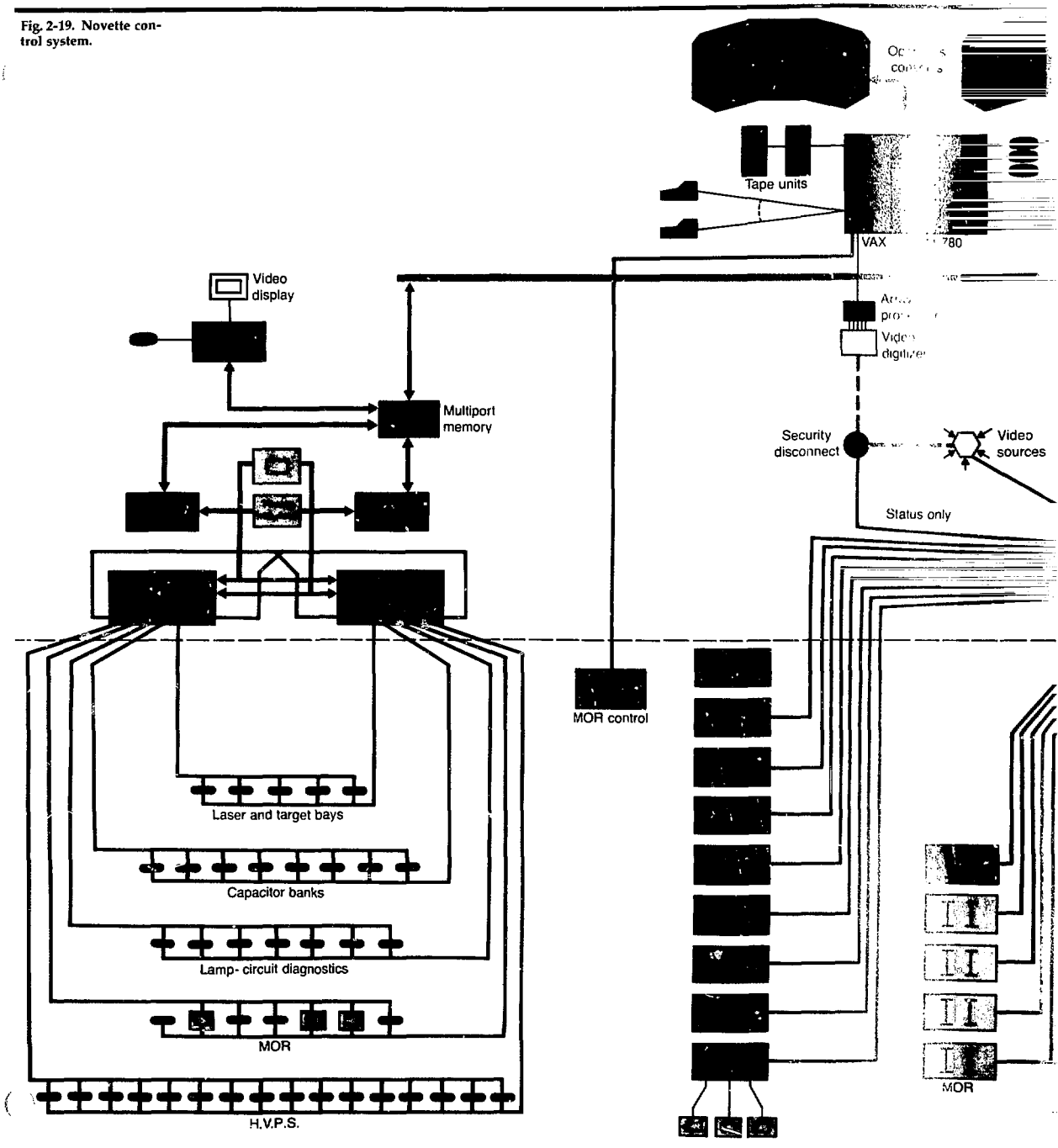

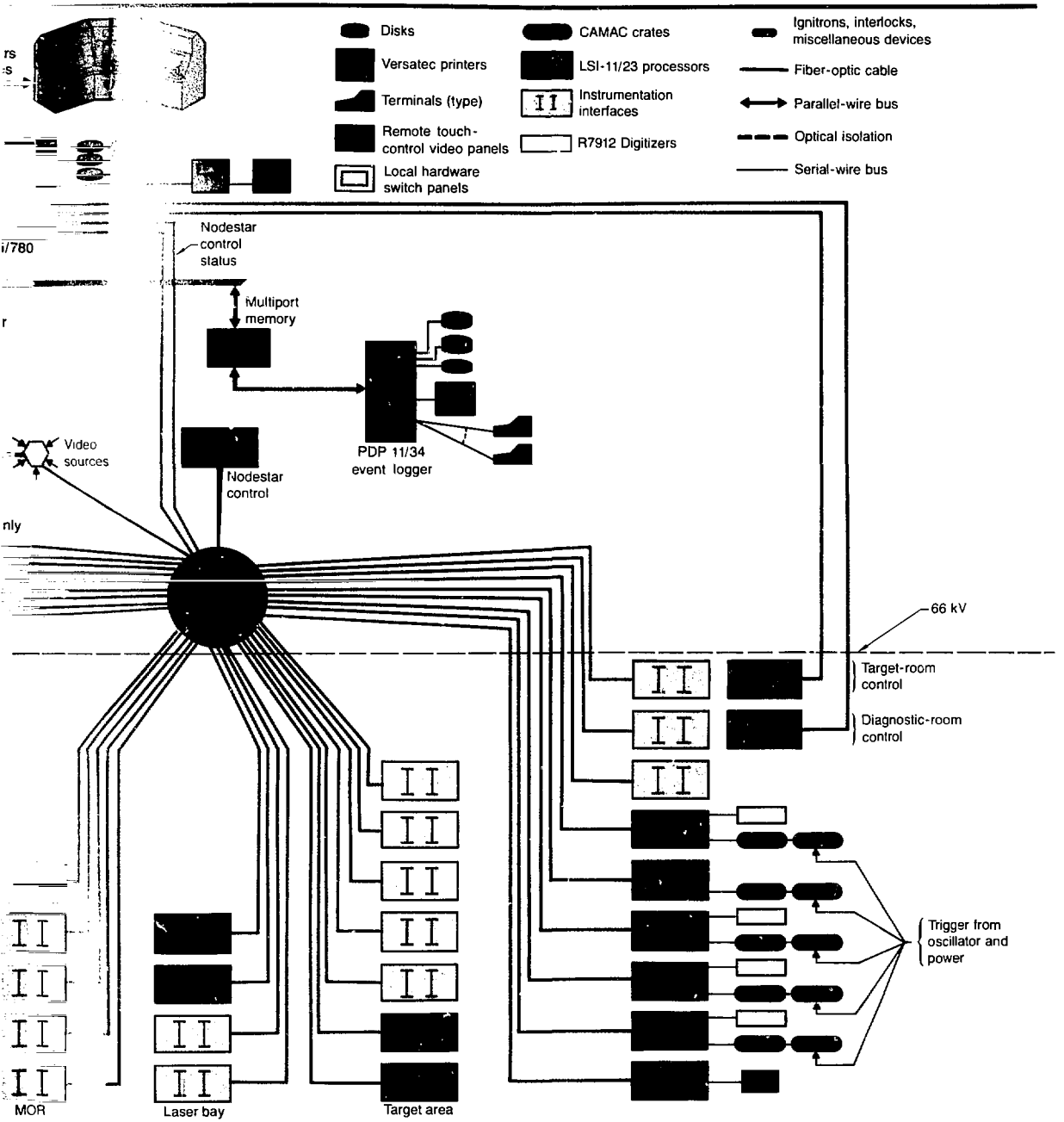

Laser diagnostics **Target diagnostics**

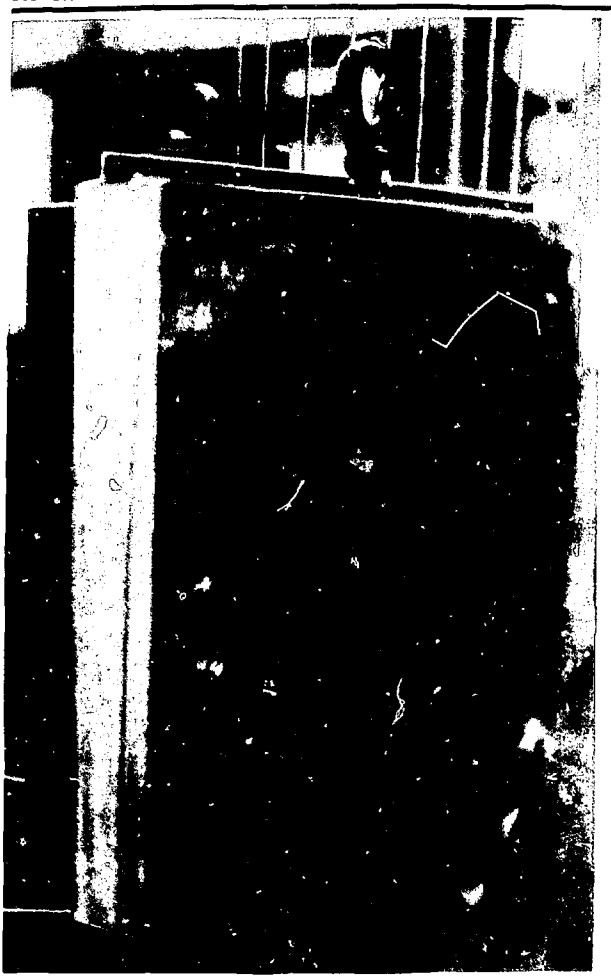

Fig. 2-20. A 15- × 15- × 1.8-cm KDP crystal blank mounted on a diamond-turning machine prior to a face-cutting operation.

systems will utilize Nova concepts, except where manpower or time limitations restrict implementation.

Of Novette's target experimentation time, we plan to devote one-half to high-density implosion studies, one-fourth to scaling experiments, and the remaining one-fourth to plasma-physics experiments in support of military applications.[26] Table 2-4 summarizes the initial diagnostics planned for these tasks. We will have the capability to measure neutrons, x rays, scattered and reflected light, and target-fuel density. We will be able to temporally resolve most of these emissions, to resolve spectra, and to acquire images. (For detailed descriptions of these diagnostics, see Section 5 and previous *Laser Program Annual Reports*.)

Chamber and Spaceframe. Laser fusion diagnostics require special care in positioning, along with careful spaceframe design to eliminate conflicts with the frame members. Figure 2-21 shows the kind of scale model that helped us plan diagnostic placement on Novette. In orienting the target chamber we chose a spherical coordinate system that provides a convenient θ, ϕ designation for diagnostic locations (Fig. 2-22). Figure 2-23 shows, in polar projection, the location of the target chamber of ports for diagnostics and target equipment. The ports suitable for large diagnostics are oriented between $\theta = 45°$ and 135°, necessitating fan-shaped mounting areas north and south of the chamber. (The spatial resolution of many diagnostics is limited to a range of just a few micrometres; these diagnostics must be very stable with respect to the target, so we have provided a wide spaceframe both to the north and south of the target chamber.)

A series of ladders and catwalks provide access to the target chamber and diagnostics. To enhance future operational capability, we have also provided for access to several isolated areas within the target-chamber area.

We positioned the target chamber in the target bay so that the entire Novette system would fit into the existing Argus high-bay area.[30] Although the center of the chamber is 12 ft above the high-bay floor, we determined that the 22× microscope and the Shiva filter-fluorescer diagnostics could be installed on Novette only if their lines of sight (LOS) penetrated the high-bay floor and their detector stations were situated in the basement. We drilled eight holes in the floor to accommodate both known and future diagnostic and equipment requirements. We also provided an LOS to the Argus neutron time-of-flight facility, even though this diagnostic is not initially needed for Novette. Implementing this LOS required cutting through the webbing of one of the high bay's supporting H-columns.

To save money and space, we combined the target and laser bays into one room by removing the curtain that separated the bays on Argus. This is a departure from the separate-room system philosophy previously implemented on Argus and Shiva and

to be implemented on Nova. Since we will no longer be able to separate laser and target activities as we have in the past, we will need much closer coordination of these operations.

Basement and Diagnostic Room. We allocated basement space between power conditioning and target diagnostics, with target systems occupying the area from beneath the target chamber to the east end of the bay. In addition to providing space for diagnostic expansion into this area, we plan to develop two laboratory areas here: one for the radiation-chemistry diagnostic and one to be shared by the optical spectroscopy and 4ω probe diagnostics. The basement location for radiation chemistry provides good shielding from background radiation (due to the three-foot concrete floor above) and allows for gravity feed of the collector up.

We will refit the old Argus diagnostic room for Novette diagnostics. Nearly all of the electronics data-acquisition system will be located here, outside the target room. No personnel hazard exists outside the target room from either neutrons or x rays for the maximum laser-shot energy of 30 kJ. Nevertheless, we added 1 in. of lead shadow shielding to the wall separating the target room from the diagnostic room to prevent target-generated x rays from inducing noise in our instruments.

A total of 22 equipment racks and 2 control racks will be installed in four groups in the diagnostic room. Each group will be individually connected to a special independent instrumentation ground established through the building foundation beneath

Table 2-4. Initial Novette target diagnostics.

Diagnostics	Previous use
Energy-balance system	Shiva; modified for 2ω and 3ω
Dante H x-ray spectrometers (2)	One from Shiva; one new
Soft x-ray streak camera	Shiva
22× x-ray microscope with streak camera	Shiva
8× x-ray microscope	Shiva
Zone-plate camera	Shiva
Pinhole cameras (2)	Shiva
Filter fluorescer x-ray spectrometer	Argus
Optical x-ray streak camera (0X-2)	New
Henway x-ray spectrograph	Shiva
ALICS x-ray spectrograph	Shiva
4ω probe	New
Cassegrain telescope (optical imaging system)	New
Optical spectroscopy	Shiva
Radiochemistry	Shiva
Lead neutron counter	Shiva
Copper neutron counter	Shiva

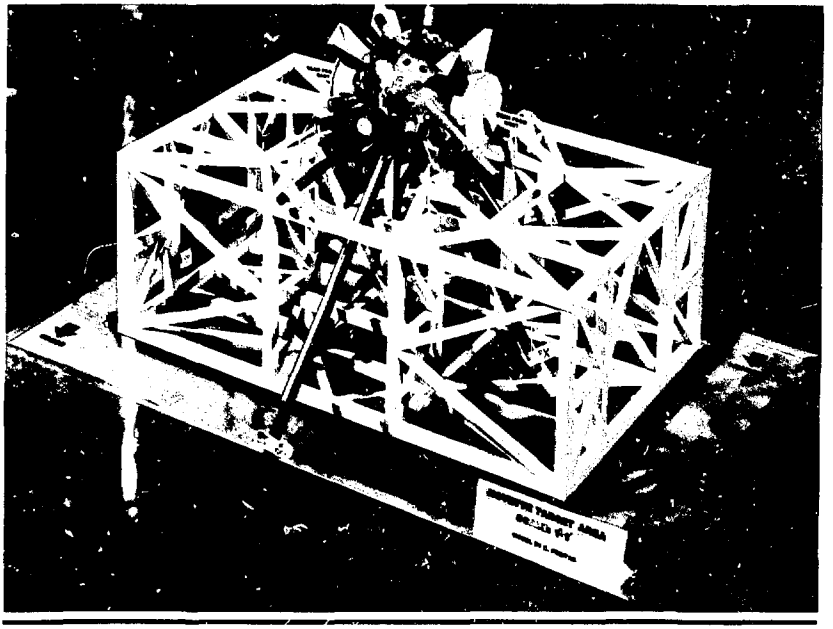

Fig. 2-21. Novette target-chamber model with selected diagnostics. Target chamber is 1.6 m in diameter.

the room. Racks will be supplied with isolated clean power; instrument cooling within the racks will be independent of the diagnostic-room climate control. Isolated signal cableways will connect the room with both the target room and the basement. Isolated fiber-optic cableways will provide communication and trigger-signal paths to the control room and other parts of the data-acquisition system.

We removed an Argus neutron time-of-flight water-barrier shield to free the space for vacuum-roughing equipment. This building at the northeast corner of the high bay will house three roughing modules and six cryopump compressors. Four access holes were drilled through the wall into the target bay for roughing and cryo lines and for control cabling.

Diagnostic Data Acquisition. Target-diagnostic data acquisition on Novette will combine established system practices with new system concepts. For example, the target-diagnostic system will be grounded independent of other Novette diagnostic systems. Detectors will be isolated from their instruments, and ground loops will be prevented by the use of fiber-optic links to communicate between parts of the system.

On the other hand, the digital data-quisition system will be of Nova design d will differ significantly from the Argus

Fig. 2-22. The Novette target-chamber coordinate system.

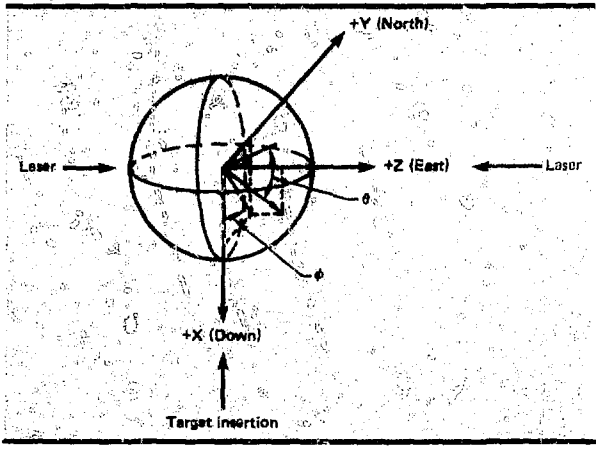

Fig. 2-23. Many diagnostics and target equipment locations have been chosen for Novette. The east laser beam is at the center of the plot.

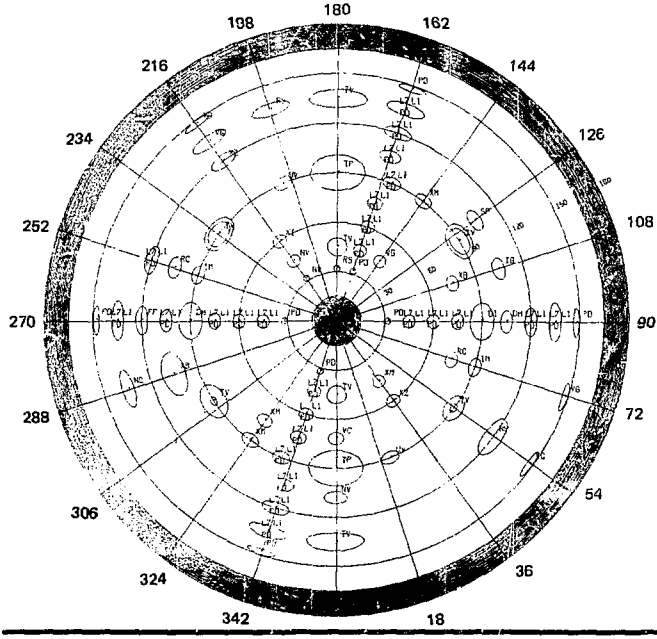

Novette target chamber diagnostic status

Laser light	65
X-ray	52
Neutron	4
Ion/plasma	25
Alpha particle	0
Target equipment	23
Total	169

and Shiva systems. Digital data-acquisition will again be a CAMAC-based system relying on existing front-end equipment: Tektronix R7912 transient digitizers, Le Croy 2249W and LLNL-programmable charge integrators, programmable gain amplifiers, calorimeter digitizers, and oscilloscopes. Figure 2-24 shows this system; a detailed description is given in "Control Systems," later in this section. The digital data-acquisition system relies on a target-systems configuration stored and accessed by ORACLE, a commercial data-base system (the target chamber diagnostic plot shown in Fig. 2-23 was generated by ORACLE).

We made provisions in the MOR to generate three optical signals for target diagnostic a trigger pulse, a fiducial pulse, and a 4ω probe pulse. Each has independent access to the laser bay.

The Novette diagnostic triggering system will use the Shiva system hardware with minor modifications. In the MOR, we will receive a portion of the switched-out long- or short-pulsed oscillator signal and transmit it to the diagnostic room via a fiber-optic cable. This optical signal will be detected, a delay will be added electronically to compensate for different propagation times, and the signal will be regenerated. Trigger signals will be distributed via fiber-optic and transformer-isolated electrical cables.

Optical and electrical timing fiducials that accurately represent the target-irradiation 2ω pulse shape are required by several diagnostics for picosecond timing measurements and for studies involving comparisons of waveshape variations. A plan for acquiring and recording these 2ω target-irradiation pulse-envelope signals at the correct time is under consideration; however, it will be extremely difficult because of the geometry of the 2ω optical components. Alternatively, we are also considering a plan for generating electrical fiducials using the trigger system as a source.

Target Chamber. We have adapted the Shiva target chamber for Novette by rotating its vertical axis to the horizontal and aligning the chamber east and west. We will remachine the diagnostic ports to correct the misalignment caused by weld shrinkage when the Shiva chamber was fabricated. During the remachining process,

- A new neutron LOS will be added.
- Eight ports will be enlarged to accommodate the new viewing optics and to provide a port for an x-ray backlighting beam.

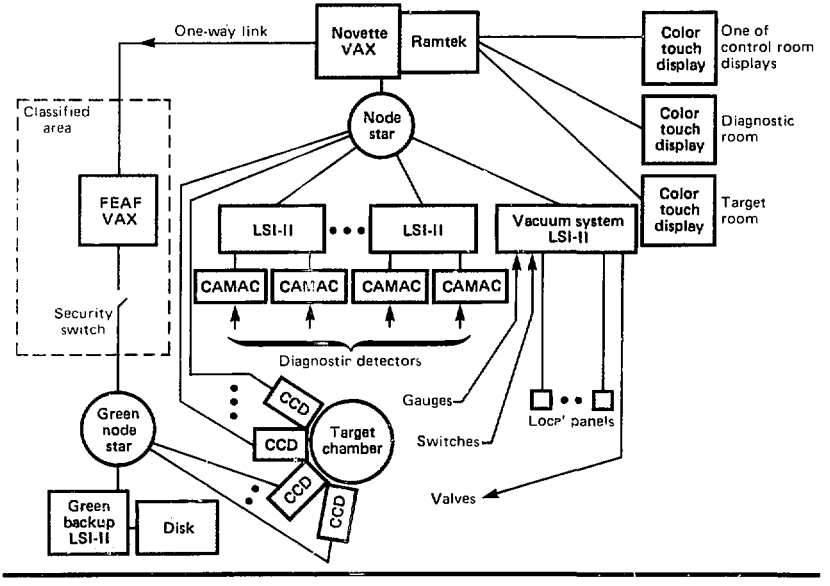

Fig. 2-24. The architecture of Novette's data-acquisition system.

- The true angles of the diagnostics ports, relative to the three major axes, will be determined.

The chamber, in this horizontal attitude, will be supported by 4 of the 10 gussets used on Shiva. However, cross bracing to the remaining gussets will redistribute the loads around the chamber and reinforce the bridge in the spaceframe. Welded supports have been fabricated out of 0.5- and 0.75-in.-thick plates; with mating parts, these supports will gird the box steel of the spaceframe in four places. The supports have several screw-adjusting feet that will allow for x-y-z alignment of the chamber to the theoretical z-centerline position.

Figure 2-25 shows the target chamber, including the sections for the vacuum pumps and the KDP frequency-conversion module. There are additional supports at the ends of the 47-in. extension spools—to couple to the chamber and the Nova lens positioners—and at the KDP module. Each spool houses a laser-diagnostic whole-beam calorimeter that can be inserted into the beamline, when required.

The Nova focus-lens system will be used on Novette; this system is comprised of an f/4 doublet lens, with the first lens acting as the vacuum barrier. The lens package is being designed to accommodate a full range of beam colors (red, green, and blue) with minimum disassembly. This requires an axial translation of the lens doublet of 14 in. In addition, the second lens must be displaced and tilted relative to the first lens to direct the diagnostic beam (which reflects off the final uncoated surface) into the incident-beam diagnostic package. A detailed discussion of the lens and frequency-conversion systems may be found in "Frequency Conversion and Target Conversion," later in this section.

We will use the Shiva target-positioning system on Novette, but with target insertion oriented vertically instead of horizontally. We anticipate no adjustment problems with this change, so no hardware modifications will be needed.[31] This system will accommodate cryogenic targets using a new pylon now under design by target fabrication.

The existing Shiva local-control target-positioning processor and software will be used with only a slight software modification. On Novette, the target viewers will no longer be orthogonal to the inserter (see Fig. 2-22). A software transformation of coordinates will allow the target to track the viewer axes; this will ease the job of manually positioning the target.

The target-positioning control system will operate only in a local mode at the front-end processor, with additional pendant controls near the chamber and at the 22× microscope. We will not integrate the target-positioning system into Novette's central controls because of the effort required to install Novanet into the existing software. Thus, all target manipulations will be done from the target room.

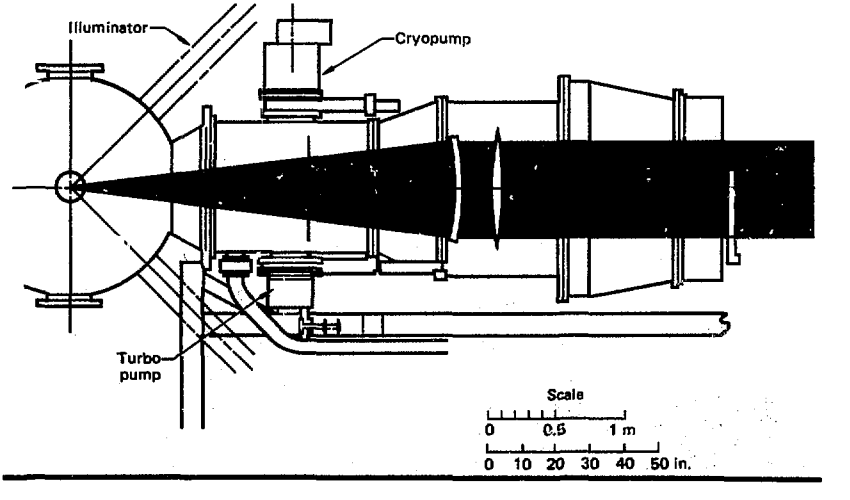

Fig. 2-25. The Novette 2ω-conversion-crystal array, focusing lenses, and vacuum system integrated with the modified Shiva target chamber.

Both Shiva target viewers will be installed on the target chamber early in the activation phase to allow definition of target-chamber center. Viewer control will be via the Shiva local-control processor used for the target inserter.

Four new target viewers will become available for installation on the target chamber later in the activation phase.[32] We will adapt a Shiva stand-alone LSI-11 stepping motor controller (B-processor) to drive the motors. Additional hardware panel controls will be provided for on-off functions, including ac power to TV cameras and illumination lasers. These panels will also provide voltage-level setting for the liquid-crystal cells that control the illumination-source output for each viewer.

The new viewer-control hardware system will be compatible with Nova-type stepping-motor controls; all cabling will be plug-compatible. This allows for future upgrading of this system with the enhanced Nova stepping motor controller (see "Control Systems," later in this section); integration into the Novette central control system will then be possible.

Vacuum System. Three independent pumping systems comprise the Novette vacuum system: two for evacuating the target chamber, and an auxiliary system for diagnostic preparation. The roughing pumps reside in a mechanical pump room at the east end of the target bay and are connected to the chamber and diagnostics via three 4-in. lines. Pressure in these lines will be about 1 Torr. High-vacuum pumping in each subsystem will be provided by cryo and turbo pumps, with the base pressure expected to be approximately 10^{-6} Torr. Two independent cryo-turbo pairs will pump the target chamber, although crossover roughing lines allow for operation of both when one roughing module is down.

The extension spools that couple the lens positioner to the chamber allow the turbo and cryo pumps to be directly coupled to the chamber system; the turbo pumps are suspended beneath and the cryo pumps are positioned on top. Our pumping rate is expected to be 5000 litre/s; with the close-coupled arrangement just described, we will exceed the Shiva pumping capacity, even with the tripling of the chamber volume due to the spools. The roughing modules for this system will come from Shiva; the 8-in. turbos come from Argus; the 12-in. cryos were purchased as test pumps for Nova. Six cryo compressors will also be housed in the pump room; these compressors will provide sufficient capacity for initial and future cryo pumping needs. A quadrupole mass spectrometer, in conjunction with one of the turbo pumps, will be used for leak checking.

Nova vacuum controls with hardware control panels will be used. All valves will incorporate either a microswitch or an air-pressure switch to provide status signals for the control system. For a more detailed discussion of vacuum-system controls, see "Control Systems," later in this section.

Authors: C. E. Thompson, J. E. Field, and P. J. VanArsdall

Major Contributors: D. E. Campbell, E. M. Campbell, K. R. Manes, M. W. Kobierecki, F. Rienecker, V. C. Rupert, T. L. Schwab, and J. R. Severyn

Nova

Introduction

The Nova laser is a large Nd:glass system that is currently under construction. When complete, Nova will be the primary laser-driven inertial-confinement fusion (ICF) experimental facility in the mid-1980s, providing the next logical increase in laser energy over the 10-kJ Shiva system. The primary programmatic objective for Nova is demonstrating the ignition of thermonuclear burn—a crucial step toward the demonstration of feasible laser-driven inertial fusion. Nova's energy levels and proposed wavelength flexibility will allow us to improve our understanding of the absorption mechanisms and implosion processes of ICF physics. Nova will also enable us to define target physics for more advanced laser drivers now under development.

Nova was originally authorized by Congress, at $195 million, as a 20-beam system operating at 1.05 μm and producing 200 to 300 kJ. Phase I of the Nova project involves construction of a 59 000-ft^2 office building, construction of a 115 000-ft^2 laboratory building, and installation of a 10-beam

Nd:glass laser system adjacent to the existing Shiva facility (see Fig. 2-26). Nova's Phase I operating criteria proposed to the Department of Energy (DOE) are:

- Energy of 80 to 120 kJ in 3-ns pulses at 1.05 μm.
- Energy of 50 to 80 kJ, with frequency conversion to the second harmonic (2ω = 0.53 μm).
- Energy of 40 to 70 kJ, with frequency conversion to the third harmonic (3ω = 0.35 μm).

During Phase II, the remaining 10 Nova beams are to be installed in the Shiva building. The full Nova complement of 20 beams will be brought to an integrated target chamber in two opposed clusters of 10 beams each (Fig. 2-27).

Nova's cost and completion date are dependent upon available funding levels in fiscal years 1982 through 1984. Entering FY 1982, we were authorized by DOE at a cumulative total of $104 million. The Congress has passed a bill authorizing an additional $37.5 million for FY 1982, although the Office of Management and Budget and DOE have not yet released these funds. Should these funds be released in a timely manner, Phase I of Nova can be completed in FY 1984 for a total cost of $176 million, if

- The scope of the project is modified to include wavelength conversion.
- The remaining funds for completion ($34.5 million) are authorized in FY 1983.

As 1981 began, we had received permission from the DOE Assistant Secretary for Defense Projects to proceed with the full Nova project: a 20-beam system that includes wavelength conversion to 2ω and 3ω. Before we could implement this configuration, however, an Energy Systems Acquisition Advisory Board (ESAAB) had to affirm the 1980 DOE decision. With the changing administration and new DOE personnel, the ESAAB hearing originally scheduled in December 1980, and subsequently rescheduled several times, did not occur.

Although full Nova remains an option, events since 1980 dictate that Phases I and II be accomplished serially. Whether Phase II is built depends on the funding situation for Nova, which is unclear as we enter calendar year 1982. We are currently authorized to obligate $108 million to Nova through FY 1982; however, the Congress has recommended that this appropriation be extended to $141.5 million in accordance with full-Nova funding plans. We have generated a plan for Nova construction that encompasses serial Phase I-Phase II implementation with both 2ω and 3ω capability, and we are proceeding with this plan pending more definitive direction.

Fig. 2-26. Phase I of the Nova laser system.

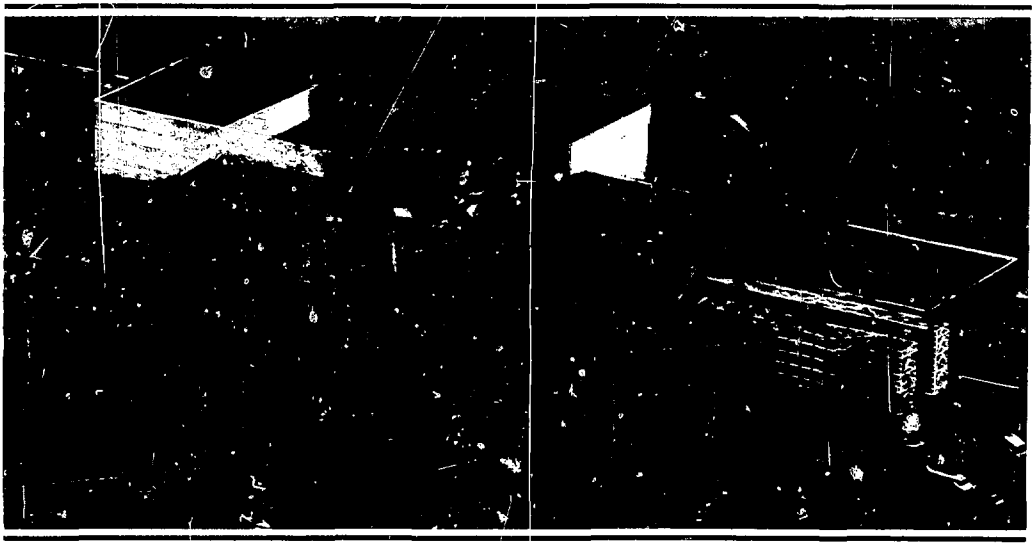

Current Status. In June of 1981, we began to execute our Nova Phase I procurement plans. Included in these procurements were options for the full-Nova materials quantities; these options expire early in 1982. We also envisioned, and began in earnest to plan and construct, a two-beam Nova prototype system, called Novette, consisting of two Nova arms. (Novette is described in detail earlier in this section.) Novette, which includes wavelength conversion to 0.53 μm, will be completed in late 1982. We have continued with plans and designs for converting both Phase I and full Nova to 2ω and 3ω, using operating funds to procure long-lead-time items such as large harmonic-conversion KDP crystals. In anticipation of implementing frequency conversion on Nova, we conducted a semiannual review on September 24, 1981, for representatives from the DOE Office of Inertial Fusion and from the DOE San Francisco Office.

As calendar year 1981 closed, we had placed orders for all of the optical components (including phosphate laser glass) for 10 Nova beams. We have also ordered the target chamber. The laboratory and office buildings are both virtually complete, and we expect to take occupancy in 1982 (see "Conventional Facilities," later in this section). The Argus laser system has been shut down, allowing construction of the Novette system to get under way. The Shiva laser system has also been shut down to provide laser and target-chamber hardware for Novette.

During 1981, we made progress in various aspects of our laser engineering effort. Through a continuation of the formalized design-review process begun in 1980 (see "Project Management Systems," later in this section), we have solidified our Nova subsystem and component criteria. In addition, we have started testing prototype components and subsystems in the power-conditioning and controls test facilities. These evaluations are aimed at

- Achieving higher-fluence damage thresholds on production-component surfaces (see "Damage Studies" in Section 7).
- Demonstrating a working, system-compatible plasma shutter for protection of the laser chain against target back-reflections (see "Plasma Shutter" in Section 7).

The remaining laser subsystems are in various stages of final design and procurement activities, as described in the following articles. Altogether, a total of $33 million in

Fig. 2-27. The full Nova system.

laser-related contracts was awarded in 1981.

Figure 2-28 is an artist's rendering of the Nova target chamber. The west beams are equally spaced on the surface of a cone whose vertex is at the target. These beams are opposed by the east beams so that east and west beams radiate through a coordinate system centered at the target. Figure 2-28 is illustrative of the full 20-beam system; for 10 beams, alternate openings would be missing, although beams would still be opposed in pairs. The initial (baseline) choice of cone angle is 100°, and the focusing length is 3 m. This configuration will allow for a full complement of experimental and diagnostic instruments, some of which are shown in Fig. 2-28. The Nova target chamber is discussed in detail in "Target Systems," later in this section. In experiments with the Argus laser system, we have demonstrated that, by using the nonlinear optical properties of potassium dihydrogen phosphate (KDP) crystals, we can double or triple the frequency of the basic 1.05-μm wavelength from high-power Nd:glass lasers with conversion efficiencies exceeding 70%. Since shorter wavelengths are much more favorable for the physics of ICF laser-target interactions, we are planning to implement frequency conversion in the Nova system. If this plan is approved by DOE, we will able to focus ~80 kJ of green (0.53 μm) light or ~70 kJ of blue (0.35 μm) light onto laser-fusion targets with 10 Nova beams. We have designed the Nova frequency-conversion scheme in some detail (see "Frequency Conversion and Target Focus," later in this section).

It is possible that advanced Nova targets will require higher-energy pulses of longer duration than those presently envisioned. Additionally, future experiments on Nova call for temporally shaped pulses that will require additional amplifiers with reserves

Fig. 2-28. The Nova target chamber and some of the major diagnostics instrumentation.

of both power and energy. In anticipation of these requirements, we have allocated space within the Nova baseline chain layout for additional amplifiers in both the penultimate 31.5-cm-amplifier stage and the final 46-cm-amplifier stage. There is also space in the laser bay for additional (but smaller) amplifier chains, as adjuncts for extended target diagnostics.

Summary. The first phase of the Nova project is well under way. The buildings are more than 90% complete, the laser is in the final detail-design phase, and most of the long-lead-time laser components have been ordered. Our calculations indicate that the Nova laser system will perform at the upper end of the predicted performance range. We are preparing to incorporate frequency conversion to 2ω and 3ω into the laser system as part of Phase II, which is still subject to DOE approval at this time.

Authors: R. O. Godwin and W. W. Simmons

Nova System Design and Performance

Design Considerations. We have designed the Nova laser system with master-oscillator, power-amplifier (MOPA) architecture. A laser pulse of controlled temporal shape is first generated by the oscillator, then preamplified, and then split into 20 beams (10 beams in Phase I). After traversing an adjustable optical-delay path (used to synchronize the arrival of the various beams at the target), the pulse enters the amplifier chain. This chain consists of

- A rod amplifier and several disk amplifiers to increase the pulse power and energy.
- Spatial filters to maintain the spatial smoothness of the beam profile while expanding its diameter.
- Isolators (Faraday rotators and Pockels cells) to prevent the entire laser from breaking spontaneously into oscillations that could drain its stored energy and damage the target prematurely.
- A plasma shutter located at the focus of the last spatial filter to protect the laser chain from target back-reflection.

A schematic layout of the entire chain is shown in Fig. 2-29. Fluence and energy along the chain were calculated with the SNOBOL code, at a maximum on-target energy of 15.6 kJ for one beam.

The beam is collimated between spatial filters; thus, each of the components in a particular section has the same diameter. In the 4.0-cm-diam section, the amplifier is a single glass rod, and the isolator is an electro-optic Pockels-cell crystal placed between crossed polarizers. This cell operates as a fast (10 ns) optical gate, preventing interchain oscillations and, at the same time, reducing unwanted amplified spontaneous emission (ASE) to tolerable levels. ASE is radiation at the laser wavelength, amplified by passage through the chain, that can strike and damage the target before the laser pulse arrives. We anticipate reusing the Pockels cells from Shiva on Nova. In all larger-diameter sections, the amplifiers consist of face-pumped disks set at Brewster's angle to the passing beam. In Fig. 2-29, we summarize the energy-storage and gain characteristics of the various Nova amplifiers.

We have optimally designed our spatial filters to provide entrance-lens-to-entrance-lens imaging. Thus, a smooth beam-intensity profile is projected along the chain, and energy extraction by the laser pulse is maximized. Figure 2-29 shows the maximum energy output, fluence, energy, and energy extraction along the various chain portions for 3-ns operation.

When the pulse exits from the final beam-expanding spatial filter, it has been amplified to an energy level of 10 to 15 kJ, and its diameter is 74 cm. Turning mirrors direct the beam to the target chamber, where focusing lenses concentrate it on the target. The first of the turning mirrors is partially transparent, allowing approximately 2% of the pulse to enter the output-sensor package. This diagnostic unit senses and reports on the alignment status, energy and power, spatial quality, and other characteristics of the beam. A plasma shutter located at the focal position of the final spatial filter protects the laser by preventing light reflected from the target from reaching the laser amplifiers. In the absence of this protection, such light would travel back down the chain (being amplified in the

process) and might destroy some of the optical components.

Neutral-Solution Processing. The fluence (energy per unit area) at which optical components suffer damage has been the subject of intense investigation and improvement. In each section of the Nova laser chains, the beam is amplified to near the lens-damage threshold for maximum energy output at a specified pulse duration. This "isofluence" design maximizes the energy output per unit cost while keeping the chain, as a whole, below the component-damage limit.

Perhaps the most exciting development during 1981 was the demonstration that neutral-solution (NS) processing of the surfaces of conventional silicate glasses could yield surfaces with both very low reflectivity and high damage thresholds. The NS processing technology, developed by Schott Optical Company, supplants previous developmental anti-reflective (AR) technologies based upon special phase-separable glasses, as discussed in the *1980 Laser Program Annual Report*.[33] Our tests with NS processing during the year have given us high confidence that

- The NS process is controllable; it can be applied to lens surfaces without substantially affecting their figure and wavefront quality.
- The damage threshold of NS-processed components is characteristic of that for "bare" surfaces (referred to in previous *Laser Program Annual Reports* as the "B"-level damage fluence) and may, in fact, be higher.
- Damage thresholds of NS-processed components appear to have a square-root-of-time dependence, as illustrated in Fig. 2-30. For the data in this figure, we measured the front and back surfaces of two samples of freshly cleaned, NS-processed BK-7 (the straight line is included for reference).
- NS processing can yield surface reflectivities less than 0.1% at a single wavelength (1.05 μm, for the spatial filter lenses within the amplifier chain).

Implementation of NS processing has substantially influenced performance projections for the baseline Nova chain. As shown in Fig. 2-31, NS processing represents an improvement of ~10% in laser performance at 1 μm. The lower curves represent "B"-fluence damage limits with uncoated spatial-filter entrance lenses; the upper curves show improved performance, at the same damage limits, when the Fresnel losses of these lenses are eliminated by NS processing (discussed further in the following article).

Baseline Chain Layout. The layout of one Nova baseline chain is shown in Fig. 2-32. In general architecture, this layout resembles the chain layout presented in previous *Laser Program Annual Reports*. The significant changes are twofold. First, the thickness of the 20.8-mm-diam amplifier disks has been increased (from 25 to 30 mm), giving increased energy performance at 1 ns. Second, the spatial-filter lenses are now NS-processed BK-7 rather than uncoated lenses; with this change, the Fresnel reflection losses at each surface are reduced from ~4% to near zero.

We have taken ghost foci into account in laying out the baseline chain, locating components near spatial filters to avoid the occurrence of such foci within any glass material. Also, the entrance lenses of the spatial filters are of meniscus design to help minimize the effect of ghost foci.

Baseline Performance at 1.05 μm. Full-system simulations using our comprehensive modeling code, MALAPROP, have resulted in the performance profiles shown in Fig. 2-33. This figure gives plots of peak and mean beam fluence, as a function of distance along the chain, for several pulse durations spanning the range of interest to Nova design. Locations of the spatial-filter lenses are indicated by the "bowties" at the top of the figure. On-target energy for the indicated pulse duration is inset. "B"-fluence thresholds for AR-coated target lenses and NS-processed spatial-filter lenses are shown as dashed lines. Average beam fluences are represented by dots. In each case, the calculations were done at that performance level representing the onset of damage to the most susceptible component; except at 1 ns, this component is the target-focusing lens system.

At the shortest pulse durations, we observed significant growth of the peak-to-average ratio throughout the beam-transport space between the final spatial filter and the target-focusing optics. This is

a manifestation of self-focusing attributed to the nonlinear index of the glass in the laser chain and to the nitrogen in the 50-m air path through which the beam is passing.

As the pulse duration increases, beam intensity decreases and this nonlinear effect dies away. At the longest pulse duration (3 ns), the chain is running near "isofluence" conditions, and the beam extracts 50% of the stored energy in the final 46-cm

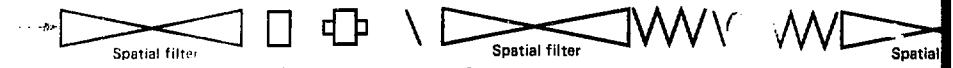

	Beam-forming aperture	Entrance lens	Pinhole	Exit lens	Rod amplifier	Pockels isolator	Input sensor splitter	Entrance lens	Pinhole	Exit lens	Disk amp	Faraday	Disk amp	Entrance lens	Pinhole
Beam diameter (cm)	2.7	2.7		3.75	3.75	3.75	3.75	3.75		9.2	9.2	9	9.2	9.2	
Long pulse (>3 ns) energy (J)	0.428	0.424		0.420	8.52	7.41	7.19	7.12		7.05	45.5	40	203	201	
Max fluence (J/cm^2)		0.11		0.05	1.10	1.1	1.0	1.0		0.15	0.64	0.5	2.9	4.7	
Component transmission (cold)	0.63	0.99	1.0	0.99	0.92	0.87	0.94	0.99	1.0	0.99	0.94	0.94	0.94	0.99	1.0
Small-signal gain					25						7.4		7.4		
Saturated gain					20.3						6.46		5.07		
Disks/module					Rod						6		6		
Stored energy/disk (kJ)					0.3						0.2		0.2		
Specific gain (cm^{-1})					0.067						0.116		0.116		
⌀D					–						2.2		2.2		
Disk thickness (cm)					48						2.4		2.4		
Extraction efficiency					0.27						0.032		0.14		

	Folding mirror	Faraday isolator	Disk amp (space)	Disk amp	Disk amp	Disk amp	Disk amp	Entrance lens	Pinhole	Exit lens	Disk amp (space)	Disk amp (space)	Slot aperture	Disk amp	Disk
Beam diameter (cm)	31.5	31.5	31.5	31.5	31.5	31.5	31.5	31.5		46	46	46	46	46	
Long-pulse (>3 ns) energy (J)	2326	2047	(–)	3012	4233	5683	7316	7243		7171	(–)	(–)	6884	10040	13
Max fluence (J/cm^2)	4.40	4.09		3.62	5.10	6.84	8.80	14.43		6.22			6.16	5.66	
Component transmission (cold)	0.99	0.88	(–)	0.97	0.97	0.97	0.97	0.99	1.0	0.99	(–)	(–)	0.96	0.97	
Small-signal gain				1.78	1.78	1.78	1.78							1.93	
Saturated gain				1.47	1.41	1.34	1.29							1.46	
Disks/module				2	2	2	2							2	
Stored energy/disk (kJ)				1.8	1.8	1.8	1.8							4.1	
Specific gain (cm^{-1})				0.056	0.056	0.056	0.056							0.062	
⌀D				3.4	3.4	3.4	3.4							3.2	
Disk thickness (cm)				4.3	4.3	4.3	4.3							4.3	
Extraction efficiency				0.27	0.34	0.40	0.44							0.38	

large-aperture frequency conversion. Various aspects of this development are re-

ing them with new instruments for specialized measurements. The Novette control

a manifestation of self-focusing attributed to the nonlinear index of the glass in the laser chain and to the nitrogen in the 50-m air path through which the beam is passing.

As the pulse duration increases, beam intensity decreases and this nonlinear effect dies away. At the longest pulse duration (3 ns), the chain is running near "isofluence" conditions, and the beam extracts 50% of the stored energy in the final 46-cm

	Beam-forming aperture	Entrance lens	Pinhole	Exit lens	Rod amplifier	Pockels isolator	Input sensor splitter	Entrance lens	Pinhole	Exit lens	Disk amp	Faraday	Disk amp	Entrance lens	Pinhole	Disk amp	
Beam diameter (cm)	2.7	2.7		3.75	3.75	3.75	3.75	3.75		9.2	9.2	9	9.2	9.2		9.2	9.2
Long-pulse (>3 ns) energy (J)	0.428	0.424		0.420	8.52	7.41	7.19	7.12		7.05	45.5	40	203	201		203	
Max fluence (J/cm^2)		0.11		0.05	1.10	1.1	1.0	1.0		0.15	0.64	0.5	2.9	4.7		2.9	1.7
Component transmission (cold)	0.63	0.99	1.0	0.99	0.92	0.87	0.94	0.99	1.0	0.99	0.94	0.85	0.94	0.99	1.0	0.94	0.99
Small-signal gain					25						7.4		7.4			7.4	
Saturated gain					20.3						6.46		5.07			5.07	
Disks/module					Rod						6		6			6	
Stored energy/disk (kJ)					0.3						0.2		0.2			0.2	
Specific gain (cm^{-1})					0.067						0.116		0.116			0.116	
αD					–						2.2		2.2			2.2	
Disk thickness (cm)					48						2.4		2.4			2.4	
Extraction efficiency					0.27						0.032		0.14			0.14	

	Folding mirror	Faraday isolator	Disk amp (space)	Disk amp	Disk amp	Disk amp	Disk amp	Entrance lens	Pinhole	Exit lens	Disk amp (space)	Disk amp (space)	Slot aperture	Disk amp		Slot aperture	amp
Beam diameter (cm)	31.5	31.5	31.5	31.5	31.5	31.5	31.5	31.5		46	46	46	46	46		46	46
Long-pulse (>3 ns) energy (J)	2326	2047	(–)	3012	4233	5683	7316	7243		7171	(–)	(–)	6884	10040	13	6884	10040
Max fluence (J/cm^2)	4.40	4.09		3.62	5.10	6.84	8.80	14.43		6.22			6.16	5.66		6.1	5.66
Component transmission (cold)	0.99	0.88	(–)	0.97	0.97	0.97	0.97	0.99	1.0	0.99	(–)	(–)	0.96	0.97		0.97	0.97
Small-signal gain				1.78	1.78	1.78	1.78							1.93			1.93
Saturated gain				1.47	1.41	1.34	1.29							1.46			1.46
Disks/module				2	2	2	2							2			2
Stored energy/disk (kJ)				1.8	1.8	1.8	1.8							4.1			4.1
Specific gain (cm^{-1})				0.056	0.056	0.056	0.056							0.062			0.062
αD				3.4	3.4	3.4	3.4							3.2			3.2
Disk thickness (cm)				4.3	4.3	4.3	4.3							4.3			4.3
Extraction efficiency				0.27	0.34	0.40	0.44							0.38			0.38

Nova

the damage threshold of uncoated surfaces and was at least twice that of thin-film

ture of 5 cm. Next come the round-disk amplifiers, which have apertures of 10 and

amplifier. When damage fluence levels at the target lens become higher, we can add additional amplifiers in the final stages to reach still higher energy outputs.

Our baseline-chain performance estimate are summarized in Fig. 2-34, which illustrates the "safe" performance region for one [illegible] chain. If the beam were perfectly [illegible]th spatially, and if it filled 70% of the [illegible]able amplifier aperture, the laser could

Fig. 2-29. Nova chain-component parameters, amplifier characteristics, and element performance for a 3-ns pulse under isofluence conditions.

Disk amp	[illegible] lens	Pinhole	Exit lens	Faraday isolator	Disk amp	Entrance lens	Pinhole	[illegible]
9.2	.2		15	15	15	15		20.8
203			199	183	559	554		548
2.9	1.7		1.63	1.61	2.97	4.89		2.32
0.94	0.99	1.0	0.99	0.92	0.95	0.99	1.0	0.99
7.4					4.2			
5.07					3.06			
6					4			
0.2					0.53			
0.116					0.100			
2.2					3.C			
2.4					3.0			
0.14					0.18			

Faraday isolator	Disk amp	Disk amp	Disk amp	Entrance lens	Pinhole	Exit lens	Folding mirror
20.8	20.8	20.8	20.8	20.8		31.5	31.5
73	898	1556	2447	2423		2398	2326
2.15	2.48	4.29	6.76	11.0		4.44	4.40
0.89	0.97	0.97	0.97	0.99	1.0	0.99	0.98
	2.3	2.3	2.3				
	1.90	1.73	1.57				
	3	3	3				
	0.77	0.77	0.77				
	0.077	0.077	0.077				
	3.2	3.2	3.2				
	3.0	3.0	3.0				
	0.18	0.28	0.39				

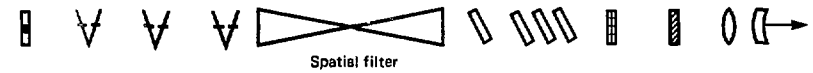

Slot aperture	[illegible] amp	Disk amp	Disk amp	Entrance lens	Pinhole (slit)	Exit lens	First turning mirror	Turning mirrors	KDP crystal [illegible]	Dichroic beam dump	Focusing lens	Debris shield (tentative)
46	-6	46	46	46		74	74	74	74	74	74	74
3894	040	13820	18040	17860		17510	16985	16305			15880	
6.	5.66	7.79	10.2	16.70		5.93	5.84	5.68			5.41	
0	0.97	0.97	0.97	0.99	0.99	0.99	0.97	0.96		(–)	0.96	(–)
	1.93	1.93	1.93									
	1.46	1.38	1.31									
	2	2	2									
	4.1	4.1	4.1									
	0.062	0.062	0.062									
	3.2	3.2	3.2									
	4.3	4.3	4.3									
	0.38	0.46	0.51									

...Surface-...threshold as a ...of pulse ...over the range ...to 25 ns.

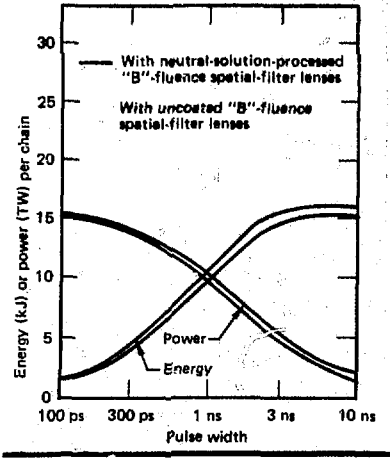

Fig. 2-31. Nova single-chain maximum power/energy performance over a pulse-duration range from 0.1 to 10 ns.

be operated at points indicated along the upper curve. However, small component imperfections introduce modulation on the beam. Thus, to avoid component damage, the laser can only be operated at or below the lower performance curve, which is determined by dividing the upper curve by the computed peak/average ratio.

Frequency-Conversion Considerations. Based on extensive analysis and experimentation during 1981, we have determined that

- Frequency or wavelength conversion should be accomplished as close as practical to the target-focusing system (i.e., at the 74-cm clear aperture).
- Conversion to either 2ω or 3ω can be accomplished with a single complex crystal array (see "Frequency Conversion," later in this section).
- Type II KDP crystals in 3×3 arrays are optimal for conversion to 2ω and 3ω, given the current state of the art in solution crystal growing (see the following article).
- Precision diamond turning is the preferred finishing technique for preparing KDP surfaces to better than ± 30-μrad angular tolerance and to better than $\pm 1.0\,\mu$m of crystal-to-crystal thickness variations.

These considerations and others have led to the proposed frequency-conversion/

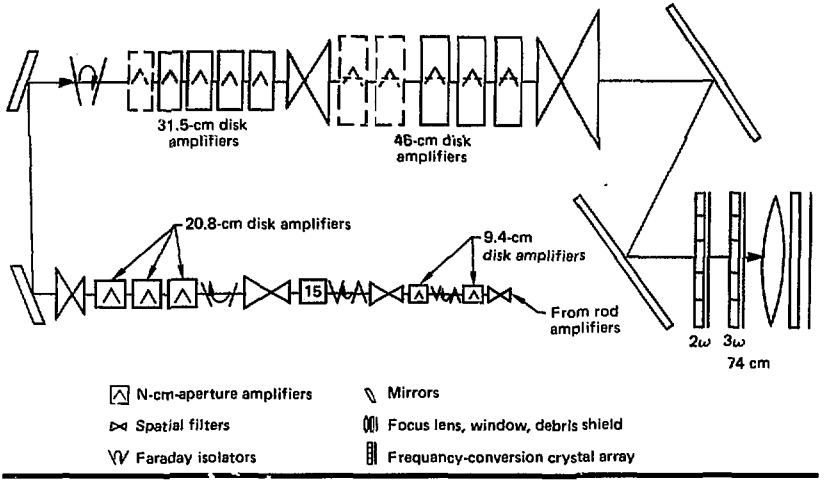

Fig. 2-32. Schematic of the Nova optical layout, including frequency-converting KDP arrays.

target-focusing subsystem configuration illustrated in Fig. 2-35. In the figure, the auxiliary alignment optics (the cross hair and retroreflector near the technician) are shown pulled out of the beamline. An insertable dichroic absorber plate is placed between the frequency-conversion array and the target-focusing lenses. Some of the features relevant to this baseline subsystem are described in the following paragraphs.

Performance analysis of self-focusing has shown that the system output at 2ω and 3ω is B-limited, insofar as power is concerned, at a B of about 2.5 rad, counting only fused silica and beam dumps. Figure 2-36 indicates the nonlinear intensity growth with B of modulation on the propagating $2\omega/3\omega$ beam. The computations were performed with the MALAPROP propagation code for a fused-silica path length of 21 cm, which is typical of the Nova optical train following the frequency-conversion array. Source terms for this calculation were multiple obscurations of 200-μm diameter. Various component-damage regimes are indicated; the component most prone to damage is the final-focusing lens. Nova operation at a B-integral of 2.2 will produce the power levels shown in the box insert. Note that operation at a B-integral of 3 will produce damage tracks in the lenses and will also destroy the surfaces.

The performance analysis described above gives the performance curve shown in Fig. 2-37 for the assumed nonlinear-index values of silica at 2ω (1.2×10^{-13} esu) and 3ω (1.5×10^{-13} esu). Note in the figure that power is limited by B-integral effects below 1 ns for 2ω and below 2 ns for 3ω. Intensive efforts are underway to measure the nonlinear index of silica early next year (see "Basic Research in Optical Materials" in Section 7).

To minimize the B-integral, we have chosen a doublet f/4 focusing-lens configuration. The first of these lenses also serves as the target-chamber vacuum barrier. The final surface will be left uncoated to provide a backward-traveling sample of the frequency-converted beam to the output sensor package. The results of extensive ghost-focus analysis have located the frequency-converting KDP array and the

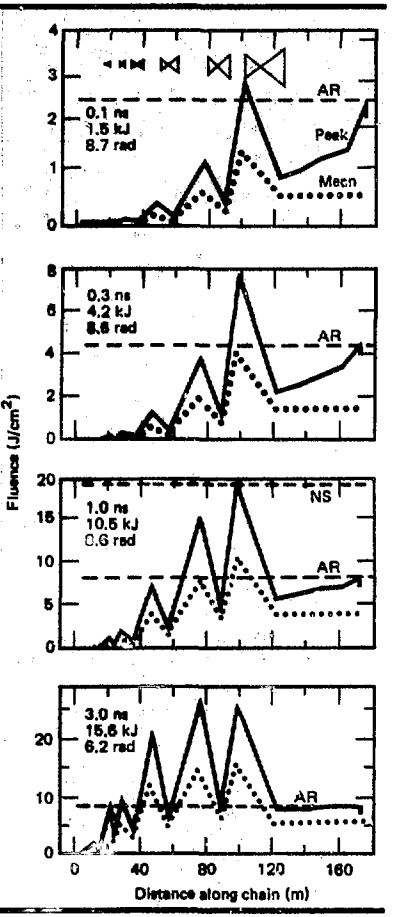

Fig. 2-33. Performance profiles of one Nova chain for four pulse durations.

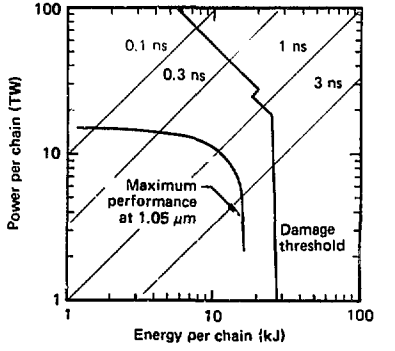

Fig. 2-34. Performance at 1.05 μm should not result in damage to optical components in the power/energy domain below the maximum-performance line.

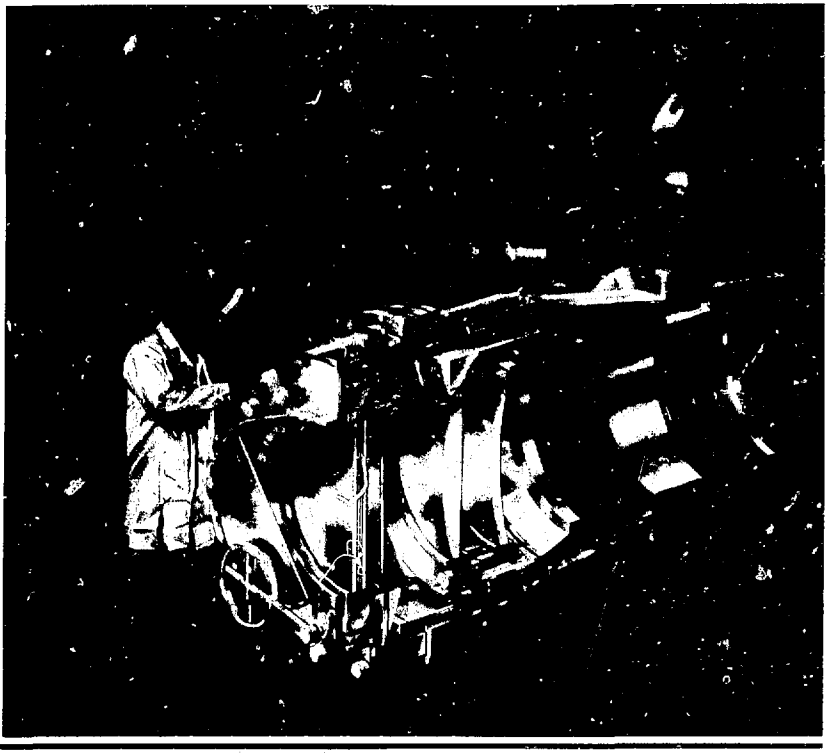

Fig. 2-35. Artist's rendering of the KDP Nova frequency-conversion array and target-focusing lenses.

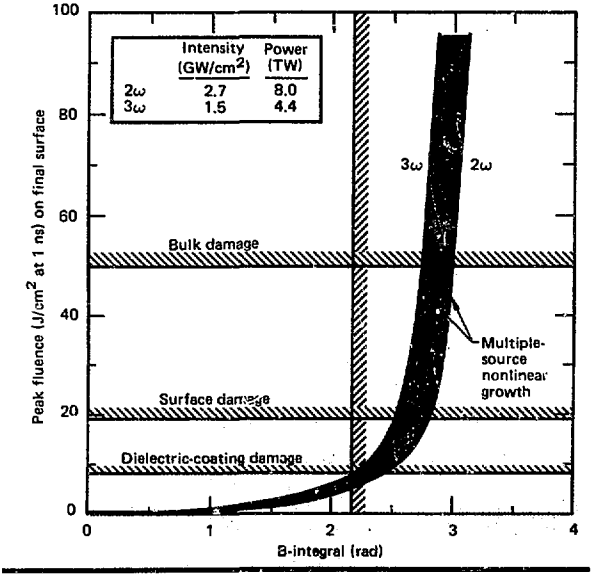

Fig. 2-36. Growth of spatial modulation (self-focusing) in the near field as a function of the B-integral.

beam dump between 1.4 and 1.5 m upstream from the focusing lenses.

Finally, fused silica (to be used for the array output window and the target-focusing lenses) remains the only identified material that does not solarize under intense 0.35-μm (3ω) radiation.

Author: W. W. Simmons

Optical Components

The Nova laser-fusion facility is probably the largest precision optical project ever undertaken. The following statistics illustrate the scale of the 20-beam optics for the Nova laser project

- 2000 major optical components.
- 4000 litres of laser glass.
- 2000 litres of fused silica.
- 20 000 litres of borosilicate glass.
- 300 litres of crystals.
- 400 m^2 of optical-quality surfaces.

- 200 m^2 of optical thin-film coating.
- Maximum component diameter of 1.1 m.
- Maximum component weight of 380 kg.
- Average flux on components of 3×10^9 W/cm^2 at 1 ns.
- Average optical-surface accuracy of 0.06 μm.

During design and construction of the Nova laser system, the LLNL optics group has had enormous cooperation and support from the optical industry in researching and developing new optical materials, fabrication techniques, and coatings. Together, we have successfully applied several new developments in these three areas, including

- Large-scale melting of phosphate laser glass.
- Monolithic edge-claddings for laser disks.
- Continuous melting of borosilicate glass.
- Precision flat-lapping machines.
- Damage-resistant thin-film high-reflectance coatings.
- Anti-reflective (AR) leached surfaces.
- Large KDP crystals.
- Diamond-turning of KDP.
- Large-sized filter glasses.

Due to the new requirements for 2ω and 3ω generation, we have also enlisted industrial support for continued development of fused silica of the quality, size, and volume necessary for Nova.

The optical technologies for the Nova laser can be divided into three categories: materials, optical surfacing and figuring, and coatings (including thin-film evaporated coatings and newly developed techniques for producing integral AR coatings). Each of these categories are discussed in detail below. The overall technology tree for Nova optics is shown in Fig. 2-38.

Advances in Material Technology. Scaling up previous technologies has provided many of the major challenges and achievements in optical materials in the past year. In some cases, we have scaled up existing technologies by as much as an order of magnitude. At the same time, we have pressed on with the development of essentially new processes and technology.

Phosphate laser glass of the type used for Nova was developed for, and has been used in recent years by, the University of Rochester, Osaka University, and others. The largest disks in these systems are about

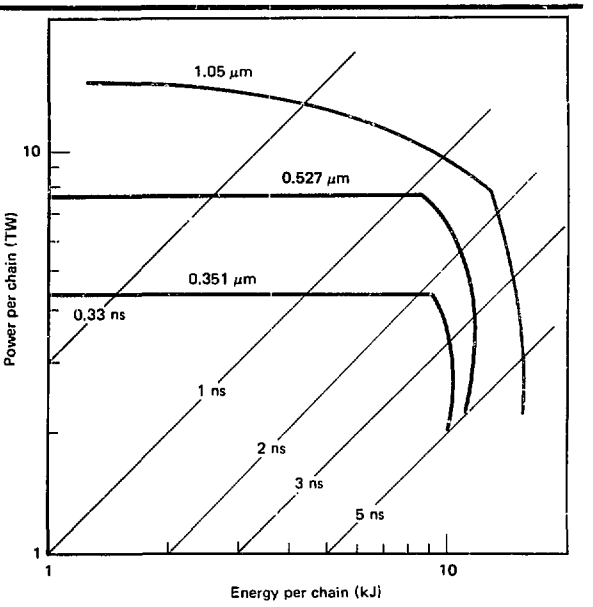

Fig. 2-37. Power/energy performance limits at 1ω, 2ω, and 3ω for one Nova chain.

2 litres in volume and have surface dimensions of approximately 20 × 40 cm. Most of the laser glass in Nova, however, resides in disks of ~8 litres in volume with surface dimensions of ~30 × 60 cm. When finished, these large disks must have an optical homogeneity within λ/6 at a wavelength of 0.63 μm and a stress birefringence within 0.5 nm per cm. The major manufacturers for the laser glass for Nova are Hoya Optics U.S.A. in Fremont, Calif., and Schott Optical Glass in Duryea, Pa. Kigre Corp. of Toledo, Ohio, will be manufacturing some of the smaller disks.

At the beginning of 1981, there were several major technical problems with phosphate laser glass that had to be solved by the glass companies

- Maintaining a long fluorescent lifetime by keeping water out of the glass.
- Finding a laser-disk edge-cladding that can survive the severe environment within the amplifier cavity.
- Producing glass with high optical homogeneity in the very large sizes required for Nova.

The most difficult problem in the largest disks has been cladding the disk with a glass that absorbs at 1.05 μm; this is necessary to prevent depumping of the disk itself

Fig. 2-38. Technology flow used for Nova optics.

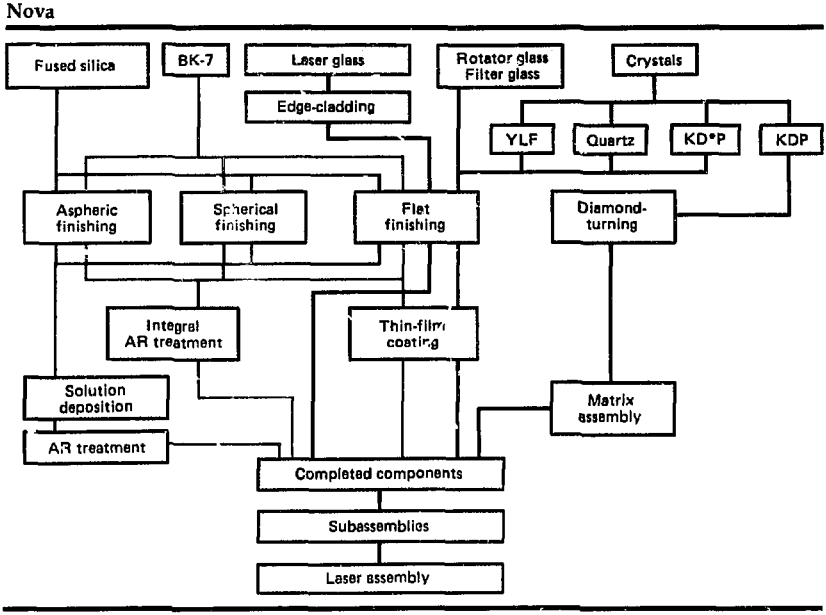

by unwanted parasitic laser oscillations within the disk. Within the Nova amplifiers, claddings will be subjected to large thermally generated stresses from exposure to very high flashlamp intensities and also from the absorption of a large fraction of the stored energy in the disk.

The glass companies were successful in developing monolithic claddings that have not been damaged in our amplifier tests. Basically, the cladding is phosphate glass that has been copper-doped to absorb 1.05 μm. The composition of this cladding glass is adjusted to match two specific characteristics of the laser glass

- First, the cladding glass must match the index of refraction of the laser glass to minimize reflectivity at the interface of the two glasses.
- Second, both glasses must have the same thermal expansion, from the annealing point to room temperature, to avoid residual stress that would make the cladding glass unusable.

To produce the monolithic claddings, the cladding is poured around the edge of annealed and shaped laser disks. The composite part is then fine-annealed and ground to its final shape.

This year, we have received edge-cladded laser disks of every size, except the 46-cm split disks. The finishers have already completed several disks, which we will use in Novette. The wavefront quality of these disks meets our specification that distortion be less than $\lambda/6$ at 0.63 μm within the specified clear aperture, as shown in Fig. 2-39. However, we find that the monolithic edge-cladding process does introduce a wavefront "roll-off" next to the interface of the cladding and laser glass. The roll-off effect does not appear to encroach on the specified clear aperture, but we will continue to monitor it in production disks.

In recent years, Schott Optical Glass has made advances in the manufacture of massive melts of borosilicate glass (BK-7), and these advances have played a significant role in making Nova a cost-effective laser. For example, Nova includes 98 massive mirrors, some of which have very high homogeneity because of transmission requirements for diagnostics. In addition, all 20 laser chains include two BK-7 lens blanks having a clear aperture of 77 cm; these lenses are the output spatial filter lens and the diagnostic objective lens. The BK-7 glass for the first 10 beams is all poured, and many of the components are already complete. The borosilicate for all these components came from one large continuous melt.

One of the more remarkable achievements of 1981 was the increased size of solution-grown KDP crystals. Up to about

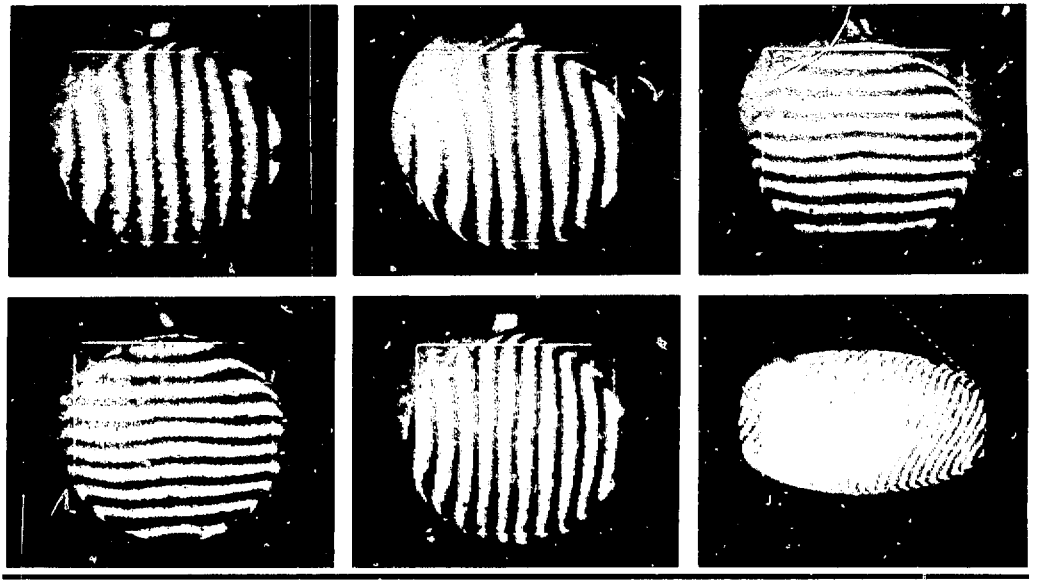

▲ Fig. 2-39. Interferogram of a finished 31.5-cm phosphate laser disk.

seven years ago, the biggest crystals of KDP and KD*P (a slower-growing, deuterated form of KDP) were about 2.5 cm in diameter. For the Shiva laser, we required 5-cm-diam KD*P for Pockels cells; we have begun developing 10-cm-diam KD*P for the Pockels cells on Nova.

With the advent of plans to implement frequency-doubling on Nova, we began to work with the glass manufacturers to increase the size of crystal boules and to determine optimum potential sizes for crystal arrays for Nova's 74-cm output apertures. We decided to start with 15-cm-square (i.e., 15 × 15 cm) KDP crystals in a 5 × 5 array for the first one or two beams, and then to proceed with 3 × 3 arrays using 27-cm-square crystals (see "Frequency Conversion," earlier in this section).

We have received a total of 35 15-cm-square plates from Interactive Radiation in Northvale, N. J., and Cleveland Crystals in Cleveland, Ohio; we are finishing them. Figure 2-40 shows the good optical quality of a 15-cm-square KDP crystal. These two companies have also harvested the first three boules large enough to yield our first 27-cm-square crystals; Fig. 2-41 compares the first of these boules with a boule typical of those obtainable five years ago.

KDP crystals grow on a seed placed in a supersaturated solution of KDP salt. Along with Lasermetrics in Englewood, N. J., both Interactive Radiation and Cleveland Crystals are working on an LLNL-funded program to increase the size, quality, and quantity of seeds for KDP production. They have grown about 35 seeds with outside dimensions greater than 30 cm and are growing over 50 more such seeds to provide sufficient KDP for doubling the Nova fundamental frequency.

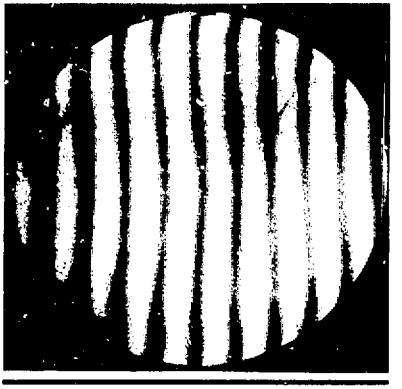

Fig. 2-40. Interferogram (double pass at 0.63 μm) through 2-cm-thick, 15-cm-aperture KDP crystal.

One of the primary factors limiting the availability of large crystals is their slow growth rate: 1 to 2 mm per day. For instance, a crystal boule 30 cm wide on a side takes 9 to 12 months to grow. This slow growth rate is both a risk and a cost

Fig. 2-41. The very large crystal at left is the first boule of a 27-cm-square KDP crystal for frequency conversion of Nova.

liability. We are, therefore, working with North American Philips Laboratories of Briarcliff Manor, N. Y., to further develop a system that has the potential of increasing the growth rate of KDP by a factor of 2 to 4.

The supersaturation of the KDP solution must be maintained while the crystal grows. The most common growth process maintains supersaturation by lowering the solution temperature. The alternative is to recharge the growth solution while holding it at a constant temperature. Philips has grown approximately eight 5-cm KDP boules at growth rates of up to 6.3 mm per day in its 100-litre system. We find that the optical quality of the Philips crystals is excellent and that the laser damage in the bulk is average (see "Damage Studies" in Section 7). Philips is continuing to refine its system and will begin growing 15-cm crystals in 1982.

Another area of current development is in massive, high-homogeneity fused silica for the output windows of the crystal array and for the focusing-lens doublet. It appears that fused silica is the only material so far identified that performs well at high energies at the third-harmonic wavelength (0.35 μm). For this reason, we are working with Corning Glass in Canton, N. Y., and with Hereaus-Amersil in Hanau, Germany, to establish acceptable quality levels and to determine production parameters for Nova's fused-silica components. Corning and Hereaus-Amersil will supply us with 80-cm-diam test blanks in 1982.

In 1981, Hoya Optics delivered three 80-cm-diam pieces of the filter glass that we will use in 2ω experiments to absorb 1-μm light and transmit 0.5-μm light. Two pieces have good optical homogeneity, and Eastman-Kodak, Rochester, N. Y., is now finishing them for Novette.

Advances in Optical Fabrication. To fabricate numerous high-precision optical components within reasonable cost and schedule constraints, it was necessary to do a great deal of planning and facility construction with the finishing companies. Those efforts are described in the following paragraphs. Much of our collaborative optical-fabrication efforts had to do with optical surfaces. From the the point of view of optical manufacturing, there are three basic types of surfaces

- Spherical and aspherical surfaces on lenses.
- Flat surfaces on polarizers, windows, and laser glass.
- Surfaces on KDP crystals, which, although flat, have very special alignment requirements.

Each Nova beam contains several lenses, the largest of which are those used for the 80-cm-diam spatial filter, the target-focusing system, and the diagnostic objective lens. The spatial-filter lenses, with ratios of diameter to focal length of about 20, have asphericities of $\sim$3 μm; these asphericities are figured into spherically polished surfaces. Figure 2-42 shows an output spatial-filter lens being inspected by the manufacturer; the interferogram of the same lens, Fig. 2-43, demonstrates its wavefront quality. The aspheric focusing lens is a doublet with three spherical surfaces and one aspheric surface of about 50-μm deviation from the best-fit sphere. The diagnostic

objective is a single-component f/2 lens whose aspheric surface has a 1-mm deviation from a spherical surface.

For aspherics as steep as these, the modern method is to generate precisely the desired asphericity into the surface prior to polishing, using numerically controlled machines. The polishing is then done with the aid of motor-driven flexible laps that are also controlled numerically, using interferometric data as feedback. The steep aspherics are being manufactured by Tinsley Laboratories in Berkeley, Calif., and Eastman-Kodak in Rochester, N. Y., both of whom have built special machines for the Nova project. Perkin-Elmer Corp. of Norwalk, Conn., is manufacturing the spatial-filter lenses through the 50-cm size.

In 1981, Eastman-Kodak and the Zygo Corp. of Middlefield, Conn., completed construction of our large lapping machines (Figs. 2-44 and 2-45) at their facilities. The Eastman-Kodak machine measures 4.1 m in diameter, and the Zygo machine measures 3.6 m in diameter; both machines are now producing Nova lenses. Each machine has associated with it an 80-cm-aperture Fizeau interferometer for the frequent checking of parts during the manufacturing process. These interferometers are located adjacent to the machines and kept at the same temperature.

One of the newer technologies used in optical fabrication is single-point diamond-turning. This technology is used very effectively on metal mirrors of certain types and on plastics, but most glasses do not machine well. KDP is much softer than glass, however, and experiments at LLNL showed that diamond-turning is a feasible approach to machining it.

Diamond-turning is especially attractive for KDP because KDP surfaces must be precisely oriented to the internal crystal structure so that the optimum phase-matching angle for each crystal is obtained when the crystals are assembled in a coplanar array. Another requirement for the KDP crystal array is very tight thickness control. Both these requirements make diamond-turning of KDP much more efficient than conventional polishing.

The KDP diamond-turning technology developed at LLNL (see "Frequency Conversion," earlier in this section) has proved to be so effective that the crystal vendors are building diamond-turning machines for the prefinishing of their crystals; prefinishing requires less accuracy, but diamond-turning lends itself to the the process very

▲ Fig. 2-42. An 80-cm-diam Nova spatial-filter lens in a test fixture.

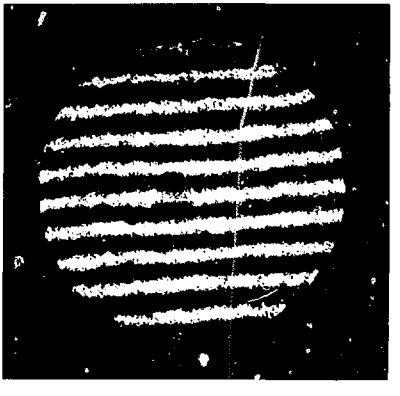

Interferogram of 80-cm-aperture Nova spatial-filter lens. (Double pass at 0.63-μm wavelength Tinsley Laboratories.)

Fig. 2-43. Interferogram (double pass at 0.63 μm) of the lens shown in Fig. 2-42.

effectively. At present, we are performing the final diamond-turning at LLNL, but we expect that one or more commercial vendors will participate as production accelerates.

Advances in Coatings and AR Surfaces. There are three basic kinds of thin-film dielectric coatings for optical components

- High-reflection coatings for mirrors.
- AR films on the air/glass surfaces of the

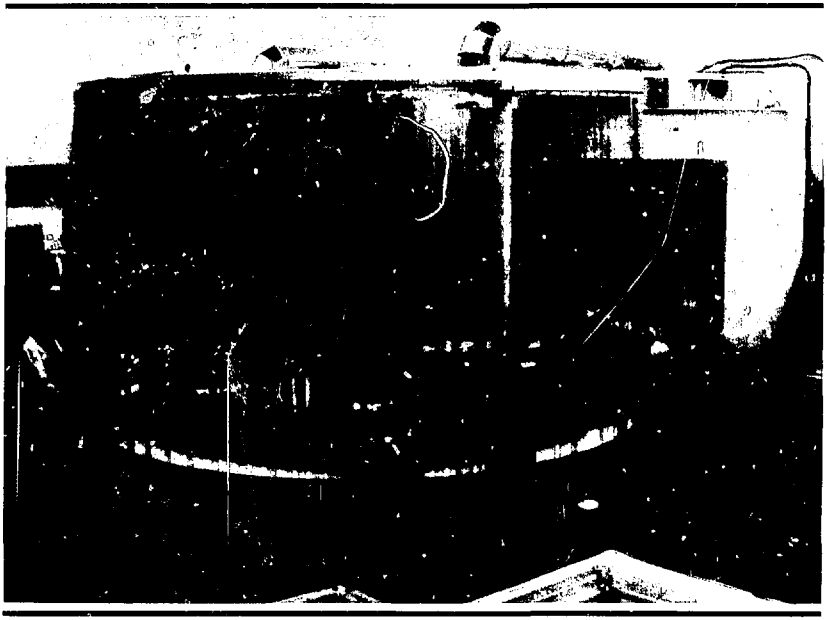

Fig. 2-44. The 4.1-m-diam flat-lapping machine at Eastman-Kodak.

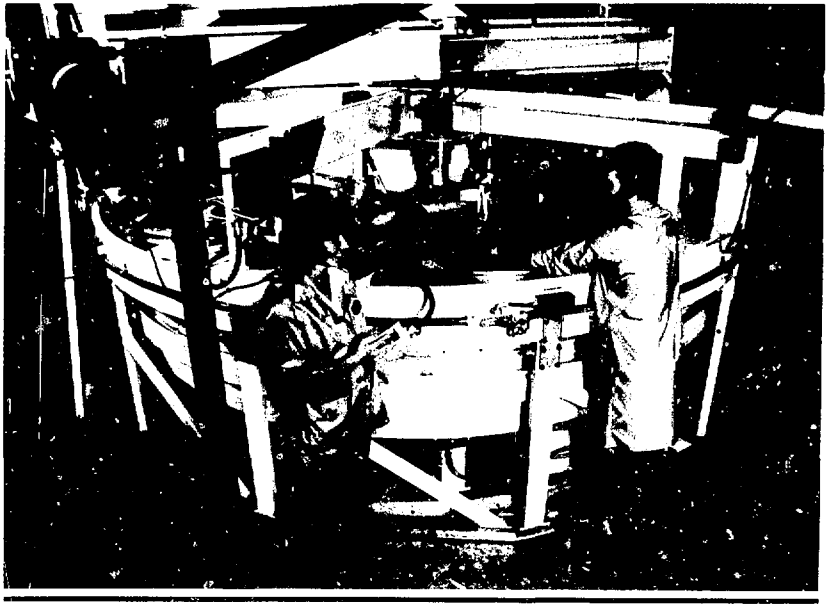

Fig. 2-45. The 3.6-m-diam flat-lapping machine at Zygo Corp.

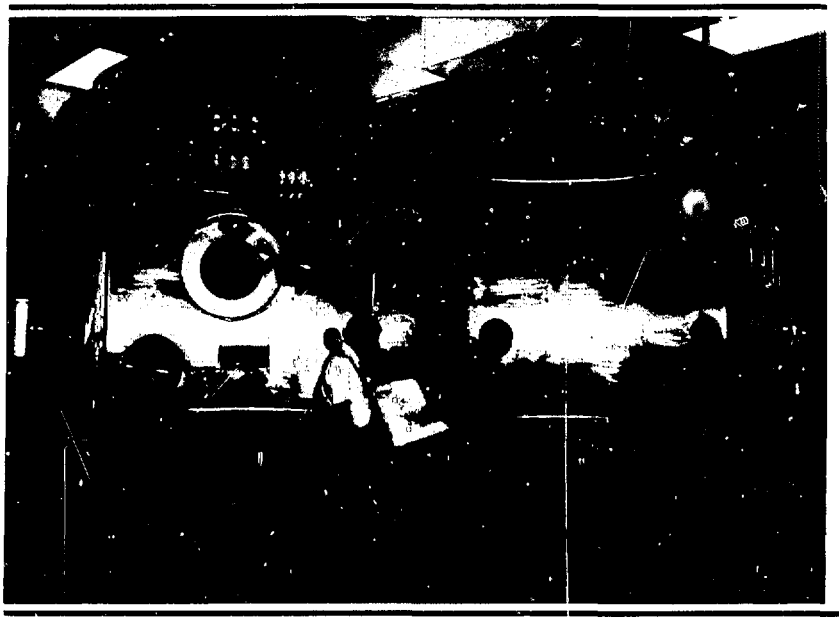

Fig. 2-46. The large lens-coating chamber at Spectra-Physics.

Fig. 2-47. The large lens-coating chamber at Optical Coating Laboratories.

Nova wavelength-separation filters.

- Polarizing filter coatings used in conjunction with Pockels cells and rotator glass.

In 1981, Spectra-Physics in Mountain View, Calif., and Optical Coating Laboratories in Santa Rosa, Calif., began operation of LLNL-funded coating chambers. The 2.4- × 2.9-m (96- × 114-in.) chamber at Spectra-Physics (Fig. 2-46) is cryogenically pumped—a unique feature in the coating industry. We believe that the employment of a cryopump will keep the vacuum coater free from oil contamination, which may improve the coating's resistance to laser-caused damage.

Optical Coating Laboratories has done two test studies in our 3-m (120-in.) chamber located in their laboratory (Fig. 2-47). They deposited 1.05-μm reflective coatings on 94- and 109-cm-diam BK-7 parts and found coating variations of 0.5 and 1.5%, respectively. Their test coatings met or exceeded the assigned goals for all criteria. In the second test series, they successfully deposited AR coatings and partially transmitting, high-reflection coatings designed to function at 1.05, 0.53, and 0.35 μm. The test coatings contained layers of zirconia and silica, instead of the common combination of titania and silica, because titania absorbs at 0.35 μm.

The absolute reflectance, transmittance, and spatial uniformity of these coatings are now being measured on a specialized scanning photometer (Fig. 2-48) designed and built by LLNL and Optical Coating Labs. The photometer operates at 1.06, 0.53, and 0.35 μm to simulate closely the fundamental, second, and third harmonics of the Nova laser. The optic element is scanned on a large x-y carriage while reflectance or transmittance data are taken continuously.

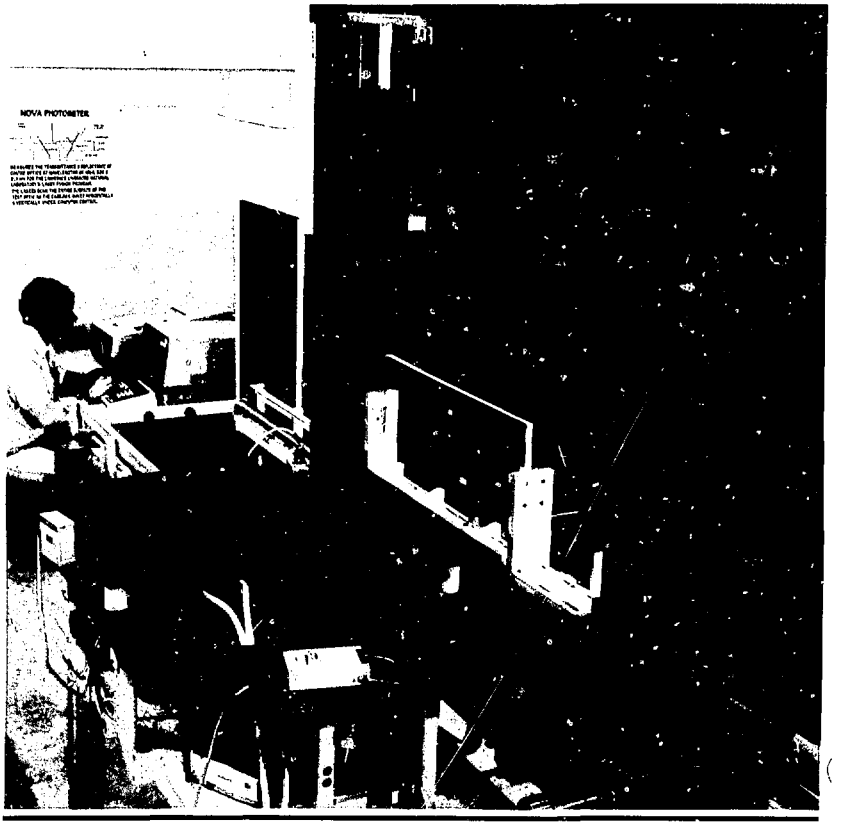

Fig. 2-48. Reflectance and transmittance photometer for measuring coating characteristics on large optical components (up to 109 cm diam and weighing up to 380 kg).

The system is controlled by an LSI 11/23 computer that processes the data and then prints out the results as hard copy or stores them on a memory disk. The detectors are temperature-controlled to within ±0.1°C, which aids in achieving an absolute accuracy of ±0.1 to 0.5% for full-scale operation, depending on the operating point. The photometer is capable of scanning a large (1-m diam) optical element in 20 to 30 min.

For AR surfaces, we will use a neutral-solution leaching process (see the previous article) that produces a low-density surface with a refractive-index gradient. Leached glass surfaces with AR properties are a new, promising development for high-power laser optics. LLNL's interest in these surfaces was stimulated by our measurements of their high laser-damage thresholds (a median of about 12 J/cm^2 for 1.06-μm operation with 1-ns pulses), which are higher than those for thin-film dielectric coatings by a factor of 2.

Along with the glass companies, we have studied two techniques for producing AR glass surfaces. One of these is based on the selective dissolution of one phase of a two-phase glass. This glass is produced by heating borosilicate glass to a temperature above the glass transformation point, which results in separation of the glass in borate-rich and silica-rich phases. Examples of this glass type are supplied by Hoya Optics as ARG-2 and by Schott as BK-3PS. Treated surfaces have less than 0.2% reflectivity over the full visible and infrared spectral regions, which indicates that a gradient-index surface has been made.

The primary drawback of phase-separated glass is the large amount of bulk scattering loss due to Rayleigh scattering from the heterogeneous glass. This scattering is small in the infrared spectrum, but the scattering increases as λ^{-4} into the ultraviolet spectrum, in which bulk-loss coefficients of 0.01 to 0.02 cm^{-1} are typical. In addition to the high scattering at short wavelengths, we also found it difficult to maintain a precision optical surface during the etching process, which resulted in a degradation of the optical figure.

In an effort to overcome these problems with phase-separated glasses, Schott investigated neutral-solution etching of BK-7 surfaces, a process previously studied by Schroeder.[34] Schott's studies found that the surface reflectivity of neutral-solution-etched BK-7 is not as wavelength-independent as the surface reflectivity of phase-separated glass (Fig. 2-49). When used in conjunction with a single-frequency laser, however, this wavelength dependence is not a disadvantage. We also found that the laser-damage threshold of etched borosilicate surfaces is comparable to or exceeds

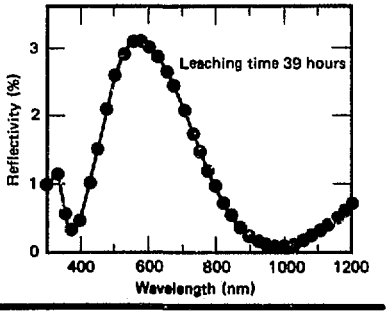

Fig. 2-49. Reflectivity of BK-7 surfaces treated with the Schott neutral-solution process.

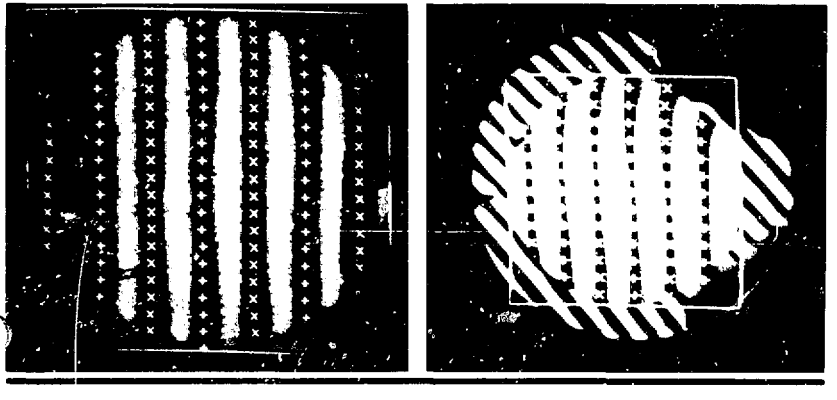

Fig. 2-50. Interferograms of a 20-cm-diam Shiva window taken (a) before, and (b) after the neutral-solution treatment. (Source: Schott Optical Glass, Inc.)

the damage threshold of uncoated surfaces and was at least twice that of thin-film coatings (see "Damage Studies" in Section 7).

Finally, the neutral-solution leaching process did not change the optical figure of the component; this is illustrated in Fig. 2-50, which shows interferograms of a 20-cm-diam window taken before and after treatment. The peak-to-valley wavefront distortion at 1.06 μm was 0.046 before leaching and 0.1 after leaching. We shall employ this treatment for all of Nova's spatial-filter lenses and windows, and we are planning a treatment facility at LLNL to process optics up to 1 m in diameter.

Author: S. E. Stokowski

Major Contributors: N. Thomas, F. T. Marchi, G. R. Wirtenson, and E. P. Wallerstein

Mechanical Systems

During 1981, we made progress with a number of mechanical systems; here, we report developments with laser amplifiers and mirrors, the spaceframe, the cleaning and assembly of components, and the nitrogen cooling system. These systems and hardware were described in the *1980 Laser Program Annual Report*[35]; our engineering effort this year has been directed primarily toward final detail design, assembly, and fabrication methods and facilities.

Amplifiers. There are three types of amplifiers in each Nova laser chain. The smallest amplifier, located at the beginning of the chain, is a rod amplifier with a clear aperture of 5 cm. Next come the round-disk amplifiers, which have apertures of 10 and 15 cm. Finally, the largest amplifiers—box-disk amplifiers—have apertures of 20.8, 31.5, and 46 cm.

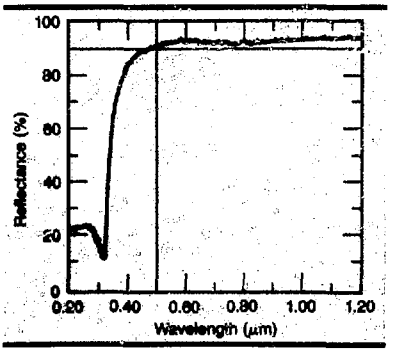

Fig. 2-51. Reflectivity of flat silver-plated reflectors for Nova box amplifiers.

There are 14 amplifiers in each of the 10 (Phase I) or 20 (Phase II) laser chains of Nova. The detailed designs for all amplifiers are complete, and all the Phase I amplifiers are in fabrication. The disk holders and reflectors are made of nickel, using the electroforming process, and are then silver-plated.

Higher reflectivity makes amplifiers more efficient. The flat reflectors in the top and bottom of Nova amplifiers are made of plated stainless steel, the surface of which is mill-finished to a 4-μin.-finish surface. We achieve a 4-μin. finish on the more complex-shaped reflectors (the crenulated flashlamp reflectors and elliptical disk holders) by machining the electroforming tooling from which the parts are made. Silver is then deposited on both flat and complex reflectors at a thickness of 0.0005 to 0.0007 in., using a super-bright silver solution.

To ensure maximum reflectivity, we must maintain strict and sensitive control of the plating-tank temperature and use micrometre-sized filters. We do not polish the reflectors after they are silver-plated, both to avoid surface contamination and because polishing does not always improve reflectivity. Our measurements of the flat reflectors show a reflectivity of ~90% at wavelengths above 500 nm (Fig. 2-51). Similar measurements of the crenulated reflectors show a reflectivity of ~86%.

Spaceframes. Spaceframes serve as stable supports for all components in the laser system. Figure 2-52 shows the locations and relative sizes of the principal spaceframe structures

- Optical components in the master oscillator room (located in the basement) are supported on a single frame of table height.
- The frames located in the east and west laser bays support the much larger optical components that make up Nova's laser beamlines.
- Individual frames in the switchyard support turning mirrors and diagnostic equipment.
- The remaining frame, located in the target room, supports the target chamber and

the final turning mirrors, which direct the laser beams from the switchyard into the target chamber.

All frames are constructed using 6-in.-square (i.e., 6 × 6 in.) tubing for the main columns and beam members; diagonal bracing members are constructed of 4-in.-square tubing for ease of fabrication. The Nova spaceframes are tied to the Nova lab building with strategically located seismic anchors, from which the frame can thermally expand on roller-bearing supports.

All frames are designed to be dynamically stable while accommodating convenient maintenance and utility access to components. The stability of laser-bearing spaceframes is measured in the deflection of the laser beams due to ground vibration. We performed computer analyses to establish the dynamic response of each frame both to ground vibrations measured at the Nova site and to LLNL design-basis seismic loadings. The calculated beam deflections we obtained indicated that our final designs for Nova's various spaceframes are acceptable. Table 2-5 itemizes the maximum translations and rotations we calculated for each final frame design used in the stability assessment.

We used modal analyses of the frames to determine the influence of frame-member size and location and to explore variations in the restraint conditions of frame supports and anchors. Table 2-6 itemizes the first three modal frequencies calculated for each final frame design.

The master-oscillator support frame consists of accessible table-height "islands" tied together structurally below a raised floor.

Frame location	Translation (μm)	Rotation (μrad)
Master oscillator room	±0.24	±0.15
Laser bay	±4.48	±0.69
Switchyard		
Mirror frame	±4.31	±0.70
Diagnostics frame[a]	—	—
Target chamber	±3.68	±0.88

[a]Analysis of the final design is in progress.

Table 2-5. Calculated maximum deformation of Nova spaceframes due to ground vibrations.

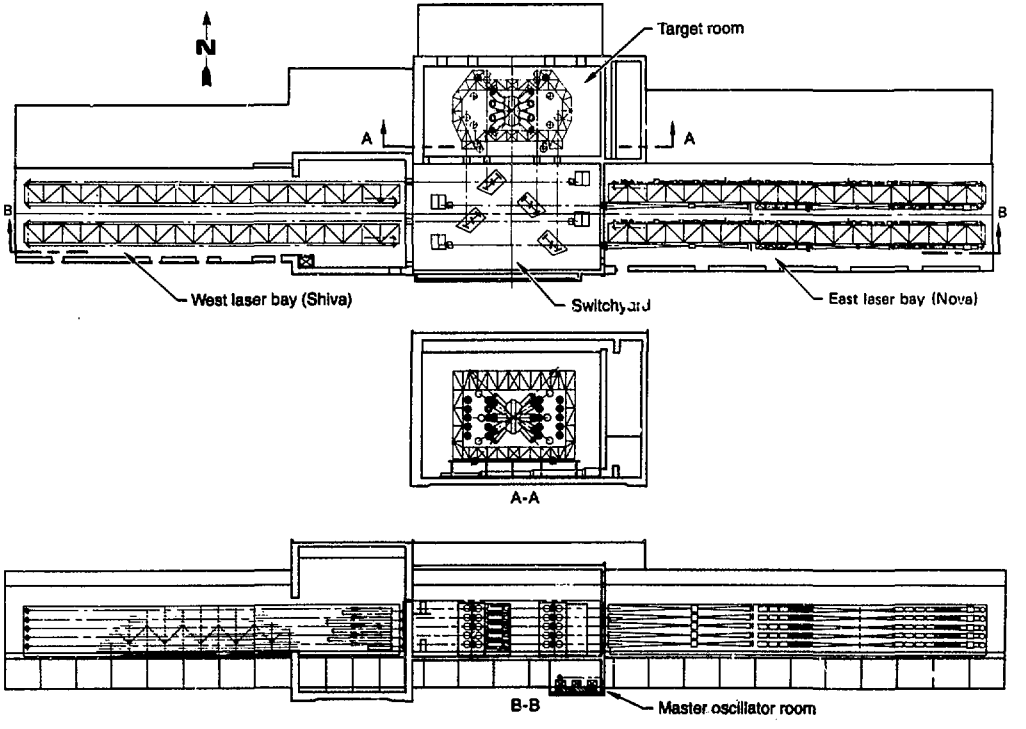

Fig. 2-52. Plan and elevation views of the Nova spaceframes.

The islands support laser hardware on surfaces composed of plate steel and a commercial honeycomb table top. A seismic anchor is located near the middle of the frame; roller-bearing supports are located in the periphery of the frame base.

Table 2-6. Modal frequencies of Nova spaceframes.

Frame location	First mode (Hz)	Second mode (Hz)	Third mode (Hz)
Master oscillator room	19.40	24.80	30.30
Laser bay	6.90	7.02	7.26
Switchyard			
Mirror frame	6.79	7.28	7.74
Diagnostic frame[a]	—	—	—
Target chamber	3.36	5.05	5.15

[a]Analysis of the final design is in progress.

Fig. 2-53. An artist's rendering of a Nova turning mirror mounted in its three-legged gimbal for tilt adjustment.

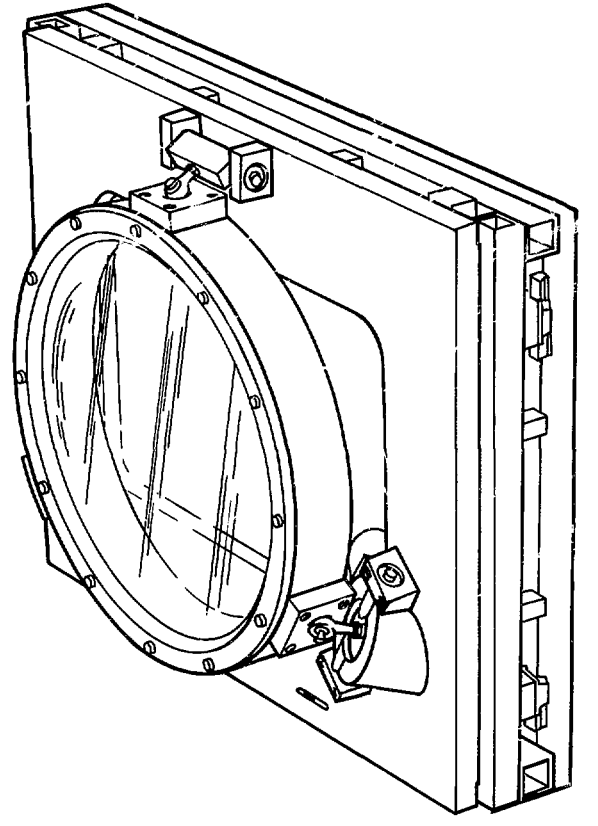

Each laser-bay spaceframe is 192 ft long, 27.5 ft high, and 10 ft wide. Diagonal bracing is provided at mid-height along the length of both sides to give the frame longitudinal stability. For lateral stability, diagonal bracing is provided in the lateral plane at 20-ft intervals along the length of the frame. Additional in-plane diagonal bracing is provided at three levels. Two seismic anchors are located near the center of each laser-bay spaceframe, and linear roller-bearing supports are spaced along the frame at 20-ft intervals.

The switchyard support frames (for the turning mirrors and diagnostic equipment) are designed to be used in either a 10- or 20-beam laser system, with different orientations for each system. All frames are seismically anchored to the floor at multiple support points, since thermal expansion is not a major concern with small frames. The switchyard spaceframes are dynamically stable, with rotation of the turning mirrors being particularly important. The maximum anticipated mirror rotation is 0.4 μrad, with the deformations given in Table 2-5.

The target-chamber frame consists of a beam-grid base structure and a large upper structure supporting the target chamber and mirrors. The overall target-chamber spaceframe measures 62 ft high, 71 ft long, and 47 ft wide. The base structure is laterally secured to the building walls and vertically supported by diagonally braced columns. The upper structure is anchored to the base structure and to four points below the centrally located target chamber; the upper structure can thermally expand from these points on roller-bearings located between the upper and base structures. Lateral stability of the upper structure is provided by diagonal bracing and by the overall geometric shape of the east and west ends of the frame.

Mirror Assemblies. The Nova target chamber, located in a room separate from the laser room, is approximately 180 ft from the output end of each laser beam. Turning mirrors are used to direct the beams the rest of the way to the target; for a 10-beam system, nine of the beams need four mirrors and one uses six mirrors. Construction of the Nova mirror assemblies has begun, and we expect the first deliveries in April 1982.

Four different-sized mirror mounts (one of which uses two different bezel sizes) are

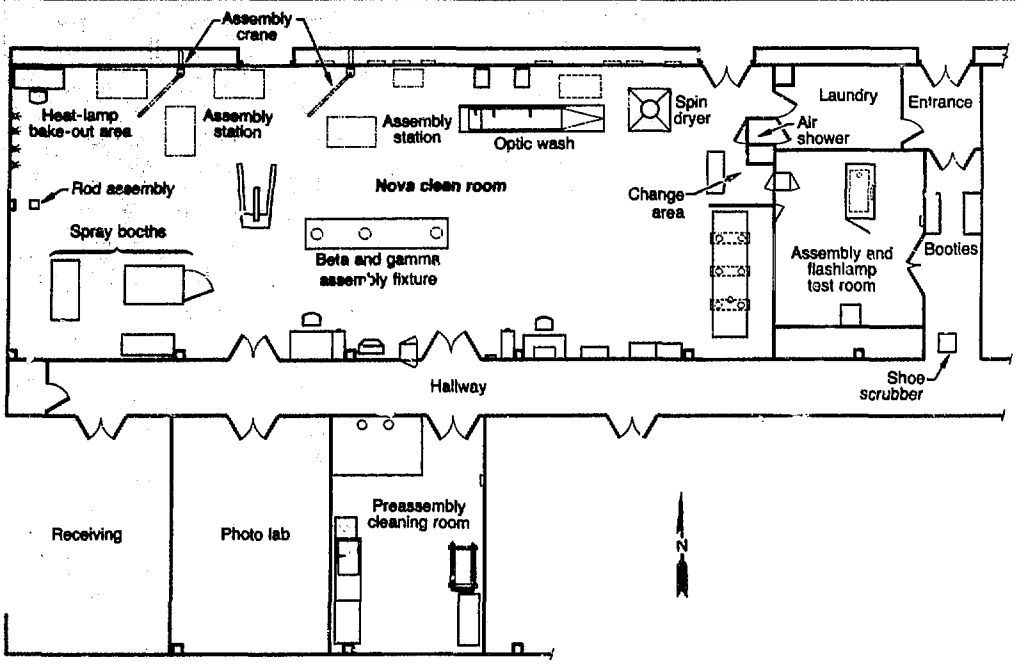

Fig. 2-54. The Nova class 100 clean room layout, including preclean room and flashlamp-assembly and test room.

required to accommodate the five different mirror sizes on Nova. Each mirror-mount bezel is attached to the mounting plate at three points 120° from each other (Fig. 2-53). Two of the three supports are linear actuators that provide angular adjustment by varying their length; the third support is a hinge. These supports are connected by a spherical rod end bearing at the bezel and by hinges at the other end. Each mount has an angular resolution of 0.5 μrad/step through a total range of ±17 mrad. The square mounting plates are attached to the spaceframe using kinematic mounts; adjustments in x and y are achieved by relative motion of the square plates. In the figure, the gimbal is shown in a transport cart.

Clean Room and Associated Hardware. The Nova clean room is an adaptation of the class-100 Shiva clean room. This facility, with an area of 335 m^2 (Fig. 2-54), has been extensively updated to accommodate the large box amplifiers to be installed on Nova and Novette. The Nova clean room has a vertical air flow with an air velocity of about 30 m/min; high-efficiency particulate air (HEPA) filters are mounted overhead.

The Nova clean room will initially process a total of 305 Nova amplifiers. These large box amplifiers are now too large and expensive, and their cleanliness level too critical, to allow them to be assembled by hand. (Tests by Milam et al. have shown the relationship between clean optics and laser-induced damage.[36]) The most critical optical elements in Nova amplifiers are the neodymium-doped phosphate glass disks. These optical components are subjected to both the incoming beam energy and the energy associated with the various arrays of xenon flashlamps located inside the amplifiers. The combined fluence of the flashlamps and beams can rapidly heat or evaporate contaminants such as dirt or film on the glass surface. This process may cause either localized melting or large local stresses in the glass surface. Repeated stress of this kind can cause fragments of glass to actually break out of the glass disk, become contaminants themselves, and escalate the destructive process even further.

The cost of the largest Nova disks now approaches $50 000 each; we have, therefore, designed special handling equipment and techniques for cleaning, assembling, and inspecting the disks and any other

amplifier components that could contaminate them. The old drag-and-wipe method of cleaning optical components has been replaced by a spin-cleaning machine that cleans the largest optics in 4 to 5 min (compared to approximately one hour using the old technique). The spin-cleaning method (Fig. 2-55) has the added advantage of permitting optical elements to be handled with a fixture instead of a hand.

In the spin-cleaning room, optical components are washed with a solution of distilled water and soap containing 30% alcohol, rinsed with distilled water, loaded into the spin cleaner where the glass is rotated at a circumferential speed of 280 m/min, and again rinsed with distilled water. The spinning dries the surfaces in about 60 s after the final rinse. The spin cleaner can handle optics weighing up to 27 kg, including the Nova 46-cm split disks (larger optics must be cleaned by hand).

Once the disk has been cleaned, the handling fixture is used to lift the disk from the spin cleaner and onto a specially designed clean-assembly cart. The disk is sealed in a reflective housing, tilted 90° on the cart, and transported to an amplifier assembly station. After assembly, the amplifier is lifted by a clean crane into its final resting place: the Nova amplifier housing

The housings—and all other metal components that make up the Nova amplifiers—will normally be given a precleaning in a room adjoining the clean room. Once the housing surfaces have been scrubbed with various cleaning solvents and are free of foreign particles and oil films, they are transported by cart to the Nova clean room. Once inside the clean room, the carts roll the amplifier components into a custom-made high-pressure spray booth.

Fig. 2-55. A 20.8-cm amplifier disk in the spin-cleaning machine.

This large spray booth uses the same cleaning principle as the smaller Shiva spray booth. A cleaning solvent (trichlorotrifluoroethane) is sprayed at 6.9 MPa (1000 psi) through spray nozzles centimetres away from the components. This high-pressure spray can remove in excess of 99.9% of particles 5 μm and larger in a matter of seconds. After spraying, the solvent is recycled through filters and a distiller to maintain the maximum level of cleanliness. As with the Shiva spray booth, we will verify cleanliness by examining a membrane filter located in the solvent return line.

The silver-coated reflectors in Nova amplifiers require special attention. Once the silver surfaces have been cleaned of foreign particles, they are moved to a cleaning area where the silver is given a low-pressure spray of thiourea solution. After the silver tarnish is removed, the silver-coated reflectors are ultracleaned like the metal components.

Xenon flashlamps also require special attention. First, all flashlamp assemblies are thoroughly cleaned in the spray booth and assembled on flashlamp-assembly carts. They are then transported to an adjoining room, where the flashlamps are tested using 30 kV of electricity in a special nitrogen-filled enclosure. After passing this test, the flashlamp assemblies are transported back to the clean room and given a final high-pressure spraying. The flashlamps are next transported to the amplifier assembly station and loaded into the amplifiers by one of two clean cranes.

The amplifier assembly sequence is not complete until all components have been inspected. Since the assembly of optical elements could cause wavefront distortion or strain birefringence, our inspection equipment includes a combined interferometer and polariscope located in the east corner of the clean room.

Assembly. There are three categories of assembly for Nova and Novette laser-chain components

- Components (such as disk amplifiers) that are irradiated by laser and flashlamp energy.

- Components (such as spatial filters, turning mirrors, isolators, rotators, and focusing optics) that are irradiated by laser energy only.
- Components that touch or are adjacent to components in the first two categories.

The class 100 assembly of highly sensitive disk amplifiers (the first category) is discussed above. Although components in the second category are not as sensitive as disk amplifiers, they are exposed to the laser-beam fluence and, thus, require class 1000 assembly conditions. Components that touch Nova optics, such as bezels or mounting hardware, must be cleaned and assembled in a manner consistent with the cleanliness of the optic. Components that are near optics but not in contact with them can be assembled under class 10 000 to class 100 000 clean conditions.

We will be assembling optical components in the Shiva high bay, which routinely operates as a class 10 000 clean room. Along with the assembly equipment, we are installing equipment for cleaning both optics and metal parts; the assembly-handling fixtures have been designed for clean operation. Figure 2-56 illustrates two methods of handling a 31.5-cm Faraday rotator-polarizer; Fig. 2-57 shows the cleaning and assembly sequence for a large turning mirror.

Nova Nitrogen Cooling System. The Nova nitrogen cooling system is used to cool laser components between shots: the system is designed to provide quick cooling

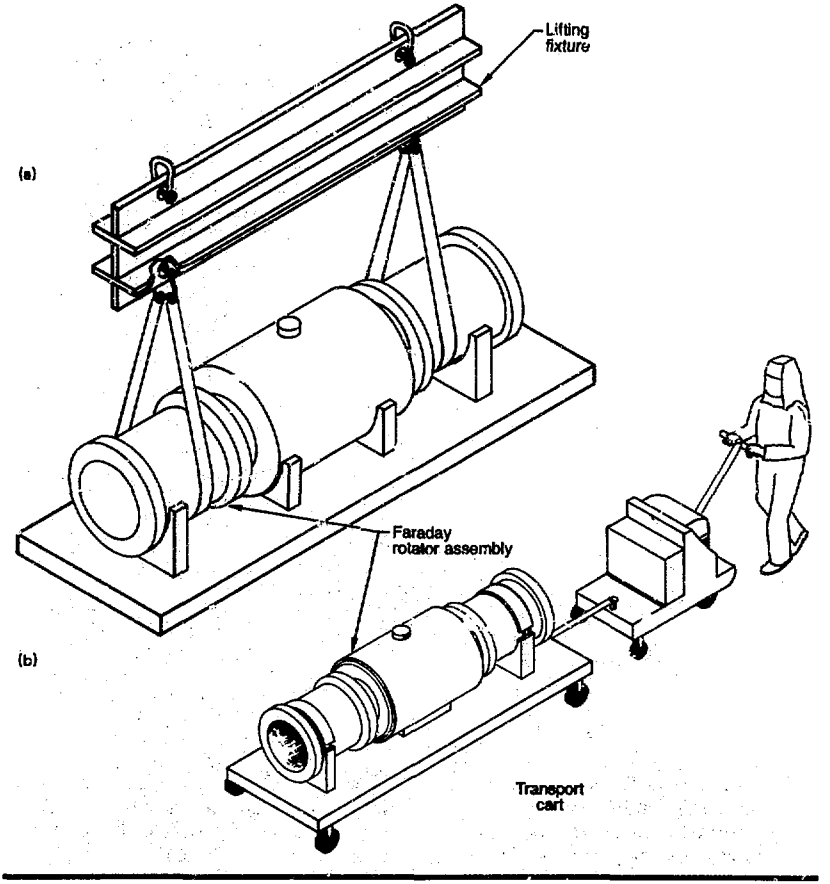

Fig. 2-56. A crane and transport cart for handling large Faraday rotators.

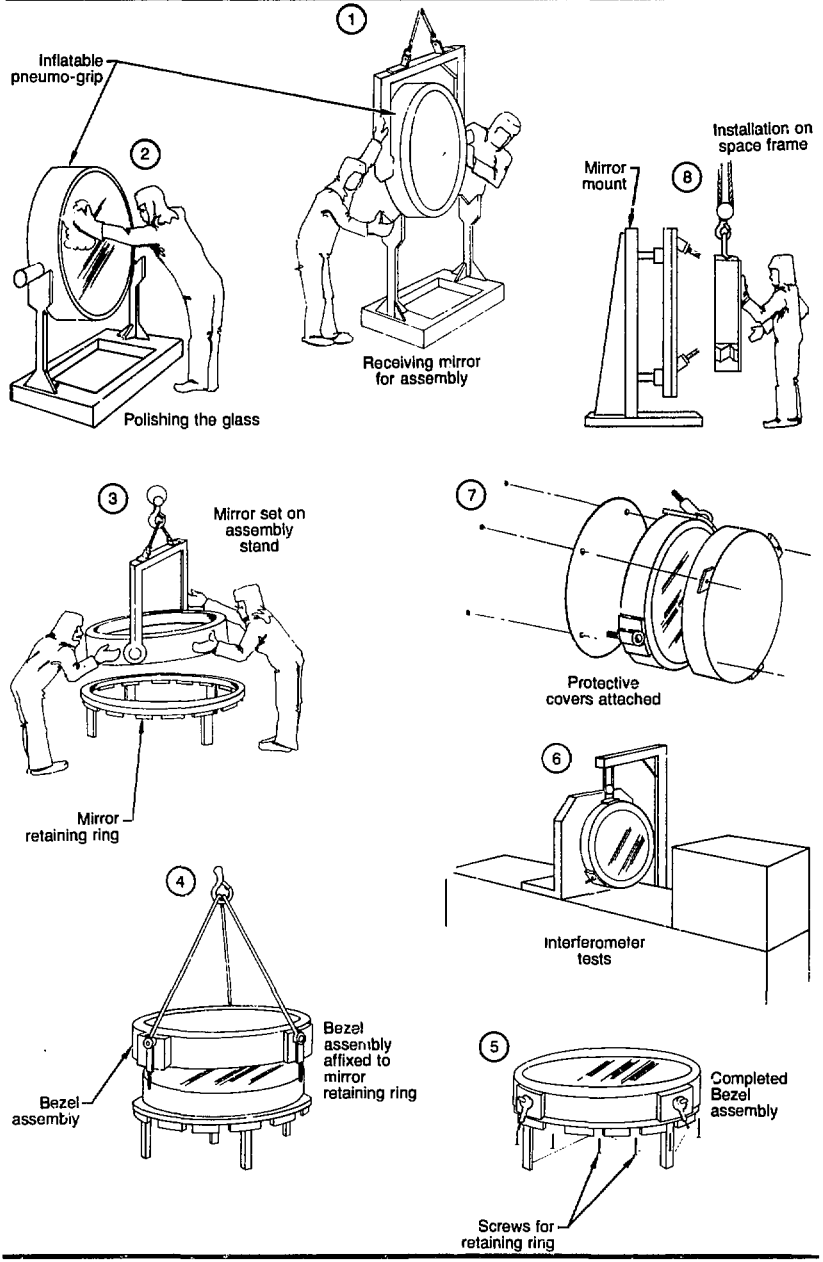

Fig. 2-57. Cleaning and assembly sequence for large turning mirrors.

at reasonable cost. In the larger amplifiers, nitrogen enters the disk cavity and flashlamp cavity through a plenum input. Gas for the flashlamp cavity on the 46-cm amplifier is manifolded in series, as shown in Fig. 2-58. Three 46-cm amplifiers are placed in series on the spaceframe and close-coupled, so that they function as one

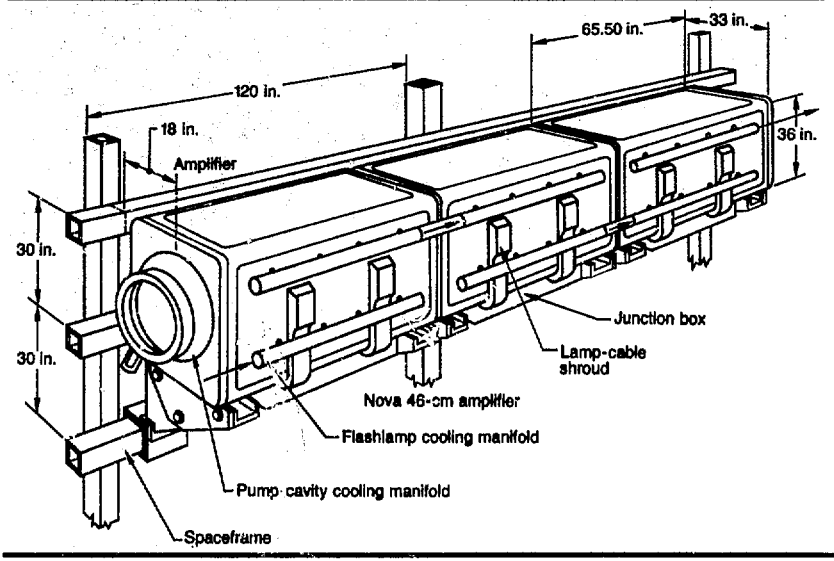

Fig. 2-58. Three 46-cm box amplifiers mounted in series on the Nova spaceframe.

Fig. 2-59. Preliminary design for the Nova nitrogen-gas cooling system. (See p. 2-54.)

amplifier with six disks. The space between disks in the Nova amplifiers is approximately 2 in., and the space between disks of adjacent amplifiers is approximately 4 in.

Nova laser components are larger than those previously used on Shiva; thus, they require higher nitrogen flow rates to achieve even moderate cooling periods. According to calculations presented in the *1980 Laser Program Annual Report*,[37] each Nova laser chain requires a continuous nitrogen flow rate of 500 cfm to cool in a period of four hours. To accomplish quicker cooling in a cost-effective manner, we have investigated two main options: recirculation of the nitrogen gas to reduce operation costs, and use of a stepped-temperature scheme to reduce the cooling period.

Recirculation of nitrogen gas requires three components

- A clean recirculation blower.
- A chiller unit for thermally reconditioning the gas.
- A low-pressure-loss piping and filtration system.

During 1981, we investigated various components and preliminary designs to evaluate both the feasibility and effectiveness of a recirculation system based on these elements.

After considering a number of options, we found acceptable a "Roots"-type blower with externally housed bearing supports for the lobe shafts. The chiller unit is required to compensate for adiabatic compression in the blower and for heat extracted from the laser components; we identified a unit of reasonable size that fits easily into the Nova

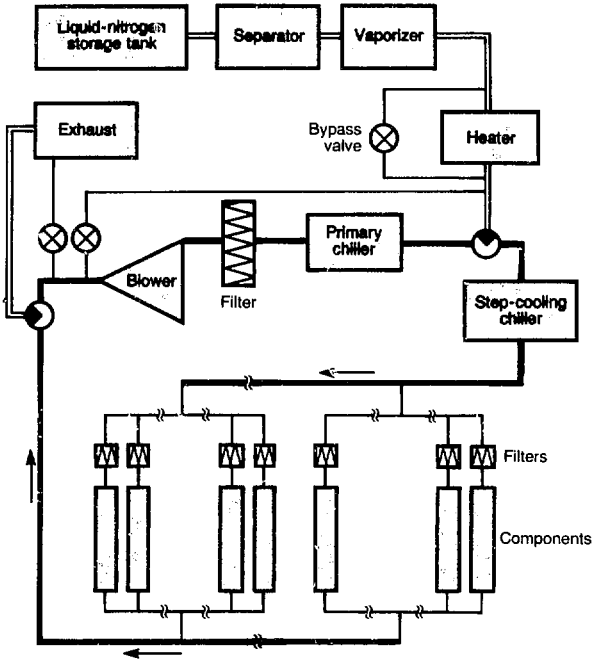

nitrogen-supply system. Our preliminary design of a piping and filtration system (Fig. 2-59) was found to require reasonable blower power (55 hp) at a total pressure loss of 1 psi, calculated for the high-flow cooling condition mentioned above. Based on these developments, we will implement a nitrogen-recirculation system on Nova.

The stepped-temperature scheme we investigated uses a stepped change in the nitrogen gas temperature to achieve improved convective heat-transfer in the laser components. The gas temperature is lowered during the first cooling phases to increase the difference in temperature between the component surfaces and the gas; then, at a predetermined system-temperature condition, the gas temperature is increased to the desired equilibrium level for the final cooling phase. For the full Nova system, we calculated that a stepped-temperature system can reduce the anticipated cooling time of four hours to just two hours. Although we must conduct experiments to confirm this effect, we plan to install on Nova the additional chiller unit required for the stepped-temperature scheme.

Authors: C. A. Hurley, F. A. Frick, H. L. Julien, C. R. McKee, A. Martos, and H. G. Patton

Power Systems and Energy Storage

During 1981, we refined designs, completed drawings, and began procurements for Nova. We revised our earlier designs to increase reliability and ease of maintenance. After extensive testing, we adjusted our procurements to select components (particularly resistors and ignitrons) of higher quality. We have also extended the use of fiber optics to further isolate the pulsed-power system from the control system.

Safety is an area of particular importance for power systems and energy storage. We have expended much effort to ensure that Nova's hazardous pulsed-power system will be safe for both personnel and equipment. For example, we have designed an extensive interlock system that integrates electrical, laser, and radiation safety; this interlock safety system will be prototyped on Novette.

During the past year, the basic flashlamp circuit has been refined, and we have staged and laid out the entire Nova pulsed-power system. Almost all components to be used on Nova—including a fiber-optic-connected, computer-driven control system— have been tested in our megajoule test facility. We have tested techniques for driving Pockels cells, and we are receiving the MVA power supplies for the Nova capacitor bank.

Figure 2-60 illustrates the layout of the Nova energy-storage system. The Nova power bank is comprised of capacitors totaling 100 MJ. The capacitor bank for Phase I of Nova is housed in 16 rows, each 53 ft long, comprised of steel shelving and circuits stacked seven high on each side of the aisle. Each circuit stores from 18 to 50 kJ of

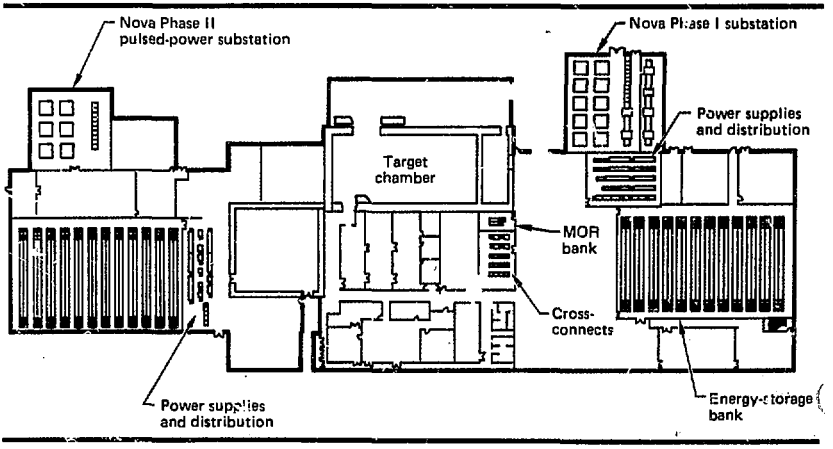

Fig. 2-60. Layout of the Nova energy-storage system.

energy, depending on the load requirement. At the end of each row of circuits is a switch control rack that contains up to five circuits along with computer-interface and diagnostic circuitry.

Each circuit is packaged in a module with its own pulse-forming network and its own vacuum-formed plastic tray that provides 25 kV of isolation between the rack and the circuit common. The rack is set on insulators and tied to ground through a 1-kΩ resistor. Each circuit also has its own safety-dump resistor. The dump circuits are mounted on a vertical channel adjacent to the capacitor circuit (shown in Fig. 2-61); this vertical channel has up to seven dump circuits on it.

To develop a system of known reliability, we constructed a 1-MJ test bank and put 4000 cycles on it using prototype Nova circuitry. Based on these tests, we have ordered parts for the first phase of Nova (10 beams). Power-conditioning staging for both phases of Nova is summarized in Table 2-7.

Capacitor Circuit. A photograph of the basic flashlamp circuit is shown in Fig. 2-61; a schematic is given in Fig. 2-62. The location of the spark gap in this circuit represents a major change from previous designs. For Nova, the spark gap will be located across the inductor and flashlamp combination; previously the spark gap was placed only across the inductor.

Relocation of the spark gap resulted from unusual failures in the Shiva capacitor bank that caused flashlamps to break. We determined that, during certain transients, the spark gaps were flashing over while the capacitors were still mostly charged, allowing the capacitors to discharge themselves into the flashlamps without being limited by the inductor. The increased current density and shortened pulse lengths caused the flashlamps to explode. Typically, all the circuits on a given switch would experience flashlamp failure.

For Nova, circuits operating with a flashlamp load will be connected as shown in Fig. 2-62. If, under transient conditions, the spark gaps should flash over, the capacitors will discharge through the spark gaps into a 5-Ω resistor, and the energy stored in the inductors will be dissipated into both the 5-Ω resistor and the flashlamp. The resistor size of 5 Ω represents a compromise among various factors; we require the resistor to provide resistance that is

- Large enough to limit the capacitor current.
- Small enough to limit the voltage across the inductor.
- Sufficiently different from the flashlamp impedance so that the lamp-circuit diagnostic circuit can discern whether the flashlamp or the dummy load (the 5-Ω resistor) is connected.

The 5-Ω resistor can also serve more than one function. We can employ it either as a dummy load, with the select switch in the alternate position, or as a surge-limiting resistor, with the select switch positioned as shown in Fig. 2-62.

Test Program. Before installing certain components in the test bank, we put them through separate test programs to establish their performance characteristics. The high-density capacitors were tested in this way;

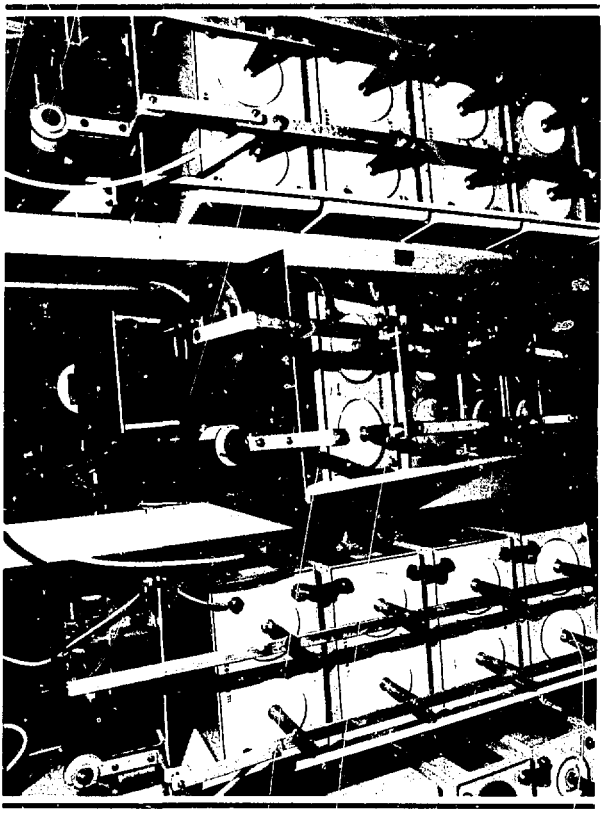

Fig. 2-61. The basic Nova energy-storage module.

Table 2-7. Power-conditioning staging for Nova.

Nova

Component	No.	Circuits	Energy	Lamps	Capacitance per circuit (μF)	Inductor size (μH)	Power supply	Switches
Faraday rotator (9.4 cm)	22	22	462-3 kJ[a]	—	108	—	3 kVA	3
Faraday rotator (15.0 cm)	20	80	1 920-3 kJ	—	116	—	2 kVA	4
Faraday rotator (20.8 cm)	20	100	4 000-5 kJ	—	200	—	4 kVA	8
Faraday rotator (31.5 cm)	20	80	3 360-3 kJ	—	200	—	4 kVA	8
Rod amplifier (3.8 cm)	28	28	1 176-3 kJ	168-19 in.[b]	203	450	3 kVA	6
Amplifier (9.4 cm)	40	320	5 760-3 kJ	640-44 in.	87	450	2 MVA	20
Amplifier (15.0 cm)	20	240	4 320-3 kJ	480-44 in.	87	450	2 MVA	20
Amplifier (20.8 cm)	60	480	12 000-12.5 kJ	960-44 in.	104	450	2 MVA	20
Amplifier (31.5 cm)	8	800	30 000-12.5 kJ	1600-44 in.	156	650	4 MVA	40
Amplifier (46.0 cm)	6	960	36 000-12.5 kJ	4800-19 in.	156	450	4 MVA	60
PILC	—	14	84-3 kJ	—	29	—	2 kVA	14
Total		3114	17 082-3 kJ 4 000-5 kJ 78 000-12.5 kJ	4968-19 in. 3680-44 in.			18 kVA 12 MVA	203

[a]The 3-, 5-, and 12.5-kJ figures indicate the energy per capacitor.
[b]The 19- and 44-in. figures indicate the size of the flashlamps.

Fig. 2-62. Schematic of a basic Nova circuit.

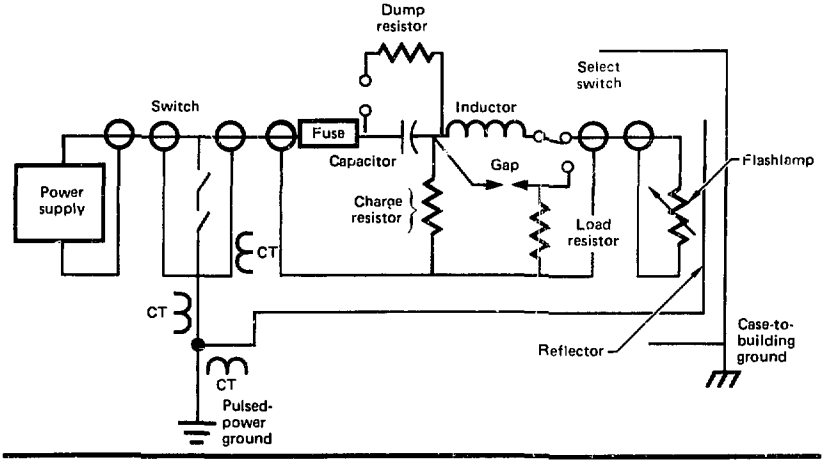

the test program is described elsewhere.[38,39] The high-power resistors also required a separate test program. On Shiva, the high-power resistors had the highest failure rate of any component. Consequently, we screened the products of over 20 vendors and performed extensive tests to find cost-effective resistors to be used as dummy loads and dumps on Nova.

Dummy loads are used as alternate loads for testing the energy-storage system; dumps are resistors used to absorb energy left in the capacitors after a shot. Dump resistors are rated at 1000 Ω to give a resistance-capacitance (RC) time-constant that is long enough to allow the mechanical dump mechanism to react and to keep the current low. Dump resistors must be capable of absorbing up to 200 kJ in a single shot under fault conditions. The dummy load is rated at 5 Ω and has similar energy requirements.

Our experience in modeling and testing circuits has shown that normal operating levels in the bank are exceeded by large margins in fault conditions; to prevent propagation of fault damage, components must be very conservatively rated. We identified two vendors whose products meet our needs: The Carborundum Co., and Allen Bradley, Ltd. We performed tests on their products that extended the data well

beyond the Nova operating point, and we identified explosion energies for each component in the high-power circuit. We have placed orders with Allen Bradley, Ltd., for dummy loads and dump resistors for Phase I of Nova; Fig. 2-63 shows dummy load and dump resistors in a typical circuit installation.

Ignitron Switches. The Nova energy-storage system uses ignitrons for the switch element; we have taken a number of steps to ensure their reliable operation. The most troublesome aspect of ignitrons in a large-population system like Nova is their propensity to prefire. We now buy ignitrons that meet a specified maximum prefire rate under incoming test conditions. In addition, the cathode of each tube is water-cooled to 16 to 18°C, and the anode is heated to 50°C. In the past, anode heating was accomplished by heat lamps. On Nova, we will use direct-contact heaters powered by isolation transformers; this reduces power consumption from 500 W per tube to 26 W. In addition, to prevent prefire, two ignitrons are placed in series in each switch, and a voltage divider is used to equalize tube voltage (Fig. 2-64). We also perform periodic high-potting to 25 kV ac to check the condition of each tube.

To detect and localize any prefire that might occur, we place a voltage monitor in each switch rack. This monitor is fiber-optic-coupled to the control system; if prefire occurs, the event is immediately recognized and remedied. We have taken similar steps to diagnose and respond to ignitor failure in ignitrons. On Nova, both ignitors on each tube are fired on each shot, and current transformers monitor each one. This trigger information is fiber-optic-coupled to the control system so that failures can be localized and repaired quickly. A large current-transformer is used to monitor the main switch current as well, so that each switch is fully diagnosed.

On Nova, we will use 200 dual size-D ignitron switches. An integral number of amplifiers must be connected to individual switches to prevent partial firing of—and possible damage to—an amplifier's flashlamps. The switches are staged so that individual beamlines may be fired independently. The subassemblies for these switches are all designed, and long-lead-time orders have been placed. We will soon order ignitors for qualification to our new specification.

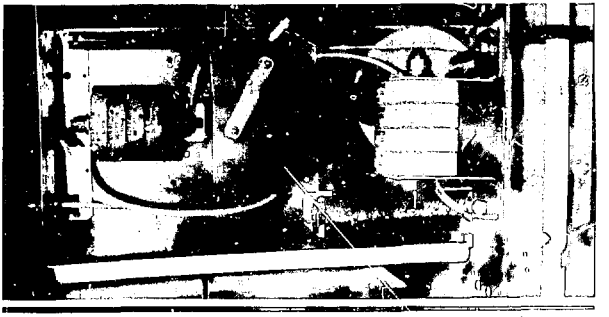

Fig. 2-63. A dummy load and dump resistor in a typical Nova circuit configuration.

Fig. 2-64. An ignitron switch assembled for Nova.

Nova Power Supplies. To achieve adequate capacitor-bank lifetime, the Nova bank must be charged within 30 s. This requires that we apply 25 to 30 MVA of dc power to the bank. We will use small Shiva-type 100-kVA supplies to charge the modules for the rod amplifiers and rotators, but most of the bank will be charged by 12 substation-sized power supplies (plus one spare) located in the substation areas outside the Nova laboratory building. For Phase I of Nova, we have ordered seven of these large units from Aydin Engineering of Palo Alto, Calif. The first unit has been

thoroughly tested and has over 3000 charge cycles on it; four of the remaining six units were delivered this year.

We have designed new control hardware for the 100-kVA power supplies, including a new phase controller, new silicon-controlled rectifier (SCR) gate-driver cards, and new isolation amplifiers. The new phase-controller module provides higher reliability and performance and requires no calibration. This is accomplished using a phase-locked loop, a precise analog-to-digital converter, and digital logic. We designed new SCR gate-driver cards to eliminate a noise problem we experienced with our earlier design. We proved this year that noise within the supply could turn on the gate drivers erroneously; the new cards eliminate this problem.

Our new isolation amplifiers achieve high-voltage isolation through a fiber-optic link. A voltage-to-frequency converter at the output-voltage divider transmits an optical pulse train having a frequency that is a linear function of the output voltage. This pulse train is sent to the isolation-amplifier module via fiber-optic cable. The module converts the pulse train to a voltage that is a linear function of the pulse frequency. The total system, converting voltage to frequency and frequency to voltage, is accurate, linear, and temperature-stable.

Optical-Isolation Pulsers. Optical isolation is required in the laser chain to prevent amplified spontaneous emission, to prevent oscillation from building up, and to prevent reflected power from damaging components. On Nova, we will obtain the required isolation using three basic techniques: Pockels cells for small apertures, Faraday rotators for apertures up to 35 cm, and plasma shutters for larger apertures. Pockels cells use electrically active crystals in a switched electric field to redirect reflected power. Faraday rotators use the Faraday effect in doped glass to redirect reflected power. Plasma shutters use exploding-wire technology to place a blocking plasma in the way of reflected laser light.

We have used a number of techniques to pulse Pockels cells in the nanosecond regime. Cells in the laser chains must each be switched simultaneously. For Nova, an N-way fan-out was designed to be switched with a hydrogen thyratron; its rise time is 15 ns, which is adequate for chain Pockels cells. In the case of Pockels cells near the oscillator front end, the rise time must be maintained at 1 to 3 ns with no more than 200 ps of jitter. For this application, we use planar triode pulsers. The planar triode is a 3000-MHz device which can be operated in a switched mode. In this mode, for pulses from 5 to 25 ns, the rated cathode current can be greatly extended, and a single tube is capable of putting out 30 A with several kilovolts of anode swing. Figure 2-65 shows a planar triode pulse chassis; Ref. 40 describes the application in greater detail.

The Faraday-rotator pulse system is very similar to the flashlamp system, with the exception that the circuit uses no inductor for pulse shaping. The load is the coil in the rotator body that generates the magnetic field. The inductance-capacitance (IC) of the energy storage and the load coil would ring at about 9 kHz if the backswing diode were not used. The ringing would not be deleterious to the rotator's performance, since there is sufficient time at the first current peak to satisfy system requirements; however, the ringing exchanges a great deal of charge through the switch, and many additional switches would be required were the diode not used.

This year, we eliminated the water circuit on the Faraday-rotator diode stacks. Our experience on Shiva showed that the low-conductivity water (LCW) used for resistive equalization eventually would leak, causing problems with wet components in the capacitor banks. The water circuit was used primarily for voltage distribution because it acts like a resistive divider; nevertheless, the cooling it provides is not necessary under the low-repetition-rate conditions of the Shiva and Nova laser systems. For Nova, we have solved this problem by using discrete high-voltage resistors rather than LCW for resistive equalization.

The plasma-shutter pulsed-power system has been described in detail elsewhere.[41,42] In summary, it utilizes four UV preilluminated rail gaps, low-inductance capacitors, an elastomer-dielectric system, and coaxial geometry to obtain the required 650 kA in 400 ns in a small package that fits in the laser chain. The system has been successfully tested on an arm of the Shiva laser, and it has stopped beams of Nova intensity in the time required.

Power-Conditioning Controls. The pulsed-power system is controlled and monitored by the computer system diagrammed in Fig. 2-66. The central control computer is a DEC VAX 11/780. Operators control the system using a display/touch video panel, selecting control functions from a series of menus. The computer responds by generating a series of commands to the hardware devices. These commands are put in a memory shared with LSI 11/23 front-end processors (FEPs) that route the commands to the hardware through fiber-optic links. The FEPs constantly poll the hardware devices for status information, placing it in the common memory. The

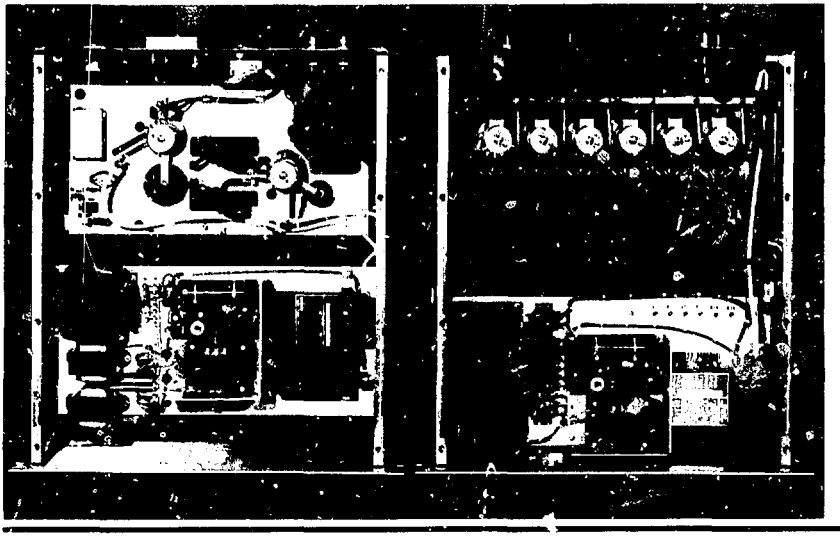

Fig. 2-65. Planar-triode pulser chassis used to pulse Pockels cells in the nanosecond regime.

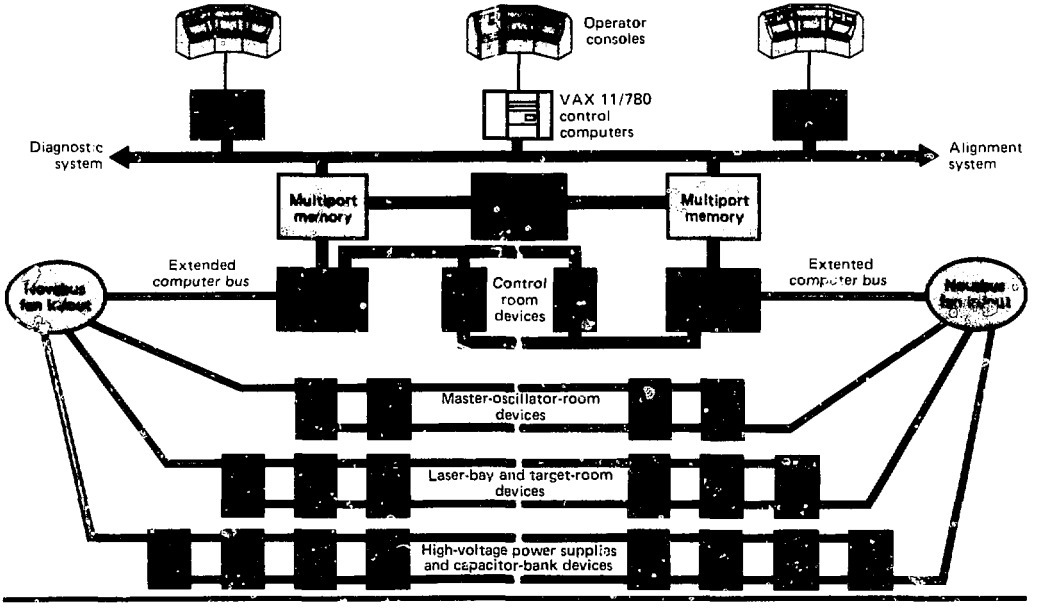

Fig. 2-66. Schematic of the Nova pulsed-power control system.

control computer thus has constant access to system status.

Pulsed-power devices are connected to the FEPs in a redundant fashion. The internal bus of the FEPs is serialized and extended to service numerous devices. The interconnection network, called Novabus,[43] divides the devices among 12 parallel chains. The DEC FEPs use a multiplexed parallel bus (known as the Q bus) for communications between devices within a chassis. The LSI-11 Q bus is comprised of some 56 discrete signals: 16 for data, 18 for address, and 22 for control. The Q bus is both asynchronous and multiplexed; each bus transaction is sequenced by handshake signals between the device initiating the bus cycle (usually the CPU) and the responding device.

Each bus transaction is complete within about 10 μs, or a time-out occurs. Any extension of the bus must take into account the additional delay incurred and ensure that bus time-outs do not result. If propagation delays were the main concern, the bus could be linearly extended for thousands of feet, but differential delays between bus lines (skew) turns out to be the limiting parameter for optically isolated parallel buses. Skew is not a problem with a serial bus, since there is only a single line. However, differential delays, resulting from differences in turn-on and turn-off switching times, cause problems that, when resolved, result in an increased propagation delay.

The main timing consideration for serial systems is multiplexing the original parallel bus data, sending it over a single signal channel, and converting the returning serial data to the parallel bus format. Such a multiplexing system requires that the serial system operate at relatively high speeds. Using a system operating at 10 Mbit/s, the Q bus can be serialized with an overhead of less than 4 μs. Complex bus structures increase this overhead to 6 to 7 μs, which is still well within the time-out interval.

The selection of which Q-bus signals to send, and in what order to send them over the serial bus, involves many trade-offs. The serialized message must contain address bits, data bits, and control bits; the number of each and their configuration determines the message format. Our design priorities for the Nova format are that it

- Be transparent to all CPU operations.
- Be compatible with multitapped bus networks.
- Incorporate global (address-independent) control capability.
- Be compatible with active or passive starred networks.
- Provide inherent error checking.
- Be compatible with redundant bus operations.

The resulting message format is shown in Fig. 2-67. Each message begins with a start bit followed by 12 address bits and an input/output bit to designate if the message is a request for input data or an output command. The next two bits are global command bits and also provide the necessary delay between the address bits and the data bits. The global master-reset command supports redundant bus operations, and the universal trigger bit supports system synchronization.

Communication between the computers and the pulsed-power devices takes place in a hostile environment of high voltage, high currents, and fields of extreme electromagnetic interference (EMI). Additionally, the communication system provides isolation between devices. Using fiber optics as a communication medium resolves the isolation requirement, but does not satisfy the noise-immunity requirements. Optical communication is inherently immune to EMI, but the signal-conversion process from optical to electrical is noise-sensitive. This is especially true if the data rate (bandwidth) is high and the optical flux is of low intensity. The Nova control system operates at 10 Mbit/s with an optical flux of 10 μW. We have tried shielding the optical receiver, with limited success. To resolve the noise-immunity problem on Nova, we will store

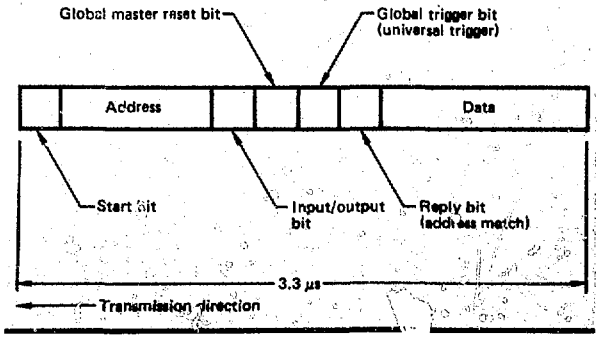

Fig. 2-67. Design of the Nova control-system message format.

in the device-interface electronics those commands scheduled to occur at peak noise periods. Thus, during the time of high noise levels, optical-to-electrical conversion errors will not adversely affect operation of the system.

Figure 2-68 is a schematic of the interface between the control system and an ignitron switch. Note that the pulsed-power elements are electrically isolated from the control electronics. Triggers to the ignitron are sent via fiber-optic cables; feedback to the control system is provided by current-transformers around the ignitron leads and by the ignitron itself; feedback is transmitted via fiber cables.

The Nova lamp-circuit diagnostic (LCD) system provides capability for flashlamp-circuit diagnosis under computer control. The LCD system provides data acquisition and threshold detection for current waveforms in the Nova pulsed-power system. The system also allows preshot testing of flashlamp circuits by doing a pulse-ionization lamp check (PILC), in which the lamps are fired at a very low energy. The LCD system will be used in Nova for diagnosing the health of flashlamps before full-energy shots and for recording pulsed-power current waveforms for analysis by computer or human operator.

Current-transformers are used to measure currents in the return leg of the lamp circuits, in the amplifier reflector ground connection, and in the connection from the ignitron switch ground to earth ground (see Fig. 2-68). If there are no faults in the pulsed-power system, the current in the return leg is an indication of the actual lamp-circuit current. If a fault occurs, some of the current may return through the reflector ground. This occurs if there is a short or an arc to the reflector, if there is a short through the connection from the ignitron ground to earth ground, or if there is a short or an arc to building ground. Thus, we can detect a fault in the pulsed-power system associated with the ignitron switch we are monitoring.

The PILC pulsed-power system generates a low-energy pulse that is sent to all of the lamp circuits on a given ignitron. The energy is distributed approximately equally among the lamp circuits on the ignitron. The LCD system determines whether the lamp currents exceeded a certain threshold, which indicates that they have ionized and are in good condition. If the lamp currents are below the threshold, no full-energy shot will be fired until the problem is located and maintenance is performed.

The LCD system is interfaced to the power-conditioning FEPs through Novabus. The computer has complete operating control of the LCD system and is able to read the data it acquires. The system can sample data for 4 ms, with a maximum time between samples of 64 μs. There are two ranges for recorded data: a high range for full-energy shots, and a low range for PILC tests. The latches used for determining whether the tested current exceeds threshold have corresponding settings; a high setting for full-energy shots, and a low setting for PILC tests. Recorded data can be analyzed both qualitatively and quantitatively. The correct lamp-circuit current pulse has an easily recognized characteristic shape; deviation from this shape indicates a definite problem. Recognition can be performed

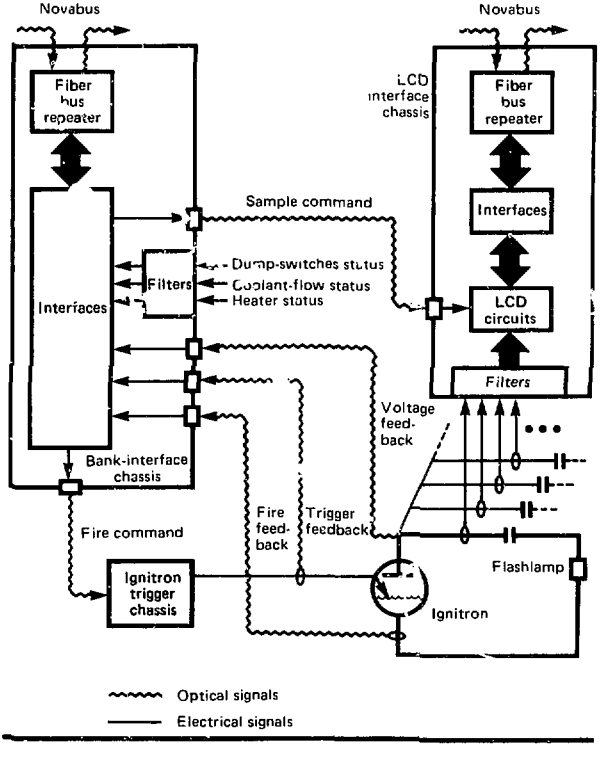

Fig. 2-68. Schematic of the ignitron control and monitoring system.

with a computer or by an operator.

Design of the control system is nearing completion, and all critical items have been tested on our 1-MJ test bank. Over 1200 circuit boards have been ordered, and the completed chassis are being fabricated.

Authors: D. J. Christie, D. G. Gritton, B. T. Merritt, and K. Whitham

Major Contributors: B. M. Carder, G. R. Dreifuerst, J. R. Holloway, J. A. Morton, J. A. Oicles, and J. A. C. Smart

Oscillator and Front-End Subsystems

The Nova front end includes all beamline components ahead of the individual amplifier chains, and its function is to provide input pulses to each chain. The front end is subdivided into a master oscillator room (MOR), where initial pulse generation and preamplification occur, and a splitter array, which splits and transports the MOR output to each chain input.

Master Oscillator Room. The functions performed in the MOR derive from Nova system requirements. The Nova MOR must provide

- Transform-limited pulse generation at 1.05 μm, with nominally Gaussian temporal pulse shapes and variable pulsewidth capability from 0.1 to 10 ns.
- Preamplifier gain that is adequate to reach 5 J/cm^2 at the MOR output for all pulsewidths and that is continuously adjustable down to 5 μJ/cm^2.
- Spatial shaping to produce a 70% fill factor for the output beam with a peak-to-average ratio less than 1.3:1.
- Prepulse discrimination of 10^{10} against unwanted portions of the oscillator waveform.
- Discrimination against amplified spontaneous emission (ASE), such that ASE at the target originating in the MOR is less than that from the chains.
- Capability of measuring the synchronization between pulse-arrival times on target to within ±10 ps.
- Table and rack space for a second oscillator system and preamplifier beamline to allow for the addition of a synchronized diagnostic pulse.

Of these criteria, only the capability for measuring on-target pulse-synchronization was added this year. Consequently, the major features of the MOR have not changed. Figure 2-69 is a schematic of the current Nova MOR layout, which satisfies all the above criteria. Details of a similar functional layout for Novette are given in "Novette Master Oscillator Room," earlier in this section.

Reliability of the MOR is extremely important because overall Nova performance depends directly on the proper functioning of the MOR. We have addressed the issue of reliability by emphasizing both

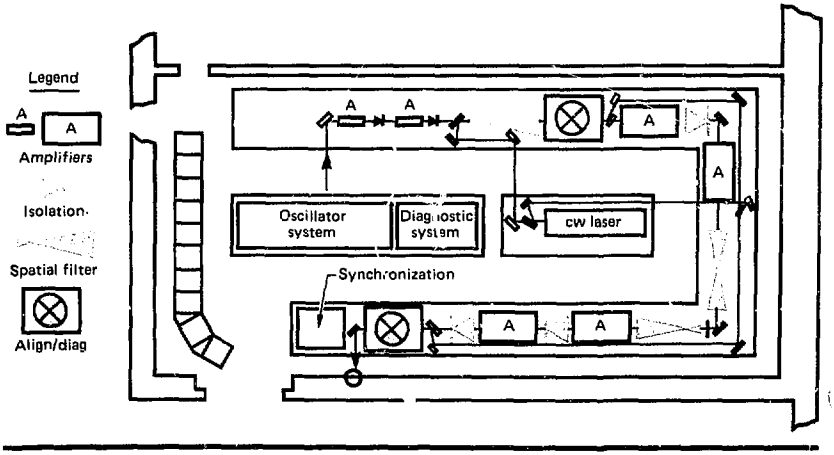

Fig. 2-69. Layout of the Nova master oscillator room.

individual-subsystem reliability and overall maintainability. Reliability is directly improved through automatic alignment systems and computer monitoring of adjustable components. The criterion of maintainability was a primary source of the basic MOR concept: an electrically and physically isolated laser system performing as many front-end functions as possible in a separate facility. One of the MOR subsystems that has been extensively engineered for reliability is the oscillator system. In addition to initial pulse generation,[44] the oscillator system provides all the fast timing signals for the total Nova system.

Oscillator Controls and Timing-Pulse Distribution. The function of the oscillator-control and pulse-distribution system (Fig. 2-70) is the integrated control of four laser oscillators along with the synchronization of high-speed system elements, including ASE Pockels cells, plasma shutters, beam diagnostics, and streak cameras used in target diagnostics. During 1981, we finalized the design of the oscillator-control and pulse-distribution system and developed a successful prototype. We needed the prototype to test the system's fast-timing circuitry and to verify that the delay-generated trigger channels would operate with subnanosecond jitter. Our measurements at the end of the year demonstrated that we could expect jitter in the range of 250 to 500 ps. The Nova controls require a greater degree of power-conditioning computer interaction than Shiva controls; much of the year was spent in optimizing this interface. We have completed our development of the system and have installed these controls in the Novette MOR.

Nova's fast synchronization is based on the operating principles of the actively mode-locked and Q-switched (AMQ) oscillator. The AMQ oscillator is a flashlamp-driven Nd:YLF laser with two key control elements within the laser cavity. The first of these is an acousto-optic (A-O) modulator driven by a 62.5-MHz reference signal. The period of this signal is matched to the cavity's round-trip time, and the resulting oscillating waveform is a single, low-energy, transform-limited pulse. To increase the pulse energy, the oscillator is simultaneously Q-switched.

The Q-switch device is the second control element within the laser cavity; it causes the laser to lose gain when driven by an rf source. When the 32.5-MHz drive to this element is removed, the laser Q-switches and dumps the energy stored in the Nd:YLF lasing medium. This process results in a laser output that grows in amplitude until the

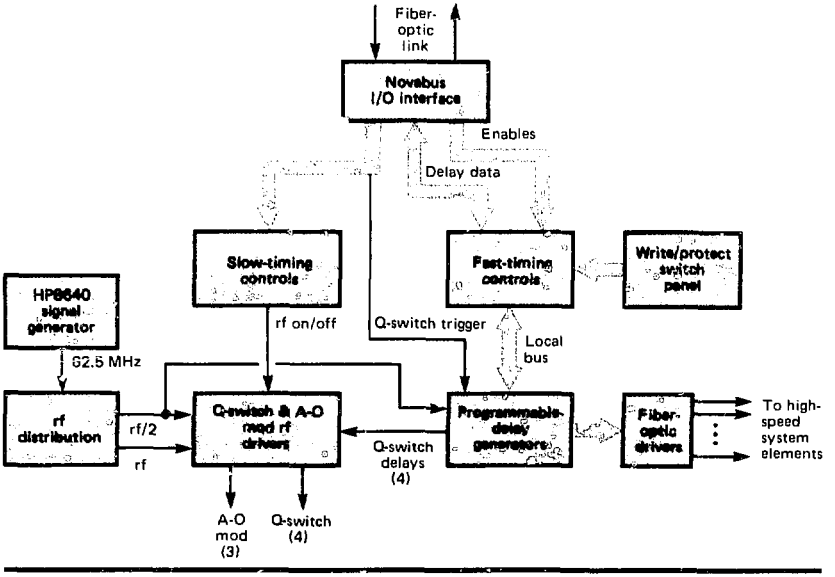

Fig. 2-70. Nova oscillator-control and pulse-distribution system.

peak pulse is many orders of magnitude larger than the quasi-cw prelase level. The pulse train then decays in amplitude as energy is depleted. A single high-energy pulse is optically switched out at the peak of the pulse train; this pulse then propagates down the Nova laser chains and is amplified before reaching the target.

Since the timing of the high-energy pulse is tied directly to the 62.5-MHz reference signal driving the A-O modulator, the laser's high-speed system elements can be easily synchronized. Nanosecond-accurate event triggers $\pm 1\ \mu s$ from switchout are achieved by clocking a bank of programmable timers with the same rf source and initiating them at Q-switch time. The sequence of events just described covers a time from approximately 10 ms before switchout to $1\ \mu s$ after. The oscillator is Q-switched at a rate of 10 pps to ensure reliable steady-state operation.

The Shiva controls were designed to support just one oscillator and were capable of synchronizing only seven high-speed system elements. The planned implementation of up to four oscillators in the Nova MOR, and our increased demand for up to 60 fast triggers with nanosecond accuracy, resulted in the need for a modular and easily expandable control system.

The number of oscillators a system can support is primarily determined by the availability of rf amplifier circuits that are needed to drive the A-O modulator and Q-switch elements in the oscillator cavity. These two elements require separate rf amplifier channels. The Q-switch is very sensitive to amplitude variations; small perturbations will initiate spurious Q-switching. The A-O-modulator rf channel, in contrast, must exhibit very stable phase characteristics.

The need for high performance in these areas led to a modular packing approach in which the rf handling circuits were separated and shielded from other elements of the subsystem. Readily available commercial rf components were found to exhibit suitable amplitude and phase-stability characteristics. These amplifier channels can be easily added according to demand.

The number of nanosecond-accurate fast timing triggers that a system can generate is dependent on the delay-generator's programming requirements. A total of 14 bits of information is required to program each timer (Fig. 2-71). Once the binary counter elements (+32 ns coarse delay) have counted down, they must be reloaded before the next Q-switch time. On the Shiva controls, this was accomplished by storing the information in thumbwheel switches. This method would be cumbersome with a larger system; instead, with the Nova controls, the delay data are stored in a 256×8 RAM. The contents are continuously reloaded into each of the delay generators

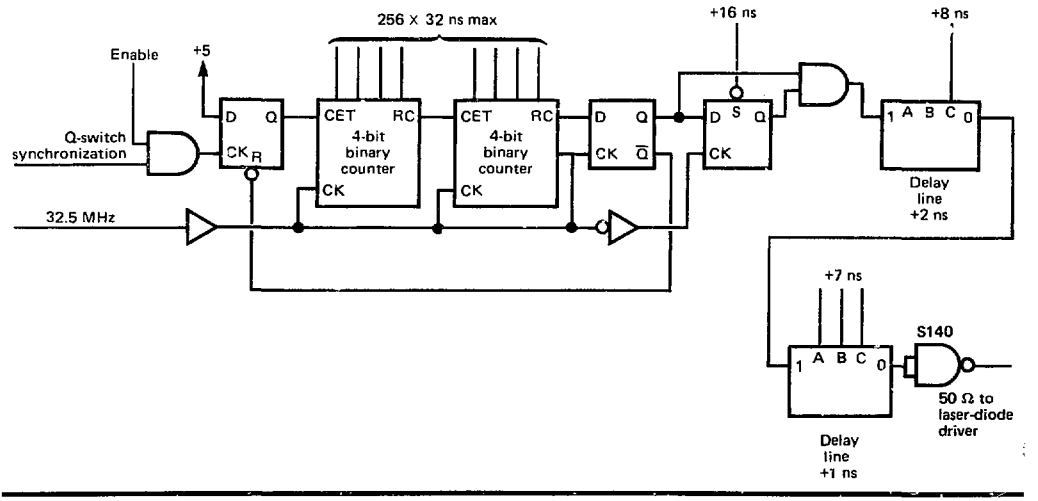

Fig. 2-71. Programmable delay-generator channel.

over a local bus structure during the interval between Q-switch times. With this expandable structure, we can realize up to 128 discrete delay channels.

The use of a RAM to store delay data required two added protection features. The first of these involves the capability to remotely alter the RAM contents over the Novabus input/output interface. It was evident that a hardware-protection feature would be needed to prevent unauthorized access to the RAM by the computer system. We accomplished this by electrically segmenting the RAM into 16 address ranges of variable length, then determining computer access to that block with a dedicated block write/protect switch. In this way, users alter only the contents of their own block. The second RAM-protection feature is a battery backup circuit to guarantee nonvolatile RAM operation during a power-down event.

We also required a new packaging approach to accommodate the large number of delay-generator channels and their accompanying fiber-optic laser-diode drivers. We found that four delay-generator channels would fit nicely on a single four-layer printed circuit board. We determined also that 16 of these boards, along with accompanying bus isolation, bus drivers, and terminator circuitry, could comfortably occupy a single deep chassis measuring 17.5 in. wide by 10.5 in. high by 20 in. long. It will take two of these chassis to provide the maximum of 128 delayed timers. The spare six slots in each chassis will be used to fan out delayed timers, as desired, to up to 16 separate laser-diode drivers. We have found that four of these laser-diode drivers *fit well on a single shielded nuclear instrumentation* module (NIM). Since 12 NIMs can be housed in a single chassis, laser-diode drivers can be added to the system in increments of 48.

Splitter Array. The splitter array divides and transports the MOR output to the individual amplifier chains. Our requirements for the splitter array, like those for the MOR, derive from overall Nova performance criteria. The splitter array must provide

- Adjustable division of the MOR output energy to allow balancing of the chain outputs for symmetric target illumination.
- Adjustable time delays for each chain to allow synchronization of pulse-arrival times on target.
- Relaying with sufficient accuracy to give a spatial profile with a peak-to-average ratio less than 1.3:1 in each chain.
- Space for a 5-cm rod amplifier after the first splits to allow for a future increase in drive to the chains.

Each division of the pulse will be done with polarizers, as in the MOR, so that computer-controlled wave plates can be used to adjust the fraction split. Adjustable splitters, rather than attenuators in the chains, allow balancing of the chain outputs without loss of total drive energy to the chains. They also allow injection of all the MOR output into selected chains for alignment purposes. Figure 2-72 shows the geometry of one of the five-way splitter assemblies to be mounted at floor level on each laser spaceframe. Adjustable time delays are provided by trombone sections that allow us to adjust the path length.

Image relaying[45] of the spatial beam profile in the splitter array is required to maintain the profile without diffraction. Perfect relaying results for only one propagation distance, and the peak-to-average criterion

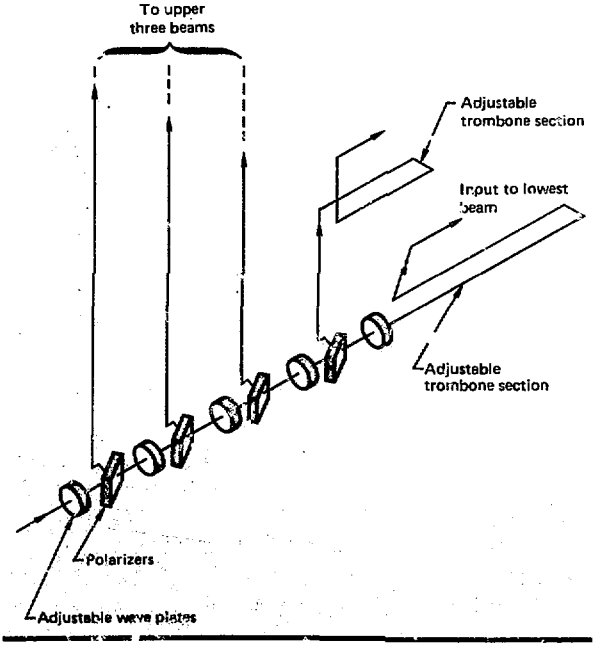

Fig. 2-72. Layout of the five-way splitter assembly, showing trombone sections and adjustable splitters.

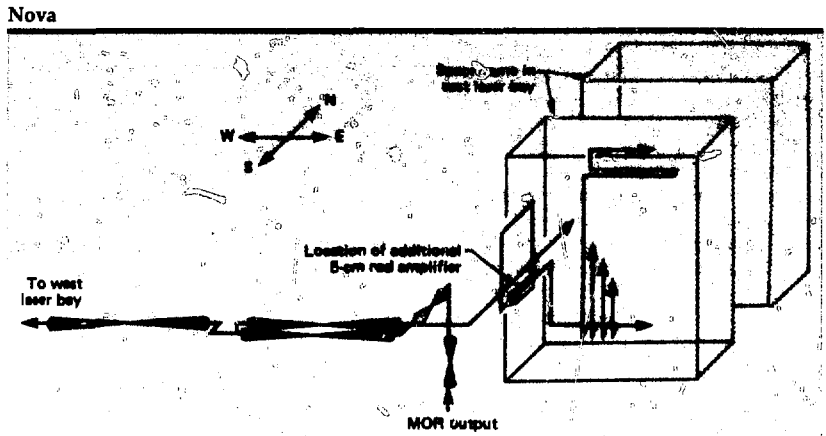

Fig. 2-73. Splitter-array layout for full Nova, showing locations of relays and space for additional amplifiers.

determines the relaying tolerance—i.e., the range of distances for which a given relay can be used. Propagation tests with our MALAPROP diffraction code show that we can maintain peak-to-average ratios <1.3:1 with relaying errors as large as ±50 ft. Since the path lengths between the MOR and chain inputs vary by only ±30 ft, we can use a single relaying scheme for all beams.

The number of individual relays for a single relaying scheme depends on the geometry of the splitter-array layout. The cost of a relay is nearly independent of its length, so cost dictates that we minimize the total number; however, the maximum lengths of relays are determined by available straight sections in the layout. Figure 2-73 shows the splitter-array layout and relay locations for the full 20-beam Nova system. Where possible, relays are located ahead of the splitters to avoid duplication. However, half the total distance relayed is taken up by the relay itself for the 1:1 relays used here. Since the first split occurs less than halfway to the chain inputs, one relay must be located after the first split and, therefore, must be duplicated to relay each beam. The layout in Fig. 2-73 requires five individual relays.

We have allocated space on the ends of each laser spaceframe for an additional rod amplifier just prior to the last five-way split. This location (shown in Fig. 2-73) is above head height to allow access to the frame interior.

Authors: J. E. Murray and J. W. Morton

Major Contributors: E. S. Bliss, G. S. Bradley, G. R. Dreifuerst, D. J. Kuizenga, J. A. Oicles, and K. D. Snyder

Alignment and Laser Diagnostics

Introduction. Nova's alignment and laser-diagnostic systems[46,47]

- Guide laser pulses through the separate amplifier chains to the target.
- Measure the pulse ' temporal, spatial, and energy characteristics.
- Ensure simultaneous arrival of the pulses at the target, to within 5 ps.

At the time of a target shot, over 200 energy values are measured simultaneously. Alignment tasks accomplished prior to each target shot involve automatic or remote-manual adjustments of approximately 2000 stepper motors and other actuators for the 20-beam, three-wavelength Nova laser system.

The sensor packages and individual detectors used for gathering alignment and diagnostic data on Nova are modular to minimize the number of different design and fabrication efforts. The output sensor, for example, comprises separate, but essentially identical, modules for each of the three operating wavelengths.

The primary detectors for alignment functions are charge-coupled-device (CCD) cameras with both digital and standard video output. Automatic alignment loops are closed by digital processing of the video data. At the same time, operators can easily

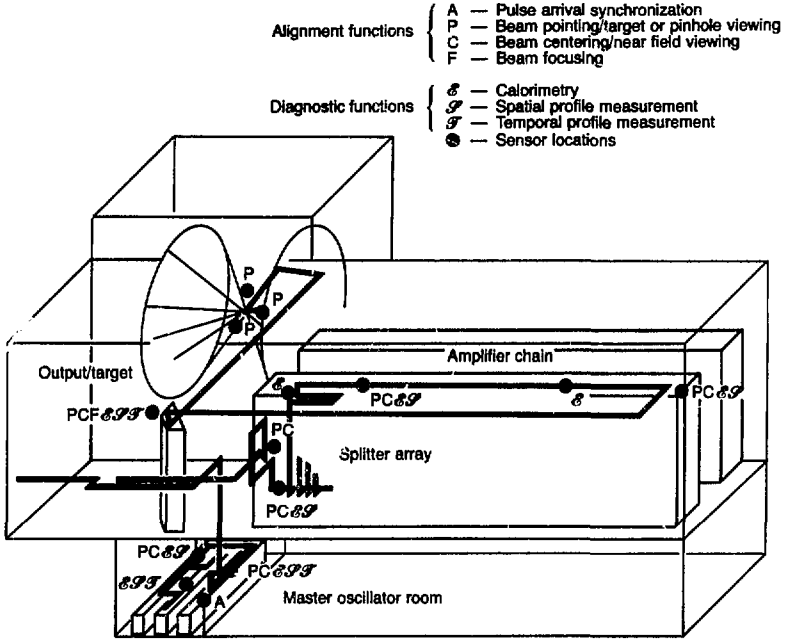

Fig. 2-74. Alignment and diagnostic subsystems functions and sensor locations for a single Nova amplifier chain in the east laser bay.

monitor the automatic operation by viewing standard video displays.

The primary detectors for diagnostic instrumentation are absorbing-glass calorimeters, calibrated photodiodes, and photographic film. High-speed streak cameras also play an important role. Diagnostic instrumentation of such a large optically pumped laser is particularly challenging because both the optical and electromagnetic background levels at shot time are very high. Handling and processing of diagnostic data are accomplished digitally, and both the alignment and diagnostic systems are integrated into Nova's facility-wide digital control network.

System Overview. Figure 2-74 shows the four major alignment and diagnostic subsystems of Nova and the tasks performed in each. These subsystems are located in different parts of the Nova facility, and they sample beams of widely varying diameter and signal level. As the figure shows, however, the same basic functions are performed in each area.

At a number of locations in the 20 laser chains, the beam position is compared with insertable cross-hair references that are permanently mounted on the laser spaceframe. Beam-position comparisons are made by examining a near-field image of the beam in the plane of each cross hair on which the beam should be centered; this function is designated "C" in Fig. 2-74. More than one cross hair can be viewed by most near-field sensors, and there are eight cross-hair locations in each chain. All of the cross-hair insertion mechanisms are of similar design; all are driven by stepper motors and are controlled through the Nova digital control network.

At most sensor locations, the precise propagation direction of the beam is also important. In the MOR and splitter-array subsystems, for example, each of the principal beam-path segments is defined as the line that passes through the center of a particular cross hair and is pointed in a specified direction. A sensor package ("P" in Fig. 2-74) in each path provides the ability to monitor beam pointing. The sensor brings the beam to a focus on the detector; then offsets of the beam at this focus are proportional to changes in the pointing angle. In the pointing mode of operation, the sensors are used as far-field viewers; the sensors

can also provide images of spatial-filter pinholes or the target, depending on location of the sensors in the system.

Table 2-8. Nova component-alignment tolerances.

	Position (mm)	Direction (μrad)	Error on Target (μm)
Master oscillator room			
West table	0.5	15	—
East table	0.5	15	—
Pulsed/cw coincidence	<1.0	<30	—
Splitter array			
Transport to laser bay	0.5	15	—
Entrance to splitter	0.5	15	—
Pulsed/cw coincidence	<1.0	<30	3
Amplifier chain			
Chain input	0.5	15	—
Midchain	(Monitor only)	—	—
Pinholes	4 f/No.	—	—
Main chain	8.0	—	—
Output/target (1ω)[a]			
cw at focus lens	8.0	—	—
Surrogate target insertion	0.010	—	10
cw on surrogate target	0.010	—	15
(Focus adjustment)	(0.080)	—	(80)
Fusion target insertion	0.010	—	10
Open-loop lens offsets	0.005	—	5
		—	21 RSS[b]
Output/target (added for 2ω/3ω)			
Auxiliary mirror reflection	—	5	15
Local 2ω/3ω insertion	8	5	15
		—	30 RRS[b]
KDP crystal array			
Local 1ω insertion	3	5	—
Crystal angle for max 2ω	—	25	—
(Crystal angle by reflection)	—	(5)	—
Open-loop tilt (3ω only)	—	2	—

[a]The focus lens is assumed to be an f/4 refracting doublet.

[b]The root of the sum of the squares gives an estimate of the net error, allowing for some cancellation of random errors.

The optical systems required to accomplish the centering and pointing measurements described above also provide much of the capability for beam focusing and for the diagnostic functions listed in Fig. 2-74. We have, therefore, designed sensor packages that perform multiple alignment and diagnostic tasks

- Input sensor packages are used in the MOR and splitter-array areas and near the input to each amplifier chain.
- The midchain sensor monitors the beam at the point where it is folded back toward the output.
- The output sensor is located in the switchyard.

With these sensor packages and other systems described in this and previous *Laser Program Annual Reports*, alignment errors will be controlled within the tolerances listed in Table 2-8, and the spatial, temporal, and energy characteristics of all beams will be measured on each shot. Pulse-arrival synchronization is performed by a separate dedicated system, which is described elsewhere.[48]

Input Sensors. The design of the input sensors has been described previously,[49] but the first units were not built until this year. Figure 2-75 shows an input sensor with the

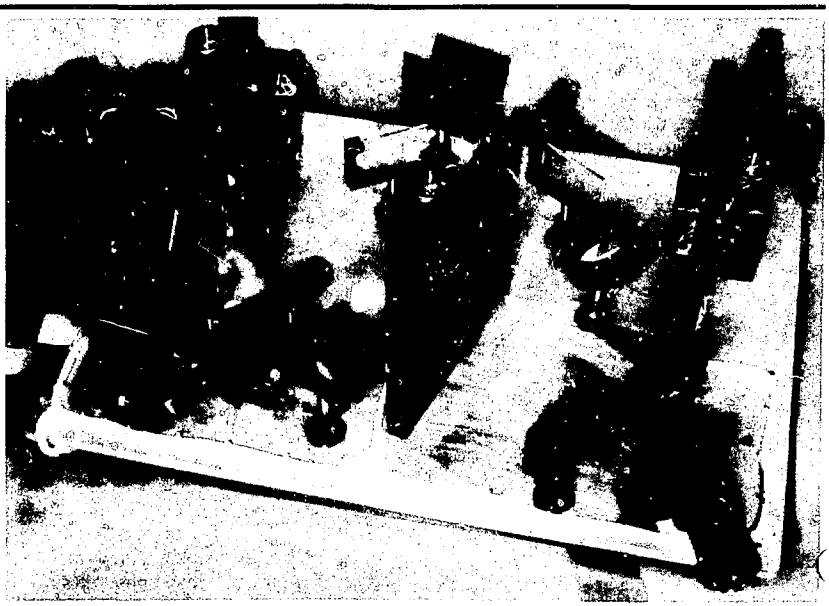

Fig. 2-75. A Nova input-sensor package with the cover removed.

cover removed. The flat cable running out of the photo to the left connects the CCD camera head to its support electronics, which are mounted separately for ease of maintenance and to keep heat sources away from other components. Figure 2-76 shows a camera electronics unit with its CCD camera head mounted behind a filter and mode selection wheel; the header box measures $2.75 \times 3 \times 1.625$ in.

The images seen by the CCD cameras in the input sensors (and in other Nova sensors) are carried over the system-wide TV network to both the control system and the system operators. A video digitizer converts the analog signals into a form suitable for use by the computers, and video-analysis software then extracts alignment data from the image. Figure 2-77 shows a sample image that has been analyzed by a cross-hair identification program. The black rectangle is added to the picture by the computer program to indicate that it has found the center of the right-hand cross hair. The difference between the center points of the two cross hairs is used by Nova's closed-loop alignment program to calculate stepper-motor commands for the gimbals that correct alignment errors. Computer analysis of video data is an essential part of the closed-loop alignment system (discussed more fully in "Control Systems," later in this section).

Midchain Sensor. The Nova midchain sensor is located at the point where the beam is folded toward the chain output. The capabilities of the midchain sensor are similar to those of the input sensor, but the midchain sensor has the additional flexibility of focus adjustment for both near- and far-field viewing. The hardware is actually a modification of an existing sensor package taken from the Shiva laser system. Figure 2-78 shows the layout of the midchain sensor for Nova and Novette. Mounted after the 20.8-to-31.5-cm spatial filters, this sensor is used to measure midchain energy, to observe the beam in both the near and far fields, and to supplement the output sensor in the tasks of spatial-filter pinhole alignment and component installation. All adjustments required for normal operation of the midchain sensor will be controlled through the alignment and diagnostics parts of the system control network.

Lenses L_1, L_2, and L_3 form a Galilean telescope with an effective focal length of 900 cm (f/26.9) and a back focal distance of 180 cm. We have chosen the telescope parameters so that the flux on the L_3 dielectric coatings is 2.2 J/cm^2 for a 15-kJ laser shot—well below damage level. In operation, these nominal conditions are achieved by translating lenses L_3 until the collimated input beam is focused in the plane of the cross hair ahead of lens L_6. The beam can also be centered on the cross hair using the motor-driven gimbals holding mirror M_3. Lens L_6 then reimages the far field at the TV with a magnification of 6.3.

The combination of lenses L_4 and L_5 has an effective focal length of about 23.1 cm and relays near-field images to the TV camera. The overall magnification of the near field is about 2×10^{-2}. Lens L_4 can be adjusted to view a range of near-field planes, including the chain-input aperture, spatial-filter inputs, and cross-hair locations.

During system alignment, the two shutters are used to select near- or far-field viewing, and filter wheel 2 controls the cw level to the TV. During a pulsed shot, filter wheel 1 controls the energy to the calorimeter and inserts a splitter to direct energy to the film holder. Both shutters are closed during pulsed shots to protect the TV camera.

Output Sensor and Related Components. The output target-alignment and diagnostics system (Fig. 2-79) is a prime example of multiple-function design. The output sensor, positioned behind a partially transmitting mirror, collects both alignment

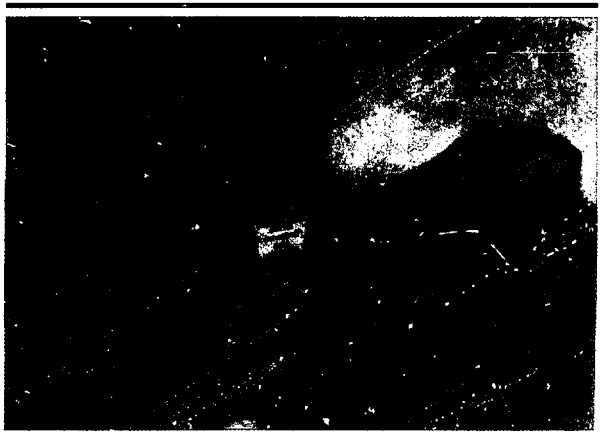

Fig. 2-76. A CCD camera head and electronics unit.

Fig. 2-77. Cross-hair images from a CCD camera after computer processing to locate the center of the right-hand cross hair.

Fig. 2-78. The midchain sensor monitors beam position, energy, and transverse profile.

and diagnostic data from the laser directly as well as from the direction of the target.

Alignment to references that are closer to the target than the sensor poses a special problem: light must somehow be returned to the sensor. For centering the beam on the cross hair near the target chamber, light is reflected from an insertable mirror. For pointing the beam at the target, we have successfully demonstrated two approaches. The target can be silhouetted against the incoming beam, with the light continuing on across the target chamber and into the opposing sensor, which is configured to image the target plane. Alternatively, a reflective spherical surrogate target can be introduced in place of the fusion target, and the reflected beam will carry information about both the pointing and focus characteristics of the incoming beam back to the sensor. Other kinds of surrogate targets are possible, and some have been described previously.[50]

Diagnostic measurements are also somewhat more complicated in the output system. For 1.05-μm (1ω) experiments, the chain output is sampled on its way to the target, and light reflected from the target is directed into the sensor by the auxiliary mirror. Discrimination between these incident and reflected signals is accomplished by temporal gating, to take advantage of the longer path traveled by the reflected light, and by angle sensing using the auxiliary mirror, to redirect the reflected beam by a specified amount.

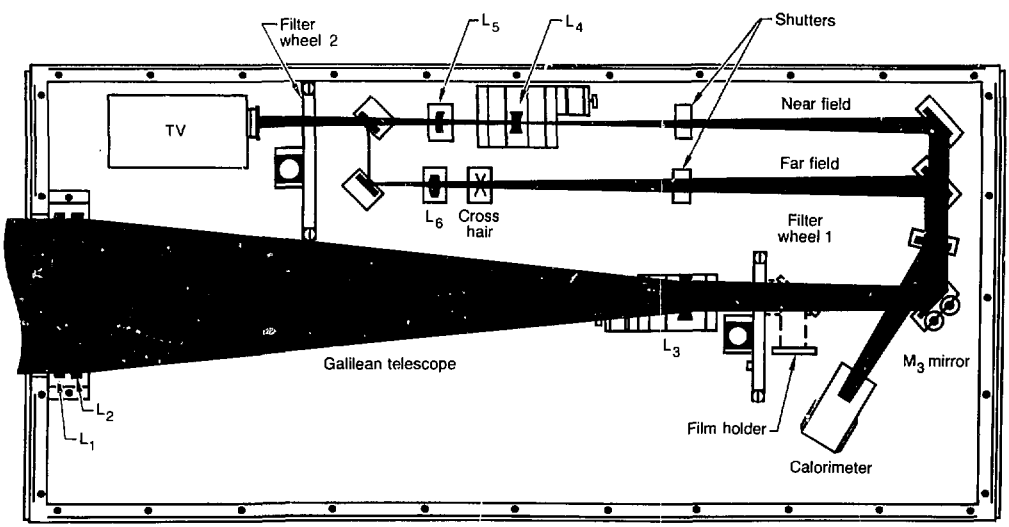

For experiments at shorter wavelengths, the optical frequency of the output beam is doubled (2ω) or tripled (3ω) in an array of KDP crystals located just ahead of the focusing optics. Gimbal and lens adjustments for aligning the beam to the target are accomplished using a local source of 2ω or 3ω light that is collinear with the 1ω beam. This full-aperture alignment beam is inserted at the final spatial filter, as shown in Fig. 2-79.

Procedures for aligning the crystal array to the beam are based on experience gained during the last year in work with crystal assemblies in the laboratory (see Ref. 51 and "Harmonic Conversion" in Section 7). We use a small-diameter, high-repetition-rate (~3 kHz) 1ω beam that is also available from the local illuminator. A portion of this beam is converted to 2ω by a crystal in the local illuminator package to provide a reference signal. The rest of the local 1ω beam is aligned to follow the same path as the main beam to the KDP array at the target chamber. Reflecting off a corner cube in the insertable centering mirror behind the crystals, the 2ω beam generated in the central crystal of the array returns to the local illuminator package for comparison with the reference 2ω beam. The crystal array angle is adjusted to maximize the ratio of the 2ω generated in the array to that generated in the reference crystal.

For those experiments requiring the generation of 3ω light, the crystals are rotated 10° before tilting to maximize the second harmonic. Then, an open-loop angle correction of 4.4 mrad about one axis places them in the correct orientation for 3ω operation (as described in "Harmonic Conversion" in Section 7).

To return a fraction of 2ω or 3ω incident light to the ouput sensor for diagnostics, the final surface of the focusing optics is figured so that it reflects a slowly converging sample of the 2ω or 3ω beam back toward the ouput sensor. Figure 2-79 shows how this sample of the light that has been frequency-converted in the crystal assembly is returned to the output sensor. The final-focusing optic is tilted slightly so that, on reaching the first output turning mirror, the converging diagnostic reflection is offset from the center of the aperture and subtends only about 5% of the beam area. That fraction of the diagnostic beam that is transmitted by the turning mirror reflects off a recollimating mirror in front of the auxiliary mirror and is directed back toward the output sensor.

The focusing-optics diagnostic surface is so close to the target that the 2ω or 3ω

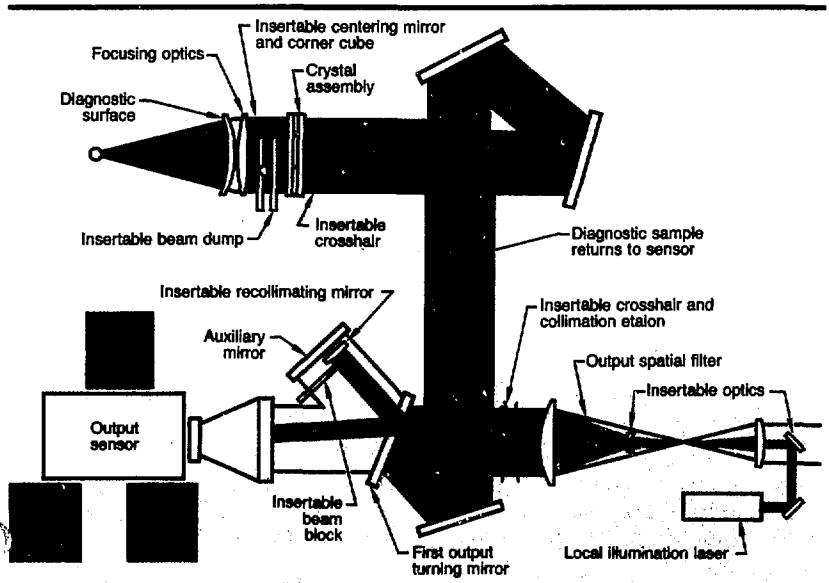

Fig. 2-79. The output alignment and diagnostics subsystem.

incident light reflected from the diagnostic surface arrives at the sensor within about 15 ns of the light reflected from the target. This period is too short for temporal discrimination by the gating techniques used for 1ω operation. Therefore, the target-reflected light and the recollimated diagnostic beam must enter the sensor with enough of an angular difference to be completely separated spatially in the far field. The recollimating mirror repoints the incident diagnostics beam at the appropriate angle. Because of its offset and reduced diameter, this mirror has an insignificant effect on the full-aperture signals that traverse the same path for other alignment and diagnostics functions. Once the various incident and reflected beams have entered the output sensor, the signals are divided among three separate modules according to wavelength. Each module provides a number of capabilities, as described in the *1980 Laser Program Annual Report*.[52]

Sensitivity to Polarization Changes. The accuracy of 2ω diagnostics is limited by polarization effects inherent in the quadrature frequency-conversion scheme described in the next article. The 2ω outputs from the first and second crystal arrays are orthogonally polarized. Since the beamline turning mirrors and the beam splitters and mirrors in the output sensor have different reflectivities for S- and P-polarization, the detectors receive unequal samples of the orthogonal 2ω components. For a constant input polarization, this is of no consequence since it can be calibrated out. The frequency-conversion process is power-dependent, however; the ratio of 2ω intensity generated in the first crystal array to that generated in the second array is dependent on the input 1ω intensity (see the following article).

For low 1ω intensity, the first and second arrays yield nearly equal amounts of 2ω light. As the 1ω intensity is increased, the ratio shifts toward increased conversion in the first crystal, causing a rotation of the net polarization vector of the 2ω light and a change in the fraction of the 2ω light reaching the diagnostics. In other words, the 2ω calorimeter-calibration coefficients are different for strong and weak pulses. Further, since temporal variations in intensity occur within each pulse, the sampling fraction changes during the pulse. This produces distortions not only in the temporal pulse shape recorded by the 2ω streak camera but also in the 2ω spatial profiles recorded on film.

We have calculated the energy-measurement error that would result from using nominal dielectric coatings on the turning mirrors and in the 2ω module of the output sensor; the transmission was assumed to be the same for orthogonal polarizations in the output sensor splitter box. In addition to errors caused by changes in the relative amplitude of contributions from the first and second crystals, these calculations include errors caused by changes in the relative initial phase of the two contributions. The calculations do not include effects due to different phase shifts for S- and P-polarized components reflecting from dielectric coatings. Because each beamline has a different set of mirror angles, the measurement error is beamline-dependent. For the worst beam, over intensities from 0 to 3 GW/cm^2 and phase variations from 0 to 2π, one output-sensor photodiode sees a maximum calibration change of 20%, the calorimeter sees a maximum change of 22%, and the second photodiode sees a change of 62%.

We are still studying this problem, but we have identified some important considerations. For example, the polarization sensitivity of the output-sensor splitter box must be minimized; it was assumed to have no sensitivity in the above calculations. The choice of coatings used on the large-aperture turning mirrors is important and should be made considering polarization sensitivity for both phase and amplitude. Finally, each segment of the KDP array is different enough in index-matching-fluid thickness, crystal thickness, crystal wedge, and crystal tilt that a different fraction of the 2ω output will reach the sensor for each segment. These sampling fractions will be distributed within the error ranges previously calculated and will ultimately lead to an improvement in overall accuracy because of averaging effects.

Diagnostic Data-Acquisition and Processing. Our requirements for acquiring and processing diagnostic data include

- Rapid turnaround.
- Effective interfacing with alignment and power-conditioning controls.
- Preservation of data under failure conditions.
- Options for local and control-room modes of operation.
- Portability of the hardware required for off-line troubleshooting and calibration.

In addition, the data-handling system must be able to operate in an environment characterized by significant electromagnetic interference at shot time, when the tens of megajoules stored in the capacitor bank are discharged into the amplifier flashlamps. The major elements of a digital system that meets these requirements have been described in previous *Laser Program Annual Reports*.[53,54]

Diagnostic signals are generated by streak cameras, photodiodes, and calorimeters and are collected in one of two ways.[53] In the first instance, single detectors that produce large blocks of data, such as CCD readouts for streak cameras (160 000 words), interface directly to the fiber-optic communications bus (Novanet); data blocks are transferred directly to the top-level Nova computers (VAX 11/780s) located in the control room. Data from transient digitizers are also handled by direct interface to Novanet and subsequent processing by the control-room computers. These computers have enough memory and speed to process the large volumes of data or to generate the complex displays associated with time-resolved signals.

The second instance involves for a diagnostic task such as calorimetry, which produces a small quantity of data per detector, but requires many such detectors. Groups of detectors are connected to a microprocessor located near the detectors. This front-end processor (FEP) collects the data and supplies control signals for the detector electronics. Operator interface at this level is through a control panel on each micro-processor chassis. Figure 2-80 is a photograph of an LSI-11 FEP with the laser-diagnostic control panel.

These FEPs are interfaced to each other and to the top-level computers in the control room via the Novanet fiber-optic bus and by a multiported shared memory.[55] The shared memory thus provides interconnection between the alignment, diagnostics, and power-conditioning controls (see "Control Systems," later in this section). With this network configuration, the mechanical functions shared by alignment and diagnostics can be readily controlled by either laser-diagnostics or laser-alignment software.

Synchronization of the diagnostic electronics to the firing of the laser is essential, and the trigger network that accomplishes this important timing function has been described previously.[53] All triggers are transmitted over fiber-optic cables. This mode of transmission provides complete electrical isolation between source and destination. In the case of triggers originating from the oscillator, this isolation is essential so that noise is not transmitted back to the oscillator timing circuitry. Noise picked up along wire cables might disrupt the gated amplifiers used with diode calorimeters.

Calibration for Calorimetry. Measurements of laser energy on Nova are made with photodiode calorimeters or absorbing-glass calorimeters; the input sensor, for example, uses a photodiode.[49] In each case, the calorimeter sees only a small fraction of the energy in the main beam at that point. The accuracy of each energy measurement can be no better than the accuracy with which the scale factor between the sensor

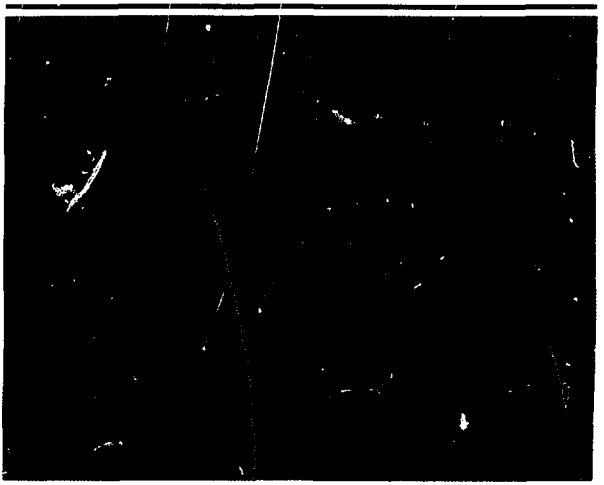

Fig. 2-80. Laser-diagnostic microprocessor chassis.

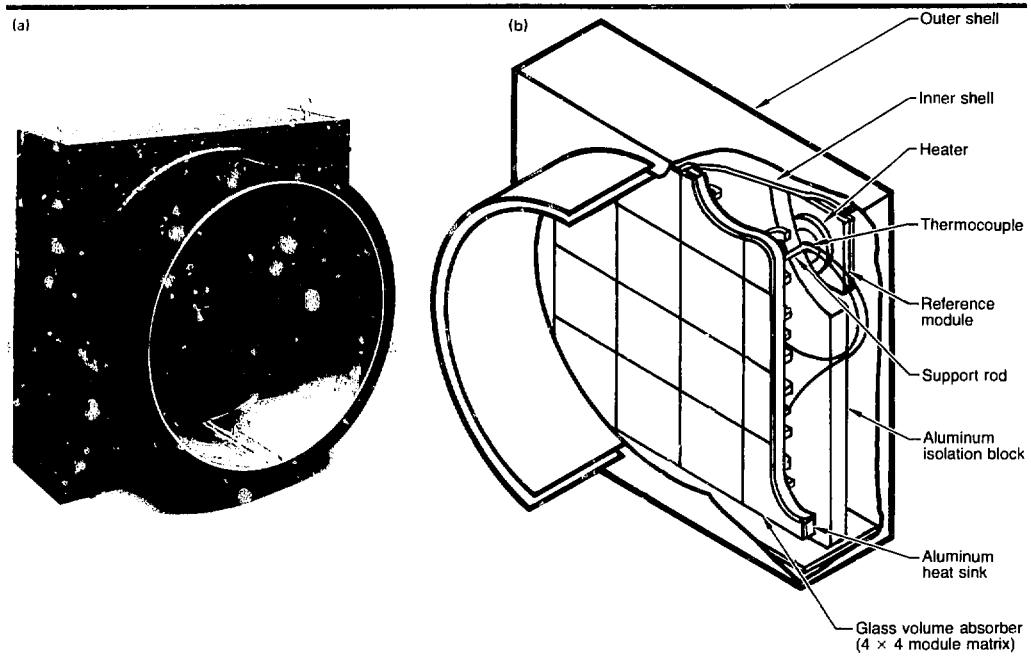

Fig. 2-81. A prototype 34-cm-aperture absorbing-glass calorimeter, and a schematic showing the segmented absorber and shared ambient reference module.

calorimeter and the main beam energy has been determined. We have, therefore, made provision at the input sensor to insert an absolutely calibrated absorbing-glass calorimeter in place of the beam tube immediately after the sensor. This enables us to determine the calibration scale factor to better than 2%.

As the beam diameter and the energy per laser pulse increase toward the output of the amplifier chain, the calibration process for energy measurement becomes increasingly difficult. For example, previous calorimeter designs fail because of excessive equilibration time if they are simply scaled to an 80-cm clear aperture. Furthermore, the requirement to measure pulses of 10 to 20 kJ at multiple wavelengths severely limits the choice of absorbing material.

Nova large-aperture absorbing-glass calorimeters utilize a matrix construction (Fig. 2-81). The equilibration time for such calorimeters is characteristic of the individual matrix-element dimensions, rather than the full-aperture dimension. After considering the absorption spectrum, laser-induced damage properties, and fluorescence radiation losses of several glasses, we have chosen 3-mm-thick Schott NG-4 as the absorbing glass. All calorimeters used for sensor calibration are themselves absolutely calibrated using an electrical-resistance heater.

Authors: E. S. Bliss, R. G. Ozarski, and C. D. Swift

Major Contributors: R. D. Boyd, D. W. Myers, J. B. Richards, and L. G. Seppala

Frequency Conversion and Target Focus

During 1981, we continued to improve our baseline design for the Nova frequency-conversion system by incorporating new ideas and working within new material constraints. The baseline configuration (shown previously in Fig. 2-32) consists of one 74-cm KDP crystal-array assembly followed by a beam dump and an f/4 fused-silica doublet. This design achieves high conversion efficiency to both 2ω and 3ω, minimizes nonlinear propagation effects, and provides a cost-effective multi-wavelength flexibility.

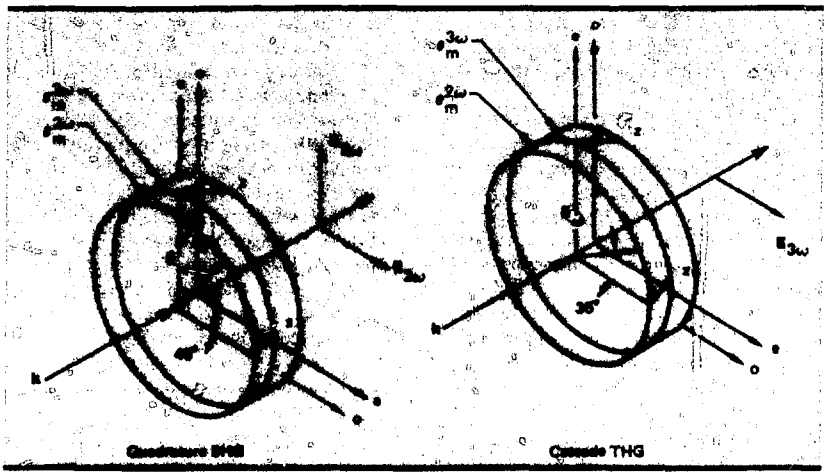

Fig. 2-82. The quadrature SHG, cascade THG frequency-conversion scheme used on Nova.

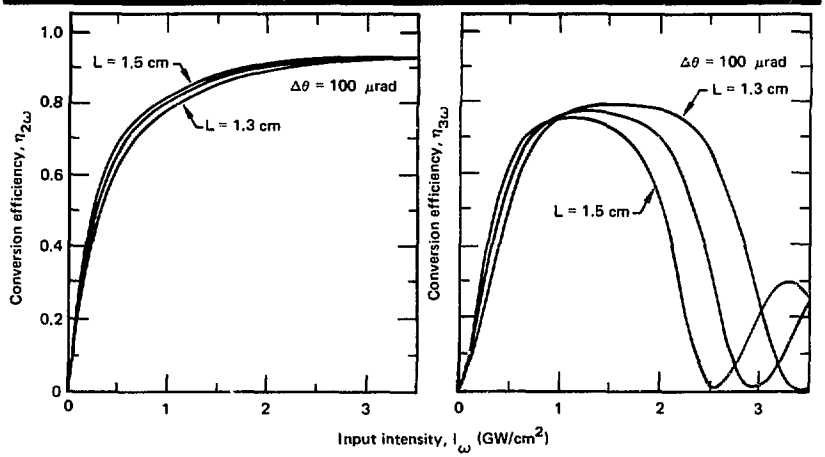

Fig. 2-83. Conversion efficiency of 2ω and 3ω generation for three crystal lengths, calculated for flat, temporal, and spatial profiles.

We have now consolidated the two separate array assemblies of our previous baseline design[56] into one assembly using a new 2ω/3ω frequency-conversion scheme known as quadrature/cascade (see "Harmonic Conversion" in Section 7, and Refs. 57 to 59). As Fig. 2-82 shows, the second harmonic is generated using two 1.4-cm-thick, 74-cm-aperture Type II KDP crystal arrays operating in series. These crystal arrays are oriented for 3ω conversion, but aligned to phase-match 2ω conversion; 3ω light is then obtained simply by aligning the second crystal to phase-match 3ω conversion. The two crystal arrays are oriented so that they function independently, producing 2ω light in two orthogonally polarized components, one from each array. The major feature of this design is the wide range of input intensities over which high conversion efficiency can be maintained (Fig. 2-83).

Third-harmonic generation is achieved easily because the two crystal arrays are already in the basic orientation for the Type II-Type II polarization-mismatch configuration.[60,61] Alignment for 3ω generation is accomplished simply by rotating the assembly 10° about the beam direction (Fig. 2-82) and angle-tuning the second crystal (only one axis of the assembly) onto the mixer phase-matching angle ($\Delta\theta$ = 4.4 mrad). Efficient conversion is achieved over a somewhat smaller range of fundamental input intensities than for 2ω generation, but the design works best at the low-intensity end of the Nova pulse-width

range (2 to 5 ns). This operating range is consistent with other system constraints, imposed primarily by nonlinear propagation effects.

We undertook the design of the Nova frequency-conversion and target-focusing systems for multiwavelength operation with the intention of minimizing both the required number of large-aperture components and the total glass thickness. We have achieved this goal by using the same components for all three wavelengths and by multiplexing functions. High efficiency is achieved by optimizing the crystal lengths for the input-intensity range of interest. For commonality of parts, both arrays use identical crystal lengths.

Our propagation analysis of the harmonic beam indicates that a maximum allowable B after the KDP crystal array is $B < 2.5$ rad. Performance at this level is achievable only if some care is taken to control diffraction from the gaps between crystals in the array, i.e., by apodization. This places a maximum value on the harmonic intensity that can propagate without damage through the remaining optics. The impact on system performance is shown in Fig. 2-84, assuming 20 cm of fused silica following the array. The maximum harmonic intensity is limited

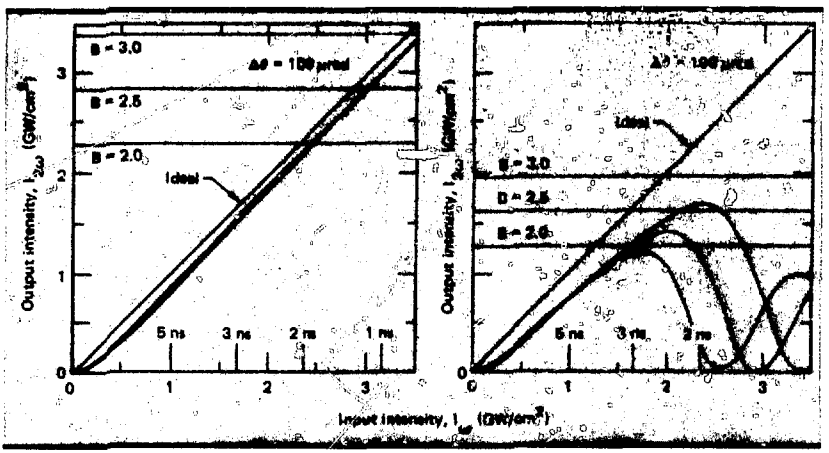

Fig. 2-84. Output intensity of 2ω and 3ω vs input for three crystal lengths, using flat, temporal, and spatial profiles.

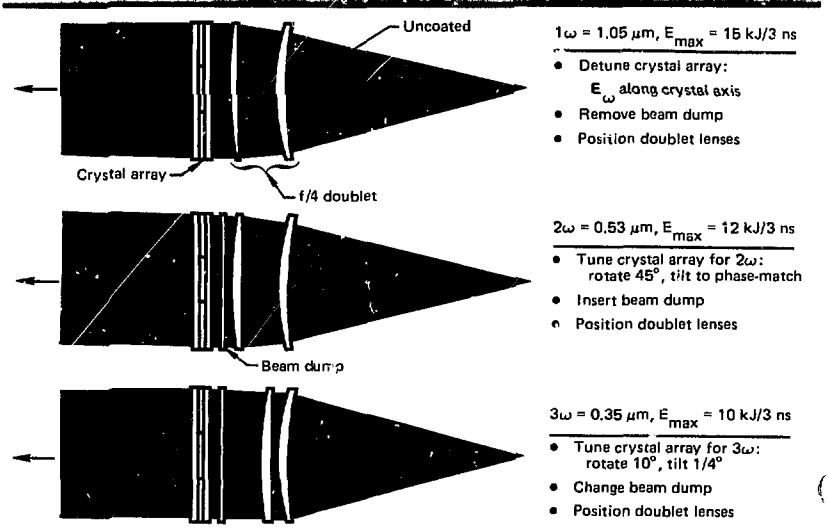

Fig. 2-85. Nova's frequency-conversion system and target-focusing optics.

by $B < 2.5$. Note that the maximum Nova fundamental intensity as a function of pulsewidth is shown along the abscissa. The lower maximum intensity of 3ω includes our estimate of the dispersion in the nonlinear index of refraction for fused silica.

Nova's multiwavelength capability is summarized in Fig. 2-85. The crystal array has the capability of transmitting the fundamental or converting it to the second or third harmonic. The array windows are made of materials that transmit the desired wavelengths, and the windows' broadband antireflection coatings are based on graded-index technology.[62] These window coatings, along with the index-matching fluid between the crystals and the windows, significantly reduce the optical insertion loss due to Fresnel reflections in the assembly. The beam dump following the array is the only wavelength-unique component in the system. The beam dump is used to absorb the undesired residual 1ω or 2ω light.

The components that follow the crystal array and beam dump must provide a vacuum barrier, provide a diagnostic reflection, and focus the light onto the target with a minimum of glass. The first element of the focus lens is an f/6 aspheric lens that serves as a vacuum barrier; the second element is an f/13 aplanatic lens with an uncoated last surface. Both lenses are made of fused silica, which is the only material we have identified that possesses high transmission at 3ω and that will not solarize under intense illumination.

The combination of these two lenses provides an f/4 focusing system with a 4% diagnostic reflection that can be focused to the alignment and diagnostic sensor. Changing the spacing between the two elements allows us to control the convergence on the diagnostic reflection to accommodate arm-to-arm variations in the distance from the lens to the sensor. This spacing change also helps compensate for the focal shift in the target plane due to dispersion in the glass.

Author: M. A. Summers

Major Contributors: D. Eimerl, L. G. Seppala, R. D. Boyd, and B. C. Johnson

Target Systems

Nova target systems include the target chamber, focusing-lens positioners, the target positioner, target-alignment optics, the vacuum system, and interfaces for the various target-diagnostic instruments. Data handling, instrumentation, and control of the radiation environment are also intrinsic aspects of Nova's target systems.

Target Room. The target chamber will be located in a concrete-shielded room north of the optical switchyard (Fig. 2-86). Laser beams will be routed to the target chamber with a series of turning mirrors mounted on the Nova spaceframe (described in "Mechanical Subsystems," earlier in this section). The target will be irradiated with 20 beams in two open cones on the east and west ends of the target chamber. The included angle of the cone centerlines is 100°. During Phase I, we will install 10 beams and modify the mirror arrangement in the switchyard so that the five beam ports on the west end will be illuminated by five of the laser chains in the east bay.

Target Chamber. As described in the *1979 and 1980 Laser Program Annual Reports*,[63,64] the target chamber will be supported 10 m above the floor in the center of

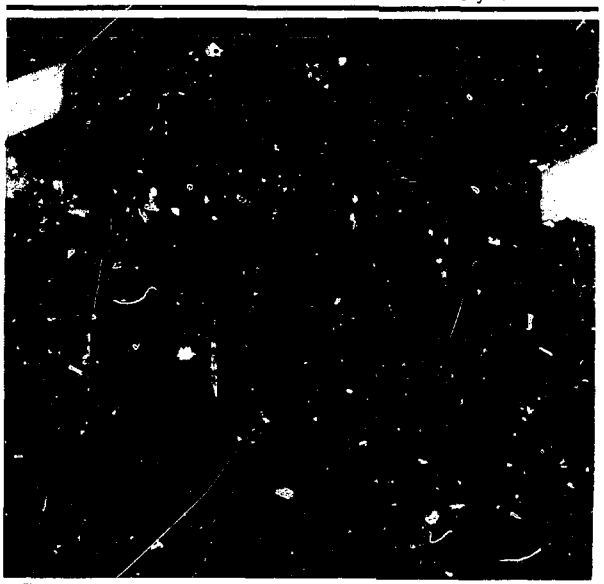

Fig. 2-86. Arrangement of the Nova target room and switchyard.

the target room. The main body of the chamber will have a 1-m-wide central ring with an inner radius of 2.2 m to provide structural support for the target positioner, target-alignment optics, high-vacuum system, and target-diagnostics instruments. Also attached to the center ring will be two removable hemispherical heads that we have designed to accommodate the laser beams, x-ray effects experiments, and target diagnostics. The 2.2-m radius is necessary to accommodate 10 lenses per side (instead of 5) and to reduce the x-ray fluence on the first wall.

Our Phase I plans for Nova include an experiment yielding 1×10^{17} neutrons from a 100-kJ, 1-ns laser pulse. The neutron, x-ray, and debris fluences generated by this neutron yield are not high enough to require local shielding or protection of the chamber by a first-wall absorber. The baseline lens has a focal ratio of f/4 with a 740-mm clear aperture. For Phase II, we will configure the target chamber for laser energies of up to 300 kJ and for yields of up to 5×10^{18} n, with as much as 3.2 MJ of cold x rays and 4 MJ of target debris. These conditions will require

- A first wall to absorb x rays and debris.
- An aluminum vessel to allow neutron-activated materials to decay rapidly to an acceptable level.
- A neutron shield around the chamber to limit activation of the steel spaceframe and concrete building.

The Phase II target chamber is illustrated in Fig. 2-28.

Fig. 2-87. Computer printout of predicted deflections in an element of the Nova target chamber.

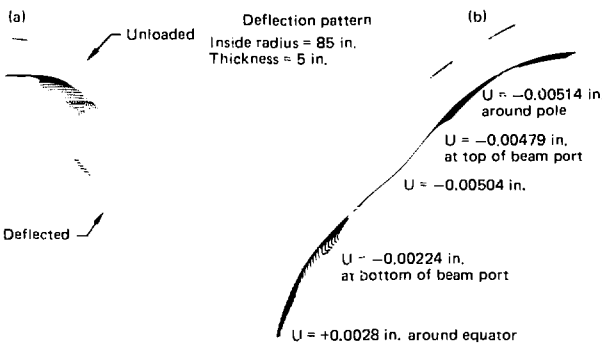

We have conducted finite-element stress and deflection analyses using the SAP IV code. Figure 2-87(a) shows a computer printout of the shell in the original, unloaded condition (the dotted image) and in the loaded condition (the line image). Figure 2-87(b) represents a section taken through a beam port; this printout shows the deflections at various key locations.

Vacuum System. The vacuum system will use mechanical pumps and Roots blowers for rough pumping and will employ turbomolecular and cryogenic pumps for high-vacuum pumping. With these machines, we will attain a pressure of 10^{-5} Torr in 30 min and we will ultimately reach a base pressure of 10^{-7} Torr. This low-pressure capability will ensure that we can easily achieve 10^{-6} Torr, which is required for survival of cryogenic targets. An overall layout of the vacuum system is shown in Fig. 2-88.

Fig. 2-88. Nova vacuum-system layout.

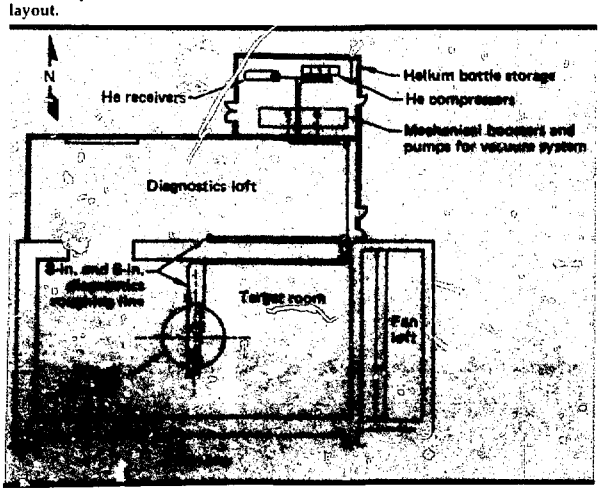

Nova's vacuum system utilizes a graphics-based closed-loop control system. As with all other Nova control subsystems, the vacuum-system controls have been designed for centralized computer control with high-speed communication (through Novanet) to a distributed-control front-end processor. Control functions are entered on a touch panel and Ramtek color monitor that displays menus, submenus, and schematic drawings of the system and controlled items. Control commands are processed and distributed by the VAX 11/780 main computer and an LSI 11/23 local processor.

The control system can handle up to 512 varied sensor-input signals, both digital and analog. A maximum of 320 output lines are provided for control of valves, pumps, and status displays. Control and status are apportioned to polling and interrupt-driven data-acquisition methods. All sensor and pressure transducer values are displayed on another color monitor that provides an overview of system functions. Safety interlocks and legal/illegal valve-state tables are also provided to protect personnel and delicate apparatus.

Overall system status, pressures, and states are displayed on a companion color monitor. Individual sensors and signal-conditioning units operate at 100 kHz to achieve an overall system rate of approximately 250 updates and control commands per second. We have designed the control-system functions for easy use by system operators.

Beam Focusing. One of the most difficult and exacting tasks associated with the target system is the simultaneous focusing of 20 beams onto a microscopically small target. All beam adjustments are powered by stepping motors and controlled from the central control room. Positions are determined by optical digital encoders to within 0.002 mm. The focusing challenge is compounded by the requirement that we minimize the amount of glass in the beam path while working at various wavelengths: 1.05, 0.53, and 0.35 μm.

We have minimized the amount of glass in the system by making the focusing lens serve also as a vacuum window. Accordingly, the focusing mechanism must work against the 5000-kg force of atmospheric pressure. The lens must be strong enough to withstand this pressure safely, and we must seal the lens to the chamber with a large bellows. The focal length of the lens at 0.35 μm is about 312 mm shorter than it is at 1.05 μm, due to the dispersion of fused silica (see the previous article). To provide a focusing range at each wavelength, the travel of the z axis will be about 350 mm. Lateral shift of the focal spot is 20 mm from center.

To diagnose the 2ω beam, we have provided an uncoated surface that will reflect about 4% of the beam back through the turning mirrors to the output sensor (described in "Alignment and Laser Diagnostics," earlier in this section). This surface is on the back of the second element of the two-element lens. Element spacing is variable to account for color changes; the second element is tiltable to aim the return beam back to the output sensor.

The baseline lens-positioner design is shown in Fig. 2-89. (An artist's rendering showing the scale of the lens positioner is shown in Fig. 2-35.) As an integral part of

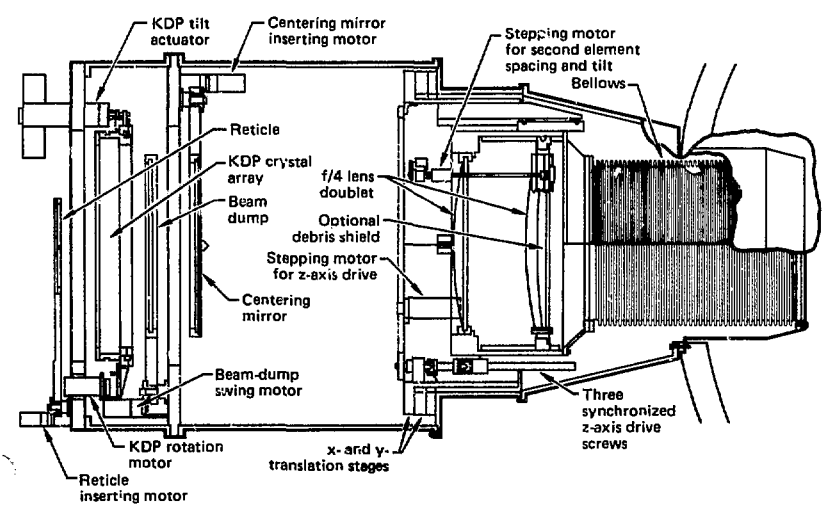

Fig. 2-89. Nova lens *positioner, using a* double-element f/4 lens. The first element is the vacuum barrier.

the lens positioner we have included the harmonic-generation package, beam dumps to absorb unconverted light, and alignment cross hairs and screens to aid in centering the beam.

Target Support. Nova's remote-controlled target positioner will have four degrees of freedom, enabling it to place targets within 5 μm of the desired location in the chamber. Controls for the target positioner will be integrated into the Novalink control system. Provision will also be made for handling cryogenic targets (and maintaining them in the frozen state) throughout installation, alignment, and exposure.

Target Alignment. We have a four-step plan for aligning the laser beams to the target

(1) A surrogate target is placed in the geometric center of the chamber.
(2) All beams are focused to this center position by means of lens positioners.
(3) The focal points are repositioned to various locations defined by the specific target to be irradiated.
(4) The surrogate is replaced by the actual target.

The position of the actual target must be identical or nearly identical to that of the surrogate—within 5 μm of true center, as verified by a reliable optical instrument.

The center of the target chamber will be established by the intersection of two optical lines of sight (LOS), as defined by two optical telemicroscopes. These instruments, called target-alignment and verification instruments (TAVI), are described in the *1980 Laser Program Annual Report*.[65] A third TAVI acts as a back-up reference and provides additional viewing flexibility. The schematic diagram in Fig. 2-90 shows a cross-sectional view of the main subunits in a single TAVI: an optical transfer, an image-viewing stage, and a control assembly.

The optical transfer requires maximum stability, which we accomplish by building the relay structure as a single unit and by mounting it ruggedly, coupled closely to the target-chamber. The optical transfer is located completely within the target-chamber vacuum; it is also isolated from its housing, which also provides protection from unauthorized adjustment and accidental impact during operations. To add rigidity to the housing and to conserve space in the experimental area, the optical path is folded. The optical transfer will form a full-size image of the target on a reticle, all within the vacuum. The image will be viewed through a vacuum window by the image-viewing stage.

The image-viewing stage will move in

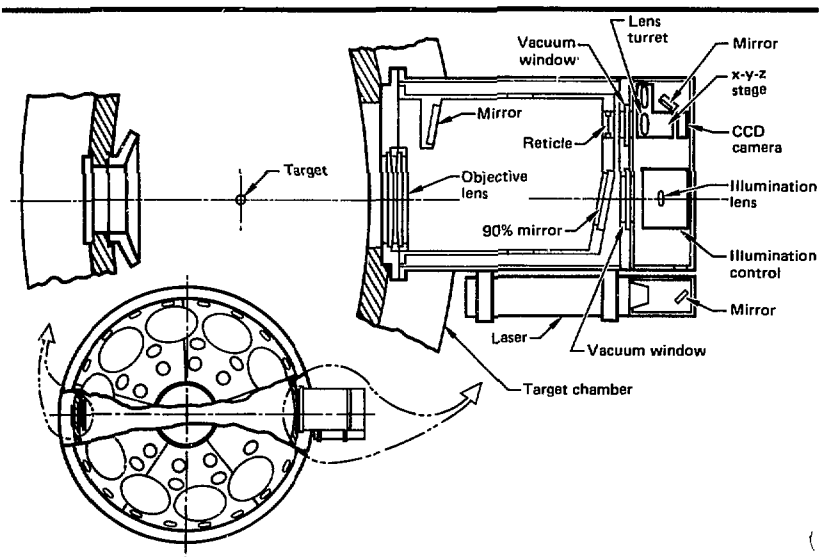

Fig. 2-90. Arrangement of the Nova target-alignment and verification instrument (TAVI).

three axes, within a volume measuring 25 mm diam by 25 mm long, to measure target-image features at various magnifications. The CCD camera will move with the turret, thereby maintaining alignment and focus at all positions in the image volume. The target will be illuminated by a small He–Ne laser, which will use beam splitters and the optical-transfer optics to provide both front and back illumination. Beam intensity will be made continuously variable by means of rotating polarization plates.

Target Diagnostics. We have provided ports in the central ring and hemispherical heads for an array of target-diagnostic instruments. All ports will be precisely located in spherical coordinates. In most cases, each port will have a standard 8-in. diameter to allow diagnostics to be interchanged between locations or even between different facilities (i.e., Nova and Novette).

Instruments sensitive to neutron or gamma pulses will be located in the diagnostics loft, behind the concrete shielding wall, and will be connected to the target chamber by vacuum LOS pipes. They include instruments with synthetic plastic fluors, photomultiplier tubes, and fast electronic circuits (such as the filter-fluorescer detector and the high-speed streak cameras). Intrinsically "hard" instruments, such as the calorimeters and Dante fast x-ray detectors, can be mounted on shorter pipes within the target room. Each instrument package will have a valve in its LOS pipe to isolate it from the target chamber. Control of these valves will be integrated into the Novalink system; this will allow individual components to be evacuated separately and help avoid vacuum accidents.

Target-Diagnostics Data-Acquisition and Control. Our basic philosophy concerning target-diagnostic data-acquisition on Nova is to adapt standard acquisition and digitizing hardware from Shiva and Argus by adding hardware and software to integrate the target diagnostics into Nova's central controls. In this way, Nova's target-diagnostics packages will also include acquisition and control functions. CAMAC and LSI-11 interfaces will be used on most computer-controlled data-acquisition units. We will support IEEE-488 Buss interfaces on Nova since many newer instruments use this standard computer interface.

The Nova target-diagnostics system will be operated primarily from the control-room consoles, using Ramtek touch-activated color-graphics screens. The system will be experiment-oriented and menu-driven. The operator will first select an experiment type and then select the diagnostics to be included in the experiment. Additions or deletions can then be made in the mix of acquisition modules for each diagnostic. An operator will be able to build an acquisition configuration from scratch or use a file that describes a previous shot configuration.

Remote-control panels will also be placed in the diagnostics loft and in the switchyard near the target diagnostics, so that operational checkouts can be performed locally. These remote panels will be interfaced to the control room, enabling the control-room computers to continuously update the status of the entire system. Nova target diagnostics will rely heavily on the hardware and software tools developed by Nova central controls.

Radiological Control. The concrete shielding walls and roofs in the Nova target room and switchyard are sufficiently thick to limit personnel exposures outside the Nova building to well below the current DOE standards for operations resulting in 5 $\times 10^{17}$ neutrons yield per day. With a 2-ft-thick-equivalent water shield around the chamber, the facility can safely operate at a level of 2 $\times 10^{19}$ neutrons per day. However, personnel occupancy in the Nova target room immediately following high-yielding neutron shots must then be limited to less than 40 h/wk per operator because of the neutron-induced residual radioactivity.

The bulk of residual radioactivity occurs in the target chamber, spaceframe, and

Table 2-9. Chemical composition of major components in the Nova target room. (See p. 2-82.)

concrete shield. The materials in each of these structures contribute differently at different locations in the room, and the activity varies with time following the shot. The material compositions of the Al vessel, the mild-steel spaceframe, and the concrete shield are given in Table 2-9. Based on the table, we have calculated the biological dose from neutron-induced residual radioactivity in the spaceframe, chamber, and the

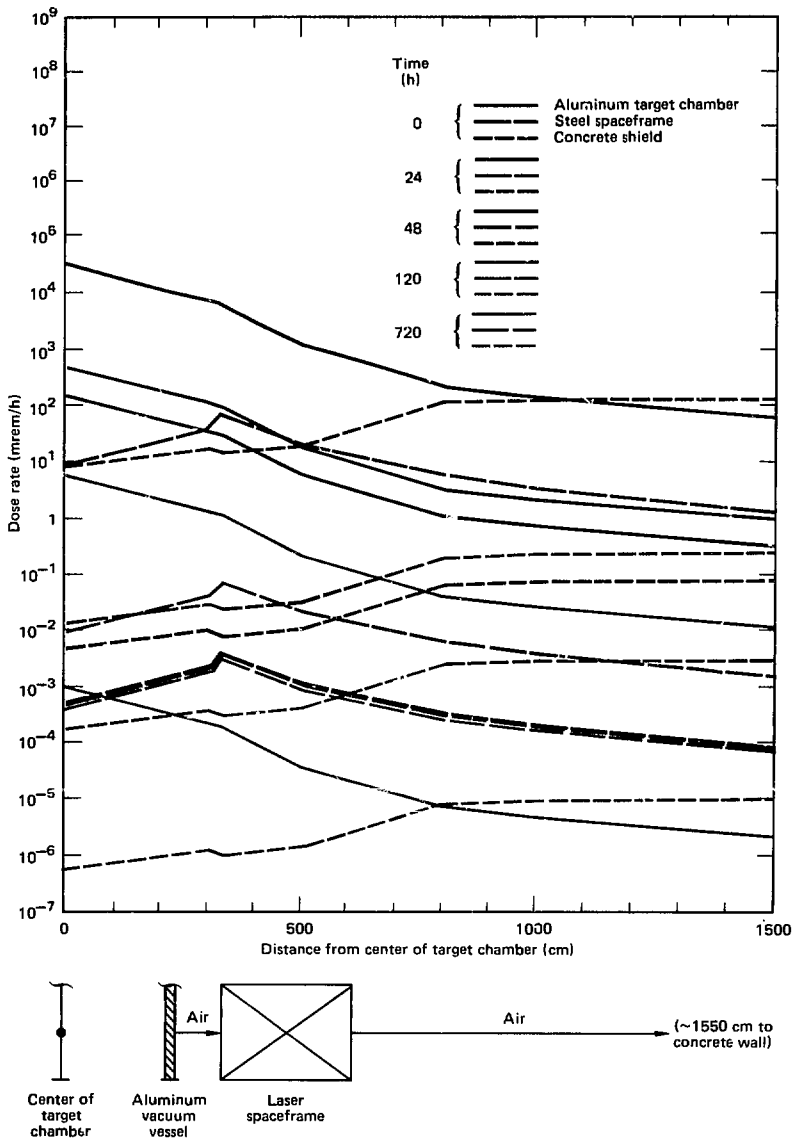

Fig. 2-91. Biological dose rates in the Nova target room following a single shot yielding 2×10^{16} neutrons.

concrete for various target neutron yields. The results of these calculations are presented in Figs. 2-91 through 2-93 for various times of operation.

The model shown in the lower part of Fig. 2-91 was used to describe the inside of the Nova target room for the neutron-flux-density calculations, neutron-induced activity calculations, and for the biological dose calculations. In this model, the Al vacuum vessel has a 218-cm inner radius and is 12.7 cm thick. The spaceframe (weighing approximately 130 tons) is distributed evenly between 335 and 610 cm from the target. The concrete walls start at 1585 cm from the center of the target chamber. Dry air was assumed in the regions between the vacuum vessel and mild-steel spaceframe and between the spaceframe and the concrete shield.

To calculate the biological doses, it was first necessary to calculate the flux density, which was evaluated using the TARTNP Monte Carlo code, and the induced residual radioactivity, which was evaluated using the ACTIVE code and analytical expressions. The biological dose was then evaluated using the MORSE-L code. The doses were calculated at the center of the vessel, at 300, 331, 500, 800, 1000, and 1500 cm from the center of the target vessel.

Figure 2-91 gives the radiation dose after a single shot yielding 2×10^{16} neutrons. Figure 2-92 shows the doses after operation for one year at 2×10^{16} neutrons (one shot) per day. Figure 2-93 gives the doses after

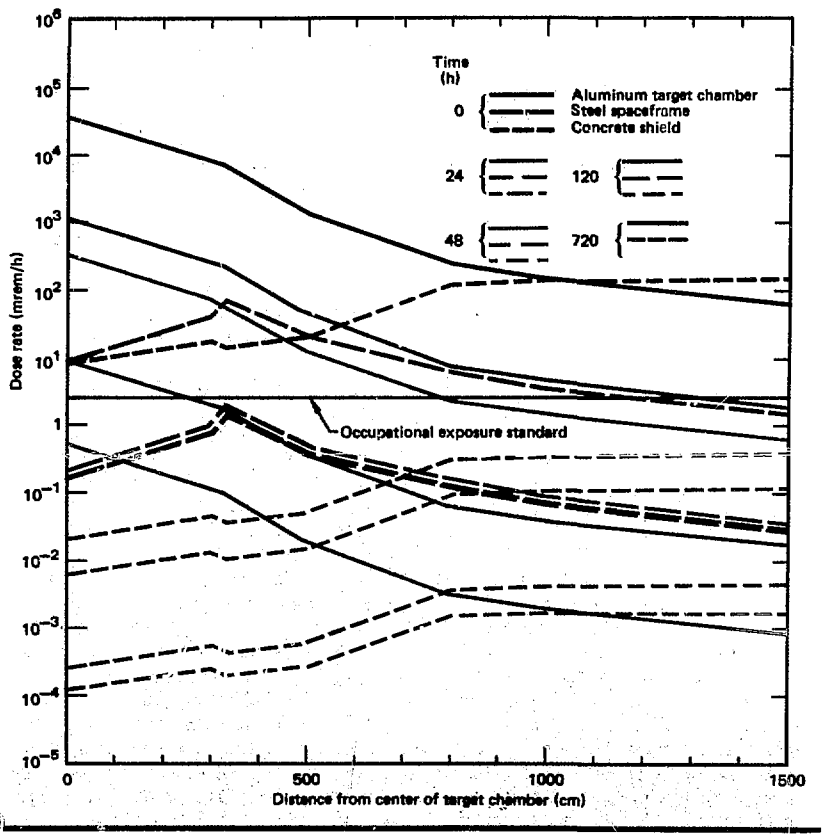

Fig. 2-92. Biological dose rates in the Nova target room after one year's operation at 2×10^{16} neutrons per day.

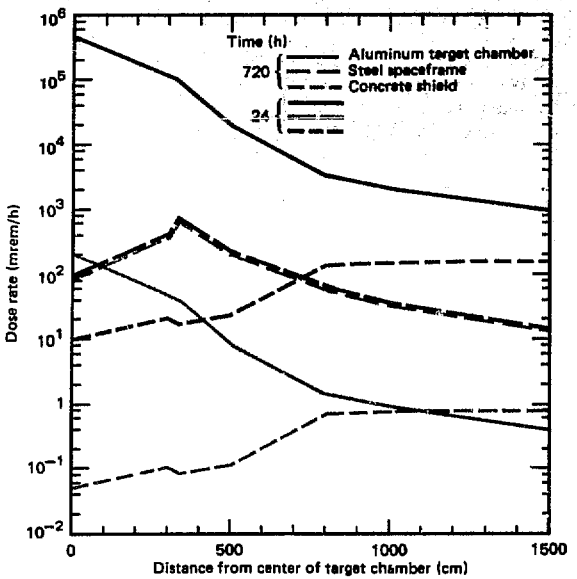

Fig. 2-93. Biological dose rates in the Nova target room after one year's operation at 1 $\times$ 10^{19} neutrons per day.

operation for one year at 1 $\times$ 10^{19} neutron (one shot of higher intensity) per day. The cooldown times following the last shot are 0, 24, 48, 120, and 720 h. (Data points are connected as a viewing aid only.)

Authors: F. Rienecker, J. R. Severyn, and M. S. Singh

Major Contributors: M. A. Summers, J. E. Field, E. A. Ries, J. F. Kane, J. Nemeth, E. A. Barna, and S. B. Rodriguez

Sequencing, Synchronization, and Safety Systems

The predefined sequence of steps required to operate the Nova laser spans many minutes. Preshot preparation includes manual setups, computer-assisted semiautomatic tasks, and fully automatic tests under computer control. Early activities include aligning the laser chains and preparing the various laser- and target-diagnostic subsystems. These operations are semi-automatic, in that computer programs assist operators in completing a series of setup checklists.

When all preliminary steps have been taken, an automatic sequencer program then controls and monitors all systems for the final minute, during which the energy-storage capacitor banks are charged. At 10 ms prior to switchout of the optical pulse, control of the laser systems is transferred from the computer to integrated logic timers. At 1 μs prior to switchout, one of these timers activates the master-oscillator fast-timing system. The oscillator electronics then generate a sequence of nanosecond-accurate triggers.

Figure 2-94 illustrates a control problem that is unique to laser fusion: the event-timing requirements for operating the laser system span 12 orders of magnitude. Early preshot events are measured in minutes and seconds, while events occurring during the propagation of the laser pulse are measured in nanoseconds and picoseconds. The Nova timing and synchronization system meets this wide range of requirements using computers and programmed logic. Operationally, the control system is organized into three categories, each associated with a different control technique and covering a different time span. Table 2-10 summarizes the major tasks, timing, and control techniques for various time periods relative to shot time.

The Nova control-system architecture (shown previously in Fig. 2-66) is based on the use of multiple computers that exchange information via a shared memory and communicate with laser devices via Novabus, an extended computer bus using fiber-optic cables. Novabus features global synchronization bits and is connected with each device that requires synchronization or control during a shot sequence. Synchronization via Novabus is accurate to 1 μs; synchronization of devices requiring submicrosecond timing is accomplished using triggers from the master oscillator electronics. This fast-timing subsystem is hardwired and employs very-broad-bandwidth circuitry, providing electronic and optical-pulse synchronization to less than 1 ns in critical applications.

Preshot Validation. All mechanical, optical, and electrical components of the Nova system must function in a coordinated manner. Failure of any component to fully perform its design function results in degraded laser performance. We therefore verify the condition of all laser subsystems prior to propagation of the laser pulse. Furthermore,

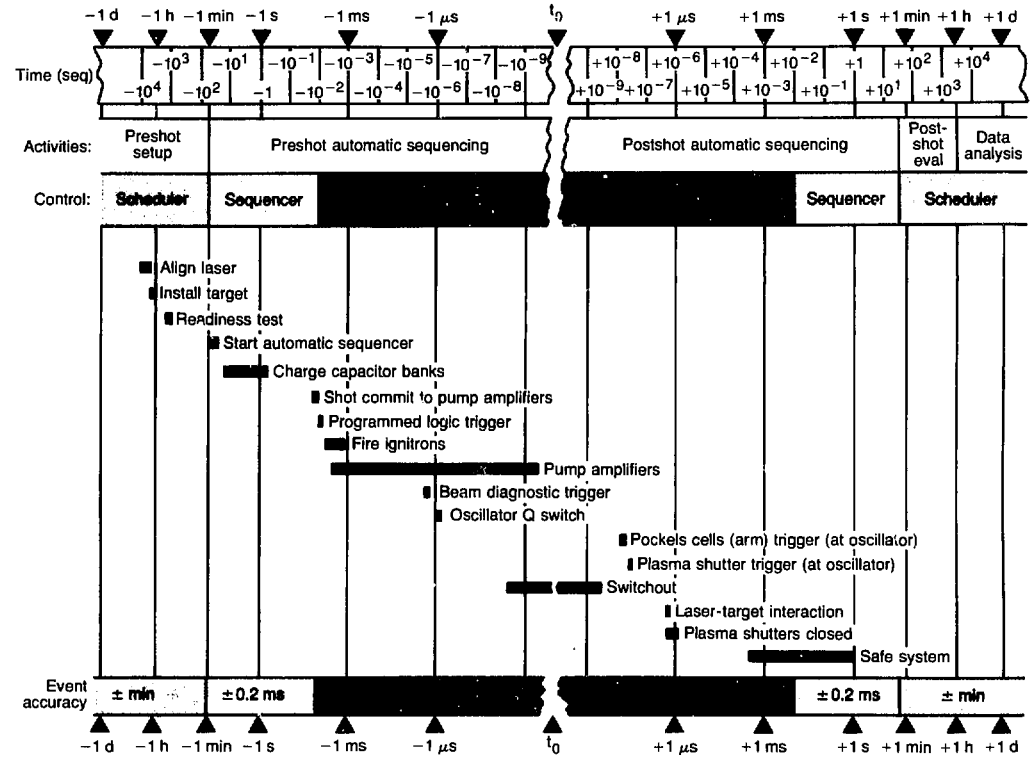

Fig. 2-94. Event timeline for Nova operations.

a performance failure by certain key components can damage the laser itself. For example, an early breakdown of the rail-gap portion of the plasma shutter could allow a reflection of the full-energy laser pulse to propagate back through the laser chain, resulting in serious damage to costly 46-cm-aperture optical components.

The readiness of subsystems and components is verified by operators using a predefined set of diagnostic tests. One such test, for preventing flashlamp failure at full power, involves testing all 3000 circuits (at reduced energy) for waveform anomalies. The testing sequence takes into account the dependency of one system on another to ensure that interfaces between components are properly configured. The end result is confirmation that all systems are ready to support operation of the laser.

Preshot Sequence. Figure 2-95 illustrates the major preshot tasks performed for operation of the Shiva laser, which is conceptually similar to Nova. The time-span for

Period relative to shot time	Major tasks	Time scale	System control
Up to −[illegible]	[illegible]	[illegible]	Computer-assisted manual operations
−[illegible] h to −1 min	[illegible]	[illegible]	Scheduler checklist
−1 min to −[illegible]	[illegible]	±2 ms	Interrupt-driven computer operations
−[illegible] to −[illegible]	[illegible]	±[illegible] μs	Computer-initialized programmed logic
−[illegible] to −[illegible]	[illegible]	[illegible]	Master-oscillator operations
[illegible]	[illegible]	±[illegible] ps	Pulse-driven operations
[illegible]	[illegible]	[illegible]	[illegible]

Table 2-10. Major events, timing, and system control for operation of Nova laser system.

Nova preparation will be shorter because of increased automation, but the tasks themselves remain essentially the same. Each block in Fig. 2-95 represents a set of tasks that is managed with a computer-controlled checklist called a scheduler. The scheduler

Fig. 2-95. Task timeline for the Shiva laser, indicating Nova requirements.

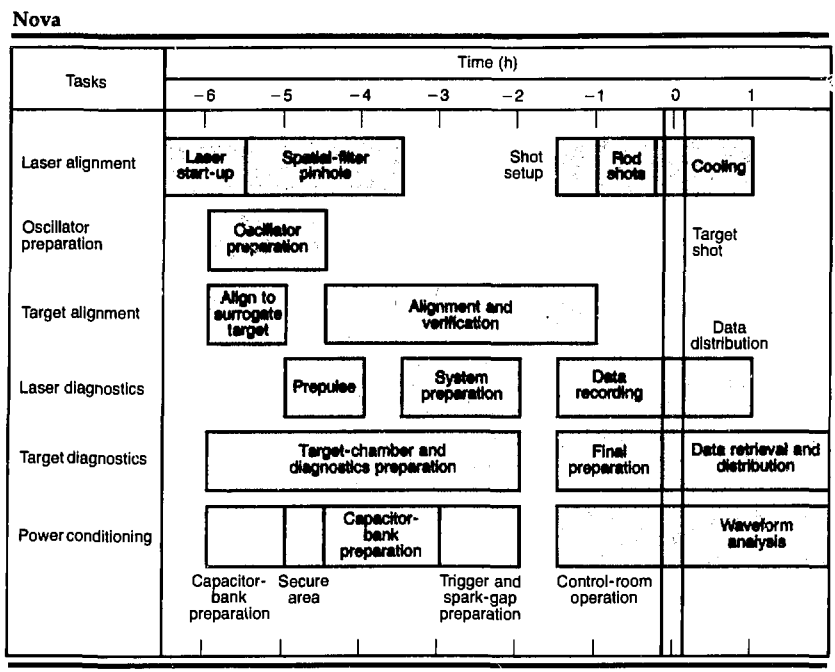

assists the Shot Director with validation of the system while simultaneously recording data related to all tests conducted. The scheduler prompts the Shot Director at each decision point in the testing sequence; when the checklist is successfully completed, the Shot Director authorizes moving on to the next step. Since the computer evaluates much of the test data, the Shot Director is free from routine tasks; in the event of an anomaly, he or she can either modify a test, repeat a test, or initiate diagnostic procedures.

The scheduler oversees the preparation of the laser and target systems; when all subsystems are determined to be ready for a shot, the scheduler initiates an automatic sequencer. The primary difference between the scheduler and the sequencer is that the scheduler is event-driven, while the sequencer is time-driven. As the scheduler progresses from event to event, the time span for completion of a given event is not fixed. The sequencer, on the other hand, operates in a context of fixed time spans; each event occurs at a specific time relative to propagation of the optical pulse. The Shot Director can hold or abort the scheduler or sequencer at any time.

The sequencer takes over for the scheduler at 1 min prior to switchout of the laser pulse, when the timing of events becomes critical. The sequencer consists of computer routes that execute a predefined set of commands and diagnostic routines to complete final system preparation. The sequencer monitors the entire system for proper operation and will automatically pause in the event of a system anomaly. Such anomalies include ignitron prefires, plasma-shutter prefires, interlock breakage, or failure of a device to respond to commands.

Each sequencer event activates a routine at a predefined time measured in seconds and milliseconds preceding laser-pulse generation. Early sequencer channels are related to setup of the power-conditioning system. Between 30 and 45 s before shot time, the sequencer initiates charging of the energy-storage capacitor banks. By 1 s before shot time, some 100 MJ of electrical energy is stored and ready for switching into the laser amplifiers.

A key decision point occurs at switchout of the laser pulse minus 10 ms. If all systems are determined to be ready at this time, the sequencer sends a universal trigger over Novabus that activates

programmable timers throughout the laser facility. At this point, the system is not yet committed to switchout of the laser pulse, but the laser-amplifier flashlamps are pumped with 100 MJ of electrical energy from the charged capacitor banks. If the shot is aborted after this time (10 ms before shot time), the time required to cool and restabilize the amplifier glass exceeds 1 h.

During the final milliseconds, the environment in which the control system must function changes drastically. Electromagnetic noise levels increase dramatically, and timing requirements are tightened to microseconds. The pumping operation requires that the electrical energy stored in capacitors be transferred to the laser amplifiers in about 1 ms, with a peak power in excess of 100 000 MW. Careful design of the pulsed-power system ensures that only a small fraction of this power is radiated as noise. Even so, the noise is extreme when compared with required environmental conditions for TTL/CMOS circuitry. Control-system logic adjacent to the ignitron switches must not only survive but also continue to operate throughout this noisy period.

The most noise-susceptible components in the Nova control system are the fiber-optic receivers of the Novabus control network. Since control signals to and from the control computer pass through these devices, control signals are subject to corruption during the high-noise period. We have eliminated this problem by storing in each device interface those commands that must be executed during the high-noise interval. Device interfaces are loaded with timing information well before the pumping operation. Each device then operates independently of the control system for the last 10 ms prior to switchout. Timing information is loaded into device-interface logic, called programmable timers. All timers are activated simultaneously when the control computer sends the universal trigger through Novabus.

Table 2-11 lists the devices (including the master oscillator) that receive synchronized triggers from the programmable timers. While the timers are running, the computer continues to check the laser alignment and diagnostics systems for abnormal conditions. If an abort condition arises, the computer sends a command directly to the oscillator to prevent switchout of the laser pulse. A timer signal initiates Q-switching of the oscillator 1 μs before the shot. The oscillator then issues a sequence of submicrosecond triggers to laser devices further down the laser chains.

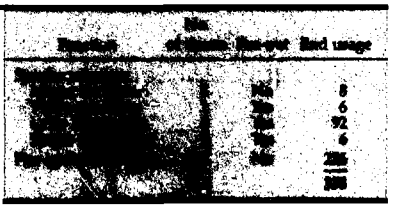

Table 2-11. Implementation of programmable timer channels on Nova.

Electronics associated with the master oscillator produce timing signals with nanosecond-accurate resolution. Figure 2-96 is a block diagram of the oscillator timing system. The exact timing of each channel is loaded by the control computer into a RAM within the fast-timing control block of Fig. 2-96. The coarse timing is provided by 8-bit Shottky TTL counters clocked by the master rf oscillator output (divided by two). By choosing either the leading or trailing edge of the symmetrical 31.25-MHz clock, we attain 16-ns resolution. Finally, programmable delay lines provide 1-ns resolution. We have also incorporated into the system the capability to abort the switchout signal in the event of a plasma-shutter prefire. This abort signal is sent by direct connection between the oscillator and plasma shutter.

Tasks associated with target diagnostics begin immediately following the shot. Data for beam diagnostics, target diagnostics, and power conditioning are recorded by numerous instruments and transferred to large computers for processing. This data base is used by both laser-fusion experimenters and system engineers; in the latter case, we use the data to determine how the overall system performed and to identify required adjustments prior to the next shot.

Safety System. The safety of all personnel is of primary importance during operation of the laser. Potential hazards include high voltage, high-intensity laser beams, and radiation from high-energy target shots. Identification of potential hazards is the responsibility for each system or project engineer. Hazard identification is an integral part of the early design process; potential hazards are presented in design reviews

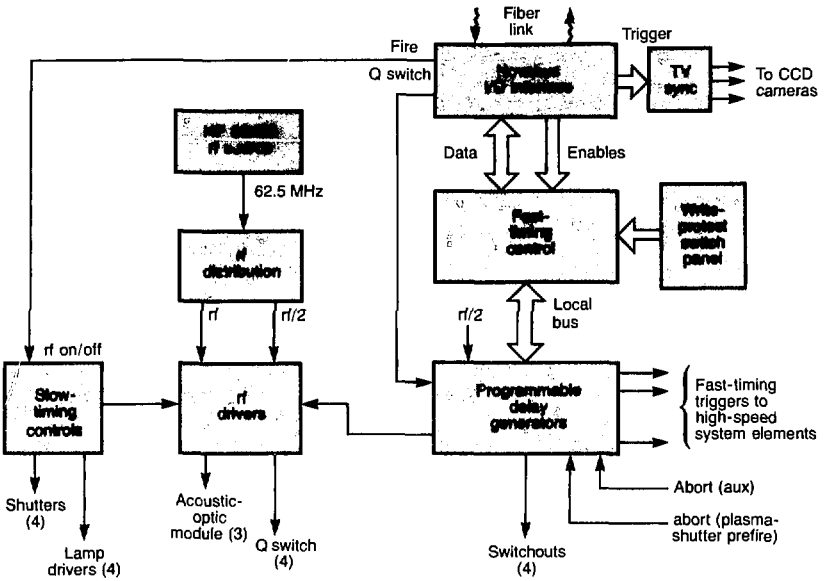

Fig. 2-96. The Nova oscillator-electronics timing system.

and documented on a preliminary hazard-analysis form that includes recommendations for ameliorating the hazards.

The system of barriers, sensors, displays, and controls specifically designed to prevent personnel hazards is called the safety interlock system (Fig. 2-97). This system uses the information available to it to decide, for example, whether oscillator shutters may open (constituting an eye hazard) or whether crowbars may be lifted from capacitors and high-voltage power supplies may be allowed to charge (constituting a high-voltage hazard). Such actions are allowed only when the permissive signals for eye and high-voltage hazards are asserted.

Information available to the interlock system includes the status of facility doors, beam shutters, runsafe boxes, panic boxes, and the power-conditioning control panel. Runsafe boxes and panic boxes provide crash buttons throughout the system; these buttons cause the boxes to go to the "safe" state when pushed, causing the interlock system to remove the permissive. The runsafe boxes are reset with a key, as shown in Fig. 2-97. The panic boxes are reset with a push button. The power-conditioning control panel, which also provides a crash button for the system, must be actuated for a high-voltage permissive to be granted.

The interlock system gives an audible message that warns personnel of the hazard that will soon arise. This message is timed to give personnel sufficient time to crash a runsafe or panic box or to leave the area, if they are not adequately protected or are not allowed in the area when the equipment operates. A chime rings when the hazard status of an area changes, and the current hazard status of the laser area is displayed on access panels at doors entering the area and on hazard-status panels within the area.

The system will use a single key for actuating the power-conditioning control panel, resetting runsafe boxes, and unlocking capacitor bank doors. There will be only one copy of the key within the system, allowing the person who holds the key to prevent operation of the high-voltage system. The single-key system also forces the control room operator to visit the site of a crashed runsafe, both to reset it and to determine the reason it was crashed.

The interlock logic is implemented with a triple-redundant voting system. There are

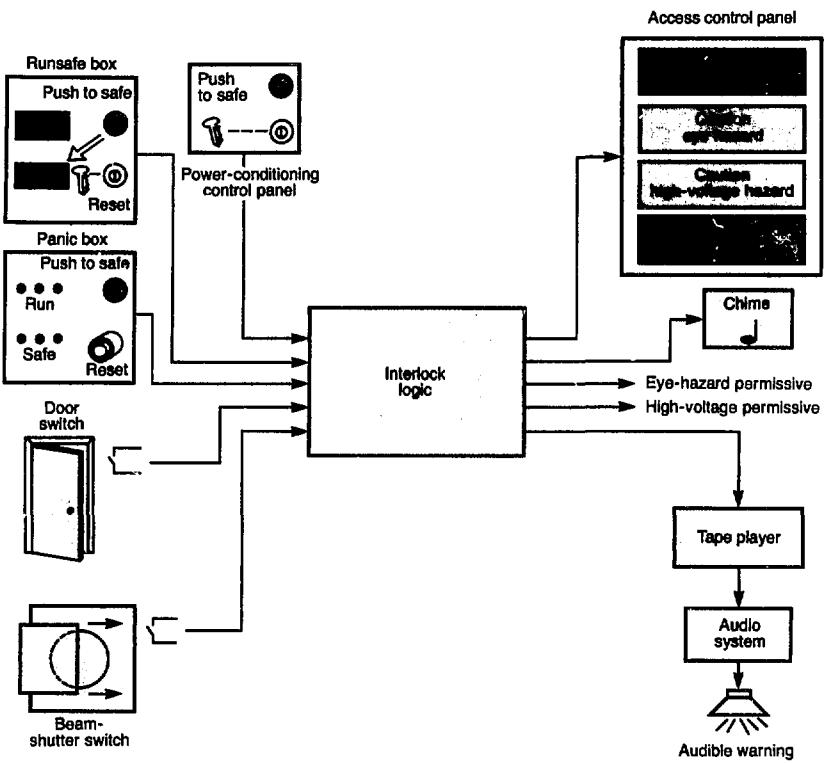

Fig. 2-97. Configuration of a typical interlock safety system.

three redundant contact closures at each monitor point, each connected to one of three identical interlock logic units. The three outputs of these logic units "vote," with a majority deciding the action of the system. In the event of a single-point failure, voting allows the system to operate until it can be repaired. The outputs resulting from the vote are used for permissives, to drive displays and chimes, and for interfacing with the audible warning system. The interlock system functions independently of the computer system, but is monitored by the computer system for detection of single-point failures.

As part of our grounding and isolation plan, the control room and MOR are electrically isolated from the rest of the system. This is accomplished largely through the use of fiber optics. The safety interlock system is interfaced to devices within the control room and MOR through fiber-optic cable to conform with this isolation scheme.

We also employ various barriers to prevent entry of a person or a part of their body into a dangerous area. The type of barrier is determined by the nature of the hazard. Signs are posted throughout the laser area to inform persons of hazards and any special precautions to be observed. Doors, gates, and removable panels are locked, interlocked, or both. The safety interlock system provides for automatic safety by removing permissives when the interlocks are broken by unauthorized entry into an interlocked hazardous area. Non-interlocked barriers include beam tubes, equipment cabinets, shields, and barricades.

Author: D. G. Gritton

Major Contributors: L. W. Berkbigler, D. J. Christie, A. J. DeGroot, and J. A. Oicles

Control Systems

Introduction and Design Objectives. The control system for the Nova laser must meet substantial requirements in the areas of technical function, flexibility, maintainability, and operability. The laser system itself is comprised of four major subsystems: power conditioning, alignment, laser diagnostics, and target diagnostics. The design of the Nova control system must meet the unique control requirements of each of these subsystems while providing consistent overall architecture and a common set of tools to reduce development and long-term maintenance costs. This hierarchical functional architecture is illustrated in Fig. 2-98; note that, in addition to the control subsystems corresponding to the four laser functional areas, there is a fifth control system called central controls.

Overall control-system architecture is based upon a series of distributed microcomputers, minicomputers, and components interconnected through high-speed fiber-optic communications systems. The microcomputers provide cost-effective local remote-control and data-acquisition functions, while the larger minicomputers provide high-level capabilities such as integration, image-processing for closed-loop alignment functions, and centralized operator controls. We have designed special-purpose hardware and software to improve the performance and maintainability of the control system; these include

- Fiber-optic networks.
- Color-display-based programmable operator consoles.
- A sophisticated computer language (Praxis) specifically designed to support control-system implementation efforts.

We successfully demonstrated a prototype of this control system in November 1980 and installed it in December 1981 for Novette (the two-beam, 15-kJ prototype of Nova, described earlier in this section). Installation of a full control system on Nova is scheduled for mid-1982.

Author: G. J. Suski

Major Contributors: J. M. Duffy, D. G. Gritton, F. W. Holloway, J. E. Krammen, R. G. Ozarski, J. R. Severyn, and P. J. VanArsdall

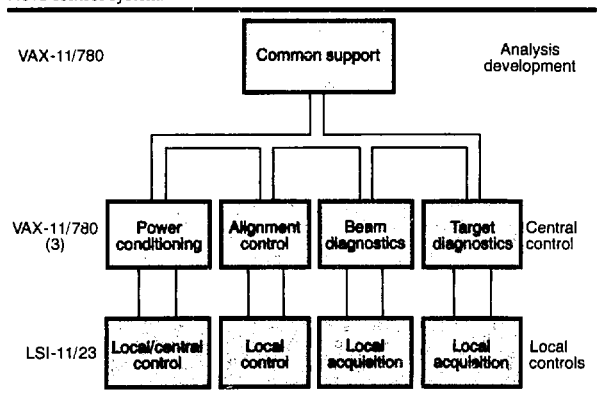

Fig. 2-98. Functional architecture of the Nova control system.

Architecture. The hardware architecture of the Nova control system is illustrated in Fig. 2-99. The fundamental building blocks for local control and data-acquisition functions are DEC LSI-11/23 microcomputers, packaged in an LLNL-designed chassis that provides power and I/O space for large configurations. The microcomputers are set up with memory, local control panels, device interfaces, and software specifically matched to their individual functions. Typical applications of these units include firing the power-conditioning ignitrons, controlling configuration of the Nova output sensors through stepping-motor manipulations, and acquiring data from beam and target-system calorimeters.

The technically diverse control functions of the four fundamental subsystems are centralized and integrated into two DEC VAX-11/780 computers. These computers, interconnected with MA780 shared memory, share the load of central-system operation and provide redundancy. Functions performed at this level include cross-subsystem interlocks (synchronization), centralized operator control, configuration management, and data storage. Common resources, such as large file storage, output-plotting devices, and analysis packages reside at the uppermost level and are supported by a third VAX-11/780 system.

High-speed data transfers to remote local tions are provided by two fiber-optic

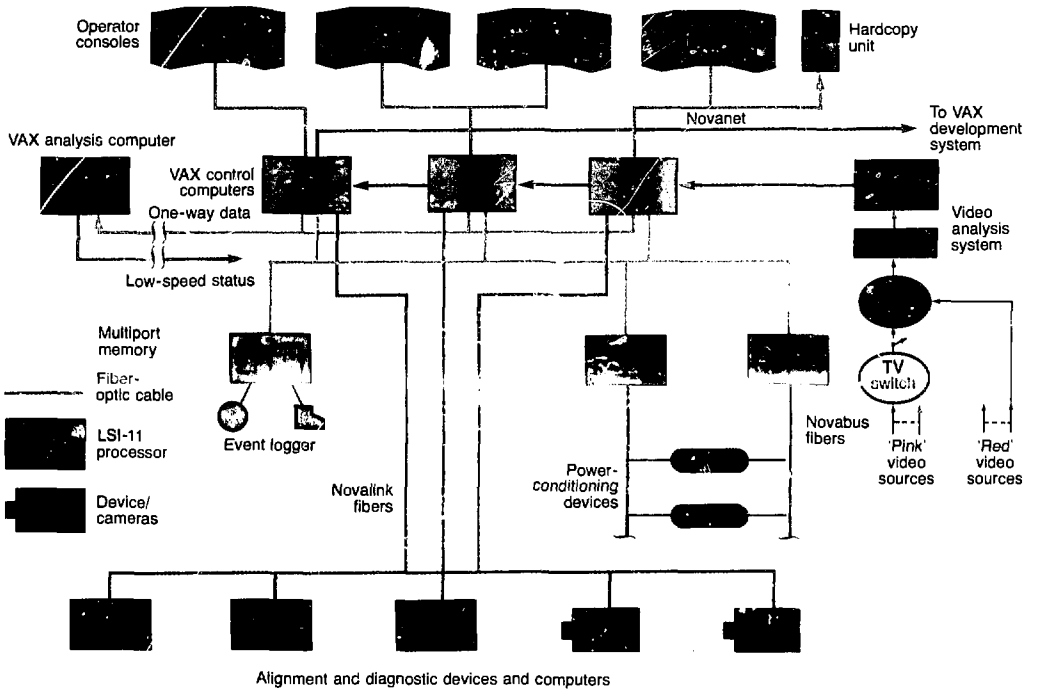

communications systems: Novanet, and power conditioning's Novabus. Novabus has been designed to transfer control-system data to remote devices at maximum speed; devices served by Novabus are connected to the central computers via multiport memories attached to controller LSI-11/23s. The Novanet system supports computer-to-computer transfers and computer-to-device transfers for the alignment and diagnostics subsystems. All elements connected via Novanet, including the three central computers, form nodes in a network in which any node can "talk" to any other node.

Author: J. M. Duffy

Major Contributors: G. J. Suski and P. J. VanArsdall

Console Display System. We have slightly modified the hardware design for the Nova operator console to improve both aesthetics and manufacturability. The desk component design now uses fewer parts, which should result in a cleaner appearance and stronger overall surface. We have designed custom front panels for the Ramtek displays and the black-and-white TV monitors, resulting in a more integrated system. Most of the vertical separation members on the front of the console are the same color as the large panels to reduce the busy appearance of the prototype console. Two console units are being completed for Novette; four more units (for the Nova control room) are due early in 1982. All that remains is integrating the joystick and numeric keypad into the desk surface.

Our console interactive-graphics software is the primary means of interaction between operators and control-system programs. During 1981, we focused on optimizing the prototype system that was demonstrated near the end of 1980 and described in the *1980 Laser Program Annual Report*.[66]

The console-display system is composed of four software packages used to generate and update color-graphics images on large-console TV screens. During the first phase of system operation, called the definition

Fig. 2-99. Nova control-system architecture.

phase, only one of the software packages is used. The picture-definition functions of the package allow programmers to write a program that completely describes the color picture that will later be drawn on any of the screens. Such a picture is called a frame, or menu; the package is called the frame-definition package.

The other three packages of the system are used during the second phase, known as the operations phase. In this mode, the console interactive-graphics system is actually used as the interface between operations personnel and laser- and target-control programs. The three packages used during the operations phase perform as follows

- Frames are drawn and maintained on console screens by the console executive (CE) package at the request of laser- and target-control programs. It is also through the CE program that control programs receive operator inputs from the touch-sensitive screen panels on each console.
- The menu-manager package keeps track of the order in which frames have been requested by control programs as the result of operator inputs. This information allows operators to request that the menu manager retrace their steps through a sequence of menus. The package also updates the time and date information on the console screens.
- The autostatus update program ensures that laser, target, and control-system status information depicted on visible frames is updated on a regular basis or as changes occur.

Communication between the CE program and all control-system programs that use the consoles occurs through shared data regions. The exchange of data through these regions is interlocked by parts of the network-shared memory (discussed below).

The speed with which data can be exchanged affects how quickly control programs can change the information on console screens; the data-exchange rate also affects the response time of programs to operator inputs. We made considerable improvements in the response of the CE program, when performing frame changes during the operations phase, by optimizing the internal operation of the network-shared memory (NSM). In fact, the rate at which data could be exchanged through the shared-data regions was at least doubled. Therefore, the amount of graphical information that can be updated on the screens by a control program during a time interval was at least doubled.

In addition, data being passed between the control programs and the CE program are buffered. That is, control programs can prepare and pass a set of data to the CE; while the CE is processing this "buffer" of data, the control programs can be processing the next set of data. This allows the processing times of the control programs and the CE to overlap. Thus, large numbers of graphical operations are performed more quickly than if they are submitted to the CE one at a time. The rate at which pictures change increased at least by a factor of 5 in cases where more than a few changes occur together.

The speed with which the CE program performs graphical operations with the Ramtek 9400 was improved through program optimizations based on results of timing measurements. We designed, wrote, and executed a set of exercise programs for the Ramtek 9400 graphics processor, and we used the resulting data to determine which programming techniques provide optimum hardware performance for the VAX/Ramtek coupling.

One of the primary uses of the graphics system for Nova and Novette will be the display of system status. We decided that the best approach would be a common routine (the autostatus update manager); we chose this approach because it frees the developers from having to put extra logic in their codes to update the status displays. This should simplify the control processes, thereby making it easier to maintain the status-update function. Using a common routine for graphic status updates also lowers system overhead.

We have shown the feasibility of a common routine for status update, and we are very close to a prototype version. To build the prototype, we extracted from the configuration and control data base the information describing where status information for a given device would be derived from. With this information, and a user-supplied routine to extract the status information, we developed a routine that listens to the appropriate NSM regions and calls the appropriate status routines for the devices. The routine then calls the CE

program with instructions for changing the displays on operator consoles.

Authors: J. E. Krammen and D. L. McGuigan

Major Contributor: P. J. VanArsdall

Novanet Local-Area Network. Novanet is a 10-Mbit fiber-optic data network that allows high-speed computer and digital-device communication. Novanet's capabilities and architecture were described in detail in the *1980 Laser Program Annual Report*.[67]

We devoted our efforts during 1981 to the manufacture and final debugging of Novanet hardware and to enhancing the companion software drivers in both the VAX and LSI-11 processors. We have fabricated and tested approximately 50 sets of the Novanet master/slave controller, which is the Novanet computer interface for all VAX, LSI-11, and PDP-11 processors. We have also completed hardware designs for the device interface modules, the Q-bus-device interface for LSI-11 backplanes, and the multiple-device interface for Augat backplanes; 25 sets of each printed-circuit card set have been manufactured.

We have tested our hardware designs using a diagnostic software package running on the VAX. Using the remote self-test capability of device-interface modules, this network analyzer package can access a remote device interface on the network and verify proper operation of most functions. The network analyzer also queries the network's computer and device nodes for their identifications. In this manner, the configuration of the Novanet hardware is mapped in real time, and we can pinpoint the location of every serialized interface. On-net diagnostics are also automatic, since the type of interface can be determined by the remote testing process. The Novanet network analyzer is now one of the standard network-debugging tools in the controls development system.

Operation of the Novanet communications system is greatly enhanced by the ancillary control process (ACP). The ACP is a separate process that implements the upper levels of protocol for the network while running in parallel with the driver and users' programs. The ACP

- Performs message blocking/deblocking and multiplexing/demultiplexing for users.
- Performs some network housekeeping and management tasks.
- Permits efficient transmission of messages of widely varying lengths.

Novanet software drivers for both the VAX 11/780 and the LSI-11s contain many enhancements over the drivers that were demonstrated in 1980.[67] For example, since the ACP will be incorporated at a later date, the proper system linkage between the driver and the ACP has been included in the drivers. New driver-function codes allow the user to access the communications medium either directly throughout the driver or via the ACP, as appropriate for the desired operation. The error handlers in the driver have been improved and now include error correction by retrying at the communications-block level. The driver now detects and discards duplicate blocks and has access to the VAX 11/780 error logger, so all unrecoverable errors are logged in the system error log. The driver for the LSI-11 implements these same enhancements in the stand-alone environment. We have written a third version of the driver that will run under the DEC RSX-11M operating systems.

In the area of network utilities, we are writing programs to control charge-coupled-device (CCD) cameras and transient digitizers (Tektronix 7912ADs). The 7912AD digitizer uses the IEEE 488 bus for communications. To control this device, we are implementing a general-purpose Novanet-to-IEEE 488 interface so that any IEEE 488 instrument may be remotely controlled directly from the VAX.

During 1981, we completed our first Nodestar; it will be used as a manufacturing model and will also be installed on Novette as part of the Novette control system. The Nodestar is capable of handling 32 nodes and is expandable as system requirements grow.

Authors: J. R. Hill, J. R. Severyn, and P. J. VanArsdall

Network-Shared Memory, Data-Base Management, and Alignment-Configuration Control. During the early design stages of Nova, we recognized that,

for subsystem engineers, the most clearly understood method of program-to-program communication was through shared tables of data. Using a set of interface routines called the network-shared memory (NSM), we now have the ability to share tables between

- Programs in the same computer.
- Programs residing in computers connected via multiport memories.
- Programs residing in computers connected by Novanet.

NSM, therefore, provides a simple control-system-oriented interface to the extensive network functions of Novanet (Fig. 2-100). Since the interface to the shared tables is independent of the physical data-transfer medium, uniform methods of communicating between programs in the same and separate computers can be used. This decreases programming effort and increases system maintainability.[68]

During 1981, we also smoothed the process of adding new NSM regions to the Nova control system. This was done by cleaning up the generation processes and simplifying the process of adding information to the configuration and control data base. We have also developed processes for easily creating groupings of NSM regions to be loaded into the LSI-11/23 local processors. These enhancements should simplify the job of developing and maintaining control programs.

Because of greatly increased demands on our data-base management techniques during the year, we decided to look for a configuration-management system that would provide even greater flexibility to the user. We felt that developers would benefit most by knowing that they could get their data without having to worry about how they got it. After careful study, we determined that our needs would best be served by a relational data base because it is inherently easy to modify the way that data are retrieved from a relational base. Thus, users can work with their data at a much higher level, which simplifies the developer's job.

After evaluating available systems, we chose the ORACLE system from Relational Software, Inc., of Menlo Park, Calif., because of its performance and its support packages. ORACLE is also used in the Fusion Experiments Analysis Facility for some data-management tasks.

As part of this data-management effort, we considered how to provide the alignment-control programs with information on the configuration of the MOR (or any other part of the laser system) and also how to display the status of devices on the controls consoles. Achieving these goals is complicated by the fact that different

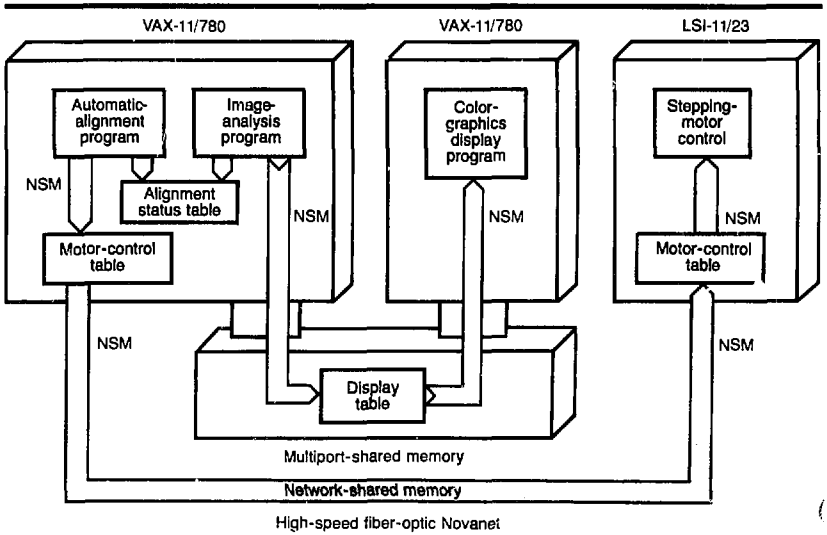

Fig. 2-100. The network-shared memory allows data transfer between programs in the same or different computers.

alignment-control tasks have different configuration requirements for waveplates, shutters, gimbals, and other alignment components. Clearly, we wanted to avoid hard-coding the configuration for a given task into the alignment-control software because, then, any changes would mean editing and recompiling the software. Furthermore, configuration information must be made available to the alignment-control software in a fashion that does not cause excessive overhead (thus slowing down the alignment).

Recognizing that our final alignment-task configurations will be substantially different from our initial choices, we decided to place all of the configuration data within the ORACLE data base. This step enables the MOR designers to find out about or make changes in any given task configuration with minimal effort. To provide configuration information to the alignment-control programs, we took the librarian parser, added some necessary capabilities, parsed an ASCII file of a single-task configuration to extract some information, and then placed the data into a binary file that alignment-control programs can access very quickly.

We also created a graphics-system status frame of the MOR that shows the Nova alignment devices in physical layout. As the status of each particular device is read back from the NSM shared regions, it is updated on the console graphics display. MOR operations personnel can thus ascertain the status of each device in the MOR with a single glance.

Authors: J. M. Duffy, P. J. VanArsdall, and D. L. McGuigan

Major Contributor: C. A. Humphreys

TV Network. The successful application of digital processing of standard TV images on Shiva[69] led to a commitment to image processing for all closed-loop alignment functions for Nova. Figure 2-101 shows the architecture of the video system attached to the VAX computers. A Quantex DS-12 video digitizer converts video images to digital form, and a Floating Point Systems array processor aids the VAX computer for image analysis.

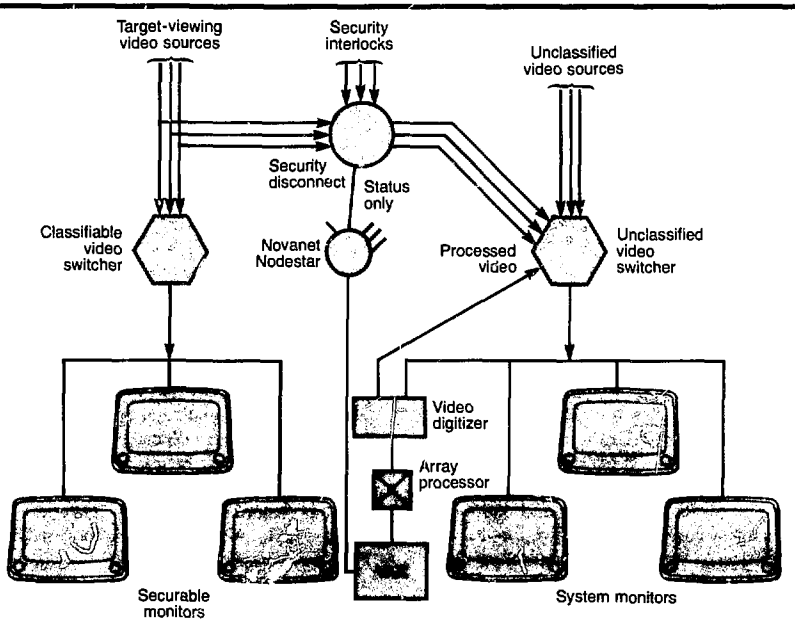

Fig. 2-101. Nova TV-system architecture.

The switching network provides a flexible and cost-effective multiplexing scheme. The unclassified switching system is responsible for collecting and distributing standard video format signals (RS-170 specification) throughout the Nova laser facility. It is based on the Telemation TVS-1000 series of commercial video cross-point switchers, and it accommodates 90 cameras and 40 monitors for Phase I (10 beams) of Nova. The classified switcher handles 40 cameras and 10 monitors.

The VAX-based image-analysis system can select any unclassified video source through one of the monitor channels of the unclassified switcher. Processed images with diagnostic text and graphic overlays are returned to the distribution system through a camera channel and can be viewed on any monitor. Since the array processor is attached to the VAX computer system, images can also be color-enhanced either for display on color monitors or for printing by the color hard-copy unit.

The TV distribution system includes security interlocks that automatically prevent target images from reaching either uncleared staff or the unclassified computer system during experiments with classified targets. As shown in Fig. 2-101, a set of securable monitors provides controlled operator access to classified images. These monitors are located in the target room, in the switchyard, and in one control console in the control room. The security-disconnect system automatically severs connections between target viewing sources and the unclassified switcher when interlock conditions are not met. However, the interlocks are keyed on a per-beam basis, so unclassified work can proceed on beamlines for which the cameras have no view of the target. The security disconnect will be implemented in hard logic, but the status of connections will be monitored in the control room over the Novanet computer link.

The Nova TV system also provides important capabilities for diagnostic data distribution. Several types of instrumentation planned for use on the laser and target diagnostic system can reproduce stored information in video form, among them the Tektronix 7912 transient digitizer and the LLNL CCD streak camera. Both these units also provide for data access over digital data buses, and the primary method of gathering data from these instruments is the digital route, over Novanet fiber-optic links. However, the TV-distribution system allows for convenient viewing of the output of these instruments during setup operations.

Important additional features of the TV network include system-wide synchronization and high-voltage isolation. Common synchronization of all cameras and monitors ensures that monitor displays do not roll during switching. Also, since the TV network and the pulsed oscillators are both synchronized to the 60-Hz line, the video cameras can be used to view both cw and pulsed sources.

High-voltage (60 kV) fiber-optic isolation will be installed at key points in the distribution network to prevent pulsed-power faults from propagating to unsuspecting personnel or damaging the central computers. Additional ground isolation will be provided for all signals by using video transformers to eliminate induced ground loops.

Author: P. J. VanArsdall

Processing of Alignment Cross-Hair Images. Aligning the Nova laser beam to the desired propagation path involves lining up each beam with insertable cross hairs that have been strategically located along the beamline and that are subsequently imaged by alignment sensors. The cross hairs are guaranteed to be rotated by at least 22.5° from one another and to have a fixed orientation once installed. However, the level of noise in the images is rather high. The method we have developed to find the center points of up to two cross hairs in each such image involves storing in advance a very condensed "snapshot" of each cross hair and then using the Nova array processor to correlate the stored snapshots with current cross-hair images. We chose a correlation method because correlation methods for finding simple shapes are relatively immune to noise; other methods (such as feature extractions) were found to be unreliable. Also, the correlation method is by far the fastest algorithm.

The correlation procedure can be used when one (stored) image contains a feature or pattern whose location we wish to find in a second (current) image. The result of

the correlation procedure is a new image with an intensity distribution proportional to how good the match is at each location in the current image between the feature in the stored image and the contents of the current image.

Figure 2-102 shows how the procedure works for the correlation of a stored image (3 rows and 3 columns) with a current image (7 rows and 7 columns). Each value obtained in the result image was obtained by overlaying the stored image onto the current image, multiplying each element that overlapped in the two arrays, and then summing up the results of those multiplications. The feature in the stored image is a cross with a slightly brighter center than the rest. The result image shows that the best correlation (the highest numerical value) was obtained at position 2, 4 (row 2, column 4). Examining the current image shows that, indeed, the highest value (the brightest cross) in the current image is also at position 2, 4.

In the Nova alignment application each stored image is a 50 × 50 position subsection of a 128 × 128 position image of a single cross hair. When the current image has two cross hairs in it, separate correlations are performed with each stored image to find the center points of the two cross hairs. For an M × M position stored image and an N × N position current image, this process would involve (M × M) (N × N) multiplications and (N × N) (M × M − 1) additions, thus consuming significant computation time. However, by reducing the images to binary images and omitting multiplications and additions involving zero, the number of calculations is reduced sixfold and the calculation time sixteen-fold, so that each correlation takes about three seconds.

In the processing of cross-hair images, we take the following steps

(1) Take the two-dimensional gradient of an image of each cross hair; this enhances edge features, such as cross-hair lines.
(2) Threshold the enhanced image, so that only the most significant edge features (those with the greatest gradient magnitude) are left; this creates a binary image, since a point either is or is not above the threshold value.
(3) Write each binary cross-hair image into a one-dimensional array that gives the offset of each nonzero image element from the upper left-hand corner of the image (see Fig. 2-103). Each element of the offset array represents a binary "1" in the stored image; the value equals the offset into a 128 × 128 position image, i.e., the row number multiplied by 128 and then added to the column number. These arrays describe the binary images by telling only where the nonzero elements are, resulting in a typical data volume reduction of 6 to 1 compared to the initial images.
(4) Save these arrays, plus the location of the cross-hair centers, as stored cross-hair images.
(5) Take the two-dimensional gradient of the current image and threshold it to generate a binary version of the current image.
(6) Perform the correlation procedure on the saved image(s) and the current image.

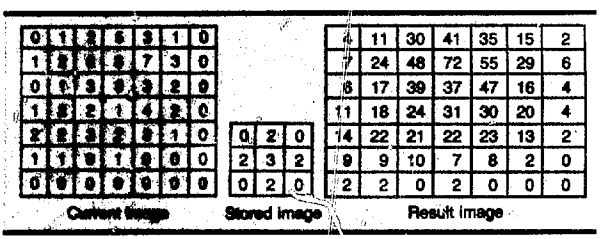

Fig. 2-102. Correlation of a stored image with a current image produces a result image used to align beam-alignment cross hairs.

Fig. 2-103. Creation of an offset array from a binary image for correlation of stored and current cross-hair images.

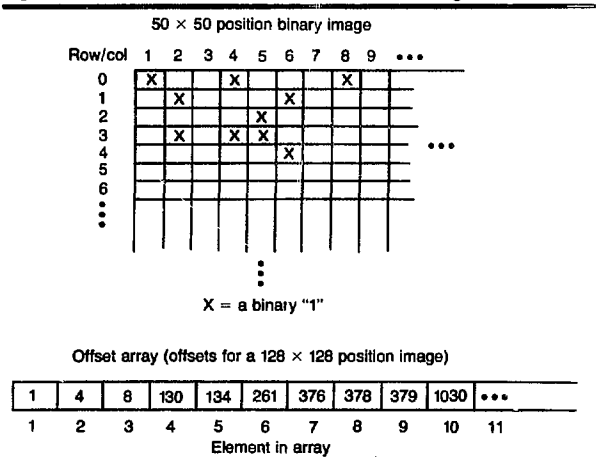

(7) Smooth the resulting image to reduce noise; then, take the location of the maximum value to be the location of the center of the cross hair.

We have tested this method thoroughly and find it very reliable for locating cross-hair center points.

Author: C. A. Humphreys

Enhanced Stepping-Motor Controller. On Shiva alignment subsystems, we employed our standard stepping-motor controller (SMC) for interfacing with alignment manipulators. All other types of interface hardware, such as on/off shutters, sense switches, and potentiometer-style position feedback, were interfaced through a custom-programmed LSI-11 processor. This approach suffered from the increased complexity and effort required to include these functions in both the hardware and the software.

Newly developed in-house products (primarily Novanet and the network-shared memory system discussed above) now permit virtual elimination of the custom LSI-11s from a performance standpoint (see also "Alignment and Laser Diagnostics" and "Target Systems," earlier in this section). To achieve this reduction in software, we had to upgrade the SMC to handle the additional interface requirements common to the alignment system. The next-generation machine is thus called the "enhanced" stepping-motor controller; it will be used to replace the older unit in new applications. Principal enhancements are as follows

- A total of 60 motors per microprocessor.
- Integration into the Nova and Novette control systems through the 10 Mbaud fiber-optic Novanet.
- Programmable alphanumeric control panel.
- Customized local controls resulting from the "device" concept.
- Programmable backlash correction.
- Higher resolution rates and local cross-coupling capability.
- Provision for optical-incremental encoders for position verification.
- Addition of binary device-interface capability.

The SMC is based on the LSI-11/23 microprocessor, a unit that offers greater execution speed over past LSI-11s. Because new technology allows higher performance, motor-interface capacity per SMC unit has been doubled with considerable savings over the two-unit cost. Software for the SMC has been rewritten in the Praxis language, both to support the upgraded functionality and to integrate the SMC into the Novanet fiber-optics link. Conversion of the software to Praxis also provided the benefit of testing the Praxis compiler.

Basic to the new SMC is the concept of an alignment "device": a collection of stepping motors strongly related in function. We have defined four classes of these devices, from those containing just one motor to those containing four. Examples of one-motor devices include wave plates, cross hairs, quartz rotators, and filter wheels. Two-motor devices can be spatial-filter pinhole manipulators or apertures. A three-motor device could be a lens adjustable in x, y, and z. A pair of two-axis mirror gimbals forms a four-motor device. Now, instead of referring to lookup tables and arrays of motors, we refer to named devices or arrays of devices.

More relevant to the laser operator, the device approach permits us to customize the local control panel found on each SMC. Based on past feedback from users, we have redesigned this panel to simplify its operation. Instead of printed labels on control switches, we have included programmable alphanumeric 18-segment displays that can be configured to reflect the function of each switch (when a switch is not used, the associated display label is turned off). The user now selects a device number on the control panel; the panel displays a meaningful device name, such as "SPATIAL FILTER 4," as well as custom labels for the slew axis controls.

A stand-alone SMC will not be customized for device level controls until the attachment to the central VAX system loads the definitions of the devices into the SMC control tables. Local controls in the "dumb" configuration are roughly equivalent to those found on the Shiva SMC.

On the previous SMC, several switches were hardwired for special functions. The new panel has a programmable function switch with an associated alphanumeric display. Only the desired function type is displayed, and there is ample room for

others to be added. We feel the programmable nature of the local control panel will minimize operator error and prove more flexible than fixed panel designs.

From past experience, we find that most alignment manipulators have a certain amount of mechanical backlash. This is exhibited as a loss of steps when the direction of motion is reversed. To alleviate this problem, we have implemented a backlash correction algorithm that always approaches a set-point position from the same direction. Our technique allows a programmed correction distance and motor rate to be set uniquely for every device. A version of this technique is found only in expensive commercial units, in which it is limited to a single predetermined value.

Because the laser path is folded and does not always lie in a plane, cross-coupling from the motor coordinate system to the video-sensor coordinate system is desirable, even from the local stand-alone control panel. If this is not done, some alignment jobs are quite difficult to accomplish manually. Coordinate transformations for automatic alignment are routinely done from VAX computer programs. The SMC has an algorithm, based upon closest fit to a line, that can approximate the desired manual slew vector at the selected motor speed. This function operates from a transformation matrix uniquely entered for each device requiring the conversion. Scaling of motor step units to real units can be accomplished concurrently with this operation.

The proper operation of most alignment components can be directly observed by the video-sensor system, as is the case for beam-transport mirrors. Simple binary motions can be verified by the normal two-position limit switches associated with the stepping motor, as is the case for passive quartz rotators. However, some devices cannot be easily observed and verified. For example, the gain-setting wave plate is a continuous function that must be checked. The multiposition filter wheels (used in the alignment and diagnostic sensor packages to insert filters, lenses, or mirrors) represent another type of device for which position encoding is desirable (see "Alignment and Laser Diagnostics," earlier in this section).

Position verification is accomplished through the use of optical incremental encoders, usually mounted integral to the stepping-motor unit. As each motion occurs, asynchronous counters connected to the encoder track the movement in terms of both direction and distance. Additionally, an index signal is generated once per encoder revolution. The index is used to recalibrate the step count with the independent encoder count. Recalibration is achieved by stepping the motor to an end-of-run limit switch and then reversing direction and stepping until the index is found. The sequence is automatic upon manual initiation. Here, again, the use of encoders is discretionary and is part of customization.

Binary I/O capability has been added to further enhance the utility of the SMC as the primary alignment front-end processor. Some alignment devices have a third indicator switch that can be sensed with a binary input channel. We have also defined a fifth class of component: "binary devices" having one binary output and two binary inputs (typically used for shutter control, etc.). The output controls a solenoid actuator; the two inputs encode the open or closed state of the shutter mechanism. The output channels are rated 24 V dc at 2 A. All signals in or out of the SMC microprocessor are optically isolated.

Several new hardware interfaces for the enhanced SMC have been designed and fabricated on printed-circuit cards. These include three boards for the optical encoders, one for the alphanumeric displays, two for the binary I/O, a new step clock and interrupt interface, and some smaller support boards. We are currently finishing debugging and will go into our first production in early 1982 in support of Novette.

Enhancement software is also undergoing extensive final development at this time. We will be fielding new SMC units on Novette prior to the November 1982 activation date, except for the target-positioning system (see "Target Systems," earlier in this section). Final debugging will be accomplished in actual system use on Novette. All of the systems should benefit from improved functionality, easier operation, and lower cost per controlled device.

Author: P. J. VanArsdall

Major Contributors: F. W. Holloway, R. D. Demaret, and W. J. Schaefer

Power-Conditioning Controls. The operator runs the power-conditioning control system by selecting from a menu of options pictured upon the operator console's center screen. By touching the pictures displayed upon the center screen, operators can perform a control function, select a new menu of control options, or perform other functions. System status is displayed on side monitors, and operators can select the type of status displayed upon those monitors. However, the status of the system is monitored by the VAX even when the status of parts of the system are not displayed. If a problem develops, the operator will be notified by a message that identifies the problem.

We have designed the command and status menus used in the power-conditioning control system; some have been prototyped. We designed the system to provide operators with maximum control of the laser while minimizing the amount of information they must remember. The power-conditioning main menu controls the system at the highest level; below that level, various control menus offer a more detailed control capability. At each level of control, appropriate status can be displayed; when the system is functioning properly, the operator will not be required to directly control the low-level functions. Control is available, however, if a malfunction occurs.

The configuration of the power-conditioning control system is defined as the state of the hardware and software components of the system. We can select any of a number of known system configurations; these given configurations are stored in an ORACLE data base and are keyed by a configuration name. Configurations are created or changed at a VAX terminal, using the ORACLE interactive application facility (IAF). The IAF menus allow the states of any controllable hardware or software component to be included or excluded in a configuration.

Configurations are loaded by selecting one of the available configuration names from the main power-conditioning control menu, or by selecting one of the names available from the configuration loading menu. We have designed and implemented the configuration loader that actually loads the NSM regions that control the hardware and software components.

We have completed the conceptual design of the power-conditioning control system VAX software. The software controls the power-conditioning hardware through the loading of NSM regions. These shared-memory regions reside in the power-conditioning multiports shared by the VAX and the power-conditioning front-end processors; the NSM regions have been defined and implemented. Since the multiport is the prime communication medium between the FEPs and the VAX for power conditioning, we will be able to control the laser equally well either from the FEPs or from the control-room graphics consoles.

Author: A. G. DeGroot

Target Data-Acquisition and Control System. The Nova target-diagnostics system has the task of recording a wide variety of signals from many diagnostics instruments surrounding the target. These instruments include x-ray and particle detectors, calorimeters, and other instruments to diagnose target shot results. Detectors in these instruments include CCD streak cameras with 10-ps resolution, photodiodes and x-ray diodes with 100-ps response, photomultipliers and silicon photodiodes with 1- to 2-ns response, and light and particle calorimeters with response times measured in full seconds. This wide range of bandwidths and wide variation in signal levels means that close attention must be given to diagnostic isolation and grounding to prevent cross talk and signal degradation.

The target-diagnostics system uses geographically distributed LSI-11 FEPs to control various analog-to-digital converters placed near the analog signal sources (Fig. 2-104). This minimizes analog-signal cable lengths and maximizes the signal-to-noise ratio. The central VAX computer supervises most FEP operations via Novanet.

The system will be menu-controlled for both system configuration and actual operation. System configuration will be accomplished by filling out a form displayed on a CRT connected to the VAX and accessing the control data base. Color-graphic touch panels will be the primary operator interface in both the control room and various remote areas around the target room near diagnostic instruments. Color touch panels

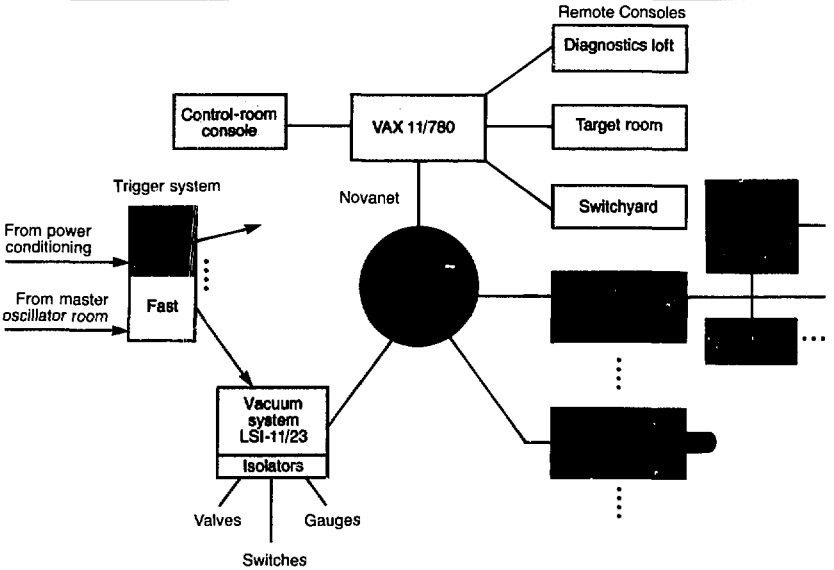

Fig. 2-104. Nova target-diagnostics control-system architecture.

will be located in the diagnostic loft, the target room, and the switchyard for convenient access and setup of diagnostics.

We designed the graphics-touch interface to allow system operation from both a diagnostic and a hardware perspective, with a clearly defined association between the diagnostics and the hardware used to implement them. Provision has been made for the operator to change from one mode to the other without losing his or her point of reference. By presenting to the operator only those options or commands that are appropriate for a given system state, we preclude much of the confusion normally associated with the operation a system of this type.

To further assist the operator, we have incorporated an on-line help feature into the menu design; this allows an operator to request information regarding use of the menu itself or of any selected option or command. The menus may be traversed as either a tree, beginning at the highest level of user interaction with the system, or by direct selection of the menu required to perform the desired operation. We have implemented eight of the control and status frames, representing a vertical slice of those enus required for system operation.

An integrated vacuum system for both the target chamber and the individual diagnostics will be controlled and interlocked using an LSI-11 FEP. Vacuum control of the chamber and each diagnostic will be available at any of the color-graphic touch panels. A major fraction of the vacuum system FEP was implemented this year, following the structure outlined in the *1980 Laser Program Annual Report*.[70] Most of the FEP hardware and software has been designed with stand-alone operation in mind. This year, we have developed and tested most of the hardware, including panels and interfaces for local control, signal processing for pressure gauges, and sensor subsystems.

We have concentrated our vacuum-system software in the vacuum-system FEP. The main control program, called the supervisor, provides operation and interlock functions for the main and auxiliary vacuum systems. The supervisor is table-driven for these two systems, as they are very infrequently (if ever) rearranged by physically changing the vacuum plumbing. On the other hand, diagnostics are frequently changed; therefore, we have written a separately programmed routine for each diagnostic, providing flexibility (and complexity) that a table-driven scheme cannot provide.

The trigger system for target diagnostics synchronizes both the FEPs and the data digitizers with the laser-shot countdown

sequence. The trigger signals come from two sources (see Fig. 2-104). The "slow" triggers originate from the power-conditioning system and inform the FEP of the status of the shot sequence; slow system signals are sent to an initiator transmitter, where the option of a local dry-run capability may be selected. The fiber-optic output from the initiator transmitter terminates at an initiator receiver in one CAMAC crate attached to each of the FEPs. The initiator receiver interrupts the processor at each change in the shot sequence status and, therefore, synchronizes each FEP to the shot countdown.

The "fast" trigger originates from the master oscillator room, where a fraction of the main laser pulse is sent to a photodiode in the diagnostic area. The photodiode's output is discriminated and gated by the slow trigger system to allow the fast trigger to propagate only on actual shot sequences; the photodiode output is then converted back to a constant-amplitude optical pulse by the laser-diode trigger transmitter. Each FEP has a trigger-receiver CAMAC module that interrupts the processor at shot time and that also converts the optical pulse back to an electrical signal for distribution to all instruments in the diagnostic station.

A diagnostic station is defined as an electrically isolated group of racks, at least one FEP, at least one CAMAC crate, and the digitizers and equipment required to support an associated diagnostic detector. Each diagnostic station is completely isolated, using fiber-optics for all input and output signals (except for the isolated detector); power is supplied through low-capacitance isolation transformers. A single safety ground is connected from each station to the local common-ground rod; "daisy chaining" of this ground wire is not permitted.

Most data acquisition is accomplished through CAMAC standard modules at the diagnostic station. CAMAC-controlled analog-to-digital and digital-to-analog converters presently supported include Tektronix 7912 transient digitizers, gated and ungated charge integrators, low-level calorimeters, and programmable high-voltage power supplies.

The basic conceptual design of the VAX resident portion of the target-diagnostic data-acquisition system software has been completed and is being implemented. We have taken a multiprogramming approach, using Praxis as the primary implementation language (see below). System operation is table-driven, and network-shared memory is used for process-to-process communication and synchronization. All of the configuration parameters, data from nonblock transfer devices, status regarding operation of the system, diagnostic hardware mapping, and command descriptions are contained within NSM regions to facilitate easy access by all of the processes that will comprise the system.

The command executive, which is the nucleus of the system, has been written. The command executive processes all command requests generated within the VAX resident portion of the system. Along with a terminal-oriented man-machine interface developed as a debugging aid, the command executive permits operation on a rudimentary level.

We are programming most of the system software in Praxis to aid in readability and maintainability. We have recoded the entire FEP software in Praxis, using the experience gained with Argus and Shiva. We have removed all data-base functions from the FEP and concentrated on device drivers and network software for all data-acquisition devices required for Nova and Novette. In addition to a CAMAC crate driver, device drivers for eight of our data-acquisition modules were coded in Praxis. This software was integrated with the Novanet communications driver and is presently being tested on a prototype diagnostic station connected to our development VAX computer.

Authors: D. J. Kroepfl, J. R. Severyn, and T. A. Sherman

Major Contributors: H. R. Burris and R. K. Reed

Experience with Praxis. We have continued work on the design and implementation of Praxis, a high-level block-structured language supporting real-time constructs, separate-module compilation, and extensive data-type checking.[71] Written in its own source language, Praxis currently generates code for both VAX and LSI-11 computers.

The prototype PDP-11 and VAX compilers were delivered to us during the

summer of 1980. Since that time, we have written on the order of 150 000 lines of working Praxis code. There were predictable disadvantages in trying to write control software while the compilers were under development. However, this effort served to exercise the compiler extensively, specifically testing many features that the compilers—written in Praxis themselves—were unable to test. The process rapidly uncovered many errors and unimplemented features; these were fixed in regular updates by Bolt Beranek and Newman, Inc. (BBN), the contractor for Praxis implementation. We were also able to demonstrate many of the advantages of using Praxis.

Praxis helps to produce maintainable and error-free programs. The extensive data-structuring capabilities and control statements allow programmers to "say what they mean." The strong type-checking and syntax analysis capabilities of Praxis find many common programmer errors. Therefore, we have found that, by the time the program compiles, it usually runs correctly.

We have demonstrated that programs written in Praxis can be compiled, run, and debugged on the VAX computer and then recompiled for the PDP-11 and run on the remote computers. One application in particular shows the transportability of Praxis code. Figure 2-105 shows a VAX computer interfaced to an LSI-11 by way of a shared memory. The data tables that reside in that memory, and the routines that access them, are defined in a single set of Praxis modules. After being compiled by the VAX Praxis compiler, these same files are compiled by the PDP-11 compiler and loaded into the LSI-11. The ability of Praxis to specify the exact location and layout of the data ensures that it is accessible from both sides.

On the VAX, Praxis follows the VMS procedure-calling standard, so that programmers may write Praxis interfaces for routines written in any other language that also follows this standard. We have written such interfaces to several packages, including the VAX/VMS system services, the VAX/RMS file system, the ORACLE relational data-base system, and the Nova console-graphics system.

The current maintenance contract with BBN continues until June 1982, at which point we will support the language entirely at LLNL. When fully completed, the Praxis products will be better than any existing system-control language available on DEC machines, and we plan to use Praxis for future projects.

Author: J. M. Duffy

Conventional Facilities

Introduction. In previous annual reports, we have described the design philosophies and functional aspects of the Nova conventional-facilities construction program, and we have listed the major engineering and construction organizations participating in the program.[72-74] During 1981, construction continued on the Nova laboratory and office buildings. Major site work got under way, including grading around each building, expansion of an adjacent parking lot, and preparation of site drainage. Paths and roads are being relocated consistent with the Laser Program Master Plan; however, progress in this endeavor was hampered by winter rains. Landscaping designs were completed, with the intent of releasing the landscape work in the spring of 1982.

Nova Laboratory Building. Completion of Nova laboratory building (Building 391, increment II) increased from 64 to 98% during the calendar year

- Interior walls were completed and painted.
- Clean-room ceilings were installed in the four clean areas, including the laser bay (Fig. 2-106).

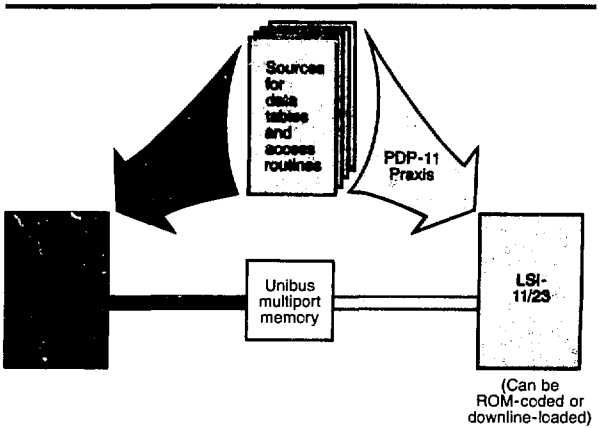

Fig. 2-105. The Praxis language supports common software for our VAX 11/780s and LSI-11/23s.

Fig. 2-106. The Nova ▲ laser bay after installation of the ceiling filter system, but before completion of the ceiling and the access floor (which forms the return-air plenum).

Fig. 2-107. The optical switchyard, looking toward the target room, with a completed ceiling filter system; the sprinkler piping is now covered ▼ by the access floor.

- The shielding doors were completed and accepted.
- Access floors were installed in the laser bay, optical switchyard (Fig. 2-107), and master oscillator room.
- All mechanical equipment (including vane-axial circulating fans, chillers, and pumps) and electronic control systems were installed.

We also awarded a contract for drilling large-diameter holes for laser beams and diagnostics[74]; this work was performed in April, May, and June. The job consisted of drilling 20 42-in.-diam holes through 4-ft-thick concrete walls for future laser-chain installations, and drilling 15 18-in.-diam diagnostic holes in the target room at oblique angles in space, all radial to the target chamber. Very precise alignment and location tolerances were met by the contractor. One hole that did not meet specified tolerance was enlarged from 18 to 24 in. to meet our technical requirements. By the end of 1981, the ceiling was complete, and return-air ducts on the floor had been installed.

To our knowledge, the hole-drilling work was unique in terms of the size of the laser-beam holes and the alignment and tolerance requirements of the diagnostic holes. We had predicted that the hole-drilling effort would not have a significant impact on the time or cost of construction. This prediction was incorrect, however, due to delays in the development and award of the contract. As a result, we sustained a delay of about four weeks to overall construction completion. We now expect that construction of the laboratory building will be complete at the end of January 1982, except for some exterior work.

Nova Office Building. Physical completion of the Nova office building (Building 481) increased from 28 to 86% during 1981. Most of the work was performed by building-finish, electrical, and mechanical contractors, who were responsible for erecting exterior window walls, glazing, interior walls and partitions, heating and ventilating duct-work and piping, electrical and communication systems, carpeting, and suspended ceilings.

All major mechanical and electrical equipment was delivered and installed. We experienced delivery delays with the window-wall framing and glass, however, which in turn delayed interior construction. To mitigate the delay, a significant amount of temporary glazing was done to allow construction to proceed effectively through the wet-weather season. We continued to evaluate office furniture, and we placed orders for delivery of furniture consistent with the occupancy schedule. We now project the completion of contract construction for early April 1982, with building occupancy in late April.

Author: C. P. Benedix

Project-Management Systems

For Nova, we have developed a financial planning and tracking system, a schedule-control system, and an integrated quality- and safety-assurance system. These systems are described in detail in the *1980 Laser Program Annual Report*.[75] During 1981, our project-management systems continued to function smoothly and effectively; the following paragraphs address the accomplishments and applications of each system individually.

Financial Planning and Tracking System. The Nova financial planning system is an earned-value system that calculates three performance-measurement parameters

- Budgeted cost of work scheduled (BCWS).
- Budgeted cost of work performed (BCWP).
- Actual cost of work performed (ACWP).

The system (illustrated schematically in Fig. 2-108) emphasizes formal review procedures for developing the project baseline. This baseline is then tracked with reports generated by automated procedures drawing on LLNL-wide accounting and procurement data bases. These tracking reports are prepared for level 3 of the Nova work-breakdown structure (illustrated in Fig. 2-109). Level-3 tracking reports, along with detailed actual-cost documents, are provided each month to lead engineers responsible for cost centers. Summary reports at levels 0, 1, and 2 are prepared for review by the project office and DOE.

During 1981, we modified our computer system to accommodate a longer planning horizon and to plan for frequency-conversion costs. From the beginning of 1981, we had tracked against a baseline comprised of a 10-beam laser system without frequency conversion; this system had a total estimated cost (TEC) of $140 million. In May 1981, we prepared and submitted to DOE the required Construction Project Data Sheet (Schedule 44) for a 10-beam system with frequency conversion (Phase I) and for a 20-beam system with frequency conversion (Phase II), assuming concurrent procurements. Table 2-12 gives the funding assumptions and TECs we used for these Schedule 44s. On October 1, 1981, we

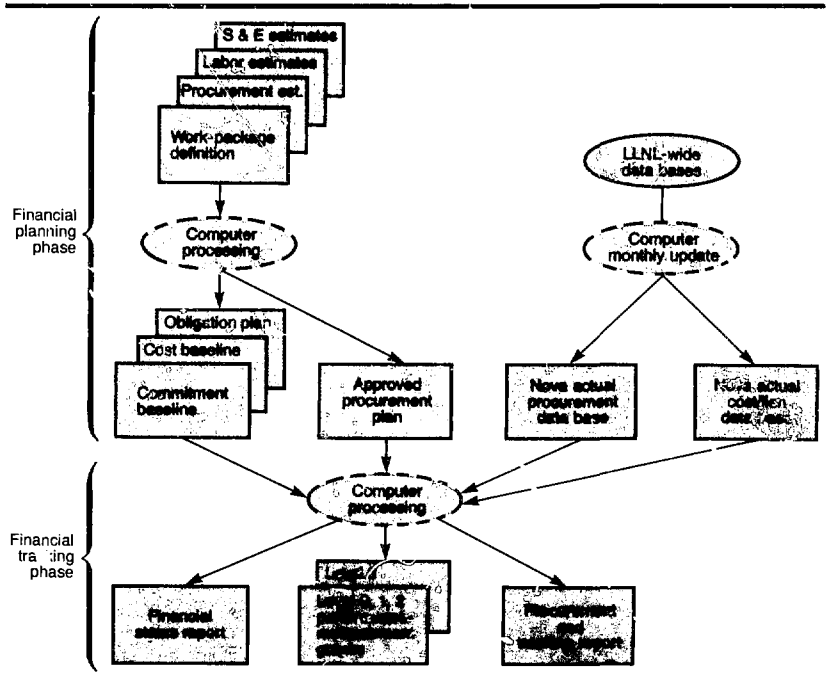

Fig. 2-108. Schematic of the Nova financial planning and tracking system.

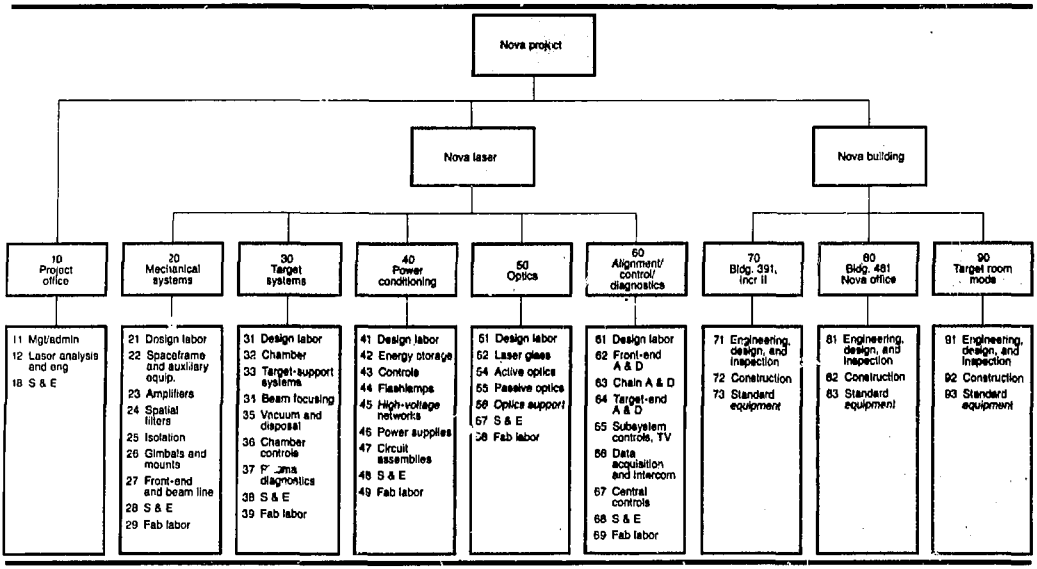

Fig. 2-109. Nova work-breakdown structure.

started formally tracking against a Phase I baseline.

Pending DOE approval of frequency conversion, we are temporarily charging all procurements associated with the frequency-conversion capability against an operating account. Procurements for frequency conversion are on the critical path, however, and operating funds can cover these procurements only partially pending formal approval. With early-1982 approval of frequency conversion by DOE as part of the Nova line item, the $189 million TEC could be reduced and the fourth-quarter FY 1985 completion date moved up.

Scheduling System. To monitor schedule performance during 1981, we relied on a comparison of the commitment BCWS and BCWP curves of the financial system. The planned commitment curve is a good base from which to measure schedule performance during periods when a large number of procurement awards are scheduled. Figure 2-110 shows the planned commitment and planned cost curves for Nova, indicating the periods when each of these is most useful for measuring schedule performance.

During 1982, we will begin using an event-based system to monitor and control schedule performance. The events will be established within the framework of an assembly breakdown structure (ABS), so they may be summarized and reviewed according to completed assembly (Fig. 2-111). The ABS provides a structure for reviewing critical events in a systematic, hierarchical manner and is useful to the Nova project engineer responsible for directing the integration of the system. The event-based schedule-control system features

(1) A list of major project milestones, updated for DOE at each change in the project baseline.
(2) A baseline project schedule showing major milestones yet to be accomplished vs a time line.
(3) An activation schedule, including the major project milestones tracked by DOE and other significant milestones.
(4) Milestone charts prepared by each lead engineer, showing feasible plans for achieving the events on the activation schedule for which they are responsible.

Features 1 and 2 were implemented in connection with the Phase I baseline adopted October 1, 1981. Features 3 and 4 were developed for Novette and are proving extremely effective; the Novette activation schedule is given in Fig. 2-112. For Nova, the progress of assemblies defined within the ABS structure will be collected on Nova Schedule Status Reports. The progress information will then be displayed with a "time now" line against the assembly milestones in the Nova Plan Versus Actual

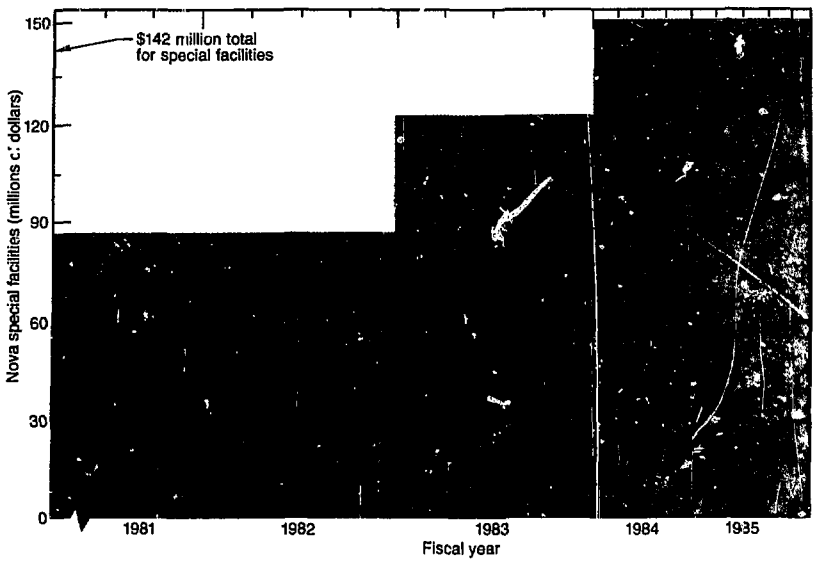

Fig. 2-110. Planned commitment and cost curves for Nova, showing that different schedule-performance parameters apply as the Nova project evolves.

Schedule Reports. The schedule updating and reporting will be computer-processed.

At weekly Novette meetings, as the activation schedule is reviewed and discussed, all lead engineers simultaneously review the detailed schedules they have prepared for their own work. If lead engineers cannot meet their own schedule, solutions are formulated and implemented. These same procedures will be used for Nova, with the added provision that key milestones reported to DOE will also be included on the activation schedule.

During 1981, three major uncertainties regarding the Nova project caused a slowdown of procurement awards and, thus, slowed the entire Nova schedule. These were

- Uncertainty regarding DOE approval for the inclusion of frequency conversion.
- Uncertainty regarding DOE approval of procurement awards for Phase II.
- Uncertainty regarding FY 1982 funding, resulting in a hold on procurements near the end of 1981.

The slowing effect of these uncertainties was incorporated into the baseline as of October 1981.

Quality- and Safety-Assurance System. We continued to implement our integrated quality- and safety-assurance system in 1981. Our primary focus was on

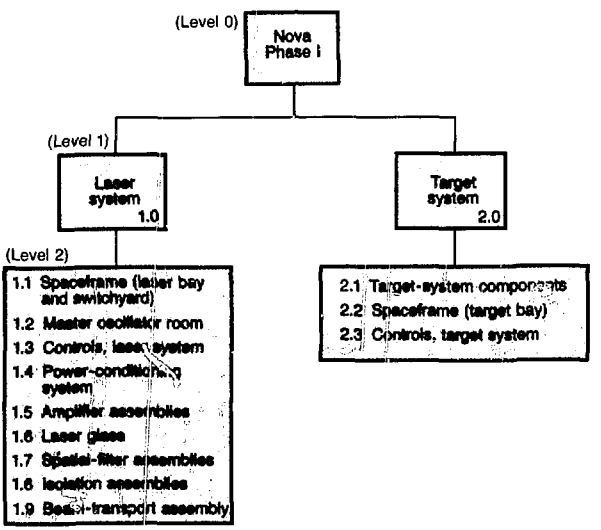

Fig. 2-111. Assembly breakdown structure for Phase I of Nova.

Table 2-12. Funding assumptions and total estimated costs for Nova Phase I and Phase II (in millions of dollars).

	Fiscal-year budget authorization					Total estimated costs	Projected completion
	[illegible]						
Phase I	[illegible]	25	17	40	—	200	[illegible]
Phase II	101	75	50	50	50	400	[illegible]

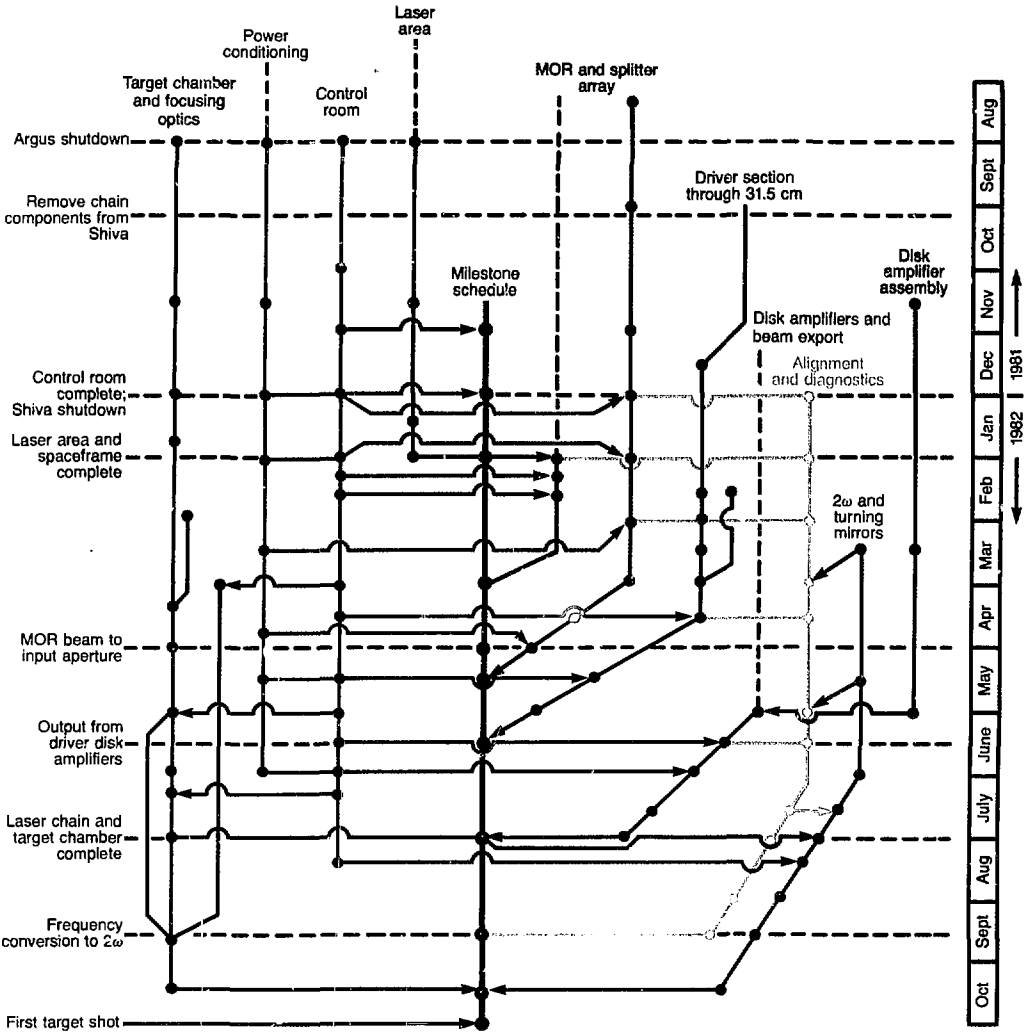

Fig. 2-112. The Novette activation schedule.

- Construction activities associated with the laboratory and office buildings.
- Design and procurement activities for the laser system.

With construction of conventional facilities nearing completion (see the previous article), we have used an updated subordinate assurance plan as our guide during construction. The subordinate plan was updated based on the findings of an internal LLNL audit conducted late in 1980. Based on that audit, we expanded the plan's requirements to cover the Nova office building along with the Nova laboratory building. We also established a dedicated team from the LLNL Plant Engineering Department to evaluate and oversee Nova design changes resulting from errors and oversights or from requests. The design-change control system was used for all changes affecting building criteria or interfaces between the laser system and the building. The design-change team prepared 48 Design Change Records (DCRs) for conventional facilities through the end of 1981.

With conventional-facilities construction

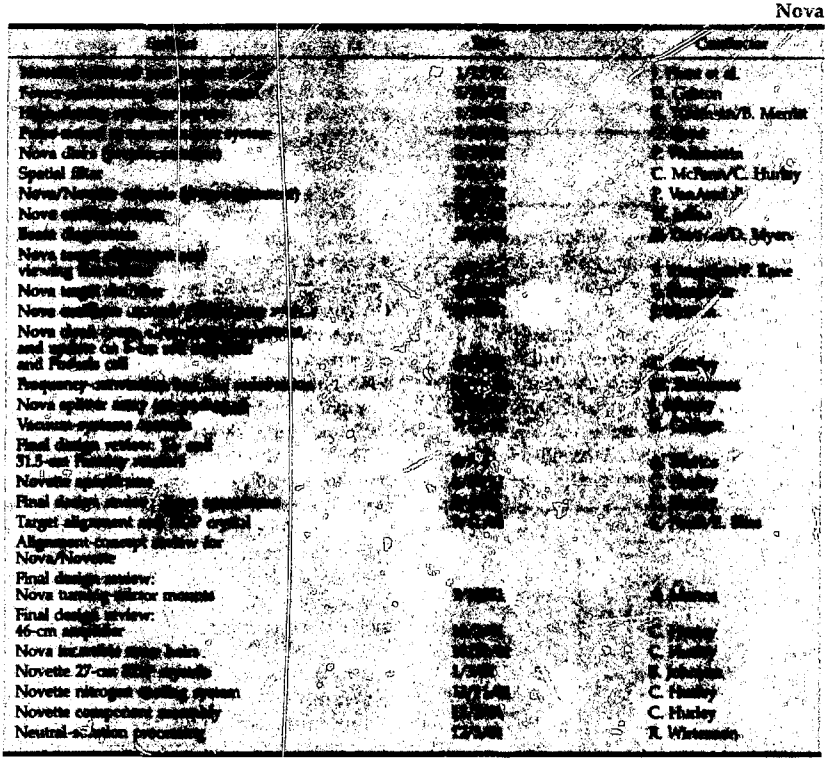

Table 2-13. Nova and Novette design reviews conducted during 1981.

coming to an end, we decided to conduct a final audit of our conventional construction. The Nova Project Manager assigned an audit team consisting of a representative from the Laser Program Facilities Group, the LLNL Plant Engineering Department, and the LLNL Quality Assurance Office. The team was asked to verify that

- Mechanisms are in place to verify completion of contractual requirements.
- Necessary documentation and as-built drawings required by LLNL and the Laser Program are forthcoming prior to close-out of all contracts.
- As-built documentation will exist showing the physical location of utility lines, conduit, plumbing, computer cabling, etc., that interface with existing LLNL facilities.

A report and briefing to the Nova Project team is planned for early 1982.

Progress with Nova special facilities (the laser system) during 1981 was hampered due to the uncertainties mentioned above. For the quality- and safety-assurance effort, these uncertainties resulted in our slowing procurements, and subsequent assembly, and placing major emphasis on the same types of activities that were conducted in 1980: design and procurement reviews.

Design reviews conducted during 1981 are listed in Table 2-13, which shows how our designs have progressed from the conceptual phase to the procurement phase. For each review, we continue to prepare preliminary hazards analyses that assess the hazards associated with the design or operation of the components. We also have used the DCR process, described above, for special-facility components; 15 special-facility DCRs were prepared during the year.

We updated our Nova Master Assurance Program Plan as a result of the audit findings from the LLNL internal audit and the DOE audit conducted in late 1980. However, we have not released the revised version or conducted a second audit. Now that we have DOE direction for Nova Phase I and frequency conversion (to be included later in FY 1982), we plan to proceed with another audit, release the updated master plan, and release the subordinate plans for

optical components, alignment diagnostics, and control systems.

Authors: A. J. Levy and F. J. Holcomb

Janus

Following the shutdown and subsequent dismantling of the Argus laser facility in September 1981, we overhauled and reconfigured the Janus laser. Janus had been a two-beam laser system designed for two-sided target illumination experiments. The new configuration is a single chain incorporating a number of Argus and Shiva optical and electro-optical components. These larger components almost completely fill the space originally occupied by the two Janus arms. The new facility (shown in Fig. 2-113) features the following improvements over the old Janus facility

- A new active mode-locked, Q-switched (AMQ) oscillator with planar-triode-driven switchout.
- An image-relayed beam path.
- Higher-performance Argus and Shiva laser amplifiers.
- Larger f/No. Argus and Shiva spatial filters for image relaying.
- Argus Pockels cells for isolation and for protecting the target from amplified fluorescence.
- Neutral-solution processed surfaces on the output spatial-filter lenses (see "Optical Components," earlier in this section).

Fig. 2-113. Schematic of the new Janus laser facility.

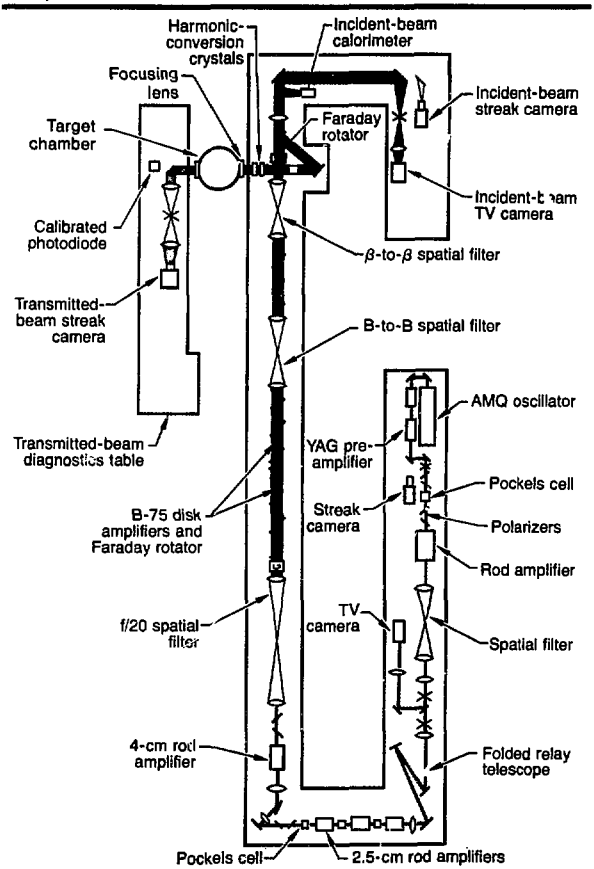

The new AMQ oscillator will significantly enhance the efficiency and reliability of the laser. The use of hard apertures and image-relaying techniques will significantly increase the output energy extractable from the laser while ensuring excellent overall beam quality. We expect that the new Janus single-chain configuration will deliver between 100 and 200 J of 1.06-μm light in ~1-ns pulses for use in a variety of experiments.

Instrumentation on the new Janus incident beam includes a streak camera, a 1.06-μm-sensitive calorimeter for measuring the output energy of the chain, several infrared-sensitive vidicons for monitoring system alignment at selected image planes, and an equivalent-plane camera. The transmitted-beam diagnostics (TBD) package features streak-camera and target-imaging optics, supporting the study of shock-wave propagation through layered planar targets.

We have reserved space for insertion of a large-aperture mirror following the output Faraday rotator. This mirror will direct the laser energy through 10-cm-aperture harmonic-conversion crystals for 2ω and 3ω experiments in the green (0.53 μm) and near-UV (0.35 μm) regions of the spectrum. With minimal modification, the Janus facility will support both target experiments and propagation experiments.

All of the new Argus and Shiva optical amplifiers, image-relaying telescopes, apodizers, spatial filters, Faraday rotators, polarizers, and Pockels cells are installed and on-line, and initial tests of the new system are underway. The new image-relaying optical train appears to be working well,

delivering a homogeneous beam to the focusing lens on the Janus target chamber. The incident-beam instrumentation has been installed, permitting ready alignment of the beam from the laser chain and of the pinholes in the several spatial filters located in the chain.

Author: G. J. Linford

References

1. J. Nuckolls et al., *Nature (London)* **239**, 139 (1972).
2. C. E. Max, C. F. McKee, and W. C. Mead, *Phys. Fluids* **23**, 1620 (1980).
3. C. E. Max and K. G. Estabrook, *Comments Plasma Phys. Contr. Fusion* **5**, 239 (1980).
4. R. O. Godwin et al., "Livermore Builds a Giant," *Laser Focus Magazine*, May 1981, pp. 58–64.
5. *Laser Program Annual Report—1980*, Lawrence Livermore National Laboratory, Livermore, Calif., UCRL 50021-80 (1981), pp. 2-38 to 2-52.
6. E. Fabre et al., in *Proc. Conf. Plasma Phy. Contr. Nucl. Fusion Research*, Vienna, Austria, 1980 (International Atomic Energy Agency, Vienna, 1981), Paper No. IAEA-CN-38/1-4.
7. A. G. M. Maaswinkel, K. Eidmann, and R. Sigel, *Phys. Rev. Lett.* **42**, 1625 (1979); D. E. Slater et al., *Phys. Rev. Lett.* **46**, 1199 (1981); W. Seka et al., *Bull. Am. Phys. Soc.* **25**, 895 (1980).
8. W. C. Mead et al., "Laser-Plasma Interactions at 0.53 μm for Disk Targets of Varying Z," *Phys. Rev. Lett.* **46**, 1289 (1981).
9. *Laser Program Annual Report—1980*, Lawrence Livermore National Laboratory, Livermore, Calif., UCRL-50021-80 (1981), pp. 2-38 to 2-53.
10. L. M. Cook, W. H. Lowdermilk, D. Milam, and J. E. Swain, *Antireflective Surfaces for High Energy Laser Optics Formed by Neutral-Solution Processing*, Lawrence Livermore National Laboratory, Livermore, Calif., UCRL-86909 (1981).
11. *Laser Program Annual Report—1980*, Lawrence Livermore National Laboratory, Livermore, Calif., UCRL-50021-80 (1981), pp. 2-57 to 2-61.
12. J. E. Swain, Lawrence Livermore National Laboratory, Livermore, Calif., private communication (1981).
13. W. W. Simmons, J. T. Hunt, and W. E. Warren, "Light Propagation through Large Laser Systems," *IEEE J. Quantum Electron.* **QE-17**, 1727–1744 (1981).
14. A. J. Glass and W. E. Warren, *MALAPROP—Light Propagation in a Nonlinear Medium*, Lawrence Livermore National Laboratory, Livermore Calif., UCRL-80316 (1977).
15. *Laser Program Annual Report—1976*, Lawrence Livermore Laboratory, Livermore, Calif., UCRL-50021-76 (1977), pp. 3-15 to 3-18.
16. J. Hunt, W. Simmons, R. Speck, W. Warren, and D. Eimerl, *Beam Propagation in the Frequency Converted Subsystems of Nova and Novette*, Lawrence Livermore National Laboratory, Livermore, Calif., UCID-19086 (1981).
17. *Laser Program Annual Report—1980*, Lawrence Livermore National Laboratory, Livermore, Calif., UCRL-50021-80 (1981), pp. 2-259 to 2-264.
18. M. Weber, *Nonlinear Refractive Index of Glasses at 2ω*, Lawrence Livermore National Laboratory, Livermore, Calif., internal memorandum ELR 81-03/5666P (1981).
19. *Laser Program Annual Report—1980*, Lawrence Livermore National Laboratory, Livermore, Calif., UCRL-50021-80 (1981), pp. 2-48 to 2-50.
20. D. J. Kuizenga, "Short-Pulse Oscillator Development for the Nd:Glass Laser-Fusion Systems," *IEEE J. Quantum Electron.* **QE-17**, 1694–1708 (1981).
21. J. E. Murray and D. J. Kuizenga, "Regenerative Compression of Laser Pulses," *Appl. Phys. Lett.* 37, 27 (1980).
22. J. E. Murray, "Temporal Compression of Mode-Locked Pulses for Laser-Fusion Diagnostics," *IEEE J. Quantum Electron.* **QE-17**, 1713–1722 (1981).
23. P. M. Johnson, *Building 381 High Bay Air Conditioning System*, Lawrence Livermore National Laboratory, Livermore, Calif., UCID-17320 (1976).
24. E. L. Molishever, *Analysis of a Stepped-Temperature Scheme for Cooling Laser Box Amplifiers*, Lawrence Livermore National Laboratory, Livermore, Calif., internal memorandum NOVA 81-385 (June 4, 1981).
25. E. L. Molishever, *Implementation of Stepped Cooling to Novette Laser Amplifiers*, Lawrence Livermore National Laboratory, Livermore, Calif., internal memorandum NOVA 81-473 (October 7, 1981).
26. J. F. Holzrichter, *Program Planning*, Lawrence Livermore National Laboratory, Livermore, Calif., internal memorandum ICF 81-91 (October 30, 1981).
27. *Laser Program Annual Report—1978*, Lawrence Livermore National Laboratory, Livermore, Calif., UCRL-50021-78 (1979), pp. 6-1 to 6-71.
28. *Laser Program Annual Report—1979*, Lawrence Livermore National Laboratory, Livermore, Calif., UCRL-50021-79 (1980), pp. 5-1 to 5-99.
29. *Laser Program Annual Report—1980*, Lawrence Livermore National Laboratory, Livermore, Calif., UCRL-50021-80 (1981), pp. 5-1 to 5-78.
30. *Laser Program Annual Report—1980*, Lawrence Livermore National Laboratory, Livermore, Calif., UCRL-50021-80 (1981), pp. 2-50 to 2-53.
31. *Laser Program Annual Report—1977*, Lawrence Livermore National Laboratory, Livermore, Calif., UCRL-50021-77 (1978), p. 3-17.
32. *Laser Program Annual Report—1980*, Lawrence Livermore National Laboratory, Livermore, Calif., UCRL-50021-80 (1981), pp. 5-72 to 5-75.
33. *Laser Program Annual Report—1980*, Lawrence Livermore National Laboratory, Livermore, Calif., UCRL-50021-80 (1981), p. 2-75.
34. H. Schroeder, "Thin-Film Formation on Glass Surfaces in Chemical Coating Processes," *Proc. 10th Intern. Conf. Glass*, (Kyoto, Japan, 1974), pp. 8-118; and H. Schroeder, "A Method of Reducing Reflection from Articles of Glass or Silicates," Federal Republic of Germany Patent 821828 (1962).
35. *Laser Program Annual Report—1980*, Lawrence Livermore National Laboratory, Livermore, Calif., UCRL-50021-80 (1981), pp. 2-65 to 2-72 and 2-97 to 2-103.
36. D. Milam, "1064 nm Laser Damage Thresholds of Polished Glass Surfaces as a Function of Pulse Duration and Surface Roughness," in *Laser Induced Damage in Optical Materials*, US Department of Commerce, National Bureau of Standards Special Publication 541 (U.S. Government Printing Office, Washington, D.C., 1978).
37. *Laser Program Annual Report—1980*, Lawrence Livermore National Laboratory, Livermore, Calif., UCRL-50021-80 (1981), p. 2-71.

38. B. T. Merritt and K. Whitham, "Performance and Cost Analysis of Large Capacitor Banks Using Weibull Statistics and MTBF," *3rd IEEE Intern. Pulsed Power Conf.* (Albuquerque, N. Mex., June 1981).
39. D. K. Haskell et al., "Development of a High Density Energy Storage Capacitor for Nova," *9th Symp. Eng. Problems Fusion Research* (Chicago, Ill., October 1981).
40. J. Oicles, D. Downs, and D. Kuizenga, "Fast, Versatile Pockels Cell Driver," *3rd IEEE Intern. Pulsed Power Conf.* (Albuquerque, N. Mex., June 1981).
41. L. Bradley, E. Orham, I. Stowers, and P. Koert, *Development of a Plasma Retropulse Shutter for Shiva and Nova*, Lawrence Livermore National Laboratory, Livermore, Calif., UCRL-52830 (1979).
42. J. Oicles, E. S. Fulkerson, and B. Mass, "A Reliable Trigger Unit for Rail Gap Switches," *9th Symp. Eng. Problems Fusion Research* (Chicago, Ill., October 1981).
43. D. G. Gritton, L. W. Berkbigler, and J. A. Oicles, "Design of a Fiber Optic Multi-tapped Computer Bus for a Pulsed Power Control System Application," *8th Symp. Eng. Problems Fusion Research* (San Francisco, Calif., 1979).
44. D. J. Kuizenga, *IEEE Journal Quant. Electron.* **QE-17,** 1694 (1981).
45. J. T. Hunt, J. A. Glaze, W. W. Simmons, and P. A. Renard, *Applied Opt.* **17,** 2053 (1978).
46. E. S. Bliss et al., "Nova Alignment and Diagnostic Systems," *Proc. IEEE 9th Symp. Eng. Problems Fusion Research* (Chicago, Ill., October 26–29, 1981).
47. R. Ozarski, *Laser Focus* 17(12), 50 (1981).
48. D. H. Mueller and S. Sheldrake, "Pulse Synchronization System," *Tech. Digest IEEE-OSA Conf. Laser Eng. and Appli.* (Washington, D.C., June 1–3, 1977), paper 11.9.
49. *Laser Program Annual Report—1979*, Lawrence Livermore National Laboratory, Livermore, Calif., UCRL-50021-79 (1980), p. 2-111.
50. *Laser Program Annual Report—1980*, Lawrence Livermore National Laboratory, Livermore, Calif., UCRL-50021-80 (1981), p. 2-123.
51. *Laser Program Annual Report—1980*, Lawrence Livermore National Laboratory, Livermore, Calif., UCRL-50021-80 (1981), p. 2-269.
52. *Laser Program Annual Report—1980*, Lawrence Livermore National Laboratory, Livermore, Calif., UCRL-50021-80 (1981), p. 2-128.
53. *Laser Program Annual Report—1979*, Lawrence Livermore National Laboratory, Livermore, Calif, UCRL-50021-79 (1980), p. 2-114.
54. *Laser Program Annual Report—1980*, Lawrence Livermore National Laboratory, Livermore, Calif., UCRL-50021-80 (1981), p. 2-125.
55. *Laser Program Annual Report—1980*, Lawrence Livermore National Laboratory, Livermore, Calif., UCRL-50021-80 (1981), p. 2-131.
56. *Laser Program Annual Report—1980*, Lawrence Livermore National Laboratory, Livermore, Calif., UCRL-50021-80 (1981), pp. 2-90 to 2-97.
57. D. Eimerl, internal memorandum LTA 81-11, Lawrence Livermore National Laboratory, Livermore, Calif. (May 1981).
58. D. Eimerl, internal memorandum LTA 81-09, Lawrence Livermore National Laboratory, Livermore, Calif. (May 1981).
59. M. A. Summers et al., "A Two Color Frequency Conversion System for High Power Lasers," presented at *Conf. Lasers Electro-Optics '81* (Washington, D.C., June 10–12, 1981).
60. W. Seka et al., "Demonstration of High Efficiency Third Harmonic Conversion of High Power Nd-Glass Laser Radiation," *Opt. Commun.* **34,** 469 (1980).
61. R. S. Craxton, "Theory of High Efficiency Third Harmonic Generation of High Power Nd-Glass Laser Radiation," *Opt. Commun.* **34,** 474 (1980)
62. S. P. Mukherjee and W. H. Lowdermilk, *Gradient-Index Antireflection Films Deposited by the Sol-Gel Process*, Lawrence Livermore National Laboratory, Livermore, Calif., UCRL-86274 (1981).
63. *Laser Program Annual Report—1979*, Lawrence Livermore National Laboratory, Livermore, Calif., UCRL-50021-79 (1980), p. 2-119.
64. *Laser Program Annual Report—1980*, Lawrence Livermore National Laboratory, Livermore, Calif., UCRL-50021-80 (1981), p. 2-158.
65. *Laser Program Annual Report—1980*, Lawrence Livermore National Laboratory, Livermore, Calif., UCRL-50021-80 (1981), p. 2-163.
66. *Laser Program Annual Report—1980*, Lawrence Livermore National Laboratory, Livermore, Calif., UCRL-50021-80 (1981), p. 2-144.
67. *Laser Program Annual Report—1980*, Lawrence Livermore National Laboratory, Livermore, Calif., UCRL-50021-80 (1981), pp. 2-133 to 2-141.
68. *Laser Program Annual Report—1980*, Lawrence Livermore National Laboratory, Livermore, Calif., UCRL-50021-80 (1981), pp. 2-141 to 2-143.
69. G. J. Suski, *Shiva Automatic Pinhole Alignment*, Lawrence Livermore National Laboratory, Livermore, Calif., UCRL-84903 (1980).
70. *Laser Program Annual Report—1980*, Lawrence Livermore National Laboratory, Livermore, Calif., UCRL-50021-80 (1981), pp. 2-160 to 2-162.
71. A. Evans, Jr., et al., *Praxis Language Reference Manual*, Lawrence Livermore National Laboratory, Livermore, Calif., UCID-15331 (1981).
72. *Laser Program Annual Report—1978*, Lawrence Livermore Laboratory, Livermore, Calif., UCRL-50021-78 (1979), pp. 2-123 to 2-126.
73. *Laser Program Annual Report—1979*, Lawrence Livermore National Laboratory, Livermore, Calif., UCRL-50021-79 (1980), pp. 2-127 to 2-134.
74. *Laser Program Annual Report—1980*, Lawrence Livermore National Laboratory, Livermore, Calif., UCRL-50021-80 (1981), pp. 2-168 to 2-172.
75. *Laser Program Annual Report—1980*, Lawrence Livermore National Laboratory, Livermore, Calif., UCRL-50021-80 (1981), p. 2-172.

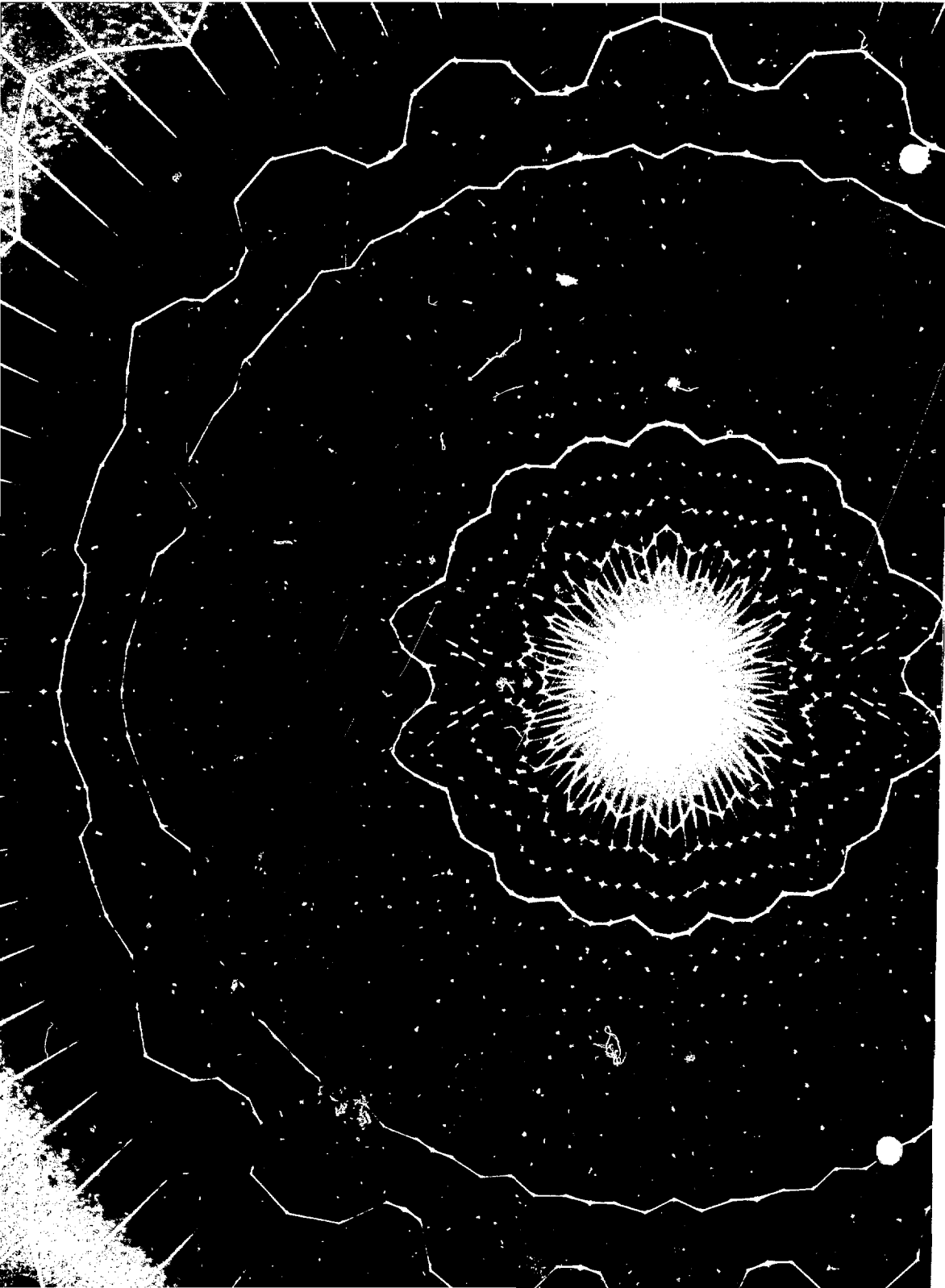

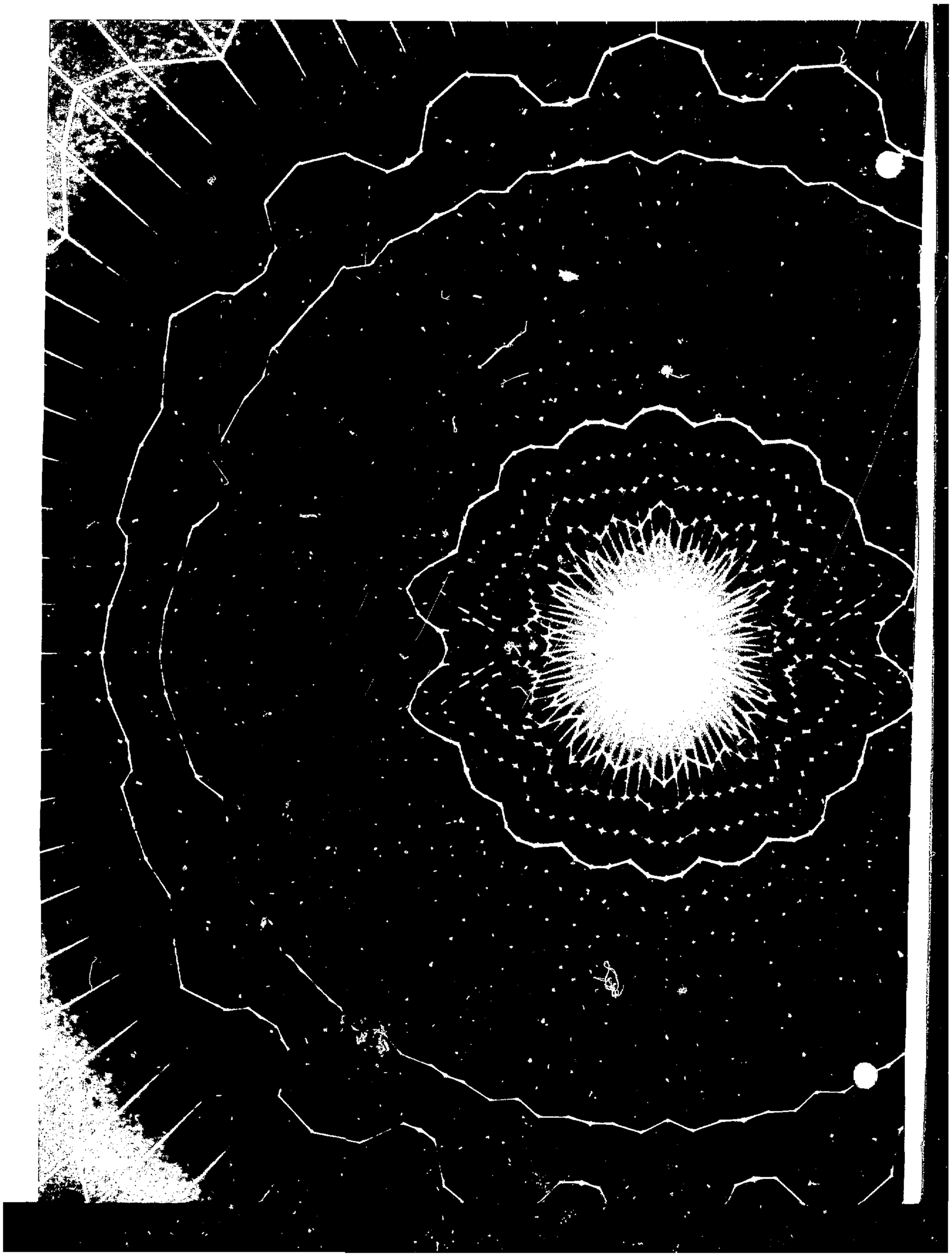

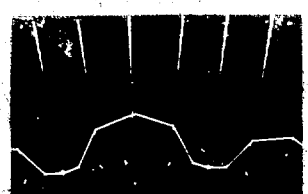

Target Design
Section 3

Target Design

Contents

Section Editor: W. L. Kruer

Target Design

Introduction

J. H. Nuckolls

The target-design program at LLNL combines the efforts of the Plasma, Code Development, and Design groups in three basic areas

- Developing theories of beam–plasma interaction, implosions, and thermonuclear microexplosions.
- Building plasma and implosion-burn computer codes.
- Using these theoretical and computational tools to design targets and simulate experiments.

A principal objective is to demonstrate the implosion of D–T to reactor-target densities, about 1000 times liquid density. In 1979–1980, we achieved 100 times liquid density. This year, we designed an improved target hohlraum and successfully tested it on Shiva. Important improvements were made. Coupled with our results on wavelength scaling, these Shiva experiments have increased our confidence that significant advances in compression are possible in Novette experiments with 2ω and 3ω light focused by the Axicon cylindrical focusing system. Preliminary calculations of some Novette target designs indicate that we can achieve implosion of D–T fuel to about 200 to 400 times liquid density. With adequate funding of target fabrication and implosion diagnostics, we anticipate that these compressions will be achieved in a year or two after the Novette facility becomes fully operational.

In 1981, an extensive series of Argus experiments on wavelength scaling was designed and analyzed. These experiments, using light of wavelengths 1.06, 0.53, and 0.35 μm, provide further confirmation of our predictions of excellent laser–plasma coupling at short wavelengths. Preliminary plans were made for Novette experiments to test the coupling of intense laser light with larger-scale-length underdense plasmas. In this planning, we have given a high priority to experiments in which the underdense plasma conditions are diagnosed. This will be an important test of our theoretical models.

These high-density and plasma-scaling Novette experiments are a precursor to Nova scientific-feasibility experiments. In these Nova experiments, we plan to implode scaled-down versions of our single- and double-shell reactor targets to the same fuel densities as in the reactor-scale target designs. We will then diagnose the central hot spot by neutron and x-ray imaging and spectra, and we will diagnose the main fuel density and mix by backlighting and self-emission. The implosion dynamics (including preheat, fluid instabilities, and symmetry) will be diagnosed by observing the inner surfaces of the imploding shells. Finally, we will diagnose laser–plasma coupling at plasma scale lengths relevant to multimegajoule drivers.

We are pursuing both single- and double-shell capsule designs. However, we have decided to focus most of our resources on single-shell capsules and carry the double-shell capsule as a backup. This choice has been driven by a number of considerations. Although the double-shell design has a higher estimated gain than the single-shell design above 4- to 5-MJ driver energy, there are serious uncertainties associated with unstable mixing of the high-Z shell with both the igniter and the main fuel. This higher double-shell gain estimate assumes that the single-shell target ignition and burn efficiency will be degraded by the same factors as for the double-shell target. Since the single-shell target has no high-Z

shell, this assumption is probably biased against the single shell, so that its gain is underestimated. In addition, the threshold for ignition of the double-shell outer fuel occurs at an uncomfortably large driver energy (above 3 MJ). If we move beyond this threshold by a factor of 2 to be conservative, then the driver cost is excessive. In addition, the threshold energy and the gain in the vicinity of the threshold cannot be validated except by doing experiments at the threshold. Finally, current funding levels are not adequate to ensure the timely fabrication of the double-shell capsules.

Both the single- and double-shell designs fail to achieve their performance potential because of premature central ignition. We are exploring target designs with potentially higher gain at lower driver energy.

A number of important improvements were made to LASNEX. These include improved treatment of the transport of suprathermal electrons and x rays.

Our studies of ion-beam-driven targets have provided a clear outline of the parameter space for effective driving of ion-beam reactor targets. They bring to a sharp focus the preference for multigap (e.g., induction) accelerators as drivers for fusion reactors. On the other hand, single-gap diode accelerators have the advantage for ignition experiments at relatively low cost.

We are continuing to pursue both hohlraum and directly driven targets. For reactor-size targets, the hohlraum approach has a significant advantage. To catch up, the laser-driven direct approach must demonstrate very efficient absorption without generation of significant hot electrons, must achieve ablation efficiencies as high as those of short-wavelength lasers, and must attain ultrasmooth illumination uniformities (~1%).

Our estimates of fusion-reactor driver requirements and our calculated target-gain curves are essentially unchanged from previous years (Fig. 3-1). We expect to achieve the best-estimate levels initially with our single- and double-shell target designs and then to follow a learning curve leading to the more optimistic levels with advanced target concepts. The best estimate in Fig. 3-1, which is based on realistic assumptions about implosion instabilities and thermonuclear ignition and burn, assumes efficient beam–target coupling with either ion beams or short-wavelength lasers.

Fig. 3-1.

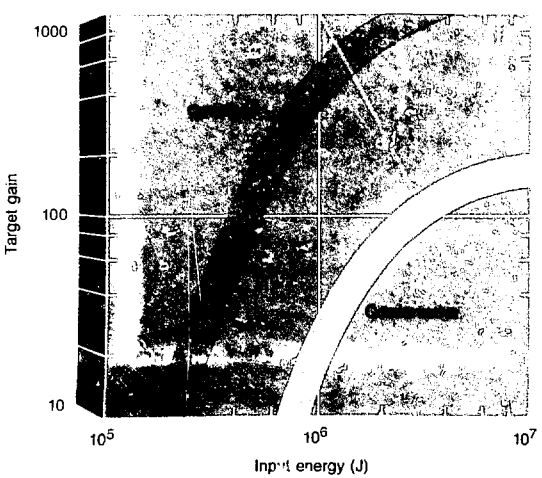

In the following articles, we report our progress in 1981 in four areas: laser targets, ion-beam targets, plasma physics, and atomic theory. Our work in the design and interpretation of experiments, which constitutes a very sizable fraction of our efforts, is reported in Section 6, "Laser-Fusion Experiments and Analysis."

Laser Targets

Introduction

Symmetry requirements have a large impact on the wavelength scaling of directly driven ICF implosions. If the requirement for

smoothing a given fractional intensity perturbation, $\delta I/I$, to tolerable levels is satisfied for a given value of r_c/r_a (where r_c = radius of critical surface and r_a = radius of ablation surface), then we must compare the implosion efficiency for various wavelengths under this constraint. We call the distance between the critical-density surface and the ablation surface the standoff distance. For a fixed value of r_c/r_a, the peak implosion efficiency is independent of wavelength. The efficiency also drops markedly as r_c/r_a is increased. Long wavelengths (at least 2 μm) have the required standoff distance at low intensity and are useful for setting the initial implosion adiabat. However, the standoff distance at higher intensities is large and results in poor implosion efficiency. Short wavelengths have the required standoff at high intensity, and are useful at the end of an implosion, but have virtually no conduction smoothing effect at the low-power beginning of an implosion. Hence, direct implosions with intensity variations $\delta I/I \gtrsim 0.1$ must start with light of about 2-μm wavelength and successively shift to shorter wavelengths, ending with $\lambda \lesssim 0.5$ μm. If short-wavelength lasers are used, irradiation uniformities with $\delta I/I \lesssim 0.01$ must be developed.

We have developed a planar electron-conduction ablation model applicable to flows with inhibited electron conduction. This model joins a steady-state solution for densities greater than the critical density to an isothermal expansion for densities less than critical. At the critical density, we allow for a discontinuity in density and temperature, a feature required when the conduction is inhibited. We also estimate the effects on implosion efficiency of an accelerating reference frame. Here, we find that the efficiency is strongly reduced when the ablated mass between the critical density and the ablation surface is comparable to the unablated mass. Physically, this happens because the ablated mass between the critical density and the ablation surface must be accelerated to nearly the velocity of the unablated material, but the former mass adds nothing to the payload energy.

Author: J. D. Lindl

Planar Laser-Driven Ablation: Effect of Inhibited Electron Thermal Conduction

Introduction. Many of the experiments to date that have studied the details of laser-driven ablation[1] have used planar geometry[2] because of practical advantages, such as ease of diagnostic access and experimental design. We present a theory describing the structure and global properties of planar laser-driven ablation as a function of the laser intensity and wavelength, the target material, and the degree of inhibition of electron thermal conduction.[3] We compare our predictions with other models[4-7] and with the results of a computer hydrodynamics code.[8]

Basic Equations and Assumptions. We introduce the following assumptions

- We consider situations where the fluid flow in the conduction zone has reached a steady state. In contrast, the underdense plasma cannot be in a steady state in planar geometry because it is expanding into a vacuum. We shall thus join together steady-state solution inside the critical surface with a time-dependent rarefaction wave in the corona.[3,5,6]
- We consider laser and target parameters such that laser-light absorption occurs at or near the critical-density surface and such that the absorbed energy is deposited primarily in the thermal-electron population.
- We assume for simplicity that the electron and ion temperatures are equal.
- We assume that the underdense plasma ($n_e < n_c \equiv m_e \omega_l^2/4\pi e^2$) is isothermal.

The basic equations describing the plasma flow in plane geometry are

$$\frac{\partial}{\partial x}(\rho v) = 0 \quad , \tag{1}$$

$$-\frac{\partial}{\partial x}(p + \rho v^2) + \rho G = 0 \quad , \tag{2}$$

and

$$-\frac{\partial}{\partial x}\left[\rho v\left(\frac{5}{2}\frac{p}{\rho} + \frac{v^2}{2}\right) + q\right] + \rho v G + I_a \delta(x - x_c) = 0 \quad . \tag{3}$$

Here, ρ and v are the mass density and velocity, respectively, p is the pressure, and x_c is the position of the critical-density surface. In Eq. (2), the momentum equation, ρG, is the inertial force due to ablative acceleration of the target. We begin by solving Eqs. (1) through (3) without inertial effects ($G = 0$); these effects will be studied later.

The pressure, p, is defined by

$$p = n_e k T_e + n_i k T_i = \rho \left(\frac{Z+1}{A m_p} \right) kT = \rho c^2 \quad , \tag{4}$$

where $c \equiv (p/\rho)^{1/2}$ is the isothermal sound speed, and the mean charge and mass of the ions are Ze and Am_p, respectively.

The heat flux, q, is taken to be the minimum of the classical value (Ref. 9) $-\kappa dT/dx$ and a phenomenological form representing inhibited heat flow[10]

$$q = \min \begin{cases} -K_0 T^{5/2}\, dT/dx \\ -5\, \phi\, \rho c^3 \dfrac{dT/dx}{|dT/dx|} \end{cases} \quad . \tag{5}$$

In this expression, (Ref. 9) T is the electron temperature and

$$K_0 T^{5/2} \cong 1.1 \times 10^{-11} \times \left(\frac{T}{1\ K} \right)^{5/2} \frac{W}{mK} \tag{6}$$

for $Z = 3.5$ and the Coulomb logarithm $\ln \Lambda = 10$. The quantities ϵ and δ_T depend on Z and are evaluated in Ref. 9.

The flux limit, ϕ, has been expressed here in terms of hydrodynamic variables. In terms of the more usual definition of the flux-limited heat flow $f n_e m_e (kT_e/m_e)^{3/2}$, Eq. (5) implies that

$$f = 0.12\, \phi \left[\frac{(Z+1)^{3/2}}{Z A^{1/2}} \right] \quad . \tag{7}$$

For $Z \gg 1$ and $A \cong 2Z$, this expression becomes $f \cong 0.08\, \phi$.

Solution in the Underdense Plasma. In the isothermal approximation, the energy equation [Eq. (3)] is replaced by the simple hypothesis that the temperature, T, is constant. Numerous authors have studied the plasma flow under these conditions.[11-16]

There exist self-similar solutions to Eqs. (1) and (2) with the property that the flow is sonic in a reference frame moving with a point of constant density. In particular, the critical-density point at position x_c fulfills this condition

$$v(x) = c + (x - x_c)/t \quad , \tag{8}$$

$$\rho(x) = \rho_c \exp\{(x_c - x)/ct\} \quad . \tag{9}$$

Thus, $v(x_c) = c$.

The flow cannot remain isothermal unless there is sufficient outward heat flow to feed the increase in kinetic energy with x. This required heat flux is[15]

$$q = \rho_c c^3 \quad . \tag{10}$$

Jump Conditions at the Critical-Density Surface. We introduce the notation $[y] \equiv y(x_c + x) - y(x_c - x) \equiv y_2 - y_1$, where the indices 1 and 2 refer to the overdense and underdense sides of x_c, respectively. Equations (1) through (3) may be integrated from one side of x_c to the other

$$[\rho v] = 0 \quad , \tag{11}$$

$$[\rho v^2 + \rho c^2] = 0 \quad , \tag{12}$$

$$\dot{m} \left[\frac{v^2}{2} + \frac{5c^2}{2} \right] + [q] = I_a \quad . \tag{13}$$

In contrast with previous calculations,[7,17-20] here we specifically allow a temperature jump

$$\alpha \equiv \left(\frac{c_1}{c_2} \right) = \left(\frac{T_1}{T_2} \right)^{1/2} \quad ; \tag{14}$$

here, in general, $\alpha \neq 1$.

For a broad range of physical conditions the underdense plasma is nearly isothermal. The Mach number $M \equiv v/c$ on the low-density side of the critical surface is then given by Eq. (8), $M_2 = 1$. Consequently, Eqs. (11) and (12) give a relation between M_1 and α

$$M_1 = \alpha^{-1} \left[1 - (1 - \alpha^2)^{1/2} \right] \quad . \tag{15}$$

The density ratio ρ_1/ρ_2 is $(\alpha M_1)^{-1}$. Thus, once M_1 is known, Eq. (15) gives a unique

value for the density and temperature ratio across the critical surface.

Solutions for the Flow in the Conduction Region. Bobin,[4] Takabe et al.,[5] and Manheimer et al.[6] have studied this region in the limit of classical thermal conduction. We begin by reviewing their results. We then derive new solutions that apply when flux-limited thermal conduction is important.

The steady-state energy equation [Eq. (3)] can be integrated for $x < x_c$

$$\dot{m}\left(\frac{5}{2}c^2 + \frac{1}{2}v^2\right) + q = A = \text{constant} \quad . \tag{16}$$

The constant A represents the difference between the outward flux of kinetic energy and enthalpy, and the inward heat flow. It may be evaluated at the cold side of the ablation front, where we shall assume there is negligible preheat. Under these conditions $A = 0$.

In the case of non-flux-limited flow, Eq. (16) with $A = 0$ becomes

$$\dot{m}\left(\frac{5}{2}c^2 + \frac{1}{2}v^2\right) - K_0 T^{5/2}\frac{dT}{dx} = 0 \quad . \tag{17}$$

Let us assume that the conduction region contains a sonic point characterized by a velocity v_0 (= c_0). Then, the integrals of Eqs. (1) and (2) imply that the flow has maximum temperature at the sonic point. On the other hand, the sonic point must also be contained in the isothermal corona, where it corresponds to a constant-density surface. Physically these two requirements can be made consistent if we take the critical-surface boundary between the two zones to occur exactly at the sonic point.[4-6] This result is verified by our numerical simulations. Furthermore, it satisfies the jump conditions established above with $M_1 = M_2 = \alpha = 1$.

Under these conditions, Eq. (13) becomes

$$I_a = [q] = q_2 - q_1 \quad . \tag{18}$$

For an isothermal corona, $q_2 = \rho_c c_0^3$. The inward heat flux, q_1, may be found from Eq. (17) to be $q_1 = -3\rho_c c_0^3$. Equation (18) gives us the relation between the intensity and the sound speed at the critical-density surface

$$I_a = 4\rho_c c_0^3 \quad . \tag{19}$$

Recalling Eq. (10), this implies that 25% of the absorbed laser flux is used to keep the corona isothermal. The remaining 75% is used to ablate the cold material.

We are now in a position to determine macroscopic characteristics of the flow, such as the ablation pressure, p_a, and ablation rate, $\dot{m}$. From Eqs. (1) and (2) we have

$$p_a \cong 12\ \text{Mbar}\left(\frac{I_a}{10^{14}\ \text{W/cm}^2}\right)^{2/3} \times \left(\frac{1\ \mu\text{m}}{\lambda_L}\right)^{2/3}\left(\frac{A}{2Z}\right)^{1/3} \quad , \tag{20}$$

$$\dot{m} \cong 150\frac{\text{kg}}{\text{cm}^2\,\text{s}}\left(\frac{I_a}{10^{14}\ \text{W/cm}^2}\right)^{1/3} \times \left(\frac{1\ \mu\text{m}}{\lambda_L}\right)^{4/3}\left(\frac{A}{2Z}\right)^{2/3} \quad , \tag{21}$$

and

$$T_e(x > x_c) \cong 2.7\ \text{keV}\left(\frac{I_a}{10^{14}\ \text{W/cm}^2}\right)^{2/3} \times \left(\frac{\lambda_L}{1\ \mu\text{m}}\right)^{4/3}\left(\frac{A}{2Z}\right)^{1/3},\ Z = 3.5 \quad . \tag{22}$$

The length of the conduction zone between $x = 0$ ($T = 0$) and $x = x_c$ ($T = T_0$) can be established by integrating Eq. (17) numerically

$$x_c = 0.15\left(\frac{K_0 T_0^2}{\rho_c}\right)\left(\frac{Am_p}{k(Z+1)}\right)^{3/2} \quad . \tag{23}$$

The quantity of matter between $x = 0$ and x_c is important in the interpretation of some current experiments on planar laser-driven ablation.[2,21] We define the thickness, e_0, as the equivalent thickness of matter between $x = 0$ and x_c if it were at the solid density ρ_s

$$e_0 \simeq 11\ \mu\text{m}\left(\frac{I_a}{10^{14}\ \text{W/cm}^2}\right)^{4/3}\left(\frac{\lambda_L}{1\ \mu\text{m}}\right)^{8/3} \times\left(\frac{1\ \text{g/cm}^3}{\rho_s}\right)\left(\frac{A}{2Z}\right)^{13/6}, \quad (24)$$

where we have used Eqs. (19) and (23), with $Z = 3.5$. Note the very strong dependence on laser wavelength.

When considering flow in the flux-limited regime, the maximum inward classical heat flux occurs at the critical surface and is equal to $3\rho_c c_0^3$. Thus, the critical surface is the place where the flux limitation in Eq. (5) should first become important. The condition for flux-limited heat flow at the critical surface is $3\rho_c c_0^3 > 5\ \phi\rho_c c_0^3$, or $\phi > 0.6$.

In the zone where the heat flux is limited according to Eq. (5), the energy equation [Eq. (16)] yields[7,22,23]

$$M(5 + M^2) = 10\phi \quad (25)$$

This equation shows that the Mach number is constant throughout any region where the heat flux is flux-limited. Solutions of Eq. (25) are shown in Fig. 3-2.

In a steady planar flow, a constant Mach number has very dramatic consequences: from Eqs. (1) and (2), if M = constant, *all* physical quantities describing the flow (ρ, v, T) must be constant in space. To avoid this unphysical situation, we introduce a discontinuity at the point in the flow where the local Mach number first reaches the value given in Eq. (25). At this point, the density will drop sharply from $\rho_1 > \rho_c$ to $\rho_2 < \rho_c$, so the laser-energy deposition occurs at the discontinuity.

This discontinuity must satisfy the jump conditions of Eqs. (11) through (13), with M_1, the Mach number just inside the critical surface, given by the solution of Eq. (25). We saw in the discussion of jump conditions at the critical-density surface that the temperature jump $\alpha \equiv c_1/c_2$ depends only on M_1. Thus, α is only a function of the flux limit ϕ and is shown in Fig. 3-2, $\alpha = 2M_1(1 + M_1^2)^{-1}$. The density ratio, ρ_1/ρ_2, is also a function only of the flux limit, ϕ.

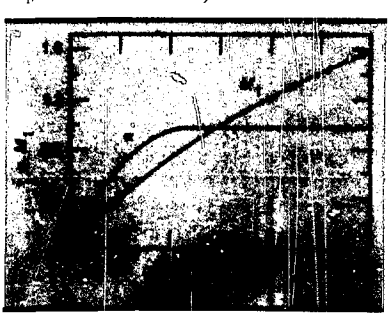

Fig. 3-2. Dependence of Mach number M_1 and temperature ratio $\alpha = (T_1/T_2)^{1/2}$ on flux limit, ϕ.

As is common in hydrodynamic descriptions of discontinuities, purely macroscopic equations are insufficient to fully determine all the characteristics of the discontinuity. In the absence of a detailed microscopic description, it is nevertheless possible to solve for ρ_2/ρ_c by hypothesizing a relation between ρ_2 and the flux limit ϕ, $(\rho_2/\rho_c) = (\phi/0.6)$, $\phi \leq 0.6$. Then, Eqs. (11) and (13) yield

$$\frac{I_a}{4\rho_c c_2^3} = \begin{cases}\left(\dfrac{\phi}{0.6}\right), & \phi < 0.6 \\ 1, & \phi \geq 0.6\end{cases} \quad (26)$$

Our numerical simulations show that Eq. (26) is verified when the laser energy in the computer code is deposited in the last Lagrangian zone having a density less than the critical density.

Using Eq. (26), we can now calculate the different parameters characterizing the flow for $\phi < 0.6$. The temperature of the isothermal corona is given by $(\phi/0.6)^{-2/3}$ times the result of Eq. (22). This indicates that, when the flux limit, ϕ, is less than 0.6, the coronal temperature, T_2, increases monotonically as ϕ decreases. This is a result of the temperature jump at the critical surface. Figure 3-3 shows the dependence of T_1 and T_2 on the flux limit, ϕ.

The mass flux is given by $(\phi/0.6)^{2/3}$ times the result of Eq. (21). The ablation pressure is equal to $(\phi/0.6)^{1/3}$ times the result of Eq. (20). Both $\dot{m}$ and p_a decrease as ϕ decreases.

Rocket Effect and Hydrodynamic Efficiency. Until now, we have implicitly assumed that the solid target was thick and very massive. In the case of thin targets, the ablation pressure results in the acceleration and motion of the high-density part of the target. We begin by assuming that the expressions for p_a and $\dot{m}$ derived earlier remain valid even when the target is thin enough to be set in motion by the laser heating. Later, we discuss the effect of acceleration on these solutions.

Consider a target with initial mass per unit area, m_0, irradiated by a laser pulse of constant absorbed intensity, I_a. The momentum equation for the target describes the velocity, $v(t)$, of the unablated dense material, $m(t)dv/dt = p_a$, with $m(t) = m_0 - \dot{m}t$. The solution is the well-known rocket equation

$$v(t) = \left(\frac{p_a}{\dot{m}}\right) \ln\left(\frac{m_0}{m(t)}\right) \quad . \tag{27}$$

The hydrodynamic efficiency, η, is the ratio of the target's kinetic energy, $(1/2)\, m(t)\, v^2(t)$, to the laser energy, $I_a t$, absorbed in the time t. The efficiency is

$$\eta = \frac{\frac{1}{2}\, m(t)\, v^2(t)}{I_a t} = \eta_0 \left(\frac{x \ln^2 x}{1 - x}\right) \quad , \tag{28}$$

$$\eta_0 \equiv \frac{p_a^2}{2 I_a \dot{m}}, \; x \equiv \frac{m(t)}{m_0} \quad . \tag{29}$$

Thus, η depends both on the fraction of the target mass ablated (via x) and on the details of the ablation model (via η_0). The efficiency, η, reaches a maximum as a function of x when $x \equiv m(t)/m_0 = 0.2$, $\eta_{max} = 0.65\, \eta_0$, and 80% of the initial target mass has been ablated.

The quantity η_0 defined in Eq. (29) can be evaluated using the model for planar ablation derived previously in this article; we obtain $\eta_0 = 1/2$ for all ϕ.

Thus, the maximum efficiency obtainable in planar ablation is

$$\eta_{max} = \frac{0.65}{2} = 0.32 \quad . \tag{30}$$

The efficiencies found here are a factor of 2 smaller than those frequently quoted in the literature, which are obtained using the cold-rocket model.[24,25] Our factor $\eta_0 = 1/2$ represents the additional energy used to heat the corona and conduction zone.[3] It is interesting that the factor $\eta_0 = 1/2$ caused by thermal effects is independent of the size of the flux limit and laser intensity.

Comparison with Numerical Simulations. We have used the Lagrangian hydrodynamics code FILM, developed by Virmont,[8] to check the validity of the principal results in our theoretical model and to evaluate the range of applicability of our initial approximations.

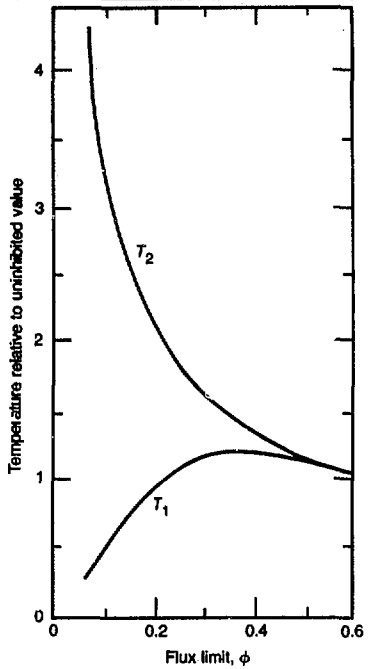

Fig. 3-3. Dependence on flux limit, ϕ, of temperatures on either side of critical surface.

Details of the algorithms and physics used in FILM may be found in Ref. 8. It is a one-dimensional Lagrangian hydrodynamics code and was used here in plane geometry with a perfect-gas equation of state. We used a constant-intensity laser pulse having a long-enough pulse length to produce steady-state conditions. The laser energy was deposited at the critical surface.

According to our model, when the flux limit, ϕ, is greater than 0.6, the flow at the critical surface is sonic and continuous. For $\phi < 0.6$, a discontinuity appears. The Mach number M_1 on the high-density side of the discontinuity satisfies $M_1(5 + M_1^2) = 10\, \phi$, while on the low-density side, the Mach number $M_2 = 1$. In our simulations, this discontinuity extends over two or three Lagrangian cells, independently of the initial zoning of the target.

Figure 3-4 represents the variation of M_1 and M_2 with ϕ. Simulation parameters were $I_a = 10^{13}$ W/cm^2, $\lambda_L = 1.06\, \mu$m; target material was a plastic, CH ($A = 6.5$, $Z = 3.5$, initial density $\rho_s = 1$ g/cm^3). We see that there is excellent agreement of M_1 with the

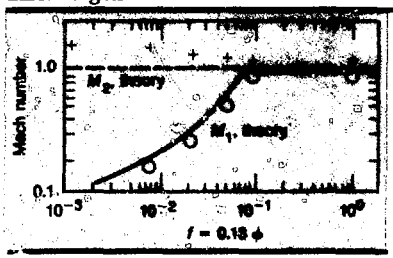

Fig. 3-4. Variation of Mach numbers M_1 and M_2 with flux limit f, where $f = 0.13\phi$; lines represent theory, symbols represent simulations.

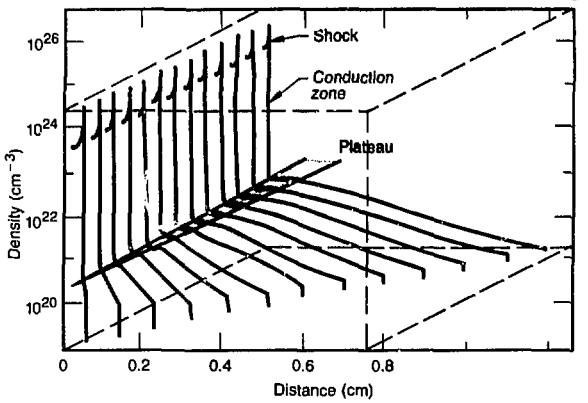

Fig. 3-5. Time sequence of density profiles from computer hydrodynamics simulation showing evolution of density plateau below critical surface when $\phi < 0.6$.

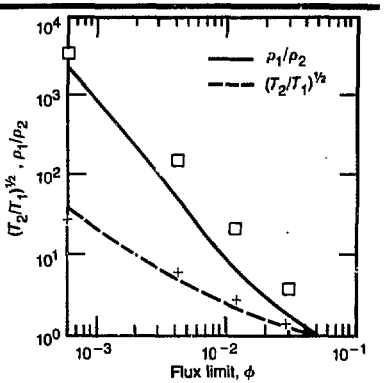

Fig. 3-6. Comparison of predicted density and temperature ratios across critical surface with computer-simulation results.

prediction of Eq. (25). In contrast, the behavior of M_2 is not exactly as predicted. Figure 3-4 shows that M_2 slowly increases above the predicted value $M_2 = 1$ as ϕ decreases, finally reaching the value $M_2 \sim 2$ at small ϕ. The behavior of M_2 is not sensitive to the initial zoning or to the numerical details of energy deposition at the critical layer.

The fact that M_2 is slightly larger than 1 for small ϕ has an interesting consequence in our simulations. A flat density plateau appears just outside the critical layer, in which the density (= ρ_2), temperature, and velocity are constant in space. The length of the plateau increases in time for the following reasons. Since $M_2 > 1$, the plateau is fed on the left by fluid entering at a speed $v_2 = M_2 c_2$. On the right of the plateau, there is a self-similar isothermal expansion wave that eats into the plateau at a speed given by c_2. The plateau length that results from these two processes thus follows the law $l_p = (M_2 - 1)\, c_2 t$. Figure 3-5 shows an example of such a density plateau in our hydrodynamics simulations. Parameters of the FILM calculation were $I_a = 10^{13}$ W/cm^2, $\lambda_L = 1.06\ \mu$m, flux limit $f = 0.012$; target material was CH.

Next, we compare the hydrodynamic simulations with our theory describing the density discontinuity at the critical layer. Figure 3-6 illustrates the theoretical and numerical results for the ratios ρ_2/ρ_1 and T_2/T_1 of density and temperature across the discontinuity. Solid line (theory) and squares (simulation) represent ρ_1/ρ_2; dotted line (theory) and crosses (simulation) represent T_2/T_1. Laser and target parameters were $I_a = 10^{13}$ W/cm^2, $\lambda_L = 1.06\ \mu$m; target material was CH. There is excellent agreement between the model and theory.

The density ratio, ρ_2/ρ_c, is strongly influenced by the method chosen to deposit the laser energy. When the absorbed laser energy is deposited in the last underdense zone, we obtain the excellent agreement shown in Fig. 3-7 between our model and numerical-simulation results for the coronal temperature, T_2 and the mass flux, $\dot{m}$. To obtain this figure, all the absorbed laser energy was deposited in the highest-density zone satisfying $\rho > \rho_c$. Laser parameters were $I_a = 10^{13}$ W/cm^3 and $\lambda_L = 1.06\ \mu$m; target material was CH.

Figure 3-8 shows the maximum hydrodynamic efficiency as a function of the laser wavelength. Points represent FILM simulations with $I_a = 10^{13}$ W/cm^2, CH target material, and flux limit $\phi > 0.6$. At laser wavelengths of 1, 1/2, 1/4, and 1/6 times the wavelength of a Nd:glass laser ($\lambda_L = 1.06\ \mu$m), the initial thicknesses, L, of the solid material were 5, 8, 20, and 15 μm, respectively. The solid curve represents theory corrected for inertial effects, as described in Eq. (34). The limit of 32% predicted by Eq. (30) for an isothermal corona is attained when $\lambda_L = 0.53\ \mu$m. For

shorter-wavelength lasers, the slight increase in η_{max} above the value of 32% seems to be because the corona becomes less isothermal. In the extreme limit of no outward heat flow, the theoretical maximum efficiency is 41%.

On the other hand, when the laser wavelength $\lambda_L \sim 1\ \mu m$, the inertial forces in the accelerated frame of the target are no longer negligible. The result is a decrease in the hydrodynamic efficiency. We discuss the role of inertial forces next.

When the inertial force is included, integration of the steady-state momentum equation from the ablation front to just outside the critical surface gives the following expression for the ablation pressure

$$p_a = p_2 + p_2 v_2^2 - G \int_{x_a}^{x_c} \rho(x)dx \quad . \tag{31}$$

Here, p_2, ρ_2, and v_2 are the pressure, density, and velocity, respectively, at the low-density side of the critical surface. The effect of acceleration is to diminish the ablation pressure by an amount

$$p_I = G \int_0^{x_c} \rho(x)dx = G\rho_s e_0 \quad . \tag{32}$$

Here, e_0 is the column density of the conduction zone at equivalent solid density ρ_s, calculated in Eq. (24).

To estimate the effect of the inertial pressure, p_I, we must determine self-consistently the acceleration, G. In the case of thin-target accelerations, the rocket model allows us to write

$$G = \frac{dv}{dt} = \frac{p_a}{m(t)} \quad . \tag{33}$$

Since the mass per unit area varies from m_0 to 0.2 m_0 (the optimum value of the hydrodynamic efficiency), we shall use a mean mass $\langle m(t) \rangle = 0.5\ m_0$. Thus, we have $G \simeq 2p_a/m_0$, and the expression for the inertial pressure becomes

$$p_I = G\,\rho_s e_0 \cong \frac{2p_a e_0}{L} \quad , \tag{34}$$

where we have defined L as the initial thickness of the solid target, $m_0 = L\rho_s$.

It is clear from Eq. (34) that the inertial pressure, p_I, can significantly reduce the ablation pressure, p_a, when the equivalent thickness, e_0, of the conduction zone at solid density becomes comparable with the initial thickness of the solid target, L. Equation (24) shows that $e_0 \propto \lambda_L^{8/3} I_a^{4/3}$. Thus, inertial effects on the ablation pressure should be smaller at low laser intensities and short-wavelength lasers. On the other hand, the decrease in hydrodynamic efficiency, η_{max}, shown in Fig. 3-8 for $\lambda_L = 1.06\ \mu m$, is due to the decrease in p_a caused by the inertial force at long laser wavelengths, since $\eta_{max} \propto p_a^2$. When the hydrodynamic efficiency is corrected using Eq. (34), excellent agreement is obtained between our theory and the computer simulations shown in Fig. 3-8.

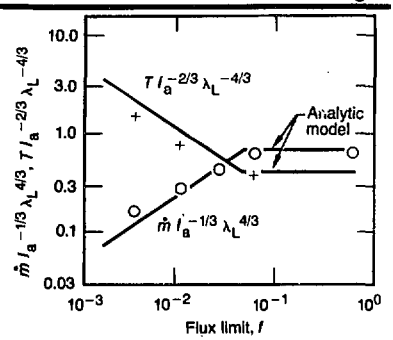

Fig. 3-7. Comparison of analytic model (solid lines) with computer-simulation results for coronal temperature, T (crosses), and mass-loss rate, $\dot{m}$ (circles), as function of flux limit, f.

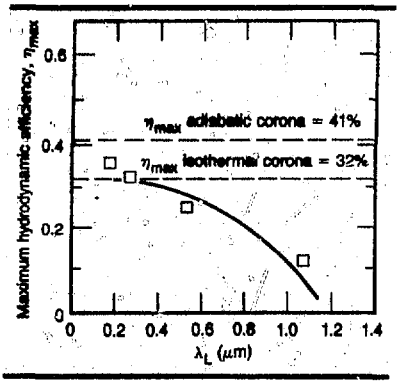

Fig. 3-8. Maximum hydrodynamic efficiency, η_{max}, as function of laser wavelength, λ_L.

Summary and Discussion. Within the assumption of localized laser-energy deposition into a thermal-electron population at the critical-density surface, we have derived a model for the spatial structure and global properties of planar laser-irradiated targets. Our model joins a steady-state region of conduction for $n_e > n_c$ to an isothermal rarefaction wave for $n_e < n_c$, with the isothermal sonic point located at the critical surface. We find in the flux-limited case ϕ

< 0.6 that a discontinuity develops at the critical-density surface, including a jump in the temperature as well as a jump in density and velocity.

Inhibited heat flow has the effect of decreasing the mass ablation rate, $\dot{m}$, and the ablation pressure, p_a. The maximum value of the hydrodynamic efficiency of target acceleration is independent of the flux limit in planar geometry, being equal to $\eta_{max} = 0.32$, independently of the laser wavelength and intensity.

The advantages of short-wavelength lasers are apparent in many different aspects of our model. Short-wavelength lasers produce higher ablation pressures and ablation rates for fixed values of the laser intensity. They also have beneficial effects on the hydrodynamic efficiency because the inertial effects caused by target acceleration are less detrimental when the laser wavelength is short.

We have not considered here the crucial issues of target symmetry and Rayleigh–Taylor instability. Initial calculations of symmetrization of inhomogeneities in the laser intensity[6,26,27] show that longer-wavelength lasers are definitely preferable for this task. This apparent disadvantage of short-wavelength lasers must be weighed in the eventual choice of an optimum wavelength for fusion applications.

Authors: C. E. Max, R. Fabbro, and E. Fabre

Effect of Symmetry Requirements on the Wavelength Scaling of Directly Driven Laser-Fusion Implosions

During the past two years, abundant evidence has accumulated concerning the beneficial effects of shorter-wavelength lasers on laser–plasma interaction processes.[28,29] The present work addresses the related question of how implosion symmetry and hydrodynamic efficiency scale with laser wavelength.[30] Our results emphasize that, for directly driven laser-fusion implosions, much of the advantage of short-wavelength laser light for implosion physics and target coupling may be dissipated if we attempt to use laser and target parameters producing good symmetrization by a hot atmosphere. We discuss some approaches to avoiding this dilemma.

Implosion Symmetry. For a situation where many laser beams irradiate a spherical target, there will inevitably be some degree of nonuniformity in the distribution of absorbed laser energy. Such an impressed nonuniformity can lead to degraded target performance, particularly for shell targets with high convergence ratios.

Several years ago, Thiessen and Nuckolls[31] and Mead and Lindl[32] explored the circumstances under which laser-illumination nonuniformities can be smoothed by heat conduction in a hot atmosphere surrounding the dense target. For spherical targets, they found that an imposed nonuniformity of 10% could be tolerated if the critical radius, r_c, were larger than roughly twice the ablation radius, R_a, during the first part of the implosion.

A second requirement for conduction smoothing[31,32] is that the atmosphere must be hot enough for the thermal-conduction time[33] to be small compared with the sonic-transit time. For a target with $Z = 10$ and $A = 20$, this requirement becomes

$$T(r_c) >> T_{min} = 4.8\left(\frac{L}{1\ \text{cm}}\right)^{1/2} \times \left(\frac{1\ \mu\text{m}}{\lambda_L}\right)\text{keV} \quad . \qquad (35)$$

Here, L is the size of the atmosphere, λ_L is the laser wavelength, and $T(r_c)$ is the temperature at the critical surface.

A third condition for symmetrization is that the initial strength of the shock sent into the dense material be less than 1 to 2 Mbar. This is necessary to achieve a low isentrope appropriate to high-gain implosions. It was found in Ref. 32 that the initial shock pressure increases strongly as the laser wavelength used for atmosphere formation is decreased.

With the above smoothing conditions in mind, we can use the simple spherical steady-ablation model of Ref. 34 to ask about the wavelength scaling of symmetrization by a hot atmosphere. (This model does not apply either where profile steepening and hot electrons dominate coronal behavior or to strongly accelerated targets. It does not include energy losses caused by x-ray radiation. Reference 34 gives an extensive discussion of the conditions under

which this model is valid.) Reference 34 predicts the radius and temperature of the critical surface as

$$\frac{r_c}{R_a} \simeq 1.3\left(\frac{I_P}{10^{14}\ \mathrm{W/cm^2}}\right)^{0.11}\left(\frac{\lambda_L}{1\ \mu\mathrm{m}}\right)^{0.38} \times \left(\frac{0.1\ \mathrm{cm}}{R_a}\right)^{0.08} \quad (36)$$

$$\frac{T_c}{1\ \mathrm{keV}} \simeq 2.2\left(\frac{I_P}{10^{14}\ \mathrm{W/cm^2}}\right)^{0.52}\left(\frac{\lambda_L}{1\ \mu\mathrm{m}}\right)^{0.83} \times \left(\frac{R_a}{0.1\ \mathrm{cm}}\right)^{0.11} \quad (37)$$

Here, R_a is the ablation radius, the surface of the cold, dense pellet. The quantity I_P is the absorbed laser power divided by $4\pi R_a^2$. The absorbed intensity at the critical surface is $I_P(R_a/r_c)^2 \equiv I_c$. We call I_P the pellet intensity.

The above expressions for r_c/R_a and T_c were derived for irradiation conditions where the heat flow, q, is flux-limited at the critical surface, assuming that

$$q = \min\begin{cases} -\kappa \nabla T_e \\ -fn\, e^{m_e(kT_e/m_e)^{3/2}} \nabla T_e/(\nabla T_e) \end{cases}, \quad (38)$$

where κ is the classical thermal conductivity.[33] In Eqs. (36) and (37), the flux-limit value was $f = 0.03$ for $Z = 10$, $A = 20$.

The first criterion for effective smoothing is that $r_c/R_a > 1.5$ to 2. Consider, for example, a target with ablation radius $R_a = 0.1$ cm, $Z = 10$, $A = 20$, and a fixed pellet intensity $I_P = 10^{14}$ W/cm^2. Then, Fig. 3-9(a) shows the ratio of the critical and ablation radii, r_c/R_a, as a function of laser wavelength, λ_L [(Eq. (36)]. For this intensity we need a laser wavelength $\lambda_L \geq 1.5$ to 3 μm to be in the desired smoothing regime $r_c \geq 1.5$ to 2 R_a. Reference 30 reached a similar conclusion for planar targets.

The second criterion for good smoothing is that the temperature at the critical surface, given by Eq. (37), be large compared with the minimum temperature, T_{min}, in Eq. (35). Figure 3-9(b) shows that, for $\lambda_L > 1$ μm, the coronal temperature, T_c, predicted by the model in Ref. 34 is indeed large compared with T_{min}. Here, T_{min} is calculated using the self-consistent atmosphere size $L = r_c - R_a$, and other conditions are as in Fig. 3-9(a).

Both Fabre[35] and Thiessen and Nuckolls[31] have noted that symmetry requirements might be relaxed if we used higher laser intensities and smaller-radius targets when using lasers of shorter wavelengths. Let us ask how fast the intensity must be increased at short λ_L to keep r_c/R_a constant when λ_L is decreased. In all these wavelength-scaling discussions, there is a somewhat arbitrary choice of what to hold constant as λ_L varies. Let us assume that the laser energy is kept constant and that the required pulse length is approximately proportional to the target radius, R_a. If we now require that r_c/R_a in Eq. (36) remain at a constant value as the laser wavelength is decreased, we find that the pellet intensity must be scaled as

$$I_P \propto \lambda_L^{-2.7} \quad (39)$$

in this scheme. The required increase in pellet intensity when short-wavelength lasers are used is illustrated in curve (a) of Fig. 3-10, where we assumed $Z = 10$, $A = 20$, $f = 0.03$, and $R_a = 0.13$ cm at $\lambda_L = 1$ μm. From Eq. (37), the temperature at the critical surface will increase as λ_L gets shorter: $T_c \propto \lambda_L^{-0.5}$. The target size must be decreased according to $R_a \propto \lambda_L^{0.9}$ and the absorbed laser power $P_{abs} \propto \lambda_L^{-0.9}$.

By decreasing target size when we use shorter-wavelength lasers, we can thus counteract the wavelength dependence of the critical-surface standoff distance, and we can cause the coronal temperature to increase rather than decrease at shorter wave-

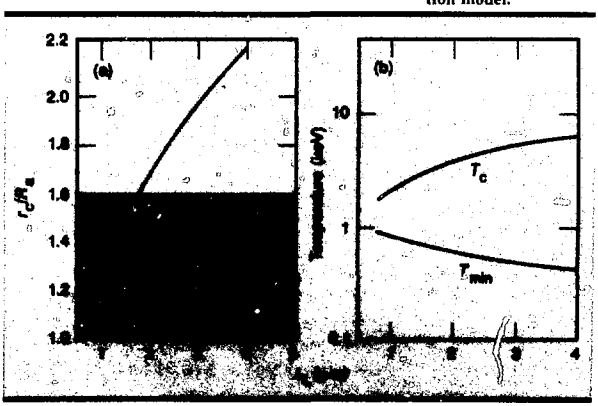

Fig. 3-9. Wavelength-scaling predictions of simple spherical ablation model.[34]

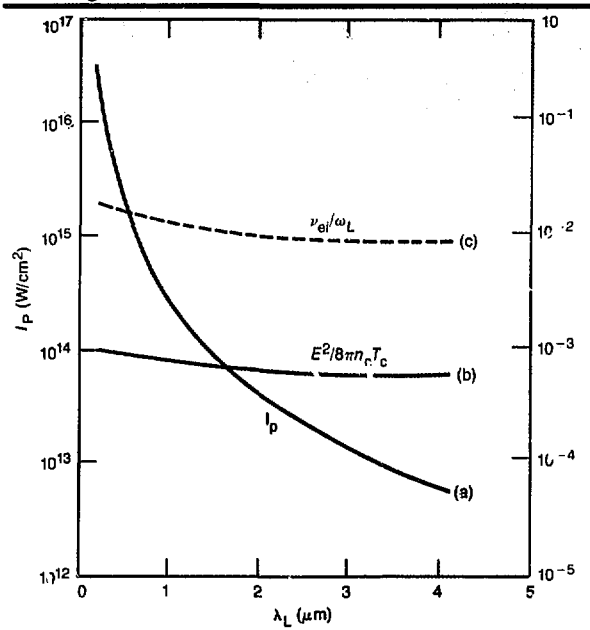

Fig. 3-10. (a)(Scale on left) pellet intensity I_p required to maintain $r_c/R_A = 1.5$; (b), (c) (scale on right) resulting values of collision frequency and electric-field energy density at critical surface.

lengths. These are both beneficial effects for symmetrization. Curves (b) and (c) of Fig. 3-10 show the consequent scaling of the plasma-coupling parameters $E^2/8\pi n_c T_c$ and ν_{ei}/ω_L, where ν_{ei} is the electron–ion collision frequency, and E is the laser electric field at the critical surface.

Hydrodynamic Efficiency. By implosion or hydrodynamic efficiency we mean the inward kinetic energy of the imploding target relative to the total absorbed laser energy. In spherical geometry, including the effects of the full temperature, density, and velocity profiles, the velocity is described by a rocket equation analogous to the usual planar result

$$\overline{v}(t) = V_{ex} \ln\left[\frac{m(t)}{m_0}\right] ,$$

$$V_{ex} = \frac{4\pi R_0^2 p_0}{\dot{m}_0} . \qquad (40)$$

Here, R_0 is the initial target radius, and p_0 and m_0 are the initial values of ablation pressure, p_a, and mass-ablation rate, $\dot{m}$. These may be evaluated using the expressions developed in Ref. 34 for a flux limit $f = 0.03$.

Equation (40) for the mean inward velocity of the shell can now be used to find the hydrodynamic efficiency, ϵ

$$\epsilon \equiv \frac{(1/2)m(t)\overline{v}^2}{P_{abs}\tau_L} = \left[\frac{2\pi R_0^2 p_0^2}{I_p m_0}\right]\left(\frac{x\ln^2 x}{1-x}\right) , \qquad (41)$$

where P_{abs} and I_p are the absorbed laser power and the pellet intensity, respectively, τ_L is the laser pulse length, and $x \equiv m(t)/m_0$ is the fraction of mass remaining in the shell after a time t.

The factor in parentheses in Eq. (41) optimizes for $x = 0.2$. We can obtain the wavelength scaling of the hydrodynamic efficiency, ϵ, by examining the factor in square brackets in Eq. (41). First consider the case where the pellet intensity and target size are held fixed and only the wavelength is varied. Using the results of Ref. 34 for p_a and $\dot{m}$ as a function of flux limit, f, and laser wavelength λ_L, it is straightforward to show that

$$\epsilon \propto \lambda_L^{-p} , \qquad (42)$$

where the exponent p varies from 1.2 to 0.5 as the flux limit, f, changes from 0.02 to 0.2. Figure 3-11 shows the exponent p as a function of f.

It is clear from Fig. 3-11 that, when the absorbed intensity and target size are held constant, the implosion efficiency increases strongly at short wavelengths. We shall show below that this is almost entirely because the critical surface lies closer to the ablation surface for shorter-wavelength lasers. The discussion of implosion symmetry earlier in this article indicates that the standoff distance, r_c/R_a, becomes smaller as λ_L is decreased. The symmetry results thus imply that, to achieve good implosion symmetry, we would require higher and higher degrees of laser-illumination uniformity as the laser wavelength is decreased.

To achieve relaxed beam-uniformity conditions with short-wavelength lasers, we can pursue the alternative scaling described by Eq. (39), where r_c/R_a is kept fixed at a value of 1.5 to 2 by increasing I_p and decreasing R_a when we use short-wavelength lasers. The implosion efficiency then scales

very differently with laser wavelength. For a constant value of $x \equiv m(t)/m_0$, we can substitute the results of Eq. (39) into Eq. (41) to show that ϵ is virtually *independent* of laser wavelength when we keep r_c/R_a fixed

$$\epsilon \propto \lambda_L^{-0.01} . \quad (43)$$

We have illustrated this result in a different way in Fig. 3-12, which shows the implosion efficiency vs the normalized standoff distance $r_c/R_a - 1$. The curve shown was calculated for $\lambda_L = 0.5\ \mu m$, $R_a = 0.1$ cm, $Z = 10$, and $A = 20$ by varying the pellet intensity. The flux limit was $f = 0.03$. Equation (43) shows that this curve is virtually independent of laser wavelength. Regardless of the value of λ_L, the hydrodynamic efficiency is highest when the critical surface is closest to the ablation surface. We conclude that, at any laser wavelength, the implosion efficiency will be limited to a relatively low value if we use a value for r_c/R_a of 1.5 to 2, which is appropriate for good symmetrization.

Discussion. To begin our discussion of these results, we reemphasize the limitations of our simple thermal-conduction model. A phenomenological flux limit as used in Ref. 34 is at most a zero-order description of inhibited electron transport. Furthermore, effects such as current filamentation and large-scale dc magnetic fields are not addressed by our smoothing model. Finally, more sophisticated treatments of electron heat flow in the limit where the electron mean free path is approaching the temperature scale length are now becoming available. It would be very interesting to apply these new methods to the symmetry problem studied here.

Within these limitations, we have shown that symmetry requirements can significantly affect the predicted wavelength scaling of directly driven laser-fusion implosions. When r_c/R_a is kept large and constant, the implosion efficiency becomes virtually independent of laser wavelength. In addition, the efficiency falls as the standoff distance is increased, as shown in Fig. 3-12. We thus lose many of the advantages of short-wavelength lasers under conditions where the separation between the critical and ablation surfaces is large enough to produce symmetrization of 10% illumination nonuniformities.

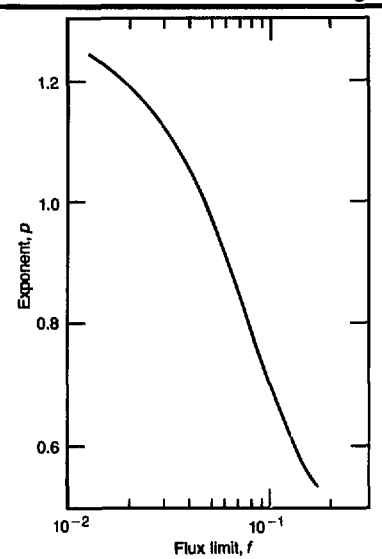

Fig. 3-11. Ablation model predicts that implosion efficiency, ϵ, is proportional to $\lambda_L{}^p$; figure plots exponent p as function of flux limit, f.

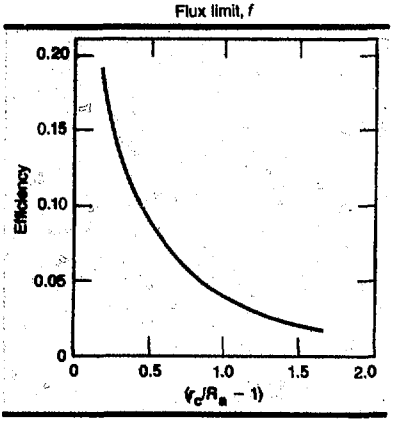

Fig. 3-12. Implosion efficiency, ϵ, vs normalized standoff distance $r_c/R_a - 1$.

We can consider several ways to surmount this dilemma. If the short-wavelength laser light is converted to x rays, and the x rays are used to implode the fuel capsule, requirements of laser-illumination uniformity can be substantially relaxed. We may then be able to reap the advantages of short-wavelength light for coupling and laser–plasma interaction physics without impairing implosion symmetry.

Within the context of directly driven laser-fusion implosions, we might follow the suggestion of Refs. 31 and 32 that lasers of two or more different wavelengths be used during the implosion. It was proposed

that a laser with $\lambda_L = 2$ to 3 μm be used to create the initial hot smoothing atmosphere, followed by a shift to shorter wavelengths as the pellet implodes and its radius decreases. We could, thus, maintain r_c/R_a at a large enough value to provide smoothing as long as necessary. This might allow a good compromise between long- and short-wavelength lasers. Uniformity requirements would be relaxed by the presence of the hot atmosphere, yet we could still have the advantages of good coupling physics for the short-wavelength light.

Finally, we reemphasize that, in directly driven laser irradiations, there is a tradeoff between the standoff distance $r_c/R_a - 1$ and the allowable size of illumination nonuniformities, $\Delta I_c/I_c$. A natural direction of evolution will be to push laser technology as far as possible in the direction of higher levels of illumination uniformity. The required standoff distance will be a function of the best value of $\Delta I_c/I_c$ attainable on a given laser system.

The investigation and exploitation of the different symmetrization techniques discussed here will be essential to the successful use of short-wavelength lasers for direct-drive fusion applications.

Authors: C. E. Max, J. D. Lindl, and W. C. Mead

Charged-Particle Targets

Introduction

The year 1981 has been a stimulating one for ion-beam target physics and related activities at LLNL. In addition to our long-standing interest in charged-particle targets and beam-propagation physics, we continued our cooperation with other US research programs for developing fusion concepts using ion-beam accelerators as inertial-confinement fusion (ICF) drivers. For example, we collaborated with Los Alamos National Laboratory, Los Alamos, N. Mex., on ion-beam target studies for heavy-ion fusion (HIF), which envisages accelerating ions of atomic number $A \geq 200$ to high kinetic energy ($T \sim 10$ GeV). We also pursued target studies in conjunction with Sandia National Laboratories, Albuquerque, N. Mex., for light-ion-beam fusion ($A \gtrsim 1$, $T \gtrsim 1$ MeV), in general using single-gap diode accelerators. Proximity also makes it easier for close collaboration with the HIF work at Lawrence Berkeley Laboratory (LBL), Berkeley, Calif., which is developing the technology for the induction linear accelerator (multiacceleration gaps), and with the HIF-related reactor beam-propagation studies at the LLNL beam physics group. Some features of our activities this year include[36-38]

- Target-gain considerations are found to somewhat favor multigap ion accelerators because they result in beams with less angular and energy spread (see "A Tamped, Split-Fuel-Layer Ion-Beam Target" and "Conservative Estimate of Double-Shell Target Gain for Ion Beams with Large Dispersions," below).
- The requirements of target and beam-transport physics (as presently modeled; see "Initial Application of Target Considerations to the Production, Acceleration, Transport, and Focusing of Ion Beams" below) give further incentive to design accelerators using less phase-space-diluting operations.
- Interesting physics experiments on disk heating, beam deposition, innovative focusing, and transport are expected in some accelerator test facilities (see "Suggested Disk-Heating, Focusing, and Beam-Transport Experiments Using Accelerator Test Facilities for Inertial Fusion," below).
- Studies of possible innovations in ion-beam targets are continuing (e.g., the tamped double-shell target).

Single-gap diode accelerators result in beams with relatively large angular divergence and energy spread. These divergences increase focal-spot radii, thus reducing specific energy deposition. They also imply energy deposition closer to the target surface, thus increasing losses and lowering hydrodynamic efficiency (see the next two articles). The convenient ion energies for diode acceleration also typically involve a short range (~ 0.02 g/cm^2) in matter, so deposition profiles are even more sensitive to these divergences in entrance angle and energy. The possibility exists that more innovative target designs might eliminate some of these differences caused by angle and

energy divergences. In the article on tamped targets, possibly higher gains than those given in our earlier surveys[39,40] are reported. However, the tamped target is still sensitive to these divergences. Illumination symmetry and other requirements also must be studied to confirm these new target-gain results.

In addition to restrictions on angular and energy spreads, target physics requires certain pulse energies and peak powers that are related to the beam current, pulse length, and particle kinetic energy. Some initial models of these phase-space requirements on the beam pulse are studied later in this section, along with some of the beam-transport consideration in the fusion chamber. Within the constraints of our present modeling procedure, accelerator concepts using fewer phase-space-diluting operations would more easily satisfy these phase-space constraints.

Ion-energy deposition and heating experiments are continuing at a number of laboratories. So far, they have not found anomalous deposition effects. For example, the Naval Research Laboratory (NRL) light-ion experiments[41] reached beam-current densities of 250 ± 100 kA/cm^2. This current density is only several times lower than those expected inside heavy-ion reactor targets after stripping of beam ions (ignoring current neutralization). However, the current density is at least an order of magnitude lower than those in similar light-ion targets. Their temperatures of deposition material at ~10 to 15 eV are still lower than in targets (we need ≥100 eV). On the other hand, numerical simulations suggest that high-temperature experiments could also be performed with some proposed heavy-ion test-facility designs. In this section, we particularly emphasize a case where 10^6 K (~80 eV) and ~10^2 kA/cm^2 are obtained in simulations (focal-spot beam energy fluxes ~10^{13} W/cm^2). Experiments on beam focusing and transport of ~1 kA beams are expected if such test facilities are built.

Author: J. W-K. Mark

A Tamped, Split-Fuel-Layer Ion-Beam Target

Target designs suitable for ion-beam-driven inertial-confinement fusion have appeared in the literature since 1968.[42-46] Ions are assumed to deposit classically in the ablator material of the target. Sufficient range flexibility is available through proper choice of ion species and accelerating voltage to allow the designer significant latitude in target size and materials. Designs to date consist of single- and double-shell arrangements containing a central D–T fuel region. We have investigated a more complex design similar to the targets[47] proposed for laser fusion, but with the addition of a tamping layer surrounding the main deposition layer to fully use the benefits of the ion transport. Figure 3-13 shows the target. To date, we have performed only one-dimensional computer simulations of this target, but, in that very optimistic light, the design exhibits net gain in excess of 200 for target energies less than 2 MJ and for beam power of 80 TW. This article will describe that target and its sensitivity to ion range, size, tamper thickness, and beam-spot size.

The uniqueness of this ion target is two-fold. First, it has a split fuel layer, allowing a central D–T core to ignite the much larger outer D–T mass. Second, the deposition layer is tamped; i.e., the low-Z material is surrounded by a dense, high-Z layer that effectively reduces some of the outward motion of the deposition layer, thereby increasing the efficiency of driving the fuel. This tamped effect was first described in 1976[46] in a single-shell design. The extension to two shells and a split fuel layer has greatly increased the gain and reduced the input requirements for a particular yield. However, to achieve the higher gains, the double-shell design requires more stringent

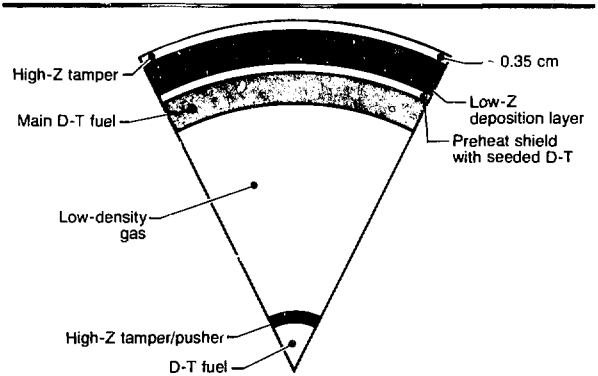

Fig. 3-13. Target geometry used in one-dimensional study.

beam symmetry than the single-shell targets. In addition, the second shell adds the potential of mixing material from this inner pusher into the fuel during implosion.

Classical theory predicts that an ion has a higher dE/dx in low-Z materials than in high-Z materials. Thus, with more energy per gram deposited in low-Z materials, we would preferentially choose a deposition material having a low Z. Furthermore, for a given shell mass, low-Z shells are thicker, thus being less subject to fluid instabilities. Because the ion beam deposits less energy per gram in high-Z material, we can replace some of the low-Z material with a high-Z shell with little penalty in energy loss. The outer shell now provides our tamper.

To investigate the effect this tamper has on ion deposition and coupling to the target, we performed a simple slab study with range, focus, and angular distribution as the variables. Table 3-1 indicates the energy balance of one of the slab problems, and we see that a great deal of energy resides as internal energy of the deposition layer. The tamper serves to minimize this energy sink, as the high-Z material has a lower specific energy than the lower-Z deposition layer; furthermore, the tamper also helps to impede the outward progress of the deposition layer. Column 2 in Table 3-1 shows the results of replacing 0.01 g/cm^2 of the low-Z deposition layer with high-Z material, in terms of energy balance. The key point is that the internal energy has dropped by 20% and the outward motion of the deposition layer has been retarded until the peak of the pulse, resulting in a net reduction in input energy of 0.6 MJ. Because it tamps the low-Z material, the high-Z shell causes the main deposition layer to act more like an expanding piston instead of a rocket-like ablator.

Table 3-1. Energy balance in slabs. (Some miscellaneous energy terms omitted.)

	No tamper	Tamped
$E_{payload}$	340 kJ	550 kJ
$E_{KE\ outward}$	600 kJ	560 kJ
$E_{absorber\ internal}$	2700 kJ	2100 kJ
E_{source}	4.75 MJ	4.75 MJ
$E_{payload}/E_{source}$	0.07	0.12

Fig. 3-14. Efficiency of driving payload vs input power.

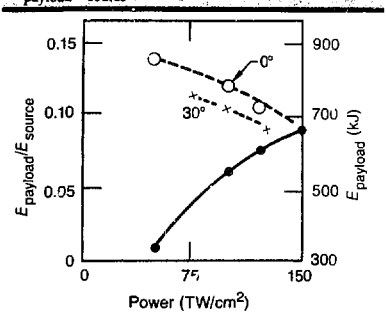

The particular example cited above used radial incidence of the ion beam. We can also study the effect of adding angular divergence to the beam. Figure 3-14 shows how the efficiency of delivering kinetic energy to the fuel layer varies as the intensity is changed for an angular distribution of 30°. The beam shown is a 5-GeV heavy-ion beam. Clearly, as the beam becomes more random, tamping becomes less important. This is obvious when we realize that the angled beam starts depositing the majority of its energy in the outer high-Z tamper instead of in the low-Z material. This then reduces the available energy to the deposition layer, and the drive pressure subsequently drops.

All the above points were observed in the design of the two-shell ion target. Figure 3-13 shows the generic shape of the target. We start with a solid (frozen) D–T fuel region surrounded by a high-Z pusher. This is isolated from the second shell by a low-density gas cushion, chosen to allow proper timing of the incoming shocks. The main fuel layer is next, again frozen to allow a density of 0.21 g/cm^3. A seeded region of D–T surrounds the fuel to isolate it from the hotter deposition layer. The last two layers make up the low-Z deposition layer and the high-Z hydrodynamic tamper. In all the calculations, the central fuel remained fixed in size and material. The gas-cushion density was changed as the pulse shape was varied to regain optimum conditions. However, the biggest variety occurred in the material chosen for the deposition layer and in the thickness of the deposition and tamper layers.

Three ions of differing range were used in this study, and the target design was reoptimized for each range. Figure 3-15 shows the gain expected from this target as a function of range, with a maximum occurring at 5 GeV. Changing the thickness of the tamper for these targets produced varying results. Figure 3-16 indicates the change in yield from the 5- and 10-GeV targets as the thickness of the tamper is varied. For

the 10-GeV case, the output is relatively insensitive over a broad range of thicknesses. However, the 5-GeV case exhibits a rather pronounced peak at 0.03 g/cm^2 and deteriorates rapidly on either side. The mechanism of the tamping is quite apparent. As the tamping becomes too thin, the hydrodynamic motion is unimpeded, and the coupling is less efficient. Adding too much tamper has a similar effect: now, the majority of the beam is deposited in the tamper, thus reducing the pressure in the deposition layer.

To study the effect of changing the diameter of the incoming ion beam, we ran examples up to 0.3-cm focus and plotted the results in Fig. 3-17. The diameter of this target is 1 cm. We note that, below a certain spot size, the effect on gain is minimal, but, for large beams, the target behavior deteriorates badly. Also, some tamping is beneficial in improving the gain.

The size of the target also affected its performance, as this performance is directly related to the beam focus and radial incidence. However, other effects also were noted. For instance, if the target was too small (<0.25-cm radius), it was very difficult to obtain both the required implosion velocity and low adiabat of the outer fuel. As the target shrinks in size, we must hit it harder to get to the required velocity as the run-in distance is reduced. This harder initial shock, in turn, shocks the main fuel harder than desired, setting it on too high an adiabat and reducing the ultimate yield. Problems are also noted in the very large sizes: the drive energy required has increased, although the power has decreased. Furthermore, the aspect ratio has increased for similar masses, making the target more susceptible to Rayleigh–Taylor instabilities. The optimum target radius appears to lie between 0.3 and 0.5 cm. Table 3-2 indicates the target behavior for an optimized 5-GeV beam with 90-TW input power and a focal-spot size of 0.2 cm.

The possibility of preheat caused by K- and L-line emissions as the ion beam passes through the outer high-Z tamper was also investigated. We found that a source of 60-keV photons, equal in strength to 1% of the beam energy and placed uniformly in the high-Z tamper, could destroy the target. Using the Bethe formula and calculating the stopping power due to each

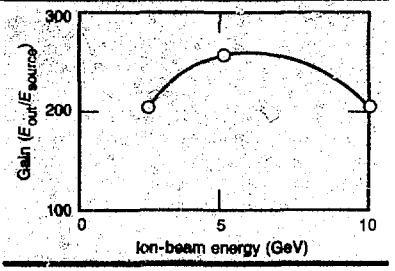

Fig. 3-15. Gain vs ion-beam kinetic energy.

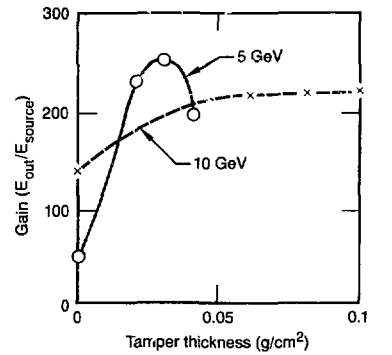

Fig. 3-16. Gain vs tamper thickness for 5- and 10-GeV beams.

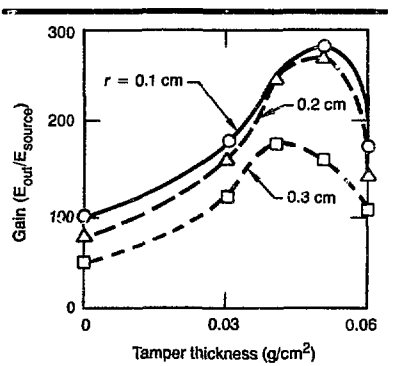

Fig. 3-17. Gain vs tamper thickness and spot size.

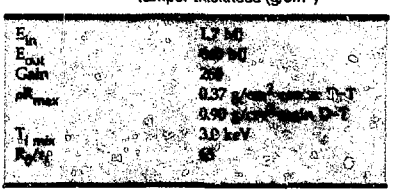

Table 3-2. Characteristics of 5-GeV target.

electron in lead, we estimate that less than 4% of the beam energy could be converted to L-line emission (10 to 15 keV) and 0.06% into K-line emission (55 to 65 keV). The above estimates are for a 10-GeV beam. Putting this photon source into our 5-GeV target to simulate an upper-limit preheat,

we saw no changes in yield and only minor changes (5%) in ignition conditions.

We might expect the stability of this double-shell target to be quite good because the density decreases with decreasing radius. The acceleration is initially in the direction of decreasing density, thus ensuring stability. Unfortunately, this situation does not persist. The density of the low-Z beam-deposition region drops below the density of the imploding shell and instabilities may develop; however, preliminary numerical simulations show that the stability is adequate.

In conclusion, we have designed an ion target that produces a conservative gain of 200 with an input of 5-GeV heavy ions (5-MeV proton equivalent), 1.7-MJ total energy, and 90-TW peak power in a one-dimensional computer simulation. Studies show the target to be relatively insensitive to changes in size and ion range, but quite sensitive to angular distribution of the beam and tamper thickness. Further work is required to study the two-dimensional effects, particularly the symmetry problem posed by multiple beamlets and the resulting beam overlap.

Fig. 3-18. Gain as a function of input energy for single-shell targets.

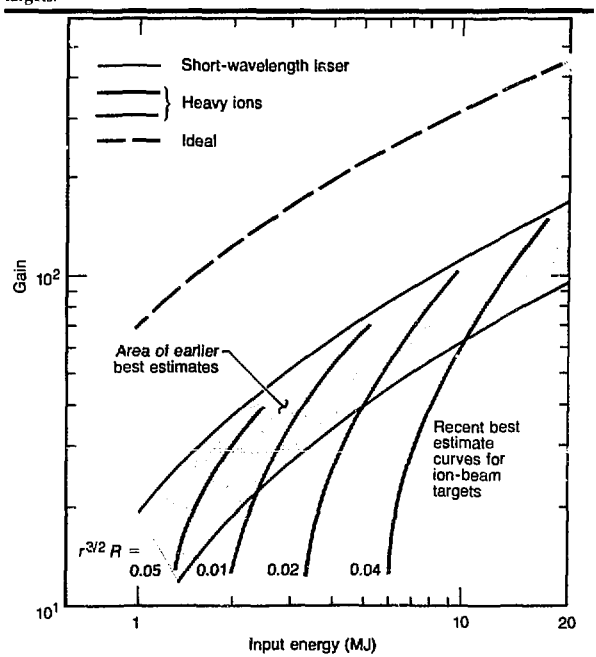

Authors: D. J. Meeker (LLNL) and R. O. Bangerter (Los Alamos)

Conservative Estimate of Double-Shell Target Gain for Ion Beams with Large Dispersions

In previous reports,[48,49] we gave a survey of gain curves for ion-beam-driven targets as a function of the relevant input energy, ion range, and focal-spot size. However, these reports considered a restricted parameter range (focal-spot radii ≤ 0.5 cm) primarily of interest for multigap accelerators.

We have been extending our calculations to the parameter range of interest for single-gap accelerators. We now find it necessary to consider larger focal-spot radii, effects of beam-energy spread, and angular divergence. Since symmetry and pulse-shaping requirements have not been fully addressed for these targets, actual target gains could be lower than estimated here. Our results have important consequences for accelerator design.

Acceleration of light ions has been actively pursued by Sandia National Laboratories, Albuquerque, N. Mex., concentrating primarily on single-gap diode accelerators.[50] For this program, there is an ongoing study by Bechtel, San Francisco, Calif., and Physics International, San Leandro, Calif., of an ion-beam-driven ICF reactor (the Eagle reactor concept).[51] Therefore, it is interesting to give a parameter survey of gain curves for relevant target designs. This article summarizes the preliminary results of such a survey. Because the considered targets depend on more parameters than our earlier results,[48,49] we have only made rough estimates of the symmetry requirements. Also, pulse shaping is difficult for present single-gap ion-diode accelerators, whereas some pulse shaping is implied in the target gains presented here. Therefore, the estimates tend to be upper bounds. Since we are presenting upper bounds to target gains, a survey of double-shell targets is sufficient.

In our earlier reports,[48,49] we have given target gain as a function of input energy, ion range, and focal-spot size. The principal results are given in Figs. 3-18 to 3-20, where target gain and power requirements are plotted as a function of input energy, E (M and a parameter, $r^{3/2}R$, where r is the focal spot radius (cm) and R is ion range (g/cm^2).

The gain of short-wavelength-laser targets is expected to lie in the band defined by the dashed lines.

The curves in Figs. 3-18 to 3-20 were obtained by a least-squares fit to the results of a number of numerical simulations performed with the LASNEX code. The simulations covered only a restricted parameter range where

$$0.1 < r/E^{1/3} < 0.2 \quad . \tag{44}$$

These relatively small focal radii have been primarily of interest for multigap accelerators, but the general nature of the curves is expected to be valid for all ions. Single-gap diode acceleration results in beams with large angular divergence and energy spread. The ion energies chosen also typically involve a short range ($\sim$0.02 g/cm^2) in matter, so the deposition profiles are particularly sensitive to dispersions in ion entrance angle and energy. Thus, the gain of such ion-driven targets depends not only on E, R, and r, but also on the angular divergence, $\delta\theta$, and the energy spread, $\delta E/E$, of the beam. These latter effects are shown in Fig. 3-21. These calculations were performed on a planar target. For a spherical target, finite focal radii cause angular spread, even for a parallel beam. Both angular divergence and energy spread lead to increased energy deposition near the surface of the target. This results in lowered hydrodynamic efficiency and increased radiative losses. These effects were not included in the calculations shown in Figs. 3-18 to 3-20 because the ion ranges used were long. In any case, the ion beams studied so far for multigap accelerators have negligible angular divergence and energy spread. We have now included these effects and extended our calculations to a wider range of r and R. Preliminary results for double-shelled targets are given in Figs. 3-22 to 3-25.

We emphasize that these results may change as we improve our simulation codes and do experiments. However, as outlined earlier,[49] we expect these gains to be conservative. Since a full study of symmetry and pulse-shaping considerations has not been made for the targets reported here, and since present diode accelerator schemes have little pulse-shaping capabilities, these estimates are likely to give upper limits to target gain. With these precautions in mind, we arrive at some tentative conclusions

- For focal spot sizes of 0.2 to 0.3 cm, the curves of Figs. 3-18 to 3-21 show that uncertainties of about a factor of 2 in range are tolerable. For example, a 10-GeV Pb ion has a range of about 0.1 g/cm^2, a focal-spot radius of 0.2 cm, and $r^{3/2}R \simeq 0.01$. An increase of range to 0.2 g/cm^2 shifts $r^{3/2}R$ to about 0.02, which has an important but not decisive, impact on target performance.
- For reasonable focal radii ($r > 1$ cm), ranges in excess of a few times 0.1 g/cm^2 yield economically unattractive target designs.
- Independent of ion range, large focal radii ($r \geq 1$ cm) are economically unattractive.
- The effects of angular divergence and energy spread could become important for large focal radii where the gains are already marginal.
- Large values of r and R imply a high peak-power requirement.

Authors: R. O. Bangerter (Los Alamos); J. W-K. Mark and D. J. Meeker

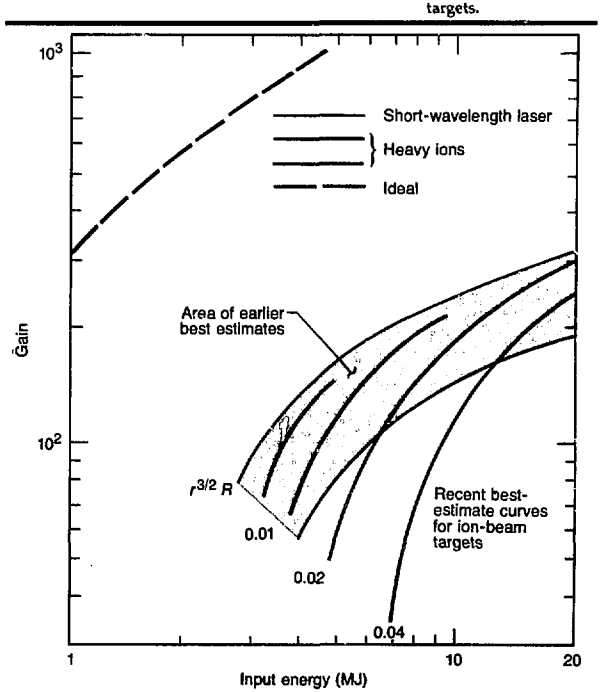

Fig. 3-19. Gain as a function of input energy for double-shell targets.

Initial Application of Target Considerations to the Production, Acceleration, Transport, and Focusing of Ion Beams

For heavy-ion fusion, the accelerator driver and the fusion reaction chamber represent the major capital cost of an ion-beam-driven ICF power plant. Therefore, to optimize the design of such a facility, it is important to consider the implications of our best-estimate gain curves on the driver and fusion chamber. This report is, therefore, a first attempt at such an optimization, assuming an rf accelerator driver and assuming chamber vapor pressures in hard vacuum of $\leq 10^{-4}$ Torr and in soft vacuum of $\sim 10^{-4}$ to 10^{-3} Torr.

Attention is concentrated on one combination of accelerator parameters, the phase-space volume of the beam pulse, in addition to the beam pulse energy, E (MJ), and ion kinetic energy, T (GeV). Also, for a preliminary survey, we have chosen one parameter of fusion-chamber conditions that, under certain conditions, has an important effect on the target gain vs accelerator relation for these beam-propagation regimes. Our initial optimizations interface between disciplines by simple analytical models or scaling laws that have approximate validity within certain restrictions.

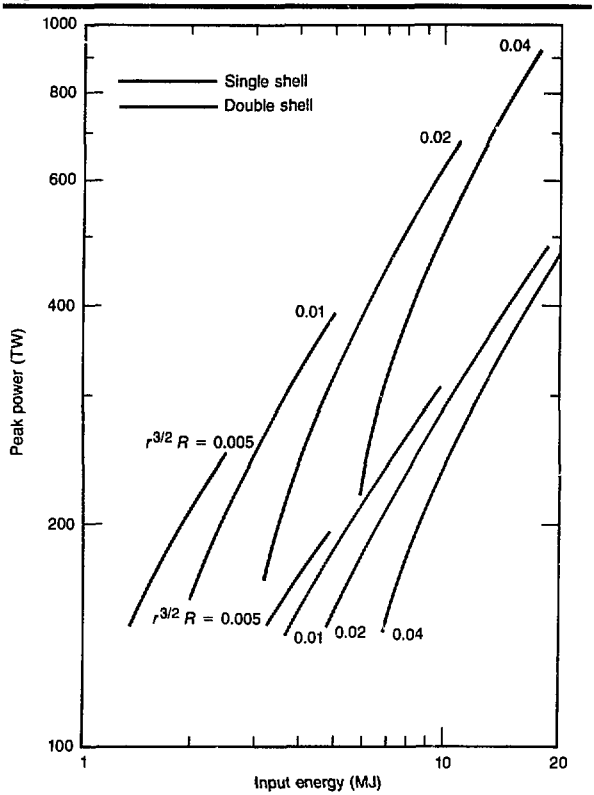

Fig. 3-20. Input peak power requirement as a function of input energy for single- and double-shell ion targets.

We begin with the phase-space constraints first introduced[52] in discussions of rf linear accelerators for ion-beam fusion. If space-charge effects on ion trajectories within the fusion reaction chamber can be neglected (as in beams fully neutralized[53-55] by injection of electrons before entrance into the fusion reaction chamber), we can directly relate the target gain to this phase-space factor. More general beam-transport considerations in a reactor chamber then follow.

A six-dimensional phase-space volume is defined by ranges in coordinates x, y, and z and momenta p_x, p_y, and p_z. For fusion targets, all six of these parameters have bounds that, if extended, will lower the gain. The curves of Figs. 3-18 and 3-19 display this effect for a spot size that limits x and y. The beam length, z, is limited by the peak-power requirement. For heavy-ion systems, constraints on angular divergence (proportional to p_x and p_y) or energy spread (p_z) are determined by known properties of final lenses, which place stringent limits on phase-space volumes. In addition, large divergence and spread would cause an excessive fraction of the beam energy to be deposited near the target surface, increasing radiative losses and reducing coupling efficiency.[54,56,57] (Large angular divergences are more typical of single-gap acceleration schemes.) However, beam focusing and transport systems will place more stringent limits on the phase-space volume. As an example, we consider heavy-ion rf linacs, for which the constraints on angular divergence and momentum spread are determined by the known properties of final lenses.

Within a numerical factor, the four-dimensional transverse phase-space volume available to a beam is given by $V_4 = p^2 r^2 \theta^2$, where p is the beam momentum and θ is a small transverse angle. The (nonrelativistic) longitudinal two-dimensional volume is

given by $V_2 = T\tau(\delta p/p)$, where T is the ion kinetic energy, τ is the pulse length, and $\delta p/p$ is the fractional momentum spread. The total six-dimensional phase-space volume per ion is given by $V_F = nV_2V_4T/E$, where n is the number of beams. For an rf linac, the six-dimensional phase-space volume per ion is given by $V_L = (Mc\epsilon_\perp)^2 \epsilon_\parallel qef/I$, where M, c, $\epsilon_\perp$, $\epsilon_\parallel$, qe, f, and I are the ion mass, light speed, transverse normalized emittance, longitudinal emittance per rf bucket, ion charge, the frequency with which buckets emerge from the linac, and mean electrical beam current, respectively.

According to Liouville's theorem, V_F must be greater than V_L. Dilution is expected in acceleration, storage, transport, and focusing so that $D = V_F/V_L$ must substantially exceed unity.

The convergence angle of an alternating-gradient lens system is given by $\theta^2 = GXqeB/p$, where B is the pole-tip field, X is the aperture radius, and G is a dimensionless constant determined by detailed lens design. For uncorrected lenses, chromatic aberrations require that $\delta p/p < r/(2X)$. We allow the possibility of some chromatic correction using sextupoles by setting $\delta p/p = F_s r/(2X)$, where F_s might be

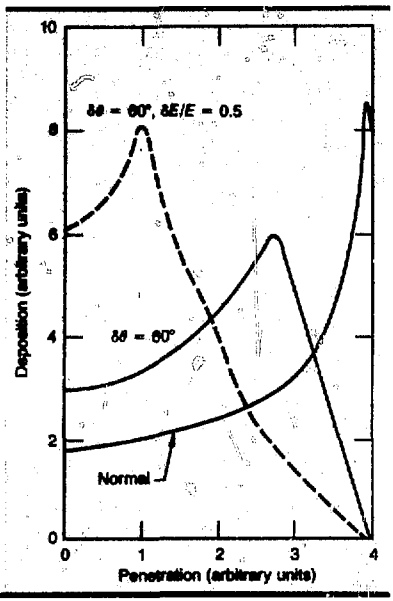

Fig. 3-21. Deposition as a function of ion penetration into target, showing effect of angular and energy spread.

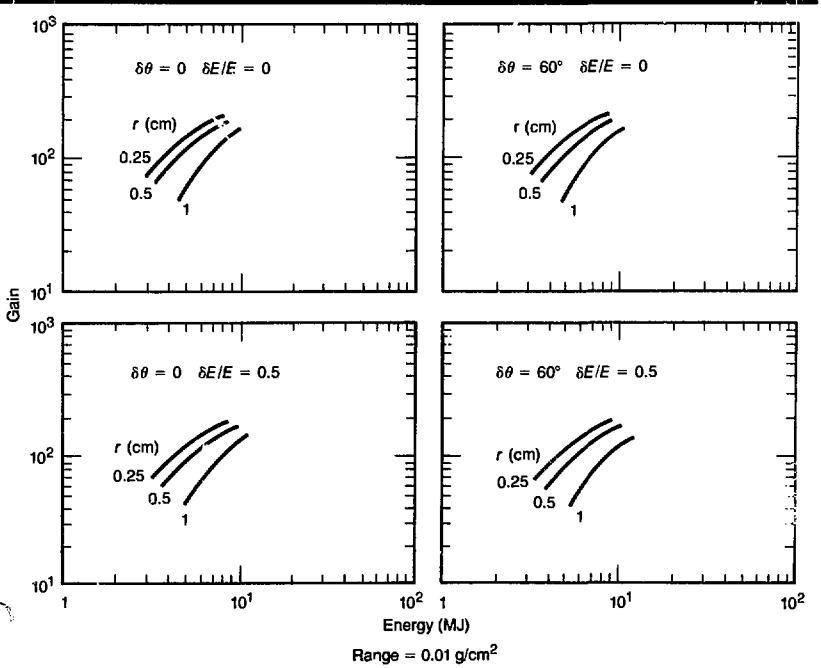

Fig. 3-22. Target gain as a function of beam energy for two-shell targets; ion range is 0.01g/cm² in all cases.

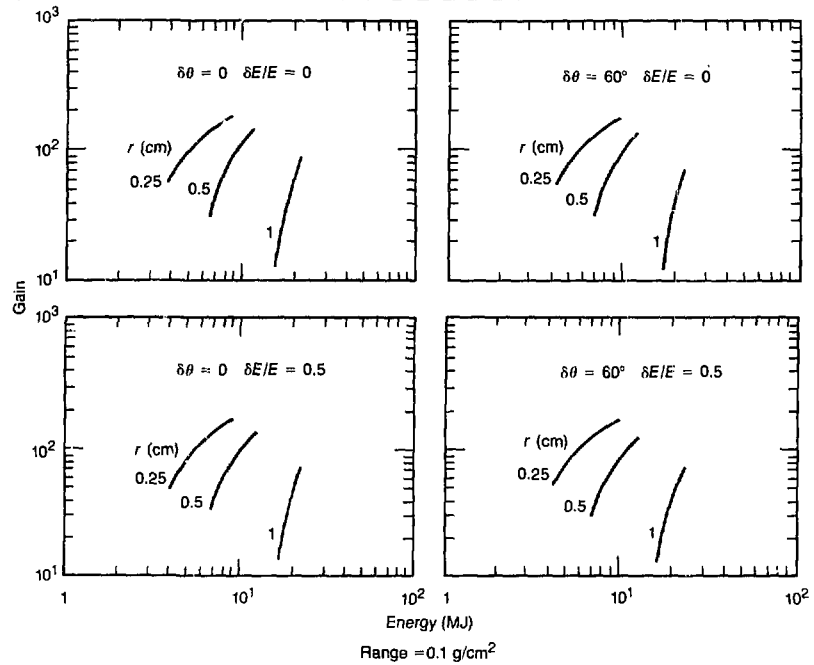

Fig. 3-23. Target gain as a function of beam energy for two-shell targets; ion range is 0.1 g/cm² in all cases.

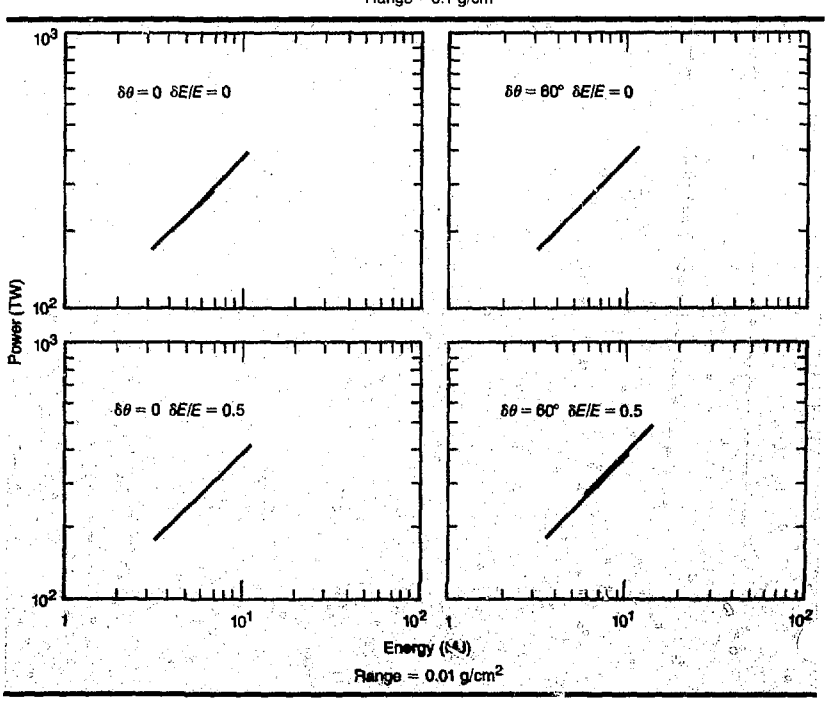

Fig. 3-24. Power as a function of beam energy for targets in Fig. 3-22 with range = 0.01 g/cm²; curves for three radii lie almost on top of each other.

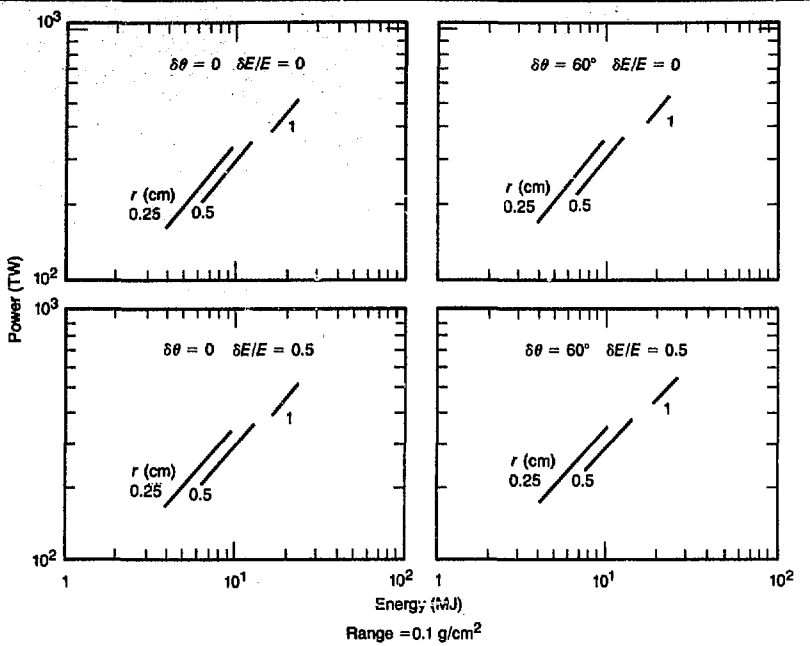

Fig. 3-25. Power as a function of beam energy for targets in Fig. 3-22 with range 0.1 g/cm^2.

1 to 3. Combining the above expressions we obtain

$$D = \frac{Gc}{4\pi^{3/2}(mc)^{2/3}}\left[\frac{\tau T}{E}\left(\frac{2\pi r^2 T}{A}\right)^{3/2}\right] \times \left[\frac{I}{\epsilon_\perp^2 \epsilon_\parallel f}\right] n B F_s = K F_{TI} F_I n B F_s \quad , \qquad (45)$$

where A is the atomic number and m is the proton mass. The first quantity in brackets,

$$F_{TI} = \frac{\tau T}{E}\left(\frac{2\pi r^2 T}{A}\right)^{3/2} \quad , \qquad (46)$$

depends on target and ion parameters. The second quantity, F_I, is a figure of merit depending on linac parameters. The factor 2π in F_{TI} is included for historical reasons.[52,58] We employ the following units: τ (ns), T (GeV), r (cm), E (MJ), I (A), $\epsilon_\perp$ (cm mrad), $\epsilon_\parallel$ (eV s), B (T), and f (MHz). The constant K is evaluated in Ref. 52 and is given by $K \sim 5 \times 10^{-3}$.

Target gain as a function of F_{TI}, E, and T can be calculated.[54,57,58] Using Figs. 3-18 to 3-20, the results of such a calculation for $A = 238$ are shown in Fig. 3-26. The dependence on T is very weak, as indicated by the horizontal lines.

To apply this analysis, we must assume a set of rf linac parameters and an expected phase-space dilution factor from linac exit to target. Available linac designs are neither detailed nor optimized. Furthermore, dilution estimates are based on educated guesses, rather than experience. The following choices can only be described as representative[52]: $I = 0.3$ A, $\epsilon_\perp = 0.2$ cm mrad, $\epsilon_\parallel f = 0.128$ eV s MHz, $B = 5$ T, $F_s = 3$, and $n = 24$. It is reasonable to provide about four factors of 3 each for all kinds of dilutions. With such numbers $81 \sim (5 \times 10^{-3}) F_{TI} \times 60 \times 24 \times 5 \times 3$, so $F_{TI} \sim 0.75$. From Fig. 3-26, we see that this value implies large E, double-shell targets, and relatively low gain. On the other hand, larger numbers of beams, better linac brightness,[59] or assurance of smaller dilutions could ease the constraint significantly. In any event, the constraint must be met. At present, it appears to be important. The work described above provides a parametric treatment of the influence of target-design parameters on this constraint for neutralized

beam propagation in the fusion chamber. It also displays the cost (in reduced gain or increased E) of easing this constraint for rf accelerators. Induction accelerators can more readily satisfy this criterion.

The above results assume ballistic focusing of a fully neutralized beam in a hard vacuum ($<10^{-4}$ Torr). Although calculations[53-55] suggest that the beam could be neutralized by coinjection of electrons, more detailed simulations and experiments are needed to confirm the applicability of the process. On the other hand, electrical efficiency for liquid-metal-wall protection schemes points to somewhat higher vapor pressures.[60] One confluence of these requirements occurs in the 10^{-4} to 10^{-3} Torr pressure regime, where there is partial beam neutralization by ionization of the propagation medium (e.g., Li vapor), somewhat modified by mild stripping of the beam ions.[53-55]

Even ballistic focusing in hard vacuum without neutralization is subject to beam-emittance growth effects, which depend on the beam profile.[53] To a first approximation, the effective available phase-space dilutions for accelerator design can be defined by Eq. (45), except that the radius, r, remains the spot radius of the final-focusing system with the fully neutralized beam. Without neutralization, the actual spot radius, r_s, is enlarged because of growth of "effective emittance." Corresponding to an "intended" target phase-space factor, F_{TI}, we have to use instead a larger target radius, $r_s > r$, to calculate the actual target gains. Thus, the target gain vs F_{TI} relation is modified and depends on values of the beam-emittance growth parameter, ϵ_g (Refs. 53, 55, and 61). In hard vacuum ($<10^{-4}$ Torr), this parameter is

$$\epsilon_{gv} = 4.55 \frac{L\lambda I_b Z}{A(\beta\gamma)^3} \quad , \tag{47}$$

where L (m) is the distance of beam propagation, and Z, A, and $(\beta\gamma)$ are the ion charge, atomic mass number, and ion velocity factor, respectively. The quantities I_b (kA) and λ are beam current and shape factor. For flat, parabolic, and Gaussian beam profiles, $\lambda = 0$, 0.149, and 0.388, respectively.

In a soft vacuum ($\sim 10^{-4}$ to 10^{-3} Torr), the ionization of the medium provides electrons that partially neutralize the beam[53-55] and reduce emittance growth. As suggested in Ref. 54, the major result of this process can be represented by using the modified emittance growth parameter

$$\epsilon_g = (1 - f_{neut})\,\epsilon_{gv} \quad , \tag{48}$$

where f_{neut} is the effective fractional neutralization of the beam. For a 1.2×10^{-3} Torr Li vapor pressure in the fusion chamber, $f_{neut} \simeq 0.5$ (Ref. 54; for details, especially saturation phenomena in f_{neut}, see Ref. 56).

The emittance growth parameter, ϵ_g, results in a stronger dependence of F_{TI} on ion kinetic energy, T (for fixed target gain and beam pulse energy, E). This is illustrated in Fig. 3-27 for a partially neutralized beam. Bearing in mind this amount of variation of the averaged values of F_{TI} for given target gain, Fig. 3-28 illustrates the "typical" reactor beam-transport modifications to Fig. 3-26 for the ballistic-focusing scenario.

Influences that change the effective focal-spot radius, r_s, at the target relative to the intended radius, r, of final focus are more

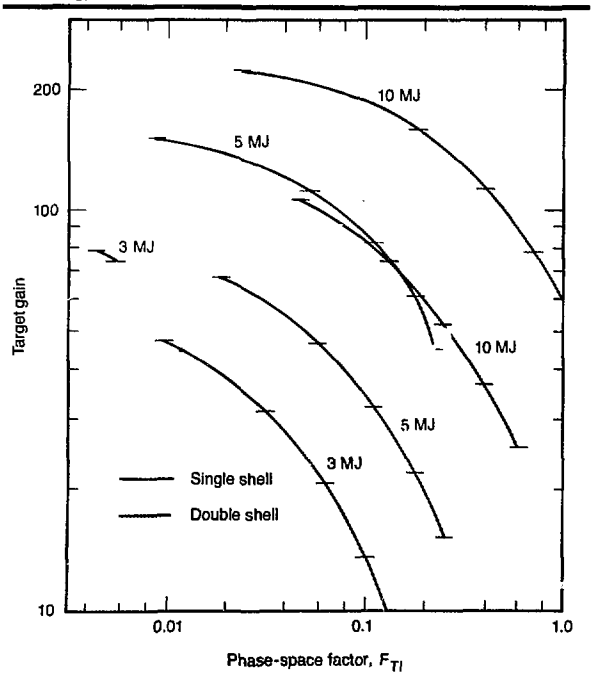

Fig. 3-26. Gain as a function of F_{TI} for single- and double-shell targets evaluated for A = 238; horizontal lines indicate small dependence on ion kinetic energy.

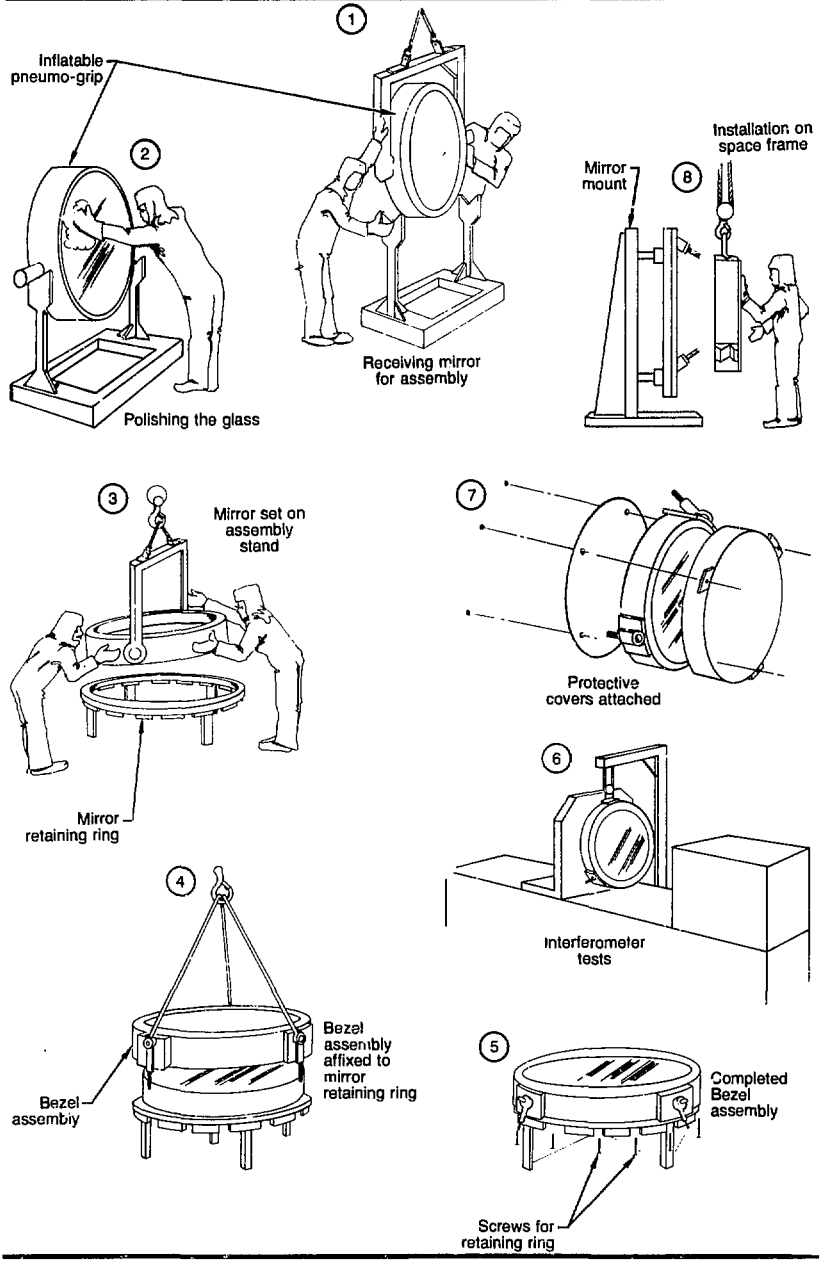

Fig. 2-57. Cleaning and assembly sequence for large turning mirrors.

at reasonable cost. In the larger amplifiers, nitrogen enters the disk cavity and flashlamp cavity through a plenum input. Gas for the flashlamp cavity on the 46-cm amplifier is manifolded in series, as shown in Fig. 2-58. Three 46-cm amplifiers are placed in series on the spaceframe and close-coupled, so that they function as one

to 3 kA of incident ion current on these disks with beam energy fluxes almost comparable to that of reactor targets (10^{13} W/cm^2 of 100-MeV Na implies 100 kA/cm^2). Thus, if any anomalous plasma effects on deposition exist, the conditions should be available for discovering some of them. Note also that these deposition experiments have low ion kinetic energy per nucleon. About 4 to 5 MeV/nucleon are appropriate if lighter ions such as sodium are used. However, for lighter ions, unexpected plasma effects in deposition might be more readily noticed because heavy-ion beams are more "stiff."

Fig. 3-29. An appropriate configuration for disk experiments using heavy-ion beams from accelerator test facilities.

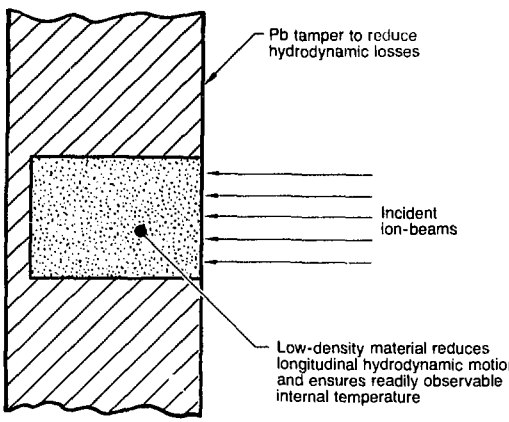

Fig. 3-30. Numerical grid after 2 ns.

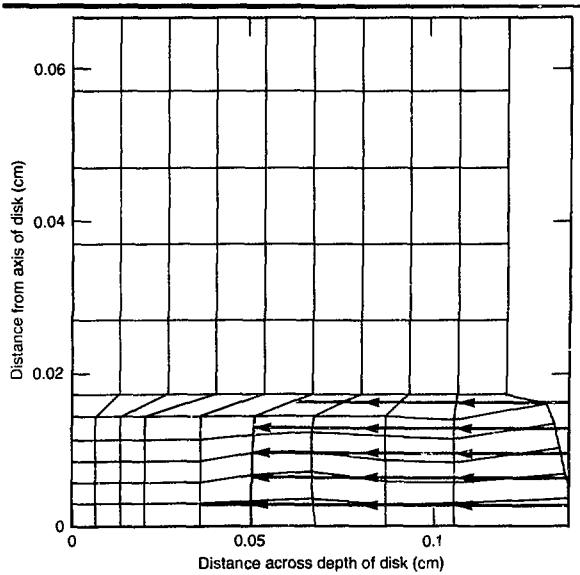

Ion-beam focal-spot energy fluxes for reactor targets in heavy-ion inertial fusion range from 10^{14} to 10^{15} W/cm^2 (10^2 to 10^3 TW/cm^2). A preliminary estimate suggests that the emergent beams from some accelerator test facilities could be ballistically focused to an energy flux of about 2×10^{13} W/cm^2 (Ref. 65). Some of our numerical examples are motivated by the parameters of a recent design proposal[64] for a multibeam induction linear-accelerator test facility. Focusing and increasing beam intensity in this case are facilitated by

- Low normalized emittance of ~2 to 4 $\times$ 10^{-2} mrad cm per beamlet.
- Use of Na or K ions.
- Compression of the beam pulse.
- The fact that energy flux increases very rapidly with decreasing focal distance because of the decrease in spot radius, consistent with space-charge effects.

Conceivably, the energy fluxes might even reach 3 to 4 $\times$ 10^{14} W/cm^2 in this design[64] if we use magnetic plasma lenses that involve pinching forces on a beam stripped to a high charge state in a plasma cell. Some estimates of these processes are given later.

A few details of the numerical simulation of disk heating in one proposed experiment are given in Figs. 3-29 to 3-34. In particular, Fig. 3-29 shows the configuration for depositing the incident beam onto low-Z "felt-metal." We start with a small hole (in this extreme case ~0.34-mm diam) drilled in a heavy material such as lead. This hole is subsequently filled with a low-Z metal, such as aluminum in low-density felt-metal form. The heavier lead prevents transverse conversion to hydrodynamic motions, while use of low-density material (say $\rho \sim 0.15$ g/cm^3) reduces conversion into longitudinal hydrodynamic motions. Together, this scheme results in lower hydrodynamic losses (actually delays their occurrence) and maximizes the internal temperature of the material used for beam-heating experiments. Simultaneously, the internal temperature of the material is more readily observed and measured.

About 3 kJ of sodium ions at 100 MeV and 0.3 TW are used. By using sodium ions

in this test facility, instead of a heavier ion such as thallium, we obtain a gain in beam power by roughly the square root of the inverse mass ratio. Unlike reactor drivers with 5- to 20-GeV ions, there is little penalty to pay in terms of ion range when lighter ions are used for a 100-MeV test facility.

The numerical grid after 2 ns (near time of peak temperature) is shown in Fig. 3-30. Actually, by 2 ns, the peak temperature is reached even though only 0.6 kJ of energy is deposited. Subsequently, the disk disintegrates even with our care to delay hydrodynamic losses. The time variation of disk temperatures is shown in Fig. 3-31 at points near the front, where the beam enters the disk. Figure 3-32 further illustrates the distribution of the internal temperature across the disk. The several curves are different cuts across the depositing materials. The rate of energy lost from the front of the disk vs the rate of energy deposited is given in Fig. 3-33, while the accumulated energy lost (deposited) up to that time, as a function of time, is given in Fig. 3-34.

The above example assumes 3.3×10^{14} W/cm^2. However, to reach 10^6 K (~80 eV), it is sufficient to have 0.7×10^{13} W/cm^2, which can be reached by ~0.3 TW of sodium ions focused to a spot diameter of 1.2 mm. Preliminary results suggest that these numbers could be attainable in an early conceptual test-facility design.[64] Figure 3-35 shows observable temperature vs beam energy flux at the focal spot. For each energy flux point in Fig. 3-35, Table 3-3 lists beam-pulse energies required to reach and maintain peak temperatures for roughly 1 to 2 ns. We must emphasize that Fig. 3-35 and Table 3-3 are just indicative results. A more detailed experimental design will have to take careful account of effects such as detector response and the angle between disk and detector, as well as whether the detector angular resolution partially sees the lead tamper. Also, if the spot diameters differ significantly from 1 mm, or if the ion range differs significantly from that of Na at 100 MeV or K at 200 MeV, more calculations are advisable.

We have also briefly considered the possibility of using magnetic focusing (with discharge currents or external magnets) of ripped beams in plasma cells to reduce the final focal-spot size on target. In one of these schemes, the many ion beamlets are combined into one or several bunches that are then injected into plasma channels in gas cells with preexisting pinch fields (Fig.

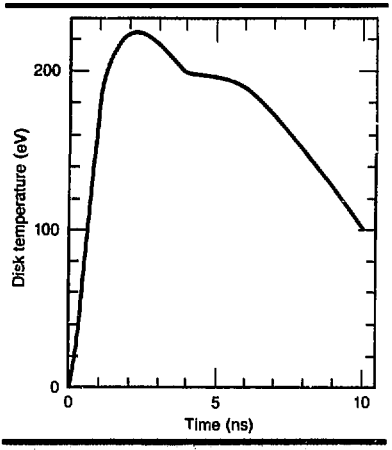

Fig. 3-31. Disk temperature reached as function of time for point near front of disk.

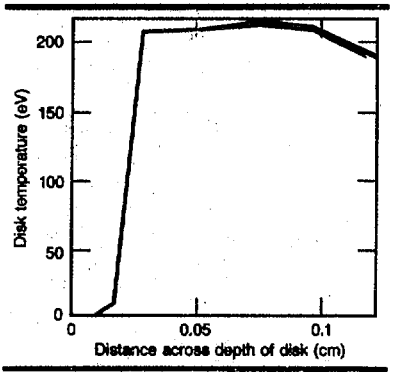

Fig. 3-32. Internal temperature as function of positions across depth of disk at time of 2 ns; different curves are for several radial positions.

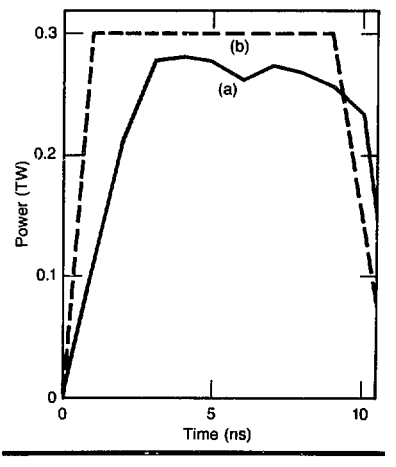

Fig. 3-33. (a) Rate of energy lost from front of disk vs time. (b) Rate of energy deposition.

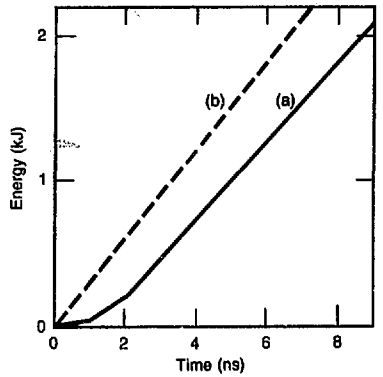

Fig. 3-34. Total energy lost. (a) From front. (b) Energy deposited by beam.

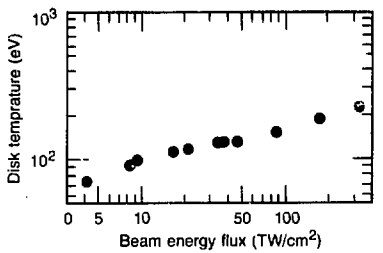

Fig. 3-35. Observable disk temperature vs beam energy flux at focal spot.

Table 3-3. Required beam energy flux, power, and energy at focal spot.

Beam energy flux (TW/cm²)	Power (W)	Energy (kJ)
4.2	0.075	0.8
8.5	0.15	1.4
9.5	0.3	2.4
17.0	0.3	1.8
22.0	0.075	0.7
34.0	0.6	6.0
38.0	0.3	2.7
47.0	0.15	1.1
88.0	0.3	1.8
175.0	0.6	3.0
330.0	0.3	0.9

3-36). The ions are quickly stripped by the gas, and the resulting stripped beams are focused by the external fields onto one single small spot. As an example, we consider a single final beam with an emittance of ~0.2 mrad cm and an initial beam radius of ~1 mm being injected into a channel with a discharge current density of 1 MA/cm^2. Assuming a charge state of $Z \sim 9$, the beam is expected to pinch down to 150 μm after propagating a few centimetres. If we have 10 beam bunches with an emittance of 0.063 mrad cm per bunch, the same external current will lead to a final spot of 80 μm. More detailed simulations of these effects are being planned. Before the results are known, it may be prudent to add some conservative factors to the above numbers: (1) there may be a distribution of charge states in the stripped beam (we assumed that 33% of the particles reach the correct focal spot); (2) the emittance may dilute by additional factors during the process of combining the beamlets. Of course, we could also consider using further external focusing magnets on this beam in the plasma cell. Thus, an initial 0.3 TW of Na beams might be focusable to a 180-μm or smaller radius, reaching ~1.4×10^{14} W/cm^2. From the results of Fig. 3-35, we feel that disk-heating experiments up to 250-eV temperatures might even be possible, although the initial goal is closer to 100 eV.

For comparison, the 3-MJ induction linear accelerator for 10-GeV ions, designed at Lawrence Berkeley Laboratory (LBL), Berkeley, Calif., as an ICF reactor driver, will focus 150 TW of ions to a 2.5-mm-radius spot, or 7.6×10^{14} W/cm^2. Thus, the possible maximum energy flux of $\gtrsim 10^{14}$ W/cm^2 envisaged for the test facility is close to reactor-scale beam fluxes. Of course, if beam flux is the only issue, a comparable 3-MJ driver could be designed to optimize the flux. To give a further comparison with the test facility, we might mention that, with some modifications the 3-MJ driver design might reach a spot of 1.7-mm radius, or $\lesssim 1.6 \times 10^{15}$ W/cm^2 (Ref. 66). Simulations of self-pinched beam propagation suggest that, alternatively, a 1.2-mm-radius spot might be obtained from the self-pinching effect of a beam propagating into a few Torr of neon gas, starting from an initial beam radius of 2 mm. Even a 0.7-mm-radius spot ($\lesssim 10^{16}$ W/cm^2) might be achievable using an external discharge current of ~35 kA in a configuration similar to Fig. 3-36.

The proposed test-facility parameters should also permit useful experiments on beam-transport considerations, such as neutralization. A 2.4-keV electron beam has the necessary longitudinal velocity to travel in parallel with a 100-MeV Na beam. This kinetic energy per electron is quite small in comparison with the electrostatic potential drop of more than 900 kV associated with an unneutralized Na beam of 3 kA. Extrapolating from results given by a two-dimensional particle-code simulation (using the HIPPO code), we expect that the

coinjection of electron beams, with transverse temperatures below 1 keV, will produce extremely good neutralization, even if the ion beam is subdivided into as many as 50 individual beamlets.

Besides neutralization experiments, the test facility should also be able to provide meaningful tests of the scaling laws for other focusing and transport issues, such as any possible emittance growth and focal-spot size variations in unneutralized beams.

Thus, with such a proposed test facility, we could look forward to performing a number of interesting deposition experiments with heating of disks to possibly greater than 10^6 K (~80 eV). Beam focusing and transport experiments are also expected. We could reach as much as 1 to 3 kA of incident ion current on these disks with beam intensities almost comparable to those of reactor targets. Thus, if any anomalous plasma effects on deposition should emerge, the conditions should be available for testing some of them. If they exist, such plasma effects might well be more noticeable for intermediate ions, such as sodium, than for truly heavy ions. The $\leq$4 to 5 MeV/nucleon achievable is still an order of magnitude smaller than the more realistic heavy-ion deposition conditions in reactor targets (where relatively classical deposition is expected).

We are grateful for helpful discussions with A. Faltens (LBL), A. Garren (LBL), W. Herrmannsfeldt (Stanford Linear Accelerator Center, Stanford, Calif.), D. Keefe (LBL), A. Sessler (LBL), and L. Smith (LBL).

Authors: J. W-K. Mark (LLNL), R. O. Bangerter (Los Alamos), W. M. Fawley, D. L. Judd (LBL), and S. S. Yu (LLNL)

Plasma Physics

Introduction

A capability to model the coupling of laser light with targets is essential both for designing laser targets and for guiding the choice of future drivers. As shown in Fig. 3-37, the laser-plasma coupling is determined by a rich variety of processes occurring in the plasma with density $\lesssim n_c$, the critical density. Our continuing program to quantify the impact of these various processes on absorption and hot-electron generation is described in this section.

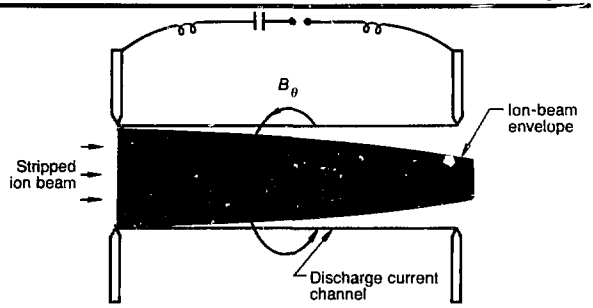

Fig. 3-36. Supplementary focusing using stripped-ion beam in external magnetic field.

We have continued to give particular attention to coupling processes that generate high-energy electrons, since these electrons have such a major impact on target performance. Hot-electron generation by resonance absorption and by the Raman and two-plasmon-decay instabilities have been both predicted and confirmed in experiments. Our recent work on these important topics is reported below in "Simulations of Hot-Electron Generation Near Critical Density," "Raman Instability with High Background Temperature or Magnetic Fields," and "Finite Bandwidth Effects in Resonant Absorption." We have also continued to examine other potentially strong mechanisms for hot-electron generation, such as parametric instabilities near the critical density and absorption on drift-excited ion turbulence ("Hot Electrons from Laser Absorption on Ion Acoustic Turbulence" and "Parametric Instabilities Near the Critical Density in Steepened Density Profiles"). In addition, we have developed improved models to calculate how hot electrons couple with laser-fusion targets ("Coupling of Hot Electrons to Laser-Fusion Targets").

The laser–plasma coupling has been predicted to improve as the wavelength of the light is decreased. A major fraction of the plasma group's resources this year has been devoted to the design and interpretation of an extensive series of Argus experiments to test our wavelength-scaling predictions. This close collaboration with the experimental program (whose results are reported in "Laser-Fusion Experiments and Analysis" in Section 6) has been very fruitful and has substantially enhanced our confidence in

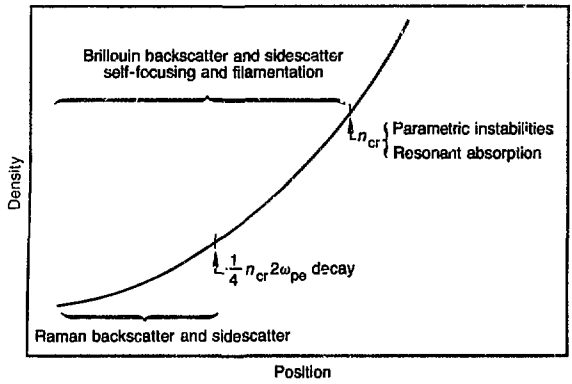

Fig. 3-37. Regions of density where various laser-plasma coupling processes are operative.

our theoretical modeling. We have begun to plan the laser-plasma coupling experiments for our future, larger, lasers. These experiments will be crucial to confidently scale our coupling models to the much larger underdense plasmas that will be characteristic of high-gain targets driven by multimegajoule lasers. We continue to emphasize that measurements of the underdense plasma conditions are crucial to both test and guide our models for the coupling.

We have also devoted some effort this year to important theoretical issues not directly linked to hot-electron generation. Recent work on Brillouin scatter is reported in "Time Evolution of Stimulated Brillouin Scattering in Bounded Systems" and "Effect of Ion Collisionality on Ion Acoustic Waves." An improved computational model for thermal-electron transport is under development. We have also continued to develop new long-time-step techniques for plasma simulation. This work is described in "Simulation of Long-Time-Scale Plasma Phenomena." Finally, we continued measurements of parametric instabilities that produce hot electrons. This work is presented in "Hot Electron Production Caused by Parametric Instabilities."

Author: W. L. Kruer

Simulations of Hot-Electron Generation Near 0.25 Critical Density

This article is an update of the *1980 Laser Program Annual Report*.[67] We are continuing our two-dimensional simulation studies of the high-frequency instabilities that occur near 0.25 critical density (n_c). These parametric instabilities are the $2\omega_{pe}$ instability; the decay of the incident electromagnetic wave at ω_0 into two electron plasma waves; and the Raman instability, in which the decay waves are a plasma wave and an electromagnetic wave at approximately half the frequency of the incident wave. From the frequency-matching conditions, the $2\omega_{pe}$ instability occurs near 0.25 n_c, and the Raman instability occurs at or below 0.25 n_c.

The major concern for laser-fusion target designs is the generation of an unwelcome high-energy electron component. Last year, we discussed our ZOHAR[68] simulations, which showed that the absorption by $2\omega_{pe}$ and Raman produces a heated electron distribution that is approximately Maxwellian, with $T_{hot} \propto (I\lambda_0^2)^{1/3}$ near 0.25 n_c. The simulation results emphasize that the amount of $\omega_0/2$ detected is an underestimate of the absorption by these high-frequency instabilities.

The intensity range over which the above results hold has been extended. The previous results were for $v_{osc}/v_e < 1$, where v_{osc} is the quiver velocity of an electron in the electromagnetic wave, and v_e is the electron thermal velocity. The new simulation has $v_{osc}/v_e \sim 2$ with incident intensity 3×10^{16} W/cm^2 (for 1-μm light) on a plasma slab with background electron temperature T_e = 3 keV and $ZT_e/T_i = 3$ with density 0.195 to 0.235 n_c in 25 vacuum wavelengths (λ_0). The high-frequency instabilities scale as expected from the earlier ZOHAR simulations. The temperature of the heated electron distribution, T_{hot}, is ~190 keV, increasing as $(I\lambda^2)^{1/3}$ from the 90-keV T_{hot} for the 3×10^{15} W/cm^2 incident intensity on the same slab. The absorption is ~40%, with ~10% of the incident light in $\omega_0/2$ emission. At 3×10^{15} W/cm^2, the corresponding results are 32% absorption and 8% $\omega_0/2$ emission. Thus, the absorption into hot electrons by the $2\omega_{pe}$ and Raman instabilities is only weakly dependent on intensity, and the $\omega_0/2$ emission is still only a lower bound on the absorption. Raman scatter below 0.25 n_c is discussed in Ref. 69, and the modulational instability of the scattered $\omega_0/2$ light is treated in Ref. 70.

However, the ion response changes dramatically at the higher intensity. Here we

are referring to Brillouin scattering or filamentation, not to the role of the ions in saturating the high-frequency instabilities. The latter effect has been identified in Ref. 71, and ion fluctuations associated with the saturation of the $2\omega_{pe}$ instability have been seen experimentally by Baldis and coworkers.[72]

At 3×10^{16} W/cm^2, the biggest change was the filamentation of the incident plane wave by $\omega_0 t = 2400$, or 1.4 ps for 1-μm light. The appearance of filamentation at the higher intensity is consistent with the threshold for filamentation in the transverse magnetic polarization

$$\lambda_D^2 < \frac{1}{2}\left(\frac{v_{osc}}{c}\right)^2 \left(\frac{1}{k_y^2} - \frac{1}{k_0^2}\right) \quad , \tag{49}$$

where $k_y = 2\pi/L_y$, and L_y is the system length in the y-direction. At 3×10^{16} W/cm^2, the intensity is approximately seven times above threshold, while 3×10^{15} W/cm^2 is below threshold. The higher-intensity simulation was not continued beyond this point. However, the filamentation of the incident light underscores how likely filamentation is in the large volumes of plasma envisioned for reactor targets. Then, the intensity at 0.25 n_c would be higher than the incident intensity, and T_{hot} would be higher than estimates based on nominal intensities.

Also, at 3×10^{16} W/cm^2, there was more Brillouin backscatter ($\sim$10%) in comparison with the level at the lower intensity ($\sim$1%). This increase in Brillouin scatter did not affect the scaling associated with the high-frequency instabilities.

In two simulations at 3×10^{15} W/cm^2, a modest change in Brillouin scattering also did not change either T_{hot} or the level of $\omega_0/2$ emission. The ratio ZT_e/T_i was increased from 3 (the usual level) to 10, and the Brillouin level went from 1% to several percent; that was the only altered result in the simulation.

All of the simulations mentioned above, and those discussed last year,[67] were done with a background electron temperature of T_e of 3 keV. Another set of simulations was aimed at establishing the dependence of T_{hot} on background temperature. The preliminary estimate is that T_{hot} should increase with increasing T_e. As T_e increases, Landau damping limits the instability decay waves to higher phase-velocity waves.

Two cases were run at 3×10^{15} W/cm^2. At 10-keV background temperature, the plasma slab was 25 λ_0 at density 0.23 n_c. The 7-keV slab had the usual shallow profile going from 0.195 n_c to 0.235 n_c in 25 λ_0. For both simulations T_{hot} *decreased* from 90 keV at $T_e = 3$ keV. At 7 keV, T_{hot} was 80 keV and decreased to 60 keV at 10-keV background temperature.

The unexpected behavior of T_{hot} is a symptom of a fundamental change in the character of the high-frequency instabilities. At 3 keV, the growth rate is typically $\gamma_{max}/3$, where $\gamma_{max} = k_0 v_{osc}/4 \approx 0.03\,\lambda_\mu (I_{15})^{1/2}$. At the higher temperatures, the growth rate falls to $\sim\gamma_{max}/10$.

We therefore hypothesize that, at these higher background temperatures, the instabilities have become kinetic, by which we mean the following. Let ω_1 be a longitudinal wave, ω_s a scattered electromagnetic wave, and (ω_0, k_0) the incident electromagnetic wave. Then Raman scattering $\omega_0 \rightarrow \omega_s + \omega_1$ becomes stimulated Compton scattering,[73] $\omega_0 \rightarrow \omega_s + kv_e$. Similarly for the $2\omega_{pe}$ instability, $\omega_0 \rightarrow \omega_1 + \omega_1$, one or both plasma waves may become kinetic. Either

$$\omega_0 \rightarrow k_1 v_e + \omega_1(k_2) \quad ,$$

where

$$k_2 < 1/\lambda_D < k_1$$

and

$$k_2 \lesssim k_0 \quad , \tag{50}$$

or

$$\omega_0 \rightarrow k_1 v_e + k_2 v_e \quad . \tag{51}$$

These kinetic branches need more theoretical attention. We expect slower growth rates for these instabilities, which are no longer confined to 0.25 n_c and below. The kinetic branch of the $2\omega_{pe}$ instability is difficult to establish experimentally, since it has no well-defined signature.

This set of ZOHAR simulations confirms that the mix of processes in the underdense plasma is a sensitive function of intensity and plasma conditions. The result, $T_{hot} \propto (I\lambda^2)^{1/3}$, holds for intensities that vary by

more than an order of magnitude for $T_e \sim$ 3 keV. Background temperatures of 7 and 10 keV lead to more benign electron distributions in these two-dimensional simulations.

Authors: B. F. Lasinski, A. B. Langdon, and W. L. Kruer

Raman Instability with High Background Temperature or Magnetic Fields

The Raman instability represents the scattering and absorption of laser light[7,8] by stimulated electron plasma waves (epw) in the underdense corona ($n/n_c \lesssim 0.25$, where n = plasma density and n_c = critical density), where $\omega_0 = \omega_{pe}$ is the local plasma frequency. The incident light of frequency ω_0 and wave number k_0 is converted to scattered light of frequency ω_s and wave number $\pm k_s$ plus absorbed light of frequency ω_{epw} and wave number k_{epw}. The $\pm$ symbol refers to Raman forward (+) or back (−) scatter. This instability is of particular concern in large targets, since very hot electrons are nonlinearly generated by the electron plasma wave. As target plasmas have increased in size, Raman scattering has become more important and has received increased attention in both calculations and experiments. We report here how this process is affected by either a very high background electron temperature, such as occurs in targets irradiated with high-intensity CO_2 light, or by self-generated magnetic fields.

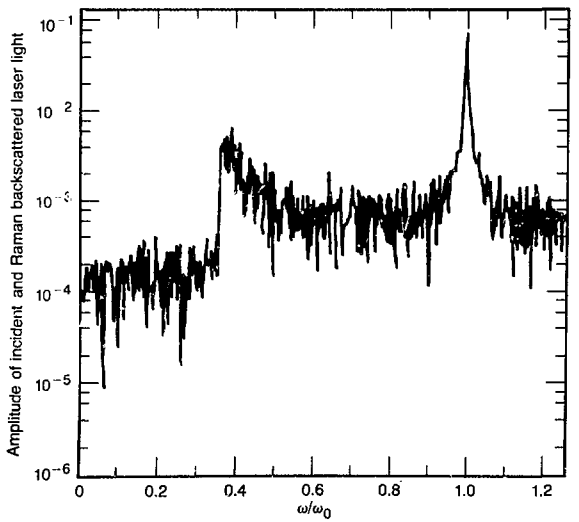

Fig. 3-38. Fourier spectrum of amplitude of incident and Raman-backscattered light from plasma of density 0.15 n_c. Scattered light is strongly red shifted and has large bandwidth.

When the background electron temperature is very high, the Raman-scattered light can peak at a frequency significantly below $\omega_0/2$. In Fig. 3-38, we show the frequency of the reflected and incident light from a 1.5-dimensional, relativistic, electromagnetic, and kinetic simulation in which laser light of intensity $I\lambda_0^2 = 1.2 \times 10^{16}$ W μm^2/cm^2 is propagated through a slab of very hot plasma. Here, I is the intensity and λ_0 is the free-space wavelength of light. The plasma density is 0.15 n_c. The background electron temperature is 64 keV, and the plasma length is 128 λ_0. The peak laser-light absorption was about 46% into hot electrons with a temperature of about 350 keV. Note that the scattered light peaks at a frequency less than 0.4 ω_0, even though the plasma is rather underdense.

In Fig. 3-39, we present simulation results for the absorption, scattered frequency, and heated electron temperature as a function of background plasma density (n). Because of the large damping that increases as $k\lambda_D \propto (T_e/n)^{1/2}$, the resonance width of ω_{epw} and, hence, of the observable $\omega_s = \omega_0 - \omega_{epw}$ (Fig. 3-39) is quite large even though the plasma density is constant. The bandwidth increases rapidly as the density decreases, since the electron Landau damping of the unstable wave increases. Other contributors to bandwidth are different density, which can be estimated from $\omega_s(n/n_c)$ in Fig. 3-39, and sidescatter at both S and P polarizations, which is not considered here.

The frequency of the scattered light that corresponds to the peak growth rate is much lower than is commonly looked for experimentally. In particular, there might be more Raman scattering in recent CO_2 experiments than is apparent from observing scattered light with frequencies ~0.5 to 0.7 ω_0.

We have compared these results with linear theory using the fully kinetic nonrelativistic dispersion relation for Raman and stimulated Compton scattering. For this very high background temperature (~64 keV), we find that the theory is inadequate to describe the wave number of the fastest-

growing mode. This discrepancy appears to be caused by relativistic effects not yet included in the linear theory. For example, the relativistic dispersion relation for electron plasma waves[82] is

$$\omega_{epw}^2 = \omega_{pe}^2 \left[1 - 2.5 (v_e/c)^2 + 3k_{epw}^2 v_e^2 \right] \quad . \quad (52)$$

Here, $(v_e/c)^2 = T_e(\text{keV})/511$. The effective density, which is proportional to ω_{pe}^2, is less by a factor of $1 - 2.5(v_e/c)^2 \approx 0.7$. Comparing the simulations to the theory, we find that the peak growth rate as a function of k can be found by mapping the density multiplied by a factor of 0.7, which crudely models the relativistic effect.

Finally, we point out that the self-generated magnetic fields can significantly reduce the level of Raman backscatter in the nonlinear regime. Any mechanism that inhibits the transport of the hot electrons produced by the instability will enhance the damping of the unstable waves by locally increasing the hot-electron density. The enhanced damping will reduce the level of the scatter and absorption. We tested this idea by putting magnetic fields into simulations and using reflecting boundary conditions for the particles. We then compared the results against simulations with no imposed magnetic fields and with the usual reemitting particle boundary conditions mocking up a free-streaming flux limit. In these simulations, the plasma density was 0.2 n_c, and the background electron temperature was 3 keV. Interestingly, the magnetic-field runs initially showed more Raman backscatter, since the magnetic field rotated the heated-electron velocities into the transverse direction, where they caused less damping. However, as time increased, the magnetic fields led to a severe reduction of Raman backscatter, although Raman forward scatter continued to increase. (However, forward scatter is much more sensitive to density gradients that were zero in these comparisons.) This choking effect caused by self-generated magnetic fields might be especially important in many disk experiments. Figure 3-40 shows the time-integrated $\mathbf{J}\cdot\mathbf{E}$ energy absorbed for two representative runs. In summary, inhibited transport of the Raman-heated suprathermal electrons by magnetic fields can lead to enhanced damping and, hence, decrease the level of Raman absorption into hot electrons.

Authors: K. G. Estabrook and W. L. Kruer

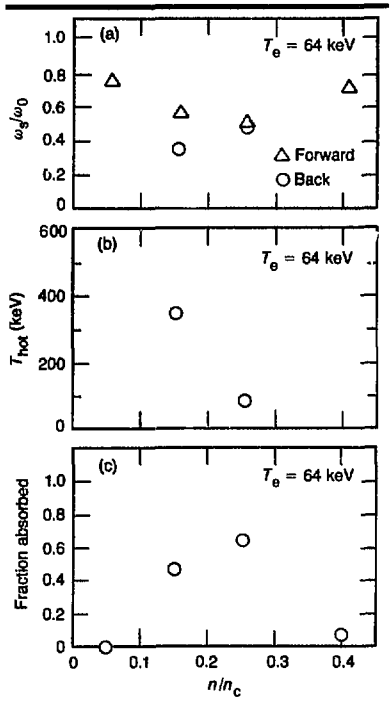

Fig. 3-39. (a) ω_s/ω_0 vs n/n_c by Raman backscatter and forward scatter from 1.5-dimensional kinetic simulations. (b) Heated electron temperatures from simulations for density 0.25, $T_{hot} \sim T_e$. (c) Fraction of laser light absorbed vs density in simulation plasmas 128 λ_0 long at constant density.

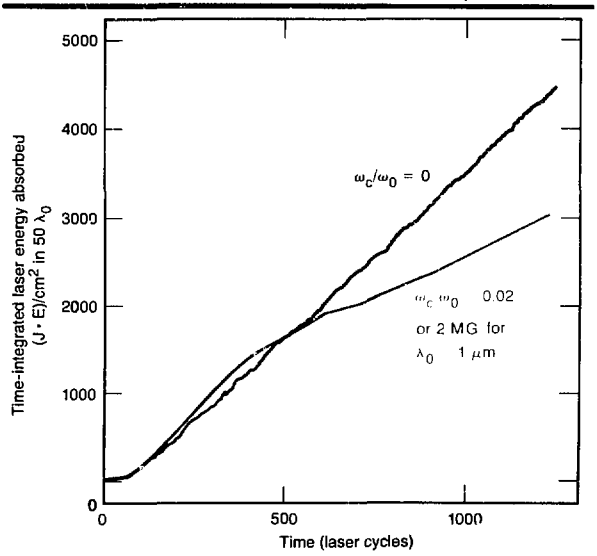

Fig. 3-40. Time-integrated $\mathbf{J}\cdot\mathbf{E}$ energy absorbed by laser light by Raman backscatter and forward scatter with and without magnetic field. Magnetic field inhibits transport of heated electrons that Landau damp the Raman electron plasma waves and decrease Raman absorption.

Finite Bandwidth Effects on Resonant Absorption

In resonant absorption, the laser electric field drives an electron oscillation at critical density, where the local plasma frequency equals the laser frequency. The amplitude of this oscillation grows until, at time t_{b0}, wave breaking occurs and energetic (hot) electrons are produced. Thereafter, a steady state is reached in which energetic electrons carry off the energy absorbed by the driven plasma oscillation. If the driving field has a finite bandwidth, $\Delta\omega$, we expect its coupling to the plasma oscillation to be less efficient and that an associated reduction in the energy of the ejected hot electrons will result.

We have investigated analytically the effect of finite pump bandwidth on the one-dimensional electrostatic (capacitor) model of resonant absorption in cold plasmas with fixed background-density profiles. We find the expected delay in wave breaking and reduction in wave amplitude at breaking for $\Delta\omega t_{b0} > 1$. The power absorbed is unchanged. Particle-in-cell (PIC) simulations are in excellent agreement with the results up to the time of breaking. In the steady state that follows, we find the surprising result that bandwidth *increases* both the average and maximum energy of the ejected hot electrons! Finally, we have performed capacitor-model simulations in warm expanding plasmas with self-consistent ion dynamics. We find that the scaling of the steady-state hot-electron temperature with absorbed pump intensity is unchanged by bandwidths of practical interest. Thus, we expect the hot-electron temperature to scale simply with the electromagnetic absorption fraction.

Under the influence of an external driver field, the displacement, $\delta(x,t)$ of an electron fluid element from its initial position, x, obeys the driven harmonic-oscillator equation[83]

$$\frac{\partial^2\delta}{\partial t^2} + \omega_p^2\delta = \omega_0^2\,\delta_0 e^{i\omega_0 t + i\varphi(t)} \quad . \tag{53}$$

Here, $\omega_p^2 = 4\pi e^2 n(x)/m$ is the local plasma frequency at the background density $n(x)$ $= ZN_i$, ω_0 is the pump frequency, and δ_0 $= eE_0/m\omega_0^2$ is the electron jitter amplitude in the pump field, E_0. The phase of the pump is given by the random variable $\varphi(t)$. We take a linear density profile $\omega_p^2 = \omega_0^2(1 + x/L)$ and decompose δ into a slowly varying amplitude D and a rapidly varying phase

$$\delta = \delta_0 D\, e^{i\varphi(t) + iq\tau^2/2} \quad . \tag{54}$$

We employ the normalized variables τ $= \omega_0 t$ and $q = x/L$. Assuming $\partial(\ln D)/\partial\tau$ $\ll 1$ and $q \ll 1$, we find that Eq. (53) yields

$$\frac{\partial D}{\partial\tau} = \frac{-i}{2} e^{i\varphi(\tau) - iq\tau^2/2} \quad , \tag{55}$$

$$\frac{\partial D_x}{\partial\tau} = \frac{i}{2} D \quad , \tag{56}$$

where we define $D_x = \partial D/\partial x$.

Wave breaking occurs when $\partial\delta/\partial x = -1$, or, effectively, $|D_x| = L/\delta_0$. In the absence of bandwidth, $\varphi = 0$, and Eqs. (55) and (56) may be integrated immediately to obtain $|D_x| = (\tau^2/8)\cdot F(q\tau)$, where $F(y)$ is a function that attains its maximum value of unity at y $= 0$ and is appreciable in the range $|y| < 4\pi$. Thus, the wave breaks first at critical density, $q = 0$, and we recover the well-known result for the breaking time, τ_{b0} $= (8L/\delta_0)^{1/2}$. The electron jitter velocity at breaking is $v_{b0} = \omega_0\delta_0|D| = \omega_0(2L\delta_0)^{1/2}$. The size of the resonant interval decreases with time and, at breaking, is given by $L_{R0} \approx 2L(4\pi/\tau_{b0}) \approx 2\pi\delta_{b0}$. The number of resonant waves within the interval is $n = k_{b0}L_{R0}/\pi$ $\approx k_{b0}\delta_{b0}$, where the wave number of the breaking waves, k_{b0}, is given by the breaking condition $\partial\delta/\partial\chi \approx k_{b0}\delta_{b0} = 1$. Thus, n $= 1$, and the resonant interval contains a single wave.

In the case of finite bandwidth, $\varphi \neq 0$, it is instructive to examine the ensemble average of $|D_x|^2$. We may again integrate Eqs. (55) and (56) to obtain

$$D_x = \frac{1}{4}\int_0^\tau d\tau' \int_0^{\tau'} d\tau''\, e^{i[\varphi(\tau') - \varphi(\tau'')] - iq\tau''^2/2} \quad , \tag{57}$$

so that

$$\langle|D_x|^2\rangle = \frac{1}{16}\int_0^\tau d\tau' \int_0^{\tau'} d\tau'' \int_0^\tau d\tau''' \int_0^{\tau'''} d\tau^{iv} \times \exp\left[-\Delta|\tau'' - \tau^{iv}| - \frac{iq}{2}(\tau'' - \tau^{iv})\right] \quad . \tag{58}$$

Here, we have employed the autocorrelation function of the phase φ

$$\langle e^{i[\varphi(\tau)-\varphi(\tau')]}\rangle = e^{-\Delta|\tau-\tau'|}; \Delta = \Delta\omega/\omega_0 \quad . \qquad (59)$$

The integrals in Eq. (58) may be done exactly, but, in the limit $\Delta\tau \gg 1$, we obtain the compact result

$$\langle|D_1|^2\rangle = \frac{1}{24}\frac{\Delta\tau^3}{\Delta^2 + (q/2)^2} \quad . \qquad (60)$$

Again, the wave is most likely to break at $q = 0$. The breaking time is $\tau_b = (24\Delta L^2/\delta_0^2)^{1/3}$, with the fractional increase being $\tau_b/\tau_{b0} = (3\Delta\tau_{b0}/8)^{1/3}$. The electron jitter velocity at breaking is reduced by a similar factor $v_b/v_{b0} = [(3)^{1/2}/\Delta\tau_{b0}]^{1/3}$. In this case, the size of the resonant interval is $L_R \approx 4\tau L$. The number of waves contained in the interval is $n = k_{b0}L_R/2\pi \approx (2\Delta/\pi)(L/\delta_{b0})(\delta_{b0}/\delta_b) \approx (\Delta\tau_{b0})^{4/3}/8$. Thus, for $(\Delta\tau_{b0})^{1/3} > 2$, the resonant interval may contain many quasi-resonant waves.

In the simple theory just presented, we calculated the average breaking time at the position where breaking is most probable, $q = 0$. However, for any given realization of the random phase φ, breaking can actually occur first at some other nearby position $|q| > 0$. Since we have not accounted for this possibility, we have slightly overestimated the average breaking time; similarly, we have slightly underestimated the breaking velocity. Details of an improved calculation that accounts for this are given elsewhere.[84] The results for the (average) breaking time are summarized in Fig. 3-41. The improved theory preserves the weak $(\Delta\tau_{b0})^{1/3}$ scaling of bandwidth effects, except for a logarithmic correction. The predicted (average) breaking time shown in Fig. 3-41 and breaking velocity (not shown) are in excellent agreement with particle-simulation results.

While the theory is invalid past breaking, we might naïvely expect from the zero bandwidth experience that the lower breaking velocities and wave amplitudes resulting from finite bandwidth would lower the energy of the ejected hot electrons in the time-asymptotic state. Figure 3-42 shows T_h/T_{h0}, the ratio of the hot-electron tem-

Fig. 3-41. Delay in breaking time caused by finite pump bandwidth; ● PIC simulations, ▲ numerical solutions of Eq. (53).

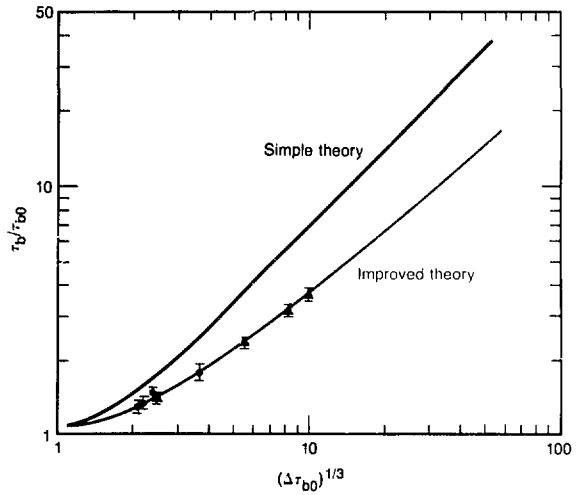

◀ Fig. 3-42. Increase in hot-electron temperature with bandwidth from PIC simulations with fixed-ion background.

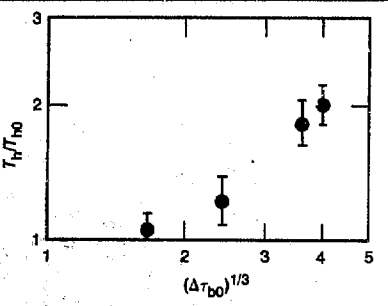

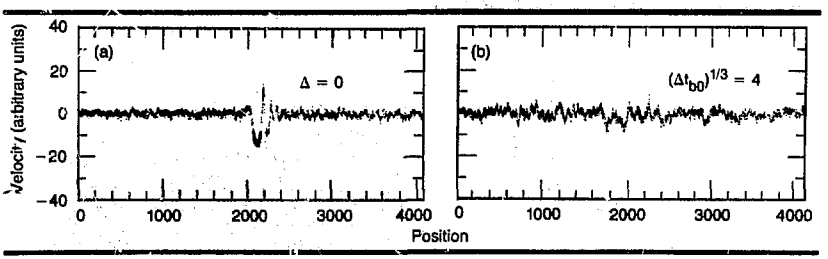

Fig. 3-43. Electron phase space from PIC simulations with $t_{b0} = 900$. For clarity, only one of four electrons with velocity $|v| < 8$ is plotted.

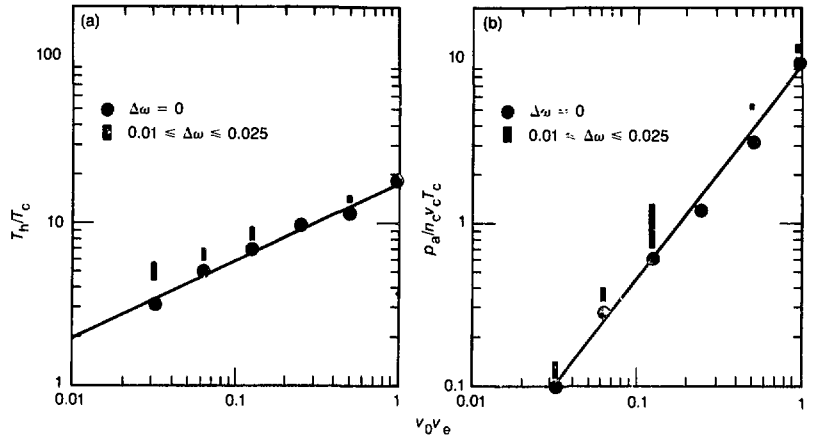

Fig. 3-44. Simulation results with moving ions.

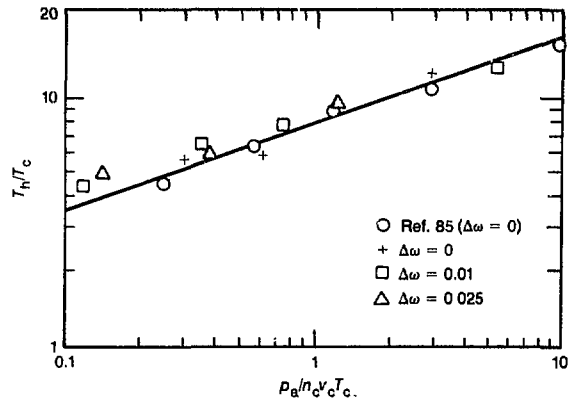

Fig. 3-45. Simulation results of moving ions.

perature with and without bandwidth, as a function of $\Delta\tau_{b0}$ for a fixed ion background. Surprisingly, the hot-electron temperature increases with bandwidth! A plausible physical explanation emerges from examination of the phase-space plots of Fig. 3-43, together with a more detailed consideration of the hot-electron dynamics in the wave structure described after Eq. (60). The amplitude of the individual waves is reduced by bandwidth, but their number increases from just one ($\Delta = 0$) to many ($\Delta > 0$). Energetic electrons born in waves breaking at any point can pick up additional energy in traversing the field structure farther down the density gradient. A simple estimate we can construct is that $T_h \sim \epsilon n$, where $\epsilon \sim mv_b^2 \sim T_{h0}(\Delta\tau_{b0})^{-2/3}$ is the energy obtained in traversing each wave and n is the number of waves traversed. From our previous discussion, we recall the scaling of n as $n \sim (\Delta\tau_{b0})^{4/3}$ and obtain the remarkable result that T_h increases with bandwidth, $T_h/T_{h0} \sim (\Delta\tau_{b0})^{2/3}$. Thus, as bandwidth is increased, the increasing number of waves that an energetic electron traverses more than compensates for the reduced amount of energy it receives from each. For $\Delta\tau_{b0} \leq 1$, these results are modified and $T_h/T_{h0} \approx 1$. Unfortunately, the range of data in Fig. 3-43 is not sufficient to determine the scaling quantitatively.

Finally, we have done simulations of resonant absorption of a noisy pump in warm expanding plasmas, including self-consistent profile modification. We have obtained scalings for T_h vs absorbed intensity in the manner described previously.[85] Our simulation results are shown in Figs. 3-44 and 3-45. The self-consistently steepened density profiles yield $\Delta\tau_{b0} < 1$ for Δ in the range of a few percent or less. Hence, according to the preceding discussion, T_h is expected to be relatively unchanged by bandwidth; yet, as Fig. 3-44 shows, for a given driver strength v_0/v_e both T_h and absorbed power can increase markedly. This may be understood, since analysis of single-particle trajectories shows that a hot electron may spend many laser cycles in the complex resonant-field structure before being ejected. Thus, if the heating time of the particles is greater than Δ^{-1}, bandwidth may affect their orb

even if $\Delta\tau_{b0} \lesssim 1$. Relaxation of the scale length itself because of reduction in the resonant-field amplitude presumably also plays a role.

Remarkably, the scaling of hot-electron temperature with the absorbed pump intensity shown in Fig. 3-45 is unchanged by bandwidth to within estimated errors. These results imply that bandwidth influences T_h only via the electromagnetic absorption fraction that cannot be addressed with our electrostatic models.

Authors: C. J. Randall, J. R. Albritton, and E. A. Williams

Hot Electrons from Laser Absorption on Ion Acoustic Turbulence

We consider laser absorption on short-wavelength ion turbulence driven by electron–ion streaming instabilities.[86–89] Contrary to linear theory, which predicts that the turbulent spectrum $\varphi(k)$ peaks at $k\lambda_D \sim 0.7$, basic plasma experiments find that $\varphi(k)$ peaks at $k\lambda_D$ values between about 0.04 and 0.2 (Table 3-4). We show by theory and simulation that the laser absorbs most strongly at densities from 0.7 to 1.2 times critical density (n_c) and produces hot electrons [with temperatures from about 5 to 70 times the cold-electron temperature (T_e), depending on the density] that are another source of preheat, which may reduce the compression and yield of laser-fusion targets. These hot electrons may be avoided by using long underdense scale lengths, a short-wavelength laser, or both to absorb the light before it reaches $0.7\,n_c$ targets.

One of the many absorption mechanisms for laser light is ion turbulence, which is driven by a relative drift between the ions and electrons. The drift is assumed to be caused by an electric field that accelerates thermal electrons into the heating region to replace hot electrons streaming out. This is the same ion turbulence often assumed to be partly responsible for transport inhibition, since it is well above theoretical threshold. Some of the laser power is irreversibly absorbed when the electrons oscillating in the laser electric field (E) couple to the ion waves to drive electron plasma waves (epw), which heat electrons as they damp and break. The wavelength of epw is predominantly determined by ion acoustic fluctuations. Reference 86 describes the fraction of light absorbed and electron distributions produced by a given wavelength of ion fluctuations. Here, we extend this work by using experimentally measured electron–ion drift turbulence spectra[90–95] as input to determine the important features of the absorption. The experiments[90–95] use much smaller densities and much longer time scales than those of laser fusion, but $k\lambda_D$ and $v_d/v_e \sim 0.1$ scale similarly. Here, $k = 2\pi/\lambda_{epw}$, λ_D is the Debye wavelength, v_d is the drift velocity, and $v_e^2 = T_e/m_e$. Data from these experiments[90–95] show that the peak of the spectrum from electron–ion drift turbulence is at a surprisingly long wavelength ($k\lambda_D \sim 0.2$). The significance of the long wavelength is that epw will have a reasonably large phase velocity

$$v_p/v_e = [3 + 1/(k\lambda_D)^2]^{-1/2} \qquad (61)$$

and, hence, a fairly hot electron temperature

Table 3-4. Summary of results for basic plasma experiments where laser pulse is absorbed on short-wavelength ion turbulence driven by electron–ion streaming instabilities.

Reference	Results
90 (Stenzel)	$v_d < 0.1\ v_e$, peak at $\omega/\omega_{pi} \sim 0.18$, $\delta n/n > 0.2$
91 (Yamada & Raether)	$v_d \sim 0.1\ v_e$, peak at $\omega/\omega_{pi} \sim 0.08$, $\delta n/n \sim 0.03$ to 0.1
92 (Amagishi)	$v_d \sim v_e$
93 (Kawai & Guyot)	$v_d \sim 0.1\ v_e$, peak at $\omega/\omega_{pi} \sim 0.05$, $\delta n/n < 0.15$
94 (Bollen)	Peak at $\omega/\omega_{pi} \sim 0.16$, $\delta n/n \sim 0.2$ to 0.3
95 (Hollenstein et al.)	$v_d/v_e \sim 0.01$ to 0.2, $\delta n/n \sim 0.001$ to 0.1, peak at $\omega/\omega_{pi} \sim 0.04$ to 0.09
96 (Slusher et al.)	$v_d/v_e \sim 0.1$ to 0.18, peak at $k\lambda_D \sim 0.5$, $\delta n/n \sim 10^{-4}$
97 (Wong et al.)	$v_d/v_e \sim 0.3$, peak at $\omega/\omega_{pi} = 0.5$, $\delta n/n = 0.01$
97 (Muraoka et al.)	Shock, $T_e = T_i$, peak at $\omega/\omega_{pi} = 0.5$
99 (Quon et al.)	$v_d/v_e \sim 4$ to 5, $\delta n/n \sim 0.05$ to 0.1, peak at $\omega/\omega_{pi} \sim 0.5$

$$T_{hot}/T_e \sim \left[1.5 + 1/\left(2k^2\lambda_D^2\right)\right] \times [1 \text{ to } 2] \quad , \qquad (62)$$

or about 20 for $k\lambda_D \sim 0.2$. The experimentalists actually measure the frequency, f, rather than wavelength. The two are related by

$$f/f_{pi} = k\lambda_D \left\{\left[1 + 3T_i/(zT_e)\right]/\left(1 + k^2\lambda_D^2\right)\right\}^{1/2} \quad , \qquad (63)$$

where z is the ion charge state, $f_{pi} = (4\pi ne^2/m_i)^{1/2}/2\pi$ is the ion plasma frequency, and n is the electron density. The experiments do not agree on where the frequency peak is located, and most[90,95] find it at f/f_{pi} and $k\lambda_D$ values between 0.04 and 0.2. Some workers[96,97] do find the spectrum peaks at $k\lambda_D \sim 0.5$, but they report such small turbulence amplitude, $\delta n/n$, that it is not surprising their results agree with linear theory.[98] Reference 99 also reports a spectrum that peaks at 0.5, but the v_d/v_e value is between 4 and 5, which is much greater than expected for laser-fusion plasmas (where v_d is probably from 1 to 5 times c_s). References 100 and 101 use laser spectroscopy to examine the $\delta n/n$ at $k\lambda_D = 0.5$ for laser-produced plasmas and report sizable amplitudes there, but do not describe amplitudes at longer wavelengths. This variation in the literature is unfortunate, since the total absorption and T_{hot} depend sensitively on the $k\lambda_D$ of the peak. However, the discrepancies serve to emphasize the still mysterious nature of the ion acoustic instability. Experiments need to be done to extend the work of Refs. 100 and 101 by looking at the wavelength and angular spectrum for laser-produced plasmas (preferably produced by a heating laser with $\lambda_0 \leq 1$ μm), much as done in Ref. 96 for low-density plasmas.

We begin our analysis with single modes and then go to a spectrum of modes. We have analytically calculated the fraction of light absorbed as a function of the ratio of plasma density to critical density (n/n_c). We also calculated the $k\lambda_D$ of the ion waves using the complex dielectric function of the electron plasma waves at that wavelength and frequency, using the methods of Refs. 86 and 89. The results are shown in Fig. 3-46. Since Fig. 3-46 shows each mode separately, thus separating out the effects of each mode, it is not applicable to our experiments.

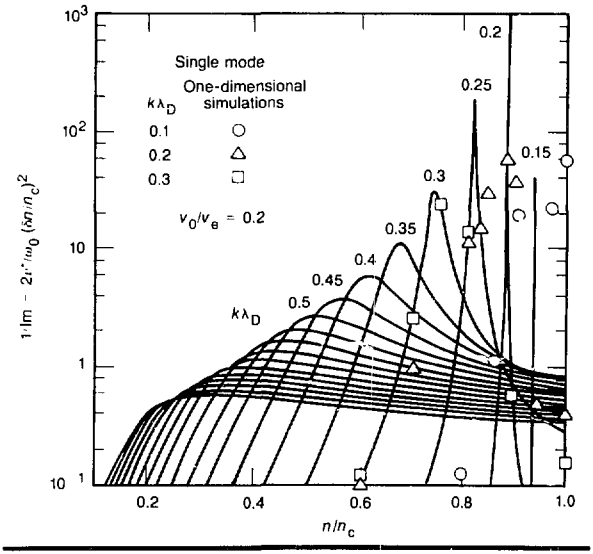

Fig. 3-46. Effective collision frequency [times $2/(\delta n/n_c)^2$] for single modes of $k\lambda_D$; solid lines are analytically calculated $1/\text{Im } \epsilon$.

Figure 3-46 also shows the results of one-dimensional electrostatic simulations[102] based on a fixed single sinusoidal mode of an ion wave. All the one-dimensional computer runs in this article had $v_{osc}/v_e = 0.2$ (where $v_{osc} = eE/m_e\omega_0$, and ω_0 is the angular frequency of E) with E added uniformly to the self-consistent electrostatic field. A plot of the electron kinetic energy in the simulations revealed that the heating was at first very slow as epw grew from noise. Then, the heating became quite rapid as the epw trapped electrons. Finally, the plasma became so hot that epw became very highly damped, and the heating rate dropped to a small value. The calculations of the effective collision frequency (ν^*) were made during the period of most rapid heating. The simulations ($k\lambda_D < 0.2$) show that the resonance width of the heating is broader in density than the linear theory because of mode coupling and increased damping by the trapped and heated electrons.

The simulations in Fig. 3-47 used a fixed spectrum of ion turbulence that matched the shape of the experimental spectrum. For $k\lambda_D = 0.5$, 32 modes were used. The longer wavelengths used 64 to 128 modes of random phase, $\Sigma n_i(k)^2 = 0.01$, rms $(n_i - 1) = 0.07$. The simulation results for absorption and temperatures depend on the high-frequency falloff [we used $(f/f_{pi})^{-2.3}$] and on the shape for frequencies below the peak. The runs for Fig. 3-47 were made with the modes in random phase. Changing the random-number generator or making the phases all zero (simulating a steepened sawtooth-shaped ion acoustic wave) caused variations in ν^* and the heated temperatures by, typically, a factor of 2. Interestingly, runs above critical density with peak $k\lambda_D = 0.17$ showed surprisingly large absorption ($\nu^* \sim 0.05$) up to $n/n_c < 1.2$ for $T_{hot}/T_e \sim 15$, with reasonable absorption up to $n/n_c \sim 2$. Of course, the light must be incident nearly perpendicular to tunnel into these overdense regions.

At constant $n/n_c = 0.87$ and $k\lambda_D = 0.17$, we tested the theoretical scaling of $\nu^*/\omega_p = [\Delta(KE/KE_0)/\Delta(\omega_p t)](v_e/v_{osc})^2$, where KE (KE_0) is the total (initial) kinetic energy. We found the scaling to be quite good for v_{osc}/v_e values of 0.1, 0.2, and 0.3. We then tested the consistency of $1/\mathrm{Im}\,\epsilon = 2\nu^*/[\omega_0 \Sigma(\delta n/n_i)^2]$ (where Im ϵ = imaginary part of the dispersion, ϵ) for rms $\delta n/n$ values of 0.015, 0.05, 0.15, 0.19, and 0.38 and found that the scaling relationship $\nu^* \sim (\delta n/n)^2$ holds for smaller amplitudes (rms $\delta n/n$ values <0.05). It reduces to $\nu^* \sim (\delta n/n)^\alpha$ (where $\alpha < 3/2$) for the higher amplitudes because of increased damping from the very rapid heating and rapid mode coupling to higher modes.[87,89] References 90 to 94 report measurements of $\delta n/n$ to be typically 0.1 to 0.3 for laser-fusion regimes. Estimates[86] of time-averaged $\langle \delta n/n \rangle_t$ give

$$\left\{\left[(1 + 3T_i/ZT_e)/(1 + k^2\lambda_D^2)\right]^{1/2} - (3T_i/ZT_e)^{1/2}\right\}^2/3 \quad . \qquad (64)$$

For large pumps, the heating rate can be reduced if the electron excursion amplitude, $eE_{tot}/\omega_0^2 m_e$, becomes larger than λ_D.

The fraction of light absorbed is

$$1 - \exp\left[-2\pi(\nu^*/\omega_0)(\ell/\lambda_0)/(1 - n/n_c)^{1/2}\right] \qquad (65)$$

in each light direction,[103] where ℓ/λ_0 is the light-path length in vacuum-wavelengths. An experimental diagnostic of ion turbulence or parametric instability absorption is the appearance of red-shifted 2ω light.[104]

The electron-heating mechanism is trapping (Fig. 3-48), which can occur even for fairly low v_{osc}/v_{e} since the electrostatic wave amplitude is proportional to $v_{osc}/$ damping.[103] Our fixed-ion single-mode kinetic simulations find the heated electron distribution (f_e, the insert plot in Fig. 3-48) to be approximately Maxwellian with a temperature $T_{hot}/T_e \approx m_e v_p^2/2$, truncated at a speed of about $v_p + 3v_e$. In runs where the broad ion spectrum of the experiments was used (Fig. 3-49) the hot distribution was nearly Maxwellian (no truncation, with $T_{hot}/T_e = m_e v_p^2/2$). The broad $\varphi(k)$ heated electron distribution can be analytically

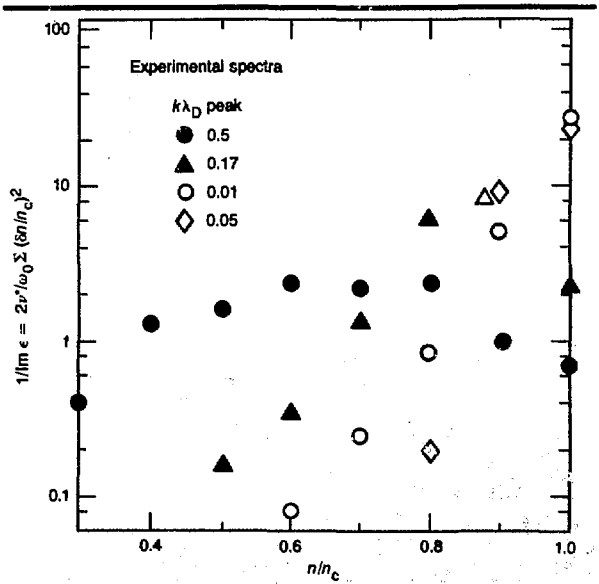

Fig. 3-47. Effective collision frequency [times $2/(\delta n/n_c)^2$] from electron-ion drift-induced turbulence spectra, from Refs. 89 to 93, with spectral peaks at $k\lambda_D$ indicated.

To convert this graph into an effective collision frequency, multiply by an assumed turbulence level $[(\delta n/n)(n/n_c)]^2/4$. The extra factor of 2 is to convert from one-dimensional to three-dimensional simulation, assuming an averaging over angles.[86]

constructed from the sum over k of the truncated single-mode distributions

$$\sum [v^*(k)][\varphi(k)] \times \exp\left[-\text{energy}/T_{hot}(k)\right] , \quad (66)$$

where (k) is from Fig. 3-46 and exp is truncated at speed $v_p + 3v_e$. The term T_{hot} increases with time, caused by v_p increasing from the heating. The heat flux is in the direction of the laser electric field. We extend the analysis to two-dimensional simulations[105] in Fig. 3-50. We find that $T_{hot}/T_e \sim 25(L/\lambda_D)^{0.2}$ for a $k\lambda_D$ peak about 0.17 and $v_{ose} = v_e$. Moving-ion runs (parametric decay and oscillating two-stream instabilities) show L/λ_D values of about 0.5 to 0.7 for v_{ose}/v_e values from 1 to 0.5 [$L = n_c(\Delta x/\Delta n)$]. Because of the inherent problem of mapping the experimental homogeneous turbulence to a density gradient ($\lambda_D \propto n^{-1/2}$), we tested the sensitivity of T_{hot}/T_e to two kinds of turbulence representations and to a 0.6 n_c density shelf[105] (⊕,⊖) before critical density. In one kind of turbulence (●, x, O, △, ◇, and □), $\varphi[k\lambda_D n(x)]$ is constant, but not isotropic (i.e., x∥ ∇n). The other kind of turbulence (⊗ , ⊖, ▽, and ⊕), which is homogeneous and isotropic [with $\varphi(k)$ constant in angle and random x,y phases] was mapped to $n(x)$ with $\delta n/n$ constant. However, $\varphi(k\lambda_D)$ peaks at $k\lambda_D \sim 0.17$ only for $n \sim 0.9\ n_c$ because of random phases and $\nabla n(x)$. If we consider the electrons to then equilibrate[105] to a hot three-dimensional temperature, the resulting T_{hot} would be 67% of that shown. In addition to ion acoustic turbulence, critical-surface ripples[106,107] by a Rayleigh–Taylor instability would also provide ion-density perturbations for this type of absorption. To avoid these hot electrons, we can decrease the laser intensity (lower T_e), the wavelength (increase n_c), or both to favor inverse bremsstrahlung absorption, which is proportional to $n/T_e^{3/2}$. Possibly reactor targets will have long enough density gradient lengths (or be irradiated with short enough laser wavelengths) to absorb the light before density of 0.7 n_c is reached.

We acknowledge valuable conversations with W. L. Kruer and J. S. DeGroot.

Author: K. G. Estabrook

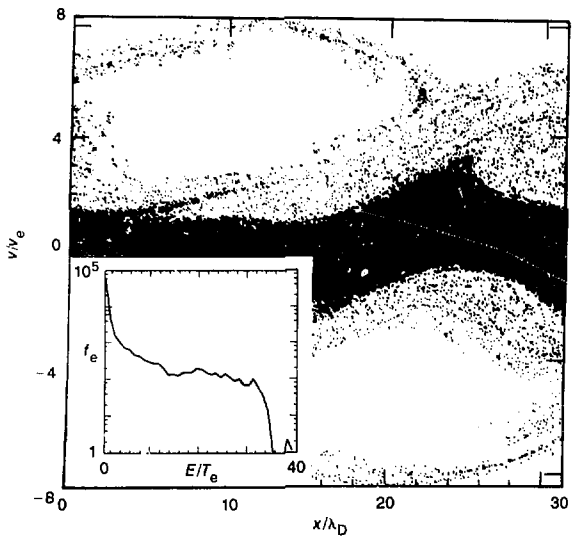

Fig. 3-48. Electron phase space from one-dimensional simulation; fixed single-ion mode, $k\lambda_D$ 0.2, $\delta n/n$ 0.1, n/n_c 0.87, and v_{ose}/v_e 0.2. Note strong trapping for relatively weak pump.

Parametric Instabilities Near the Critical Density in Steepened Density Profiles

The generation of energetic electrons by laser–plasma coupling processes is a topic of great interest, since such electrons preheat the laser-fusion capsules. Any process that generates electron plasma waves with a high phase velocity is a potential source of preheat, since such waves characteristically heat the faster, more nearly resonant electrons. Hot-electron generation via the electron plasma waves generated by resonance absorption and by the Raman and $2\omega_{pe}$ instabilities has been both predicted and observed[108–110] in laser experiments. On the other hand, in recent years, relatively little attention has been given to another potential source of hot electrons, i.e., the ion acoustic decay and oscillating two-stream instabilities. These instabilities[111] represent the decay of laser light into electron and ion waves near the critical density. As we will show, these instabilities can occur ever

in ponderomotively steepened density profiles. We will first discuss the results of two-dimensional simulations, which both show the instabilities in operation and illustrate salient properties of interest, such as the fractional absorption and the heated electron energies. Then, we will estimate the steepened density scale length near the critical density and obtain a criterion for instability generation.

Simulations of Instability Absorption. We use a two-dimensional electromagnetic relativistic particle code to simulate laser light normally incident on a plane slab of plasma. The light propagates from vacuum onto an inhomogeneous overdense slab of plasma. The particles reflect at the vacuum-plasma interface and are reemitted with their initial temperature at the high-density boundary, simulating contact with denser plasma in the interior of a target. In the simulations, we follow variations both along the direction of the propagation vector of the incident light (the x direction) and along its electric vector (the y direction). Periodic boundary conditions are imposed in the y direction. The simulations are run until well after the density profile is steepened by the ponderomotive force of the light wave.

In typical simulations, we observe the simultaneous growth of both electron and ion waves near the critical density. The unstable waves have wave vectors preferentially along the electric vector of the incident light. In Fig. 3-51, we show a contour plot of the electrostatic potential, Fourier analyzed in the y direction, as a function of both the electron density in the steepened profile and the wave vector in the y direction. These results are from a simulation in which $\theta_e = 4$ keV and $I\lambda_\mu^2 = 10^{15}$ W μm^2/cm^2, where θ_e is the background electron temperature, and $I(\lambda_\mu)$ is the intensity (wavelength in micrometres) of the incident laser light. As expected from the linear-instability theory, the potential reaches a peak near the critical density. In addition, the electrostatic potential exhibits two distinct lobes in wave vector space, reflecting both the ion acoustic decay and oscillating two-stream instabilities.

Correlated with the growth and saturation of the electrostatic waves, a tail of hot electrons is generated. In contrast to electron heating by resonance absorption,[112] the electrons are now heated preferentially in the direction of the electric vector of the light. We find that the heated tail has a roughly Maxwellian velocity distribution, with a temperature similar to that produced by resonance absorption. Figure 3-52 shows the hot-electron temperature found in a number of different simulations where $I\lambda_{0\mu}^2$ was varied over three orders of magnitude. In these simulations, the fraction of the incident laser light energy absorbed into the hot-electron tail was typically $\simeq$10 to 20%.

Steepened Scale Length. Since the density profile steepening plays an important role in parametric instability absorption near the critical density, it is instructive to

Fig. 3-49. Heated electron temperature vs density from one-dimensional simulations (Fig. 3-47).

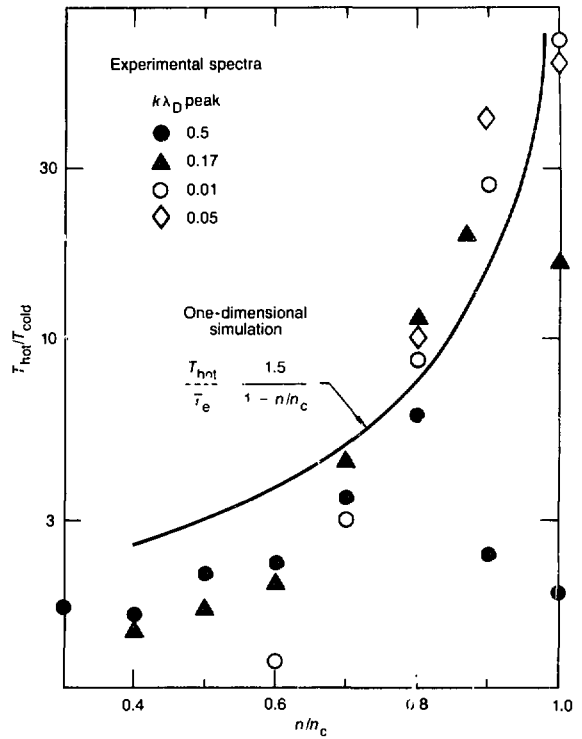

The turbulence spectrum is broad enough so that, at high densities, the pump couples to its resonant long wavelengths. At low densities, it couples to the shorter wavelengths and gives, roughly, $T_{hot}/T_e \sim 1.5/(1 - n/n_c)$, which is simply found from the Bohm-Gross relation with $T_{hot}/T_e \sim (v_p/v_e)^2/2$.

estimate the steepened scale length. We have investigated the simplest model of profile steepening, assuming a normally incident light wave reflecting from the critical surface of an isothermal, freely expanding, collisionless plasma. Our analysis parallels that of Ref. 113, except that we explicitly obtain the scale length near the critical density by removing the Wentzel-Kramers-Brillouin (WKB) assumption on the field structure.

The basic idea is that twice the pressure of the light wave is taken up by the plasma near the reflection point, and this momentum deposition locally steepens the density profile near the critical density. Adopting a fluid description of the plasma and considering planar geometry, we readily obtain equations of the density (n) and flow velocity (u) in the frame moving with the steepened structure

$$\frac{\partial}{\partial x} nu = 0 \quad , \tag{67}$$

$$\frac{\partial}{\partial x}\frac{u^2}{2} = -c_s^2 \frac{\partial}{\partial x} \ln n - \frac{Zm}{4M}\frac{\partial}{\partial x} v_w^2 \quad . \tag{68}$$

Here, m is the electron mass, $M(Z)$ is the ion mass (charge state), c_s is the ion sound velocity $= (Z\theta_e/M)^{1/2}$, and v_w is the oscillation velocity of an electron in the electric vector of the light wave. If we normalize the flow velocity to the sound speed and substitute from Eq. (67) into Eq. (68), we obtain

$$(1 - u^2)\frac{1}{n}\frac{\partial n}{\partial x} + \frac{\partial}{\partial x}\frac{v_w^2}{4v_e^2} = 0 \quad , \tag{69}$$

where v_e is the electron thermal velocity. Since the density gradient remains finite, it is clear that the sonic point ($u = 1$) must be at the maximum of the field of the standing light wave, i.e., where $\partial v_w/\partial x = 0$. Integrating Eqs. (67) and (69), we then obtain

$$\left(\frac{n_s}{n}\right)^2 + 2\ln\left(\frac{n}{n_s}\right) + \frac{v_w^2}{2v_e^2} = 1 + \frac{v_{max}^2}{2v_e^2} \quad . \tag{70}$$

Here, n_s is the density at the sonic point, and v_{max} is the value of v_w at the maximum of the standing wave. As noted in Ref. 113, there are two solutions of Eq. (70): $n_1 < n_s$ ($u_1 > 1$), which corresponds to a lower density plateau; and $n_2 > n_s$ ($u_2 < 2$), which corresponds to the upper density shelf. Figure 3-53 shows a schematic of the steepened density profile.

To make further progress, we must now relate the density at the sonic point to the critical density (n_c) by considering the solution for the standing electromagnetic wave. We do this by approximating the density profile as locally linear from n_s to n_c and fitting to the well-known Airy-function solution[114]

$$E = \alpha A_i\left[\left(\frac{\omega^2}{c^2 L}\right)^{1/3}(L - X)\right] \quad , \tag{71}$$

where α is a constant determined by fitting to the incoming light wave. This locally linear assumption is a good approximation when $v_{osc}/v_e < 1$, where v_{osc} is the oscillation velocity of an electron in the free-space value of the electric field of the light. The assumption fails when $(v_{osc}/v_e)^2 \gg 1$, since the jump in density becomes too large.

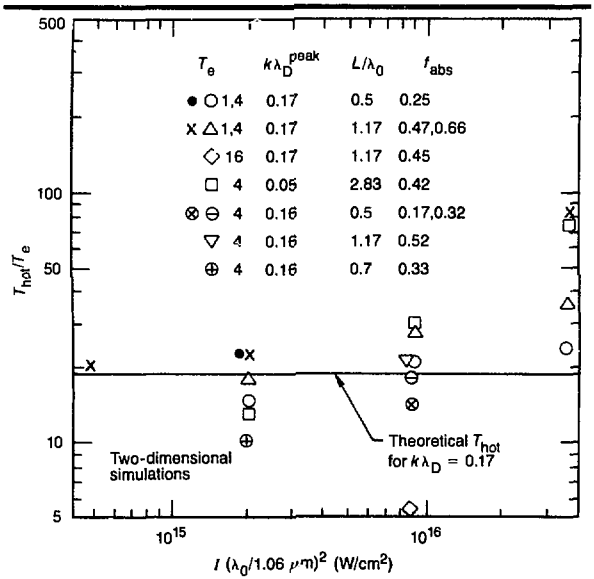

Fig. 3-50. Heated electron temperatures from two-dimensional simulations of fixed ion turbulence; f_{abs} is average fraction light absorbed.

If the ordinate is $T_{hot}/(T_e + m_e v_{osc}^2/2)$ the points form a more horizontal line nearer the theory shown; ◇, □ may not have enough statistics to resolve higher temperatures.

Matching the peak of the Airy-function solution to the field at the sonic point, we obtain $v_w^2(n = n_c) = 0.44\, v_{max}^2$. In addition, we note that the sonic point and the critical point are separated by $\Delta x = (c^2 I/\omega^2)^{1/3}$. Equation (70) then becomes

$$\left(\frac{n_s}{n_c}\right)^2 + 2\ln\frac{n_c}{n_s} = 1 + 0.28\frac{v_{max}^2}{v_e^2} \quad . \tag{72}$$

The solutions for n_1, n_s, and n_2 are now straightforward. For weak fields ($v_{osc}/v_e \lesssim 0.1$), analytic results can be given

$$\begin{aligned}
\frac{n_s}{n_c} &\simeq 1 - 0.77\left(\frac{v_{osc}}{v_e}\right)^{0.8} \quad , \\
\frac{n_s}{n_1} &\simeq 1 + 0.97\left(\frac{v_{osc}}{v_e}\right)^{0.8} \quad , \\
\frac{n_s}{n_2} &\simeq 1 - 0.97\left(\frac{v_{osc}}{v_e}\right)^{0.8} \quad ,
\end{aligned} \tag{73}$$

$$\frac{\omega L}{c} \simeq 1.5 \Big/ \left(\frac{v_{osc}}{v_e}\right)^{1.2} \quad .$$

For more intense fields, numerical solutions of the transcendental equations are required. Results for the densities, shown in Fig. 3-54, are in good agreement with the earlier results of Ref. 113. The steepened scale length is plotted as a function of v_{osc} in Fig. 3-55. In the interesting regime typical of many current applications ($0.1 \lesssim v_{osc}/v_e \lesssim 1$), $\omega L/c \sim 2/(v_{osc}/v_e)$.

We note that, in this intensity regime, the steepened scale length[115] found in simulations of resonance absorption is about the same as what we calculate here. This is not surprising, since for intensities $\gtrsim 3 \times 10^{15}$ W $\mu m^2/cm^2$, the momentum deposition by the reflecting light wave is comparable to that deposited into the resonantly generated plasma wave. This means that our estimate for L is not overly sensitive to the assumption of normal incidence.

Using the steepened scale length, we can now estimate the instability threshold set by the density gradient. Unless the ion waves are very weakly damped, the gradient threshold is about the same for both instabilities, so we simply consider the oscillating two-stream instability. The threshold condition is then[116]

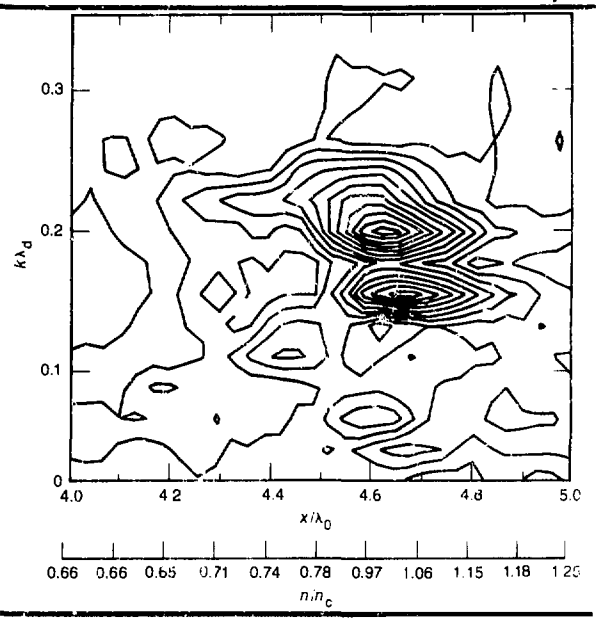

Fig. 3-51. Contour plot of electrostatic potential, Fourier analyzed in y direction as function of plasma density and wave number.

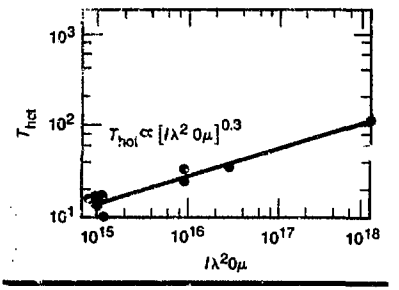

◀ Fig. 3-52. Heated electron temperature as function of $I\lambda_{0\mu}^2$ as found in two-deminsional simulations with normally incedent light; background electron temperature = 4 keV.

$$\frac{v_w^2}{v_e^2} > \frac{2}{k\,L} \tag{74}$$

where k is the component of the wave number of the electron plasma wave along the electric vector of the light. Noting that the lowest threshold is obtained for the largest value of k consistent with weak Landau damping, we take $k\,\lambda_D \sim 0.2$, where λ_D is the electron Debye length. Substituting for v_w^2 and L, we obtain

$$\frac{v_{osc}}{c} \gtrsim 3.8\left(\frac{v_e}{c}\right)^{2.5} \quad . \tag{75}$$

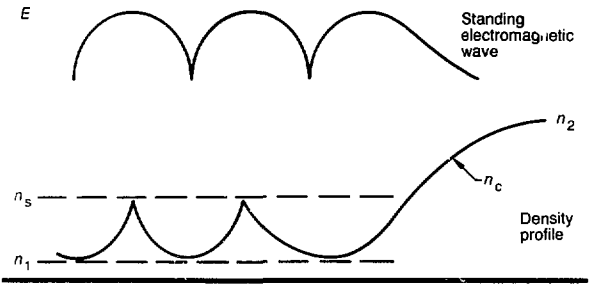

Fig. 3-53. Schematic of ponderomotively steepened density profile illustrating characteristic densities.

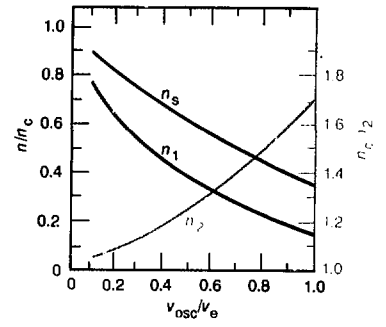

Fig. 3-54. Model predictions for sonic density and densities of upper and lower shelves as function of v_{osc}/v_e.

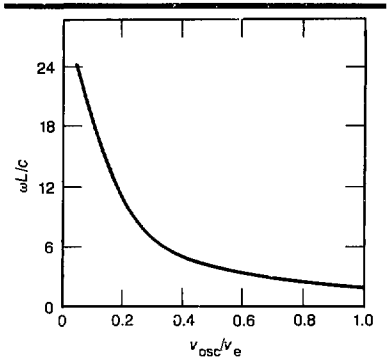

Fig. 3-55. Model predictions for steepened density scale length at critical density as function of v_{osc}/v_e.

Our simulations are consistent with this estimate of the threshold. In one simulation, the threshold condition was not satisfied, and, indeed, no instability was observed.

These instabilities are less of a concern as the intensity and wavelength of the laser light are decreased. If the inverse bremsstrahlung absorption length is a fraction of the size of the underdense plasma, most of the light is absorbed before it reaches the critical-density surface. Furthermore, even if sufficient light reaches the critical-density surface to drive the instabilities above their collisional and gradient thresholds, the heated temperatures generated would be modest for short-wavelength, low-intensity light (see Fig. 3-52).

Discussion and Summary. Finally, we discuss some of the limitations on our work. We have focused on instability absorption near the critical density in a steepened density profile. Of course, the instabilities may also occur[117] in the lower density plateau below the steep rise. In typical simulations, this plateau has a density of ~0.5 to 0.7 n_c, but our two-dimensional simulations are not large enough to include a long plateau, such as may form in long-pulse-length experiments. We have briefly examined these instabilities in large regions of plasma with density 0.5 to 0.7 n_c by using one-dimensional simulations where the light is modeled as a spatially homogeneous pump. We find that the instability heating is rather weak at these densities. An effective collision frequency describing the plasma heating is ~10^{-3} to $10^{-4}\,\omega_{pe}$, but the collision frequency increases dramatically when the plasma density becomes larger. At the lower densities, the heated electron temperature is typically approximately three to five times the background temperature. Further work is needed to assess the competition of this instability heating with other effects, such as Brillouin scatter.

In summary, we find that parametric decay of intense laser light into electron and ion waves near the critical density can operate at modest levels even in steepened density profiles. Hot electrons are generated with a characteristic temperature similar to that produced by resonance absorption. The efficiency of these instabilities may be enhanced when long plateaus with density $\gtrsim 0.5\,n_c$ are formed.

Authors: W. L. Kruer and K. G. Estabrook

Coupling of Hot Electrons to Laser-Fusion Targets

Coupling of hot electrons to laser-fusion targets is of considerable interest because such electrons may detrimentally preheat high-density implosions at modest or low driving intensity. At high intensity, hot electrons may represent the majority of absorbed laser energy and, thus, determine significant target dynamics.

Here, we investigate the thermalization of hot electrons by the background electrons in dense material in some idealized systems. Figure 3-56 shows the model problem of a hot-electron gas (neutralized by fast ions) in contact with the target. A related model problem is that of the albedo of targets to incident hot-electron beams. Solutions of these problems readily display the essential physics of hot-electron transport in systems of practical interest.

In these problems, the penetration of hot electrons into the dense material results in loss of particles and energy because of collisional drag by the background electrons, so that a source, taken to be at the interface, sustains the steady states shown in Fig. 3-56. The penetration of the hot electrons also depends on their elastic scatter on the atomic nuclei and, thereby, on the nuclear charge, Z. In Fig. 3-56, the number density of hot electrons in the coronal plasma, their average energy, and the energy-deposition profile in the target material are found as functions of the source and target parameters. In the albedo problems, the albedo and the energy-deposition profile in the target are found.

Multigroup diffusive transport is solved both analytically and numerically, and a useful improvement over the usual formulation is presented. Direct numerical solutions of the complete transport equation, including multiple small-angle scatter, are also shown. These transport schemes and results are compared.

Hot-Electron Transport Equations. The Fokker-Planck equation for the steady-state, low-density hot-electron distribution, f, in position x, speed $v = |\underline{v}|$, and pitch angle $\mu = \underline{v} \cdot \underline{x} / |\underline{v}|\,|\underline{x}|$ is

$$v\mu \frac{\partial f}{\partial x} = \frac{v}{\lambda_{90}} \frac{\partial}{\partial \mu} \times \left(1 - \mu^2\right) \frac{\partial f}{\partial \mu} + \frac{2v^2}{\lambda_r} \frac{\partial f}{\partial v} \quad . \tag{76}$$

Here, $\lambda_{90} = m^2v^4/2\pi e^4Z^2N(1 + 1/Z) \ln \Lambda_{ei}$ is the mean free path for elastic scatter of hot electrons on atomic nuclei of charge Z and density N. The factor $(1 + 1/Z)$ accounts approximately for the effect of scattering by the neutralizing electrons. The dominance of (multiple) small-angle collisions over large-angle collisions is expressed by the Coulomb logarithm $\ln \Lambda_{ei}$ (>1). The thermalization mean free path, $\lambda_r = [Z(1 + 1/Z) \ln \Lambda_{ei}/ \ln \Lambda_{ee}]\, \lambda_{90}$ is related to the energy loss rate along the hot-electron path (stopping power) by $\lambda_r = 2mv^2/(dE/dx)$. We will use $\ln \Lambda_{ei} = \ln \Lambda_{ee}$ throughout this article.

Equation (76) is to be solved subject to boundary conditions in space appropriate to a source of hot electrons. It has been solved numerically to obtain results for comparison with those of the reduced descriptions.

Equation (76) may be reduced to the multigroup diffusion model whenever λ_{90} is small compared with scale lengths of interest and whenever boundary and source effects are unimportant. In this limit, the distribution is dominantly isotropic and may be written $f = f_0(x,v) + \mu f_1(x,v)$. The number and energy density of the hot electrons are calculated from f_0

$$n_h = 4\pi \int_0^\infty dv\, v^2 f_0 \quad , \tag{77a}$$

$$E_h = n_h \left\langle \frac{mv^2}{2} \right\rangle_h$$

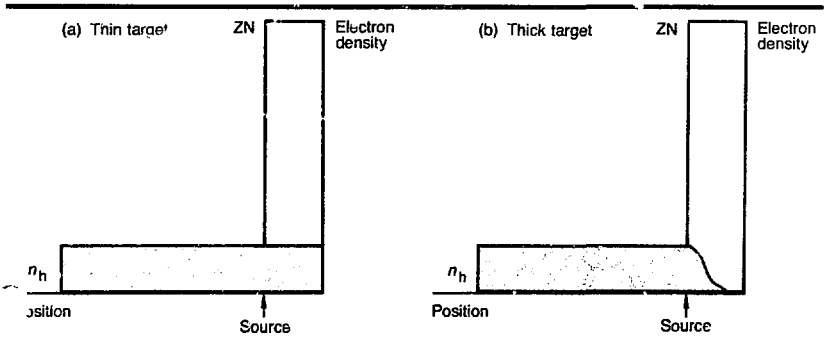

Fig. 3-56 A laser source, taken to be at target-corona interface, supports uniform coronal hot electrons against thermalization in dense target.

$$= 4\pi \int_0^\infty dv\, v^2 \frac{mv^2}{2} f_0 \quad , \qquad (77b)$$

$$\frac{v}{3}\frac{\partial}{\partial x} f_1 = \frac{2v^2 \partial f_0}{\lambda_e \partial v} \quad . \qquad (78)$$

The number and energy fluxes of hot electrons are calculated from f_1

$$j_h = \frac{4\pi}{3} \int_0^\infty dv\, v^2 v f_1 \quad , \qquad (79a)$$

$$q_h = \frac{4\pi}{3} \int_0^\infty dv\, v^2\, v \frac{mv^2}{2} f_1 \quad , \qquad (79b)$$

$$v \frac{\partial f_0}{\partial x} = \frac{-2v}{\lambda_{90}} f_1 + \frac{2v^2}{\lambda_e} \frac{\partial f_1}{\partial v} \quad . \qquad (80)$$

When Eq. (80) is solved for f_1 and substituted into Eq. (78), the usual multigroup diffusion equation is obtained for f_0

$$\frac{-\partial}{\partial x} \frac{v\lambda_{90}}{6} \frac{\partial f_0}{\partial x} = \frac{2v^2}{\lambda_e} \frac{\partial f_0}{\partial v} \quad . \qquad (81)$$

Here, we have neglected the second term on the right-hand side of Eq. (80), as it is smaller than the first by roughly the factor $(Z+1)^{-1} \sim (\lambda_e/\lambda_{90})^{-1}$. Equation (81) is to be solved subject to the source boundary condition at the interface.

Because the higher-energy hot electrons carry considerable flux, and because we are interested in pushing the model to as small a Z as practicable, we will retain the second term on the right-hand side of Eq. (80), and we will also solve

$$\frac{-\partial}{\partial x}\left[\frac{v}{3}\int_v^\infty dv' \exp\left(-\int_v^{v'} dv'' \frac{\lambda''_e}{v''\lambda''_{90}}\right)\frac{\lambda'_e}{2v'}\frac{\partial f'_0}{\partial x}\right] = \frac{2v^2}{\lambda_e}\frac{\partial f_0}{\partial v} \quad . \qquad (82)$$

Equation (82) will be seen to be a useful improvement of Eq. (81).

Thermalization of Hot Electrons by Laser-Fusion Targets. In Fig. 3-56, we imagine that the hot-electron gas models the coronal blowoff and that the gas is populated only by the hot electrons and fast ions. Thus, there is no thermalization in this region. The time-dependent rarefaction and spatial inhomogeneity in the corona are ignored here, and the distribution in the corona is the same as at the interface. As the hot electrons are absorbed in the dense material, a current of background electrons must flow to the source at the interface to maintain charge neutrality. Since the electrons in this flow are collision dominated in the dense material, the electric field required to drive them to the source may become large enough to also affect the penetration of the hot electrons. However, for a relatively small absorbed flux of hot electrons, or after the associated resistive heating of the return current, the field may become negligible for the hot-electron transport of interest. For these reasons, and to expedite the calculation, we have neglected this field.

We present solutions of Eq. (81) below, subject to the boundary condition appropriate to thermalization of the entire source in the target. At the $x = 0$ interface, we have

$$\left|\frac{-v\lambda_{90}}{6}\frac{\partial f_0}{\partial x}\right|_{x=0} = v_s f_s(v) \quad . \qquad (83)$$

The absorbed flux density is given by $v_s f_s(v)$, where v_s is a velocity characteristic of the source, and f_s is a function of v and v_s. We shall use the Maxwellian $f_s = n_s/(2\pi T_s/m)^{3/2} \exp(-mv^2/2T_s)$, with $T_s = mv_s^2$. The average energy of source electrons is $\langle mv^2/2\rangle_s = 3T_s/2$. The source-energy flux is $Q_s = n_s v_s 3T_s/2$, which may be viewed as determining the density of source electrons n_s, in terms of the source strength, Q_s.

Thin-Target Thermalization. If the mean free path of the hot electrons in the target is large compared with its thickness, Eq. (81) can be solved subject to Eq. (83) and the no-flux condition at the rear of the target, $\partial f/\partial x = 0$ at $x = \Delta r$.

The solution is readily found by expanding in the small parameter $\Delta r/\lambda$. In lowest order, the distribution is independent of position, as indicated in Fig. 3-56(a) and

$$f_0(v) \cong \frac{\lambda_{es}}{2\Delta r}\int_v^\infty \frac{dv'\, v'^2}{v_s^3} f_s(v') \quad . \qquad (84)$$

Here, the target density and atomic number are employed, and v is replaced by v_s in λ_{es}.

By direct integration, we find the number density and average energy of hot electrons in the corona, supported by the Maxwellian source flux, to be

$$n_h = \frac{8}{3(2\pi)^{1/2}} \frac{\lambda_{ei,s}}{\Delta r} n_s \quad , \tag{85a}$$

$$\left\langle \frac{mv^2}{2} \right\rangle_h = \frac{6}{5} \left\langle \frac{mv^2}{2} \right\rangle_s = \frac{6}{5} \cdot \frac{3}{2} T_s \quad . \tag{85b}$$

Equation (85a) reveals that a large reservoir of hot electrons is formed to balance the source and the weak thermalization in the target. Equation (85b) shows that the Maxwellian source flux leads to an average energy in the system 20% higher than that of the source! This is the result of the velocity-dependent thermalization rate and source flux. Note also that the total number of hot electrons in the system and the time to reach the steady state of Eqs. (85) depends on the actual extent of the coronal plasma.

Thick-Target Thermalization. When the mean free path of hot electrons in the target is small compared with its thickness, Eq. (81) may be solved subject to Eq. (83) and $f(x_0,v) = 0$. Here, x_0 is to approach infinity in the final results.

The solution may be written conveniently in dimensionless space- and time-like variables ζ and τ, respectively

$$f(\zeta,\tau) = \int_t^\infty d\tau' \sum_{m=0}^{\infty} \frac{2}{\zeta_0} e^{-\lambda_m^2(\tau' - \tau)} \cos \lambda m\zeta \cdot F(\tau') \quad . \tag{86}$$

In Eq. (86), $\zeta = (12/\lambda_{90,s}\,\lambda_{es})^{1/2}x$, $\tau = v^8/8v_s^8$, ζ_0 is ζ evaluated at x_0, and $\lambda_m = (m + 1/2)\pi/\zeta_0$. The boundary condition expressing the absorbed flux gives $F(\tau) = -(3\,\lambda_{es}/\lambda_{90,s})^{1/2} f_s(\tau)/(8\tau)^{5/8}$.

Equation (86) may be employed to study the detailed structure of the thermalization of the hot electrons. We are presently concerned with the characteristics of the coronal plasma that are given by the interface distribution, $f(x = 0,v)$. This corresponds to the large ζ_0 and small ζ limit of Eq. (86).

$$f(0,v) = \left(\frac{8}{\pi}\right)^{1/2} [3(Z+1)]^{1/2} \int_v^\infty \frac{dv' v'^2}{v_s^3} \frac{f_s(v')}{\left(\frac{v'^8}{v_s^8} - \frac{v^8}{v_s^8}\right)^{1/2}} \quad . \tag{87}$$

As before, direct integration yields the density and typical energy of hot electrons in the corona for the Maxwellian source flux.

$$n_h = \frac{4}{\pi} 3^{1/2} I_2 (Z+1)^{1/2} n_s \simeq 1.06 (Z+1)^{1/2} n_s \quad , \tag{88a}$$

$$\left\langle \frac{mv^2}{2} \right\rangle_h = \frac{I_4}{I_2} m v_s^2 = 0.47 \left\langle \frac{mv^2}{2} \right\rangle_s \quad . \tag{88b}$$

Note that Eq. (88a) is independent of v_s, while Eq. (88b) is independent of Z. Here, $I_N = \int_0^1 dx\, x^N/(1 - x^8)^{1/2}$, with $I_2 = 0.4$ and $I_4 = 0.34$. Equation (88a) expresses again that a large ($Z > 1$) reservoir of hot electrons is established, so that the weak thermalization in the target balances the source.

Figure 3-57 shows the energy-deposition profile in the target. From our analysis, we observe that the penetration scales with $(Z + 1)^{1/2}\lambda_{90,s}$ so that the curve shown is universal. Although most of the source is absorbed near the interface, there is also a long tail penetrating deep into the target.

LASNEX Checks. To compare our analysis with common numerical models of hot-electron transport, we ran several test problems with the LASNEX code. Weak hot-electron sources were introduced in thin and thick targets and coronal plasmas similar to those in Fig. 3-56. As configured, the code essentially solved only Eq. (81), subject to Eq. (83) and overall conservation, and gave results for the hot-electron density and energy density in the corona.

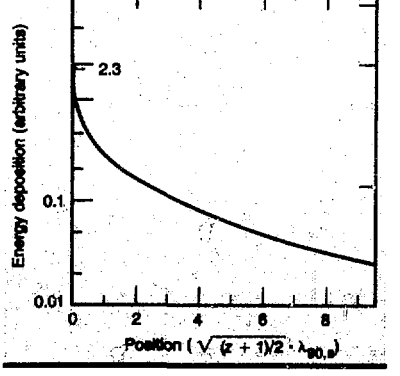

Fig. 3-57. Energy-deposition profile in target for thick-target thermalization problem.

The thin-target data agreed to within a few percent with the analytic results in all cases. This was accomplished without significant sensitivity of the results to zoning. Employment of considerable fine zoning of the target near the source at the coronal interface was required to achieve essentially equivalent results for the thick targets.

We believe these recent tests to be some of the more detailed and successful for the hot-electron transport in LASNEX.

Albedo of Materials to Energetic Electrons. In the preceding discussion, we have shown how the transport equation may be solved to obtain the characteristics of the coronal hot-electron population that obtains in steady state because of thermalization of the source by the target. The albedo concept and empirical data may also be employed to this end.

Here, we compute the albedo of materials to energetic electrons according to Eqs. (76), (81), and (82) and display the relation between albedo and transport.

A commonly defined albedo is the ratio of the magnitude of the flux of particles returning from a thick target to the flux of an incident beam. The transport equation is to be solved for the flux emerging from the target when the incident flux is given. In the preceding thermalization investigation, the absorbed flux was given, since the hot electrons could not escape the system. The albedo problem is one in which the emerging flux escapes.

Explicitly for Eq. (76), we have

$$A = \frac{-2\pi \int_{-1}^{0} d\mu\, \mu \int_0^\infty dv\, v^2 v f(x = 0, \mu, v)}{2\pi \int_0^1 d\mu\, \mu \int_0^\infty dv\, v^2 v f(x = 0, \mu, v)} \quad . \tag{89}$$

When Eq. (76) is solved subject to $f(x = 0, 0 < \mu < 1, v)$ given on the boundary of a thick target, Eq. (89) yields the albedo. It is common to employ $f \propto \delta(v - v_0)\,\delta(\mu - 1)$ as representing a collimated beam.

Substituting the usual diffusion-theory distribution associated with Eq. (81) into Eq. (89), we obtain the diffusion-theory albedo, A_D

$$A_D = \frac{\pi \int_0^\infty dv\, v^2 v f_0 - \frac{2\pi}{3} \int_0^\infty dv\, v^2 v f_1}{\pi \int_0^\infty dv\, v^2 v f_0 + \frac{2\pi}{3} \int_0^\infty dv\, v^2 v f_1} \quad . \tag{90}$$

Here, $f_1 = -(\lambda_{90}/2)\partial f_0/\partial x$. To evaluate A_D, Eq. (81) is to be solved for f_0 subject to the boundary condition appropriate to the incident flux given; for example, at $x = 0$, $(1/2)f_0 - (1/3)(\lambda_{90}/2)(\partial f_0/\partial x) \propto \delta(v - v_0)$. We have found that the boundary condition employed in the diffusion theory is of relatively little consequence, so that the absorbed flux condition already solved may be used to evaluate the albedo. Using Eqs. (81), (83), and (87) to evaluate Eq. (90), we find

$$A_D = \frac{0.54\,(Z + 1)^{1/2} - 1}{0.54\,(Z + 1)^{1/2} + 1} \quad . \tag{91}$$

Thus, for example, the diffusion-theory albedo of gold is $A_D^{Au} = 0.66$. The diffusion-theory albedo is nonphysical (less than zero) for $Z < 2.4$, and Eq. (91) presumably is in error for Z not much greater than 2.4. This result is not a surprise, since Eq. (81) is essentially a high-Z expansion of the transport equation. The theory fails for f_1 sufficiently larger than f_0 such that the numerator of Eq. (90) becomes negative.

If we heuristically cancel the velocity from the fluxes in Eq. (90), we can obtain the relation between the albedo and the transport result for the thermalization problem, $A_D \simeq (n_h/4 - n_s/2)/(n_h/4 + n_s/2)$, which can be written

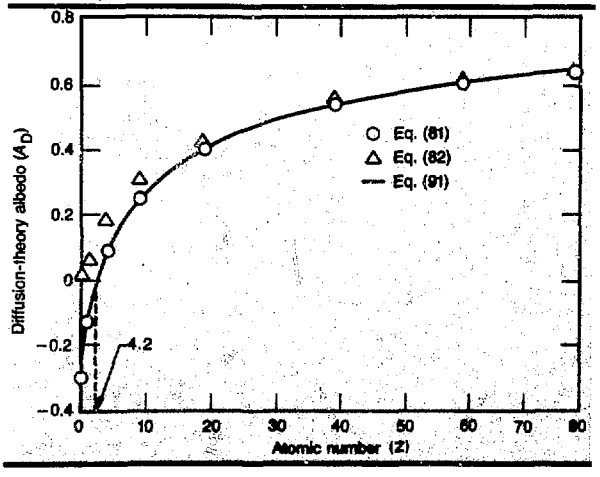

Fig. 3-58. Analytically calculated diffusion-theory albedo [Eq. (91)] agrees extremely well with numerically computed values from Eq. (81), the usual diffusion theory.

$$n_h \simeq 2n_s \frac{1+A}{1-A} \quad . \qquad (92)$$

Equation (92) accurately expresses the coronal hot-electron density in terms of the source density and the target albedo.

The diffusion-theory albedo described above can be improved significantly for low Z by retaining the drag on f_1 in Eq. (80) to obtain Eq. (82), rather than Eq. (81). The improved diffusion-theory albedo from Eq. (82), with the appropriate incident-flux boundary condition, is plotted in Fig. 3-58, together with Eq. (91). Note that the nonphysical behavior at small Z is removed.

In Fig. 3-59, we show the albedo resulting from direct solution of Eq. (76) for incident collimated and isotropic beams, together with the improved diffusion-theory albedo. Except for the smallest albedos at low Z, the accuracy of the improved diffusion theory is of the order of 10% or less. Note also the superior agreement between the improved diffusion theory and isotropic beam albedos. This is reasonable in view of the preceding discussion of the validity of diffusion theory.

Figure 3-60 shows the energy-deposition profiles in the target associated with the $Z = 1$ albedo calculations of Eqs. (76), (81), and (82). Agreement of the results from Eqs. (76) and (82) is seen to be good. In particular, it may be seen from Eq. (76) that no deposition should occur beyond $\lambda_{\epsilon,s}/8$, the penetration depth permitted by thermalization in the absence of elastic scattering. The breakdown of the usual diffusion theory, Eq. (81), already seen in the albedo value, is clearly evident in the energy-deposition profile.

Discussion. The poor behavior of the usual diffusion theory, Eq. (81), for Z less than about 10 is eliminated by the improved diffusion theory, Eq. (82), to obtain agreement with the exact transport theory, Eq. (76), for the problems and physical quantities considered here. Low-Z thermalization problems recalculated with the improved diffusion theory exhibit results very much like the low-Z (and low albedo) problems shown here. Thus, the improved diffusion theory appears to be both a desirable and a tractable model for transport calculations.

Authors: J. R. Albritton, C. J. Randall, and A. B. Langdon

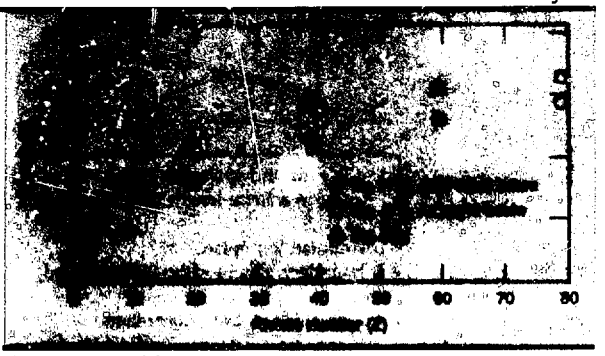

Fig. 3-59. Improved ▲ diffusion-theory albedo [Eq. (82)] is in acceptable agreement with numerically calculated results from Eq. (76), even for small Z.

Fig. 3-60. Energy-deposition profiles associated with albedo calculations of Eqs. (76), (81), and (82) for $Z = 1$ shown in ▼ Figs. 3-58 and 3-59.

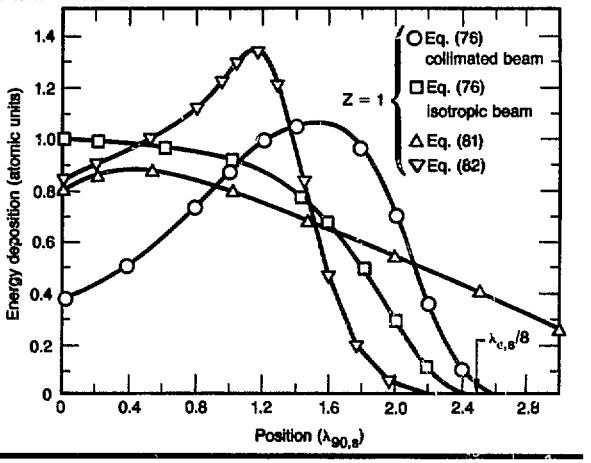

Time Evolution of Stimulated Brillouin Scattering in Bounded Systems

The well-known theory of stimulated Brillouin scattering (SBS), as described in Ref. 118, for example, has often been used to interpret backscatter observations in experiments and computer simulations. The growth rates found in Ref. 118 are correct after an initial transient period; however, this transient period may be significant in microwave plasma experiments, computer simulations, or short-pulse-length laser–plasma-interaction experiments. Here, we

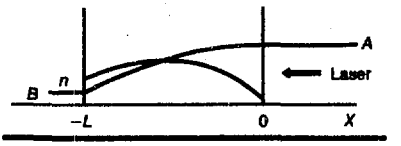

Fig. 3-61. Geometry of calculation.

solve in time and space the equations for scattering in a finite-length system, allowing for

- Distributed ion noise.
- A boundary value for the backscattered wave.
- An initial ion-density fluctuation.

An analytic expression for the time evolution of the reflectivity is derived that shows an initially larger growth rate than that of Ref. 118, but which asymptotically approaches that of Ref. 118 with time. The transient period is about the time it takes an ion wave to traverse the system, L/c_s, where L is the system length, and c_s is the sound speed.

We use the same notation as Ref. 118, except that the backscattered wave is A and the ion wave is n. The deceptively simple equations for A and n are

$$\frac{\partial A}{\partial x} = n + S \quad , \tag{93}$$

$$\frac{\partial n}{\partial t} - \frac{\partial n}{\partial x} + \beta n = A \quad . \tag{94}$$

Here, β is proportional to the ion wave damping; x is normalized to a growth length, L_1; and time is normalized to L_1/c_s. Here, S is the distributed ion wave noise, which arises naturally from thermal-plasma fluctuations. The time derivative of A may be neglected after the short time it takes a scattered wave pulse to leave the system ($2L/c$, where c is the speed of light). Henceforth, we also normalize L to L_1.

We Laplace transform by the operation $\int_0^\infty e^{-pt}\,dt$, obtaining

$$\frac{\partial A_p}{\partial x} = n_p + S_p \quad , \tag{95}$$

$$(p + \beta)n_p - \frac{\partial n_p}{\partial x} = A_p + n_0 \quad , \tag{96}$$

where $n_0 = n(x, \tau = 0)$, thus taking account of initial density perturbations at the proper frequency and wave number. For example, in the microwave experiment of Ref. 119, microwaves were reflected from the chamber wall, setting up a large standing ion wave from which SBS was initiated. The same effect has been observed in simulations, where the initial standing wave can result from dielectric reflection at the plasma edge[120] or from imperfect numerical boundary conditions. We suppose that both S and n_0 are independent of x.

Taking the spatial derivative of Eq. (96) and substituting Eq. (95), we have

$$\frac{\partial^2 n_p}{\partial x^2} - 2\sigma \frac{\partial n_p}{\partial x} + n_p = \frac{-S}{2\sigma - \beta} \quad , \tag{97}$$

where $\sigma = (p + \beta)/2$. The solution to Eq. (97) is

$$n_p = C_+ e^{\alpha_+ x} + C_- e^{\alpha_- x} - \frac{S}{2\sigma - \beta} \quad , \tag{98}$$

where

$$\alpha_\pm = \sigma \pm (\sigma^2 - 1)^{1/2} \quad . \tag{99}$$

The appropriate boundary conditions are (see Fig. 3-61)

$$n_p(0) = 0 \quad , \tag{100}$$

$$A(-L) = B \quad , \tag{101}$$

where B is the boundary value of A at $x = -L$. This corresponds, for example, to a reflected wave from a critical-density surface.[121] Only the amount of reflected light at the backscattered frequency ($\Omega_0 - \Omega_s$) is included in B.

We use Eq. (101) in Eq. (96) to obtain

$$\left(\frac{\partial n_p}{\partial x} - 2\sigma n_p\right)_{x = -L} = -n_0 - \frac{B}{2\sigma - \beta} \quad . \tag{102}$$

The goal of this calculation is to find $A(x = 0,t)$, since this is the square root of the reflectivity. Using Eqs. (100) and (102) to evaluate the numerical constants in Eq. (98) and then using Eq. (96) to calculate $A_p(x)$, we find

$$A_p(x=0)$$

$$= n_0\left(\frac{\alpha_+ - \alpha_-}{\alpha_+ e^{-\alpha_- L} - \alpha_- e^{-\alpha_+ L}} - 1\right)$$

$$- \frac{S}{2\sigma - \beta}$$

$$\times\left[\frac{\alpha_+^2\left(1 - e^{-\alpha_- L}\right) - \alpha_-^2\left(1 - e^{-\alpha_+ L}\right)}{\alpha_+ e^{-\alpha_- L} - \alpha_- e^{-\alpha_+ L}}\right]$$

$$+ \frac{B}{2\sigma - \beta}$$

$$\times\left(\frac{\alpha_+ - \alpha_-}{\alpha_+ e^{-\alpha_- L} - \alpha_- e^{-\alpha_+ L}}\right) \quad . \qquad (103)$$

We then have to inverse transform Eq. (103). Let us first consider the term proportional to n_0 and call it A_{pn}

$$A_{pn}$$

$$= n_0\left\{\frac{\alpha_+ - \alpha_-}{\alpha_+ e^{-\alpha_- L}\left[1 - \frac{\alpha_-}{\alpha_+} e^{-(\alpha_+ - \alpha_-)L}\right]} - 1\right\}$$

$$= n_0\left\{\frac{2(\sigma^2 - 1)^{1/2}}{\left[\sigma + (\sigma^2 - 1)\right]^{1/2}} e^L\right.$$

$$\times\left[\sigma - (\sigma^2 - 1)\right]^{1/2}$$

$$\left.\times\left[1 + \frac{\alpha_-}{\alpha_+} e^{-2L}(\sigma^2 - 1)^{1/2} + \ldots\right] - 1\right\} \quad . \qquad (104)$$

The inverse transform is

$$A_n(0,t) = \frac{2e^{-\beta t}}{\Pi i} n_0 \int_{C-i\infty}^{C+i\infty}\left\{\frac{(\sigma^2 - 1)^{1/2}}{\sigma + (\sigma^2 - 1)^{1/2}}\right.$$

$$\times e^{L\left[\sigma\zeta - (\sigma^2 - 1)^{1/2}\right]}$$

$$+ \frac{(\sigma^2 - 1)^{1/2}\left[\sigma - (\sigma^2 - 1)^{1/2}\right]}{\left[\sigma + (\sigma^2 - 1)^{1/2}\right]}$$

$$\left.\times e^{L\left[\sigma\zeta - 3(\sigma^2 - 1)^{1/2}\right]} + \ldots\right\} d\sigma \quad , \qquad (105)$$

where $\zeta \equiv 1 + 2\tau/L$.

We use the following identity[122]

$$F_n(\tau, k) \equiv \frac{1}{2\pi i}$$

$$\times \int_{C-i\infty}^{C+i\infty} \frac{e^{\tau s - k(s^2 - 1)^{1/2}}}{(s^2 - 1)^{1/2}\left[s + (s^2 - 1)^{1/2}\right]^n} ds$$

$$= \left(\frac{\tau - k}{\tau + k}\right)^{n/2} I_n\left[(\tau^2 - k^2)^{1/2}\right] U(\tau - k) \quad , \qquad (106)$$

where I is the Hankel function, and U is the step function. Equation (105) may be solved exactly

$$A_n(0,t) = 4e^{-\beta t} n_0 \sum_{i=1}^{\infty}\left(\frac{\partial}{\partial\tau} + \frac{\partial}{\partial k}\right)^{i-1}$$

$$\times \frac{\partial^2}{\partial k^2} F_i\,|\tau = L\zeta_{k=i+2i}L \quad . \qquad (107)$$

The first term is

$$A_n(0,t)_1 = 4e^{-\beta t} n_0\left\{I_1\left[L(\zeta^2 - 1)^{1/2}\right]\right.$$

$$\times\left[\frac{1}{(\zeta + 1)(\zeta^2 - 1)^{1/2}}\right.$$

$$\left.+ \frac{2(\zeta - 1)}{L^2(\zeta^2 - 1)^{1/2}(\zeta + 1)^2}\right]$$

$$\left. - I_0\left[L(\zeta^2 - 1)^{1/2}\right]\frac{(\zeta - 1)}{L(\zeta + 1)^2}\right\} U(\zeta - 1) \quad . \qquad (108)$$

The argument of the Hankel functions is $L(\zeta^2 - 1)^{1/2} = 2[t(t + L)]^{1/2}$. Using the asymptotic form

$$A(0,t) \sim e^{2[\tau(t + L)]^{1/2}} \quad . \qquad (109)$$

For $t < L$, the reflectivity (A^2) increases approximately as $\exp[4(t)^{1/2}]$; for $t \gg L$, it increases approximately as $\exp(4t)$, which is just the result of Ref. 118 for large L. Thus, we see that the condition to go over to this time-asymptotic behavior is $t > L$, which is just the time for an ion wave to leave the system (in physical units, $t > L/c_s$).

The second term in Eq. (107) contains the factor $U(\zeta - 3)$, which means it turns on at $\zeta = 3$, or $t = L$, again the time at which an ion wave leaves the system. Each succeeding term can be seen to turn on at integral

multiples of this time: $2L$, $3L$, etc. For large L, the leading contributions to the first and second terms of Eq. (107) are

$$A_{n1}(0,t) = 4e^{-\beta t} n_0 \frac{I_1\left[L(\zeta^2-1)^{1/2}\right]}{(\zeta+1)(\zeta^2-1)^{1/2}} U(\zeta-1) \tag{110}$$

and

$$A_{n2}(0,t) = 36e^{-\beta t} n_0 \frac{(\zeta-3)^{1/2}}{(\zeta+3)^{5/2}} I_1\left[1(\zeta^2-9)^{1/2}\right] U(\zeta-3) \quad . \tag{111}$$

In Fig. 3-62(a), we have plotted the reflectivity $R(t) = A_n^2(t)$ given by Eq. (107) for a system of length $L = 10$, $B = 0$, and an initial noise level $n_0 = 1$. Shown by the dashed lines for comparison are the reflectivities growing exponentially at the asymptotic growth rate of Ref. 118 [four times the largest root of $(1-\sigma^2)^{1/2} + \sigma \tan[L(1-\sigma^2)^{1/2}] = 0$]. Both the reflectivity [Fig. 3-62(a)] and the integrated reflectivity [Fig. 3-62(b)] are about two orders of magnitude larger than the estimates predicted by the asymptotic growth rate. Figure 3-62(c) compares the growth rate $\gamma = \partial/\partial t[\ln A^2(t)]$ given by Eq. (107) to the asymptotic result. The growth rate is initially very large and falls to the asymptotic results in about one ion-wave transit time, $t \sim L$. A series expansion of Eq. (107) shows that, for the $n_0 = 1$ noise source, the initial growth rate is $\gamma(t=0) = L$. For very large systems, this can be much larger than the asymptotic result $\gamma = 2$. Finally, in Fig. 3-62(d), we show the growth rate for the

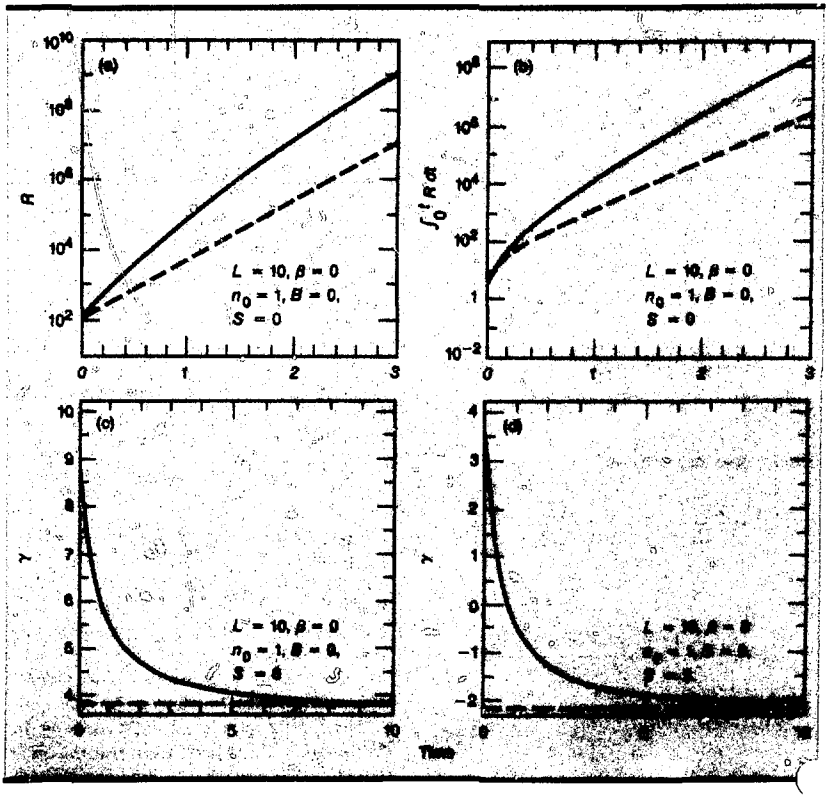

Fig. 3-62. Reflectivity $R(t) = A_n^2(t)$ given by Eq. (107) for system of length $L = 10$, $B = 0$, for initial noise level $n_0 = 1$.

identical case, except that $\beta = 3$. In this case, since $2 < \beta < L$, the reflectivity actually grows briefly before reaching its asymptotic exponentially decaying state.

Similar calculations can be carried out for the contributions to the reflectivity caused by B and S. These are considerably more complicated than the above. In the large L limit with $\beta < 2$, a good approximation is

$$A_S(0,t) \cong 4S^{-\beta t} \frac{I_1\left[L(\zeta^2-1)^{1/2}\right]}{(\zeta+1)(\zeta^2-1)^{1/2}} \times \left[1 - \beta/2 \frac{(\zeta^2-1)^{1/2}}{\zeta}\right]^{-1}, \quad (112)$$

$$A_B(0,t) \cong 2B^{-\beta t} \frac{I_0\left[L(\zeta^2-1)^{1/2}\right]}{\zeta(\zeta+1)} \times \left[1 - \beta/2 \frac{(\zeta^2-1)^{1/2}}{\zeta}\right]^{-1}. \quad (113)$$

Figure 3-63(a) and (b) shows the reflectivity and growth rate for a boundary noise source $B = 1$ for the case $\beta = 0$ and $L = 10$. In this case, the asymptotic reflectivity is more than three orders of magnitude above the estimate given by the initial reflectivity growing at the asymptotic rate. The initial growth rate is $\gamma = 20 = 2L$, in agreement with a series expansion of Eq. (112). Figure 3-63(c) and (d) has the identical parameters, except that $\beta = 3$. In this case, Eq. (112) fails, since $\beta > 2$, and the denominator eventually vanishes. In Fig. 3-64, we show similar results for a distributed noise source $S = 1$.

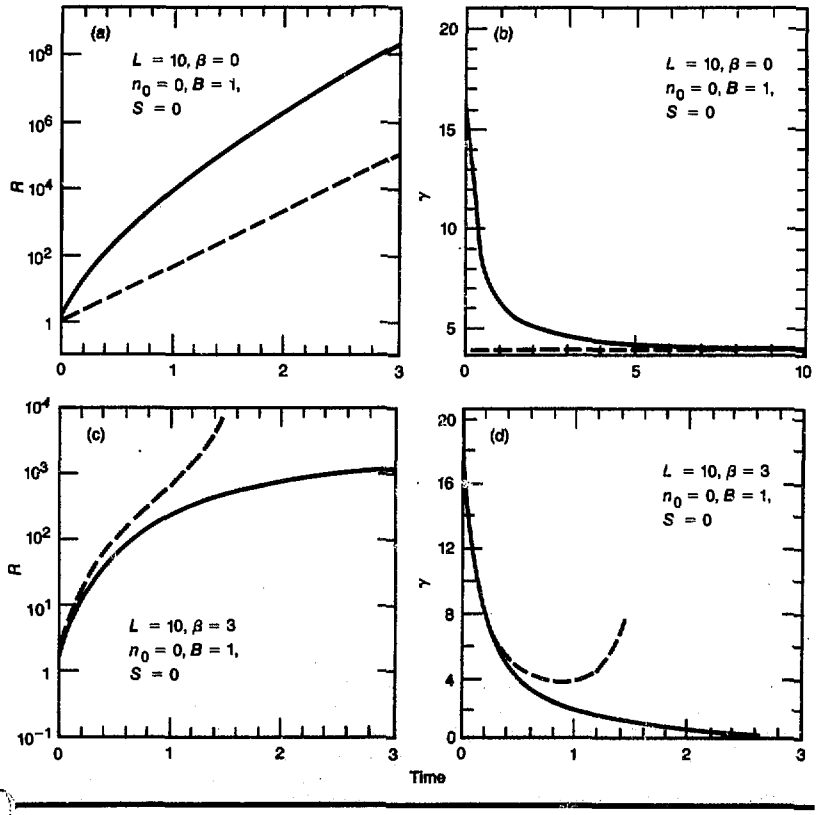

Fig. 3-63. (a), (b) Reflectivity and growth rate for boundary noise source $B = 1$ for case $\beta = 0$ and $L = 10$. (c), (d) $\beta = 3$.

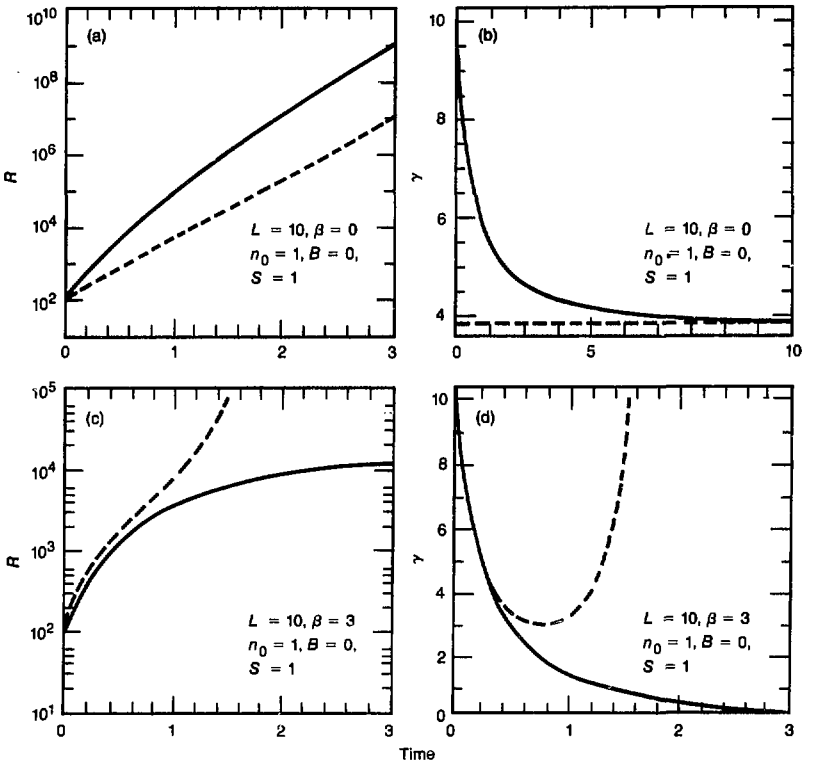

Fig. 3-64. Reflectivity and growth rate for boundary noise source $B = 0$ and for distributed noise source $S = 1$. (a), (b) $\beta = 0$. (c), (d) $\beta = 3$.

While Eqs. (112) and (113) fail for $\beta > 2$, the exact time-asymptotic state may be obtained from Eq. (103) by taking the residue at $\alpha = \beta/2$. For very large β, the result is

$$A(0,t) \simeq Be^{L/\beta} + \beta S\left(e^{L/\beta} - 1\right) \quad . \qquad (114)$$

A simple picture can be given of the preceding calculations. The usual analysis giving reflectivities that are proportional to exp(growth rate $\times$ t) concentrates on the fastest-growing mode of the system. After a sufficient number of growth times, this will be the dominant mode. However, in a finite-size system, a number of modes will grow initially. Our calculation has included the initial growth of all the available modes and follows the evolution to dominance of the fastest-growing mode.

Authors: C. J. Randall and J. J. Thomson

Effect of Ion Collisionality on Ion Acoustic Waves

In high-Z plasmas irradiated by short-wavelength lasers, the ion-acoustic waves associated with stimulated Brillouin scatter and other low-frequency collective processes can be collisional; i.e., $k\ell_i \leq 1$, where k is the wave number and ℓ_i is the ion mean free path defined by $\ell_i = v_i \tau_i$. Here, v_i is the ion thermal velocity, and τ_i is the ion–ion collision time defined in Ref. 123. In Ref. 124, the authors have numerically solved the ion acoustic dispersion relation in the regime $0.1 \lesssim k\ell_i \lesssim 10$. Their data smoothly connect onto the theoretical results at both the weak ($k\ell_i \gg 1$) and strong ($k\ell_i \ll 1$) collisional limits. In the modest electron–ion temperature-ratio regime that they considered ($1/2 \lesssim ZT_e/T_i = R_T \lesssim 4$)

the damping-rate parameter for the ion acoustic wave, $\gamma = -\mathrm{Im}(\omega)/\mathrm{Re}(\omega)$, decreased monotonically from the collisionless Landau damping value as the plasma became more collisional. Here, we show that, for larger values of R_T, the damping initially increases by as much as a factor of 4 as the plasma becomes more collisional and then finally decreases according to collisional theory as $\gamma \sim k\ell_i$.

Writing the ion and electron distributions as $F_\alpha + f_\alpha \exp(ikz)$, where $\alpha = (i,e)$, taking Maxwellian background distributions $F_\alpha = n_\alpha \exp(-v^2/2v_\alpha^2)/(2\pi v_\alpha^2)^{3/2}$, and assuming *collisionless electrons* $k\ell_e \approx R_T^2\, k\ell_i \gg 1$, we have the linearized kinetic equations

$$\frac{\partial f_i}{\partial t} + ikv_z f_i - i\frac{Ze\phi k}{M}\frac{\partial F_i}{\partial v_z} = C(F_i, f_i) + C(f_i, F_i) \quad , \qquad (115)$$

$$\frac{\partial f_e}{\partial t} + ikv_z f_e + i\frac{e\phi k}{m}\frac{\partial F_e}{\partial v_z} = 0 \quad . \qquad (116)$$

Here, Z is the ionic charge and $M(m)$ is the ion (electron) mass. We solve Eq. (116) in the low-frequency limit $|\beta_e| \ll 1$, where $\beta_e = \omega/(2kv_e)^{1/2}$, and we use quasi-neutrality to obtain the potential ϕ in terms of the perturbed ion density $n_1 = \int f_i d^3v$. Dropping the subscript i, Eq. (115) becomes

$$\frac{\partial f}{\partial t} + ikv_z f + iR_T \frac{n_i}{n_0\left(1 + i\beta_e \pi^{1/2}\right)} F = C(F, f) + C(f, F) \quad . \qquad (117)$$

The first collision term (F colliding on f) is given by

$$C(F, f) = \Gamma\left[4\pi F f + \frac{h}{2v}\frac{\partial F}{\partial v} + \frac{\partial^2 g}{\partial v^2}\left(\frac{\partial^2 F}{\partial v^2} - \frac{1}{v}\frac{\partial F}{\partial v}\right)\right] \quad . \qquad (118)$$

Here, g and h are the Rosenbluth potentials,[125] defined by $\nabla_v^2 h = -8\pi f$ and $\nabla_v^2 g = h$, and we have used the spherical symmetry of F. The collision-strength parameter is $\Gamma = 4\pi(Ze)^4\Lambda/M^2$, where Λ is the Coulomb logarithm. The second collision term (f colliding on F) is given by

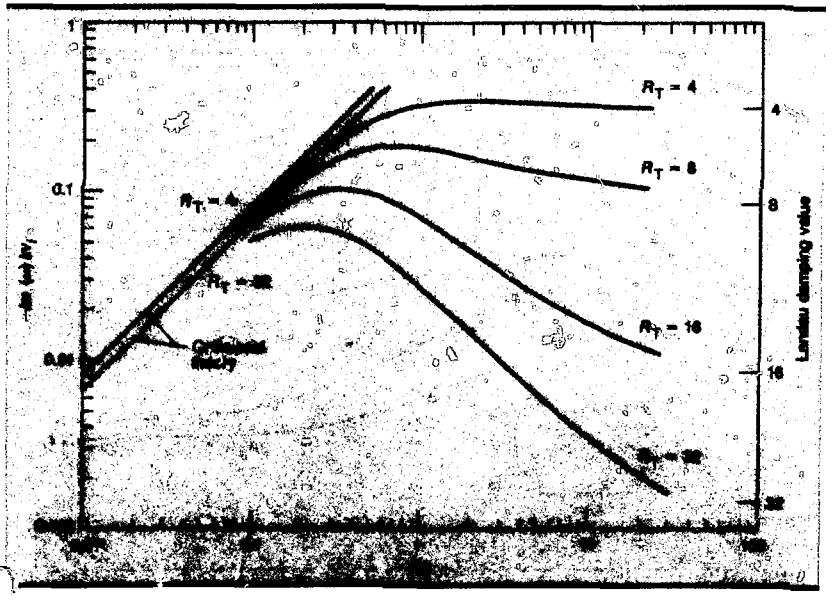

Fig. 3-65. Plots of $-\mathrm{Im}(\omega)/kv_i$ vs $k\ell_i$ for $Zm/M = 0$, and four temperature ratios, and results of collisional theory [Eq. (120)] for two temperature ratios.

$$C(f, F) = -\frac{1}{v^2}\frac{\partial}{\partial v}$$

$$\times\left\{f\left[v^2\frac{\partial H}{\partial v}+\frac{\partial G}{\partial v}-\frac{1}{2}\frac{\partial}{\partial v}\left(v^2\frac{\partial^2 G}{\partial v^2}\right)\right]\right.$$

$$\left.-\frac{v^2}{2}\frac{\partial^2 G}{\partial v^2}\frac{\partial f}{\partial v}\right]$$

$$+\frac{1}{2v^3}\frac{\partial G}{\partial v}\left[\frac{\partial}{\partial \mu}(1-\mu^2)\frac{\partial f}{\partial \mu}\right] . \qquad (119)$$

Here $\mu = v_z/v$. Again, we have used the spherical symmetry of F and, in addition, the azimuthal symmetry (about $\underline{k}$) of f. The Rosenbluth potentials G and H are defined in direct analogy with g and h: $\nabla_v^2 H = -8\pi F$, and $\nabla_v^2 G = H$. Substitution of Eqs. (118) and (119) into Eq. (117) yields a linear two-dimensional (v,μ) integro-differential equation for the perturbed ion distribution, f.

We advance a finite-difference analog of Eq. (117) numerically to obtain ω, the complex frequency of the normal mode of the system, i.e., the ion acoustic wave. Following Ref. 124, we write in Eq. (117) $\partial f/\partial t \rightarrow \partial f/\partial t - i\omega' f$, where ω' is an estimate of the acoustic frequency. Throughout the calculation, ω' is improved until $\partial f/\partial t$ is made small, at which time ω' is the normal mode frequency.

In Fig. 3-65, we give our results for $\mathrm{Im}(\omega)/kv_i$ vs $k\ell_i$ for $R_T = 4$, 8, 16, and 32. We have set Zm/M equal to zero in these calculations to isolate the damping caused only by ions. For $R_T > 4$, $\mathrm{Im}(\omega)/kv_i$ has a maximum for $k\ell_i$ between 0.1 and 1. For comparison, we also display the results of the collisional theory for $R_T = 4$ and 32

$$\left(\frac{\omega}{kv_i}\right)^2 = 1+\frac{2}{3}\left[1+i\frac{2}{3}\delta_k^i(k\ell_i)\frac{kv_i}{2\omega}\right]^{-1}$$

$$-i\frac{4}{3}\delta_\mu^i(k\ell_i)\frac{\omega}{kv_i}+R_T \quad . \qquad (120)$$

In Eq. (120), δ_k^i and δ_μ^i are the ion coefficients of conductivity and viscosity, respectively, given in Ref. 123 as 3.906 and 0.96, again respectively. For $k\ell_i \lesssim 0.1$, the damping approaches the collisional result quite closely.

A finite electron–ion mass ratio introduces electron Landau damping, which sets a minimum damping rate independent of $k\ell_i$ so long as the electrons remain collisionless ($k\ell_e \cong R_T^{\frac{1}{2}} k\ell_i \gg 1$). In Fig. 3-66, we plot $\gamma = -\mathrm{Im}(\omega)/\mathrm{Re}(\omega)$ vs $k\ell_i$ for several values of R_T but with $Zm/M = 10^{-4}$.

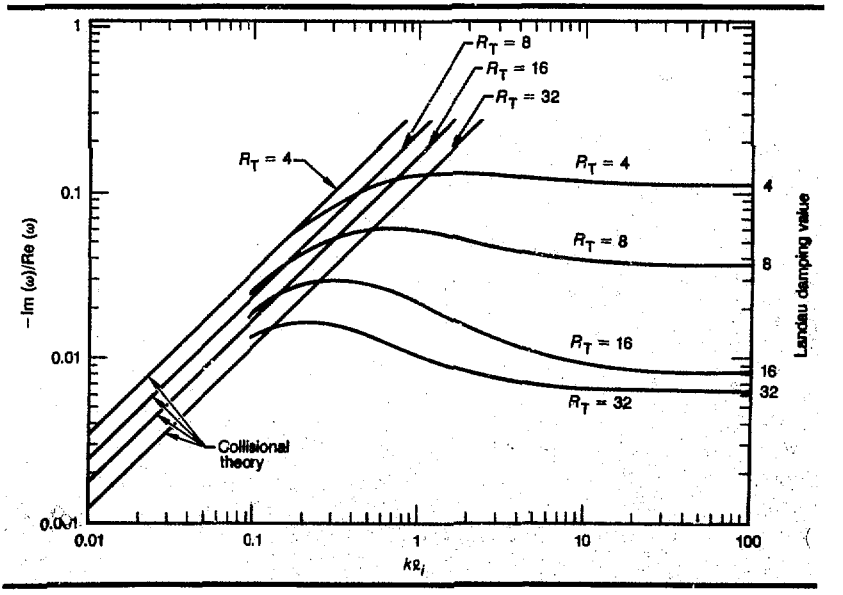

Fig. 3-66. Plots of $-\mathrm{Im}(\omega)/\mathrm{Re}(\omega)$ vs $k\ell_i$ for $Zm/M = 10^{-4}$, and results of collisional theory.

The maxima in the damping rates are now less pronounced, but still can amount to as much as a factor of 4 increase over collisionless values. The agreement with collisional theory near $k\ell_i \sim 0.1$ becomes progressively poorer as R_T increases, since Eq. (120) does not take Landau damping into account.

It is easy to generalize these results to any Zm/M by simply adding the appropriate electron Laudau damping decrement $(\pi Zm/8M)^{1/2} \cdot \mathrm{Re}(\omega)$ to the ion contribution $\mathrm{Im}(\omega)$ given in Fig. 3-65. This follows since $|\beta_e| \ll 1$ for any realistic Zm/M.

Author: C. J. Randall

Simulation of Long-Time-Scale Plasma Phenomena

Implicit Simulation. In Ref. 126, we briefly described a new direct method for implicit large-time-step particle-in-cell plasma simulation. During the past year, we have furthered our understanding of implicit simulation in general and of direct methods in particular. Reference 127 gives a brief discussion of the simplest direct method and its application to the electron–electron two-stream instability and to ion acoustic waves. Our analyses of the stability and accuracy of implicit time-integration schemes and our synthesis of new schemes with desirable properties are described in detail in Ref. 128. This work is equally relevant to moment-implicit methods described in Refs. 129 and 130. A detailed description of a generalized direct scheme, including discussions of prediction, iterative refinement, spatial difference representations, residual time-step limitations, and consistent spatial filtering, is given in Ref. 131. Here, we briefly summarize our work described in Refs. 128 and 131.

A desirable difference scheme should satisfy the following design criteria

- Provide high accuracy for modes with normal frequency $\omega_0 < \Delta t^{-1}$, e.g., $\mathrm{Im}(\omega/\omega_0)$ should be minimal.
- Provide substantial dissipation of modes with $\omega_0 \gg \Delta t^{-1}$, since these modes cannot be represented accurately.
- Minimize past data to be stored.
- Minimize spurious numerical cooling and heating (secular acceierations, described below).
- Be Galilean invariant so it does not spuriously destabilize fast or slow space-charge waves.
- Be robust with respect to an approximate solution of the implicit particle-field equations, which cannot be solved exactly for reasons of computational economy.

We have addressed all but the last issue in our analysis of difference schemes in Ref. 128, and we have constructed new schemes possessing the properties described above.

The analysis of cold-plasma wave dispersion in Ref. 128 led to a number of important conclusions. Relaxation of the $\omega_p\Delta t$ stability constraint in a plasma simulation requires implicitness without exception. The coefficients in our difference equations that control the degree of implicitness and that govern dissipation jointly determine stability. For $\omega_0^2\Delta t^2 \gg 1$, implicit schemes may be stable, but high-frequency oscillations are necessarily distorted. Thus, damping is generally desirable. We have devised several schemes that efficiently damp high-frequency oscillations. These can be compared in Fig. 3-67, where $|z| = |e^{-\omega\Delta t}|$ for the least-damped normal mode is plotted as a function of $\omega_0^2\Delta t^2$ for the I_1 and I_2 schemes of Denavit,[129] the Curtiss and Hirschfelder (C–H) scheme,[132,133] first-order schemes with $\alpha = 3/7$ and 1/10, the optimized C_1 scheme ($c_0 = 0.302$, $c_1 = 0.04$), and the D_1 scheme ($d_0 = 2$, $d_1 = -1$). Low-frequency oscillations can be simulated with high accuracy. With the proper choice of coefficients, the dissipation rate can be removed to high order in Δt for $\omega_0\Delta t \ll 1$.

We have generalized our implicit schemes to include a magnetic field in such a way as to

- Reproduce the cyclotron gyration of single particles in a stable fashion, with no damping for any value of the product of cyclotron frequency, ω_c, and the time step, Δt.
- Model collective modes (waves) in a numerically stable fashion for any wave frequency and time step, with frequency error $\propto \Delta t^2$ and damping $\propto \Delta t^3$ at low frequency and with substantial dissipation at high frequency.

Another important aspect of numerical accuracy is shown by a calculation of the

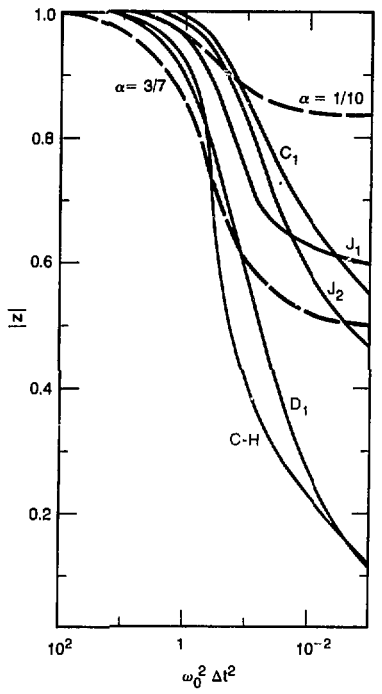

Fig. 3-67. Absolute value $|z| = |\exp(-i\omega\Delta t)|$ of least-damped simple-harmonic oscillator normal mode vs $\omega_0^2\Delta t^2$ for various schemes.

trajectory of a particle drifting through a sinusoidally varying electric field, as reproduced by finite-difference equations. Unphysical modifications are introduced by finite time-step effects that depend on wavelength, time step, and particle velocity. The particle is untrapped and should interact adiabatically with the wave. However, we find that a drifting particle will experience a spurious time-averaged force and will accelerate.

The unphysical acceleration (drag) rates for second-order schemes are all proportional to Δt^3 for slow particles. This scaling, and detailed dependence on the difference schemes, correspond directly to those for the dissipation rates we found for low-frequency, simple-harmonic oscillations. Thus, the same mechanism causing damping of low-frequency modes is also responsible for artificial cooling or heating of the plasma as it interacts with electric-field structures. The use of higher-order schemes reduces both effects. The absolute cooling or heating rates we obtain depend on the strength of the electric field, as measured by $\omega_{tr}\Delta t$, where ω_{tr} is the trapping frequency of oscillation of a particle near the bottom of a potential well.

In contrast, the plasma cooling/heating rates for the first-order schemes are generally much larger than those for the second-order accurate schemes, which argues strongly for using the higher-order algorithms. Drag rates of first- and second-order schemes are compared in Fig. 3-68, where we plot the normalized accelerations

$$-\langle a^{(2)}\rangle/|\tilde{a}|(\omega_{tr}\Delta t)^2 = -\mathrm{Im}(\tilde{x}/\tilde{a}\Delta t^2) ,$$

which are functions only of $Kv^{(0)}\Delta t$. Plotted in Fig. 3-68 are the J_1 and J_2 schemes of Denavit,[129] the Curtiss and Hirschfelder (C–H) scheme,[132,133] first-order schemes with $\alpha = 3/7$ and 1/10, the optimized C_1 scheme ($c_0 = 0.302$, $c_1 = 0.04$), the D_1 scheme ($d_0 = 2$, $d_1 = -1$), and the D_2 scheme ($d_0 = 5/2$, $d_1 = -2$, $d_2 = 1/2$). The drag rate has odd symmetry and is periodic with respect to $kv^{(0)}\Delta t$ with period 2π. In Ref. 130, observations of numerical cooling of warm plasmas in simulations with a first-order dissipative implicit algorithm are described. Significantly reduced cooling rates can be achieved by using the higher-order accurate integration schemes.

Our research has also aimed at developing improved schemes for solving the coupled implicit particle-field equations. A simple, but approximate, scheme has been described in Ref. 127. We have devised a means of iterating toward an exact solution of the field equation at the advanced time level. The ability to iterate to an exact answer ensures that desirable features built into the time-differencing scheme are realizable in practice and provides a useful benchmark for inexact (but perhaps faster) schemes. We have studied a simplified scheme where we require a significantly smaller set of quantities from the particles. Also, the bandwidth of the resulting field equations is reduced to the point where solution, even in two-dimensional magnetized problems, is convenient with known methods. Iteration might be used to refine the resulting fields. We have also delineated residual time-step constraints arising from direct-implicit schemes; these are noted below.

The essence of our iterative scheme is the correction of an rth approximation to the potential $\phi^{(r)}$ by an amount $\delta\phi$, where

$$-\nabla \cdot (1 + \chi)\nabla\delta\phi = \rho^{(r)} + \nabla^2\phi^{(r)} \qquad (121)$$

and

$$\chi(x) = \beta\omega_p^2(x)\,\Delta t^2 \quad . \qquad (122)$$

Here, β is a positive constant ≤ 1 and is a function of the implicit difference scheme chosen. The particles are readvanced using $\phi^{(r+1)} = \phi^{(r)} + \delta\phi$ and an improved $\rho^{(r+1)}$ is computed. In our simplest scheme, $\phi^{(0)} = 0$, and we take only one iteration.

There are three residual limits on the time step in our simulation schemes. To some degree, they are coincident with the fundamental limit of a step small enough to resolve the physical processes being studied. The first limitation is on the electron transit frequency $v_t\,\Delta t/L$, where v_t is the thermal velocity and L is a scale length of field variation. This arises as a consequence of requiring that electrons reproduce Debye shielding and, possibly, Landau damping. The implicit code shields too strongly at short wavelengths. Accurate shielding requires $k^2v_t^2\,\Delta t^2 \lesssim 1$. When $\omega_p^2\Delta t^2 \gg 1$, we are restricted to wavelengths large compared to a Debye length, since

$$k\lambda_D = \frac{kv_t\Delta t}{\omega_p\Delta t} \ll 1 \quad . \qquad (123)$$

Unfortunately, this eliminates applications such as ion acoustic turbulence, for which $k\lambda_D \sim 1/2$.

At short wavelengths, the implicit algorithm is at least stable and errs in the direction of making E too small. Thus, it appears that the presence of short wavelengths may not interfere with the longer wavelengths that are simulated accurately. Finite $kv_t\Delta t$ does not appear to affect convergence of our solution process, whereas $kv_t\Delta t \gtrsim 1$ does upset convergence of the moment-implicit method.[128,130]

The second residual Δt limit is a restriction on $\omega_{tr}\Delta t$. It arises from the neglected field-gradient term in the equation for the particle displacement at the advanced time. The neglected term is important when Δt is too large to resolve trapping oscillations.

The final limitation on the time step, that of nonphysical secular acceleration, has been described above.

We have also described in detail our strict and simplified spatial-difference schemes, as well as an energy-conserving Hamiltonian scheme, and we have considered how inclusion of a magnetic field affects our solution for the advanced field. We have also proven that the matrix operator in the field equation is positive. In the simplified scheme, the matrix is also an M matrix, with off-diagonal terms negative. The Hamiltonian and simplified schemes can yield symmetric matrices, depending on how $\underline{B}$ is introduced.[131]

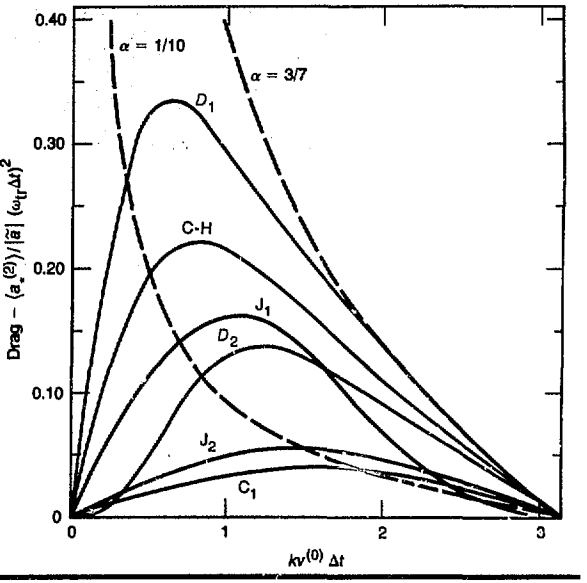

Fig. 3-68. Normalized drag $-\langle a^{(2)}\rangle/|\bar{a}|(\omega_{tr}\,\Delta t)^2 = -\mathrm{Im}(\bar{x}/\bar{a}\Delta t^2)$ vs $kv^{(0)}\Delta t$ for various schemes.

Electron Subcycling. A simpler approach is electron subcycling, which still provides a saving of computer time.[134] The standard leap-frog scheme is used for both electrons and ions, but the electron time step is a fraction of the ion time step. For each complete cycle of time integration, there is one cycle for ions and several subcycles for electrons. The cost of integrating the ions becomes negligible. The electrons are integrated on their time scale, while the slower massive ions can be integrated with a larger time step, using the field caused by their own charge plus the low-pass-filtered field of the electrons. This coupling of the species can be made second-order accurate. Stability and design of the low-pass filter are analyzed by the methods of Ref. 135 and examined empirically in an algorithm the implementation. Unlike the implicit codes, there is no limitation on wavelength

or field gradient, and high-frequency electron modes are retained. Although the potential gain in computer time is much smaller than for the implicit codes, subcycling is more widely applicable.

Authors: A. B. Langdon, A. Friedman, B. I. Cohen, J. C. Adam, and A. Gourdin-Serveniere

Hot-Electron Production Caused by Parametric Instabilities

Parametric instabilities, where the laser light decays to electron plasma waves and ion waves, can be an important absorption mechanism in laser fusion. These instabilities can occur on the long underdense shelf that is predicted for moderate-intensity lasers ($I \lesssim 10^{15}$ W/cm^2 for a 1-μm laser). We observed hot-electron production and microwave absorption caused by these instabilities in microwave experiments.[136] We have continued these measurements and have used simulation calculations and theory to model hot-electron production. The importance of these results is that the long underdense shelf predicted to occur for moderate-intensity lasers can result in significant hot-electron production.

We model this phenomenon using a one-dimensional particle-simulation code. Hot electrons leaving both ends are replaced by returning thermal electrons. We can measure the hot-electron temperature as a function of distance from both boundaries. The parameters for typical runs are plasma length $L = 512\ \lambda_D$, ion-to-electron mass ratio $m_i/m_e = 100$, and ion-to-electron temperature ratio $T_i/T_e = 0.1$. The hot-electron temperature vs the distance the electrons travel is given in Fig. 3-69 for $v_0/v_e = 0.6$ for $n = 0.7\ n_c(0)$. The hot-electron temperature increases almost linearly with distance. In these calculations, the results are obtained after the system reaches steady state, but before effects caused by the approximate boundary conditions perturb the solution. A better current-conserved boundary condition is being constructed.

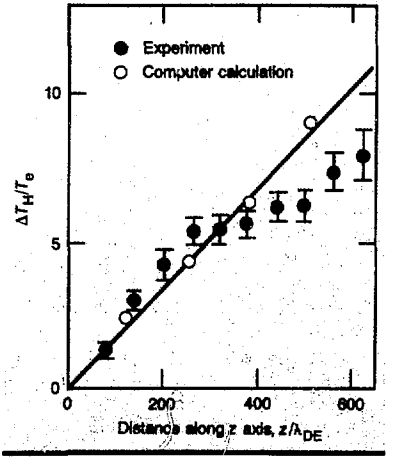

Fig. 3-69. Hot-electron temperature as a function of position in the turbulent region.

The simulation results can be understood by solving the spatially dependent quasi-linear equation. The effective diffusion coefficient is the usual spectral-energy term minus a term caused by the emission of plasmons by electrons. We can approximate both terms numerically in an effective spectral-energy term by using only the part of the spectral energy that is obtained in the simulations after the pump is turned off.[137] We find good agreement between theory and simulation calculations.

For comparison, in Fig. 3-69, we have included microwave experimental results obtained from Prometheus I. These measurements were made at a microwave power of 4 kW. The underdense shelf density was $n_s \simeq 0.7\ n_c$ in the experiments. The measured spatial rate of increase of the hot-electron temperature is comparable with the simulation results.

In summary, we have investigated the hot-electron production caused by parametric instabilities. The results for particle-simulation calculations, theory, and experiments are in reasonable agreement.

Author: J. S. DeGroot

LASNEX and Atomic Physics

Introduction

During the past year, the LASNEX Code group has concentrated on improving

transport models in the code. We have made significant advances in both photon and charged-particle transport, including refinements to the underlying atomic physics and development of new mathematical methods for solving the relevant transport equations. The work reported in the following four articles was performed in support of current target-design needs and was directed toward improving the general modeling capabilities of the LASNEX code.

When matching code calculations to experimental results, it has often been necessary to restrict the electron heat flow below the level normally expected by classical physics. Some of this restriction is now understood, but a factor of 2 to 20 remains to be explained. Understanding the causes of inhibited electron transport is essential if we are to accurately predict how future targets will perform. To this end, we have calculated a complete and consistent set of electron-transport coefficients for a magnetized, partially degenerate plasma, including models of the solid and liquid phases ("A New Electron-Transport Model for LASNEX"). We have also made several numerical improvements in the suprathermal-electron transport routine, including speeding convergence to a self-consistent electric field and the ability to handle arbitrary energy group spacings ("Suprathermal Electron-Bin Transport Allowing Arbitrary Bin Structure").

The ion-beam deposition package in LASNEX requires fast-ion stopping formulas in the heated target material. Heavy-ion beams may not be fully ionized; thus, their range may be longer than predicted by the fully ionized formulas currently used. Even a small range increase can have a substantial impact on target efficiency. Thus, we have made calculations of the dynamic charge state of a heavy ion as it experiences various ionization and recombination processes while slowing down in heated target material ("Ab Initio Calculations of the Charge State of a Fast, Heavy Ion Stopping in a Finite-Temperature Target").

In some target designs, radiation can be used to carry a substantial amount of the laser energy to the target. This has put additional accuracy requirements on the radiation flow models used in LASNEX. We have improved the efficiency of the routine used to solve the matrix representation of the diffusion equation ("A Vectorized Incomplete Cholesky-Conjugate Gradient Package for the Cray-1 Computer").

Author: G. B. Zimmerman

A New Electron-Transport Model for LASNEX

Hydrodynamic codes used to analyze laser-fusion plasma experiments require a complete set of electron-transport coefficients that can be used over a wide range of temperatures and densities, that are consistent with each other (Onsager symmetry relation), and that are expressed in a computationally simple form. We have developed a new electron-transport coefficient package for LASNEX that satisfies these difficult constraints.

The physical effects included in the model are

- Electron degeneracy.
- Debye–Hückel screening.
- Ion–ion coupling.
- Electron–neutral scattering.

We calculate the electron–ion collision rate in plasmas using a Coulomb cross section with carefully chosen cutoff parameters. For the solid and liquid phases, we employ the Bloch–Grüneisen formula[138] for the electron mean free path. Our model gives a complete set of transport coefficients, including not only electrical conductivity and thermal conductivity but also thermoelectric-power, Hall, Nernst, Ettinghausen, and Leduc–Righi coefficients. These coefficients are obtained by solving the Boltzmann equation in the relaxation-time approximation.

Our transport coefficients reduce to the well-known formulas of Spitzer[139] and Braginskii[140] at high temperature and low density. However, our results give significant improvement over the plasma formulas at high density. For example, when Spitzer's formula is applied to calculate electron thermal conductivity at temperature $T \leq 10$ eV and at near-solid density, it gives results that are incorrect by large factor ($\sim$10). Our transport coefficients also agree with results from a partial-wave calculation in which the electron–ion collision frequency is obtained by numerical solution

of the Schrödinger equation for Thomas–Fermi potentials.

For a plasma with small gradients of density and temperature and an arbitrary value of magnetic field, expressing the electric field in terms of the electrical current gives

$$\mathbf{E}_{\parallel} = \mathbf{j}_{\parallel}/\sigma_{\parallel} + S_{\parallel} \nabla_{\parallel} T \quad ,$$

$$\mathbf{Q}_{\parallel} = T S_{\parallel} \mathbf{j}_{\parallel} - K_{\parallel} \nabla_{\parallel} T \quad ,$$

$$\mathbf{E}_{\perp} = \mathbf{j}_{\perp}/\sigma_{\perp} + S_{\perp} \nabla_{\perp} T + R_{\perp} \mathbf{B} \times \mathbf{j} + N_{\perp} \mathbf{B} \times \nabla T \quad ,$$

$$\mathbf{Q}_{\perp} = T S_{\perp} \mathbf{j}_{\perp} - K_{\perp} \nabla_{\perp} T + N_{\perp} T \mathbf{B} \times \mathbf{j} + L_{\perp} \mathbf{B} \times \nabla T \quad , \qquad (124)$$

where σ = electrical conductivity, K = thermal conductivity, and S = thermoelectric power. The terms R, N, NT, and L are the Hall, Nernst, Ettinghausen, and Leduc–Righi coefficients, respectively.

The calculation of these coefficients requires knowledge of the momentum-transfer cross section. Since our goal is to obtain transport coefficients for use in large-scale hydrodynamic codes, we need a pragmatic method for calculating cross sections. By comparison with numerically calculated cross sections, we find that a Coulomb cross section with appropriate cutoff parameters gives a good approximation for the transport coefficients, except at high densities, where strong ion correlation can have a dramatic effect. The Coulomb cross section is

$$\sigma_{tr} = \frac{4\pi (Z^*)^2 e^4 \ln \Lambda}{m^2 v^4} \quad , \qquad (125)$$

where Z^* = ionization state. The Coulomb cross section is a reasonably accurate description of plasma scattering for conditions where the typical free electron has an energy small compared to the ionization potential of bound electrons.[41] The Coulomb logarithm, $\ln \Lambda$, is calculated with cutoff parameters that reflect influences of electron degeneracy, Debye–Hückel screening, and strong ion–ion coupling.

Using this Coulomb cross section, we obtain the complete set of electron-transport coefficients for plasmas. For example, the electrical conductivity is

$$\sigma_{\perp} = \frac{n e^2 \tau}{m} A_{\perp}(\mu/kT, \omega_e \tau) \quad , \qquad (126)$$

where μ is the chemical potential, $\omega_e = eB/mc$, and τ is given by

$$\tau = \frac{3 (m)^{1/2} (kT)^{3/2}}{2 (2)^{1/2} \pi (Z^*)^2 n_i e^4 \ln \Lambda} \times F_{1/2}(\mu/kT) \{1 + \exp(-\mu/kT)\} \quad , \qquad (127)$$

where $F_{1/2}(\mu/kT)$ is a Fermi function, and n_i is the ion density. The function $A_{\perp}(\mu/kT, \omega_e\tau)$ is expressed in terms of integrals involving the electron relaxation time, magnetic field, and local electron equilibrium distribution. For arbitrary values of electron degeneracy and magnetic field, we numerically evaluate $A_{\perp}$ and tabulate the results as a function of μ/kT and $\omega_e\tau$.

The conductivity model gives transport coefficients for partially ionized and partially degenerate plasmas of arbitrary composition. As an example, we calculate the electrical conductivity of aluminum.

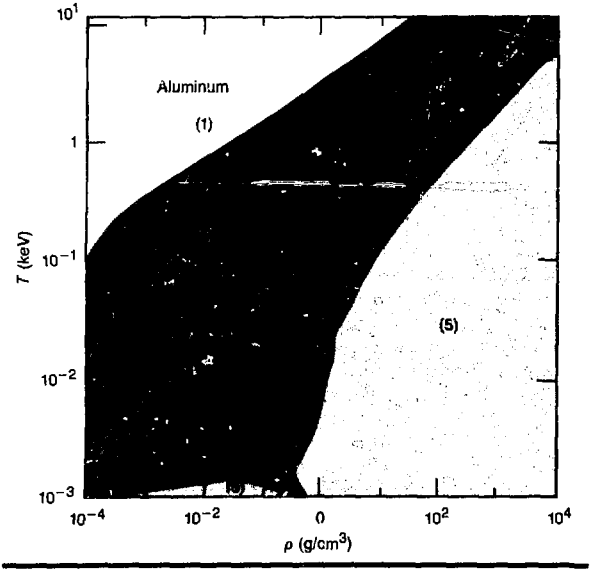

Fig. 3-70. Temperature and density regions where different theories described in text are used to calculate electron relaxation time.

Figure 3-70 shows the temperature–density regions where different theories are used in our model. Region (1) is the high-temperature/low-density plasma where the screening length is obtained from the Debye–Hückel theory. In region (2) (the dense plasma), the Debye–Hückel treatment of screening breaks down because of strong ion correlation effects. The Debye–Hückel screening length becomes less than the interatomic distance in this region. To be consistent with results from the one-component plasma (OCP) theory,[142] we replace the Debye–Hückel screening length in this region by the interatomic distance.

In region (3), the Coulomb logarithm reaches a minimum value equal to 2.0. With this minimum value for the Coulomb logarithm, the conductivity agrees with results from partial-wave calculations for Thomas–Fermi potentials. The same conclusion was reached in Refs. 143 and 144.

In region (4), the calculated electron mean free paths are less than the interatomic distance. Without detailed analysis of the conduction mechanism appropriate to this region, we adopt a minimum conductivity following the argument developed for amorphous semiconductors in Ref. 145.

Regions (5) represent liquid and solid phases. The electron mean free path in these regions is calculated using the Bloch–Grüneisen formula,[138] together with a semiphenomenological melting model[146] derived from the Thomas–Fermi theory. The electrical conductivity calculated by the Bloch–Grüneisen formula agrees adequately with experimental data for monovalent metals.

Figure 3-71 shows the electrical conductivity of aluminum as a function of temperature and density. The ionization state is obtained from the screened hydrogenic model.[147] In general terms, the model has a maximum error of a factor of 2 because of the approximations used in the calculation. Our results for a fully ionized plasma agree with Spitzer and Braginskii. At low temperature and high density, the conductivity model gives a significant improvement to the results of Spitzer and Braginskii.

Authors: Y. T. Lee, R. M. More, and B. Zimmerman

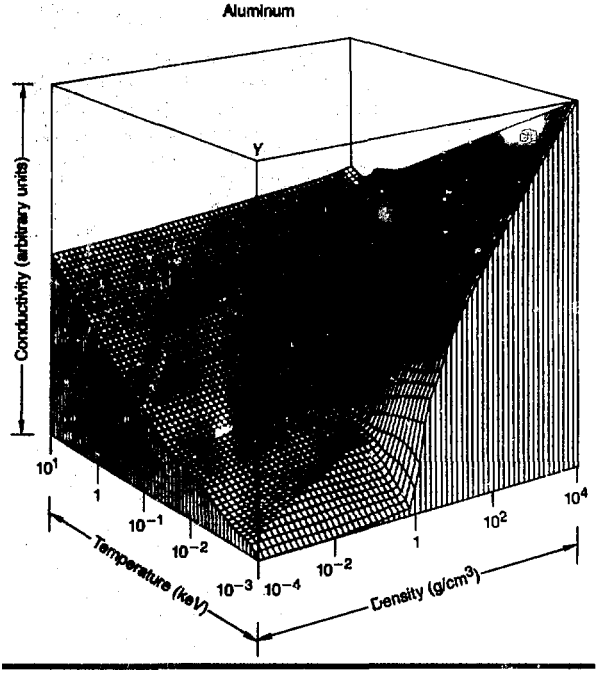

Fig. 3-71. Electrical conductivity calculated as function of temperature and density (zero magnetic field).

Suprathermal Electron-Bin Transport Allowing Arbitrary Bin Structure

LASNEX calculates the transport of suprathermal electrons in laser-fusion plasmas by solving a set of relativistic multigroup diffusion equations.[148] The method used to solve these equations is described in Ref. 149.

The simplifying assumption of equal-width energy bins[149] limits the usefulness of the model. Laser-fusion target designers encounter plasmas with T_{hot}/T_{cold} ratios ranging from 2 to 200 or more. Thus, the electron bins must span several orders of magnitude to represent the hot distribution. The requirement of equally spaced electron bins prevents the designers from finely resolving the low energies while simultaneously including the high energies. By using a bin structure with wider bins at the higher energies, the designer has the advantages that he or she can resolve the spectrum at the energies of interest, cover the entire energy range, and often use fewer

bins, thus making the calculations smaller and faster.

The new suprathermal electron transport allows unequally spaced electron bins. To do this, we wrote a completely general mapping from kinetic-energy space (KE) to total-energy space (TE) and back. To take full advantage of the Cray computer, the mapping routine is vectorizable over the mesh index, which is typically larger than the number of bins.

The mapping algorithm from KE to TE space is a generalization of the equally spaced mapping. The TE space bin structure is determined by the bin structure in the zone with the lowest potential energy, with the top bin repeated as many times as necessary to cover the entire total energy range. In mapping, the bin populations are weighted by the area of overlap. The bin quantities are weighted by the fraction of electrons from each KE bin contributing to the TE bin. The remap from TE to KE space of the newly transported bin population is also area weighted with the added constraint of $E \cdot J$ energy conservation. The energy conservation is applied first on a local zone-by-zone basis. If the energy is still not conserved, the remap for all zones is shifted to conserve energy. We now include the thermalization and the suprathermal hole loss terms in the energy-conserving remap. This eliminates nonphysical oscillations in the bin populations, which we observed with the old remap when thermalization was the dominant process.

To lessen the resolution problem, the old equally spaced bin routine rezoned the bin structure up and down, following the average suprathermal temperature $\langle T_s \rangle$ where

$$EN_{max} = P \langle T_s \rangle = P \left\{ \frac{\sum_l \sum_i \eta_i^l \epsilon_i}{\sum_l \sum_i \eta_i^l} \right\} , \quad (128)$$

EN_{max} = maximum bin energy, and ϵ_i and η_i^l are the bin energy and population for the ith bin in the lth zone, respectively. The factor P is set by the user with a drop-through value of 20.

The new routine allows the user to control the bin rezoning, or to let the code control it, or to eliminate it entirely and preserve the original bin structure throughout the calculation. Also, we have changed the definition of the average suprathermal temperature used in the rezone calculation to

$$EN_{max} = P \langle T_s \rangle = P \frac{1}{2} \left\{ \frac{\sum_l \sum_i \eta_i^l \epsilon_i \epsilon_i}{\sum_l \sum_i \eta_i^l \epsilon_i} + T_{hot} \right\} . \quad (129)$$

This definition emphasizes those bins with the most energy, not just those with the largest population, as in Eq. (128). For the same maximum bin energy, an unequally spaced bin structure with larger bins at the higher energies has much-lower-energy bins than in the equally spaced case. For this case, adding a given amount of energy to the lowest bin requires more electrons than in the unequal case. Therefore, using Eq. (128) with the unequally spaced bins, the code will predict a maximum bin energy that is too low when absorption in the lowest bin is dominant. This happens when inverse bremsstrahlung absorption takes place in a cold plasma. The maximum bin energy calculated by Eq. (129) is a more realistic value, as it emphasizes the bins that contain the most energy, not the most electrons.

Finally, the new suprathermal electron-transport routine, allowing unequally spaced electron bins, models typical problems in less than one-third the time required by the old, simpler routine. We achieved this speed in the more complex calculation by coding the inner loops over the mesh so that they could be vectorized by the compiler and take advantage of the vector nature of the Cray computer.

Authors: J. A. Harte and D. S. Kershaw

Ab Initio Calculations of the Charge State of a Fast, Heavy Ion Stopping in a Finite-Temperature Target

Because of recent interest in heavy-ion-driven ICF targets, we are improving the

stopping-power calculations used in the simulation codes for target design. Knowing the effective charge of the projectile ion is very important for these calculations, since it is the square of the charge that enters into the stopping-power calculation. This article discusses a calculation from first principles of the charge state of a fast, heavy ion traversing a finite-temperature target plasma.

To perform this calculation, we use an average-atom representation,[150] together with scaled hydrogenic rates[151] for the continuum and bound processes (see Table 3-5) to follow the time history of the projectile charge state. Since our main interest lies in a high-Z projectile and a warm, low-Z target, we have excluded various resonance processes that are important for near-neutral ions and enhanced charge transfer from target to projectile where there is a coincidence in the energy levels. In our case, since we expect the target and projectile atoms to be highly ionized, such resonance effects are small.

Next, we present arguments to show that even at approximately solid density in the target, three-body recombination is strongly suppressed by kinematic effects. To calculate the rate for this process, we must integrate the cross section over the initial electron-distribution function in both energy and angle. In our case, however, we essentially have delta functions, which, with requirements of energy and momentum conservation and the form of the cross section, lead to a small result. To get a quantitative estimate, we proceed as follows. From detailed balance, we can relate the recombination differential cross section to that for ionization. Using a Born approximation for the ionization differential cross section, and performing the phase-space integral, we finally obtain an analytic expression for the three-body rate. There are two parts to this: an angular part, shown in Fig. 3-72; and an energy factor, listed in scaled form in Table 3-6. Here, R(three-body/radiative recombination) $= R_0(E/I) \times (n_e/n_0) - (n/Z^*)^4$, where n_e = electron density (cm^{-3}), E = electron energy (keV), I = ionization potential (keV), n = level, and Z^* = ion charge. Even at threshold ($E/I \sim 1$, appropriate at equilibrium), the combination of angular and energy factors yields a suppression of 1000 to 10 000 for fast ions of high

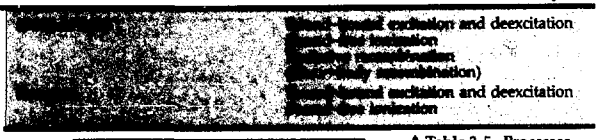

▲ Table 3-5. Processes included in rate calculations.

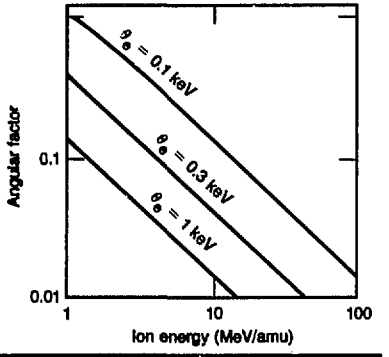

Fig. 3-72. Dependence of three-body recombination rate on angular point of phase space as function of projectile-ion energy for free-electron temperatures (θ_e) of 100, 300, and 1000 eV.

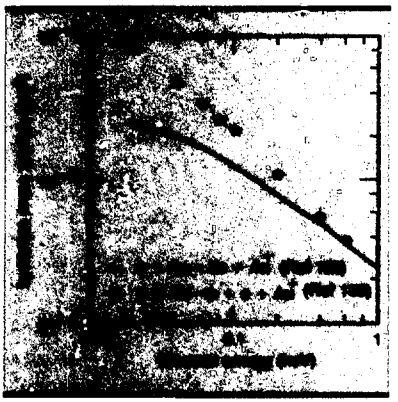

Fig. 3-73. Comparison of total ionization cross sections for incident electrons and protons as a function of collision energy per electron mass.

E/I	R_0
1.0	2.8×10^{-1}
5.0	4.74×10^{-3}
10.0	3.18×10^{-4}
15.0	1.02×10^{-4}
20.0	2.90×10^{-5}
30.0	6.52×10^{-6}

Table 3-6. Comparison of three-body recombination rate with radiative recombination rate.

charge of three body relative to radiative recombination.

Finally, we include the ion-ion processes by Z scaling from the electron results (i.e., $\sigma_{\text{ion-ion}} = (Z^*)^2 \times \sigma_{\text{electron-ion}}$). As shown in Fig. 3-73, this is a good approximation for fast ions on fully stripped targets, which is the case of greatest interest here.

In summary, the important processes are collisional ionization balanced at equilibrium by radiative recombination. Although similar to coronal equilibrium, the peaked electron-energy distribution means, in the

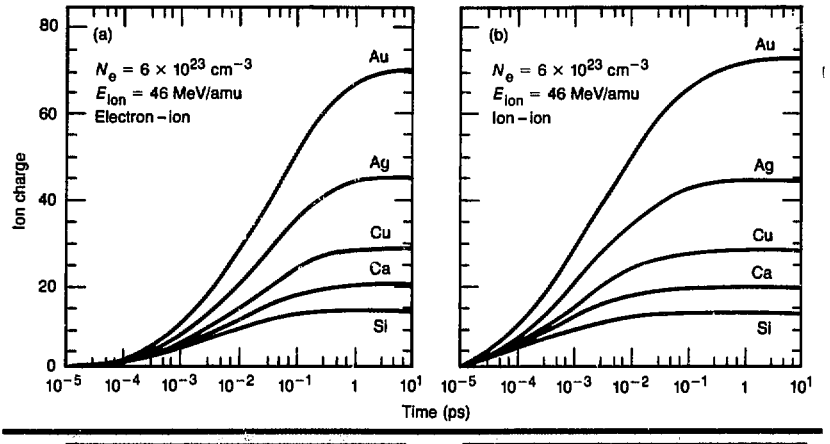

Fig. 3-74. Time-dependent charge state for several ions. (a) For electron collisions. (b) Ion collisions for target corresponding to fully stripped Al at solid density.

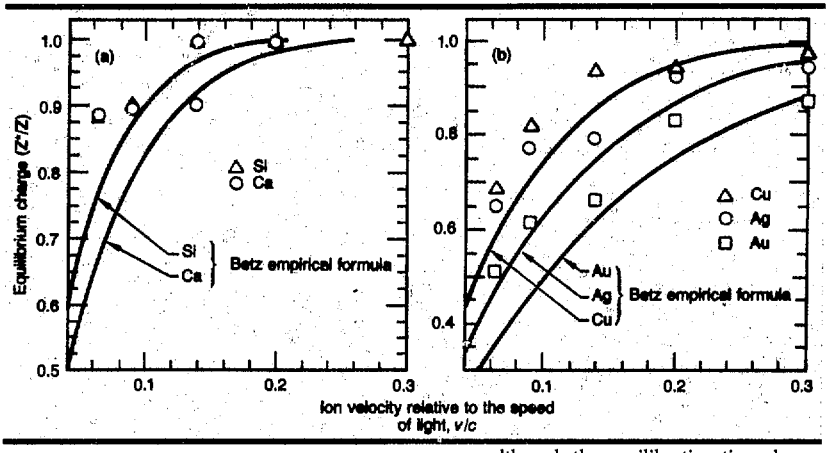

Fig. 3-75. Equilibrium charge state as a function of ion velocity for ions of Fig. 3-74. (a) Low-Z ions. (b) High-Z ions.

Table 3-7. Equilibrium distance (units of cold range).

Gold	Au	~0.16
Silver	Ag	~0.1
Copper	Cu	~0.025
Calcium	Ca	~0.01
Silicon	Si	~0.005

present case, that the same electrons excite as recombine, whereas, with Maxwellian electrons, it is the high-energy ones that do the excitation and the low-energy ones that recombine.

The results of solving the rate equations for various projectile ions with an energy of 46 MeV/amu (corresponding to 9 GeV for a gold ion) are shown in Fig. 3-74(a) for electron–ion excitation and in Fig. 3-74(b) for ion–ion excitation for a target ion with a Z^* of 10. For such fast ions, the equilibrium charge state is very close to fully stripped in all cases, although the time to reach equilibrium increases with projectile Z. Furthermore, although the equilibration time decreases for the ion–ion case [Fig. 3-74(b)], the equilibrium charge is almost identical to the electron–ion case, in agreement with the Bohr criterion. To express the equilibration time in more physical units, we list in Table 3-7 the equilibration distance (for a constant-velocity ion) in units of the cold range for the ions in Fig. 3-74. The delay distance increases rapidly with Z and, for gold ions, is 1/6 of the total range, which is a substantial effect. By repeating the calculations of Fig. 3-74 for lower-energy ions, we can obtain the equilibrium charge for each ion as a function of projectile velocity. These results are shown in Fig. 3-75(a) and (b) for the same ions used in Fig. 3-74. We also show for comparison the semi-empirical Betz formula.[154] At high velocities, the agreement is very good; at medium

velocities, shell effects cause our results to deviate from Betz; and, at low velocities (where the Betz formula starts to fail), our results are systematically high.

Finally, we mention a useful result that we obtain as a by-product of solving the rate equations, i.e., the radiation emission of the projectile ion as it traverses the target. We show in Fig. 3-76 the time-integrated emission spectrum of a 46-MeV/amu gold ion penetrating somewhat more than a cold target range depth in Al. Since the total radiation emission is ~2% of the original ion energy, it is a potential source of preheat in the rest of the target.

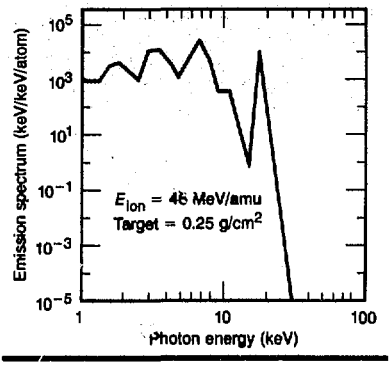

Fig. 3-76. Time-integrated emission spectrum for gold ion traversing 0.25 g/cm^2 of cold Al.

Authors: D. S. Bailey, Y. T. Lee, and R. M. More

A Vectorized Incomplete Cholesky-Conjugate Gradient Package for the Cray-1 Computer

In LASNEX, the two-dimensional radiation transport, electron thermal conduction, ion thermal conduction, and neutron transport all use the incomplete Cholesky-conjugate gradient (ICCG) method to solve the transport equations. We have been using ICCG[155] to solve the diffusion equation with a 9-point coupling[156] scheme on the CDC-7600. In going from the CDC-7600 to the Cray-1, a large part of the algorithm consists of solving tridiagonal linear systems on each L line of the Lagrangian mesh in a manner that is not vectorizable. Therefore, a direct translation from the CDC-7600 to the Cray-1 would not give much increase in running speed because the vectorization potential of the Cray-1 cannot be used. We have developed an alternative ICCG algorithm for the Cray-1 that uses a block form of the cyclic reduction algorithm described previously.[157] This new algorithm allows full vectorization and runs as much as five times faster than the old algorithm on the Cray-1. It is now being used in Cray-1 LASNEX to solve the two-dimensional diffusion equation in all the physics subroutines mentioned above.

In the article following Ref. 157, we described[158] our first attempt at vectorizing ICCG. In that earlier method, we applied the cyclic reduction permutation only within each block, with the blocks retaining the standard ordering. Thus, within each block, we had K = 1, 3, 5, 7,..., 2, 6, 10, 14,...2^P, but the blocks are ordered L = 1, 2, 3, 4,..., $LMAX$. The new method described here is conceptually much simpler, easier to program, and easier to maintain. Its speed of execution on the Cray-1 is about the same as the vectorization method described in Ref. 158.

Basic Algorithm. We have an equation, $MX = Y$, where M is positive definite, and symmetric, and the sparsity pattern is such that $M_{i,i}$, $M_{i,(i\pm1)}$, $M_{i,(i\pm KMAX)}$, $M_{i,(i\pm KMAX\pm1)}$ are the only nonzero elements.

The ICCG method consists of finding an approximate Cholesky decomposition for $M \approx LDL^T$ and then using the conjugate-gradient algorithm. Let $r_0 = Y - MX_0$ and $p_0 = (LDL^T)^{-1}r_0$, then

$$a_i = \left[r_i,(LDL^T)^{-1}r_i \right] / (p_i,Mp_i) \quad ,$$

$$X_{i+1} = X_i + a_i p_i \quad ,$$

$$r_{i+1} = r_i - a_i M p_i \quad ,$$

$$b_i = \frac{\left\{ r_{(i+1)},(LDL^T)^{-1}r_{(i+1)} \right\}}{\left[r_i,(LDL^T)^{-1}r_i \right]} \quad ,$$

$$p_{i+1} = (LDL^T)^{-1} r_{(i+1)} + b_i p_i \quad ,$$

$$\text{for } i = 0, 1, 2,.... \qquad (130)$$

This algorithm is trivially vectorizable except for the evaluation of the approximate inverse on the residual $(LDL^T)^{-1}r_i$. With the choice for the approximate Cholesky decomposition given in Ref. 155, this is a recursive operation that can only go at scalar speeds on the Cray-1. To improve it, we

must use a different approximate decomposition that allows for vectorization.

To see how this is done, we first write our equation in block form, in which our matrix, M, can be written

$$M = \begin{pmatrix} A_1 & B_1^T & 0 & 0 & \\ B_1 & A_2 & B_2^T & 0 & \\ 0 & B_2 & A_3 & B_3^T & \\ 0 & 0 & B_3 & A_4 & \ddots \\ & & & \ddots & \ddots \end{pmatrix} , \qquad (131)$$

where the A_i and B_i are tridiagonal matrices of dimension $KMAX$ and $i = 1, 2, 3,..., LMAX$.

To obtain an algorithm that allows vectorization, we apply the cyclic reduction permutation, but we apply it only to the $KMAX$ by $KMAX$ blocks, and, within a block, we retain the standard ordering.[158] Thus, the blocks are now ordered $L = 1, 3, 5, 7,..., 2, 6, 10, 14,..., 1\cdot 2^q, 3\cdot 2^q, 5\cdot 2^q, 7\cdot 2^q,..., 2^p$. Here, p is the highest power with $2^p \le LMAX$. Within a block, the elements are still ordered $K = 1, 2, 3, 4,..., KMAX$. Let P be the matrix that performs this reordering of the unknowns.

Our equation $MX = Y$ then becomes $(PMP^{-1})(PX) = (PY)$, and we now perform block LDL^T decomposition of this block-permuted matrix.

The decomposition is incomplete because, as we perform the block LDL^T decomposition, the blocks (which were originally all tridiagonal) would all quickly become dense, but we simply ignore (neither compute nor store) all elements that lie outside the tridiagonal band.[159]

Implementation. The implementation of the above algorithm into a practical code is straightforward. We have chosen to split the program into two levels. The first (ICCGAF) performs the actual matrix solution, while the second (SICCG) serves as a supervisor and interface to LASNEX.

The algorithm used in ICCGAF differs from that described in Ref. 159 in only one way. We found it useful, in rendering unique the decomposition $L_i^q\, D_i^q\, (L_i^q)^T = A_i^q$, to specify that the diagonal elements, $(L0_j)$, of the lower triangular matrices, L_i^q, equal the reciprocals of the corresponding elements (D_j) of the D_i^q, rather than equal unity. By this choice, the off-diagonal elements, $(L1_j)$, of L_i^q become equal to the corresponding elements, $(A1_j)$, of A_i^q. The sweep for each block then becomes

$$D_1 = 1/A0_1$$

For $J = 2,..., KMAX$,

$$D_j = 1/(A0_j - A1_{j-1}^2\, D_{j-1}) \quad , \qquad (132)$$

where the $A0_j$ are the diagonal elements of A_i^q, and $A0_j$ and D_j share the same storage (a copy of the input $A0$ is saved for later matrix multiplications). The $L0_j$ are not needed later, since, in $B^T = LDC^T$ (etc.), only $L0_jD_j = 1$ appears and, in the solve, the necessary division by $L0_j$ becomes a multiplication by D_j.

The other choice ($L0_j = 1$) would have led to the sweep

$$D_1 = A0_1 \quad ,$$

$$L1_1 = A1_1/D_1 \quad .$$

For $J = 2,..., KMAX$,

$$D_j = A0_j - L1_{j-1}^2\, D_{j-1} \quad ,$$

$$L1_j = A1_j/D_j \quad . \qquad (133)$$

If the $L1$ overwrite the $A1$, extra storage to save a copy of the input $A1$ is required. This choice would also lead to one extra multiplication in the formation of the C. Because most of the time is spent in the iteration and not in the decomposition, this is a minor savings.

On input to ICCGAF, each array is of length $2*KMAX*LMAX$. The last half of the Y array is used to save $A0$ for matrix multiplications. A workspace, W, of length $4*KMAX*LMAX$ is required. The first quarter is used to store the diagonals of the C matrices. For odd blocks at each level, the subdiagonals of C are equal to those of B, while, for even blocks, the superdiagonals are equal. Hence, the second quarter of W contains the off-diagonals of the C matrices. The last two quarters of W are used for the r and p vectors of the conjugate-gradient iteration.

The interlaced storage of the sub- and superdiagonal bands of the C for alternate blocks suggests we specify that the first significant element of the superdiagonal of the B be the first element, not the second. Since

this does not agree with previous LASNEX convention, SICCG supplies the necessary offset in its calls to ICCGAF.

The code was written using structured programming techniques. Special care needed to be taken in the coding to ensure that "overreaches" (references to undefined elements beyond the ends of an array's storage) do not lead to errors. Appropriate directives instructing the compiler to ignore apparent vector dependencies in the sweeps were employed, so that all loops could be processed in vector mode on the Cray-1.

The supervisor routine SICCG performs a number of functions

- We note that the program is most efficient for problems with $LMAX \gg KMAX$ because this implies a large number of small blocks and, thus, long vector lengths and simple sweeps. For smaller block sizes, less fill-in is discarded in the incomplete decomposition; hence, convergence is faster in the conjugate-gradient iteration. Thus, when appropriate, we transpose the computational mesh by interchanging K and L. The transposition is always rapid, so it is performed whenever $KMAX > LMAX$.
- To prevent excessive memory-bank access time, no bank can be referenced more frequently than every four machine cycles. In particular, we should avoid references to array elements spaced by multiples of 8. The entire storage scheme described in Ref. 159 was worked out with this in mind. Since we often need reference elements spaced by increments 2*$KMAX$, it is important to ensure that $KMAX$ is odd. In LASNEX, there is always a column of boundary zones for which the diffusion equation need not be solved. This column is either preserved or eliminated, depending on whether $KMAX$ on input is odd or even, before the call to ICCGAF. The row of boundary zones corresponding to $L = 1$ is eliminated by calling ICCGAF with offset arrays as arguments. If transposition is called for, the $L = 1$ row is kept or discarded, depending on whether the input $LMAX$ is odd or even, so that the new $KMAX$ seen by ICCGAF is always odd.
- Boundary matrix elements needed to calculate fluxes can be overwritten when ICCGAF is called after the above-described operations. Thus, SICCG saves these elements and restores them after solution. Vacuum-field values are similarly saved and restored.
- Since hand-coded (assembly language) routines for solution of tridiagonal systems are available, they (rather than ICCGAF) are called by SICCG for solution of one-dimensional problems. For $LMAX = 2$, a simple call with an offset of $KMAX + 1$ is made, while, for $KMAX = 2$, a transposition is performed before the call. For single-zone (zero-dimensional) problems, the hand-coded routines fail, so a single division in SICCG solves the remaining trivial equation.
- SICCG chooses the maximum number of levels of cyclic reduction to be performed (S). On problems with small $LMAX$, this number may be greater than the number needed to process all levels, and ICCGAF uses the smaller of the two. At present, S is hardwired at four levels (see below).
- As mentioned above, SICCG changes the storage convention for the superdiagonal elements of the B arrays to and from that of ICCGAF.

Performance. The new algorithm has been tried on a variety of test problems. These include the model problem from Ref. 155, a typical real problem taken from a laser-fusion simulation, and a set of M matrices whose elements were randomly generated and whose mean degree of diagonal dominance was adjustable to obtain matrices with different degrees of ill-conditioning.

Incomplete cyclic reduction worked very well. For all the matrices we tried, it was true that the B blocks decreased very rapidly relative to the A blocks (in fact they decreased quadratically as predicted in Ref. 158). Even for the stiffest model problems, it was never necessary to go beyond $S = 3$ to get the fastest possible running time. Performance was typically a weak function of S for $S > 0$. More recent LASNEX user experience showed that, on very stiff problems, the routine would fail to converge with S set at 2; when S was raised to 4, the routine performed well.

Figure 3-77 shows relative running times for the new vectorizable algorithm and the scalar algorithm given in Ref. 155. $KMAX$ was held fixed at $KMAX = 5$ and $LMAX$ was varied from 4 to 8000. The matrices were generated by setting each subdiagonal element $M_{(i+1)i}$, $M_{(i+KMAX)i}$,

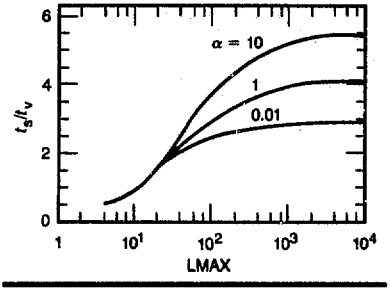

Fig. 3-77. Ratio of scalar execution times, t_s, to vector execution times, t_v, for solution of block tridiagonal linear system. *LMAX* is number of blocks, α is stiffness parameter.

$M_{(i+KMAX-1)i}$, and $M_{(i+KMAX+1)}$ to a different random number between -1 and 0.

This fixes the superdiagonals, since M is symmetric. Then, we set

$$M_{ii} = \alpha * RANF - \sum_{j} M_{ji} \quad , \tag{134}$$

where the summation is over all the off-diagonal elements in the ith column, *RANF* is a random number between 0 and 1, and α is a stiffness parameter. By construction, M is a diagonally dominant M matrix and so is positive definite. We chose a random X vector, found Y from $Y = MX$, and then solved $Y = MX$ using ICCG until $\| X^n - X \| / \| X \| \leq 10^{-7}$, where X^n was the ICCG solution for X after n iterations and $\| X \|$ was the Euclidean norm. Both the old and new algorithms were written in FORTRAN, compiled with CFT, and run on the Cray-1 computer. The new algorithm was completely vectorized. The old algorithm was completely vectorized except for the incomplete factorization, $LDL^T \approx M$, and the incomplete solve $(LDL^T)^{-1} r_i$. These operations are recursive and cannot be vectorized. The ratio of the central processor times is shown in Fig. 3-77 for three different values of α. Asymptotically, the new algorithm runs three to five times faster than the old. As the problem got stiffer, the new algorithm tended to take a few more iterations than the old. This is why the speed increase is less for small α.

Authors: A. Friedman and D. S. Kershaw

1. J. H. Nuckolls, L. L. Wood, A. R. Thiessen, and G. B. Zimmerman, *Nature* **239**, 139 (1972); J. H. Nuckolls, in *Laser Interaction and Related Plasma Phenomena* Vol. 3, H. Schwarz and H. Hora, Eds. (Plenum, New York, 1974), p. 399.
2. J. P. Anthes, M. A. Gusinow, and M. K. Matzen, *Phys. Rev. Lett.* **41**, 1300 (1978); J. Grun, R. Decoste, B. H. Ripin, and J. Gardner, U.S. Naval Research Laboratory, Washington, D.C., Report No. 4410 (1981)(unpublished); R. Decoste et al., *Phys. Rev. Lett.* **42**, 1673 (1979); F. Amiranoff, R. Fabbro, E. Fabre, C. Garban, J. Virmont, and M. Weinfeld, *Phys. Rev. Lett.* **43**, 522 (1979); B. H. Ripin et al., *Phys. Fluids* **23**, 1012 (1980); B. H. Ripin et al., *Phys. Fluids* 24, 990 (1981) **24**, 990 (1981); H. Nishimura et al., *Phys. Rev. A* **23**, 2011 (1981); W. C. Mead et al., *Phys. Rev. Lett.* **47**, 1289 (1981); M. D. Rosen et al., *Phys. Fluids* **22**, 2020 (1979).
3. C. E. Max, R. Fabbro, and E. Fabre, *Bull. Am. Phys. Soc.* **25**, 895 (1980).
4. J. L. Bobin, *Phys. Fluids* **14**, 2341 (1971).
5. H. Takabe, K. Nishihara, and T. Taniuti, *J. Phys. Soc. Japan* **45**, 2001 (1978).
6. W. M. Manheimer, D. G. Colombant, and J. H. Gardner, "Steady-State Planar Ablative Flow," U.S. Naval Research Laboratory, Washington, D.C., Memorandum Report 4644 (1981).
7. F. S. Felber, *Phys. Rev. Lett.* **39**, 84 (1977).
8. J. Virmont, R. Pellat, and P. Mora, *Phys. Fluids* **21**, 567 (1978); D. Shvarts, C. Jablon, I. B. Bernstein, J. Virmont, and P. Mora, *Nucl. Fusion* **19**, 1457 (1979); E. Goldman, *Plasma Phys.* **15**, 289 (1977).
9. L. Spitzer, Jr., *Physics of Fully Ionized Gases* (Wiley-Interscience, New York, 1967), Ch. 5.
10. W. L. Kruer, *Comments Plasma Phys. Controlled Fusion* **5**, 69 (1979); C. E. Max, in *Proc. Les Houches Summer School Theoret. Phys.*, Vol. 34., R. Balian and J. C. Adam, Eds. (North-Holland, Amsterdam, 1981).
11. A. V. Gurevich et al., *Sov. Phys.—JETP* **22**, 449 (1966); A. V. Gurevich et al., *Sov. Phys—JETP* **27**, 476 (1968); S.I. Anisimov and Yu. V. Medvedev, *Sov. Phys.—JETP* **49**, 62 (1979).
12. J. E. Crow, P. L. Auer, and J. E. Allen, *J. Plasma Phys.* **14**, 65 (1975).
13. J. E. Allen and J. G. Andrews, *J. Plasma Phys.* **4**, 187 (1970).
14. J. Denavit, *Phys. Fluids* **22**, 1384 (1979).
15. P. Mora and R. Pellat, *Phys. Fluids* **22**, 2300 (1979).
16. L. Landau and E. Lifshitz, *Fluid Mechanics* (Addison-Wesley, Reading, Md., 1959), pp. 33–43; R. Courant and K. O. Friedrichs, *Supersonic Flow and Shock Waves* (Wiley-Interscience, New York, 1948), pp. 92–95.
17. F. J. Mayer, R. L. Berger, and C. E. Max, *Phys. Fluids* **23**, 1244 (1980).
18. C. E. Max and C. F. McKee, *Phys. Rev. Lett.* **39**, 1336 (1977).
19. J. D. Perez and G. L. Payne, *Phys. Fluids* **22**, 361 (1979).
20. L. Montierth and R. L. Morse, *Phys. Fluids* (to be published).
21. B. H. Ripin et al., *Phys. Fluids* **25**, 1012 (1980); M. H. Key, R. G. Evans, P. T. Rumsby, and W. Toner, *Topical Meeting on Inertial Confinement Fusion* (San Diego, Calif., 1980), Rutherford Laboratory Report No. RL-80-023 (1980); R. Fabbro et al., *Rapport d'Activité 1979*, GRECO Interaction Laser Matière, Ecole Polytechnique, Palaiseau, France, pp. 113–129.
22. L. L. Cowie and C. F. McKee, *Astrophys. J.* **211**, 135 (1977).
23. C. E. Max, C. F. McKee, and W. C. Mead, *Phys. Fluids* **23**, 1620 (1980); C. E. Max, C. F. McKee, and W. C. Mead, *Phys. Rev. Lett.* **45**, 28 (1980).
24. B. H. Ripin et al., *Phys. Fluids* **23**, 1012 (1980); B. H. Ripin et al., *Phys. Fluids* **24**, 990 (1981).
25. B. H. Ripin et al., U.S Naval Research Laboratory, Washington, D.C., Memorandum Report No. 4212 (1980).
26. J. H. Gardner and S. E. Bodner, *Phys. Rev. Lett.* **47**, 1137 (1981); S. E. Bodner, *J. Fusion Energy* **1**, 221 (1981).
27. C. E. Max, J. D. Lindl, and W. C. Mead, *Effect of Symmetry Requirements on the Wavelength Scaling of Directly Driven Laser Fusion Implosions*, Lawrence Livermore National Laboratory, Livermore, Calif., UCRL-86715 Rev. 1 (1981).
28. C. Garban-Labaune, E. Fabre, R. Fabbro, F. Amiranoff, and M. Weinfeld, in *Rapport d'Activité 1979*, GRECO Interaction Laser-Matière (Ecole Polytechnique, Palaiseau, France), pp. 64–75; F. Amiranoff, R. Fabbro, E. Fabre, C. Garban, J. Virmont, and M. Weinfeld, *Phys. Rev. Lett.* **43**, 522 (1979); A. G. M. Maaswinkel, K. Eidmann, and R. Sigel, *Phys. Rev. Lett.* **42**, 1625 (1979); A. G. M. Maaswinkel, *Opt. Commun.*, **33**, 62 (1980); D. C. Slater et al., *Phys. Rev. Lett.* **46**, 1199 (1981); W. C. Mead et al., *Phys. Rev. Lett.* **47**, 1289 (1981); W. Seka et al., *Bull. Am. Phys. Soc.* **25**, 895 (1980).
29. C. E. Max and K. G. Estabrook, *Comments Plasma Phys. Controlled Fusion* **5**, 239 (1980).
30. S. E. Bodner, *J. Fusion Energy* **1**, 221 (1981).
31. *Laser Program Annual Report—1974* Lawrence Livermore National Laboratory, Livermore, Calif., UCRL-50021-74 (1975), pp. 391–395.
32. W. C. Mead and J. D. Lindl, *Symmetry and Illumination Uniformity Requirements for High Density Laser-Driven Implosions*, Lawrence Livermore National Laboratory, Livermore, Calif., UCRL-78459 (1976); *Bull. Am. Phys. Soc.* **21**, 1102 (1976).
33. L. Spitzer, Jr., *Physics of Fully Ionized Gases* (Wiley-Interscience, New York, 1967), Ch. 5.
34. C. E. Max, C. F. McKee, and W. C. Mead, *Phys. Fluids* **23**, 1620 (1980); C. E. Mac, C. F. McKee, and W. C. Mead, *Phys. Rev. Lett.* **45**, 28 (1980).
35. E. Fabre, *Bull. Am. Phys. Soc.* **25**, 992 (1980).
36. W. A. Barletta, *Thermalization of Heavy-Ion Beams in the Final Lens of Vacuum Reactor Vessels*, Lawrence Livermore National Laboratory, Livermore, Calif., UCRL-86016 (1981).
37. J. W-K. Mark, *Plasmas in Particle Accelerators: Adiabatic Theories for Bunched Beams*, Lawrence Livermore National Laboratory, Livermore, Calif., UCID-18947, Part II (1981).

References

38. G. Krafft, J. W-K. Mark, L. Smith, and T. F. Wang, *Proc. 1981 Palaiseau (France) Intern. Topical Conf. High-Power Electron Ion-Beam Res. Tech.* (1981).
39. J. W-K. Mark, *Bull. Am. Phys. Soc.* **25**, 968 (1980).
40. *Laser Program Annual Report—1980*, Lawrence Livermore National Laboratory, Livermore, Calif., UCRL-50021-80 (1981), pp. 3-17 to 3-19.
41. F. C. Young, S. J. Stephanakis, S. ... Goldstein, and D. Mosher, *Bull. Am. Phys. Soc.* **2v**, 920 (1981).
42. F. Winterberg, *Phys. Rev.* **174**, 212 (1968).
43. J. W. Shearer, *Nucl. Fusion* **15**, 952 (1975).
44. M. J. Clauser, *Phys. Rev. Lett.* **35**, 848 (1975).
45. J. M. Kindel and E. L. Lindman, *Nucl. Fusion* **19**, 597 (1979).
46. R. O. Bangerter and D. J. Meeker, *Ion Beam Inertial Fusion Targets*, Lawrence Livermore National Laboratory, Livermore, Calif., UCRL-78474 (1976).
47. J. D. Lindl, *Low Aspect Ratio Double Shells for High Density and High Gain*, Lawrence Livermore National Laboratory, Livermore, Calif., UCRL-80104 (1977).
48. J. W-K. Mark, *Bull. Am. Phys. Soc.* **25**, 968 (1980).
49. *Laser Program Annual Report—1980*, Lawrence Livermore National Laboratory, Livermore, Calif., UCRL-50021-80 (1981), p. 3-17.
50. *Particle-Beam Fusion Progress Report, July 1980 through December 1980*, Sandia National Laboratories, Albuquerque, N. Mex., SAND 81-0683 (1981).
51. *Light Ion Design Review and R&D Plan Workshop*, Electric Power Research Institute at Sandia National Laboratories, Albuquerque, N. Mex., October 1981, EPRI RP 1527-1 (1981).
52. D. L. Judd, *Proc. Heavy Ion Fusion Workshop*, Argonne National Laboratory, Argonne, Ill., ANL-79-41 (1978), p. 237.
53. *Laser Program Annual Report—1980*, Lawrence Livermore National Laboratory, Livermore, Calif., UCRL-50021-80 (1981), p. 3-19.
54. J. W-K. Mark, *Bull. Am. Phys. Soc.* **25**, 968 (1980).
55. W. A. Barletta, W. M. Fawley, E. P. Lee, and S. S. Yu, *Proc. 4th Intern. Top. Conf. High-Power Elect. Ion-Beam Res. Tech.*, Palaiseau, France, H. J. Doucet and J. M. Buzzi, Eds. (1981).
56. *Laser Program Annual Report—1976*, Lawrence Livermore National Laboratory, Livermore, Calif., UCRL-50021-76 (1977), p. 4-36.
57. *Laser Program Annual Report—1980*, Lawrence Livermore National Laboratory, Livermore, Calif., UCRL-50021-80 (1981), p. 3-17.
58. D. L. Judd and R. O. Bangerter, *Impact of New HIF Target Requirements on the Phase-Space Constraint*, Lawrence Berkeley Laboratory, Berkeley, Calif., HIFAN 163 (1981).
59. A. W. Maschke, *Megalac: A New Approach to Low-Beta Acceleration*, Brookhaven National Laboratory, Upton, N.Y., BNL-51029 (1979).
60. *Laser Program Annual Report—1980*, Lawrence Livermore National Laboratory, Livermore, Calif., UCRL-50021-80 (1981), p. 9-1.
61. E. P. Lee, S. S. Yu, and W. A. Barletta, *Nucl. Fusion* **21**, 961 (1981).
62. W. A. Barletta, *Thermalization of Heavy-Ion Beams in the Final Lens of Vacuum Reactor Vessels*, Lawrence Livermore National Laboratory, Livermore, Calif., UCRL-86016 (1981).
63. A. W. Maschke, *Megalac: A New Approach to Low Beta Acceleration*, Brookhaven National Laboratory, Upton, N.Y., BNL-51029 (1979).
64. W. B. Herrmannsfeldt, *High Intensity Multi-Megajoule Heavy Ion Accelerator*, Lawrence Berkeley Laboratory, Berkeley, Calif., HIFAN-153 (1980).
65. D. L. Judd, *Phase-Space Constraints on Induction-Linac Heavy-Ion Inertial Fusion Igniters*, Lawrence Berkeley Laboratory, Berkeley, Calif., HIFAN 178 (1981).
66. D. L. Judd, *Phase-Space Constraints on Induction-Linac Heavy-Ion Inertial Fusion Igniters*, Lawrence Berkeley Laboratory, Berkeley, Calif., LBL-14038, p. 28.
67. *Laser Program Annual Report—1980*, Lawrence Livermore National Laboratory, Livermore, Calif., UCRL-50021-80 (1981), p. 3-30.
68. A. B. Langdon and B. F. Lasinski, "Electromagnetic and Relativistic Plasma Simulation Models," in *Methods in Computational Physics*, Vol. 16, B. Alder and S. Fernbach, Eds., J. Killeen, Vol. Ed. (Academic Press, New York, 1976), p. 327.
69. W. L. Kruer, K. G. Estabrook, B. F. Lasinski, and A. B. Langdon, "Raman Backscatter in High Temperature, Inhomogeneous Plasmas," *Phys. Fluids* **23**, 1326 (1980); K. G. Estabrook, W. L. Kruer, and B. F. Lasinski, "Heating by Raman Backscatter and Forward Scatter," *Phys. Rev. Lett.* **45**, 1399 (1980).
70. A. B. Langdon and B. F. Lasinski, *Frequency-Shift of Self-Trapped Light*, Lawrence Livermore National Laboratory, Livermore, Calif., UCRL-82076 (1980). (Submitted to *Phys. Fluids*.)
71. A. B. Langdon, B. F. Lasinski, and W. L. Kruer, "Nonlinear Saturation and Recurrence of the Two-Plasmon Decay Instability," *Phys. Rev. Lett.* **43**, 133 (1979).
72. H. A. Baldis and C. J. Walsh, "Experimental Observations of Nonlinear Saturation of the Two Plasmon Decay Instability," *Phys. Rev. Lett.* **47**, 1658 (1981).
73. A. T. Lin and J. M. Dawson, "Simulated Compton Scattering of Electromagnetic Waves in Plasma," *Phys. Fluids* **18**, 201 (1975).
74. W. L. Kruer, K. G. Estabrook, and K. H. Sinz, "Instability Generated Laser Reflection in Plasmas," *Nucl. Fusion* **13**, 952 (1973).
75. K. G. Estabrook, W. L. Kruer, and B. F. Lasinski, "Heating by Raman Backscatter and Forward Scatter," *Phys. Rev. Lett.* **45**, 1399 (1980).
76. W. L. Kruer, K. G. Estabrook, B. F. Lasinski, and A. B. Langdon, "Raman Backscatter in High Temperature, Inhomogeneous Plasmas," *Phys. Fluids* **23**, 1326 (1980).
77. *Laser Program Annual Report—1980*, Lawrence Livermore National Laboratory, Livermore, Calif., UCRL-50021-80 (1981), p. 3-34.
78. *Laser Program Annual Report—1979*, Lawrence Livermore National Laboratory, Livermore, Calif., UCRL-50021-79 (1980), p. 6-32.

79. D. W. Phillion, D. L. Banner, E. M. Campbell, and R. E. Turner, "Stimulated Raman Scatterin in Large Plasmas" (submitted to *Phys. Fluids*).
80. M. C. Richardson, L. M. Goldman, W. Seka, J. M. Soures, K. Tanaka, R. Bingham, and E. Williams, "Raman Side-Scattering and Evidence of $2\omega_p$ Instability in UV Plasmas," *Bull. Am. Phys. Soc.* **26**, 954 (1981).
81. J. F. Drake, P. K. Kaw, Y. C. Lee, G. Schmidt, C. S. Liu, and M. N. Rosenbluth, "Parametric Instabilities of Electromagnetic Waves in Plasmas," *Phys. Fluids* **17**, 778 (1974).
82. P. C. Clemmow and J. P. Dougherty, *Electrodynamics of Particles and Plasmas* (Addison-Wesley, Reading, Md., 1969), p. 278.
83. J. R. Albritton and P. Koch, "Cold Plasma Wavebreaking: Production of Energetic Electrons," *Phys. Fluids* **18**, 1136 (1975).
84. C. Randall, J. R. Albritton, and E. A. Williams, "Finite Bandwidth Effects in Resonant Absorption." (To be submitted to *Phys. Fluids*.)
85. *Laser Program Annual Report—1979*, Lawrence Livermore National Laboratory, Livermore, Calif., UCRL-50021-79 (1980), p. 3-16.
86. R. J. Faehl and W. L. Kruer, "Laser Light Absorption by Short Wavelength Ion Turbulence," *Phys. Fluids* **20**, 55 (1977).
87. W. L. Kruer, "Efficient Energy Transfer Between Fast and Slow Electron Plasma Oscillations," *Phys. Fluids* **15**, 2423 (1972).
88. W. M. Manheimer, D. G. Colombant, and B. H. Ripin, "Efficient Light Absorption by Ion-Acoustic Fluctuations in Laser-Produced Plasmas," *Phys. Rev. Lett.* **38**, 1135 (1977).
89. J. M. Dawson and C. Oberman, "High-Frequency Conductivity and the Emission and Absorption Coefficients of a Fully Ionized Plasma," *Phys. Fluids* **5**, 517 (1962); P. K. Kaw, A. T. Lin, and J. M. Dawson, "Quasi-Resonant Mode Coupling of Electron Plasma Waves," *Phys. Fluids* **16**, 1967 (1973).
90. R. L. Stenzel, "Experiments on Current-Driven Three-Dimensional Ion Sound Turbulence. Part II: Wave Dynamics," *Phys. Fluids* **21**, 99 (1978).
91. M. Yamada and M. Raether, "Saturation of the Ion-Acoustic Instability in a Weakly Ionized Plasma," *Phys. Rev. Lett.* **32**, 99 (1974).
92. Y. Amagishi, "Turbulent-Like Spectrum of Ion Waves in a Beam-Plasma System," *Phys. Rev. Lett.* **29**, 405 (1972).
93. Y. Kawai and M. Guyot, "Observation of Anomalous Resistivity Caused by Ion Acoustic Turbulence," *Phys. Rev. Lett.* **39**, 1141 (1977).
94. W. M. Bollen, *Plasma Turbulence Driven by a High Density, Low Energy Electron Beam in a Double Plasma Device*, Ph.D. thesis, University of California, Davis, Calif. (1979).
95. C. Hollenstein, M. Guyot, and E. S. Weibel, "Stationary Potential Jumps in a Plasma," *Phys. Rev. Lett.* **45**, 2110 (1980).
96. R. E. Slusher, C. M. Surko, D. R. Moler, and M. Porkolab, "Study of the Current-Driven Ion-Acoustic Instability Using CO_2-Laser Scattering," *Phys. Rev. Lett.* **36**, 674 (1976).
97. A. Y. Wong, B. H. Quon, and B. H. Ripin, "Evolution of Bernstein-Greene-Kruskal-Like Ion Modes with Trapped Electrons," *Phys. Rev. Lett.* **30**, 1299 (1973); K. Muraoka et al., "Anisotropy of Turbulence in a Collisionless Shock," *J. Plasma Phys.* **10**, 135 (1973).
98. J. DeGroot, University of California, Davis, Calif., private communication (1980).
99. B. H. Quon, A. Y. Wong, and B. H. Ripin, "Backscattering Decay Processes in Electron Beam-Plasma Interactions including Ion Dynamics," *Phys. Rev. Lett.* **32**, 406 (1974).
100. A. A. Offenburger, A. Ng, and L. Pitt, "Ion Turbulence in a CO_2-Laser-Plasma Interaction Experiment," *Phys. Rev. Lett.* **40**, 873 (1978).
101. D. R. Gray et al., "Observation of Severe Heat-Flux Limitation and Ion Acoustic Turbulence in a Laser-Heated Plasma," *Phys. Rev. Lett.* **39**, 1270 (1977).
102. K. G. Estabrook and J. E. Tull, *An 880 Nanosecond Particle in Cell Mover for the CDC-7600*, Lawrence Livermore National Laboratory, Livermore, Calif., UCID-17050 (1977).
103. W. L. Kruer, Lawrence Livermore National Laboratory, Livermore, Calif., private communication (1980).
104. N. G. Basov et al., *Plasma Physics: Nonlinear Theory and Experiments*, H. Wilhelmsson, Ed. (Plenum, New York, 1977).
105. K. G. Estabrook and W. L. Kruer, "Properties of Resonantly Heated Electron Distributions," *Phys. Rev. Lett.* **40**, 42 (1978).
106. K. G. Estabrook, "Critical Surface Bubbles and Corrugations and Their Implications to Laser Fusion," *Phys. Fluids* **19**, 1733 (1976).
107. B. Grek, F. Martin, T. W. Johnston, H. Pepin, G. Mitchel, and F. Rheault, "Fine-Scale Structures in Plasmas Stimulated by a CO_2 Laser," *Phys. Rev. Lett.* **41**, 1811 (1978).
108. J. J. Thomson and W. L. Kruer, *Comments Plasma Phys. Controlled Fusion* **3**, 129 (1978).
109. N. H. Ebrahim, H. A. Baldis, C. Joshi, and R. Benech, *Phys. Rev. Lett.* **45**, 1179 (1980).
110. D. W. Phillion and D. L. Banner, *Stimulated Raman Scattering in Large Plasmas*, Lawrence Livermore National Laboratory, Livermore, Calif., UCRL-84854 (1980).
111. W. L. Kruer, *Advances in Plasma Physics*, Vol. 6, A. Simon and W. Thompson, Eds. (Wiley, New York, 1976), pp. 237-269.
112. K. G. Estabrook, E. J. Valeo, and W. L. Kruer, *Phys. Fluids* **18**, 1151 (1975); D. W. Forslund, J. M. Kindel, K. Lee, E. L. Lindman, and R. Morse, *Phys. Rev. A* **11**, 679 (1975).
113. K. Lee, D. W. Forslund, J. M. Kindel, and E. L. Lindman, *Phys. Fluids* **20**, 51 (1977).
114. V. L. Ginzburg, *The Properties of Electromagnetic Waves in Plasmas* (Pergamon, New York, 1964), p. 260.
115. K. G. Estabrook and W. L. Kruer, *Phys. Rev. Lett.* **40**, 42 (1978).
116. F. W. Perkins and J. Flick, *Phys. Fluids* **14**, 2012 (1971).

References

117. *Laser Program Annual Report—1980*, Lawrence Livermore National Laboratory, Livermore, Calif., UCRL-50021-80 (1981), p. 3-65.
118. D. W. Forslund, J. M. Kindel, and E. L. Lindman, *Phys. Fluids* **18**, 1002 (1975).
119. H. E. Huey, A. Mase, N. C. Luhmann, Jr., W. F. DiVergilio, and J. I. Thomson, *Phys. Rev. Lett.* **45**, 795 (1980).
120. A. B. Langdon and B. A. Lasinski, *Methods in Computational Physics*, Vol. 16, B. Alder, S. Fernbach, and M. Rotenberg, Eds. (Academic Press, New York, 1976).
121. C. I. Randall and J. J. Thomson, *Phys. Rev. Lett.* **43**, 924 (1979).
122. M. Abramowitz and S. A. Stegun, *Handbook of Mathematical Functions* (Dover, New York, 1965).
123. S. I. Braginskii, *Reviews of Plasma Physics*, Vol. 1, M. A. Leontovich, Ed. (Consultants Bureau, New York, 1965), p. 205.
124. M. Ono and R. M. Kulsrud, *Phys. Fluids* **18**, 1287 (1975).
125. M. N. Rosenbluth, W. M. MacDonald, and D. L. Judd, *Phys. Rev.* **107**, 1 (1957).
126. *Laser Program Annual Report—1980*, Lawrence Livermore National Laboratory, Livermore, Calif., UCRL-50021-80 (1981), p. 3-57.
127. A. Friedman, A. B. Langdon, and B. I. Cohen, *Comments Plasma Phys. Controlled Fusion* **6**, 225 (1981).
128. B. I. Cohen, A. B. Langdon, and A. Friedman, *J. Comput. Phys.* (To be published.)
129. J. Denavit, *J. Comput. Phys.* **42**, 337 (1981).
130. R. J. Mason, *J. Comput. Phys.* **41**, 233 (1981).
131. A. B. Langdon, B. I. Cohen, and A. Friedman, "Direct Implicit Large-Timestep Particle Simulation of Plasmas," (To be published in *J. Comput. Phys.*)
132. C. F. Curtiss and J. O. Hirschfelder, *Proc. Natl. Acad. Sci. US* **38**, 235 (1952).
133. C. W. Gear, *Numerical Initial Value Problems in Ordinary Differential Equations* (Prentice-Hall, Englewood Cliffs, New Jersey, 1971), p. 217.
134. J. C. Adam, A. Gourdin-Serveniere, and A.B. Langdon, *J. Comput. Phys.* (In press.)
135. A. B. Langdon, *J. Comput. Phys.* **30**, 202 (1979).
136. *Laser Program Annual Report—1980*, Lawrence Livermore National Laboratory, Livermore, Calif., UCRL-50021-80 (1981), p. 3-67.
137. J. I. Katz, J. S. DeGroot, and R. J. Faehl, "Simulation of Turbulence Plasma Heating by Moderately Strong Oscillating Two-Stream Instabilities," *Phys. Fluids* **18**, 1173 (1975).
138. J. M. Ziman, *Principle of Theory of Solids* (Cambridge University Press, Cambridge, England, 1964).
139. L. Spitzer and R. Harm, *Phys. Rev.* **89**, 977 (1953); L. Spitzer, *Physics of Fully Ionized Gases*, 2nd ed. (Interscience, New York, 1962).
140. S. I. Braginskii, *Sov. Phys.—JETP* **6**, 358 (1958).
141. R. M. More, *Atomic Physics in Inertial Confinement Fusion*, Lawrence Livermore National Laboratory, Livermore, Calif., UCRL-84991 (1981).
142. S. G. Brush, H. L. Sahlin, and E. Teller, *J. Chem. Phys.* **45**, 2102 (1966); J. Hansen, *Phys. Rev. A* **8**, 3096 (1973).
143. J. Green, *Free-Free Gaunt Factors for Gold Plasmas at Laser Fusion Conditions*, unpublished report RDA-TR-108600-03, R&D Associates, Marina del Rey, Calif. (1979).
144. P. H. Lee, *Thermal Conductivity of Highly Compressed Matter*, Ph.D. thesis, University of Pittsburgh, Pittsburgh, Pa. (1977).
145. N. F. Mott, *Phil. Mag.* **13**, 989 (1966).
146. C. W. Cranfill and R. M. More, *IONEOS: A Fast, Analytic Ion Equation-of-State Routine*, Los Alamos National Laboratory, Los Alamos, N. Mex., unpublished report LAMS-7313 (1978).
147. W. A. Lokke and W. H. Grasberger, *XSNQ-U, A Non LTE Emission and Absorption Coefficient Subroutine*, Lawrence Livermore National Laboratory, Livermore, Calif., UCRL-52276 (1977).
148. D. S. Kershaw, *Interaction of Relativistic Electron Beams with High Z Plasmas*, Lawrence Livermore National Laboratory, Livermore, Calif., UCRL-77047 (1975).
149. D. S. Kershaw, *Computer Simulation of Supra thermal Transport for Laser Fusion*, Lawrence Livermore National Laboratory, Livermore, Calif., UCRL-83494 (1979).
150. D. H. Sampson and L. B. Golden, *Astrophys. J.* **161**, 321 (1970).
151. W. A. Lokke and W. H. Grasberger, *XSNQ-U, A Non LTE Emission and Absorption Coefficient Subroutine*, Lawrence Livermore National Laboratory, Livermore, Calif., UCRL-52276 (1977).
152. W. Lotz, *Z. Phys.* **216**, 241 (1968).
153. E. J. McGuire, *Phys. Rev. A* **22**, 868 (1980).
154. H. D. Betz, *Rev. Mod. Phys.* **44**, 465 (1972).
155. D. S. Kershaw, "The ICCG Method for the Iterative Solution of Systems of Linear Equations," *J. Comp. Phys.* **26**, 43 (1978).
156. D. S. Kershaw, *Differencing of the Diffusion Equation in Lagrangian Hydrodynamics Codes*, Lawrence Livermore National Laboratory, Livermore, Calif., UCRL-82747 (1980).
157. *Laser Program Annual Report—1979*, Lawrence Livermore National Laboratory, Livermore, Calif., UCRL-50021-79 (1980), p. 3-77.
158. *Laser Program Annual Report—1979*, Lawrence Livermore National Laboratory, Livermore, Calif., UCRL-50021-79 (1980), p. 3-79.
159. D. S. Kershaw, "*The Solution of Single Linear Tridiagonal Systems and Vectorization of the ICCG Algorithm on the Cray-1*," Lawrence Livermore National Laboratory, Livermore, Calif., UCID-19085 (1981).

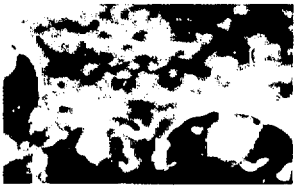

Target Fabrication
Section 4

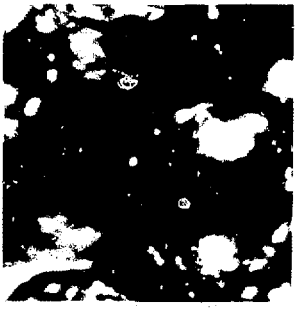

Target Fabrication

Contents

Section Editor: J. W. Sherohman

Target Fabrication

Introduction

C. D. Hendricks

The primary task of the Fusion Target Fabrication program is the production of targets for our current experimental program. However, development of techniques by which future targets can be produced is also one of our most important activities. Material, design, and experimental limitations provide challenges that must be surmounted to achieve success. In spite of the limitations, we have successfully produced many targets, but have also experienced delays in the successful completion of some other tasks.

There are two major classes of targets: directly driven and soft x-ray driven. In the second class, the laser light or other beam energy is converted to soft x rays that then drive the implosion. The x-ray-driven targets are generally classified and are not discussed. In this section, we discuss the fabrication problems for the direct-drive targets.

Much of our research, development, and production is in the general field of material sciences. In particular, we are concerned with density and surface uniformity in deposited materials—usually coatings on small (50- to 500-μm-diam) spherical shells. Polymeric materials, metal coatings, glass, and some ceramics are also critical to our present and future targets.

As in the past few years, we continue to have a strong interest in glass-shell development and production. In addition, we are developing techniques for the production of hollow metallic shells. Recently, we have had some success in making hollow gold spheres using liquid-jet techniques. The extension of our earlier work on copper and other materials by liquid-jet techniques further emphasizes the generality of this very useful method.

Producing small parts by micromachining is a remarkable adaptation of machine-shop technology that was considered almost impossible only a few years ago. Other techniques, such as ion milling and drilling, adapted from the physics of electron- and ion-beam technology, have made it possible to drill holes as small as 1 μm to depths of tens of micrometres.

While we have solved many of the cryogenics problems, there are still many techniques to be developed. Some fabrication techniques that may be required for future targets include completely filling a hollow sphere with solid D–T and then assembling multiple layers of organometallic polymers and other materials concentrically around the cryogenic sphere.

Characterization of complete targets and components throughout the fabrication processes has provided, and will continue to provide, very difficult technical problems. As we work with more opaque targets, radiography or other nonoptical techniques become critical tools. Beam techniques, such as scanning electron microscopy and Auger spectroscopy, are also important analytical techniques for both developmental and production aspects of target fabrication.

We would be remiss if we did not point out the support and assistance that we enjoy from equipment manufacturers and other industrial suppliers. We are also fortunate to have excellent interactions with other laboratories, particularly Los Alamos National Laboratory, Los Alamos, N. Mex.; Sandia National Laboratories, Albuquerque, N. Mex.; and KMS Fusion, Ann Arbor, Mich. In the cryogenics area, the National Bureau of Standards, Boulder, Colo., has provided developmental and fabrication support. In general-fabrication areas, the Future Systems group at the Department of Energy plant in Rocky Flats, Golden, Colo.

(managed by Rockwell International), has been exceptionally helpful and has been instrumental in solving many of our problems. The Charged Particle Research Laboratory at the University of Illinois, Urbana, Ill., has assisted us strongly in liquid-drop technology development, and, at the Jet Propulsion Laboratory, Pasadena, Calif., we have had significant help in the generation of hollow metal shells and the study of liquid-drop behavior. We would like to acknowledge the help of these and others who have helped us to accomplish our goals.

Fuel Container

Introduction

Past and current directly driven laser-fusion targets have relied on bare or coated glass microspheres to contain the D–T fuel. Investigation of these types of targets requires that we maintain our ability to produce glass shells in a variety of sizes. In some cases, the shells require that diagnostic tracer gases be added to the fuel. We are still seeking an optimal method for adding the tracer gases.

Most of our new development efforts for these targets are in the area of metal shells. We are investigating the possibility of forming fuel containers from molten metal by a concentric jet process. We are also pursuing plating or vapor coating thin evaporable mandrels as an alternative method.

The new fusion-target development facility (FTDF) tritium laboratory is under construction. The tritium laboratory will provide diffusion fill capability and the facilities for developing other filling techniques.

Author: T. P. Bernat

Metal-Shell Development

In August 1981, in anticipation of the high-gain directly driven capsules for Nova experiments, we started the development of techniques for producing high-quality metal shells. Thin-walled hollow spheres of select metals and alloys are required as the basic layer in the construction of Nova targets. By high quality, we mean that the metal shells must display nearly perfect sphericity and concentricity (within ±1%), high yield strength ($>4.2 \times 10^6$ g/cm^2), uniform thickness (within ±2%), and good surface finish. Although hollow glass spheres with superior qualities were produced routinely in our laboratories, new techniques must be established for metal shells because of the vast differences in properties between metals and glasses.

Three methods have been conceived as possible solutions to the problem of metal-shell preparation. The simplest and the most direct method is called the metal-droplet generator method. A metal-droplet generator simply consists of two concentric tubes so designed that a double-jacket orifice emerges at the lower end. The outer tube contains the metallic charge from which the hollow spheres are to be made. The small inner tube is for the passage of an inert gas under pressure p_1. The function of the inert gas is to push the liquid metal through the orifice so that a hollow liquid jet will be formed beneath the generator. To facilitate the jet formation, the liquid metal is acted on by the same inert gas supplied under a different pressure p_2 from a second source. By adjusting the pressure ratio p_1/p_2, we not only allow a hollow liquid jet to be formed, but also cause instability of the jet, which leads to the jet breakup into a series of droplets. The liquid droplets will eventually solidify into hollow spheres with a small amount of inert gas trapped inside. The materials suitable for the construction of the generator vary with the type of metallic material to be handled. The generator materials could be stainless steels for such metallic charges as lead, tin, and Au–Sb–Pb eutectic alloys, which have relatively low melting points, T_m. For metals with T_m greater than 1000°C, the generator may be constructed from quartz, graphite, refractory metals, or ceramics.

We have successfully used an all-quartz generator to produce gold shells. The qualities of the initial product were surprisingly good with respect to the sphericity and

surface finish. However, the yield of metal shells with the specified wall thickness and aspect ratio is still too low, and the overall qualities of the shells have not met all the requirements for Nova targets.

For our second method, we use undersized spherical mandrels of a volatile metal, such as zinc, on which the shell material will be deposited by either electroplating or some other technique. A small hole will then be drilled through the plated layer. The sphere will then be heated in a vacuum to drive out the volatile mandrel metal through sublimation in a closed system equipped with a trap. The applicability of this method has been demonstrated with zinc wires, from which hollow cylinders of a noble-metal alloy were produced. We are continuing the feasibility test of this method with zinc spheres and searching for a method to minimize the diffusion of zinc into the noble-metal alloy during the heat treatment.

The third method involves essentially the same principle as the second method, i.e., the use of disposable mandrels. The mandrel material, however, is changed from a metal to an organic compound that could be eliminated by gas reactions at moderate temperatures. The latter material offers the advantage that diffusion of polymeric molecules into the plated layer is unlikely to proceed to any appreciable extent during the gas treatment, thus alleviating the problems caused by metal diffusion of the mandrel metal into the noble-metal alloy encountered in the second method. The feasibility of this method is being tested with latex microspheres furnished by Dow Chemical Co.

Author: C. W. Chen

Major Contributor: W. E. Elsholz

Fuel Filling of Impervious Capsules

With the exception of a few particular alloys, metal fuel capsules will be impervious to hydrogen, even at relatively high temperatures, and therefore not fillable by diffusion. In the same way, some glass microspheres with more stable compositions than our current product,[1] or with high-atomic-number additives, might not be fillable by high-temperature diffusion. We have therefore continued developing a technique for drilling submicrometre-diameter holes in impervious fuel capsules.

As described in Ref. 2, we have been collaborating with Hughes Research Laboratories, Malibu, Calif., on the microdrilling. Hughes has developed a focused ion-beam facility with interchangeable liquid-metal sources. We have used it to perform drilling and milling experiments on gold foils with 60-keV ions from a Au–Ge source and on glass with 60-keV ions from a Au–Si source.

Figure 4-1 shows a representative hole drilled through a 10-μm-thick gold foil that had been prepared by evaporation onto a flat substrate. The foil was removed from the substrate and mounted on a small grid for drilling. The back-surface hole is seen just after the ion-beam breakthrough, and comparison of it with the front-surface hole suggests a profile as depicted. However, longer drilling time opened the diameter of the back-surface hole until it equaled the diameter of the front-surface hole.

By making electrical contact to the foil and to an electronically floating base under the foil, we were able to measure the portion of the beam current hitting the foil and the portion hitting the base after the foil was penetrated. For these experiments, the total current was about 150 pA. We defined $T_{1/2}$ as the time it took for the current to the base to equal the current to the foil. The term $T_{1/2}$ is an arbitrary indication of the hole-drilling time, although the time for initial beam breakthrough was less. We measured $T_{1/2}$ for four foils from 1 to 10 μm thick, with the results shown in Fig. 4-2. The approximate straight-line fit suggests an exponential dependence of $T_{1/2}$ on foil thickness. For verification, we tried drilling a new 14-μm-thick foil. The exponential equation predicts $T_{1/2}$ of about 150 s. Unfortunately, we were not able to drill through the foil, even after 700 s. The Hughes facility had been modified between the two sets of experiments and we are therefore repeating the earlier work to try to elucidate the discrepancy.

Drilling experiments with glass have not been as extensive as with gold foils. However, we have established that 60-keV ions will sputter cuts and holes in thin glass flats

Fig. 4-1. Ion beams can drill high-aspect-ratio, small-diameter holes in gold foils.

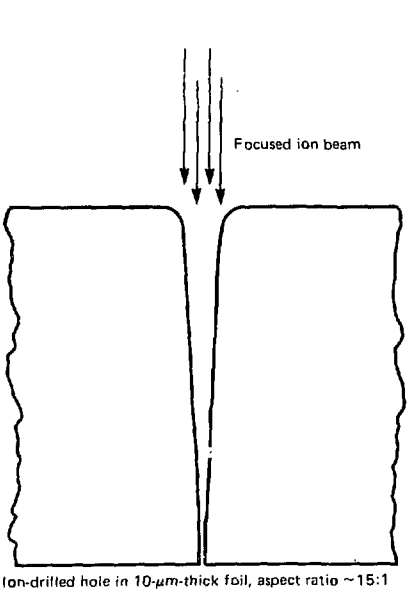

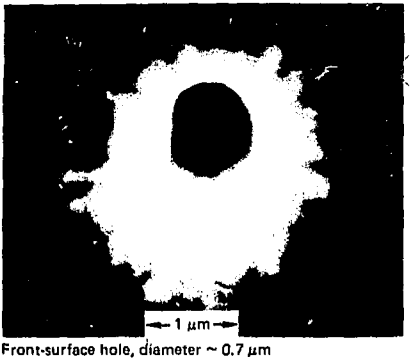

Front-surface hole, diameter ~ 0.7 μm

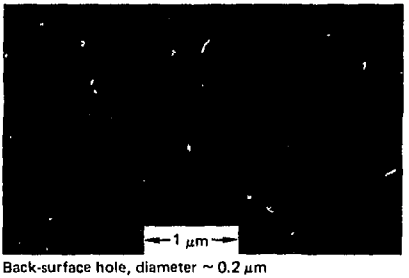

Back-surface hole, diameter ~ 0.2 μm

Fig. 4-2. Ion-beam burnthrough time experimentally increases with foil thickness.

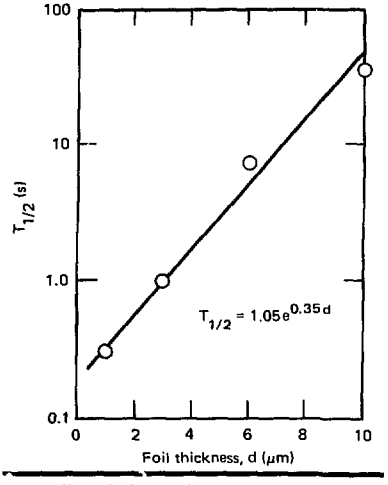

Fuel Container

ar.d will drill glass spheres. Target charging does not seem to degrade the sputtering process, possibly because the very low beam current is drained away by target surface currents.

Author: T. P. Bernat

Major Contributors: W. L. Johnson, B. H. Ives, and W. E. Elsholz

Tritium Laboratory

Target Fabrication is faced with developing unique processing and construction schemes to meet Nova target-design specifications. One important area is D–T fuel processing. Target fill, target-fuel containment, and target-fuel solidification are processes that we need to study to achieve a fabrication capability for the Nova target. A tritium laboratory (TL) has been designed and is currently being built for the new fusion target development facility (FTDF) to permit experimentation with D–T fuel processing. The design of the TL is based on safety features that are necessary for handling tritium. A discussion of these safety features is presented to emphasize the redundant safeguards incorporated in the TL to ensure a safe working environment.

To acquire state-of-the-art safeguards for handling tritium, we visited a number of laboratories having tritium facilities: Sandia Laboratories (Livermore, Calif.), Mound Laboratory (Miamisburg, Ohio), and Los Alamos National Laboratory (Los Alamos, N. Mex.). Common to each was the provision of systems for tritium containment,

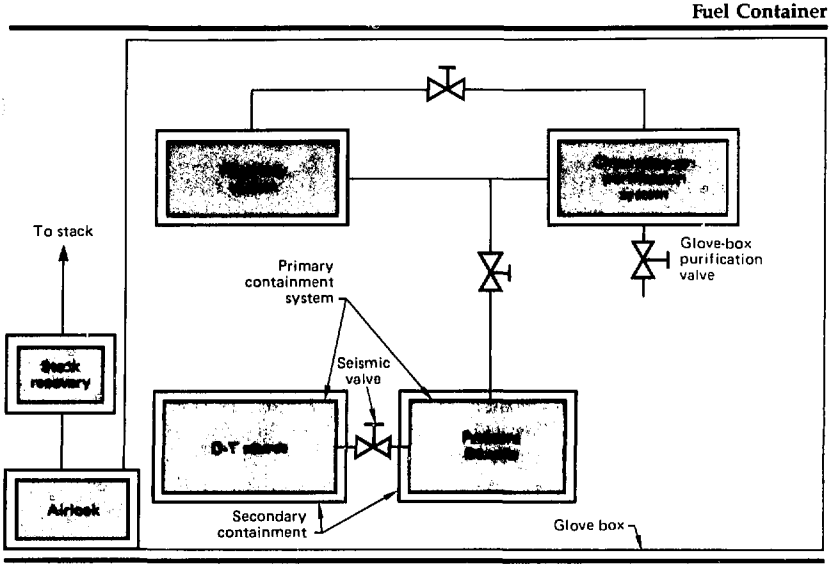

Fig. 4-3. Basic block diagram of tritium laboratory indicating various safeguard systems inside glove box.

recovery, gas purification, monitoring, and accountability. In the design of the TL to supply fuel for laser-fusion targets, we used a combination of approaches to assure the same capabilities. Figure 4-3 shows a TL block diagram representing our various safeguard systems.

The confinement of tritium in the TL begins with a primary containment system using certified high-pressure stainless-steel tubing, vessels, and valves. A stainless-steel autoclave is used as the tritium source vessel in which the tritiated fuel is absorbed on a granular-vanadium bed to form vanadium deuteride–tritide. The target-fill section of the primary system is composed of individual beryllium pressure cells that contain the targets during the diffusion-fill process. In case of possible leaks, localized secondary containment is provided for both the autoclave and beryllium pressure cells to ensure entrapment of the tritiated gas. A seismic valve is also included in the system to provide closure of the autoclave in the event of a seismic disturbance.

The primary containment system with its localized secondary containment section is redundantly contained in a sealed stainless-steel glove box. Any leak from the primary because of a mechanical failure or operator error is thus enclosed within the box.

Recovery of the tritiated gas from the primary containment system is accomplished by a system that uses both a gettering and a holding-tank approach. Initial recovery of the tritiated gas from the primary system is by gettering (a tritiated gas–solid-metal reaction forming a metal hydride) the gas back on the vanadium bed. However, because of the equilibrium vapor pressure of vanadium hydride (approximately 2.1×10^3 g/cm^2 at 25°C), not all of the gas can be reabsorbed. Consequently, the residue gas remaining in the primary system is recovered by gettering on a granular-uranium bed, which has a very low hydride equilibrium vapor pressure (1.0×10^{-6} g/cm^2 at 25°C). The uranium bed is also inside a secondary contained autoclave. In addition, a holding tank is provided in the recovery system to collect a primary flushing gas used in the event that traces of tritium might still be present. The holding tank and uranium bed are each designed to contain the total primary D–T gas supply.

Tritiated gas in the holding tank, secondary containment vessels, and the glove box itself is purifiable by a gas-purification system (GPS). The GPS is a gas-circulating system using two titanium-metal disposable canisters, each held at different temperatures, thus thermodynamically favoring the gettering of oxygen and the isotopes of hydrogen. The effluent from the GPS goes through yet another purification system, a catalyst molecular sieve unit, before it is allowed to enter the exhaust stack. The redundant purification approach is to ensure

that the tritium concentration level in the stack is below the acceptable tritium concentration that can be released to the environment.

Tritium concentration levels are determined by tritium monitors that are placed in various locations in the TL. Two monitors are positioned inside the glove box. One of them is set at a sensitive low-curie range for the GPS, while the other is at a higher range for detecting tritium levels in the secondary containment vessels and in the glove box. Others are strategically located outside the glove box to monitor the working environment. In addition, monitors are placed in the stack to determine the amount of tritium being released outside the building. By knowing gas-flow rates or volumes and tritium-concentration levels, all tritium can be accounted for in the TL.

We have designed the tritium laboratory for D–T fuel processing for laser fusion targets with the intent of providing redundant safeguard systems. The design is the result of employing a combination of tritium-handling approaches that are currently used by experienced laboratories. Construction of the TL is expected to be completed by September 1982.

Author: J. W. Sherohman

Major Contributors: D. H. Roberts and B. H. Levine

Glass-Sphere Technology

The past year has seen a considerable reduction in our effort to extend glass-sphere technology. As we anticipate the shutdown of the Shiva system, we have shifted resources toward the solution of advanced target-fabrication problems that have not yet been addressed. However, we have maintained our liquid-droplet technique for making glass microspheres and have designed improvements for it. We have also continued our attempts to add small amounts of diagnostic gases to the interiors of the glass microspheres.

The basic arrangement of the liquid-droplet generator, drying column, and furnace region for making glass spheres has not changed.[3] However, all regulation and control have, in the past, been by hand settings. Data on system performance have not been logged automatically, thus leading to imperfect record keeping. We have therefore designed a system to provide programmable control and automatic data logging. Each sphere-production station, whether liquid-droplet or dried-gel based, will have a programmable controller capable of handling up to 22 inputs and outputs for reading and controlling all system parameters. The separate controllers will be interfaced via a multiplexer to a central minicomputer, which will act as a data logger. Continuous records of the status of the systems[3] will be kept on hard copy, disk, or tape, as required. The full system will be implemented in the fusion-target test facility.

In Ref. 4, we discussed the possibility of adding bromine to the interior of the glass spheres in the form of HBr to avoid the condensation expected for pure Br_2 at room temperature. We attempted this by evacuating and backfilling an alumina oven column with pure HBr and dropping preformed glass microspheres through it at 1300°C. We had hoped that when the glass remelted, diffusion would proceed fast enough that by the time the spheres were caught they would have a substantial HBr content. Unfortunately, the hot HBr was much too reactive and severely degraded the glass. In addition, in a separate attempt, krypton also failed to penetrate into the sphere interiors, although it did not affect the glass. This indicates a low diffusion coefficient for krypton through the molten glass, and any reactive molecule, such as HBr, would be even worse. A successful method of diagnostic gas filling remains to be found.

Author: T. P. Bernat

Major Contributors: R. L. Morrison, K. A. Miller, and J. J. Sanchez

Coatings and Layers

Introduction

Inertial-confinement fusion (ICF) directly driven target designs show the need to apply a variety of layers to the D–T fuel

container to maximize the prospects for thermonuclear ignition. Microscopic spherical shells (microshells), currently hollow glass microspheres, contain the D–T fuel and form the target core (the only layer of early ICF targets). Three functional categories of materials can be added to enhance ICF performance: pusher-tamper layers, usually higher atomic-number (Z) coatings; mixed-Z interfacial and support layers; and low-Z ablators. Figure 4-4 shows one ICF target concept that includes current R&D goals plus existing target technologies.

Besides the wide range of Z needed for ICF target coatings with thicknesses of a few to many micrometres, each layer including the D–T-filled microshell must be uniformly dense and extremely smooth, with surface defects typically restricted to the 10- to 100-nm range. With the recognition of the difficulty of meeting so many stringent concurrent requirements, ICF target coatings R&D proceeded through 1979 on the concept of a two-step effort. The first was effort on processes to form candidate materials based on deposits on substrates other than ICF target cores, and the second was effort on techniques to successively coat the microshells.

Despite deposition of some smooth and dense polymers and metals in 1979–1980, results in 1980 strongly indicated that thick-film materials R&D cannot be entirely separate from the development of techniques to coat microspheres, particularly for sputtered metals. Beryllium was deposited on microshells and on hemispherical mandrels. However, near-target-quality layers have so far been achieved only with the mandrels by using bias sputtering. Meyer summarized approaches and problems regarding metal coatings for microspheres at LLNL through 1980.[5] Magnetron sputtering, mostly on unlevitated microspheres, mandrels, and flat substrates, was used to make Pt layers with submicrometre smoothness. It continues to be the favored process for metal deposition. Accumulation of charge and resultant electrostatic forces on levitated microspheres continues to be a key problem.

By 1981 polymer ablator layers had been made, mostly by batch-pan methods, but stress cracking and smoothness variations were problems. To form higher Z polymers, a system for metal-seeded organic-coating deposition was designed and experiments with chlorocarbons had begun.

For 1981, the main areas of effort were polymers, sputtered metals, lithium/lithium hydride (an ablator), and apparatus developments.

Principal results in the expanded scope of polymers for ICF target development were the achievement of a stress-free 500-μm-thick $CF_{1.3}$ coating and a 1-μm surface-finish $CH_{1.3}$ ablator over 50 μm thick (also stress free), both on microspheres. Furthermore, chlorohydrocarbon layers have been developed along with special potting and micromachinable polymers. Potting polymers hold microspheres for grinding and

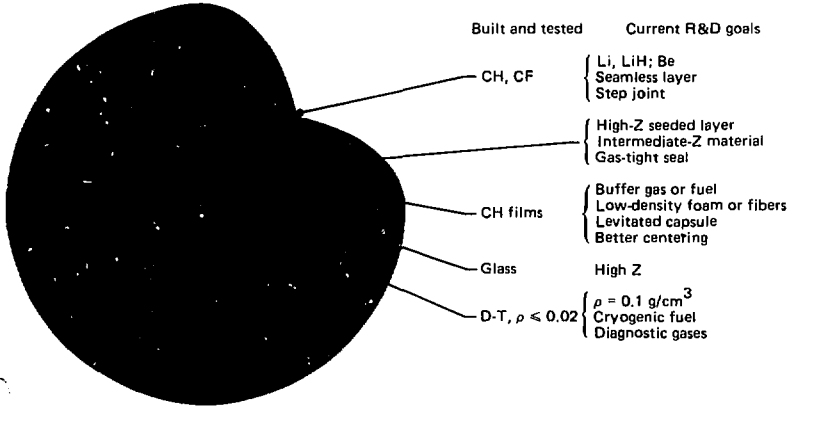

Fig. 4-4. An ICF ta concept that inclu three types of mat layers that can be added to enhance performance.

lapping. Micromachining is used to make polymer hemispheres for outer (ablator) layers of double-shell targets.

With metals, charging of the levitated microspheres during sputtering has been significantly reduced by the development of a mesh-screen plasma shield attached to the microsphere-levitation gas-flow structure. Alloying minor amounts of Ti with Cu has solved cold-welding problems for batch Cu coating, while Al added to Au in a new co-sputtering system gave stronger and harder coatings with finer microstructure than pure Au. Gas-jet levitation of large spheres has been done in an evacuated chamber while sputtering copper, which also showed gas-jet masking to get preferred polar-region deposition. When sectioned, the spheres demonstrated a uniform copper coating.

Bulk properties of lithium and its hydride show both to be good ablator candidates. Lithium was chosen for initial experimentation using both hydroforming and evaporation methods. Hemishells will be formed by these methods in a glove-box-enclosed apparatus that has been designed and built.

Finally, some apparatus developments were

- Completion of a system to do metal-seeded organic coatings.
- Portable molecular-beam levitation (MBL) station interchangeable between the plasma-activated chemical-vapor deposition (PACVD) systems.
- Inclined rolling pan to give low-fracture-incidence polymer coatings of large spheres.
- New electroplating-cell designs to handle buoyant and dense microspheres.
- Initial construction of a planar magnetron sputter system to give longer run times between sputter target changes and higher deposition efficiencies.

Author: D. E. Miller

Polymers

Polymers are used in directly driven laser-fusion targets in a wide variety of applications. Plasma-polymerized coatings having a composition of $CH_{1.3}$ or $CF_{1.3}$ are deposited on microspheres as ablators. Micromachinable polymers are applied to mandrels and machined into hemishells. Also, we have recently developed polymer potting compounds that allow individual microshells to be held for grinding. By grinding or sectioning microshells, coating microstructure and uniformity can be determined for nontransparent targets. As an extension of the potting technology, we made uniform hemishells by recovering sectioned microshells from the polymer support.

Plasma Polymerization. Recent efforts in polymer coating technology have focused on streamlining and simplifying coating techniques and increasing coater versatility. We have upgraded two coaters to deposit both hydrocarbon and fluorocarbon coatings. Another coating apparatus was modified to deposit chlorocarbon materials. A new technique for handling spheres in the plasma-assisted coater using an inclined rotating pan was developed (see "Apparatus Developments," below) and used to coat large solid-steel spheres.

In the process of consolidating our coating effort, we have compared the performance of separate coaters for the deposition of the same material. The gas composition in the plasma zone and, consequently, the coating quantity, depend on downstream pumping capacity and flow conductance. We have found that different coaters perform alike if each is using a turbomolecular pump. Thus, turbomolecular pumps are now used to obtain reproducibility between different deposition systems.

Using our improved plasma-polymerization technology, we have coated relatively large solid stainless-steel spheres with hydrocarbon polymer. Sphere handling is done by the inclined rotating pan technique. Figure 4-5 shows two solid-steel spheres coated with hydrocarbon polymers at two different pan rotation rates. The large missing pieces of coating did not result from the rotating pan technique; rather the coating was deliberately scratched down to the steel substrate to characterize the coating for thickness, homogeneity, and adhesion to the substrate. The surface finish of the coating deposited at 20 rpm [Fig. 4-5(a)] is very rough. Close examination of the surface revealed many 1- to 5-μm particles distributed over the surface. We found that the particles are pieces of coating fractured by the weight of the rolling sphere. The particles adhere to the surface and cause the coating to be rough. However, by

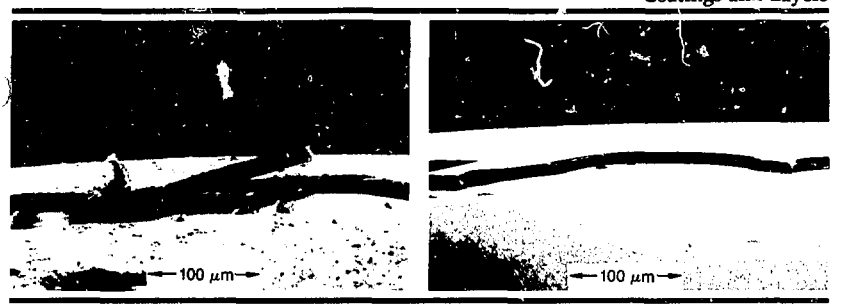

Fig. 4-5. Surface finish of solid-steel spheres coated by rotating-pan technique is affected by rotation rate.

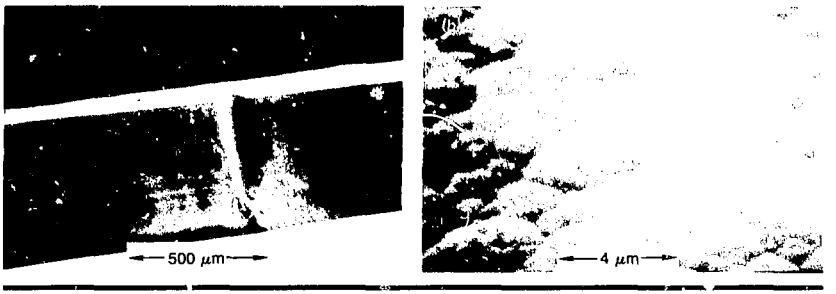

Fig. 4-6. Capacitively coupled discharge was used to deposit stress-free 500-μm-thick fluorocarbon coating.

reducing the rotation rate of the pan to 1 rpm, fatiguing of the coated polymer was eliminated and the surface finish improved to approximately 1 μm as shown in Fig. 4-5(b).

We have experimented with several new discharge configurations in the last year to simplify apparatus maintenance and for special applications (deposition of conductive materials). Using a capacitively coupled discharge, we have deposited in a 300-h continuous coating run a 500-μm-thick adherent, stress-free $CF_{1.3}$ polymer coating. Figure 4-6(a) shows a cross section of the coating in a region flawed by a substrate defect. The overall surface finish is 2 μm [Fig. 4-6(b)], which should be improved by further experimentation.

We are currently developing a chloro carbon coating (CCl). The properties of CCl (ρ = 2.3 g/cm^3, Z = 11.5) are similar to aluminum. Initial attempts to deposit CCl with an inductively coupled discharge resulted in all of the material depositing on the process-chamber walls upstream of the substrate. Adjusting power, pressure, and flow rate brought little improvement. However, by installing a jacket filled with a sodium chloride solution around the discharge tube, we were able to alter the distribution of the rf energy. A range of salt concentration was found that caused the primary coating deposition region to be located closer to the substrate. For a high salt concentration (0.5 wt%), the solution absorbed most of the rf energy and resulted in a lower deposition rate. We found that the optimum concentration for a good deposition rate was a 0.1-wt% solution.

The material composition using chloroform ($CHCl_3$) as a feedstock is CHCl. We are now working with carbon tetrachloride (CCl_4) to develop materials having a composition of CCl.

Full-Density Micromachinable Polymer Development. Techniques for micromachining hydrocarbon polymer into small hemishells are described in Ref. 6. The techniques involved coating and curing or melt-coating small amounts of polymer onto a premachined copper mandrel. Recently, we attempted to extend the same techniques to larger hemishells. We found that surface tension alone was incapable of supporting the polymer liquid, a mixture of poly (1,2 butadiene) and vinyl toluene. A Teflon mold was constructed to hold the polymer until solidification was complete. The mold, while supporting the polymer, prevented gases generated by the free-radical curing agent [2,5-dimethyl-2,5-di (t-butylperoxy) hexane] to diffuse out of the polymer. The trapped gas caused many bubbles to grow within the polymer. We

eliminated the bubbles by using a curing agent, cumene hydroperoxide, that does not generate gas. We continue to search for a curing agent that is effective at room temperature to eliminate post-cure shrinkage during cooling. We are also continuing to evaluate polymers for micromachining applications.

Development of Polymers to Support Microspheres for Grinding. For mass production of hemispheres and characterization of target materials, it is important to be able to precision-lap a microshell. We have developed a transparent, solid, soluble potting medium in which microshells are rigidly suspended. The microshells, after lapping, are released by dissolving the potting medium. The polymers that we have found best suited for potting applications are methyl methacrylate and polystyrene.

Methyl methacrylate, because of thermal contraction and volume reduction during conventional peroxide-catalyzed polymerization, tends to distort and create voids. To avoid distortion, we used room-temperature ultraviolet polymerization of a prepolymer syrup. We aligned the microshells into a single plane by two techniques: sprinkling microshells on a thin film of gravity-leveled syrup or by sandwiching microshells between two Teflon surfaces surrounded by a monomer. After an ultraviolet cure, the solid mixture was potted in plastic tubes for grinding.

We avoided the large-volume contraction during methyl methacrylate polymerization by using instead molten polystyrene. A special low-molecular-weight mixture of polystyrenes was formulated to provide a minimum melting range to reduce shrinkage on cooling. A plastic tube was nearly filled with cured epoxy, then a thin layer of the molten polystyrene was formed on top, allowing a meniscus to project above the tube rim. Microshells were sprinkled onto the molten polymer, then brought into a uniform plane by forcing a Teflon-coated glass slide down on the top of the Bakelite tube. Cooling left the resulting composite ready for grinding.

Authors: S. A. Letts and L. E. Lorensen

Major Contributors: A. T. Buckner, G. R. Cameron, D. M. Gouveia, C. W. Jordan, and R. M. Krenik

Sputtered Metals

During the year, we have gained a better understanding of the physics and mechanics involved in our existing coating processes. Our effort has advanced some R&D processes to the production status and made other production processes more efficient and reliable. We have also extended our capabilities to meet the new coating requirements of producing high mechanical-strength coatings on microspheres along with thick coatings on larger spheres (>1 mm).

Improved Understanding of Coating Processes. There are three areas where we have made significant advancement in our understanding of coating processes: resputtering phenomena[7] in Pt coating, cold welding with soft metals,[5] and electrostatic sticking in molecular-beam levitation (MBL) coating of microspheres.[8]

During sputter coating of Pt on microspheres, we had noticed that the coating rate was not proportional to the sputtering power. After an initial increase in coating rate with an increase in power, the rate of coating will begin to decrease for higher power levels. The effect can logically be explained by resputtering, which takes place when the reflected ions and neutrals strike the microspheres. Resputtering will cause a rise in substrate temperature because of the high kinetic energy of the striking ions and neutrals and will also roughen the coating surfaces by an etching action. If a microsphere is D–T filled, the rise in temperature caused by resputtering will also cause a loss of fuel. Our experiments showed that both a substrate temperature rise and a roughness of coating surface increased with sputtering power. Consequently, to minimize the effects of resputtering, it is necessary to select the proper sputtering power level.

In batch coating of microspheres in a bouncing pan, the soft metals like Au, Cu, and Al are usually excluded as a coating metal because of cold-welding problems. When coating with a soft metal, the microspheres tend to stick together on impact, forming a permanent bond. Usually there is no problem of cold welding when a harder metal is used like Ta, Ni, or Cr. In our experimenting with O_2-doped Pt coatings, we found that cold welding existed in pure

Pt coatings but not in O_2-doped Pt coatings. Our recent experiments to harden Cu by doping it with less than 1% of Ti suggest that hardness of the coating determines the susceptibility of cold welding.

Molecular-beam levitation is a powerful scheme that allows sputter coating of microspheres without making contact with the supporting apparatus, thus circumventing the cold-welding and debris problems. The main drawback of the MBL scheme is the electrostatic sticking problem in coating metals. The metal-coated microsphere is charged by the plasma and acted on by a complicated electrical force (which varies with sputtering power), pinning the microsphere to the levitating head.[8] To alleviate the problem, we have installed a shutter (metal-mesh screen) and positioned it just above the levitation head. By connecting the shutter to the same electrical potential as the levitation head, we can effectively shut off the plasma from the microsphere and isolate the coating process, thus eliminating the electrostatic sticking problem. The MBL scheme is now a more effective and reliable process for coating microspheres.

High-Strength Coatings R&D. Coatings with high mechanical strength become important in some target designs. Both the atomic number and the density of target materials are basic design requirements and take precedence over other material properties. As a result, we can only attempt to increase the strength of chosen target materials by coating techniques, rather than selecting materials that are known to have greater mechanical strength.

The mechanical strength of a material can be controlled through grain refinement, selective doping, and alloy formation.[10] Coatings that are deposited onto spherical substrates usually have a porous columnar structure (caused by the oblique incident coating flux) and reduced mechanical

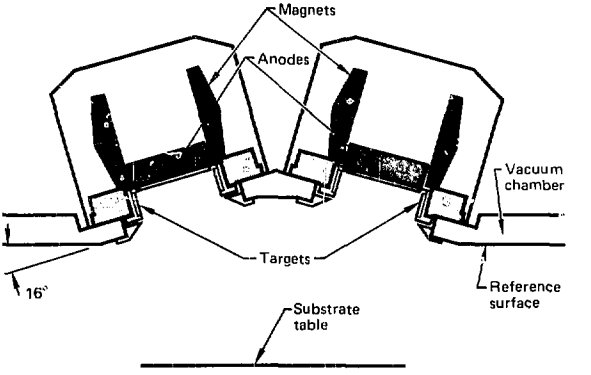

Fig. 4-7. Schematic of magnetron co-sputtering system (see p. 4-12 for discussion).

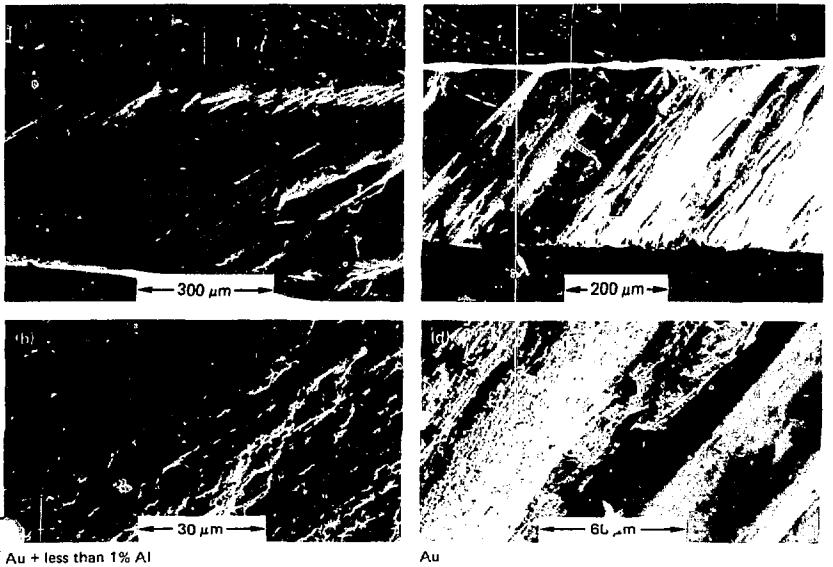

Fig. 4-8. Fractographs of layer of Au and layer of Au doped with Al (discussed on p. 4-12).

strength.[5] We will discuss the approach to strengthen a base metal by doping and alloying and also by coating techniques to improve the microstructure.

From a materials standpoint, composition may be the most important factor for getting a strong coating. We have constructed a magnetron co-sputtering system to selectively dope a base metal with another.[11] The co-sputtering system, as shown schematically in Fig. 4-7, can also provide a range of compositions of a binary alloy during a single run. From preliminary experiments, we have found that a base-metal layer (Au) can indeed be strengthened (hand bending test) and hardened (diamond-point hardness test) by doping with another metal (Al). We have examined fractographs (Fig. 4-8) of layers of both Au and Au-Al. Figure 4-8(a) and (c) shows the overall cross-section views of the Au and Au-Al layers. Figure 4-8(b) and (d) shows the corresponding enlarged views. The fractographs indicate a refinement of microstructure (a prerequisite for a strong coating) for the doped layer. We plan to increase our effort in this area as more base-metal materials and mechanical-testing capabilities are made available.

In coating spherical substrates, an oblique incident coating flux is unavoidable. An oblique flux promotes porous and columnar coating growth that is inherently weak in mechanical strength. We are examining two approaches to overcome the oblique coating flux difficulty.

Author: E. J. Hsieh

Major Contributors: C. S. Alford, G. T. Jameson, A. L. Plake, and M. J. Rocke

Ablator Development—Li and LiH

Because Nova target designs require a low-atomic-number ablator layer, both lithium hydride (LiH) and lithium (Li) are considered to be suitable candidate materials. Accordingly, we are presently involved in a development program to produce Li or LiH hemispheres that can be joined together to form the target ablator layer.

Li and LiH are both chemically reactive materials that must be handled in an inert-atmosphere glove box to prevent oxidation reactions. Consequently, we have recently completed the construction of a controlled-atmosphere glove-box assembly for Li and LiH processing.

In addition, we have constructed a unique transport container to allow the transfer of Li and LiH samples from the glove box to a scanning electron microscope (SEM). The container is connected to a lift mechanism fitted inside the SEM. The lift mechanism can then be manipulated to expose the sample inside the SEM vacuum chamber and thus permit surface characterization without oxidation.

Our initial approach in the Li and LiH development program is to examine Li as an ablator candidate. The physical properties of lithium metal may allow use of a relatively simple technique to form hemispheres that cannot be used on brittle LiH.

Lithium is a metal that has a low melting temperature, has a low solid-phase vapor pressure, and is more ductile than lead. It is a single-element material, as opposed to LiH, and can be obtained in foil form. At higher temperatures, the vapor pressure of the liquid phase of Li allows vapor deposition onto a substrate. Because of its physical properties, we have been examining various methods to form Li hemispheres.

It is hoped that one of the methods may provide a means of producing Li target-quality hemispheres. If not, our approach will shift to other techniques suitable for forming the brittle compound LiH. We expect to be able to determine if Li is an acceptable candidate for the target ablator layer in the coming year.

Author: J. W. Sherohman

Apparatus Developments

The apparatus used to coat laser fusion targets was designed specifically for the unique coating challenges presented by fusion targets. Changes in the coating apparatus are often required to improve process reliability and surface quality and to supply the desired new materials for target layers. During 1981, significant development work was expended on the following:

- Completion of the hazardous-material plasma-assisted chemical-vapor deposition (PACVD) system.
- Development of a rotating-pan technique for large-sphere coating.

- Improvement of the molecular-beam levitation (MBL) system.
- Design of new electroplating cells.

Each of the improvements will be discussed individually.

Hazardous-Materials Plasma-Activated Chemical-Vapor Deposition. We have completed construction of the PACVD coater to be used to handle hazardous materials. We described the design of the metal-seeded organic coater that included safety interlocks and three levels of containment.[12] Construction of the apparatus was completed in 1981. We have now tested the coater with nonhazardous materials and have found it performs identically with our other coating systems. Some weaknesses in the vacuum-system design were discovered in the testing phase and are now corrected.

New Sphere-Handling Technique. We have recently developed the capability of coating spheres using an inclined rotating pan as shown in Fig. 4-9. The rotating-pan technique was used for both polymer and metal coatings (see "Polymers" and "Sputtered Metals," above). Spheres too large for the MBL have been coated by this technique. The rotating pan is simple and introduces no additional gas to the coater, as does MBL. Loss of spheres is also minimized because of the simple design and ease of operation. Using the technique, we have coated spheres with up to 30 μm of hydrocarbon polymer and up to 5 μm of copper–titanium alloy.

Molecular-Beam Levitation. We have constructed a portable MBL device that allows us to use this sphere-handling capability on all polymer coaters. The new MBL is much simpler than previous MBL designs, having only two valves. It has fewer incidences of microshell loss during initial pumpdown because of balanced pumping between the coater chamber and the MBL plenum. Addition of a television monitor has simplified observation of the microshell during both pumpdown and startup of the system. Also, a piezoelectric vibrator is now used, instead of a hammer, to break the microshell free at the beginning of levitation. The improved MBL apparatus is currently used on all production PACVD coaters.

Electroplating. Glass microshells have served as the pressure vessel and pusher for several years in laser fusion targets. However, some design calculations indicate that higher-yield targets will require microshells of higher density and higher Z. One approach we are pursuing is to fabricate hollow gold microshells by electroplating on a mandrel. To successfully adapt electroplating to laser-fusion targets, two problems must be overcome:

- The solution composition must be adjusted to deposit a smooth and uniformly dense coating of the desired material.
- An electroplating cell must be designed so that it reliably and repeatably coats mandrels.

These aspects are currently being addressed.

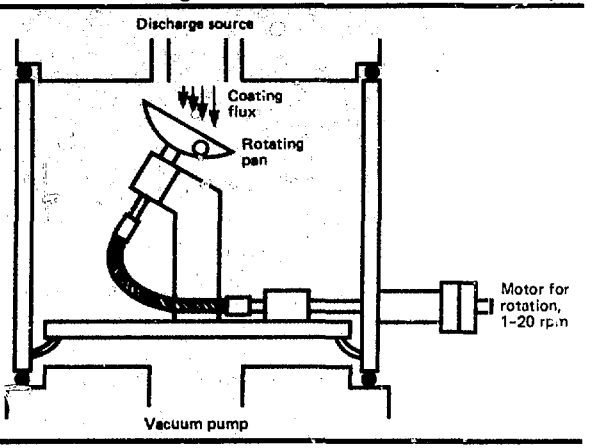

Fig. 4-9. Rotating-pan technique used to coat solid spheres.

Authors: S. A. Letts and E. J. Hsieh

Major Contributors: G. R. Cameron, J. D. Illige, and C. W. Jordan

Target Characterization and Materials Analysis

Introduction

Production of ICF targets and development of advanced fabrication technology rely on our ability to characterize targets and analyze materials. Only after measuring the physical, chemical, and structural characteristics of target materials can we improve target fabrication.

Several measurement development projects produced valuable results during 1981. Improvements have been achieved in

x-ray microradiography, which is a necessity for opaque targets. An automated sphere-mapping interferometer is in the testing stage, and a special station for interferometric examination of hemispheres has been constructed. A development project to enhance our ability to study the internal structure of materials has returned valuable preliminary results.

The following sections describe these projects in detail. The final section describes other additions and improvements made to our previously existing measurement capabilities.

Author: W. G. Halsey

Microradiography

The increasing use of opaque coatings on laser-fusion targets has expanded the need for microradiography. Two areas of major improvement during the year have been the sorting of opaque batches and the development of the Ag anode in the monoenergetic x-ray source.

Because of the time and handling involved in doing a complete radiographic analysis on a microsphere, we have found it necessary to develop a sorting technique. Sorting ensures that only candidates with a reasonable probability of meeting the target specifications are subjected to the complete analysis. The situation is analagous to the optical sorting of glass spheres on an interferometer prior to inspection on the 4π interferometer TOPO I.

The sorting of the spheres is done by mounting them between two thin Formvar films. One of the films is about 10 μm thick and the other is less than 1 μm thick. A contact radiograph is made of the batch, and the radiograph is examined under a standard microscope.[13] If a usable candidate is found on the radiograph, it is located in the holder using the radiograph as a map. A vacuum chuck is then used to pierce the 1-μm film and retrieve the candidate sphere. The procedure does not disturb the arrangement of the other spheres. Thus other candidates can be selected from the same batch. Because the sorting technique does not require the same film-grain size as our final-analysis system, we have been able to use faster (larger-grain) films. The radiographing of the batch can be accomplished in less than 30 min and is comparable in speed to our optical-sorting technique.

The second area of improvement has been on the monoenergetic x-ray system. Last year we developed the system using a Cu anode.[14] We have since changed to a Ag anode that was fabricated by sputtering Ag onto one of our Cu anodes. The Ag anode produces a 22-keV K_α line that is useful for examining materials with a higher atomic number. To maximize the ratio of 22-keV x rays (the Ag K_α line) to the bremsstrahlung background, we had to run the system at 40 kV (the maximum voltage of our power supply). We developed severe arcing problems in the x-ray unit at the high-voltage connectors and in the water-cooled anode column. We eventually redesigned the system to allow backfilling of the connector box and anode column with SF_6 gas. The use of SF_6 gas has eliminated the high-voltage arcing problem.

A second problem in the use of the Ag anode became apparent when we analyzed the x-ray spectrum while operating at 40 kV. As indicated in Fig. 4-10(a), we found we were exciting the Ag $L_{\alpha,\beta}$ line, traces of the Cu lines from the anode

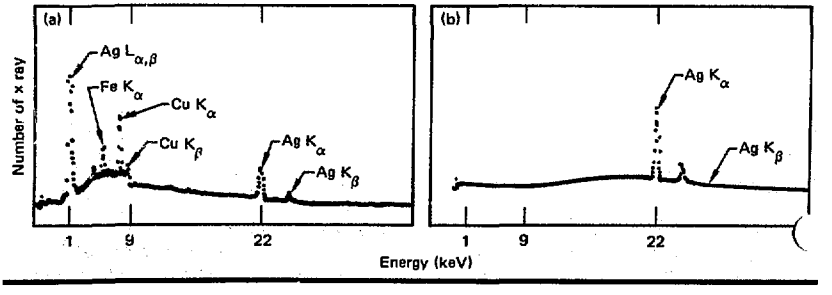

Fig. 4-10. Spectrums from Ag anode using 40-kV accelerating voltage. a) Without Al filter. b) With Al filter.

substrate, Fe lines from the chamber walls, and a large bremsstrahlung background. However, we found that we could suppress the unwanted part of the spectrum by filtering our beam with a 0.05-cm-thick sheet of Al. The attenuation of the x rays in the lower portion of the spectrum is evidenced by the spectrum shown in Fig. 4-10(b). The monoenergetic system is now capable of running at 40 kV and giving a clean spectrum of the Ag $K_{\alpha,\beta}$ lines.

Author: J. T. Weir

Automated Sphere Mapping

During the past year, we have continued construction on the automated sphere-mapping (ASM) system.[15] The ASM will allow us to rapidly measure height defects on the total surface of opaque or transparent microspheres. The ASM system has been fully discussed in Refs. 15 and 16 and will not be discussed in depth here.

The ASM system is diagrammed in Fig. 4-11. Most of the system has been built and is currently under test and evaluation. The phase-shift-generator optics and electronics, are operational and partially integrated into the system. We have tested the phase detectors and phase-measurement electronics, and both are ready for integration. The phase-shift interferometer and viewing optics have been assembled and are currently being aligned. The alignment process is tedious and time consuming, but is progressing well. The controlling computer software is 80% complete and partially integrated into the system. Once the system has been totally aligned, we will begin testing for stability and accuracy.

However, we have encountered a long-term drift problem with the sphere-rotator system. The sphere rotator,[17] shown in Fig. 4-12, allows the center of the target microsphere to move off the interferometer optic axis after operation for long time periods (approximately 1 h). Precise long-term centering of the sphere is critical for large spheres and for tests that require considerable sphere manipulation. By allowing the center of the sphere to drift, an error offset creeps into the data, eventually corrupting

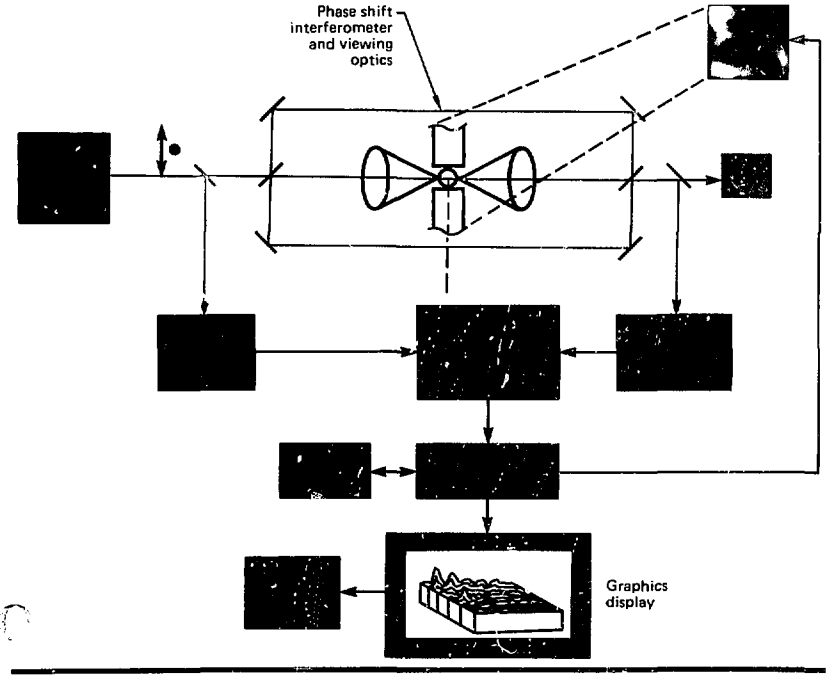

Fig. 4-11. Block diagram of the automated sphere-mapping system.

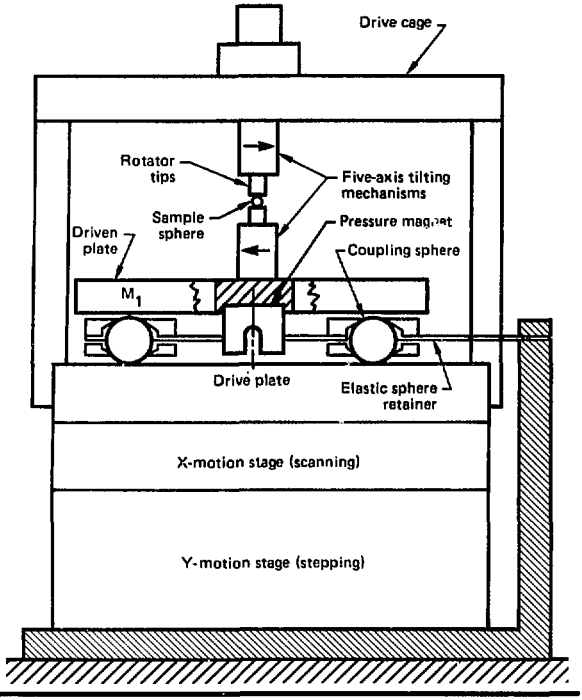

Fig. 4-12. Sphere rotator for manipulation of microspheres, with automated interferometric target characterization.

the test results. The exact cause of the drift is not known, but we are investigating the problem.

Complete system integration has been temporarily halted to research the drift problem of the rotator. However, many system tests can be performed as the drift problem is researched. Total system integration should be complete by the second quarter of 1982. Overall results, to date, look very encouraging. The interferometer appears to be stable, the phase shifter is performing as expected, and phase-detector accuracy exceeds design specification.

Author: D. L. Willenborg

Major Contributors: W. G. Halsey, A. Hernandez, G. F. Jacobson, J. A. Monjes, A. L. Richmond, M. D. Saculla, B. W. Weinstein, J. T. Weir, and K. R. Zeringue

Hemisphere Examination

The use of opaque materials (Be or LiH) as hemispheres for directly driven ablation shells in laser-fusion targets prevents us from using our standard optical-characterization techniques.[18] As a result, we have found it necessary to develop a new measuring system for opaque materials.

Features such as surface finish, diameter, and condition of the rim can be measured on opaque hemispheres using the same methods we use for transparent shells. However, the major problem in examining opaque hemishells is determining the wall uniformity.

To examine the wall uniformity, we developed a method of mounting the hemisphere to be inspected on an air-bearing spindle. The air-bearing spindle has a total indicated runout of less than 0.05 μm, which is just above the resolving power of our interferometer. By using reflection interferometry from the surface of the hemisphere, we can position the center of the outside surface on the axis of rotation of the spindle. The positioning is done using differential screw micrometers using the interference pattern as an indicator. Once the outer surface is indicated in, we rotate the spindle 180° and observe the pattern on the inner surface. Any change in the inner pattern as we scan the inner surface is caused by a nonuniformity of the wall. By rotating the shell on the mounting chuck, we can scan any portion of the shell and measure the wall uniformity at any point.

Author: J. T. Weir

Structure of Materials

During the year, we have improved our capability to measure the structure of materials used in targets and to relate this material structure to the mechanical properties of targets. The structure of materials becomes more important as design specifications become more demanding. Structural properties such as grain size, preferred orientation, and phase segregation influence vital target specifications, such as strength, hardness, surface finish, and homogeneity of both density and atomic number. Only by understanding the internal nature of the materials in a target can we optimize the properties of that target.

Our structure-analysis project has three complementary branches. The first is

transmission electron microscopy (TEM), which permits imaging small grains and internal defects in metals, polymers, and glass. Electron diffraction in TEM yields crystal-lattice structure and orientation. The second branch is x-ray diffraction, which is a family of techniques for accurate crystal structure and orientation analysis. The third branch is a set of mechanical-testing developments to measure physical properties of interest, such as tensile strength, hardness, and surface finish.

The major results obtained during the year are in the area of transmission microscopy. The largest challenge in applying TEM to any problem is preparing suitable and representative samples that are thin enough (~1000 Å) to be transparent to 100- to 200-keV electrons. In laser-fusion targets, sample preparation is a challenge, considering the size, shape, and structural complexity of a typical target. We have successfully applied three techniques to obtain thin samples. First, thin-metal-coating samples have been deposited on a flat substrate and subsequently removed for TEM use. Second, an ultramicrotome has been used to slice thin sections of polymers and metals using a diamond knife. Third, an ion mill has produced thin-metal samples by sputter erosion using argon-ion guns.

Figures 4-13 and 4-14 are examples of the kinds of information that can be obtained from TEM. The material is an 800-Å-thick foil of co-sputtered gold–copper alloy that is being developed as a candidate target coating, as described in an earlier article, "Sputtered Metals." To aid in producing a strong smooth coating, there is considerable interest in measuring the dependence of the alloy structure on deposition conditions. Figure 4-13 shows an extremely fine grain size with crystallite dimensions ranging from 50 to 500 Å. The presence of moire fringes indicates more than one grain in the 800-Å foil thickness. Figure 4-14(a) shows a normal electron diffraction pattern of the gold–copper alloy taken from an area a few micrometres in diameter. The powder-type pattern reveals lattice parameters and can show preferential grain orientation. As shown in Fig. 4-14(b), a very small-diameter electron beam results in a single-crystal-type pattern, which allows examination of the orientation of an individual grain or

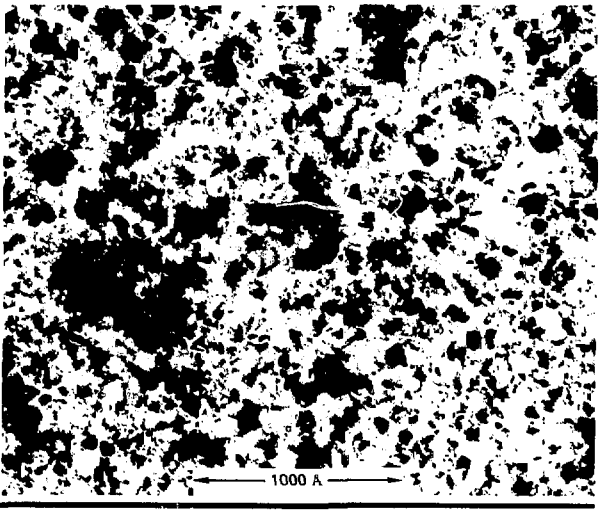

Fig. 4-13. High-resolution transmission electron micrograph of co-sputtered Au-Cu alloy.

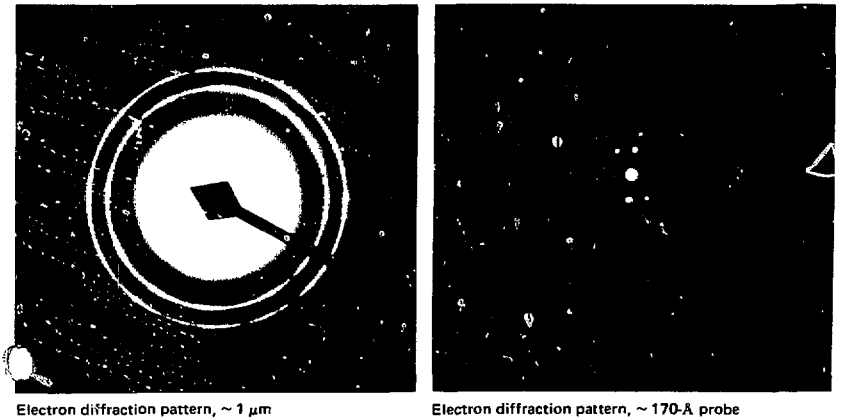

Electron diffraction pattern, ~ 1 μm

Electron diffraction pattern, ~ 170-Å probe

Fig. 4-14. Electron diffraction patterns from Au-Cu foil.

inclusion. Information obtained from TEM helps guide the development of new materials and processes.

Mechanical testing of target materials has been expanded with the construction of a single-sphere crush tester, an apparatus that measures the force needed to crush a target sphere. Microhardness measurements on metal coatings are helping to optimize alloy selection. The improvements in mechanical testing, combined with TEM and x-ray diffraction, represent a substantial increase in our capability to understand materials for laser targets.

Author: W. G. Halsey

Major Contributors: K. L. Montgomery, E. J. Hsieh, and J. A. Bonemetti

Analysis Improvements

Accurate analysis of target materials and precise measurement of target dimensions have proven vital to the development and production of laser-fusion targets. Surface finish, diameter, sphericity, wall thickness, and uniformity must be measured for spheres and hemispheres. Flat-disk targets and coatings on spheres must also be characterized for thickness, uniformity, and surface condition. Furthermore, the composition, density, homogeneity, and trace impurities, both at the surface and in the bulk, must be analyzed in glass, metal, and polymer materials.

We have recently added several new analytical capabilities, other than those described in previous articles ("Microradiography," "Automated Sphere Mapping," "Hemisphere Evaluation," and "Structure of Materials"). Previously described capabilities[19,20] have also been expanded and updated to address the evolving requirements of target fabrication.

Scanning Electron Microscopy. The scanning electron microscope (SEM) has proven to be the most frequently used tool for laser-target analysis. Poor surface finish or adhering debris is the most common cause for rejection of target microspheres, and both are examined using an SEM. Fractured or microsectioned spheres and coatings are measured in an SEM to obtain wall thickness and uniformity data. We use a variety of custom and commercial accessories to enhance the versatility of our SEMs. Techniques such as energy-dispersive x-ray spectroscopy (EDS), wavelength-dispersive x-ray spectroscopy (WDS), 4π sphere rotators, and backscattered electron (BSE) microtopography have been reported in the past.[21,22]

During 1981, we installed a new Cambridge S-250 scanning electron microscope. The S-250 is an advanced high-resolution instrument with 60-Å point-to-point resolution and a very clean ion-pumped and turbomolecular-pumped vacuum system. The new machine is performing steadily after an initial break-in period and has helped relieve the workload on our other instruments. Turnaround time for routine SEM analysis has been halved to two to three days since the addition of the SEM, and all high-magnification work is being routed to it. The state-of-the-art resolution of the new SEM is important as surface-finish requirements have recently advanced beyond the capability of existing equipment.

Our Cambridge S-180 is operating nearly full time as a composition-measuring microprobe using x-ray spectroscopy. To relieve the workload on the S-180, we have moved the BSE microtopography system[22] to the new SEM. At the same time, we upgraded the electron detectors and computer software to improve system performance and simplify operation. The BSE technique is now an operational tool for surface mapping. The new SEM also interfaces with a solid-state x-ray detection system to provide rapid semiquantitative composition analysis of microscopic areas.

Two new stage fixtures were built for handling special samples. One fixture is a simplified stationary version of the tips used in the 4π sphere rotator. Elastic pads on opposed tips hold a glass microsphere for SEM observation and allow recovery without damaging the sample. The second fixture is a small transportable vacuum-transfer device for remote loading of chemically active samples. The sample can be mounted in an inert dry box and loaded into the SEM without exposure to the atmosphere.

Composition Measurements. From target-development projects and production specifications, we have found increasing demand for composition measurements. One

example of this is a search for trace impurities in disk targets. Another need has developed for measuring small fractions of diagnostic gases in D–T-filled microspheres. In response to the composition-analysis requirements, we have added several new analytical techniques.

For rapid and reliable quantitative analysis of bulk samples and multiple microspheres, we have acquired an x-ray fluorescence (XRF) analyzer. The XRF system exposes a sample to the output of an x-ray tube and measures the spectrum of x rays fluoresced by the sample. Composition can be calculated from the characteristic x-ray emission signal in comparison to known standards. Accurate measurement of diagnostic gases in targets can now be obtained by crushing a small number (~10) of filled microspheres in the inlet of a gas chromatograph that has been modified for this purpose with a sphere-crushing fixture at the inlet.

Our ability to measure surface contaminants and perform near-surface profiling of composition vs depth has been improved by the addition of a secondary-ion mass spectrometer (SIMS) to our Auger electron spectrometer. The SIMS technique complements previously existing surface-analysis capabilities.

Author: W. G. Halsey

Major Contributors: E. Austin, G. J. Greiner, R. Lim, C. L. McCaffrey, P. L. McCarthy, E. A. Pyle, C. M. Ward, and F. J. Wittmayer

Cryogenic Target Development

Introduction

Many high-compression ICF targets require that the D–T fuel be condensed in a thin liquid or solid layer on the interior surface of a spherical fuel capsule to ensure adequate implosion symmetry. The condensed-fuel layer must be highly uniform, requiring the development of special techniques for its production and characterization.

Target survivability requires additional care in selecting materials compatible with the cryogenic environment.

During the past year, we have continued to investigate the production of uniform solid D–T layers inside thick-walled fuel containers.[23] The feasibility of using holographic interferometry for high-resolution characterization of the frozen fuel layer inside thick-walled transparent targets has been demonstrated and shown to be superior to classical interferometric techniques.

Investigations have continued on cryogenic fuel layering in regimes not accessible with diffusion-filled glass microspheres by using spheres fitted with fill tubes.

We have initiated efforts to develop analytic and computer-code modeling of the thermal behavior of cryogenic single- and double-shell targets as part of a theoretical effort to understand fuel-layering dynamics.

Engineering development of hardware for target-chamber support of cryogenic targets is continuing. Checkout tests to evaluate the baseline cryogenic performance of a cryogenic pylon were completed at the National Bureau of Standards (NBS), Boulder, Colo. The final pylon assembly has been received at LLNL, where it awaits additional testing.

Cryogenic target experiments using a prototype shroud-retractor assembly were also undertaken at NBS. The information generated is being used in specifying a final-version retractor and in addressing target-chamber interfacing issues.

Author: D. H. Darling

Formation of Solid D–T Layers Inside Fuel Capsules

To obtain high fuel compression and eventual ignition, target designs using thin layers of D–T condensed on the inside surface of a fuel capsule have been proposed. Stability requirements of the laser-driven implosion require that the condensed fuel layer be both smooth and uniform in thickness.

Both liquid and solid condensed-fuel layers have been previously investigated for ICF target applications. Liquid D–T layers are very smooth, but, in a short time, sag under the influence of gravity to equilibrium configurations displaying considerable nonconcentricity. The fuel layer is thick on

the bottom of the fuel capsule and thin near the top. Previously, some degree of success has been obtained in reducing the sag-induced liquid-layer concentricity defect by applying a temperature gradient across the fuel capsule.[24,25]

Solid layers of D–T at temperatures considerably below the D–T triple point are quite stable. The production of smooth and concentric solid-fuel layers inside fuel capsules is a major goal of the cryogenic-target development effort.

The cryogenic system employed for studying solid layering was previously described in Ref. 26. The cryogenic fuel-layer smoothness and concentricity characterization can be performed optically for transparent-walled targets. Classical optical interferometric techniques have been extensively used to investigate condensed fuel-layer configurations; Mach–Zehnder, shearing cube, and wedge interferometers have all been employed for fuel-layer characterization.

In thick-walled fuel capsules, the rearrangement of the fuel from the vapor phase to an eventual solid layer produces only a small change in the interference pattern obtained using classical interferometry. The small fringe shift produced by the fuel rearrangement is caused by the relatively small phase lag produced in the fuel compared to the large background phase lag developed in traversing the thick high-refractive-index (n = 1.3 to 1.5) capsule walls. Assessing the fuel-layer configuration requires measuring small (interference pattern) shifts generated by the fuel redistribution. The fuel-capsule contribution to the interference pattern, inherent in classical interferometry, severely limits the precision of measuring the fuel-layer nonconcentricity. For example, consider a 200-μm i.d. fuel capsule with 25-μm-thick walls of refractive index 1.5 and having sufficient D–T fuel to produce a uniform 1.5-μm-thick layer when frozen. The shift in the center of the bull's-eye interference pattern produced when the uniform fuel layer is replaced by a maximally nonconcentric layer (zero thickness on top and 3 μm thickness at the bottom of the fuel capsule) is only 3% of the capsule radius.

If the large background phase-shift contribution of the fuel-capsule walls were to be subtracted out, then the fuel-layer configuration could be determined to a much higher accuracy.

Holographic interferometry is an extremely sensitive method for displaying changes in an object.[27] Real-time holographic interferometry is an optical technique that fulfills the above requirement of being sensitive only to the redistribution of the fuel inside a target. When coherent light from an object is superimposed on its holographic reconstruction an interferogram is formed. Interference fringes will be observed if there is any difference between the object wave front and the reconstructed holographic wave front. For our investigations, a holographic image was recorded of a fuel capsule with all of the fuel in the gas phase at a temperature of about 35 K. The fuel was frozen into a solid layer by reducing the target temperature to 10 K. The fringes produced when the object and reconstructed holographic wave fronts interfere are generated solely by changes in the optical path length created as the fuel went from a void-filling gas to a thin solid layer. To within the approximation that refraction is unimportant, the transparent thick-walled fuel capsule plays no role. The system we used to investigate holographic interferometry is diagrammed in Fig. 4-15. The argon-ion laser was used to pulse heat the target to produce uniform solid-fuel layers. We employed a holographic camera based on a thermoplastic recording medium instead of a photographic plate. The camera system, available from Newport Research Corporation, Fountain Valley, Calif., allows in-place development of a hologram in about 20 s, has an optimal spatial frequency of 800 line pairs/mm, and is erasable, allowing several hundred exposures on the same thermoplastic plate.

To illustrate the sensitivity of holographic interferometry, reconsider the fuel capsule used in the classical interferometry example, i.e., 200-μm i.d., 25-μm-thick wall of refractive index 1.5, and an 11.6-mg/cm^3 D–T fill, which, when frozen out uniformly, produces a 1.5-μm layer. Using holographic interferometry, the difference in fringe position for the uniform and maximally nonconcentric fuel layer is 30% of the capsule radius. Holographic interferometry displays a factor-of-10 resolution improvement over classical interferometry for the above example. The results obtained were based

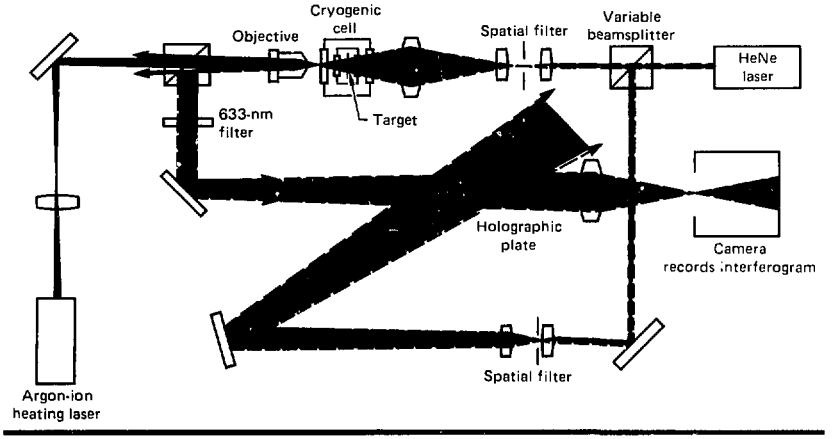

Fig. 4-15. Schematic of cryogenic cell and optics chain demonstrating feasibility of holographic interferometry to characterize frozen D-T fuel configuration in transparent spherical fuel capsules.

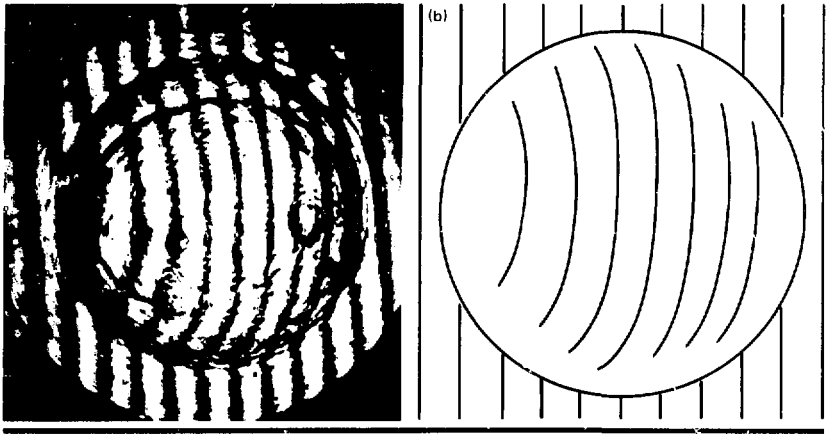

Fig. 4-16. Comparison of holographic interferogram with calculated fringe pattern.

on a nonrefractive approximation similar to models previously used for analyzing imperfect glass shells.[28] The approximation becomes less valid for thicker walls and near the target limbs, where large deviations from normal incidence heighten refractive contributions. To demonstrate the qualitative agreement obtainable using the nonrefractive model, we compare in Fig. 4-16 a holographic interferogram of a liquid layer in a glass fuel capsule with a fringe pattern calculated using the nonrefractive approximation and an offset-sphere model for the liquid layer.[29] In Fig. 4-16(a), we show a holographic interferogram of a nonuniform liquid layer in a glass fuel capsule at 25 K. The fuel capsule is a 153-μm-i.d. glass microsphere with 4.4-μm-thick walls and a D–T fill density of 10 mg/cm^3. The vertical lines are reference fringes produced by introducing a linear phase gradient in the reference beam used to reconstruct the hologram. Figure 4-16(b) shows the calculated holographic interferogram using a nonrefractive approximation and treating the nonuniform liquid-layer profile as a nonconcentric spherical shell, with average D–T thickness of 1.0 μm and with fuel-layer offset of 0.6 μm.

Inclusion of refractive effects using ray-tracing codes should allow fuel-layer determination to very high accuracy, even inside thick-walled capsules.

Author: D. H. Darling

Major Contributors: T. P. Bernat, B. H. Ives, M. J. Moss, J. J. Sanchez, and K. Zeringue

Cryogenic-Target Support Systems

The cryogenic hardware for supporting, positioning, and maintaining targets in the target chamber is described in Refs. 30 and 31. The hardware consists of two parts: a target-mount pylon, and a cryogenic shield and retractor, as shown in Fig. 4-17. The pylon fits into the presently used Shiva target positioner and can provide cryogenic cooling to the target. The National Bureau of Standards (NBS), Boulder, Colo., has completed construction of the pylon, and we have tested it there. We cooled the pylon with liquid helium while it was in a horizontal position and again in a vertical position with the helium flowing uphill. In both positions, the tip temperature reached about 4.2 K, as indicated by thermocouples. The pylon should, therefore, be usable in either orientation in a target chamber. The liquid-helium consumption was around 4 liters/h in the horizontal position and slightly higher in the vertical position. The pylon has been delivered to LLNL for further testing.

The prototype cryogenic shield and retractor, which provides shielding of the target against 300 K radiation (until a few tens of milliseconds before the target is shot), has also received extensive testing at NBS in addition to what we reported last year.[31] We were interested in assessing whether the shield could maintain a fuel-filled microsphere below the triple point of the fuel, particularly when the microsphere was mounted on a noncryogenic target holder.

For our first test, we glued a D_2-filled microsphere to an approximately 10-μm-diam, 1-cm-long glass fiber, which was in turn attached to a room-temperature target holder. The cryogenic shield cell was sealed to the target holder by a Mylar stack, which we have described previously.[30] With the shield cooled with liquid helium, and approximately 1 Torr of helium exchange-gas pressure in the cell, the D_2 did indeed freeze. However, the D_2 would remelt within 2 to 3 min of opening the valve to evacuate the cell. The calculated time to melt the fuel if the target were completely exposed to room-temperature radiation is about 100 ms, which indicates that the shield was performing well.

In our second experiment, we mounted D_2-filled glass microspheres between two 500-Å-thick Formvar films stretched over a thin copper washer. The washer was then attached to the mounting pylon by a small thin-walled hollow plastic tube for good thermal insulation. The thin-film mounting arrangement has the advantage of allowing a fairly isotropic thermal environment for the microsphere. With fiber mounting, as in our first experiment above, a small thermal gradient on the microsphere is always present.

With the target thus mounted, we recorded its behavior with a high-speed (150 m/s) movie camera. We found that, after the D_2 had been frozen and the cryogenic shielding cell rapidly removed, the measured time to melt the D_2 was 50 ms. We also found about 200 μm of target motion upon unshielding, indicating we will have to be very careful with our final mounting and sealing arrangement. With the cell covering the target, we performed laser heat-pulsing experiments to try to make uniform frozen layers and monitor their stability. Unfortunately, the

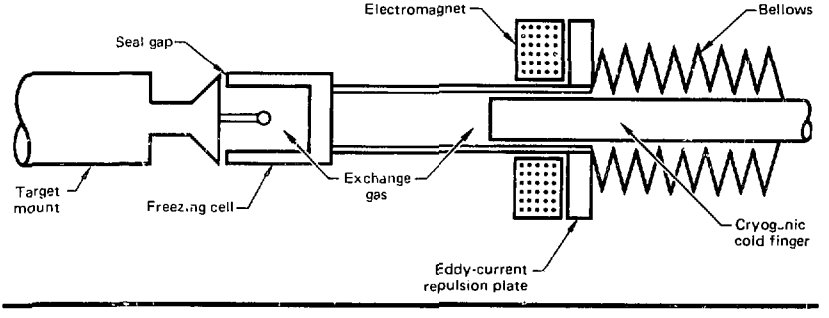

Fig. 4-17. Schematic of cryogenic retractor, cooling is provided by retractor mechanism, but can also be supplied by target mount.

viewing-light levels were too low to evaluate these experiments.

In conclusion, we have found that the prototype cryogenic shield and retractor mechanism can provide cooling to a room-temperature-mounted target and, with the cell evacuated, can sustain frozen fuel on the order of 1 min. We are presently working on interfacing the cryogenic shield mechanism to the laser target chamber and are preparing to perform experiments with a combined cryogenic pylon and shield configuration.

Author: T. P. Bernat

Major Contributors: P. Ludtke (National Bureau of Standards, Boulder, Colo.) and D. H. Darling

Target-Production Activities

Introduction

During 1981, our fabrication effort produced targets for the Shiva and Argus irradiation facilities and supplied a few targets to other facilities. We fabricated targets for direct-drive implosions, for development of diagnostic capabilities, for beam and diagnostic alignment, and for beam characterization. This subsection describes the techniques and production quantities involving unclassified experiments.

The types of targets produced include:

- Ball-in-film for direct irradiation or cryogenic-layer studies.
- Flat disks for analyses of the interaction of the laser light with various materials.
- Multilayer disks with micrometre steps for shock velocities.
- Thin metal foils on plastic support films for x-ray laser experiments.
- Platforms for producing intense bursts of x rays for backlighting.
- Elementally doped disks for evaluating underdense plasma conditions.

The production of targets involves the efforts of the Coatings, Material Analysis, Characterization, and Assembly groups in Target Fabrication. In addition, we have received support from the plastics and glass shops at LLNL, as well as from the Future Systems Group of at the Department of Energy plant in Rocky Flats, Golden, Colo.

Although a number of fuel capsules were used in these targets, no production efforts were required for the manufacture of glass spheres or coated glass spheres, since a stockpile of fully characterized glass spheres remained from the previous year. However, many coatings were required from the thin-film-coatings area to produce the different films used for the disk targets. Characterization efforts to certify that the materials and dimensions of all targets were to specification were also required (see next article). In addition, we discuss the assembly techniques for some of these targets, along with a development effort to construct a high-precision lathe for advancing our machining capabilities.

Author: C. W. Hatcher

Characterization

During 1981, the Target Characterization group handled over 500 characterization requests and delivered over 100 target balls to the Assembly group.

Because of the increased complexity of the target balls, we had to commit more resources, in terms of time and people, to completely characterize a target. A good example of the type of characterizations we were doing was the work we did with the 140 × 5 + Cu + CH target. Targets of this type are glass spheres with an inside diameter of 140 μm and with a 5-μm wall. There is a thin layer (1 to 3 μm) of Cu on the glass and a 20-μm layer of hydrocarbon (CH) on the Cu.

The process begins by selecting from a batch a D–T-filled glass ball. The selection is determined by using an interferometer to measure the sphere-wall thickness. The D–T content of the glass ball is measured on the gas proportional counter. The ball is then placed on the Vickers split-image microscope, and its diameter is measured. Using the 4π interferometer system, TOPO I, the surface of the ball is inspected for local defects, such as dirt specks or glass shards. The wall uniformity of the ball is measured and recorded. If it meets the surface and

dimensional specifications, the ball is delivered to the Metal Coatings group. A layer of Cu is deposited on the ball and then returned to the Characterization group for surface inspection of any pits or cracks in the Cu layer. If the surface is acceptable, the ball is loaded in the radiographic ball roller. By rotating the ball 90° between exposures, we can make two radiographs. The radiographs are done on the monoenergetic x-ray source using a Cu-anode system, and the glass plates are developed in our darkroom. The plates are then placed on the AXIAS system,[32] and the Cu coating is analyzed for thickness and uniformity. If the ball meets the specifications, it is taken to the Organic Coatings group where it is coated with a CH layer. The CH-coated ball is returned to the Characterization group and the thickness of the CH layer is measured using an interferometer. Once again, it is radiographed in two orientations, and the plates are inspected to measure the coating uniformity. At this point, the ball is placed in the TOPO I inspection station, and its surface is mapped for localized defects. If the ball still meets specifications, it is then delivered to the user.

The characterization process requires about one man-day of effort, exclusive of the time required to coat the ball with Cu and CH. This represents a factor of 2 increase in effort per delivered ball when compared to last year.

New complexities in target characterization have led to intensive development of automated measuring systems. Our advanced radiography program plan includes fully automated image analysis to decrease the effort required for ball characterization and increase our measurement accuracy.

Author: J. T. Weir

Assembly

The majority of the targets were flat disks mounted on a glass stem. Disks made of gold are produced by electron-beam (e-beam) coating onto a silicon wafer that has been shaped by photolithography to provide the correct size.[33] Another method of producing a disk is by precoating a glass substrate with a release agent and then overcoating it with the desired material. By immersing the slide in a suitable solvent for the release agent, a thin film is produced. The film is placed in a punch-and-die-fitted arbor press and formed into the disk shape. Further processing of the disk may be done by ion-etching slots or layers to provide steps a few micrometres high. The disks are then positioned under a high-power microscope using a micromanipulator and bonded to a glass capillary tube at the required angle.[34] The production of these types of targets with full documentation generally requires 8 to 20 man-hours of effort.

Thin (20- to 50-μm) hydrocarbon films with a few atomic percent of different elements, including titanium, calcium, chlorine, and silicon, were prepared as disk targets. The hydrocarbon film was initially prepared by ball-milling powders containing the elements (particle size of 1 μm) into a styrene monomer until homogeneous. The styrene was then cured. Afterwards, the polystyrene thermoplastic was thermoformed to the desired thickness, and disks were punched from the film. Table 4-1 shows a list of targets constructed.

In addition to assembling the targets listed in Table 4-1, we are also designing a high-precision computer-controlled air-bearing, air-spindle diamond-turning

Table 4-1. Targets constructed in 1981.

Target	Jan.	Feb.	Mar.	Apr.	May	June	July	Aug.	Sept.	Oct.	Nov.	Dec.	Total
B	4	2	9	0	0	2	5	2	2	2	0	1	29
BF	0	0	1	0	2	2	0	0	0	1	5	0	11
EP	0	0	0	0	0	0	0	0	0	0	0	1	1
Flasher x ray	0	0	0	0	0	0	0	0	0	0	0	2	2
LLP	28	19	6	23	36	23	27	20	5	7	5	75	274
LP	60	161	38	75	0	27	25	0	41	0	0	0	427
Mirror	0	0	0	4	0	0	0	0	0	0	0	0	4
Pinlite	0	8	11	22	2	0	0	0	0	0	0	0	43
Shiva alignment	0	0	0	0	0	0	0	0	0	0	0	1	1
Total	92	190	65	124	40	54	57	22	48	10	10	80	792

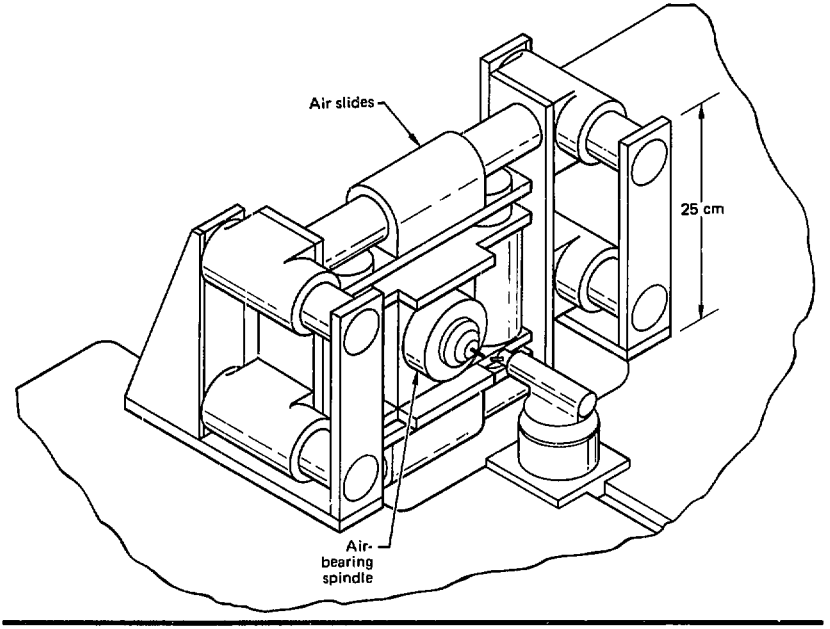

Fig. 4-18. Precision-lathe schematic.

machine. The machine (Fig. 4-18) will be designed especially for the size and space parameters characteristic to Target Fabrication, as opposed to systems such as the large-optics diamond-turning machine (213-cm diam).[34] The initial design parameters have been completed, and purchase orders for the various components will be issued in early 1982. This will provide a test facility for developing precision-machining techniques applicable to the special materials required for ICF experiments. The diamond-turning machine will also provide a badly needed additional source of mandrels necessary for coating and machining of various target parts.

Author: C. W. Hatcher

Target-Factory Studies

Parametric expressions have been derived for target production and tritium processing in a target factory.[35,36] From the expressions we have completed a study to estimate the inventory of tritium needed in the operation of a proposed fuel-processing system during the production mode of a target factory. The inventory of the proposed target fuel-processing system was determined as a function of production efficiency, storage factor, and time interval for the slowest processing step. We feel that a parametric study of this type will be necessary in evaluating possible processing schemes for the production of tritiated laser-fusion targets.

Tritium System

A description of the tritiated fuel-processing system and the derivation of the following tritium inventory equations were given in Refs. 35 and 36. As shown in Fig. 4-19, we represent the tritium system as being composed of four sections: source, fill process, storage, and recovery.

Source. The tritium source supplies fuel to the fill-process section. In a steady-state production mode, the source output rate, $\dot{m}_S$, to the fill-process section is equal to the sum of the tritium input rates, $\dot{m}_R$ from recovery and $\dot{m}_E$ from the reactor:

$$\dot{m}_S = \dot{m}_R + \dot{m}_E \quad . \tag{1}$$

Consequently, during steady-state production, the tritium-source inventory can be set

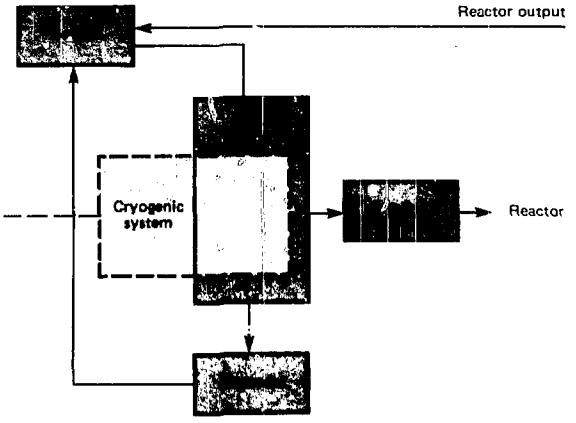

Fig. 4-19. Basic block diagram of tritium system interfacing cryogenic process of target factory.

to a minimal level and is, therefore, considered negligible.

Fill Process. The inventory of tritium in the fill-process section during target production is given by the expression

$$I_f = \frac{m_f R t_C}{\left(\prod_{i=m}^{s} q_i\right)}\left[1 + \sum_{i=m}^{s-1}\left(\prod_{j=m}^{i} q_j\right)\right] , \qquad (2)$$

where

m_f = amount of tritium per target (g),
R = target injection rate into the reactor (s^{-1}),
t_C = time interval for the slowest processing step in the cryogenic production line (s),
q = production efficiency for a cryogenic process step (yield factor),
s = the number of process steps in a cryogenic production line,
m = the cryogenic process step where the tritiated fuel-processing begins.

Storage. The storage section has an inventory of tritium-filled targets for maintaining the reactor-target injection rate in case of a production interruption. The tritium inventory is expressed as

$$I_S = m_f N R t_C , \qquad (3)$$

where N is the storage factor or the number of additional times that the fill-process section is activated to meet a required stockpile of targets.

Recovery. The recovery section is composed of two parts: the recovery processing of rejected tritiated targets from the fill-process section, and a redundant recovery system (RRS). The RRS is an environmental gas purification and gettering system.

The tritium inventory, I_R, for the recovery section is the sum of the tritium in the initial recovery process and in the *RRS*:

$$I_r = \frac{m_f R t_C}{\left(\prod_{i=m}^{s} q_i\right)}\left[1 - \left(\prod_{i=m}^{s} q_i\right)\right]$$

$$\times\left[2 - \left(\prod_{i=1}^{x} r_i\right) + \sum_{i=1}^{x-1}\left(\prod_{j=1}^{i} r_j\right)\right] , \qquad (4)$$

where x is the number of process steps in the initial recovery processing and r represents the efficiency of each process step.

Target-Factory Tritium Inventory

A target-factory tritium inventory can be estimated using Eqs. (2) through (4). However, to use these expressions, a proposed tritium system must be conjectured by arbitrarily assigning values to certain parameters:

$s = 10$ cryogenic process steps,
$m = 6$ as the initial cryogenic tritiated fuel-processing step,
$x = 5$ initial recovery process steps.

A value of $s = 10$ is selected as an estimate of the possible total number of processing steps in the cryogenic system that would be needed for target transport, manipulation, preparation, inspection, selection, tritium fill, and temperature treatment. A value of $x = 5$ recovery steps is used to approximate the possible number of processes to recover tritium, e.g., crushing, separating, gettering, purifying, etc. Also, for simplicity, each step in a processing system is assumed to be equally efficient, $q_i = r_i$.

The parameters m_f and R, whose product represents the tritium injection rate into the reactor, are dependent on the tritium burn fraction and the fusion power of the ICF power plant:[37]

$$\dot{m}_b = 1.78 \times 10^{-6} P_f , \qquad (5)$$

$$m_f R = \frac{\dot{m}_b}{f_b} \quad . \tag{6}$$

Substitution of Eq. (5) into Eq. (6) yields

$$m_f R = 1.78 \times 10^{-6} \frac{P_f}{f_b} \quad , \tag{7}$$

where

m_b = tritium burn rate (g/s),
P_f = fusion power [MW(f)],
f_b = burn fraction.

For instance, if it is assumed that an ICF power plant operates at $P_f = 3000$ MW(f) with a burn fraction $f_b = 0.3$, the tritium injection rate from Eq. (7) becomes

$$m_f R = 0.0178 \text{ g/s} \quad . \tag{8}$$

Furthermore, if the proposed target factory operates at a 0.9 efficiency with a storage factor of $N = 10$, the tritium inventories of each section can be determined using Eqs. (2) through (4) for various values of t_C, as shown in Table 4-2. We have plotted in Fig. 4-20 the total tritium inventory I_T from Table 4-2 as a function of t_C. The time interval for the slowest processing step in the cryogenic production line is shown to be an important factor in determining the total inventory of tritium. Consequently, to obtain a low I_T, cryogenic production must be thought of in terms of processes that will result in a minimal value for t_C. Likewise, the operating efficiency of the target factory is also an important factor in determining the total tritium inventory, as indicated in Table 4-3. The numbers are based on an arbitrary assigned value of 1 h for t_C.

Note that, from Tables 4-2 and 4-3, the total tritium inventory could be in the kilogram range. Because constraints will undoubtedly be placed on the quantity of tritium allowed, high-efficiency and high-rate processes must be developed for target production. A parametric study of this type will be necessary to evaluate possible processes for target production to estimate the total tritium inventory of a fuel-processing system.

Author: J. W. Sherohman

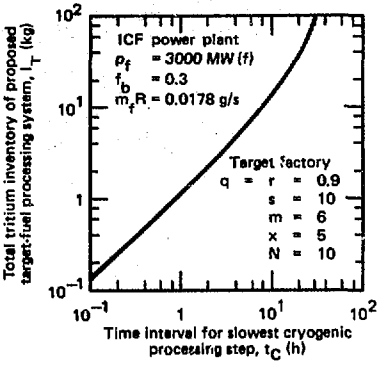

Fig. 4-20. Total tritium inventory plot of proposed tritiated fuel-processing system.

t_C (h)	I_F (kg)	I_S (kg)	I_R (kg)	I_T (kg)
0.5	0.22	0.32	0.10	0.64
1.0	0.44	0.64	0.20	1.08
10.0	4.46	6.41	2.01	12.88

[a] $q_i = r_i = 0.9$.

Table 4-2. Tritium inventory of proposed target factory operating to maintain 3000-MW(f) ICF power plant.[a]

$q_i = r_i$	I_F (kg)	I_S (kg)	I_R (kg)	I_T (kg)
0.9	0.44	0.64	0.20	1.08
0.8	0.65	0.64	0.53	1.82
0.7	1.06	0.64	1.14	2.84

[a] $t_C = 1$ h.

Table 4-3. Tritium inventory of proposed target factory operating at various efficiencies while interfacing 3000-MW(f) power plant.[a]

References

1. *Laser Program Annual Report—1977*, Lawrence Livermore National Laboratory, Livermore, Calif., UCRL-50021-77 (1978), pp. 5-13 to 5-16.
2. *Laser Program Annual Report—1980*, Lawrence Livermore National Laboratory, Livermore, Calif., UCRL-50021-80 (1981), p. 4-18.
3. *Laser Program Annual Report—1977*, Lawrence Livermore National Laboratory, Livermore, Calif., UCRL-50021-77 (1978), pp. 5-5 to 5-12.
4. *Laser Program Annual Report—1980*, Lawrence Livermore National Laboratory, Livermore, Calif., UCRL-50021-80 (1981), p. 4-6.
5. S. F. Meyer, "Metallic Coating of Microspheres," *J. Vac. Sci. Tech.* **18**, 1198 (1981).
6. *Laser Program Annual Report—1980*, Lawrence Livermore National Laboratory, Livermore, Calif., UCRL-50021-80 (1981), p. 4-31.
7. *Laser Program Annual Report—1980*, Lawrence Livermore National Laboratory, Livermore, Calif., UCRL-50021-80 (1981), pp. 4-23 to 4-26.
8. *Laser Program Annual Report—1980*, Lawrence Livermore National Laboratory, Livermore, Calif., UCRL-50021-80 (1981), pp. 4-26 to 4-29.
9. E. J. Hsieh and S. F. Meyer, "Recent Advances in Pt Coating of Microspheres by a Batch Magnetron Sputtering Process," *J. Vac. Sci. Tech.* **18**, 1205 (1981).
10. E. G. Dieter, *Mechanical Metallurgy* (McGraw-Hill, New York, 1976), 2nd ed., p. 190.
11. E. J. Hsieh et al., *A Magnetron Co Sputtering System for Coating ICF Targets*, Lawrence Livermore National Laboratory, Livermore, Calif., UCRL-86160 (1981).
12. *Laser Program Annual Report—1980*, Lawrence Livermore National Laboratory, Livermore, Calif., UCRL-50021-80 (1981), p. 4-16.
13. *Laser Program Annual Report—1979*, Lawrence Livermore National Laboratory, Livermore, Calif., UCRL-50021-79 (1980), p. 4-38.
14. *Laser Program Annual Report—1980*, Lawrence Livermore National Laboratory, Livermore, Calif., UCRL-50021-80 (1981), p. 4-36.
15. *Laser Program Annual Report—1980*, Lawrence Livermore National Laboratory, Livermore, Calif., UCRL-50021-80 (1981), pp. 4-39 to 4-40.
16. *Laser Program Annual Report—1979*, Lawrence Livermore National Laboratory, Livermore, Calif., UCRL-50021-79 (1980), pp. 4-42 to 4-45.
17. J. A. Monjes, B. W. Weinstein, D. L. Willenborg, and A. L. Richmond, *Microsphere Rotator for Automated Interferometric Target Characterization*, Lawrence Livermore National Laboratory, Livermore, Calif., UCRL-83375 (1979).
18. *Laser Program Annual Report—1979*, Lawrence Livermore National Laboratory, Livermore, Calif., UCRL-50021-79 (1980), p. 4-37.
19. *Laser Program Annual Report—1980*, Lawrence Livermore National Laboratory, Livermore, Calif., UCRL-50021-80 (1981), pp. 4-34 to 4-49.
20. C. M. Ward, *Applications of Surface Analysis to Fusion Target Fabrication*, Lawrence Livermore National Laboratory, Livermore, Calif., UCRL-82664 (1979).
21. *Laser Program Annual Report—1979*, Lawrence Livermore National Laboratory, Livermore, Calif., UCRL-50021-79 (1980), pp. 4-49 to 4-55.
22. C. M. Ward and D. L. Willenborg, *Microtopography Measurement of Small Defects Using Backscattered Electrons*, Lawrence Livermore National Laboratory, Livermore, Calif., UCRL-85290 (1981).
23. J. F. Miller, "A New Method for Producing Cryogenic Laser Fusion Targets," K. O. Timmerhaus, Ed., *Advances in Cryogenic Engineering* (Plenum Press, New York, 1978), p. 669.
24. *Laser Program Annual Report—1980*, Lawrence Livermore National Laboratory, Livermore, Calif., UCRL-50021-80 (1981), p. 4-51.
25. E. R. Grilly, "Condensation of Hydrogen Isotopes in Laser Fusion Targets," *Rev. Sci. Instr.* **48**, 2 (1977).
26. *Laser Program Annual Report—1978*, Lawrence Livermore National Laboratory, Livermore, Calif., UCRL-50021-78 (1979), p. 4-48.
27. C. M. Vest, *Holographic Interferometry* (John Wiley and Sons, New York, 1979).
28. R. R. Stone, D. W. Greg, and P. C. Souers, "Nondestructive Inspection of Transparent Microtargets for Laser Fusion," *J. Appl. Phys.* **46**, 2693 (1975).
29. T. P. Bernat, D. H. Darling, and J. J. Sanchez, *Applications of Holographic Interferometry to Cryogenic ICF Target Characterization*, Lawrence Livermore National Laboratory, Livermore, Calif., UCRL-86168 (1981).
30. *Laser Program Annual Report—1979*, Lawrence Livermore National Laboratory, Livermore, Calif., UCRL-50021-79 (1980), pp. 4-59 to 4-61.
31. *Laser Program Annual Report—1980*, Lawrence Livermore National Laboratory, Livermore, Calif., UCRL-50021-80 (1981), pp. 4-58 to 4-59.
32. *Laser Program Annual Report—1980*, Lawrence Livermore National Laboratory, Livermore, Calif., UCRL-50021-80 (1981), pp. 4-36 to 4-39.
33. W. E. Tindall, *Fabrication of Laser Target Components by Semiconductor Technology*, Lawrence Livermore National Laboratory, Livermore, Calif., UCRL-82644 (1979).
34. C. W. Hatcher and C. D. Hendricks, *Micromanipulators for ICF Target Fabrication*, Lawrence Livermore National Laboratory, Livermore, Calif., UCRL-84385 (1981).
35. J. W. Sherohman and W. R. Meier, *A Parametric Study of a Target Factory for Laser Fusion*, Lawrence Livermore National Laboratory, Livermore, Calif., UCRL-84264 (1980).
36. J. W. Sherohman, *Parametric Expressions of Tritium Flow Rates and Inventories in a Target Factory*, Lawrence Livermore National Laboratory, Livermore, Calif., UCID-18877 (1980).
37. W.R. Meier, *Build-Up of Tritium in a Liquid Lithium Breeding Blanket for an Inertial Confinement Fusion Chamber*, Lawrence Livermore National Laboratory, Livermore, Calif., UCRL-85245, Rev. 2 (1981).

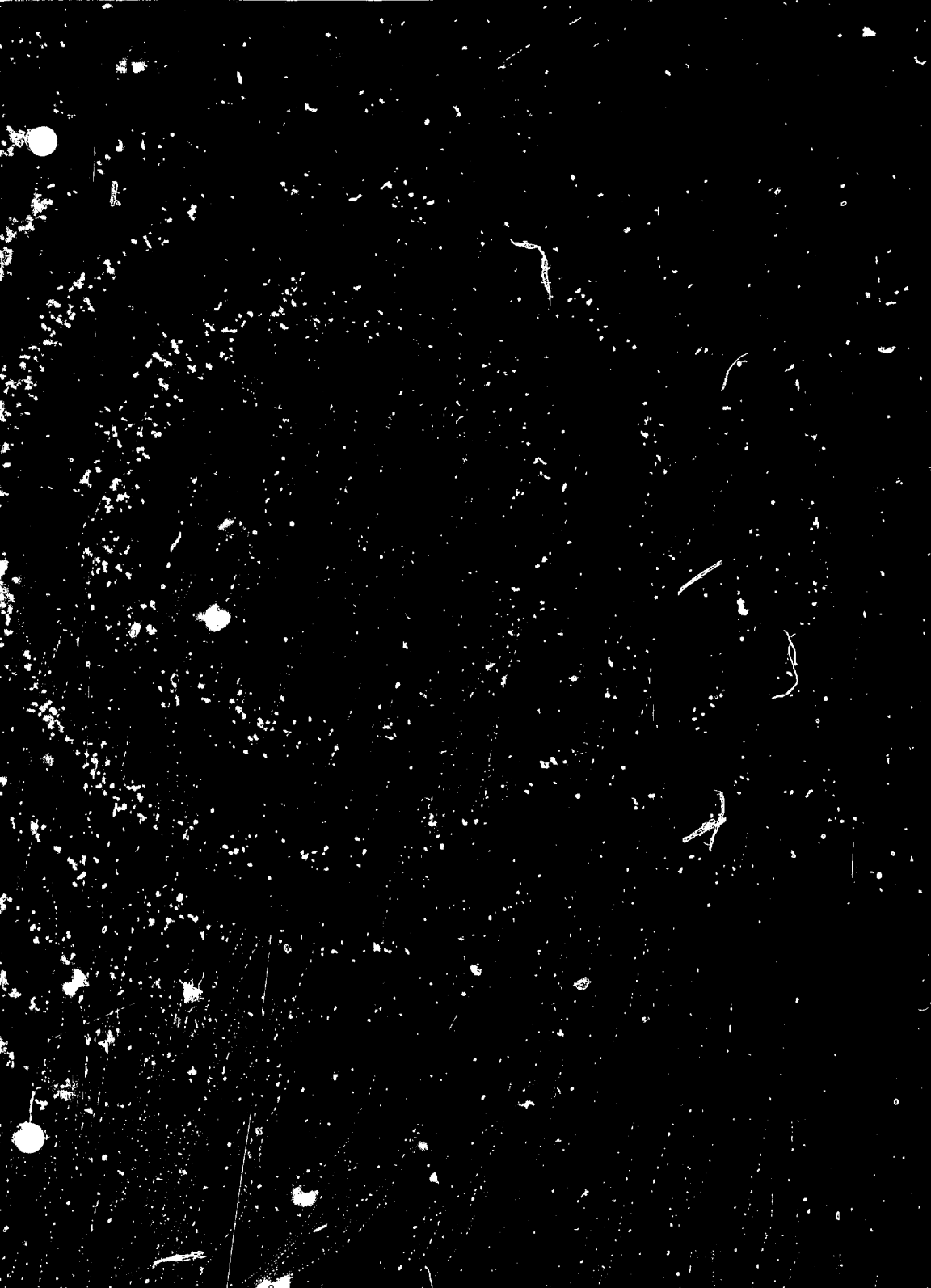

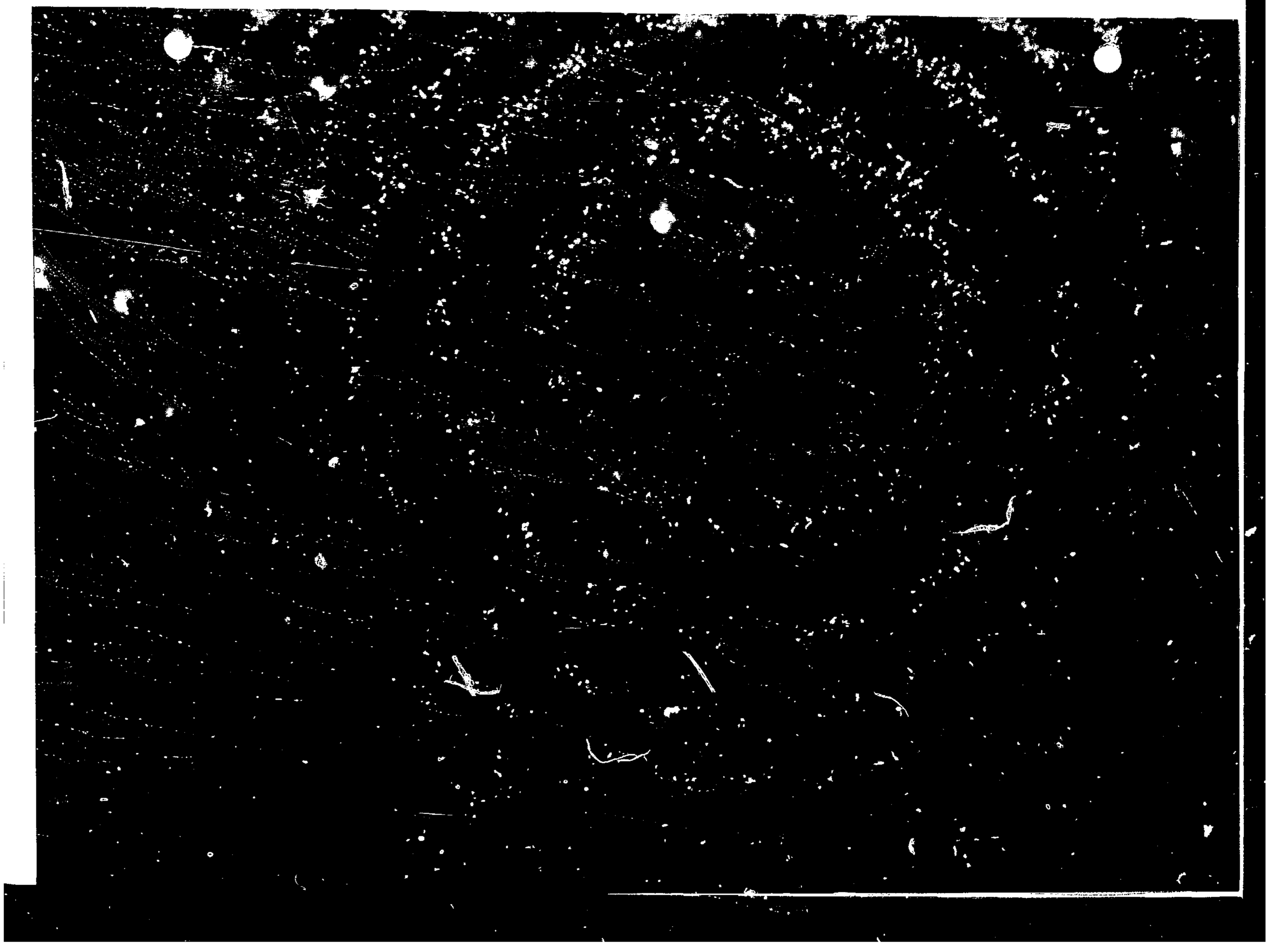

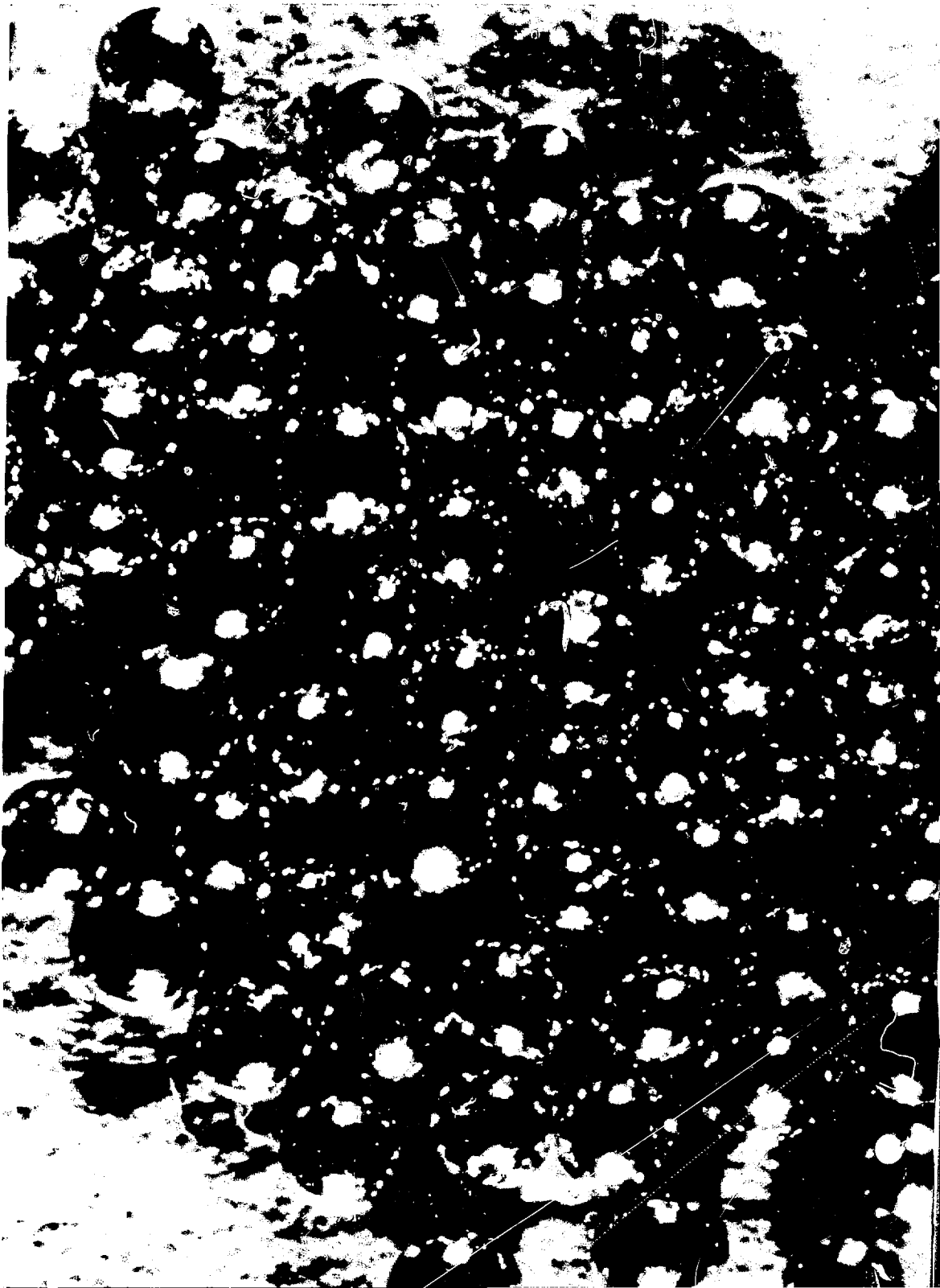

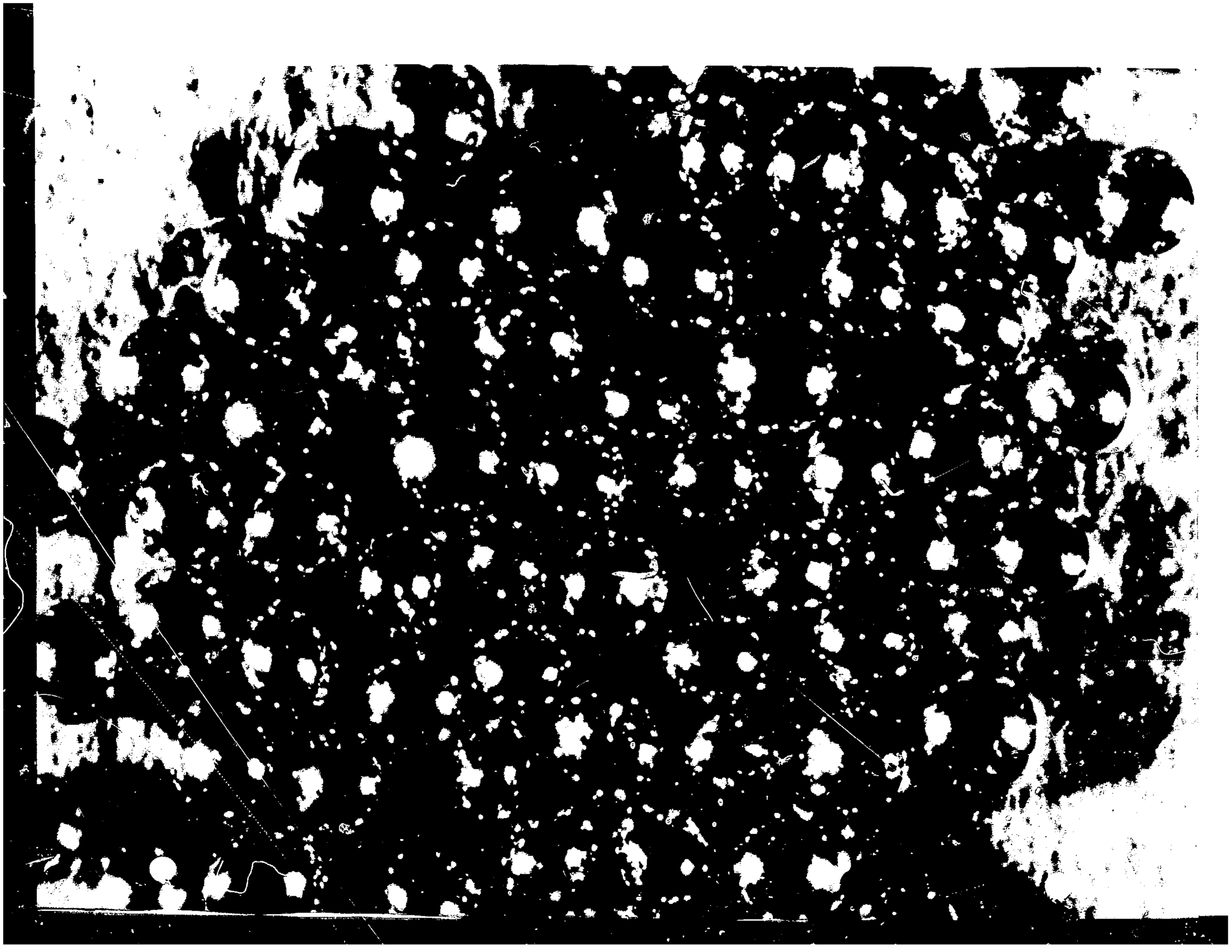

Diagnostic Development
Section 5

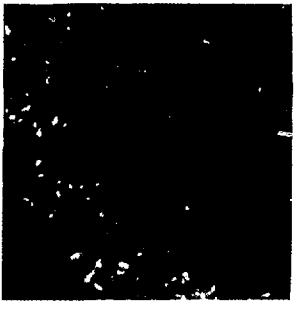

Diagnostics

Contents

Section Editor: D. T. Attwood

Diagnostics

Introduction

V. W. Slivinsky

The primary purpose of our diagnostics effort is to accurately measure the emissions from laser-fusion targets for the purpose of understanding laser-plasma interaction physics and the history of fuel-capsule implosions. The stringent diagnostics requirements dictated by the regimes of temperature, density, space, and time in which we operate force us to develop and field instrumentation not commonly found in other fields of physics. Because of the Laser Program's role in the national inertial-confinement fusion (ICF) program, we are often the first to identify new diagnostics requirements, develop the necessary instrumentation, and make the initial physics measurements in the new parameter regimes. During the last year, we made major advances in the development or utilization of diagnostics in the four general areas discussed below.

- ***X-Ray Diagnostics.*** The ongoing development of our filtered-diode sub-keV (Dante) spectrometers culminated this year in a versatile design that provides improved channel definition and temporal resolution. Each improvement gained from our experience with previous Dante systems has been incorporated into this new design. We have improved the spectral definition of x rays above 1 keV using bandpass diodes and photomultiplier tubes; this scheme employs a combination of filter and cathode x-ray absorption edges. We have also constructed a flat-response detector for x rays in the range from 400 to 1000 keV.

  For the first time, we obtained a combination of high temporal resolution and continuous sub-keV spectrograph coverage, using free-standing gold transmission gratings as an energy-dispersing element for an x-ray streak camera. This instrument complements our other discrete-energy diagnostics. We obtained time resolution of high-energy x rays using a modified optical/x-ray streak camera for x rays in the range from 20 to 30 keV and using a microchannel-plate photomultiplier tube for x rays from 20 to 70 keV. In addition, we made extensive use of a Wolter microscope/streak-camera combination to record space-time histories of accelerated disks and imploding fuel capsules.
- ***Optical Diagnostics.*** In 1981, we moved closer to a full understanding of suprathermal-particle generation, developing a single instrument (an optical/x-ray streak camera) for recording $3/2\omega$ stimulated optical emissions concurrently with the observed onset of high-energy x rays. In frequency-doubled (2ω) irradiation experiments, we made spectrally and temporally resolved measurements of stimulated Raman scattering; these measurements indicate broadband features from the time that the laser beam hits the target. Using our optical diagnostics in thin-foil experiments, we have observed high absolute levels (10%) of stimulated Raman scattering in underdense plasmas.
- ***Radiochemistry and Neutron Diagnostics.*** To significantly reduce the background for our determinations of fuel density in laser-fusion targets, we built and tested a thin-wall gas-proportional counter. We also made progress on new collimator designs for neutron imaging. Calculations show that neutron imaging of fusion reactions will be possible with the Nova laser. Our design analysis of an ultrafast neutron streak camera leads us to believe that such an instrument will be capable of measuring the fusion burn time of Nova targets.

- *The Fusion Experiments Analysis Facility.* Our newly acquired VAX 11/780 computer system has become a significant factor in processing and analyzing experimental data. In particular, we adopted a formal approach to sorting and correlating large amounts of experimental data; this effort has corroborated some of our scaling relationships. We have implemented a powerful image-processing capability to handle large arrays of digitized image data. Users can now produce color-enhanced images for instant analysis and examination.

Shiva Filtered X-ray Diode Low-Energy Spectrometer

In 1981, we installed on the Shiva target chamber an improved 10-channel filtered x-ray diode (XRD) low-energy x-ray spectrometer, using it for several important target-irradiation series to measure time-dependent x-ray spectra in the range from 0.2 to 1.5 keV. We have thus reached a significantly higher plateau in the evolution of XRD-based spectrometer systems used at LLNL laser facilities. In this article, we present our spectrometer design, which is based largely on considerations of channel response vs x-ray energy. In addition, we summarize the temporal responses of various detector, cable, and oscilloscope systems that we employ.

The new system is known as the "H" (hybrid) spectrometer because of its combination of filtered XRD channels, some with and some without small-angle scattering mirrors for high-energy cutoff. We have previously discussed the use of small-angle reflection from x-ray mirrors to greatly reduce signal contributions above filter edges.[1] Although our measurements to date have been made without mirror cutoff, we have now completed the mirror-adaptation mechanical design, and we plan to employ mirror cassettes on Novette, the prototype of the Nova laser system (both discussed in detail in Section 2). Our mirror cassettes are self-contained small-angle x-ray scattering mirrors developed by Lockheed. We tested the mirrors for several months in a five-channel x-ray spectrometer on Shiva. On Novette, we will be able to replace two to five XRD channels with mirror cassettes to provide the mirror cutoffs mentioned above.

Mechanical Improvements

The H system, shown schematically in Fig. 5-1 as it was fielded on Shiva, incorporates

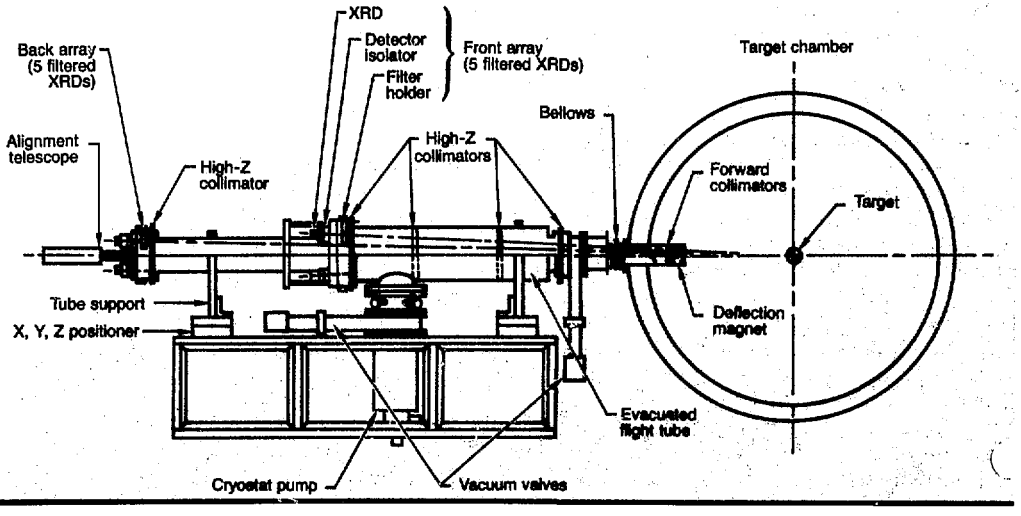

Fig. 5-1. Schematic of the hybrid H spectrometer, as fielded on the Shiva target chamber.

a large number of mechanical improvements. The system has greatly improved forward collimation, with a 1-cm field of view at the target, and negligible channel-to-channel soft x-ray cross-talk. Each beam line is very well shielded for higher-energy photon-beam definition and is particularly suitable for the new microchannel-plate (MCP) photomultiplier (PM) channels in the range from 2 to 5 keV (discussed in the following article).[2] In fact, we can provide good beam geometry for photon channels up to 500 keV if necessary.

As Fig. 5-1 shows, the evacuated x-ray flight tube is independently supported for *shot-to-shot alignment capability by means* of *x,y,z* position controls on the front and back. Alignment is verified by the use of an optical telescope or laser on the system center axis. Portability is improved by means of a frame that supports everything, including a vertically mounted cryostat pump. The internal system alignment can thus be maintained from the bench to the target chamber. The detector is electrically isolated with Rulon, a commercial plastic material that does not have a tendency to crack.

XRD Channels

The filtered-XRD channel arrangement used for spectra between 0.2 and 1.8 keV has been described previously.[3,4] Because of their long-term stability, we employ aluminum XRDs to cover as much of this range as possible. Using these same aluminum XRDs with a different set of filters, we can conveniently adjust the array for spectral emission measurements in the lower-temperature range from 10 to 50 eV. For x-ray channels close to the Al K-edge jump, we use chromium and solid-nickel cathodes. During 1981, we minimized the use of Cr cathodes because of a problem with response stability. The Al and Ni detectors are diamond-turned for more uniform absolute sensitivity (see "Absolute Photoelectric X-Ray Diode Sensitivity," later in this section). The H system also employs an NE-111 fluor-MCP detector combination and a 2-μm-thick Ti filter, in a special light-tight assembly, to measure a 2-keV-wide band of x rays extending from 2.5 to 4.7 keV.

Channel Energy Responses and Mirror Cutoff

We obtained channel sensitivity as a function of energy by combining results from separate detector and filter calibrations. The spectra that we measured are in the temperature range from 80 to 180 eV and fall rapidly above a photon energy of 1 keV. In Fig. 5-2, we compare the response of filtered aluminum XRD channels with and without mirror cutoff to a typical case (a 150-eV temperature spectrum). Note that none of the channels has a significant signal contribution above the aluminum K edge despite the large sensitivity increase there. A proposed beryllium-filtered channel (111 eV) is not shown.

Each of the first two channels (boron[5] and Formvar) has a significant signal contribution above the filter edge that is reduced to very acceptable levels using the appropriate mirror cutoff. The corresponding improvement in response of the vanadium channel is marginal. We conclude that the addition of mirror cutoff provides, in general, a significant improvement in channel definition for the lowest two or three channels, a marginal improvement for perhaps one more channel, and not much benefit for channels above 700 eV.

These considerations led to the hybrid configuration obtained by adding mirror cutoff to as many as four detectors. The main disadvantages of mirrors, besides greater mechanical complexity, are their additional calibration difficulties, as well as uncertainties in mirror reflectivity due (in practice) to a lack of timely recalibration efforts. However, we feel that these additional problems are worth the improved channel definition and can be solved before Novette startup in October 1983.

Temporal Response

We now discuss the time response that we obtain using various combinations of fast XRDs and fast recording instruments. Our 50-ps-response XRD is intended for use in future target-diagnostic experiments in which we will require the fastest impulse response and optimum electrical fidelity for recording soft x-ray data. We have modified

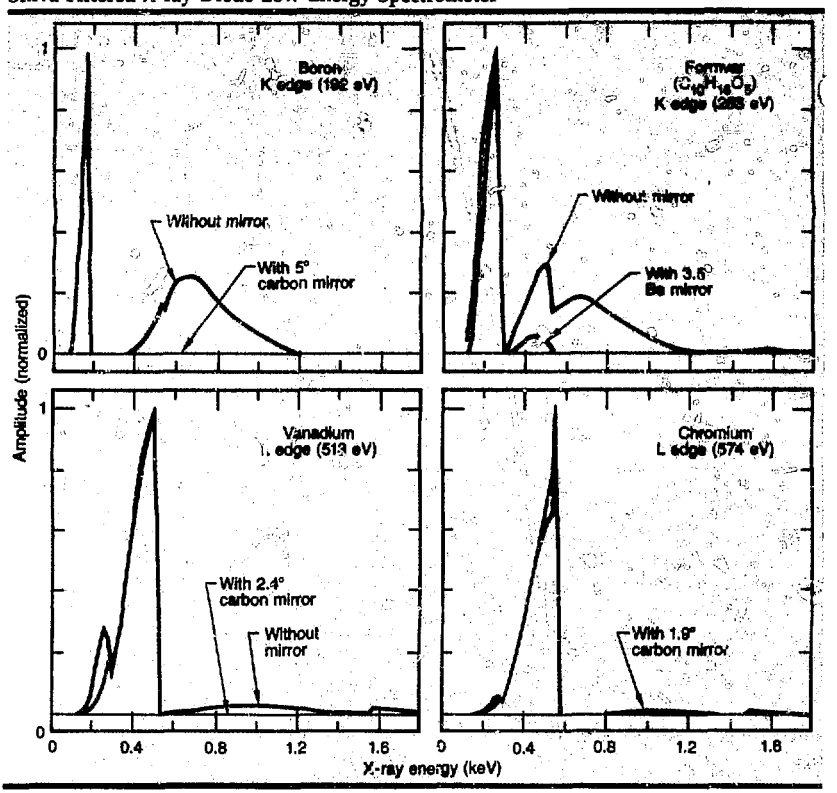

Fig. 5-2. Sensitivity of filtered-aluminum XRD channels to a 150-eV temperature spectrum as a function of x-ray energy for filter edges below 600 eV.

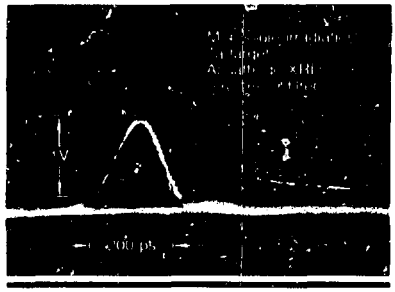

Fig. 5-3. Response of a modified 50-ps XRD and a Thomson TSN-660 oscilloscope, showing improved return to the baseline.

the 50-ps XRD, originally reported in the *1978 Laser Program Annual Report*,[6] to reduce after-pulse ringing and to simplify assembly. We determined the cause of the ringing to be an electrical resonance of the anode-cathode capacitance and the anode inductance. Accordingly, we redesigned the geometry to reduce the equivalent anode inductance by a factor of 10. We replaced the discrete ceramic-chip bypass capacitors with a cup-geometry capacitor using Parylene as the dielectric material.

The electrical performance of this improved XRD was verified by impulse measurements made using x rays from target irradiations at the Monojoule laser facility; a sample impulse record is shown in Fig. 5-3. Although the FWHM of the x-ray source is not sufficiently narrow to permit good measurements of the detector impulse response, the recorded data confirm that the new design is electrically superior.[7] The improved 50-ps XRD, when used with a short, high-quality signal cable and a Thomson TSN-660 oscilloscope, should have an impulse-response FWHM of <120 ps.

Figure 5-4 compares the measured impulse time responses of the improved 50-ps XRD system with three other XRD-oscilloscope systems that we use. In previous studies, we measured a system impulse response of 135 ps FWHM for a system

comprised of an XRD-31, 30 ns of 0.5-in. air-heliax signal cable, and a Thomson TSN-660 oscilloscope.[8] As can be seen in Fig. 5-4, there is a significant contribution to the trailing edge of the response, most probably due to a reflection from the signal feedthrough. We obtain, to first order, a 107-ps FWHM response for the detector and cable by unfolding the 90-ps oscilloscope response.

Using short laser pulses and making measurements with a soft x-ray streak camera, we obtained, by deconvolution, a value of 335 ps FWHM for the average temporal response of our Shiva systems, each consisting of an XRD-31, 90-ns of 0.5-in. air-heliax signal cable, and a direct-access Tektronix 7912 oscilloscope. (Most of the response width is not due to the detector, but to the oscilloscope.) The direct-access unit is relatively insensitive at a fixed 4 V/div. The amplified 7912, with a vertical sensitivity of up to 10 mV/div, yields a system time response of 730 ps FWHM. Nonetheless, the 7912 systems that we used at Shiva have been very adequate for multinanosecond experiments, including all of the series above 2 ns. In detailed tests of the 5-ns series data, we found that signals obtained by deconvolution, to remove the system response, were nearly identical to their originals.

We are currently developing a preamplifier that can be substituted for the Tektronix model 7A19 now used in the 7912 oscilloscope; we expect this preamplifier to yield a response of ~500 ps FWHM at 500 mV/div. Because of the lack of active electronic components in our new design, we should obtain much greater noise immunity. In addition, we are evaluating a commercial amplifier (the B & H Electronics model AD-5120H) that will improve the sensitivity of the TSN-660 oscilloscope by a factor of ~10, but will reduce the bandwidth to ~3 GHz.

Author: K. G. Tirsell

Major Contributors: D. E. Campbell, R. A. Heinle, M. W. Kobierecki, and P. H. Y.

Detector	System Oscilloscope	FWHM (ps)	Rise time, 10 to 90% (ps)	Fall time, 90 to 10% (ps)
50 ps	TSN-660	<120	<100	<120
XRD-31	TSN-660	135	110	—
XRD-31	DA-7912	335	305	430
XRD-31	Amp-7912	730	585	505

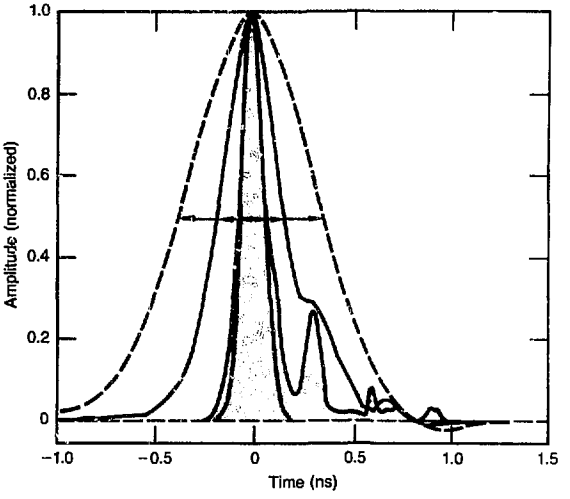

Fig. 5-4. Measured impulse time response of four XRD detector-signal cable-oscilloscope systems.

Fluor/Microchannel-Plate and CsI X-ray Diode Detectors for Measuring X Rays of 2 to 5 keV from Laser-Target Interactions

Since 1978, we have routinely measured the emission of soft (sub-keV) x rays from laser–target interactions using filtered x-ray diodes (XRDs).[9] From these measurements, we have derived a data base for LASNEX calculations,[10] furthered our understanding of thermal-electron conduction and transport phenomena,[11] and obtained x-ray conversion efficiencies.[12] On the other hand, we have routinely measured hard x rays (above 6 keV) using a filter-fluorescer (FFLEX) diagnostics system.[13,14] However, XRD systems that use conventional (Al, Cr, and Ni) cathodes are not sensitive enough to measure x rays above ~1.5 keV, while

FFLEX is difficult to use below ~6 keV because of the rapidly decreasing fluorescence yield with decreasing atomic number.

Thus, the x rays in the range from 2 to 5 keV have never been measured, despite their importance as a potential source of deleterious photon preheat.[15] Recent wavelength-scaling studies of the laser-target interaction[16,17] show that the hard x-ray fluence decreases dramatically with decreasing wavelength, while the soft x-ray fluence increases. It is not known whether the x-ray fluence from 2 to 5 keV increases or not. The importance of measuring this fluence led us to develop detectors for use in the range of 2 to 5 keV.

We selected two candidates for this purpose: a cesium-iodide-cathode XRD, and a fluor/microchannel plate (fluor/MCP). The MCP detector consists of a 36-μm-thick NE-111 plastic scintillator, a 3-mm-thick blue-light filter (Corning 754 glass), and an 8-mm-thick Pb-glass x-ray filter, all sandwiched together and coupled to a one-stage ITT 4126 MCP photomultiplier with an S-1 photocathode. The fluor/MCP assembly is housed in an arrangement that effectively reduces stray light to less than 10^{-6} by differentially pumping around the filter, using an effective light baffle.

Figure 5-5 compares the calibrated x-ray detector sensitivities of a thin fluor/MCP, a 0.3-μm-thick CsI cathode, and a conventional aluminum cathode (other metallic cathodes, such as Ni and Cr, all have sensitivities on the same order as Al). As the figure shows, the CsI XRD is almost two orders of magnitude more sensitive than a solid-Al XRD in the region of 2 to 5 keV, while the fluor/MCP detector is three orders of magnitude more sensitive than an Al XRD. This means that both the fluor/MCP and the CsI XRD are potentially capable of measuring x rays of 2 to 5 keV from laser-target interactions.

Cesium iodide is a hygroscopic material; unless it is hermetically sealed, its sensitivity changes with time. The long-term stability of CsI-cathode sensitivity, however, needs further investigation.

Table 5-1 gives examples of the design of different x-ray detector channels at

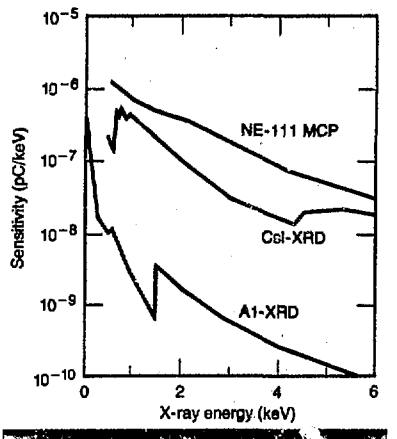

Fig. 5-5. Comparison of detector sensitivities using fluor/MCP, CsI-cathode XRD, and Al-cathode XRD.

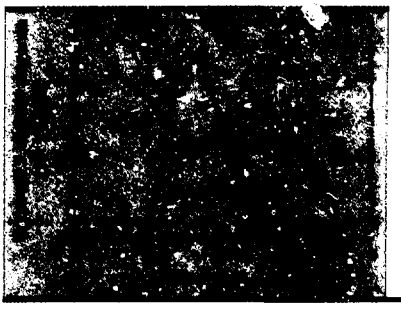

Fig. 5-6. Channel response folded with trial gold-disk spectra.

Table 5-1. Design of x-ray detector channels at intermediate energies (1.5 to 5 keV).

					Channel characteristics (folded with trial spectrum)		
	Filter					Fraction of	
Detector	Material	K edge (keV)	Thickness (μm)	Channel center (keV)	Channel width (keV)	signal below filter k edge (%)	Total signal charge (V-ns)
CsI XRD	Al	1.56	25	1.43	0.2	88	0.73
CsI XRD	Zr	2.2	5	1.93	0.49	87	0.52
Fluor/MCP (36-μm NE-111)	Zr	2.2	4	1.97	0.50	90	12.4
Fluor/MCP (36-μm NE-111)	Ti	4.96	14	3.3	1.73	99.3	6.38
Fluor/MCP (36-μm NE-111)	Ti	4.96	50	4.28	1.37	99.9	0.27

intermediate energies (1.5 to 5 keV). Using various x-ray diodes with different filters, we can obtain different channel coverages and channel widths. The objective of our present design is to obtain a total signal level above the oscilloscope detection threshold (>20 mV at Shiva), but, at the same time, maximize the fraction of signal below the filter K edge.

As an example, we show the details of our design for a relatively broad channel centered on 3.5 keV. Figure 5-6 shows the channel response folded with a trial spectrum (estimated from earlier x-ray data of gold-disk target shots). We obtained the channel response by folding the calibrated sensitivity of a 14.2-μm-thick Ti filter with the calibrated fluor/MCP sensitivity. Integrating the fold in Fig. 5-6 with respect to x-ray energy, we obtain the channel-center energy, defined as the 50% point of the running integral. As Fig. 5-7 shows, the channel center (the energy one-half value) is at 3.3 keV; the fraction of total signal below the filter K edge is 99.3%; and the total detector charge is 8.4×10^7 pC, which corresponds to 6.38 V-ns for this channel.

The 3.5-keV channel described above was installed on the Shiva 9-channel filtered-XRD H system (described in the previous article) and used to measure x-ray emission from laser-target interactions. Figure 5-8 shows the result obtained with a gold-disk target, 1.5 mm in diameter and 25 μm thick, irradiated with 1.06-μm light. The disk was tilted so that its normal made an angle of 30° with respect to the irradiation axis. The H system viewed the target at an angle of 66° with respect to the disk normal. In Fig. 5-8, the spectral data are compared to a theoretical spectrum calculated using non-LTE ionization physics and inhibited thermal-electron conductivity.[18] Below 1.5 keV, the experimental data match the numerical simulation quite well; at 3.5 keV, however, the experimental data are a factor of 2.5 higher than the theoretical value. The reason for this discrepancy is not clear at present.

Based on the successful measurement of the 3.5-keV channel, we plan to incorporate other channels (~1.5 and ~2 keV; see Table 5-1) into the filtered-XRD system. We will then be able to cover the spectral region both below and at the energy where gold M lines occur, allowing for better comparisons between theoretical calculations and more complete spectral data.

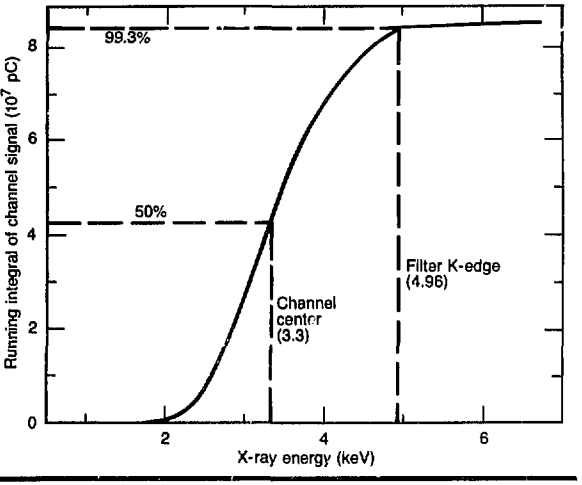

Fig. 5-7. Running integral of channel signal gives channel center, fraction of total signal below filter K edge, and total signal level.

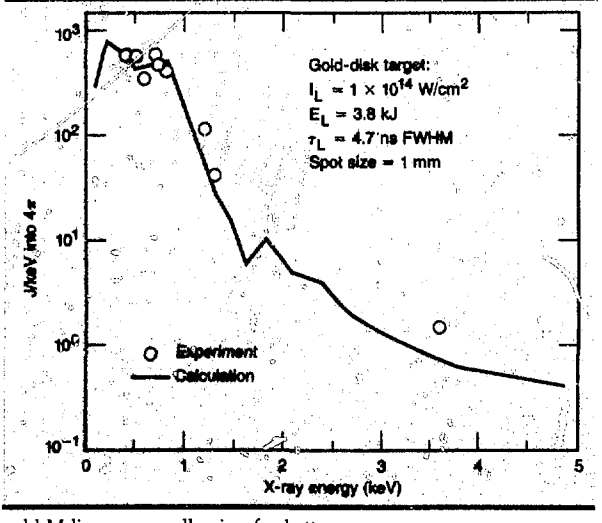

Fig. 5-8. Comparison of measured and calculated soft x-ray spectra for a gold-disk target; spectra are normalized at 800 eV.

Author: P. H. Y. Lee

Major Contributors: K. G. Tirsell, G. R. Leipelt, and W. B. Laird

Absolute Photoelectric X-ray Diode Sensitivity

We use a large number of filtered x-ray diodes (XRDs) to measure low-energy x-ray emission from laser-irradiated targets. To calibrate these detectors absolutely, we measure each photocathode's sensitivity from ~0.2 to 8 keV at the LLNL X-Ray Calibration and Standards Laboratory. In this article, we first discuss our calibration techniques and then present energy-dependent, quantum-efficiency values measured for the photocathode materials we have used most frequently, including aluminum, nickel, chromium, and gold. Here, detector quantum efficiency (in detected electrons per incident photon) is simply related to the photocathode sensitivity (usually expressed in units of coulombs per keV of incident photon energy).

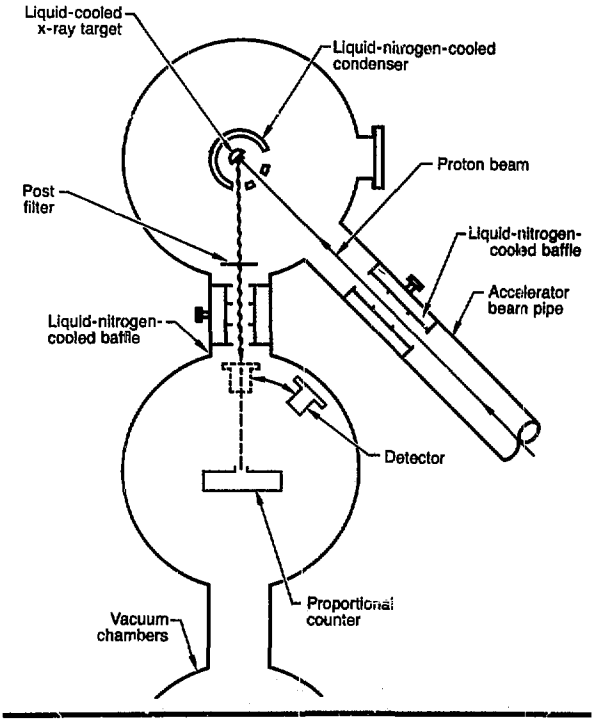

Fig. 5-9. Ionac sub-keV XRD-calibration arrangement.

Detector Calibration Techniques

High x-ray flux levels from LLNL x-ray calibration facilities are capable of producing low steady-state detector-output currents that can be accurately measured. To measure the absolute sensitivity of an XRD from 185 to 932 eV, we use proton-induced x-ray lines from the Ionac facility.[19,20] The Ionac utilizes high-fluorescence x ray yields with low bremsstrahlung background to provide an excellent set of intense, nearly monoenergetic sub-keV calibration lines. For each x-ray line, the absolute x-ray flux directed towards the XRD is determined using a reference detector in the counting mode. Similarly, we use electron-induced fluorescence lines from our low-energy x-ray facility for calibrations in the range of 1.5 to 8.1 keV (Ref. 21).

Figure 5-9 shows the Ionac calibration arrangement, consisting of a target chamber, a detector chamber, and (for completeness) a third chamber used for grazing-incidence mirror-reflection measurements. Briefly, x rays are produced by steering and focusing a 225-keV proton beam onto a water-cooled, interchangeable metallic target. Impurities (consisting mainly of carbon K lines) are greatly suppressed by liquid-nitrogen-cooled traps and suitable x-ray filters located appropriately in the target chamber. Minor spectral-contaminant lines (such as oxygen K lines) tend to vary greatly with target type.

The x-ray flux at the detector position is measured absolutely in the counting mode using a calibrated gas-flow proportional counter; the transmission of the thin Parylene counter window is measured separately. The monitor solid angle is defined by a small pinhole of known area, chosen to adequately obtain low instrumental dead time. After rotating the monitor out of the beam, we measure the current from the XRD using an electrometer. The detector collimator defines a beam covering 80% of the XRD cathode area—the area consistent with practical use. The low-energy lines we use are listed in Table 5-2.

The calibration technique used at the laser energy x-ray facility (LEXF) for the x-ray range from 1.5 to 8.1 keV is similar to the technique just described, except that the

x-ray flux is monitored using a windowless, cooled Si detector.[21] In the LEXF, the purity of the x-ray lines is greater than 87% (96% for aluminum K lines) due to the shielded tungsten cathode and back-directed target geometry.[22] The low-level bremsstrahlung background is accounted for by a code that simultaneously takes the measured spectrum for each source line, along with the corresponding monitor and XRD detector data, and then iterates to obtain corrected sensitivity values.[23] We use the LEXF to calibrate all of our XRD detectors from 1.5 to 4.1 keV and to calibrate many detectors from 1.5 to 8 keV.

XRD Calibration Results

Figure 5-10 and Table 5-2 show quantum-efficiency values that we have measured for our most commonly used cathodes. The aluminum and nickel calibration data are averages of 30 and 6 diamond-turned solid cathodes, respectively. The chromium data are for a batch consisting of 2 μm of Cr vapor deposited on diamond-turned copper. The gold results are typical of 1 μm of gold deposited on nickel on diamond-turned copper. In each case, the calibration values are compared with arbitrarily normalized values of $E\mu(E)$, determined from the incident photon energy, E, and from the photoionization cross-section data of Henke, et al.[24] for $\mu(E)$.

As has been observed by other workers,[25,26] this simple model tends to work better away from edges. The $E\mu$ curves for both pure Al and for Al_2O_3 fit the slope of the calibration data above the aluminum K edge rather well. The model for pure Al seems to fit better between the oxygen and aluminum K edges and tends

Table 5-2. Quantum-efficiency measurements for XRD cathodes commonly used at LLNL.

Source	Energy (eV)	Quantum efficiency in electrons/photon (%) Al	Au	Cr	Ni
Ionac[a]					
β-K	183	4.67	2.76	3.03	3.92
C-K	277	2.79	7.32	1.98	2.89
V-L	510	2.95	12.7	2.12	3.24
Cr-L	574	4.05	13.0	4.07	3.64
Fe-L	704	3.05	11.4	7.17	2.63
Cu-L	932	1.76	8.67	5.04	5.37
LEXF[b]					
Al-K	1486	0.570	5.93	2.31	3.25
Zr-L	2402	2.13	3.25	1.07	1.79
Ag-L	2982	1.11	10.6	0.520	0.960
Sc-K	4090	0.643	7.28	0.345	0.638

[a]Other sources used less frequently include nickel L and cobalt L, while beryllium K is under development.

[b]Other source lines used for many calibrations include vanadium K (4951 eV), manganese K (5898 eV), cobalt K (6929 eV), and copper K (8046 eV).

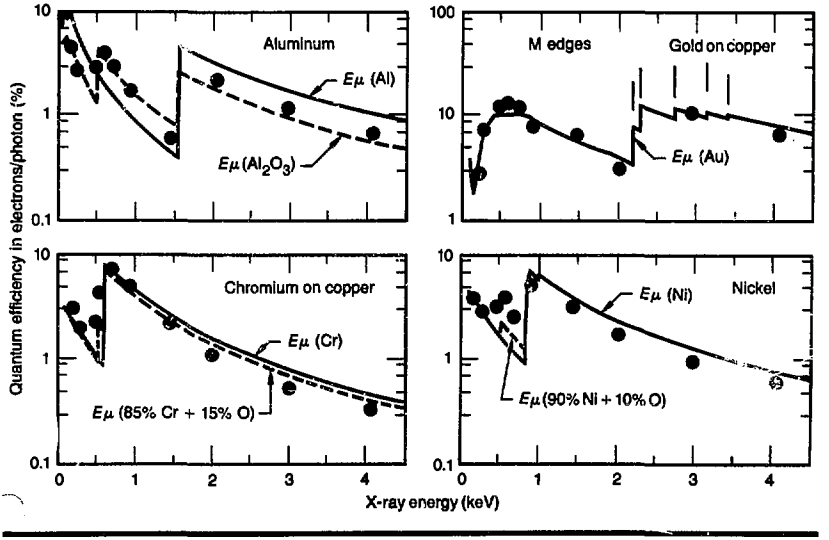

Fig. 5-10. Measured absolute XRD quantum efficiencies compared to normalized values of $E\mu(E)$, where $\mu(E)$ is the photoionization cross section at x-ray energy E.

to exaggerate the K-edge jump. The Al_2O_3 model underestimates the K-edge jump, which suggests that a better fit for this type of cathode lies between pure Al and Al_2O_3.

In the case of gold, the $E\mu$ model gives a somewhat better representation of the quantum-efficiency shape, even across the main gold M edge. The model for chromium fits the data reasonably well across the Cr L edges, but does not match the slope above 1 keV; this may be because the Cr performance is affected by contributions from the copper substrate. The pure Ni model fits the solid-nickel calibration very well above its L edges, but poorly below them. The addition of 10% oxygen tends to improve the agreement. Our results support the validity of the model away from absorption edges and also confirm the difficulties with edge jumps and effects due to the presence of oxygen in surface layers.

Variations in Sensitivities of New XRDs

Since we use so many XRDs, one of our goals has been to produce more uniform absolute sensitivity. Figure 5-11 shows sensitivity deviations from the batch average for one of our first sets of Al XRDs, characterized by a variety of cathode surface treatments and no diamond-turning, and for a later set that was diamond-turned. The shape of the sensitivity curves does not change drastically from detector to detector; consequently, the deviation curves are rather flat. The absolute amplitudes vary as much as ±40%, however, most probably due to significant variations in effective cathode surface area.

We subsequently tested cathodes whose surfaces were polished in a treatment

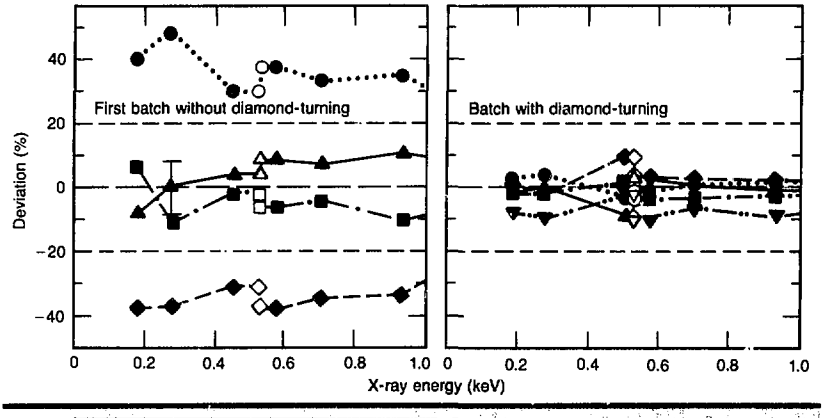

Fig. 5-11. Deviations of solid-Al-XRD sensitivities from the batch average.

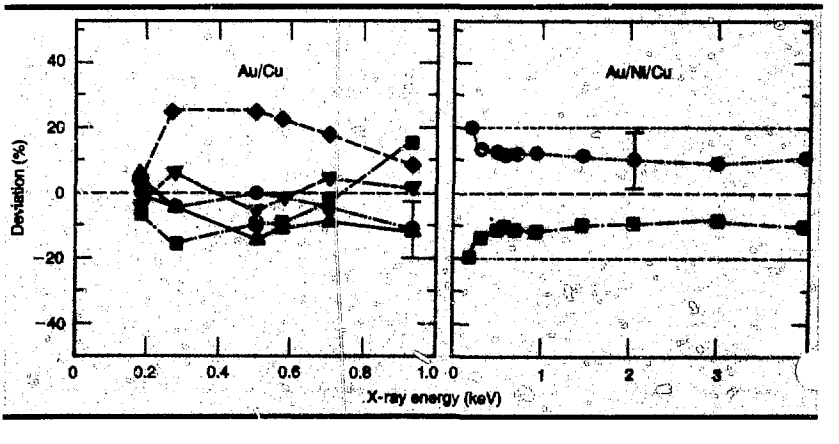

Fig. 5-12. Deviations of gold-XRD sensitivities from the batch average.

consisting of dry machining to an 8-μin. finish using a 5-mil-radius diamond tool and no chemical cleaning. This polishing treatment tends to decrease the Al sensitivity, but it gives batch variations of less than ±15% for all calibration points and variations of less than ±10% above the oxygen edge. The results for Cr XRDs prepared by vapor deposition on diamond-turned copper have been almost as good, while the data for a recently made set of diamond-turned, solid-Ni XRDs shows sensitivity variations as low as ±8%.

Figure 5-12 shows that our first batch of gold XRDs made by vapor deposition on diamond-turned copper tends to have significantly greater variations than other materials. The second gold batch, made by depositing gold on nickel on diamond-turned copper, appears somewhat better, but is not well tested due to the small sample. As Fig. 5-12 shows, the gold-sensitivity curves tend to fall into either a low group or a high group. Perhaps these variations are related to the significantly greater changes with use that we observe in gold cathodes, which are most probably due to the affinity of these cathodes for water vapor.

Settling the issues described above requires further work on the surface preparation of gold cathodes. However, our experience with several early batches of XRD detectors has shown that diamond-turning of the cathode surfaces tends to significantly reduce XRD sensitivity variations.

Author: K. G. Tirsell

Bandpass X-ray Diodes and X-ray Multiplier Tubes

During 1981, we developed a simple method of obtaining bandpass x-ray detectors: the lower and upper bounds of the bandpass are determined by the absorption edges of the photocathode and the filter, respectively. We have employed this method for windowless and vacuum-bandpass x-ray diodes (XRDs), and we have extended it to obtain an electron multiplier tube as well. These general-purpose bandpass XRDs may find special applications for pulsed x-ray sources associated with inertial-confinement fusion, magnetic-confinement fusion, or plasma-focusing devices.

The quantum yields, or sensitivities, of various photocathodes are known to have discontinuities at the x-ray absorption edges. Figure 5-13 gives a partial compilation of available data on relevant photocathode sensitivities.[27-29] Even though the

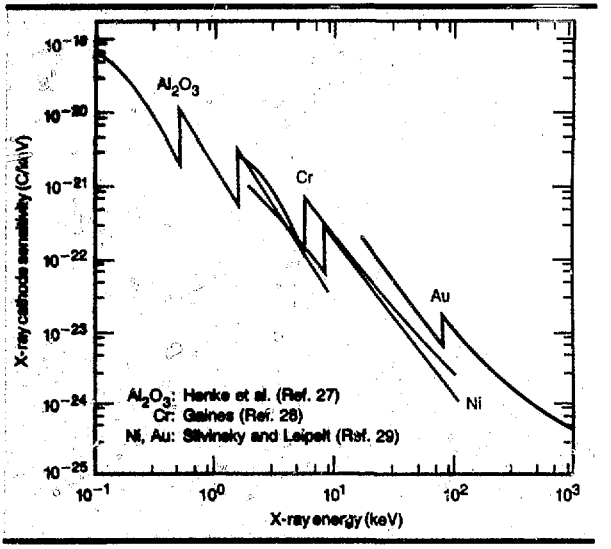

Fig. 5-13. A partial compilation of available data on photocathode sensitivities to x-ray energy between 0.1 and 1000 keV.

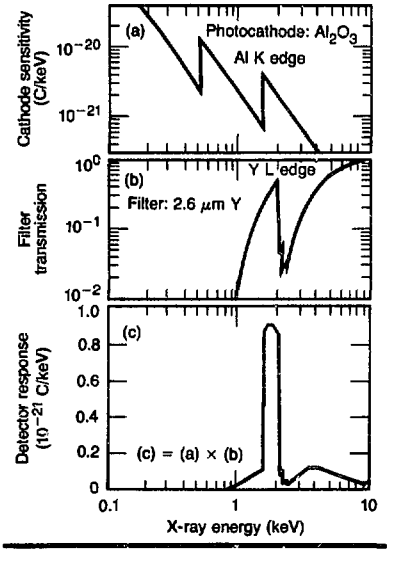

Fig. 5-14. Simple method of obtaining a 1.56- to 208-keV bandpass XRD utilizing the Al K edge of the photocathode and the L edge of an yttrium filter.

sizes of the quantum-yield jumps are typically smaller than the corresponding cross-sectional jumps by a factor of up to ~3, the former can still be quite effective in defining the x-ray bandpass when coupled to filters of sizable transmission jumps.

In Fig. 5-14, we illustrate our bandpass XRD method for a 1.56- to 2.08-keV detector, utilizing the aluminum K edge of the photocathode and the L edge of an yttrium filter. We obtain a well-defined bandpass by multiplying the cathode sensitivity and the filter transmission [Fig. 5-14(c)]. At higher x-ray energies, it is easy to construct vacuum XRDs with thin windows. Figure 5-15 shows the response of a bandpass vacuum XRD that utilizes a Cr photocathode.

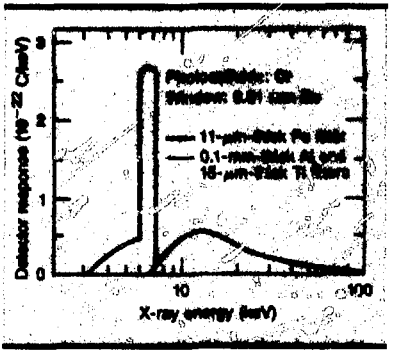

Fig. 5-15. A 5.99- to 7.11-keV bandpass vacuum XRD utilizing an Fe filter, a Be window, and a Cr photocathode.

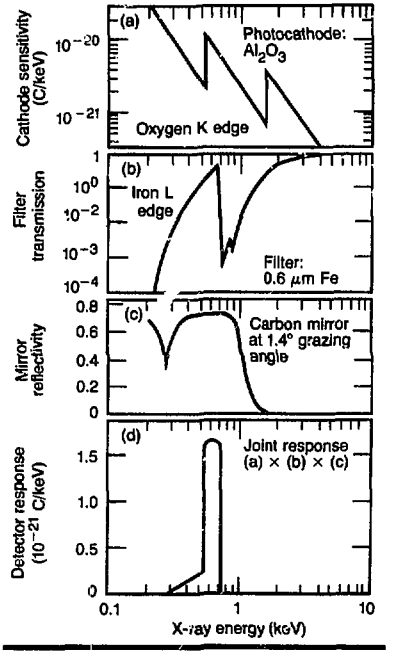

Fig. 5-16. A 532- to 708-eV bandpass windowless XRD utilizing an Fe filter and an Al_2O_3 photocathode.

The method described above is perhaps the simplest way of obtaining bandpass XRDs. The bandpass is not completely clean, however, because of the low-energy tail and the bump on the high-energy side. It is virtually impossible to reduce the low-energy tail without cutting into the flat top of the bandpass. The high-energy bump, on the other hand, is not difficult to cope with.

First, the high-energy bump can be removed fairly easily with x-ray mirrors; this procedure is very effective for low-energy (especially sub-keV) bandpass XRDs, as Fig. 5-16 illustrates for a 532- to 708-eV bandpass detector. The clean cutoff [Fig. 5-16(d)] is accomplished by placing a carbon mirror at a grazing angle to the incident x rays [Fig. 5-16(c)].

We can also remove the high-energy bump by means of an "off-line" subtraction. First, the bump is duplicated by proper choice of filter; this is illustrated by the dotted curve in Fig. 5-15. Simple subtraction using the solid-line and dotted-line responses then yields a clean cut-off on the high-energy side. The validity of the subtraction method depends, of course, on the shape of the x-ray spectrum. If the signal from the dotted-line response is comparable to that from the solid-line response, the method cannot be used.

When working in the sub-keV region, we must take special care of the detectors to ensure their stability, such as by handling them in a dry-nitrogen atmosphere outside the vacuum systems.[27] We must also give careful study to data points near the absorption edges.

For high-flux x-ray measurements, the bandpass XRDs have adequate sensitivities. For low-flux applications, however, it is desirable to increase the detector sensitivities, thus leading to the concept of x-ray-multiplier tubes (XMTs). An XMT is to a photomultiplier tube what an XRD is to a photodiode. Both XMT and the photomultiplier tube are, of course, electron-multipliers in nature; they do not multiply photons. An XMT is, thus, an electron-multiplier tube

whose cathode is sensitive to x rays. In Fig. 5-17, we show a possible configuration of the XMT. To preserve good quantum-yield jumps in the x-ray cathode response, it is vital that the electron dynodes are not exposed to x rays.

We have shown that well-defined bandpass XRDs of large dynamic range can be obtained by coupling the absorption-edge jumps of the filters and of the photocathodes. The bandpass response is very similar to that obtainable with the filter-fluorescer (FFLEX) technique.[30] The bandpass characteristics of the FFLEX scheme are generally better than those of our filter-photocathode scheme because the fluorescence-yield jumps are larger than the photocathode quantum-yield jumps at the absorption edges and because post-filters can be used to clean up the fluorescence lines. Our bandpass detectors, on the other hand, may have some advantages in certain applications. They are simple, fast, relatively sensitive to x rays (with electron multipliers), and less sensitive to neutrons. (The neutron background is an important concern in the controlled-fusion plasma environment.)

FFLEX is generally not very sensitive because of the low fluorescence yield for low-Z elements and because of the small solid angle subtended by the x-ray detector at the fluorescer. To improve sensitivity, the FFLEX scheme usually employs highly sensitive scintillators, such as NaI(Tl) or plastics, that are slow or relatively sensitive to neutrons remove the parenthesis.

Lindsey[31] attempted to construct a bandpass x-ray triode by utilizing the quantum-yield jumps of the cathode and the central electrode and by subtracting the electric currents instantaneously. This approach is disadvantageous because the quantum-yield jumps on both electrodes are small and fixed. Our bandpass detector, on the other hand, enjoys a degree of freedom in that the filter thickness can be varied to make the transmission jump at the absorption edge arbitrarily large; in Fig. 5-16(b), for example, the jump is $\sim 10^3$. In addition, the precision of the electrode thickness is critical in the triode scheme.

At present, the experimental data on the quantum-yield jump of photocathodes at the absorption edges are rather limited. A systematic study of the phenomenon as a function of element and cathode thickness should be quite useful. Optimized quantum-yield jumps can certainly improve the characteristics of our present bandpass XRDs. The bandpass characteristics of the filter-photocathode combination should also have useful applications with x-ray streak cameras.

Author: C. L. Wang

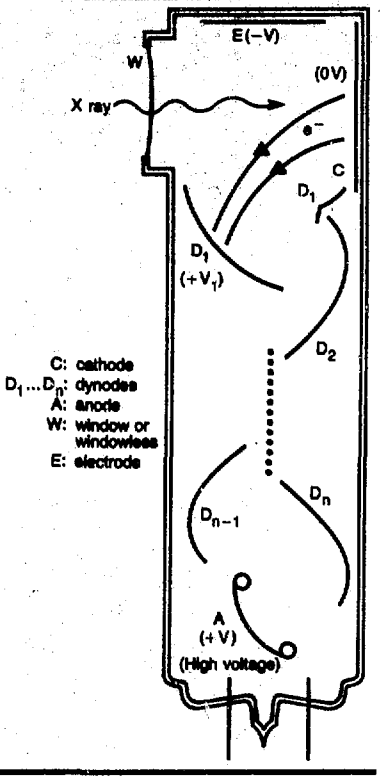

Fig. 5-17. A possible configuration of the x-ray multiplier tube (XMT).

Flat-Response Detector for X Rays from 400 to 1000 keV

In experiments involving the laser-plasma interaction, we routinely measure the

suprathermal x-ray spectrum up to 350 keV using a filter-fluorescer (FFLEX).[32] The continuum spectra can often be described as a two-temperature distribution comprised of a relatively cold Maxwellian main body and a hot Maxwellian tail. For some targets, however, we have consistently observed the existence of yet another component—a "superhot" tail.

It is not practical to construct FFLEX channels at energies greater than 350 keV because either hyper-FFLEX (which extends FFLEX to higher x-ray energies[33]) becomes too insensitive or the response of the simple filter-detector becomes too broad, giving a poorly defined peak. For our diagnostic purposes, it is sufficient to know the energy content of the superhot tail, rather than the spectral detail. We have, therefore, designed a flat-response detector for measuring x rays from 400 to 1000 keV. The detector signal is proportional to the incident x-ray energy and is independent of the spectral shape in the energy interval of interest.

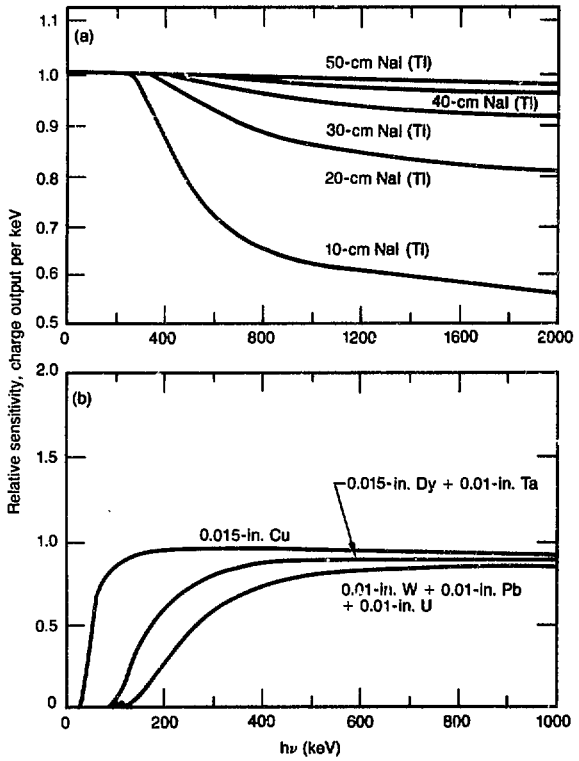

Fig. 5-18. Crystal characteristics. (a) Sensitivity of a NaI(Tl) crystal to x rays. (b) Response of a 30-cm NaI(Tl) crystal coupled to various filters used fro cutting off low-energy x rays.

Thick Calorimeter

There are two ways of making flat-response detectors. The well-known method is the total-absorption (thick) calorimeter; after a thick calorimeter absorbs all the energy of the incident radiation, the detector sensitivity per unit energy is naturally flat. Figure 5-18(a) illustrates this effect for a NaI(Tl) crystal; Fig. 5-18(b) shows the responses of a 30-cm-thick NaI(Tl) crystal coupled to various filters used for cutting off low-energy x rays. Such a large crystal is not a practical solution in our experimental environment, however, because of background consideration.

Thin Calorimeter

We have chosen the second method of obtaining a flat-detector response: balancing the response of a limited-absorption (thin) detector with proper filter transmission. Figure 5-19 shows the quasi-complementary nature of detector sensitivity and filter transmission, resulting in a slowly varying sensitivity near 1000 keV. By coupling a 2-mm-thick Pb and a 1-mm-thick U filter to a 3-mm-thick NaI(Tl) crystal, we obtain a flat detector response between 400 and 1000 keV, as shown in Fig. 5-20. Even though the thin detector absorbs only a small part of the incident energy, its output signal is still proportional to the total input energy; hence, the name "calorimeter." During 1981, we constructed one such thin calorimeter and operated it at Shiva.

The major deficiency of this flat-response high-energy x-ray detector is that the low-energy cut-off is not at all sharp. However, the x-ray energy content below 400 keV can be obtained by the spectral information supplied by FFLEX. Thus, we use the flat-response detector together with FFLEX to obtain the total energy content of the

superhot tail in the x-ray spectrum. An error analysis of this effect is in progress.

Author: C. L. Wang

Major Contributors: V. W. Slivinsky and K. G. Tirsell

Microchannel-Plate Photomultiplier Tube for Time-Resolved Suprathermal X-ray Measurement

In laser-fusion experiments, it is important to know exactly when the suprathermal x rays or electrons are produced during target irradiation, so that their effect on fuel preheat can be studied. Microchannel-plate photomultiplier tubes (MCP PMTs) are candidate detectors due to their fast impulse responses (0.3 to 0.5 ns FWHM) and to their sensitivity to both x rays and optical light. These combined characteristics offer us a convenient opportunity for performing absolutely calibrated, time-resolved suprathermal x-ray measurement of laser-produced plasmas.

Figure 5-21 illustrates our method of temporarily calibrating the instrument. Since the MCP PMT is not sensitive to the characteristic 1ω laser wavelength of Nd:glass (1.06 μm), we calibrate the instrument using 2ω (0.53 μm) light generated by a KDP frequency-doubling crystal. The 2ω light scattered from the target ball thus defines the zero time at the MCP PMT. The laser pulse derived from the incident-beam diagnostics serves as a reference time, or fiducial, relative to the above-defined zero time. We can now measure the production time of suprathermal x rays using the setup shown in Fig. 5-22; this arrangement is similar to the setup previously used by Kornblum[34] for measuring the relative production time of suprathermal x rays from various targets.

In addition to developing the absolute temporal measurement of suprathermal

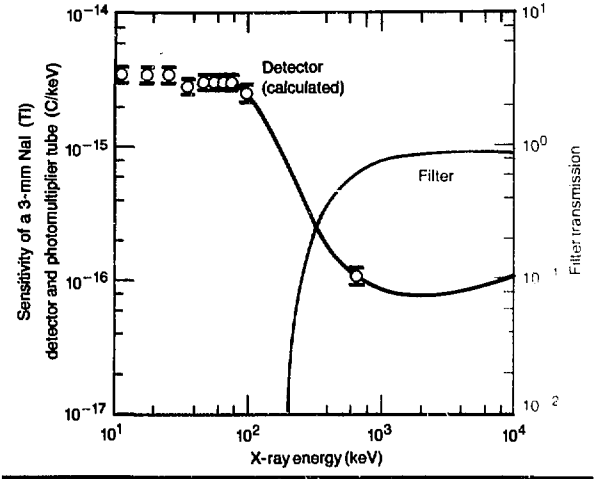

Fig. 5-19. Complementary nature of detector sensitivity and filter transmission near 1000 keV.

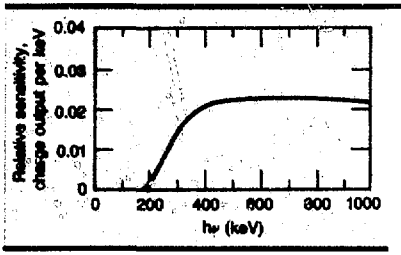

◀ Fig. 5-20. Response of a thin calorimeter for 400- to 1000-keV x rays, using a 3-mm NaI(Tl) crystal coupled to a 2-mm Pb and a 1-mm U filter.

x rays, we made significant progress during 1981 in understanding the MCP PMT response to x rays above 100 keV. Without this knowledge, the energies of the detected x rays can be misinterpreted. For example, the 40- to 70-keV channel[34] of the old *FFLEX* has been corrected to 50 to 210 keV for the x-ray spectrum of a 35-keV suprathermal temperature.

The sensitivity of the two-stage (ITT F4128) MCP PMT used in this experiment is given in Fig. 5-23. Note the absorption edge of Pb, which is a major component of the MCP glass tubes. Above 100 keV, the sensitivity remains high. The response of the new 20- to 70-keV channel is shown in Fig. 5-24 for a 35-keV reference spectrum. The filters are 13-μm Fe and 8-μm Ti (used in front for the filter-fluorescer experiment); the vacuum window is 0.4-μm Al.

Figure 5-25 shows experimental results obtained in a gold-disk experiment with a 2ω fiducial. X rays from 20 to 70 keV were produced early in the laser irradiation of the

Microchannel-Plate Photomultiplier Tube for Time-Resolved Suprathermal X-ray Measurement

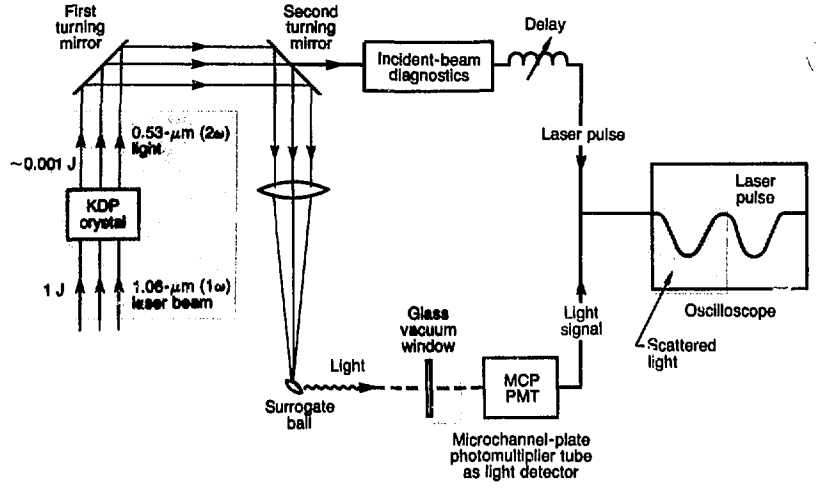

Fig. 5-21. The method of obtaining zero time for calibration of the MCP PMT.

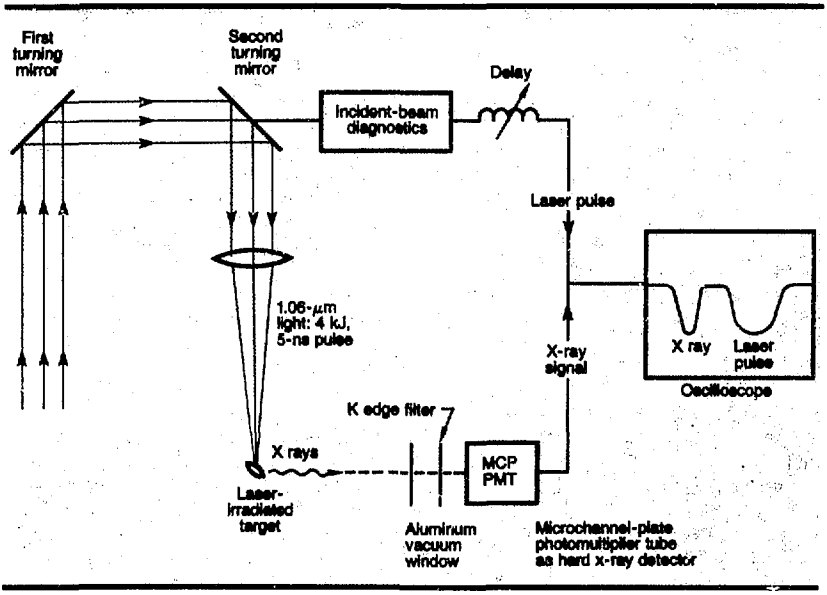

Fig. 5-22. Arrangement for measuring the production time of suprathermal x rays.

target. The zero time is taken here as 10% of the amplitude of the x-ray pulse and of the scattered light pulse. It is interesting to note that the x rays peaked out at 1.3 ns, even though the 1ω pulse length was nominally 5 ns. We were not able to compare this result with optical/x-ray streak camera (OX-1) data because OX-1 is not sensitive enough for the disk targets.

The MCP PMT has proven to be a very versatile detector for the time-resolved measurement of suprathermal x rays. Its simplicity, high sensitivity, and adequate time resolution should be very useful for upcoming 5-ns experiments on Nova.

Authors: C. L. Wang and G. R. Leipelt

Major Contributors: O. C. Barr, D. E. Campbell, H. N. Kornblum, V. W. Slivinsky, C. E. Thompson, and J. D. Viedwald

X-ray Transmission Gratings for Spatially or Temporally Resolved X-ray Spectra from Laser-Fusion Targets

Introduction

We have fabricated x-ray transmission gratings and are using them for the spectroscopy of high-temperature laser-produced plasmas.[35,36] We have coupled a gold transmission grating to a soft x-ray streak camera (SXRSC), producing the first temporally resolved, continuous x-ray spectrum from 0.1 to 1.5 keV from a laser-produced plasma. The time resolution of this grating/streak-camera combination is 20 ps. In addition, we have coupled a transmission grating to a high-resolution Wolter x-ray microscope to produce an imaging spectrometer of unprecedented spatial resolution and spectral range. In laboratory experiments, this imaging spectrometer demonstrated a spectral resolving power, $\lambda/\Delta\lambda$, of 200 and a spatial resolution of 1 μm over a spectral range extending out to ~3.2 keV.

Figure 5-26 shows a simple x-ray transmission-grating spectrometer viewing a small laboratory source. The principal components of the spectrometer are

- The aperture, which could be a focusing optic, a coded aperture, or the simple slit shown in Fig. 5-26.
- The gold transmission grating, which is 0.6 μm thick and has a 0.3-μm spatial period.
- The detector, which could be film or an active readout system, such as a charge-coupled device (CCD) array or an x-ray streak camera.

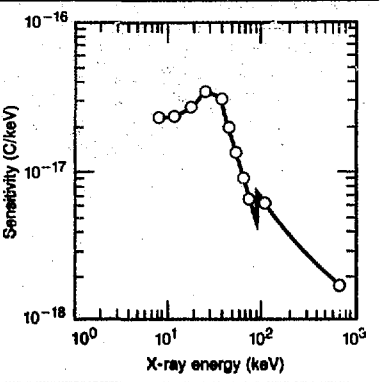

Fig. 5-23. X-ray sensitivity of the MCP PMT.

Fig. 5-24. Response of a 20- to 70-keV filtered MCP PMT channel for a temperature spectrum of 35-keV suprathermal x rays.

Fig. 5-25. Absolutely calibrated production time of suprathermal x rays, from 20 to 70 keV, from a gold-disk target.

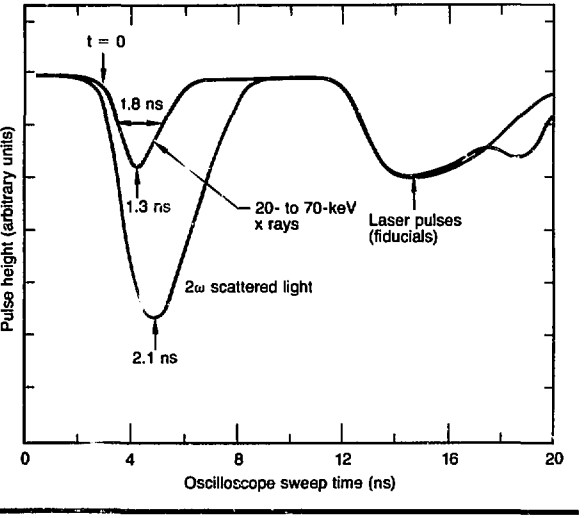

Fabrication of x-ray transmission gratings is a multistep process involving holographic lithography at UV wavelengths, ion beam etching, x-ray lithography, and gold electroplating on a submicrometre scale. Detailed descriptions of these transmission-grating fabrication procedures are provided elsewhere.[37]

Theory

An x-ray transmission grating is a linear, periodic array of alternately transparent and opaque lines with a submicrometre spatial period. In practice, an x-ray transmission grating is a linear grid of wires or bars of high-Z material (usually gold) supported either by a thin polymer membrane or a coarse grid orthogonal to the grating lines. Scanning-electron micrographs of a gold transmission grating supported by a thin (0.5 μm) polyimide membrane are shown in Fig. 5-27; the grating period for these transmission gratings is 0.3 μm. Figure 5-27(b) gives an edge-on view of a grating that has been fractured to illustrate its high aspect ratio. The gold grating lines shown are 0.15 μm wide and 0.65 μm high.

Owing to its simple geometry, the transmission grating is an extremely versatile dispersion element, accepting radiation at all angles of incidence. As a result, an x-ray transmission grating

- Requires no detailed angular alignment in its operation.
- Is easily coupled to instruments of high spatial and temporal resolution.
- Is capable of a large collection solid angle.
- Can cover a broad spectral range.

There is an important difference between the dispersive properties of transmission gratings and reflective dispersion elements such as multilayer mirrors[38] or natural crystals. All these structures satisfy similar Bragg conditions relating wavelength, period, and angle of diffraction, as follows

$$\text{Gratings: } \sin\theta = \frac{m\lambda}{d} \qquad (1)$$

$$\text{Crystals or multilayers: } \sin\theta = \frac{m\lambda}{2d} \ ,$$

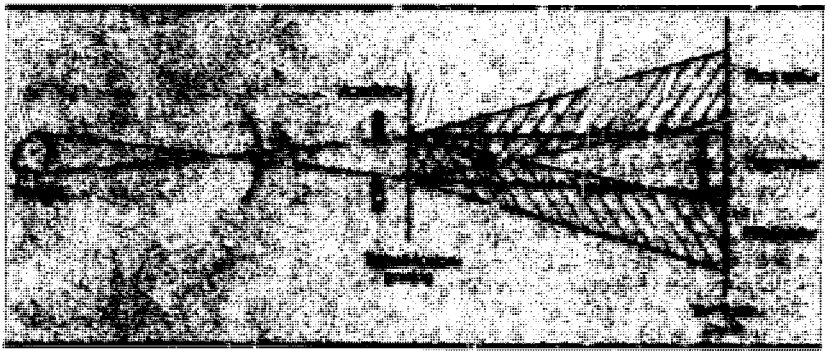

Fig. 5-26. Design of a simple spectrometer employing an x-ray transmission grating.

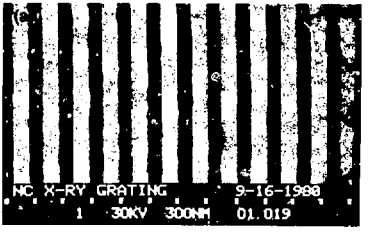

0.3 μm

0.65 μm

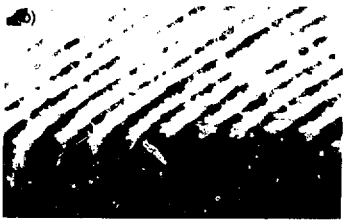

Electroplated gold grating: 0.3 μm period, 0.65 μm thick

Fig. 5-27. Scanning-electron micrographs of an x-ray transmission grating supported on a polyimide membrane. (a) Top view. (b) Side view.

where λ is the x-ray wavelength, m is the diffraction order, d is the period of the dispersive element, and θ is the diffraction angle measured relative to the incident beam for transmission gratings and relative to the reflecting surface for crystals or multilayer mirrors.

In addition to the Bragg condition, reflective components require the incident x rays to satisfy a reflection condition equating the angles of incidence and reflection. Figure 5-28 illustrates the different dispersive properties of transmission and reflective elements in two extreme cases: an incident cone (converging or diverging beam) of monochromatic x rays; and an incident beam of collimated, polychromatic x rays. In each case, the transmission grating disperses the entire incident spectrum, whereas the reflective element selects only a narrow band of x rays satisfying both the Bragg and reflection conditions. (Imperfections in the periodic structure of the reflector allow for a finite "rocking curve" and, thus, for a finite spectral band that satisfies both conditions.[39])

The dispersive simplicity of transmission gratings accounts for their strengths as well as their limitations in spectroscopic applications. A particular limitation is the dependence of the spectral resolution of transmission-grating instruments on incident-beam collimation. The fundamental limit to grating resolution is due to diffraction at the grating aperture; thus, $\Delta\lambda = \lambda/N$, where N is the number of grating periods participating in the diffraction. The practical limit to spectral resolution in laboratory x-ray applications is the finite size and collimation of laboratory sources. In such cases, the limit to spectral resolution may be written as the product of the spectral dispersion, $d\lambda/dy$, and the "blur" spot size, Δy, at the detector plane, such that

$$\Delta\lambda = \frac{d}{D}\Delta y \quad , \tag{2}$$

where d is the grating period, D is the grating-to-detector distance, and Δy is the size of the shadow cast by the source through the aperture onto the detector (in the absence of the grating).

Another issue of practical importance in the use of x-ray transmission gratings is the spectral dependence of grating diffraction efficiency. This is important not only for optimization of instrument efficiency but also for the interpretation and unfolding of recorded x-ray spectra. In those spectral

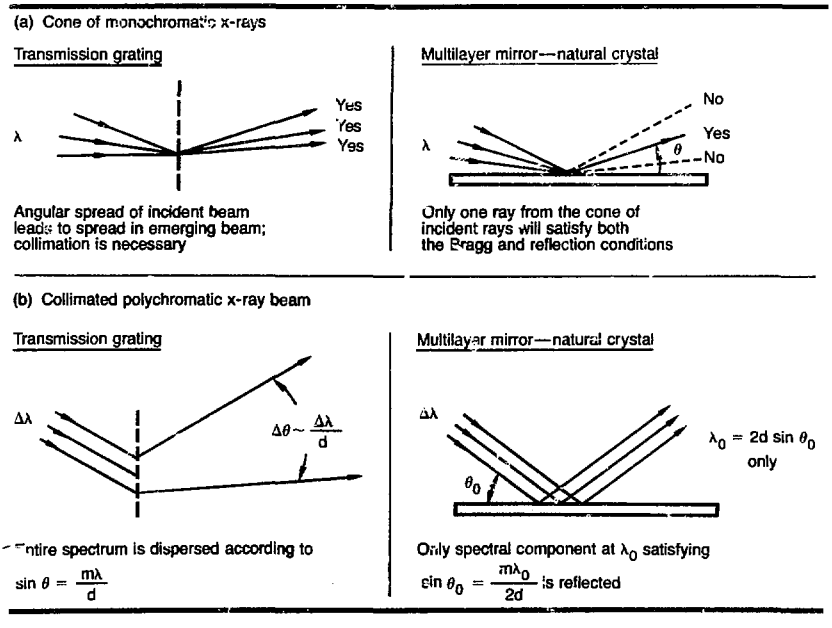

Fig. 5-28. Comparative illustrations of dispersive properties of x-ray transmission gratings vs reflective dispersion elements.

regions where there is finite x-ray transmission and appreciable phase shift through the gold grating lines, grating diffraction efficiency can be strongly dependent on grating thickness, t, and line/space ratio, γ. The relative mth-order diffraction efficiency is then

$$\frac{\eta_m}{\eta_0} = \left[\frac{\gamma + 1}{m\pi} \sin\left(\frac{m\pi}{\gamma + 1}\right)\right]^2 \times \left(\frac{1 + b^2 - 2b\cos\Phi}{1 + \gamma^2 b^2 + 2b\gamma\cos\Phi}\right), \quad (3)$$

where $b(t,\epsilon)$ is the fractional amplitude transmission through the gold grating lines, $\Phi(t,\epsilon)$ is the phase shift through the gold, and ϵ is the x-ray energy.

Spectroscopic Measurements

We coupled a freestanding x-ray transmission grating to an SXRSC, successfully recording the first time-resolved continuous x-ray spectrum from 0.1 to 1.5 keV from a laser-produced plasma. A schematic representation of the experimental arrangement is shown in Fig. 5-29, along with the data record from a gold-disk target. This data record covers a spectral range from 8 to 120 Å with 20-ps temporal resolution. In these time-resolved experiments, the spectral resolution was collimation-limited to $\Delta\lambda \sim 1$ to 2 Å, allowing the observation of subkilovolt spectral detail hitherto unavailable in a time-resolved mode.

The ease with which x-ray transmission gratings can be coupled to high-resolution streaking (or spatially imaging) cameras leads to instruments of powerful spectroscopic capabilities. This point is illustrated by the SXRSC data in Fig. 5-29. The total information-recording capability (i.e., the number of distinct resolution elements) of the two-dimensional data record in the figure may be estimated by dividing the duration of the x-ray emission (~2.5 ns) by the temporal resolution (~20 ps) and multiplying that quantity by the quotient of the full spectral range (~120 Å) with the spectral resolution ($\Delta\lambda \sim 2$ Å). The result of this calculation—approximately 8×10^3 resolution elements in the data record—represents an information capacity one to two orders of magnitude greater than any competing time-resolved spectrometer.

We have also coupled an x-ray transmission grating to a 22× Wolter grazing-incidence x-ray microscope to produce a high-resolution imaging spectrometer for laboratory x-ray sources.[40] This instrument is similar in concept to imaging spectrometers used in x-ray astronomy,[41] but it has superior spatial and spectral

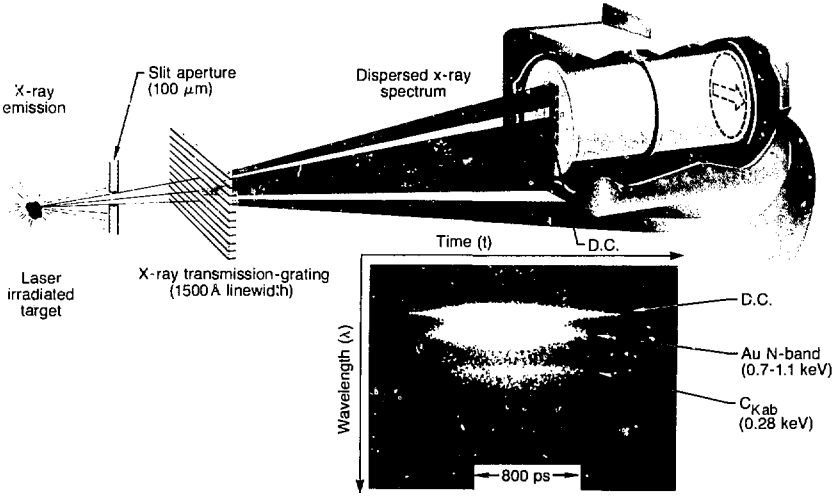

Fig. 5-29. Schematic of a time-resolved x-ray transmission-grating spectrometer, and a sample data record.

resolution (due to higher-quality mirror surfaces) and greater spectral range (due to thicker gold gratings).

Figure 5-30 illustrates the experimental setup for testing the spatial and spectral resolution of the imaging spectrometer. We backlit a test-pattern mask with M_α (1.75 keV), M_β (1.835 keV), and M_γ (2.035 keV) line emission from a tungsten anode. The transmitted x-ray pattern was imaged by the microscope and dispersed by the grating. The resulting spatially resolved x-ray spectra are shown in Fig. 5-31.

In the test setup we used, the x-ray grating intercepted only a 20° segment of the annular ring of reflected x rays emerging from the rear of the microscope. The remaining 340° segment of the annular ring was blocked. As is well-known, surface scattering effects from a microscope mirror segment are anisotropic.[42] Significantly greater image-blurring occurs in the plane of incidence than normal to it. As a result, the spectral- and spatial-resolution characteristics of the spectrometer vary, depending on the relative orientation of the grating lines and on the plane of incidence at the mirror surfaces.

This dependence is illustrated in Fig. 5-31, which shows spatially resolved spectra from three different grating orientations. The best spatial resolution (nominally 1 μm) was achieved with the grating lines normal to the plane of incidence. Under that condition, a "point" x-ray source (~0.5 μm in diameter) was imaged as a line roughly 1 μm × 10 μm FWHM. The best spectral resolution was achieved with the grating lines parallel to the plane of incidence. Under that condition, we measured a spectral resolution of $\Delta\lambda \sim 0.03$ Å, limited strictly by source size. The resulting spectral resolving power, $\lambda/\Delta\lambda \sim 200$, is the highest ever achieved with this type of instrument.

Spectral Unfolding

The "spectra" reported in the previous section are raw data, for which no account has been made of the spectral response of the detectors, the spectral variation of the grating diffraction efficiency, or contributions from multiple diffraction orders. The presented spectra are, in this sense, merely the measured response distribution, $R(y)$,

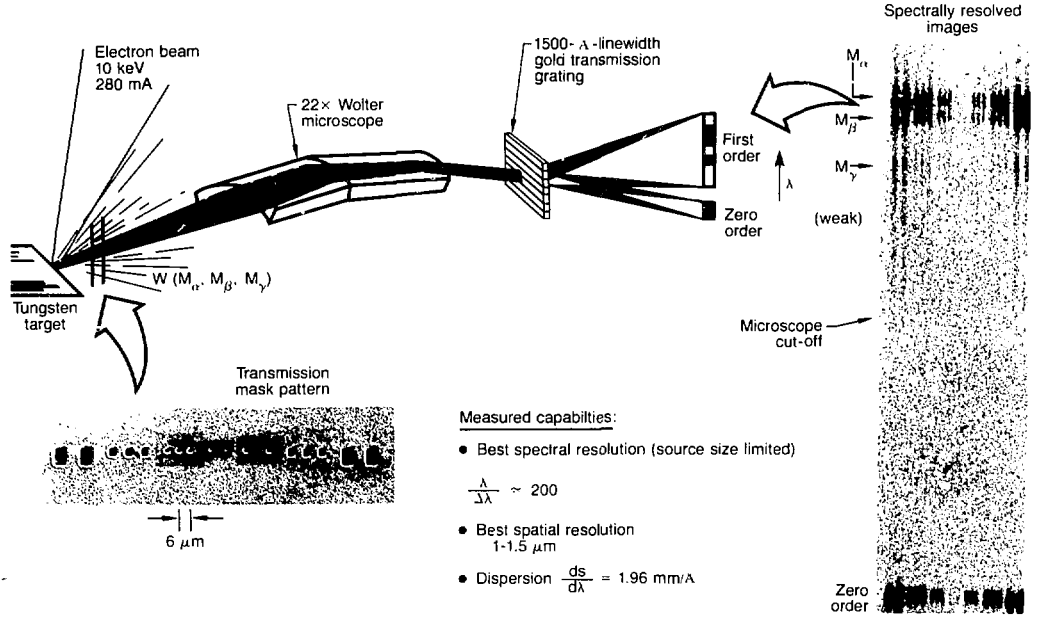

Fig. 5-30. Schematic of a high-resolution imaging spectrometer.

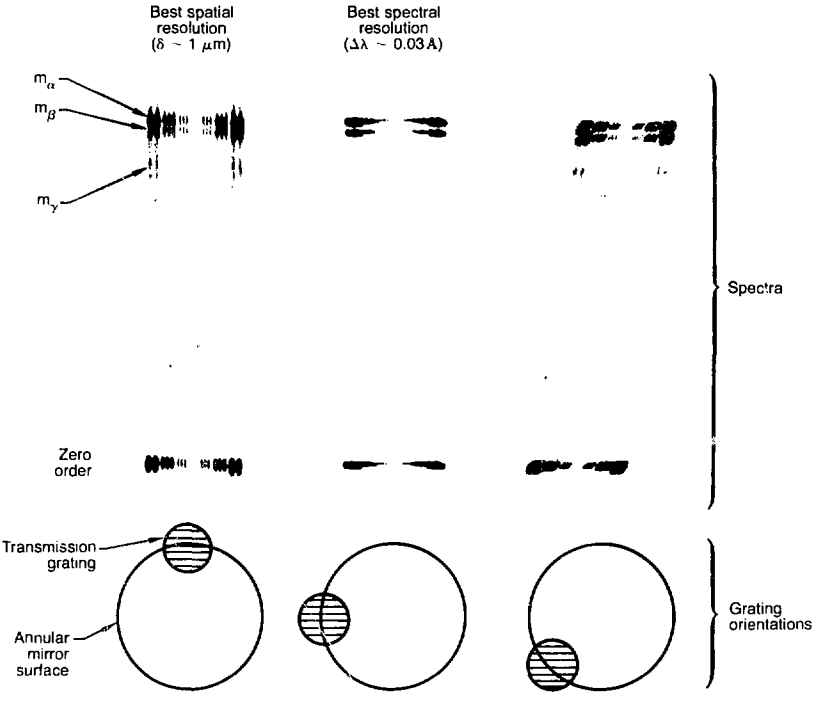

Fig. 5-31. Spatially resolved x-ray spectra recorded at three different relative orientations between grating lines and x-ray plane of incidence.

displayed along the length of the detector. From these distributions, it is necessary to extract the spectral distribution, $S(\epsilon)$, of the laboratory source. The response distribution and source spectrum are related by

$$R(Y_0) = \frac{\Delta\lambda}{\lambda_0 r^2} \sum_{\substack{\text{orders} \\ m=1}} \times S(m\epsilon_0)\,\eta_m(m\epsilon_0)\,\alpha(m\epsilon_0) \quad , \qquad (4)$$

where the sum is over the various diffractive orders, $Y_0 = D/d \cdot \lambda_0$. In Eq. (4), r is the source-detector distance, $\Delta\lambda$ is the spectrometer resolution, $\eta_m(m\epsilon_0)$ is the mth-order diffraction efficiency for x rays at energy $m\epsilon_0$, $\alpha(m\epsilon_0)$ is the detector response for x rays at energy $m\epsilon_0$, and $\epsilon_0 = hc/\lambda_0$. Now, $S(\epsilon)$ can be unfolded from Eq. (4) by an iterative procedure when $R(Y_0)$, $\eta_m(\epsilon)$, and $\alpha(\epsilon)$ are known. Such unfoldings are presently under way for gold and titanium target shots performed at Argus during 1981.

Summary

We have fabricated freestanding x-ray transmission gratings with a 0.3-μm spatial period, and we are now well under way to using these gratings for spectroscopic investigation of laboratory x-ray sources. We have coupled x-ray transmission gratings to a grazing-incidence x-ray microscope to provide spatially resolved spectra and to a soft x-ray streak camera to provide time-resolved spectra from laser-produced plasmas.

Additional work remains to fully characterize the transmission-grating spectrometer, including experimental determinations of the grating efficiency, $\eta(\epsilon)$, the detector response, $\alpha(\epsilon)$, and the successful unfolding of the source spectrum, $S(\epsilon)$, from the recorded "spectrum," $R(y)$.

Author: N. M. Ceglio

Major Contributors: A. M. Hawryluk, R. L. Kauffman, R. H. Price, and H. Medecki

Progress on X-ray Microscope Development

Our streaked x-ray microscope was first fielded in 1980; since that time, we have continued to improve its capabilities. Areas in which we desire further improvement include overall spatial resolution, intensity calibration, sweep-speed calibration, accurate orientation of the film and input slit relative to the sweep axis, higher-energy imaging, definition of the x-ray bandpass, increased signal level, and improved signal-to-noise ratio. During 1981, we applied varying degrees of effort to each of these areas.

One of our major accomplishments was the completion and characterization of the new mirror for our Wolter axisymmetric x-ray microscope (ASXRMS). This mirror (described below) has much better surface quality than previous mirrors, resulting in better resolution (1 μm vs 2 to 3 μm), improved thoroughput (increased by a factor of 10 to 20), and a higher-energy cutoff for the reflectivity (3 vs 2 keV). We are not yet able to take advantage of the improved resolution of the ASXRMS due to the limited spatial resolution of the soft x-ray streak camera (SXRSC). The 150-μm resolution of the SXRSC, together with the 22× magnification of the ASXRMS, yields a 7-μm resolution at the target. In the future, we hope to improve or replace the SXRSC and, thus, improve the overall resolution.

Intensity calibration of the x-ray microscope is presently accomplished, on a given shot, through the comparison of data from the streaked microscope with data from the calibrated x-ray diodes in the Dante x-ray spectrometer. This comparison method yields factor-of-2 accuracy, which could be improved considerably through laboratory measurements.

Sweep-speed calibration is now carried out using laser-pulse trains whose temporal spacing we know with good accuracy. The calibration, in this case, can be improved simply through more accurate analysis of the data. It may also be possible to use a microwave-modulated electron source to produce accurate temporal calibrations.

For the precise velocity measurements required for equation-of-state and hydrodynamic-efficiency measurements, the streak-camera sweep axis and slit orientation must be accurately aligned and referenced. Depending on the sweep speed, a 1% error in sweep-axis alignment can result in a 5% error in measured velocity. Misalignment of the streak-camera slit can cause a significant loss in temporal resolution integrated over the slit length. We plan to establish the sweep axis accurately relative to fiducials that will mark the axis on the film for reference during digitization. The streak-camera slit will also be carefully oriented to the streak-camera tube and fixed by pins or a mechanical reference surface.

The new ASXRMS forms the first step in our pursuit of higher-energy imaging, raising the energy cutoff for x-ray reflectivity from 2 to 3 keV. The next step will be the use of a Kirkpatrick–Baez (KB) x-ray microscope with multilayer (Barbee) x-ray reflecting coatings. As was described in the *1980 Laser Program Annual Report*,[43] this new KB x-ray microscope was designed to fit into the streaked x-ray microscope interchangeably with the ASXRMS. At first, we will use the KB instrument, which uses multilayer-coated, 2° grazing-incidence mirrors to record images backlit by x rays from ionized titanium lines at 4.73 keV. With different coatings, the KB/Barbee system can eventually be used at energies up to 10 keV. The multilayer coatings on the Barbee mirrors have the additional advantage of having a narrow energy bandpass ($E/\Delta E \gtrsim 20$), thus requiring very little additional filtering.

The signal level in the streaked-microscope system has been improved by a factor of 20 by the new ASXRMS mirror. In the apertured mode, in which a sector (1/20) of the mirror is used to increase the depth of field, the new ASXRMS mirror has a solid angle of $\sim 6.5 \times 10^{-6}$ sr for $h\nu <$ 2 keV. This value includes reflectivity, but no filtering; filtering reduces the solid angle by a factor of about 3, to 2.2×10^{-6} sr. Between 2 and 3 keV, the reflectivity drops rapidly, so, when filtered for 3-keV operation, the ASXRMS mirror has an effective solid angle of 4.5×10^{-7} sr.

The KB/Barbee microscope will have an effective solid angle of 5.5×10^{-7} sr at 4.73 keV. Because of its narrow bandpass, it

will require effectively no filtering, other than a heavy beryllium blast shield with 90% transmission at 4.73 keV. The effective solid angle for this type of microscope may increase by a factor of 2 to 4 at the higher x-ray energies (~10 keV). The increased effective solid angle is due to improved coating reflectivity at higher energies, which, in turn, results from decreased absorption in the coating material.

The effective solid angles of the ASXRMS and the KB/Barbee microscope may be compared with the effective solid angle of 2.8×10^{-7} sr for a conventional unfiltered KB microscope at 4.73 keV. With minimal filtering, this solid angle would be reduced to less than 1×10^{-6} sr. The conventional KB microscope also has a substantially smaller field of view ($\pm 80\ \mu m$) than the KB/Barbee microscope ($\pm 200\ \mu m$).

Quantum Noise Considerations

In our present SXRSC system, quantum noise considerations are of the utmost importance. Note that we are speaking here of the SXRSC and of the image-intensifier voltages and gains as they have been used in the streaked x-ray microscope since mid-1980; the discussion that follows would vary depending on these voltages and gains.

As it is now used, the streak camera detects single photoelectrons produced by the absorption of x-ray photons at the gold photocathode, which has a quantum efficiency of ~5% at 3 keV. The signal levels in many backlighting experiments are measured to be 50 to 100 detected x-ray photons per picture element (pixel), but fluctuations are higher than the anticipated shot noise. A photoelectron from the x-ray photocathode is accelerated to an energy of ~17 keV; it strikes the output phosphor (P-11) screen of the streak camera, producing an average of about 400 visible-light photons. These photons pass through two fiber-optic faceplates (with a combined transmission of 60 to 70%) and onto the S-20 photocathode of a microchannel-plate (MCP) intensifier. The S-20 photocathode has a quantum efficiency of ~15%, yielding ~40 photoelectrons.

The low number of quanta at this point forms a statistical bottleneck, yielding significant noise variation in the output from the original x-ray photon detected at the x-ray photocathode. The 40 photoelectrons spread out from the intensifier photocathode into a region on the MCP face that is ~50 to 70 μm in diameter, containing ~10 to 20 microchannels. Each channel then multiplies the incident photoelectron(s) that enter it by a factor of approximately 500. Statistics enter strongly at this point as well, due both to statistical fluctuations in the gain of a given channel and to variations in the average gain from channel to channel. The channel-to-channel gain variation results from slight material and processing variations and from small differences in channel length and diameter.

The 40 photoelectrons entering the MCP result in $\sim 2 \times 10^4$ electrons at its output. These electrons emerge from the MCP and are accelerated to 5 keV before striking a P-20 phosphor screen in a region ~70 to 150 μm in diameter. The MCP intensifier has a net luminous gain of 10^3, so $\sim 4 \times 10^6$ visible photons are transmitted through the final fiber-optic faceplate to the film. Thus, a single photoelectron from the x-ray photocathode of the streak camera is recorded on the streak-camera film as a spot ~100 μm in diameter having a specular film density of ~1 above the fog level. (This number is, of course, dependent on the MCP gain.)

Threshold sensitivity of the streak camera is typically taken to be the signal level at which the signal-to-noise ratio = 1, i.e., where there is one photon recorded per pixel at the film plane of the streak camera. The pixel in this case is an area ~150 μm on a side, or ~18 ps by ~150 μm at a sweep speed of 120 ps/mm. During a recent experiment (described below), we used 3-keV x rays to backlight a carbon-foil target that was ablatively accelerated by 10 beams of the Shiva laser. In that experiment, the measured maximum signal level was ~40 x-ray photons recorded per pixel. This implies an intensity uncertainty of 15% even in the brightest parts of the image, ignoring the statistics of the gain of the streak camera and image-intensifier. In the less-bright regions of the image, statistical variations in intensity are considerably worse.

We are systematically studying the relation between resolution, signal level, signal-to-noise ratio, and other parameters of our

imaging systems. By doing this, we hope to identify areas of maximum leverage and, thus, improve the quality of the images.

ASXRMS Characterization

During 1981, we completed characterization of the 22× Mod II Wolter axisymmetric x-ray microscope. This instrument was jointly fabricated by LLNL, Visidyne, Inc., and Random Devices, Inc. Characterization was divided into three parts

- Metrology of the mirror.
- Measurement of the point-spread function.
- Measurement of the x-ray transmission of the mirror.

A detailed metrology report[44] was provided by Visidyne in April. The report is based on measurements carried out on the axisymmetric mirror using the slope scanner, provided by Random Devices, shown schematically in Fig. 5-32. The scanner works on the principle of the optical lever. A carefully prepared He-Ne laser beam, entering the system through a series of apertures and lenses (at the right edge of the figure), is focused to a 50-μm-diam spot on the surface of the Wolter x-ray-microscope mirror. As the beam scans along the mirror surface, the reflected beam is deflected by variations in the slope of the surface. Deflections of the reflected beam are detected by a pair of pin diodes arranged as a differential beam-position sensor. Thus, the reflected beam is a lever magnifying the tiny slope deviations on the surface. Integration of the signal converts the slope measurements to surface displacements. Absolute measurements are obtained through calibration using a small tilted glass window of known thickness to displace the reflected laser beam by a known amount. The

Fig. 5-32. Schematic of the optical slope scanner used to measure the surface profile of the Wolter x-ray mirror.

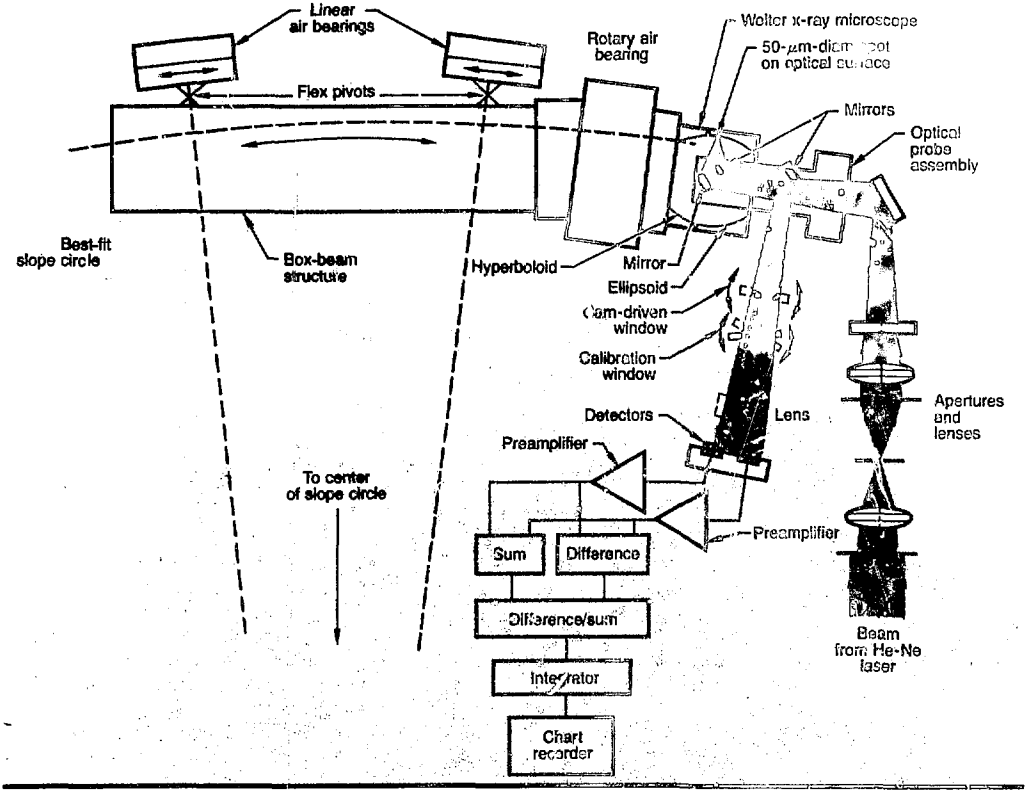

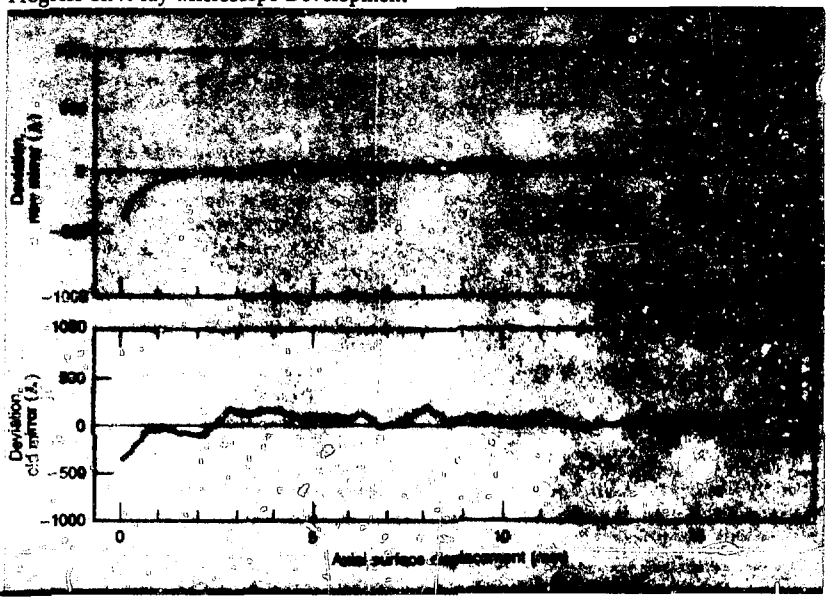

Fig. 5-33. The deviation of the new Wolter mirror from the desired profile is much less than for the older mirror.

Fig. 5-34. The slope-error distribution of the new Wolter mirror, 0.65 to 0.82 arc-seconds, is a great improvement over the old mirror (13.2 to 16.0 arc-seconds).

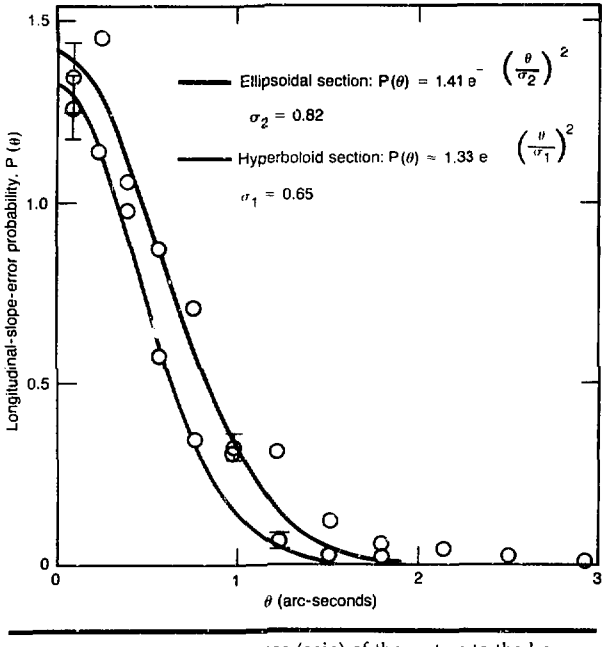

response (gain) of the system to the known beam displacement, together with the known length of the lever arm, yields the sensitivity of the scanner to slope errors on the surface.

The x-ray mirror to be measured is scanned past the laser probe on a carriage supported in the horizontal plane by very accurate linear air bearings. Other linear air bearings, attached to the carriage through flex pivots, cause the mirror to move in an arc having a radius of curvature equal to that specified for the sagittal profile of the x-ray microscope. Azimuthal scans of the mirror surface were obtained by holding the carriage stationary and rotating the x-ray microscope by means of a rotary air bearing mounted between the microscope and the carriage. This allows us to measure the microscope's deviation from cylindrical symmetry.

Measurements of the mirror surface made with the Random Devices slope scanner are repeatable to within ±20 to 30 Å, with rms deviations of 10 to 15 Å. The slope scanner has been verified to agree with the Clevite profilometer to within ±70 Å when averaged over the 50-μm dimension of the slope-scanner probe beam. The main advantage of the slope scanner is, however, that it is a noncontact instrument and can be used without dismounting the mirror from its rotary air bearing and carriage. The rotary air bearing and carriage are also used to move the mirror during the lapping process. The lapping tool is easily interchangeable with the scanner probe, thus giving the

lapping operator rapid feedback about mirror-polishing progress. This has not been possible in the past with other polishing and measuring devices.

The output of the slope scanner is a graph showing the deviation of the surface from the desired profile; with the curvature of the mirror removed from these plots, a perfect surface would appear as a straight line. Figure 5-33 shows an axial scan of the surface of the new LLNL/Visidyne/Random Devices mirror, along with a similar scan from an older mirror fabricated at LLNL.[45,46] The new mirror clearly has a much smoother figure than the old mirror.

Groups of 10 axial scans were taken at 90° intervals around the circumference of the mirror on both the hyperboloid and ellipsoid sections, for a total of 80 scans. The 6 scans that showed the least drift from each group of 10 were then digitized for further processing. Measured profiles were consistently within ±50 Å of the desired profile, with less than a 30-Å rms deviation. The digitized data from the eight groups of scans (four each for both the hyperboloid and ellipsoid sections) were independently reduced to yield slope-error distributions, which could then be used to calculate the response function of the x-ray optic. The longitudinal (axial) slope-error distributions (shown in Fig. 5-34) have standard deviations of 0.65 arc-seconds for the hyperboloid section and 0.82 arc-seconds for the ellipsoid section. The distributions are principally Gaussian—indicating random, incoherent slope errors—but have some small peaks due to periodic structures on the surface.

We also made azimuthal scans of the surface to determine the degree of cylindrical symmetry of the mirror. Scans were made at the large end, at the center, and at the small end of each of the hyperboloid and ellipsoid sections of the mirror. Figure 5-35 shows a representative azimuthal scan from the center of the hyperboloid section. The large-scale waviness of the curve (peak-to-peak amplitude of 0.2 μm) is largely due to a slight decentering of the mirror on the air bearing during measurement. The decentering error in the measurement is removed by the computer before extracting further data from the curve. The residual wavy structure on the surface is a remnant of the diamond-turning process by which

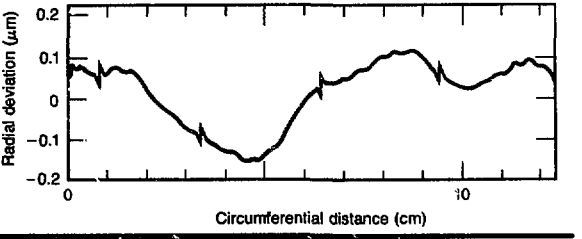

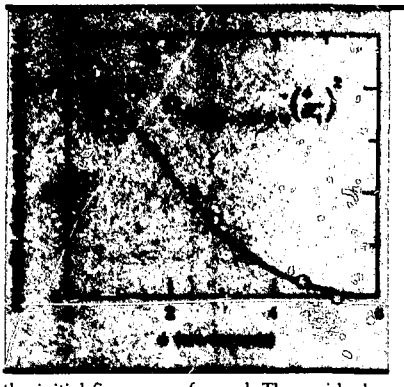

Fig. 5-35. A representative scan from the center of the hyperboloid, showing the deviation from roundness of the x-ray mirror. Large-amplitude waviness is due to decentering of the part during measurement.

◀ Fig. 5-36. The slope-error distribution of the x-ray mirror (standard deviation of 2.8 arc-seconds), showing peaks at 0.75 and 1.7 arc-seconds due to periodic structure.

the initial figure was formed. The residual structure was reduced but not eliminated by polishing.

Analysis of the azimuthal scan data indicates the presence of both random and periodic slope errors. Figure 5-36 shows the distribution of the azimuthal slope error from the center scans of the hyperboloid, together with a best-fit Gaussian with the same normalization. Correlation peaks are obvious in the data at 0.75 and 1.7 arc-seconds. The peak at 1.7 arc-seconds in Fig. 5-36 corresponds to the ripples in Fig. 5-35, having a period of 4 to 5 mm. The overall distribution has a standard deviation of 2.8 arc-seconds.

If the slope errors on the mirror surfaces are nearly random in nature, the response function can be calculated in a simple analytical way.[47,48] The object-plane equivalent-radial-energy distribution is approximately given by

$$P(r)rdr = \frac{4rdr}{\sigma_T \alpha_T \pi d_0^2 \tan\theta_g} \times \frac{\frac{\pi}{2} e^{-\left(\frac{r}{d_0 \sigma_T}\right)^2}}{\sqrt{1+\pi a^2}} f(a) \quad , \qquad (5)$$

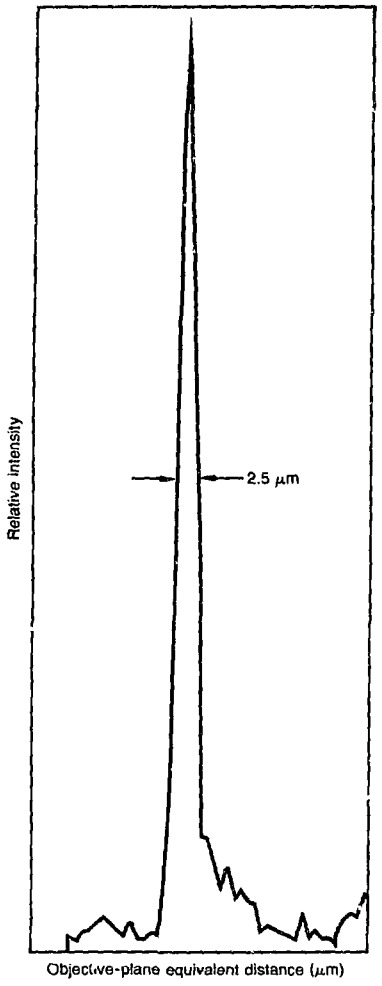

Fig. 5-37. The image of a 2-μm pinhole has a FWHM of 2.5 μm, indicating a response function of 1.0 to 1.5 μm FWHM.

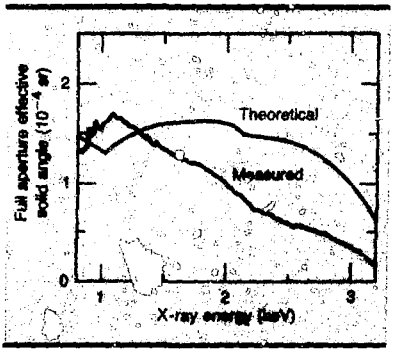

Fig. 5-38. Comparison of measured and theoretical transmission of the new Wolter mirror as a function of energy.

where

$$f(a) = 1 + \frac{a^2}{1 + 0.58a^2 + 1.63a^4} \quad , \qquad (6)$$

$$a = \frac{r}{\alpha_T d_0 \tan \theta_g} \quad , \qquad (7)$$

$$\sigma_T = 2\sqrt{\sigma_1^2 + \sigma_2^2} \quad . \qquad (8)$$

and

$$\alpha_T = 2\sqrt{\alpha_1^2 + \alpha_2^2} \quad . \qquad (9)$$

In these equations, d_0 is the object distance r is the radial distance from the center of the distribution; θ_g is the grazing angle; σ_T is the standard deviation of the longitudinal total-deflection distribution; α_T is the standard deviation of the azimuthal total-deflection distribution; σ_1 and σ_2 are the standard deviations of the hyperboloid and ellipsoid longitudinal-slope-error distributions, respectively (Fig. 5-34); and α_1 and α_2 are the standard deviations of the hyperboloid (Fig. 5-36) and ellipsoid azimuthal-slope-error distributions, respectively.

If α_T and σ_T have similar magnitudes, and if θ_g is an angle on the order of 1°, then ($\alpha_1 d_0 \tan \theta_g \ll \sigma_T d_0$) and the response function resolves itself into a sharp central spike with wide Gaussian wings. The central spike has a FWHM of approximately $7.5(\alpha_1 d_0 \tan \theta_g)$, where we have assumed that $\alpha_1 \sim \alpha_2$. The half-power circle diameter is approximately $2.7(\sigma_1 d_0)$, where we assume $\sigma_1 \sim \sigma_2$. The theoretical FWHM for this mirror is about 0.5 μm, while the theoretical half-power circle diameter is about 2.9 μm. The measured point-spread function of the mirror has a FWHM of 2.5 μm (Fig. 5-37) when measured with a 2-μm pinhole as the source, yielding a point-spread-function FWHM of about 1 to 1.5 μm.

This difference from theory indicates that tolerances other than random slope errors make significant contributions to the response function, unlike the case of our older Wolter mirror for which random slope errors were the dominant effect. A close examination of the mirror azimuthal scans indicates that the average slope of the conic (hyperboloid and ellipsoid) surfaces varies with azimuthal position by an amount large enough to account for the discrepancy

between measurement and theory. This variation in the average slope of the conic surfaces also accounts for the lack of point symmetry that we would expect from a point-spread function determined by random slope errors and that we find in the case of the older Wolter mirror. The lack of point symmetry can be viewed as the result of inaccurate superposition in the image plane of images formed by different portions of the surface. Thus, if only a small sector of the surface is used, many of the images that do not superimpose accurately will be eliminated. For many laser-fusion applications, we have used an 18° sector of the Wolter mirror. The main purpose of using this small sector is to increase the effective depth of field of the mirror, but the small sector also reduces the effect of the azimuthal slope errors on the image.

Another measure of the quality of an x-ray mirror is its transmission as a function of x-ray energy. The transmission of the ASXRMS mirror, as measured in a manner described in the *1977 Laser Program Annual Report*,[14] deviates somewhat from theoretical expectations in that its reflectivity is low at energies above 1.2 keV (see Fig. 5-38). This is presumably due to the finite roughness of the surface.

The transmission spectrum represents an integral over the response function out to a radius of 30 μm (the object-plane equivalent radius). The spatial response function (Fig. 5-37) is determined photographically in the image plane. From the photographs, we find the half-power circle diameter to be 8.6 μm, which again is somewhat larger than the value expected theoretically from a random-slope-error distribution. The fact that the measured transmission spectrum comes as close as it does to the theoretical curve indicates that the surface of the mirror is very smooth, with roughness less than ~15 Å and, perhaps, considerably better.

After completing characterization of the new Wolter mirror, we installed it in the 22× streaked x-ray microscope at Shiva. It has been used on several shot series since that time with excellent performance and results.

X-Ray Microscope Experiments

In a collaborative experiment with the Naval Research Laboratory (NRL), we used our high-resolution streaked x-ray backlighting system, together with a

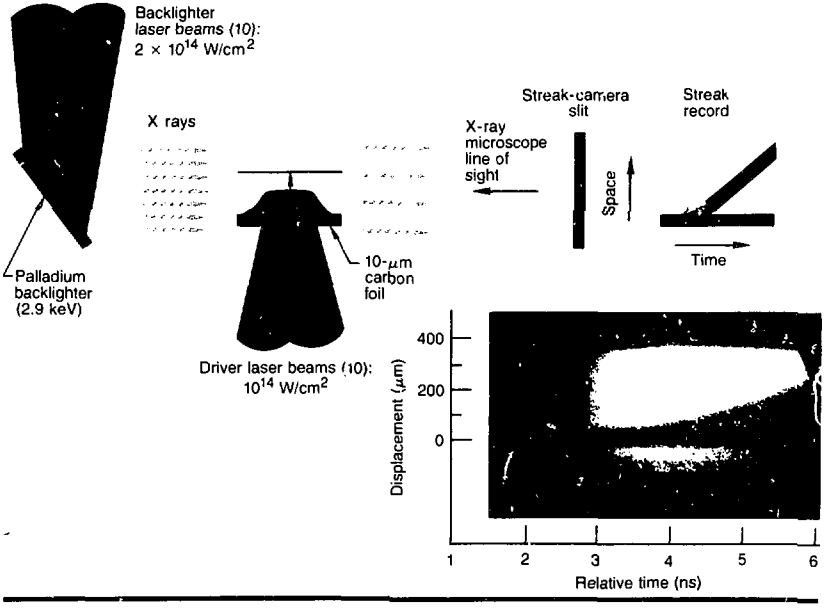

Fig. 5-39. Schematic of, and data from, single-foil experiment observed with x-ray backlighting and the streaked x-ray microscope (p. 5-30)

streaked imaging optical pyrometer[50] and other techniques, to investigate the laser-driven ablative acceleration of matter in a regime characterized by moderate laser intensity (10^{14} to 10^{15} W/cm^2), a long-scale-length plasma ($\geq$0.3 mm), long pulse lengths ($\geq$3 ns), and stringent requirements on beam uniformity.

To obtain these conditions, we irradiated ~10-μm-thick carbon foils in a 1-mm-diam focal spot at 10^{14} W/cm^2 in the near field of the lower 10 beams of Shiva. The incident pulse contained 3 to 3.5 kJ and was 3 to 3.5 ns long. The use of 10 overlapped beams provided significant statistical improvement (by a factor of about 3) in irradiation uniformity. X-ray microscope images indicate ~50% modulation on similar shots with the pulse length reduced to 100 ps to limit lateral energy transport. In some cases, the irradiated foil was allowed to impact a second foil in which the shock breakout and recoil could be observed. Although we have not yet completed the detailed analysis of these experiments, we here summarize them and make some basic observations about this application of the high-resolution x-ray microscope/streak-camera system.

We used the streaked (Wolter) x-ray microscope at 3 keV to make x-ray backlighting observations of the ablative acceleration and recoil history of single- and double-foil experiments (Figs. 5-39 and 5-40, respectively). As we mentioned earlier, the overall spatial resolution of the x-ray microscope is ~6 to 7 μm; time resolution is ~20 ps. A palladium L-line backlighter, irradiated at 2×10^{14} W/cm^2 by Shiva's upper beams, had the same pulse length as the drive pulse, but delayed by 1 ns. A 75-μm-thick Be shield protected the accelerated foil from preheat due to the backlighter soft x rays (<1 keV) and suprathermal electrons (<50 keV).

Preliminary analysis of the backlighting data from the single-foil experiment (Fig. 5-39) involves the fitting of second- and third-order polynomials to the upper edge of the shadow of the moving carbon foil.

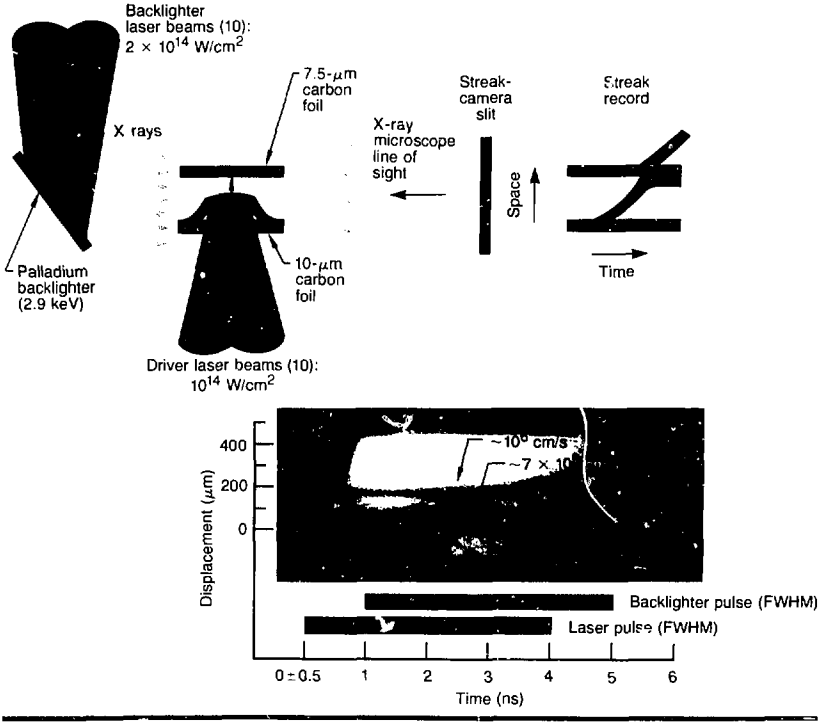

Fig. 5-40. Schematic of, and data from, double-foil experiment observed with x-ray backlighting and the streaked x-ray microscope.

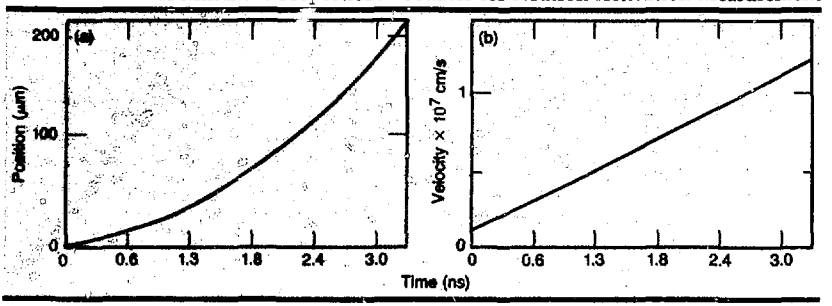

Fig. 5-41. Single-foil experiment (Fig. 5-39) analysis. (a) A second-order polynomial fit to the data. (b) The derivative of the second-order polynomial, giving the velocity as a function of time.

To extract data from the photo, we first visually fit a smooth, continuous curve to it. The curve is then digitized, and the polynomial fit is performed on the digital data. We follow this procedure because image-processing software is not yet available to extract the edge and correct for backlighter intensity variations in the presence of substantial statistical noise.

The curves we have obtained using our rough method appear to be quite reproducible and accurate to about one pixel (~6 to 7 μm). The histories of position and 'ocity vs time are quite reasonable and agree well with LASNEX calculations; we obtain a good average acceleration value, also. It is true, however, that small errors in position for the points digitized from the original data lead to increasingly large errors for higher derivatives of the position data. Thus, our rough method limits extraction of the acceleration data to its average value with limited temporal history.

Figure 5-41(a) shows a second-order polynomial fit to the data sample in Fig. 5-39, giving the position of the foil as a function of time. The time-derivative of the polynomial (the velocity) is shown in Fig. 5-41(b). The second derivative of the polynomial is the average value of the acceleration (a constant) and has a value of 3.3 $\times 10^{15}$ cm/s^2. The laser pulse (and therefore the acceleration) is falling rapidly at the end of these curves, so the terminal velocity of the foil is $\sim 1.2 \times 10^7$ cm/s for the shot shown in Figs. 5-39 and 5-41. A velocity of 1.2×10^7 cm/s gives the 1-mm-diam spot in the center of the moving portion of the foil a kinetic energy of 90 J. This result represents a conversion efficiency of incident laser energy to kinetic energy of 7%. With a preheat level of 15 eV, the foil has approximately 10 times as much directed kinetic energy as internal thermal energy. This value is lower than the ratio of ~80 reported by NRL[51] because of higher preheat; our experiments were performed at 10^{14} W/cm^2, while previous NRL experiments were done at 10^{12} to 10^{13} W/cm^2.

We also performed x-ray backlighting experiments on double-foil targets (Fig. 5-40). Preliminary analysis of the data indicates that the irradiated foil reaches a velocity of 7×10^6 cm/s before impact with the second foil at somewhat more than halfway through the laser pulse. At the time of collision, both foils have a nearly equal areal density of 1.5×10^{-3} g/cm^2. The second foil thus attains a velocity of $\sim 7 \times 10^6$ cm/s from the collision, as shown in Fig. 5-40. The figure shows also the pre-collision decompression of the upper foil (due to preheat) at a velocity of $\sim 1 \times 10^6$ cm/s.

The improvements in the streaked x-ray microscope made over the last year, and the continued development of this instrument now in progress, will significantly enhance the quality of measurements in the area of hydrodynamic instabilities.

Author: R. H. Price

A Miniature Proportional Counter for Neutron-Activation Measurements

Measurement of the pusher areal density, $\langle \rho \Delta R \rangle$, of imploded laser-fusion targets provides an important indicator of our progress toward thermonuclear ignition. We currently measure $\langle \rho \Delta R \rangle$ using neutron-activation techniques.[52-57] In our experiments, thermonuclear neutrons, generated by an imploded target consisting of

deuterium–tritium (D–T) gas encapsulated in a glass microshell, activate the ^{28}Si atoms in the glass via the $^{28}Si(n,p)^{28}Al$ ($t_{1/2}$ = 2.2 min) reaction. A portion of the debris from the exploding target is collected on a 20-μm-thick titanium foil placed near the target. The foil is then rapidly transferred to a radiation detector that determines the number of activated atoms created in the target. From this determination, and from an independent measurement of the neutron yield, we can determine $\langle \rho \Delta R \rangle$.

Anywhere from 50 to 500 activated atoms are created in some of our fusion targets, which translates to 5 to 50 detected events. This small signal places a premium on low-background, high-efficiency detectors.

Aluminum-28 decays by the emission of a 0 to 2.8-MeV β particle and a 1.78-MeV γ ray. To detect these decays, we require a coincidence between our 25- by 25-cm NaI(Tl) detector, which has an Al photopeak efficiency of 40%, and the β detector located in the 5- by 15-cm well of the NaI(Tl) crystal. The collector foil is placed inside the β detector. In the past, we have used an NE-102 plastic fluor to detect the β particles; recently, we have substituted a miniature proportional counter that reduces the background by a factor of 4 to 5. In this article, we describe the present proportional counter and compare its measured efficiency to results of a computer simulation. We also describe the design of an improved version of the counter, which we expect will have a much higher detection efficiency.

Proportional Counter

The proportional counter is shown schematically in Fig. 5-42; it is constructed of copper and consists of a single inner chamber and eight separate outer chambers, each with a 25-μm central wire held at a potential of +4 kV above the grounded chamber walls. The collector foil containing the radioactive target debris is placed in the space between the inner and outer chambers, the wall thicknesses of which are 330 and 254 μm, *respectively. Methane at atmospheric pressure* flows through the detector at a rate of 60 cm^3/min.

We measured the detection efficiency of the miniature proportional counter by irradiating a 5- by 5-cm by 25-μm piece of aluminum foil with thermal neutrons to produce ^{28}Al. Counting rates are given by

$$N_\beta = \epsilon_\beta A \quad ,$$

$$N_\gamma = \epsilon_\gamma A \quad ,$$

and

$$N_{\beta\gamma} = \epsilon_\beta \epsilon_\gamma A - N_\beta N_\gamma \tau \quad ,$$

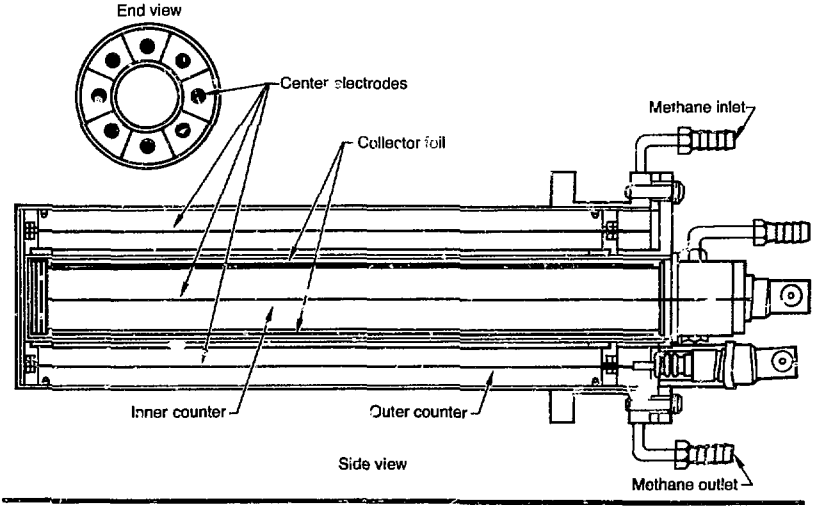

Fig. 5-42. The proportional counter consists of eight separate outer chambers and a single inner chamber; the collector foil is wrapped around the inner chamber.

where N_{β}, N_{γ}, and $N_{\beta\gamma}$ are the β, γ, and coincidence count rates; ϵ_{β} and ϵ_{γ} are the β and γ detector efficiencies; A is the ^{28}Al activity; and τ is the resolving time (0.1 μs). We measured the counting rates after placing the ^{28}Al source on the inner surface of a collector foil, centered between the two ends of the proportional counter. We then solved the above equations to obtain the β efficiencies shown in Table 5-3. For comparison, the plastic β detector has a measured efficiency of 85%.

Due to the increased background at low energies, we adjusted the discriminators to allow the proportional counter to respond to signals in the range from 0.2 to 3.0 MeV. In this energy range, the background count rate for the proportional detector was 0.14 cpm—much lower than the count rate of 0.56 cpm for the plastic detector.

Table 5-3. Detection efficiencies for ^{28}Al β particles.

Detector	Efficiency	
	Measured	Calculated
Inner copper	0.16	0.19
Outer copper	0.29	0.34
Inner aluminum	0.43	0.41
Outer aluminum	—	0.51

Computer Model

The efficiency of the proportional counter was estimated from a simple Monte Carlo computer model that used the Katz–Penfold estimate of electron ranges.[58] Electrons having an energy distribution identical to the ^{28}Al β spectrum were launched in random directions from the source. Regions representing the aluminum source, the titanium collector foil, and the walls of the counter were included. All β particles reaching the sensitive detector region with an energy above 32 eV (the ionization threshold for methane) were considered to be detected. These calculations usually overestimated the measured efficiencies by about 20%.

High-Efficiency Counter

In addition to the copper detector, we have built a 150-μm-thick aluminum inner detector for the proportional counter. The measured background of this inner detector was the same as for the copper inner detector; however, the efficiency of the aluminum detector was measured to be 43%, which agrees well with the computer model. Based on these results, we are now designing a detector constructed completely of aluminum; all the walls adjacent to the collector foil will be made of 125-μm-thick aluminum. The aluminum detector has a calculated efficiency of >90% and should afford a considerable improvement in detection sensitivity over the plastic-fluor system now in use.

Author: S. M. Lane

Major Contributors: J. H. Dellis, C. K. Bennett, and E. M. Campbell

Collimator Design for Neutron Imaging

For low-density laser-fusion targets, we have employed α-particle imaging to diagnose the thermonuclear burn of the fuel region.[59] This technique is not feasible for imaging intermediate- and high-density targets, however, because the compressed pusher of these targets will not transmit the relatively short-range α particles. We have, therefore, directed our efforts to imaging the highly penetrating 14-MeV deuterium–tritium (D–T) neutrons. The predicted D–T neutron yield for Nova targets suggests that, in some cases, enough neutrons may be available to achieve good image resolution. To evaluate the potential for pinhole imaging of neutrons, we studied the image quality for various collimator designs and found that 5- to 10-μm resolution is possible for near-term neutron yields.

A collimator (the three-dimensional analog of an optical-pinhole camera) consists of a high-Z material having an aperture whose diameter is a function of the position along the collimator axis. For neutron-imaging experiments presently envisioned, the collimator would be approximately 100 mm long and placed 500 mm from the emitting source with its aperture axis carefully aligned with the source. A detector would be placed 100 to 200 m from the source, giving magnifications in the range of 200× to 400× and a source-plane resolution of 5 to 10 μm. For an instrument with 5-μm resolution, a 20-μm-diam source (16 resolution elements) must emit 2.5 × 10^{14}

neutrons to have an average of 100 neutrons per resolution element reach the detector plane.

Collimator Configurations

We have examined the effect of collimator design on field of view, neutron efficiency, and spatial resolution.[60] Of the collimator configurations we explored, the most promising are the four shown in Fig. 5-43: the cylinder, the hyperbola of revolution, a pair of intersecting cones, and a segmented approximation to intersecting cones. The cylinder is the most obvious geometry and the easiest to construct; for these reasons, we consider it the basis for comparison. We consider segmented approximations because they may prove easier to construct than configurations in which the aperture diameter varies continuously along the collimator axis.

For comparison, all collimators discussed here have the same length, ℓ, and the same aperture diameter, $2a$, at a distance, s, from the source plane. We define a parameter, d, as the radius of the circle formed by the intersection of the source plane and the mathematical function describing the collimator; this parameter is a somewhat qualitative definition of the field of view. For point-source positions less than d, we can expect good imaging; for positions greater than d, we should observe image degradation. Note that, for the cylinder configuration, the parameter d is fixed by a, whereas, for the other geometries, d can be varied for a given a. The numerical values used for the plots in Figs. 5-44 through 5-46 are $\ell = 100$ mm, $a = 2.5$ μm, $s = 500$ mm, and $d = 10a$ (except for the cylinder). The

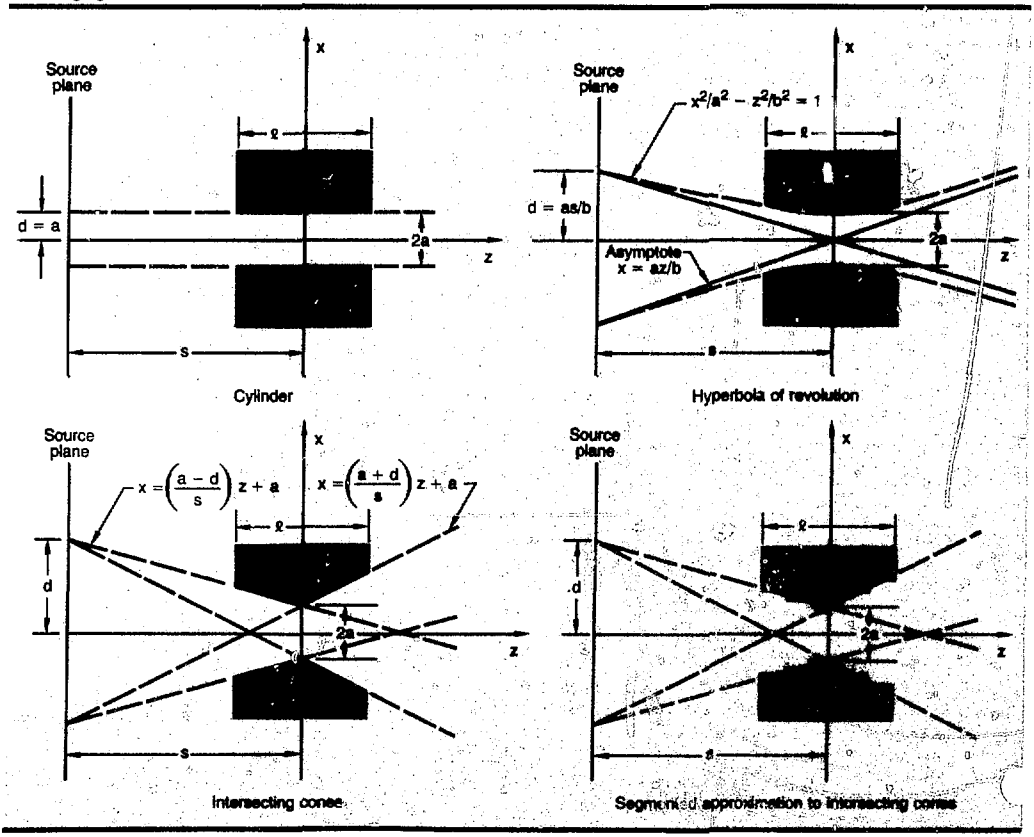

Fig. 5-43. Four collimator configurations studied for use in neutron imaging.

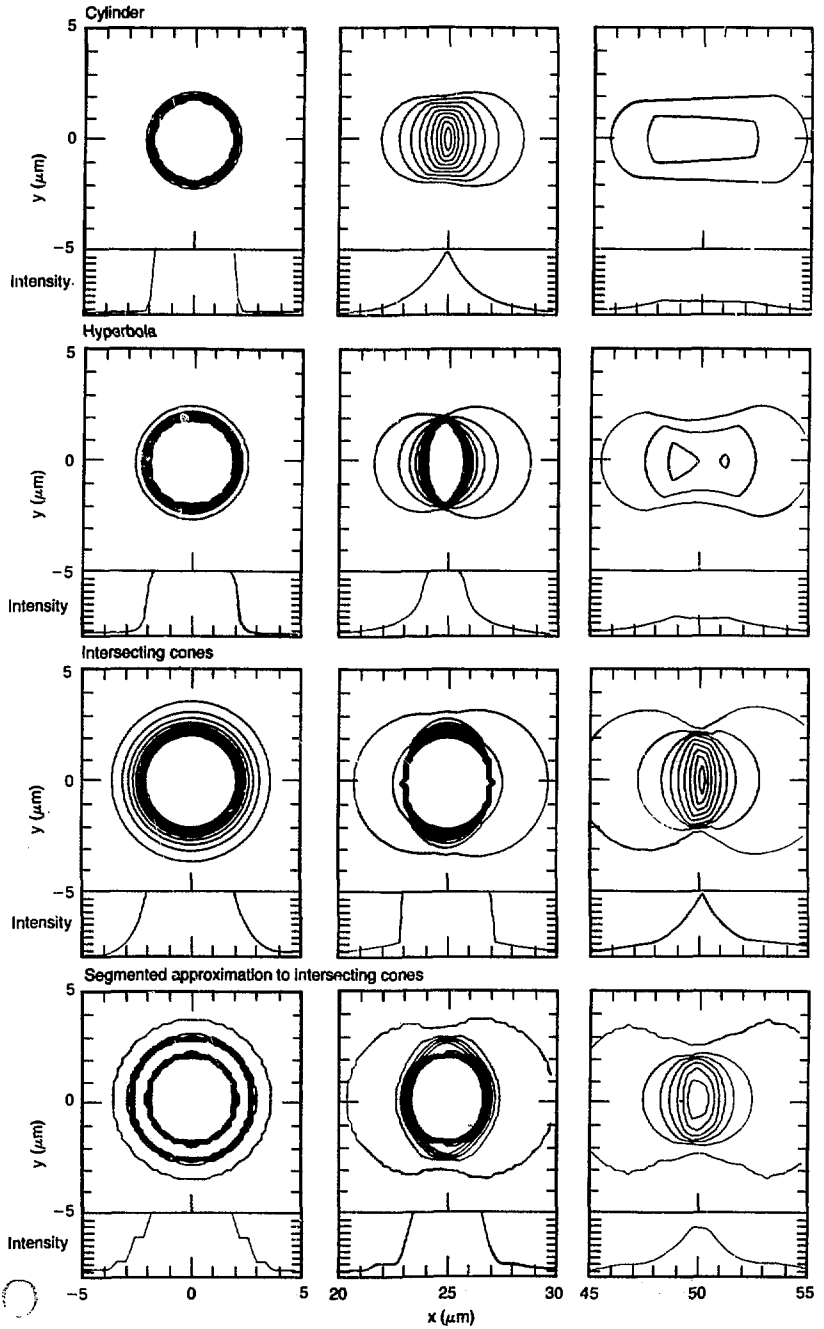

Fig. 5-44. Comparison of response functions of potential collimator configurations for source positions of $x = 0$, 25, and 50 μm.

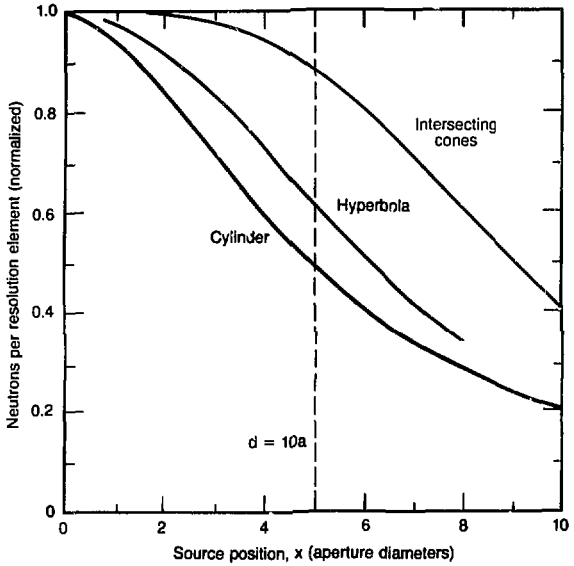

Fig. 5-45. Relative degree of isoplanatism for three potential collimator configurations.

collimator material is assumed to have a 14-MeV-neutron mean free path of 35 mm, and the detector plane is located at z = 200 m (magnification of 400×).

As in any imaging system, the response function should be as narrow as possible because it is directly related to the spatial resolution that can be achieved. Spatial resolution, in the classical sense, is the minimum separation of two point sources that appear distinct in the image. Enhanced spatial resolution can be achieved by post-target-shot data analysis, particularly by deconvolving the image and the response function. Deconvolution is most easily performed when the response function is isoplanatic; i.e., it depends only on the difference between the coordinates in the source and image planes. This implies that isoplanatic response functions have the same shape independent of the source position.

Figure 5-44 shows sample response functions for the cylinder, hyperbola,

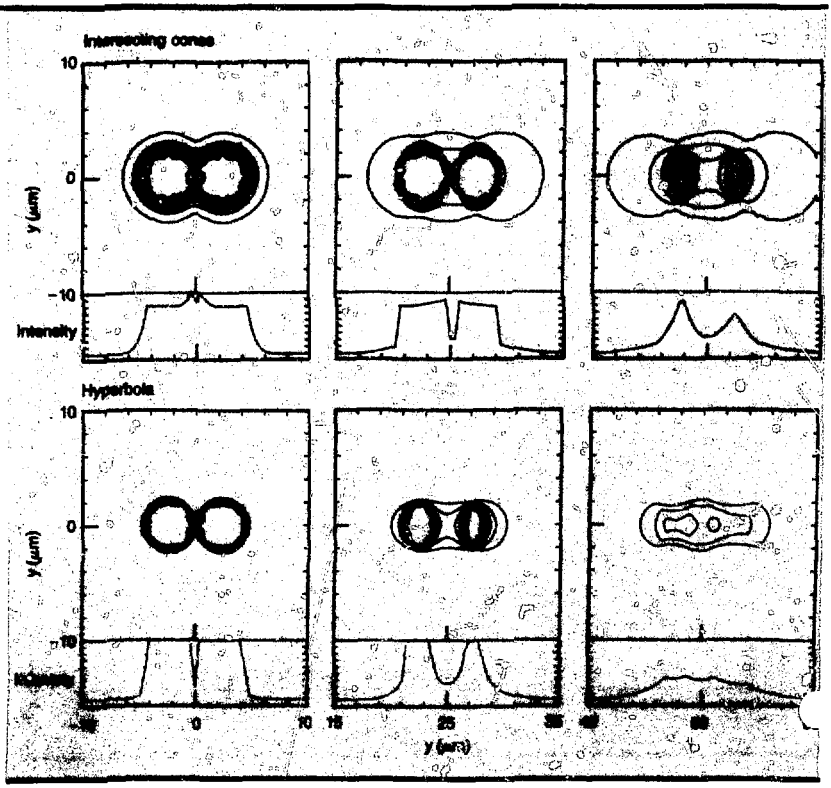

Fig. 5-46. Comparison of two-point resolution for intersecting-cones and hyperbola collimator configurations; distance between the point sources is 6 μm.

intersecting cones, and a five-zone segmented approximation to the intersecting cones. Plots are given for point-source positions of $x = 0$ (on axis), 25 μm, and 50 μm. For each contour plot, there is an intensity plot for $y = 0$. A comparison of these plots shows that the shape of the response function changes as the source is moved off axis. The shape change is most pronounced for the cylinder configuration and least for the intersecting cones. To quantify this observation, we have plotted the integrated neutron intensity over one resolution element, normalized to its on-axis value (see Fig. 5-45). The curves in the figure show the relative degree of isoplanatism for the three designs. Note that, for the intersecting cones, the curve remains above 88% out to its d-parameter value (25 μm), whereas, for the hyperbola and cylinder configurations, the curve drops more significantly.

We have addressed classical two-point resolution as well. Figure 5-46 shows images of two source points spaced slightly more than one aperture diameter (6 μm) apart for the hyperbola and intersecting cones. For source positions less than d (the field of view), the points are better resolved by the hyperbola configuration. This can be attributed to the steeper sides of its response function (compare the on-axis response functions in Fig. 5-44). Note, however, both the symmetry and constancy of the images for the intersecting cones compared to the hyperbola configuration. This is a direct consequence of the higher degree of isoplanatism.

We have studied these collimator configurations as a step toward designing for future Nova neutron-imaging experiments. Of the collimator geometries modeled, the pair of intersecting cones appears to be the most promising with respect to neutron efficiency, field of view, and isoplanatism. Although the intersecting-cones configuration did not have the best classical resolution, it was not far off, and the prospects for enhanced resolution by deconvolution are particularly attractive. We have also shown that stepped collimators can be designed with attractive characteristics.

Summary

We see that the obtainable spatial resolution in a neutron-imaging experiment will be approximately that of the collimator aperture. A 5-μm-diam collimator placed 0.5 m from a source will require approximately 6×10^{13} neutrons emitted from each resolution element to put 400 neutrons into each resolution element in the detection plane. Considering detection efficiency (~25%) and other factors, this will provide a channel confidence level of 20 to 30%. For a 10-μm-diam source under these conditions, we could then anticipate forming a reasonable-confidence image with as few as 3×10^{14} neutrons.

This is an intriguing capability; current target designs for Nova, using one-dimensional calculations for 50 kJ of frequency-doubled (0.53 μm) light in a 1.5-ns pulse, predict yields of 6×10^{14} and 2×10^{15} neutrons (a 4.5-kJ thermonuclear yield) for gas and cryogenic double-shell target designs, respectively. The latter calculation includes a near-doubling of the ion temperature to 8.4 keV due to α-particle absorption in the burning fuel. These one-dimensional calculations may be somewhat optimistic. Nevertheless, they indicate that, with the Nova system, we are approaching the possibility of neutron imaging of fusion reactions with relevant spatial resolution, enabling us to study issues of thermonuclear-burn physics in a laboratory environment.

Authors: R. A. Lerche and G. E. Sommargren

Design Analysis of Neutron Streak Camera

The D–T fusion reaction produced with the Nova laser is expected to be complete within 50 ps. To obtain some clues about how the fusion reaction progresses, we will measure the time-dependence of the neutron flux from the target. In this article, we describe the design of a neutron streak camera (with a temporal resolution of 16 ps) that will be used to study the temporal history of the thermonuclear burn-up of laser-fusion targets.

A neutron streak camera is essentially the same as an optical or x-ray streak camera, except that

- The cathode is sensitive to neutrons.

- The cathode is curved such that the difference in the neutron path lengths from a point source to various parts of the cathode is compensated by electron transit times within the streak tube.

In this way, the cathode can be made large (several cm^2) for high sensitivity without sacrificing temporal resolution. Time compensation is thus a key element in the development of a high-sensitivity neutron streak camera.

Neutron Cathode

Fission materials such as UO_2 are known to make good cathodes for neutron diodes. This suitability is due to uranium's large fission cross sections (2.1 barns for 14-MeV neutrons); the highly charged fission fragment drags out a large number (>200) of low-energy secondary electrons, as shown in Fig. 5-47. To be useful for an ultrafast streak camera, however, the energy spread of these electrons has to be small. Using the data of Jamerson et al.,[61] we estimate the spread to be $\Delta E_e \approx 6$ eV FWHM. Fortunately, as we shall see, this spread is adequate for our purposes.

The thickness of the cathode should be less than the range of the fission fragments—about 10 μm. The thinner the cathode, the smaller the electron transit-time spread and, thus, the better the temporal resolution. Unfortunately, thinner cathodes result in poorer detection efficiency; for a given cathode thickness, we can increase the detection efficiency by making the cathode area larger. This poses an additional problem, however. Because 14-MeV neutrons move rather slowly, at only 0.17 times the speed of light, a 1-mm path difference introduces a time spread of 20 ps. How can we then obtain a large cathode without jeopardizing the time resolution?

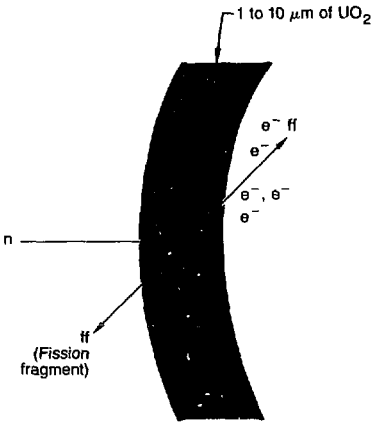

Fig. 5-47. Mechanism of secondary-electron generation from the neutron cathode. Each fission fragment, ff, drags out 400 to 200 low-energy secondary electrons from cathodes of 1 to 10 μm, respectively, of UO_2.

Compensating Neutron and Electron Transit-Time Differences

Basically, we must cancel out differences between the neutron and electron transit times; Fig. 5-48 illustrates the basic relation for this compensation mechanism. First, we make a curved cathode so that the neutron and electron path differences are given by ΔS_N and ΔS_e, respectively. Let

β_N = neutron velocity

and

β_e = electron velocity .

Then,

$$\Delta t_N = \frac{\Delta S_N}{\beta_N}$$

= neutron transit-time difference,

and

$$\Delta t_e = \frac{\Delta S_e}{\beta_e}$$

= electron transit-time difference.

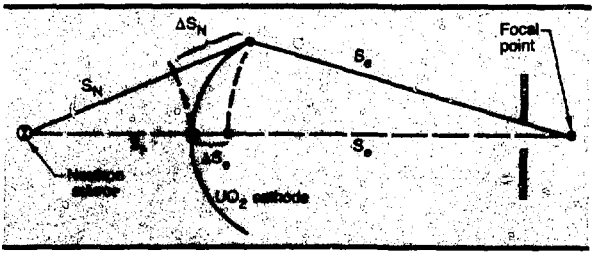

Fig. 5-48. Basic relation for analyzing and cancelling out neutron and electron transit-time differences.

Next, choose β_e such that

$$\vartheta_e = \beta_N \frac{\Delta S_e}{\Delta S_N} \quad . \tag{10}$$

Then,

$$\Delta t_e = -\Delta t_N \quad . \tag{11}$$

Thus, by choosing the electron velocity to satisfy Eq. (10), we can compensate for the neutron transit-time difference using the electron transit-time difference [Eq. (11)]. Figure 5-49 depicts the schematic of a neutron cathode and anode configuration that performs this compensation.

Electron-Beam Optics

We have modified the code GUNSLC[62] to compute the electron-beam optics for a 5-cm-diam cathode having a 2.5-cm radius of curvature. With a 10-kV extractor and a 30-kV anode, the secondary electrons can be focused at the 0.1-mm-radius pinhole located 3.7 cm from the cathode. The ray traces obtained with the modified GUNSLC[62] code are plotted in Fig. 5-50. Rays 1 through 6 were traced to clear the pinhole. Table 5-4 gives the electron transit-time difference, Δt_e, for these rays, along with the corresponding neutron transit-time difference, Δt_N, for 14-MeV neutrons emitted from a source 30 cm away from the cathode. It is evident from Table 5-4 that the transit-time differences, Δt_{Ne}, can be compensated to within 4.2 ps.

Neutron Streak Camera

Figure 5-51 is a schematic representation of a possible configuration for the neutron streak camera. The cathode is coated with 1 μm of UO_2 (or up to 10 μm for higher detection efficiency and poorer temporal resolution). For a 1-μm cathode, each fission fragment leaving the UO_2 cathode generates 400 secondary electrons; this number decreases to 200 secondary electrons for a 10-μm cathode. The electrons focused at the first pinhole by the extractor and the anode are refocused at the second pinhole by the first electrostatic lens. The vertical deflector separates the electrons from surviving positive ions [due, if present, to O (n,p) and O (n,α) reactions in the UO_2 cathode]. The electron beam can now be streaked and detected with standard streak-camera techniques.

With the neutron and electron transit-time differences cancelled out, the temporal resolution of the neutron streak camera is

Fig. 5-49. Schematic of a neutron cathode and anode configuration.

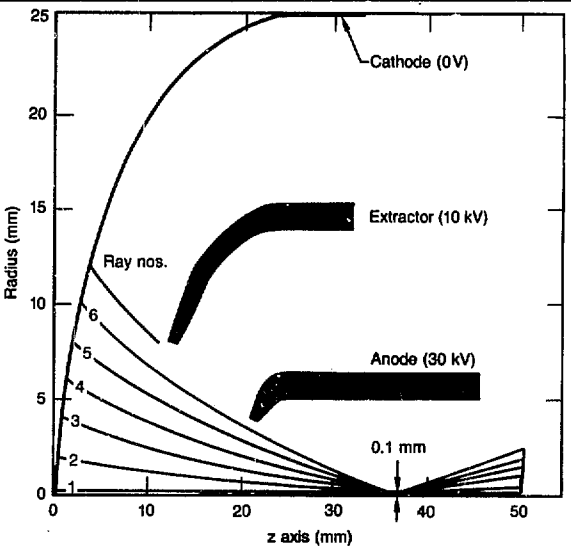

Fig. 5-50. Ray traces calculated using the electron-beam-optics code GUNSLC.

◀ Table 5-4. Ray traces calculated with GUNSLC; secondary-electron angular spread restricted to ±10° with respect to cathode normal.

Ray	Radius (mm)	Δt_e (ps)	Δt_N (ps)	$\Delta t_{Ne} - \Delta t_N + \Delta t_e$ (ps)
1	0	0.0	0.	0.0
2	2	2.0	1.7	3.7
3	4	−3.1	6.8	3.7
4	6	−11.6	15.1	3.5
5	8	−20.0	22.5	2.5
6	10	−29.6	33.8	4.2

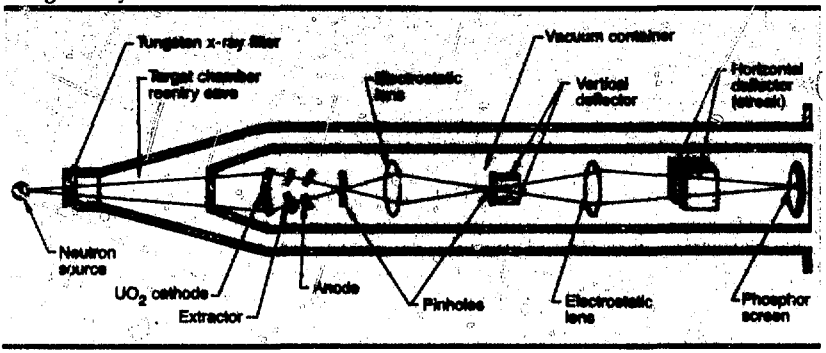

Fig. 5-51. A possible configuration of the neutron streak camera.

now dominated by the following two factors

- Δt_k, the transit-time dispersion[63] due to the electron energy spread, ΔE_e. Here, $\Delta t_k = 23\,000\sqrt{\Delta E_e/E} = 11$ ps for an electric field, E, of 5000 V/cm at the cathode, and $\Delta E_e = 6$ eV.
- Δt_t, the electron transit-time spread in the cathode material. For 1 μm of UO_2, $\Delta t_t = 10$ ps, assuming an electron-scattering-limited velocity of 10^7 cm/s.

Given these two factors, the overall temporal resolution of the neutron streak camera is then $(4.2^2 + 11^2 + 10^2)^{1/2} = 16$ ps.

Using the above geometry, then, for 10^{11} neutrons emitted isotropically from a point source 30 cm away, 60 fission fragments would leave the 1-μm-thick cathode of 1-cm effective radius, generating 24 000 secondary electrons. In the ray trace calculated by GUNSLC, however, the secondary-electron angular spread was restricted to within $\pm 10°$ with respect to the normal to the cathode. Under this restriction, the transmission of the secondary electrons through the 0.2-mm-radius first pinhole is 27%.

Shielding the Neutron Streak Camera

We can adequately shield the neutron streak camera from target-generated x rays using 1-cm-thick tungsten. A Monte Carlo calculation for the neutron transport shows that the neutrons inelastically scattered from the shielding into the cathode, along with the γ rays generated in the shielding, contribute less than 1% to the background. We have yet to carry out a detailed study to determine the shielding required to protect the phosphor screen from the direct (unscattered) neutrons and general x-ray background. However, the vertical deflector can bend the electron beams downward enough ($\geq$5 cm) so that an adequate shielding can be placed between the neutron source and the phosphor screen.

Our optical streak camera works well at 80 cm from the target (outside the target chamber). With a reentry hole in the target chamber, and with adequate shieldings for the electromagnetic pulse (EMP), we expect the neutron streak camera to function properly when located 30 cm from the target. We are planning an EMP-shielding test with an optical streak camera. Should it prove necessary, the electron beam in the neutron streak tube could be guided out of the target chamber.

Conclusion

In conclusion, it is possible that the neutron streak camera could be a viable and unique tool for studying the temporal history of fuel-region burns in D-T plasmas having an ion temperature of a few keV and a neutron yield of 10^{11}. For higher ion temperatures, the dispersion of the neutron energy due to Doppler broadening would require the streak camera to be placed closer to the target. How near the target it could remain operational may perhaps be determined only with experiments.

Authors: C. L. Wang, R. Kalibjian, and M. S. Singh

Fast-Camera Development

Streak cameras remain our primary diagnostic instruments for recording optical and x-ray energy with maximum temporal resolution. During 1981, we continued to gain a greater understanding of the capabilities, limitations, applications, and techniques relating to streak cameras. In addition, we have furthered our studies of coupling laser energy to the streak camera via optical fibers. The high-priority need for fast-gated imaging to diagnose target-implosion dynamics led us to investigate techniques and issues relative to the implementation of a fast framing instrument. In this article we discuss these latter two developments.

Fiber-Optic Links

During the year, we improved our understanding of the use of fiber-optic links to couple laser light to streak cameras. This understanding was particularly useful in our attempts to measure the temporal emission of x rays relative to the incident laser pulse. To make this determination with good resolution (10 ps for optical signals), we used one of our standard S-1 streak cameras to simultaneously record light and x-ray signals.[64] With the experimental configuration required to observe target x rays, we find it experimentally convenient to introduce the incident laser signal into the streak camera via a short (5 to 10 m) optical fiber.

The important fiber characteristics for this application are the temporal dispersion and the power-handling capacity at the desired laser wavelength. Pulse dispersion is minimized differently by two types of fiber.[65] In single-mode fibers, small-diameter cores limit the number of modes that propagate. In graded-index fibers, a radial variation of the index of refraction matches the group velocities of the propagating modes. Since several nanojoules of 1.06-μm (1ω) energy in a 50-ps pulse produce a detectable streak-camera signal, a 4-μm-diam single-mode fiber must carry an average power density of 10^9 W/cm^2; about 10^7 W/cm^2 is required for a 50-μm-diam graded-index fiber. Since the damage threshold for the glass surface at the entrance to the fiber is approximately 10^9 W/cm^2, we selected graded-index fibers to interface the incident laser light to the streak camera.

A lens system mounted behind a 99%-reflecting turning mirror focuses incident 1ω energy onto the end of a 5-m graded-index optical fiber. The light exits the fiber at a variable-delay unit mounted on the camera; here, the light is collimated, turned 180° by a set of mirrors mounted on a slider, and refocused onto a short (0.5 m) section of optical fiber that goes to the streak camera. Energy leaving this fiber is focused onto the streak-camera photocathode. The fiber lengths and variable delay can be adjusted so that the incident laser light and the light reflected from the center of the target chamber reach the streak camera simultaneously (± 5 ps).

In our laboratory, we demonstrated that nominal 50-ps laser pulses at 1ω and 2ω (0.53 μm) can be transmitted through short (up to 30 m) optical fibers without significant temporal distortion.[66] The graphs in Fig. 5-52 each show the overlay of two laser pulses recorded simultaneously with a streak camera; one pulse travels through air, while the other is transmitted through the optical fiber being tested. To minimize temporal dispersion—especially at 2ω—care must be taken to avoid excitation of fiber-cladding modes when the laser energy is coupled into the fiber. We find it best to collimate (rather than focus) the laser energy on the end of the fiber, and we use mode-stripping techniques at all fiber ends. Our optical/x-ray streak camera (OX-1) is fully operational, simultaneously recording high-energy x rays and incident and reflected laser light.

Comparison of Open-Grid vs Mesh-Grid Structures for a Streak-Camera Image-Converter Tube

During 1981, we also advanced our understanding of the streak tube's dynamic range as a function of extraction-grid design. It has been conjectured that a fine mesh

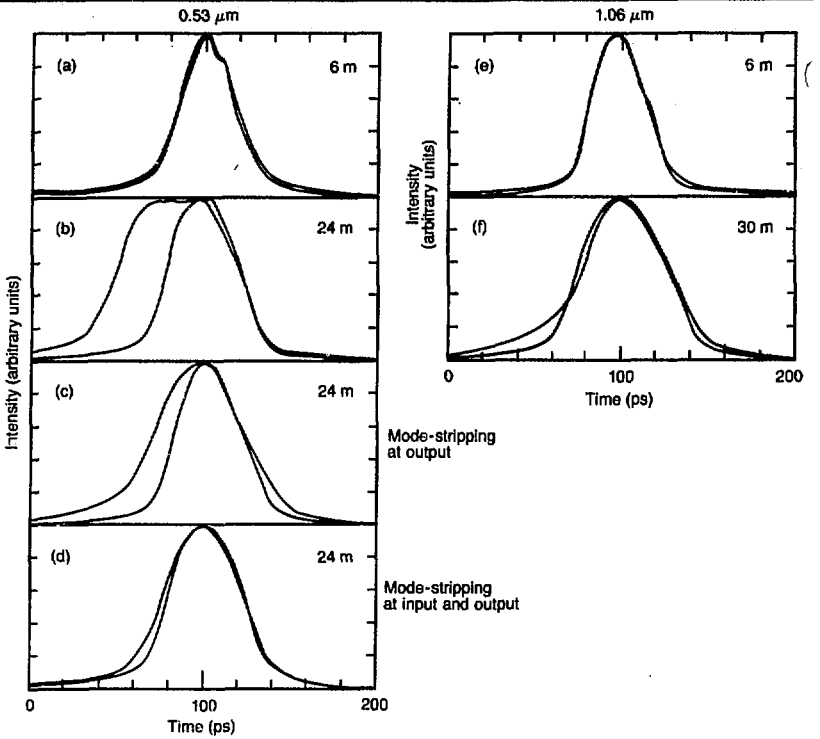

Fig. 5-52. Collimated laser pulses transmitted through 6, 24, and 30 m of optical fiber, compared with laser pulse at input to the fiber.

would scatter some electrons, which would then not be focused as well at the output phosphor as the nonscattered electrons; this condition would raise the background noise level and, thus, reduce the dynamic range. Although this condition cannot be ruled out for other tube designs, it does not appear to be the case for the RCA tube.

To establish requirements for new streak- and framing-tube designs, we wanted to decide whether to use a fine mesh or a coarse, "open" structure for the extraction field. From previous tests, it became evident that streak tubes with an open-grid structure had a much larger dynamic range than those with a fine mesh.[67] However, the tubes in these tests were all of different electron-optics design and were all made by different manufacturers. No one had tested the same tube design with both extraction-grid options.

We therefore fitted the body of an RCA C-73435 streak tube with two extraction-grid structures by replacing the conventional open grid (parallel wires separated by 5 mm) with a steel plate containing two apertures. Figure 5-53(a) shows the aperture plate installed in the streak-tube body. The lower of the two apertures in the photo simulated the open-grid structure, while the upper aperture was a 2- by 20-mm slit covered with a 38%-transmissive mesh having 40 wires per millimetre. The two sections were located an equal distance above and below the tube axis. An S-1 cathode was formed and sealed onto the tube body. We then mounted and tested the tube in the body of an LLNL optical streak camera.

Figure 5-53(b) shows the streak-tube output as presented on the output screen of the 40-mm image-intensifier used in the streak camera. For this photo, the streak-tube cathode was uniformly illuminated. The nearly rectangular top image in Fig. 5-53(b) is that of the 2- by 20-mm slit covered with the fine mesh; this image is magnified about 1.3 times in both vertical and horizontal directions. The lower image is of the aperture with the open grid; this image is magnified approximately 0.25 times in the

vertical direction due to the cylindrical-lens effect of this aperture, while magnification returns to approximately 1.3 at the ends of the image, as shown by the flaring.

We next performed dynamic testing, imaging a 152-μm slit for each section. We used a Nd:YAG laser operating at 1ω with a 35-ps pulse width to measure dynamic range. A single pulse was selected from the pulse train and passed through a 150-ps etalon with 70%-reflecting surfaces. For the recording medium, we used Royal-X Pan film developed to an ASA rating of 2000. The film was then scanned and digitized. Knowing the etalon timing permitted us to convert the position on the film into time and, finally, into a plot of FWHM vs intensity, as shown in Fig. 5-54. Similar data symbols indicate information obtained in the same single-pulse experiment. As we anticipated, saturation occurred at the same output intensity for both the open and mesh sections. The saturation level was defined by a 20% broadening of the pulse

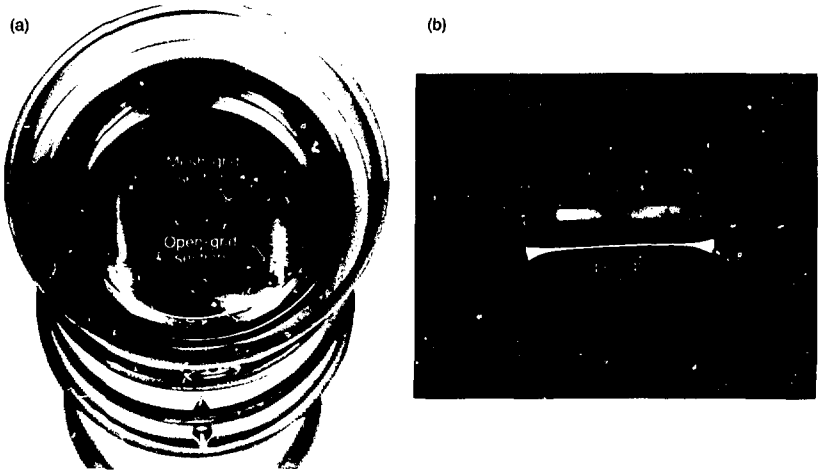

Fig. 5-53. Fine-mesh and open extraction-grid sections. (a) Experimental arrangement for comparing meshes. (b) Image-intensifier output of the two grid sections.

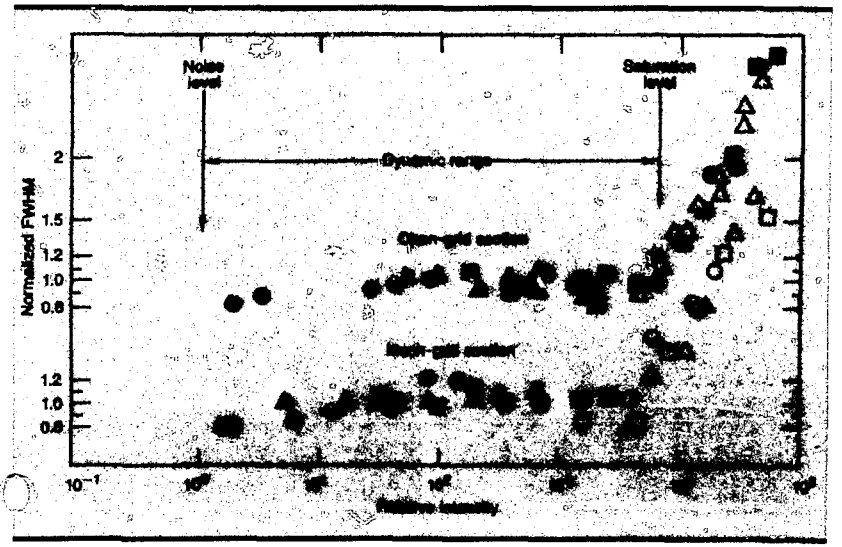

Fig. 5-54. Dynamic-range plots of the open and mesh extraction-grid sections.

width (FWHM), as compared with lower-amplitude pulses. In Fig. 5-54, saturation occurs at about 6000 intensity units.

Dynamic range is defined here as the ratio of the saturation intensity to the noise intensity level. The data revealed that the noise levels for both sections were very nearly equal and were nearly the same as for the system noise level of about one intensity unit, giving a dynamic range of about 6000 for both sections. As a consequence, we conclude that, for the RCA streak tube, dynamic range is not a function of extraction-field structure, but must be due to some other aspect of the design of the camera and image-converter (streak) tube—such as intensifier noise, microlensing, or other charge-limiting effects.

Gate-Off Circuit for an X-ray Streak Camera

In some applications with soft x-ray streak cameras (SXRSCs), we have experienced a retrace problem that is potentially destructive to the recovery of output data. The deflection system used in our SXRSCs scans the beam in a nanosecond time scale across the phosphor screen and keeps the beam off the screen for at least 0.5 μs. The beam then slowly retraces to its predeflected position on a microsecond time scale. If there is any input to the photocathode during the retrace time, additional writing could occur on the phosphor screen. Because of the slower time for the retrace, the signal strength to overwrite need be only 0.1% of the data-signal strength to produce equal intensity on the film.

Overwriting during the retrace period is illustrated in Fig. 5-55(a); a peculiarly shaped streak is shown overwriting the initial streak record. The source of the retrace streak is not fully understood, except that it is known to depend on incident fluxes, the vacuum condition, and the vacuum history of the image-converter tube.

We are presently working to identify the source of the retrace streak. In the meantime, we have developed a "gate-off" circuit that reverse-biases the streak-tube extraction grid shortly after the sweep circuit is triggered and before retrace occurs. In this gate-off circuit, a trigger pulse derived from

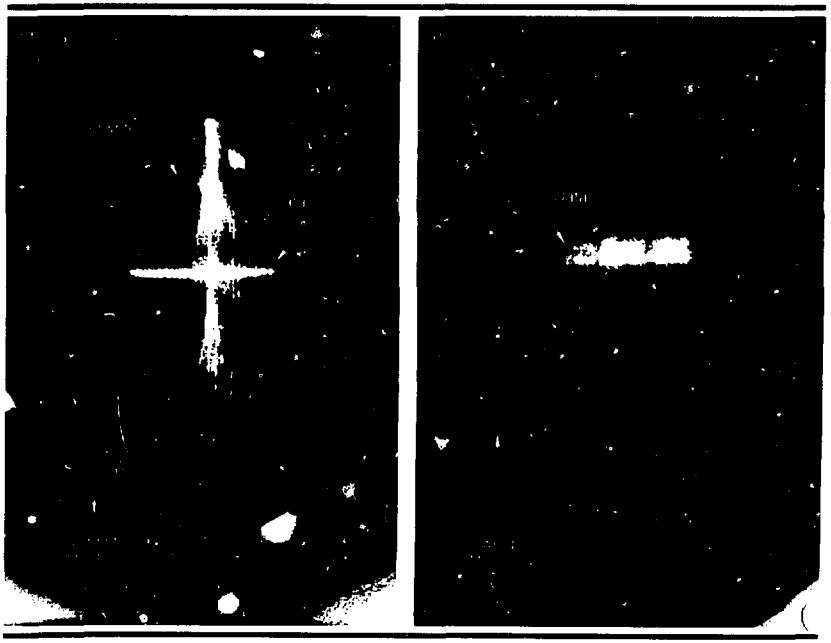

Fig. 5-55. Effect of the gate-off circuit on the retrace-overwriting problem. (a) Before installation. (b) After installation.

the sweep circuit triggers a four-transistor avalanche string. This string in turn fires a Krytron tube, producing a negative 5 kV step that is applied to the streak-tube grid through a high-voltage ceramic capacitor; the capacitor isolates the gate-off circuit from the 17-kV potential on the streak tube.

The gate-off circuit has worked well, although we have had some problems with it. For example, we experienced erratic and excessive turn-on delay. A slight increase in Krytron-tube bias (or "keep-alive" current) was all that was necessary to solve this problem. Figure 5-55(b) shows a test with the gateoff circuit functioning normally. The retrace overwriting has been effectively eliminated. We will continue testing this system to verify both the effectiveness of the changes made and that no other problems exist.

High-Speed Framing

In the area of high-speed framing, we continued the development of techniques that will lead to a framing capability for use at the Novette and Nova lasers. We have developed a dissector/restorer framing-camera tube (FCT) that has 100-ps frames with a three-frame format of 4.5-mm size.[68] However, the driver used to demonstrate these early results suffered from significant (10 μs) jitter. For the FCT to have a major impact on plasma diagnostics, it must be able to frame images with low jitter (<50 ps) and a larger frame size (~1 cm).

Recent characterization of the FCT was aimed primarily at determining its spatial resolution; we conducted these tests using a Nd:YAG mode-locked laser with Ronchi rulings and stencil patterns. The 150-ps laser pulse, in concert with a 100-ps etalon, provides an almost constant 1.5-ns pulse for backlighting tests. We checked the FCT's spatial resolution in both the framed and the streaked modes of operation. A microwave tube driver with less than 20-ps jitter drove the dissector deflectors at a sweep speed of 59 ps/mm. As referenced to the photocathode, the FCT has a field of view of 0.5 × 1 cm and a framed-mode spatial resolution of 7.5 line pairs/mm.

Figure 5-56(a) shows two identical 250-ps frames for a 0.32- × 0.42-cm stencil pattern backlighted by 2ω laser light (the otherwise visible third frame is clipped out by the limiting diameter of the image intensifier). The smallest dimension of the original stencil is a 135-μm space (resolved in the figure). Spatial resolution is more clearly demonstrated in Fig. 5-56(b), which shows two frames of well-resolved alternating opaque and transparent lines 105 μm wide (one frame is clipped by the edge of the image intensifier). In other tests, not shown here, line widths of 65 μm are just resolved.

Limitations in Image Recording

Imaging tubes optimized for very high temporal resolution often have insufficient gain to render a recordable image from the limited flux. Therefore, an element common to many fast imaging cameras is an image intensifier, used to intensify the image so that it is bright enough to be recorded on film or other media. A typical solution is to intensify the gated or streaked image by factors of several thousand, using a proximity-focused microchannel-plate (MCP) image-intensifier.

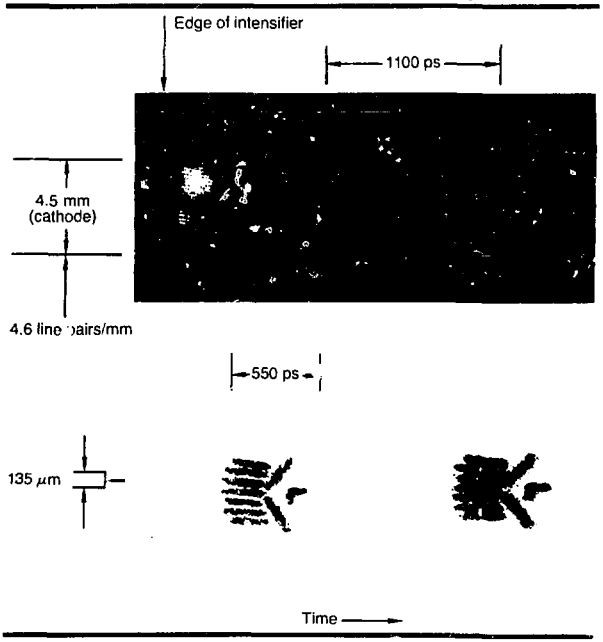

Fig. 5-56. Framed images obtained with pattern backlighted by a 150-ps (90-ps etalon) laser pulse.

As part of the development of a framing camera with high resolution and wide dynamic range, we have investigated the effects of MCP image-intensifiers on the resolution and dynamic range of recorded images. The object of our tests was an ITT F-4113 40-mm image-intensifier tube—the tube used to intensify streak-camera records at LLNL. The results of this investigation led us to a clearer understanding of the limitations of our current recording system and showed how modest changes in the tube design could lead to significant improvements in performance.

We found two significant limitations due to the tube construction

- The resolving ability of the tube is greatly reduced when contact recording is used.
- Bright portions of the image smear into adjacent dark areas, with a resultant loss of dynamic range.

The first limitation is illustrated by the fact that the tube we evaluated has a limiting visual resolution of 22 line pairs/mm when viewed with a microscope; however, on film, the resolution is only 12 line pairs/mm. We attribute the difference to the combination of a relatively thick (25 to 40 μm) phosphor layer and a fiber-optic numerical aperture of unity. The 180° acceptance angle of these fibers permits light from far off the fiber axis to be collected and delivered to the film, resulting in a loss of resolution.

We determined the second limitation by measuring the edge response of the intensifier, then finding its Fourier transform to obtain the modulation transfer function (MTF). This is shown as the solid curve in Fig. 5-57; along with it is the MTF of a classical Gaussian optical system (the dashed curve) having the same limiting resolution of 12 line pairs/mm.

Figure 5-57 illustrates that the oft-assumed Gaussian system response is not valid at low spatial frequencies. The contrast ratio of the intensifier, here defined as $MTF(f)/[1 - MTF(f)]$, is significantly reduced from that of the Gaussian at low spatial frequencies. For example, at 1 cycle/mm the respective contrast ratios are 3.4 and 49. Thus, the ability to resolve differences in intensity at 1 line pair/mm is 15 times poorer for the actual intensifier than for the ideal Gaussian case. The most likely cause of this is the elastic reflection of photoelectrons from the input surface of the MCP.[69] These reflected photoelectrons eventually strike the MCP some distance from the initial impact point, producing a background that lowers the contrast and dynamic range. We believe that improvements in resolution can be obtained by

- Using thinner phosphor layers (8 to 10 μm appears optimum).
- Using lower numerical-aperture fiber-optic faceplates.
- Reducing significantly the spacing between the photocathode and the MCP.

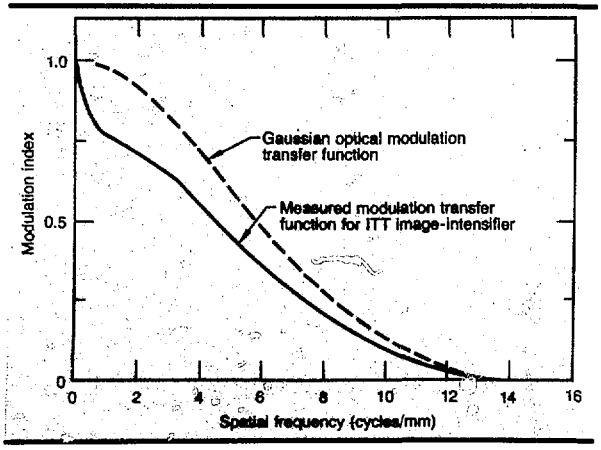

Fig. 5-57. Modulation transfer functions for proximity-focused image-intensifier and classic Gaussian optical system, both having limiting visual resolution of 12 line pairs/mm.

Summary

We have made significant progress this year in the area of optical/x-ray temporal comparison measurements. We are still improving the reliability of the basic streak-camera electronics and gaining understanding of other problem areas such as S-1 photocathode degradation and x-ray camera retrace problems. We are encouraged by our work in the framing of images, and we will continue our development in this area.

Authors: D. E. Campbell, R. Kalibjian, R. A. Lerche, S. W. Thomas, and J. D. Wiedwald

Major Contributors: R. L. Griffith, J. P. Henz, H. Medecki, R. L. Peterson, and G. E. Phillips

Overview of Data Management and Analysis

Activities of the Data Management and Analysis group during the year were directed towards making our VAX 11/780 computer system a significant factor in processing and analyzing experimental data. We first transferred all of the data processing for Shiva experiments onto the VAX from the Shiva PDP 11/70 computer. The virtual-memory feature of the VAX allowed us to rewrite the software to be much more efficient; the result was much faster turnaround of experimental data output from Shiva. Memory in the VAX has been increased to 5.5 Mbytes, giving it the capability to handle more than 30 users simultaneously. Three 176-Mbyte-capacity disk drives are now in operation, providing ample storage space for many sets of experimental data and user software. More disks are planned for the future, when data-storage requirements will increase.

The virtual-memory feature also allowed us to begin image processing on the VAX. We have achieved an excellent image-analysis capability due to the VAX's ability to handle large two-dimensional arrays and to the integration of the Ramtek color-display system into our processing software. Before we had the VAX, it took several days to obtain a color-enhanced image, mainly because the process required several nonconnected computer systems. Now an analyst can have color-enhanced or processed images minutes after the digitized data are received by the VAX. In addition to image-processing software, we wrote programs to process other types of digitized film data, such as x-ray spectrometer films; after this highly automated, user-friendly software was written, operators processed hundreds of x-ray spectra on the VAX. The VAX image-processing capability is discussed in detail in "Image Processing on the FEAF VAX," later in this section.

During 1981, we also concentrated on formulating data bases that will be used for setting up experiments, analyzing and correlating processed data from sets of experiments, and instrument design. For the purpose of designing x-ray instruments, we have set up rapid-access libraries of x-ray cross-section data on the VAX storage disks. The user software allows operators to easily display these data, as well as to incorporate it into application programs. Applications in 1981 included calculation of channel-response functions for a Kirkpatrick-Baez x-ray microscope (see "Progress on X-ray Microscope Development," earlier in this section).

After evaluating several data-base management systems for use with the Fusion Experiments data bases, we purchased the ORACLE relational-data-base system. The Fusion Experiments data bases will contain the configuration of diagnostics, the detector calibrations, and the physics parameters for each experiment. With ORACLE, we can display these data in tables, lists, and on graphs in sets and subsets specified by the user. ORACLE data bases and application programs are already used by the Laser Program for wavelength-scaling studies and for management of the Novette target-chamber configuration. ORACLE is discussed further in the following article.

In preparation for setting up the permanent Fusion Experiments Analysis Facility (FEAF) in 1982, we have acquired new hardware and software to make the VAX a versatile and powerful user's facility. Programmers have a choice of four high-level languages: FORTRAN, PASCAL, PRAXIS, and BASIC. The DISSPLA/TELLAGRAF graphics software package can be used with four types of devices: our Ramtek color-display system, Tektronix or Hewlett-Packard graphics terminals, and Versatec printer/plotters. With this versatility, the user can have high-quality, on-line graphics output at a terminal, as well as high-quality hard-copy graphics for subsequent use.

Construction started on the 2500-ft^2 addition to our office building, where most of the computer system will be housed. In addition, we have started design of data links between the Nova and Novette control computers and the Fusion Experiments computer; these links will automatically transfer experimental data to the Fusion Experiments computer shortly after the experiment has taken place.

In summary, during 1981, the efforts of the Data Management and Analysis group have contributed significantly to the Fusion Experiments goal of fast, accurate, and detailed analysis of target experiments.

Author: J. M. Auerbach

Major Contributor: R. A. Lerche

Data-Base Management

Current work in laser fusion emphasizes the search for scaling laws relating the experimental parameters (energy on target, laser pulse width, neutron yield, suprathermal-electron level, and others). The discovery of scaling laws involves sorting, processing, and correlating large amounts of experimental data. The ever-increasing amount of data requires a formal computerized approach to both management and analysis of data. In response to this need, we are currently implementing the ORACLE data-base management system on the Fusion Experiments VAX 11/780 computer. The ORACLE system satisfies our requirements for

- A versatile and user-friendly interface; the system must allow physicists, engineers, and technicians to retrieve and examine data efficiently and easily.
- An interface to high-level-language software, so that analysis programs can directly access the various data bases of experimental data.
- The ability to store and manipulate the wide range of data acquired in laser-fusion research in a compact and controllable manner.
- Easy storage and transport of data bases between computers.

Before selecting ORACLE, we conducted an evaluation of three commercial data-base management software packages: FRAMIS, INGRESS, and ORACLE; INGRESS and ORACLE were readily available for use on a VAX computer system such as ours. We judged the ORACLE system to be optimum for our Fusion Experiments Analysis Facility (FEAF) VAX computer and also for the Nova VAX control computers.

ORACLE is a relational data-base management system. In the relational data base, the data can be thought of as being configured in a table or several tables. Each column of the table corresponds to a specified entity (such as the laser energy or pulse width), and each row corresponds to a group of entities for a specific item or event (such as an experiment or experimental series). Data in one table can be used with the data in another table or tables by having one or more corresponding columns in each table.

Figure 5-58 shows a sample data base and tables that could form a simple Fusion Experiments data base. ORACLE uses the SQL query language for queries and manipulation of the table data. The SQL language allows the user to extract data according to a wide variety of specified conditions, which frees us from having to write specialized query routines for each application.

ORACLE also has an option, called FORM GENERATOR, that allows the user to query the data base using the auxiliary terminal keypad and, thus, produce simple displays of data on the terminal video screen. Figure 5-59 shows a sample form used with the Novette diagnostic data base.

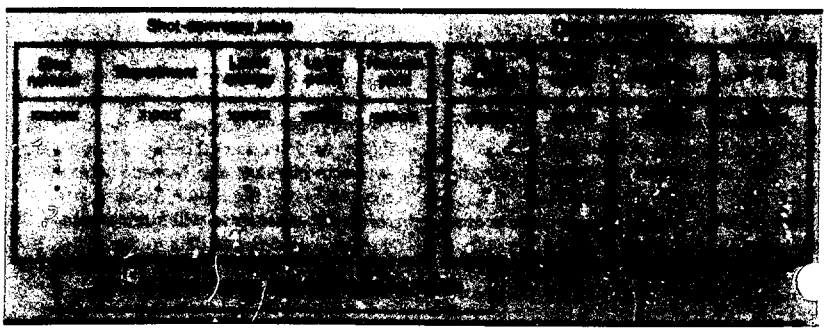

Fig. 5-58. A sample Fusion Experiments data base, showing tables and relational structure of the ORACLE data-base management system.

In the figure, the user has typed in the letters "FFLEX1" in the "CODE" block; ORACLE then returns all the other information on the form to him. Forms are initially specified by the user to satisfy individual needs; they subsequently allow the user to easily examine specific items of data without having to peruse long lists or printouts.

The Fusion Experiments data-processing and analysis scheme requires that we maintain three types of data bases: for raw data and experiment configurations, for detectors and calibration parameters, and for physics parameters. Each of these types of data base is described in detail below.

Raw-Data and Experiment-Configuration Data Base

In the raw-data data base is collected the digital data (from electronic instruments) and digitized films; in the experiment-configuration data base is collected the parameters that relate the instrument channel giving that data or film to the detector or sensor near the target. Thus, the combined raw-data and experiment-configuration data base relates electronic data-processing instruments and cameras to the corresponding physical measurement. This relationship is the first requirement for processing electronic data output into physics parameters.

During 1981, we formulated a raw-data and experiment-configuration data base and integrated it into the ORACLE data-base management system. This data base has two functions. The first function is target-chamber data management; the raw-data and experiment-configuration data base will allow experimenters and technicians to record and monitor the status of all instrumentation mounted on either the Novette or Nova target chamber. Earlier versions of a target-chamber data base have been described in the *1979* and *1980 Laser Program Annual Reports*.[70,71]

The second function of the raw-data and experiment-configuration data base is to associate diagnostics with electronic readouts, so that raw shot data initially indexed according to electronic module and channel can be indexed according to the sensor. It is this latter indexing that is meaningful to the experimenter. An item of diagnostic data is identified by three key quantities: a code (up to six letters) identifying the diagnostic; the detector number; and a channel number corresponding to a detector. For example, the output of a detector may be sent to three electronic devices through three different attenuators; thus, there is one detector and three channels. The three key parameters appear in various tables of the data base associating a diagnostic channel with location on the target chamber, connections to readout equipment, and descriptive data.

DIAGNOSTIC/EQUIPMENT CONFIGURATION

CODE	SYMBOL	FULL DESCRIPTIVE NAME
FFLEX1	FF	FILTER FLUORESCER SPECTROMETER (3 METER)

CATEGORY	RESPONSIBLE PERSON
X-RAY	CHING WANG

REC_MEDIUM	STATUS
ELECTRONIC	SCALING: 1ST

NDET	NCHAN	DATE	COMMENTS
20	60	06/01/82	3 METER INSTRUMENT—FROM ARGUS

Char Mode: Replace Page 1 Stored Count: 1

Fig. 5-59. A sample ORACLE query form displayed on a computer terminal.

Figure 5-60 shows the table structure for the raw-data and experiment-configuration data base. For illustration, the figure shows five principal tables; key parameters are shown in enclosed rectangles at the top of each table. When joined, the DETECTOR and PORT STATUS tables give complete information about the location of a diagnostic on the target chamber. The DETECTOR and DIAGNOSTIC DESCRIPTION tables, when joined, give descriptive information about a specified detector. Finally, joining the DETECTOR, ELECTRONIC CONFIGURATION, and MODULE tables tells where

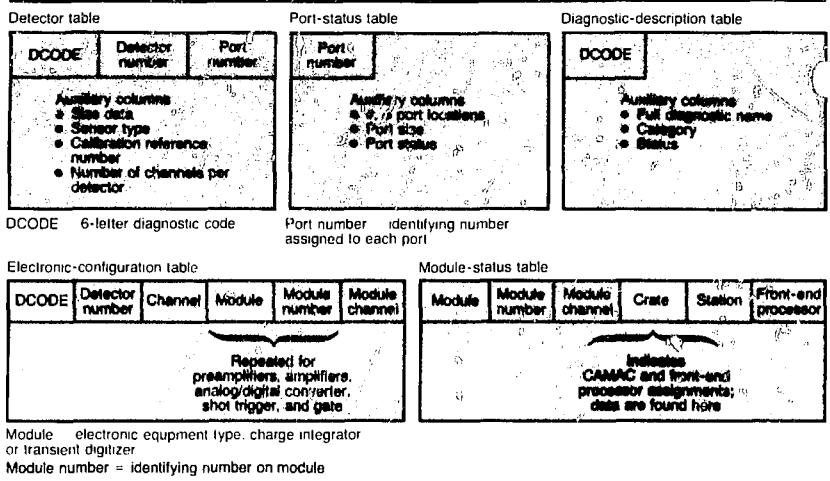

Fig. 5-60. Primary data tables used in the raw-data and experiment-configuration data base.

(in the data-acquisition system) the digital data are to be found (CAMAC crate, station, or microprocessor number). The ORACLE software does the joining operations in response to a search request and displays only on the subset of the data base that is requested.

The raw-data and experiment-configuration data base is broken down into tables of distinct groups of data for easy data-management and to make the software more efficient. For example, experimenters would make frequent use of the DETECTOR, DIAGNOSTIC DESCRIPTION, and PORT STATUS tables in setting up an experiment; it would slow down their application codes if the ORACLE software had to work with large tables containing combined diagnostic-location and electronic-configuration data. On the other hand, the electronic tables would be used by automated data-processing codes.

Detector and Calibration-Parameters Data Base

The detector and calibration-parameters data base contains calibration and response-function data for all the detectors and sensors used in an experiment. With the combined contents of this data base and the raw-data and experiment-configuration data base, processing software will turn digital data into quantities relevant to conditions at the target at experiment time. For example, the output of a neutron detector is given in counts or units of charge; with the calibration data, the output is converted to fusion neutron yield. The detector and calibration-parameters data base will be maintained by diagnosticians and updated each time a sensor is recalibrated or added to the diagnostic inventory. The data base will be used for both data processing and sensor design.

Physics-Parameters Data Base

The physics-parameters data base contains the final version of processed and analyzed data. Rows of data can be indexed by shot number, target type, or both. The data base will be accessible by application software that includes a versatile graphics package; experimenters will be able to plot the data in any user-specified configuration.

Conclusion

When fully implemented, the ORACLE data-base management system and the Fusion Experiments data bases on our VAX computer will significantly improve our ability and efficiency in reducing and analyzing experimental data.

Author: J. M. Auerbach

Major Contributors: R. W. Carey, C. E. Thompson, J. R. Severyn, and G. S. Chinen

Image Processing on the FEAF VAX

During 1981, we implemented a powerful image-processing capability on the Fusion Experiments Analysis Facility (FEAF) VAX computer; users can now quickly produce color-enhanced images of data for examination and analysis shortly after the data are generated. We achieved this capability by combining an on-line Ramtek color-display system with the VAX's ability to handle large arrays of digitized image data.

At the present time, our film records are digitized on a PDS densitometer system by the LLNL Technical Photography group. The film data are stored on magnetic tapes in a format specifically designed for the OCTOPUS system computers. During 1981, we wrote software that decodes the magnetic tapes for use on the VAX, storing each image on a disk file in a format easily adaptable to application programs. These disk files are stored on disks or magnetic tape for later use and reference.

Digitization is the longest step in the image-processing cycle, mainly because the magnetic tape from the Technical Photography group's computer must be hand carried to the FEAF VAX. Next year, we will implement our own film-digitizer system and digitize some film locally; we will use an Eikonix digitizer system controlled by a PDP 11/34 computer that is linked, in turn, to the VAX computer. In addition, some image diagnostics for the Novette and Nova laser facilities will use charge-coupled device (CCD) image-recording devices, rather than film. The output of the CCD devices will be transferred electronically to the FEAF VAX minutes after an experiment; once in the FEAF VAX, the CCD data can be processed for display and analysis.

Image processing includes not only spatial images but also images of the output of streak cameras and spectrometers (x rays and light). The first level of user software in the FEAF image-processing system is a set of utilities that allows users to color-enhance film data and look at profiles of film density as a function of position. The next level of user software is a set of diagnostic-specific processing modules that prompt the user for necessary information at each step. These processing modules are designed to allow nonexpert users to easily obtain the desired output, even if they are not familiar with the diagnostic or the VAX operating system. Modules are presently in use for processing image data from the following diagnostics[72-76]

- Optical and x-ray streak cameras.
- X-ray microscope/streak camera for time-resolved x-ray microscopy.
- Beam far-field cameras.
- Kirkpatrick–Baez x-ray microscopes.
- X-ray crystal spectrographs.

In the remainder of this article we give an example of an image-processing utility and then describe the processing of images from an optical streak camera to illustrate the use of a diagnostic module.

Figure 5-61 shows a sample color-enhanced image of an x-ray micrograph, including a lineout in the horizontal direction (the user can select a lineout of the image in either the horizontal or vertical direction). The user first selects a location relative to the 10 tick marks on the frame surrounding the image. Upon selecting the direction and location of the lineout, the image-processing utility "draws" the lineout shown in the figure. The user can also produce a hard-copy plot of the lineout data; a sample hard copy is shown in Fig. 5-62.

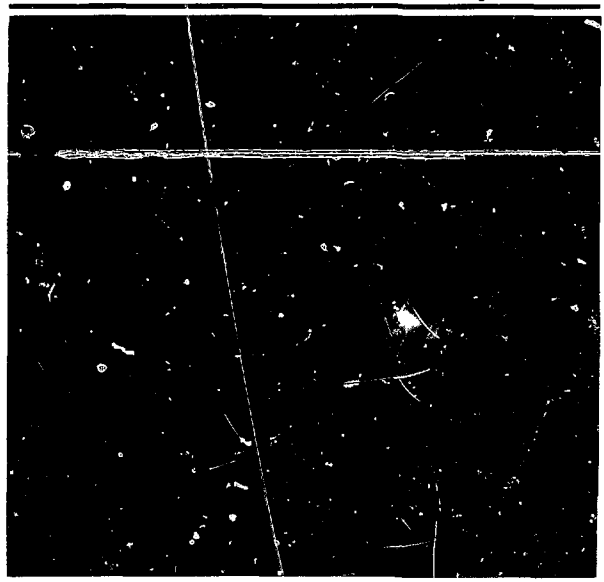

Fig. 5-61. Color-enhanced image of an x-ray micrograph, including lineout.

Note in Fig. 5-61 that the lineout is underscored by three lines. In this case, the user selected a range of pixels to average over, perpendicular to the lineout direction; this option produces a profile with an enhanced signal-to-noise ratio. The three lines indicate the lineout center and the boundaries of the averaging region. The horizontal scale in Fig. 5-62 indicates the number of pixels that were averaged over in the cross-lineout direction.

Fig. 5-62. Film-density profile from lineout data of Fig. 5-61.

The diagnostic module for our optical streak camera uses as input two sets of data

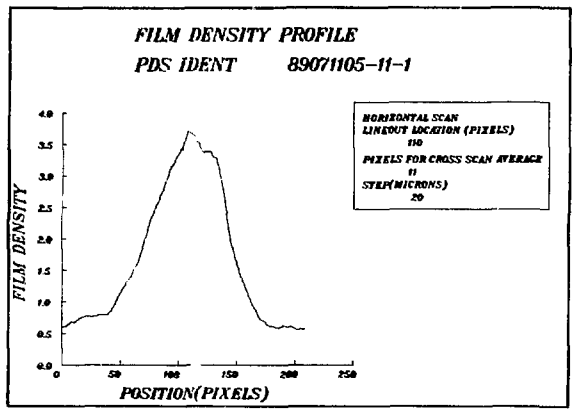

Fig. 5-63. Film step-wedge data for use in processing images from an optical streak camera.

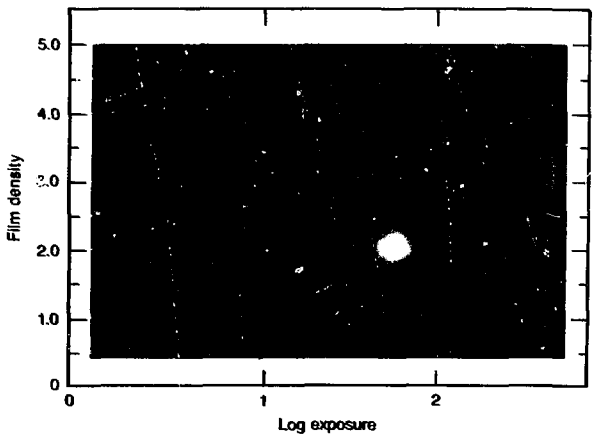

- The film-calibration step-wedge data, giving the relationship of film density to relative exposure.
- The digitized film data, containing the streak-camera image.

In the case of the optical streak camera, the objective of the module is to use these data to obtain a history of the light incident on or reflected from the target. The diagnostic module first prompts the user to produce a function of film density vs relative exposure (from the step-wedge data). Figure 5-63 shows the output the user sees after completion of the step-wedge data processing: the fit to the wedge data (the red curve) is later used to remove the film response from the step-wedge data.

The user is next presented with a color-enhanced image of the streak data, as shown in Fig. 5-64. The user then selects a lineout region to produce a profile of film density vs position for subsequent conversion into a profile of power vs time. In the final phase of image-processing, the diagnostic module asks the user to enter the streak-camera speed and the laser energy, as measured by calorimetry. The module then unfolds the film response (step-wedge data) from the film-density profile selected earlier. This profile of relative exposure vs film position is then converted to a profile of power history, using the laser energy and streak speed.

Figure 5-65 shows the module output for the data of Figs. 5-63 and 5-64, a streak speed of 190 ps/mm, and an energy of 35 J. This output shows the unfolded profile (in red), a 7th-order polynomial fit to the data (in green), the full width at half maximum of the fitted curve (in yellow), and the peak power. This Ramtek color display is duplicated as hard copy for later use. Image-processing by the diagnostic module takes ~ 1 min.

The combination of the FEAF VAX and the Ramtek color-display system is proving to be a valuable tool in analyzing image data. With full incorporation of the Eikonix digitizer, the FEAF will provide an even more complete image-processing capability for fast and thorough evaluation of data.

Author: J. M. Auerbach

Major Contributors: G. L. Hermes and W. M. Trimble

UV Probe

Our UV probe is a holographic interferometer that will be used to investigate electron densities in laser-produced plasmas. Performing this probing in the UV permits measurement of higher electron densities than would be possible with a visible-light probe. For relatively large-volume plasmas, the probe system under construction is expected to measure electron densities approaching 10^{21} e/cm^3 with a spatial resolution better than 4 μm (limited primarily by motion effects). Utilizing a probe pulse of 10 to 15 ps, we should be able to observe density contour velocities of $\sim 10^7$ cm/s.

Unlike previous UV probes,[77] the frequency of the present probe pulse will be shifted away from the fourth harmonic ($4\omega = 0.263$ μm) to eliminate plasma harmonic emission as a noise source in the hologram. Frequency-shifting will be performed using stimulated Raman scattering (SRS) in hydrogen. The resulting probe wavelength will be 0.296 μm.

As the schematic in Fig. 5-66 shows, the UV probe consists of two sections: the frequency-conversion equipment, and the holographic interferometer. The input to the system will be nominally 10 mJ of 1.053-μm light in a 20-ps (FWHM) pulse; this pulse will be frequency-converted into UV light by a sequence of two angle-tuned KDP crystals. Operating the crystals at less than maximum efficiency will result in some degree of pulse compression.[78] The UV beam will be focused through a pressurized hydrogen cell, where transient SRS will produce a coherent pulse at the first-Stokes wavelength of 0.296 μm. This process will result in an additional degree of pulse compression.[79]

The probe beam is split into two parts by a variable beam splitter consisting of a half-wave plate and a thin-film dielectric polarizer. This variable arrangement allows for adjustment of the beam-balance ratio—an important parameter in the production of high-quality holograms. The reference beam also traverses a variable optical delay that allows the paths of the target and reference beams to be adjusted to the same length.

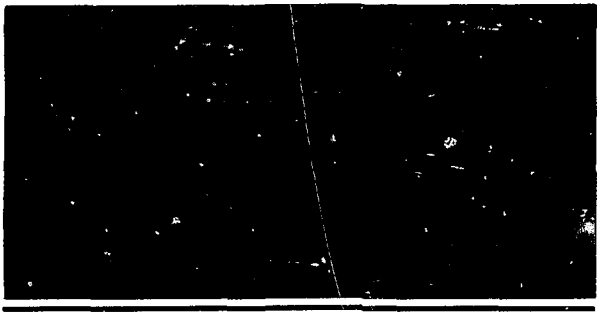

Fig. 5-64. Pixel-averaged lineout from a streak record.

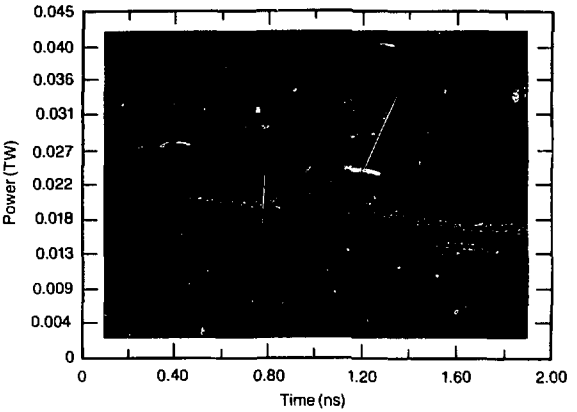

Fig. 5-65. Processed streak-camera data showing the history (power vs time) of light scattered from a target shot.

As the probe pulse width is only ~15 ps, the difference in path length must not be greater than 1 to 2 mm; otherwise, the two beams will not interfere properly in the plane of the hologram.

The target beam traverses the plasma and records the density information integrated through the plasma as a phase distortion in the wavefront. This wavefront is imaged by f/5 near-diffraction-limited optics onto the hologram image plane, where the amplitude and phase information are recorded. A second exposure, taken either before or after the plasma probe, records the wavefront traversing the undisturbed target chamber. This information is recorded on the same hologram, using an identical reference beam.

The reconstruction is performed using a He–Ne laser at 0.633 μm. The difference in

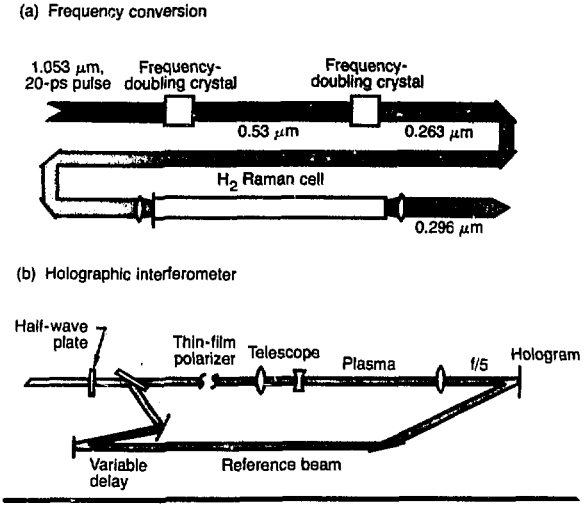

Fig. 5-66. Schematic of UV probe diagnostic comprised of two systems used to create a double-exposure hologram. (a) A frequency-conversion system. (b) An optical system.

wavelength affects only the magnification of the image. The two recorded wavefronts are reconstructed simultaneously; their interference results in a fringe pattern of isodensity contours integrated through the plasma. For the case of an axisymmetric-phase object, we will use the Abel inversion to extract point-by-point information on the local densities in the plasma.[80]

With simple modifications, the UV probe can also be used for shadowgraph, Schlieren, or Faraday-rotation photography. We also anticipate using the UV probe pulse for synchronous triggering of other diagnostics, such as Auston switches.[81] Work is presently proceeding on all aspects of the detailed design of the UV probe; we expect to use the system in the earliest Novette experiments.

Author: M. W. Taylor

1. *Laser Program Annual Report—1979*, Lawrence Livermore National Laboratory, Livermore, Calif., UCRL-50021-79 (1980), p. 5-5.
2. P. H. Y. Lee et al., *Measurement of 2-5 keV X-ray Emission from Laser-Target Interactions by Using Fluor-MCP and CsI-XRD Detectors*, Lawrence Livermore National Laboratory, Livermore, Calif., UCRL-86306 (1981).
3. K. G. Tirsell, H. N. Kornblum, and V. W. Slivinsky, *Time Resolved, Sub-keV X-ray Measurements Using Filtered X-ray Diodes*, Lawrence Livermore National Laboratory, Livermore, Calif., UCRL-81478 (1979).
4. *Laser Program Annual Report—1978*, Lawrence Livermore National Laboratory, Livermore, Calif., UCRL-50021-78 (1979), p. 6-5.
5. M. J. Rocke, *Production of Free-Standing Boron Films*, Lawrence Livermore National Laboratory, Livermore, Calif., UCRL-79448 (1977).
6. *Laser Program Annual Report—1978*, Lawrence Livermore National Laboratory, Livermore, Calif., UCRL-50021-78 (1979), p. 6-64.
7. D. E. Campbell, K. G. Tirsell, and W. B. Laird, *Improved 50 ps Response X-ray Detector with Optical Applications*, Lawrence Livermore National Laboratory, Livermore, Calif., UCRL-86340 (1981).
8. *Laser Program Annual Report—1979*, Lawrence Livermore National Laboratory, Livermore, Calif., UCRL-50021-79 (1980), p. 5-2.
9. K. G. Tirsell, H. N. Kornblum, and V. W. Slivinsky, *Bull. Am. Phys. Soc.* **23**, 807 (1978).
10. G. B. Zimmerman and W. L. Kruer, *Comments Plasma Phys.* **2**, 51 (1975).
11. G. McClellan, P. H. Y. Lee, and G. Caporaso, *Phys. Rev. Lett.* **44**, 658 (1980).
12. *Laser Program Annual Report—1980*, Lawrence Livermore National Laboratory, Livermore, Calif., UCRL-50021-80 (1981), p. 7-10.
13. *Laser Program Annual Report—1977*, Lawrence Livermore National Laboratory, Livermore, Calif., UCRL-50021-77 (1978), p. 3-64.
14. *Laser Program Annual Report—1978*, Lawrence Livermore National Laboratory, Livermore, Calif., UCRL-50021-78 (1979), p. 6-8.
15. L. Suter, Lawrence Livermore National Laboratory, Livermore, Calif., private communication (1980).
16. K. Manes et al., "X-Ray Production by Frequency Converted Nd-Glass Laser Systems," *Bull. Am. Phys. Soc.* **26**, 873 (1981).
17. E. M. Campbell et al., *Effect of Laser Wavelength on the X-ray Yield of Variable Z Targets*, Lawrence Livermore National Laboratory, Livermore, Calif., UCRL-85991 (1981).
18. M. D. Rosen, Lawrence Livermore National Laboratory, Livermore, Calif., private communication (1981).
19. R. W. Kuckuck, J. L. Gaines, and R. D. Ernst, *High Intensity Sub-keV X-ray Calibration Using a Cockroft Walton Proton Accelerator*, Lawrence Livermore National Laboratory, Livermore, Calif., UCRL-78764 (1976).
20. J. L. Gaines and R. D. Ernst, *X-ray-Detector Calibrations in the 183-to-932-eV Energy Range*, Lawrence Livermore National Laboratory, Livermore, Calif., UCRL-78616 (1976).
21. J. L. Gaines, "A Generator for Producing Monoenergetic, High Intensity, Soft X Rays," *Nucl. Instrum. Meth.* **102**, 7 (1972).
22. J. L. Gaines and R. A. Hansen, "An Improved Annular-Shaped Electron Gun for an X-Ray Generator," *Nucl. Instrum. Meth.* **126**, 99 (1975).
23. J. L. Gaines, *Unfolding the Effects of Spectral Contaminants in X-ray Calibrations*, Lawrence Livermore National Laboratory, Livermore, Calif., Internal Report UOPE 73-10 (1973).
24. B. L. Henke et al., "The Atomic Scattering Factor, $f_1 + if_2$ for 94 Elements and for the 100 to 2000 eV Photon Energy Region," in *Low Energy X-ray Diagnostics*, D. T. Attwood and B. L. Henke, Eds. (American Institute of Physics, New York, 1981), pp. 340-388.
25. R. H. Day et al., "Photoelectric Quantum Efficiencies and Filter Window Absorption Coefficients from 20 eV to 10 keV." (To be published in *J. Appl. Phys.*)
26. B. L. Henke, J. P. Knauer, and K. Premaratne, "The Characterization of X-Ray Photocathodes in the 0.1-10 keV Photon Energy Region," *J. Appl. Phys.* **52**, 1509 (1981).
27. B. L. Henke, J. P. Knauer, and K. Premaratne, *J. Appl. Phys.* **52**, 1509 (1981).
28. J. L. Gaines, *Windowless X-ray Detectors*, Lawrence Livermore National Laboratory, Livermore, Calif., Internal Report UOPE 74-4 (1974).
29. V. W. Slivinsky and G. R. Leipelt, *A Study of the Consistency of Ni and Au XRD Calibrations up to 1.25 MeV*, Lawrence Livermore National Laboratory, Livermore, Calif., Internal Report UOPE 70-17 (1970).
30. H. N. Kornblum et al., "Filter Fluorescer Experiment on the Argus Laser," *Bull. Am. Phys. Soc.* **23**, 806 (1978); C. L. Wang, *Rev. Sci. Instrum.* **52**, 1317 (1981).
31. J. Lindsey, *Photoelectric Detectors with Bandpass Sensitivity Characteristics*, Lawrence Livermore National Laboratory, Livermore, Calif., Internal Report UOPE 70-6 (1970).
32. H. N. Kornblum et al., "Filter Fluorescer Experiment on the Argus Laser," *Bull. Am. Phys. Soc.* **23**, 806 (1978).
33. C. L. Wang, *Rev. Sci. Instrum.* **52**, 1317 (1981).
34. *Laser Program Annual Report—1979*, Lawrence Livermore National Laboratory, Livermore, Calif., UCRL-50021-79 (1980), pp. 5-29 to 5-32.
35. N. M. Ceglio, "The Impact of Microfabrication Technology on X-Ray Optics," in *Low Energy X-ray Diagnostics*, D. T. Attwood and B. L. Henke, Eds. (American Institute of Physics, New York, 1981), pp. 210-222.
36. N. M. Ceglio, A. M. Hawryluk, and R. H. Price, "Space and Time Resolved Soft X-Ray Spectra Using X-Ray Transmission Gratings," in *Proc. SPIE Symposium on Soft X-ray Optics, Vol. 316* (SPIE, Bellingham, Wash., 1982), pp. 134-142.
37. A. M. Hawryluk et al., *J. Vac. Sci. Technol.* **19**, 897 (1981).
38. E. Spiller, *App. Phys. Lett.* **20**, 365 (1972).
39. Cosslett and Nixon, *X-ray Microscopy* (Cambridge University Press, Cambridge, England, 1960), p. 126.

References

40. A. M. Hawryluk et al., "Soft X-Ray Spectroscopy Using Thick Gold Transmission Gratings of 0.2 to 0.3 μm Spatial Periods," in *Low Energy X-ray Diagnostics*, D. T. Attwood and B. L. Henke, Eds. (American Institute of Physics, New York, 1981), pp. 286–289.
41. H. Gursky and T. Zehnpfennig, *Appl. Opt.* **5**, 875 (1966).
42. W. Ehrenberg, *J. Opt. Soc. Am.* **39**, 746 (1949).
43. *Laser Program Annual Report—1980*, Lawrence Livermore National Laboratory, Livermore, Calif., UCRL-50021-80 (1981), p. 5-23.
44. T. Zehnpfennig, *X-ray Microscope Assemblies: Final Report and Metrology Report*, Lawrence Livermore National Laboratory, Livermore, Calif., UCRL-15408 (1981).
45. *Laser Program Annual Report—1978*, Lawrence Livermore National Laboratory, Livermore, Calif., UCRL-50021-78 (1979), p. 6-23.
46. *Laser Program Annual Report—1978*, Lawrence Livermore National Laboratory, Livermore, Calif., UCRL-50021-78 (1979), p. 6-27.
47. R. H. Price, in *Low Energy X-ray Diagnostics*, D. T. Attwood and B. L. Henke, Eds. (American Institute of Physics, New York, 1981), pp. 189–199.
48. R. H. Price, *X-ray Microscopy Using Grazing Incidence Reflection Optics*, Lawrence Livermore National Laboratory, Livermore, Calif., UCRL-86046 (1981).
49. *Laser Program Annual Report—1977*, Lawrence Livermore National Laboratory, Livermore, Calif., UCRL-50021-77 (1978), p. 3-73.
50. *Laser Program Annual Report—1979*, Lawrence Livermore National Laboratory, Livermore, Calif., UCRL-50021-79 (1980), p. 5-26.
51. F. A. McLean et al., *Preheat Studies in Laser Ablatively Accelerated Foils*, Naval Research Laboratory, Washington, D. C., NRL Memorandum Report 4356 (1980).
52. *Laser Program Annual Report—1979*, Lawrence Livermore National Laboratory, Livermore, Calif., UCRL-50021-79 (1980), pp. 5-39 to 5-42.
53. *Laser Program Annual Report—1980*, Lawrence Livermore National Laboratory, Livermore, Calif., UCRL-50021-80 (1981), pp. 5-40 to 5-45.
54. E. M. Campbell et al., "Exploding Pusher Tamper Areal Density Measurement by Neutron Activation," *Appl. Phys. Lett.* **36**, 965 (1980).
55. I. M. Auerbach et al., "Compression of Polymer-Coated Laser-Fusion Targets to Ten Times Liquid DT Density," *Phys. Rev. Lett.* **44**, 1672 (1980).
56. S. M. Lane, E. M. Campbell, and C. K. Bennett, "Measurement of DT Neutron Induced Activity in Glass-Microshell Laser Fusion Targets," *Appl. Phys. Lett.* **37**, 600 (1980).
57. E. M. Campbell et al., "Use of a Radioactive Tracer to Determine the Fraction of Fusion Target Debris Collected," *J. Appl. Phys.* **51**, 6065 (1981).
58. L. Katz and A. S. Penfold, "Range-Energy Relations for Electrons and the Determination of Beta-Ray End-Point Energies by Absorption," *Rev. Mod. Phys.* **24**, 28 (1952).
59. N. M. Ceglio and L. W. Coleman, "Spatially Resolved α Emission from Laser Fusion Targets," *Phys. Rev. Lett.* **39**, 20 (1977).
60. G. E. Sommargren and R. A. Lerche, *Collimator Design for Neutron Imaging of Laser Fusion Targets*, Lawrence Livermore National Laboratory, Livermore, Calif., UCID-19317 (1981).
61. F. E. Jamerson, C. B. Leffert, and D. B. Rees, *J. Appl. Phys.* **36**, 355 (1965); J. N. Anno, *J. Appl. Phys.* **33**, 1678 (1962).
62. W. B. Herrmannsfeldt, *Electron Trajectory Program*, Stanford Linear Accelerator Center, Stanford, Calif., SLAC-16 (1973).
63. V. V. Korobkin, A. A. Malyutin, and M. Ya. Schelev, *J. Phot. Sci.* **17**, 179 (1969).
64. *Laser Program Annual Report—1980*, Lawrence Livermore National Laboratory, Livermore, Calif., UCRL-50021-80 (1981), pp. 5-19 to 5-21; R. A. Lerche and G. E. Phillips, *Simultaneous Recording of Optical and X-ray Signals in Laser Fusion*, Lawrence Livermore National Laboratory, Livermore, Calif., UCRL-86405 (1981).
65. S. E. Miller and A. G. Chynoweth, Eds., *Optical Fiber Telecommunications* (Academic Press, New York, 1979).
66. R. A. Lerche and G. E. Phillips, *Streak Camera Measurements of Laser Pulse Temporal Dispersion in Short Graded Index Optical Fibers*, Lawrence Livermore National Laboratory, Livermore, Calif., UCID-19176 (1981).
67. S. W. Thomas and G. E. Phillips, *Comparison of Image Converter Tubes for Ultrahigh Speed Streak Cameras*, Lawrence Livermore National Laboratory, Livermore, Calif., UCRL-77741 (1976).
68. R. Kalibjian, "A 100 ps Framing Camera Tube," *Rev. Sci. Instrum.* **49**, 891 (1978).
69. M. Fouassier, J.-C. Rosier, and J. Dietz, *Acta Electronica* **20**, 369 (1977).
70. *Laser Program Annual Report—1979*, Lawrence Livermore National Laboratory, Livermore, Calif., UCRL-50021-79 (1980), p. 5-68.
71. *Laser Program Annual Report—1980*, Lawrence Livermore National Laboratory, Livermore, Calif., UCRL-50021-80 (1981), p. 6-28.
72. *Laser Program Annual Report—1976*, Lawrence Livermore National Laboratory, Livermore, Calif., UCRL-50021-76 (1977), Sec. 3.
73. *Laser Program Annual Report—1977*, Lawrence Livermore National Laboratory, Livermore, Calif., UCRL-50021-77 (1978), Sec. 3.
74. *Laser Program Annual Report—1978*, Lawrence Livermore National Laboratory, Livermore, Calif., UCRL-50021-78 (1979), Sec. 6.
75. *Laser Program Annual Report—1979*, Lawrence Livermore National Laboratory, Livermore, Calif., UCRL-50021-79 (1980), Sec. 5.
76. *Laser Program Annual Report—1980*, Lawrence Livermore National Laboratory, Livermore, Calif., UCRL-50021-80 (1981), Sec. 5.
77. E. L. Pierce, *Appl. Opt.* **19**, 952 (1980).
78. A. Yariv, *Quantum Electronics*, 2nd ed. (John Wiley and Sons, New York, 1975), Ch. 16.
79. R. L. Carmen et al., *Phys. Rev.* **2**, 60 (1970).
80. R. N. Bracewell, *Fourier Transform and Its Applications* (McGraw-Hill, New York, 1965), p. 176.
81. *Laser Program Annual Report—1980*, Lawrence Livermore National Laboratory, Livermore, Calif., UCRL-50021-80 (1981), p. 5-68.

Laser Fusion Experiments and Analysis

Section 6

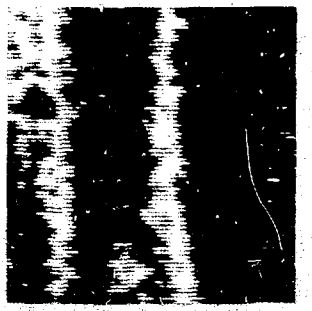

Laser-Fusion Experiments and Analysis

Contents

Section Editor: D. T. Attwood

Laser-Fusion Experiments and Analysis

Introduction

L. W. Coleman

Our primary experimental accomplishment with the Shiva laser system has been the establishment of important aspects of target-performance scaling and related physics issues. With Argus, we obtained basic, important wavelength-scaling data. During 1981, we continued to operate the Argus and Shiva facilities in support of our experimental program, albeit at reduced level. The reduced operating level resulted from a lower level of program support coupled with the need to provide resources for Novette and Nova.

During the first half of 1981, we completed our wavelength-scaling experiments on laser-target interaction at moderate laser energies, using one arm of the Argus laser. Argus was also used to study issues relating to frequency-conversion physics and technology and to test optical materials. The final target experiment on Argus was conducted on August 30, 1981, after which the system was dismantled so that we could begin building Novette. During Argus' exceptionally productive 80-month career, we accomplished much, including firsts in laser design, laser operation, and target experiments.

During 1981, the target-experiments program on Argus centered on completing our series of wavelength-scaling studies at 1.06, 0.53, and 0.35 μm. We worked with a variety of target types and obtained a wide range of x-ray and optical data for the study of absorption, energy transport, suprathermal-electron production, and the stimulated plasma processes related to production of suprathermal electrons. We have also made more complete analyses of our earlier wavelength-scaling experiments. In general, at the energy levels available for these experiments (40 to 200 J), we find our results are in basic agreement with theoretical predictions of the benefits of submicrometre laser wavelengths in laser–plasma interactions.

We operated the Shiva laser system in a sustained mode during 1981, making few modifications. The system supported an active program of target experiments, as well as development and testing of some laser components and devices. Completing an enormously successful and productive four-year life, Shiva was shut down on December 23, 1981, to make way for our new, higher-capability systems.

The 1981 experimental program on Shiva primarily addressed target performance and the physics of energy and pulse-length scaling to solidify our calculational design base for Novette and Nova targets. In addition, there were these developments

- We analyzed a technique for measuring characteristic x-ray lines as a suprathermal-electron diagnostic.
- We employed optical diagnostics with disk targets to study stimulated laser-plasma processes.
- We conducted experiments to study non-LTE physics and x-ray line production for laser- and backlighting-diagnostics applications.
- At the end of the year, we collaborated with Naval Research Laboratory personnel on experiments to accelerate directly irradiated single- and double-foil targets; 10 Shiva beams were overlapped on the targets to provide an irradiation intensity as uniform as possible. Analysis of these experiments is under way.

A laser-irradiated gas-jet target at KMS Fusion in Ann Arbor, Mich. (a support laboratory in the lead-laboratory program on short-wavelength laser experiments), provided an accessible, controlled, long-scale-length plasma. In the final article in this section, we discuss the results of using x-ray spectroscopy to characterize density and temperature distributions in the plasmas of laser-irradiated gas-jet targets.

Operating Systems

Introduction

During 1981, we operated the Argus and Shiva laser facilities at reduced rates to accommodate both budget limitations and the demands of the Nova and Novette lasers for personnel, equipment, and space. Argus was shut down permanently on August 31, 1981; Shiva was reduced to four shifts per week at the same time. Despite these reduced schedules, 640 high-energy shots were taken on Argus and 171 high-energy shots were taken on Shiva. These shots supported 11 experimental series on Shiva and 6 series on Argus. In addition, Argus supported four major physics experiments for Nova and Novette development; high-energy shots on Shiva supported four experiments for Nova development. These efforts at the Argus and Shiva facilities are discussed in the following articles.

The Janus laser facility was upgraded during 1981 to help fill the experimental gap until Novette and Nova come on line in 1982 and 1985, respectively (see "Janus" in Section 2). We removed one arm, and we fully image-relayed the remaining arm for performance at 100 to 200 J in the nanosecond regime. Janus may replace Argus as a large-aperture, moderate-energy laser for supporting development activities while the larger, less flexible systems are devoted to target-irradiation experiments.

Author: O. C. Barr

Argus Operations

We began 1981 by cleaning the 10- and 20-cm disk amplifiers in the north and south laser chains of Argus. After cleaning, the 20-cm disk amplifiers from the south arm were stored for use as north-arm spares, since all target shots remaining on the schedule for the south arm were to be low-energy shots. Removal of these large-aperture amplifiers allowed a shorter cooling period between laser shots, which resulted in a higher shot rate without noticeable degradation of the beam wavefront. To analyze the increased volume of data generated, we added a number of small software programs to the Argus PDP 11/34. This allowed us to produce more useful information, while at the same time releasing personnel for other duties on the Novette or Nova teams.

During January, we attempted to alternate north- and south-arm shots, believing this to be the most efficient use of the laser facility. In effect, we divided Argus in half, using the south amplifier chain for target shots and the north amplifier chain for measurements of conversion efficiency and for engineering-development tests associated with the Nova/Novette effort. The division of Argus proved, finally, to increase the error rate beyond an acceptable level; confusion arose from continual adjustment of components between mutually incompatible settings and from interference between south-arm target-alignment procedures and the north-arm alignment and test shots. At the end of the month, the target-experiment effort was reduced to a single shift, allowing time in the evening for a second shift devoted to north-arm developmental work.

In January, we continued a series of wavelength-scaling experiments on the south arm, confirming the desirability of operating Novette and Nova at the second (2ω) or third (3ω) harmonic of the laser frequency. One of our concerns about operating at these shorter wavelengths was personnel safety. We tested an optical material (Schott OG-560 laminated with KG-3 glass) for protection at all harmonics of the laser frequency. We soon found that this material bleaches when exposed to high-intensity green (2ω) light and momentarily

becomes nearly transparent. Thus, in early January, we issued a warning to the general laser community against using this filter glass for eye protection from 2ω light (see "Laser Safety Goggles," later in this section).

The 3ω target-shot series begun in September 1980 (Ref. 1) was completed in late January of 1981. We extended this experiment for several weeks to include a series of energy-transport experiments using a visible-light streak camera supplied by H Division of LLNL. In addition to the H-Division streak camera, we fielded several other new experiments in the target-diagnostics area

- An x-ray transmission grating that provides low-energy (0.1 to 2.0 keV) x-ray spectra with moderate ($E/\Delta E \approx 20$ to 50) spectral resolution.
- An x-ray-transmission-grating/streak-camera assembly that provides low-energy x-ray spectra with good ($\Delta t \approx 15$ to 30 ps) temporal resolution.
- An optical-spectrograph/streak-camera system that provides time-resolved optical spectroscopy for stimulated Raman shifting (709 nm) of the frequency-converted laser energy.
- An x-ray streak-camera/"Barbee-crystal" system featuring a synthetic x-ray structure that provides energy channels with moderate ($E/\Delta E \approx 40$) resolution.
- An x-ray transmission-grating/grazing-incidence spectrometer providing high-resolution, time-integrated measurement of subkilovolt x rays.

In February, to complete a consistent set of target-scaling experiments, we reconfigured the beam-diagnostics assemblies and target chamber for 1.06-μm (1ω) laser light and measured target response to an equivalent set of laser shots. The final shots in the low-power wavelength-scaling study were fired in early June.

During this same period, we measured the conversion efficiency from 1ω to 4ω (0.27 μm). This frequency conversion was a two-step process, in which we first doubled the fundamental to 2ω and then doubled the second harmonic to get 4ω. The best 2ω-to-4ω conversion efficiency we measured was 64% at 1 GW/cm^2. These tests demonstrated to us that the potassium dihydrogen phosphate (KDP) doubling crystal itself has a nonlinear absorption of 4ω light that becomes effective at intensities above 0.8 GW/cm^2. This nonlinear absorption reduced the 2ω-to-4ω conversion efficiency attainable at high power to 20% for the particular crystal used. To investigate the variation of conversion efficiency with intensity, we illuminated the first doubling crystal with 1ω intensities in excess of 8 GW/cm^2, reaching new levels of 2ω beam fluence.

In March of 1981, the second shift returned to an investigation (begun in December 1980) of several conversion-crystal orientations to determine the configuration most suited to system operation. In these experiments, we studied details of the variation of conversion efficiency with alignment and intensity. Following these experiments, we began tests of a prototype 15-cm clear-aperture crystal array. We converted Argus to supply a 15-cm-diam beam by reversing the north-arm final spatial filter. These tests supplied data from which to determine whether the operational 74-cm clear-aperture array required an internal support.

In the final north-arm study, we tested the index-matching fluid chosen for the Novette crystal array under transverse Raman and Brillouin gain conditions simulating the intensity/diameter product of Novette. Measurements of gain for these fluids indicated that either FC 104 or HC 56 should be acceptable.

Following design guidelines originated during the 4ω conversion-efficiency experiments, we reconfigured the main beamline and beam diagnostics for a short final series of target shots with 2ω light at nearly four times the energy of previous experiments. We moved the Q-switched laser on the north-arm beam-diagnostics tables to the south arm to help align the crystal and target for these experiments; we also reinstalled the south-arm 20-cm disk amplifiers.

In the following articles, we describe the configurations, procedures, and experimental details of the various tasks performed during the year.

Author: J. S. Hildum

Wavelength-Scaling Experiments. We completed the third-harmonic (3ω) portion of our wavelength-scaling experiments on January 21, 1981. This four-month experimental series was completed with a final

round of 36 target shots, bringing the total to 151 target shots supported by 233 rod shots for system alignment and checkout.

We began to prepare the south arm for 1ω target shots in February. Our reconfiguration of the laser-output beamline and the target-alignment diagnostic packages to return to 1ω operation was greatly simplified by the fact that, in most cases, the only change necessary was the replacement of the optical elements with similar 1ω coated optics. Significant simplifications of the beam paths (Fig. 6-1) were also possible. We removed the doubling and mixing crystals and the crystal-alignment optics. The actively mode-locked, Q-switched (AMQ) oscillator was replaced by a 4-W cw YAG oscillator that we used for centering and focusing the north target-chamber lens and for preliminary alignment of the south lens. The backlighting function of the AMQ oscillator was performed by a similar cw laser located on the north side of the target chamber. The incident-beam energy and temporal profile were already measured in the 1ω incident-beam-diagnostic (IBD) package, so the portion of the incident beam reflected by the diagnostic beam splitter was used only for the equivalent-plane multiple-image camera (MIC). The backreflected streak-camera fiducial, which we had obtained from the 3ω IBD during the previous experiments, was changed to a fiber-optic path. We eliminated the beam periscope we had used for backlighting the target in the 3ω layout, and we no longer needed a beam dump to remove unwanted frequencies. All other elements of the beam-diagnostic packages were functionally the same.

We aligned the laser beam to the target with a technique developed for the 3ω experiments and described in the *1980 Laser Program Annual Report*.[2] Since we did not

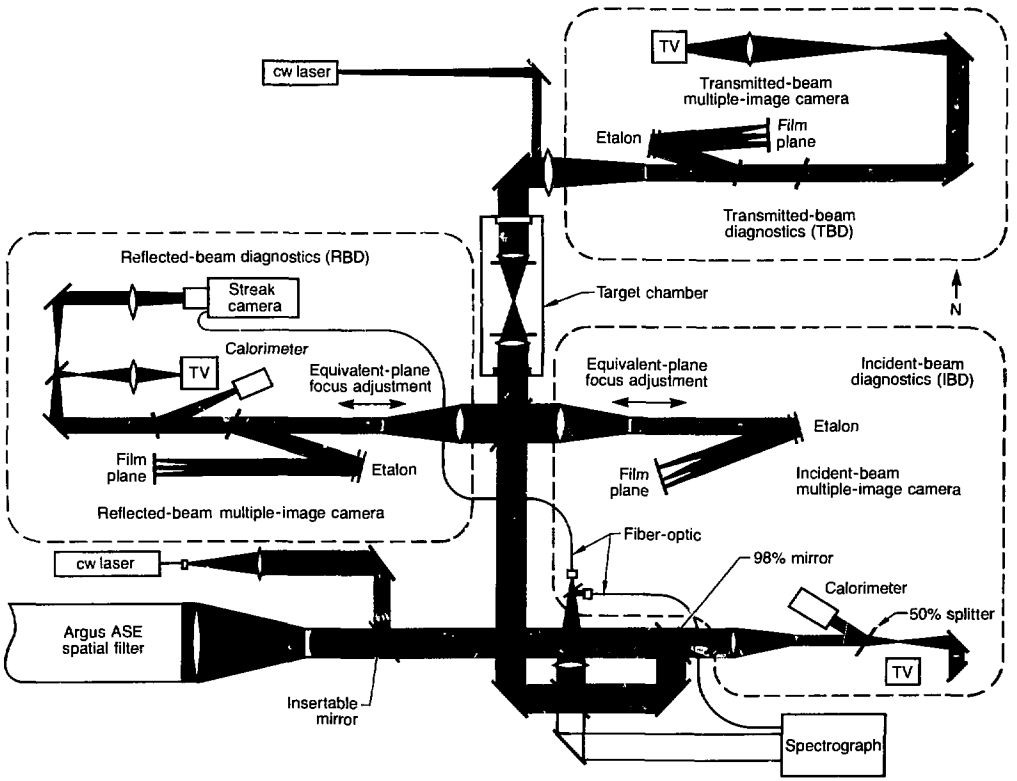

Fig. 6-1. Schematic of the laser beam and optical diagnostics for Argus 1ω wavelength-scaling experiments.

have to align the frequency-conversion crystals, the alignment procedure was greatly simplified and shortened. Coupled with the faster cooling of the laser, resulting from removal of the 20-cm-aperture disk amplifiers, this enabled us to increase the daily shot rate to as many as five shots in a 9-hour day.

Upon completion of the 1ω shot series, which included 221 target shots and 974 rod shots (for alignment, timing, and diagnostic purposes), we began conversion of the south arm for a short series of high-power 2ω target shots. We modified the optical configuration originated for the 3ω target experiments to allow for the higher beam fluences and for target energies of 200 J in 700 ns. This required reinstallation of the 20-cm disk amplifiers previously removed from the south arm. Since we were still limited in diameter to an 8-cm beam, both by our wish to perform experiments directly comparable to the wavelength-scaling series and by the size of the available doubling crystals, the peak fluences and intensities required to achieve 200 J at the target exceeded 8 J/cm^2. As a result, we used uncoated fused-silica optics for all five optical elements following the 8-cm doubling crystal (Type I, 10-mm-thick KDP). With a crystal conversion efficiency of approximately 75% and an 8% loss of the 2ω energy at each optical element, we needed a crystal output of 300 J of 2ω light and about 430 J of crystal-input laser energy at 1ω to reach the correct target energy. The fluences in the 8-cm-diam beam were 8.6 J/cm^2 at 1ω and 6 J/cm^2 at 2ω. The 1ω fluence was

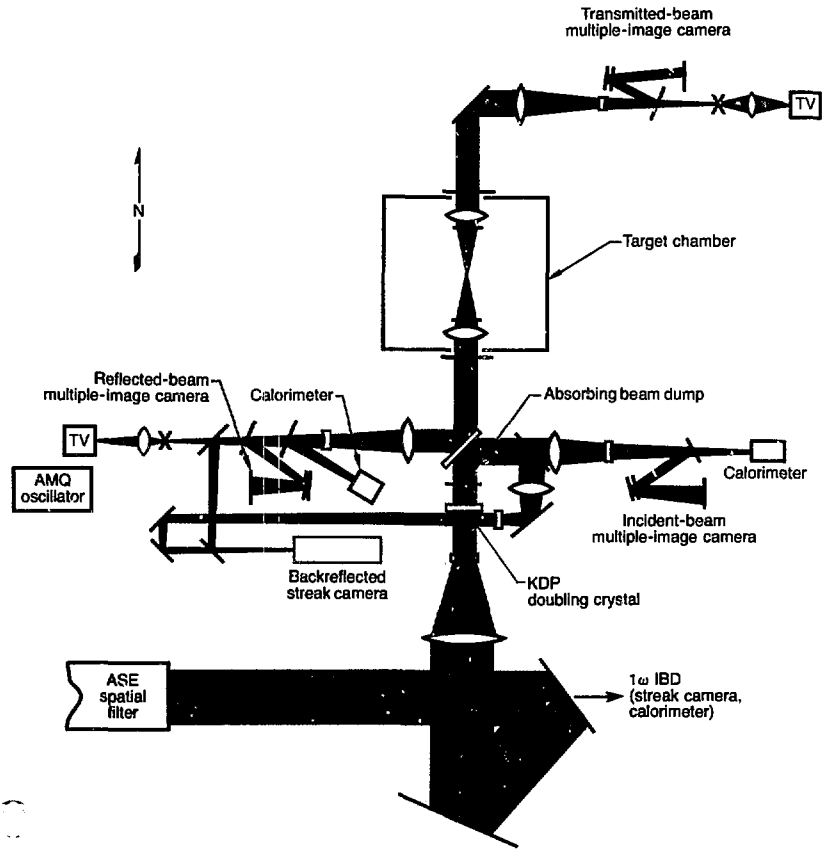

Fig. 6-2. Argus schematic for 200-J 2ω target experiments.

about 50% greater than a typical coating could survive. At 2ω, the fluence was about three times the damage threshold for presently available dielectric coatings.

To achieve an operable optical system with damage thresholds above these levels, we moved the beam-reducing telescope from the laser output to a point between the final turning mirror and the doubling crystal (Fig. 6-2). The positive lens of this telescope was the final coated optic in the beamline. To remove the residual 1ω energy from the target-illuminating beam with uncoated optics, we placed an uncoated absorption filter (LCF1 glass supplied by Hoya Optics USA, Inc.) immediately following the KDP crystal. During the ensuing experiments, we generated damage tracks in the KDP crystal and in all of the optical components between the 1ω beam dump and the target, but we did not damage the beam dump.

The beam splitter for the 2ω incident-beam fiducial on the backreflection streak camera was placed before the 2ω-IBD reducing telescope so that equivalent-plane focusing changes would not affect the fiducial beam.

For target backlighting and crystal alignment, we used a commercially available AMQ laser capable of generating 2.25 W average power at 2ω. We adjusted the target spot size by moving the target-illuminating lens and inspecting pictures from a transmitted-beam MIC exposed with rod shots prior to the target shot. The preshot alignment procedure for the 2ω target series was essentially the same as that discussed in the *1980 Laser Program Annual Report* for the 3ω series.[2]

The original schedule for the 2ω series included six preliminary shots at a nominal target energy of 100 J and four shots at 200 J. We were able to deliver nine extra 100-J shots and two extra 200-J shots for these prototype Novette targets. In addition, we fired 15 shots in the range from 100 to 200 J onto gold disks to check target-diagnostic equipment. A preliminary series of 16 lower-energy shots on gold disks provided energy-scaling information for comparison with earlier low-energy 2ω data and also "burned in" the doubling crystal (see "Damage Studies" in Section 7). For installation alignment, timing, target-chamber transmission, and preshot alignment, we also fired 529 rod and partial-system shots.

Author: J. S. Hildum

Fourth-Harmonic Conversion-Efficiency Experiments. We designed a series of frequency-quadrupling experiments using 10-cm-aperture KDP crystals to explore the possibility of generating and subsequently delivering to a target approximately 30 J of 4ω light in a 1-ns laser pulse. These experiments included measurements of 2ω-to-4ω conversion efficiency as a function of 2ω intensity and crystal thickness and also in terms of near-field photographs of the 4ω spatial-intensity distributions. Figure 6-3 displays the conversion-efficiency results from this series.

We obtained external conversion efficiencies from 2ω to 4ω (uncorrected for Fresnel reflection losses) of up to 64%, with 2ω intensities near 1.5 GW/cm^2, using a 1-cm-thick KDP crystal. We obtained output 4ω energies of slightly more than 50 J (over 80 GW) with 2ω input energies above 310 J (nearly 500 GW). Table 6-1 summarizes the published 4ω conversion efficiencies and multiphoton-absorption coefficients, β, for various quadrupling crystals. With optimum crystal thicknesses, we believe overall external conversion efficiencies of more than 50% are possible.

We arranged the Argus diagnostic optics for the 4ω studies in a format similar to the earlier 3ω experiments,[2] although the alignment of the crystals was more complex. This series of conversion-efficiency measurements was the first on the north arm since we had determined that the photographic procedure used earlier was inherently flawed.[2,3] We replaced the photographic procedure with a direct-alignment technique using the auxiliary AMQ YAG oscillator that was later used on the south arm for optical alignment of the high-power 2ω experiments (described above). We adjusted the AMQ laser to be collinear with the Argus main alignment laser, using a long-focal-length lens and TV camera for pointing alignment. The peak power from the AMQ laser was enough to generate a detectable level of 4ω light. This output was maximized by angle-tuning the two crystals.

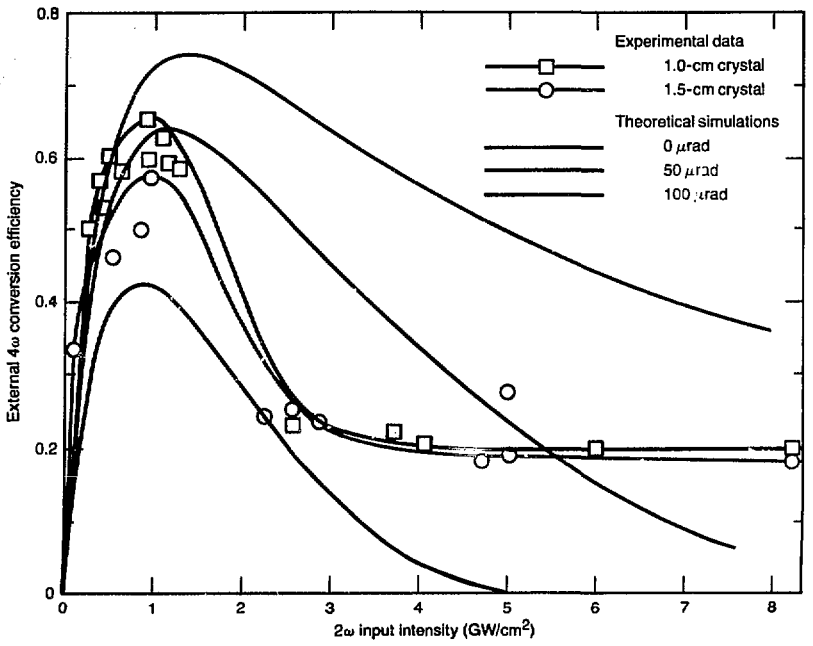

Fig. 6-3. Variation of 4ω conversion efficiency with 2ω intensity for two crystal thicknesses.

Table 6-1. Comparisons of nonlinear absorption coefficients and 4ω conversion efficiencies for selected crystals.

Crystal	Absorption coefficient, α_2 (cm/GW)	Wavelength (μm)	Thickness (cm)	Intensity (GW/cm²)	External 4ω conversion efficiency (%)	Reference
KDP	—	—	0.7	1.5	45	4
KD*P	—	—	2.0	0.02	40	5
KDP	5.9×10^{-12}	0.53	—	—	—	6
KD*P	6.4×10^{-12}	0.53	—	—	—	6
ADP	6.6×10^{-12}	0.53	—	—	—	6
KDP	2.7×10^{-10}	0.27	—	—	—	6
ADP	2.4×10^{-10}	0.27	—	—	—	6
KDP	5×10^{-10}	0.27	1.0	1.1	64	7
KDP	4×10^{-10}	0.27	1.5	1.1	55	7
KDP	4×10^{-10}	0.27	1.0	0.3	22	7
KD*P	2.7×10^{-11}	0.27	0.4	0.6	69	8
ADP	4.0×10^{-11}	0.27	0.4	0.6	78	8
KD*P	—	—	2.0	0.01	5	9
KDP	—	—	0.8	2.0	26	10
ADP	—	—	1.2	3.0	24	10
KD*P	—	—	2.0	0.03	30	11
KD*P	—	—	1.7	0.05	33	12
ADP	—	—	2.0	0.11	18	13
ADP	—	—	1.8	0.11	27	13

*All of data in this column are ± 30%.

We measured fundamental and harmonically converted input and output energies using a total of six calorimeters. The important energy measurements were

- Input to first crystal: 1.06 μm.
- Output from first crystal: 1.06 μm.
- Output from first crystal: 0.53 μm.
- Output from second crystal: 1.06 μm.
- Output from second crystal: 0.53 μm.
- Output from second crystal: 0.27 μm.

Energy measurements were complicated by the appearance of a nonlinear energy-loss mechanism, whose cause we had to determine. We found significant nonlinear losses

in the second KDP crystal at incident 2ω intensities higher than 2 GW/cm^2. Using the optical layout shown in Fig. 6-4, we discovered that the energy imbalance was present when significant 4ω output was generated; however, at the same 2ω energy input to

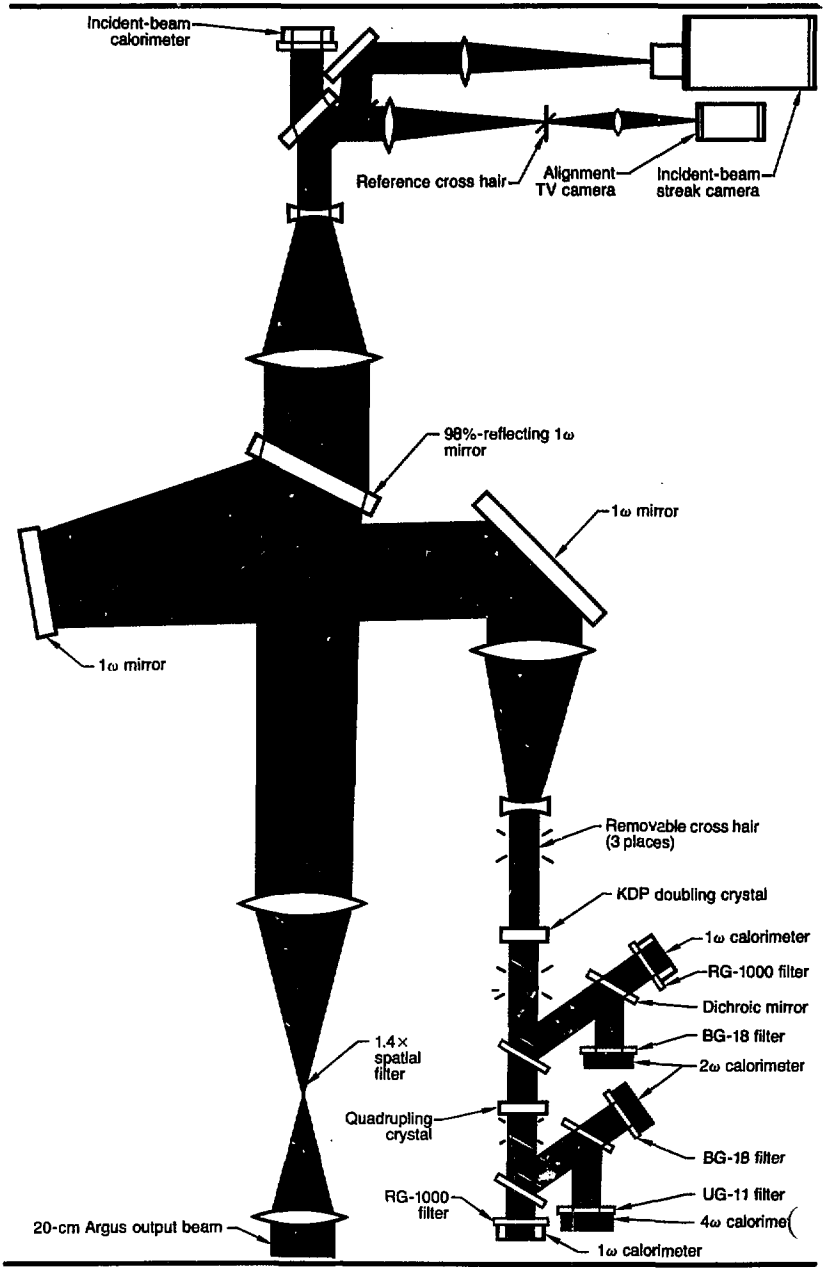

Fig. 6-4. Schematic of the Argus north-arm 4ω experiments.

the same crystal, detuned to a 180° phase mismatch, little 4ω output was generated, and our calorimeters showed energy balance. Therefore, the imbalance consisted of energy converted to 4ω and then absorbed by the crystal.

Multiphoton absorption may be the cause of our observed losses in 4ω energy, since it was evident that we had spatial high-intensity spikes in our 4ω output beam. From the significant amount of internal damage (discussed below) observed in the fused-silica optics following the quadrupling crystal, it is evident that small-scale self-focusing contributed to the observed bulk damage. Given the physical evidence of damage to both the bulk glass and the dielectric coating, it is likely that small-scale multiphoton absorption was the major loss mechanism in our experiments.

Computer simulations of two-photon absorption, using the values published in the literature[4–13] for the two-photon absorption coefficient (β), have exhibited general agreement with our measurements. Complete agreement with details of the relatively rapid onset of nonlinear absorption observed in our 4ω experiments will require a more sophisticated code. The present code does not include the effects of nonlinear self-focusing, nor does it include the second-order variations in two-photon absorption caused by beam spatial nonuniformities.

Our computer models suggest also that higher 4ω intensities may be achieved if we use thinner quadrupling crystals. Thus, a 0.5-cm-thick crystal of 10-cm aperture should be able to deliver between 75 and 100 J of 4ω light before reaching the asymptote. KDP is still a good candidate for such an experiment, since, as indicated in Table 6-1, the measured values for the two-photon absorption parameter for ammonium dihydrogen phosphate (ADP) and potassium dideuterium phosphate (KD*P) are the same as KDP within experimental error. Delivery of this energy to a target requires careful consideration, since, given intensity modulations similar to those on the Argus 1ω beam, such a beam may be capable of damaging all of the subsequent fused-silica optics if we attempted high-fluence target experiments at this level.

The damage that we experienced included damage to dielectric coatings and heavy internal damage to uncoated fused-silica optics. We were surprised that this damage and the nonlinear loss mechanisms appeared at the relatively low 4ω intensities present in our experiments. The data showed that, if the UV intensities are kept at or below the 1.0-GW/cm^2 level, target-irradiation experiments at 4ω may be feasible using thin-quartz (Supersil-I) optics.

Substantial bulk damage ("angel hair" and large, arrow-shaped tracks) was suffered by the uncoated fused-silica diagnostic beam splitter placed in the main laser beam following the quadrupling crystal. Most of the internal damage to the quartz optics was observed following a 50-J 4ω shot. No internal damage was observed in either the doubling crystal or in the quadrupling crystals; however, a small crack appeared on the input face of the 1.0-cm-thick KDP quadrupling crystal as evidence of the 175 J of 4ω light absorbed by the crystal during a pulse in which only 50 J of energy was measured by the 4ω-sensitive calorimeter.

Although we used uncoated optics for the entire main beamline during the 4ω experiments, all of the coated optics placed at off-line locations downstream from the 4ω crystal and coupled to the main beam with 4%-reflectance uncoated beam splitters were heavily damaged by a mixture of 1ω, 2ω, and 4ω light. These coated optics damaged at average fluences of less than 0.3 J/cm^2. The 4ω dielectric-coated beam dumps were especially susceptible to damage, with damage occurring at average fluences of less than 0.1 J/cm^2.

In spite of the foregoing difficulties, we have generated 4ω light at an intensity high enough (1 GW/cm^2) to permit the consideration of 4ω target-irradiation capabilities for Nova. A frequency-quadrupler enjoys one operational advantage over a frequency-tripler: alignment for the first crystal in the quadrupler is set for maximum generation of 2ω light, independent of input intensity or crystal thickness.

We conducted a series of experiments to obtain near-field photographs of the 4ω beam. To avoid the need for large-aperture, narrow-band UV filters, we designed and assembled a stigmatic fused-silica imaging system to project the equivalent near-field plane onto a photographic plate. Beam attenuation was achieved using reflections from high-quality uncoated optical flats.

Most photographic plates are extremely sensitive to exposure to UV light, and we experienced considerable difficulty in reducing the beam intensity sufficiently to obtain a linear 4ω exposure suitable for scanning and digitizing. The 4ω beam has an appearance similar to the near-field pictures obtained on the Argus north arm for the harmonically converted 2ω and 3ω output beams.

In collecting these data, we fired 67 system shots to measure conversion efficiency, together with 160 preamplifier and system shots used to align and adjust the laser and the diagnostics.

Author: G. J. Linford

Major Contributor: C. L. Vercimak

Frequency-Conversion-Array Experiments. This year, we completed tests (begun in November 1980) on a research model of the Novette frequency-conversion crystal assembly. The purpose of these tests was to demonstrate that the same pair of crystals could be used in tandem to give efficient doubling and in a cascade configuration to convert efficiently to 3ω. The change from one configuration to the other required rotating the second crystal 90° with respect to the first crystal.

Another, newer configuration also yielded efficient doubling. This configuration involves the use of the crystal pair in its cascade configuration, but with a different beam angle of incidence. A simple rotation of the assembly in this quadrature doubling mode converts the output from 2ω to 3ω. The advantage of this configuration is that we may convert from one harmonic to another without disassembling the crystal housing. The output in the quadrature doubling mode is elliptically polarized 2ω light. The frequency-doubled light from a single doubling crystal is plane polarized. (See "Frequency Conversion and Target Focusing" in Section 2 and "Harmonic Conversion" in Section 7 for detailed discussions of this conversion scheme.)

We enjoyed a high data-collection rate for our crystal-array experiments because they required only the preamplifier output energy. The rod amplifiers in this portion of the laser may be fired every 5 min

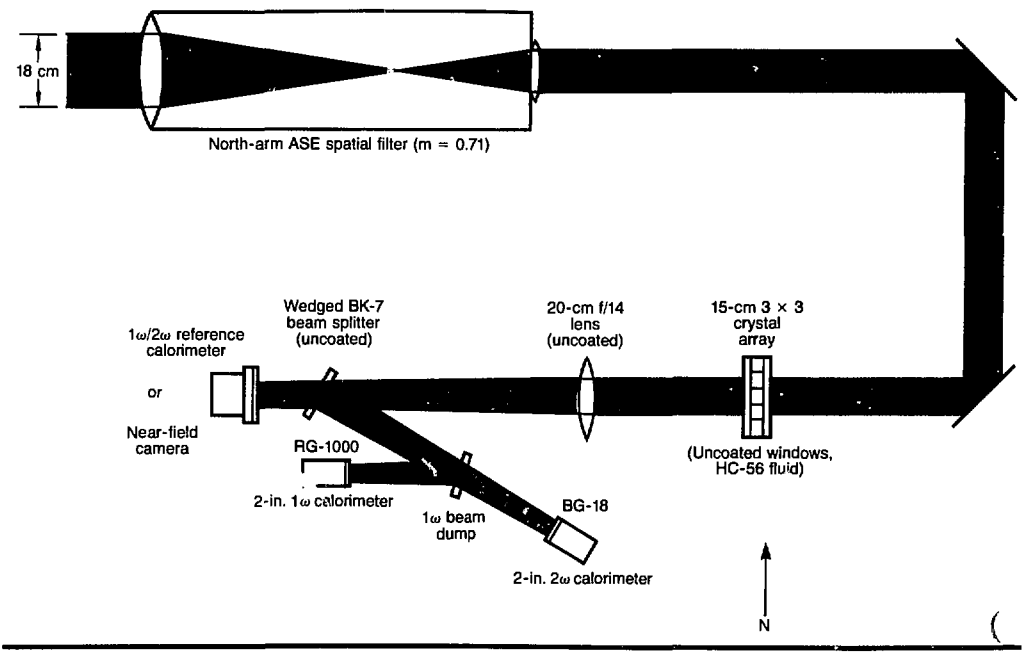

Fig. 6-5. Schematic of the Argus north-arm crystal-array experiments.

(compared to the 1-h cycle time for the 10-cm disk amplifiers).

We next investigated a developmental model of the Novette crystal array to determine the effect of crystal spacing and support structure on beam propagation and the contributions of individual crystal segments to net conversion efficiency. For this experiment, we used a 15-cm-aperture array of nine square crystals. To optimize the tradeoff between beam intensity and beam diameter, we reversed the north-arm final spatial filter to reduce the output-beam diameter from 25 to 12.6 cm. This beam was then used without further reduction; the setup is shown schematically in Fig. 6-5. An uncoated Shiva f/14 output spatial-filter lens having a 296-cm focal length was installed 60 cm after the crystal array to reduce the beam diameter for the smaller-aperture diagnostics (calorimeters and cameras). The center crystal of the array was aligned with an auxiliary Q-switched Nd:YAG alignment laser that was adjusted to be collinear with the main beamline. Frequency-doubled (2ω) alignment pulses were monitored with a photodiode/oscilloscope combination. Alignment of the crystal array was checked and adjusted prior to system shots.

On several of our system shots, we placed a 2ω near-field camera approximately 1.6 m from the f/14 lens. Figure 6-6 is an enlarged photograph of a beam taken on a rod shot. This photograph shows that each of the segments was aligned well enough to produce a similar 2ω output, so the array is behaving to a first approximation as a single crystal. In photographs taken at high power, we saw a similar balance between the crystal segments. For these high-power shots, we measured internal conversion efficiencies approaching 70% for some crystal segments.

The small irregularities observable near the edges of the middle crystal segment in Fig. 6-6 were generated when a reflection from the camera's filter glass was inadvertently directed (and imaged by the f/14 collecting lens) onto the metal "egg-crate" support-structure bar. The front side of the egg-crate was protected from the input beam by a specially designed 1ω-absorbing mask. A second mask was added to the back side of the array to preclude additional damage, and flat surfaces in the diagnostics paths were tilted to avoid unwanted backreflections (see "Novette Crystal Arrays for Harmonic Generation" in Section 2).

Collection of these data required a total of 39 system shots to measure conversion efficiency and to generate photographs. We fired an additional 85 shots for setup and alignment of the diagnostic optics and the laser.

After completion of the crystal-array tests, we again reversed the output spatial filter, returning it to the normal Argus configuration. The resulting 24-cm output beam was then reduced with a $0.33\times$ telescope to the 8-cm diameter used in most of our frequency-conversion tests. After doubling the frequency, we expanded this beam with a cylindrical lens and recollimated the major-axis rays of the resulting elliptical beam with a spherical lens when the beam size reached 16×8 cm. The minor-axis rays, which were converging following the spherical lens, passed through a line focus. A test cell for the index-matching fluid was placed at the point where the minor axis was 10 mm in diameter. A vacuum chamber behind the test cell prevented an air spark

Fig. 6-6. Beam-profile photograph of 2ω light from the prototype crystal array.

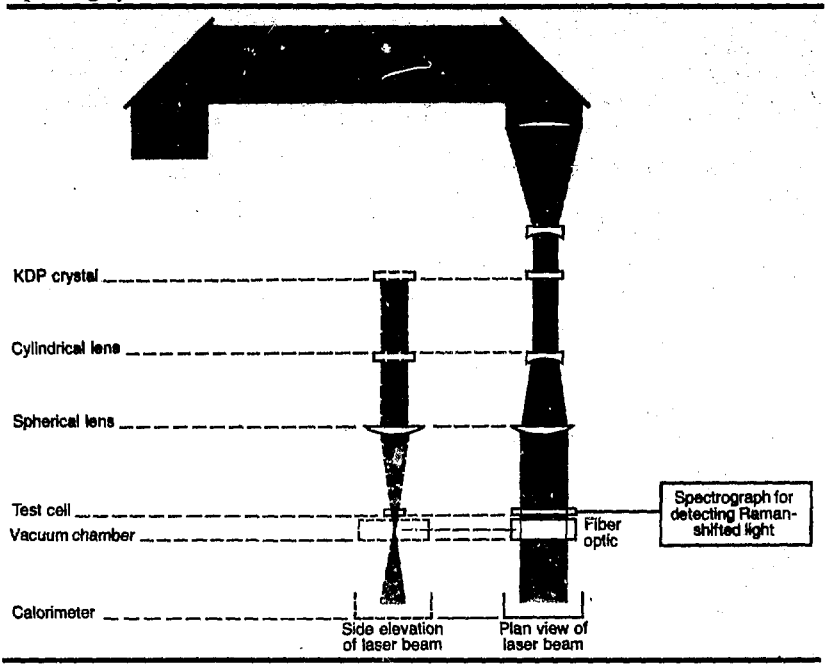

Fig. 6-7. Schematic of the Argus north-arm index-matching-fluid experiments.

at the line focus of the beam. This arrangement is shown in Fig. 6-7.

We chose the dimensions of the illuminated volume of the test cell so that the available frequency-converted energy from Argus would be capable of simulating the conditions of the Nova intensity/diameter product. Limited by available calorimeters and other components to a beam whose major axis was only 16 cm, we operated this system near the damage threshold of several optical components. We destroyed test-cell windows while obtaining the data required to identify index-matching fluids suitable for Nova conversion-crystal arrays.

This experimental series included 31 system shots for fluid tests and 60 rod and partial-system shots for setup and calibration.

Authors: W. L. Smith, M. A. Summers, and B. C. Johnson

Major Contributors: W. C. Behrendt, R. D. Boyd, B. L. Freitas, C. P. Hale, G. J. Linford, L. K. Smith, K. D. Snyder, C. L. Vercimak, and J. D. Williams

Completion of the Argus Project. We shut down the Argus laser facility and removed the laser equipment from the high bay of Building 381 during August and September of 1981. This area is being upgraded in preparation for installation of the Novette laser system.

The Argus project officially began in January of 1975; the final shots were fired 80 months later. In the interim, the facility exceeded its performance design goals by almost a factor of 2 and proved to be a highly versatile research instrument. We amassed a large body of data on directly driven and radiation-driven targets. Furthermore, Argus was the first laser facility to compress the fusion fuel to a density significantly higher than that of liquid D–T. The laser's last contribution to the understanding of target physics was made in a study of the effect of the irradiation wavelength on target response.

We used the laser not only for the primary purpose of target-physics investigation but also as a test bed for new laser-design concepts, including multiple spatial filters, beam apodization, and image-relaying of

beam-defining hard aperture from one spatial-filter input lens to the next. This latter concept is currently employed in virtually every large facility within the laser community. In addition, we used Argus to study many aspects of Shiva and Novette/Nova engineering, laser-staging optimization, crystal-array configurations, index-matching fluids, and component cooling.

During more than five years of Argus operations, we fired 2850 system shots, including 1270 target shots and 980 shots used to characterize the laser-system output and calibrate the beam diagnostics. During the last two years, 600 shots were directed toward laser-development studies. We fired an additional 9100 rod-amplifier shots to determine gain settings for target shots, take beam-profile pictures, and troubleshoot the system. Among the many events in Argus' history, the milestones listed in Table 6-2 are especially significant.

Author: W. W. Simmons

Major Contributor: J. S. Hildum

Nov 1974	Building 381 high bay completed.[14]
Jan 1975	Argus program inception.[15]
July 1975	First parts fabricated.[15]
Oct 1975	First components installed.[15]
Jan 1976	Rod-amplifier stages operational.[15]
Apr 1976	North-arm B-disk amplifiers operational (0.8 TW) (Ref. 15).
June 1976	Single-beam target experiments (1.3 TW, 1×10^8 neutrons).[15,17]
July 1976	Full system operational (2.2 TW) (Ref. 16).
Aug 1976	Two-beam target experiments (5×10^8 neutrons).[16,17]
Sep 1976	Neutron time-of-flight diagnostic on line.[16,18]
Sep 1976	Project goal reached (3 TW focusable power).[16]
Oct 1976	Target shot (10^9 neutrons).[16,17]
Nov 1976	Partial relaying (4.2 TW, 2×10^9 neutrons).[16,17]
Nov 1976	Zone-plate imaging of x rays and alpha particles.[16,19,20]
Jan 1977	Actively mode-locked oscillator installed.[21]
June 1977	Two-step-shaped pulses (3 TW) (Ref. 21).
Sep 1977	Stimulated-Brillouin-scattering studies.[22]
Dec 1977	Full relaying (5+ TW, 100 ps; 900 J, 300 ps) (Ref. 23).
Feb 1978	Long-pulse operation (2 kJ, 1 ns) (Ref. 24).
Sep 1978	High-density campaign (Dante fielded).[25]
Nov 1978	Radiation-chemistry experiment fielded.[26]
Dec 1978	Ultraclean operations (5 TW, 2 kJ) (Ref. 27).
Mar 1979	Transport-inhibition measured on layered target.[28]
June 1979	Planar-triode-driven switchout.[20,29]
Oct 1979	2ω target experiments (30 J, 700 ps, 0.53 μm) (Refs. 29 and 31).
Jan 1980	Earthquake recovery.[32]
Apr 1980	2ω conversion-efficiency experiments (80%, 113 J, 600 ps, 0.53 μm) (Ref. 33).
July 1980	3ω conversion-efficiency experiments (70%, 54 J, 600 ps, 0.35 μm) (Ref. 33).
Sep 1980	3ω target experiments (70%, 54 J, 600 ps, 0.35 μm) (Ref. 33).
Nov 1980	Tandem-crystal doubling studies.[34]
Mar 1981	4ω conversion-efficiency experiments (320 J, 6.4 J/cm^2, 0.53 μm; 24%, 50 J, 0.27 μm).
May 1981	Crystal-array studies.
June 1981	Completion of wavelength-scaling studies.
Aug 1981	2ω target experiments (240 J, 600 ps, 0.53 μm).
Aug 1981	Index-matching-fluid studies.
Aug 30, 1981	Argus program completion.
Aug 31, 1981	Disassembly begun.

Table 6-2. Argus project milestones, 1974-1981.

Laser Safety Goggles. Research with laser harmonic conversion requires that personnel be protected from high-intensity light spanning a wide spectral range. In the case of our harmonic-conversion experiments on the Argus laser, the range of wavelengths for which eye protection is essential extended from 1.06 μm in the infrared to 0.27 μm in the UV. The green-colored KG-3 glasses that we use for protection against 1ω radiation (1.06 and 1.05 μm) and 4ω radiation (0.27 and 0.26 μm) have too low an optical density for protection against 2ω and 3ω laser radiation. We therefore considered using filter glass as one component of a laminated safety lens, with KG-3 as the other portion, to eliminate the harmonics of both frequencies while retaining sufficient transmission of visible light to permit personnel to work efficiently in the laboratory.

The safety-goggle vendors selected Schott OG-560 filter glass, since their transmission measurements indicated that the optical density of OG-560 was adequate to remove the harmonics of both 1ω wavelengths while transmitting the red-yellow portion of optical spectrum. The goggle vendors measured the transmission of OG-560 using low-intensity incoherent light; their specifications are given in Table 6-3.

At LLNL, however, we measured the transmission of the glass material at intensities similar to the most stringent conditions that we would expect to find in our laboratory. For our tests, we used a pulsed alignment laser generating 1ω, 2ω, and 4ω beams at moderate intensity (up to 50 MW/cm^2); the test apparatus is shown in Fig. 6-8. The filter glass was inserted into the 2ω or 4ω beam emanating from this laser. An uncoated, fused-silica beam splitter reflected approximately 8% of the incident beam to a fast PIN-8 Schottky-barrier photodiode. The main beam was directed either into a beam dump or into a calorimeter to measure the average output power. We ran the laser at 10 pps, producing 200-mJ 2ω pulses of 20 ns

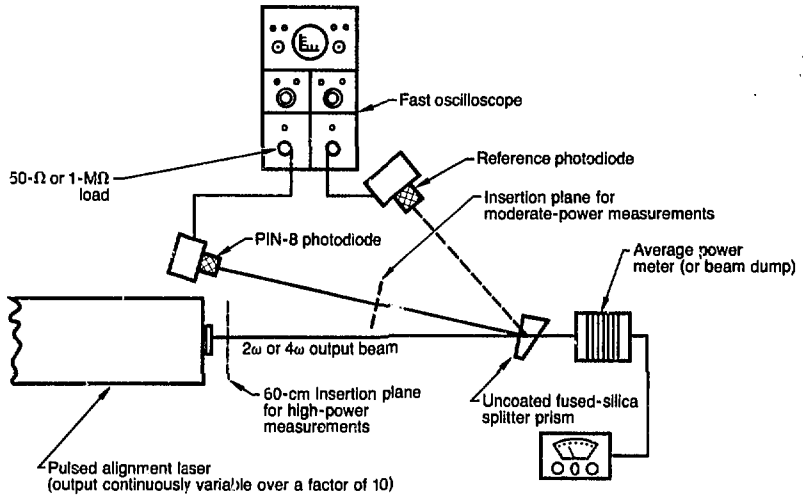

Fig. 6-8. Schematic of high-power transmission measurements of OG-560 filter glass.

Table 6-3. Vendor transmission specifications on OG-560 filter glass.

Wavelength (μm)	Transmission
1.06	$10^{-6.75}$
0.53	$10^{-6.75}$
0.35	10^{-13}
0.27	10^{-20}

Table 6-4. LLNL transmission measurements of OG-560 glass at 2ω and 4ω.

Wavelength (μm)	Flux (MW/cm^2)	Transmission
0.53	1.25	10^{-5}
0.53	10.0	0.17
0.27	0.3	0.016
0.27	2.5	0.064

duration, resulting in an average power of 2 W at 2ω and a peak power of 10 MW. For the 4ω measurements, we again operated the laser at 10 pps, producing 50-mJ pulses of 20 ns duration, for an average power of 0.5 W and a peak power of 2.5 MW.

Table 6-4 gives a summary of our preliminary transmission measurements. Note that 4ω light produces a large amount of fluorescence in the glass; hence, the indicated transmissions may not be composed entirely of 4ω radiation (no interference filters at 4ω or 2ω were available for this experiment). However, our high-intensity measurements were taken with the sample located approximately 130 cm from the photodetector, whereas the lower-intensity measurements were made approximately 30 cm from the photodetector. When we introduced a borosilicate (BK-7) window into the 2.5-MW/cm^2 4ω beam, essentially no transmitted light was measured by the photodetector. Our apparatus could not measure an optical density greater than five.

The original specifications on the Schott OG-560 filter glass are provided in Table 6-4. For fluxes less than 1 MW/cm^2, our measurements of the OG-560 glass agree with these specifications. At incident intensities higher than 1 MW/cm^2, however, the laminated OG-560/KG-3 laser-safety lenses bleached. This indicates that safety glasses utilizing OG-560 (or other OG- or RG-series glasses) are not adequate for eye protection from 2ω radiation if there is any possibility of the incident laser intensity reaching 1 MW/cm^2. This intensity level is easily attained in a specular reflection, for example, or by direct exposure to the harmonically converted alignment beam in our laboratory.

We therefore recommend that no personnel working with moderate- or high-power sources of laser radiation from 0.30 to 0.55 μm use the OG-560/KG-3 composite glasses to protect their eyes from direct illumination. Furthermore, we do not recommend the OG-560 material for use in unlaminated safety glasses; it is not annealed and may shatter if struck with a flying object. We are presently using KG-3 glasses to protect against 1ω light, and we

are using argon safety goggles, worn over the KG-3 glasses, to protect against 2ω and 3ω radiation.

Many of the currently available filter glasses (OG-515 to 590 and RG-610 to 780) that have the required spectral-absorption characteristics for protection against visible laser light are distinctly orange in color. They contain CdSe and CdS as dopants; both these substances are well-known semiconductor-saturable absorbers.[35] The resulting band gap of the mixture of CdSe and CdS is determined by the relative ratio of CdSe to CdS.

The bleaching action in the CdS and CdSe occurs when a sufficient number density of valence electrons is raised into the conduction band. Presuming that the lifetime for electron-population redistribution is comparable with or longer than the saturating laser pulse, then bleaching of the semiconductor absorption occurs when the number density of valence electrons has been reduced to a small fraction of its initial value, i.e., when the incident laser intensity lying in the spectral vicinity of the band gap is sufficiently great. In the present instance, this threshold appears to occur for OG-560 for 2ω (0.53 μm) intensities ranging from 1 to 40 MW/cm^2.

Author: G. J. Linford

Major Contributor: C. L. Vercimak

Shiva Operations

During 1981, Shiva was operated primarily in support of fusion experiments, with few changes in the system. We also devoted some shots to tests of Nova components, required laser-system tests, and calibrations. In the following articles, we discuss the operations of the Shiva laser and target systems and the maintenance history of Shiva's optical components.

Author: O. C. Barr

System Configuration and Performance. We continued to dedicate Shiva to target-irradiation experiments during 1981. The experimental series performed on Shiva included Nova Cone Angle, Nova Cone Angle II, Pinlite, Long-Pulse Cairn Scaling, NPIRE II (with and without backlighter), HEET II, Inferno, Forward Raman, and a test of x-ray laser pumps. We also performed a joint experimental series with the Naval Research Laboratory (NRL). In addition to these target-irradiation experiments, we used Shiva to test components for the Nova laser, including the plasma shutter, 34-cm-aperture calorimeters, target-chamber debris shields, and prepulse diagnostics.

Table 6-5. Summary of high-energy shots on Shiva in 1981.

Total experiments		201
Dedicated shots	171	
Secondary shots	30	
Target shots		126
Target experiments	103	
Diagnostic checkouts	23	
Laser tests and calibrations		31
Dedicated shots	22	
Secondary shots	9	
Nova development shots		44
Dedicated shots	23	
Secondary shots	21	

The total number of experiments was 201, consisting of 171 high-energy laser shots plus 30 secondary experiments that did not require dedicated shots. Table 6-5 gives a breakdown of these 201 experiments by category, and Table 6-6 gives configuration and operation information for each experimental series.

Figure 6-9 shows the 1981 monthly production of high-energy shots, divided into target and nontarget shots; the numbers of secondary experiments not requiring dedicated shots are also shown. For comparison purposes, Fig. 6-10 shows the historical monthly averages of target and nontarget high-energy shots. In early years, the nontarget shots were dedicated to laser testing and preparation for experimental series. In 1981, half of the nontarget high-energy shots were dedicated to Nova laser development, reflecting the maturation of our understanding of Shiva's operation.

Figure 6-11 shows the 1981 profile of full-time labor assigned to Shiva to sustain the shot rate shown in Fig. 6-9. We eliminated the evening shift in late May for a number of reasons. First, summer vacation, travel, and training plans indicated an impending shortage of staff. Second, Argus operations required the assignment of as many as four Shiva technicians at a time to support program-critical experiments from May to August. Finally, the skill mix among our

Experiment	Date	No. of beams	Pulse width (ns, FWHM)	Energy (kJ)	Power (TW)	No. of shots: Primary experiment	Target experiment[a]	Secondary experiment	Total
Setup for Nova cone angle	Jan Feb	2, 3, 10, 18, or 20	5 to 6	0.6 to 7.4	0.1 to 1.5	12	3	1	13
Nova plasma shutter	Feb Mar May July	1	5 to 6	0.2 to 0.5	0.04 to 0.1	21	0	4	25
Nova cone angle	Feb	10 or 11	5 to 6	3.5 to 4.0	0.6 to 0.7	9	9	0	9
Pinlite setup	Feb Mar	1, 3, 10, or 20	—	0.4 to 9	—	9	4	0	9
Pinlite	Mar Apr	9 or 10	—	4 to 5	—	24	24	0	24
Nova debris shields	Apr	1	34	0.5	0.01	1	0	0	1
Scaling setup	Apr May June July	9, 10, or 20	5 to 6	3 to 7	0.5 to 1.4	13	10	5	18
Long-pulse scaling	May June July	19 or 20	5 to 6	5 to 10	0.8 to 1.8	20	20	0	20
Nova 34-cm calorimeter	June July	1	5 to 6	0.3 to 0.5	0.06 to 0.08	1	0	2	3
Prepulse diagnostic	July Aug	1	5	—	—	0	0	15	15
Nova cone angle II setup	July	9	5	3.8	0.8	1	1	0	1
Nova cone angle II	July Aug	10 or 11	5 to 6	3 to 4	0.6 to 0.9	8	8	0	8
NPIRE II/ HEET II setup	Aug	10 or 20	1	3 to 8	3 to 8	3	2	2	5
NPIRE II	Aug Sep Oct	20	0.9 to 1	7 to 9	7 to 10	6	6	0	6
HEET II	Aug Sep Oct	20	0.9 to 1	7 to 9	7 to 9	8	8	0	8
NPIRE II/ backlighter setup	Oct Nov	8 or 10	0.9 or 5	2 to 4	0.3 to 3	4	2	0	4
NPIRE II/ backlighter	Nov	8 or 18	1 and 5	1 to 7	0.2 to 5	4	4	0	4
Cairn	Nov Dec	7 or 10	0.9 to 1.0	2 to 4	2 to 4	3	3	0	3
Inferno setup	Nov	4	0.9	1	1	1	1	1	2
Inferno	Nov Dec	10	0.9	3 to 4	3 to 4	4	4	0	4
Forward Raman	Dec	7 or 10	0.9	3 to 4	3 to 4	2	2	0	2
NRL joint series	Dec	10 or 17	3 to 4	3 to 8	1 to 2	5[a]	5[a]	0	5[a]
X-ray pump setup	Dec	10	0.1	0.1 to 0.2	1 to 2	2	0	0	2
X-ray pump	Dec	10	0.1	0.1 to 0.3	1 to 3	10	10	0	10
Total						171	126	30	201

[a]Target experiment is a subset of primary experiment.
[b]One additional target shot was taken with rod-shot energy only.

Table 6-6. Summary of experimental series on Shiva in 1981.

technicians became unbalanced such that the clean room could not sustain double-shift operation and meet other program requirements.

The shutdown and removal of Argus in August and September, and the construction of Novette, required reassignment of most of Shiva's personnel to the Nova and Novette projects on September 1, 1981 (see "Project Management Systems" in Section 2). Throughout the entire year, virtually all Shiva technicians had collateral assignments to support Argus, Nova, and Novette on a time-available basis; several technicians were assigned on loan to other groups for periods of one week to three months. Conversely, other parts of the laser program loaned technicians to Shiva operations for

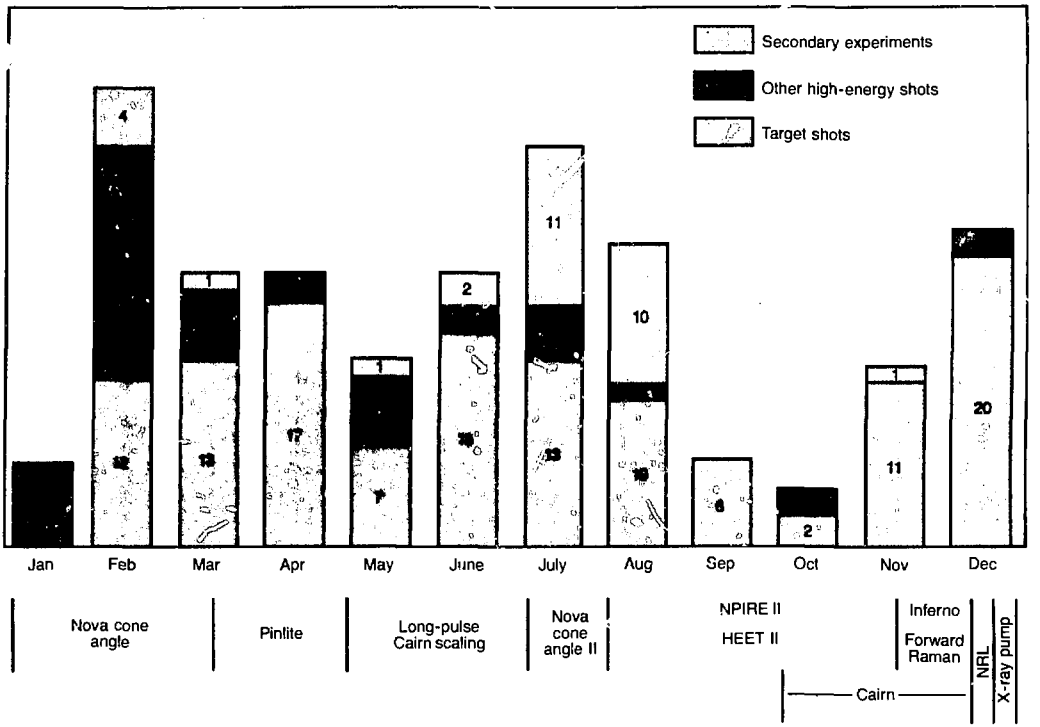

Fig. 6-9. Shiva high-energy shots in 1981.

few hours at a time—frequently on short notice—to repair failed equipment and restore the system to operation.

In addition to requiring personnel, Novette affected Shiva operations by requiring parts. Despite this, we met all Shiva's electronics needs, either from our inventory of onhand spares or by rewiring the system to operate with the electronics available. To satisfy Novette requirements for optics, however, we had to deactivate all of arm 13 and the disk amplifiers on arm 14 in late October. Deactivating these two arms provided spare optics and electronics to sustain operation of the remaining 18 arms. Final shutdown of all Shiva operations on December 23 resulted from plans to remove the Shiva target chamber and install it on Novette in January 1982.

The Nova Cone Angle, Nova Cone Angle II, and Long-Puise Cairn Scaling series required operation at a pulse width of 5 ns. We devoted our efforts in January to finding the best configuration of pinholes in the spatial filters to limit both damage and pinhole closure. This effort was also necessary

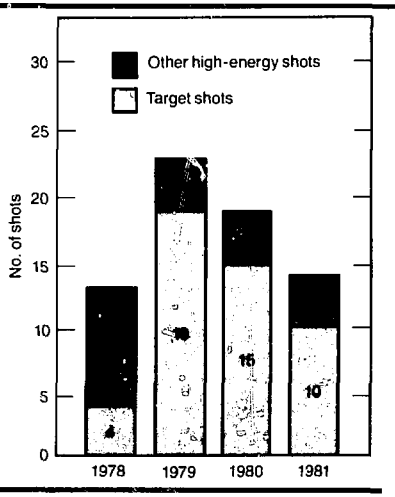

Fig. 6-10. Historical monthly averages for Shiva high-energy shots.

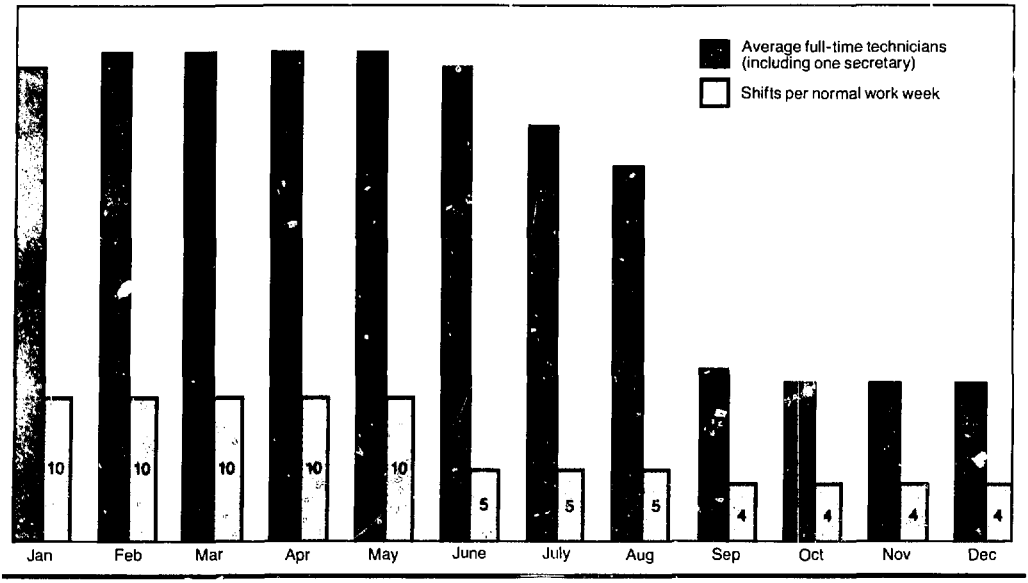

Fig. 6-11. Shiva labor profile for 1981.

for the backlighter portion of the NPIRE II series and for the joint series conducted with NRL in December. Due to increasing damage in the system because of reduced maintenance dating from December of 1980, some pinhole closure did occur on some arms during the Long-Pulse Cairn Scaling series. This effectively shortened the optical pulse width on target, since some arms had pulses as short as 3.5 ns.

Our principal method of detecting pulse-shortening was to observe the gain of the disk-amplifier sections as a function of rod output energy. Those arms showing a marked decrease in disk-section gain with increasing input were presumed to have pinhole closure. The input to these arms was reduced until the disk gain returned to normal and the arms were then operated with reduced output. This was permissible due to the lack of any requirement for a high degree of illumination symmetry for these targets.

For the NPIRE II backlighter series, we used the short-pulse oscillator to generate a 1-ns pulse that was amplified by the lower 10 arms and used to drive target-capsule implosions. The long-pulse oscillator and pulse-slicer generated a 5-ns pulse that was amplified by eight upper arms and used to illuminate an x-ray converter foil to backlight the target for the 22× microscope. Since the preamplifiers and penthouse amplifiers are common to the upper and lower beam clusters, the pulses were combined on the oscillator table and separated by the Pockels cells in the arms. The short pulse was triggered 54 ns before the long pulse, so that the two pulses propagated through the preamplifiers, the penthouse, and into the upper arms with a 54-ns separation. The Pockels-cell timing was coincident with the long pulse, so that it passed through the upper arms to illuminate the backlighter. The backlighter foil, thus, also had a precursor pulse (the drive pulse attenuated by the loss through one Pockels cell) arriving 54 ns before the target shot.

Both pulses were delayed by 54 ns at the lower arms by insertion of optical delays in the four ladder arrays between the upper and lower beam clusters. Thus, the short pulse reached the lower Pockels cells coincident with the arrival of the long pulse at the upper Pockels cells. The short pulse was then amplified and used to irradiate the target. The target was also irradiated by a postpulse (the long-pulse leakage through the lower-arm Pockels cells) arriving 54 ns after the target shot. We adjusted pulse timing at the target by fine adjustment of the interoscillator timing. Typically, the leading edge of the short (drive) pulse arrived 2.3 ± 0.5 ns after the leading edge of the long

(backlighter) pulse, giving good backlighting throughout the entire target implosion.

Since the 22× microscope has a limited field of view, the x-ray-emitting region of the backlighter plasma would blow out of the field of view of the microscope. Thus, we had to empirically determine an offset between the x-ray line of sight and the optical line of sight to center the x-ray emission in the 22× field of view during the target implosion. Further, since the 22× microscope is normally used to determine target position (on those experiments for which it is an online diagnostic), this offset significantly complicated target and beam alignment for the NPIRE experiments.

For the joint experimental series with NRL, we again used separate drive and backlighting pulses. However, we used the same pulse duration (3 ns) for both pulses. The 10 lower arms were used to drive the targets in this series. The backlighting pulse from seven upper arms was delayed 0.9 ns by moving the "trombone" delay optics in each of the available seven upper arms (arms 13 and 14 were out of service, while arm 20 was undisturbed so as not to alter the timing of the optical pyrometer diagnostic).

For the x-ray pump series, we used the lower 10 arms at low fluence and a 0.1-ns pulse duration. The low output energy necessitated low output from the rod amplifiers—so low that the beta Pockels-cell energy monitors did not indicate the energy. This forced us to set up the target shots blindly, resulting in excessively high output energy on the first shot of the series. Despite the low fluence, we observed low gain on some arms. In those cases, we substituted large pinholes for the normal small ones and saw no adverse effects.

Throughout 1981, the development of Nova and Novette was supported by Shiva operations. The prototype Nova plasma shutter was installed on Shiva, in the final f/14 spatial filter on arm 16, for seven months. This installation included a diagnostics platform on arm 16 at the output of the delta amplifier. Most high-energy shots for the plasma shutter were dedicated shots, for three reasons

- Due to the prototype nature of the plasma shutter, it was difficult to integrate its operation into our normal target-shot firing sequence.
- The plasma shutter's requirement for 5-ns pulses created a conflict with other experiments.
- We often required arm 16 to be fired on target.

We made performance checks of a Nova 34-cm-aperture calorimeter, and we set up a prepulse diagnostic in one of the Shiva incident-beam diagnostic (IBD) packages. Neither of these tests interfered with normal operations. Although the prepulse diagnostic required low energy only, its realistic installation in an IBD required that it piggyback on full-energy shots. We tested Nova charge amplifiers for noise immunity, initially on arm 4 after arm 14 was shut down in October, we dedicated its rod section to the charge-amplifier tests exclusively. These tests continued on a noninterfering basis until December 21, 1981, on which day we took a three-day series of dedicated rod shots to conclude Shiva support of the charge-amplifier check.

During 1981, we tested an experimental Auston switch. This switch, installed in the IBD of arm 15, is designed to generate timing fiducial marks. Also, we installed a neutral-solution-processed vacuum window in arm 4 and performed damage testing for six months. (The neutral-solution process is described in "Optical Components" in Section 2.)

Shiva completed its productive four-year career on December 23, 1981. It is fitting that Shiva ended as it began, firing rod shots to noise-test laser-diagnostic amplifiers.

Author: O. C. Barr

Shiva Target Diagnostics. The responsibilities of the Shiva target-diagnostics group included operation and maintenance of the electronics data-acquisition system and the target-chamber diagnostics systems. These systems are described in previous *Laser Program Annual Reports*.[36-38] During 1981, we participated in a wide variety of experimental series that produced data for Nova target designs, target-scaling experiments, drive characterization, density measurements, and plasma physics. These experiments, described briefly in the article above, required a variety of laser pulse lengths ranging from 0.1 to 35 ns. Each change of pulse length required retiming of the entire

system, particularly when changing between the long-pulse and short-pulse oscillators. As we installed more-sophisticated diagnostics on the system, the number of timing shots required for each experimental series increased.

Table 6-7 summarizes the target diagnostics installed on Shiva during 1981; the full complement of diagnostics available may be found in previous *Laser Program Annual Reports*.[39] Our Dante H spectrometer (along with other Dante instruments) and imaging soft-x-ray streak cameras (SXRSC) were used extensively in the drive-characterization experiments. These transmission-grating and high-resolution x-ray spectrometers were fielded especially to diagnose the x-ray laser drive experiments on Shiva.

Operation of the target systems became routine during 1981; because of the expected deactivation of Shiva and the build-up of Novette, we made few improvements. One significant improvement we did make was to integrate the system for acquiring target data into the shot sequence generated by the power-conditioning system. With this modification, power conditioning automatically initialized the target-diagnostics system for the shot and sent it the shot number. This prevented shot-number discrepancies, provided configuration control, and differentiated between rod-shot and target-shot data, thus allowing easy identification of relevant data files.

We removed two equipment racks so that holes for Nova Phase II beamlines could be drilled in the east wall of the target bay. The equipment in these racks included the LSI-11 front-end processor, the mother CAMAC crate, serial-highway fiber-optic lines, and power distribution, all of which are vital to the operation of the data-acquisition system. We encountered no problems in moving this equipment.

At other times, we experienced problems with the CAMAC serial-highway fiber-optic links because of deteriorating terminations and the accumulation of dirt and old optical grease in the connectors. We solved the problem by reterminating the links, with careful attention to the removal of old optical grease.

During reduction of Dante spectrometer data, the need arose for tracking changes in the time-base and amplitude stability of Tektronix R7912 transient digitizers. We set up a system to monitor the calibration of these instruments. Now, before a shot series, we apply a time- and amplitude-calibration signal to all R7912s. For amplitude calibration, we use a precise, stable square wave; for time-base calibration, we use a time-mark generator with a wide-band amplifier. These signals are included with the target-shot data for the series and are used during Dante data-reduction to improve the accuracy of data from individual R7912s.

We mounted three new microchannel-plate (MCP) detectors on the filter-fluorescer (FFLEX) diagnostic to make time-resolved measurements of high-energy x-ray emission. We determined the absolute timing of these MCP detectors by frequency-doubling beam 4 of Shiva and reflecting rod shots off a surrogate target located at the center of the target chamber. This measurement, in conjunction with our timing fiducial, allowed us to determine x-ray emission times with respect to the laser-irradiation pulse.

Other activities involving the target-diagnostics group included

- Fielding a calorimeter system from KMS Fusion, Ann Arbor, Mich. We installed the

Table 6-7. Shiva target diagnostics added during 1981.

Diagnostic	Detector	No. of detectors	Measurement	Month activated
X rays				
Dante H	XRD-31 diode	10	Spectrally resolved, time-resolved	Mar
Transmission-grating spectrometer	Streak camera/film	1	Spectrally resolved, time-resolved	Dec
High-resolution spectrometer	Film	2	Spectrally resolved, time-resolved	Dec
Laser light				
Backscatter angular	Pin diode	18	Time-resolved	Apr
3/2ω angular	Pin diode	12	Time-resolved	Nov
3/2ω spectrograph	Spectrometer/diode array	1	Spectrally resolved, time-resolved	Dec

KMS detectors on our energy-balance modules and integrated their electronics into our data-acquisition system; the data will be compared with our calorimeter data to allow future data correlation.

- Moving the optical fiducial source for one of our optical/x-ray spectrometers (OX-1) from beam 11 to beam 6 to allow the OX-1 to continue acquiring the output pulse shape after the upper arms were deactivated.
- Measurements of pinhole closure during long-pulse experiments (see "System Configuration and Performance," above). We characterized our IBD fiducial detectors and compared them with one used by the laser diagnostics group to measure the oscillator pulse; we confirmed previous evidence of pulse shortening.
- Preliminary testing of a gallium-arsenide Auston switch. This device is a candidate for use as an optical fiducial detector; it is capable of response below 100 ps with several amperes of output current.
- Comparison of a Tektronix R7912 transient digitizer incorporating a prototype CCD readout array with a standard R7912 for susceptibility to target-generated noise.
- Calibration of groups of light (LC21) and plasma (LC27) calorimeters whenever there was sufficient time in the operations schedule to do so (i.e., between experimental series).

Authors: C. E. Thompson and M. Fiore

Major Contributors: T. L. Schwab and E. J. Powell

Shiva Mechanical Modifications and Maintenance Summary. The operational strategy for Shiva during 1981 was to minimize modifications and expenditures on beamline optics, while allowing the system to degrade toward eventual shutdown at

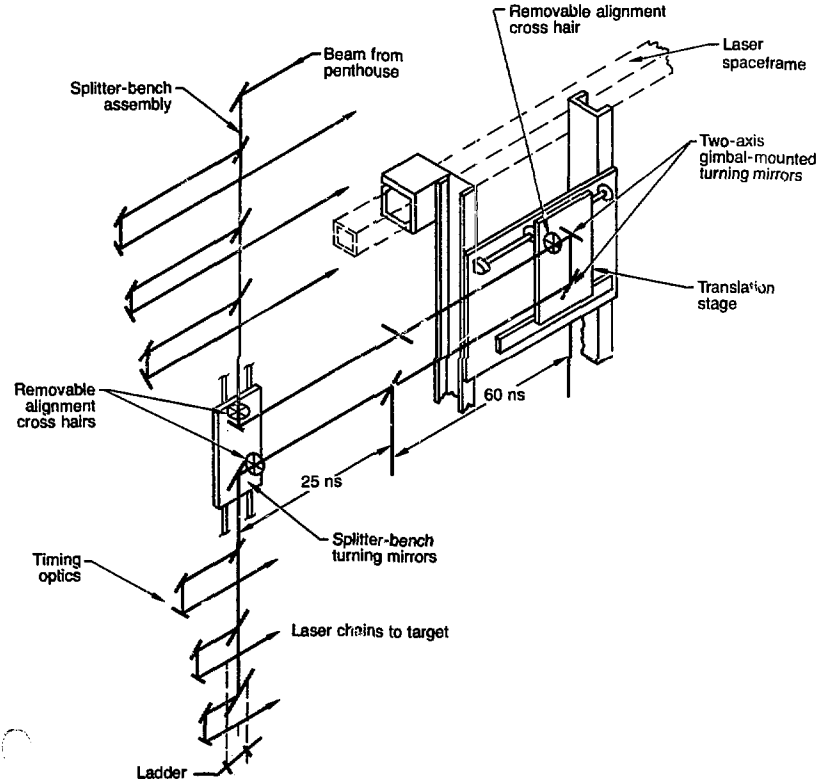

Fig. 6-12. Schematic of the optical-delay system added to Shiva to complete the x-ray backlighting capability.

the end of December. To comply with this strategy, we made only one significant modification, completing installation of the optical-delay hardware for our x-ray backlighting system.

Figure 6-12 shows the optical-relay system that provided time-delayed pulses to the target for our studies of implosion dynamics. We used four sets of these assemblies to delay the lower 10 arms of Shiva relative to the upper 10 arms. We also employed two oscillators: one for long pulses, and one for short pulses. A more detailed discussion of the harware design is given in the *1980 Laser Program Annual Report*.[10]

The only Shiva optical components given significant attention this year were rod-amplifier rods, spatial-filter lenses, and 15-cm polarizers. We recoated some spatial-filter lenses and polarizer plates because of accumulated damage; we had to rework the amplifier rods because of lower-quality optical coatings used during the past two years.

Table 6-8 shows the average number of firings for each laser component, both in 1981 and over Shiva's lifetime. Table 6-9 shows the number of component failures by year, failure mode and position. A complete damage history of Shiva laser components will be summarized in a separate report; the data here are relevant for 1981. Note that these statistics will be biased due to the fact that we intentionally allowed the system to degrade during 1981.

We have begun to disassemble some of the Shiva disk amplifiers; this process will give us a broader perspective of component damage rates vs time and firings. For example, we have disassembled a 10-cm-diam beta disk amplifier that was installed in July 1977 and had been fired 502 times. The six disks of this amplifier had no damage spots greater than 500 μm in diameter, and they had an average of only 20 spots per surface in the 100-μm range. We estimate this amplifier could have continued operation for another 500 shots before reaching an obscuration factor of 0.05% per surface. This preliminary test is significant, since it

Table 6-8. Shiva component firings in 1981 and for the system lifetime (1977-1981).

Component	No.	Component firings: 1981	Component firings: Lifetime
Preamplifier rods	7	1003	3938
2.5-cm rod amplifiers	20	975	4605
5-cm rod amplifiers	20	965	4481
10-cm disk amplifiers	40	96	692
15-cm disk amplifiers	20	96	646
20-cm disk amplifiers	20	91	331

Table 6-9. Major Shiva component failures, 1977-1981.

Year	Failure mode	2.5-cm Rod amplifiers	5-cm Rod amplifiers	10-cm Disk amplifiers	15-cm Disk amplifiers	20-cm Disk amplifiers
1977	Water leak	5	1	—	—	—
	Exploded flashlamp	1	3	—	—	—
	Laser-damaged optic	1	1	1	—	—
	Broken blast shield	1	—	—	—	—
1978	Water leak	15	11	—	—	—
	Flashlamp failure	4	4	—	1	—
	Exploded flashlamp	—	3	—	—	1
	Laser-damaged optic	4	—	4	—	4
	Low gain	—	—	1	—	—
	Broken blast shield	—	—	—	—	1
1979	Water leak	12	18	—	—	—
	Flashlamp failure	1	1	13	2	1
	Exploded flashlamp	1	—	2	1	—
	Laser-damaged optic	6	4	8	7	3
	Low gain	5	2	12	2	—
	Broken blast shield	5	4	1	—	—
1980	Water leak	7	6	—	—	—
	Flashlamp failure	1	2	—	3	3
	Exploded flashlamp	2	—	—	1	2
	Laser-damaged optic	4	1	4	9	5
	Low gain	18	12	4	1	2
	Broken blast shield	8	3	—	4	1
1981	Water leak	—	5	—	—	—
	Flashlamp failure	2	3	2	—	1
	Exploded flashlamp	—	—	—	—	1
	Laser-damaged optic	7	2	1	—	3
	Low gain	17	8	1	—	—
	Broken blast shield	4	1	—	—	—

establishes that disk amplifiers can operate for extended periods when properly designed, constructed, and operated.

Authors: H. G. Patton and W. A. Jones

Major Contributor: R. L. Combs

Argus and Shiva Experiments

Overview

From late 1979 until its shutdown in August 1981, we devoted the Argus facility to exploring the effects of laser wavelength in both indirect and direct-drive target designs. By employing type II KDP frequency-conversion crystals with the output of the Nd:glass Argus laser, we have been able to conduct experiments at laser wavelengths of 1.06, 0.53, and 0.35 μm (Ref. 41). In Table 6-10, we summarize the relevant dates and maximum energies on target that were available in a single-beam pulse of approximately 700 ps FWHM.

The energies on target at 0.53 and 0.35 μm (2ω and 3ω) were limited by the size (~100 mm) of the available KDP crystals and by damage to the dielectric coating of optical components (beam dumps, focusing optics, and blast shields) in the laser chain.[41] The high-energy (~200 J) 2ω experiments were done with an uncoated 1.06-μm-absorbing beam dump and an uncoated focusing lens. We performed 1.06-μm (1ω) experiments with similar energies on target for comparison with shorter-wavelength shots. Further details concerning the Argus facility configuration and operation are given in "Argus Operations," earlier in this section.

The irradiation conditions for our frequency-conversion experiments are summarized in Table 6-11; the rationale for these conditions is given in Ref. 42. Although we attempted to irradiate the targets under similar spot-size, pulse-width, and energy conditions, passive aberrations in the optical components resulted in intensity distributions on target that became progressively worse with decreasing wavelength. In Fig. 6-13, we show the target-plane energy distribution at 1ω and 2ω for a nominal 10^{15} W/cm^2 peak intensity; experimental conditions are $E_L \sim 50$ to 55 J, $\tau_L \sim 700$ ps, and the spot diameter (in the target plane) is ~100 μm.

In Fig. 6-14, we show the running integral of the intensity-distribution function at all three wavelengths for a nominal peak intensity of $\sim 3 \times 10^{14}$ W/cm^2 (Ref. 43). As the figure shows, a larger fraction of the 3ω energy is at substantially higher intensity than the nominal value. Irradiation conditions such as this complicate the analysis and comparison of some features of the data, particularly those involving parametric instabilities and suprathermal-electron production.

During the frequency-conversion series, we conducted a wide range of experiments, including measurements of absorption, stimulated Brillouin scattering, suprathermal-electron production and scattered light from parametric instabilities, thermal-electron transport, and total x-ray conversion efficiency. For the majority of these experiments, the targets were simple disks, ~25 μm thick and 1000 μm in diameter, of Be, plastic (CH), Au, Ni, or Ti. For the electron-transport experiments, we employed variable thickness (0 to 6 μm) Be-coated Al targets.

Some experiments were also conducted with the Shiva laser at 1.06 μm. The goal of these experiments was to explore the coupling physics in long-scale-length plasmas

Table 6-10. Maximum energy (on a 700-ps pulse) at various wavelengths for one beam of Argus.

Date	Wavelength	Energy (J)
Nov 1979 to Aug 1980	2ω	40
Oct 1980 to Jun 1981	3ω	40
Mar to June 1981	1ω	100
July to Aug 1981	3ω	240

Table 6-11. Frequency-conversion irradiation conditions.[a]

Intensity[b]	Wavelength	Spot size (μm)[c]
$\sim 3 \times 10^{13}$	1ω, 2ω, 3ω	150 to 200
$\sim 3 \times 10^{13}$	1ω, 2ω, 3ω	450 to 600
$\sim 10^{14}$	3ω	240 to 260
$\sim 3 \times 10^{14}$	1ω, 2ω, 3ω	150 to 180
3×10^{14}	1ω, 2ω	240 to 300
$\sim 10^{15}$	1ω, 2ω, 3ω	80
$\sim 3 \times 10^{15}$	2ω	40

[a]These experiments were made with linear polarization, with f/2.2 focusing optics, and with pulse widths ranging from 600 to 900 ps.
[b]Based on incident power divided by the area containing 95% of the beam energy.
[c]Spot diameter containing 95% of the beam energy.

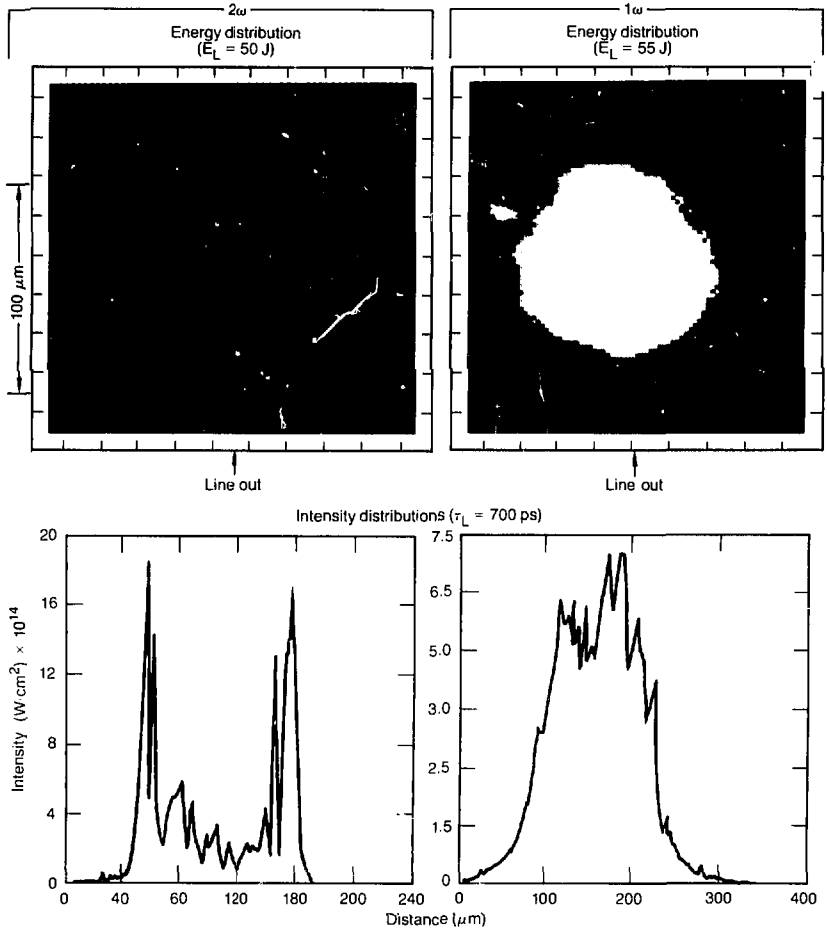

Fig. 6-13. Target-plane energy and intensity distribution at 1ω and 2ω.

($L/\lambda \sim 400$) at moderate to high values of $I\lambda^2$ (10^{14} W/cm^2-μm^2 $\lesssim I\lambda^2 \lesssim 3 \times 10^{15}$ W/cm^2-μm^2).

Some of the results of these experiments are discussed in the following articles, although data-reduction and analysis will continue into 1982. In "Layered-Disk Target Experiments," we discuss the results of layered-target studies of thermal-electron transport at an absorbed irradiance of ~1 to 2×10^{14} W/cm^2 for both 1ω and 3ω. These experiment are presently being modeled, and we report only our preliminary results. Higher ablation rates and shock pressures are implied by a wide range of x-ray and optical diagnostics for the shorter-wavelength irradiations. At present, many of the observed features of the experiments are consistent with flux limiters in the range of ~0.01 to 0.03 for both 1ω and 3ω, although effects due to lateral energy flow are still under investigation.

In "Absorption and Stimulated Brillouin Scatter," we present absorption results from disk targets. The wavelength, intensity, and Z-dependence of the results are consistent with inverse bremsstrahlung and stimulated Brillouin scattering (SBS) being the dominant interaction mechanisms. Both scattered light and suprathermal x-ray production

indicate that absorption by parametric instabilities plays a minor role in the total energy balance over the entire parametric range of the Argus experiments.

Modeling of the absorption experiments with the hydrodynamic code, LASNEX, match the experimental results reasonably well. For our modeling, we employed nominal inverse bremsstrahlung, SBS, a thermal flux limiter of 0.03, and a critical-density dump-all fraction of 0.03 to 0.1 to account for suprathermal-electron production.

In "X-ray Conversion Efficiency at 1ω, 2ω, and 3ω," we present early results of our Argus x-ray conversion-efficiency measurements. We have obtained x-ray yields of up to 60% of the absorbed energy from Au disks at a 3ω peak intensity of $\sim 1 \times 10^{14}$ W/cm^2. The previously observed fall-off in x-ray yield at $I \lesssim 10^{14}$ at 2ω has also been observed at 3ω. We confirmed the earlier 2ω conversion efficiency[44] at intensities of $\sim 3 \times 10^{13}$ and $\sim 3 \times 10^{14}$ W/cm^2 using larger irradiation spots (300 and 450 μm) during the 200-J experiment. Preliminary 1ω results are in good agreement with past experiments at Argus and Shiva,[45] albeit for slightly different irradiation conditions.

In "Comparison of Suprathermal X-ray Emission at 1ω, 2ω, and 3ω," we present the results of high-energy x-ray measurements (4 keV $< h\nu <$ 70 keV) as a function of both laser wavelength and peak intensity. The data generally show a reduction in x-ray yield (and inferred suprathermal-electron production) with decreasing wavelength, although beam modulation and the mix of the many parametric instabilities that produce high-energy electrons complicate any $I\lambda^2$-type scaling. In all of these experiments, the inferred suprathermal-electron production involves less than ~5% of the absorbed energy. Similar levels of hot-electron production are also inferred from K_α measurements on Shiva using high-intensity 1ω light with pulse widths of 100 and 600 ps (see "Suprathermal Electrons from Disks (Comparison of K_α to Bremsstrahlung)," later in this section).

We have made extensive measurements of the scattered light at 3/2ω and from 1/2ω to 4/5ω, which are generated by instabilites ($2\omega_{pe}$ and stimulated Raman scattering) at $n_e \sim 0.25\ n_c$. The results of these measurements, made at both Argus and Shiva for incident 1ω and 2ω light, are presented in and "3/2ω Emission at 1ω and 2ω" and "Stimulated Raman Scattering at 1ω and 2ω." Interesting features of the 3/2ω spectra include a strong dependence on incident wavelength, target Z, and observation angle. The Z- and wavelength-dependence support simple theories[46] from which coronal temperatures can be inferred, while the angular dependence of the emission shows the limitations of such modeling.

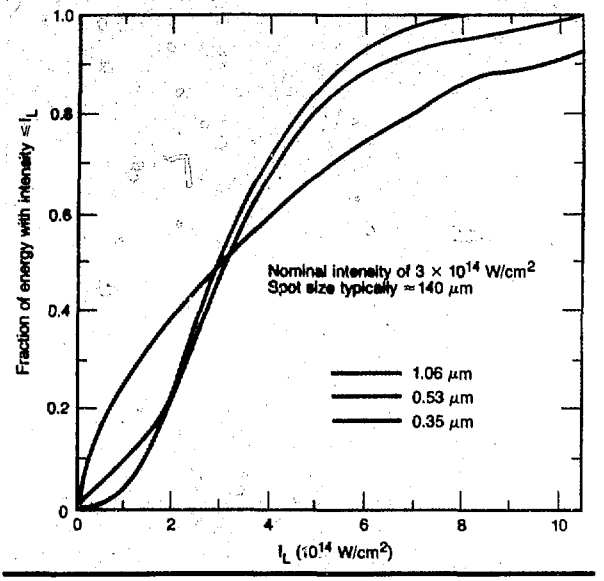

Fig. 6-14. Running integral of the intensity distribution for 1ω, 2ω, and 3ω for a nominal intensity of 3 × 10^{14} W/cm^2.

We have observed evidence of both absolute and convective Raman instabilities at both 1ω and 2ω. Time-resolved and spectrally resolved scattered light from the Raman instability with 2ω irradiation show near-simultaneous scattering from a range of densities (~0.03 to 0.15 n_c), with a rapid onset near the peak of the driving pulse. The Raman emission, which shows temporal pulsations (with a period of 50 to 150 ps) lasts for nearly 1 ns after its onset. In 1ω experiments at both Argus and Shiva, we have observed a very strong dependence of the emission levels of both 3/2ω and 1/2ω light on the dimensions of the plasma (altered by changing the irradiation spot size). Thin-foil experiments at Shiva have demonstrated that the Raman and $2\omega_{pe}$ instabilities

can be very efficient (absorption efficiency >10%) in long-scale-length, underdense plasmas. Experiments on Novette will address the coupling of large-scale-length laser plasmas with short-wavelength light.

Finally, in "Backlighting Characterization at 1ω, 2ω, and 3ω," we describe the use of x-ray backlighting to determine the symmetry, stability, and size of imploded targets. In our present work, we have investigated the production efficiency of aluminum K, gold M, titanium K, and nickel K lines as a function of laser wavelength and pulse width.

Author: E. M. Campbell

Layered-Disk Target Experiments

Electron transport plays a central role in the physics of laser-driven inertial-confinement fusion.[47] Electrons transport energy from the absorption region ($n_c \leq n_c$) into the overdense plasma, regulating the target ablation and affecting the temperature, density, and velocity profiles of the ablating plasma. These profiles in turn control the overall target absorption and affect its partition between collisional and collective processes (thermal heating and suprathermal-electron production, respectively). Important quantities such as thermal x-ray production and hydrodynamic efficiency are thus strongly influenced by the effectiveness of electron-energy transport. Furthermore, electron thermal conduction can affect the overall symmetry of the capsule implosion by determining how nonuniformities in the laser-deposition region (caused by passive beam modulation or filamentation) are transmitted to the ablation front.

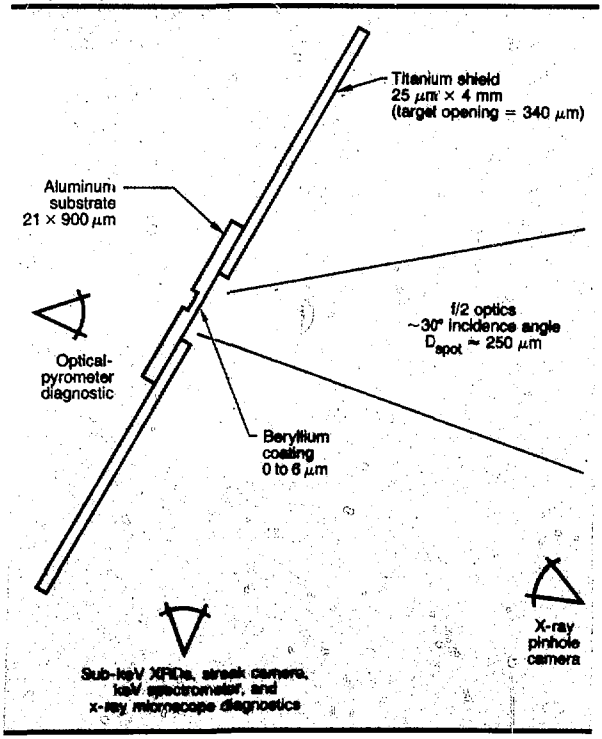

Fig. 6-15. Target and diagnostic configuration for the electron-transport experiments.

The heat-flow rate inferred from experiments has generally been parametrized by comparing it with that calculated by a hydrodynamic computer code that employs flux-limited diffusion. Such codes generally use Spitzer's thermal conductivity[47] until the heat-flux reaches a free-streaming limit in the form of

$$Q_{fs} = f_e\, n_e\, m_e\, v_e^3 = f_e\, n_e (m_e)^{1/2} (\kappa T_e)^{3/2} , \quad (1)$$

where f_e is a flux-reduction factor (commonly referred to as the flux limiter) and v_e is the thermal velocity, $(\kappa T_e/m_e)^{1/2}$. Heat flow in such a code shifts from conduction-limited to flux-limited in regions of the plasma where the temperature scale-length becomes steep compared with the mean free path of electrons having velocity ~2 to $3v_e$. This shift to flux-limited transport occurs most strongly in the overdense region, just beyond the laser-deposition region. Heuristic estimates suggest $f_e \sim 0.2$ to 0.6 in the absence of significant turbulence or electric or magnetic field effects. More recently, Fokker–Planck computer calculations have obtained heat-transport rates that can be approximated by similar flux-limited diffusion.

An "anomalous" reduction in the flux limiter by a factor of 5 to 10 from classical values may be due to the inadequacy of the simple single-group, flux-limited diffusion model in the presence of the steep temperature gradients normally found in laser-produced plasmas. However, a wide varie of experiments have generally led to inferred flux-limit values of $f_e \approx 0.03$. This

value is even lower than what at present can be justified theoretically, even with the more recent advances.

The majority of the experiments, however, have been conducted with 1ω light in short pulses ($\tau \sim 100$ to 300 ps) at high intensity ($I \sim 5 \times 10^{14}$ to 10^{15} W/cm^2); for these conditions, both thermal- and suprathermal-electron transport play an important role. Such irradiation conditions are far removed from the long pulses ($\tau \geq 1$ ns), moderate intensity ($I\lambda^2 \leq 5 \times 10^{14}$ W/cm^2-μm^2), and short wavelengths ($\lambda_L < 1.06$ μm) planned for future high-gain target implosions. The presence of substantial levels of suprathermal electrons complicates both the physics and the interpretation of the experiments to the extent that detailed transport properties of the thermal electrons cannot be reliably inferred.

In this article, we present the early experimental results of layered-disk experiments designed to observe the characteristics of energy transport in the highly collisional plasmas produced by long-pulse, moderate-intensity light at 1ω and 3ω. Analysis of the experiments using our hydrodynamic code, LASNEX, is in progress and will be reported at a later date.

The targets for these experiments, shown in Fig. 6-15, consisted of aluminum microdisks overcoated with varying thicknesses (0.27 to 6.5 μm) of beryllium. For shock-measurement experiments (described below), the aluminum disks had an ion-milled channel 40 μm wide and 3.7 μm deep; the thickness of the Al was 21 μm (at the base of the channel). On some of the shots, we placed a 4-mm-diam titanium shield with a 340-μm-diam hole over the Al disk to examine lateral transport and to prevent energy flow to the rear of the target.

A multitude of diagnostics were employed in these experiments

- We measured target absorption using an enclosing, scattered-light box calorimeter.
- We measured the x-ray spectra from 3.5 to 70 keV with three multichannel K-edge filtered spectrometers using pin diodes and fluor-photomultiplier combinations.
- We obtained the spectroscopy and yield of $3/2\omega$ light arising from parametric processes near $1/4n_c$ during 1ω experiments.
- We measured time-integrated line emissions from the Al and Ti targets with x-ray crystal spectrometers.
- We measured the yield and time-dependence of the subkilovolt x rays with

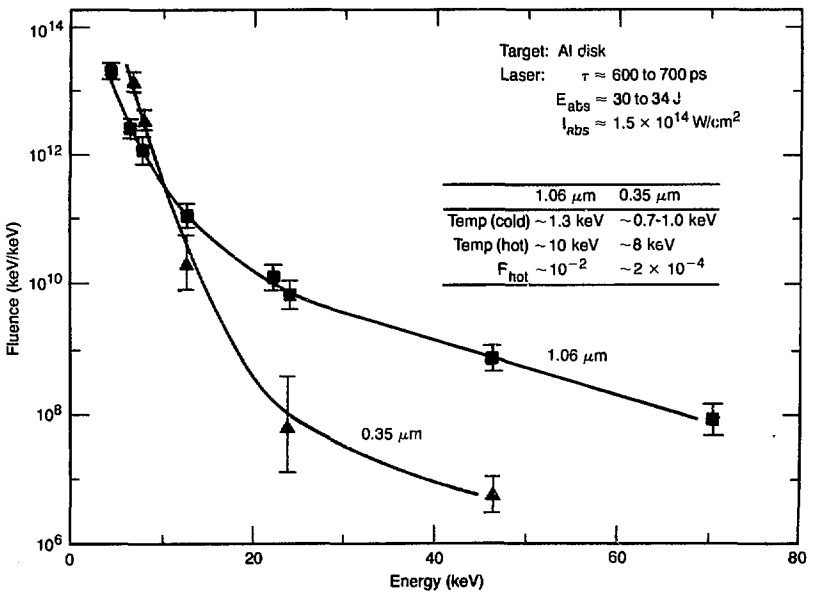

Fig. 6-16. High-energy x-ray spectra from Al targets irradiated with 1ω and 3ω light.

Table 6-12. Laser parameters for electron-transport experiments.

	1.06 μm	0.35 μm
Energy (J)	~90 ± 2	30 ± 3
Pulse length (ps)	600 to 700	600 to 700
Spot-size diameter (μm)	240 ± 50	240 ± 50
Peak incident intensity (W/cm^2)[a]	~3 × 10^{14}	~1 × 10^{14}

[a]These are nominal values: incident laser power divided by the area containing 95% of the beam energy.

Table 6-13. Absorption values obtained with an LLNL box calorimeter. ▼

Wavelength (μm)	Material	Incident intensity (W/cm^2)	f_{abs}[a] (%)	Absorption intensity (W/cm^2)
1.06	Be	~3 × 10^{14}	32 ± 5	~1 × 10^{14}
1.06	Al	~3 × 10^{14}	39 ± 5	~1.2 × 10^{14}
0.35	Be	~1 × 10^{14}	90 ± 5	~0.9 × 10^{14}

[a]f_{abs} = fraction of incident energy that is absorbed.

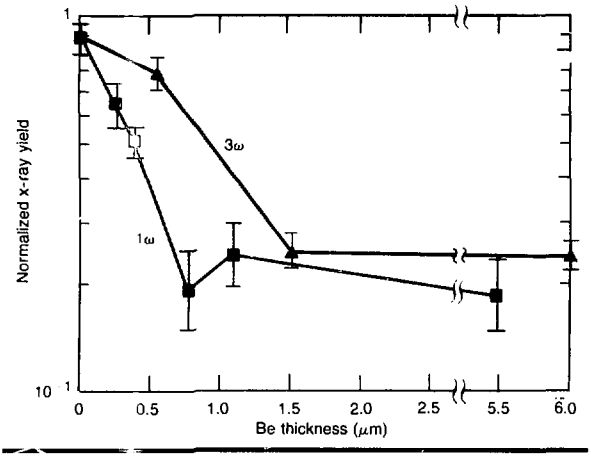

Fig. 6-17. Relative subkilovolt x-ray emission as a function of Be thickness for 1ω and 3ω.

two multichannel K- and L-edge filtered x-ray diodes, and also with three- and six-channel x-ray streak cameras.

- We measured the spatial profile of the x-ray emission with a four-channel x-ray microscope (0.28, 0.6, ~1.2, and ~2.5 keV).
- We used an imaging optical streak camera to measure the time of arrival and speed of the laser-ablation-launched shock wave at the rear of the target.

We chose the irradiation conditions at both 1.06 and 0.35 μm so that the absorbed irradiances at both wavelengths were identical and so that the interaction physics were as nearly classical as possible (i.e., suprathermal-electron production was minimal). The incident laser parameters are summarized in Table 6-12, and the absorption values obtained with the box calorimeter are presented in Table 6-13.

At the moderate $I\lambda^2$ values employed in these experiments, suprathermal-electron production should be small. This is confirmed by the high-energy x-ray spectra from Al targets shown in Fig. 6-16. For 1ω irradiation, the x-ray spectrum implies a suprathermal-electron distribution, within an equivalent temperature of 10 keV, that contains about 10^{-2} of the absorbed energy; fast ion losses are not accounted for. A surprising but similar x-ray slope is seen for 3ω, although at a much lower energy content (~10^{-4} of the absorbed energy). The hard x-ray tails seen in many of the 3ω experiments can be understood in terms of the severely modulated spatial-intensity distribution of the incident beam and the many processes that can give rise to suprathermal-electron production. The suprathermal electrons, however, should not greatly influence the transport experiments described in this article because of their low energy content.

In Fig. 6-17, we show the fall-off in the relative subkilovolt x-ray emission as the Be layer thickness is increased. We obtained these data using the Dante systems and the x-ray streak cameras. Note that, for the same absorbed irradiance, the Be thickness required to reduce the emission by e^{-1} has increased from ~0.4 to 0.5 μm to 1 to 1.2 μm as the laser wavelength decreases from 1.06 to 0.35 μm.

A similar fall-off in emission occurs in the aluminum spectra near 1.6 keV as the Be thickness is increased. In Fig. 6-18, we show examples of the time-integrated Al line spectra obtained at 3ω as the Be layer is thickened from 0 to 1.4 μm. For bare aluminum and thin Be layers, the spectra are dominated by both helium-like and hydrogenic emission; transitions occur up to the series limits for both species.

In Fig. 6-19, we show the fall-off in the Al He-α emission with increasing Be thickness for 1ω and 3ω. The e-folding thickness for this emission is ~0.4 μm at 1ω and 1 to 2 μm for 3ω light. These results are similar to that obtained from the low-energy x-ray emission. The low but measurable emission seen asymptotically for large Be thicknesses is not yet understood. Possible causes include radiation pumping and suprathermal electrons. Further analysis may clarify this although the lack of time resolution in these data may limit our conclusions.

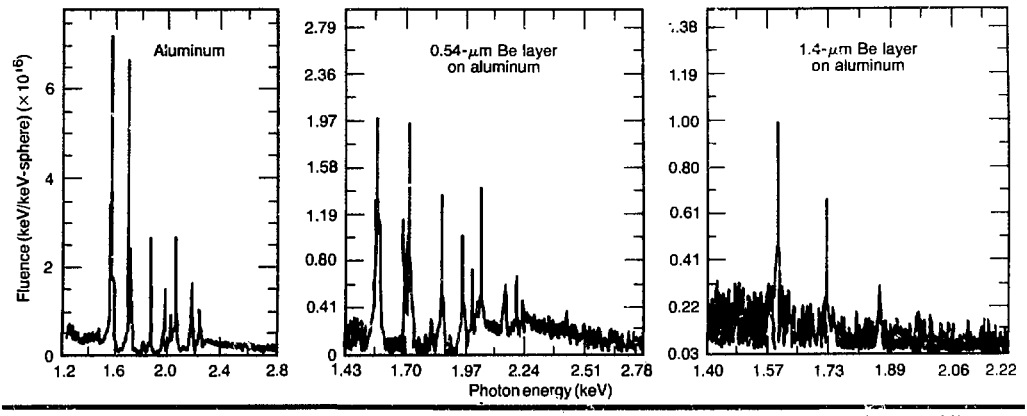

Fig. 6-18. Al line spectra obtained with increasing Be thickness at 3ω.

Finally, in Table 6-14, we summarize the results of the shock-transit measurements. For equivalent absorbed irradiances, the shock speed obtained from the 3ω experiments was 25 km/s, compared with ~20 km/s at 1ω. The implied shock strength thus increased from approximately 6 to 10 Mbar as the wavelength was decreased.

Authors: E. M. Campbell and W. C. Mead

Major Contributors: R. E. Turner, N. C. Holmes, F. Ze, and R. J. Trainor

Absorption and Stimulated Brillouin Scatter

During 1981, we performed experiments and calculations on the variation of laser-light absorption and backscatter with laser wavelength; the experiments were conducted on the Argus laser facility at 1ω, 2ω, and 3ω. We recorded absorption data for gold and beryllium disk targets at all three wavelengths, and we interpreted the data using a hydrodynamics code (LASNEX) that included a recently developed model for stimulated Brillouin scatter (SBS).[48] Preliminary reports on our 2ω and 3ω results are given in the *1980 Laser Program Annual Report*,[49] which also contains a description of the laser configuration and conversion-efficiency measurements.[50] A more complete analysis of the 2ω data was recently published.[51]

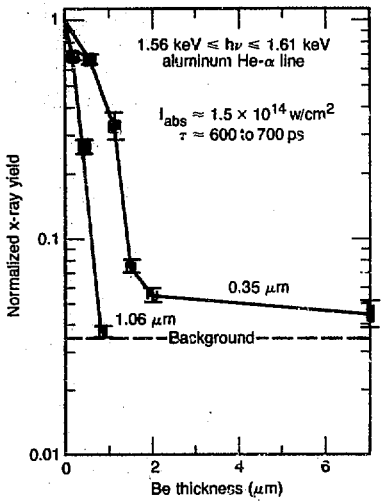

◁ Fig. 6-19. Fall-off of Al He-α line emission as a function of both laser wavelength and Be thickness.

Wavelength (μm)	Absorbed irradiance (W/cm²)	Shock speed (km/s)
1.06	~1.2 × 10^14	20
0.35	~0.9 × 10^14	25

Table 6-14. Shock-transit measurements.

Experimental Conditions. We chose the target-irradiation conditions for the wavelength-scaling experiments so that conditions would be similar at all three wavelengths

- Incident laser energies on target were ≤40 J (limited by optical-component damage thresholds); diagnostic thresholds required that the minimum energy on target exceed 3 J.
- Laser pulse lengths ranged from 500 to 700 ps FWHM.
- Focusing optics were f/2.2, with linear polarization.

The focal-spot sizes used to obtain each irradiance are shown in Table 6-15. For 1ω and 2ω, we determined the spot sizes using images from the transmitted-beam multiple-image camera (MIC).[49] For the 3ω experiments, we determined the spot size from the reflected-beam MIC and from the size of the x-ray microscope pictures. At the two lower laser intensities given in Table 6-15, we deliberately overlapped the spot sizes to study the effects of changing the focal conditions. Further details of the irradiation conditions on target may be found in "Argus Operations," earlier in this section.

Table 6-15. Focal-spot diameters and laser energies for absorption and backscatter experiments.

Laser wavelength (μm)	Approx. intensity (W/cm^2)	Focal-spot diameter (μm)[a]	Laser energy (J)
1.06 and 0.53 (1ω and 2ω)	3×10^{15}	50	30 to 40
	3×10^{14}	80	10 to 12
	3×10^{14}	150	25 to 30
	3×10^{13}	150	3 to 4
	3×10^{13}	430	25
0.35 (3ω)	3×10^{14}	160 to 170	40
	1×10^{14}	240 to 260	30
	3×10^{13}	210 to 230	4 to 6
	3×10^{13}	600	30 to 40

[a] ...am diameter that encloses 90% of the laser energy.

We performed the absorption measurements using a target-enclosing box calorimeter in conjunction with calorimetry of the incident and backreflected laser beams. The combination of the box calorimeter and focusing optics covered 98% of the solid angle around the target. The box calorimeter employed Schott GG-19 absorbing glass for the 3ω experiments and Shott NG-1 absorbers for the 1ω and 2ω light. A WG-280 shield prevented the plasma and x-ray energy from reaching the light absorbers.

Absorption. Figures 6-20 and 6-21 show the measured absorption fraction vs incident laser intensity for the three laser wavelengths. Here, the intensity is defined as the total laser power divided by the on-target focal-spot area. Intensity modulations in the beam (spatial scale ~0.1 of the beam diameter) can give peak intensities several times greater than this. The data points on Fig. 6-20 are for gold disks 15 to 20 μm thick and 600 to 1000 μm in diameter; data points in Fig. 6-21 show the absorption for beryllium disks. We varied the angle of incidence between 0 and 30°; within that range, we noted no significant differences in absorption. In Figs. 6-20 and 6-21, three trends are clear: absorption increases at shorter laser wavelengths, at lower laser intensities, and for higher-Z targets.[52]

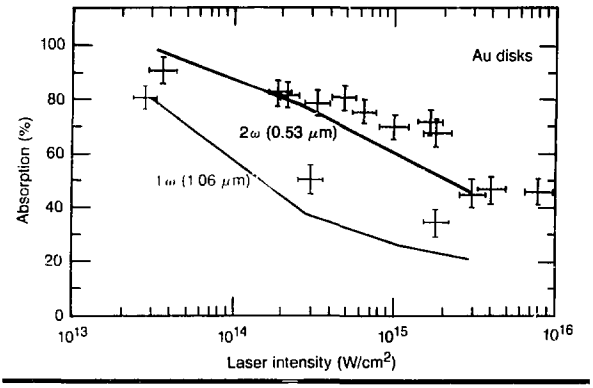

Fig. 6-20. Absorption vs incident intensity for gold-disk targets; lines represent LASNEX calculations.

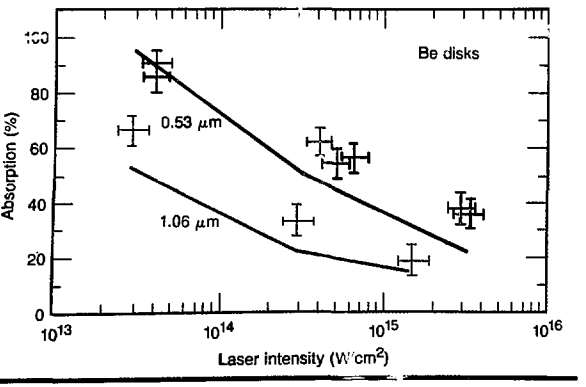

Fig. 6-21. Absorption vs incident intensity for beryllium-disk targets; lines represent LASNEX calculations.

These three trends are consistent with strengthened inverse bremsstrahlung absorption. To model the absorption quantitatively, we performed extensive computer simulations using LASNEX.[53] The solid lines in Figs. 6-20 and 6-21 show the absorption predicted by LASNEX, given the following set of physics assumptions

- A flux limit, f, of 0.03 for the thermal and hot-electron transport.
- Nominal inverse bremsstrahlung absorption.
- Non-LTE atomic physics.

The calculations were one-dimensional, used an effective radius of curvature equal to twice the focal-spot diameter, and included the SBS package recently developed

by Estabrook and Harte.[48] In addition, we used a simple model for resonance absorption[54] that deposits a fraction, f_D, of the light energy approaching the critical surface into a hot-electron population, with the characteristic temperature chosen to match the slope of the measured hard x-ray spectrum. For 2ω and 3ω, $f_D = 0.03$, while for 1ω, we used $f_D = 0.1$. Details of these choices for f_D are discussed in "Comparison of Suprathermal X-ray Emission at 1ω, 2ω, and 3ω," later in this section.

The LASNEX calculations (shown as solid lines in Figs. 6-20 and 6-21) match the experimental trend toward higher absorption at short wavelengths, low intensities, and high Z. Quantitatively, our absorption model including SBS tends to underestimate the absorption at the higher intensities and longer wavelengths. Under the same conditions, LASNEX calculations without a Brillouin-scattering model tend to overestimate the measured absorption. Two effects may contribute to this discrepancy. First, the nonlinear saturation of SBS might occur at lower scattered-light levels than our model has assumed; other features not treated are detailed frequency-matching for light reflected from the critical surface[55] and for Brillouin sidescatter. Second, additional absorption mechanisms, such as short-wavelength ion turbulence, may be contributing to the experimental absorption, as discussed in "Hot Electrons from Laser Absorption on Ion Acoustic Turbulence" in Section 3. For the Be disk, there is also a possibility that small amounts of contamination by Cu and Fe impurities could have raised the effective Z of the plasma, thus increasing inverse-bremsstrahlung absorption.

Backscattered Light. The data on backreflected light should contain additional information about Brillouin backscatter. Figures 6-22(a) and 6-23(a) show the fraction of incident laser light backreflected through the f/2.2 focusing optics as a function of laser wavelength ($\lambda_{\mu m}$) and intensity (I_{14}), for gold and beryllium targets.

Since the angle of incidence was 0° (relative to the target normal), this light contains contributions from several processes, including Brillouin-scattered light when SBS is occurring. Also, the nonabsorbed light, both specularly reflected from the critical surface and diffusely scattered by inhomogeneities in that surface, is also collected by the focusing lens. Because inverse bremsstrahlung is stronger at short laser wavelengths, there should be less nonabsorbed light as the laser wavelength becomes smaller.

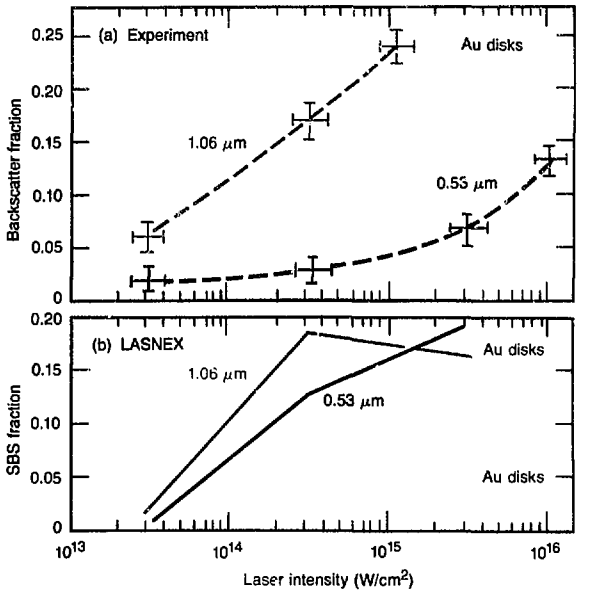

Fig. 6-22. (a) Measured backscatter fraction and (b) LASNEX calculation of stimulated Brillouin scatter for gold-disk targets. ▲

Fig. 6-23. (a) Measured backscatter fraction and (b) LASNEX calculation of stimulated Brillouin scatter for Be-disk targets. ▼

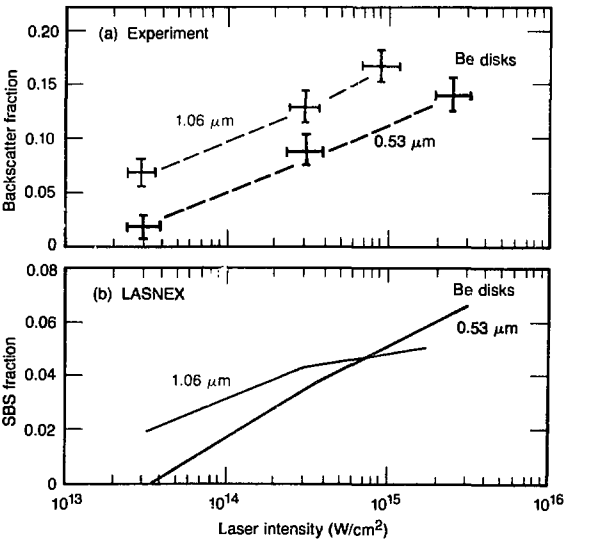

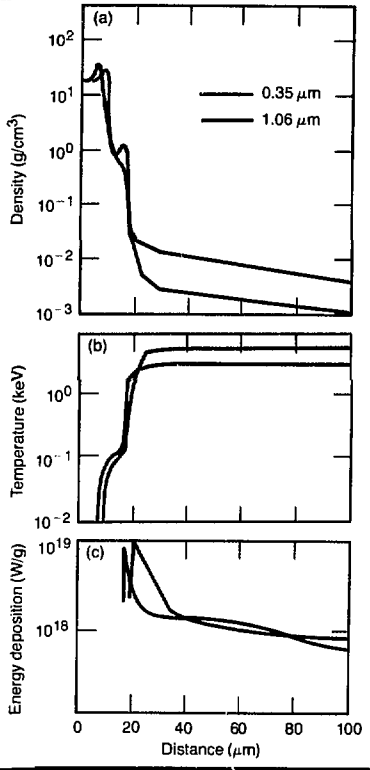

Fig. 6-24. LASNEX calculation of (a) mass density, (b) electron temperature, and (c) energy deposition rate for a gold-disk target at $I_L = 3 \times 10^{14}$ W/cm^2.

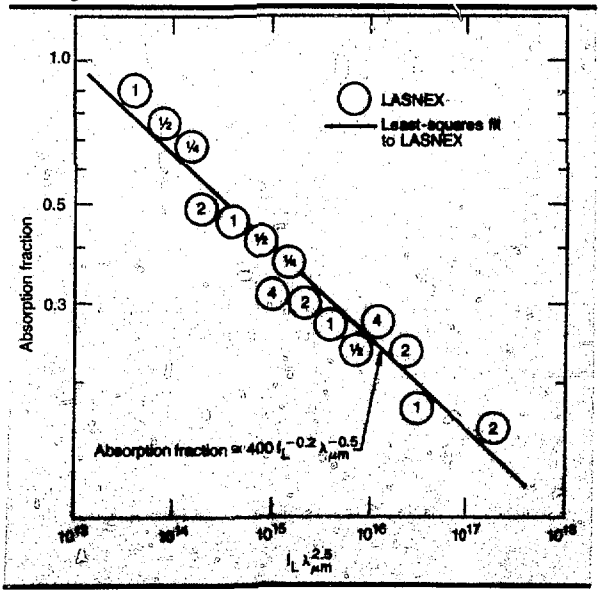

Fig. 6-25. LASNEX predictions for the scaling of total absorption with laser intensity and wavelength. Numbers within circles are wavelengths in μm.

Figures 6-22(b) and 6-23(b) show our predictions for the amount of SBS occurring locally in the coronal plasma. For the 1ω irradiations and the high-intensity 2ω irradiations, the scattered light suffers negligible inverse bremsstrahlung absorption while leaving the plasma; thus, these curves should be a good measure of the amount of Brillouin-scattered light measured by an external detector. For the 3ω irradiations and the low-intensity 2ω cases, the amount of externally measurable Brillouin-scattered light will be decreased from that shown in Figs. 6-22(b) and 6-23(b) due to classical absorption of the Brillouin-scattered light.

At laser intensities of 3×10^{13} and 3×10^{14} W/cm^2, SBS is predicted to increase monotonically as the laser wavelength increases. Since inverse bremsstrahlung decreases at longer wavelengths, we expect the total backscattered light to increase for longer wavelength. This behavior is shown in Figs. 6-22(a) and 6-23(a) for $I_L \leq 3 \times 10^{14}$ W/cm^2.

At laser intensities above about 10^{15} W/cm^2, there are two competing effects. As the laser wavelength is increased, there is more nonabsorbed light. On the other hand, Figs. 6-22(b) and 6-23(b) show that, for $I_L \geq 10^{15}$ W/cm^2, the contribution of SBS increases as we go from 3ω to 2ω, but then decreases as we go from 2ω to 1ω. Our SBS model indicates that this is because the efficiency of ion-heating saturation for SBS is largest for high laser intensities and long laser wavelengths, consistent with an earlier prediction[5b] that ion heating scales as $I_L^2 \lambda_L^3$. Thus, ion heating is able to limit SBS to a lower level for 1ω light, provided the intensity is high enough.

To obtain the total backscattered light for $I_L \geq 10^{15}$ W/cm^2, we must add together the nonabsorbed light and the Brillouin-scattered light. For our experimental parameters the decrease in inverse bremsstrahlung absorption as we go from 2ω to 1ω more than counterbalances the predicted decrease in SBS, and we find that the total backscatter fraction rises. We stress that this effect need not persist under conditions where inverse bremsstrahlung constitutes a smaller fraction of the total absorption.

Density and Temperature Profiles. Details of the density and temperature profile are often crucial in determining the mix of absorption and stimulated scattering

processes. We did not measure these quantities in the Argus wavelength-scaling series. However, in Fig. 6-24, we present LASNEX profiles for calculational parameters yielding a good match with experimentally measured macroscopic quantities, such as x-ray emission and laser-light absorption.

Figure 6-24(a) shows the predicted profile of mass density for 1ω and 3ω irradiations of a gold-disk target with $I_L \approx 3 \times 10^{14}$ W/cm^2. The two profiles are aligned so that their electron-conduction ablation fronts coincide. Both profiles are shown at the peak of the laser pulse. The calculation for 1ω light has poorer zoning resolution than that for 3ω. Nonetheless, it is clear that, for short-wavelength light, a stronger shock is sent into the dense matter, and the critical density lies closer to the ablation front. The corona is also considerably more dense for the 3ω irradiation, reflecting the fact that the critical density is nine times larger than at 1ω and the mass ablation rate is correspondingly larger as well. The large jump at critical density is due to the use of a flux limit of 0.03 at both laser wavelengths.

Figure 6-24(b) compares the electron-temperature profiles predicted by LASNEX for these same 3ω and 1ω calculations. The coronal temperature is higher at 1ω because, for the longer laser wavelength, a similar amount of laser energy must be used to heat a corona of lower heat capacity. The radiation heat front has penetrated farther into the dense material at 3ω than at 1ω.

For both laser wavelengths, it is interesting to note that the temperature rises sharply to its coronal value just outside the critical-density surface. This reflects the fact that inverse bremsstrahlung absorption is strongly peaked near critical density: the absorption coefficient is proportional to $(n_e/n_c)^2(1 - n_e/n_c)^{-1/2}$, where n_e is the local electron density and n_c is the critical electron density. Figure 6-24(c) illustrates the variation of the specific energy-deposition rate (in W/g) with distance from n_c. In the more finely zoned 3ω calculation, virtually all of the inverse bremsstrahlung absorption occurs within 5 μm of n_c; in the less well-resolved 1ω calculation, the majority of the inverse bremsstrahlung absorption occurs within 10 μm of n_c. This illustrates the strong density-dependence of inverse bremsstrahlung: even for a high-Z target at short wavelength and moderate laser intensity, collisional absorption occurs quite near n_c when the density profile is steepened, as in these calculations.

Scaling Laws. Experiments on the wavelength scaling of laser-light absorption are currently under way at a wide variety of other laser laboratories around the world. It is thus of interest to obtain some simple overall scaling laws for quantities such as total absorption, coronal conditions, and expected Brillouin scatter for a wide range of experimental conditions. Previous scaling laws[57] have been applicable within rather narrow portions of parameter space.

We used our LASNEX model of absorption and SBS to obtain scaling laws with laser wavelength and intensity. Other computational input parameters were held fixed: the laser spot was 450 μm in diameter, the pulse length was 1 ns, the target was a gold disk, $f_D = 0.3$, and the electron heat-flux inhibition was obtained from LASNEX's ion-acoustic turbulence model,[53] which tends to give a minimum flux limit of about 0.03 when $ZT_e/T_i \gg 1$.

Figures 6-25 and 6-26 show the predicted absorption fraction[48] and the mean electron temperature at the quarter-critical-density (0.25 n_c) surface (typical of the coronal conditions) for a series of LASNEX calculations. For this series, laser intensity varied from 3×10^{13} to 3×10^{16} W/cm^2 and with laser wavelength varied from 0.25 to 4 μm for the absorption and to 10 μm for the temperature. The circled numbers in Figs. 6-25 and 6-26 represent the laser wavelength in micrometres. The straight lines are least-

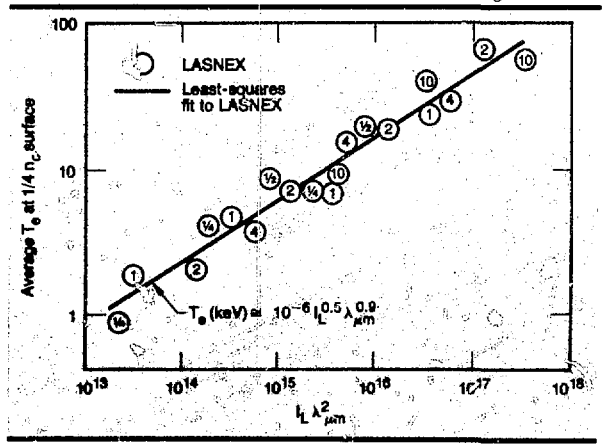

Fig. 6-26. LASNEX predictions for the average electron temperature at the 0.25 n_c surface as a function of laser intensity and wavelength. Numbers within circles are wavelengths in μm.

squares fits to the LASNEX results

$$\text{absorption fraction} \approx 400\, I_L^{-0.2}\, \lambda_{\mu m}^{-0.5} \qquad (2a)$$

and

$$\text{electron temperature (keV)} \approx 10^{\,6}\, I_L^{0.5}\, \lambda_{\mu m}^{0.9} \ . \qquad (2b)$$

Here, I_L is the peak laser intensity in W/cm^2, and $\lambda_{\mu m}$ is the laser wavelength in μm. The rms errors are ± 0.04 for the absorption and ± 6 keV for the temperature. A similar analysis of the SBS fraction calculated by LASNEX yields the prediction

$$\text{Brillouin-scattered fraction} \approx 8 \times 10^{\,6}\, I_\lambda^{0.3}\, \lambda_{\mu m}^{0.2} \qquad (3)$$

for laser wavelengths $\leq 2\ \mu$m.

This type of overall scaling relationship may be useful in the design of future wavelength-scaling experiments and in extrapolating present experimental results to future target parameters.

Author: C. E. Max

Major Contributors F. Ze, E. M. Campbell, W. C. Mead, R. E. Turner, K. G. Estabrook, V C. Rupert, and D. W. Phillion

Fig. 6-27. Preliminary measurements of x-ray conversion efficiencies from gold-disk targets.

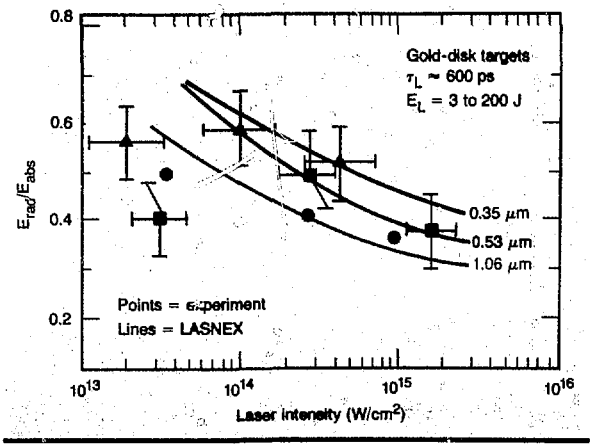

X-ray Conversion Efficiency at 1ω, 2ω, and 3ω

The Argus wavelength-scaling experiments were completed in 1981; the data analysis is still in progress. These experiments included measurements of the absolute x-ray energy ($0.1 < h\nu < 150$ keV) radiated from high-Z (gold) and low-Z (beryllium) disk targets. For experiments at 1ω (1.06 μm) and 2ω (0.53 μm), the peak average laser intensities ranged from 3×10^{13} to 3×10^{15} W/cm^2 in pulses of 600 to 700 ps (FWHM). We used a maximum intensity of $\sim 3 \times 10^{14}$ W/cm^2 for the 3ω (0.35 μm) experiments. Examples of the data, and the theoretical interpretation of the 2ω experiments have been presented in detail in the *1980 Laser Program Annual Report*[58]; data reduction and analysis is presently under way for the 1ω and 3ω experiments.

In the experiments, all but a negligible fraction of the radiated energy is in the region of the spectrum below 1.5 keV, although x-ray yields of up to several percent of the absorbed energy can be found in M-shell radiation from Au ($h\nu \sim 2.5$ keV). Details concerning x-ray line production as a function of laser wavelength are given in "Backlighting Characterization at 1ω, 2ω, and 3ω," later in this section.

The x-ray yield from photon energies of 0.1 to ~1.5 keV is measured by arrays of multichannel x-ray diodes.[59] In Fig. 6-27, we show a preliminary compilation of the gold-disk conversion efficiency—defined as radiated energy $0.1 < h\nu < 1.5$ keV divided by absorbed energy—as a function of average laser intensity for the three wavelengths. Data points are from the experiments, while the lines are LASNEX calculations. Note that the 1ω data points are representative of only a small number of measurements. They appear, however, to be in good agreement with previously reported 1.06-μm conversion-efficiency measurements.[60]

Several interesting features in the data are apparent in Fig. 6-27. First, as we noted from initial 2ω experiments,[61] the general trend is toward increasing sub-keV x-ray emission at shorter wavelengths. At 3ω and for $I_L \sim 10^{14}$ W/cm^2, we obtained a maximum conversion efficiency of 60%. Some

what surprisingly, the conversion efficiency at 2ω and 3ω decreases for $I_L < 10^{14}$ W/cm^2. This reduction is not observed at 1ω.

We performed the LASNEX calculations shown in Fig. 6-27 using fully time-dependent, non-LTE atomic physics with a constant reduction factor of 0.7 applied to the calculated emission opacity. The simulations are in agreement with the experimental results for intensities above 10^{14} W/cm^2. The increase in conversion efficiency at shorter wavelength occurs because the laser energy is deposited in denser, cooler plasma. This increases radiative rates relative to losses to internal energy and hydrodynamic blow-off.

Note that the LASNEX calculations overestimate the conversion efficiency at lower intensities, particularly at the shorter wavelengths. We are currently exploring difficulties in modeling the Au atomic physics.

Authors: R. E. Turner and W. C. Mead

Major Contributors: C. E. Max, E. M. Campbell, F. Ze, G. K. Tirsell, and P. H. Y. Lee

Comparison of Suprathermal X-ray Emission at 1ω, 2ω, and 3ω

Theoretical arguments have long predicted a reduction in suprathermal-electron production at a fixed peak intensity as the irradiating laser wavelength is decreased.[62] Confirmation of this trend has been one of the goals of the Argus experiments. To monitor the suprathermal-electron level, we measured the x-ray bremsstrahlung produced by electrons as they slow down in the overdense matter.[63] Other loss channels for suprathermal electrons, such as fast ions, were not measured in these experiments. The x-ray emission was measured by three K-edge filtered spectrometers (FFLEX, 7 Shooter, and 4 Shooter) employing both scintillator-photomultiplier and PIN-diode detectors.[63] Spectral coverage ranged from ~4.5 to ~70 keV.

As discussed in the *1980 Laser Program Annual Report*[63] cross-calibration and isotropy of the high-energy x-ray emission (except for attenuation through thick, high-Z targets) have been adequately verified during the course of the Argus wavelength-

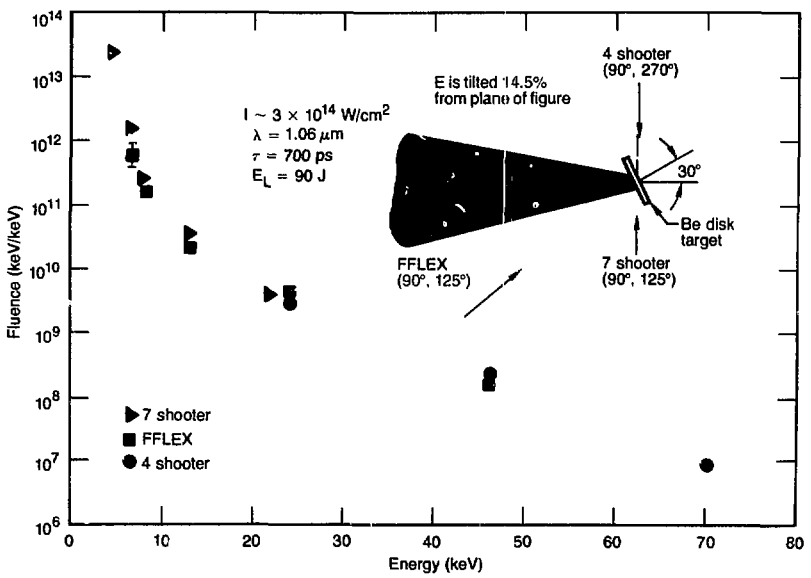

Fig. 6-28. Composite x-ray spectra from a Be disk using three K-edge spectrometers on Argus.

scaling experiments. Therefore, in generating the x-ray spectra from disk targets, we have combined the data from three systems. Figure 6-28 demonstrates the agreement between the three spectrometers, showing a typical x-ray spectrum compiled from a Be target irradiated at 1ω. In the inset of this figure, we show the target irradiation and detector geometries. Figures 6-29 through 6-31 show the x-ray spectra recorded from Au disks at nominal intensities of 3×10^{13}, 3×10^{14}, and 10^{15} W/cm^2 for incident 1ω, 2ω, and 3ω wavelengths. As shown in Table 6-16, we performed these experiments under nearly identical irradiation conditions to facilitate ready comparison.

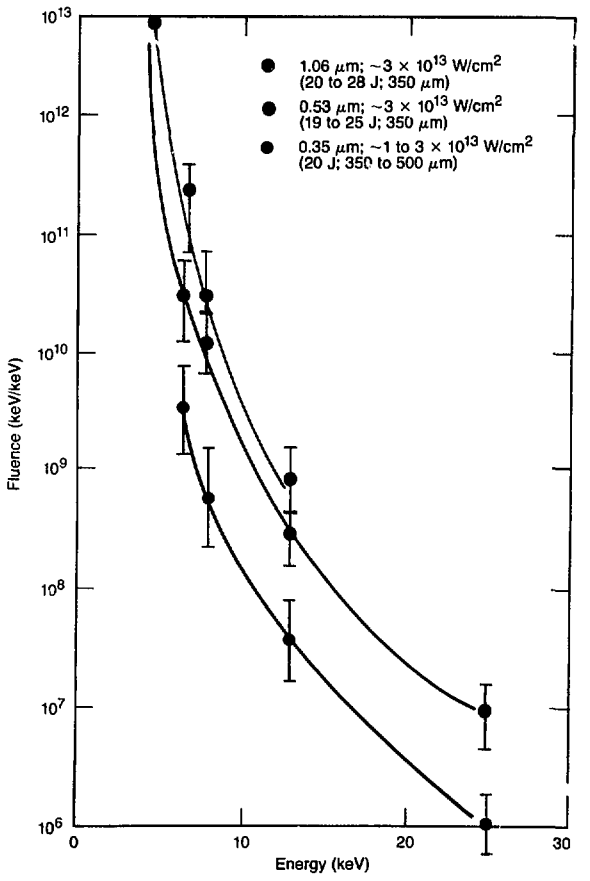

Fig. 6-29. 1ω, 2ω, and 3ω x-ray spectra from a gold disk at nominal intensity of 3×10^{13} W/cm^2.

For these nominal conditions, the data show a reduction in the high-energy x rays—and in the inferred high-energy electrons—as the laser wavelength is decreased. For example, the inferred fraction of the absorbed energy that appears as suprathermal electrons at intensities of 3×10^{14} ranges from $\sim 2 \times 10^{-4}$ to $\sim 1.4 \times 10^{-2}$ as the wavelength increases from 0.35 to 1.06 μm. At the higher intensities, these values range from $\sim 1.5 \times 10^{-3}$ at 3ω to 3×10^{-2} at 1ω. Furthermore, within the uncertainties in the measurements and the range of parameters studied, the slopes of the x-ray spectra do not show any strong dependence on wavelength or average intensity.

The minimal slope variations are not surprising, considering the observed spatial variation of intensity across the focal spot of the beam at the various wavelengths used and considering the many processes that can generate suprathermal electrons. This latter hypothesis is supported by additional experimental evidence of the scattered light from the stimulated Raman instability, discussed in "3/2ω Emission at 1ω and 2ω" and "Stimulated Raman Scattering at 1ω and 2ω," later in this section.

Author: E. M. Campbell

Major Contributors: B. L. Pruett, R. E. Turner, F. Ze, and W. C. Mead

Suprathermal Electrons from Disks (Comparison of K_α to Bremsstrahlung)

Suprathermal electrons generated in laser-fusion experiments are principally observed by measuring x-ray bremsstrahlung created when the suprathermal electrons deposit their energy in cold, dense target material. These high-energy electrons also produce x-ray lines characteristic of the material. Characteristic K_α x-ray lines have been observed in high-resolution spectra of medium-Z (Z = 22 to 30) disks.[64]

We have used a simple analytical model to relate the K_α intensity to the total energy in suprathermal electrons deposited in the material. For simple disks, this total hot-electron energy agrees reasonably well wi.

the suprathermal energy derived from the bremsstrahlung continuum. Using layered-disk targets, we have proved that these characteristic x rays are produced by suprathermal electrons. Our experiments also show that the electrons are not confined to the irradiation area of the target, but that a significant fraction reach the rear surface of the disks.

An example of the high-resolution K_α x-ray spectrum from a Ni disk is shown in Fig. 6-32. Note the two prominent features in the spectrum

- Spectral features from 7.65 to 7.85 keV are emitted by hot, ionized atoms (He-like nickel) in the laser-interaction region.
- The feature at 7.47 keV is the characteristic K_α x-ray line emitted from the relatively cool solid.

Also shown in Fig. 6-32 is a Ni spectrum produced when a thin (~0.5 μm) Au layer and a buffer layer (2 μm) of CH are placed on top of a Ni disk. In this example, the Au layer absorbs the laser energy so that no thermal Ni lines are observed. Only the characteristic K_α lines are produced by the suprathermal electrons penetrating the Ni.

We have modeled the problem analytically by calculating the K_α-x-ray production probability as the electron stops in the solid. The problem is analagous to an electron tube used as an x-ray source. For a monoenergetic electron of energy E_0, the K_α conversion efficiency, $\eta_K(E_0)$, is calculated by

$$\eta_K(E_0) = \frac{1}{4\pi E}\int_{I_0}^{I_K}\frac{\sigma(E)_K}{S(E)}\left(\frac{2E}{m}\right)^{1/2} dE \quad . \qquad (4)$$

The nonrelativistic Born approximation[65] is used for the x-ray production cross section, σ_K, and the Bethe–Bloch[66] formulation is used for the electron stopping power, $S(E)$, in Eq. (4). The results agree with semi-empirical results derived from electron-tube data.[67]

The average K_α conversion efficiency, η_K, is calculated by averaging η_K over the electron-energy distribution, $n(E)$, and normalizing to the total electron-energy (or heat) flux, Σ. The expression for η_K is

$$\eta_K = \frac{1}{4\pi\Sigma}\int_{I_K}^{\infty}\eta_K(E)n(E)\left(\frac{2E}{m}\right)^{1/2} dE \quad , \qquad (5)$$

where the heat flux is given by

$$\Sigma = \int_0^{\infty} E\,n(e)\left(\frac{2E}{m}\right)^{1/2} dE \quad . \qquad (6)$$

Fig. 6-30. 1ω, 2ω, and 3ω x-ray spectra from a gold disk at nominal intensity of 3×10^{14} W/cm^2.

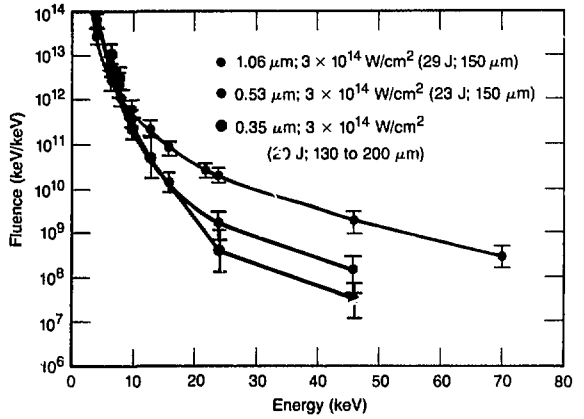

Wavelength	Laser energy (J)	Pulse length (ps)	Spot diameter (μm)
Nominal laser intensity: 1 to 3 × 10^{13} W/cm^2			
1ω	20 to 28	700 to 800	350
2ω	19 to 25	650 to 750	350
3ω	14 to 23	600 to 700	350 to 500
Nominal laser intensity: 1 to 3 × 10^{14} W/cm^2			
1ω	25 to 35	700 to 800	150 to 200
2ω	23 to 25	650 to 750	140 to 180
3ω	20 to 30	620 to 750	130 to 200
Nominal laser intensity: 1 × 10^{15} W/cm^2			
1ω	35	700 to 800	80 to 100
2ω	28 to 35	600 to 720	60 to 80
3ω	35 to 44	700	90 to 120

Table 6-16. Irradiation conditions for studies of suprathermal x-ray emission.

Fig. 6-31. 1ω, 2ω, and 3ω x-ray spectra from a gold disk at nominal intensity of 3 × 10^{15} W/cm^2.

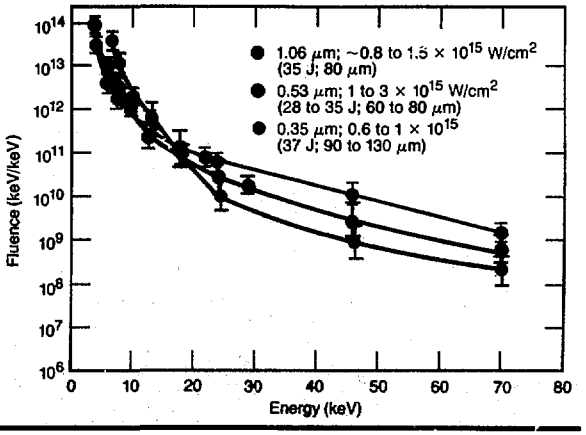

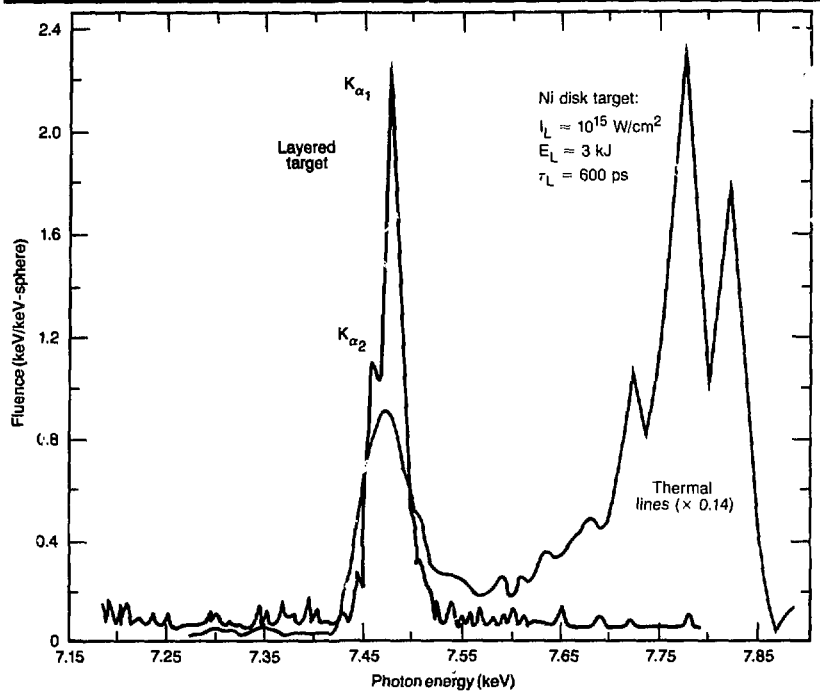

Fig. 6-32. Comparison of an x-ray spectrum from a directly irradiated Ni disk (solid line) with the spectrum from a Ni disk overcoated with Au (dashed line).

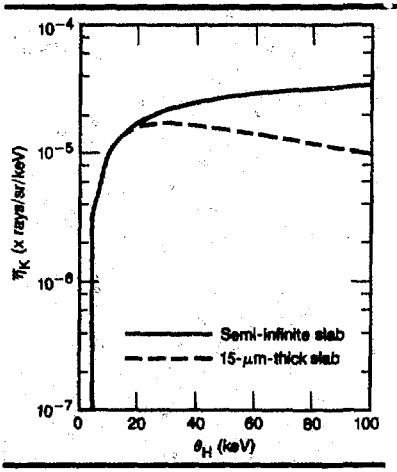

Fig. 6-33. Conversion efficiencies for production of Ni K_α x rays by suprathermal electrons. The solid curve assumes that the Ni disk is infinitely thick, absorbing all electrons; the dashed curve is for a 15-μm-thick Ni slab.

The results for a Ni disk are plotted in Fig. 6-33, assuming a Maxwellian electron distribution with hot-electron temperature θ_H.

For thin disks, the electron range can be greater than the disk thickness. The electrons, thus, may not necessarily deposit all of their energy in the disk in a single pass, potentially reducing the conversion efficiency. We have estimated the reduction of the conversion efficiency for a 15-μm-thick disk; this is shown by the dashed curve in Fig. 6-33. For typical hot-electron temperatures used in the high-irradiation experiments at Shiva ($\theta_H \sim 50$ keV), the reduced conversion efficiency is not very sensitive to θ_H, so that errors in the measurement of the bremsstrahlung slope do not affect this method for determining suprathermal energy. Including assumptions about finite target effects, errors in measuring the bremsstrahlung slope are at most a factor of 2 for disks of these thicknesses.

We have used the conversion efficiencies obtained in our experiments to analyze several sets of simple disk data, such as those shown in Fig. 6-32. The energy in hot electrons, E_H, compares favorably with results using the bremsstrahlung spectrum as measured in filter fluorescer (FFLEX) experiments[68]; an example of the agreement is shown in Fig. 6-34. The solid lines are the predicted bremsstrahlung spectrum using the total energy in hot electrons derived from the K_α signal. The integral K_α technique cannot measure the electron

distribution. We assumed a single hot-electron temperature of 50 keV, as suggested by FFLEX. The intensity of the bremsstrahlung predicted from the K_α yield agrees with the FFLEX data for the two shots. The agreement is not surprising, since both bremsstrahlung and K_α x rays are produced by electrons stopping in the dense solid material.

In other targets (such as layered disks), the two measurements may not necessarily agree, since bremsstrahlung is produced in all layers of the target, while K_α x rays are produced only in the material of interest. In this way, K_α x rays can be used to probe only part of the target. For example, we have measured Ni K_α x rays from a layered disk in which, alternately, the front and the back of the Ni is protected from electrons by low-Z plastic. The ratio of the signals from the front and back of the target shows that, for the irradiation conditions given in Fig. 6-32, about 30% of the signal is from electrons striking the rear target surface. In this experiment, the outside diameter of the laser-irradiation area is about 750 μm on a 1000-μm-diam disk. The fraction of energy transported to the rear surface will depend on the exact experimental conditions, but the experiment described here indicates that the suprathermal electrons are not confined to the irradiation region.

We have derived the energy in hot electrons for a number of disk shots at Shiva, as shown in Fig. 6-35; we used FFLEX data to derive θ_H. Most of the data indicate that the fraction of incident energy in hot electrons, f_H, is about 1%. Of course, the K_α technique only measures the suprathermal energy deposited in the solid, as do the bremsstrahlung results. Energy transferred to ion blowoff or to electric-field generation is not measured.

In summary, we have correlated the intensity of K_α x rays from laser-irradiated disks with the production of suprathermal electrons. The K_α intensity and bremsstrahlung spectra correlate well for simple disk targets. The K_α x-ray technique offers the potential for measuring localized deposition of fast electrons, since its signal is characteristic of the material.

Author: R. L. Kauffman

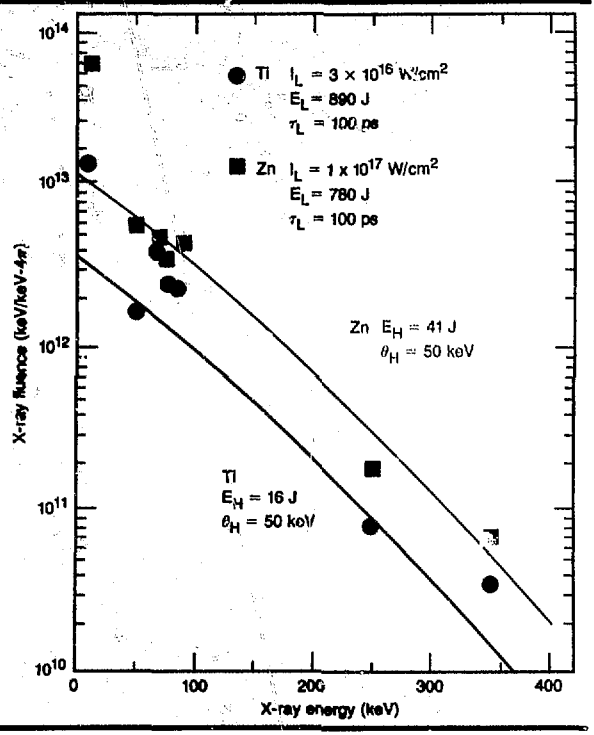

Fig. 6-34. Comparison of the total ▲ energy in suprathermals, predicted from K_α intensities, and the measured bremsstrahlung spectrum.

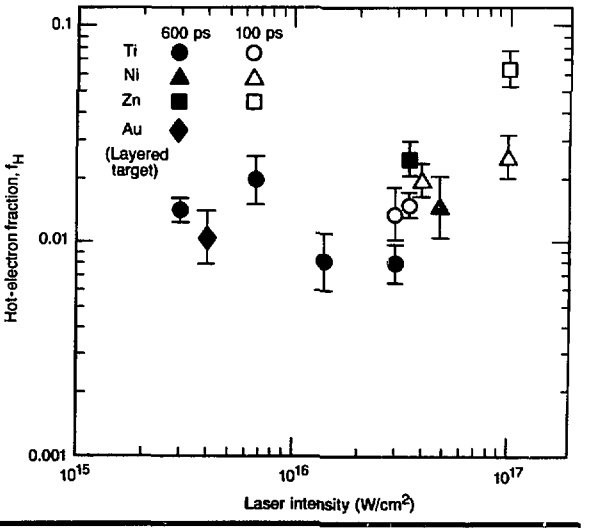

Fig. 6-35. Energy dependence of the fraction of energy in hot electrons from various disk shots, derived from the K_α yield.▼

3/2ω Emission at 1ω and 2ω

The observation of electromagnetic radiation at the 3/2 harmonic of the laser frequency (0.71 μm for 1ω = 1.06 μm) can provide data relevant to the presence of plasma waves at the quarter-critical density (0.25 n_c) of the incident laser light. Such plasma waves can be a source of suprathermal electrons, which, in turn, are capable of preheating the D–T gas, thus impairing the high-density implosions that are critical to success in inertial-confinement fusion.

In principle, measurements of the level of 3/2ω emission can yield information regarding the amount of laser energy deposited in plasma waves at 0.25 n_c; measurements of the spectral features of the 3/2ω emission can yield the electron temperature in the same region. Deducing these parameters from measurements requires an understanding of the mechanism(s) by which the 3/2ω emission is generated. We have compared our spectral data with the predictions of two different models.[69,70] The results show that we need additional theoretical understanding of the generation mechanism before temperatures can be quantitatively obtained.

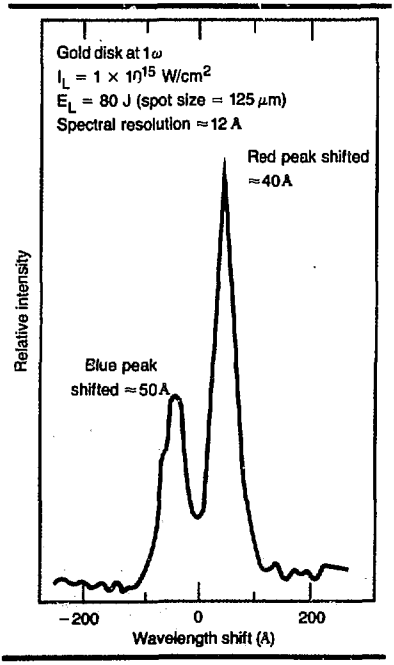

Fig. 6-36. 3/2ω spectra measured at 30° from 1ω irradiation of a gold-disk target.

It is believed that the plasma waves at 0.25 n_c are generated by the two-plasmon-decay instability,[71] in which the incident 1ω laser light decays into two plasma waves of frequencies 1/2ω ± δω, where δω/ω is a small, temperature-dependent shift. The 3/2 harmonic can be generated by the nonlinear mixing of an incident photon at 1ω and a plasma wave at 1/2ω ± δω; a higher-order (and therefore weaker) process, the nonlinear coalescence of three plasma waves, is also possible.

Stimulated Raman scattering (SRS) can also generate plasma waves at 0.25 n_c. However, it has a higher intensity threshold than two-plasmon decay. In addition, the double-peaked spectral features of the 3/2ω light we observe are those predicted for two-plasmon decay; SRS-produced plasma waves should not produce this spectrum.

We have spectrally resolved the light emissions near 3/2ω for 1ω disk experiments on both Argus and Shiva and for 2ω (0.53 μm) disk experiments on Argus. The Shiva results are similar to those obtained during Argus experiments. In this article, we discuss the Argus experiments with 700-ps pulse widths.

At an angle of 30° to the laser beam, for a disk target irradiated at normal incidence at 1ω, we observe two peaks: one red-shifted, the other blue-shifted (Fig. 6-36). The explanation[69] for this is that the red-shifted light has been directly backscattered (with a scattering angle $\theta > \pi/2$) from the lower-frequency, outward-moving plasma wave, while the blue-shifted light has been forward scattered from the higher-frequency, inward-moving plasma wave. We observe the blue-shifted light only after it has reflected off its critical surface (at 2.25 n_c).

Evidence in support of this hypothesis includes the following observations. The blue-shifted light is reduced in amplitude compared to the red-shifted light, presumably due to absorption. In 2ω experiments, where the short-wavelength 3/2ω emissions are strongly absorbed, the blue-shifted light is not observed, again due to absorption (see Fig. 6-37). In burn-through experiments on thin plastic foils, in which 3/2ω emission is observed in the forward direction, it is

the red-shifted peak that is reduced or completely absent, as shown in Fig. 6-38. Similar observations have been reported by others.[70]

The exact mechanism by which the plasma waves, the incident light, or both combine to produce $3/2\omega$ emission is an area of active research. Avrov et al.[69] use a model wherein the plasma-wave number is taken to be that which gives the highest $2\omega_{pe}$ growth rate[71] in a cold plasma, but that does not necessarily allow for phase-matching with an incident photon. This model gives

$$\Delta\lambda = -22.7\, T_e \cos\theta \ (\text{Å}) \qquad (7)$$

for the wavelength shift away from the exact 3/2 harmonic, where T_e is the electron temperature (in keV) and θ is the angle of the scattered light with respect to the incident laser light. The higher-order (but momentum-conserving) process of three-plasmon coalescence is calculated to give the same results (within 5%). In a warm plasma, we expect the $2\omega_{pe}$-plasma wave numbers to be smaller than in a cold plasma, and the numerical coefficient in Eq. (7) to be correspondingly smaller.

Additional experimental evidence, however, points out the limitations of this simple model. Spectral measurements of $3/2\omega$ emission, looking for scattered light near 90° to a nominal-incidence laser beam should [according to Eq. (7)] show only one peak. However, measurements reveal two well-separated peaks, as shown in Fig. 6-39. At this time, we do not have an acceptable explanation for these observations. In addition, present measurements neglect Doppler shifts, refraction, three-dimensional effects, ion wave scattering, and the finite f/No. of the focusing lens. Because of these limitations and assumptions, the temperatures derived from these measurements should be regarded as model-dependent, as discussed below.

Figure 6-40 shows the temperature inferred from Eq. (7) for Be, Ti, and Au disks irradiated at a nominal intensity of 1×10^{15} W/cm^2. We used the red-peak/blue-peak separation, rather than the absolute value of either peak, since the separation value is less sensitive to Doppler-shift effects. The absorbed energy for these shots is 16 J for Be, 22.5 J for Ti, and 30 J for Au. This energy is partitioned into heating the material, hydrodynamic expansion, and radiation. For the gold target, radiative losses account for approximately 10 J (see "X-ray Conversion Efficiency at 1ω, 2ω, and 3ω," earlier in this section). We did not measure hydrodynamic losses, but they are presumably highest for the (low-Z) beryllium and lowest for the (high-Z) gold. Thus, even after accounting for its radiation losses, we expect gold to be hotter than the lower-Z plasmas because of its higher absorption.

This expectation is confirmed by the data, although the absolute value of the

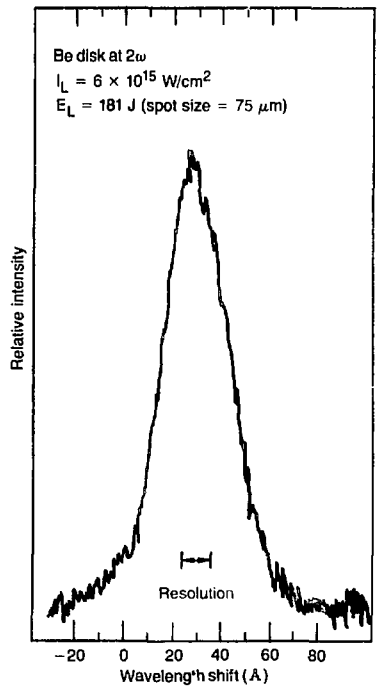

Fig. 6-39. $3/2\omega$ spectra (direct backscatter) at 2ω; note the absence of a blue-shifted peak.

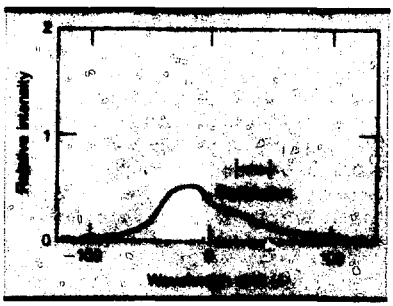

Fig. 6-38. $3/2\omega$ spectra measured in the forward direction, for a thin (0.5 μm) plastic-disk target designed to "burn through" to less than 0.25 n_c during the laser pulse. Note the reduction of the red-shifted peak.

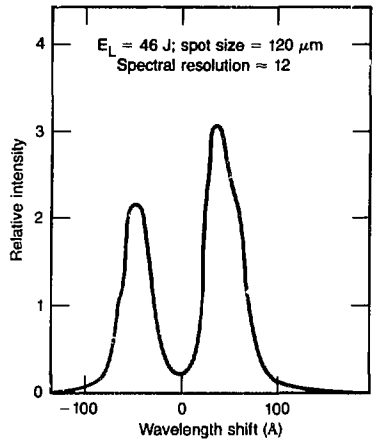

Fig. 6-39. 3/2ω, spectra, measured at 85° to 1ω irradiation, of a gold-disk target, showing two distinct peaks in contradiction to simple-model prediction.

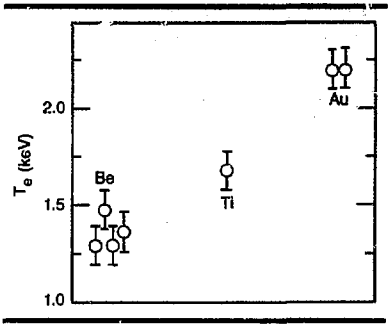

Fig. 6-40. Electron temperatures at 0.25 n_c, inferred from Eq. (7), for 1ω experiments at 1 × 10^{15} W/cm² (Doppler effects not deconvolved).

temperature is somewhat lower than that predicted by simulations or inferred from SBS measurements. We have made no attempt to remove Doppler effects from the data; to do this requires knowledge of the velocities at both 0.25 n_c and 2.25 n_c. Nevertheless, Doppler-shift corrections should be reasonably small (<10%). Since we expect the lower density to have a higher velocity, Doppler effects should cause us to slightly underestimate the temperature.

In summary, measurements of 3/2ω emission have the potential of providing electron temperatures at 0.25 n_c, a region of considerable importance for laser-plasma interactions. However, improved models are necessary for accurate interpretation of the data. Even without accurate interpretive models, however, these harmonic measurements are indicative of the presence of potentially detrimental plasma waves near 0.25 n_c. If inertial fusion is to succeed, we must understand such preheat-producing instabilities and how to control them.

Author: R. L. Turner

Major Contributors: D. W. Phillion, B. F. Lasinski, and E. M. Campbell

Stimulated Raman Scattering at 1ω and 2ω

Introduction. Experiments during the past year have not only confirmed that instabilities in the underdense plasma can occur at high levels but also proved that these instabilities, operating alone in a completely underdense plasma, can produce high-energy electrons and absorb at least 10% of the incident laser energy.

We have observed stimulated Raman scattering (SRS) in the forward direction, which can produce an extremely hard electron distribution with an average electron energy greater than 100 keV. Near quarter-critical density (0.25 n_c), the phase velocity of the electron-plasma wave is nearly independent of the scattering angle, and the wave-breaking energy is about 100 keV. At lower electron densities, the wave-breaking energy is lower for backscatter but higher for forward scatter. At 0.10 n_c, the electron-plasma wave for forward scatter has a wave-breaking energy of about 1 MeV.

The fractional amounts of incident laser-light energy appearing as 3/2ω and 1/2ω emission have been observed to increase strongly with the electron-density scale length, both in Argus experiments with varied laser-spot sizes and in Shiva experiments with varied pulse lengths. Time-resolved measurements of the Raman light spectrum for the Argus 2ω (0.53 μm) experiments show that the SRS occurs late during the laser pulse and that it can onset abruptly and simultaneously over a broad spectrum. Particularly for the very-late-time SRS emission, the average intensity on target in our experiments seems to be far below threshold. Filamentation may be the cause of this effect.

In the next three sections of this article, we describe 1ω experiments, beginning with SRS measurements in the underdense

plasma, using exploding CH foils, and then examining the plasma scaling of $1/2\omega$ and $3/2\omega$ emission. In the final section, we discuss time-resolved SRS measurements at 2ω.

Thin-Foil Experiments at 1ω. Our intent in the 1ω thin-foil experiments was to measure the scattered-light signatures of the Raman and two-plasmon-decay ($2\omega_{pe}$) instabilities, including the amount and spectrum of the forward-scattered SRS. To create a completely underdense plasma that was hot and had a long electron-density scale length, we exploded 0.69-μm-thick Formvar (CH) foils with a 900-ps FWHM Gaussian 1ω pulse with intensities of 2 to 3 $\times 10^{15}$ W/cm^2. The lower or upper cluster of 10 Shiva beams was overlapped on a focal spot 400 μm in diameter.

The CH foils were stretched across 25-μm-thick gold washers, 2 mm in outer diameter and 0.9 mm in inner diameter. We chose gold as the material for the supporting washers to generate a detectable number of high-energy bremsstrahlung x rays. In these experiments, the gold stopped ~10 J of 40-keV electrons. Additional diagnostics included a high-energy ($h\nu \approx$ 350 keV) x-ray spectrometer and an optical/x-ray (OX) streak camera that simultaneously records the intensities of the $3/2\omega$ light, the x rays from 30 to 70 keV, and the incident 1ω laser light.

The two successfully completed thin-foil experiments are summarized in Table 6-17. The exploding foils had nearly constant electron densities over the center several hundred micrometres. We performed one-dimensional LASNEX simulations for conditions of 900-ps pulses and an intensity of 3×10^{15} W/cm^2, using a flux limiter $f = 0.03$. Figure 6-41 shows the experiment and calculated electron-density profile at the peak of the laser pulse ($t = 0$). The simple fit $n_e = n_c\,[8(t + 0.8)]^{-1}$ is accurate to ±5% for $|t| < 0.5$ ns. The maximum electron density is 0.25 n_c at $t = -300$ ps and 0.10 n_c at $t = +500$ ps. Using LASNEX, we

	Shot A	Shot B
Energy on target	3.13 kJ	2.47 kJ
Pulse width	892 ps FWHM	911 ps FWHM
Average intensity	2.1×10^{15} W/cm^2	2.7×10^{15} W/cm^2
Spot diameter	406 μm	406 μm
Raman light energy	325 J	250 J
$I_{84\ keV}$	4.66×10^{12} keV/keV into 4π	3.26×10^{12} keV/keV into 4π
$I_{350\ keV}$	3.44×10^{9} keV/keV into 4π	4.46×10^{9} keV/keV into 4π
T_{hot}	37 keV	40 keV

Table 6-17. Summary of the exploding-foil experiments.

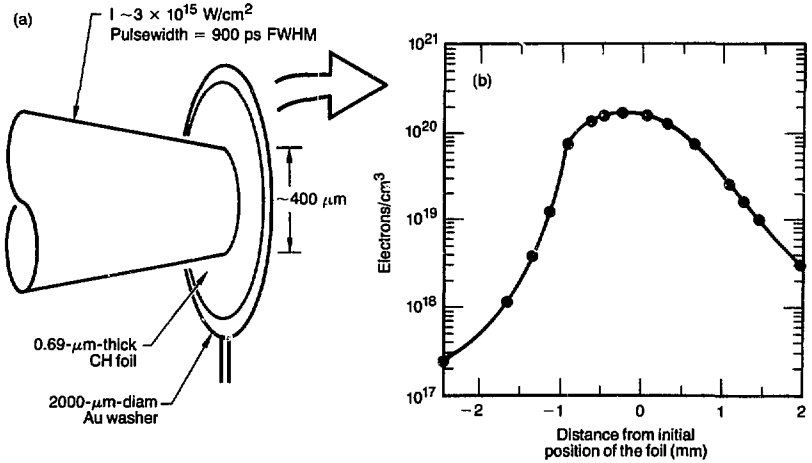

Fig. 6-41. (a) Schematic of the exploding-foil experiment. (b) Electron density profile at the peak of the laser pulse, calculated in one dimension.

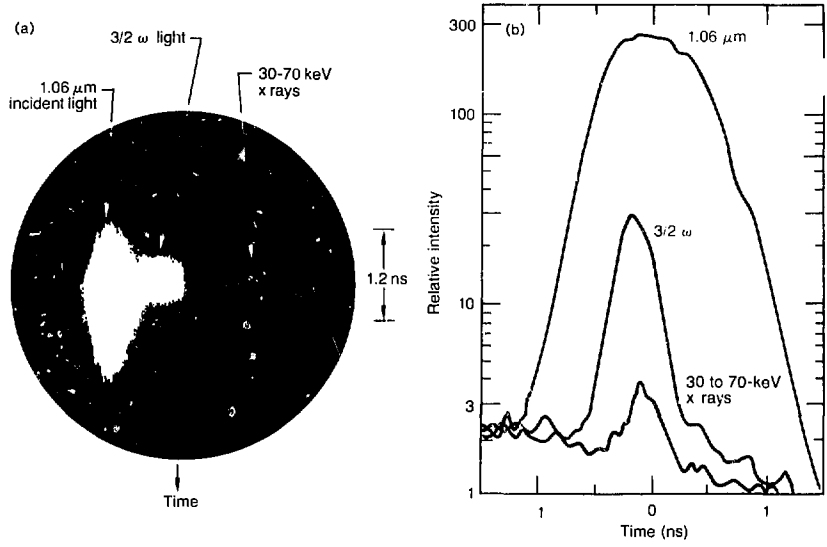

Fig. 6-42. (a) OX streak-camera record. (b) Lineouts of three images. The peak of the laser pulse is at $t = 40 \pm \frac{200}{50}$ ps.

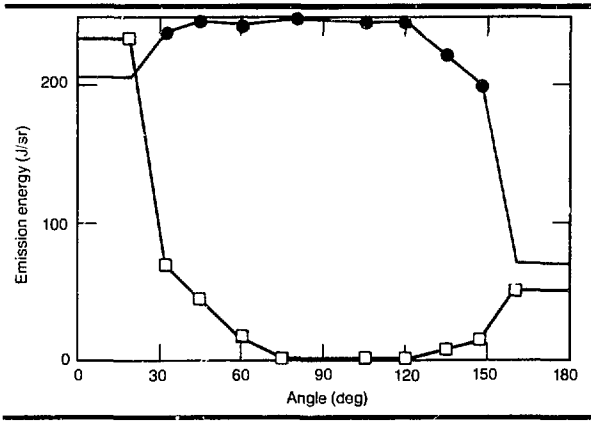

Fig. 6-43. Angular distribution of SRS; the laser beams came from near $\theta = 0°$.

calculated the coronal electron temperature, $T_{e\omega}$ to be about 4 keV and the total absorption to be 7%, which is the sum of the 3% inverse bremsstrahlung absorption and the 4% absorption that the SRS puts into electron-plasma waves. LASNEX includes a Brillouin model (which was turned on), but does not have a $2\omega_{pe}$ model. With both Raman and Brillouin turned off, LASNEX calculated 7% absorption.

Our major experimental finding was made by the OX streak camera. The $3/2\omega$ emission and x rays from 30 to 70 keV occurred simultaneously and lasted only about one-third the incident laser pulse width of 900 ps. Before discussing these results, we first describe OX, which is a conventional optical streak camera outfitted to also detect hard x rays.

A 12.5-mm-thick sheet of lead-glass blocked the x rays for the two light channels. The $3/2\omega$ emission was selectively transmitted by a bandpass interference filter with a 300 to 350-Å FWHM bandpass and 7115-Å center wavelength (the $2/3\lambda$ wavelength is 7093 Å). The $3/2\omega$ emission was fully blocked, with a rejection of 10^5, against 1ω and 2ω light; we used a KG-3 Schott color filter ahead of the interference filter to provide another factor of 10^4 rejection against the 1ω light.

The response of the OX S-1 photocathode to x rays is due to the presence of the high-Z metals cesium and silver. A 2.8-mm-thick SiO_2 vacuum window on the streak tube sets the lower limit of about 25 keV on the energy range of the x rays that can be detected. The 1.5-mm-wide contact slit was cut through 6 mm of lead; the streak tube demagnifies this slit width to about 160 μm on the streak-tube output phosphor. The time resolution for the sweep rate of 121 ± 4 ps/mm is thus about 20 ps.

The OX streak record for shot B (from Table 6-17) is shown in Fig. 6-42(a). The

three images are (from left to right) the incident 1ω fiducial, the 3/2ω emission, and the x rays from 30 to 70-keV. The 3/2ω emission seen by the OX streak camera was generated in the forward direction at 60° incident to the beam axis.

Lineouts of the three images are shown in Fig. 6-42(b). The peak of the laser pulse is at $t = -40^{+200}_{-50}$ ps. The FWHM of the fiducial is 980 ps, which compares well with the 892-ps FWHM measured at the laser oscillator. The 3/2ω emission signal is 300 ps FWHM, and the high-energy-x-ray signal is 280 ps FWHM. The x rays are nearly coincident with the time of 3/2ω emission: the x rays lag the 3/2ω emission by only 75 ± 25 ps. The peak of the 3/2ω emission is at $t = -160$ ps, which is 120^{+200}_{-50} ps before the peak of the laser pulse. This streak record establishes unequivocally the importance of densities of 0.25 n_c or near −0.25 n_c in producing high-energy electrons.

The angular distributions of the SRS emission energy (Fig. 6-43 and Table 6-18) were measured by an array of light calorimeters at the angles θ = 20, 32, 45, 60, 75, 90, 105, 120, 135, 148, and 160°. The calorimeters are of the self-compensating, dual-receiver design with 1-mm NG-1 absorber glass. Each calorimeter had Corning color filters 7-56 and 4-64, both of which are coated for 99.5% reflectivity at 1ω and >80% transmission for the dielectric coating over the wavelength range 1.5 μm < λ < 2.6 μm. We assumed a transmission of 30% through the filters that select the Raman light. The filter transmission depends on wavelength and is 42% at 2.0 μm, 30% at 1.8 μm, 18% at 1.6 μm, and 11.5% at 1.5 μm. For shot A, there is little sidescattered SRS, but about 50 J in forward-scattered Raman light, while, for shot B, the SRS energy is much greater at angles more to the side. Measurements at some angles are not available due to the loss of one or two stations of calorimeter data during each experiment.

In performing the integral over the solid angle to get the Raman-light energy, we assumed the intensity was flat between 0 and 20° and between 160 and 180°. The average values for the measurements at the same angle, θ, were connected by straight lines for the integration. However, the

Angle		Shot A (J/sr)	Shot B (J/sr)
θ (deg)	ϕ (deg)	(Beams from θ = 0°)	(Beams from θ = 180°)
20	154	233	No data
	0	No data	7
32	72	No data	21
	270	70	No data
45	306	44	5.5
60	306	16	9
75	306	1.5 ± 1.5	2.5
	324	1.5 ± 1.5	11
105	198	1.0 ± 1.5	3
	306	0.0 ± 1.5	4
120	126	0.0 ± 1.5	8
	198	No data	9
135	126	No data	31
	270	5.5	No data
148	90	No data	55
	108	No data	≳30
160	90	50	No data

Table 6-18. Angular distribution of Raman-light energy.

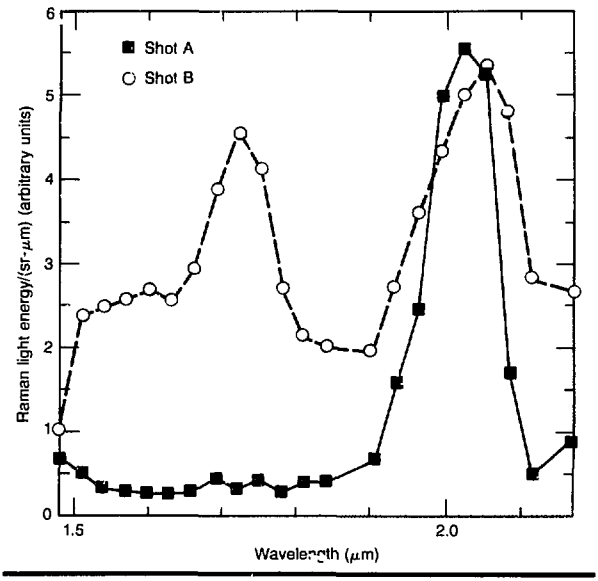

Fig. 6-44. Spectra of the forward-scattered SRS.

θ = 160° and θ = 20° measurements for shot B were lost; for shot B, we took the SRS intensity to be 180 J/sr at θ = 160° and 14 J/sr at θ = 20°.

The forward-scattered SRS spectrum shows a peak at 2.05 μm for both experiments (Fig. 6-44), but, for the higher-intensity shot B, there was also considerable forward-scattered Raman light at shorter wavelengths. The spectrograph looked 45°

away from the directly forward direction for shot A and 20° away for shot B.

The angular distribution of the scattered 1ω light for shot B is shown in Fig. 6-45. An array of photodiodes measured an absorption fraction of 20% ± 15% for both shots. This number is corrected for the energy in SRS light, which is not counted as absorption. The photodiodes had 200-Å FWHM bandpass interference filters centered at 1.06 μm; two-thirds of the unabsorbed light was transmitted through the foil. The backscattered light shows a pronounced peak at 60° away from the direct-backscatter direction. The angular distribution for the other foil experiment was nearly the mirror image of this one, since the laser light came from $\theta = 0°$, rather than from $\theta = 180°$.

From our experiments, we know that SRS caused about 10% of the incident light energy to go into electron-plasma waves. The $2\omega_{pe}$ instability may have occurred strongly, since 0.04% of the incident laser energy appeared as 3/2ω emission, but, at present, we do not know how to estimate an absorption from this measurement. The 3/2ω emission energy was measured by an array of photodiodes. The angular distribution was fairly isotropic, with about as much in the forward hemisphere as in the backward hemisphere. Thus, with the 2% calculated inverse bremsstrahlung absorption, the actual absorption in the underdense plasma was greater than 12%.

Fig. 6-45. Angular distribution of the 1ω scattered laser light for shot B.

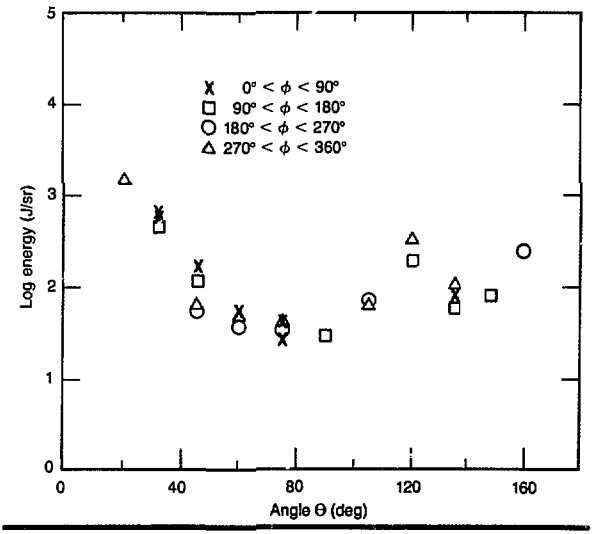

Stimulated Raman scattering was far above threshold in these experiments. About 20% of the incident laser-light energy either went into the electron-plasma waves or into SRS. Considering that SRS was operative for only part of the laser pulse, this indicates that Raman absorption can be quite efficient when the threshold for convective instability is far exceeded. For instance, the Raman light wave convectively grows 40 intensity e-folding lengths given the conditions $I = 3 \times 10^{15}$ W/cm^2, $L = 1000\ \mu$m ($L^{-1} = 1/n_e \cdot dn_e/dx$), and direct backscatter.

This calculation may at first appear to be questionable, since it assumes that the incident laser light is a linearly polarized plane wave. In fact, we know that the 406-μm-diam focal spot was simultaneously irradiated by 10 independent, differently polarized laser beams. Brillouin scattering would be expected to make the distribution of wave vectors for the incident light even more chaotic. We argue that neither a chaotic distribution of incident-light $\mathbf{k}$ vectors nor a small amount of bandwidth (i.e., less than 10% of the incident laser frequency) will cause the threshold for convective SRS to increase greatly. (We will, however, find out that the 40 e-folding lengths are really only 20, when account is taken of the differing polarizations of the Shiva laser beams.)

Imagine a Raman light wave propagating through a plasma in which the incident light wave has a variety of wave vectors and frequencies, such that

$$\frac{\partial}{\partial x}\tilde{A}_R(\omega_R, \mathbf{k}_R) = \sum_\ell \tilde{\gamma}_{1\ell}\tilde{n}_e^*(\omega_{0\ell} - \omega_R, \mathbf{k}_{0\ell} - \mathbf{k}_R) \times \tilde{A}_{0\ell}(\omega_{0\ell}, \mathbf{k}_{0\ell}) \quad . \qquad (8)$$

The sum is over the many beams, whose vector potentials have the complex amplitudes $\tilde{A}_{0\ell}$. The coupling coefficients $\gamma_{1\ell}$ include the polarization dot product $\mathbf{e}_R^* \cdot \mathbf{e}_{0\ell}$

as well as other physics. The tilda designates a complex quantity; the asterisk superscript denotes complex conjugation. The subscript R refers to the Raman light wave, and $\tilde{n}_e$ is the amplitude of the electron-density fluctuation for the electron-plasma wave.

Each incident laser beam, ℓ, drives its own electron-plasma wave, whose angular frequency is $\omega_\ell = \omega_{0\ell} - \omega_R$ and whose wave vector is $\mathbf{k}_\ell = \mathbf{k}_{0\ell} - \mathbf{k}_R$. The electron-plasma wave associated with each beam ℓ is assumed damped at a sufficiently strong rate, ν_ℓ, so that it does not have a chance to propagate far enough to fall out of phase with the beat term in the ponderomotive driving force. It is driven to the steady-state amplitude

$$\tilde{n}_e^*(\omega_\ell, \mathbf{k}_\ell) = \tilde{\gamma}_{2\ell}\left(\frac{2i\omega_{BG\ell}}{\omega_\ell^2 - \omega_{BG\ell}^2 + 2i\nu_\ell\omega_\ell}\right) \tilde{A}_R(\omega_R, \mathbf{k}_R)\,\tilde{A}_{0\ell}^*(\omega_{0\ell}, \mathbf{k}_{0\ell}) \quad , \qquad (9)$$

where $\omega_{BG}(x, k_\ell)$ is the Bohm–Gross frequency,

$$\omega_{BG\ell}^2 = \omega_{pe}^2(x) + 3\,v_{te}^2\,k_\ell^2 \quad , \qquad (10)$$

and the factor in parenthesis is the resonance factor. The coupling coefficient, $\gamma_{2\ell}$, is proportional to k_ℓ^2 (where k_ℓ is the wave number of the electron-plasma wave) and to the electric-vector dot product, $\mathbf{e}_0^* \cdot \mathbf{e}_R$.

Substituting Eq. (9) into Eq. (8), we obtain

$$\frac{\partial}{\partial x}\tilde{A}_R(\omega_R, \mathbf{k}_R) = \left[\sum_\ell \tilde{\gamma}_{1\ell}\tilde{\gamma}_{2\ell}\left(\frac{2i\omega_{BG\ell}}{\omega_\ell^2 - \omega_{BG\ell}^2 + 2i\nu_\ell\omega_\ell}\right) \times |\tilde{A}_{0\ell}(\omega_{0\ell}, \mathbf{k}_{0\ell})|^2\right] \tilde{A}_R(\omega_R, \mathbf{k}_R) \quad . \qquad (11)$$

We now compute the number of intensity e-folding lengths, G, by which the SRS wave grows

$$G \equiv \int \frac{1}{|\tilde{A}_R|^2}\frac{\partial}{\partial x}|\tilde{A}_R|^2\,dx = 2\int \mathrm{Real}\left(\frac{1}{\tilde{A}_R}\frac{\partial \tilde{A}_R}{\partial x}\right)dx \quad . \qquad (12)$$

Thus, the integrated intensity gain coefficient is

$$G \cong \int 2\sum_\ell (\tilde{\gamma}_{1\ell}\tilde{\gamma}_{2\ell}) I_\ell \times \mathrm{Real}\left(\frac{i}{\omega_\ell - \omega_{BG\ell} + i\nu_\ell}\right)dx \quad , \qquad (13)$$

where $I_\ell = |\tilde{A}_{0\ell}|^2$ and we have used the fact that $\tilde{\gamma}_{1\ell}\tilde{\gamma}_{2\ell}$ is real and positive. The Lorentzian approximation to the resonance denominator has been made. For each ℓ, there is assumed to be an $x = x_\ell$ for which $\omega_{BG}(x = x_\ell, k_\ell) = \omega_\ell$. We assume a scale length, L_ℓ, such that:

$$\omega_{BG}(x = x_\ell + \Delta x, k_\ell) = \omega_\ell \cdot \left(1 + \frac{\Delta x}{2L_\ell}\right) \quad . \qquad (14)$$

(This is in accord with the usual definition that $1/L = 1/n_e \cdot dn_e/dx$, where n_e is the electron density).

Now let $\Delta x = 2L_\ell \nu/\omega_\ell y$ in each integral in the sum, to obtain

$$G = 2\sum_\ell (\tilde{\gamma}_{1\ell}\tilde{\gamma}_{2\ell})\, I_\ell \times \left(\frac{2L_\ell}{\omega_\ell}\int_{-\infty}^{+\infty}\frac{1}{1+y^2}\,dy\right) \quad , \qquad (15)$$

or

$$G \cong \frac{4\pi(\tilde{\gamma}_1\tilde{\gamma}_2)}{\omega^*}|A_0|^2 L \quad , \qquad (16)$$

where $|A_0|^2 = \Sigma\,|\tilde{A}_{0\ell}|^2$ is proportional to the total incident laser intensity, and $\gamma_1\gamma_2$, ω_R, and L are all average quantities. The asterisk superscript in Eq. (16) now refers to an electron-plasma wave quantity.

Notice that G is independent of the damping, since the interaction length is proportional to ν. We now explicitly evaluate G for the conditions of this experiment. The coefficients $\tilde{\gamma}_1$ and $\tilde{\gamma}_2$ are given by

$$\tilde{\gamma}_1 = \frac{i\pi e^2}{m_e c^2 k_R}\mathbf{e}_R^* \cdot \mathbf{e}_0 \qquad (17)$$

and

$$\tilde{\gamma}_2 = \frac{-ik^{*2}n_0e^2}{4m_e^2c^2\omega^*}\mathbf{e}_0^* \cdot \mathbf{e}_R \quad . \tag{18}$$

The product $\tilde{\gamma}_1\tilde{\gamma}_2$ is real and positive, as we assumed earlier when we took the real part of $1/\tilde{A}_R\,\partial\tilde{A}_R/\partial x$; the units are unrationalized cgs. Using the equations $\omega_{pe}^2 = 4\pi n_0e^2/m_e$ and $v_0 = eA_0/mc$, where v_0 is the peak oscillatory velocity in the incident light field, we find

$$G = \frac{\pi^2}{2}|\mathbf{e}_0 \cdot \mathbf{e}_R^*|^2 \cdot \left(\frac{\omega_{pe}}{\omega^*}\right)^2 \cdot \left(\frac{k^{*2}}{k_0k_R}\right)\left(\frac{v_0}{c}\right)^2\frac{L}{\lambda_0} \quad . \tag{19}$$

The 10 Shiva beams are each linearly polarized so as to synthesize an effective f/1.5, radially polarized beam. Thus, $\langle|\mathbf{e}_0 \cdot \mathbf{e}_R^*|^2\rangle = 1/2$ [given that everything in Eq. (12) is to be considered an average quantity].

Dependence of 1/2ω Emission on Plasma Size. Argus experiments at 1ω, 10^{15} W/cm^2, and 700 ps FWHM have shown that the 1/2ω light intensity is very strongly dependent on the size of the plasma (Table 6-19). All experiments were done with less than 100 J of laser energy. The 1/2ω emission was measured by an indium-arsenide detector with a 0.203-μm FWHM bandpass interference filter centered at 2.15 μm. The 1/2ω emission intensity increases by 1000 times for a 20× increase in the laser energy, from 1 to 830 μJ/sr. The spot diameter increases by a factor of 4.4 (best focus is about 30 μm). We observed light only near the exact 1/2ω frequency; shorter-wavelength SRS from the convective instability in the underdense plasma was not observed.

Figure 6-46 shows the Raman-light spectrum for beryllium-disk targets tilted 30° away from normal incidence to the f/2 laser beam and irradiated at 3×10^{14} W/cm^2 with 90 J of 1ω light in a 700-ps FWHM Gaussian pulse. Each point represents a measurement by an In-As detector with an 800-Å bandpass interference filter to determine its spectral window. This spectrum was built up from a large number of separate target experiments. The true 1/2ω spectrum is less than 0.1 μm wide.

Dependence of 3/2ω Emission on Plasma Size. To study the dependence of 3/2ω emission on plasma size, we compared 3/2ω emission experiments performed with 3500- and 120-ps FWHM pulse widths. The spot size was always 1 mm in diameter. We performed the 3500-ps experiments on carbon foils at 10^{14} W/cm^2; the 120-ps experiments were done on nickel and iron disks at 1 to 2 × 10^{14} W/cm^2. For the 3500-ps experiments, the 3/2ω emission was almost isotropic in front of the target, with little in back of the target. (The target chamber is spherical and refocuses light, so we expect some of this reflected light to be seen by the photodiodes in back of the target.)

The 1/2ω emission was measured by an array of photodiodes with 300- to 350-Å FWHM bandpass interference filters centered at 7115 Å. The photodiodes were fully blocked with a rejection of 10^5 against the 2ω light generated by the target and against the 1ω laser light. A KG-3 Schott color filter ahead of the interference filter provided an additional 10^4 rejection against the 1ω light. X rays were blocked by leaded glass and the tungsten-alloy holders.

The level in the backscatter hemisphere at 3500 ps was about 0.2 J/sr, for a total of about 1 J in 3/2ω emission. This represents about 0.03% of the incident laser energy. For the 120-ps experiments, the 3/2ω emission intensity never exceeded 350 μJ/sr and always peaked to the side, never in the backscatter direction. The fractional amount in 3/2ω emission was always less than

Table 6-19. Dependence of 1/2ω emission on laser spot size.

Target description	Laser energy and pulse length	Nominal spot size and intensity	Energy histogram	1/2ω light intensity (μJ/sr)
Gold disk	450 J 700 ps	Best focus; 10^{15} W/cm^2	80% at $I > 2.1 \times 10^{14}$ W/cm^2 50% at $I > 2.2 \times 10^{15}$ W/cm^2 20% at $I > 4.0 \times 10^{15}$ W/cm^2	1
Titanium disk	33 J 700 ps	85 μm diam; 10^{15} W/cm^2	80% at $I > 1.7 \times 10^{14}$ W/cm^2 50% at $I > 5.4 \times 10^{14}$ W/cm^2 20% at $I > 1.4 \times 10^{15}$ W/cm^2	85
Gold disk	88 J 705 ps	120 μm diam; 10^{15} W/cm^2	80% at $I > 3.7 \times 10^{14}$ W/cm^2 50% at $I > 8.7 \times 10^{14}$ W/cm^2 20% at $I > 1.6 \times 10^{15}$ W/cm^2	830

0.0005%, about 100 times less than in the 3500-ps experiments.

SRS Experiments at 2ω. We performed ıe 2ω SRS experiments with gold and beryllium disks nominally irradiated at 5×10^{15} W/cm^2 with about 150 J of 2ω light in an 1100-ps FWHM pulse. We measured the following

- The time-resolved spectrum of the directly backscattered SRS.
- The time-integrated spectrum of the SRS backscattered at an angle of 30° to the incident f/2.2 beam.
- The angular distribution of the total SRS emission, both in and out of the plane of electric polarization (the incident 2ω light was linearly polarized at $\phi = 104.8°$).

In addition to the array of spectrally integrating SRS photodiodes, we used an array of spectrally resolving photodiodes. We first discuss the measurements of the time-resolved spectrum.

The light directly backreflected through the target-chamber focusing lens was imaged onto a 0.5-m Spex spectrograph with a grating of 80 line/mm blazed for 0.87-μm transmission, which was used in the first order. The 2ω laser light and the shorter-wavelength light, which would appear in higher order, were absorbed by an OG-590 sharp-red cut-on filter. The streak-camera entrance slit was in the exit-slit plane of the spectrograph.

A 1ω wavelength and time fiducial was provided by focusing some of the original 1ω laser light on the spectrograph entrance slit. By irradiating a foil target at normal incidence with a small amount of 1ω light, we were able to measure the absolute timing separation in arrival times between the fiducial signal and the light back-reflected from the target. In all the data we present, $t = 0$ is the peak of the laser pulse within 100 ps. We obtained the dispersion at the streak-camera film plane by taking two laser shots with different wavelength settings for the spectrograph.

The targets were irradiated at 5×10^{15} W/cm^2 with 130 J of 2ω light in an 1100-ps FWHM pulse. This pulse length is for the 1ω laser beam; on shots for which we could compare the 1ω and 2ω pulse lengths, they were the same. The beam was diverging at the target with a 70-μm-diam spot size. We discuss the time-resolved Raman-light spectrum for two experiments: a beryllium disk irradiated at normal incidence, and a gold disk irradiated at a 30° tilt angle.

A color-enhanced streak record for the beryllium-disk experiment is shown in Fig. 6-47. The SRS emission from the very underdense plasma occurs mostly between 0.75 and 0.90 μm. There is also strong 1/2ω emission near 1.06 μm, but the streak-camera sensitivity is too low to detect this emission, which was seen with the time-integrated spectrograph.

Several things stand out from this streak record. The SRS occurs late in time and has an extremely sudden onset. Further, it starts simultaneously over a broad range of wavelengths (0.70 to 0.90 μm), corresponding to electron densities of very roughly $0.01 < n_e/n_c < 0.1$. The SRS occurs vigorously for a very short period of time and then saturates at a lower level, persisting until very late in the laser pulse, when the intensity on target is less than 10% of its peak value.

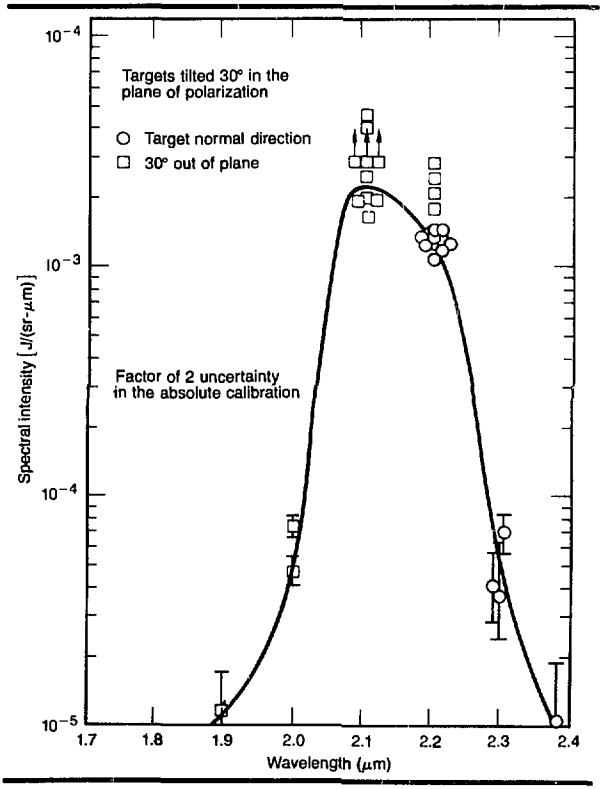

Fig. 6-46. SRS spectrum for 1ω Be-disk experiments at 3×10^{14} W/cm^2, 90 J, 700 ps FWHM; each point represents one experiment.

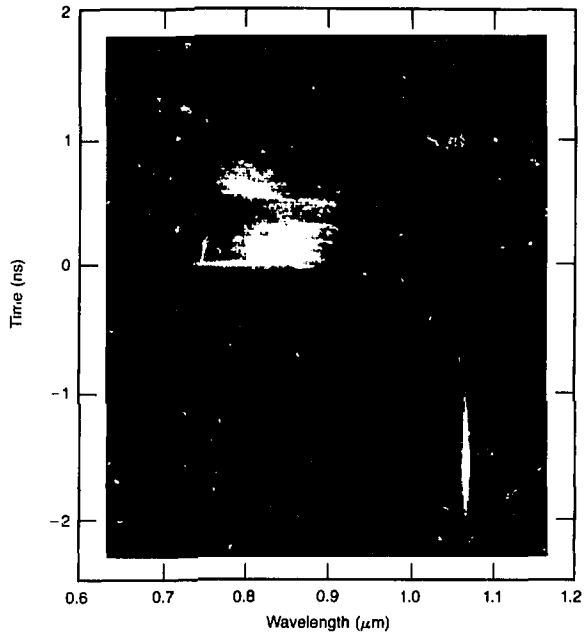

Fig. 6-47. Streak record of SRS spectrum for a Be disk tilted 30°; 2ω irradiation with 130 J, 1100 ps FWHM pulse before frequency-doubling, diverging beam, 70-μm-diam spot. The peak of the laser pulse is at $t = 0$.

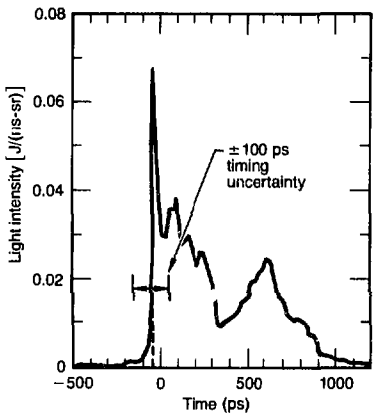

Fig. 6-48. Lineout in the time direction for the streak record shown in Fig. 6-47.

Even spectrally integrated, the Raman emission has an abrupt onset, rising from 10 to 90% in about 40 ps (Fig. 6-48). The image is digitized every 22 ps, and the streak camera has a time resolution of about 30 ps. The time dispersion of 7 ps due to the grating is negligible. There is significant SRS even 1 ns after the peak of the laser pulse. The pulse width before frequency-doubling was 100 ps FWHM. The absolute intensity units on the vertical scale are derived from photodiodes measuring the spectrally integrated Raman-light intensity at 25° to the direct-backscatter direction. The time-integrated spectrum (Fig. 6-49) shows the Raman light to be mostly between 0.75 and 0.90 μm, with a mean wavelength of 0.82 μm.

All the lineouts have been corrected for the transmission of the optics that relay the light to the streak camera and for the spectral response of the streak tube's S-1 photocathode. No corrections have been made for the grating efficiency or for the chromatic aberrations of the lenses.

The color-enhanced streak record for a similar experiment (but with a gold disk) is shown in Fig. 6-50. The first bright flash of Raman-scattered light occurs at $t = 180$ ps. Here also, the onset of the SRS is extremely abrupt, although the longer-wavelength light appears first by about 30 ps. The shorter-wavelength light appears in essentially one time-step of 22 ps and then disappears equally fast. Although there is a small precursor of SRS at $t = 80$ ps, most of the SRS emission begins later and ends earlier than was the case for the beryllium-disk experiment discussed above.

Figure 6-51 shows the time-dependence of the spectrally integrated Raman light. The emission substantially ends 600 ps after the peak of the laser pulse, compared to 1 ns for the Be-disk experiment. The time-integrated spectrum in Fig. 6-52 shows that we probably missed much Raman light of wavelengths shorter than 0.72 μm, which was dispersed off the streak-camera slit. As with the beryllium disk, there is little light at wavelengths longer than 0.90 μm.

One possible explanation for some of these results is filamentation of the incident laser beam. This would help explain why SRS can suddenly occur over a wide range of electron densities and also at such low average intensities late in the laser pulse. Raman scattering in the very underdense plasma at low intensities ($\sim 10^{14}$ W/cm^2) would seemingly require at least 100 μm of plasma, even for a fractional Landau damping of 0.01. What is more, for such small Landau damping, the electron-density profile would have to be exceedingly flat: $\Delta n_e/n_e < 2\nu_L/\omega_{pe}$. Thus, although we cannot prove filamentation, it is strongly suggest

The SRS energy in these two experime was only about 10^{-4} of the incident laser

energy, but the SRS was not saturated. In one experiment, we had 180 J on target, rather than 130 J, and the SRS energy was higher by a factor of at least 4.

As mentioned previously, the S-1 photocathode was too insensitive to detect the $1/2\omega$ emission (which has wavelengths near 1.06 μm) unless so much attenuation had been removed that the shorter-wavelength SRS would have completely overexposed the film. The $1/2\omega$ spectrum for the two experiments just discussed was measured from 0.98 to 1.14 μm by a 0.5-m Spex spectrograph equipped with a Princeton Applied Research optical-multichannel analyzer, using a 1205E enhanced-infrared silicon detector. The $1/2\omega$ emission was collected by a small telescope in the target chamber that detected the $1/2\omega$ emission that was backscattered at 30° to the incident beam and that was in the plane of polarization formed by the electric and wave vectors of the linearly polarized incident light.

In Fig. 6-53, we present the data for a third experiment covering the much broader spectral range from 0.8 to 1.1 μm, giving us the spectrum of both the $1/2\omega$ emission and the shorter-wavelength Raman light generated by the convective instability in the very underdense plasma. This spectrum is for a gold disk irradiated with 28 J of 2ω light in a 700-ps pulse; 20% of the laser energy in a central hot spot exceeded 3.5×10^{15} W/cm^2 and 50% exceeded 5×10^{14} W/cm^2. The laser beam was converging on the target.

The small peak exactly at 1.06 μm is due to the residual 1ω laser light. Except for this small peak, the resonance Raman light is split into distinct red- and blue-shifted components of about equal energy. The peaks of the red and blue components are shifted +175 and −250 Å from 1.06 μm, respectively. We have no definite explanation of the double-peaked $1/2\omega$ emission spectrum; one-dimensional simulations of the Raman instability do not predict this structure.

Raman scattering is also occurring in the underdense plasma at a density of about 0.10 n_c, or 4×10^{20} electrons/cm^3. This underdense Raman peak is centered at 0.88 μm and is about 0.1 μm FWHM. The spectrally integrated Raman-light photodiodes show that the level was about 3 mJ/sr.

The target was tilted 30° toward the light collector, so that we were observing the $1/2\omega$ emission that emerged directly along the target normal. Since the $1/2\omega$ emission is generated very near its own critical electron density, refraction will strongly collimate the light along this direction. Indeed, when the disk target was irradiated at normal incidence, the red-shifted component of the $1/2\omega$ emission disappeared. We were then looking at 30° to the target normal. The spectrum in Fig. 6-53 is not corrected

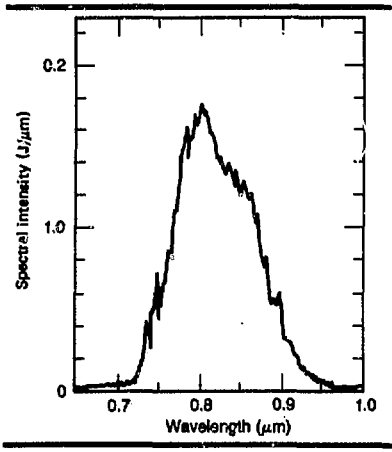

Fig. 6-49. Lineout in the wavelength direction for the streak record shown in Fig. 6-46.

Fig. 6-50. Streak record of SRS spectrum for a gold disk tilted at 30°: 2ω irradiation at 5×10^{15} W/cm^2, 130 J, 1100 ps FWHM pulse before frequency-doubling, diverging beam, 70-μm-diam spot. The pulse is at $t = 0$.

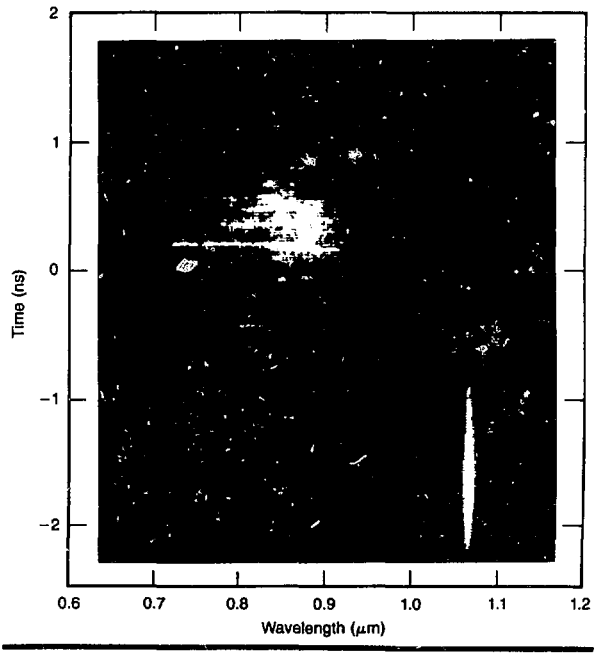

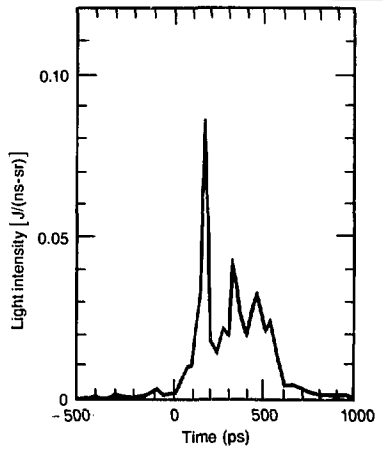

Fig. 6-51. Spectrally integrated lineout in the time direction for the streak record shown in Fig. 6-50.

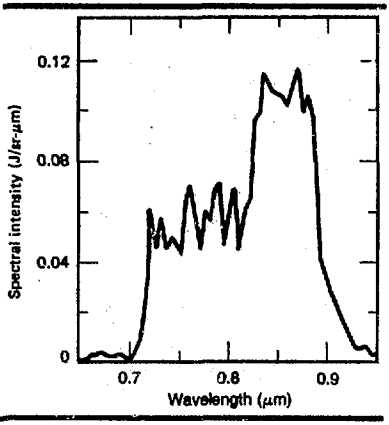

Fig. 6-52. Time-integrated lineout in the wavelength direction for the streak record shown in Fig. 6-50.

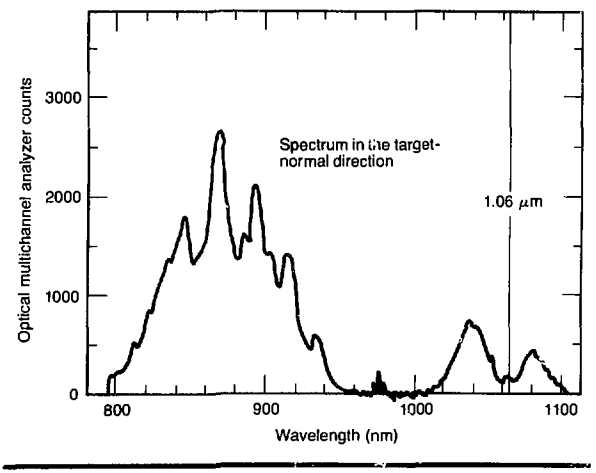

Fig. 6-53. SRS spectrum for a gold disk tilted at 30° and 2ω irradiated at 5×10^{14} W/cm^2 with 5320-Å light, giving 28 J in a 700-ps FWHM pulse.

for the spectral response of the 1205E detector.

Conclusion. We have observed efficient absorption by the Raman instability. Although convective SRS has a high density threshold, once this threshold has been greatly exceeded, it is difficult to saturate the SRS instability except by pump depletion. Furthermore, neither spatial incoherence nor a small amount of bandwidth for the pump will be very effective in preventing the instability. In experiments with completely underdense plasma from exploded foils, we observed that bremsstrahlung x rays with 40-keV mean photon energy were produced simultaneously with the 3/2ω emission. Instabilities in the underdense plasma, thus, can produce energetic electrons, although the relative importance of the $2\omega_{pe}$ and Raman instabilities has not been established.

The fractional absorption due to the $2\omega_{pe}$ instability can be determined for the exploding-foil targets by measuring the time-dependence of both the total absorption and the SRS absorption. The time-resolved 3/2ω emission will tell when $0.25\ n_c$ occurs. The change in the difference of the two absorptions at that time will give the absorption due to the $2\omega_{pe}$ instability. Thompson scattering with a short-pulse UV probe can give the spectral distribution function, $S(\omega, k)$, for the electron-plasma waves.

Time-resolved spectra from the 2ω experiments indicate that filamentation may play a role in SRS. Further 2ω experiments at the Novette laser facility in 1983 will give us a much better understanding of both SRS and the $2\omega_{pe}$ instability.

Authors: D. W. Phillion, E. M. Campbell, K. G. Estabrook, and R. E. Turner

Backlighting Characterization at 1ω, 2ω, and 3ω

As laser-fusion target performance proceeds towards higher-density fuel conditions, x-ray backlighting emerges as a unique method of determining the symmetry, stability, and size of imploded targets. In general, we use high-intensity x-ray pulses to map the implosion history of one or more parts (called "shells") of a target.

Although x-ray backlighting is a simple concept, difficulties arise in its implementation. Target design, for example, places numerous constraints on both the backlighting source and the imaging instrument. In previous *Laser Program Annual Reports*, we have shown that sources in the laser-produced plasma are the most practical for generating x-ray backlighting pulses.[72,73] In those earlier articles, we described the production efficiency of K-, L-, and M-shell lines as a function of laser intensity and pulse length.

In this article, we concentrate on the production efficiency of aluminum K (~1.8 keV), gold M (~2.5 keV), titanium K (~4.7 keV), and nickel K (7.80 keV) lines as a function of laser wavelength and pulse width. Preliminary results from our work,[74] and a recent publication by Yaakobi et al.,[75] suggest that using laser wavelengths shorter than 1.06 μm (1ω) significantly improves the line-production efficiency. This discovery is particularly significant for the production of short-pulse-length backlighters because we have had difficulty[74] in generating backlighting line-emitters with short-pulse-length 1ω irradiation.

We performed the x-ray measurements reported here with an absolutely calibrated x-ray/crystal spectrograph.[76] For the aluminum K_α (1.4 to 3.0 keV) and gold M-band radiation, we used a potassium-acid-phthalate Bragg-diffraction crystal; the x-ray recording element was Kodak no-screen film. For measurements at the Argus laser, we mounted the spectrograph on the target chamber at an angle approximately 63° to the target normal; the normal to target was rotated 30° relative to the incident laser beam. For measurements at the Shiva laser, the spectrograph viewed the target along the target normal, which was rotated 45° relative to the incident laser beam. Laser shots were fired at the characteristic Nd:glass wavelength of 1.06 μm, as well as at the second and third harmonics (0.53 and 0.35 μm, respectively). We made measurements at pulse lengths of 100, 600, and 700 ps with incident intensities ranging from ~10^{14} to 10^{16} W/cm^2.

Figures 6-54 through 6-57 show the results of these measurements. The brackets in Figs. 6-54 and 6-55 indicate the energy regions over which the photon yield has

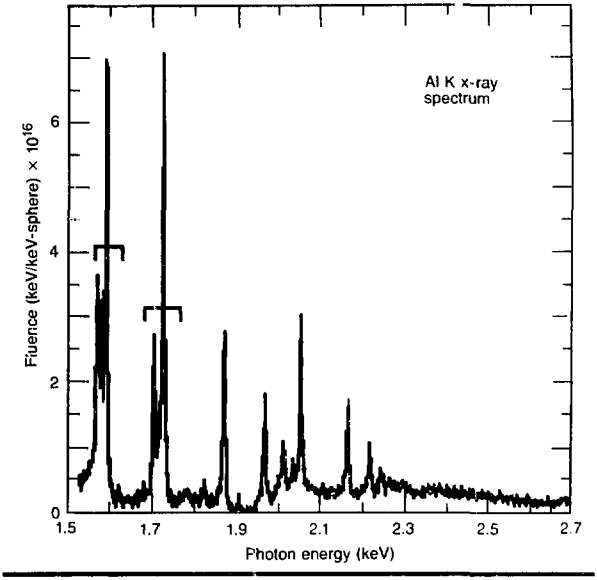

Fig. 6-54. Aluminum ▲ K x-ray spectrum from a laser-irradiated disk target; brackets illustrate spectral regions over which the x-ray yield is integrated.

Fig. 6-55. Gold m-band x-ray spectrum from a laser-irradiated disk target; the bracket illustrates spectral regions over which x-ray yield is integrated. ▼

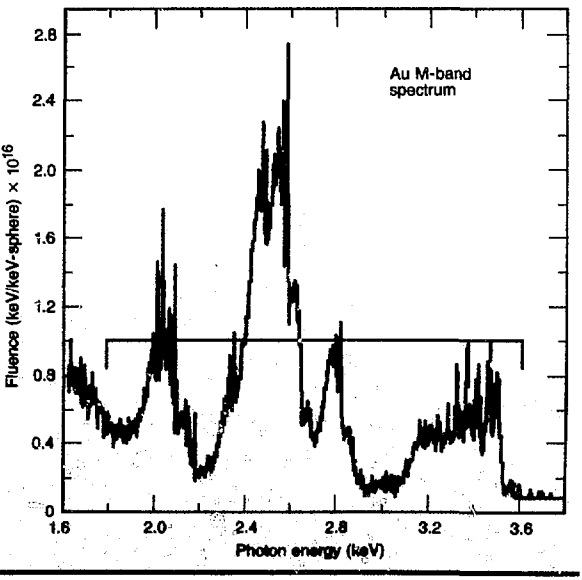

been integrated; the K_α peak is ignored in Fig. 6-57 because it is produced by suprathermal-electron fluorescence of cold material. In all cases, the photon yield includes the bulk of the line emission that could be useful for a relatively narrow-band x-ray imaging device. In particular, the yield numbers quoted include

- The He-like resonance and intercombination ($2^1P_1, 2^3P_1 \rightarrow 1^1S_0$) transitions and Li-like satellite lines for Ti (~4.7 keV) and Ni (7.80 keV).
- The same lines for Al at ~1.6 keV, plus the H-like Lyman-α transition ($2^2P_{3/2\,1/2} \rightarrow 1^2S_{1/2}$) at ~1.73 keV.
- The Au M-band radiation from 1.8 to ~3.6 keV.

Optical depth affects the total radiated line intensities for the He-like resonance lines. In particular, a given observation angle can yield different spectral intensities for optically thick lines. Figure 6-58 shows a Ti spectrum produced by 1ω irradiation with a 600-ps pulse. Clearly, the He-like resonance line suffers most from opacity, and it experiences significant attenuation when the disk is viewed at 90° to normal. It is for this reason that we perform all our measurements with the spectrograph stationed as close to the target normal as is possible.

In Table 6-20, we give the variation in production efficiency, ξ_v, with laser intensity or wavelength for aluminum K (1.598 and 1.729 keV) and titanium K (4.749 keV) x-ray resonance transitions. For both Al and Ti, we note a modest increase in ξ_v (by a factor of 3 to 4) at 0.53 μm (2ω). Note, however, the dramatic increase by at least a factor of 50 for titanium K production at 2ω with a short (100 ps) pulse. Unfortunately, the emission strength at short pulse lengths never exceeds that produced by longer wavelengths and pulse lengths. For the Ti data, in particular, the modest increase in ξ_v with decreasing laser wavelength and a 700-ps pulse is in sharp contrast to the increase by a factor of ~15 noted by Yaakobi et al.[75] under similar conditions. This discrepancy is discussed further below.

Table 6-21 represents production-efficiency data for the nickel K line, obtained at Argus and Shiva for a variety of irradiance conditions. Again, we measured no real increase in ξ_v with short pulse lengths.

The gold M-band emission results are given in Table 6-22. Note the increase in line strength by a factor of ~35 when the wavelength is changed from 1ω to 3ω (0.35 μm). This substantial increase is no doubt attributable to the numerous transitions in the gold M-band that are seldom optically thick and that involve significant oscillator strengths. Radiation in this band is, in fact, a significant portion of the incident laser energy (as much as 5% in numerous cases). We are currently performing detailed calculations of line spectra produced by both the K- and M-shell transitions; these calculations should provide an explanation for the above results.

Fig. 6-56. Titanium K x-ray spectrum from a laser-irradiated disk target.

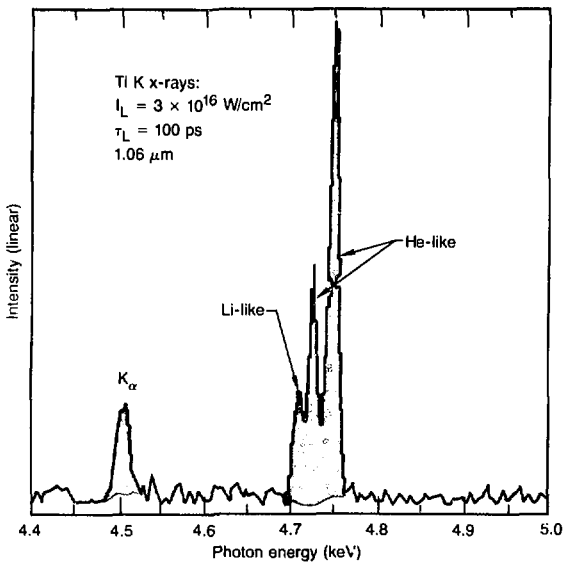

Fig. 6-57. Nickel K x-ray spectrum from a laser-irradiated disk target.

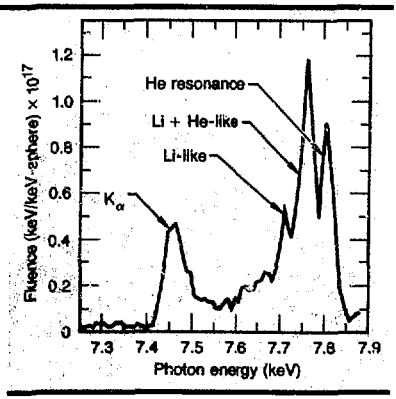

We observed marked improvements in x-ray line-production efficiency (see Figs. 20 and 6-22) for low-energy x-ray lines produced with 2ω or 3ω irradiation. Figure 6-59 represents a comparison of the x-ray line-production efficiencies obtained as a function of laser wavelength and x-ray line energy. We have also compared the data with similar measurements done at the Laboratory for Laser Energetics (LLE) in Rochester, England. The Rochester data were acquired with constant irradiance conditions for a given laser wavelength: for 1ω irradiation, $E_L = 175$ J, $\tau_L = 800$ ps, and $I_L = 10^{15}$ W/cm^2; for 3ω, $E_L = 40$ J, $\tau_L = 500$ ps, and $I_L = 10^{15}$ W/cm^2. On the other hand, the LLNL data represent the largest value for ξ_x obtained out of a variety of irradiance conditions for a given wavelength. As shown in Tables 6-20 and 6-21, we observed no significant difference for the ξ_x values produced at either 3ω or 2ω, so we have mixed their values in producing the "LLNL data" curve in Fig. 6-59.

Comparison of LLNL Results at Various Wavelengths. Considering first the comparison between LLNL data at different wavelengths, we note several interesting phenomena. First, we observe a general trend towards decreasing production efficiency with increasing line energy. In fact, using 1ω laser light to produce the line radiation results in a simple exponential decrease in ξ_x with x-ray line energy. This dependence is surprisingly independent of the type of line involved, namely gold M-band emission or, in other cases, the K x-ray transition. Deriving a slope to the curve from the data yields an empirical

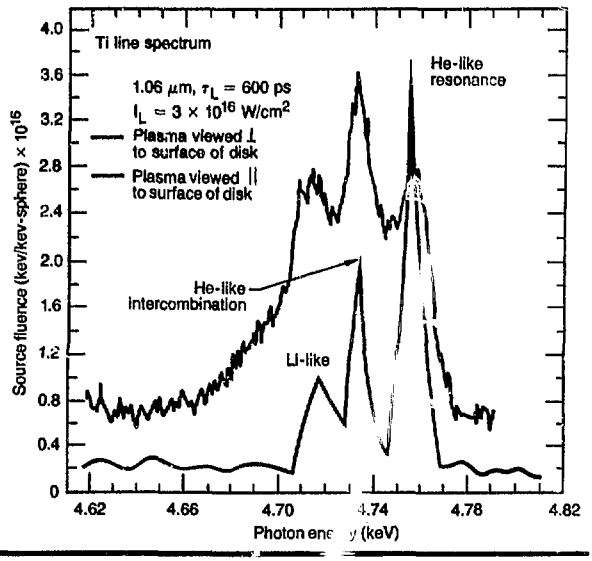

Fig. 6-58. Illustration of opacity effects on the He-like Ti resonance transition.

Laser intensity (W/cm^2)	Wavelength[a]	Pulse length (ps)	ξ_x (x-ray photons/incident laser joule)
Aluminum data			
3×10^{14}	1ω	700	1.1×10^{13}
3×10^{14}	1ω	700	1.1×10^{13}
3×10^{14}	3ω	700	5.3×10^{13}
5×10^{14}	3ω	700	4.4×10^{13}
1×10^{15}	3ω	700	3.5×10^{1}
Titanium data			
3×10^{14}	1ω	600	$7.4 \times$
1×10^{15}	1ω	700	3.2×10^{11}
2.7×10^{15}	1ω	600	5.6×10^{11}
3×10^{15}	1ω	600	5.7×10^{11}
7×10^{15}	1ω	600	4.8×10^{11}
7×10^{16}	1ω	600	2.7×10^{11}
3×10^{16}	1ω	600	3×10^{11}
1×10^{16}	1ω	100	2.2×10^{11}
3×10^{16}	1ω	100	2.4×10^{11}
3×10^{16}	1ω	100	1.8×10^{11}
3×10^{14}	2ω	700	1.9×10^{12}
1×10^{15}	2ω	700	1.1×10^{12}
1×10^{15}	2ω	700	1.5×10^{12}
1×10^{15}	2ω	100	9.5×10^{11}
1×10^{15}	3ω	700	1.1×10^{12}
1×10^{15}	3ω	700	1.2×10^{12}

[a]Wavelength at 1ω is 1.06 μm, at 2ω is 0.53 μm, and at 3ω is 0.35 μm.

Table 6-20. Variation in production efficiency for Al K and Ti K resonance lines as a function of laser wavelength and pulse length.

scaling relationship for ξ_x at 1ω of $\xi_x \sim \exp[-(2/3)E_x]$, where E_x is the line energy in keV.

Below, we will make some semi-quantitative physical arguments for why we expect a large decrease in ξ_x for increasing x-ray line energy. Theoretically, however, we do not find a simple exponential dependence. Apart from the aluminum K- and gold M-band radiation, we observe the same general decrease in ξ_x values as a function of line energy for the short-wavelength irradiance conditions. Generally, the ξ_x values for short wavelength and low transition energies far exceed the ξ_x values produced at 1ω. However, the production efficiency rapidly merges to the 1ω curves for higher transition energies, namely titanium K (4.749 keV) and nickel K (7.804 keV).

The above observations are in marked contrast to the values observed at LLE. The LLE wavelength comparison illustrates a large overall improvement in ξ_x values for short wavelength. Their ξ_x values range from a factor of ~20 higher at low transition energies to a factor of ~5 larger for the nickel K (7.804 keV) lines. Besides the disagreement in the energy scaling of the ξ_x values, the LLE numbers also conflict with our absolute values.

Part of the disagreement at 1ω can be attributed to the different irradiation conditions used in the two sets of measurements. For example, the 1ω ξ_x values from both laboratories are in strong agreement if we compare Ti values taken with an intensity $\sim 3 \times 10^{15}$ W/cm^2 and a 600-ps pulse length (see Table 6-20). In fact, the laser-intensity scaling of the Ti ξ_x values has been previously reported by Matthews et al.[74] to decrease by more than a factor of 2 when the 1ω laser intensity is increased from 3×10^{14} to 3×10^{15} W/cm^2.

For the lower transition energies, the discrepancy between the two sets of data will no doubt increase, again due to the rather high intensities used in the Rochester 1ω experiments. There are significant differences in the absolute values obtained by the two labs for the titanium and nickel K lines at 2ω and 3ω. Basically, the LLE values are four to five times higher than the LLNL values at the titanium and nickel K lines. No doubt some of this difference can be ascribed to uncertainties in absolute calibration (LLNL values are basically ±100%) and to statistical fluctuation. We are not

Table 6-21. Comparison of Ni (7.4 keV) x-ray line-production efficiency as a function of wavelength and pulse length.

Laser intensity (W/cm^2)	Pulse length (ps)	ξ_x (x-ray photons/incident laser joule)
1.06 μm (1ω)		
4×10^{14}	600	Not observed
3×10^{15}	600	Not observed
2×10^{16}	600	2.5×10^{11}
3×10^{16}	600	4.0×10^{11}
5×10^{16}	600	2.0×10^{11}
1×10^{16}	100	7.1×10^{10}
2×10^{16}	100	1.3×10^{11}
4×10^{16}	100	6.6×10^{10}
1×10^{17}	100	1.1×10^{11}
0.53 μm (2ω)		
3×10^{15}	700	1.6×10^{11}
3×10^{15}	700	1.8×10^{11}

Table 6-22. Comparison of Au M-band (1.8 to 3.6 keV) radiation as a function of wavelength and intensity with $\tau_L \sim 700$ ps.

Laser intensity (W/cm^2)	Laser energy (J)	θ_L (deg)	ξ_x (x-ray photons/incident laser joule)
1.06 μm (1ω)			
3×10^{15}	600	45	5×10^{12}
3×10^{14}	32	12	3.8×10^{12}
0.53 μm (2ω)			
$\sim 3 \times 10^{14}$	25.7	8	9.1×10^{13}
3×10^{14}	24.0	8	8.0×10^{13}
2×10^{14}	21.2	30	9.4×10^{13}
2×10^{14}	22.1	30	1.0×10^{14}
2×10^{15}	35.5	30	8.2×10^{13}
1×10^{15}	37.0	8	6.7×10^{13}
1×10^{15}	38.8	15	6.7×10^{13}
0.35 μm (3ω)			
$\sim 3 \times 10^{14}$	29.2	30	2.3×10^{13}
3×10^{14}	31.1	30	4.3×10^{13}
2×10^{15}	35.9	30	8.7×10^{13}
2×10^{15}	33.1	30	9.7×10^{13}
2×10^{15}	36.5	12	1.3×10^{14}
2×10^{15}	38.5	12	1.3×10^{14}
3×10^{14}	26.7	12	3.9×10^{13}

suggesting that the LLE values are wrong, but we do suspect the plasma conditions they produced at 3ω are significantly different from those produced at LLNL.

For example, the report[75] of the work at LLE includes a figure of a titanium K spectrum produced with 3ω laser light. This figure shows a significant production of Ti^{+21} Lyman-α radiation (~10% relative to the He-like resonance); this indicates a fairly high-temperature plasma ($T_e < 1.5$ keV). Observations at LLNL and other laboratories[77] in this same spectral region have never observed the Lyman-α transition when using 2ω or 3ω light at $I_L \times 10^{15}$ W/cm^2. In fact, results at LLNL and other laboratories indicate that line radiation is most efficiently produced in a relatively cool ($T_e \sim 0.8$ keV) and dense ($n_e > n_c$) plasma. This leads us to believe that local "hot spots," or high-intensity regions, at the target-interaction surface could lead to increased plasma temperature without significantly reducing total laser-light absorption. These conditions could explain the LLE titanium K spectrum and could also produce significantly higher values for ξ_ν.

Quantitative Model of LLNL Results. Under uniform plasma-heating conditions, the variation of ξ_ν values with transition energy and irradiation conditions can be modeled. We have developed a simple model that quantitatively illustrates the LLNL results

- A rapid decrease in ξ_ν with increasing line energy.
- Significant increase in ξ_ν only at low transition energies.

Basically, the line emission strength at a given energy, $h\nu = E_\nu$, is given by the expression

$$I(E_\nu) = \int_0^{\tau_E(D)} S_{I_\nu} e^{-\tau_l} d\tau_l \ (\mathrm{s^{-1}cm^{-2}}) \ , \quad (20)$$

which is arrived at by solving the radiation-transport equation for a plasma of thickness D having no external radiation incident on it and measured along a unique (as opposed to angular-averaged) line of sight. Here, $\tau_E(D) = \int_0^D \chi\,(x, E)dx$ is the optical depth of the plasma, having thickness x, and S_E is the source function. In general, a maximum line output from the plasma occurs during LTE conditions and for optical thicknesses large at the lines and small at the continuum. Under these circumstances, Eq. (20) reduces to the intensity curves for blackbody radiation at photon and electron temperature T, given by

$$I_{BB}(E_\nu) = -\frac{2E^3}{h^2c^2}\left(e^{E/kT} - 1\right)^{-1} \times \int_0^{\tau_E(D)} e^{-\tau_l} d\tau_l \ . \quad (21)$$

For K x-ray emission at densities typical of laser-heated disks ($n_e \sim 10^{22}$ cm^{-3}), LTE conditions and blackbody radiation do not prevail. Instead, we have the expression for the less-efficient line emission from an optically thin, non-LTE plasma,

$$I(E_\nu) \sim \frac{E_\nu}{4\pi} \cdot A_{21} \cdot L \cdot N_2 \cdot D \ , \quad (22)$$

where A_{21} is the x-ray transition rate for the decaying level of interest, N_2(cm^{-3}) is the density of ions in the upper excited state of

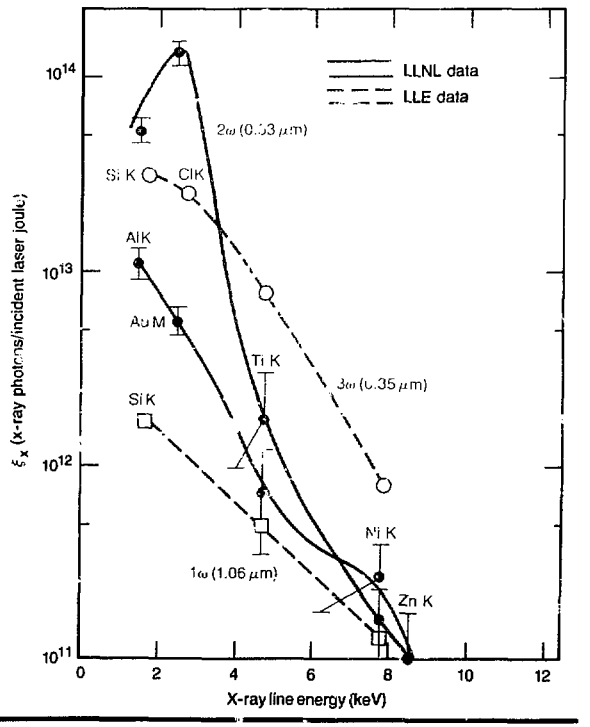

Fig. 6-59. Comparison of LLNL and LLE conversion-efficiency data at 1ω (lower curves), 2ω, and 3ω.

Table 6-23. Dependence of He-like resonance-line ($2^1P_1 - 1^1S_0$) intensities on Z, κT, and N_e.

Element	Resonance-line energy (keV)	Intensity $\sim N_z \cdot A_{21}$ arbitrary units $\times (N_e \cdot N_i)$ κT 0.7 keV	1.0 keV	2.0 keV	5.0 keV
Aluminum (Z = 13)	1.598	1.2×10^{7}	1.9×10^{7}	2.8×10^{7}	3.0×10^{7}
Chlorine (Z = 17)	2.789	5.0×10^{9}	1.4×10^{8}	4.0×10^{8}	5.8×10^{8}
Titanium (Z = 22)	4.749	8.1×10^{11}	5.2×10^{10}	3.9×10^{9}	1.0×10^{8}
Nickel (Z = 28)	7.804	2.9×10^{13}	7.0×10^{12}	7.4×10^{10}	1.6×10^{9}
Zinc (Z = 30)	8.997	3.7×10^{14}	1.5×10^{12}	9.4×10^{11}	8.9×10^{10}

the transition, and $L(E)$ is the line integral through the emitting plasma. For plasmas where significant line broadening by Stark or Doppler mechanisms is absent, which is the case here, the only significant parameters affecting line intensity are A_{21} and N_2. The radiative transition rate depends only on the element producing the transition through its $\sim Z^4$ scaling of the hydrogenic values ($\sim 10^8$ s^{-1}), whereas the upper-state populations N_2 depend on the detailed ionization, excitation, and radiative recombination kinetics of the plasma (and generally scale as Z^{-3}). Expressions for N_2 (Z, κT) have been derived for steady-state plasmas by Griem.[78]

It is important to note, however, that the formation of a transient plasma affects the x-ray line-production efficiency. In essence, the maximum N_2 values require the achievement of steady-state ionization, the time for which scales[78] as

$$t_e \sim \frac{Z^3 \kappa T}{N_e (13.55) Z^2} \exp\left|\frac{(27.12)Z^2}{\kappa T}\right| \qquad (23)$$

for a given transition. For densities of $N_e \sim 10^{21}$ cm^{-3} and constant $\kappa T_e = 1.0$ keV, t_e scales from $\sim 10^{-11}$ s for aluminum to $>10^{-6}$ s for zinc.

Thus, the efficient production of high-transition-energy, short-pulse ($\Delta t < 10$ ps) backlighting lines may not be possible, since they will exist as a result of nonsteady-state reduction in the upper-level population. It is possible to produce lines at short pulse lengths using only suprathermal-electron ionization. Although this method is significantly less efficient than line production by thermal ionization, it may be the only way to produce any monochromatic radiation with short-pulse lasers.

The dependence of $I(E_\nu)$ on transition energy and laser wavelength (i.e., the density where emission takes place) is best obtained from the product $A_{21} \cdot N_2$. According to Griem,[78] assuming coronal equilibrium,

$$I(E_\nu) \sim N_2 A_{21} = \exp\left(-\frac{E_\nu}{\kappa T}\right) Z^{-3} \times \left|\frac{(13.50)Z^3}{E_\nu}\right|^3 \left|\frac{(13.56)Z^2}{\kappa T}\right|^{1/2} n_i n_e , \qquad (24)$$

where N_i is the total ion density for the charge state necessary to produce the transition of interest (such as He-like or H-like). For the purpose of this discussion, we choose an expression assuming coronal equilibrium (as opposed to LTE or other conditions) only to illustrate the dependence of $I(E_\nu)$ on Z and N_e. The conditions governing collisional-radiative equilibrium probably best describe the plasma conditions, but expressions for the line intensity are more difficult to derive and, thus, are outside the scope of this work.

Table 6-22 gives the product of $A_{21} \cdot N_2$ for Al, Cl, Ti, Ni, and Zn He-like resonance-line emission ($1S2P^1P_1 - 1S^2, {}^1S_0$) at four different plasma temperatures from $\kappa T = 0.7$ to 5.0 keV. The absolute values are unimportant (and inaccurate); it is only the relative values that are of interest. All values in the table are in terms of the product $N_e \cdot N_i$ to separately compare the Z- and N_e-dependence of the intensity $I(E_\nu)$.

Two important phenomena are illustrated in the values for $N_2 \cdot A_{21}$ given in Table 6-23. First, as we observed experimentally, there is a rapid decrease in the product for increasing line-transition energy. The slope of the decrease depends on the plasma temperature. This analysis is too crude, however, to use as a method to determine κT by comparison of theoretical and measured slopes.

Second, and more importantly, we observe only a slight temperature-dependence in the $N_2 \cdot A_{21}$ values for low Z or small transition energies. On the contrary, we note a dramatic dependence for elements

like Ni and Zn. This implies that line-transition yields will be mostly due to the plasma $N_e \cdot N_i$ values for low-transition-energy elements and, conversely, primarily due to plasma temperature for the higher-Z transitions. Assuming that plasmas are slightly cooler when produced under equivalent irradiance conditions at 2ω and 3ω, we could expect only low-energy line-production intensities to scale with the increased plasma density that is produced at these wavelengths.

This qualitative argument obviously agrees with the measurements made at LLNL (Fig. 6-59). Moreover, if irradiation a 2ω or 3ω increases the local temperature compared to 1ω irradiation, then we would expect improved production efficiency because of the larger plasma densities produced at the shorter laser wavelengths. In practice, we must admit that all of the above arguments are sensitive to the density and temperature gradients produced in long- and short-wavelength laser-produced plasmas. Obviously, the maximum high-energy line emission will occur from the region of highest density and temperature available in the plasma. The extent of this region naturally depends on laser irradiance conditions and details of the laser-light absorption mechanism.

Author: D. L. Matthews

Gas-Jet Experiments

The characterization of plasmas associated with ablatively driven targets has become a major issue for laser fusion. Because of the large sizes associated with these plasmas, interferometric plasma-characterization methods that use UV light ($\lambda \sim 0.25\ \mu m$) are effective only for studying electron densities (n_e) on the order of $n_e \sim 10^{20}\ cm^{-3}$; for 1ω ($1.06\ \mu m$) irradiation, this value approximates 0.1 critical density (0.1 n_c). In addition, no viable methods to study temperature gradients (T_e) have been suggested.

Although x-ray line spectroscopy is to some extent underdeveloped and untested, it can be used to characterize large-volume plasmas over a relatively broad range of parameter space. Specifically, x-ray line spectroscopy can be used to determine n_e and T_e in one dimension, as long as both density and temperature are relatively constant along the other dimension.

Recent gas-jet experiments at the KMS Fusion laser facility in Ann Arbor, Mich., provide an excellent opportunity to develop x-ray line spectroscopy. Density gradients for the KMS gas jets were determined using laser interferometry; the electron temperature was not measured. In this article, we compare deduced profiles of n_e and T_e to the profiles previously determined at KMS by interferometry and laser-plasma simulations.

Experimental Method

In the gas-jet experiments, we measured n_e in one dimension by spatially resolving He-like line-intensity ratios from either pure or mixed gases. In the same manner, we can determine T_e by spatially resolving lines from different charge states, thereby producing ratios of He-like to H-like line intensities and Li-like to He-like line intensities.

We can easily obtain time-averaged measurements of the axial temperature gradient for a steady-state plasma (which the gas jet, using low- and moderate-Z species, approximates) by spatially resolving (along the Y axis) x-ray lines from different ionic charge states. The x-ray lines most frequently observed in laser-produced plasmas originate from H- and He-like ions; we have computer codes[7-9] that accurately calculate line-intensity ratios for these transitions.

Consider the ratio of the Lyman-α (2p—1s) line intensity to the He-like resonance [$(1s2p(^1P_1) \rightarrow 1s^2(^1S_0)$] line intensity. For an isothermal, isobaric plasma, the sensitivity to electron temperature of this line-intensity ratio is well known. For electron temperatures <1 keV, in particular, this line-intensity ratio is a very sensitive function of temperature. Therefore, we can use even a crude measurement of the line-intensity ratio to accurately determine T_e.

Figure 6-60 illustrates the measurement principle for the gas-jet experiments. The one-dimensional spatially resolving spectrograph integrates the x-ray emission from a plane perpendicular to the laser beam. If no radial energy transport takes place, the diameter of this plane would be equivalent to

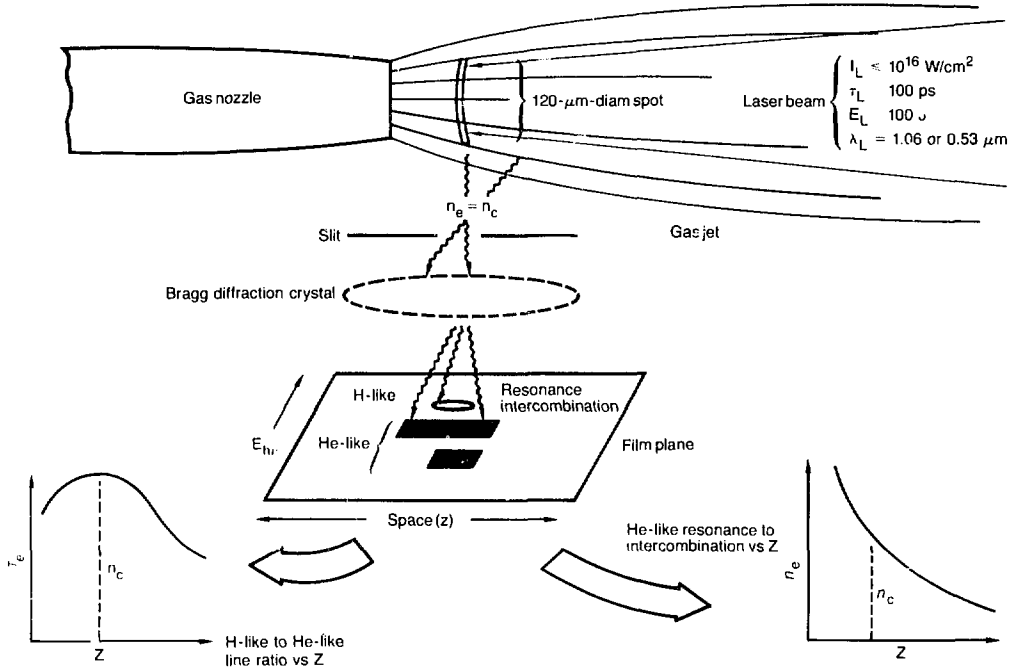

Fig. 6-60. Schematic of the gas-jet experimental method.

the laser-spot diameter (120 μm for the KMS experiments). It is relatively easy to achieve spatial resolution on the order of 20 μm, which is quite sufficient for studying plasmas with density and temperature scale lengths of 100 μm.

We can choose a gas having appropriate sensitivity to almost any temperature regime from 200 eV to 7 keV. Disk experiments at Shiva with laser intensities and pulse lengths similar to those discussed here suggest that the plasma only reaches $T_e \sim 500$ eV in the region where the maximum line-emission occurs ($n_e \geq 1$ to $2n_c$, from both simulations and experiments). Gases containing Si, P, or S are ideal for mapping this temperature region. In our first experiments, we used neon and then argon to bracket the temperature region of interest. If we had overstripped neon, we could have used the slope of the free-bound emission to estimate temperature. Moreover, if we had understripped argon, it would have been evident from the absence of H-like lines.

Spectroscopy Methods

Time-averaged measurements of n_e using x-ray line spectroscopy can proceed in several different ways, all of which use spatial resolution of transition lines to determine $n_e(Y)$. Indeed, one reason for developing x-ray line spectroscopy with the gas jet is to determine which spectroscopy technique is the most practical and accurate. In the following paragraphs, we discuss two such methods.

First, if we know T_e from a separate measurement, and if $\partial n_e/\partial t$ is small over the duration of the laser pulse (steady-state density conditions), then an absolute line-intensity measurement can give n_e. Recall that, for optically thin radiation, $I_{21} \propto A_{21} \cdot N_2$, where I_{21} is the intensity of the transition 2→1, A_{21} is the radiative rate (s^{-1}), and N_2 is the initial-state population density (cm^{-3}). The radiative decay rate, A_{21}, is known with reasonable accuracy for most He-like and all H-like transitions; thus, an

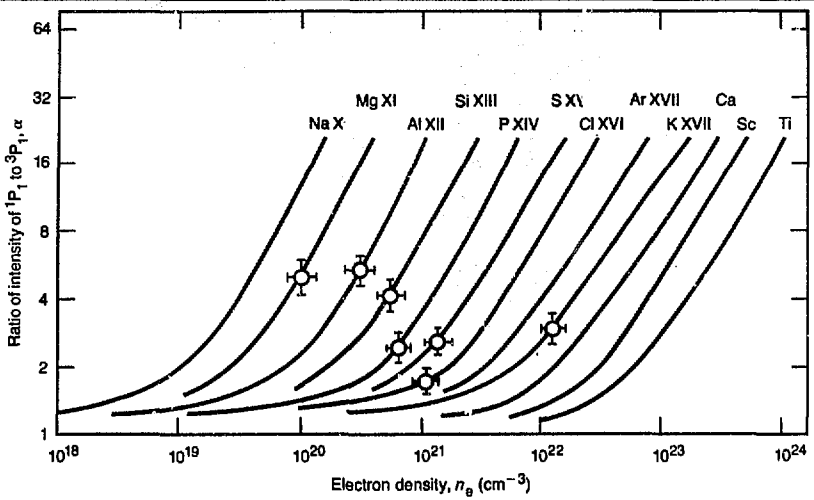

Fig. 6-61. The line-intensity ratio of the resonance and intercombination lines of He-like ions as a function of n_e for various elements.

accurate measurement of I_{21} constitutes a measurement of N_2 that can be related to the ground-state ion density and, ultimately, to the plasma electron density. This method, however, requires that we know both the emission volume and time duration with good accuracy.

A more reliable technique is to measure a line-intensity ratio that is density-sensitive, but not temperature-sensitive. V. Boiko et al.[80] and other plasma spectroscopists have advocated studying the ratio of the intensities of the He-like resonance line [$1S2p(^1P_1)$—$1S^2(^1S_0)$] and the intercombination line [$1S2p(^3P_1)$—$1S^2(^1S_0)$] because this line-intensity ratio is sensitive only to electron density. There are, of course, other density-sensitive lines, such as the Lyman-α satellite lines or doubly excited-state transitions (i.e., $2p^2-1s2p$), as well as some of the Li-like lines. The doubly excited-state transitions are weak in intensity compared to the He-like transitions suggested by Boiko and may, therefore, be impractical for our purposes. The Li-like lines are indeed practical, and these lines were studied as part of our gas-jet experimental series.

There are two problems with this spectroscopy method. First, the electron temperature must be high enough throughout the density scale length of interest to turn on the lines; we can solve this problem by using different gases. Figure 6-61 illustrates the line-intensity ratio as a function of n_e for various elements. Thus, we can choose an element having a line-intensity ratio that is sensitive to the n_e regime of interest. For example, we would use sulphur or phosphorus to cover the n_e regime near n_c for 1ω irradiation. These elements are also appropriate for determining the temperature gradient. For measurements using 2ω (0.53 μm) laser light, where $n_c = 4 \times 10^{21}$ cm^{-3}, either Cl or Ar gases would be suitable. The second problem is that we must determine the accuracy of the calculation of n_e, which we can do directly by comparing it to the interferometric determination of $n_e(Y)$.

Experimental Data

Figure 6-62 is a color-enhanced reproduction of an x-ray pinhole photograph from a laser-irradiated gas jet filtered to view x rays <1.0 keV. X rays emitted from the tip of the nozzle are evident on the left side of the photograph. The x-ray-emitting plasma has a "rocket-exhaust" appearance typified by flat emission contours on the high-density side of the nozzle and by more rounded contours towards the lower-plasma-density regime (on the right side). Note also the strong gradient in emission strength transverse to the long axis of the gas jet. Presuming a relatively shallow transverse

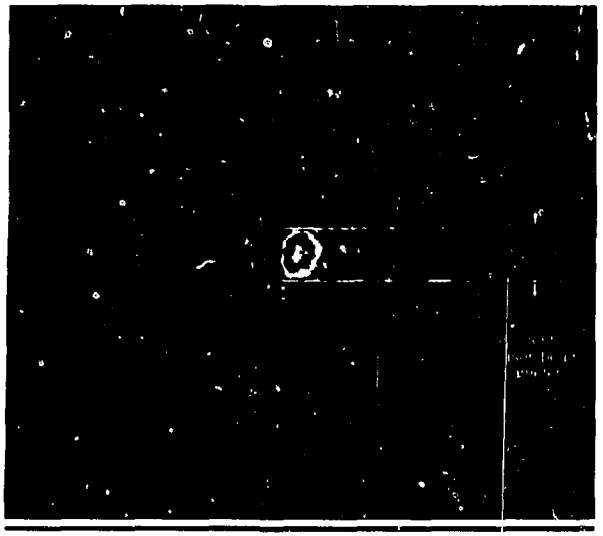

Fig. 6-62. X-ray pinhole photograph ($h\nu \sim 1.0$ keV) of a laser-irradiated gas jet.

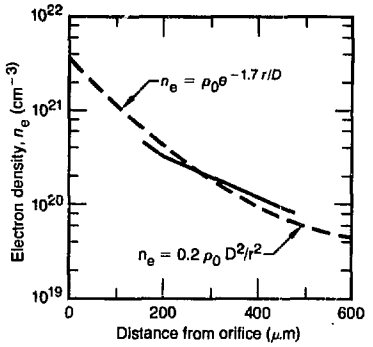

Fig. 6-63. A comparison of the longitudinal electron density profile determined by laser interferometry for a neutral gas (dashed line) and a plasma (solid line).

density gradient, this feature implies a steep temperature profile. Obviously, we must also consider the time evolution of the plasma before we have accomplished full interpretation of the pinhole photograph in Fig. 6-62.

Figure 6-63 represents the longitudinal plasma-density profile (solid line), as compared to the neutral-gas profile. Both profiles were determined by interferometry using transverse probing at the fourth harmonic ($4\omega = 0.27\,\mu$m). The neutral-gas density is asymptotically modeled as $1/r^2$ far from the nozzle tip ($r/D \gg 1$, where D is the orifice diameter) and as e^{-r} near the orifice. Further details of the gas-jet density profiles can be found in Ref. 81. Note that the gas jet produces a plasma of rather shallow density gradient ($L \sim 100\,\mu$m). In addition, as previously stated, interferometry cannot produce plasma-density information for $n_e > 3 \times 10^{20}$ cm^{-3} (0.33 n_c for 1ω light).

Figure 6-64 represents a typical x-ray spectrum from 2ω irradiation of a gas jet of $SF_6 + N_2$. The ground-state ion density of sulfur is small, so the resonance lines are optically thin. This spectrum represents both a time and volume average. The "average" temperature derived from an analysis of the H- to He-like line-intensity ratios indicates that $T_e \sim 600$ eV. This analysis estimates the temperature only crudely because it assumes plasma with uniform temperature and density.

Figure 6-65 shows a measurement of the variation in T_e along the axial direction of an argon gas jet. Recall that one-dimensional x-ray imaging techniques average over the other two space dimensions; thus, the temperature measurements in Fig. 6-65 represent the average for a thin, disk-like volume whose edge is perpendicular to the imaging spectrograph. The downward arrow in the figure is the point in space where the maximum x-ray line intensity occurs. We deduced the electron temperatures using the variation in the Li- to He-like line-intensity ratio. The temperature-dependence of this spectra has been calculated.[82]

The measurements in Fig. 6-65 could be influenced by optical-depth effects on the He-like resonance line. Preliminary analysis of the data indicates, however, that these optical depths are small. The measurements in Fig. 6-65 are influenced also by transverse temperature gradients because the method averages over that dimension. We have applied a detailed line-simulation code to the data in Fig. 6-65 to take account of density and temperature gradients. The simulation indicates that temperatures range from ~800 to 1200 eV near n_c for argon plasmas irradiated at 2ω. These calculations are time-independent, however, and necessarily assume steady-state ionization. The weakness of this type of steady-state calculation will be discussed later.

Figure 6-66 illustrates an axial-density profile that was determined by using the ratio of the He-like sulfur resonance line intensity to the intercombination line

intensity. The measurements in this figure are tentative, as they have not been confirmed by comparison with interferometry.

We estimated the density-dependence of these ratios from the calculations of Vinogradov et al.[83] We have applied no corrections for opacity because the sulfur ground-state ion density is low. Vinogradov et al. note also a weak dependence on electron temperature; we applied no temperature correction to these data, however, because of the small axial variation in temperatures demonstrated in Fig. 6-65.

The inferred maximum density that we achieved for the sulfur line-intensity ratio was only 1.4×10^{21} cm^{-3}, whereas n_c for 2ω irradiation is 4×10^{21} cm^{-3}. This low value could be due to the transverse-averaging aspect of the one-dimensional imaging technique and to the steep density gradients that may exist for these irradiation conditions. The decrease in density for distances closer to the gas-jet nozzle disagrees with measurements discussed above (see Fig. 6-63). The decrease may simply indicate that the average ionization state, and, hence, the free-electron density, is decreasing due to the inhibition of heat flow to the higher-density regions. Density gradients along the line of sight may also cause the observed decrease in density. The axial-density scale length deduced from these measurements is $L \sim 120$ μm, in agreement with the interferometric determinations discussed above. Note that, unlike interferometry, the spectroscopy method easily determines n_c in excess of 10^{21}.

Simulations

In the data described thus far, we have not attempted to illustrate the effects of transverse temperature profiles on the measured spectra, nor have we illustrated changes due to time integration. In an attempt to incorporate this, we have taken the dependence of T_e on time and radial position from a particle-in-cell (PIC) hydrodynamics code and input these values into a code for line production and transport.[79] The PIC simulations were done at KMS[84]; the input (boundary) and modeling conditions are shown in Table 6-24. A plot of the radial T_e

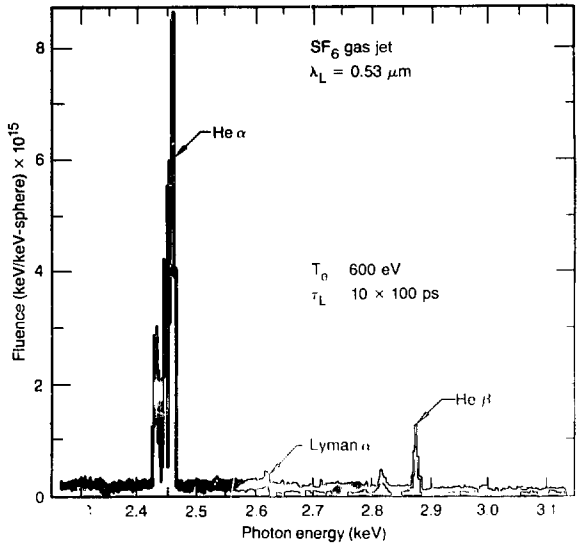

△ Fig. 6-64. A typical x-ray spectrum of the sulfur K x-ray line emission from a N_2 + SF_6 gas jet irradiated at 0.53 μm with $I \sim 10^{14}$ W/cm^2.

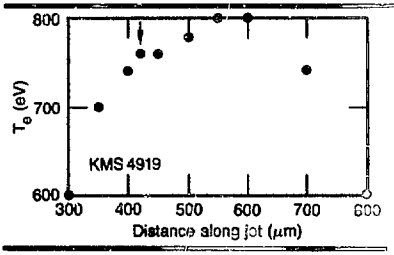

◁ Fig. 6-65. T_e deduced from the line-intensity ratios of He- and Li-like lines for an argon gas jet.

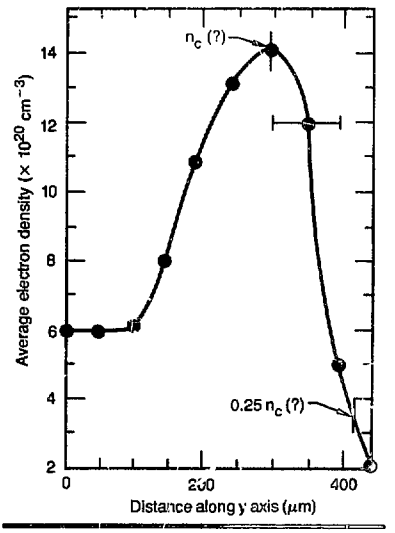

Fig. 6-66. Longitudinal density profile determined by x-ray spectroscopic technique for a N_2 + SF_6 gas jet irradiated at 0.53 μm with $I \approx 5 \times 10^{14}$ W/cm^2.

Fig. 6-67. Simulated radial temperature and density profiles for a gas jet several times during the laser pulse (slice taken at 325 μm downstream from the gas-jet nozzle).

and n_e values calculated during one run for a slice through the plasma is given in Fig. 6-67. The calculations assumed a 90-ps 2ω irradiation of an argon gas jet. Energy is assumed deposited via inverse bremsstrahlung absorption only. On these time scales, the hydrodynamics are considered negligible compared to heat conduction; thus, the density profile remains unchanged from the initial profile.

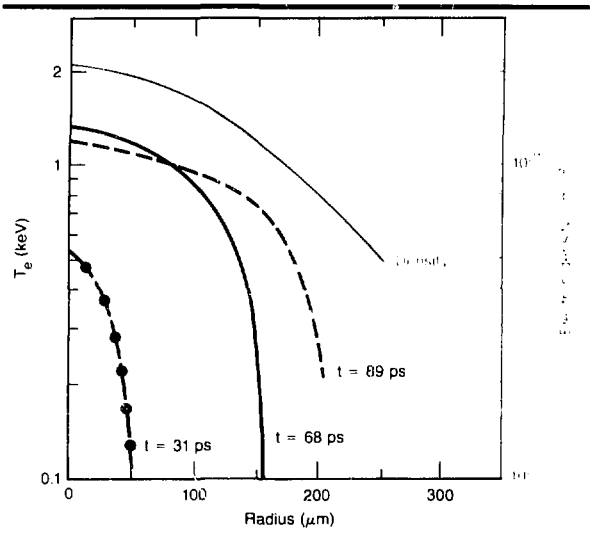

Table 6-24. Parameters used in the PIC simulations.

Orifice density = 4.0×10^{21} cm^{-3}
Initial target temperature = 1×10^3 K
$Z = 18$ (argon)
Ion density at the critical-density surface $= \frac{n_c(1\omega)}{\lambda_i^2 Z} = \frac{1 \times 10^{21}}{(0.53\ \mu\text{m})^2 18} = 2.2 \times 10^{20}$ ions/cm^3
Laser intensity = 3.8×10^{15} W/cm^2
Laser radius = 50 μm
Laser pulse length = 90 ps
Flux limiter = 0.32
$T_e = T_e$

Figure 6-68 shows calculated time-stepped x-ray spectra for a plasma having the density and temperature produced by the PIC code. The calculated spectra represent what an x-ray measurement observes at 90° to the longitudinal axis of the gas jet and at a fixed position on the longitudinal density profile (namely, $n_e = n_c$). The PIC simulations indicate the following

- The plasma expands rapidly in the transverse dimension.
- The plasma never obtains densities greater than $n_e \sim 2\ n_c$.
- There is a strong radial temperature-dependence, with $T_e \sim 2$ keV at $r = 0$, cooling to $T_e \sim 100$ eV at $r = \sim 200$ to 300 μm; under these high-temperature conditions, we observe significant populations of H-like ion species.

Figure 6-69 illustrates a measured time-averaged argon spectrum produced under conditions similar to those employed in the PIC simulation. The absence of a H-like line could indicate a cooler plasma environment than that predicted by time integration of the calculated line spectra. The lack of H-like line emission may also be due to the increased time necessary to achieve steady-state ionization equilibrium for the H-like ion configuration. Recall that the calculated spectra assume that steady-state ionization is achieved; we are performing improved calculations to account for nonsteady-state effects.

Fig. 6-68. Simulations of the argon gas-jet K x-ray spectrum emitted perpendicular to the longitudinal axis of the gas jet.

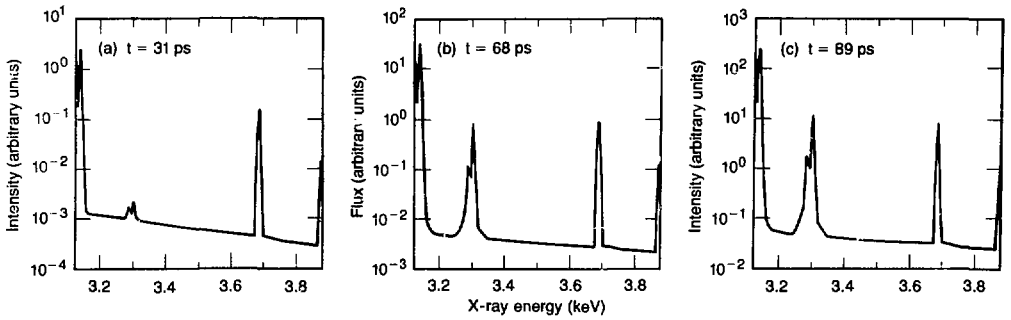

Summary

We have performed more detailed analyses of previously reported gas-jet data.[85] We conclude that transverse temperature and density gradients, as well as time-varying plasma conditions, significantly affect spectral features. We have begun more accurate calculations to improve the comparison with experimental data.

Author: D. L. Matthews

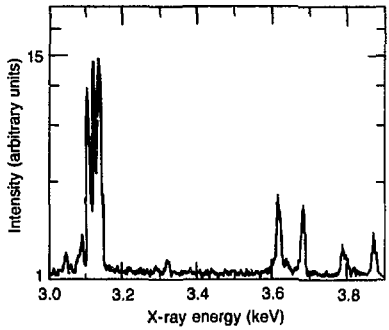

Fig. 6-69. Experimentally determined time-averaged argon K x-ray spectrum for 0.53-μm irradiation with $I \approx 1 \times 10^{15}$ W/cm^2 in a 900-ps pulse.

References

1. *Laser Program Annual Report—1980*, Lawrence Livermore National Laboratory, Livermore, Calif., UCRL-50021-80 (1981), p. 2-59.
2. *Laser Program Annual Report—1980*, Lawrence Livermore National Laboratory, Livermore, Calif., UCRL-50021-80 (1981), pp. 2-6 to 2-13.
3. *Laser Program Annual Report—1980*, Lawrence Livermore National Laboratory, Livermore, Calif., UCRL-50021-80 (1981), p. 2-262.
4. C. Lotta, D. Runeau, and E. Fabre, "Ultraviolet 45 GW Coherent Pulse for Laser Matter Interaction," *Appl. Opt.* **19,** 1022 (1980).
5. J. P. Machewirth, R. Webb, and D. Anafi, "High Power Harmonics Produced with High Efficiency in KD*P," *Laser Focus*, 104 (1976).
6. P. Liu et al., "Absolute Two-Photon Absorption Coefficients at 355 and 266 nm," *Phys. Rev. B* **17,** 4620 (1978).
7. G. J. Linford, *Low Omega Status Report*, LLNL internal memorandum, Lawrence Livermore National Laboratory, Livermore, Calif., GJL81-11/21481 (May 29, 1981).
8. J. Rientjes and R. C. Eckardt, "Two Photon Absorption in ADP and KD*P at 266 nm," *IEEE J. Quantum Electron.* **QE-13,** 791 (1977); "Efficient Harmonic Generation for 532 to 266 nm in ADP and KD*P," *Appl. Phys. Lett.* **30,** 91 (1977).
9. M. D. Jones and G. A. Massey, "Milliwatt 213 nm Source Based on a Repetitively Q Switched, CW Pumped Nd:YAG Laser," *J. Quantum Electron.* **QE-15,** 204 (1979).
10. V. D. Volosov et al., *Sov. Phys. JETP* **19,** 38 (1974).
11. P. Liu, R. Yen, and N. Bloembergen, "Two Photon Absorption Coefficients in UV Window and Coating Materials," *Appl. Opt.* **18,** 1015 (1979).
12. K. Kato, "Tunable UV Generation in KB_5O_8 to 1966 Å," *Appl. Phys. Lett.* **30,** 583 (1977).
13. K. Kato, "Conversion of High Power Nd:YAG Laser Radiation to the UV at 2661 Å," *Opt. Commun.* **13,** 361 (1975).
14. *Laser Program Annual Report—1975*, Lawrence Livermore National Laboratory, Livermore, Calif., UCRL-50021-75 (1976), Section 13.3.2.
15. *Laser Program Annual Report—1975*, Lawrence Livermore National Laboratory, Livermore, Calif., UCRL-50021-75 (1976), Section 3.2.
16. *Laser Program Annual Report—1976*, Lawrence Livermore National Laboratory, Livermore, Calif., UCRL-50021-76 (1977), Section 2.1.7.
17. *Laser Program Annual Report—1976*, Lawrence Livermore National Laboratory, Livermore, Calif., UCRL-50021-76 (1977), Section 5.3.2.
18. *Laser Program Annual Report—1976*, Lawrence Livermore National Laboratory, Livermore, Calif., UCRL-50021-76 (1977), Section 3.5.4.
19. *Laser Program Annual Report—1976*, Lawrence Livermore National Laboratory, Livermore, Calif., UCRL-50021-76 (1977), Section 2.5.9.
20. *Laser Program Annual Report—1977*, Lawrence Livermore National Laboratory, Livermore, Calif., UCRL-50021-77 (1978), p. 6-31.
21. *Laser Program Annual Report—1977*, Lawrence Livermore National Laboratory, Livermore, Calif., UCRL-50021-77 (1978), p. [illegible] and pp. 2-19 to 2-21.
22. *Laser Program Annual Report—1977*, Lawrence Livermore National Laboratory, Livermore, Calif., UCRL-50021-77 (1978), pp. 6-12 to 6-17.
23. *Laser Program Annual Report—1977*, Lawrence Livermore National Laboratory, Livermore, Calif., UCRL-50021-77 (1978), p. 3-4.
24. *Laser Program Annual Report—1978*, Lawrence Livermore National Laboratory, Livermore, Calif., UCRL-50021-78 (1979), pp. 2-1 to 2-3.
25. *Argus Weekly Status Report*, Lawrence Livermore National Laboratory, Livermore, Calif. (September 8, 1978).
26. *Argus Weekly Status Report*, Lawrence Livermore National Laboratory, Livermore, Calif. (December 1, 1978).
27. *Laser Program Annual Report—1978*, Lawrence Livermore National Laboratory, Livermore, Calif., UCRL-50021-78 (1979), pp. 2-133 to 2-137.
28. *Laser Program Annual Report—1979*, Lawrence Livermore National Laboratory, Livermore, Calif., UCRL-50021-79 (1980), pp. 6-12 to 6-14.
29. *Laser Program Annual Report—1979*, Lawrence Livermore National Laboratory, Livermore, Calif., UCRL-50021-79 (1980), pp. 2-3 to 2-12.
30. *Laser Program Annual Report—1979*, Lawrence Livermore National Laboratory, Livermore, Calif., UCRL-50021-79 (1980), pp. 2-197 to 2-203.
31. *Laser Program Annual Report—1979*, Lawrence Livermore National Laboratory, Livermore, Calif., UCRL-50021-79 (1980), pp. 6-41 to 6-46.
32. *Laser Program Annual Report—1980*, Lawrence Livermore National Laboratory, Livermore, Calif., UCRL-50021-80 (1981), pp. 2-14 to 2-18.
33. *Laser Program Annual Report—1980*, Lawrence Livermore National Laboratory, Livermore, Calif., UCRL-50021-80 (1981), pp. 2-259 to 2-268.
34. *Laser Program Annual Report—1980*, Lawrence Livermore National Laboratory, Livermore, Calif., UCRL-50021-80 (1981), p. 2-11.
35. G. Bret and F. Gires, *Comp. Rend.* **258,** 3469, 4702 (1964).
36. *Laser Program Annual Report—1977*, Lawrence Livermore National Laboratory, Livermore, Calif., UCRL-50021-77 (1978), pp. 3-11, 3-22, and 3-90.
37. *Laser Program Annual Report—1978*, Lawrence Livermore National Laboratory, Livermore, Calif., UCRL-50021-78 (1979), p. 2-56.
38. *Laser Program Annual Report—1979*, Lawrence Livermore National Laboratory, Livermore, Calif., UCRL-50021-79 (1980), p. 2-29.
39. *Laser Program Annual Report—1980*, Lawrence Livermore National Laboratory, Livermore, Calif., UCRL-50021-80 (1981), p. 2-18.
40. *Laser Program Annual Report—1980*, Lawrence Livermore National Laboratory, Livermore, Calif., UCRL-50021-80 (1981), p. 2-33.
41. *Laser Program Annual Report—1980*, Lawrence Livermore National Laboratory, Livermore, Calif., UCRL-50021-80 (1981), pp. 2-2 to 2-38.
42. *Laser Program Annual Report—1980*, Lawrence Livermore National Laboratory, Livermore, Calif., UCRL-50021-80 (1981), pp. 7-3 to 7-7.
43. *Laser Program Annual Report—1980*, Lawrence Livermore National Laboratory, Livermore, Calif., UCRL-50021-80 (1981), pp. 7-2 to 7-22.

44. W. C. Mead et al., *Phys. Rev. Lett.* **47,** 1289 (1981).
45. M. D. Rosen et al., *Phys. Fluids* **22,** 2020 (1979).
46. A. I. Avrov et al., *Sov. Phys. JETP* **45,** 508 (1977).
47. C. E. Max, *Physics of Laser Fusion, Vol. I, Theory of the Coronal Plasma in Laser Fusion Targets*, Lawrence Livermore National Laboratory, Livermore, Calif., UCRL-53107 (1981).
48. K. Estabrook et al., *Phys. Rev. Lett.* **46,** 724 (1981).
49. *Laser Program Annual Report—1980* Lawrence Livermore National Laboratory, Livermore, Calif., UCRL-50021-80 (1981), pp. 7-2 to 7-9.
50. *Laser Program Annual Report—1980* Lawrence Livermore National Laboratory, Livermore, Calif., UCRL-50021-80 (1981), pp. 2-259 to 2-264.
51. W. C. Mead et al., *Phys. Rev. Lett.* **47,** 1289 (1981).
52. C. Garban-Labaune et al., *Rapport dActivité 1979*, GRECO Interaction Laser—Matière, École Polytechnique (Palaiseau, France, 1979), pp. 64-68.
53. G. B. Zimmerman, *Numerical Simulation of the High Density Approach to Laser Fusion*, Lawrence Livermore National Laboratory, Livermore, Calif., UCRL-74811 (1973); G. B. Zimmerman and W. L. Kruer, *Comments Plasma Phys. Contr. Fusion* **2,** 85 (1975).
54. R. A. Haas et al., *Phys. Fluids* **20,** 322 (1977).
55. C. J. Randall, J. R. Albritton, and J. J. Thomson, *Phys. Fluids* **24,** 1474 (1981).
56. C. E. Max, *Physics of Laser Fusion, Vol. I, Theory of the Coronal Plasma in Laser Fusion Targets*, Lawrence Livermore National Laboratory, Livermore, Calif., UCRL-53107 (1981), p. 25.
57. C. E. Max and K. G. Estabrook, *Comments Plasma Phys. Contr. Fusion* **5,** 239 (1980).
58. *Laser Program Annual Report—1980*, Lawrence Livermore National Laboratory, Livermore, Calif., UCRL-50021-80 (1981), p. 7-23.
59. *Laser Program Annual Report—1978*, Lawrence Livermore National Laboratory, Livermore, Calif., UCRL-50021-78 (1979), pp. 6-5 to 6-7.
60. M. D. Rosen et al., *Phys. Fluids* **22,** 2020 (1979).
61. *Laser Program Annual Report—1980*, Lawrence Livermore National Laboratory, Livermore, Calif., UCRL-50021-80 (1981) p. 7-2.
62. K. Estabrook et al., "Sources of Hot Electrons in Laser-Plasma Interaction with Emphasis on Raman and Turbulence Absorption," *Japan-US Seminar on Theory and Application of Multiply-Ionized Plasmas Produced by Laser and Particle Beams*, Nara, Japan, May 3-7, 1982 (Institute of Laser Engineering, Osaka University, 1982).
63. *Laser Program Annual Report—1980*, Lawrence Livermore National Laboratory, Livermore, Calif., UCRL 50021-80 (1981), pp. 7-26 to 7-30.
64. J. D. Hares et al., *Phys. Rev. Lett.* **42,** 1216 (1979).
65. C. J. Powell, *Rev. Mod. Phys.* **48,** 33 (1976).
66. F. Ronrlich and B. C. Carlson, *Phys. Rev.* **93,** 38 (1954).
67. M. Green and V. E. Cosslett, *Proc. Phys. Soc.* **78,** 1206 (1961).
68. *Laser Program Annual Report—1978*, Lawrence Livermore National Laboratory, Livermore, Calif. UCRL-50021-78 (1979), pp. 6-8 to 6-12.
69. A. I. Avrov et al., *Sov. Phys. JETP* **45,** 507 (1977).
70. P. D. Carter, S. M. L. Sim, and E. R. Wooding, *Opt. Commun.* **32,** 443 (1980); H. C. Barr, *Rutherford Laboratory Annual Report to the Laser Facility Committee 1979*, Rutherford Laboratory, Chilton, Great Britain, RL-79-036 (1979), Sec. 8.3.3.
71. C.S. Liu and M. N. Rosenbluth, *Phys. Fluids* **19,** 967 (1976).
72. *Laser Program Annual Report—1979*, Lawrence Livermore National Laboratory, Livermore, Calif., UCRL-50021-79 (1980), p. 5-42.
73. *Laser Program Annual Report—1980*, Lawrence Livermore National Laboratory, Livermore, Calif., UCRL-50021-80 (1981), p. 5-38.
74. D. L. Matthews et al., *Bull. Am. Phys. Soc.* **25,** 898 (1980).
75. B. Yaakobi et al., *Opt. Commun.* **38,** 196 (1981).
76. L. Koppel and J. Eckels, *High Resolution X Ray Crystal Spectrographs*, Lawrence Livermore National Laboratory, Livermore, Calif., UCRL-79781 (1977).
77. I. Kilkenny, Central Laser Facility, Rutherford Laboratory, Rutherford, England, private communication (January, 1982).
78. Hans Griem, *Plasma Spectroscopy*, (McGraw Hill, New York, 1964), Chapter 6
79. R. Lee and D. L. Matthews, *Bull. Am. Phys. Soc.* **26,** 907, (1981).
80. V. Boiko, S. Pikuz, and N. Faenov, *J. Phys. B* **12,** 1889 (1979).
81. *Inertial Fusion Research Annual Technical Report 1980*, KMS Fusion Corp., Ann Arbor, Mich DOE/DP/40030-3 (no pub. date).
82. C. Bhalla, A Gabriel, and L. Presnyakov, *Mon. Not. R. Astron. Soc.* **172,** 359 (1975).
83. A. Vinogradov, I. Skobelev, and E. Yukov, *Sov. J. Quantum Electron.* **2,** 1169 (1975).
84. M. Dunning, Univ. of Michigan, Ann Arbor, Mich., and E. Mayer, KMS Fusion, Ann Arbor Mich., private communication (1981).
85. G. Charatis et al., in *Low Energy X ray Diagnostics*, D. T. Attwood and B. L. Henke, eds. (American Institute of Physics, New York 1981).

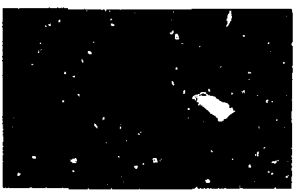

Fusion Laser Research and Development

Section 7

Fusion Laser Research and Development

Contents

Section Editor: D. Eimerl

Fusion Laser Research and Development

Introduction

J. T. Hunt

During 1981, research and development for solid-state lasers and advanced lasers were combined into one program. The new Fusion Laser Research and Development program element was given three assignments

- Short-term research and development for Nova, Novette, and presently existing Nd:glass laser systems.
- Midterm research and development of a cost-effective single-shot laser suitable for target irradiation studies in the 1- to 10-MJ range.
- Long-range research and development directed towards a high-repetition-rate cost-effective laser suitable for use in a commercial laser-fusion power plant.

The short-term program included projects such as harmonic conversion, damage studies at 1.06 μm (1ω), and the plasma shutter. The megajoule group, formed to address the design of a 1- to 10-MJ single-shot driver, concentrated on Nd:glass lasers and, in particular, on multipass amplifier configurations and improved amplifier and flashlamp design. In the area of advanced fusion drivers, we continued research on the free-electron laser; Raman compression of rare-gas halide lasers; new glass-laser media; and new pulsed-power sources, such as the compensated pulsed alternator.

Because the Fusion Laser Research and Development program was formed late in the calender year, the organization of research material follows the 1980 structure. It is divided into three categories: research and development of solid-state lasers, advanced lasers, and pulsed power.

Solid-State Laser Research and Development

Harmonic Conversion

Progress in harmonic generation during 1981 was made in several areas. Various ideas for frequency conversion on the Nova and Novette subsystems were thoroughly analyzed and tested in small-scale (3-cm aperture) experiments on Argus. A new method of second-harmonic generation was invented and incorporated into the Nova baseline design. Various designs for constructing segmented crystal arrays of large apertures were analyzed, and prototypes were constructed and tested.

Quadrature Conversion Scheme. The quadrature conversion scheme is a method of generating the second harmonic (2ω) of a fundamental wave (1ω). The scheme, which uses two crystals in series, has several advantages over single-crystal or other two-crystal schemes

- High conversion efficiency over a large dynamic range of drive intensity and detuning angle.
- Easier crystal alignment.
- Same crystal configuration as other two-crystal methods of generating the third harmonic (3ω), making much simpler the transition from 2ω to 3ω output.

Consider a pair of potassium dihydrogen phosphate (KDP) crystals cut for Type II phase matching. In the quadrature scheme, the optical axes of the crystals are arranged so that the planes containing the direction of the laser beam and their optical axes (the kz planes) are mutually perpendicular. This arrangement has two important properties. First, in Type II phase matching, the incident wave is polarized at 45° to the kz plane of the crystal. Thus, in the quadrature

scheme, if the incident wave is correctly polarized for efficient conversion in the first crystal, it is also correctly polarized for efficient conversion in the second crystal.

Second, the 2ω waves generated in the two crystals are orthogonally polarized (hence, the term quadrature). The output from the first crystal thus has the wrong polarization to experience gain in the second crystal. If the conversion efficiency is η_1 in the first crystal and η_2 in the second, the output from the first crystal is $\eta_1 I$ (where I is the incident intensity of the fundamental wave) and the input intensity to the second crystal is $(1 - \eta_1)I$. Because the second crystal does not change the output of the first, the overall output is simply the sum of the output from each crystal. The overall conversion efficiency is then

$$\eta = \eta_1 + \eta_2 (1 - \eta_1) \quad . \tag{1}$$

The advantage of quadrature conversion is that it enables us to arrange for the second crystal to convert whatever light is left unconverted from the first.

The conversion properties of a single 1.4-cm-thick crystal of KDP are plotted in Fig. 7-1 as a function of angular detuning and incident intensity, where the curves are contours of constant conversion efficiency = 0.1, 0.2, ..., 0.9. Consider a large-aperture laser beam incident on the crystal. Because of the unavoidable slight aberrations present in any laser beam, the intensity and local direction of the laser light (angular detuning) will vary over the face of the beam. As the crystal acts locally in converting the laser light to the second harmonic, the conversion efficiency experienced by the laser light varies from point to point over the face of the beam. Therefore, the relevant conversion efficiencies are defined by the range of intensities and angular detunings present in the beam, and this range defines an area on the detuning-intensity plot. For efficient conversion, the efficiency within that range must be high.

Clearly, any energy in the laser beam that meets the crystal with an intensity and detuning for which the conversion efficiency is low will remain unconverted. For efficient operation, the crystals must convert efficiently over a sufficiently large area in the intensity-detuning plane. The required size of this area depends on the quality of the incident laser beam. As shown in Fig. 7-1, a single 1.4-cm-thick crystal converts efficiently in a roughly rectangular region (defined by the 90% contour) 200 to 400 μrad wide for an incident intensity ranging from 2 GW/cm^2 to about 10 GW/cm^2. Any laser light falling in this region will be converted to the second harmonic with an efficiency greater than 80% for intensities above 2 GW/cm^2.

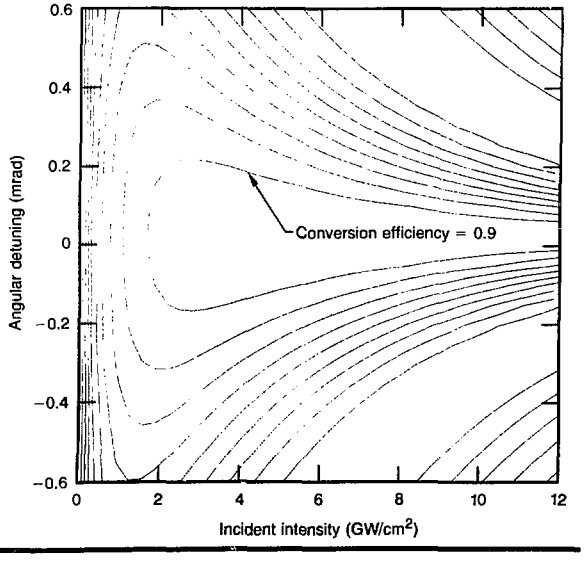

Fig. 7-1. Conversion efficiency of a single 1.4-cm-thick crystal of KDP.

The conversion properties of two 1.4-cm-thick crystals of KDP arranged in quadrature are plotted in Fig. 7-2 as a function of angular detuning and incident intensity, where, once again, the curves are contours of constant conversion efficiency = 0.1, 0.2, ..., 0.9. The quadrature system is clearly much more forgiving of beam aberrations than is a single crystal. For the beam quality of Nova, the angular detunings are not expected to exceed 0.2 mrad. Thus, the quadrature design permits efficient generation of the second harmonic over the entire operating range of Nova.

Argus Experiments and the Nova Baseline. The primary purpose of the Argus experiments was to study ideas for converting Nova to a 2ω or 3ω laser. These experiments included tandem second-harmonic generation (SHG), described in the *1980 Laser Program Annual Report*,[1] as well as the quadrature scheme just presented. The

experiments confirmed our qualitative and quantitative understanding of harmonic generation and were instrumental in the development of the quadrature/cascade ($2\omega/3\omega$) conversion scheme.

The Argus experiments used the rod section of the laser at a 3-cm aperture, the largest aperture available at an acceptably high shot rate. The experimental configuration is shown in Fig. 7-3, and the beam profile used in the experiments is shown in Fig. 7-4. The deeply modulated beam observed at high intensity is due to diffraction from the system input aperture and nonlinear growth. It would have been advantageous to avoid this problem, but we were unable to locate the crystal in an image plane where the beam would be reasonably smooth. Consequently, we developed a semiempirical beam model, which included the effects of this modulation and the beam divergence, as measured at the crystal location.

SHG-efficiency measurements were made on single KDP crystals of different thicknesses using the system configuration shown in Fig. 7-3. The results agreed closely with the widely used and well understood theory of harmonic generation. With confidence in our technique, we tested the tandem SHG scheme using two relatively thin KDP crystals. The results shown in Fig. 7-5(a) agree closely with theory using the semiempirical model of the Argus beam.

Quadrature second-harmonic conversion efficiency was measured using the same two crystals by simply rotating the second crystal 90° about the beam direction and

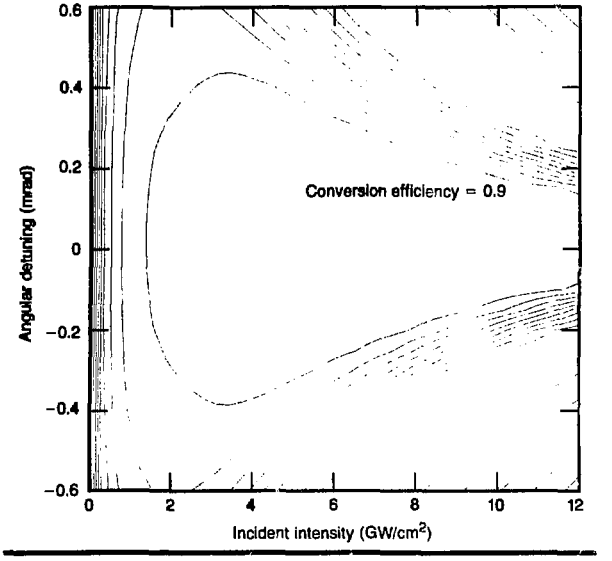

Fig. 7-2. Conversion efficiency of two 1.4-cm-thick crystals of KDP arranged in quadrature.

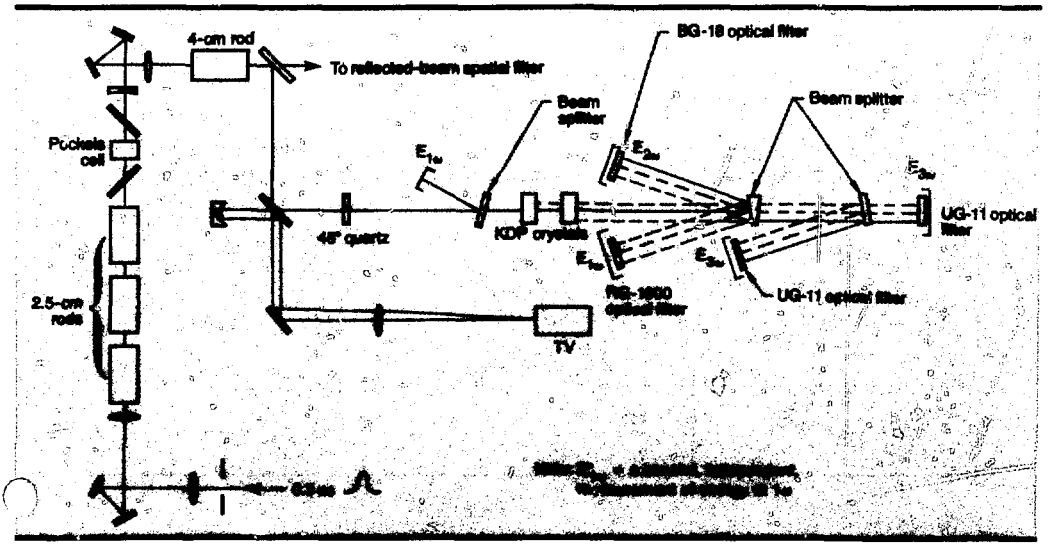

Fig. 7-3. Laboratory configuration for 3-cm-aperture experiments on Argus.

aligning it to the second-harmonic phase-matching angle. These data are compared with quadrature SHG theory in Fig. 7-5(b). Quadrature second-harmonic data agree closely with the plane-wave model over our intensity range because the conversion efficiency does not roll over at the higher-than-average intensities found in the rings present on the laser spatial profile.

The cascade third-harmonic conversion efficiency was measured using the same two crystals by rotating and tilting the two crystals together as a unit. The data shown in Fig. 7-5(c) are compared with theory for third-harmonic generation (THG), where we are using the same semiempirical beam model we used for analyzing the tandem second-harmonic experiments. For the third harmonic, conversion-efficiency rolloff with increasing intensity is a result of back-conversion of the high-intensity rings.

Our experiments confirmed an understanding of harmonic generation and demonstrated the great flexibility of the

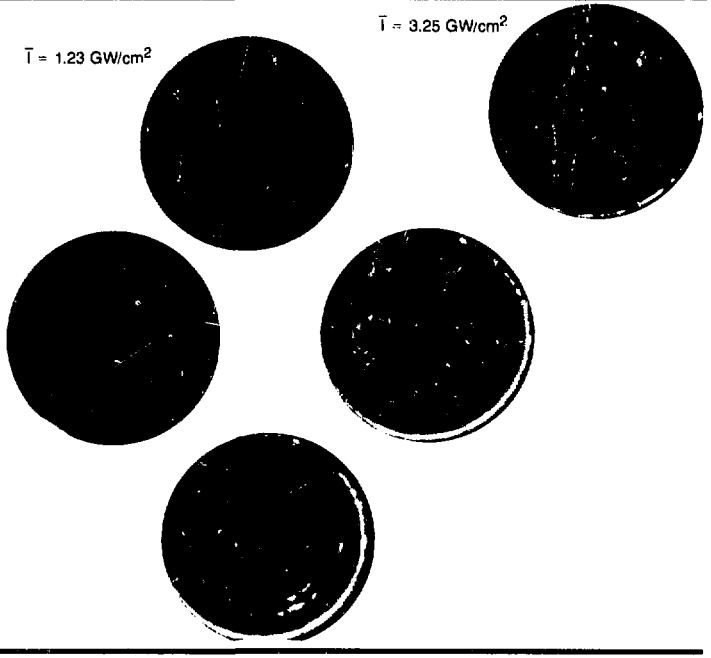

Fig. 7-4. Argus beam profile used in harmonic-generation experiments. The deeply modulated beam at high intensity is illustrated at three exposure levels.

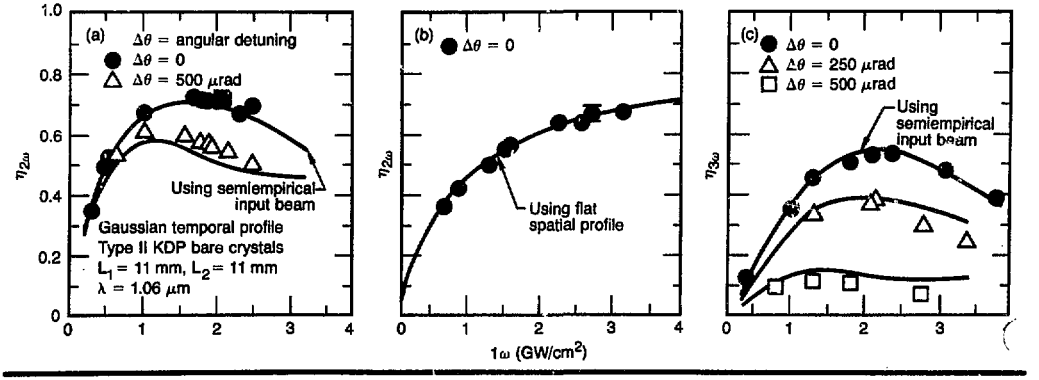

Fig. 7-5. Comparison of experiment and theory. (a) Tandem SHG. (b) Quadrature SHG. (c) Cascade THG.

quadrature scheme. The range of intensities experiencing high conversion efficiency is broad and, thus, allows for efficient operation over a large operating range of Nova.

Novette Harmonic Generation with KDP Crystal Arrays. Providing multiple-wavelength target-irradiation capability for our Nova and Novette systems requires harmonic generation at a 74-cm aperture. However, single nonlinear KDP optical crystals of this size have yet to be grown and are not likely to become available in time for either Novette or for Nova activation in 1985. To overcome crystal-size limitations, we have developed and tested KDP crystal arrays.

The arrays consist of a matrix of KDP crystal segments placed edge-to-edge and mounted between two windows in an index-matching fluid-filled housing, as indicated schematically in Fig. 7-6. The great advantage of the array is that it provides harmonic-generation capability at arbitrarily large apertures, even though individual crystal-segment size may be restricted to a small fraction of the desired aperture.

To be effective, however, a crystal array must satisfy three unique performance requirements. First, all crystal segments must be properly oriented at the angle for correctly phase-matched harmonic generation such that the array produces frequency-conversion efficiencies that are as close as possible to a single crystal of the same total aperture. This requirement places strict orientation tolerances on the crystal segments and requires good dimensional accuracy on both crystals and assembly hardware if complex individual-alignment adjustments for each segment are to be avoided.

Second, the array must produce and maintain a good optically transmitted figure while minimizing the nonlinear self-focusing (B-integral) contribution from the windows. Nova output intensities require relatively thin (90- by 4-cm thick, 22:5 aspect ratio) windows to control the B-integral.

Third, the gaps between crystals in the array matrix should obscure as little of the incident beam as possible to reduce insertion loss and should minimize the production of undesirable diffraction fringes arising from amplitude and phase discontinuities in this region.

Two prototypes were designed, constructed, and tested for optical performance and frequency-conversion efficiency. Both prototypes were subjected to a series of optical performance tests, with the following results

- Both arrays produced 70% energy-conversion efficiency to the second harmonic at high power (from 2 to 3 GW/cm^2) on the Argus laser system. In both cases, 12.6-cm-diam 2ω beams of uniform overall intensity were generated, confirming that each crystal segment participated equally in the conversion process.

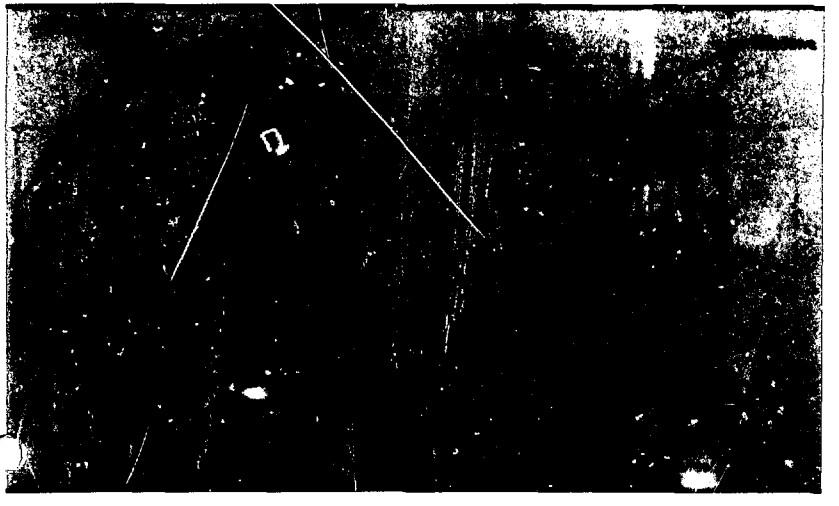

Fig. 7-6. Large-aperture KDP arrays.

- Applying a partial vacuum to the housing interior produced good transmitted-wavefront figures for both arrays in spite of the high-aspect-ratio (22:5) windows.
- Strong diffraction observed from the intercrystalline gaps will require apodization of the input beam to avoid damage to subsequent optical elements.

KDP Orientation and Finishing. To evaluate the feasibility of meeting the performance requirements just described, we built and tested smaller-aperture prototype arrays. The prototypes were designed to contain nine 5- by 5- by 1.87-cm KDP crystal segments in a 3 × 3 matrix arrangement. Providing crystal segments for the prototype required that precise dimensional and orientation tolerances be maintained for each segment. To fabricate the individual crystals with the required precision, we employed a combination of laser orientation and diamond machining. A total of 14 5-cm segments were processed; subsets of 9 were then selected for testing in the prototype arrays.

The laser-orientation setup used to measure the crystals' phase-matching direction with respect to their surface normals was described in detail in the *1980 Laser Program Annual Report*.[1] This setup is capable of determining orientation angles to within ±10 μrad, well within our tolerance of ±30 μrad for orientation of the prototype-array segments.

The procedures for diamond machining KDP crystals were also described in the *1980 Laser Program Annual Report*.[1] The basic machining operation employed is a "fly cut," whereby the work piece (KDP crystal in our case) is held against a flat (vacuum-chuck) reference surface and then translated across a rotating single-point cutter in a direction perpendicular to the cutter-spindle axis of rotation. Figure 7-7 shows KDP crystal angular-tuning curves before and after orientation and diamond machining. The expected dependence for second-harmonic output power vs angle θ is observed, with the location of the crystal-surface normal indicated by the fiducial. Before processing, the phase-match direction (peak of the tuning curve) was displaced from the surface normal by −5.539 mrad (−0.32°). After processing, the surface-normal and phase-match directions are identical to within experimental error. The dimensional, angular, and orientation accuracies obtained for the 14 prototype KDP crystals are summarized in Table 7-1.

The successful fabrication of the crystals into virtually identical segments was a direct result of the exceptional precision available from both the laser measurement and the diamond-turning machine. The results in Table 7-1 would have been difficult, if not impossible, to achieve with conventional crystal-finishing techniques and represent a key step in the successful development of large-aperture crystal arrays.

Table 7-1. Specifications and results for 14 prototype KDP crystals.

Parameter	Specification	Results
Length and width	±0.1 mm	±0.004 mm
Thickness	±0.005 mm	±0.001 mm
Transmitted wavefront at 0.6328 μm	λ/2	λ/6
Phase-matching angle, θ	±60 μrad	0 to 30 μrad
Face to edge	±300 μrad	50 to 150 μrad
Edge to edge	±50 μrad	25 to 150 μrad
Parallelism	±50 μrad	10 to 40 μrad

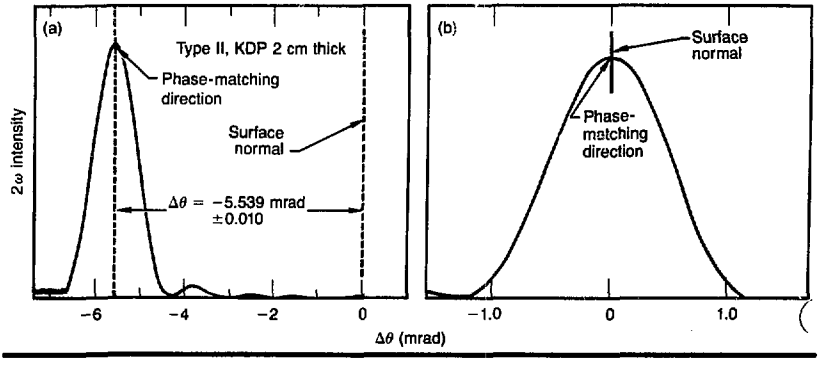

Fig. 7-7. Effects of orientation and machining on KDP crystal angular-tuning curve. (a) Before (b) After.

Prototype Array Design and Construction. We designed, built, and tested two versions of the array at a 15-cm aperture. Once again, each version contained nine precision-fabricated 5- by 5- by 1.87-cm KDP crystal segments arranged in a 3 × 3 matrix. These prototype arrays were designed to test different methods of achieving the three unique performance requirements (see "Novette Harmonic Generation with KDP Crystal Arrays," above).

Alignment of the crystal segments in the fluid-filled cell was achieved by minimizing mechanical clearance between the crystals and the windows to limit any rotation about the sensitive crystal axis. A fluid gap of 10 μm per side mechanically limited crystal rotation to about 400 μrad in the prototype arrays. In addition, the fluid film itself constrained the crystals by limiting the observed rotation to about 175 μrad. This angular misalignment did not have substantial impact on the second-harmonic energy-conversion efficiency for either "egg crate" or "close-packed" crystal arrays (see Fig. 7-8). Theory and data were in good agreement and demonstrated that both multielement arrays approached the performance of a single crystal with equivalent aperture. The Nova and Novette arrays will constrain the crystal segments to a maximum rotation of 30 μrad, as dictated by possible use of the arrays to generate 3ω.

The requirements for both minimum array-window thickness and good optical figure necessitate careful mounting to minimize stresses on the windows. The index-matching fluid must be contained by the window and mount, so that conventional sling or pad supports are not applicable.

The hydrostatic load on the windows from the index-matching fluid causes the windows to deflect outward from the cell, thereby causing substantial wavefront error in the laser beam. In the prototype array, maximum deflection was calculated to be 3.0 μm, using the SAP4 finite-element code. For the 90-cm-diam, 4-cm-thick windows that will be used on the 74-cm-aperture array, the code predicts a maximum deflection of about 50 μm. The code prediction and measured deflection of the prototype-array window show good agreement (see Fig. 7-9) and suggest that our theoretical models can be used with confidence to predict optical performance of the crystal array at the 74-cm Nova and Novette aperture. We have also investigated the application of a partial vacuum between the array windows, using the resulting atmospheric pressure load to balance the hydrostatic load.

The first prototype array used an internal egg-crate support structure, within which individual crystals were nested (see Fig. 7-10). The egg crate was fabricated to be slightly thicker (20 μm) than the crystals and was lapped flat and parallel.

The second prototype version employed the same nine crystals in a close-packed arrangement, with the crystals simply stacked edge-to-edge between the windows (see Fig. 7-11). In this case, there was no

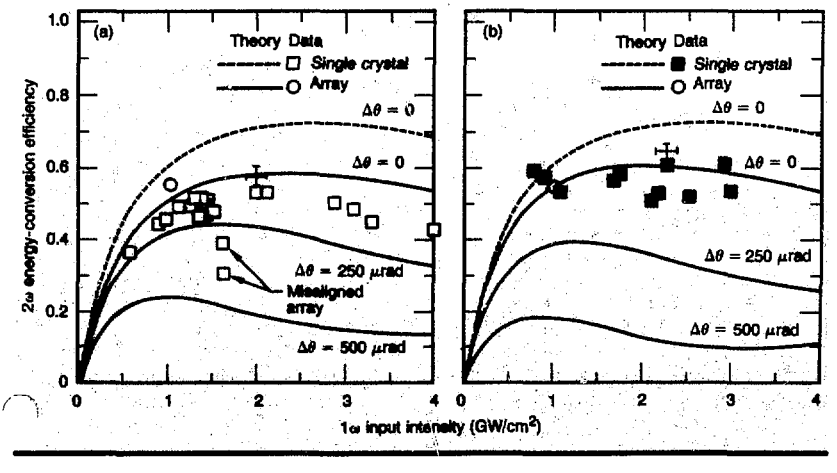

Fig. 7-8. Second-harmonic energy-conversion efficiencies. (a) Egg-crate array. (b) Close-packed array. Theory and data are in good agreement.

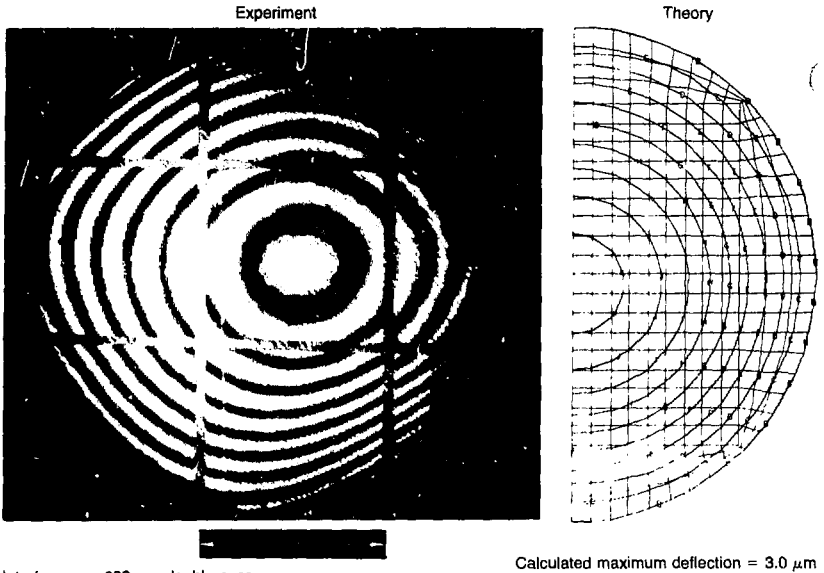

Fig. 7-9. Comparison of experiment and *theory for hydrostatic*-loading deformation of a thin window (aspect ratio = 22:5).

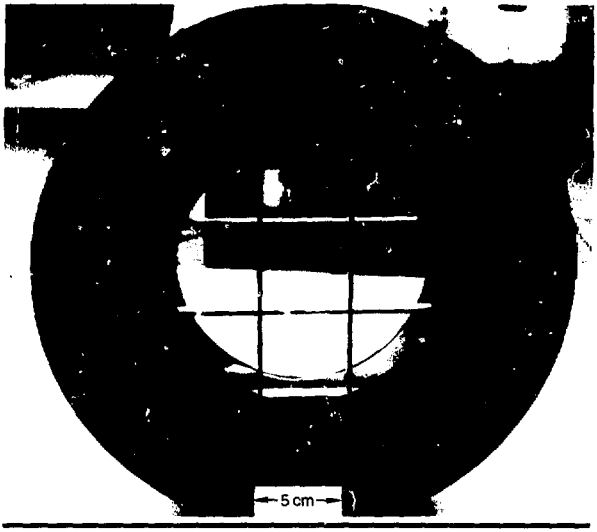

Fig. 7-10. Photograph of egg-crate prototype array with 5- by 5-cm KDP segments nested between egg-crate bars in a honeycomb arrangement.

separate internal support structure to obscure the beam, but the crystals themselves became structural elements of the assembly.

In both cases, window deflections and resulting optical distortion were reduced by the application of a partial vacuum between the windows. Analysis of the resulting interferograms indicated that window sealing and mounting techniques used in the prototype arrays contributed substantially to the optical distortion. We have developed a seal that is vacuum tight to 1×10^{-8} cm^3/s at STP of helium, is chemically resistant to the index-matching fluid, and yet leaves the window distortion-free after mounting. We believe the seal will facilitate better registration of the windows on the egg-crate or on the crystals and result in less optical distortion on the windows.

Code calculations indicate that window deflection in the 74-cm-aperture arrays will be less than 0.5 μm when the vacuum-balancing technique is applied to a full-scale egg-crate structure. The egg-crate structure minimizes any stresses placed on the crystals and stiffens the entire array, much as a honeycomb core stiffens aircraft components. Because the egg crate will obscure from 3 to 5% of the beam area in the 74-cm array, a mask will be required to prevent direct irradiation of egg-crate webs and to reduce diffraction from crystal edges.

Conversion Efficiency and Beam Quality. Energy-conversion efficiency for the

egg-crate and close-packed prototype arrays was measured in a series of experiments on the Argus laser north arm. Figure 7-8(a) shows 2ω energy-conversion efficiency vs 1ω input intensity for 20 high-power shots on the egg-crate array. The theoretical conversion curves (bottom three curves) account for the misalignment of the individual segments and also incorporate the spatial-distribution spectrum of the input beam. The three curves plotted are for the relative alignment of the central ray with respect to the ideal phase-match direction. For our analysis, insertion loss due to the egg-crate obscuration (~14%) has been removed to permit comparison with the equivalent (18.7-mm-thick) single-crystal performance (top curve). Fresnel losses due to surface reflections on the uncoated input and output windows were not backed out; i.e., theoretical and experimental efficiencies would be about 8% higher with anti-reflective (AR) coated windows. The vertical error bar represents the energy imbalance in the calorimeters. The data boxes were plotted conservatively by assuming that all the energy not accounted for was at the fundamental wavelength. The horizontal error bar arises from uncertainties in the input beam area.

Figure 7-8(b) is a plot of 2ω conversion efficiency vs 1ω input intensity for the close-packed array. In this case, the obscuration loss was negligible (~0.1%). Fresnel losses, individual-segment misalignment, and energy and intensity errors were treated in the same manner as for egg-crate data.

Our results indicate that, after subtracting Fresnel and egg-crate insertion losses, both arrays produced conversion efficiencies approaching 70%. More importantly, even though they consisted of an assemblage of individual crystal segments, both arrays closely approached the performance of an equivalent single crystal.

Array Optical Distortion. Prior to high-power conversion tests, both arrays were tested for their transmitted wavefront on a 6-in., 0.633-nm Twyman–Green interferometer. Test results are summarized in Figs. 7-12 and 7-13.

Figures 7-12(a) and (b) are double-pass interferograms showing the transmitted wavefront obtained initially with the egg-crate array at 1 atm. A combination of hydrostatic-loading effects of the index fluid and window-clamping stresses produces the distorted optical figure shown. The 22.5-cm-diam by 1.0-cm-thick windows used in the assembly had an aspect ratio similar to that (22:5) anticipated for the 4.0-cm-thick window on the full-aperture arrays.

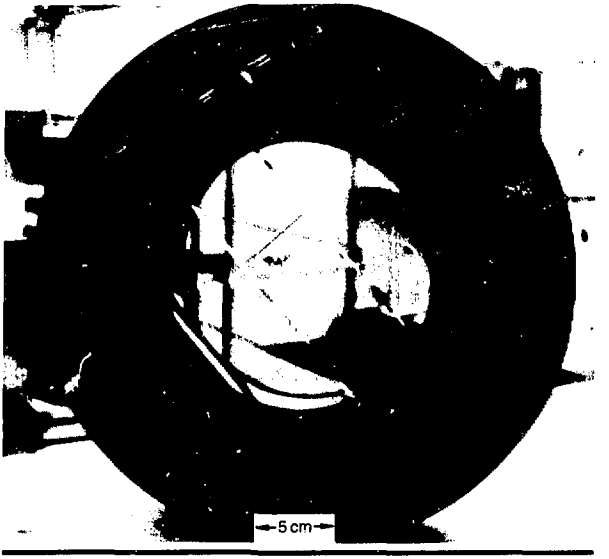

Fig. 7-11. Photograph of close-packed prototype array with 5- by 5-cm KDP segments stacked edge on edge.

Figures 7-12(c) and (d) are the corresponding interferograms with a slight (0.033 atm) vacuum applied to the fluid-filled center section of the array. With the vacuum, a substantial improvement in the wavefront resulted. Improved window-mounting techniques and a modified egg-crate support with better flatness, all presently in progress, are expected to result in further improvements in these wavefront figures.

Figure 7-13(a) is the interferogram for the close-packed array at 1 atm. It shows clamping and hydrostatic-loading stresses similar to those observed for the egg-crate array. With a slightly higher (0.1 atm) vacuum applied, we again observed a substantially improved optical figure, as illustrated in Figs. 7-13(b) and (c). As in the egg-crate case, modified window-mounting techniques are expected to improve the optical figure. Phase jumps observable between

some of the segments appear as discontinuities in the fringe pattern. These jumps arise from crystal-thickness variations and are partially responsible for the diffraction effects discussed below in conjunction with Figs. 7-14 and 7-15.

Near-Field Beam Quality. Figures 7-14 and 7-15 are near-field photographs of the 12.6-cm-diam second-harmonic output beams from the egg-crate and close-packed prototype arrays. These photographs show that all of the segments are sufficiently aligned to produce 2ω outputs and that the arrays are behaving, to a first approximation, as single crystals. Photographs taken at high power (1.2 GW/cm^2) and low power (100 MW/cm^2) exhibited similar characteristics.

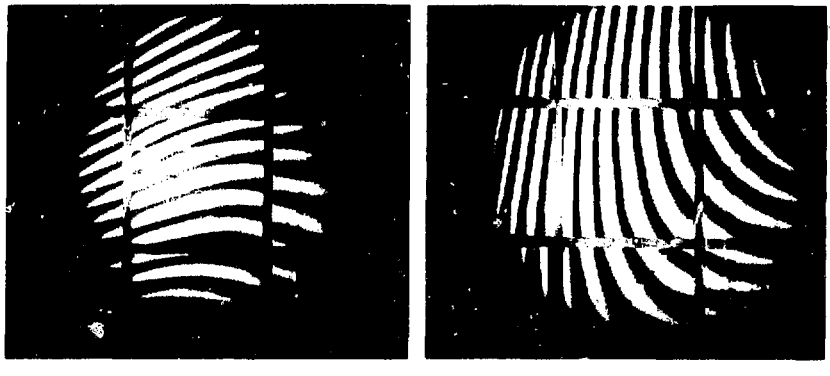

Fig. 7-12. (a) and (b) Transmitted wavefront (0.633 μm, double-pass) of the egg-crate array at 1 atm. (c) and (d) Corresponding interferograms with 0.033-atm vacuum applied to the array interior.

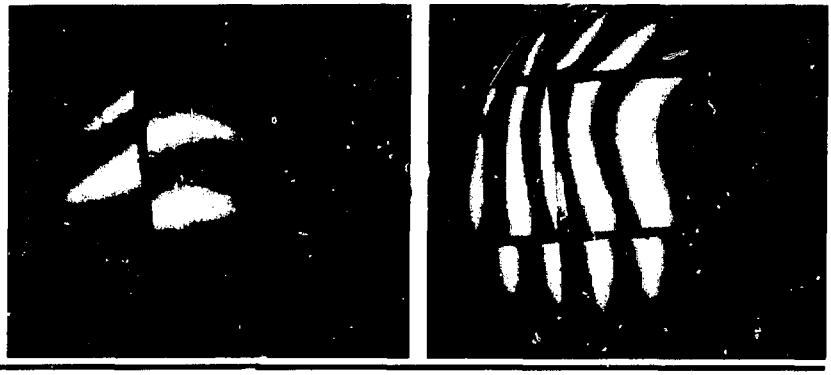

Fig. 7-13. Transmitted wavefronts (0.633 μm, double-pass) of close-packed array with different pressures applied to the array interior. (a) At 1 atm. (b) and (c) At 0.1 atm.

The small irregularities observable near the edges of the middle-crystal segment in Fig. 7-14 were generated when a reflection from the camera-filter glass was inadvertently back-reflected onto the metal egg-crate bar. The relative uniformity of the beam from segment to segment in Fig. 7-15 confirms that all these crystals were accurately aligned and participating equally in the conversion process. The qualitative differences in the gap diffraction patterns arise from differing phase jumps between crystals. A smeared outline indicates a close match in phase; a strong, dark band in the gap region indicates a substantial phase change.

Calibrated microdensitometer scans of these near-field photographs showed that diffraction ripples with approximately 2:1 peak-to-average intensity ratios were generated from the crystal gap regions in both test arrays. Diffraction effects resulting from amplitude and phase discontinuities in the gap region will require apodization of the input beam in the gap region to restrict ripple amplitude and spatial frequency to acceptable levels.

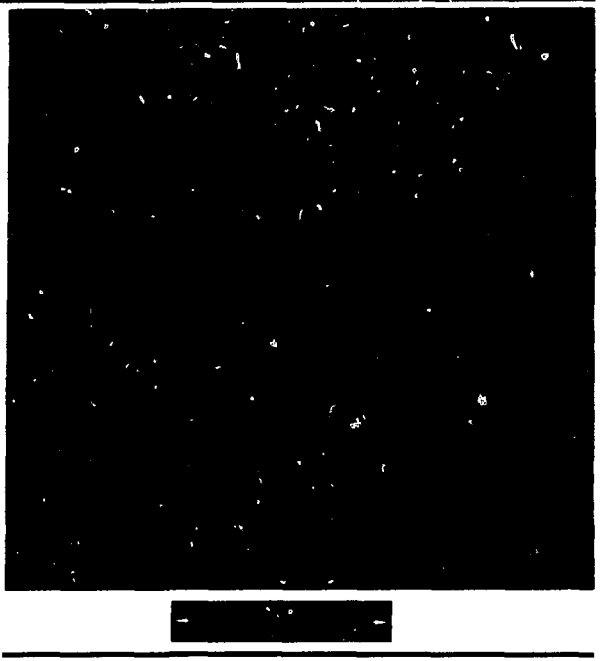

Fig. 7-14. Near-field photograph of 2ω output beam from egg-crate prototype array.

Crystal-Mounting Stress. To evaluate the extent of strain birefringence resulting from mounting stresses that might be present in crystal segments, we examined both arrays in an optical polariscope. As hoped, the egg-crate array exhibited no measurable strain-induced birefringence in any of the segments, indicating that the egg-crate matrix had effectively held the crystals in a strain-free condition.

The close-packed array segments did exhibit observable local-strain effects. Local strains occurred on a few crystal corners and edges. Their magnitude, from 2 to 5 nm/cm, and limited spatial extent were not sufficient to adversely affect conversion efficiency (as borne out by the Argus experiments). However, strain effects point out the potential risk of crystal breakage in the close-packed array should local strains become too large. In our case, local strains remained below material-strain limits of KDP, but will have to be carefully considered for the large-aperture array.

Apodization. Diffraction fringes from the egg-crate and close-packed arrays and from the egg-crate support structure produce undesirable modulation on the harmonically converted beams. After undergoing nonlinear intensification in the subsequent target-focusing optics, the modulation of the beam can significantly reduce the focusability of the beam and raise peak optical intensities above the damage threshold for coated optics.

Our solution to this problem has been to design a "soft apodization" mask. By generating phase-scrambling optically diffuse stripes that are specifically contoured, the crystal interstices are masked on the windows themselves. Theoretical simulations (using codes assuming that the diffuse stripes randomize the phases of the scattered light over a scale length that is small in comparison with stripe width) have given us insights regarding optimum contour shapes of the strip boundaries.

As shown in Fig. 7-16(a), for a sufficiently soft boundary, the diffraction-induced fringes almost entirely disappear. Fringes reappear in Fig. 7-16(b) when a more abrupt boundary is generated. Both the theoretical simulations and diffraction experiments agree that it is the contour and scale length

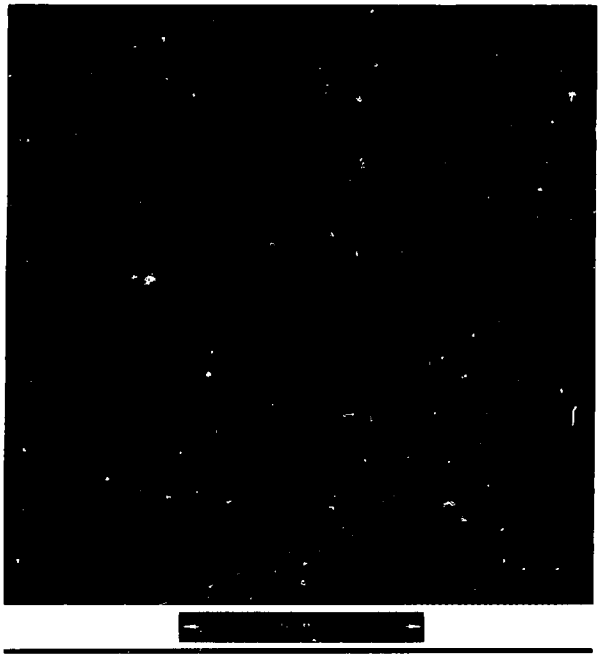

Fig. 7-15. Near-field photograph of 2ω output beam from close-packed prototype array.

of the diffuse boundary that determines the magnitude of resulting diffraction fringes.

A series of experimental measurements has confirmed the accuracy of our theoretical simulations with regard to both diffraction-fringe visibility and the phase randomization of the diffracted waves. Our experimental measurements included

- Apodization characteristics of the boundary contours that produce minimal fringes.
- Evaluation of near-field and far-field diffraction phenomena as functions of apodizer boundary contour.
- Optical-damage thresholds of the stripes at 1.06 μm and fluences of $\leq 10\ J/cm^2$ in a 1-ns pulse.
- Testing and evaluation of appropriate techniques (acid etching, grinding, and bead blasting) to generate contoured diffuse stripes on optical substrates.

Tests of a suitably contoured soft strip proved that the technique was capable of suppressing the very strong diffraction fringes originating from a wire crosshair placed in the probe laser beam. As a consequence of our work on soft apodization of harmonic crystal arrays, we anticipate that the optical performance of the resulting large-aperture harmonic-conversion crystal array for Nova and Novette will be comparable to that of a monolithic KDP crystal, less any obscuration losses produced by the apodized intercrystalline gaps.

Authors: D. Eimerl, M. A. Summers, B. C. Johnson, J. D. Williams, and G. J. Linford

Major Contributors: R. L. Combs, F. T. Marchi, J. E. Murray, S. Warshaw, and B. W. Woods

Damage Studies

Introduction. The primary responsibility of the laser-damage group is to provide components with damage resistance adequate to allow for successful operation of

- The Nova laser.
- The KDP crystal array needed for generation of 2ω and 3ω from the fundamental (1ω) Nova output.
- Lenses and windows needed to deliver beams of all three frequencies to fusion targets.

To meet our responsibilities, we studied damage induced by 1ω, 2ω, and 3ω laser pulses. We continued to operate the 0.248-μm KrF laser-damage experiment and to complete 0.248-μm experiments that were started in 1980 because results of 0.248-μm experiments are instructive in the section of materials for use at 3ω.

At 1ω, a major improvement was made in AR films. In collaboration with Schott Optical Glass, Inc. (Duryea, Pa.), we found that neutral-solution processing[2,3] of common borosilicate (BK) glasses produced AR surfaces whose damage thresholds[4] were more than twice the thresholds of conventional vacuum-deposited AR films. Application of neutral-solution processing to laser optics was remarkably straightforward. We treated 20-cm-diam lenses without loss of surface figure and successfully used a prototype lens on the Shiva laser. BK glasses treated by neutral-solution processing should provide damage-resistant transmissive components for both 1ω and 2ω frequencies of Nd:glass lasers.

Unfortunately, most BK glasses exhibit linear or nonlinear absorption of intense 3ω beams. Such absorption might, however, be acceptably low in thin layers of glass. Thus,

we tested two types of graded-index AR films etched into glass layers that had been deposited on silica substrates from liquid[5-9] solutions. Layers of lead silicate glass were fabricated and etched by Owens-Illinois, Inc.; several multicomponent BK layers were prepared[10] and etched by Battelle Laboratories (Columbus, Ohio).

At 1ω, damage thresholds of the etched-glass layers on silica were comparable to damage thresholds of etched surfaces on bulk-phase-separated glass. At 3ω, thresholds of the glass surface layers were one to three times greater than thresholds of electron-beam-deposited AR films. Therefore, use of glass layers deposited from liquids appears to be a promising technique for producing damage-resistant 3ω transmissive optics, although much more developmental work remains to be done.

We continued our study[11] of damage in KDP, which is the only harmonic-generation material presently available in the sizes needed for Nova. After numerous KDP crystals have been tested, the inclusions that cause internal damage remain unidentified. However, we have found[12] that the damage resistance of the crystals can be increased by subjecting them to repeated low-fluence laser irradiation. Damage thresholds of laser-hardened crystals should satisfy Nova requirements.

We operated the ILS laser throughout the year as a source of 3ω pulses, and, in September, we also converted the Cyclops laser to 3ω. Most of our time on these lasers was spent in studies of nonlinear absorption in glasses and index-matching liquids and in initial measurements of nonlinear refractive indexes at 3ω. A few damage measurements were made to improve 3ω thresholds. In general, at 3ω and 0.6 ns, thresholds of conventional reflective and antireflective coatings remained at 2 to 3 J/cm^2 throughout the year.

We continued to operate the KrF laser-damage experiment.[13] Thresholds for approximately 100 coatings from 11 vendors were measured[14] to establish baseline thresholds at 0.248 μm and 20 ns. A major study[15] showed that scandium oxide is an attractive high-index component for 0.248-μm films. Numerous coating materials are being tested at 0.248 μm, and those that show promise of UV-compatibility will be evaluated at 0.355 μm.

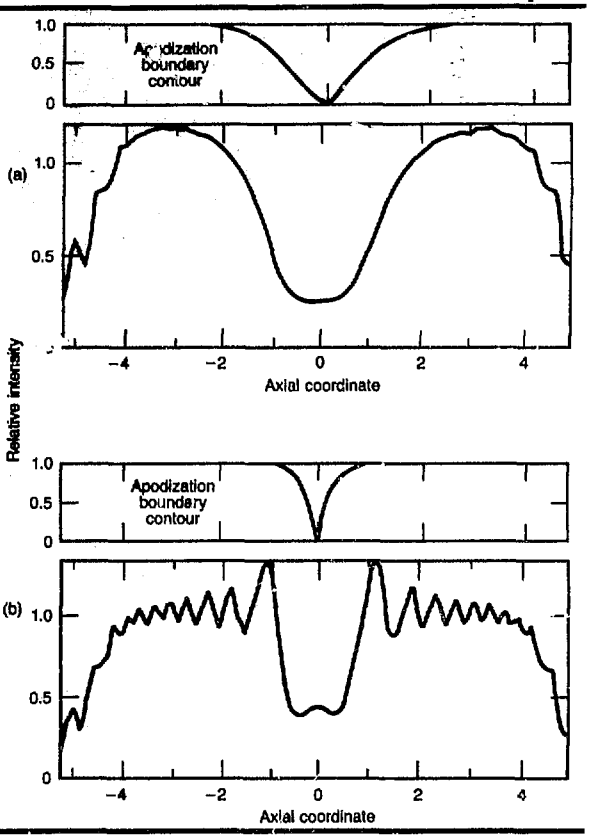

Fig. 7-16. Apodization effects on near-field intensity profiles. (a) A gradual (soft) transmission contour. (b) A sharper (hard) gradient contour.

Neutral-Solution Processing of AR Films. Schott Optical Glass, Inc., developed a neutral-solution-processing procedure wherein AR films are formed on polished-glass surfaces on homogeneous BK glasses.[2,3] The glasses are immersed in a solution that leaches some constituents from the glass to form a low-index microporous layer. Some gradation of the refractive index in the altered-surface layer is provided through partial etching, which increases the size of those pores formed nearest the glass boundary. Thickness of the microporous layer depends upon duration of immersion.

We studied[4] AR surfaces formed by immersing BK-10 and BK-7 in a solution of 0.034 M $NaHAsO_4$ and 1.3 × 10^{-3} M Al^{+3} in distilled water at 87°C. Surface reflectivity (%) as a function of wavelength for a BK-7 sample leached for 39 h is shown in Fig. 7-17. The reflectivity spectrum is similar to that exhibited by a surface bearing a

homogeneous low-index layer with an optical thickness of $d = 0.250\ \mu m$. For the homogeneous layer, reflectivity minima occur at wavelength λ such that $m\lambda/4 = d$. A maximum, where reflectivity equals that of the bare substrate, occurs at $\lambda = 2d$. For the neutral-solution-processed surface, which was designed to produce minimum reflectance at $\lambda = 1.06\ \mu m$, there was a second minima at $\lambda \cong 0.35\ \mu m$ and a maximum at $\lambda \cong 0.53\ \mu m$. However, at the maximum, the reflectivity was much less than that of the untreated substrate. The reduction of reflectivity at the maximum demonstrates the partial gradation of index in the low-index layer formed by neutral-solution processing. Gradation of index causes a reduction of reflection that is independent of wavelength.

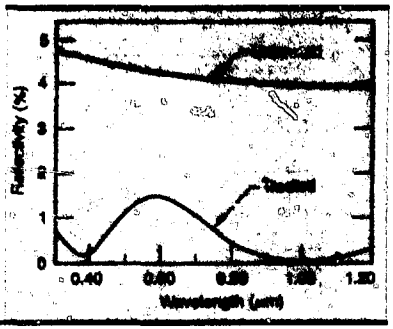

Fig. 7-17. Reflectance spectrum of BK-10 glass before and after neutral-solution processing.

Fig. 7-18. Laser damage thresholds for leached AR surfaces of BK-7 and BK-10 glass prepared by neutral-solution processing and for conventional multilayer AR coatings.

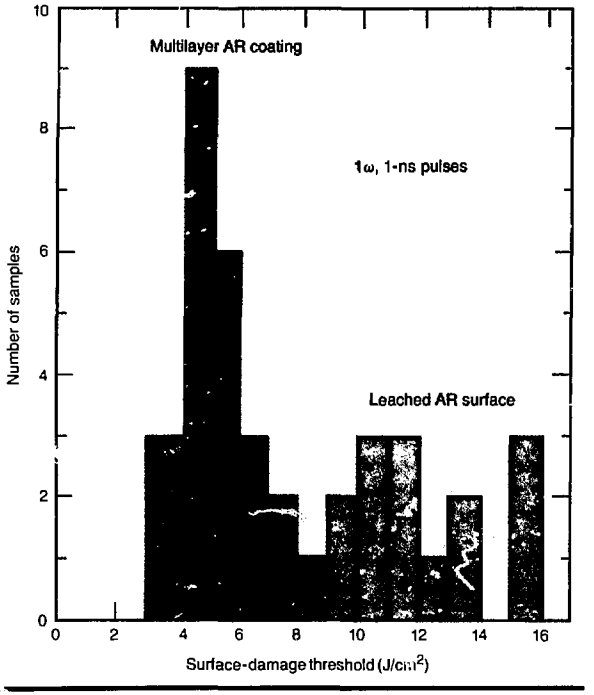

Figure 7-18 shows laser-damage thresholds (for 1ω, 1-ns pulses) of several BK-10 and BK-7 surfaces prepared by neutral-solution processing and of several conventional multilayer thin-film AR coatings prepared by electron-beam deposition. The median damage threshold for neutral-solution-processed surfaces is more than twice that for conventional films.

For two BK-7 surfaces prepared by neutral-solution processing, thresholds were measured with 1ω pulses having durations of 1, 3, 6, 9, or 20 ns. Each surface on each sample was tested twice, once as an entrance surface and once as an exit surface. The surface-damage thresholds measured in all four tests are shown in Fig. 7-19. Within experimental uncertainty, entrance and exit thresholds were equal at all pulse durations. Functional variation of threshold as the square root of pulse duration is illustrated by the agreement between the data and the square-root function (solid line) in Fig. 7-19.

The neutral-solution process was readily scaled to provide AR films on actual laser components. Whereas typical etching of glass in caustic acids proceeds rapidly and is difficult to control, the slow treatment of glass in an almost neutral solution is easily controllable. Films have been formed on components 20 cm in diameter without alteration of surface figure. A spatial-filter lens prepared by neutral-solution processing was used on the Shiva laser. The surfaces are more fragile than those coated with hard, multilayer oxide films but are more durable than etched surfaces of phase-separated glass and can be cleaned by conventional techniques.

We have recently determined that thresholds for surfaces prepared by neutral-solution processing can usually be increased by first irradiating the focal area at fluences below the single-shot-damage threshold. Study of this process is continuing to determine an optimum and reliable irradiation

procedure and the maximum threshold increase.

Sol-Gel Coatings. Layers of noncrystalline inorganic oxides can be deposited on glass surfaces by the sol-gel[5–9] process. The layers can be phase-separated and etched to produce AR surfaces similar to those formed by etching surfaces of bulk-phase-separated glasses.

The sol-gel process consists of polymerization of a viscous liquid sol of alkoxysilane with other metal alkoxides or metal salts in alcohol solutions to form a transparent elastic gel that can be applied to glass surfaces. Residual organic material is driven off by heating to leave a microporous layer. The pores can be eliminated, if desired, by further heating to form a glass-like material.

S. P. Mukherjee[10] of Battelle Laboratories prepared films of sodium borosilicate glasses on silica substrates, and Thomas Hahs of Owens–Illinois, Inc., prepared films of a lead borosilicate glass on both BK-7 and fused-silica substrates. Damage testing of some Owens–Illinois samples remains to be done. Figure 7-20 compares 1ω, 1-ns damage thresholds of 15 Battelle sol-gel films with thresholds of 23 conventional, multilayer thin-film AR films. The median threshold for sol-gel films is about four

Fig. 7-19. Damage thresholds of neutral-solution-processed BK-7 surfaces as a function of pulse duration.

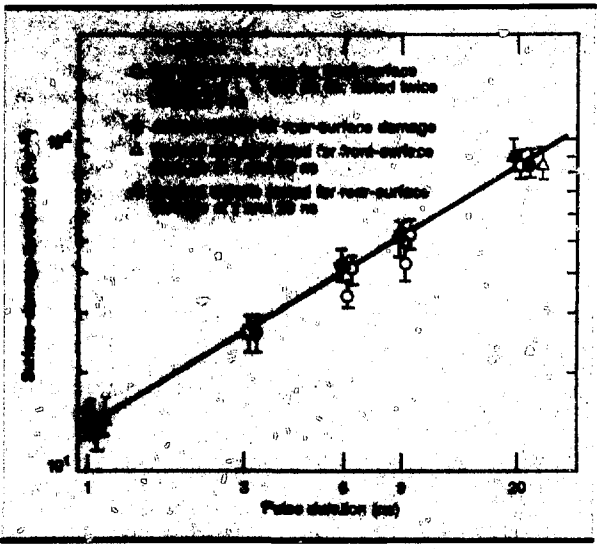

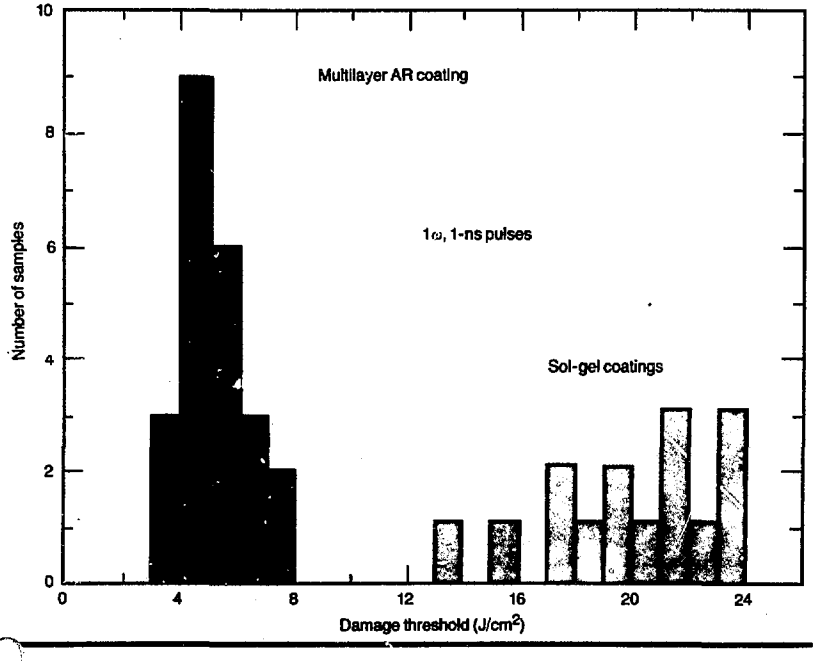

Fig. 7-20. Damage thresholds of sol-gel and conventional AR films.

times greater than the median threshold of conventional films.

The reflectivity of etched sol-gel films varied greatly both from site to site on a given sample and from sample to sample. Considerable developmental work will be required to produce uniform sol-gel coatings that are useful for laser applications. Nevertheless, sol-gel films are one of our most promising prospects for providing damage-resistant UV-compatible AR films.

KDP Crystals. When KDP crystals are irradiated by 1ω, 1-ns laser pulses of high fluence, isolated damage centers[11] are produced in the bulk of the crystal. We have tested[12] more than 100 crystals using our usual procedure of irradiating each focal volume only once (one-on-one tests). The crystals were grown by five manufacturers and were tested during an attempt to identify the source of inclusions that cause damage. A histogram of measured bulk-damage thresholds in Fig. 7-21 shows that the median damage threshold is 7 J/cm^2. No firm correlations between parameters of growth conditions and damage thresholds were found, and the inclusions remain unidentified.

Fig. 7-21. Histogram of one-on-one KDP bulk-damage thresholds measured with 1ω, 1-ns pulses.

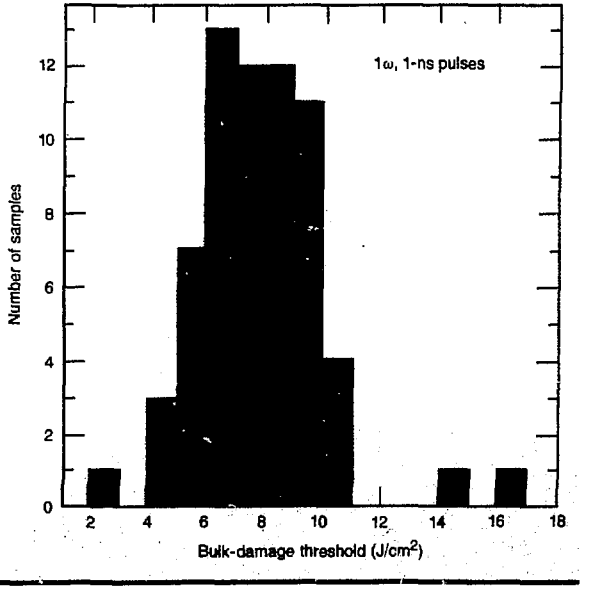

We did find that thresholds could be increased by baking the crystals and that damage resistance of a given focal volume could be increased by subjecting that focal volume to repeated laser irradiations (n-on-one experiments) at fluence levels below the one-on-one threshold.[12] The effects of baking and laser-hardening are somewhat cumulative, as shown by the histograms in Fig. 7-22. For these treatments, one-on-one thresholds are given for unbaked crystals [see Fig. 7-22(a)] and for subsets of the same crystals after baking in air for 24 to 96 h at three temperatures [see Figs. 7-22(b), (c), and (d)]. Figure 7-22 also gives n-on-one thresholds measured on a few sites of each crystal. The process of baking at 140° or 165°C followed by laser hardening produced crystals with thresholds greater than those obtained by other baking and irradiation sequences.

At 1ω, measurements of bulk-damage thresholds for two crystals (see Fig. 7-23) demonstrated that laser-hardening of thresholds occurs at all pulse durations between 1 and 20 ns.

We also measured the bulk-damage thresholds of three KDP crystals at wavelengths other than 1ω. One crystal was damaged at 1ω and 2ω. Two other crystals were tested at 1ω and 3ω. Damage thresholds were the same at 1ω and 2ω and were 25% lower at 3ω than at 1ω. Laser hardening at wavelengths other than 1ω has not been attempted.

We recommend, therefore, that KDP crystals be baked for 24 h or more at 140°C. The baking temperature must be well below 180°C to avoid a phase change that ruins the KDP crystal. Irradiation should begin with a sequence of low-fluence-level laser pulses (less than 3 J/cm^2 at 1.0 ns) that eventually increases to the desired operating fluence.

Damage Studies at 0.355 and 0.248 μm. To support development of fusion lasers operating at frequencies less than 1ω, we continued to upgrade the KrF facility[13] for testing with 0.248-μm, 20-ns pulses and to use the *ILS* facility[13] for testing with 0.355-μm, 0.6-ns pulses. Thresholds were measured for a large number of highly reflective (HR), antireflective, and single-layer films; for oxide films deposited from

liquids, and surfaces prepared by neutral-solution processing; and for bare, polished surfaces of UV-compatible solids.

At 0.248 μm, we tested[14,15] numerous HR and AR samples supplied by 11 commercial and research institutions. Test results are illustrated in Figs. 7-24 and 7-25 and are summarized in Table 7-2. Thresholds for both HR and AR coatings exhibited similar trends. The commercial samples, many of which had been used on LLNL lasers for several years, had generally low thresholds; only a few exceeded our goal of 5 J/cm^2. Research samples that were produced to improve thresholds had varied quality. HR films made by sputtering had low thresholds. In an extensive study[15] to evaluate use of scandium oxide as a high-index film, we found that Sc_2O_3/MgF_2 HR films with MgF_2 overcoats and Sc_2O_3/SiO_2 AR films with SiO_2 undercoats had thresholds that consistently exceeded 5 J/cm^2.

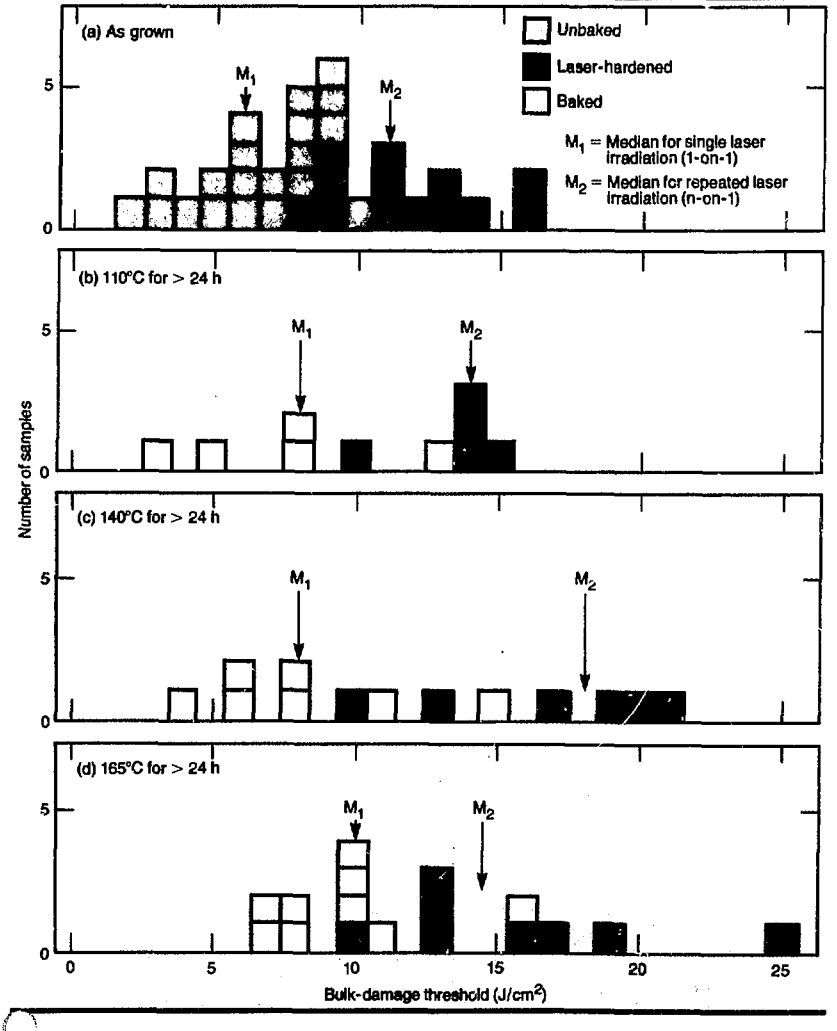

Fig. 7-22. Histograms of bulk-damage thresholds with 1ω, 1-ns pulses for unbaked and baked KDP crystals given single or repeated laser irradiation.

We also used 0.248-μm, 20-ns pulses to measure surface and bulk thresholds for several UV-transmitting glasses and crystals. Lithium fluoride, in its crystalline form or in a multicrystalline form obtained by hot-press forging, had bulk and surface thresholds exceeding 20 J/cm^2. Fused silica had good bulk-damage resistance, but its surface-damage threshold appeared to be highly dependent upon the polishing procedure. Use of cerium oxide polishing compounds may produce surfaces that are highly absorptive at 0.248 μm.

Fig. 7-23. *Dependence of one-on-one and n-on-one bulk-damage thresholds on pulse duration for KDP crystals.*

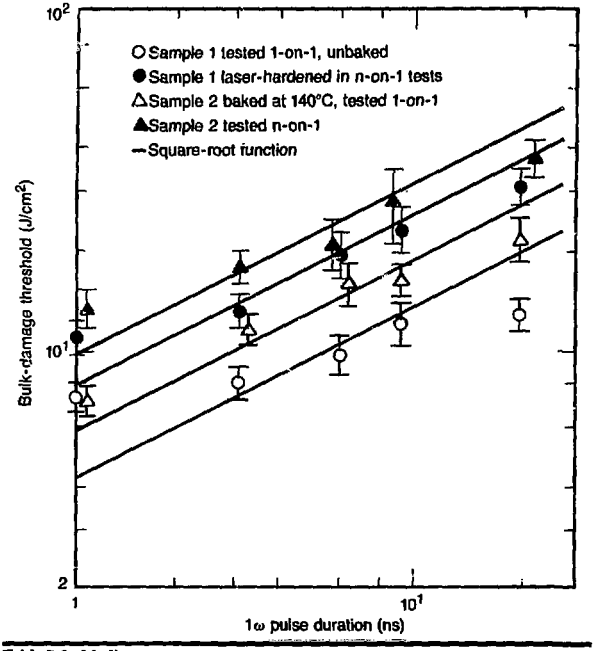

Table 7-2. Median laser-damage thresholds of thin-film optical coatings at 0.248 μm and 20 ns.

Sample type	HR threshold (J/cm^2)	HR number tested	AR threshold (J/cm^2)	AR number tested
Commercial	1.8	20	3.3	19
Sputter deposited	1.8	12	—	—
E-beam deposited				
nonoverstressed HR	3.1	15	—	—
nonoverstressed AR	—	—	4.2	8
E-beam deposited				
overstressed HR	4.5	10	—	—
overstressed AR	—	—	5.4	16

Films and surfaces of several types were tested with 0.355-μm, 0.6-ns pulses. AR films consisting of SiO_2 in combination with ZrO_2, HfO_2, Ta_2O_5, or Sc_2O_3 had thresholds near 2.5 J/cm^2, while HR films made with the same materials were damaged at 3 J/cm^2. AR films formed on BK-10 by neutral-solution processing had thresholds exceeding 6 J/cm^2. Thresholds from 2 to 6 J/cm^2 were measured on graded-index AR surfaces etched into glass layers, which were deposited on fused-silica substrates from liquid solutions. We found that the bulk-damage thresholds of KDP crystals were 6 to 7 J/cm^2, or about 30% less than the thresholds measured on the same crystals with 1ω, 1.0-ns pulses.

Authors: D. Milam, W. H. Lowdermilk, F. Rainer, and J. E. Swain

***Major Contributors:* S. E. Peluso, S. E. Stokowski, and M. C. Staggs**

Optical Materials Research

Introduction. The physical and spectroscopic properties of optical materials used in fusion lasers limit performance and determine operating conditions. Therefore, our program continues to (1) quantify parameters of optical materials for the laser designer and (2) determine the fundamental limitations of materials for high-power lasers. The latter research, which is broader in scope and of a long-range nature, is supported by the Division of Materials Sciences of the DOE Office of Basic Energy Sciences (OBES).

Specifically, our projects include

- Studies of fusion-laser materials.
- OBES-supported research on optical materials.
- OBES-supported experiments on laser-excited fluorescence in amorphous solids.

Our two OBES programs and the program on "Damage Studies," above, complement the activities of the Fusion Laser Research and Development program element by exploring phenomena that are basic for developing improved optical materials.

During 1981, we concentrated on questions about optical materials for Nova and Novette and extended our studies of

features that are of importance for future fusion lasers. In both instances, the materials issues arose from the use of wavelengths shorter than 1ω, efforts to increase overall lasing efficiency, and the consequences of higher output power. For example, large arrays of nonlinear crystals used as harmonic generators for Nd:glass fusion lasers require low-loss index-matching fluids. Fluids suitable for Nova and Novette operation have now been successfully identified.

As the laser wavelength approaches one-half the fundamental band-gap energy of a transmitting material, two-photon absorption and two-photon-induced solarization become energetically possible. We quantified absorption and solarization losses in numerous optical materials under both the Fusion Laser Research and Development and the OBES programs.

Another consequence of shorter wavelengths is the increase in the nonlinear refractive-index coefficient, n_2. To measure the wavelength dispersion of n_2, we considered the use of interferometric techniques (similar to those we used previously) and sensitive photorefractive techniques (of interest for studies on multiphoton-absorption processes). We demonstrated that time-integrated fringe shifts recorded with a vidicon yield results comparable to those obtained with time-resolved fringe shifts. Therefore, several possible approaches for measuring n_2 are now available.

Efficient operation of large glass lasers requires extracting a significant fraction of the stored energy, and questions of saturation fluence and hole burning become increasingly important. Our measurements of the saturated gain for a number of Nd-doped phosphate glasses of interest for Nova show that phosphate glasses behave more homogeneously than other glasses we have studied. In addition, we have shown that a distribution of stimulated-emission cross sections exists not only because of spectral inhomogeneities but also because of spatial anisotropy and the random orientation of different laser ion sites in glass. Polarization dependence of hole burning and estimates of its effect on energy extraction can be determined from laser-induced fluorescence-line-narrowing (FLN) experiments using polarized light. Therefore, we now have procedures for surveying and quantifying the relative saturation behavior of different laser glasses.

The threshold for laser action and the rate of stimulated emission are governed by the associated cross sections. Our

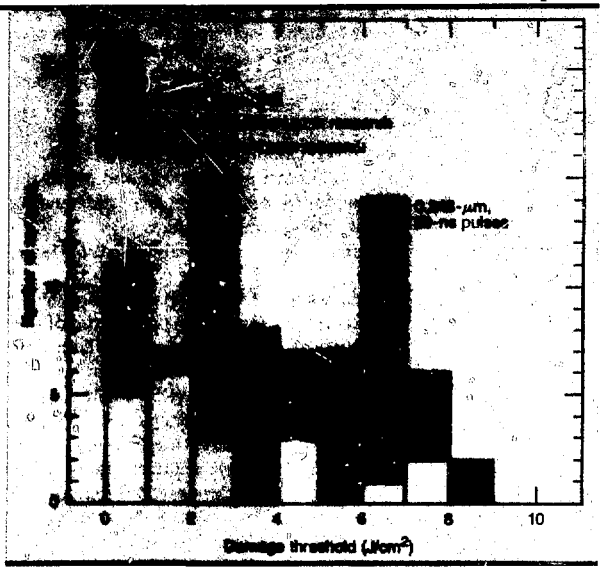

Fig. 7-24. Laser-damage thresholds of HR films.

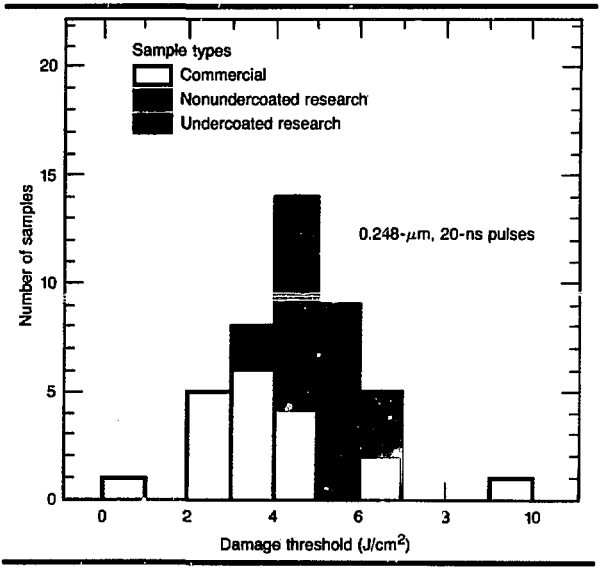

Fig. 7-25. Laser-damage thresholds of AR films.

examination of spectroscopic properties of Nd-doped glass compositions now spans most of the periodic table and includes both oxide and halide glasses. Therefore, we have now extended our ability to predict bounds on stimulated-emission cross sections and other spectroscopic and physical properties to include inorganic oxide and halide glass-forming systems.

Although our empirical data base is large, a detailed understanding of the lasing characteristics of ions in glass requires a knowledge of the microscopic nature of the local fields and interactions at the laser ion site. Our previous work has shown how the structure at a rare-earth (RE) site in glass can be successfully simulated using Monte Carlo and molecular-dynamics methods. Using simple models of the crystal field, we find that many of the observed compositional variations in spectroscopic properties can be predicted from simulated structures.

With computer simulations, we discovered defect structures with unusual and time-dependent ion coordination numbers. These numbers may be associated with anomalies in the low-temperature properties and optical line widths in glasses reported during the past decade and attributed to the existence of different equilibrium ion configurations. We have, therefore, examined the effects of ligand motion on optical line widths and ion diffusion in glass based on computer simulations of simple fluoride glasses.

To round out our investigations of laser glass, we have compared infrared and Raman spectra with vibronic spectra of RE ions and determined the relative value of different spectroscopies for studies of vibrations in glass.

Our data on spectroscopic and physical properties of Nd-doped glasses, amassed prior to 1981, have been condensed and distributed in the form of a handbook.[16] During 1981, we prepared a second set of additions to this volume and completely updated the indexes and all summary tables and figures. In addition, data on Faraday rotator materials, which were also the subject of earlier studies, have now been accumulated in a new handbook.[17] Both handbooks have been distributed to workers in the areas of lasers and optical materials.

Author: M. J. Weber

Two-Photon Absorption and Solarization in UV Glasses. In 1981, we investigated nonlinear absorption and solarization in optical glasses that are of potential use in the UV region. By solarization, we mean an increase in the linear absorption coefficient, α, as a result of prior exposure to optical radiation. Attenuation of an optical pulse of intensity $I(r,z,t)$ as it propagates through a material is described by the relation

$$\frac{dI}{dz} = -(\alpha + \beta I + s_1 + s_2)\, I \quad , \tag{2}$$

where α and β are the one- and two-photon absorption coefficients, and s_1 and s_2 describe one- and two-photon-induced solarization, respectively. Hence, s_1 and s_2 are of the time-integral forms

$$s_1(t) \equiv c_1 \int_{-\infty}^{t} I(t)dt \quad , \tag{3}$$

and

$$s_2(t) \equiv c_2 \int_{-\infty}^{t} I^2(t)\, dt \quad , \tag{4}$$

where we have ignored the decay of absorption terms by recombination. At room temperature, we have found the solarization in borosilicate glasses to be permanent; however, after a few hours at elevated temperature (>350°C), transparency can generally be recovered.

Our experiments are concerned with measuring the transmission, T, of a laser pulse of known intensity through a nonlinear absorber of length L, where

$$T = \frac{\int_{-\infty}^{\infty} dt \int_0^{\infty} 2\pi r dr\, I(r,L,t)}{\int_{-\infty}^{\infty} dt \int_0^{\infty} 2\pi r dr\, I(r,0,t)} \quad . \tag{5}$$

Ignoring solarization terms and multiple reflections, the solution to Eq. (2) has been used to evaluate T for four different

spatio-temporal intensity profiles, and the results are collected in Table 7-3. The nonlinear component of the transmission is characterized by the parameter Q, defined in Table 7-3. These solutions are plotted in Fig. 7-26 for an arbitrary set of parameters α, β, and L.

At any intensity, the Gaussian–Gaussian pulse (Gaussian in space and time) exhibits the least nonlinear loss. Because the flat-square (flat in space, square in time) pulse exhibits the most nonlinear loss, it is preferred for measurements of nonlinear absorption.

In 1981, we investigated nonlinear absorption using both Gaussian–Gaussian and flat–square pulses. Due to laser availability, we used Gaussian–Gaussian pulses from the ILS laser. Our study was completed in 1981 and is discussed below. Later we used flat–square pulses from the Cyclops laser for a refined measurement series that focused on solarization behavior.

Figure 7-27 illustrates the apparatus we used in early 1981. We frequency-tripled the single 1ω pulses of smooth spatial shape from the Nd:YAG glass ILS laser. At 3ω, the 0.60-ns pulses of up to 200 mJ were separated from the parent pulses by dichroic mirrors. The pulses were then collimated to a $1/e$-diameter of approximately 1.3 mm to generate intensities up to 25 GW/cm^2. A linearized, calibrated Si vidicon, associated computer equipment, and an absorbing-glass calorimeter were used to measure the peak intensity of each pulse with an absolute accuracy of ±25% or better. The transmission of each pulse through a sample was measured with an accuracy better than ±3% using linear vacuum photodiodes. The results from our computer-code solutions for transmission vs incident intensity were then used to extract the nonlinear transmission coefficient from the data.

Relevant features of the samples are presented in Table 7-4. Four borosilicate glasses were tested, two of which (BK-10, and BK-10* solarization-resistant) were designed for use in the UV region. The fluorophosphate (FK-54) sample showed general immunity to nonlinear loss, but, because linear transmission in the UV region of our sample was poor, we defer discussion of FK-54 until better samples are tested.

Figure 7-28 shows measured transmission vs input intensity for the BK-10 sample. A yellow-brown track of color-centers, the spectrum of which is shown in Fig. 7-29, was generated in the sample by these pulses. The solarization was, in general, removable by overnight annealing in air at ~350°C. Quantitative investigation of

		Transmission from Eq. (5)
Space	Time	$= T_{\text{lin}} \sum_{n=1}^{\infty} (-Q)^{n-1} n^{-3/2}$, for $Q < 1$
Gaussian	Gaussian	$T_{\text{lin}} \frac{2}{\sqrt{\pi}\, Q} \int_0^{\infty} \ln\left[1 + Qe^{-x^2}\right] dx$
Flat	Gaussian	$T_{\text{lin}} \frac{1}{\sqrt{\pi}} \int_{-\infty}^{\infty} \frac{e^{-x^2}}{\left[1 + Qe^{-x^2}\right]} dx$
Gaussian	Square	$T_{\text{lin}} \frac{\ln(1+Q)}{Q}$
Flat	Square	$T_{\text{lin}} \frac{1}{1+Q}$

Table 7-3. Transmission through a one- and two-photon absorber where $T_{\text{lin}} = (1-R)^2 e^{-l}$ **and** $Q = \frac{\beta(1-R)I(1-e^{-l})}{\alpha}$.

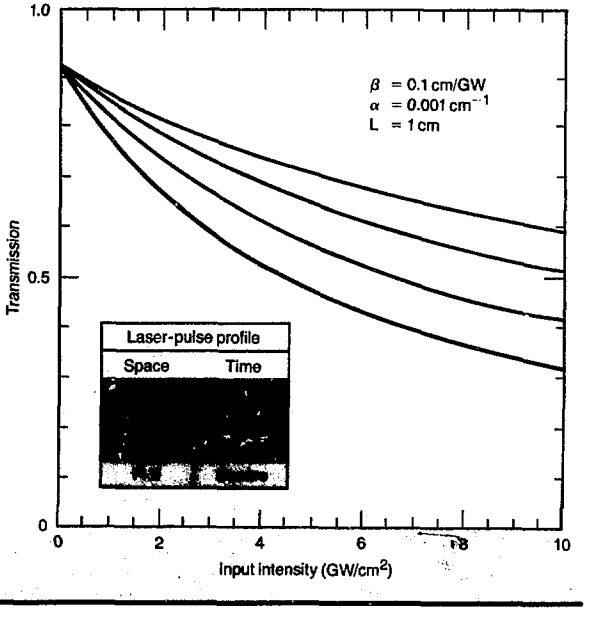

Fig. 7-26. Transmission of laser pulses through a one- and two-photon absorber for four laser-pulse profiles.

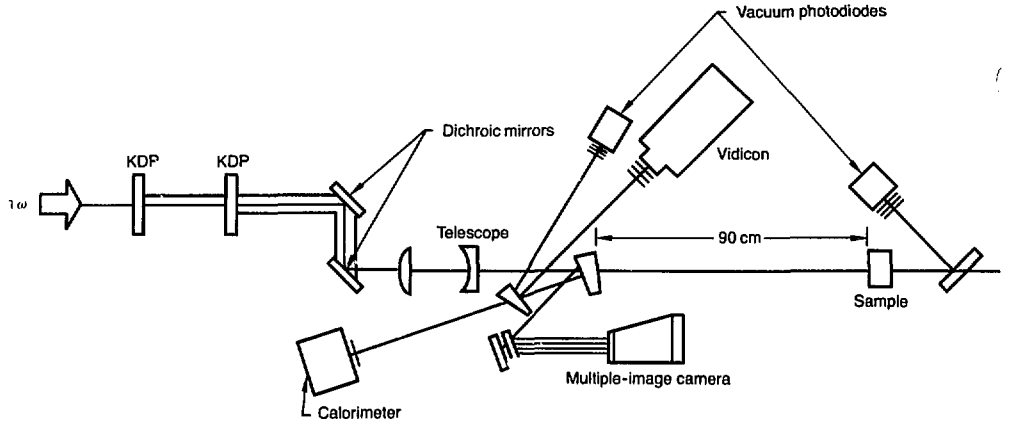

Fig. 7-27. Apparatus for measuring the two-photon absorption coefficient at 3ω.

Table 7-4. Two-photon absorption samples.

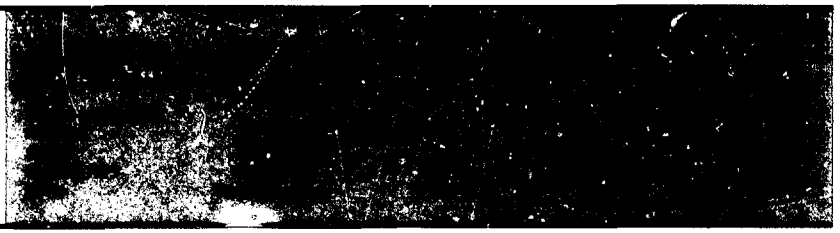

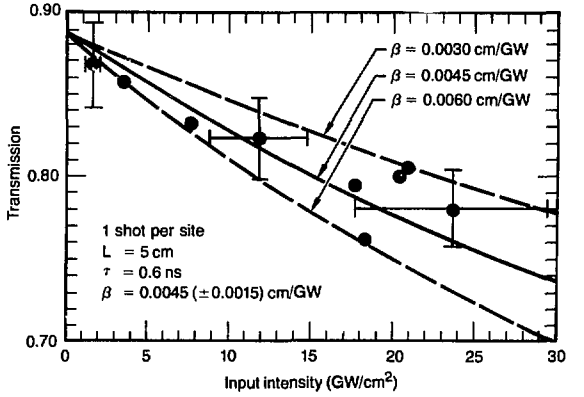

Fig. 7-28. Transmission vs input intensity at 3ω for BK-10 glass.

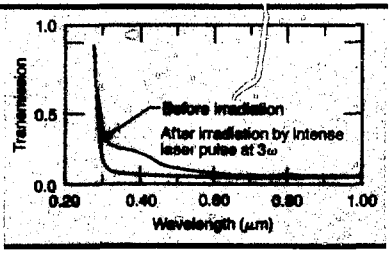

Fig. 7-29. Spectra of laser-induced coloration (solarization) in BK-10 glass.

annealing effectiveness will be part of our later tests.

Figure 7-30 shows the performance of fused silica. The minimal apparent drop in transmission in this 10-cm-long sample is smaller than the uncertainty in the data, allowing us to ascribe only an upper bound for β in this material. The upper bound ($\beta \leq 0.0005$ cm/GW) measured in our work is 2.5 times smaller than that published by Liu et al.[18] The small value of β underscores the suitability of silica for high-intensity UV-laser applications.

The results for β along with UV-edge ($0.1\ cm^{-1}$) positions are shown in Table 7-5. In all materials except silica, the two-photon energy (6.99 eV) exceeds the UV edge, and two-photon absorption is energetically expected. However, the magnitude of β in these glasses is typically less than one one-hundredth of that[18] in small-band-gap alkali-halide crystals, such as KI (5.2 eV), RbI (5.0 eV), or RbBr (5.4 eV), and from two to four times less than that[18] in KDP and its family of isomorphs. Such comparisons of β present a challenge to band-structure theory of crystalline and amorphous solids.

Figure 7-31 shows calculated transmission based on the measured β of 0.0045 cm/GW through different lengths of BK-10 glass for two laser-pulse types. The nonlinear absorption strength, though smaller than expected, is still not favorable for the use of these glasses in high-intensity UV-laser applications.

Thus far, all discussion has concerned data taken with one shot per sample site. Figure 7-32 shows the transmission on 22 sequentially numbered shots through the same site in a solarization-resistant BK-10 sample. Also shown in Fig. 7-32, for purposes of comparison, is the experimentally determined transmission as a function of intensity for one shot per site (β = 0.010 cm/GW). After several shots at ~2.0 GW/cm^2, input intensity was reduced to ~0.6 GW/cm^2, and transmission did not return to its initial value. This effect is two-photon absorption induced solarization, described earlier in Eq. (2) with the term s_2. The effect may pose as restrictive a limitation for the UV utility of these glasses as the magnitude of β itself. Therefore, we are beginning an investigation that will measure two-photon absorption-induced solarization with more precision.

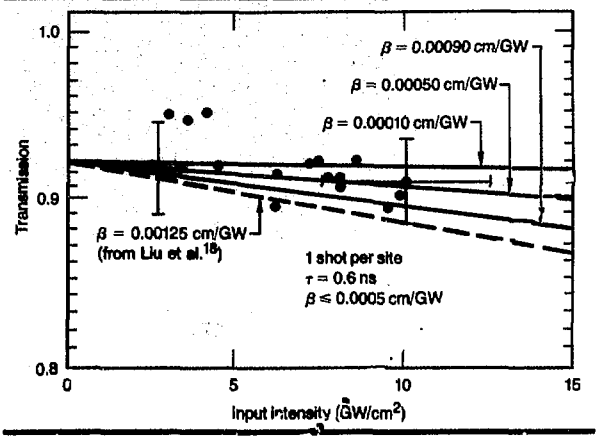

Fig. 7-30. Transmission vs input intensity at 3ω for 10-cm fused-silica glass.

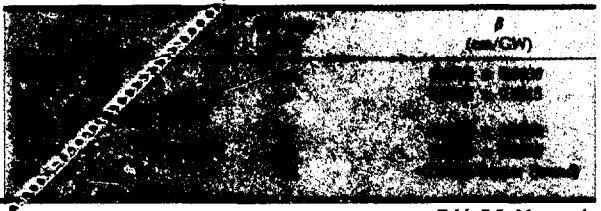

Table 7-5. Measured two-photon absorption coefficients at 3ω.

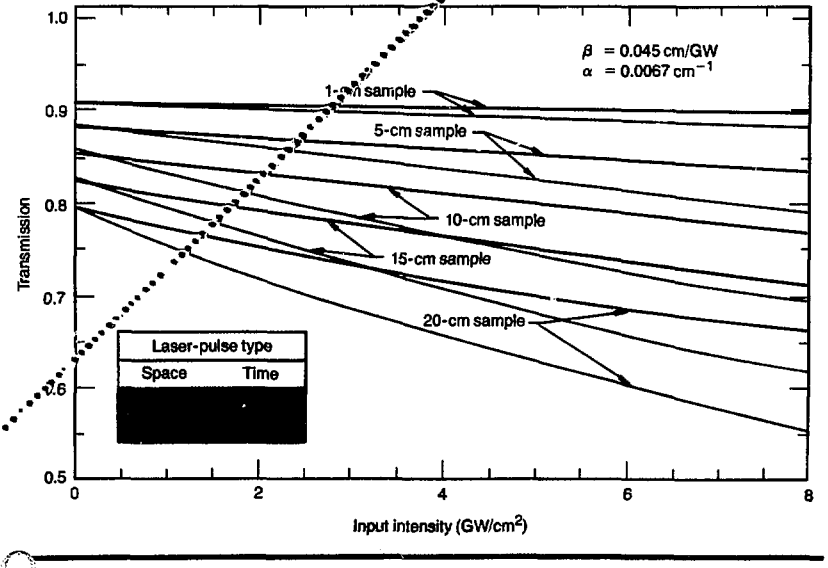

Fig. 7-31. Transmission vs input intensity for BK-10 glass samples of five different lengths.

Gain Saturation in Nd:Doped Laser Glass. We completed[19] measurements of saturation fluence in seven Nd:doped phosphate laser glasses and in one sample of Nd:doped fluoroberyllate glass. Properties of the glasses are summarized in Table 7-6. Saturation of gain was observed while amplifying well-characterized 1.053-μm pulses with durations of either 1.4 or 20 ns. For each shot, we measured the fluence into the test amplifier, E_{in}, the output fluence, E_{out}, and the small-signal gain G_0. Saturation fluence, E_s, was then computed from these data by numerical integrations from the relation[20]

$$\ln G_0 = \int_{E_{out}}^{E_{in}} \frac{dE}{E_s\left[1 - e^{-E/E_s}\right] - \delta E/\alpha_0} , \quad (6)$$

where α_0 is the gain coefficient, and δ is a loss coefficient computed by attributing measured passive-transmission loss to uniform bulk absorption.

Figure 7-33(a) shows output vs input fluence, and Fig. 7-33(b) shows saturation vs output fluence for Q-88 glass. These data are typical of outcomes for six other phosphate glasses shown in Figs. 7-34(a) through (f). The saturation fluences measured with 20-ns pulses were slightly greater than those measured with 1.4-ns pulses, and saturation fluence increased slightly with increases in output fluence.[21] For all phosphate materials, measured saturation fluences varied as the inverse of cross section. At $E_{out} = 5$ J/cm^2, measured values of saturation fluence and cross section are related by the equation $E_s\sigma = k$, with 15.8×10^{-20} J $< k < 17.5 \times 10^{-20}$ J.

Data for the fluoroberyllate-glass test amplifier are given in Fig. 7-35. The B-101 material is not well developed and contained stria within the rod that distorted the saturating beam, thus increasing our experimental uncertainty. For B-101 glass, the product $E_s\sigma = 14.6 \times 10^{-20}$ J at $E_{out} = 5$ J/cm^2 is slightly less than product values for phosphate-glass samples.

The constant k is a measure of the effective gain homogeneity of a material. In general, saturation fluence can be written as $E_s = k\,(\nu, g_u, g_l, E_m, \text{and } t)/\sigma$, where g_u and g_l are the degeneracies of the upper and lower

Fig. 7-32. Transmission losses with 22 3ω laser shots fired through the same site in solarization-resistant BK-10 glass.

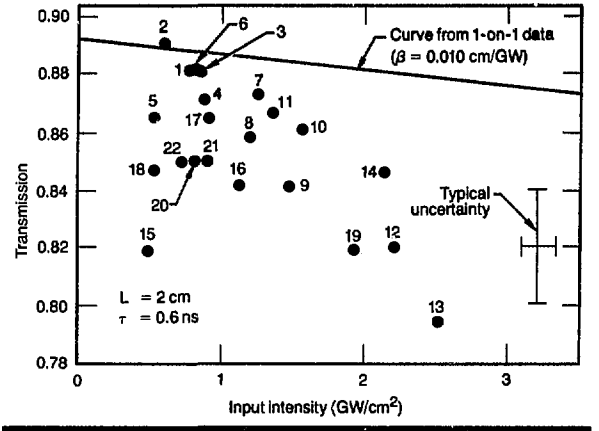

Glass sample	Glass supplier	1.053-μm-gain cross section (10^{-20} cm^2)	Refractive index	Transmission at 1.053 μm	Rod size (cm)
P-101	Hoya Corp.	3.0	1.53	0.985	4.0 × 25
LHG-8	Hoya Corp.	4.0	1.52	0.984	4.0 × 25
Q-88	Kigre, Inc.	4.0	1.54	0.985	2.5 × 25
Q-94	Kigre, Inc.	3.8	1.54	0.985	2.5 × 25
Q-98	Kigre, Inc.	4.1	1.55	0.982	2.5 × 25
LG-750	Scott Optical	4.0	1.52	0.985	2.5 × 25
EV-4	Owens-Illinois	4.2	1.50	0.980	2.5 × 25
B-101	Corning Glass	2.6	1.54	0.98	2.5 × 25

Note: All rods had Brewster-cut ends.

Table 7-6. Properties of phosphate- and fluoroberyllate-glass test amplifiers.

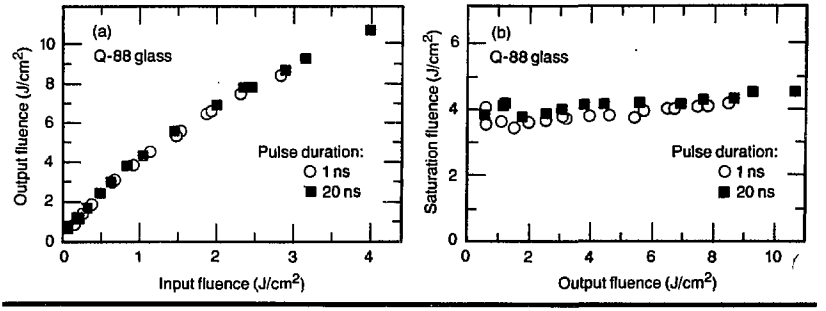

Fig. 7-33. Output vs input fluence and saturation vs output fluence for Q-88 glass.

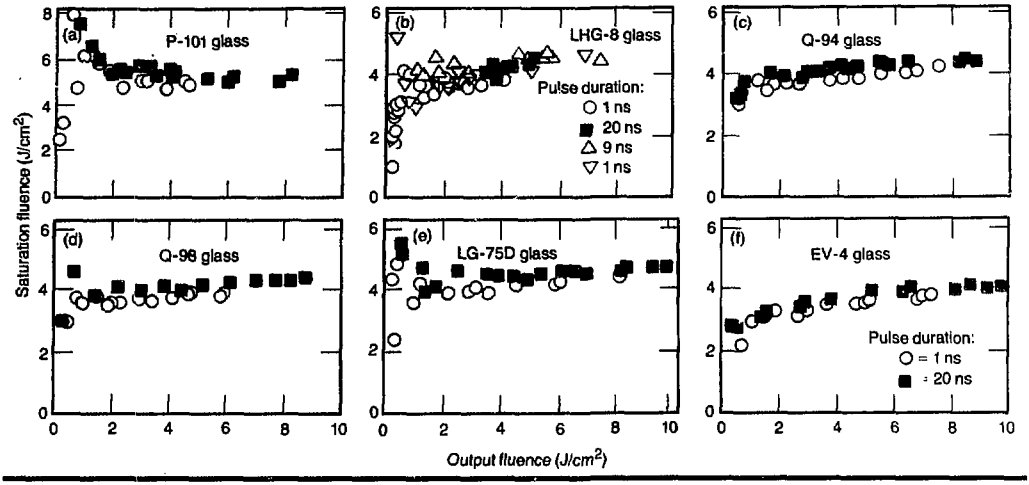

Fig. 7-34. Saturation vs output fluence for six phosphate glasses.

laser level, ν is the laser frequency, E_m is the fluence at which E_s is measured, and t is the pulse duration. The dependence of E_s upon E_m arises from hole burning in the ensemble of excited states. Saturation fluence can depend on the laser-pulse duration if t is less than the lifetime of the lower laser level or the lifetime of states created by excited-state absorption from the upper laser level. When several glasses are tested with the parameters ν, E_m, and t held constant, variations in the measured product $E_s\sigma$ are the result of hole burning and, therefore, a measure of the effective gain homogeneity of the glasses. By this criterion, phosphate glasses are less subject to hole burning than are other common Nd:doped glasses.

Faraday Rotator Materials Databook. In the past several years, we have surveyed the Faraday rotator properties of numerous optical materials.[22,23] Faraday rotator materials are used for optical isolators in many fusion lasers and for other applications. For fusion-laser applications at $\leq 1\omega$, materials having large Verdet constants and small nonlinear refractive indexes were of principal interest. The materials we investigated included oxide and fluoride glasses and crystals.

To disseminate our accumulated data, we prepared manual M-103, *Faraday Rotator Materials*,[17] in a format similar to that of our earlier manual M-095, *Nd-Doped Laser Glass Spectroscopic and Physical Properties*.[16] Because the materials described in M-103

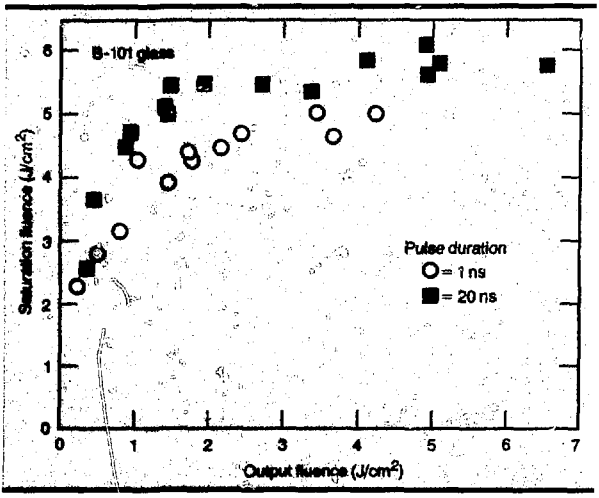

Fig. 7-35. Saturation vs output fluence for the fluoroberyllate-glass test amplifier.

are representative of those used in fusion-laser and other Faraday rotator applications, M-103 was not as extensive as M-095, nor was the manual generated from computer-based archives. Optical materials described in the Faraday rotator manual include eight diamagnetic glasses, 16 paramagnetic glasses, and 12 crystalline materials.

The major topics discussed in each section of *Faraday Rotator Materials* are

- Preface—a short bibliography and previous tabulations of Verdet constants for solids and liquids.

- Introduction—magneto-optic effects in solids, applications of Faraday rotator materials, historical notes, illustrations, and 57 references.
- Measurement Techniques and Data Analysis—experimental apparatus and analytical methods.
- Tables of Faraday Rotator Materials—lists of all materials by the following properties: Verdet constant at 633 nm, Verdet constant at 1064 nm, nonlinear refractive index, and figure of merit for high-power-laser rotator applications.
- Description of Data Sheets—definition of terminology, and sample illustrations showing where to find data in the standard format.
- Data Sheets—glass composition or crystallographic properties, Verdet constants for various wavelengths, estimates or measurements of nonlinear refractive index coefficient, and optical absorption spectra from 0.20 to 3.00 μm. Where available, supplemental data are given for other optical, thermal, mechanical, and solubility properties.
- Index—listing and identification of Faraday rotator materials by diamagnetic glass and paramagnetic glass.

Faraday Rotator Materials has been distributed to both LLNL personnel and more than 100 outside researchers working in the areas of lasers, Faraday rotator devices, and magneto-optic properties of solids.

Index-Matching Fluids. Index-matching fluids (IMF) are required for the crystal-array harmonic generators that will be used on next-generation fusion lasers. Successful application requires that the fluid withstand the Nova and Novette intensity levels at 1ω, 2ω, and 3ω without exhibiting loss[24] due to transverse-stimulated scattering or other deleterious behavior across the 74-cm aperture.

Transverse-stimulated Raman intensity increases exponentially with pump intensity, I, aperture, D, and the Raman gain coefficient of each liquid. For assured performance, a candidate IMF must be tested at the maximum expected product of laser intensity and aperture ($I \times D$). Since the IMF encounters different wavelengths in the harmonic-generator array, frequency-dependence of the gain coefficient must be considered. In addition, the light-propagation time across the array aperture must be compared with the laser pulse-duration range to identify the correct and

Table 7-7. Nova index-matching fluid excitation parameters.

Parameter	Definition of parameter	Wavelength	1-ns intensity (GW/cm^2)	3-ns intensity (GW/cm^2)	5-ns intensity (GW/cm^2)
A	Nova-design maximum intensity (mean) in IMF for three wavelengths.	1ω	3.2	1.6	1.0
		2ω	$\leq$2.8	1.4	0.8
		3ω	$\leq$1.6	1.3	0.7
B	Product of A and the 74-cm Nova aperture.	1ω	237	118	74
		2ω	207	104	59
		3ω	118	96	52
C	Product of A and the distance ($c\tau/n$) light propagates in IMF over pulse duration, τ.	1ω	68/75[a]	102/112	106/118
		2ω	60/67	89/99	88/94
		3ω	34/38	83/92	75/83
D	Product of A and the effective transverse dimension (lesser of parameters B or C).	1ω	68/75	102/113	74
		2ω	60/67	89/99	59
		3ω	34/38	83/92	52
E	Product of D and factor $G(\lambda) = 532/\lambda$ (λ in nm) to account for dependence of stimulated-Raman gain on Nova wavelengths.	1ω	34/37	51/57	37
		2ω	60/67	89/99	30
		3ω	51/57	125/138	78
F	Product of E and 2.0 safety factor. The highest entry is the IMF test goal.	1ω	68/75	102/113	74
		2ω	120/137	178/198	60
		3ω	102/114	250/276	156

[a]For table entries with two values, the refractive index, n, for Halocarbon 56 was used in the first entry, and that for FC-104 in the second.

effective aperture, D, for each calculation. These parameters are collected in Table 7-7 for the Nova laser, with the largest product ($\phi \times D = 125$ GW/cm) occurring for 3ω, 3-ns operation. To protect against possible intensified stripes across the aperture that arise from diffraction by the crystal interstices within the array, we incorporated a safety factor of 2.0 to arrive at 250 GW/cm as the excitation goal for our IMF tests.

Our previous work[24] identified two fluids as promising candidates. These fluids were polychlorotrifluoroethylene, or Halocarbon 56 (Halocarbon Products, Hackensack, N. J.) and a perfluoroalkane, FC 104 (3M Co., St. Paul, Minn.). Tests at 2ω using 8-cm-diam pulses from the Argus laser showed these two fluids to be passive up to 18 GW/cm, the excitation limit of that experiment.

In 1981, we extended our work to 235 GW/cm. To achieve such extremely high excitation, high-energy pulses and an a typical beam geometry were required. Figure 7-36 illustrates the experimental apparatus. The 0.7-ns Argus laser pulses we used were nominally flat in spatial profile and delivered up to 400 J at 1ω. These pulses were reduced to an 8-cm diameter, frequency-doubled in KDP, and then sampled for energy content by absorbing-glass calorimeters. Next, a negative cylindrical lens followed by a 20-cm-diam positive spherical lens served to double the horizontal aperture of the beam and collimate it in the horizontal plane and yet to focus it ($f = 1.6$) in the vertical plane. The result was a horizontal line focus. A cell composed of two 1- by 8-cm windows containing the 12.5-μm layer of fluid was placed in front of the focal point, where the beam shape was a 16- by 1-cm ellipse. A vacuum cell (not shown in Fig. 7-36) immediately followed the IMF cell to prevent breakdown at the focal line. Additional calorimeters measured the energy transmitted through the cell. Fiber-optic cables (FOC) were

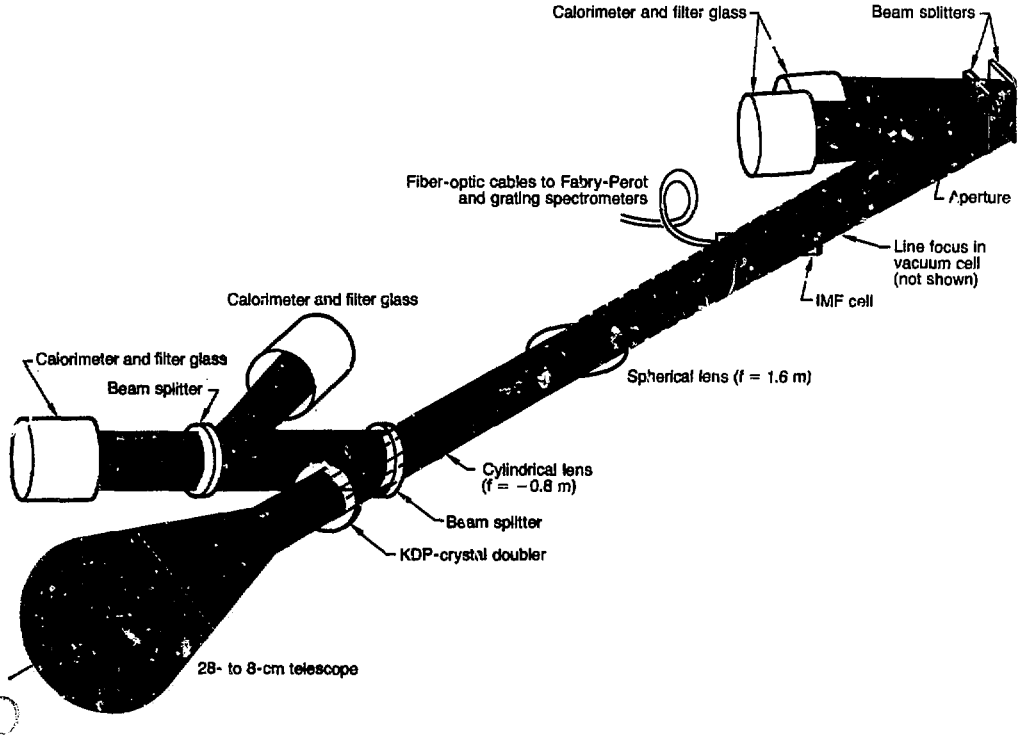

Fig. 7-36. Schematic of apparatus for IMF experiments.

inserted into the cell to receive any side-scattered light and transport it to Fabry–Perot and grating spectrometers.

Tests with He–Ne laser light injected into the FOC determined that the Fabry–Perot apparatus would produce a usable exposure if approximately 10^{-3} J/cm^2 (or 0.01 ω) of the most intense pulses used in the tests were side-scattered into the FOC. Similarly, the exposure threshold of the McPherson spectrometer was approximately 10^{-4} J/cm^2 incident on the FOC. A moderate-intensity (2.6 GW/cm^2) shot using a 100-μm layer of 5610 fluid (Cargille Laboratories, Cedar Grove, N. J.) produced the expected Raman-shifted signature and verified correct operation of these diagnostics.

At 2ω, pulses of mean fluence up to 11 J/cm^2 were directed through the fluid layer. Although laser-induced breakdown in the vacuum-cell windows and shattering of the IMF cell occurred repeatedly, it was possible to obtain the necessary data because cell-shatter occurred many tens of nanoseconds after transmission data were secure. Energy loss due to breakdown in the glass windows of the IMF cell and the vacuum cell were checked by high-intensity shots with no IMF in the cell and with the cell removed from the system. These data are plotted in Fig. 7-37, along with data for the cell filled with a 12.5-μm layer of Halocarbon 56 fluid. Before each high-intensity shot, a weak (~1.7 GW/cm^2) shot was fired to establish the low-intensity ratio of the calorimeter signals. The ratio measured on the following intense shot was then compared, and the percentage of energy loss at the intensity of that shot was determined.

Figure 7-37 shows that approximately two-thirds of the energy lost on each shot was associated with breakdown in the vacuum-cell windows. The first window is the component located nearest to focus, and it experiences the highest intensity. The beam "footprint" was enscribed in this window on each intense shot, requiring us to translate the window between shots. Approximately one-sixth of the energy loss resulted from breakdown in the IMF-cell windows, and the remaining one-sixth was lost in damage and bubble formation in the IMF. To account for approximately one-twelfth of the intensity that was removed from the pulse by the first IMF-cell window, we derated the intensity by the appropriate amount (0.083 × 45% ≅ 4%) at 16 GW/cm^2 in the 12.5-μm layer of Halocarbon 56.

Our final results for IMF experiments are summarized in Table 7-8. The 50-μm layer of Halocarbon 56 produced strong Raman-shifted and frequency-broadened signals on the spectrometers, indicating the presence of stimulated-Raman scattering (SRS). Energy transmission was, however, not markedly reduced, thus emphasizing that SRS had not become dominant.

The final two entries in Table 7-8 represent successful performance by two fluids in thin-layer geometry under probably the highest transverse excitation ever generated in optical-materials research. No SRS signal and no abnormal energy loss were detected in these tests. With the 2.0 safety factor incorporated into the test goal of 250 GW/cm, we have now shown that index-matching fluids will perform adequately in the

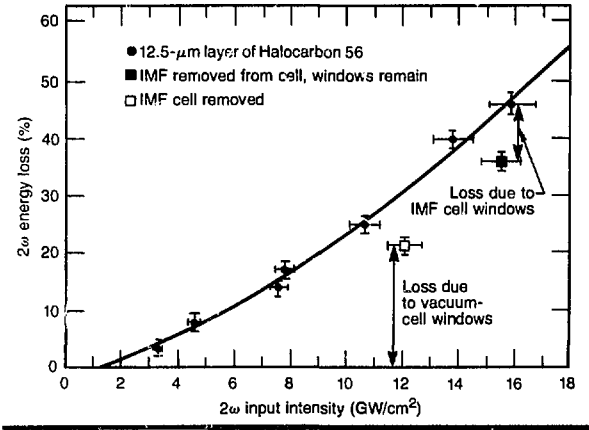

Fig. 7-37. Energy losses at 2ω for IMF tests.

Table 7-8. Index-matching fluid test results.

Fluid	Thickness (μm)	Fluence (J/cm^2)	Intensity (GW/cm^2)	Intensity × length (GW/cm^2)	Results
None	—	10.9	15.6	250	No SRS or SBS
Cargille 5610	100	1.8	2.6	41	SRS—[illegible] failure
Halocarbon 56	50	9.5	13.6	218	SRS—[illegible] failure
Halocarbon 56	12.5	10.8	15.4	246	Success
FC 104	12.5	10.3	14.7	236	Success

crystal arrays that will be used for harmonic generation in Nova and Novette.

Neutron-Induced Transmission Loss. Focusing lenses, beam dumps, and input windows on the KDP array near the Nova target chamber will be exposed to 14-MeV neutron fluences from 10^9 neutrons/cm^2 (1% target yield) to possibly 10^{14} neutrons/cm^2 on each shot. We have assessed the susceptibility of several optical materials to neutron-caused transmission degradation.

We tested the following glasses: BK-7, UBK-10, BK-10*, ARG-2, FK-54, FCD-10, BG-38A, and silica. BK-7 is the standard glass for Nova spatial-filter lenses, polarizer substrates, and array windows. The BK-10 glass selected for UV transmission, UBK-10, and its solarization-resistant version, BK-10*, are candidates for UV-transmitting optics. A phase-separated glass, ARG-2, was considered as a 1ω-transmitting material with integral AR surfaces, but it cannot be used at 3ω because of high scattering losses. FK-54 and FCD-10 are fluorophosphate glasses with good UV-transmission characteristics and low nonlinear refractive indexes. BG-38A is a filter glass (Schott Optical Glass, Inc.) that we plan to use as a 2ω-transmitting, 1ω-absorbing filter following the KDP array. Fused silica is our choice for UV optics if a damage-resistant AR surface can be developed. The fused-silica samples we tested were Optical Grade material from Corning Glass Works, Corning, N. Y.

Glass samples (typically 1- by 1- by 3-cm in size) were irradiated by 14.7-MeV neutrons in the RTNS II (rotating target neutron source) facility at room temperature, which provided a neutron environment similar to the radiation environment anticipated in the Nova laser facility. Using three sets of samples, we performed four exposures at levels of 3.4×10^9, 3.4×10^{12}, 2.8×10^{13}, and 1.4×10^{14} n/cm^2. Sample transmission was measured with lasers or a spectrophotometer before and after each neutron irradiation.

The absorption coefficient of several glasses at 2ω and 3ω are plotted as a function of neutron dose in Fig. 7-38. The functional relationship between the two variables is unexpectedly nonlinear. In contrast, fused silica had no degradation in transmission, even at the highest dose. Therefore, fused silica is clearly the best material to use in our neutron environment.

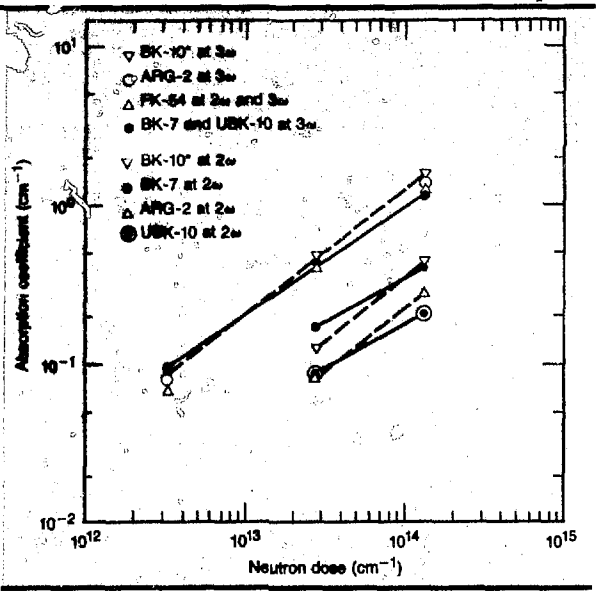

Fig. 7-38. Absorption loss in several optical materials induced by 14.7-MeV neutron irradiation.

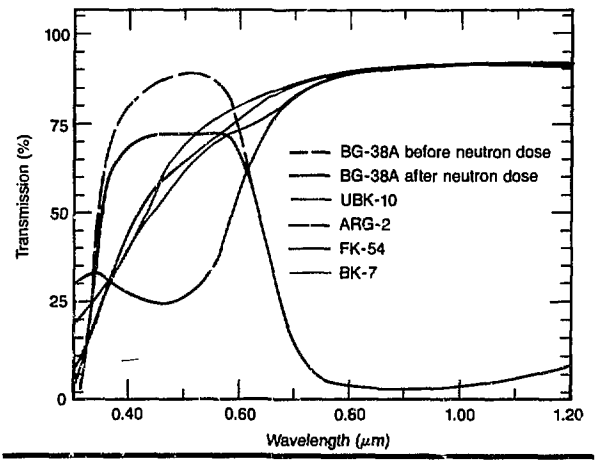

Fig. 7-39. Transmission spectra of optical materials after 14-MeV neutron irradiation at 1.4×10^{14} neutrons/cm^2. Samples were 1 cm thick, except for BG-38A, which was 2 cm thick.

Transmission spectra of five glass samples after a 1.4×10^{14}-n/cm^2 dose are shown in Fig. 7-39. Samples were 1 cm thick, except for BG-38A, which was 2 cm thick. The 2ω beam-filter transmission before the test is also shown. The neutron-damaged borosilicates and fluorophosphates contain a UV-absorbing color center with

spectral characteristics similar to those of centers caused by UV-light irradiation. The neutron-induced absorption band in FK-54, FCD-10, and BG-38A is typical of phosphate-containing glasses and is probably caused by a singly ionized nonbridging oxygen.

In many cases, color centers in a material can be eliminated by heating. Therefore, we annealed the damaged samples at temperatures ranging from 100° to 400°C for up to four days. After annealing, BK-7, FK-54, FCD-10, ARG-2, and BG-38A transmissions were close to their original values. However, UBK-10 showed a 5%/cm loss after one day of annealing at 400°C. Thus, most of the optical materials we tested can be used near the Nova target chamber if they are periodically annealed.

Authors: D. Milam, W. L. Smith, S. E. Stokowski, M. J. Weber, and S. M. Yarema

Major Contributors: H. D. Bissinger, L. W. Coleman, B. L. Freitas, C. P. Hale, G. J. Linford, J. E. Lynch, F. P. Milanovitch, S. E. Peluso, M. S. Singh, L. V. Smith, M. C. Staggs, and C. L. Vercimak

Comparison of Two Methods for Measuring n_2. Measurements of the nonlinear refractive index, n_2, may be categorized as either time-resolved or time-integrated. During 1981, our experiments using subnanosecond pulses at 1ω from the ILS laser showed that both time-integrated and time-resolved methods yield, within experimental uncertainty, the same value of n_2 for a given sample.[25]

Our experiments used interferometric techniques similar to those previously reported.[26-31] The sample was a rod of ED-2, a Nd-doped silicate laser glass.

Figure 7-40 shows the experimental layout. At the output of a two-beam interferometer, intensity-induced motion of the fringes provided a measure of the intensity-dependent refractive index of the sample inside the interferometer. A removable mirror allowed us to use either a streak camera or a common vidicon to analyze the fringes. The streak camera permitted time-resolved measurement, whereas the vidicon permitted time-integrated measurement of fringe displacement. We determined n_2 by correlating the measured peak-fringe shift with the peak intensity averaged over the round-trip through the length of the sample.

Figures 7-41 and 7-42 show typical fringe patterns. Figure 7-41 is an enlarged photograph of the streak-camera output, where

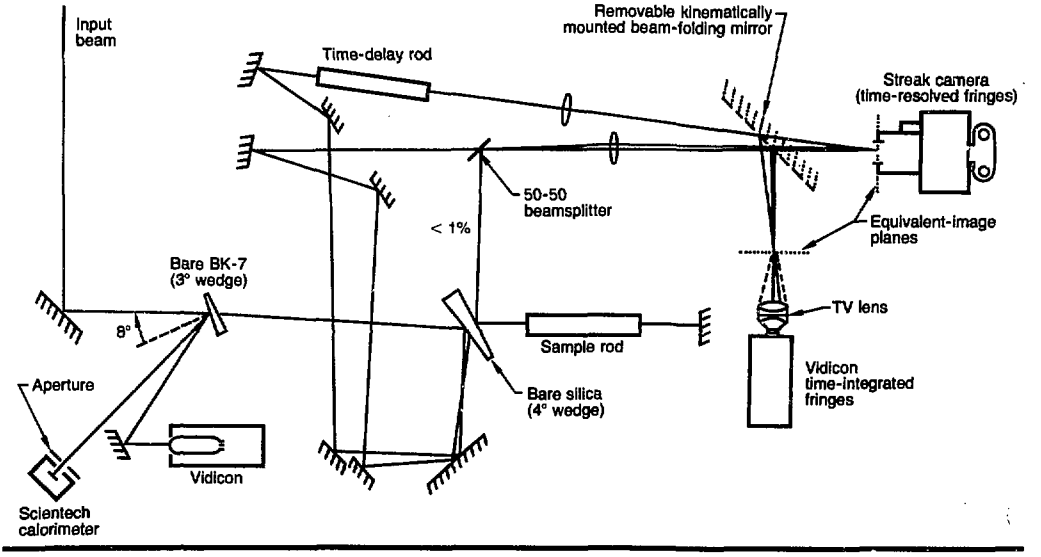

Fig. 7-40. Experimental layout for comparing time-resolved and time-integrated interferometry.

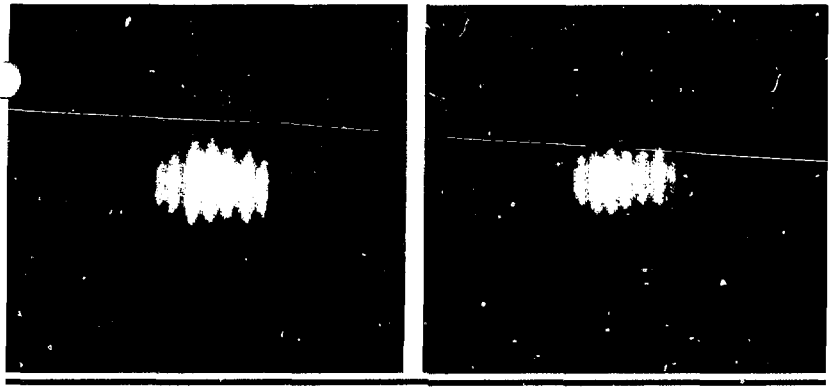

Fig. 7-41. Photograph of streak-camera output showing time-resolved fringe shift. (a) Fringe shift = 0.0 fringes. (b) Fringe shift = 0.5 fringes.

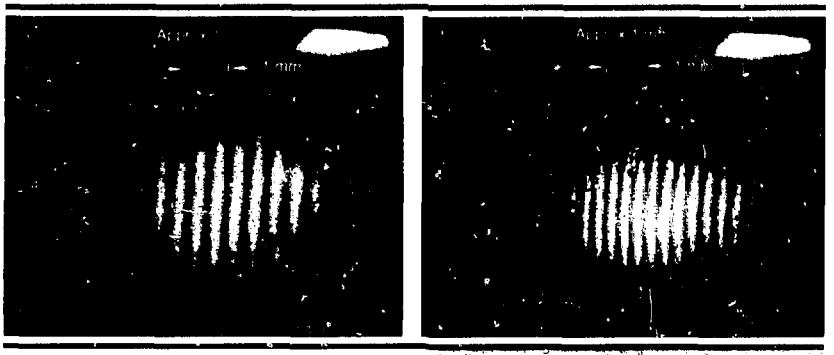

Fig. 7-42. Photograph of vidicon output showing time-integrated fringe pattern. (a) Fringe shift = 0.1 fringes. (b) Fringe shift = 0.5 fringes.

the pattern represents instantaneous position of fringes in a central 10- by 0.1-mm slice of the beam. The nominal FWHM (full width at half maximum) pulse length is 0.1 ns. The time axis runs parallel to the fringes. Figures 7-41(a) and (b) show the output of the streak camera in the absence of fringe displacement (low laser intensity) and in the presence of fringe displacement (high laser intensity), respectively. Figures 7-42(a) and (b) show low displacement and large displacement, respectively, of the entire time-integrated interferogram recorded by the vidicon.

Due to beam breakup and self-focusing problems, we restricted intensities to those causing fringe shifts ≤ 0.5 fringes. Consequently, our data show substantial random scatter, since the ability to read a fringe shift was limited to between 0.1 and 0.15 fringes. In addition, uncertainties in measuring peak intensity contributed about 25% to the scatter of data.

Table 7-9 compares our measurements with predicted values of n_2 that are derived from Boling et al.[32] These authors present

Table 7-9. Comparison of two methods for measuring n_2 in ED-2 at 1ω.

Method	Measured n_2 (10^{-13} esu)	Predicted n_2 (10^{-13} esu)
Time-resolved	1.75 ± 35%	1.51 to 1.73
Time-integrated	1.68 ± 31%	1.51 to 1.73

two empirical approximations for n_2 at 1ω. The first approximation has a sound physical basis, while the second better describes n_2 at 1ω in a wider variety of materials. Since both empirical formulae have been used throughout the literature, the two predicted values are included in Table 7-9 to facilitate comparison. Our time-resolved and time-integrated interferometric measurements of n_2 yielded outcomes similar to the Boling et al. predictions.

Measurements of Nonlinear Optical Effects. To measure the linear and nonlinear optical properties of fusion-laser materials, we are investigating the high-sensitivity techniques of photorefractive lensing[33] and beam deflection.[34] The optical properties we studied include linear absorption, two-photon absorption two-photon-induced linear absorption (solarization), and nonlinear refractive index (n_2).

A typical experiment is shown in Fig. 7-43. A high-intensity "pump" beam is derived from a frequency-doubled Nd:YAG laser or from a frequency-doubled Nd:YAG-pumped dye laser. The pump beam induces either a thermal lens or a nonlinear-refractive-index lens in an optically thin sample. A high-stability He–Ne "probe" laser, collinear with the pump beam and orthogonally polarized, counterpropagates through the induced lens and undergoes beam deflection or change in far-field divergence. The probe-beam modulation is detected with a fast-semiconductor photodiode following an appropriately positioned pinhole aperture. For induced lensing, the pump and probe are focused to approximately the same radii in the sample, and the pinhole aperture is centered on the probe beam in the far field. For beam deflection, however, the probe is focused much more tightly than the pump, overlapped off-center to the pump in the sample, and the pinhole is positioned off-center in the probe in the far field. Configurations other than that shown in Fig. 7-43, in which the pump and probe beams copropagate, have also been used successfully and allow freedom in choosing pump and probe polarizations.

To quantify laser intensities, our beam-diagnostic system is composed of a vidicon, Grinnell video-signal digitizer, and PDP-11/10 processor. The system captures, digitizes, color codes, and displays real-time laser-beam profiles at a rate of 10 Hz. The temporal-pulse profile is recorded with a Tektronix R7912 transient digitizer.

The thermal-lens effect is caused by momentary nonuniform heating of a small region of the sample due to combined linear and nonlinear absorption of pump radiation. Immediately following traversal of the pump pulse, the temperature-dependent linear refractive index images the absorbed pump-beam energy distribution. Radial heat flow from the hot region by thermal diffusion subsequently smears the induced-index profile. For a near-Gaussian pump spatial profile, the induced-index profile may be modeled as a "thin" lens. An n_2 profile at the probe wavelength (similarly modeled as a thin lens) is induced by the high-intensity pump field through third-order

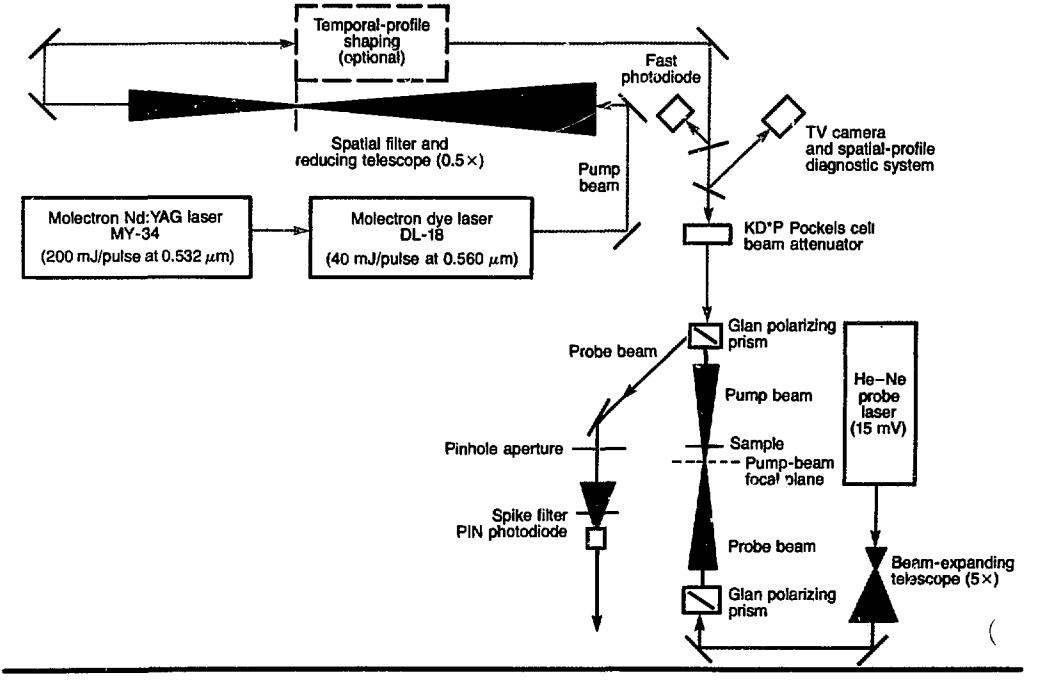

Fig. 7-43. Experimental arrangement for two-photon-absorption spectroscopy.

nonlinear susceptibility[35] and evolves spatially and temporally following the pump pulse.

We have considered photorefractive beam deflection in both experiment and theory. Generally, the beam-deflection effect is three to five times more sensitive than lensing techniques. However, the overall signal-to-noise ratio is unimproved because the beam-deflection technique is very sensitive to small-scale shot-to-shot fluctuations in the spatial profile of the pump.

Figure 7-44 illustrates typical thermal-lensing data obtained for a pump wavelength of 2ω. We used a 0.1 neutral-density (ND) filter, a yellow Corning filter glass (3-75), and three visible-transmitting Corning filter glasses (0-52, 0-53, 0-54). Except at the highest intensities (~3 to 10 GW/cm^2), the ND filter exhibited a linear rise ($n = 1$) in thermal-lensing signal, Q (unnormalized), with increasing intensity. The Corning filters all showed slight two-photon nonlinearity at the highest intensities, while filter 0-54 showed a marked two-photon effect ($n = 2$).

We have estimated the minimum detectable levels of linear and nonlinear absorption from the experimental data illustrated in Fig. 7-44. For a signal-to-noise ratio of 10, an estimated peak-energy density of 20 J/cm^2, and a peak intensity of 3.9 GW/cm^2, we estimate a minimum $\alpha L \cong 5 \times 10^{-3}$ and $\beta L \cong 1 \times 10^{-3}$ cm^2/GW, where α and β are the linear and nonlinear absorption coefficients, respectively, and L is the sample length. The corresponding minimum detectable absorbed energy is $\sim 5 \times 10^{-5}$ J, or a temperature difference $\Delta T \cong 4 \times 10^{-2}$ °C. For glass such as BK-7 with $\delta n/\delta T \cong 2.8 \times 10^{-6}$ °C, the ΔT translates to a minimum refractive index change of $\Delta n \cong 1 \times 10^{-7}$. For n_2-induced lensing, a nonlinear refractive index equal to the minimum detectable index change is equivalent to a nonlinear index coefficient $\cong 3 \times 10^{-21}$ m^2/W, which is approximately 10 times that observed in BK-7. Hence, the induced-lensing technique should have adequate sensitivity for accurate determination of n_2. We are presently carrying out an experiment to determine n_2 at 1ω and 2ω in a variety of glasses.

Tailoring Stimulated-Emission Cross Sections of Nd^{3+} Laser Glass. Studies in the past decade have demonstrated that there are large variations in the spectroscopic properties of rare-earth (RE) ions in different glasses. Spectroscopic properties can be tailored, within limits, by the choice of glass network-forming and network-modifying ions.[36] Properties that determine the peak cross section include the line strength and line width of the transition and the refractive index of the host.

Line strength is the most host-dependent quantity in determining the stimulated-emission cross section and, for an RE, is usually given in terms of Judd–Ofelt intensity parameters.[37] Both homogeneous and inhomogeneous line widths of optical transitions vary with host.[38] Inhomogeneous broadening caused by site-to-site variations in the local field dominates the effective

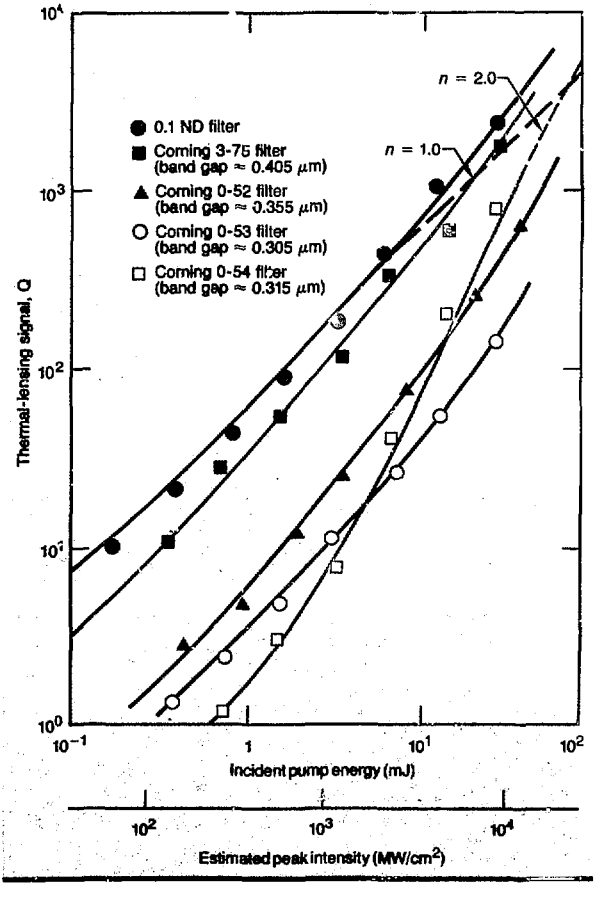

Fig. 7-44. Thermal-lensing signal, Q (unnormalized), in several filter glasses as a function of incident pump energy and estimated peak intensity.

line width measured at temperatures ≤300 K. In general, the smaller the anionic field strength, the smaller the Stark splitting and the narrower the effective line width. The weaker the coordinating power of the glass-forming cation, the tighter and more symmetrical the RE-coordination shell and the narrower the line width. Finally, for a given glass-network former, the effective line width generally increases with increasing charge and decreasing size of the modifying cations.[39]

The compositional versatility of glass-forming systems can be exploited to tailor stimulated-emission cross sections. Tailoring has been most thoroughly demonstrated for the $^4F_{3/2} \rightarrow {}^4I_{11/2}$ lasing transition of Nd^{3+}. Some examples of emission spectra in different glasses are shown in Fig. 7-45. The range of cross sections and other spectroscopic properties observed to date for various oxide and halide glasses[16] are summarized in Table 7-10. Although the ranges are not necessarily the extreme values achievable, they illustrate the magnitude of possible changes.

For silicate glasses, which have been studied most extensively, cross sections in Table 7-10 range from $<1.0 \times 10^{-20}$ cm^2 for simple alkali silicates to 3.6×10^{-20} cm^2 for a bismuth-cadmium silicate glass. Larger cross sections are obtained for phosphate-glass compositions. Although the Judd-Ofelt parameters for Nd^{3+} in phosphate glasses can be slightly larger than in silicate glasses, the larger cross sections are mainly due to narrower effective-emission line widths. Cross sections for tellurite glasses can be larger than the largest values observed for phosphate glasses. The difference is not due to narrower line widths or larger line strengths, but is a result of the larger refractive index of the host.

The effective line width is narrowed by using monovalent halide, rather than divalent oxide, anions. As shown in Table 7-10, the width of the Nd^{3+} emission for fluoroberyllate glasses can be narrower than the narrowest width for oxide glass. The peak cross sections, however, are not larger because the line strengths are smaller. The use of larger, more polarizable anions, such as

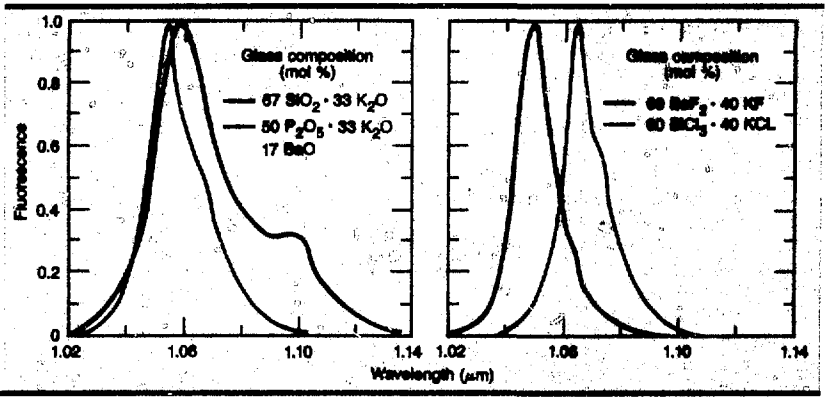

Fig. 7-45. Comparison of the $^4F_{3/2} \rightarrow {}^4I_{11/2}$ fluorescence spectrum of Nd^{3+} in oxide and halide glasses at 295 K.

Table 7-10. Ranges of spectroscopic properties for the $^4F_{3/2} \rightarrow {}^4I_{11/2}$ transitions of Nd^{3+} in different glasses at 295 K.

Glass	n_d	Cross section (10^{-20} cm^2)	Wavelength, λ_p (nm)	Line width, Δ_{eff} (nm)	Lifetime, τ_R (μs)
Oxides					
Silicates	1.46 to 1.75	0.9 to 3.6	1057 to 1088	34 to 55	170 to 1090
Phosphates	1.49 to 1.63	2.0 to 4.8	1052 to 1057	22 to 35	280 to 530
Borates	1.51 to 1.69	2.1 to 3.2	1054 to 1063	34 to 38	270 to 450
Germanates	1.61 to 1.71	1.7 to 2.5	1060 to 1063	36 to 43	300 to 460
Tellurites	2.0 to 2.1	3.0 to 5.1	1056 to 1063	26 to 31	140 to 240
Halides					
Fluoroberyllates	1.28 to 1.38	1.6 to 4.0	1046 to 1050	19 to 29	460 to 1030
Fluoroaluminates	1.41 to 1.48	2.2 to 2.9	1049 to 1051	30 to 33	420 to 570
Fluorozirconates	1.52 to 1.56	2.9 to 3.0	1049	26 to 27	430 to 450
Chlorides	1.67 to 1.91	6.0 to 6.3	1062 to 1064	19 to 20	180 to 220

Cl^- or Br^- instead of F^-, results in both narrow line widths and increased Judd-Ofelt parameters. Cross sections also increase due to the larger refractive index of glasses made from these halide ions. Thus, chloride glasses have the largest cross sections in Table 7-10.

The only stimulated-emission cross sections determined using the Judd-Ofelt approach that are larger are those reported for two chalcogenide glasses, where values of $\sim 8 \times 10^{-20}$ cm^2 were obtained.[40]

Nd-doped glass compositions that have now been examined span most of the periodic table. The limiting values of stimulated-emission cross sections and other spectroscopic and physical properties achievable in inorganic oxide and halide glass-forming systems can therefore be predicted.

Hartree-Fock Calculations in Solids. As part of our theoretical investigation of the optical properties of RE ions in solids, we are developing a computer program to perform exact-exchange Hartree-Fock (HF) calculations in crystals. Our general theoretical problem is the quantitative determination of RE crystal-field (CF) energy levels.

It is common to use an approximation to a general ionic model (the point-charge model) to establish CF parameters. The ionic model states that the CF is due to the electrostatic field of the other ions at the RE site. The point-charge model assumes that the electrostatic field arises from point charges at the ion sites. Recent studies have shown that the point-charge model is quantitatively unreliable, and it has been suggested that covalency plays a significant role in CF splittings, even in fluoride crystals.[41]

An HF treatment of an RE fluoride or RE oxide crystal allows the calculation of accurate crystal-wave functions. With wave functions, we can obtain an accurate crystal/charge distribution and, thus, critically test the ionic model of the CF. By expanding our calculation to include the effects of configuration interaction, an ab initio calculation of the CF can also be made.

The HF program we are writing includes several features that distinguish it from other programs reported previously. Our program uses the conventional LCAO-MO equations of quantum chemistry adopted for the solid state. In our treatment, the wave function is expanded in terms of atomic orbitals, which are a set of functions localized on each atom. Up to 20 basis functions per unit cell can be handled. Combining the functions with effective core potentials means that crystals with three, and possibly four, atoms per unit cell can be realistically treated.

The developments that allow for our expanded treatment include a unique numerical treatment of exchange integrals, including accelerated-convergence schemes. For a moderate problem, there are $>10^9$ exchange integrals. It is not possible to store this number of integrals, as would be done in a smaller, conventional molecular calculation. Instead, the integrals would have to be recalculated for each iteration. (An HF calculation involves iterating a set of partial differential equations to self-consistency.) For most of the iterations, rapidly obtained approximations to the integrals are used for converging to the nearly correct result. At the end, however, when converging to the accurate HF result, the full integrals to about eight significant figures are needed.

The exchange integrals are calculated as sums over reciprocal lattice vectors. For many cases, there are hundreds or thousands of terms in the sums, so that normal calculations would be prohibitively lengthy. By using the recently developed accelerated-convergence schemes, however, it is possible to calculate only the first few terms of the series and, from them, to accurately determine the value of the full series. In this way, the calculation can be made practical.

Authors: M. A. Henesian, W. T. White, M. J. Weber, and S. A. Brawer

Major Contributors: A. Rosencwaig, T. W. Hindley, and W. L. Smith

---

Comparison of Optical Spectra and Computer Simulations of Glass Structure. The optical spectra of rare-earth (RE) ions in glass vary from site to site because of differences in local environments. The inhomogeneous broadening associated with local environments makes detailed studies of spectroscopic properties difficult. To interpret RE spectra in glass, we have performed computer simulations of ion structure in the

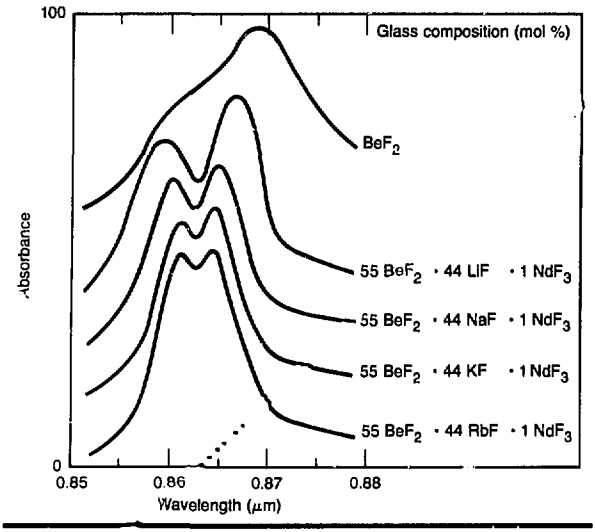

Fig. 7-46. A portion of the $^4I_{9/2} \rightarrow {}^4F_{3/2}$ absorption spectrum of Nd^{3+} in five glasses at 295 K.

Simulated glass (molar proportion)	Average energy splitting			Line width, $\Delta\lambda_{eff}$ (nm)
	nn F^-	All ions	Half width	
130 BeF_2 · 1 NdF_3	1.0	1.0	1.0	26.2
76 BeF_2 · 74 NaF · 1 NdF_3	0.82	0.90	0.78	20.8
76 BeF_2 · 74 RbF · 1 NdF_3	0.82	0.97	0.79	19.7
76 BeF_2 · 37 CaF_2 · 1 NdF_3	1.07	1.06	1.1	—

Table 7-11. Average energy-level splitting (relative units) and line width of the $^4F_{3/2}$ state of Nd^{3+} in beryllium fluoride glasses, calculated from computer-simulated structures using a point-charge model.

vicinity of the RE. Our previous Monte Carlo simulations of simple RE-doped BeF_2 glass showed that there are large variations in the number and geometric arrangement of ions around the RE. To test the validity of the simulated structure, energy levels of 160 different sites of Eu^{3+} were calculated using a point-charge model. The resulting range and distribution of energy-level splittings were in good agreement with both broadband and laser-excited fluorescence spectra.[42]

We have extended the computer simulations using molecular dynamics (MD) to treat more complex multicomponent glasses. Alkali and alkaline-earth ions were added as network-modifier cations. Details of the calculations, radial distribution functions, and average coordination of the various ions are described in Ref. 43.

Systematic variations of RE spectra with glass composition have been known for many years. Variations in the Stark splitting of the $^4F_{3/2}$ state for some simple glass compositions are shown in Fig. 7-46. The two inhomogeneously broadened peaks correspond to transitions from the lowest Stark level of $^4I_{9/2}$ to the two Stark levels of $^4F_{3/2}$. To account for the results in Fig. 7-46, we simulated the structures of RE-doped BeF_2 glass and glasses modified with Na^+, Rb^+, and Ca^{2+} cations. Our simulated glasses were chosen to test the effects of changing modifier-cation size (Na^+, Rb^+) and modifier-cation charge (Na^+, Ca^{2+}). The Stark splitting of the $^4F_{3/2}$ state was calculated for 100 simulated sites using a point-charge model.

The half-width of the energy distribution, expressed in relative units and excluding the homogeneous line width, and the effective-fluorescence line width are summarized in Table 7-11. In the first column of data in Table 7-11, only nearest-neighbor (nn) fluorine ions within 3 Å were used; in the second column, all ions in the primary cell (~17 Å) were used. The half-width of the energy distribution is given in the third column, and the $^4F_{3/2} \rightarrow {}^4I_{11/2}$ fluorescence line width is shown in the final column.

With respect to simple BeF_2 glass, the smaller splittings in the alkali-containing glasses and the larger splitting in the alkaline-earth glass (not shown) are successfully predicted. Both the magnitude and distribution of $^4F_{3/2}$ splittings change together. Thus, those glasses with large average splittings of $^4F_{3/2}$ also have large inhomogeneous line widths, in agreement with Fig. 7-46. Exact agreement between our results and experimental spectra is not expected because we have only considered energy levels and not transition probabilities. Nevertheless, computer simulations appear capable of predicting variations in RE line widths with composition of fluoroberyllate glasses. One feature in Fig. 7-46 that is not predicted is the smaller splittings for the larger alkali ions. Resolution of the discrepancy probably requires a more sophisticated model of the crystal field.

Vibrations in Glass. Vibrations of a host material around an optically active ion in a solid-state laser medium affect the ion's lifetime, homogeneous line width, and quantum efficiency. The three parameters, in turn, affect energy storage and extraction properties of the laser system. The most direct way to investigate vibrations about RE ions in glass is through observation of

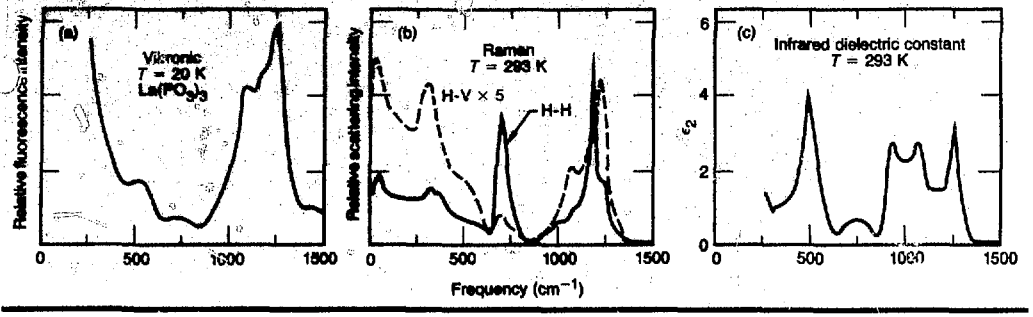

Fig. 7-47. Comparison of three spectra for $La(PO_3)_3$:Gd glass. (a) Vibronic spectrum. (b) H-V and H-H Raman spectra. (c) Infrared spectrum.

vibrational-electronic (vibronic) sidebands in line-narrowed fluorescence spectra.[44] A vibronic sideband occurs when an excited RE ion relaxes to a lower energy state by creating a phonon in the host and emitting a photon as well. By monitoring the intensity and energy shift of photons from the strong zero-phonon line, we map the vibrational density of states around the RE, weighted by a factor that accounts for the different coupling of specific vibrations to the ion. Those vibrations that create a large microscopic electric field at the ion site should have the largest coupling.

A major observation in our previous work[44] was the striking similarity of vibronic spectra and the H-V polarization of Raman-scattering spectra in a series of metaphosphate glasses.[45] H-V polarized Raman spectra reveal vibrations of the bulk glass (vibrations not just around the RE, but those that may be due to its presence) weighted by a selection rule that emphasizes asymmetric vibrations with a position-dependent polarizability. During 1981, we extended our investigation to include another bulk-vibrational spectroscopy, infrared reflectance. Infrared reflectance emphasizes vibrations that create a macroscopic electric field. Relating vibrational properties of an ion/host system to those of the host itself is an important step in tailoring materials for particular laser applications.

With the assistance of Dr. Dave Ottesen (Sandia Laboratories, Livermore, Calif.), we obtained infrared reflectance at 15° from normal using a Digilab FTS14 Fourier-transform spectrometer in the range of from 170 to 4000 cm^{-1}. Because of dispersion associated with reflectance, the quantity most indicative of vibrations is the imaginary part of the dielectric constant, ϵ_2. To obtain ϵ_2 numerically from reflectance data, we used a Kramers–Kronig transformation run on a PDP-11/40 minicomputer.

Results of all spectroscopies for one representative metaphosphate glass are shown in Fig. 7-47. Since infrared spectra emphasize vibrations that create large electric fields, one might predict a similarity with vibronic spectra. The difference in location of peaks in the structure of the two spectroscopies stresses the microscopic nature of the field that affects the RE. The localized vibrational probe provided by vibronic spectra is most relevant to the dynamic influence of a host on a laser ion.

FLN Spectra and Hole Burning Using Polarized Light. Fluorescence-line-narrowing (FLN) experiments yield the parameters necessary to predict saturation behavior in spectrally inhomogeneous media.[46] Among the measures we have obtained are homogeneous line width, inhomogeneous-broadening width, and cross-relaxation rate. The FLN technique can also be used to obtain parameters relevant to an orientationally inhomogeneous system. During 1981, we performed FLN experiments with polarized light on two Nd:silicate laser glasses of technological importance, ED-2 and LG-650.

Our FLN experiments use polarized light from a Nd:YAG laser to excite ions in a lightly doped sample out of the thermally populated lower laser level ($^4I_{11/2}$) and into the upper level ($^4F_{3/2}$). Resonant fluorescence is observed with polarization parallel and perpendicular to the polarization of the exciting beam. The detection system consists of a 1-m grating monochromator, a cathode-gated S-1 phototube, and photon-counting electronics.

The very weak signal that necessitates photon counting is the result of three factors

- Only 10^{-4} of the Nd ions are in the $^4I_{11/2}$ state at room temperature.
- Light doping is necessary to prevent cross relaxation and to maintain site selectivity.
- Photocathodes are relatively insensitive to 1ω light from the resonant fluorescence.

Our experimental results are expressed as the depolarization ratio, ρ, of perpendicular and parallel signals. We found that $\rho = 0.88 \pm 0.02$ for ED-2 glass and $\rho = 0.94 \pm 0.02$ for LG-650 glass. Our ratios compare closely with those obtained by others[47] in experiments using more easily measured RE transitions in glass. The small resonant FLN signals required long sampling times and precluded measurement of polarized spectra across the lasing band. Increased detector sensitivity at 0.88 μm did, however, allow measurement of polarized spectra for the nonresonant $^4F_{3/2} \rightarrow {}^4I_{9/2}$ transition. Results are shown in Fig. 7-48. The maximum ρ for the transition in ED-2 is ~0.95, reflecting the loss of site selectivity due to accidental coincidences in nonresonant excitation-observation transitions.

To predict laser-amplifier performance from our results, we needed a microscopic model to represent the interaction between an ion in a site with particular orientation and polarized light. For simplicity, we used a two-level system that is spectrally homogeneous with all ion sites identical except for orientation.

The site symmetries in glass are low (e.g., C_1, C_{2v}) so that a local orthogonal coordinate system can be uniquely assigned to each ion, and a polarized cross section can be associated with each axis direction. The cross section σ_i is proportional to the probability of absorption or emission (spontaneous or stimulated) of light polarized in the ith direction. A further simplification is to treat the two cross sections for light polarized perpendicular to the principal site axis, denoted by σ_v, as equal; the parallel cross section is denoted by σ_p. An assumption of equality simplifies the angular integration, and the results are expressible in terms of a single parameter, the ratio σ_v/σ_p.

The macroscopic response, ρ, of an isotropic distribution of sites in a resonant polarized FLN experiment was calculated and is shown in Fig. 7-49. Therefore, once the microscopic parameter σ_v/σ_p is determined from the measured ρ, calculations of orientational hole-burning effects during large signal/gain conditions can be made using the same model.

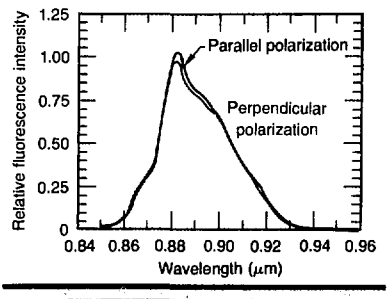

Fig. 7-48. Spectra showing polarized fluorescence for the nonresonant transition $^4F_{3/2} \rightarrow {}^4I_{9/2}$ of Nd^{3+} in ED-2 glass excited with linearly polarized 1ω radiation.

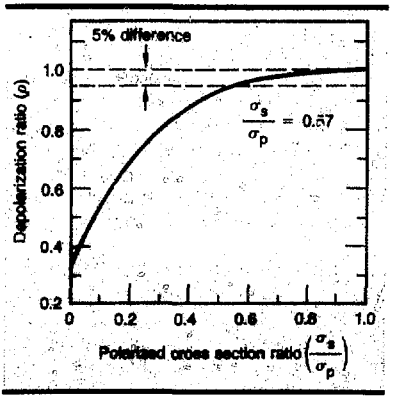

Fig. 7-49. Calculated depolarization ratio as a function of the polarized cross-section ratio for an isotropic ensemble of partially anisotropic oscillators.

Interaction of Rare-Earth Ions with Two-Level Systems in Glass. The homogeneous line widths of RE ions in glasses have an unusual temperature dependence in that they are approximately proportional to T^2 from about 8 K to room temperature.[48,49] The behavior is surprising because temperature dependence of the homogeneous line width is much steeper for Pr^{3+} in LaF_3, while, for Eu^{3+} in $YAlO_3$, it is $e^{-400/T}$. Moreover, at the lowest temperatures, homogeneous line widths in glasses are several orders of magnitude larger than in crystalline materials, although the widths are about the same at room temperature.

Based upon usual theory,[50] it is not possible to rationalize the T^2 dependence of line widths and still account for the anomalous behavior of Eu^{3+}. It is well known, however, that virtually all low-temperature (<2 K) properties of dielectric glasses are anomalous.[51] Phenomenologically, anomalies have been attributed[52,53] to the presence of a group of atoms that undergo phonon-assisted tunneling between two unequal

potential wells. These so-called two-level systems (TLS) give rise to excitations whose energies range from less than 1 kHz to greater than 35 GHz.[54] Temperature dependence of the anomalous homogeneous line widths of RE ions in glasses has been rationalized in terms of a possible interaction of the RE with TLS.[55,56]

We have theoretically examined the experimental ramifications of an RE-TLS interaction in glass. Our general theory includes two previous theories[56,57] as special cases. An important result is that, if the RE-TLS interaction is indeed significant, then temperature-dependent sidebands whose intensities depend on the number of TLS (with which the RE interacts) should be observable. The presence of sidebands provides a stringent test for the existence of a significant RE-TLS interaction.

The physical origin of sidebands is shown in Fig. 7-50. The RE-energy levels are shown as E_1 and E_2 for the ground state and excited state, respectively, and the TLS energies are + and − when the TLS is in the well with the higher and lower energy, respectively.

In Fig. 7-50(a), the top two solid lines are the $^7F_0$ (E_1) and $^5D_0$ (E_2) energy levels of Eu^{3+} when the TLS is in the + well. The double-well potential showing the relative TLS energies is drawn below the RE energies. In Fig. 7-50(b), the TLS is in the − well. Due to the RE-TLS interaction, the energy of each RE level changes when the TLS switches from one well to the other. Thus, the four possible energy levels are E_1^+, E_2^+ [in Fig. 7-50(a)], E_1^-, and E_2^- [in Fig. 7-50(b)].

The case of negative coupling is shown; therefore, E_1 and E_2 increase when the TLS goes from the + to the − well. Note that the increase in E_1 is much greater than E_2.

Figure 7-50(c) shows the four "collective" energy levels of the combined RE + TLS system. We have purposely chosen the negative-coupling case for which the RE levels increase in energy as the TLS goes from the + to the − well. Positive coupling is just as likely as negative coupling, but does not lead to sidebands. For Eu^{3+}, the change in energy of the excited state is proportional to the change in energy of the ground state. Both changes result when the TLS hops from one well to the other. It can be shown that the magnitude of the change of the excited state is 2.5% of the change in the ground state. As a result, it is possible for the total energy (RE + TLS) to appear as shown in Fig. 7-50(c), where the level δ is above α, while γ is below β.

Consider what happens when the RE of Fig. 7-50 is excited. At low temperatures, such that kT is much less than $E_1^- - (E_1^+ - \Delta)$, the system is in the ground state, α. A photon of frequency $E_2^+ - E_1^+$ excites the system to level β. The excited state β (or γ) has a lifetime of more than 1 ms for a radiative transition to the lower state, while, in general, tunneling times for TLS are less than 1 μs. Thus, the system transfers to the lowest excited state, γ, by the TLS tunneling from one well to the other. The system then radiates by making a transition to level δ and emitting a photon of frequency $E_2^- - E_1^-$, which is smaller than the excitation frequency. The system returns to the ground state by another tunneling process.

The fact that the emission frequency is smaller than the excitation frequency means that the emission appears as a sideband. These sidebands have not actually been observed experimentally. The evident weakness of the sidebands implies any hypothetical RE-TLS interaction cannot possibly produce the observed behavior of the homogeneous line widths. Therefore, at present, the temperature-dependent behavior of homogeneous line widths in glass has no qualitative explanation.

Kinetics of Ligand Motion about RE Ions in Liquids and Glass-Forming Fluids. The FLN technique[57] can be used

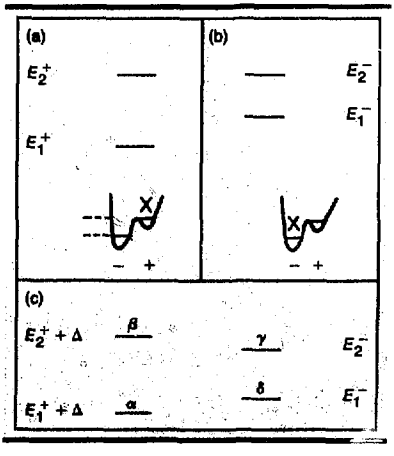

Fig. 7-50. Origin of temperature-dependent sidebands. (a) $^7F_0$ (E_1) and $^5D_0$ (E_2) energy levels of Eu^{3+} with TLS in the + well. (b) TLS in the − well. (c) Four energy levels of the combined TLS + RE system.

to study the kinetics of ligand rearrangement about optically active ions in liquids. FLN involves selective excitation of ions in an inhomogeneously broadened spectral profile by narrow-band radiation typically derived from lasers.

The broadband $^5D_0 \rightarrow {}^7F_0$ emission of Eu^{3+} in aqueous nitrate solution [concentration = 3.4×10^{20} $Eu(NO_3)_3/cm^3$] at room temperature is shown in Fig. 7-51. The remarkable feature is the very narrow width of the band, at less than 6 cm^{-1}. Similar narrow bands have been observed in the absorption of Nd^{3+} in aqueous solutions.[58] Narrow bands can be compared with an inhomogeneous width of more than 50 cm^{-1} for the same transition in oxide glasses.[59]

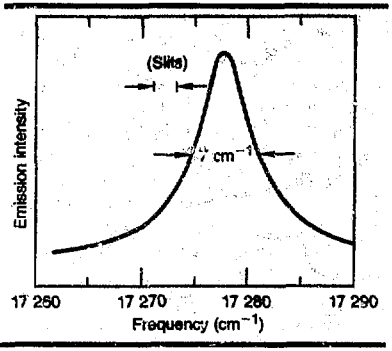

Fig. 7-51. The $^5D_0 \rightarrow {}^7F_0$ emission of Eu^{3+} excited by pumping the $^7F_0 \rightarrow {}^5D_2$ absorption.

Fig. 7-52. RE emission intensity following selective excitation at frequency E_0 + 100 cm^{-1}, where E_0 is the line center for various times following excitation.

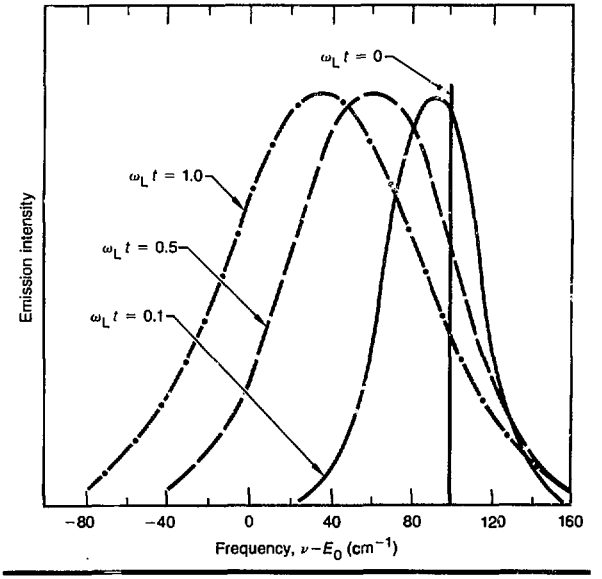

Two possible explanations for the narrow band in Fig. 7-51 are

- The RE forms a very regular molecular complex in the solution so that each RE has the same environment.
- The spectrum is motion-narrowed, analogous to the phenomenon of nuclear magnetic resonance (NMR).

Motion-narrowing arises when ligands move very rapidly relative to inhomogeneous broadening (divided by Planck's constant). At high temperatures, where the viscosity of a fluid is quite small (<1 P), ligand motion can be rapid. Therefore, a relatively narrow emission line, such as that shown in Fig. 7-51, can conceivably be observed even when considerable inhomogeneous broadening exists. As the temperature of the fluid is lowered, however, the rate of ligand rearrangement decreases. If the spectrum is originally motion-narrowed, the emission bands should be observed to broaden until the full inhomogeneous line reappears. Broadening contrasts with the behavior of RE ions in crystals, where emission bands narrow with decreasing temperature.

As temperature is further lowered (to some tens of degrees above the glass transition of the fluid) the time characteristic, ω_L^{-1}, of the ligand motion becomes large compared to the temporal resolution of the experimental apparatus. Thus, at low temperatures, motion of the ligands may be studied using time-resolved FLN. The phenomenon of FLN arises from the fact that, under narrow-band excitation, only a small subset of all the ions that contribute to an inhomogeneously broadened emission band are selectively excited. If the laser pulse is short compared to ω_L^{-1} (the time characteristic of ligand rearrangement), then only those RE ions will be excited that are in instantaneous "sites" having a particular energy-level separation. As time increases, the ligands move about, and the energy levels of the excited ions fluctuate, eventually passing through all the values typical of the inhomogeneously broadened line. Therefore, the excited ions emit at frequencies different from the excitation frequency.

Time and frequency dependence of emission are shown in Fig. 7-52, where the different curves correspond to successive times following excitation. All curves are normalized to the same peak intensity. The

dependence is quite different from that due to energy transfer among a single type of ion[57] (in which the full inhomogeneous line increases in intensity with increasing time relative to the resonant emission)

The results of Fig. 7-52 have been calculated from equations that describe the behavior of RE emission as a function of time. We have derived the relevant equations and used them to show that, by studying the dependence of the evolutionary process on temperature and excitation frequency, information can be obtained about the kinetics of ligand rearrangement for different types of RE-ligand structures. For example, we can determine whether different RE instantaneous sites (part of the same structureless, inhomogeneous line) are kinetically different.

A related question that can be studied is whether the apparent homogeneous width measured at short times is due to the fast mechanical relaxation of ligands. The existence of two different time scales for ligand relaxation is interesting because it relates to the so-called two-level systems (TLS) that exist in many glasses.[60] Recently, it has been suggested[61] that the TLS do not affect RE homogeneous line widths, in contrast to previous suggestions.[62] Fast relaxations would be analogous to the TLS. The determination of such a fast time scale would prove that mechanical relaxations can affect RE homogeneous line widths. On the other hand, the absence of two time scales would indicate that homogeneous widths are not so affected.

Defects and Fluorine Diffusion in Sodium Fluoroberyllate Glass. During our MD simulations of the RE sites in BeF_2-based glasses,[63] we studied the mechanism of fluorine diffusion. The mechanism, which applies to silicates as well, is qualitatively consistent with the following experimental observations

- Oxygen diffusion in vitreous silica increases with increasing pressure.
- The viscosity of fluoride and oxide glasses decreases rapidly with addition of modifier ions.
- The diffusion mechanism is related to the sites of secondary relaxations and to anomalous low-temperature excitations (so-called two-level systems) present in all glasses.[64,65] The latter observation may be important because the homogeneous line widths of RE ions have been observed to vary as T^2, and TLS have been invoked to explain such anomalous behavior.[66]
- The diffusion mechanism may provide an explanation of relative crystallization rates in alkali fluoroberyllates and silicates.[67]

In studies of fluoroberyllate-glass structure,[67] we found Be ions coordinated by five fluorines. In simulated BeF_2 for a glass with a fictive temperature of 1670 K, only about 8% of the Be ions were fivefold coordinated by F. The remaining Be ions were tetrahedrally coordinated by F, so that the structure was qualitatively similar to the continuous, random network often used to characterize silica. In simulated binary glasses, from 30 to 50% of the Be ions were fivefold coordinated by F, depending upon glass composition.

The importance of fivefold-coordinated ions is that a neighboring Be–F pair will separate only if the Be ion is fivefold coordinated. Thus, F diffusion is bound up with the existence of weakly bound defects. A tetrahedral Be ion never becomes threefold coordinated with the loss of F. Since the number of defects in alkali fluoroberyllates is much greater than in pure BeF_2, the diffusion coefficient of the former glass is much larger than the latter.

A mechanism for F diffusion necessarily involves F ions separating from five- or sixfold Be ions. If the separation were all that occurred, then, after the available five-fold Be ions become fourfold coordinated, diffusion would cease (at 1350 K, in 20 ps, some 450 separations occur, involving virtually all the F and Be ions). If diffusion were to continue, then F ions around tetrahedral Be would be required to mobilize in some manner. However, such mobilization is impossible unless such tetrahedral Be becomes five-fold again.

Thus, the diffusion process necessarily involves two steps. First, a four-fold Be is converted to a five-fold Be by an F ion drifting into its coordination sphere. After conversion, a different F ion leaves the coordination sphere of the Be to make it four-fold again. According to the two steps, F ions can be passed from Be to Be without ever having to separate from a four-fold Be ion.

A specific example of a replacement event is shown in Fig. 7-53, where Be–F distance is plotted vs time for the same Be ion

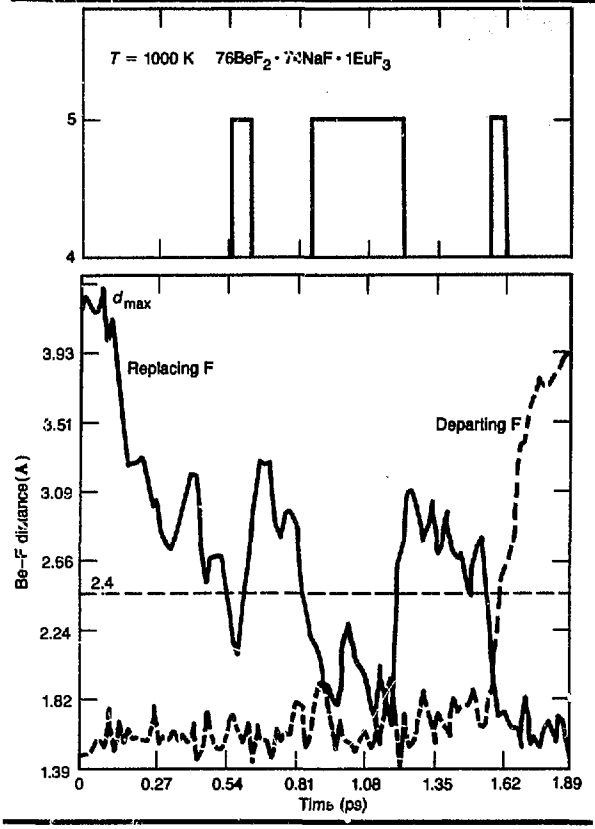

Fig. 7-53. Replacement event showing Be-F distance for two F ions and a single Be ion during an MD run at 1000 K. The coordination number of Be uses a coordination sphere of 2.4 Å.

and two F ions. The figure also shows the coordination number of Be vs time. As the replacing F ion approaches Be, a departing F ion originally close to Be detaches itself and drifts apart. Note that the departing F ion was originally quite close to Be (a typical, but not universal, case). We find scores of replacement examples during 20 ps at all temperatures above 1000 K. The vacillation before final separation is typical of a large number of cases, although a cleaner event is sometimes seen. The coordination number changes whenever one of the ions becomes separated from the Be by more than 2.4 Å. The change reflects the fact that the coordination sphere is defined as 2.4 Å. Similar replacement events have been observed by Woodcock et al.[68] in their simulations of SiO_2.

Replacement events rapidly become less common at temperatures below 1000 K. At lower temperatures, an F ion can still separate from a five-fold Be by a considerable distance, but few such separations are preceded by a replacing F ion. Rather, the ion separate and then often rejoin at a later time, leading to roughly periodic motion. Similar events have been previously described for BeF_2 (Ref. 69).

The activation energy for separations at low temperatures is about 0.1 eV. Defects involving five-fold Be may be responsible for the TLS, which give rise to the low-temperature thermal anomalies of glass[64,65] and may also produce anomalous RE optical properties.[66]

It is interesting that, for BeF_2 glass, the sites giving rise to low-temperature motion are also those giving rise to diffusion at high temperatures—namely, the five-fold Be ions. The same rule is obviously applicable for Na diffusion as well. Anderson et al.[34] qualitatively predicted the connection between diffusion and TLS in their paper on the anomalous low-temperature properties of glass.

Authors: S. A. Brawer, D. W. Hall, and M. J. Weber

Amplifier Development

Flashlamp Research. Xenon flashlamps convert electrical to optical energy with measured efficiencies of 80% (Ref. 70). Because of their high efficiency and simplicity, flashlamps have been used to pump most solid-state lasers since the invention of the ruby maser in 1960. During the 1970s, LLNL and its contractors performed extensive development and optimization on large-bore (1 to 2.7 cm) flashlamps for the pumping of Nd-doped glass lasers. Our work led to the design of lamps used in the Shiva and Nova laser systems. As we now consider the development of a new generation of large aperture ($\geq$1 m) amplifiers, it is appropriate that, in seeking to maximize performance and minimize cost, we reexamine our flashlamp and amplifier designs.

As a first step, we have briefly characterized the 2-cm bore, 48-cm arc-length flashlamp used in the 46-cm Nova amplifier. Our main focus was to contrast a lamp in the amplifier cavity with a lamp removed from the cavity and placed in free space. Thus, we measured the effect of optical

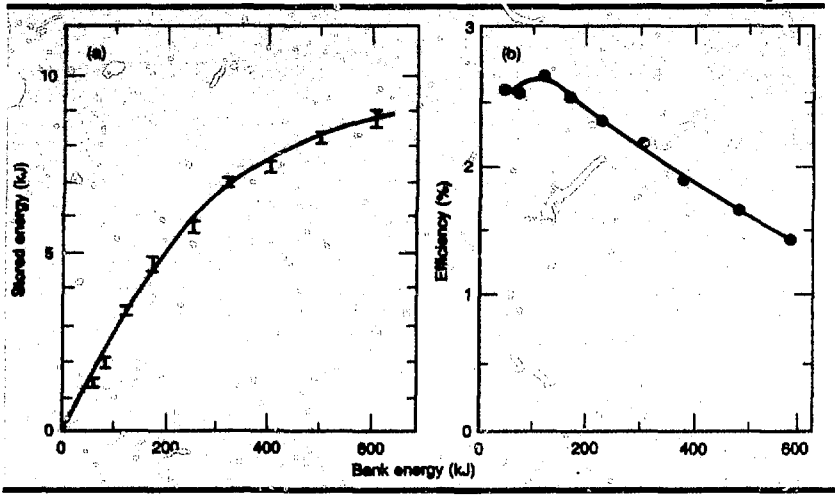

Fig. 7-54. Amplifier characteristics. (a) Energy stored in the 46-cm amplifier vs bank energy. (b) Efficiency (stored energy/bank energy) vs bank energy.

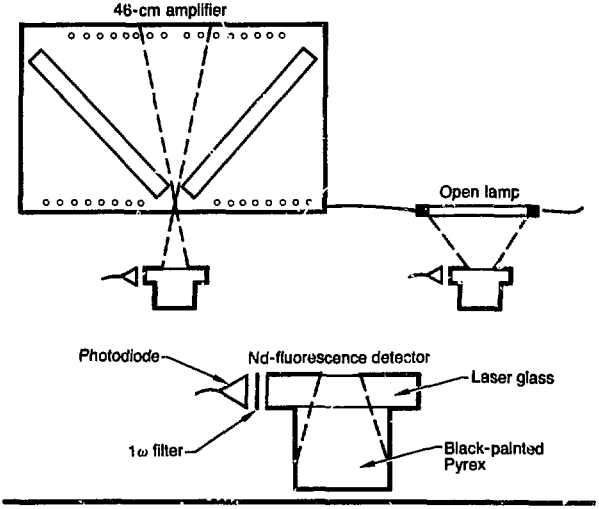

Fig. 7-55. Experimental arrangement for Nd-pumping efficiency of lamps inside or outside a cavity. Enlarged view of Nd-fluorescence detector is shown.

feedback on the lamp and the changes caused in the Nd-pumping efficiency.

The use of the 46-cm amplifier for our characterization was simply a matter of convenience; we expect most large disk amplifiers to behave similarly. The stored-energy vs bank-energy curve for the 46-cm amplifier with fluorophosphate glass is shown in Fig. 7-54(a). The observed decline of amplifier efficiency with input energy, shown in Fig. 7-54(b), is presumed to result from two effects: loss of excited states by amplified spontaneous emission (ASE) at high gain, and a blue-shift of the pumping spectrum with input energy. Our experiments were designed to separate these two effects.

To examine the variation in pumping efficiency of Nd ions with input energy to the flashlamps, we used two simple detectors. The first was a small elliptical laser disk, of Nd-doped fluorophosphate glass with a 4-cm minor diameter, that was installed in the plane of, and adjacent to, the large disk. The small signal gain of the small disk was measured to determine the gain vs bank-energy curve for a small sample pumped under conditions similar to the main disks, but having minimal ASE loss. A second fluorophosphate disk located outside the amplifier was exposed to flashlamp light passing through an aperture in the side wall of the amplifier. Nd fluorescence from the second disk was monitored by a silicon photodiode placed behind a 1.06-μm filter having a 10-nm-wide bandpass. As shown schematically in Fig. 7-55, the disk configuration was similar to previous experiments[70] in that Nd fluorescence (but no flashlamp light) would reach the photodiode. Additionally, 1 of the 80 flashlamps was removed from the cavity, but electrically connected to the rest of the lamps in the cavity. The single flashlamp was monitored by the Nd-fluorescence detector to observe the dependence of Nd pumping without a reflecting cavity surrounding the lamps.

Gain data were reproducible to within 4% and fluorescence data to within 2%. The use of very small gain and fluorescence monitors precludes gain effects, such as

ASE, from influencing the data. Since the disk located outside the cavity is pumped by a very low optical fluence, nonlinear effects, such as excited-state absorption of pump light, could not possibly affect the data either.

As an evaluation of ASE loss, Fig. 7-56 shows the ratio of centerline-gain coefficient of the large disks to peak Nd-fluorescence signal (light from lamps in the cavity) as a function of bank energy. Within experimental error, the peak gain coefficient of the small disk and the peak Nd fluorescence for the detector outside the cavity followed identically shaped curves. We compare, however, the large-disk gain (rather than small-disk gain) to the fluorescence signal because of greater precision obtained from measuring the large-disk gain. Notice in Fig. 7-56 that the ratio of large-disk gain to peak fluorescence declines by no more than 15% with bank energy. Thus, as expected, the effect of ASE and parasitics on the large-disk gain is quite small. (The product of gain coefficient and maximum disk dimension was approximately 2.5.) Hence, ASE is not a major contributor to the observed saturation in amplifier gain with bank energy.

Fig. 7-56. Ratio of large-disk gain coefficient to peak Nd-fluorescence signal as a function of bank energy.

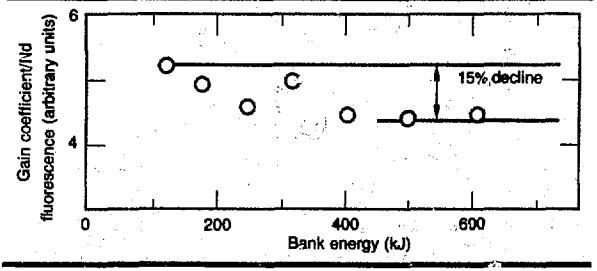

Fig. 7-57. Peak Nd fluorescence vs bank energy for an open lamp and for lamps in the amplifier cavity.

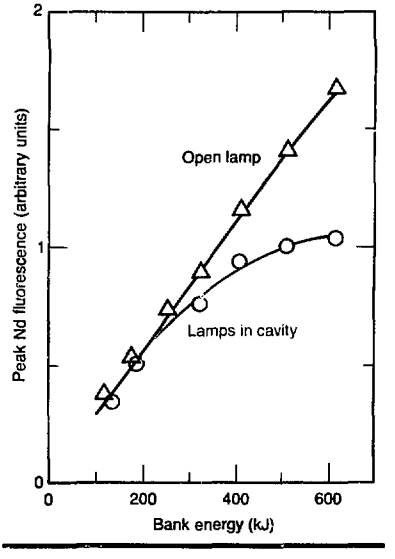

Figure 7-57 shows data from the Nd-fluorescence detector for the lamps in a cavity and for the open lamp as a function of bank energy. The data for lamps in the cavity were normalized to the open-lamp data at low input energy. The observed linearity of the Nd-fluorescence signal with bank energy for the open lamp is in agreement with previous results.[7] However, there is strong saturation of the Nd-pumping efficiency for lamps in an amplifier cavity. It has been generally assumed that the difference in the shape of the two curves arises from increased absorption of cavity light by the flashlamps at higher current density and by a high-power shift to the blue, combined with low cavity efficiency in the blue. Additional input power to the lamps then reduces the cavity Nd-pumping efficiency. The dependence on bank energy of Nd fluorescence pumped by lamps in the cavity was essentially the same as the measured gain coefficient. This similar dependence proves that excited-state absorption of pump light does not produce the observed decline in pumping efficiency. Hence, lamp reabsorption and spectral change of the pump light are of primary importance.

We placed a broadband blue (short-pass) or red (long-pass) filter in front of the Nd-fluorescence detector to observe the change in flashlamp pumping by light over two spectral regions. The division between red and blue was 0.63 μm. The absorption spectrum of the Nd-doped fluorescence detector is shown in Fig. 7-58, for reference. Note that the blue filter allows pumping of the bands at 0.53 and 0.58 μm, while the red filter allows pumping of the bands at 0.74, 0.80, and 0.88 μm.

Figure 7-59(a) shows the peak Nd-fluorescence signal produced by an open lamp using either the blue or red filter. For either filter, the Nd pumping by an open lamp is linear with electrical input energy, similar to the unfiltered open-lamp case shown in Fig. 7-57. However, as shown in Fig. 7-59(b), the dependence of the Nd-

fluorescence signal produced by lamps in the cavity is quite different for the blue and ed filters. Although both curves show saturation behavior similar to the unfiltered lamps-in-cavity case shown in Fig. 7-57, saturation of Nd pumping by the red-filtered spectrum is considerably greater than saturation of pumping by the blue-filtered spectrum.

Our results can be explained qualitatively by a simple picture. Flashlamp spectral emission may be described as a gray body where the output intensity is given by emissivity times blackbody intensity. The temperature of the flashlamp (~1 eV) is known to vary only weakly with pump energy over the range tested.[72] Lamp emissivity, however, is largest at long wavelengths,[72] so that lamp emission first approaches the blackbody limit at long wavelengths as the bank energy is increased. Thus, the emission in the red portion of the spectrum becomes clamped against the blackbody limit, while the blue region of the spectrum continues to increase. Since the primary, and most efficient, pump bands for Nd are in the red portion of the spectrum, Nd-pumping efficiency declines at high input energies. This decline is exaggerated for lamps in a cavity because the lamps form a large fraction of the load in the cavity and are especially absorbing in the red.

We can characterize the total input power to the lamps in a cavity as electrical plus optical energy fed back into the lamps from the cavity. The result of optical feedback is a higher input energy per unit volume for lamps in a cavity. Presumably, additional input energy is recycled with an efficiency less than unity and also causes a greater saturation in the pumping of Nd ions due to blue-shift.

Authors: L. P. Bradley and H. T. Powell

Major Contributors: S. M. Yarema, R. D. Behymer, D. B. Clifton, R. J. Poli, and J. B. Woods

Change in Flashlamp *V–I* Characteristic Due to Reabsorbed Light. Reabsorption of amplifier-cavity pump light by flashlamps is an important process that greatly influences the efficiency of amplifier pumping. We show here that a simple model of the reabsorption process is consistent with measurements of the change of the *V–I*

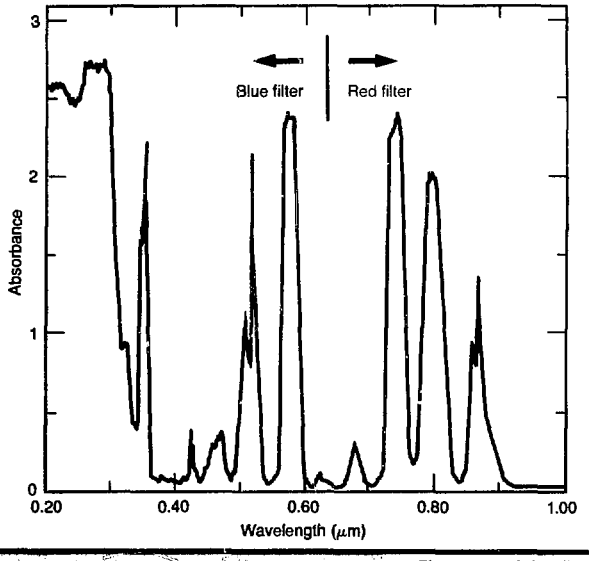

Fig. 7-58. Absorbance of Nd-doped glass sample as a function of wavelength, where absorbance = $-\log_{10}$ (transmission).

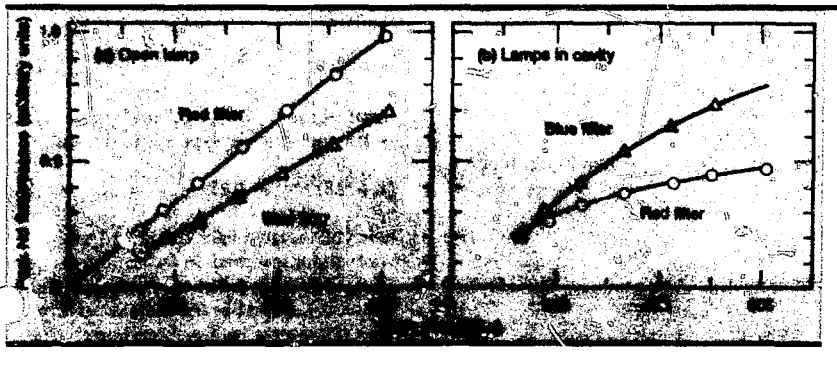

Fig. 7-59. Peak Nd fluorescence vs bank energy with a red or blue filter. (a) Open lamp. (b) Lamps in amplifier cavity.

characteristic when a lamp is strongly self-loaded.

Suppose the resistivity of plasma in a lamp is given by Spitzer's result for a fully ionized Lorentz gas

$$\rho = \frac{\mathcal{E}}{J} = \frac{38\, Z \ln \Lambda}{T^{3/2}} \quad , \tag{7}$$

where Z is the ionic charge ($\sim$1 for singly ionized xenon), Λ is the cutoff parameter ($\ln \Lambda \approx 5$), and T is the temperature. Suppose that the lamp radiates from its surface as a gray body, with efficiency η compared to a blackbody (η accounts for nonopacity and nonradiative losses). The lamp output power is then

$$P_0 = 2\pi R L \eta \sigma T^4 \tag{8}$$

where R is the radius, L is the length, and σ is the Stefan–Boltzmann constant. Input, when electrical only, is given by

$$P_E = \pi R^2 L \mathcal{E} J \quad . \tag{9}$$

Equate the input and supposed output to obtain

$$R \mathcal{E} J = 2 \eta \sigma T^4 \tag{10}$$

and solve for the temperature

$$T = \left(\frac{R \mathcal{E} J}{2 \eta \sigma}\right)^{1/4} \quad . \tag{11}$$

Our only assumption thus far is that η does not depend upon T.

Now substitute T into the Spitzer conductivity to obtain

$$\mathcal{E} \left(\frac{R \mathcal{E} J}{2 \eta \sigma}\right)^{3/8} = 38\, Z \ln \Lambda\, J \quad , \tag{12}$$

which solves to yield

$$\mathcal{E} = (38\, Z \ln \Lambda)^{8/11} \left(\frac{2 \eta \sigma}{R}\right)^{3/11} J^{5/11} \quad . \tag{13}$$

Equation (13) can be written in terms of voltage

$$V = \mathcal{E} L \tag{14}$$

and current

$$I = \pi R^2 J \tag{15}$$

through the lamp, as

$$V = C \left(\frac{L}{D}\right) I^{5/11} \quad , \tag{16}$$

where

$$C = \left[\frac{(152\, Z \ln \Lambda)^8 (\eta \sigma)^3}{\pi^5 D^2}\right]^{1/11} \quad . \tag{17}$$

Note that Eq. (16) is quite close to the commonly assumed V–I characteristic of lamps

$$V = K \left(\frac{L}{D}\right) I^{1/2} \tag{18}$$

with $K \approx 1.3$. Since η appears only to the 3/11 power in Eq. (17), large deviations from the assumed constancy of η can take place without substantial change in the V–I characteristic. Note also that temperature in our model varies according to

$$T \approx I^{4/11} \quad . \tag{19}$$

Now, add the effect of reabsorbed power. Suppose a fraction, f, of the input is reabsorbed, so that total input is

$$P_I = P_E (1 + f) \quad . \tag{20}$$

Equating Eq. (20) to the output again, we easily find that the temperature goes to

$$T = \left[R \mathcal{E} J \frac{(1 + f)}{2 \eta \sigma}\right]^{1/4} \quad , \tag{21}$$

so that, once more,

$$V = C' \left(\frac{L}{D}\right) I^{5/11} \quad , \tag{22}$$

but with

$$C' = C(1 + f)^{-3/11} \quad . \tag{23}$$

Since, at most, f is the radiative efficiency $\sim$ 0.8, the most we expect K to drop is

$$(1 + 0.8)^{-3/11} = 0.85 \tag{24}$$

when all radiated light is returned to the lamp and reabsorbed. In fact, in our model $P_0/P_E = 1 + f$, so that the increase in light output is f as long as the radiative efficiency does not change with reabsorption.

Unpublished data by Holzrichter (see Fig. 7-60) shows that K decreases according to

$$= 0.87\,K \qquad (25)$$

on the average, a value similar to what the model predicts (0.92 for $f = 0.34$).

We expect that changes in the absorption-emission coefficient with loading will cause output (both heat and radiated) to vary in a manner different from a blackbody. We also expect that changes in ionization fraction will cause deviations from the Spitzer temperature-dependence of the resistivity. To include the two effects, we use a more general set of assumptions. First, suppose the lamp output (radiative and nonradiative) comes from

$$P_0 = 2\pi R L A T^p \qquad (26)$$

where p is a power chosen to fit reality. Some value of p (probably $p \approx 4$) will surely work over a reasonable loading range. Then, suppose the resistivity varies as

$$\rho = B\,T^{-Q} \quad , \qquad (27)$$

with Q chosen to fit reality. When we equate input (including reabsorption) to output, we find that

$$V = \left[W (1 + f)^{-1/(B+1)} \right] \left[\frac{L}{D^{(2B-1)/(B+1)}} \right] I^S \quad , \qquad (28)$$

where W is some constant, $B = P/Q$, and $S = (B - 1)/(B + 1)$. To obey the known V-I rule, we must have $S \simeq 1/2$, so that

$$B = \frac{1 + S}{1 - S} \cong 3 \quad . \qquad (29)$$

To keep K from depending too much on D, we must have

$$\frac{2B - 1}{B + 1} \approx 1 \quad , \qquad (30)$$

so that $B \cong 2$. A value of $B \sim 2.5$ will work well. We then obtain

$$\frac{1}{B + 1} \approx 0.25 \text{ to } 0.33 \quad , \qquad (31)$$

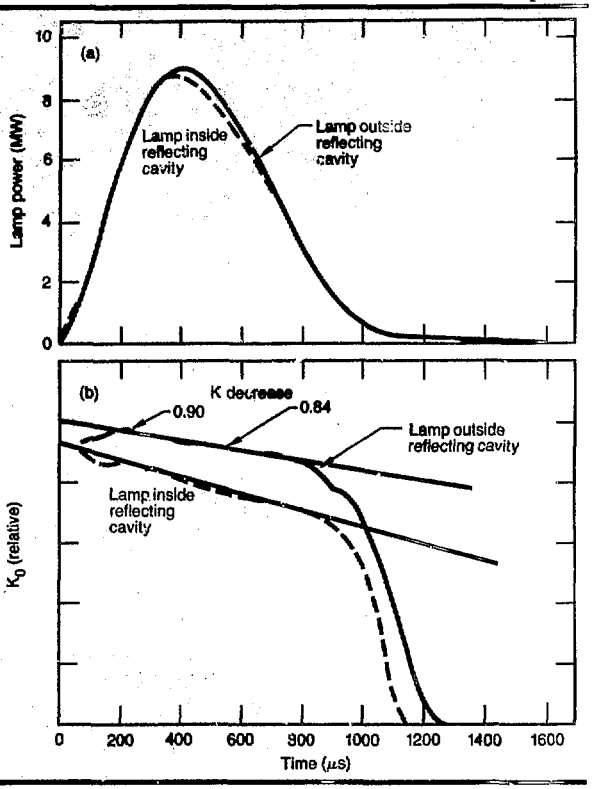

Fig. 7-60. Lamp performance outside and inside a reflecting cavity. (a) Lamp output outside and inside the cavity (b) Lamp constant as a function of time.

which allows a maximum decrease in K (80% radiative efficiency, 100% reabsorption) of

$$(1 + 0.8)^{-1/3} = 0.82 \quad . \qquad (32)$$

With Holzrichter's measured value of $f = 0.34$, we obtain

$$(1 + 0.34)^{-1/4} = 0.93 \quad ,$$

or

$$(1 + 0.34)^{-1/3} = 0.89 \qquad (33)$$

for the decrease in K. The agreement is fair.

How does the change in K affect the bank-lamp circuit? The normalized equations[73] were integrated with $B = 3$ (so that $V = K\sqrt{I}$), assuming f is independent of the lamp current. Figure 7-61 shows the effect on normalized lamp current for various values of f. The calculated increase in current, using Holzrichter's $f = 0.34$, is 1.04.

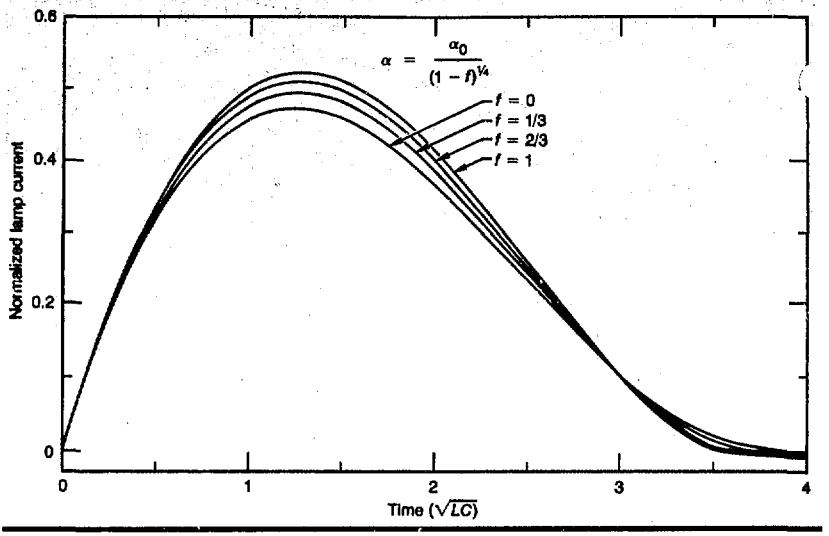

Fig. 7-61. Predictions of a simple model for lamp current as a function of time for various optical feedback conditions.

Even with 100% feedback, the effect on the circuit is small.

Author: J. B. Trenholme

Contributions of Saturation-Fluence Error. When saturation measurements are made in glass, results are often reported as equivalent saturation fluence. It is important to know the error contributions to a quantity so reported. We have, therefore, calculated the effect of errors in measurement of input fluence, output fluence, small signal gain, and transmission on the calculated value of equivalent saturation fluence.

Suppose we know the errors in the measured values taken during a saturation measurement. Specifically, we know

- Input fluence = $\phi_1 \pm \sigma_1$.
- Output fluence = $\phi_2 \pm \sigma_2$.
- Small signal gain = $G \pm \sigma_G$.
- Unpumped transmission = $T \pm \sigma_T$.

When T is near unity, we apply a transmission $K = \sqrt{T}$ at each end of the rod (or disk) and use the Frantz-Nodvik equation to define an equivalent saturation fluence, ϕ_E. The equation

$$\phi_2 = K\phi_E \ln\left[1 + G\left(e^{K\phi_1/\phi_E} - 1\right)\right] \qquad (34)$$

is transcendental in ϕ_E and must be solved by iteration. When T is not near unity, we split the rod into several calculation zones and distribute the losses more uniformly. We perform only the low-loss case in the present analysis.

If errors are Gaussian and independent, they add as the root of the sum-of-squares. If σ_E is the error in ϕ_E, we have

$$\sigma_E^2 = \left(\frac{\partial\phi_E}{\partial\sigma_1}\sigma_1\right)^2 + \left(\frac{\partial\phi_E}{\partial\sigma_2}\sigma_2\right)^2 + \left(\frac{\partial\phi_E}{\partial G}\sigma_G\right)^2 + \left(\frac{\partial\phi_E}{\partial T}\sigma_T\right)^2 , \qquad (35)$$

and, to obtain σ_E, we need several partial derivatives.

For convenience, let

$$A = \frac{K\phi_1}{\phi_E} \quad ; \quad B = \frac{\phi_2}{K\phi_E} , \qquad (36)$$

and recall that the gain left after the pulse is

$$G_S = \left[1 - e^{-A}\left(1 - \frac{1}{G}\right)\right]^{-1} . \qquad (37)$$

Then, we have

$$\frac{\partial\phi_1}{\partial\phi_E} = \frac{\phi_1}{\phi_E} - \frac{\phi_2}{T G_s \phi_E} , \qquad (38)$$

so that

$$\frac{\partial\phi_E}{\partial\phi_1} = \frac{-T G_s \phi_E}{\phi_2 - T G_s \phi_1} .$$

Next, we calculate

$$\frac{\partial \phi_2}{\partial \phi_E} = \frac{\phi_2 - T G_s \phi_1}{\phi_E} \quad , \tag{40}$$

from which we obtain

$$\frac{\partial \phi_E}{\partial \phi_2} = \frac{\phi_E}{\phi_2 - T G_s \phi_1} \quad . \tag{41}$$

The variation with gain gives

$$\frac{\partial G}{\partial \phi_E} = \frac{-Be^B}{\phi_E (e^A - 1)} + \frac{A (e^B - 1) e^A}{\phi_E (e^A - 1)^2} \quad , \tag{42}$$

which, by use of the Frantz-Nodvik equations, is written as

$$G = \frac{e^B - 1}{e^A - 1} \tag{43}$$

and (equivalently)

$$e^B = 1 + G (e^A - 1) \quad , \tag{44}$$

which becomes

$$\frac{\partial G}{\partial \phi_E} = \frac{\phi_2 (G - 1) - G (\phi_2 - T\phi_1) e^{K\phi_2/\phi_E}}{\phi_E^2 \left(e^{K\phi_1/\phi_E} - 1\right) T^{1/2}} \quad , \tag{45}$$

so that

$$\frac{\partial \phi_E}{\partial G} = \frac{\phi_E^2 \left(e^{K\phi_1/\phi_E} - 1\right) T^{1/2}}{\phi_2 (G - 1) - G (\phi_2 - T\phi_1) e^{K\phi_1/\phi_E}} \quad . \tag{46}$$

Finally, variations in transmission are found from the differentiation of

$$e^B - 1 = G(e^A - 1) \quad , \tag{47}$$

which yields

$$\partial \phi_E \left(\frac{G \phi_1 K e^A}{\phi_E^2} - \frac{\phi_2 e^B}{K \phi_E^2}\right) = \partial K \left(\frac{G \phi_1 e^A}{\phi_E} + \frac{\phi_2 e^B}{K^2 \phi_E}\right) \quad , \tag{48}$$

which solves to yield

$$\frac{\partial \phi_E}{\partial T} = \frac{\left(\frac{G\phi_1 e^A}{\phi_E} + \frac{\phi_2 e^B}{K^2 \phi_E}\right)}{2T^{1/2}\left(\frac{G\phi_1 K e^A}{\phi_E^2} - \frac{\phi_2 e^B}{K \phi_E^2}\right)} \quad , \tag{49}$$

where we have used the fact that $K = \sqrt{T}$. Now substitute

$$e^B = 1 + G (e^A - 1) \tag{50}$$

and solve to find

$$\frac{\partial \phi_E}{\partial T} = \frac{-\phi_E \left[G (\phi_2 + \phi_1 T) e^{K\phi_1/\phi_E} - \phi_2 (G - 1)\right]}{\partial T \left[G (\phi_2 - \phi_1 T) e^{K\phi_1/\phi_E} - \phi_2 (G - 1)\right]} . \tag{51}$$

A typical case with values of $G = 8$, $\phi_E = 5\ \mathrm{J/cm^2}$, and $T = 0.9$ yields the curves shown in Fig. 7-62 as input fluence, ϕ_1, is varied. The curves are drawn assuming equal relative errors in ϕ_1, ϕ_2, G, and T. Under our assumption of equality, the errors from the four sources are of comparable magnitude, although errors in ϕ_2 and T are more important than those in ϕ_1 and G. The most important point is that all errors are larger at low fluence, so that the accuracy of the measurement improves as fluence level increases.

Author: J. B. Trenholme

Multipass-Systems Analysis

The next generation of fusion lasers requires efficient energy storage and extraction. Here, we discuss the characteristics of multipass systems in simplified and generalized terms; more specific examples are presented in "Megajoule Lasers," below.

Because high-energy-storage glasses can be used with multipass systems, these systems provide improved overall efficiencies at output fluences that are limited by damage to components. Multipass systems also provide high saturated gains, which reduce the number of stages required for a large

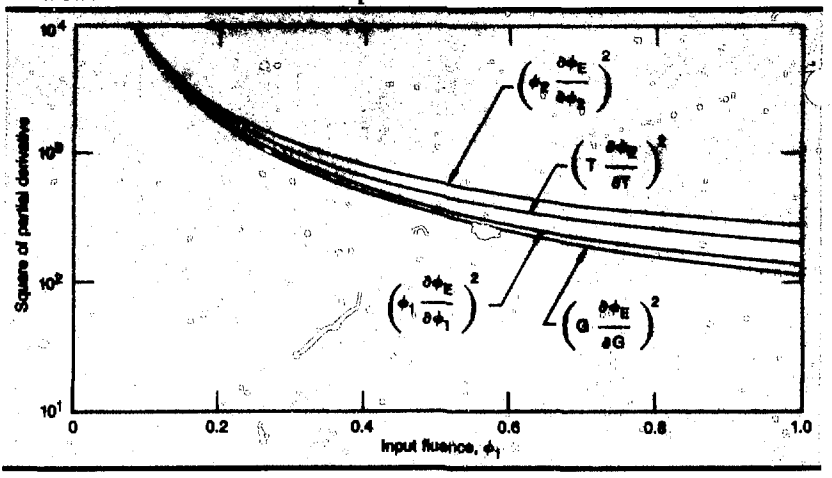

Fig. 7-62. Variance contributions to error in equivalent saturation fluence due to relative errors in ϕ_1, ϕ_2, G, and T.

system and, hence, reduce cost and complexity.

Extraction Efficiency. Multipass laser systems use the same amplifier medium by repeatedly passing the laser beam through the same material. The multipass approach reduces the fluence at which high extraction of stored energy takes place. Because fluence is usually limited by damage to optical components, more efficient extraction of expensive stored energy is possible. However, in the absence of temporal effects, such as lower-level recovery, multipassing does not cause large increases in the highest attainable extraction efficiency. In fact, in a simplified model (in which external-component losses and bulk and surface losses in the amplifier medium are lumped equally before and after each pass through the medium), the maximum extraction efficiency is independent of the number of passes.

To understand how the independence comes about, we model each pass using the Frantz-Nodvik equations.[74] Expressed in terms of the ratio, R, of fluence, F, to saturation fluence, F_s, the equations relate the fluence and gain after pass J and pass $J+1$ by

$$R_{J+1} = \sqrt{T} \ln\left[1 + G_J\left(e^{\sqrt{T}R_J} - 1\right)\right] \quad (52)$$

and

$$G_{J+1} = \left[1 - e^{-\sqrt{T}R_J}\left(1 - 1/G_J\right)\right]^{-1} = G_J e^{-\Delta_J}, \quad (53)$$

where

$$\Delta_J = \frac{R_{J+1}}{\sqrt{T}} - \sqrt{T}\,R_J \quad , \quad (54)$$

where G is the gain, and T is the lumped equivalent transmission of one pass.

In the absence of temporal effects, gain is reduced according to the total fluence, independent of pulse shape, entering the amplifier. The gain after N passes is then

$$G_N = \left[1 - \left(1 - 1/G_0\right) e^{-\sqrt{T}S_N}\right]^{-1} = G_0\, e^{-\sum_1^N \Delta_J} \quad , \quad (55)$$

where

$$S_N = \sum_0^{N-1} R_J \quad (56)$$

and

$$\sum_1^N \Delta_J = \frac{R_N - R_0 + (1 - T)\,S_N}{\sqrt{T}} \quad . \quad (57)$$

The extractable energy per unit area in the medium is

$$F_S \ln G_0 \quad , \quad (58)$$

so that the extraction efficiency, η, after N passes is

$$\eta_N = \frac{F_N - F_0}{F_S \ln G_0} = \frac{R_N - R_0}{\ln G_0}$$

$$= \frac{\sqrt{T}\ln\left[1 + G_0\left(e^{\sqrt{T}S_N} - 1\right)\right] - S_N}{\ln G_0} \quad (59)$$

By simple differentiation, the maximum extraction is at

$$\hat{S}_N = \frac{1}{\sqrt{T}}\ln\left(\frac{1 - 1/G_0}{1 - T}\right) \quad (60)$$

and has the value

$$\hat{\eta} = \frac{\sqrt{T}\ln\left(\frac{G_0 - 1}{1/T - 1}\right) - \frac{1}{\sqrt{T}}\ln\left(\frac{1 - 1/G_0}{1 - T}\right)}{\ln G_0} . \quad (61)$$

Clearly, our result is *independent of the number of passes.*

There are no simple expressions for the fluences at maximum extraction efficiency, but the output fluence must lie between the single-pass result

$$\hat{R}_1 = \sqrt{T}\ln\left(\frac{G_0 - 1}{1/T - 1}\right) \quad (62)$$

and the multipass result

$$\hat{R}_\infty = \sqrt{T}\ln\left(\frac{G_0 - 1}{1/T - 1}\right) - \frac{1}{\sqrt{T}}\ln\left(\frac{1 - 1/G_0}{1 - T}\right) . \quad (63)$$

Figure 7-63 shows how extraction efficiency and the output-fluence ratio are related for various numbers of passes. Note that the maximum efficiency remains the same, but occurs at lower fluence levels as the pass count increases.

Similar results are found if the laser beam is transmitted through lossy amplifiers in the same direction. However, differences occur when the laser beam propagates through a lossy amplifier in alternating directions or when external losses arise from spatial filters or Faraday isolators between stages. The differences of alternating the direction of the beam through the amplifier are relatively small; however, external losses are much more detrimental to a single-pass

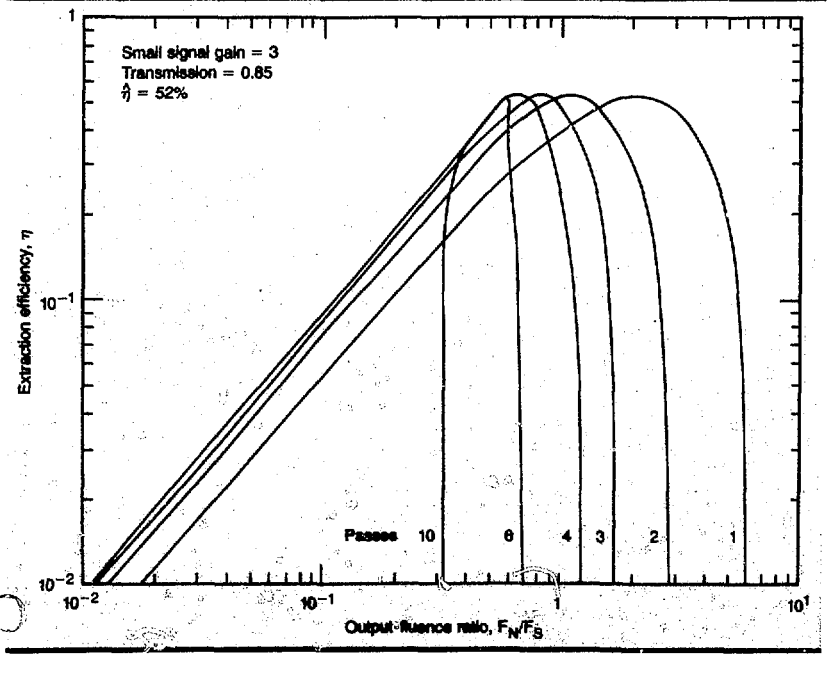

Fig. 7-63. Extraction efficiency as a function of output-fluence ratio, R_N in a lumped-loss multipass amplifier.

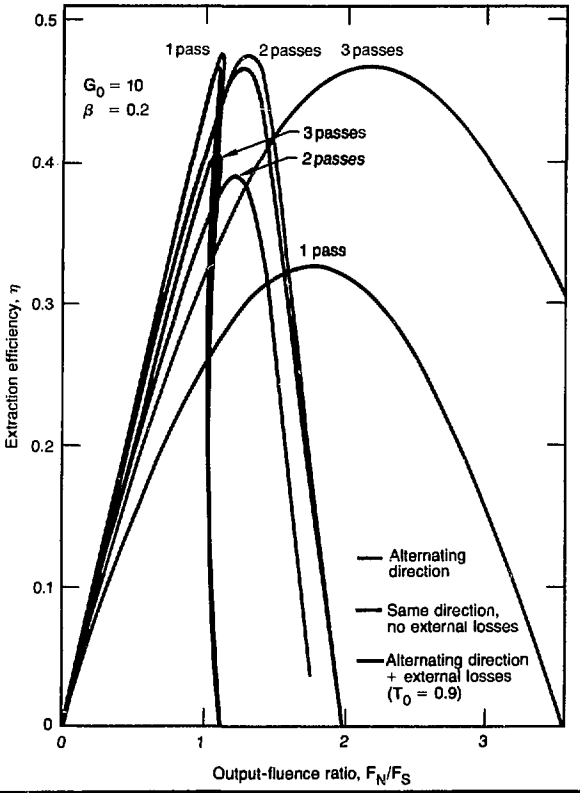

Fig. 7-64. Maximum extraction efficiency increases with each pass for alternating beam direction and with external losses between stages; no increase for one-way propagation through lossy amplifiers.

system than for multipass systems with high saturated gains, as shown in Fig. 7-64. For this example, a loss-to-gain ratio of

$$\beta = \gamma/\alpha \approx -\ln T/\ln G_0 \approx 0.2 \qquad (64)$$

was applied, where α is the gain coefficient, and γ is the effective loss coefficient.

The most significant effect of multipass systems is the reduction in the optimum fluence ratio, $\hat{R}_N$. For an amplifier element ($G_0 T \rightarrow 1$), the optimum fluence ratio is inversely proportional to the number of passes, N. The $\hat{R}_N$ values for multipass systems, in comparison to single-pass systems, are shown in Fig. 7-65. Fluence ratios do increase with gain and loss from their initial values of $\hat{R}_1/N$, but are, in general, lower by a factor of 2 to 3 than for single-pass systems.

The general reduction in fluence ratio provides an important advantage of multipass systems because, while maintaining the same output fluences, it allows the selection of materials with higher saturation fluences. Materials with high saturation fluences have, in general, long fluorescence lifetimes and, hence, improved energy-storage capabilities leading to a significant improvement in overall efficiency for multipass systems.

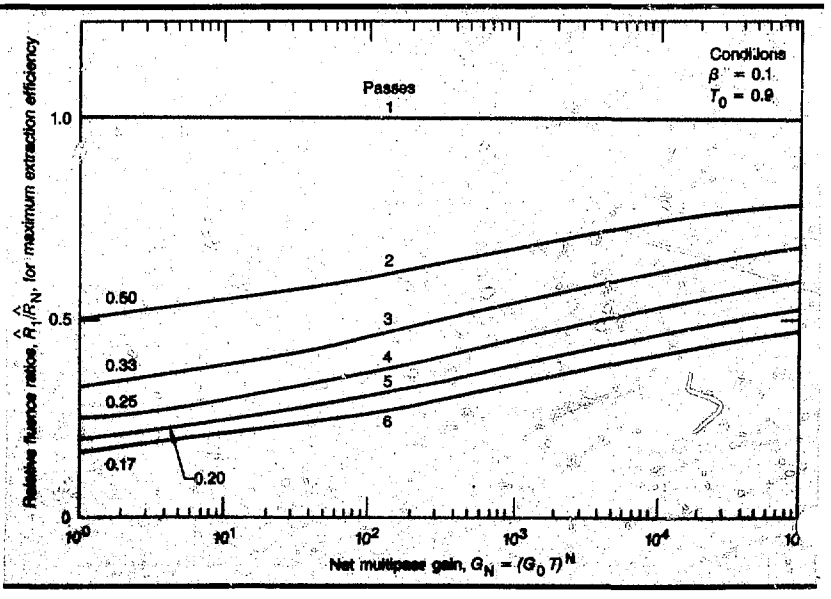

Fig. 7-65. Fluence ratios for maximum extraction efficiency are significantly lower for multipass systems than for single-pass systems. For low gains, fluence ratios are inversely proportional to the number of passes.

For a more general analysis, a simpler approach can be applied by evaluating the extraction efficiency of an amplifier element, dx, at average fluence values $\overline{R} = N\overline{R}_N$ in the form

$$\eta = \frac{d\overline{F}}{\alpha F_S\, dx} = 1 - e^{-\overline{R}} - \beta\overline{R} \quad . \tag{65}$$

Maximum energy extraction is obtained at

$$\overline{R}^* = N\overline{R}_N^* = -\ln\beta \tag{66}$$

and has the value

$$\hat{\eta}^* = 1 - \beta(1 - \ln\beta) \approx \hat{\eta} \quad . \tag{67}$$

The approximation in Eq. (67) is quite accurate for small signal gains of up to 10 and is essential for the independent optimization of amplifiers.

Cost Minimization. Actual laser systems should be designed for the maximum output-to-cost ratio rather than for the point of maximum extraction. Per unit area, output is proportional to the fluence, F_N, after the Nth pass. In our analysis, we model cost as the sum of three terms.

The first term is the cost of the amplifier. The stored energy per unit area is proportional to $F_s \ln G_0$, and the amplifier cost per unit area is

$$C_A = \frac{F_s}{Q_s} \ln G_0 \quad , \tag{68}$$

where Q_s is the cost-effectiveness of storing energy.

From our evaluation of different laser glasses shown in Fig. 7-66, the cost of stored energy in an amplifier was found to be proportional to the square root of the stimulated-emission cross section, σ. A correlation can be approximated for Nd:glass lasers by

$$Q_S = \frac{Q_S^*}{\sqrt{\sigma}} \approx 10\frac{\sqrt{J\,\mathrm{cm}}}{k\$}\sqrt{\frac{F_N}{R_N}} \quad . \tag{69}$$

The second term is fixed cost per unit area, C_F, which does not depend on stage gain, but may depend on the number of passes. The third term is the cost of drive fluence, which we take as $C_D = F_0/Q_D$, where F_0 is the input fluence, and Q_D is the cost-effectiveness of the driver. The ratio of output energy to laser cost is then

$$Q = \frac{F_N}{C_A + C_F + C_D}$$

$$= F_N\frac{1 - k/G_S}{C_A + C_F} = \eta Q_S\frac{1 - \Delta k/(G_S - 1)}{1 + C_F/C_A} \quad , \tag{70}$$

where

$$k = 1 + \Delta k = \frac{Q}{Q_D} \tag{71}$$

is the relative drive-cost factor, and $G_S = F_N/F_0$ is the saturated gain of the output stage.

For any gain, G_0 there is an optimum input-output combination, since low input leads to low extraction efficiencies, while overdrive increases the cost of the driver. Because of fixed costs and drive costs, the highest Q value is at input and output values lower than those that lead to highest extraction efficiency.

Note that the cost-effectiveness of a laser system is dominated by the fluence-limited cost-effectiveness of extracting energy

$$Q_E = \eta Q_S = Q_S^*\sqrt{\frac{F_N}{R_N}}\frac{R_N - R_0}{\ln G_0}$$

$$\approx Q_S^*\sqrt{F_N}\frac{1 - e^{-\overline{R}} - \beta\overline{R}}{\sqrt{\overline{R}}} \quad . \tag{72}$$

With our correlations it is possible to determine the optimum fluence ratios, $\overline{R}^*$, for maximum values of Q_E from

$$\overline{R}^* = \ln\frac{1 + 2\overline{R}^*}{1 + \beta\overline{R}^*} \approx \frac{1.26}{1 + 2.5\beta} \quad , \tag{73}$$

which leads to

$$\hat{Q}_E \approx Q_S^*\sqrt{F_N}\frac{0.64}{1 + 1.9\beta} \tag{74}$$

for single-pass systems. An evaluation of Eq. (72) is shown in Fig. 7-67, along with the fluence ratio for maximum energy extraction corresponding to Eq. (66). It is obvious from Fig. 7-67 that the optimum fluence ratios for maximum cost effectiveness are much lower than for maximum energy extraction. This figure also shows the loss in

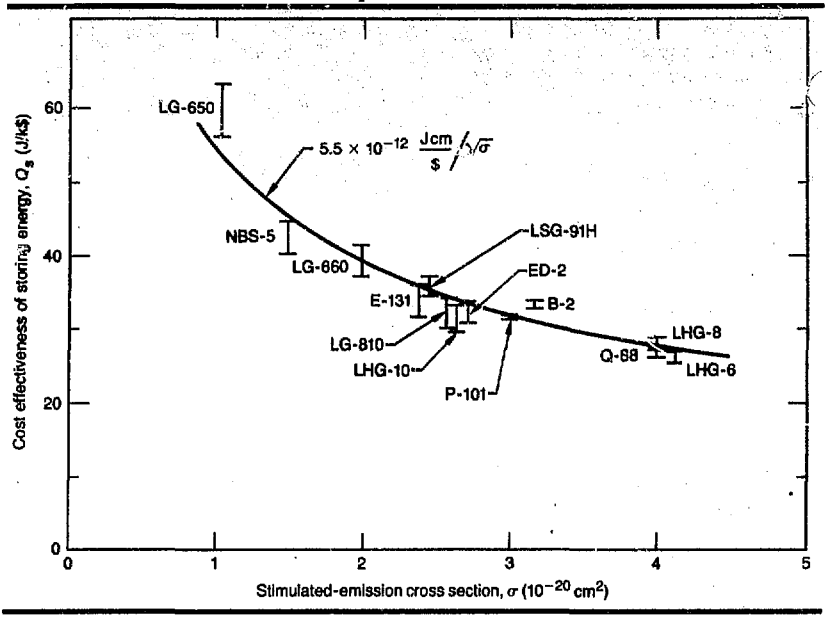

Fig. 7-66. Cost effectiveness of storing energy in large-disk amplifiers (30 ± 10 cm) is inversely proportional to $\sqrt{\sigma}$ for various laser glasses.

extraction efficiency with increasing loss-to-gain ratio corresponding to Eq. (67), while the reductions in the relative Q_E values of Eq. (73) are less severe.

Amplifier Design Considerations. The gain coefficients of Nd:glass disk amplifiers are limited by amplified spontaneous emission and parasitics to typical values of

$$\alpha = \frac{p}{n\hat{D}} \quad , \tag{75}$$

where $\hat{D}$ is the major axis of the disk and p is a numerical coefficient, $p \approx 4 \pm 1$. The loss coefficients are determined by impurities and are in the range of

$$\gamma \approx 0.2 \pm 0.1\, m^{-1} \quad . \tag{76}$$

High gain coefficients can be obtained by segmentation, which improves the extraction efficiency, but reduces the fill factor

$$f = \left(1 - \frac{\Delta D}{D}\right)^2 \quad , \tag{77}$$

where ΔD is the reduction in the clear aperture, D, for alignment and apodization. From these trade-offs, it is possible to determine an optimal disk size, D_o, which can be approximated for $\Delta D \ll D$ by

$$D_0 \approx \left[\frac{2p\,\Delta D(1 - e^{-\overline{R}^*})}{n\,\gamma\,\overline{R}^*(1 + n^2)^{1/2}}\right]^{1/2} \approx \left(1.8\,\frac{\Delta D}{\gamma}\right)^{1/2} \tag{78}$$

for $n \approx 1.5$ and $\overline{R}^* \approx 1.1 \pm 0.1$. For example, a 0.5-cm-wide rim around each segment leads to optimal segment sizes of 30 ± 10 cm for the above-nominal conditions. Smaller segments have lower fill factors, while larger segments have poorer extraction efficiency due to lower gain coefficients.

Figure 7-68 shows the evaluation of Q_E for various numbers of passes and small signal multipass gains, but with equal output fluences. Optimal amplifier gains do exist that balance extraction efficiency with storage efficiency. Lower gains lead to higher drive costs and poor extraction, while higher gains lead to higher fluence ratios, higher emission cross sections and, hence, reduced energy-storage efficiency.

The improvement in the performance-to-cost ratio is due to the reduction in the optimal fluence ratio, R_N^*, with increasing number of passes, as shown in Fig. 7-69 for several cavity-transmission values, T_o. The fluence ratio of the optimal six-pass system is lower (by a factor of about 4) than for the optimal single-pass system. The lower value

leads us toward a laser glass with a four-times-lower stimulated-emission cross section and, hence, a much higher energy-storage efficiency. The optimum stimulated-emission cross section can be determined from

$$\sigma^* = \frac{h\nu}{\kappa F_S} \approx \frac{[2.2 \times 10^{-19}\ J]\ R_N^*}{F_N}$$

$$\approx 1 \times 10^{-20}\ cm^2 \qquad (79)$$

for a fluence limit of $F_N \approx 20$ J/cm^2 and an effective degeneracy factor $\kappa = 1 + g_u/g_l \approx 1.3 \pm 0.3$, which depends on the fluence through the amplifier and the composition of the glass. The dual-ion-saturation characteristics observed for Nd:glass have not yet been included in our analysis because the scaling to different glasses is not well established and because the complexity of dual-ion saturation obviates a general analysis.

From our simplified analysis, it appears possible to realize at least a 50% improvement in cost-effectiveness with multipass systems. The relative improvement is sensitive to cavity-transmission losses. A lossless system would allow a relative improvement proportional to the square root of the number of passes, corresponding to an inverse relationship of the fluence ratios. The most significant loss in cost-effectiveness is observed for the first 10% loss in cavity transmission due to the spatial filter, mirrors, and switch.

While the cost of the driver, as well as the fixed cost and vignette for off-axis geometries, has been ignored here, those correctional terms are included in "Megajoule Lasers," below. Such terms contribute <10% variations and have little effect on a relative comparison, since the higher fixed cost of multipass systems is compensated for by the higher drive cost of single-pass systems. Only a detailed layout and cost analysis would resolve the contribution of such correctional terms; however, such an analysis has not yet been completed.

Our analysis assumes that all systems operate at the same output fluence, since high-reflective (HR) and graded-index coatings have similar damage thresholds. At present, HR coatings have damage thresholds that are about 20 to 40% lower than bare surfaces for 1-ns laser pulses and 1ω light. Data are insufficient to scale to longer pulse durations and shorter wavelengths. If HR and graded-index coatings do not remain close to the damage threshold of bare surfaces, then beam expansion with an uncoated element may provide the highest performance-to-cost ratio, despite the higher losses.

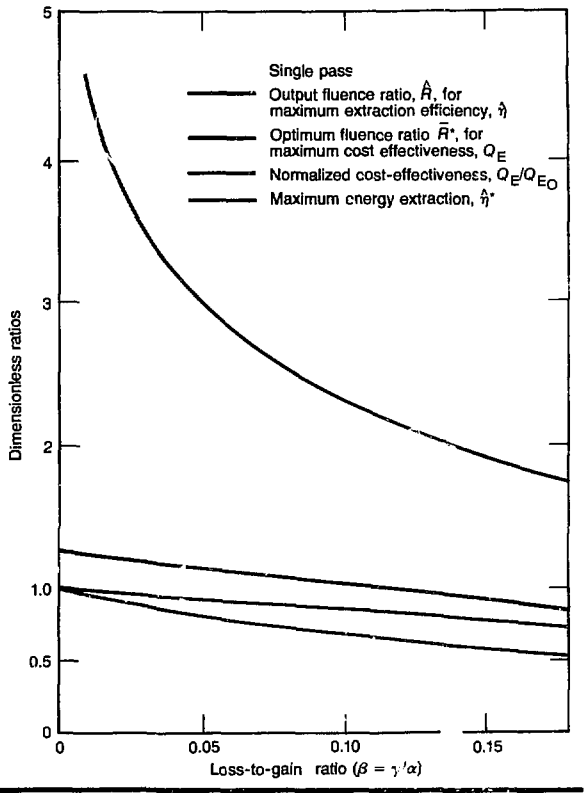

Fig. 7-67. Fluence ratio for maximum energy extraction is several times larger than the optimum fluence ratio for maximum cost effectiveness. Reduction in extraction efficiency with increasing losses is also greater than reduction in cost effectiveness.

In addition, issues regarding beam propagation need more detailed analysis and experimental verification. The number of passes are probably limited by optical distortions. Optical distortions in multipass systems will be larger than for single-pass systems because the laser beam samples a larger volume of laser glass. On the other hand, multipass systems have strong output-fluence-limiting characteristics that should significantly reduce the intensity modulations on the beam. Multipass systems could then operate at much higher average fluences than single-pass systems, so that any potential differences in the damage

Fig. 7-68. Optimum multipass gain increases with number of passes, even though amplifier gains are reduced. Improvement in performance-to-cost ratio for multipass systems is primarily due to improved energy storage.

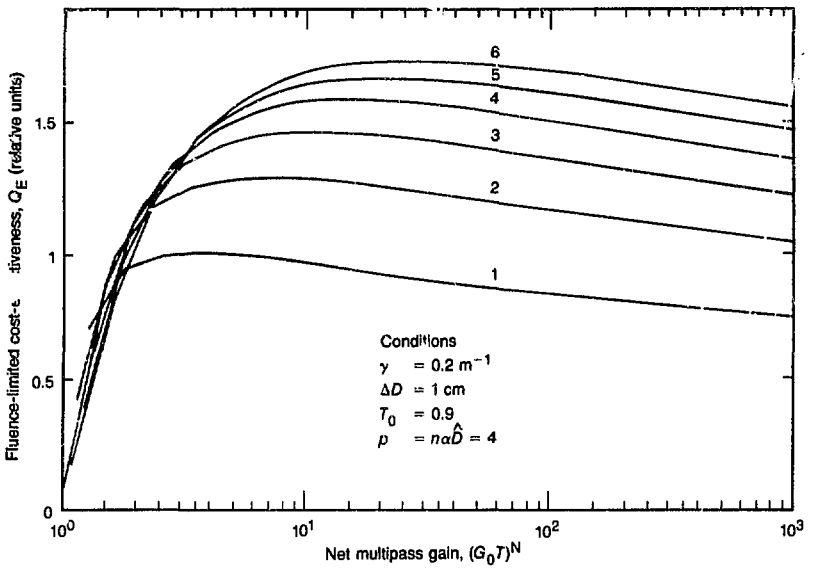

Fig. 7-69. Reduction in optimum fluence ratio R_N with increasing number of passes allows the selection of low-cross-section, high-storage glasses. R_N for a lossless system is inversely proportional to the number of passes.

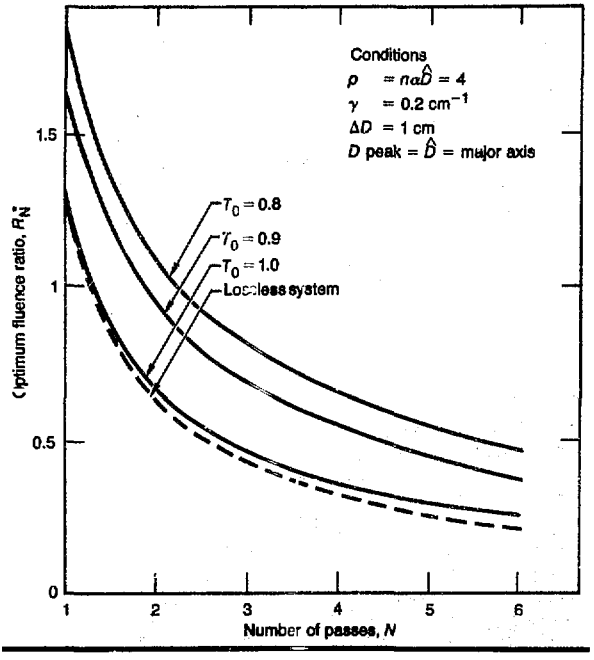

thresholds of AR vs HR coatings could be easily outweighed. In principle, it should be possible to obtain very smooth beam profiles with multipass systems.

The combination of high cost-effectiveness, high saturated gains, simplicity of operation, and a potentially smooth beam profile provides distinct advantages for the use of multipass systems.

Authors: W. F. Hagen and J. B. Trenholme

Megajoule Lasers

The trend in the design of fusion lasers is toward higher energies and longer pulse durations. For megajoule lasers with pulse durations in the 10-ns range, the primary constraints are damage limitations and cost. Nonlinear effects, which greatly influenced the design of the Shiva and Nova lasers, become less important with ~10-ns pulses. For long pulse durations, it is possible to increase the overall efficiency for Nd:glass lasers by an order of magnitude because efficient energy storage and extraction can be obtained. For short-pulse lasers, only a small fraction of the stored energy could be extracted due to nonlinear limitations. High-gain glasses were then preferable, despite their low energy-storage efficiencies.

The change in emphasis also leads to changes in system architecture and makes

multipass systems more attractive. These systems provide high extraction efficiencies from high-storage materials at damage-limited output fluences. The optimum glass for a multipass system will have a much lower emission cross section and, hence, a significantly higher storage efficiency than the glass for a single-pass system.

Multipass systems also provide high saturated gains, which reduce the number of stages required for a large system and, hence, reduce cost and complexity. In addition, it should be possible to obtain relatively smooth beam profiles because multipass systems operate at nearly maximum energy extraction, where the output fluence is essentially independent of the input fluence over a large range.

Critical issues concerning multipass systems are the optical distortions accumulated for many passes and the isolation characteristics. However, many options exist, and only a few passes are required to take advantage of efficient extraction at reduced fluence ratios. Additional passes only reduce the input energy from a few percent of E_{out} to an insignificant fraction of E_{out}, while accumulating more distortions and increasing the risk of self-oscillation.

Multipass Geometries. While many multipass systems have been evaluated in the past,[75] their geometries fall into two distinct categories

- Regenerative type amplifiers (REGEN).
- Off-axis multipass geometries.

The REGEN geometry requires a fast optical switch to inject and extract the laser beam from the cavity. The laser beam retraces its path exactly and could be amplified in a cavity for a very large number of passes. The advantage of such a configuration is that it could potentially eliminate all preamplifier stages of a system. However, the optical distortions may limit the number of passes because the laser beam would sample a much greater volume of laser glass than for an expanding linear-chain design. In addition, with present state-of-the-art technologies, it is unlikely that we can provide sufficient isolation for a REGEN system.

Off-axis multipass geometries eliminate or reduce the requirements on the optical switch, but limit the number of passes. The limit is tolerable because many of the advantages of multipass systems can be realized in a few passes. Thus far, the most cost-effective option consists of a system whereby the laser beam is separated in the far field by tilting one mirror of a reimaging cavity containing a spatial filter and a harmonic converter for an output coupler.

Far-field Separation Systems. Multipass systems with far-field separation are designed for injection of the laser beam close to the focus of the spatial filter and relay system, as shown in Fig. 7-70. The size of injection optics is determined by the ratio of the fluence limitation relative to the output optics and the saturated gain of the system. The small angular separation required for these optics leads to vignette losses in the amplifiers by reducing the effective clear aperture in one plane. Vignette losses are proportional to the total angular separation of the beams and the length-to-diameter ratio of the amplifier. An optimal design is obtained by balancing the saturated gain

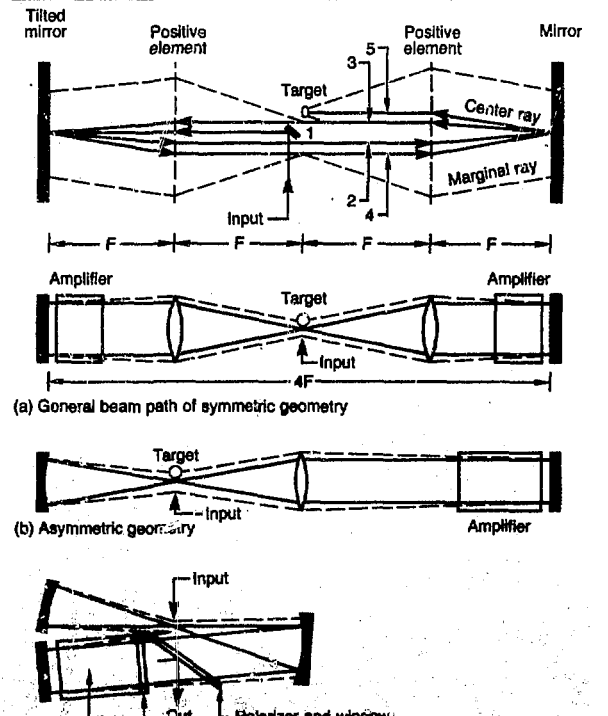

Fig. 7-70. Far-field separation geometries. Symmetric geometries provide better performance, while asymmetric geometries are less costly.

against the length of the amplifier, while the f/No. of the spatial-filter is traded off against the cost of the spatial filter and length of the laser bay.

There are basically two options in placing the components of a far-field system: the symmetric arrangement shown in Fig. 7-70(a), and the asymmetric arrangements shown in Figs. 7-70(b) and (c). The two options differ with respect to vignette losses and accumulation of nonlinear phase retardation, B. For systems of equal overall length and gain, the vignette losses are twice as high for the asymmetric approach because the equivalent amplifier is twice as long. In addition, the B accumulation in the last pass is significantly larger for the asymmetric approach. These two effects cannot be ignored and probably outweigh the simplicity and lower cost of the asymmetric approach. For our analysis, the symmetric geometry has been selected.

Three options for injecting and extracting the laser beam are shown schematically in Fig. 7-71. Option 1 is illustrated in Figs. 7-71(a) and 7-72. The laser beam is injected via a small mirror near the focal plane of the cavity, and the amplified beam is directed onto the target at or near the focus of the last pass. A second or fourth harmonic converter increases the separation between target location and pinholes by about 1 m for typical cases. The improved access for target diagnostics is illustrated in Fig. 7-72.

Fig. 7-71. The high angular sensitivity of harmonic converters provides an effective switch for off-axis geometries.

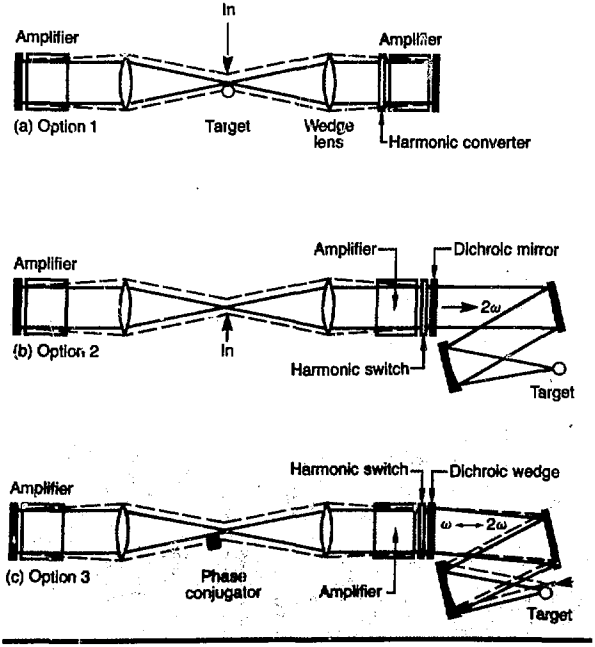

Option 1 has the least number of components and, hence, the lowest cost. Several systems could be arranged at different angles relative to each other to illuminate the target in relatively close bundles or at large angles. However, the flexibilities in target irradiation are somewhat limited, and some compromise in selecting an f/No. for the lenses may be required to satisfy requirements of both spatial filtering and focusing.

Option 2 [see Fig. 7-71(b)] applies the same injection of the beam, but provides the flexibility of external focusing optics at a significant increase in cost. Here, we employ a dichroic mirror or polarizer to transmit or reflect the laser beam, which is harmonically converted to 2ω or 4ω. The damage limits of the required dichroic coatings are presently uncertain.

Option 3 [see Fig. 7-71(c)] injects the laser beam near the target and uses a phase conjugator near the focus in the multipass cavity. The phase-conjugated beam then retraces its path toward the target. The target position is displaced from the point of beam injection by dispersion obtained with a wedged element. Option 3 could reduce the optical distortions in a multipass system, but has target-access limitations that are similar to Option 1. Option 3 is clearly more complex and costly. At present, it is difficult to assess whether phase conjugation provides a sufficiently large payoff.

Performance Analysis. The performance simulation of all far-field-separation systems is quite similar, since the harmonic converter is, in all cases, the last element. Thus, losses and conversion efficiency affect all systems in a similar manner.

The design of multipass far-field-separation systems with harmonic conversion is confined to a limited regime bounded by

- Fluence limitations.
- Linear beam aberrations.
- Nonlinear effects.
- Vignette losses.
- Transmission losses.
- Amplified spontaneous emission.

- Isolation.
- Spatial filter requirements.
  Discrimination against SHG in previous passes.

Most of the constraints limit the performance of the system simultaneously.

In general terms, the performance analysis can be done by trading off energy storage, energy extraction, vignette losses, and relative cost fixed-output fluences and loss-to-gain ratios. For our analysis, an average output-fluence limitation of 20 J/cm^2 was applied. The saturation fluence was approximated by $F_s = h\nu/\sigma$, and a loss-to-gain ratio of $\beta = -\ln T/\ln G_0 = 0.1$ was used as a typical example.

The assumption that the damage threshold on the input mirror or phase conjugator is equal to the damage threshold on the cavity mirrors requires that beam-area ratios be equal to the saturated gain, G_S, of the system. The beam-diameter ratios are

$$\frac{d}{D} = \theta F_\# = \frac{1}{\sqrt{G_S}} \qquad (80)$$

where θ is the angle between adjacent beams and $F_\#$ is the f/No. of the spatial filter. Obviously, we would like high saturated gains to reduce the size, d, of the input mirror and the losses due to vignette, which are determined by

$$v = \theta(N-1)\frac{L}{D} \approx \theta(N-1)\,nN_D \quad , \qquad (81)$$

where N is the number of passes, L/D is the length-to-diameter ratio of the amplifier, n is the index of refraction, and N_D is the number of disks along the beam. Note that vignette losses are independent of the clear aperture, D, which applies for single-disk amplifiers as well as segmented amplifiers consisting of many identical rectangular segments.

The number of disks depends simply on the required small signal gain, G_0, of the amplifier and the logarithmic gain per disk, g_0, which can be scaled with the stimulated-emission cross section, σ, by

$$g_0 \approx 1.5 \times 10^{-11}\ \mathrm{cm}^{-1}/\sigma \quad . \qquad (82)$$

Vignette losses are

$$v = \frac{n(N-1)}{g_0 F_\# \sqrt{G_S}} \ln G_0 \qquad (83)$$

for all cases where the angular separation is determined by damage to the input mirror. However, other constraints on angular separation must be satisfied. To provide sufficient beam separation for spatial filtering, the angle θ was limited to values above 10 times the diffraction limit of 20-cm segments, or $\theta \geq 10\,\theta_D \approx 20\,\lambda/D \approx 0.1$ mrad.

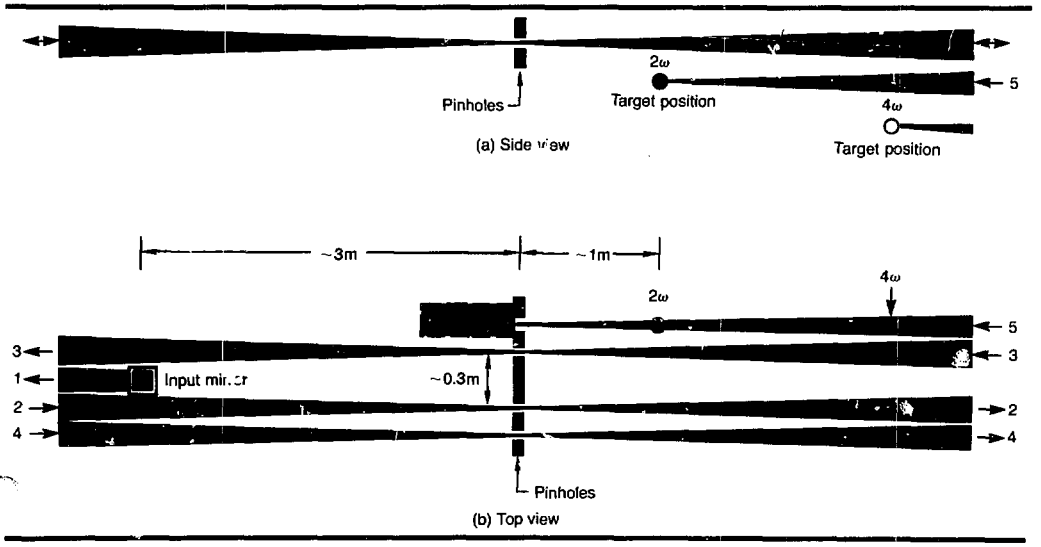

Fig. 7-72. Expanded view of the focal area containing pinholes, input mirror, and target. Several feet of separation between components should prevent serious interference.

For a second-harmonic output coupler, the angle θ or $\theta_N = (N - 1)\,\theta$ must be sufficiently large to prevent significant conversion in the previous pass. The angles are in the range of a few milliradians and, hence, dominate the above considerations of diffraction and spatial filtering. The optical arrangement shown in Fig. 7-70(a) provides an angular separation of $(N - 1)\,\theta$ for the last two passes and, hence, is preferable to the reverse arrangement, where the last two passes are only separated by θ.

To reduce second-harmonic losses, the angle $(N - 1)\,\theta$ should be selected close to a high (ith) order zero of the SHG angular-tuning curve, which is determined for Type I KDP crystals and 1.06-μm light by

$$\theta_i \approx 1.2 \text{ mrad cm} \frac{i}{l} \approx (N - 1)\,\theta \qquad (84)$$

where l is the effective crystal length. The first zero of the SHG tuning curve depends, to a large degree, on the beam intensity and, hence, is not suitable for effective discrimination. To avoid SHG losses, we limited the angle $\theta_N = (N - 1)\,\theta$ in our analysis to values greater than 2 mrad.

An upper limit on the angle θ is set by optical aberrations caused by the off-axis beams. The angular blur-circle diameter can be approximated by

$$\theta_B \approx \frac{\theta_N^2}{8F_\#} = \frac{[(N - 1)\theta]^2}{8F_\#} = \frac{(N - 1)^2}{8G_S F_\#^3} \qquad (85)$$

and was kept below 10 μrad to avoid beam degradation. This constraint is usually satisfied for cost-optimal designs with $\theta <$ 10 mrad and does not impose any serious limitations.

The selection of a cost-optimal f/No. was obtained by trading off the vignette losses against the fractional cost of the spatial filter and laser bay, which was approximated by

$$\frac{\Delta C}{C} \approx 0.06 \frac{F_\#}{1 + N_D} \qquad (86)$$

Our scaling is based on the cost analysis of Nova components and a cost of \$200/ft^2 for a section of the laser bay, which is twice as wide as the beam. A lower limit on the f/No. was set such that the amplifier would only occupy one-half of the space between the lens and the mirror to maintain good reimaging qualities.

Another very important, but somewhat uncertain, constraint is the total small signal

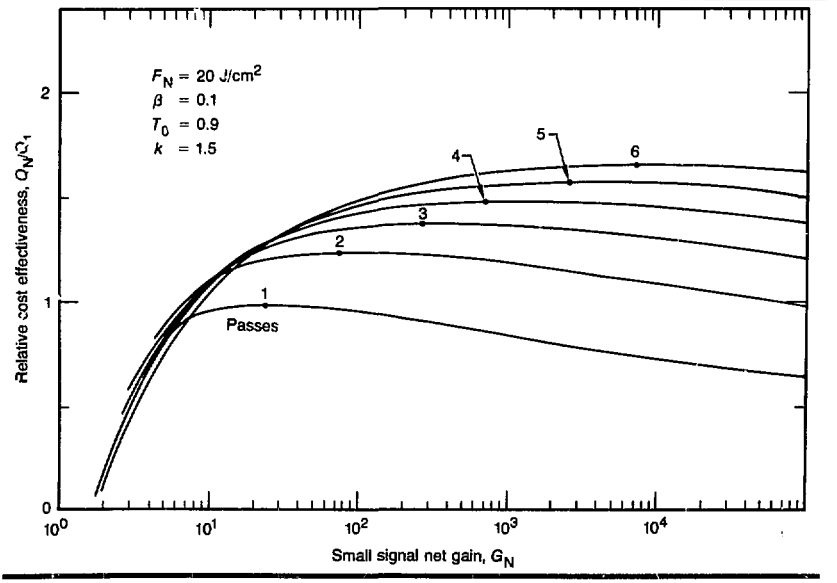

Fig. 7-73. Relative cost effectiveness of various multipass systems as a function of small signal net gain.

net gain, G_N, of the multipass system, which can be maintained without self-oscillation. Typical values are in the range of 40 to 50 dB, which means

$$G_N = (G_0 T)^N < 10^5 \quad , \tag{87}$$

where G_0 and T are the single-pass small signal gain and transmission of the multipass system, respectively.

With our assumptions and constraints, the system is quite well defined and can be optimized for maximum efficiency or highest cost-effectiveness. The multipass systems were evaluated for various values of G_N, which makes it easier to compare various systems for similar isolation constraints.

The relative cost-effectiveness of optimized multipass systems is illustrated in Fig. 7-73. A 66% improvement in the performance-to-cost ratio is obtained for a six-pass system operating at a multipass small signal net gain of $G_N \approx 10^4$. Figure 7-74 shows the corresponding saturated gains, which do not increase significantly after several passes for identical isolation requirements. The most cost-effective systems are marked by a dot along each curve. The optimal saturated gains are below 1000. The balancing of vignette losses and saturated gain leads to a reduction in the extraction efficiency for low-gain systems, as shown in Fig. 7-75. The vignette losses are typically below 10% for cost-optimal designs. The product of optimal extraction and vignette is essentially independent of the number of passes.

The optimal fluence ratios for multipass systems are much lower than for single-pass systems, as shown in Fig. 7-76. The corresponding stimulated-emission cross sections range from 2 to 1×10^{-20} cm^2 for one- to six-pass systems, respectively leading to glass compositions with higher energy-storage capabilities. The improved energy storage provides the primary advantage for multipassing, since improvements in extraction efficiency are almost compensated by vignette losses. The corresponding cost-optimal f/Nos. are displayed in Fig. 7-77, where the constraint $F_\# > 2L/D$ becomes effective for $G_N > 10^4$, and the blur-circle limitation, θ_B, for $G_N < 5$. Lower f/Nos. increase the vignette losses, while longer spatial filters become too costly. The constraints due to astigmatic distortions, reimaging quality, spatial filtering, and harmonic conversion are satisfied in all designs.

The specifications of the most cost-effective multipass systems are summarized in Table 7-12. The required amplifier gain, G_0 for the single-pass system is much higher than for multipass systems and leads to higher transmission losses. The saturated gain, G_S, however, is small in comparison to

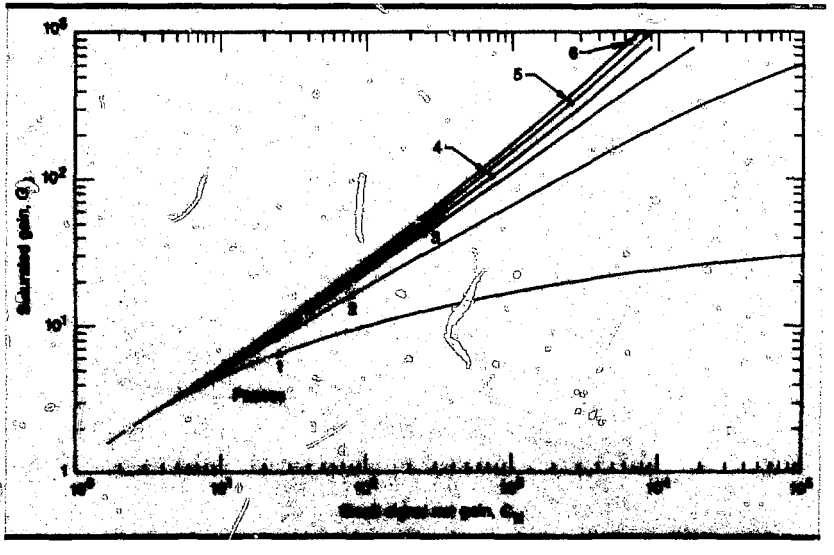

Fig. 7-74. Saturated gains of cost-optimal multipass systems are below 1000. Isolation requirements may limit saturated multipass gains to somewhat lower values without significant reduction in cost effectiveness.

multipass cases. The extraction efficiency, η is quite similar, while the optimal saturation fluence, F_S increases with the number of passes. Cost decreases with increasing number of passes because lower-gain amplifiers are required for multipassing. The end

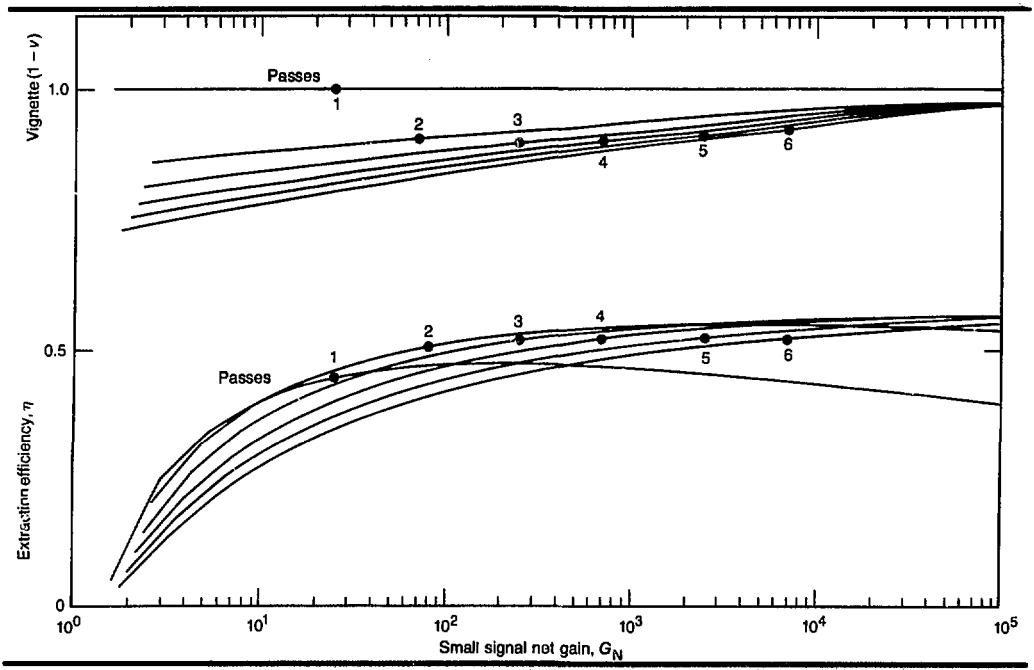

Fig. 7-75. Vignette losses decrease with increasing gain. Optimal extraction efficiency increases for the first few passes, but remains constant (~52%) for additional passes.

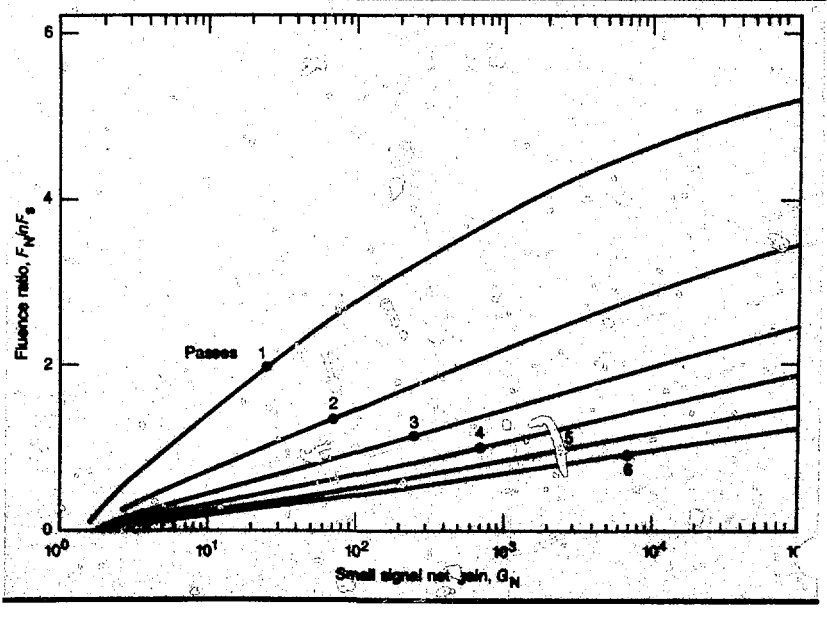

Fig. 7-76. The cost optimal fluence ratio decreases with number of passes.

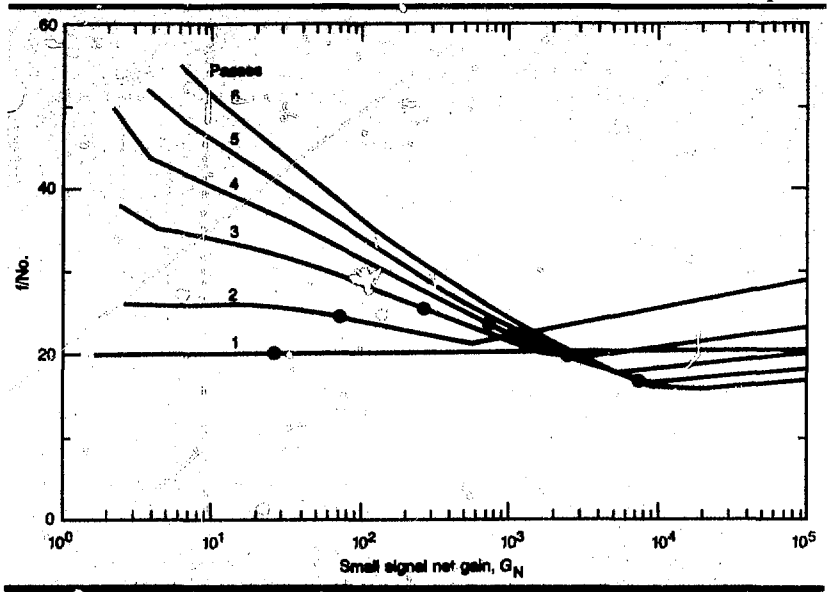

Fig. 7-77. The f/Nos. of cost-optimal designs are in the range of 20 ± 5.

Table 7-12. Specifications of the most cost-effective multipass systems.

result leads to about a 66% improvement in cost-effectiveness for a six-pass system in comparison to the single-pass case. The number of passes is primarily limited by optical distortions that require experimental determination.

Our estimated improvements depend somewhat on the maximum output fluence, cavity transmission, loss-to-gain ratio, and relative drive-cost factor. In addition, adjustments are necessary because of differences in system architecture. However, from our analysis to date, a 50% improvement for multipassing appears to be quite realistic.

A cost-optimal six-pass system could provide a saturated gain of about 900 at an overall efficiency of approximately 2%. The system would operate at an extraction efficiency of 52% and a vignette loss of 7%, corresponding to f/17 optics. The ratio of output fluence to saturation fluence is about 0.9, which corresponds to an emission cross section of 10^{-20} cm^2 for an average output-beam fluence of 20 J/cm^2 and an effective degeneracy factor of $k = 1.3$. The system would require two five-disk amplifiers, each providing a small signal gain of 2.4. A 2-m-aperture device would consist of about 500 square segments with a total volume of 2 m^3. The amplifiers would occupy half of the space between the lens and the mirror. The angle between adjacent beams is about 5 mrad, which translates to a blur circle of less than 3 μrad.

Megajoule lasers using segmented amplifiers with clear apertures of about 2 m would extend over 150 m in length. Such a system operating at an average fluence of 20 J/cm^2 could produce 1ω output energy of 0.5 MJ per beam. A 5-MJ system would

require about 20 m^3 of laser glass and 250 MJ of bank energy. Such a system could be built now without requiring any technical breakthroughs or major developmental efforts.

Author: W. F. Hagen

Advanced Lasers

Rare-Gas Halide Kinetic Studies

Excimer lasers operate on radiative transitions of molecules in which the upper state is bound and the lower state is repulsive. We label these excited molecules (excimers) by an asterisk. During 1981, we extended our earlier studies[76] of rare-gas halide (RGH) excimers with an examination of the factors contributing to the efficiencies of the ArF* and KrF* lasers. The factors include the rate at which the excimer molecule is formed, the rate at which it is quenched by the various gas components, and the absorption coefficient of the gaseous lasing medium at the laser wavelength.

For the rare-gas fluorides, in contrast to the chlorides,[76] the time scale for producing the excimer is not the most important factor in limiting short-pulse laser efficiency. In general, the RGH dimer is produced mainly by recombination of positive rare-gas ions with negative halogen ions, requiring about 10 ns (Ref. 77) for typical plasma densities of 10^{14} cm^{-3}. The rather slow attachment of electrons to chlorine donors to produce Cl^- is usually the rate-limiting step in rare-gas chloride production. In contrast, the rate of electron attachment to fluorine donors to produce F^- is quite fast and presents no such limit (e.g., $k_a \approx 5 \times 10^{-9}$ cm^3/s for a Maxwellian distribution of electrons at 1 eV (Ref. 78), corresponding to an attachment time of 1.2 ns at a typical F_2 pressure of 5 Torr).

Collisional quenching of RGH excimers occurs primarily by collisions with the halogen donor, with electrons (two-body processes), and with the rare-gas atoms (three-body process). The three-body quenching of the dimers by rare gases produces RGH trimers, such as Ar_2F^* and Kr_2F^*. Like the dimers, the trimers can be viewed as ion-pair molecules[79] (e.g., $Ar_2^+F^-$). Because of trimer formation, three-component gas mixtures (e.g., Ar, Kr, and F_2 mixtures for KrF* lasers) perform better as laser media than simple two-component mixtures. In three-component mixtures, the formation of trimers proceeds at a slow rate compared to the formation rate of trimers in a two-component mixture of comparable density (i.e., comparable stopping power).

Optical absorption at the laser wavelength by excited states in the laser medium is presently the least understood of the major determinants of RGH laser efficiency. Experiments have shown[80] that Kr_2F^* causes at least 50% of the background absorption at the KrF* laser wavelength in the absence of strong stimulated emission. Viewed simplistically, this absorption is saturable, since the optical saturation of KrF* removes the source of Kr_2F^* production. However, because the saturation of KrF* is limited both by its finite vibrational relaxation rate[81] and by the nonsaturable absorption of the medium, the Kr_2F^* absorption is not completely saturable. For both KrF* and ArF*, the nonsaturable optical absorption at the laser wavelength is very important in determining the laser extraction efficiency.

Thus, RGH trimers are important from the standpoint of dimer kinetics, excited-state absorption, and, ultimately, laser performance. During 1981, we studied the kinetics of ArF* and Ar_2F^*, as well as KrF* and Kr_2F^*, as a function of current density and gas mixture. We analyzed the time dependence of the trimers Ar_2F^* and Kr_2F^* to determine their collisional quenching rates by F_2 and NF_3 and their natural radiative lifetimes. At high current densities, we observed qualitative indications of electron quenching for the trimers, but not for the dimers. In addition, we measured the optical absorption spectra and absorption cross sections of Ar_2F^* and Kr_2F^*.

Finally, in a more exploratory vein, we have considered possible gaseous energy-storage media that might be pumped by RGH lasers. Such media potentially allow the temporal compression of high-energy RGH laser pulses to short pulses appropriate for a laser-fusion driver. We discuss two examples of storage media that are typical of diatomic and large-molecule candidates.

RGH Trimer Kinetics. We used the MEG I electron beam (e-beam) facility at

LLNL to excite RGH laser mixtures at a fixed voltage (~600 kV), fixed pulse length (50 ns), and variable current density (5 to 30 A/cm^2). A schematic diagram of the setup is shown in Fig. 7-78. The e-beam, having a cross section of 2.5 × 10 cm^2, passed through a 1.3 × 10^{-2}-cm-thick titanium diode foil and drifted 10 cm in 30 Torr of air to reach the experimental cell. Carbon screens were placed in the drift region to attenuate the beam from 500 to 5 A/cm^2 in steps. The e-beam passed through a 7.6 × 10^{-3}-cm-thick Inconel foil into the gas cell, where the current could be measured with a carbon-collector Faraday cup.

To observe the kinetic properties of a homogeneously excited volume of gas, we reduced the excited volume by placing a stainless-steel insert in the cell. This insert defined an excited volume 2.5 cm long, 1 cm high, and 1.5 cm deep. The e-beam excitation within this region was presumed to be uniform. We observed fluorescence from this region through 1-cm-diam holes in the block and transversely through a 0.3-cm-diam hole. The hole diameters were chosen to be small compared to the observed depth of gas to minimize edge effects. Also, the fluorescence volume was chosen to be small to minimize the effects of amplification and absorption on the observed fluorescence signals. To check these assumptions, we compared the shape of fluorescence signals from the 2.5-cm and 1-cm directions and found no apparent difference. The gain and absorption coefficients determined by direct measurement also suggest that the medium was optically thin for these dimensions.

The gas cell and its fill system, constructed of stainless steel, were passivated with F_2 and evacuated between fills to less than 10^{-4} Torr. Subatmospheric pressures were measured with a capacitance manometer, and higher pressures were measured with a strain gauge. Gas mixtures were composed in 1-litre mixing bottles using commercially pure F_2 and NF_3 and research-grade rare gases. To ensure complete mixing, the bottles were left standing for several hours before use. We generally used gas from the same mixture batch for each data set, and refilled the cell with gas from the mixture bottle for each shot.

Photodiodes viewed the fluorescence from the excited volume through selected bandpass filters. Biplanar vacuum photodiodes were used with a 50-Ω load, giving a 1-ns response. The cable lengths for the signals were adjusted so that the observed signals occurred simultaneously within 1 ns. As shown in Fig. 7-79, a 5-56 Corning filter isolated the Kr_2F^* emission. A 7-54 filter isolated the Ar_2F^* emission. Figure 7-79 shows the emission spectrum of Kr_2F^* taken with an optical multichannel analyzer

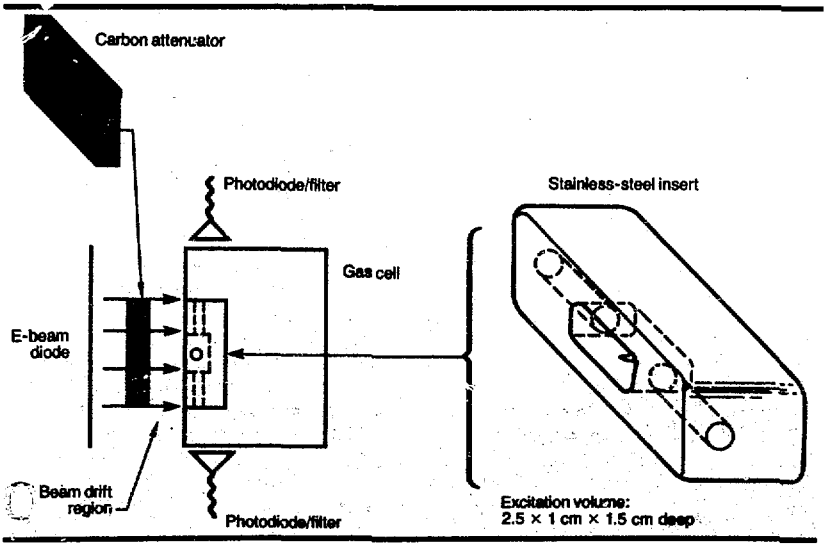

Fig. 7-78. Schematic of experimental setup used to study RGH kinetics.

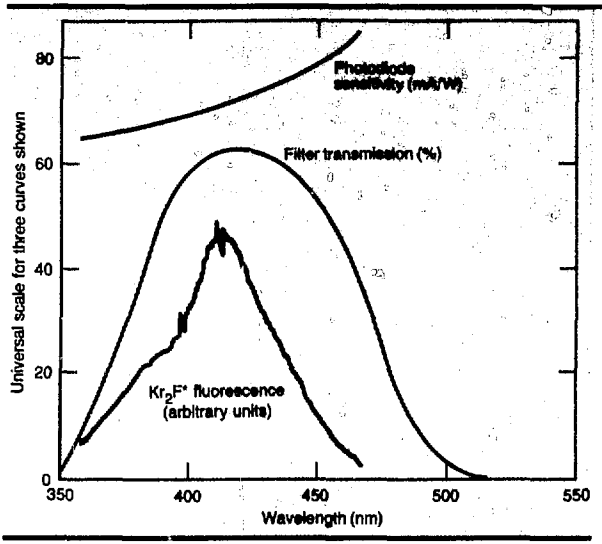

Fig. 7-79. Spectral response of photodiode and filter transmission used to isolate KrF* fluorescence.

and also shows the photodiode response as determined by the manufacturer. Interference filters having bandwidths of 20 and 10 nm, centered at 195 and 250 nm, respectively, isolated the ArF* and KrF* *B-X* emissions.

Comparisons of the e-beam current, ArF* fluorescence, and Ar_2F^* fluorescence are shown in Fig. 7-80 for low (33 A/cm^2) and high (470 A/cm^2) e-beam current densities. The negative pulse at the end of each trace is a common fiducial pulse that was used to adjust the scope sweeps to be simultaneous. As shown in Fig. 7-80, the ArF* signal typically followed the current pulse with about a 10-ns delay and had a relatively constant shape for high and low current; the KrF* signals behaved similarly. This behavior is in contrast with XeCl*, where the temporal shape of the fluorescence changes with current density,[76] presumably because of the change in the HCl attachment rate.

The Ar_2F^* signal is unlike the ArF* signal mainly because of its longer radiative lifetime (~200 ns compared to ~5 ns for the dimer). At low current density, the trimer signal integrates the dimer signal with a decay constant, which appears to be the same during and after the e-beam current. This behavior is consistent with the view that the trimer is formed from the dimer by three-body collisions and then decays by a time-independent loss process consisting of radiative decay plus collisional quenching.

The trimer fluorescence has a qualitatively different time dependence at high current density. The trimer appears to approach a steady state more rapidly during the current pulse than after. This immediately suggests a larger quenching rate for the trimer during the e-beam pulse, quite probably by electron collisions.

The peak amplitude of the trimer fluorescence plotted vs average current density also suggests an e-beam-related quenching. Figures 7-81 and 7-82 show the peak ArF* and Ar_2F^* signals and peak KrF* and Kr_2F^* signals, respectively, as a function of average current. While the dimer signals increase almost linearly with current, the trimer signals roll off strongly at the highest current densities. Because the normal decay time of the trimer is much longer than that of the dimer, electron quenching (or any other excitation-dependent quenching) is comparatively more important for the trimer. Indeed, to predict the trimer concentration accurately, it appears necessary to include this additional quenching in a description of the trimer kinetics for current densities as low as 50 A/cm^2. Interestingly, Figs. 7-81 and 7-82 also suggest that, at least with 5 Torr of F_2, electron quenching of the dimer is not a serious problem up to 500 A/cm^2.

Analysis of the trimer kinetics is considerably simpler than the dimer kinetics. First, the trimer decays on a relatively long time scale, so that the trimer can be observed after its production has completely ceased. Second, the dimer emission provides the time dependence of the source of the trimer production. We make the following assumptions

- The dimer and trimer fluorescence signals are proportional to the corresponding species density.
- The trimer is formed solely from the dimer,[82] the formation rate being proportional to the dimer density.
- At low current densities, the trimer is quenched with a time-independent rate.

Under our assumptions, at low current densities, the trimer fluorescence signal (S_{X_2F}) and the dimer fluorescence signal (S_{XF}) are related at low current densities by the single equation

$$\dot{S}_{X_2F} = \alpha S_{XF} - \tau^{-1} S_{X_2F} \quad . \tag{88}$$

The source term, α, is given by

$$= \frac{\mathcal{S}_{X_2F}}{\mathcal{S}_{XF}} k \quad , \tag{89}$$

where k is the pressure-dependent trimer formation rate, and the $\mathcal{S}_i$ are detector-sensitivity factors defined according to $S_i = \mathcal{S}_i n_i$, where n_i is the number density of the species i. The decay term τ^{-1} in Eq. (88) is the sum of radiative decay (τ_{rad}^{-1}) and two-body quenching processes ($k_i n_i$).

Using the dimer fluorescence as input, we fitted the observed trimer time dependence at low current densities to obtain best-fit values for α and τ^{-1}. The oscillograms of fluorescence were first digitized at approximately 40 points chosen to allow full definition of the curves. A 1-ns-spaced set of "experimental" points was then obtained by quadratic interpolation. We represent the experimental dimer fluorescence at t_i by x_i, the experimental trimer fluorescence by S_i, and the computed trimer fluorescence by y_i. We determined values for α and τ^{-1} by minimizing the error

$$\Delta^2 = \sum_i (S_i - Y_i)^2 \quad . \tag{90}$$

It is convenient to define the variable $u(t) = y(t)/\alpha$, so that Eq. (88) can be rewritten

$$\dot{u} = x(t) - \tau^{-1} u(t) \quad . \tag{91}$$

Then, minimizing Δ^2 with respect to α simply gives

$$\alpha = \left(\sum_i S_i u_i \right) \left(\sum_i u_i^2 \right)^{-1} \quad . \tag{92}$$

Therefore, the value of α giving a best fit is simply a normalization factor relating $u(t)$ to $y(t)$, which is applied after solving Eq. (91) for $u(t)$ with an arbitrary value of τ^{-1}.

Approximating the dimer fluorescence, $x(t)$, by a linear function between t_i and t_{i+1} we can solve Eq. (91) analytically in Δt interval. We obtain the recursion relationship

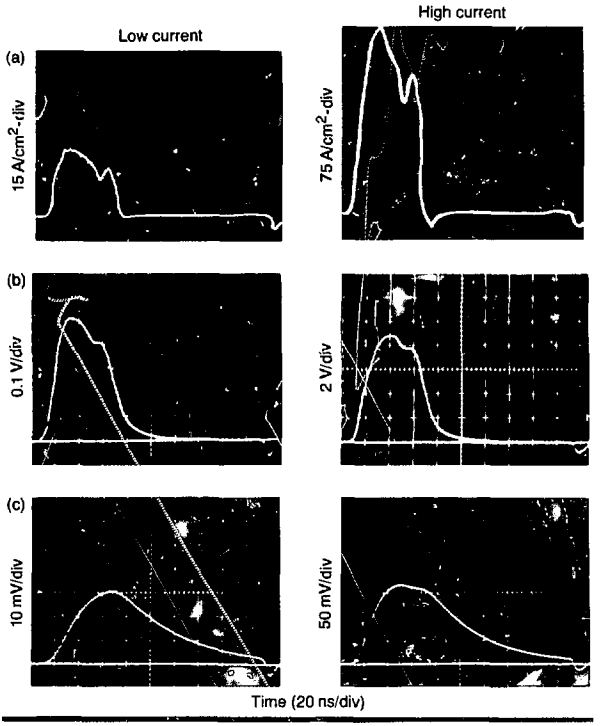

Fig. 7-80. Time dependence at low and high current densities (1500 Torr Ar/2.5 Torr F_2). (a) E-beam current density. (b) Dimer fluorescence. (c) Trimer fluorescence.

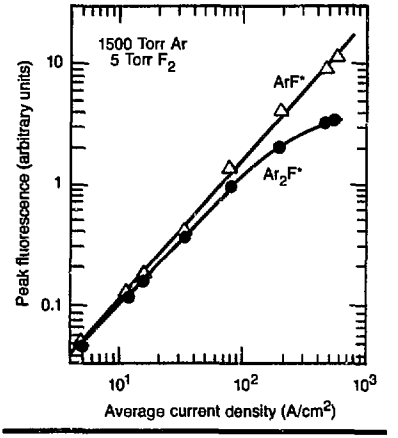

Fig. 7-81. Peak ArF* and Ar_2F^* fluorescence signals vs average current density.

$$u_{i+1} = u_i e^{-\Delta t/\tau} + x_i \tau \left[\frac{\tau}{\Delta t} (1 - e^{-\Delta t/\tau}) - e^{-\Delta t/\tau} \right] + x_{i+1} \tau \left[1 - \frac{\tau}{\Delta t} (1 - e^{-\Delta t/\tau}) \right] \quad , \tag{93}$$

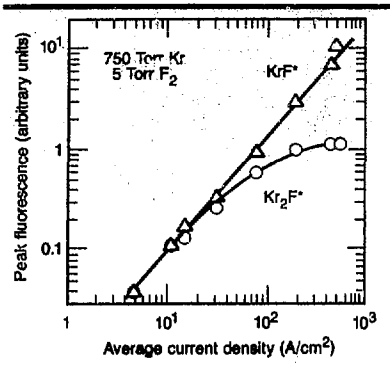

Fig. 7-82. Peak KrF* and Kr_2F^* fluorescence signals vs average current density.

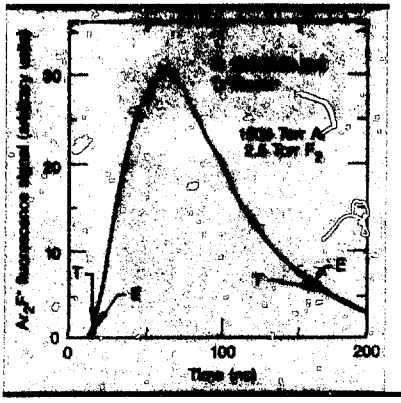

Fig. 7-83. Comparison of experimental and model values for Ar_2F^* fluorescence signal at low current density (33 A/cm²).

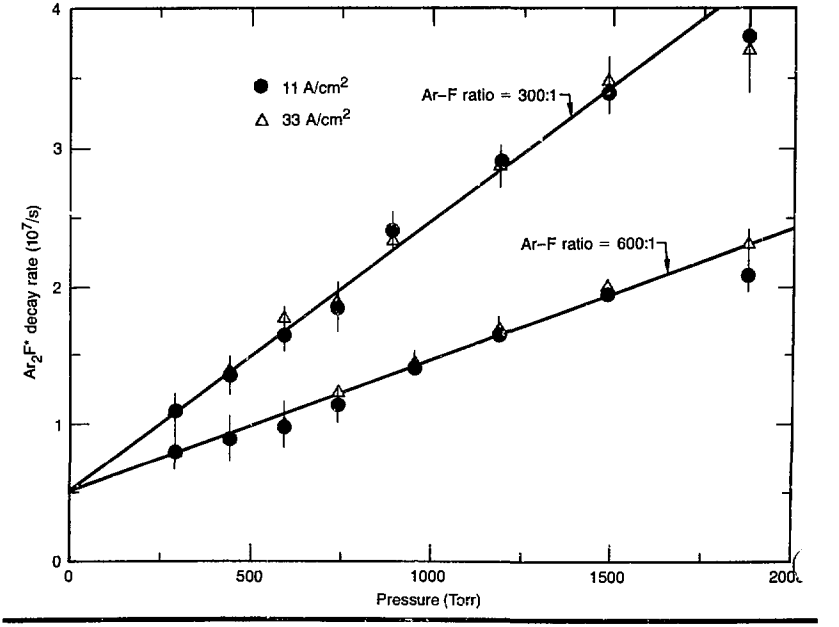

Fig. 7-84. Ar_2F^* decay rate, τ^{-1}, vs gas pressure at low current densities; straight lines represent linear fit to data.

where $\Delta t = t_{i+1} - t_i$.

Using Eqs. (92) and (93) to find u_i and α, we determined the error, Δ^2, associated with a given value of τ^{-1}. The error Δ^2 was then minimized with respect to τ^{-1} using a modified Gauss–Newton method, where the derivatives were calculated numerically using finite differencing (IMSL routine ZXSSQ, Ref. 83).

The error in the best-fit value of τ^{-1} was estimated as that increase (or decrease) required to increase the error sum to twice its minimum value. This estimated error is consistent with assuming an error in each residual equal to the error incurred in digitization. The error in the best fit for α was simply that associated with the error range for τ^{-1}.

The agreement between the model and the experimental trimer fluorescence was extremely good, as demonstrated in Fig. 7-83. The excellent match between the model and experiment is typical of all the results at low current density. Plots of the resulting best-fit value for τ^{-1} vs pressure are shown in Fig. 7-84 for Ar–F_2 mixture ratios of 300:1 and 600:1. Representative error bars are only shown for the circles that indicate data taken at a current density of 11 A/cm². The triangles represent data at

33 A/cm^2. Note that, for these low current densities, the fitted decay rates do not vary with the excitation current density. This was found for all gas mixtures. The solid lines are the result of a multiple linear regression fit, where each point was weighted according to its error range. Specifically, we assumed τ^{-1} to be of the form

$$\tau^{-1} = \tau_{rad}^{-1} + k_r n_r + k_d n_d \quad , \tag{94}$$

where the subscripts r and d imply a rare gas or a fluorine donor.

The trimer quenching coefficients and radiative lifetimes obtained from the analysis of the low-current-density data are shown in Table 7-13. The radiative lifetimes are somewhat longer than both the calculated values[79] (132 ns for both K_2F^* and Ar_2F^*) and previous measurements [165 ns (Ref. 84) and 181 ns (Ref. 85) for Kr_2F^* and 185 ns (Ref. 84) for Ar_2F^*]. Our F_2 quenching-rate coefficients are in the range of the several previous measurements.[84–86] There appear to be no previous data for trimer quenching by NF_3. It is interesting to note the small quenching rate of Kr_2F^* by NF_3. To measure that rate accurately without the influence of electron collisions, we reduced the e-beam current density to 2 A/cm^2.

Examples of the values of α determined as a function of pressure are shown in Fig. 7-85 for Ar–F_2 mixtures at 11 and 33 A/cm^2 and Ar–NF_3 mixtures at 11 A/cm^2. To prevent confusion because of the large number of overlapping points, we have shifted the data in Fig. 7-85(a) down in pressure by a factor of 2 and the data in Fig. 7-85(c) up in pressure by a factor of 2. For comparison, we have associated with each data group a common line having a p^2 dependence, which has been shifted similarly with pressure. Although we expect a simple p^2 dependence for a three-body formation rate, the curves for the various conditions all deviate from the p^2 line at high pressure. The Kr_2F^* formation rates behave similarly. Although we have no clear explanation of this effect, it is consistent with a decrease in the effective radiative lifetime of the dimer species at high pressure, presumably because of vibrational relaxation. Such a decrease in dimer lifetime has been reported by others.[87] This would imply that the ratio between the dimer fluorescence and the dimer density is not constant with pressure. This would then cause only an apparent rather than a true deviation in the trimer formation rate from a p^2 law.

Kr_2F^*		Ar_2F^*	
τ_{rad}	= 208 ± 21 ns	τ_{rad}	= 205 ± 20 ns
k_{Kr}	≤ 10^{-13} cm^3/s	k_{Ar}	≤ 10^{-14} cm^3/s
k_{F_2}	= (1.49 ± 0.10) × 10^{-10} cm^3/s	k_{F_2}	= (1.79 ± 0.06) × 10^{-10} cm^3/s
k_{NF_3}	= (2.7 ± 1.0) × 10^{-12} cm^3/s	k_{NF_3}	= (1.07 ± 0.07) × 10^{-10} cm^3/s

Table 7-13. Trimer decay constants determined from analysis of fluorescence at low current densities.

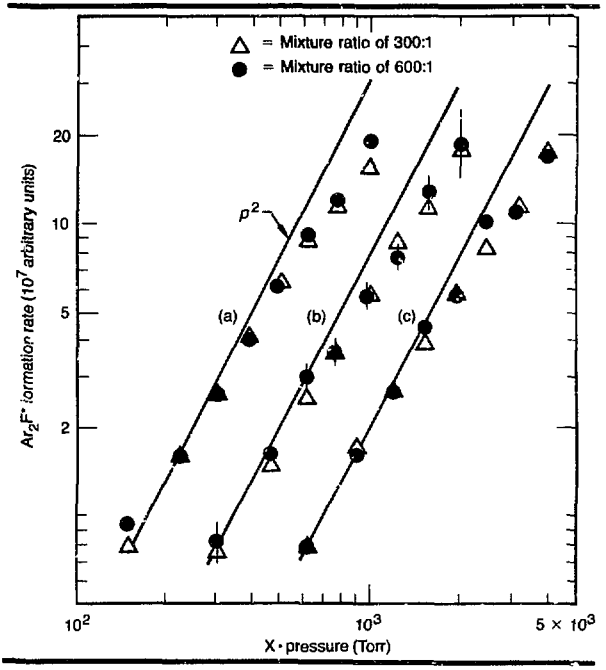

Fig. 7-85. Ar_2F^* formation rate α, vs gas pressure for various mixtures and e-beam current densities. (a) Ar-F_2, 11 A/cm^2, x = 0.5. (b) Ar-F_2, 33 A/cm^2, x = 1. (c) Ar-NF_3, 11 A/cm^2, x = 2.

The analysis of the trimer time dependence at high current density was performed in a different manner because of the presence of additional quenching during the current pulse. Labeling the trimer signal as y and the dimer signal as x, we expect them to be related by

$$\dot{y} = \alpha x - \tau^{-1} y - \gamma_e(t)\, y \quad . \tag{95}$$

Note that we have made no assumptions about the time dependence of the additional quenching, labeled $\gamma_e(t)$, but we presume the values of α and τ^{-1}, determined at low current density, will apply. We then determined $\gamma_e(t)$ by numerical

differentiation of the digitized trimer curves. The trimer points are labeled y_i, and the experimental dimer points are labeled x_i. Assuming linear interpolation between t_i and t_{i+1}, and defining $t_i^+ = (t_{i-1} + t_i)/2$, we have

$$\gamma_e(t_i^+) = \frac{\alpha(x_{i+1} + x_i)}{(y_{i+1} + y_i)} - \frac{2}{\Delta t}\frac{(y_{i+1} + y_i)}{(y_{i+1} + y_i)} - \tau^{-1} \quad (96)$$

Figure 7-86 shows the result of analyzing the high-current data of Fig. 7-80(c) by this procedure. Note that the additional quenching during the current pulse is about three times greater than the fixed quenching rate. Also, this additional quenching goes to zero after the current pulse, as we expect for a plasma-related process. A characteristic rate was obtained by averaging the values of $\gamma_e(t_i^+)$ in the time range of 30 to 50 ns into the current pulse.

A plot of the characteristic quenching rate of Ar_2F^* determined in this manner as a function of average current density is shown in Fig. 7-87 for several partial pressures of F_2. The horizontal bars represent the range of current densities exhibited by the e-beam over the averaging period. Within the scatter of the data, the additional quenching increases linearly with current density. However, it does not vary inversely with F_2 in the manner that we expect the electron density to vary when the primary electron loss is attachment to F_2 with a constant-attachment coefficient. The Kr_2F^* data show a similar behavior.

Because our results do not fit a simple model, we have considered possible quenchers of the trimers other than electrons such as Ar_2F^* or F^-. However, to fit our data, the rate coefficients for trimer quenching by these species would have to be greater than 10^{-7} cm^3/s, an unreasonably high number for a heavy-particle rate. Hence, we are left to conclude that trimer quenching during the e-beam pulse is caused by free electrons. However, we must also conclude that the electron density dependence on F_2 is not given by a simple model.

One complication in the description of the electron kinetics is that the addition of F_2 causes deviations from a Maxwellian electron-energy distribution because of the large loss rate for electrons near zero energy.[78] Loss of electrons in the low-energy range may suppress the effective attachment-rate coefficient at high F_2 concentrations. By this argument the normal (i.e., Maxwellian distribution) attachment rate is most appropriate at the lowest F_2 pressure. Using the data at 2.5 Torr F_2, assuming an attachment coefficient of 5×10^{-9} cm^3/s, and presuming the e-beam deposition rate in our cell is twice that given by the Berger and Selzer stopping power,[88] we estimate the electron quenching rate of Ar_2F^* is 4.1×10^{-8} cm^3/s (Ref. 78) and that of Kr_2F^* is 1.3×10^{-7} cm^3/s. These quenching coefficients are similar to those previously measured for the ArF* and Kr. dimers.[89]

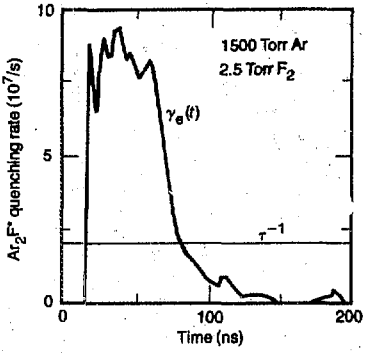

Fig. 7-86. Comparison of additional quenching rate, $\gamma_e(t)$, at high current density to fixed quenching rate, τ^{-1} (e-beam current density = 470 A/cm^2).

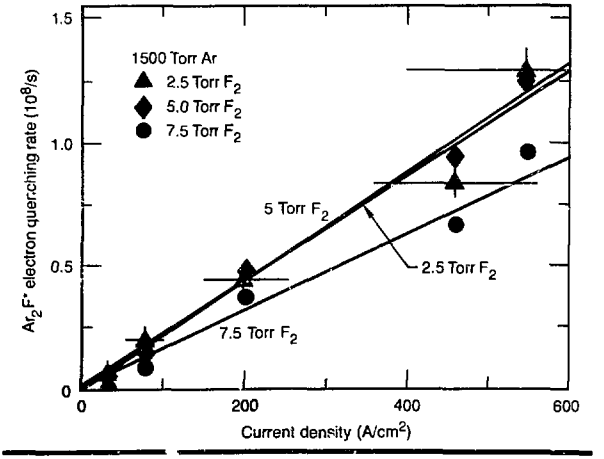

Fig. 7-87. Ar_2F^* electron quenching rate, γ_e, vs current density for various F_2 concentrations; solid lines are linear fits to data at fixed F_2 pressures.

RGH-Medium Absorption. The ratio of small signal gain to nonsaturable loss at the laser wavelength is paramount in determining the extraction efficiency of e-beam-excited lasers. Generally, the background loss is spectrally broad so that "off-line" measurements suffice to determine the "on-line" gain-to-loss ratio.[90] During 1981, we measured the absorption spectra of ArF* and KrF* laser mixtures, identified absorption maxima caused by Ar_2F^* and Kr_2F^*, and measured their peak absorption cross sections.

To probe the excited medium, we used several wavelengths produced by stimulated Raman scattering of a KrF laser in either H_2 or D_2, as described in Ref. 76. Raman scattering of a 100-mJ KrF laser produced probe pulses of approximately 15-ns duration at 11 wavelengths between 206 nm (second anti-Stokes in H_2) and 423 nm (fourth Stokes in H_2). The intensity of each line was large enough (>1 kW) to eliminate any problems caused by background fluorescence from the e-beam-excited gas. Spectrometers equipped with vacuum photodiodes were used to sample the input intensity (reference signal) and transmitted intensity for any specific line. The pulsed laser was generally timed so that absorption was measured at the end of the 50-ns current pulse. A triple-pass arrangement gave an absorption path that was 30 cm long.

We first used this technique[76] to measure the absorption spectra in e-beam-excited Ar and Ne. The interpretation of these data was clouded by our inability to separate the contributions to the absorption from the rare-gas molecular ions (e.g., Ar_2^+) and the rare-gas excimers (e.g., Ar_2^*). Modeling indicates that the molecular ions and excimers are generally present in comparable concentrations and that both contribute to the observed absorption.

Calculations predict that the absorption cross sections for the molecular excimer,[91] as well as the rare-gas halide trimer[79] (e.g., Ar_2F^*), are similar to those of the corresponding rare-gas molecular ion in the 300-nm region. The rare-gas excimers may be visualized as Rydberg molecules with a molecular ion core, the trimers as rare-gas-ion, halogen-ion pairs (e.g., $Ar_2^+F^-$). For both molecules, we expect the absorption to be the result of a process analogous to the strong $^2\Sigma_u^+ \rightarrow {}^2\Sigma_g^+$ transition, which has been predicted for the rare-gas molecular ions.[92-94]

The addition of halogen donors to the rare gases simplifies the identification of the absorber in comparison to the case of the pure rare gases. The RGH trimers then generally have the highest concentration of any excited species, as illustrated in Table 7-14. (The species concentrations were calculated with a RGH kinetics code similar to that described in Ref. 86.) This dominance of the trimers results from their being the lowest-energy excited species and from their having a relatively long lifetime.

Negative halogen ions and excited rare-gas atoms also contribute to the medium absorption. Figure 7-88 displays the experimentally determined[95] absorption cross section of F^-, together with the theoretically predicted spectra of Ar* and Kr* (Ref. 96), Ar^{**} (Ref. 97), and Ar_2^+ and Kr_2^+ (Ref. 94).

Figure 7-89 shows the absorption spectrum of an Ar–F_2 mixture measured at the end of the e-beam current pulse. The error bars represent the scatter in the data over several shots. The solid line in Fig. 7-89 is the spectral profile of Ar_2^+ calculated by Wadt.[94] Both the peak position and the width of the absorption, presumed to be caused by Ar_2F^*, are in good agreement with the Ar_2^+ calculation. The experimental absorption is higher in the wings, presumably because of contributions from other species.

The measured absorption at 226 nm in Fig. 7-89 is significantly higher than the overall experimental curve. We expect absorption by excited rare-gas atoms to be unstructured in this region, since, at this wavelength, the final state lies in the

Species	Concentration (cm^{-3})
Ar*	2.9×10^{15}
Ar**	2.3×10^{15}
Ar^+	1.3×10^{15}
Ar_2^*	3.7×10^{14}
Ar_2^+	2.2×10^{15}
F^-	1.6×10^{14}
ArF*	6.3×10^{14}
Ar_2F^*	1.7×10^{16}

[a]Total deposition of energy into gas is estimated at twice rate given by Berger and Seltzer stopping powers.

[b]Model used does not include electron quenching of trimer, and, thus, probably overestimates Ar_2F^* density by a factor of about 2.

Table 7-14. Excited species concentrations predicted at 50 ns into a 500 A/cm² e-beam pulse (1500 Torr Ar, 5 Torr F_2).[a,b]

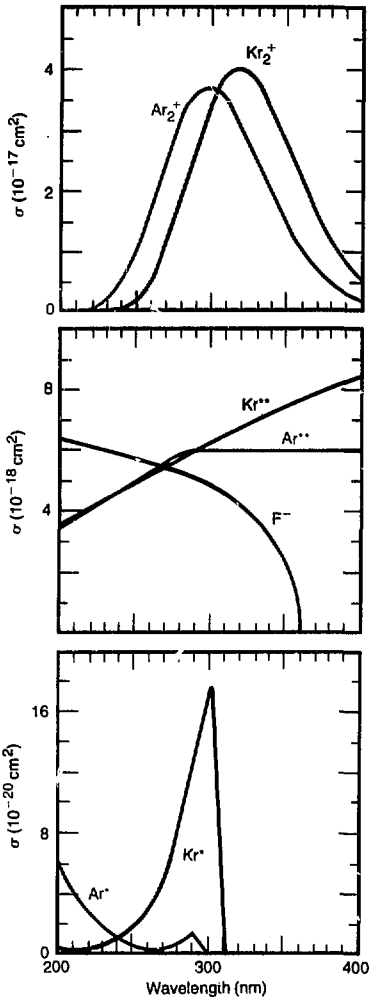

Fig. 7-88. Experimental absorption cross section for F^-, with theoretical absorption cross sections for excited rare-gas atoms and rare-gas molecular ions.

ionization continuum. Thus, the observed feature must come from either ArF*, Ar_2F^*, or, possibly, F_2^*. Our hypothesis is supported because no similar deviation was observed in the pure-Ar absorption data. Bound–bound absorptions for RGH trimers from the ionic state to Rydberg states have been predicted[98] in this spectral region.

Figure 7-90 shows the absorption spectrum of an Ar–Kr–F_2 mixture. Since the mixture concentrations are appropriate for laser operation, we observed gain at the KrF laser wavelength. The two different gain values were obtained using either H_2 or D_2 as a scatterer and probably reflect small spectral changes in the probe spectrum at the pump line caused by rotational Raman scattering. The absorption maximum is at 315 nm, compared to 300 nm for Ar–F_2 mixtures. We attribute the maximum to Kr_2F^*, the primary trimer species. (The concentration of the mixed trimer $ArKr^+F^-$ is believed to be small because of the rapid process $ArKr^+F^- + Kr \rightarrow Kr_2^+F^- + Ar$.) The theoretical absorption[94] for Kr_2^+ (solid line) again matches the wavelength of the peak, but underestimates the wings. Note that the anomaly at 226 nm is still present for this mixture.

Interpolating the measured absorption at 249 nm, we estimate the ratio of small signal gain to small signal loss to be 6. Assuming that half of the absorption at 249 nm is caused by Kr_2F^*, as suggested by the calculated Kr_2^+ spectrum, would imply that the ratio of gain to nonsaturable loss is 12. Ratios of 10 to 20 are inferred from KrF* laser performance.[80]

To confirm our identifications of Ar_2F^* and Kr_2F^* as the primary absorbers at 300 and 315 nm, we compared the time dependence of the absorption to that of the trimer emission. For simplicity, we used the 351-nm line of the cw Ar^+ laser as a probe to obtain the full time dependence of absorption on a single shot. A spectrometer and fast-response vacuum photodiode were again used to detect the transmitted beam. Oscillograms of the transmitted light signal were digitized and then converted to absorption coefficients vs time. Figure 7-91 compares the measured absorption coefficient at 351 nm to the Kr_2F^* emission at 420 nm, normalized to the same peak value. The temporal shapes are in excellent agreement, further confirming the absorber as Kr_2F^*. The comparison for Ar–F_2 mixtures was equally good.

To obtain absolute absorption cross sections, it is necessary to determine the trimer densities. We did so by measuring their absolute emission intensities for a well-defined geometry. Pinholes of 0.36-cm radii were located at the cell-output window and at the detector. The pinholes were separated by 54 cm. The projection of an illuminated field at the detector through the pinholes demonstrated that the field of view through the 2.5-cm excited length was unobstructed. For our simple geometry, the detected

signal is given by

$$= D R h\nu \tau_{rad}^{-1} n \left(\frac{\pi r_1^2 r_2^2 L}{4d^2} \right) \quad (97)$$

with the following definitions

D = detector sensitivity in mA/W averaged over the emission band,
R = load resistance,
$h\nu$ = quantum energy,
n = trimer density,
r_1, r_2 = pinhole radii,
L = length of excited gas, and
d = pinhole separation.

The factor in parentheses is an effective volume that can be derived by simple application of the brightness theorem.[99] Data such as those shown in Fig. 7-79 were used to obtain the detector response, D. Using Eq. (97), we determined simple factors to convert measured photodiode voltages to number densities of trimers.

An additional correction was necessary, since fluorescence was measured from a 2.5-cm length, while absorption was measured over 10 cm. Using the data in Figs. 7-81 and 7-82, we made a small adjustment (~20%) in the number densities corresponding to the change in average current density pumping these lengths.

The resulting trimer-absorption cross sections are summarized in Table 7-15. A major part of the estimated uncertainty in the cross sections arises from using the fluorescence from a small volume to infer number density in a larger volume. The wavelengths for peak absorption by Ar_2F^* and Kr_2F^* are in excellent agreement with the calculations for Ar_2^+ and Kr_2^+, while the experimental peak cross sections are slightly larger than calculated. Since excited rare-gas atoms and halogen ions also make a small contribution to the absorption in this spectral region, the experimental values should be regarded as upper limits on the trimer cross sections.

RGH-Pumped Storage Lasers. We have studied the feasibility of using as a storage system those gaseous gain media that have high quantum efficiency when pumped by either ArF or KrF lasers and have energy storage times greater than 0.1 μs. These media potentially can offer simplicity and economy, relative to pulse stackers, in achieving power compression of long-pulse lasers. This general approach, often classified as a hybrid laser, could be competitive with other RGH pulse-compression concepts in reaching the goal of 5% overall efficiency for 1- to 10-ns pulses. The longstanding task for the hybrid scenario is to identify practical storage media. We have found two interesting candidate molecules to use in a hybrid scheme. First we describe some general properties of hybrid systems, then we discuss the possibility of using KrF to pump SO or DABCO (1,4-diazabicyclo [2.2.2] octane).

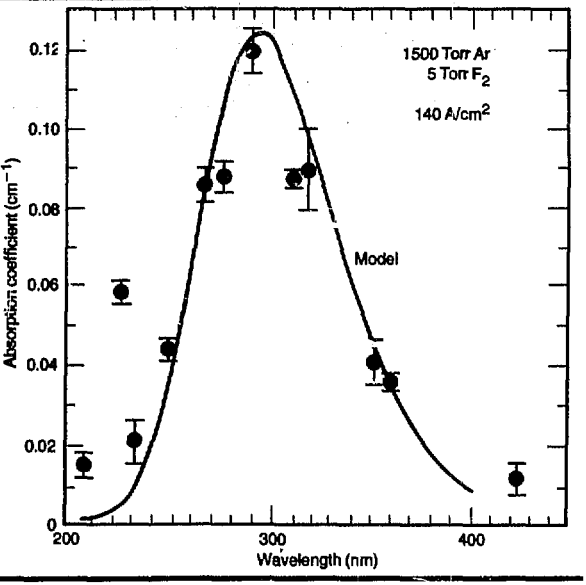

Fig. 7-89. Absorption spectrum of Ar-F_2 mixture measured at end of e-beam current pulse; solid line is spectral profile of Ar_2^+ calculated by Wadt.[94]

We first note that the hybrid concept is closely related to Raman compression. Raman excitation can be viewed as optical pumping to a virtual state of the conversion medium. Because such states have a very short storage time, this method of pumping requires simultaneous extraction with a backward-propagating Stokes pulse to extract a power greater than the pump power. The major advantage of virtual-state pumping is that it is nonresonant and, thus, useful with lasers of arbitrary wavelength. It also can have a high quantum efficiency using vibrational Raman emission. The major disadvantage of nonresonant virtual-state pumping is that it also works at the output wavelength. Thus, spontaneous conversion to second-Stokes light is possible when the output intensity becomes high. Theoretical analysis[100] suggests that, in a simple

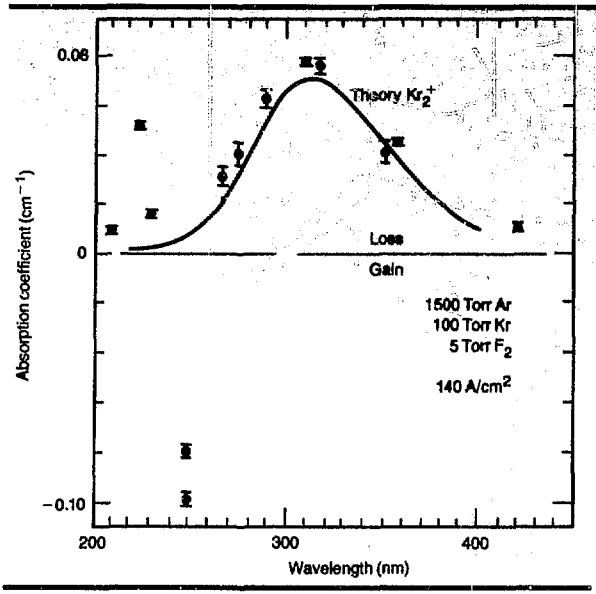

Fig. 7-90. Absorption spectrum of Ar-Kr-F_2 mixture measured at end of e-beam current pulse; solid line is spectral profile of Kr_2^+ calculated by Wadt.[94]

amplifier without second-Stokes suppression, the ratio of photon fluence between the Stokes pulse and the pump pulse is limited to about 5. Experiments[101] using KrF-pumping of methane have achieved power gains of about 3.

Because of the uncertainty principle, $\Delta E\, \Delta t > h$, optical pumping of real states allows much longer storage times. Provided that a low-lying vibrational level is still used as the lower laser state, the quantum efficiency also can be high in this case. We exclude photodissociation, as in the iodine or Group VI lasers, because their quantum ratio is inherently much lower. The power intensification ratio using real-state pumping can be on the order of the medium storage time divided by the short-pulse extraction time multiplied by the quantum ratio. Hence, with a very modest storage time of 100 ns and a relatively long extraction time of 10 ns, we have a potential power gain (neglecting the quantum ratio) of 10. In principle, much higher power gains are possible, since there is presumably no second-Stokes limit for resonant pumping. However, the analogous problem becomes the absorption of either pump-laser or output-laser photons by the excited states in which energy is stored. We note that our present objective is the conversion of a KrF or ArF laser operating nominally at 10 MW/cm^2 (as limited by nonsaturable loss) to a fusion driver operating nominally at 1 GW/cm^2, a power gain of 100.

Many of the attributes commonly associated with Raman pulse compression are actually quite general to laser pumping of gain media. For the best analogy with present Raman schemes, consider longitudinal pumping of a storage medium. "Stacker-compressors" are clearly possible using storage media, since we may use a single extraction beam to obtain an optical summation of various pump beams incident on the conversion cell at different angles or opposing directions. Moreover, as commonly advertised for Raman compressors, the spatial coherence of the output can be much better than the pump. Some averaging of spatial inhomogeneities in the pump by the storage medium is automatically accomplished by extracting slightly off-angle to the pump beam. These benefits generally accrue when using longitudinal excitation of a medium by a coherent pump and are not specific to Raman conversion.

Longitudinal pumping of a conversion medium appears potentially to be the most efficient hybrid configuration. Provided the transverse aperture of the conversion medium is greater than the width of the input beam, complete geometric overlap of the extraction pulse with the pump pulse can be obtained without suffering diffraction or scattering by walls. As with all such face-pumped amplifiers, depletion of the pump by absorption does not cause spatial inhomogeneity of the output beam in contrast to transversely pumped amplifiers. Moreover, Brewster-angle or AR-coated input windows can be used to provide efficient input coupling. Hence, in the longitudinal pumping configuration, there are no inherent geometric considerations that limit the extraction efficiency. Rather, the performance of the amplifier will be determined by the physical properties of the conversion medium.

We first estimate the general range of absorption and gain cross sections desired for a hybrid system. The simplest type of molecular storage laser is a "two-state" system. Absorption and emission occur via the same overall electronic transition moment, gain being provided by a Franck–Condon shift. Since the absorption and gain cross sections are inherently comparable in this

case, we may ask if they are compatible for longitudinal pumping as well as for providing energy storage. The output fluxes of GH lasers are typically in the range of 0.2 to 1 J/cm^2, corresponding to about 0.2 to 1 $\times$ 10^{18} photon/cm^2 at 193 nm. If we produce a concentration of excited species of 10^{16}/cm^3 in the storage medium (the concentration is based on experience with Group VI and other gaseous-storage lasers), the input flux can excite an amplifier depth of 0.2 to 1 m to this concentration. The actual amplifier depth would likely be a factor of 2 or so greater, allowing for exponential depletion of the pump. Hence, we require an absorption coefficient of 0.01 to 0.05/cm. Since the minimum concentration of ground-state molecules must be 10^{16}/cm^3, we find that the absorption cross section must be *less than* 5 $\times$ 10^{-18} cm^2. If we only want to excite 10% of the ground-state molecules, an absorption cross section of about 5 $\times$ 10^{-19} cm^2 is desired. We immediately observe that the cross sections above are consistent with weak transitions having oscillator strengths of 10^{-2} or less. Such transitions are consistent with our needs for energy-storage time and gain. Hence, a two-state molecular-storage laser is feasible using longitudinal pumping.

A "three-state" molecular laser would obviously rely on absorption to one molecular state followed by internal conversion or collisional relaxation to a second state, which provides gain. Our previous estimate of the desired absorption cross section is still applicable. However, in this case, it is possible to absorb on the wing of a strongly allowed band, since energy storage and, hence, a long radiative lifetime, are not required for the state that is directly pumped.

We can naïvely classify potential gaseous hybrid lasers into three types: diatomic molecules, small molecules (up to 4 atoms), and large molecules. The three categories have significantly different problems and attributes. Stable diatomic molecules having a useful vapor pressure are relatively few in number. It is generally improbable to have a good spectral overlap of convenient diatomic molecules with available pump lasers. However, diatomic molecules are the most attractive in terms of their ionization potentials and relatively simple spectroscopy. Small molecules might be the most attractive. However, we have not yet identified any that have a high fluorescence yield in the ultraviolet. Large molecules have continuous absorption bands, improving the likelihood of overlap with pump lasers. However, with large molecules, questions frequently arise about photodissociation, photoionization, and excited-state absorption. The tradeoffs between diatomic and large molecules as hybrid laser candidates are well illustrated by SO and DABCO.

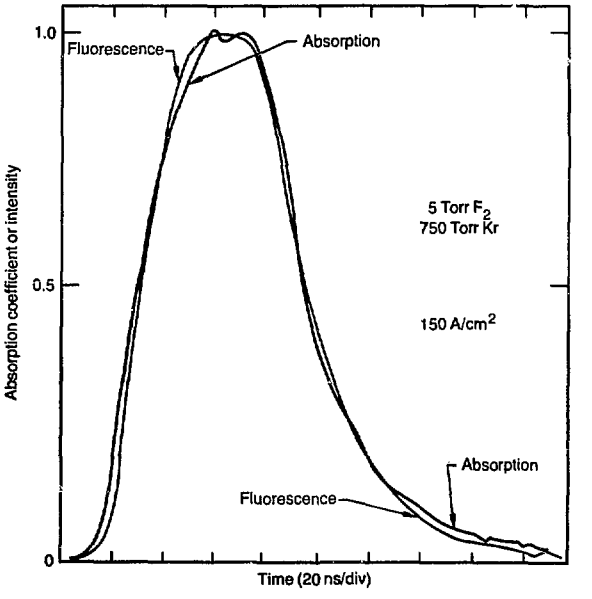

Fig. 7-91. Comparison of time dependence of Kr_2F^* emission at 420 nm (F) with absorption coefficient (A) at 351 nm.

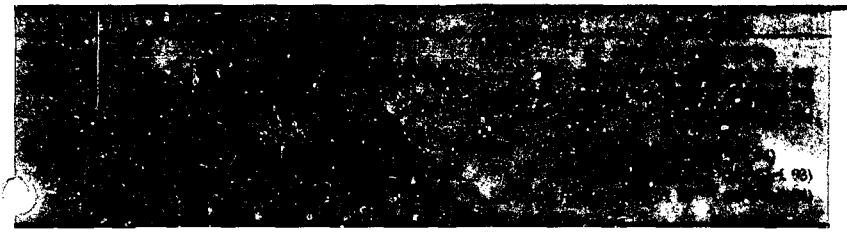

Table 7-15. Wavelengths for peak absorption, and peak absorption cross sections, for Ar_2F^* and Kr_2F^*.

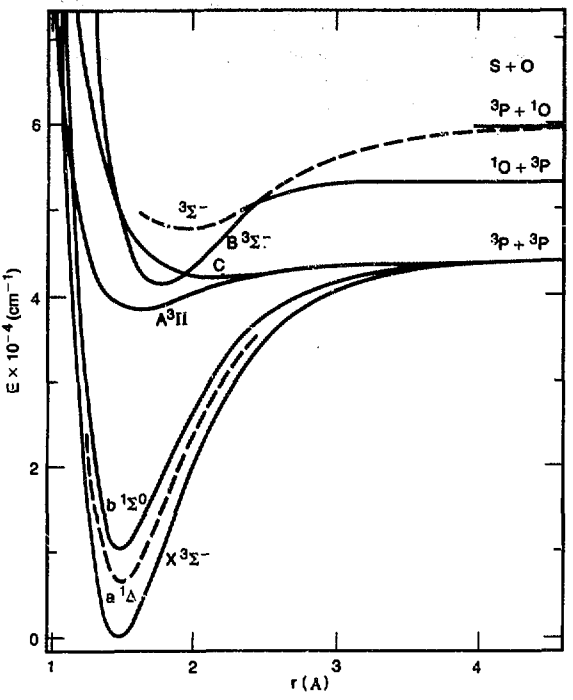

Fig. 7-92. Morse potential-energy curves of known electronic states of SO.

Clyne and McDermid[102] have suggested the use of the $A\,^3\Pi \rightarrow X\,^3\Sigma^-$ transition in the SO radical for a two-state molecular-storage laser pumped by KrF excimer radiation. The potential curves of the known states of SO are shown in Fig. 7-92. Being analogous to O_2, SO has the familiar $^3\Sigma^-$ ground state and low-lying $^1\Delta$ and $^1\Sigma^+$ metastable states. The primary ultraviolet transition of SO is the $X\,^3\Sigma^- \rightarrow B\,^3\Sigma^-$ band (analogous to the Schumann-Runge bands of O_2) extending in absorption from about 200 to 240 nm. The $A\,^3\Pi$ state, first identified and analyzed by Colin,[103] is interesting as a storage-laser candidate because of its 16-μs radiative lifetime, as measured by Clyne and McDermid. Perhaps the long lifetime arises because both the A and X states correlate with ground-state atoms (thus leading to the possibility of producing an SO laser based on the recombination of ground-state atoms).

Ground-state SO is a relatively stable free radical and has been observed[102] to exist in flow systems for times greater than 0.1 s. The presence of O atoms causes recombination to SO_2. The radical SO has been produced by the reaction of O atoms with CS_2, reaction of S atoms with O_2 following flash photolysis of COS, discharges of SO_2, and by numerous other techniques. Although, for the present purposes, we must avoid the presence of SO_2, which absorbs in the spectral region of interest, it still seems likely that SO concentrations approaching 1 Torr can be produced.

The vibrational spacings in the ground and excited states of SO are 1148 and 413 cm^{-1}, respectively, and the rotational constants are 0.72 and 0.61 cm^{-1}, respectively. The KrF excimer radiation overlaps well with the 6-0 bands of the $A\,^3\Pi_0 \rightarrow X\,^3\Sigma^-$ band that extends from 247.7 nm to beyond 249 nm. Many close rotational lines of this band would be excited by a conventional broadband KrF laser. Several 6-v'' bands have sufficiently large Franck-Condon factors for laser emission. Band origins are: 6-1, 254 nm; 6-3, 269 nm; 6-4, 277 nm; and others up to wavelengths of ~600 nm are found to have Franck-Condon factors >0.05. For the extracted photons not to be absorbed by unexcited SO molecules, the 6-3 transition at 269 nm seems to be the best choice, giving the highest quantum ratio. We assume that energy in the upper state is localized in $v' = 6$ and that mixing occurs only within its substates. The range of buffer-gas pressures and pump times for which this is true would have to be determined experimentally, but pressures on the order of about 10 Torr and pump times on the order of 100 ns seem reasonable. Thus, the gain cross section for the 6-3 transition is comparable to the 6-0 absorption cross section ($>10^{-18}$ cm^2) with the above assumptions. During the 10-ns energy-extraction period, complete mixing may not occur, so that multirotational-line extraction might be required.

The ionization potential of SO is 10.34 eV, so photoionization of the excited state by pump or laser photons is not possible. In addition, the excited state lies almost 0.5 eV below the lowest dissociation limit, so predissociation will not occur. Finally, the excited state is reasonably stable to quenching. Rate constants for quenching by O_2, N_2, and N_2O were measured[78] at 5×10^{-11} cm^3/s and by CS_2 at 2.7×10^{-10} cm^3/s. Thus, the total system pressure

should not exceed 10 Torr, so that sufficient storage times can be achieved.

We foresee that the primary difficulties of naking a KrF-pumped SO-storage laser are, first, obtaining the required concentration of SO in a suitable buffer and, second, obtaining a good spectral overlap of the KrF output with SO. We also note that Clyne and Heaven[104] have suggested recently a BO laser ($A\ ^2\Pi \rightarrow X\ ^2\Sigma^+$, 1.8-$\mu$s radiative lifetime), which might operate at 470 nm when pumped on its 4–0 band by an XeF laser. The advantages and disadvantages of this system for fusion applications appear to be similar to the SO case, except that a less-efficient RGH pump would be employed, and a longer output wavelength would be obtained.

We also have considered the compound known as DABCO (1,4-diazabicyclo [2.2.2] octane) or triethylenediamine ($C_6H_{12}N_2$) as a laser medium that can be pumped using KrF excitation. The molecular structure of DABCO is a cage formed by three ethylene (C_2H_4) bridges connecting two nitrogen atoms. The system has high symmetry (D_{3h}) with the two nitrogen atoms on the major-symmetry axis. DABCO has a broad absorption band whose origin is at ~252 nm, which is identified as the $B \rightarrow X$ transition.[105] This state rapidly relaxes to the A state, which, in the gas phase, emits around 315 nm with a radiative lifetime of approximately 1 μs.[106] The quantum yield of fluorescence has been measured at >0.9, and the excited state appears to be resistant to collisional deexcitation.

The absorption and emission properties of interest in DABCO involve only the nonbonding electrons associated with the nitrogen atoms. Both photoelectron spectroscopy and theoretical calculations[107] have determined that the highest occupied molecular orbital is the symmetric combination of the nonbonding lone-pair orbitals [$n(+)$]. Because of the high symmetry in the molecule, excitation to some of the lower Rydberg states is not dipole allowed. (There are no known valence states in saturated amines.) The unusually long lifetime of the fluorescing state can be explained by considering the symmetries of the states involved. The ground state of DABCO is $^1A_1'$. Interpretation of two-photon fluorescence-excitation spectra by Parker and Avouris[108] shows that the first excited state, which is one-photon forbidden and two-photon allowed, must be the $^1A_1'[3s(+)]$ symmetric combination of the Rydberg 3s orbitals on the nitrogens. The B state, which is both one- and two-photon allowed from the ground state, has been identified as being $^1E'[3p_{x,y}(+)]$.

We estimate that the absorption cross section at 249 nm is about 1.5×10^{-19} cm^2, and the cross section for stimulated emission is about 4×10^{-19} cm^2 at 314 nm. Using these cross sections, we determined that it is necessary to heat the DABCO to ~80°C to obtain 4 Torr of vapor pressure,[109] so that the absorption will be sufficiently large to allow reasonable gain.

The ionization potential of DABCO is sufficiently low (7.2 eV) that photoionization by either the pump light or the laser photons is possible. Since the A state is a 3s Rydberg state, most of its oscillator strength will be carried by the 3s–3p transition, so photoionization of the proposed upper-laser state is expected to be very small ($<10^{-19}$ cm^2). On the other hand, p-Rydberg states generally have larger photoionization cross sections, so that ionization of the B state may be a serious problem. We anticipate that, by adding a buffer gas to cause collisional relaxation from the B to the A state, we can greatly reduce the photoionization problem.

The unique aspect of DABCO that makes it interesting as a laser system is its high symmetry. The transition to the ground state from the lowest excited state is symmetry forbidden. In addition, the high quantum yield for producing the A state, and the comparatively small Raman shift, make this system ideal. Spectral overlap with a KrF pump laser is good, and short-pulse extraction seems likely because of the generally rapid internal relaxation for large molecules. However, photoionization is a matter of significant concern. If the photoionization problem cannot be solved, it may be possible to find similar large molecules of high symmetry whose ionization potentials are not as low.

Authors: H. T. Powell, K. S. Jancaitis, and K. C. Kulander

Major Contributors: R. J. Poli and J. J. Dub

Rare-Gas Halide Theory

Photoabsorption by Kr_2^* Excimers. Photoabsorption by rare-gas excimers plays an important role in the kinetics of high-pressure rare-gas excimer and rare-gas halide (RGH) lasers. To improve the performance of RGH lasers, such as KrF or ArF, it is necessary to identify the absorbing species and to determine their photoabsorption and photoionization cross sections.

Several years ago, extensive calculations were performed[110,111] to study the photoionization of the excimer states of Ne_2^* and Ar_2^*. These studies predicted a very strong and fairly broad absorption peak near 300 nm, which has been observed recently in electron-beam-excited high-pressure argon.[112] As an extension of our earlier work, we have undertaken a new study of the photoionization of Kr_2^* excimers.

Our current calculations of Kr_2^* have several novel features. First, we are using relativistic effective core potentials to describe the effects of the inner-shell electrons of Kr, thus simplifying the extensive configuration-interaction calculation of the molecular-wave functions. Second, we are studying the effects of spin–orbit coupling on the calculated photoionization cross sections by using a semiempirical procedure to treat the spin–orbit splittings of both the excimer states of Kr_2^* and the lowest four states of Kr_2^+.

We have completed calculations of the vertical electronic absorption spectrum of Kr_2^* at five internuclear separations. We have obtained partial photoionization cross sections for the channels leading to the formation of $Kr_2^+(^2\Sigma_u^+)$

$$Kr_2(^{1,3}\Sigma_u^+) + h\nu \rightarrow Kr_2^+ + e(k\sigma_u) \quad , \qquad (98)$$

$$Kr_2(^{1,3}\Sigma_u^+) + h\nu \rightarrow Kr_2^+(^2\Sigma_u^+) + e(k\pi_u) \quad . \qquad (99)$$

As in the case of Ne_2^* and Ar_2^*, the first of these two channels exhibits a strong absorption near 300 nm caused by transitions between the $^{1,3}\Sigma_u^+$ excimer states and $^{1,3}\Sigma_g^+$ autoionizing states associated with the $^2\Sigma_g^+$ excited state of Kr_2^+. Figure 7-93 shows the vertical photoionization profile of $Kr_2^*(^1\Sigma_u^+)$ at the equilibrium internuclear distance of 5.25 bohr. Two noteworthy features are the large peak centered near 3.7-eV photon energy ($\sigma_{max} = 0.6 \times 10^{-16}$ cm^2) and the relatively small magnitude (2 to 5 $\times$ 10^{-18} cm^2) of the background cross section.

To study the effects of spin–orbit coupling, we performed first-order configuration-interaction calculations of the $^{1,3}\Pi_u$ states of Kr_2, which correlate with the lowest $Kr(^1S) + Kr(^{1,3}P)$ asymptotes at infinite internuclear separation. We then used the atomic spin–orbit coupling constant appropriate for the $4p^5 5s$ configuration of Kr to determine the mixing between these $^{1,3}\Pi_u$ states and the $^{1,3}\Sigma_u^+$ excimer states. We also calculated the electronic transition energies and optical transition moments for the $^{1,3}\Pi_u \rightarrow {}^{1,3}\Pi_g$ and $^{1,3}\Pi_u \rightarrow {}^{1,3}\Sigma_g^+$ excitations to identify the strongest perturbers in the photoabsorption spectrum of Kr_2^*.

Additional calculations that are required to treat properly the spin–orbit mixing among the $^{1,3}\Sigma_g^+$ and $^{1,3}\Pi_g$ states are currently in progress.

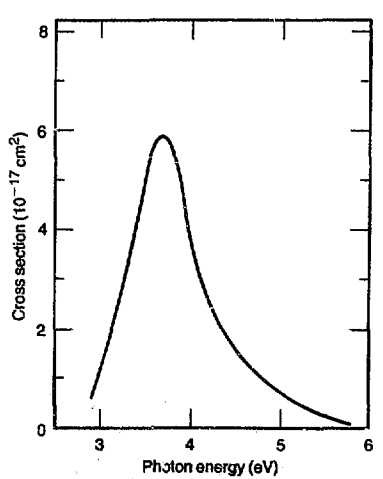

Fig. 7-93. Vertical photoionization cross section of $Kr_2^*(^1\Sigma_u^+)$ at equilibrium internuclear distance of 5.25 bohr; vertical ionization potential is 3.0 eV.

Transient Absorption between the Excited States of KrF. Absorption processes among the excited states of RGH molecules are of particular interest as a possible probe of the kinetics of the upper laser level in the RGH laser. We have characterized the absorption from the ion-pair states $B(^2\Sigma_{1/2}^+)$ and $C(^2\Pi_{3/2})$ into the $D(^2\Pi_{1/2})$ state. In addition, we have investigated the absorption from the upper laser level $B(^2\Sigma_{1/2}^+)$ of KrF

into the $^2\Sigma^+$ and $^2\Pi$ Rydberg states. An important parameter in the RGH laser kinetics is the relative population of the B and C states, as well as the coupling of the two states by collisions with electrons and heavy particles. The B-state population can be monitored using its strong fluorescence. However, for the long-lived C state, it would be advantageous to use its transient absorption to a higher state.

Using the Dunning and Hay[113,114] definition of the spin-orbit wave functions for the B, C, and D states, the transition moments can be expressed as

$$\mu(B \rightarrow D) = cd\left[\mu(2^2\Pi) - \mu(2^2\Sigma)\right] \quad , \quad (100)$$

and

$$\mu(C \rightarrow D) = \frac{d}{\sqrt{2}}\langle 2^2\Pi \,|\times|\, 2^2\Sigma\rangle \quad , \quad (101)$$

where $2^2\Sigma$ and $2^2\Pi$ are the ion-pair wave functions without spin-orbit coupling. The coefficients c and d are found from the mixing of these states to form the spin-orbit states B and D. The parameters $\mu(2^2\Sigma^+)$ and $(2^2\Pi)$ are the dipole moments of the ion-pair states for KrF. Dunning and Hay[113] give $\mu(2^2\Sigma^+) = 1.68$ a.u. and $\mu(2^2\Pi) = 1.82$ a.u. at 4.75 bohr. The value of the transition moment $\langle 2^2\Pi \mid x \mid 2^2\Sigma^+\rangle$ was calculated in the present study to be 0.01 a.u. for KrF. Using these values, the transition moments for the spin-orbit states are $\mu(B \rightarrow D) = 0.14$ a.u. and $\mu(C \rightarrow D) = 0.0036$ a.u. After squaring the transition moments and including the y component, the $C \rightarrow D$ transition is predicted to be 750 times weaker than the $B \rightarrow D$ transition. Consequently, only the $B \rightarrow D$ transition is expected to be observed.

The next step was to investigate the Franck-Condon (FC) factors for the $B \rightarrow D$ transition. Table 7-16 lists values of the FC factors, along with the predicted transition

v″	v′ = 0	1	2	3	4	5
0	0.872 (5702)	0.107 (5366)	0.013 —	0.002 —	— —	— —
1	0.130 (6043)	0.659 (5707)	0.179 (5378)	0.026 —	0.004 —	— —
2	0.004 —	0.220 (6045)	0.504 (5716)	0.210 (5390)	0.049 —	0.007 —
3	— —	0.011 —	0.264 (6051)	0.401 (5726)	0.231 (5403)	0.062 —
4	— —	— —	0.016 —	0.340 (6061)	0.335 (5738)	0.230 (5418)
5	— —	— —	— —	0.020 —	0.360 (6075)	0.303 (5754)

Table 7-16. Wavelengths and FC factors for B—D transitions in KrF; frequencies in parentheses are for stronger transitions, in cm^{-1}.

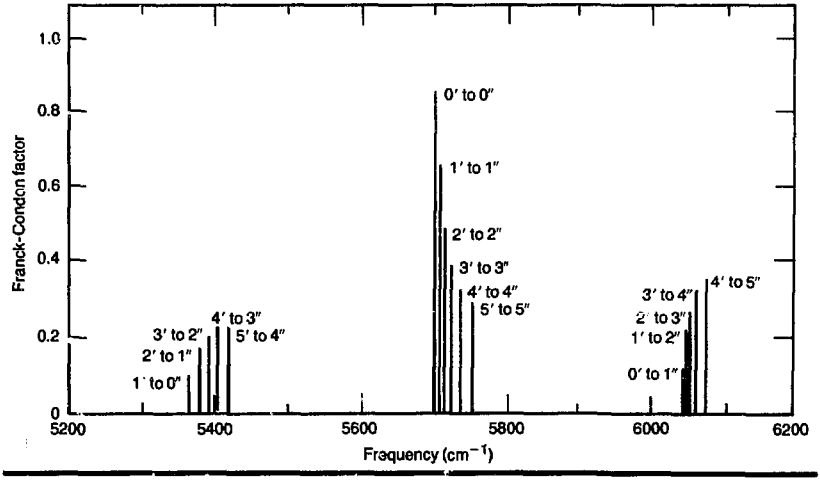

Fig. 7-94. FC factors for $B \rightarrow D$ transition in KrF.

frequencies. The FC factors and frequencies are also summarized in Fig. 7-94. Rotational effects have not been included.

Fig. 7-95. Potential-energy curves for B state and two lowest Rydberg states of KrF.

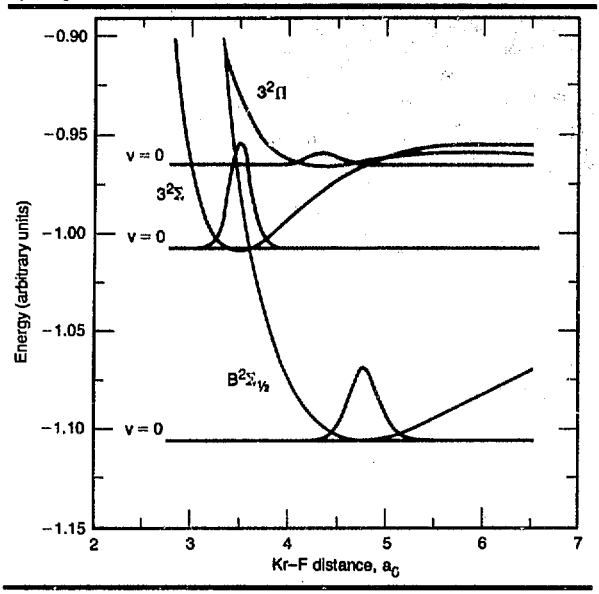

Fig. 7-96. Comparison of $B(v = 0)$ and $3^2\Sigma(v = 19)$ vibrational wave functions.

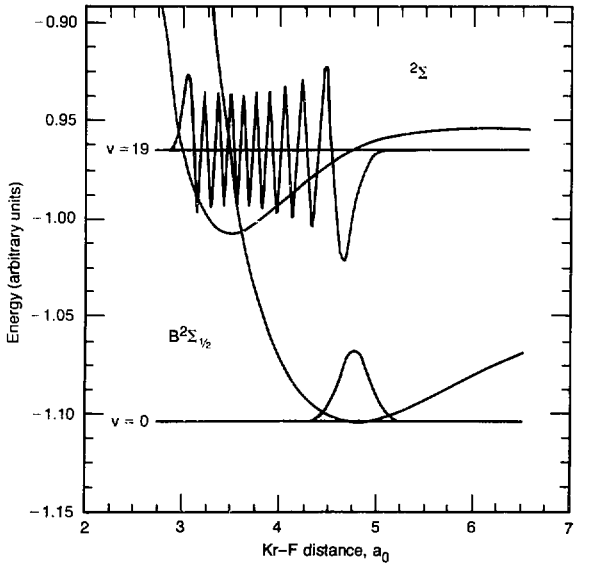

The transitions cluster into three groups separated in energy by about 300 cm^{-1}. Within a group, the lines are only a few wave numbers apart and probably could not be resolved. The weakness of the $C \rightarrow D$ transition presents the most important stumbling block to using these transitions in a kinetic study. The wavelength for the strong $B \rightarrow D$ absorption, $\lambda = 17\,543$ Å, also presents a serious problem in finding a probe laser.

In their papers on the electronic structure of KrF, Dunning and Hay[113,114] reported several Rydberg state potential-energy curves in addition to the curves for the ion-pair levels, each of which dissociate to $Kr^*(^1P)$ and $F(^2P)$. We have calculated both the transition moments and FC factors between the B state and the lowest two Rydberg states. The calculation of the $2^2\Sigma^+ \rightarrow 4^2\Pi$ transition moment is not complete, but the FC factors have been determined and are reported here. The transition moment between the $2^2\Sigma^+$ ion-pair state and the $3^2\Sigma^+$ Rydberg state at 4.75 a.u. is given by Dunning and Hay[114] as 0.3 a.u. and by the present calculations as 0.26 a.u. The $3^2\Pi$ state is not coupled strongly to the $2^2\Sigma^+$ ion-pair state $\mu(\Pi \rightarrow \Sigma)$ and is equal to 0.0017 a.u. When spin-orbit coupling is introduced into the ion-pair states, the $B \rightarrow 3^2\Sigma^+$ transition moment is reduced to 0.2 a.u., which can be compared to the value of 1.0 for the $B \rightarrow X^2\Sigma^+$ laser transition.

The $3^2\Pi$ Rydberg state is strongly coupled to the $2^2\Sigma^+$ ion-pair state, giving $\mu(\Sigma \rightarrow \Pi) = 0.38$ a.u. Including spin-orbit coupling reduces this to 0.33 a.u. The $3^2\Pi$ Rydberg state is also radiatively coupled to the lowest $^2\Pi$ state arising from the interaction of ground-state $Kr(^1S)$ and $F(^2P)$, $\mu(\Pi \rightarrow \Pi)$ and is equal to 0.45 a.u.

Figure 7-95 shows the potential curves for the $B\ ^2\Sigma_{1/2}$, $3^2\Sigma^+$, and $3^2\Pi$ states as calculated by Dunning and Hay[114], along with the lowest vibrational wave function for each state determined in this study. Because of the large displacement of their potential wells, the FC overlap for the $B(v = 0)$ and $3^2\Sigma^+(v = 0)$ levels is clearly zero. However, for higher vibrational levels of the Rydberg state, the FC factor becomes significant. For example, the $v = 19$ level has an FC factor of 0.21 with the $B(v = 0)$ level. The overl can vary dramatically with the nodal

pattern of the upper levels, as illustrated in Figs. 7-96 and 7-97. The $v = 18$ level of the $3^2\Sigma^+$ state has a favorable overlap, as do the levels $v = 19$, 20, 21, and 22. However, by $v = 23$, a node has developed near the midpoint of the $B(v = 0)$ wave function, and the FC factor is only 0.02. Table 7-17 summarizes the FC factor for these levels with $B(v = 0)$.

The $3^2\Pi$ state has a shallow minimum that is more or less at the same internuclear separation as that of the B state (see Fig. 7-95). The $B(v = 0)$ and $3^2\Pi$ ($v = 0$) FC factor is only 0.03, but, as given in Table 7-18, the higher vibrational levels of each state have much better overlap. Because of the large errors in the asymptotic limits of the calculated potential-energy curves, the FC factors and transition moments are probably more accurate than the predicted transition wavelengths for both the $3^2\Sigma^+$ and $3^2\Pi$ states.

We have also considered the other $^2\Pi$ state arising from this asymptotic limit. As shown in Fig. 7-98, it has a shallow well in the FC region of the B state that can support at least one vibrational level. The FC factor is a strong 0.27, and the calculated wavelength for the transition is 245 nm.

Recently, Shimauchi, Karasawa, and Miura[115] have observed absorption bands and lines in a discharge-pumped KrF laser spectrum. They ruled out impurities such as C, HF, CF, and CF_2 and concluded that the bands were caused by v' progressions of an excited state of KrF. The dissociation limit for the upper state of the absorption was estimated to be 40 308 cm^{-1} above the B-state $v = 0$ level. This corresponds to the $Kr^*(^3P_{3/2}) + F(^2P)$ limit at 10.18 eV, provided the absorption does arise from the B state. However, their derived spectroscopic parameters are in serious disagreement with those of the $^2\Sigma^+$ or $^2\Pi$ Rydberg states calculated by Dunning and Hay.[114] This error undoubtedly comes from analysis of the very high levels using expansion formulas derived from the harmonic oscillator and appropriate only for the lower vibrational levels.[116] For example, Shimauchi et al.[115] predict the values $\omega_e = 519.6\ cm^{-1}$, $X_e\omega_e = 2.165\ cm^{-1}$, and $D_e = 3.865$ eV. The correct values for the $3^2\Sigma^+$ state are $\omega_e = 506\ cm^{-1}$, $X_e\omega_e = 9\ cm^{-1}$, and $D_e = .33$ eV. The observation of the absorption in KrF is consistent with the present calculations, even though the authors of Ref. 115 cannot conclusively prove that the Rydberg states of KrF are responsible. Further calculations are planned on the vibrational levels $v > 100$ of the $3^2\Sigma^+$ state to compare to the experimental band positions.

It is not clear what role the Rydberg-state absorption plays in the KrF laser. It is possible that it may explain the presence of two peaks in the laser spectra at 248.4 and 249.1 nm, with the absorption occurring between these peaks. However, Goldhar and Murray[117] have suggested that absorption by CF_2 is responsible for the hole in the KrF spectra. Rydberg states that are formed by absorption from the B state quickly

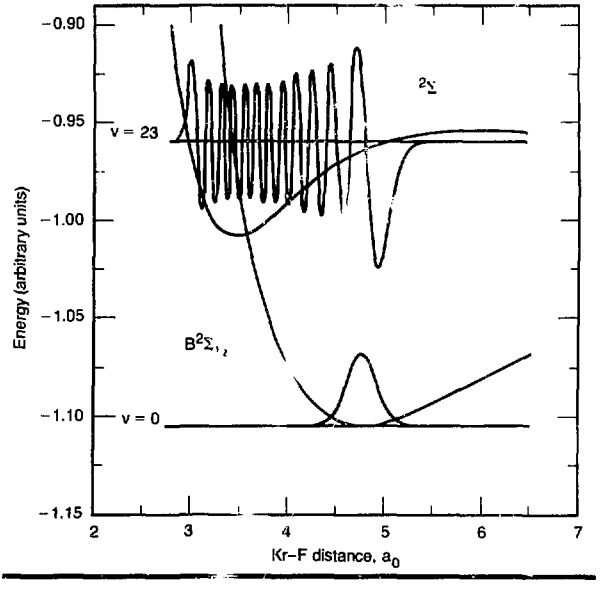

Fig. 7-97. Comparison of $B(v = 0)$ and $3^2\Sigma(v = 23)$ vibrational wave functions.

Table 7-17. FC factors for $B(v = 0)$ level with higher levels of $3^2\Sigma^+$ state.

N	$\|\langle B(v = 0) \| 3^2\Sigma^+(v = n)\rangle\|^2$	λ^a (nm)
18	0.13	264
19	0.21	261
20	0.25	259
21	0.21	257
22	0.10	255
23	0.02	253

[a] Calculated wavelengths include correction factor of 0.97 eV to adjust $Kr^*(^3P) + F(^2P)$ asymptotic limit to its correct value.

v	v'	$\|(v\|v')\|^2$	λ^a (nm)
0	1	0.19	258
0	2	0.41	257
0	3	0.32	255
1	1	0.18	261
1	3	0.16	257

[a]Calculated wavelengths include correction factor of 0.97 eV to adjust $Kr^*(^3P)$ + F (^2P) asymptotic limit to its correct value.

Table 7-18. FC factors for vibrational levels of B and $3^2\Pi$ states of KrF.

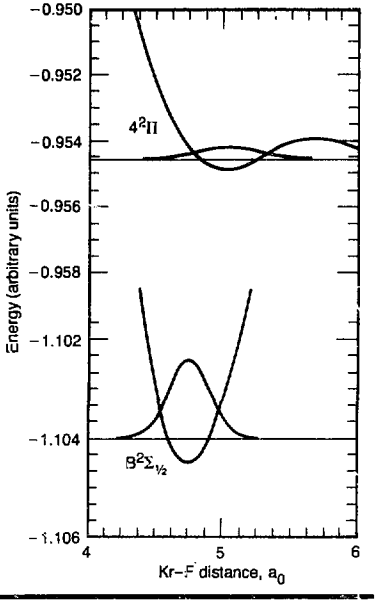

Fig. 7-98. Lowest vibrational wave functions of *B* state and $4^2\Pi$ state.

dissociate and produce $Kr^*(^3P_{3/2})$. Depending on the conditions, the excited Kr atoms can reform the KrF upper laser level, thus resulting in no significant loss. In any case, the total absorption in this region does not appear to be significant after accounting for F_2 and rare-gas dimer ion absorption.[115]

Authors: A. U. Hazi, J. R. Harvey, and N. W. Winter

RAPIER Experiments

This year, we describe further experiments on the limits of Raman pulse compression of KrF lasers and pulse stacking where the output of an electron-beam-pumped KrF laser is angle-coded and compressed. New developments in modular pulse-power technology for a KrF laser-fusion driver are presented later in this article. Our experiments provide practical information needed to assess the value of such systems for large-scale laser-fusion drivers.

Raman Compression in Double-Pass Amplifier Geometry. In Ref. 118, we presented theoretical and experimental analyses of the basic physics of Raman amplifiers and Raman pulse compression. This year we have concentrated on experiments that illustrate the properties of these devices in practical systems with large Fresnel number and pump beams of poor spatial quality. We have also chosen to study these effects in a double-pass Raman amplifier geometry. The analysis of such geometries is more complex than the analysis of the simple single-pass geometries we used previously for basic physics experiments. However, double-pass geometries have more favorable staging properties in practical systems than do single-pass designs. Thus, we can use the former design to begin an evaluation of the practical advantages of multipass geometries in this system.

Figure 7-99 shows the double-pass geometry we have chosen for our series of experiments; this geometry is particularly powerful for a Raman compressor. A short Stokes pulse enters a Raman cell coincident with the leading edge of the pump pulse and sees small signal forward gain as it propagates through the cell. The input intensity of the Stokes pulse is chosen so that it reaches the saturation fluence of the amplifier and depletes energy from the pump just as it reaches the end of the cell. The Stokes pulse then strikes a mirror and travels back through the remainder of the pump pulse in the Raman cell, extracting energy from it and increasing in intensity to several times the pump intensity.

We now present a numerical comparison using a Raman extraction code of a single-pass backward Raman amplifier and an amplifier with the double-pass geometry of Fig. 7-99. We chose the parameters for this comparison (Fig. 7-100) to represent typical pulse shapes, gains, and compressions for a practical high-efficiency compressor stage. The pump pulse has a flat top with linear rise and fall, each equal to 20% of the total pulse length, which is representative of the pulse we expect from a pulse-stacked, e-beam-pumped KrF amplifier, as

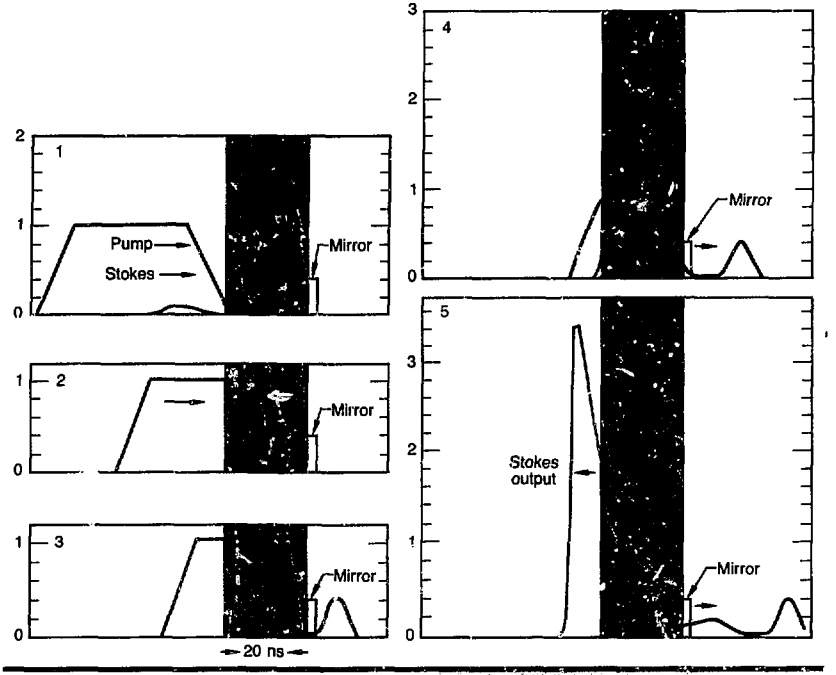

Fig. 7-99. Pulse amplification in two-pass Raman amplifier.

demonstrated in experiments discussed below. The Stokes pulse is a Gaussian pulse with a width equal to one-fourth of the full width at half power of the pump pulse. The Raman cell has a length of 50% of the full width at half power of the pump pulse. The backward Raman small signal gain is 3.7 Np, and the forward Raman gain is higher by a forward/backward ratio of 1.5, or 5.5 Np.

Figure 7-101 shows a comparison of the extraction efficiency of a single-pass backward amplifier and the double-pass amplifier of Fig. 7-99 under these conditions as a function of Stokes-pulse input energy. The total second-Stokes gain is plotted on these curves as a parameter, assuming that the Stokes mirror reflects 100% of the second Stokes as well as the first Stokes, which is the worst case. If the second-Stokes reflectivity were reduced to 5%, for example, the points at high extraction efficiency on the double-pass amplifier extraction curve have a second-Stokes gain 3 Np less than that shown on the graph. An ideal amplifier may operate with a second-Stokes gain near 20 Np, but intensity variations in the

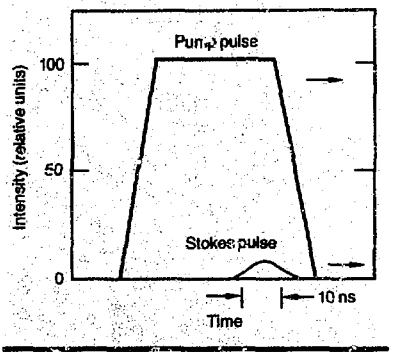

Fig. 7-100. Pulse shapes of pump and Stokes inputs to Raman amplifier.

Stokes pulse will lead to higher local intensities in the amplifier that push the average second-Stokes gain we can tolerate to a smaller value.

The single-pass saturated amplifier can achieve very high extraction efficiency, but has very low saturated gain, which is the usual deficiency of highly saturated amplifiers. The backward small signal gain of 3.7 Np implies that only 3.7 saturation fluences are stored in the pump beam, yet the Stokes beam must enter at or above 1

saturation fluence to get reasonably efficient extraction. Thus, the stage gain can only be a factor of 3 or 4. The double-pass amplifier allows a stage gain more than an order of magnitude greater for similar extraction efficiency and permits an enormous reduction in the number and size of preamplifiers in a laser chain, with consequent savings in complexity and cost. Experimental studies of a double-pass amplifier of this type confirm these predictions, as we shall now discuss.

Fig. 7-101. Pump depletion in Raman amplifier.

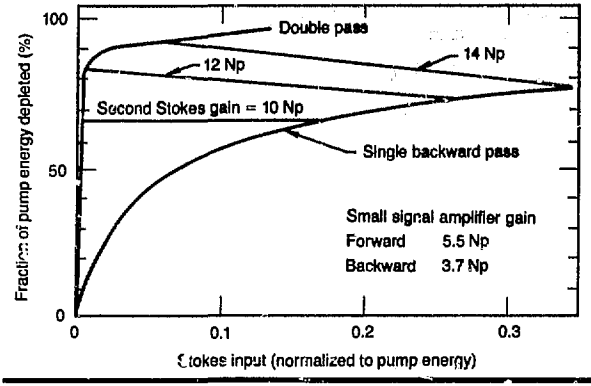

The KrF laser system (Fig. 7-105) that was used in our experiments is an upgraded version of the Raman amplifier pumped by intensified excimer radiation (RAPIER) front end using fast UV-preionized discharge lasers, which were described in Ref. 123. The system uses a KrF etalon-tuned oscillator followed by regenerative amplifiers. Lasers L1 and L2 are small discharge lasers with an excited volume having dimensions of $0.5 \times 2 \times 30$ cm, while L3 to L5 are higher-energy lasers with an excited volume having dimensions of, nominally, $1 \times 5 \times 100$ cm. These larger devices typically generate 600 mJ each in a 15- to 20-ns pulse. The smaller lasers, L1 and L2, have stable resonators with mode-limiting apertures, and the larger lasers, L3 to L5, have unstable resonators with a magnification of 10.

Two etalons (0.1-mm and 1-mm gaps) reduce the line width of laser L1 to less than 0.1 cm^{-1}. Another etalon (1-cm gap) can be

Fig. 7-102. RAPIER front-end KrF laser system.

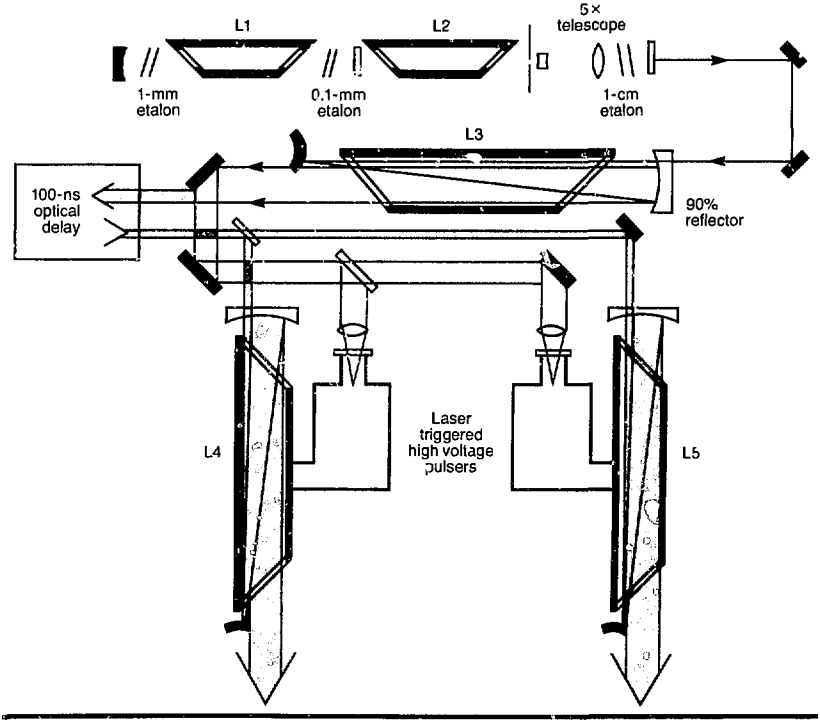

inserted into the cavity of laser L2 to further reduce the line width to 0.02 cm^{-1}.

Line widths are measured using a Fabry–Perot interferometer uniformly illuminated by a diffusing screen. The far field of the Fabry–Perot output is photographed on Plus-X film that is calibrated at the same wavelength (249 nm) with a series of spots of decreasing relative intensity. The photographs of the Fabry–Perot rings are then digitized and converted to a linear intensity scale. A digital processing algorithm is then used to average over radial position in the rings and convert the fringes from a quadratic to linear frequency scale, as shown in Fig. 7-103. The frequency scale is determined by the mode spacing between adjacent peaks, which is $1/2L$ in cm^{-1}, where L is the etalon spacing. We measured line widths from the full width at half maximum (FWHM) of the smallest fully resolved interference fringe. This width is actually the line width of the laser convolved with the intrinsic line width of the Fabry–Perot interferometer, which is related to the finesse and etalon spacing. We estimate the finesse of the Fabry–Perot interferometer to be approximately 20. Thus, for the 6-cm etalon-spacing data shown, the actual laser line width is about 0.016 cm^{-1}.

Lasers L1 to L3 are electrically triggered, but all components of the system past L3 are optically timed to L3 using laser-triggered spark gaps or photodiodes. We find optical timing to be less troublesome than electrical timing for our complex short-pulse KrF systems.

We have encountered some problems with amplified spontaneous emission, which gives a broadband background signal in the output from L4 and L5. The broadband background from L2 is very weak, but approximately 5% of the output from L3 and 15% of the energy from L5 was measured to be outside a 1-cm^{-1} bandwidth. We attribute this to amplified spontaneous emission or diffuse parasitics in these very high-gain devices. In addition, we find that about 5% of the narrow-band part of the output from L5 is not in the desired linear polarization, even though the output from L3 passes through a polarizer before entering L5. This could be caused by stress-induced birefringence in the laser windows.

The energy available for Raman extraction in the L5 output beam is, therefore, about 20% less than the calorimetrically measured output.

The Raman part of the experiment shown in Fig. 7-104 begins with a low-energy high-quality forward Raman oscillator generating 0.25 to 0.5 mJ of Stokes radiation. The Raman oscillator is similar to one we have used previously, but incorporates a Pockels cell placed in front of the input to the Raman cell to control the pulse length of the Stokes output. This modification allows us to control the oscillator Stokes pulse width over the range of 2 to 5 ns that we used in extraction experiments.

The beam emerging from the oscillator Raman cell is dispersed with a prism and the Stokes beam uniformly illuminates a 1-mm slit aperture. The image of that aperture is magnified by a 5× telescope and relayed down the amplifier chain to the output of the Raman power amplifier. The beam exiting the 5× telescope is mildly expanding and exits the power amplifier as a 1.5- by 1.3-cm rectangle.

A high-gain Raman preamplifier is used to boost the oscillator output to the level required to saturate the power amplifier. We generate uniform Raman gain in the preamplifier by splitting the pump beam into six beams that cross at small angles (1 to 0.5 mrad) in the center of the cell. A dichroic mirror was used to separate the

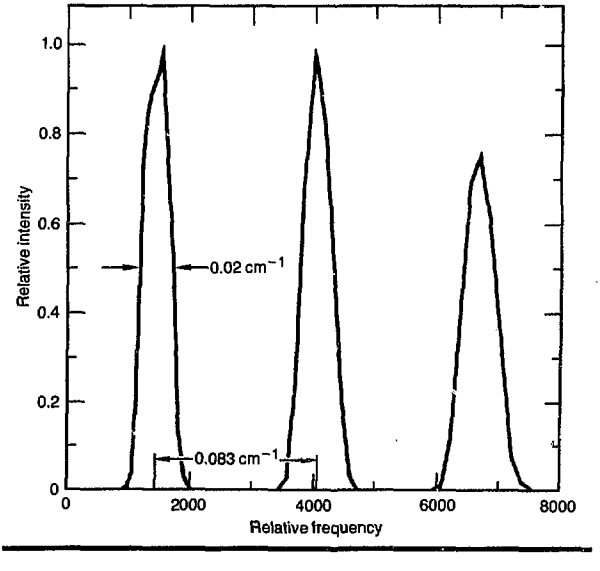

Fig. 7-103. Conversion of Fabry-Perot rings from quadratic to linear frequency scale.

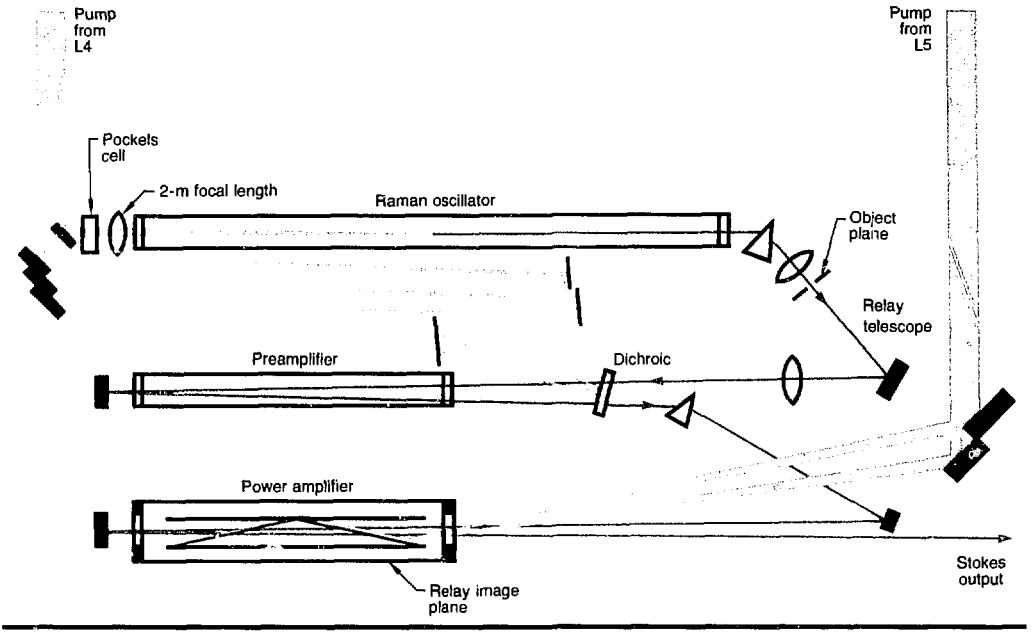

Fig. 7-104. RAPIER ▲ front-end Raman system.

Fig. 7-105. Input and output pulses in Raman power amplifier. ▼

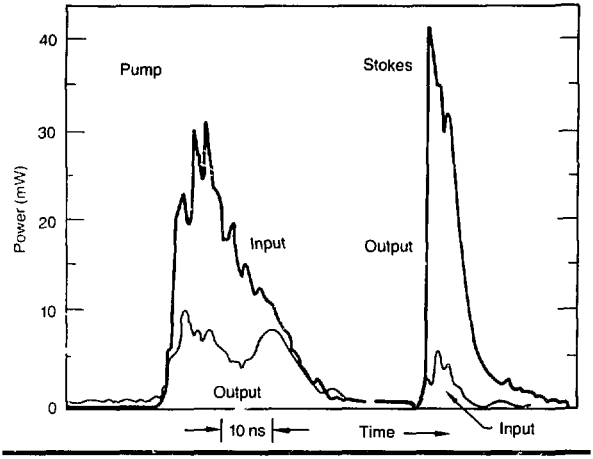

Stokes output. The angles of pump and Stokes beams were carefully designed to avoid the four-wave mixing effects that we have described previously. These effects were negligible in this amplifier.

We must have good spatial overlap between the pump and the Stokes beam in the power amplifier to have a high extraction efficiency. This was accomplished by bouncing the pump beams between a pair of reflecting light-guide walls, while the Stokes beam propagated in a double pass down the middle of the cell, avoiding the reflecting walls. The two pump beams bounce three times from the walls while transiting the cell, which has a 2-cm aperture. The walls of the light guide consist of 10 glass plates ($4 \times 1 \times 30$ cm) held in a rigid frame. The glass surface was coated with a layer of rhodium to enhance the reflectivity. In three bounces propagating down the light guide, the pump lost ~10% of its energy. Nonoptical-quality glass was used for these plates, and the pump phase distortion for reflection at normal incidence was about 20 waves.

The pump and Stokes beams do not fully overlap in a light-guide cell such as this at any given instant. The transverse oscillation of the pump in the light guide must, therefore, be faster than the Stokes pulse length to ensure efficient energy transfer. In this experiment, the Stokes beam filled 70% of the gain cross section, and the time between the bounces of the pump was 1.7 ns, so that the overlap was adequate for 5-ns Stokes pulses, but marginal for 2-ns pulses We observe these overlap effects and find that, to first order, they fit a simple computer model of extraction in the amplifier.

We studied extraction in the power amplifier of Fig. 7-104 in some detail for comparison to models. Four signals corresponding to input and output Stokes and pump beams were monitored on each shot with appropriate beam splitters and fast photodiodes. The signals were either displayed on a Tektronix 7904 oscilloscope or digitized with Tektronix R7912 transient digitizers and analyzed using a PDP-11 computer. Each photodiode was absolutely calibrated by comparing the integrated-signal calorimetric-energy measurements. Typical input and output pulses for the Stokes and pump beams are shown in Fig. 7-105, where the large Stokes amplification and pump depletion are evident. Figure 7-106 shows the output Stokes energy from the amplifier vs the input Stokes energy in a 5-ns pulse. Curve (a) corresponds to two pump beams with 340 mJ of available energy, curve (b) to a single pump beam with 240 mJ, and curve (c) to a single pump beam with 70 mJ in a 1- by 1-cm^2 beam propagating at a small angle (3 mrad) to the Stokes beam without bouncing from the light guide. A dichroic mirror was necessary for case (c) to separate the output Stokes beam. However, when the light guide is used, cases (a) and (b), the angle between the pump and Stokes beams is 40 mrad, and the beams can be geometrically separated. Solid lines on the graph represent the theoretical predictions from a one-dimensional model for a Raman amplifier, showing good agreement between the model and the experiment for all cases studied.

The spatial beam profile of the output Stokes beam was analyzed by relaying the image of the Stokes beam exiting the power amplifier onto a finely ground diffusing screen and photographing it from the back with a UV camera using Plus-X film. The spatial resolution due to granularity of the diffuser was about 0.2 mm, which was adequate for our purpose. The diffuser-camera combination attenuates the light intensity impinging on the film by the required factor of $\sim 10^6$ without introducing as much beam distortion as neutral density filters. The image of the Stokes beam is shown in Fig. 7-107(c), and the digitized linearized intensity profiles are shown in Fig. 7-108. The intensity variation across the profile is typically $\pm 40\%$ of the average intensity. This beam profile should be contrasted with that of the pump beam. Figure 7-107(a) and (b) shows the intensity profile of the pump beam as it enters and exits the light guide, as recorded on Dylux film. This is a good demonstration of beam-quality improvement in the Raman amplifier.

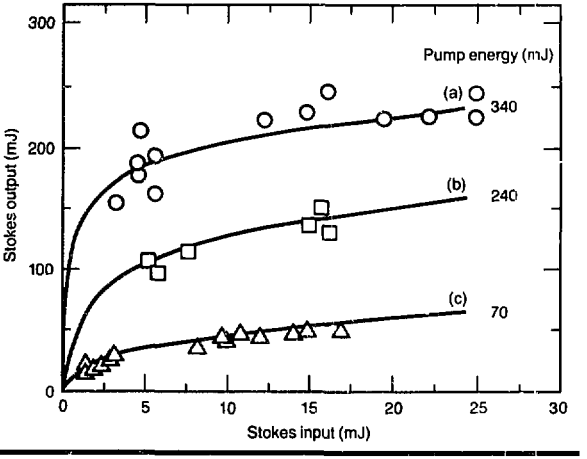

Fig. 7-106. Input and output characteristics of Raman amplifier. ▲

Fig. 7-107. Pump and Stokes beam quality in Raman amplifier. ▼

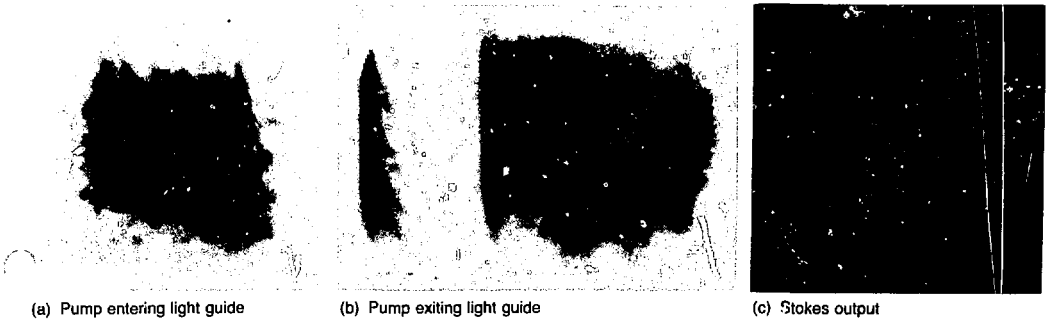

(a) Pump entering light guide (b) Pump exiting light guide (c) Stokes output

The far field of the Stokes output was also studied and was close to the diffraction limit. Some astigmatism was present in the beam from passing through the prisms. There was no observable change in the beam profile with and without gain in the power amplifier, confirming that the angles were properly chosen to avoid four-wave mixing effects.[119]

At a pump energy of 340 mJ with 30 mJ of Stokes input (290 mJ in 5-ns Stokes output), traces of second-Stokes radiation are observed in the spectrum of the output Stokes beam, although it is too weak to be important. With 2-ns Stokes input pulses, the second Stokes is observed at a somewhat lower output energy, as expected. The second-Stokes gain corresponding to these cases can be calculated from our model. For the peaks of the spatial profile, it implies that the second Stokes becomes observable at a gain of about e^{14}, which is in reasonable agreement with our earlier predictions, stating that the second-Stokes intensity becomes comparable to the first-Stokes intensity at a gain of about e^{20}.

Another parasitic that is possible in this system is the conversion of pump energy to forward first-Stokes intensity. The average gain for such a process is the same as the first-pass gain through the Raman amplifier, or about $e^{5.5}$ for the 340-mJ pump. The beam distortion for this light guide is expected to increase the peak gain coefficient for the parasitic by about a factor of 2, which should still be below the gain required for forward first-Stokes superfluorescence. We analyzed the spectrum of the pump beam exiting the Raman cell without any Stokes input and confirmed the absence of any forward parasitic waves.

A-Amplifier Pulse-Stacking Experiment. A schematic of the experiment is shown in Fig. 7-109. The input to the e-beam-pumped amplifier was generated by

Fig. 7-108. Cross section of intensity distribution of Stokes beam.

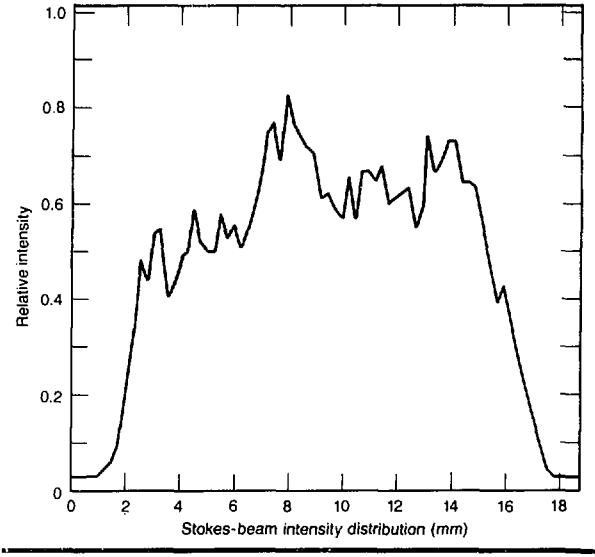

Fig. 7-109. Schematic of four-stacker system.

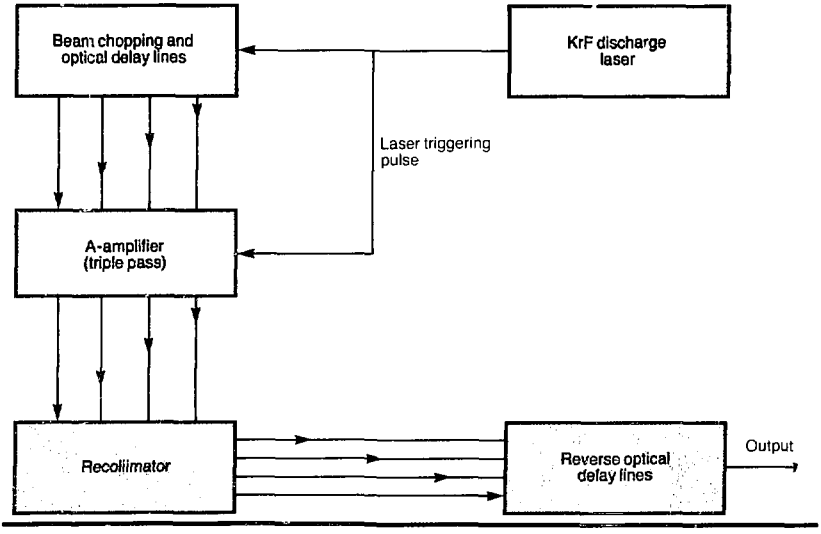

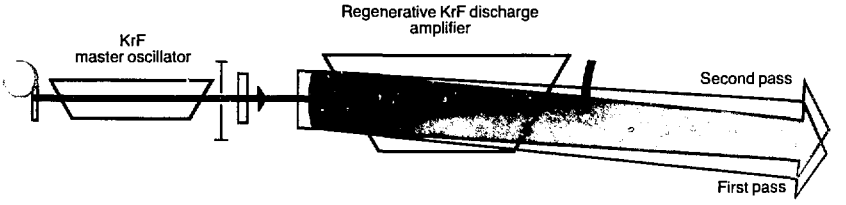

Fig. 7-110. Master oscillator-power amplifier configuration for 10-ns pulses.

a KrF discharge laser, described in more detail below. The output from this laser was two sequential angle-encoded beams. The first beam was used as input to the amplifier, and the second beam was used to trigger the e-beam guns. The beam intended for amplifier input was sent through an optical delay system that split the beam into four separate sections and stacked them sequentially in time. Each beam was expanded by a factor of 10 during a triple pass in the amplifier. On exiting, they were recollimated and passed through a reverse-delay system, resulting in a single amplified pulse.

A KrF discharge oscillator-amplifier combination, shown in Fig. 7-110, that normally operates at 600 mJ in a single 20-ns pulse at 249 nm, was modified to yield two angle-coded 10-ns pulses by a calculated misalignment of the unstable-resonator cavity in the amplifier. A weak beam from the oscillator was injected into the amplifier at an angle substantially different from the natural mode of the unstable resonator. Successive round trips in the resonator quadratically approach the natural mode.

Since the various modes of the unstable resonator compete, it was necessary to carefully control the level of injection signal from the oscillator and the amount of feedback in the amplifier so the energy would be extracted in the proper modes at the desired times. The injection misalignment was such that the first round trip (10 ns) differed from the second by approximately 2.5 mrad. After propagating 20 m, the first and subsequent round trips were completely separated.

The amplifier in this experiment was a dual e-beam-driven KrF device in the RAPIER facility that has been described in detail previously.[120] The gain duration of the amplifier is nominally 50 ns (FWHM). To accurately synchronize the amplifier to the input laser, one of the pulses from the probe was used to trigger the Blumlein lines.[121] The probe beam was split and focused through two holes in each Blumlein output switch, which was pressurized with SF_6 gas. Because of the low breakdown threshold of SF_6 in the UV, subnanosecond jitter can be obtained with this switching arrangement.

The amplifier input beams made a triple-pass through the telescoping optical configuration shown in Fig. 7-111. The lower portion of the 10- × 10- × 50-cm volume was used as a preamplifier. The telescope was adjusted to render the output beams slightly focusing. As each beam traverses the amplifier at a slightly different angle, the beams separate with increasing distance from the amplifier. Thus, at 12.5 m from the exit of the amplifier, the location of the recollimating optics, the beams were completely separated and reduced to one-half their size at the amplifier.

The temporal pulse shapes were monitored routinely at strategic locations with S-20 UV-grade vacuum photodiodes. These detectors were located in positions to observe the original input pulse, the time-sequenced pulses as they exited the amplifier, and the restacked single-output pulse.

In this experiment, we operated the amplifier as both a triple-pass four-stacker amplifier and an injection-locked unstable resonator. The resonator cavity was formed by the same optics as the three-pass amplifier, with the alignment changed to allow feedback. In the amplifier configuration, the input–output pulse-shape characteristics and saturation effects were studied. The device was then operated as an unstable resonator to determine what fraction of the available energy was being extracted in the amplifier configuration.

Figure 7-112 shows the typical input and output pulse shapes of the triple-pass amplifier. The two pulses in Fig. 7-112(a) are the input and restacked outputs for the case of no gain in the amplifier. Figure 7-112(b) shows the time-sequenced pulses directly after the output of the amplifier, again with no gain. Figure 7-112(c) and (d) shows the

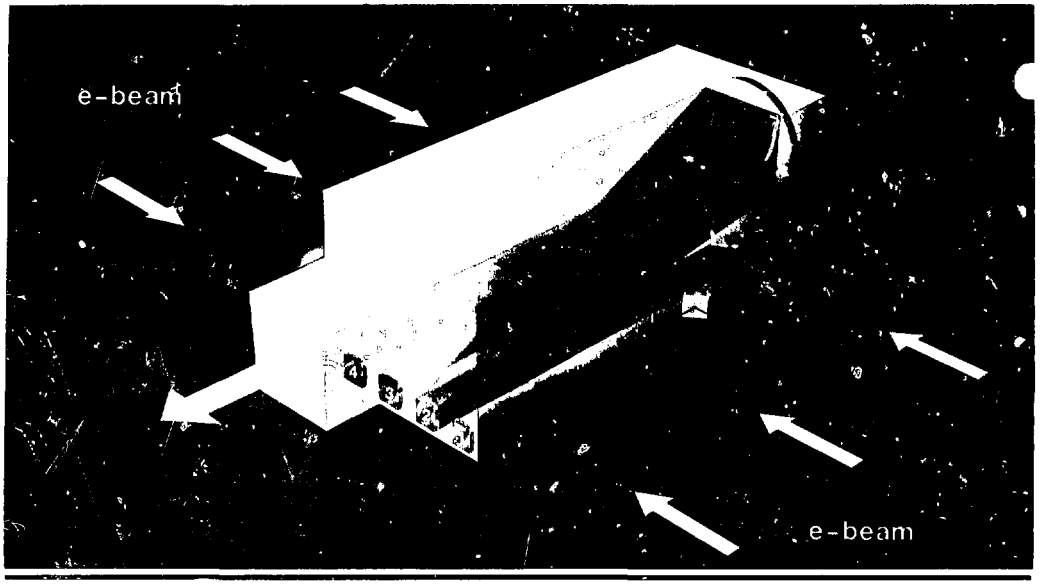

Fig. 7-111. Triple-pass amplifier configuration.

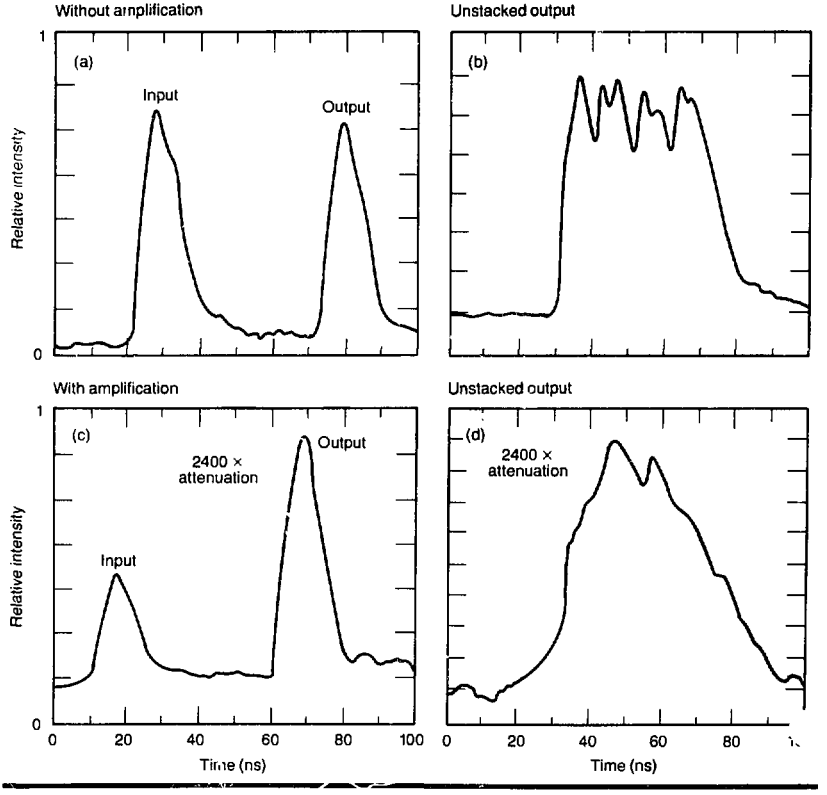

Fig. 7-112. Typical input and output pulses for four-stacker triple-pass oscillator.

same pulses with gain for a total input of approximately 100 mJ. Note that the amplified pulses have been attenuated by a factor of 2400 from the previous case. Figure 7-112(c) shows that the amplified pulse underwent virtually no pulse broadening because of saturation effects in the amplifier, although the amplifier was fully saturated, as shown below. This lack of pulse broadening can be attributed to the geometry of the triple-pass configuration. The input to the amplifier was held at a level such that the first pass acted as a preamplifier stage. The pulses were fully saturated on the final pass, during which the tail of one pulse was forced to compete for the available gain with the front of the following pulse. There was also no apparent degradation of the pulse shape caused by crosstalk between the various optical channels.

Figure 7-113 shows a plot of the input vs output energy for the triple-pass amplifier, displaying typical saturation characteristics. Also plotted in Fig. 7-113 is the average output energy for the amplifier operated as

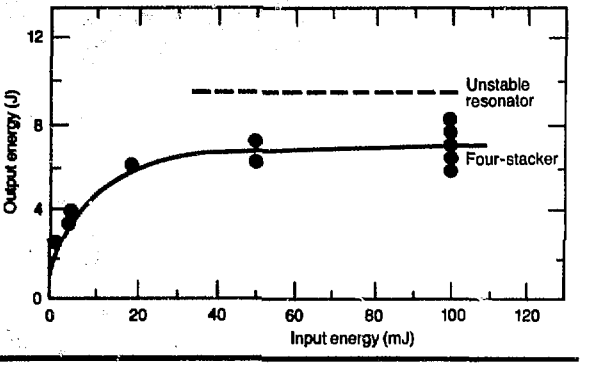

Fig. 7-113. Input vs output energy for triple-pass four-stacker amplifier.

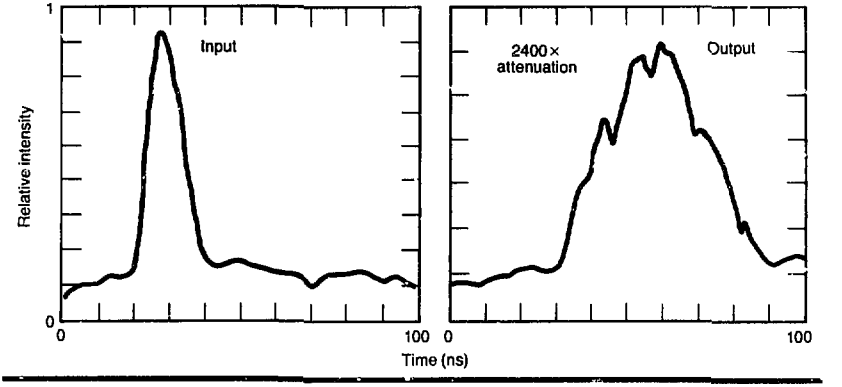

Fig. 7-114. Typical input and output pulses for A-amplifier as injection-locked unstable resonator (p.7-92).

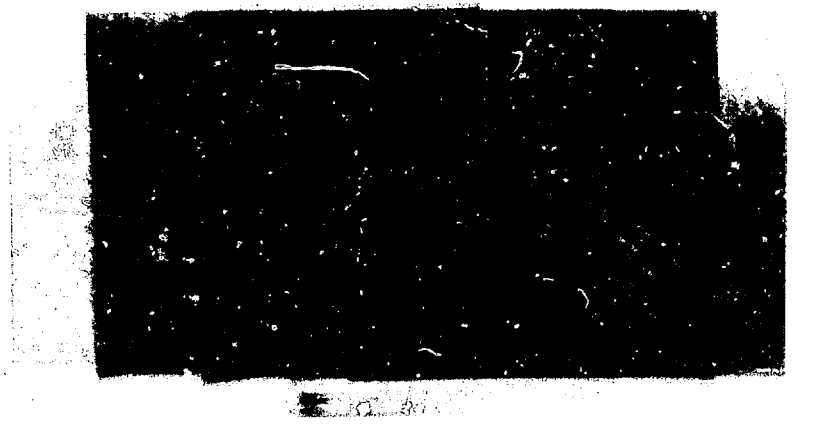

Fig. 7-115. Output beams of triple-pass four-stacker 2 m from amplifier (p. 7-42).

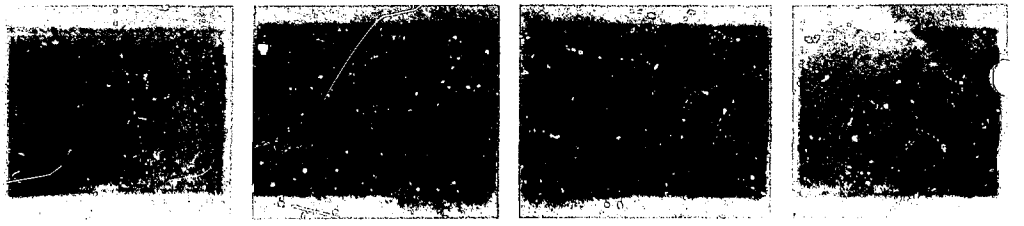

Fig. 7-116. Output beams of triple-pass four-stacker 12.5 m from amplifier.

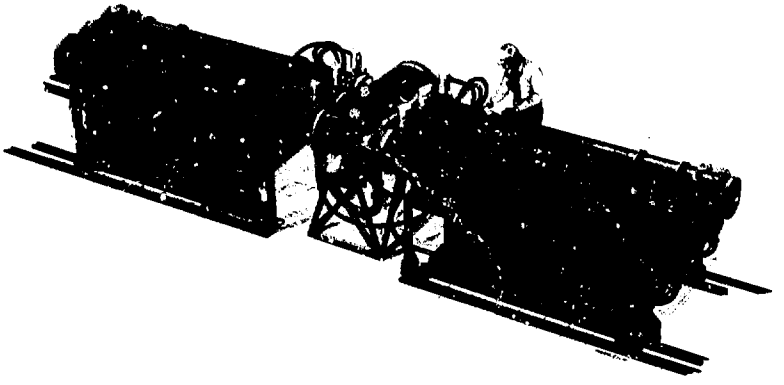

Fig. 7-117.RAPIER-B amplifier.

an injection-locked unstable resonator. Approximately 80% of the energy available was extracted by the triple-pass amplifier. The fraction could be increased by further optimization of the triple-pass geometry, including moving the separate optical channels closer together. Figure 7-114 shows the input and output pulse shapes for the unstable resonator.

Figures 7-115 and 7-116 show the four-stacker beam profiles at distances of 2 and 12.5 m, from the exit of the amplifier. The images were recorded on Dylux 608 Registration Master Film and rephotographed for publication.[122] In Fig. 7-118, near the amplifier, the beams are still overlapping and nearly the size of the amplifier cavity. After propagating an additional 10.5 m (Fig. 7-116), the beams are reduced in size and are spatially separated. Note the presence of strong diffraction fringes around the edges of the beams produced by the hard edges of the amplifier. Such fringes will be important in high-gain saturated KrF amplifiers, since the beam must saturate the gain up to the edge of the volume. Apodization of the output beam can control such effects at some cost inefficiency. We encountered several modes of parasitic oscillation in the amplifier arising from stray reflections from the many mirrors and components surrounding the high-gain cavity. However, these were easily controlled with low-reflectance baffles in proper locations.

RAPIER-B Amplifier and Pulsed-Power Experiments. The RAPIER-B amplifier is intended not only to deliver 500 J of KrF laser output but also to demonstrate the development of a compact modular pulsed-power and e-beam system that would permit the construction of even larger KrF amplifiers. The width of individual modules has been minimized so that modules can be arrayed side-by-side to produce a nearly continuous e-beam of arbitrary width. Only minor design changes would be required to permit vertical stacking of modules as well.

Figure 7-117 shows an artist's concept of the B-amplifier system. Two sets of three modules are located on each side of a 30-cm-wide by 40-cm-high by 125-cm-long laser cell that will be filled with a mixture

of noble gases and fluorine at a pressure of 2 atm. Each pulsed-power module consists of a Marx generator located in an oil-filled tank beneath a cylindrical 5-Ω water-dielectric pulse-forming line. At the rear of each line is an oil-filled chamber containing all of the charging connections, as well as connections to the adjacent triggered output switch. At the front of each line, adjacent to the laser cell, is an evacuated chamber containing the magnetically isolated diodes, individual diode insulators, and cathodes that produce 25-cm-high by 41-cm-wide e-beams. The kinetic energy of the beam electrons is 450 keV, and the current produced by each module is 90 kA. Thus, each beam delivers 6 kJ of energy in a 150-ns pulse, for a total energy of 36 kJ. Each module is 42 cm wide. The complete machine is 8.2 m long, 1.85 m wide, and 1.45 m high.

During 1981, we completed the development of the pulsed-power subsystems described in Ref. 123. Using a 60-ns pulse-forming line, we have extensively tested a full-scale prototype 150-ns pulse-forming line with both resistive and diode loads. We have also assembled and tested three of the six modules that will be used in the B-amplifier and have nearly completed the installation of these modules in the RAPIER system.

The prototype 150-ns machine was nearly identical to one of the six modules of the B-amplifier. We first tested the prototype with a 5-Ω resistive load to determine pulse shapes and verify machine performance before coupling it to the more complex diode load. Output voltage and current pulse shapes are shown in Fig. 7-118. We conducted the tests at 525 kV, or about 15% above the intended operating point to assure reliability at 450 kV. We did most of the testing with an e-beam diode load. The pulse shapes shown in Fig. 7-119 differ from those in Fig. 7-118 because of diode inductance, a finite formation time for the plasma cathode, and a changing load impedance caused by expansion of the plasma in the diode. More than 7.5 kJ were delivered to a calorimeter located at the anode plane under these conditions. The energy we measured at the anode plane was approximately 75% of the energy stored in the Marx generator. We fired well over 1000 shots in the development of the prototype line, with over 200 shots following the last modification of a component of the machine.

We encountered two types of problems with the prototype line. First, difficulties occurred with several plug-in electrical connections that we incorporated into the design of the B-amplifier to facilitate assembly and maintenance of the pulsed-power modules. These difficulties required extensive testing and some minor design changes. The second problem was the electrical breakdown of the water dielectric of the pulse-forming line caused by air bubbles trapped in the line during filling by the high surface tension of the high-purity (resistivity > 10 MΩ cm) water. Substantial enhancement of the electric field occurs at the surface of bubbles because of the difference in permittivity of air and water. To solve this problem, we devised hardware and a filling procedure to prevent the formation and entrapment of bubbles during filling. We also used deaerated water to prevent the evolution of bubbles after filling.

Following the successful development of the prototype line, we assembled three complete pulsed-power modules that will form one-half of the completed B-amplifier.

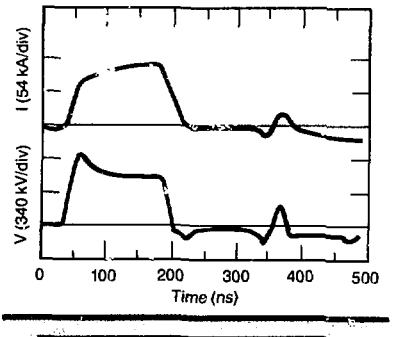

Fig. 7-118. Output pulse, diode load.

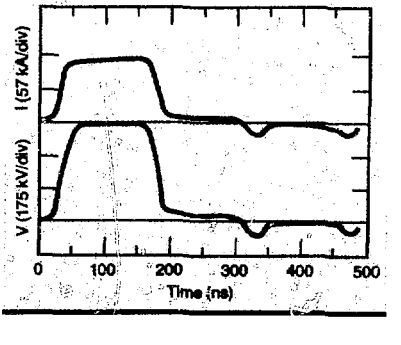

Fig. 7-119. Output pulse, resistive load.

Each of these modules was tested separately for 50 shots at 525 kV output and 20 shots at 450 kV. The three Marx generators have been installed in the B-amplifier tanks and tested with resistive loads to verify the operation of the charging, triggering, and diagnostic systems. We are currently installing the three pulse-forming lines, diodes, and supporting systems.

Authors: J. Goldhar and L. G. Schlitt

Advanced Solid-State Lasers

Introduction. Single crystals of vanadium-doped magnesium fluoride (V:MgF_2) possess many of the properties required of an efficient (≥5%) high-average-power multimegajoule fusion laser. We based this observation, first put forward[124] in 1979, on the limited spectroscopic data available in the literature,[125,126] combined with solid-state laser-system design codes existing at LLNL. With this encouraging potential, measurements of the critical spectroscopic and laser parameters and exploratory crystal-growth studies on V:MgF_2 were carried out in 1980 by the Quantum Electronics and Electronic Materials Groups, Solid State Division of Lincoln Laboratory, Lexington, Mass.

As described in Ref. 127, the following key results were obtained[128]

- Solid solutions of up to 9 wt% VF_2 in MgF_2 were demonstrated in single crystals.
- High-quality optical crystals containing 0.5 wt% VF_2 in MgF_2 were grown, suitable for laser experiments.
- A literature value of the vanadium radiative lifetime of 2.48 ms was confirmed.
- The temperature dependence of the fluorescence lifetime was measured.
- Concentration quenching of fluorescence was found to be negligible for doping levels up to 5 wt% VF_2 in MgF_2 (adequate for large lasers).
- Absolute polarized spectral-absorption cross sections were measured as a function of temperature, thus eliminating discrepancies in the literature.
- Relative polarized spectral-emission cross sections were measured.
- A preliminary value of the σ-polarized spontaneous-emission cross section ($\sim 0.4 \times 10^{-20}$ cm^2) of the $^4T_2 \rightarrow {}^4A_2$ laser transition was determined by zero-phonon-line absorption/emission spectroscopy. The value is half that given in the literature[126] and implies a homogeneous saturation fluence of 42 J/cm^2.
- Argon-laser-pumped V:MgF_2 amplifier and laser experiments were initiated to quantify any excited-state absorption, which was cited in the literature[126] as being small.

Given our encouraging results, we continued work at Lincoln Laboratory to: (1) learn how to grow optical-quality crystals containing ≥1 wt% VF_2, (2) construct the absolute polarized spectral-emission cross-section curves, and (3) assess potential excited-state absorption processes in V:MgF_2 laser amplifiers and oscillators. We report the results of our work in this article.

Spectral Fluorescence and Gain Distributions. Fluorescence was excited by pumping the $^4A_2 \rightarrow {}^4T_1a$ transition with a 50-mW-output cw He–Ne laser. A portion of the laser output was sampled, and the detected fluorescence signal was electronically normalized to this output for improved accuracy and reproducibility. Fluorescence from the crystal, which was oriented using x-ray techniques, was passed through a Polaroid-type HR sheet polarizer, analyzed by a Heath EU-700 grating spectrometer, and detected by a PbS photoconductor. The stepping motors driving the spectrometer scan and chart recorder were synchronized to obtain an accurate wavelength axis. The polarized wavelength response of the detection system was determined by placing a tungsten standard lamp at the location normally occupied by the crystal. Recorded data were digitized and then corrected for the system response by an HP9830 computer. In addition, the change in absorption of the He–Ne pump laser was measured as a function of temperature, and fluorescence intensities at different temperatures were corrected to take the change into account. Absorption at 632.8 nm increased nearly 20% as the temperature rose from 20 to 240 K. The wavelength accuracy of the recording system was checked by scanning through a variety of

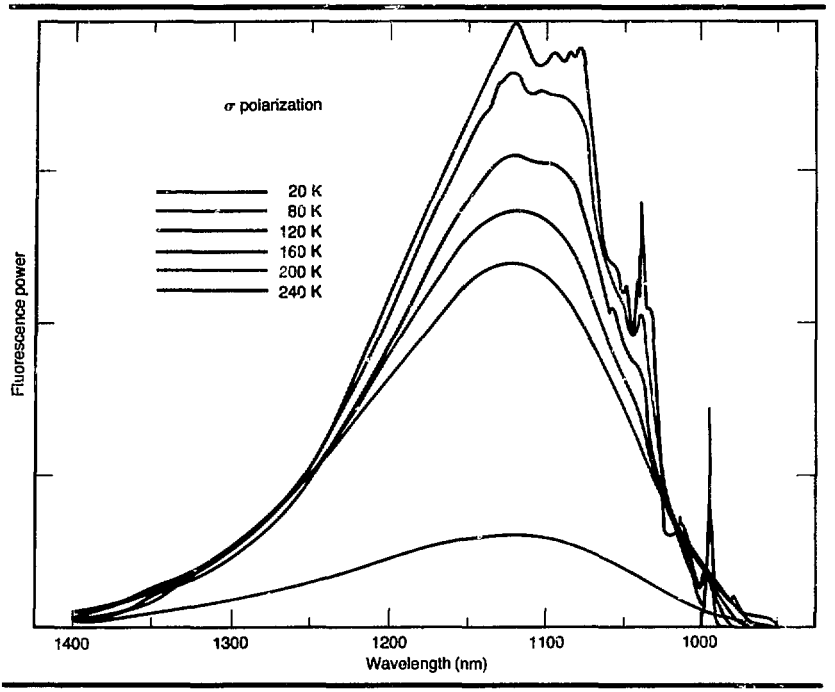

Fig. 7-120. Fluorescence spectrum of V:MgF_2 as function of temperature for σ-polarized light.

neon emission lines from the He–Ne laser discharge. In the region between 1000 and 1250 nm, accuracy was better than 0.5 nm.

Figure 7-120 shows the relative fluorescence power vs temperature for σ-polarized light. It is apparent that the amount of total emission in the zero-phonon lines rapidly reduces as the temperature increases. An accurate value of the absorption cross section for one of these $^4A_2 \rightarrow {}^4T_2$ zero-phonon lines is required to determine the peak spontaneous-emission cross section of the $^4A_2 \rightarrow {}^4T_2$ transition. An elaborate spectroscopic setup, described in Ref. 128, was implemented to make this measurement and will not be described here.

Analysis of the measurements resulted in a σ-polarization emission cross section $\sigma_p = 5.6 \times 10^{-21}$ cm^2 at the peak of the $^4A_2 \rightarrow {}^4T_2$ emission transition ($\lambda_{peak} = 1130$ nm), with an estimated uncertainty in the measurement of $\pm 20\%$. One can also calculate the gain cross section by using the Einstein relation between cross section and spontaneous-emission lifetime, under the assumption that the measured lifetime is due entirely to radiative processes. Suitable averaging is required for anisotropic media. For V:MgF_2 at 20 K, the value of σ_p (σ-polarized light, $\sigma_p = 1130$ nm) is 3.1×10^{-21} cm^2 if the axial and σ-polarized emission are equivalent (electric-dipole transition) and is 4.2×10^{-21} cm^2 if the axial and π-polarized emission are equivalent (magnetic-dipole transition).

It is not clear why there is such a large discrepancy between the cross section determined by zero-phonon-line measurements and those determined by the Einstein relation. Some, if not all, of the discrepancy may be caused by experimental error. However, it is clear that an assumption of unity for quantum efficiency in fluorescence must be reasonably accurate.

Laser Properties of V:MgF_2. We constructed a cw V:MgF_2 laser to determine the effective-gain cross section of the $^4T_2 \rightarrow {}^4A_2$ transition for an optically pumped crystal to compare with the spontaneous-emission cross section derived from spectroscopic measurements. In particular, a determination of the cross section in laser operation

accounts for effects of excited-state absorption caused by transitions from the $^4T_2$ level to higher-lying states. The magnitude of such absorption cannot be derived from standard spectroscopy.

Figure 7-121 shows a schematic diagram of the V:MgF_2 laser experiment. A 2-cm-long Brewster-angle crystal was longitudinally pumped via the $^4A_2 \rightarrow {}^4T_1a$ optical transition using 0.5145-μm radiation from a cw argon-ion laser. The crystal was doped with ~0.5 wt% VF_2 and absorbed 45% of the incident radiation. We cooled the crystal to ~80 K by thermally contacting the material with the copper cold finger of a liquid-nitrogen Dewar. All of the cavity optics were maintained in a vacuum to eliminate the need for intracavity windows. A single-plate crystal-quartz birefringent tuning element was placed in the cavity for tuning experiments.

The pump-beam mode area in the crystal was adjusted to be considerably smaller than the TEM_{00} cavity mode size in the crystal. Under such conditions, the following relation exists between the effective gain cross section, σ_{eff}, and the pump power incident on the crystal at threshold P_{TH}

$$\sigma_{eff} = \frac{\pi n w_c^2 E_p (L + T)}{4 P_{TH} \tau F} , \qquad (102)$$

where n is the refractive index of the crystal; w_c is the cavity mode radius at the crystal; E_p is the energy of a pump photon; L is the fractional round-trip loss in the cavity due to all losses, except that from the fractional transmission, T, of the output mirror; τ is the upper-state lifetime; and F is the fraction of incident pump power absorbed.

The term σ_{eff} is the difference between the cross section for stimulated emission, σ_E, and that for excited-state absorption, σ_A. It is assumed that the excitation efficiency is unity; i.e., one absorbed pump photon yields one excitation in the upper laser level.

For our experimental conditions, $\pi w_c^2 = 6.7 \times 10^{-4}$ cm^2, $n = 1.38$, $\tau = 2.4 \times 10^{-3}$ s, and $F = 0.45$. The value of $L + T$ was determined by measuring the frequency of relaxation oscillations observed in the output of the V:MgF_2 laser. Such oscillations appear as the result of perturbations in the laser operating conditions and, in the small-perturbation limit, consist of exponentially damped sinusoidal variations in output power. It can be shown that, even under conditions where excited-state absorption is present, the following equation is appropriate

$$L + T = \frac{\tau \tau_c \Omega^2}{R - 1} , \qquad (103)$$

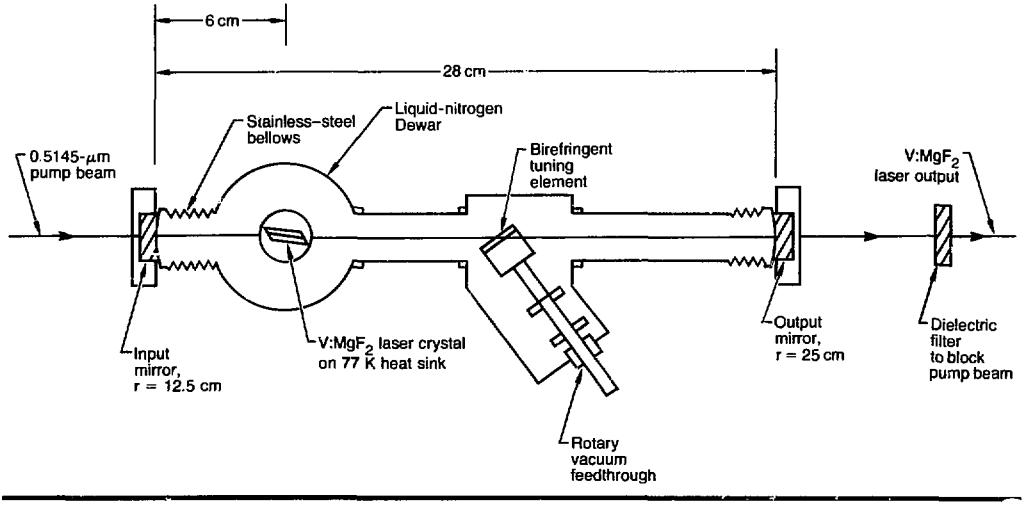

Fig. 7-121. Schematic diagram of V:MgF_2 experiment where stimulated-emission cross section, σ_{eff}, was determined to be 8.7 × 10^{-22} cm^2.

where Ω is the angular frequency of the oscillations, R is the ratio of pump power to threshold pump power, and τ_c is the cavity round-trip time. We measured Ω for five values of R ranging from 1.23 to 4 and found an average value for $L + T$ of 1.07×10^{-2}, with a deviation of less than 10% of that amount. The value of T was 0.35% and, thus, all unwanted losses, L, in the laser cavity were ~0.7%.

We observed the laser threshold at an incident power of 1.0 W, resulting in a value for σ_{eff} of 8.7×10^{-22} cm^2 (the laser wavelength was 1.115 μm). This cross section is considerably smaller than the spontaneous-emission cross section deduced from spectroscopic data (which indicated a range of cross sections from 3 to 5.6×10^{-21} cm^2) and is an indication of the existence of appreciable excited-state absorption.

We observed the laser slope efficiency to be 16%. However, from the ratio of T to $L + T$, we would expect a slope efficiency of 33%. It is possible to show from the rate equations for a laser with excited-state absorption that the slope efficiency is reduced by a factor of σ_{eff}/σ_E. This calculation assumes that the decay from the levels excited by excited-state absorption occurs rapidly compared to the upper-state lifetime and that all decay is back down to the upper level. (If this assumption is not correct, efficiency is reduced even further.) Thus, from the reduction in slope efficiency, we calculate that $\sigma_{eff}/\sigma_E \approx 1.2$ and $\sigma_E \approx 1.7 \times 10^{-21}$ cm^2. Such a value is much lower than the estimated values of σ_E, which could imply the existence of other loss mechanisms *in the operation of the V:MgF$_2$ laser.*

One such loss could be a less-than-unity quantum efficiency of excitation by the pump laser because excitation into the $^4T_1$ level might find other paths for decay than into the $^4T_2$ upper laser level. However, preliminary measurements of relative excitation efficiency vs wavelength indicate that the efficiency of excitation is equal for both $^4A_2 \rightarrow {}^4T_2$ and $^4A_2 \rightarrow {}^4T_1$ transitions. Another loss of efficiency could be caused by excited-state absorption of the pump radiation. Experiments are now in progress using other excitation wavelengths to determine if excited-state pump absorption is a significant effect.

The tuning curve of the V:MgF$_2$ laser supports the contention that a good portion of the reduction in gain is caused by excited-state absorption. Figure 7-122 plots the relative gain curve for V:MgF$_2$ predicted from the measured fluorescence spectrum (e.g., in the absence of excited-state absorption). Also plotted is the observed tuning curve of the cw V:MgF$_2$ laser. The peak in output power around 1.09 μm is not intrinsic to V:MgF$_2$. Rather, the peak is caused by an increase in output-mirror transmission for wavelengths shorter than 1.1 μm, which results in more optimal output coupling. The lowest threshold for operation was at 1.115 μm. At the wavelength we expect the laser gain to be maximum (in the absence of excited-state absorption), around 1.15 μm, the laser output is almost zero; for wavelengths longer than 1.16 μm, no output is observed. Therefore, at longer wavelengths, the value for σ_A is equal to or greater than that of σ_E, and no gain can be observed. It is unlikely that any mechanism other than excited-state absorption could so distort the V:MgF$_2$ tuning curve.

The presence of a large amount of excited-state absorption in V:MgF$_2$ crystals precludes the construction of an *efficient* V:MgF$_2$ amplifier chain for a fusion driver system. However, the wavelength, bandwidth, and strength of an excited-state

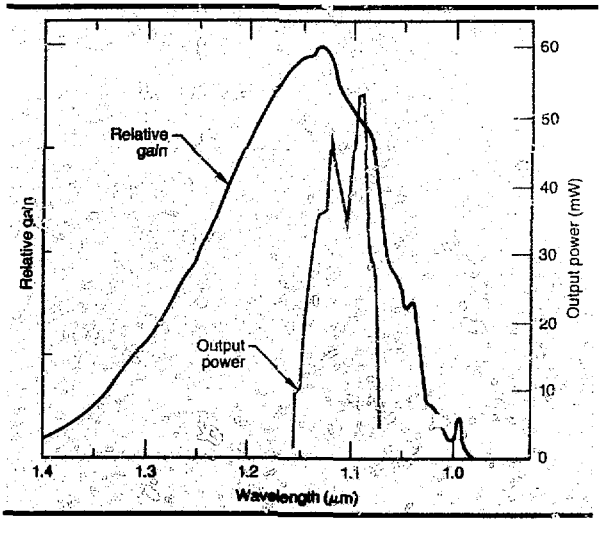

Fig. 7-122. Relative gain of V:MgF$_2$ laser predicted from measured fluorescence spectrum in the absence of excited-state absorption; measured gain peaks around 1.09 μm.

absorption transition are strongly dependent on the detailed crystal structure of the host crystal (MgF_2 in this case). Thus the V^{2+} ion, which otherwise exhibits very favorable electronic properties, may yet serve as an active ion for an efficient solid-state laser when dispersed in a host crystalline material that has more favorable crystal field properties (e.g., MnF_2, $KMgF_3$, or $KZnF_3$). Based on these results, we plan to investigate other V^{2+}-doped host crystals.

Authors: P. F. Moulton and R. E. Fahey (Lincoln Laboratory, Lexington, Mass.); and W. F. Krupke (LLNL)

Free-Electron Lasers

Introduction. Last year,[129] we conceptualized and studied the free-electron laser (FEL) as a driver for inertial-confinement fusion targets. The results presented at that time were based on one-dimensional simulations of FEL amplifier performance. We also noted that, although the FEL performance predicted with one-dimensional simulations was encouraging, the influence of several major physics issues remained to be resolved

- Three-dimensional phenomena, including laser-beam quality, diffraction, refraction, self-focusing, and other nonlinear propagation phenomena.
- Three-dimensional propagation of electron beams.

To study the laser-beam propagation effects, we have developed a two-dimensional model of a high-gain (e-beam power > input laser-beam power) FEL that includes the effects of diffraction, refraction, and off-axis e-beam current density and magnetic-field variations. Here, we discuss the details of our theoretical formulation and results obtained from numerical calculations.

Background. Laser amplification in a tapered-wiggler-magnet FEL is accomplished by trapping electrons in a potential well (called a bucket) that is created by the joint action of the magnetic field of the wiggler magnetic field and the electric field of the laser. Kinetic energy is transferred from the trapped electrons to the laser field by tailoring the magnetic-field parameters so the bucket and the trapped electrons decelerate. Throughout this process, a precise relationship between the energy of the electrons (u), the magnetic-field strength (B_w), the magnetic-field period (λ_w), and the laser wavelength (λ_s) must be maintained. The relationship is

$$\gamma^2 = \frac{k_s}{2k_w}\left(1 + \frac{b_w^2}{k_w^2} - \frac{2e_s b_w}{k_s k_w}\cos\psi + \frac{e_s^2}{k_s^2}\right), \quad (104)$$

where

$\gamma = u/mc^2$,
$k_s = 2\pi/\lambda_s$,
$k_w = 2\pi/\lambda_w$,
$b_w = eB_w/(2)^{1/2}mc$,
$e_s = eE_s/(2)^{1/2}mc^2$,
m = rest mass of the electron,
e = charge of the electron ($e > 0$),
c = speed of light, and
E_s = laser electric-field amplitude.

Equation (104) is derived by insisting that the motion of the electron is synchronized to the bucket motion.[130]

One-dimensional models[129-131] of the FEL assume that all the parameters of the e-beam, the wiggler magnet, and the laser are uniform in the radial direction. (The radial direction is perpendicular to the laser axis.) This assumption implies that, if synchronization is achieved [Eq. (104) satisfied] at one radial position, then synchronization is maintained at all radial positions. Furthermore, the assumptions inherent in the one-dimensional model imply that the gain of the laser is uniform across the amplifier aperture. In fact, all the characteristics of the FEL may have radial variations, so that Eq. (104) cannot be simultaneously maintained for arbitrary values of the radius of the electron beam as electrons travel through the wiggler magnet. The performance of FELs may be severely affected by this loss of synchronization.

The computer model discussed in this article is being used to investigate fusion-class FEL amplifiers and is not limited to low-gain amplifiers. Substantial growth of the laser field is permitted. The model includes the effects of detrapping caused by loss of electron-bucket synchronization at large radial positions. The effects of diffraction and refraction on laser gain and laser-beam quality are also included.

Two-Dimensional Resonant Electron Model. Our modeling is based on the analysis of the tapered-wiggler-magnet FEL

given by Kroll et al.[130,131] An extension of this model to two dimensions (cylindrical geometry) is relatively straightforward. Thus, we will only discuss the modifications to the one-dimensional FEL equations of motion that are required by the two-dimensional model.

The interaction between the laser field and the e-beam in an FEL amplifier is governed by Maxwell's equation

$$\nabla^2 E - \frac{1}{c^2}\frac{\partial^2 E}{\partial t^2} = \frac{Z_0}{c}\frac{\partial J}{\partial t} \tag{105}$$

and the equations of motion of the beam electrons[130]

$$\frac{d\gamma}{dZ} = \frac{-e_s b_w}{k_w \gamma}\sin\psi \quad , \tag{106}$$

$$\frac{d\psi}{dZ} = k_w - \frac{k_s}{2\gamma^2}\left(1 + \frac{b_w^2}{k_w^2} - \frac{2e_s b_w}{k_s k_w}\cos\psi - \frac{e_s^2}{k_s^2}\right) + \frac{d\phi}{dZ} \quad , \tag{107}$$

$$\psi = k_w Z + \psi_s \quad , \tag{108}$$

and

$$\psi_s = k_s Z - \omega_s t + \phi_s \quad . \tag{109}$$

In Eq. (105), Z_0 is the impedance of free space (mks units, $Z_0 \approx 377\ \Omega$), and J is the average current density of the e-beam. For a monochromatic laser beam, the electric field and current density are given by

$$E = Pe\left(E_s e^{i\psi_s}\right) \tag{110}$$

and

$$J = Re\left[\hat{J}\, e^{i(k_s z - \omega_s t)}\right] \quad , \tag{111}$$

where ψ_s is given in Eq. (109).

The electric-field amplitude, E_s, electric-field phase, ϕ_s, and complex current density, $\hat{J}$, are functions of position (r,Z). Typically, E_s, ϕ_s, and $\hat{J}$ vary much more slowly along the direction of propagation (the Z direction) than in the transverse direction (the radial r direction). Under these circumstances, we can neglect the second derivative and products of first derivatives of E_s and ϕ_s with respect to Z. This is the paraxial approximation.[132] We can now write the field equation, Eq. (105), in the form

$$\nabla_\perp^2 \hat{E} + 2ik_s\frac{\partial \hat{E}}{\partial Z} = i\omega_s \hat{J}\frac{Z_0}{c} \tag{112}$$

and

$$\nabla_\perp^2 = \nabla^2 - \frac{\partial^2}{\partial Z^2} \quad , \tag{113}$$

where the complex field amplitude is

$$\hat{E} = E_s e^{i\phi_s} \quad . \tag{114}$$

The complex current density is found from Eqs. (106) and (107) $\left\{\mathrm{Re}\left[\hat{J}e^{i(k_s Z - \omega_s t)}\right] = J_s\right\}$, Ref. 130, Eq. (16) if we ignore the f_0 (plasma) component

$$\hat{J} = -\sqrt{2}\frac{b_w}{k_w} J\left\{\left\langle\frac{\sin\psi}{\gamma}\right\rangle_r + i\left\langle\frac{\cos\psi}{\gamma}\right\rangle_r\right\} e^{i\psi_s} \quad . \tag{115}$$

The notation $\langle\rangle_r$ indicates that an average must be taken over all electrons at the position r. Equation (112) is the paraxial wave equation for the complex field amplitude, $\hat{E}$. Various forms of this equation have been used to model laser-beam propagation in other laser media with a high degree of success.[133,134]

The equations governing the field amplitude, E_s, and phase, ϕ_s, are obtained by combining Eqs. (112) and (115) and then equating the real and imaginary parts to obtain

$$2\nabla_\perp E_s \nabla_\perp \phi_s + E_s \nabla_\perp^2 \phi_s + 2k_s\frac{\partial E_s}{\partial Z} = \sqrt{2}\, Z_0 \frac{b_w}{k_w} k_s J\left\langle\frac{\sin\psi}{\gamma}\right\rangle_r \tag{116}$$

and

$$-\nabla_\perp^2 E_s + E_s(\nabla_\perp \phi_s)^2 + 2E_s k_s\frac{\partial \phi_s}{\partial Z} = \sqrt{2}\, Z_0 \frac{b_w k_s}{k_w} J\left\langle\frac{\cos\psi}{\gamma}\right\rangle_r \quad . \tag{117}$$

These equations specify the evolution of the laser field, while Eqs. (106) and (107) describe the motion of the electrons.

To find a solution to the field equations, Eqs. (116) and (117), we must first solve Eqs. (106) and (107) for a large number of electrons, each with a different initial energy, phase, and radial position. This process requires a large amount of computation. A less desirable but quicker method is to solve Eqs. (106) and (107) for one average electron at each of many radial positions and then assume that the motion of this one electron is representative of the motion of a large number of electrons. The averages appearing in Eqs. (116) and (117) may then be replaced by functions of the phase-space coordinates of the average electron.

The current density, J, must also be replaced by a bunched current density, J_Λ, which should be proportional to the number of electrons that follow the motion of the average electron.

For one-dimensional models,[130] we usually choose the average electron to be resonant, i.e., the electron for which

$$\frac{d\psi}{dZ} \approx 0 \quad . \tag{118}$$

The bunched current density is then chosen to be

$$J_\Lambda + \frac{A_\Lambda J}{4\Pi\Delta\gamma} \quad , \tag{119}$$

where

$$\Delta\gamma = \frac{(\gamma_{max} - \gamma_{min})}{2} \quad , \tag{120}$$

$$A_\Lambda(\psi_{avg}) = 2\int P(\psi,\psi_{avg})\,d\psi \quad , \tag{121}$$

$$P(\psi,\psi_{avg}) = \left(\frac{e_s b_w}{k_w^2}\right)^{1/2} F^{1/2}(\psi,\psi_{avg}) \quad , \tag{122}$$

and

$$F(\psi,\psi_{avg}) = \cos\psi + \cos\psi_{avg} - (\Pi - \psi - \psi_{avg})\sin\psi_{avg} \quad . \tag{123}$$

This particular choice for the bunched current density implicitly assumes that the trapped current is proportional to the bucket area (A_Λ). Usually, we make the additional assumptions that

$$J_\Lambda \le J \text{ for all values of } Z \tag{124}$$

and

$$J_\Lambda(Z + \Delta Z) \le J_\Lambda(Z) \quad . \tag{125}$$

When we choose the average electron to be the resonant electron, we may also replace the averages over all electrons with averages over full buckets, as follows

$$\left\langle\frac{\cos\psi}{\gamma}\right\rangle \rightarrow \frac{1}{\gamma_{avg}}\int\cos\psi\,F^{1/2}(\psi,\psi_{avg}) \times d\psi\,\frac{\langle\cos\psi\rangle_{avg}}{\gamma_{avg}} \tag{126}$$

and

$$\left\langle\frac{\sin\psi}{\gamma}\right\rangle = \frac{1}{\gamma_{avg}}\int\sin\psi\,F^{1/2}(\psi,\psi_{avg})\,d\psi = \frac{\langle\sin\psi\rangle_{avg}}{\gamma_{avg}} \quad . \tag{127}$$

The approximations in Eqs. (118) to (127) give good estimates of FEL performance when only one-dimensional effects are considered. The validity of the approximations in two-dimensional models is much less obvious than in the equivalent one-dimensional model. The reason is that resonance [Eqs. (104) and (118)] can only be strictly maintained at one radial position (henceforth called the design radius). The substitutions outlined above are, therefore, only fully justified at the design-radial position. Nevertheless, even in two dimensions, the resonant-electron approximations lead to appropriate behavior of the source terms in Eqs. (116) and (117). If the field intensities are small, the bucket area decreases, leading to detrapping, as expected. Lack of synchronization also leads to detrapping because ψ_{avg} will become large, leading to small F values and small bucket areas. Therefore, we continue to use the resonant-electron model in two dimensions in spite of its obvious faults.

The two-dimensional modeling procedure can be summarized, as follows

- Numerically solve the ordinary differential equations, Eqs. (106) and (107), for one electron at an arbitrarily chosen radial position (the design radius), picking the wiggler-magnet field at each axial position to maintain $d\psi_{avg}/dZ = 0$. This electron becomes the single resonant electron; λ_w is chosen constant.
- Numerically solve Eqs. (106) and (107) for 700 additional electrons, each at a different radial position. The magnetic field of the wiggler magnet is consistent with the first step, above, and has a quadratic radial dependence.
- Solve the partial differential equations

$$2\nabla_\perp E_s \nabla_\perp \phi_s + E_s \nabla_\perp^2 \phi_s + 2k_s \frac{\partial E_s}{\partial Z} = \sqrt{2Z_0}\frac{b_w}{k_w}\frac{J_\Lambda}{\gamma_{avg}} k_s \langle \sin \psi \rangle_{avg} \qquad (128)$$

and

$$-\nabla_\perp^2 E_s + E_s(\nabla_\perp \phi_s)^2 + 2E_s k_s \frac{\partial \phi_s}{\partial Z} = \sqrt{2Z_0}\frac{b_w}{k_w}\frac{J_\Lambda k_s}{\gamma_{avg}} \langle \cos \psi \rangle_{avg} \quad , \qquad (129)$$

where ψ_{avg}, γ_{avg} at each radial point are determined from the results of the second step, above.

Our procedure, with appropriate error control, will yield all the parameters of laser performance. Note that the electrons are constrained to travel in straight lines; thus, betatron oscillations are not included.

Preliminary Results. The accuracy of the numerical techniques[135] used to solve Eqs. (128) and (129) was verified by two methods

(1) J was set equal to zero so the numerical solutions could be compared to known solutions of the homogeneous paraxial wave equation. Under these conditions, the model correctly predicted the Fresnel diffraction pattern produced by an aperture $\left[E = E_0 e^{-(r/0.25)^{20}}\right]$. This confirmed that the code could properly calculate interference effects.

(2) Σ, J, and B were initially made independent of r, thus producing a one-dimensional problem. Under these conditions, the two-dimensional code reproduced previous one-dimensional FEL amplifier design results.[130]

Table 7-19. Design characteristics for 156-m amplifier.

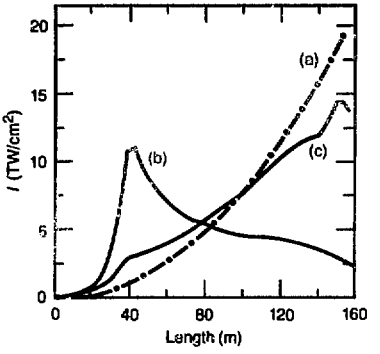

Fig. 7-123. (a) On-axis 250-nm laser intensity as predicted by one-dimensional model. (b) Two-dimensional model with on-axis design. (c) Two-dimensional model with design axis of 0.175 cm.

We have used our one- and two-dimensional FEL models to investigate fusion-class laser amplifiers. The basic characteristics of one of these amplifiers are listed in Table 7-19. This is not an optimally designed amplifier, but it is a convenient choice for comparing one- and two-dimensional performance estimates.

Curve (a) in Fig. 7-123 shows the laser intensity vs amplifier length predicted by our one-dimensional model under the conditions in Table 7-19. The output power is 3.1 TW ($\pi r^2 I$). Curve (b) shows the intensity (at $r = 0$ for the initial conditions given in Table 7-19) predicted by our two-dimensional code. We will discuss curve (c) later in this article.

We have chosen the design axis to be at $r = 0$ to obtain curve (b). The laser intensity is seen to come to a sharp peak and then slowly decrease. An examination of Fig. 7-124, which shows $I(r,Z)$, reveals that the laser beam first focuses and then

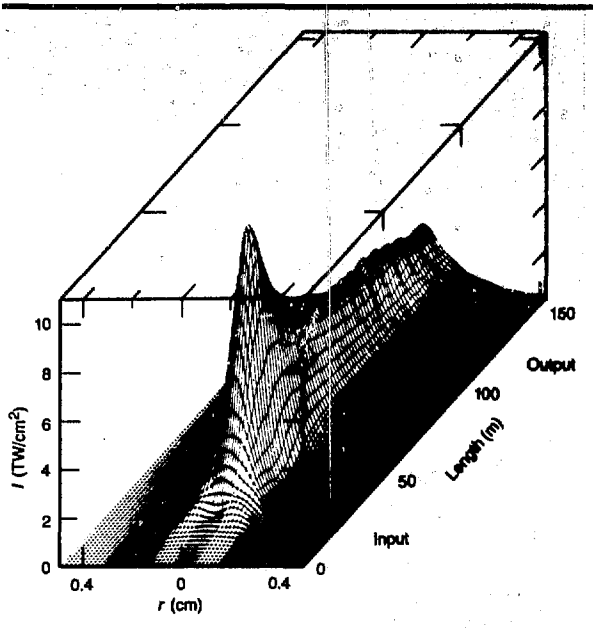

Fig. 7-124. On-axis 250-nm laser intensity as a function of amplifier length and radial position.

defocuses. The total output power is only 0.47 TW.

As the laser intensity is not the same in the one- and two-dimensional amplifier designs, neither is $d\gamma/dZ$. Therefore, the final electron energy is different for the two models. However, predicted performance can be compared for different amplifiers by defining

$$\eta_t = \frac{P_0}{i_e mc^2 (\gamma_{initial} - \gamma_{final})} , \qquad (130)$$

where P_0 is the laser output power, and i_e is the e-beam current; η_t is a measure of the amplifier trapping efficiency. We find $\eta_t = 0.41$ for the one-dimensional model, and $\eta_t = 0.06$ for the two-dimensional model.

Several factors cause the reduced performance predicted by the two-dimensional model

- The inhomogeneous magnetic field does not permit synchronization of the buckets and the electrons located away from the axis.
- The effective focusing of the laser field reduces the off-axis bucket size.
- The sharply peaked laser field creates large differences in $d\gamma/dZ$ across the e-beam.

All of the above factors lead to detrapping and reduction of FEL efficiency. The focusing results from two phenomena. First, the severe off-axis detrapping produces a gain medium of very small aperture. The laser beam is effectively truncated by this aperture even with the physical boundaries set at infinity. This causes Fresnel interference patterns, in this case an apparent focusing.[136,137] Sharp detrapping boundaries (the radial position where synchronization can no longer be maintained) introduce interference effects in a manner completely analogous to sharp (real) apertures. This effect might be expected to be smaller in an actual amplifier because, as the exact circular symmetry assumed by the model disappears, so will some of the interference effects.

The second reason for focusing is that trapping the e-beam on axis retards the laser beam on axis relative to the edges of the laser beam. This produces a "lens-like" focusing.

The detrapping boundary moves inward as the electrons propagate down the amplifier. The resultant reduction of the gain aperture increases axial gain relative to the beam edges and enhances both the Fresnel focusing and the lens-like (refractive) focusing. The net result of these phenomena is that detrapping increases the focusing, which, in turn, increases the detrapping, and the FEL performs poorly.

One way to improve FEL performance is to increase the useful aperture of the amplifier by preventing the initial detrapping at large radial positions.

The radius over which synchronization can be achieved (for a planar wiggler magnet) is usually estimated[138] by

$$r_s = \left[\frac{2\left(1 + \frac{b_w^2}{k_w^2}\right)}{b_w^2} \frac{\Delta\gamma}{\gamma} \right]^{1/2} , \qquad (131)$$

where $\Delta\gamma$ is the e-beam energy spread that the amplifier is designed to trap. If we choose r_{design} equal to r_s, we can trap over a larger aperture $[(2r_s)^{1/2}]$, and performance is improved. The optimum design radius may not be precisely r_s because there is more current at larger radii; therefore, detrapping in the center of the beam is less detrimental than detrapping at the beam edges.

We attempted to increase the gain aperture by choosing our design radius to be off-axis. Our results are presented in Fig. 7-125, where we have plotted laser output intensity for a 156-m FEL amplifier vs design radius. Peak power output is obtained for a design radius of 0.14 cm.

In Fig. 7-126, we have plotted FEL amplifier trapping efficiency, η_t, vs design radius. It is clear that off-axis designs are efficient. Best amplifier performance (as measured by trapping efficiency for our test parameters) is achieved with a design radius of 0.175 cm. For this design, the trapping efficiency is found to be 0.32, or five times greater than that achieved with the on-axis design.

Figure 7-127 shows $I(r,Z)$ for the FEL amplifier designed with $r_{design} = 0.175$ cm. Curve (c) of Fig. 7-123 shows the laser intensity on axis for the same design. Focusing of the laser beam has been avoided by increasing the gain aperture of the amplifier, and FEL performance approaches that predicted by the one-dimensional model.

Conclusions. Based on our approximate method of solving the two-dimensional FEL equations of motion, we believe that two-dimensional effects significantly alter one-dimensional predictions.[131] Our modeling procedure permits large amplifier gains and includes the effects of increases in laser-field strength, diffraction, refraction, and radial magnetic-field variations. The transverse gradient of the magnetic field may cause significant detrapping. Refractive focusing and Fresnel interference also lead to detrapping. These difficulties appear to be controlled by using an off-axis amplifier design that results in significantly larger gain apertures and much improved FEL performance.

Authors: D. Prosnitz, R. A. Haas, S. Doss, R. J. Gelinas, and W. Richardson

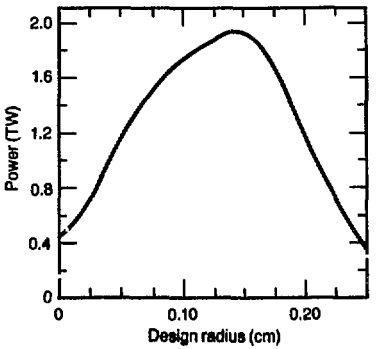

Fig. 7-125. Power output of 156-m, 250-nm FEL amplifier as a function of amplifier design radius; different amplifiers may result in different final electron energies.

Fig. 7-126 Trapping efficiency [η_t, Eq. (130)] in 156-m, 250-nm FEL amplifier as a function of amplifier design radius; equivalent one-dimensional model predicts $\eta_t = 0.41$.

Fig. 7-127. Intensity of 250-nm laser (design axis = 0.175 cm) as a function of amplifier length and radial position.

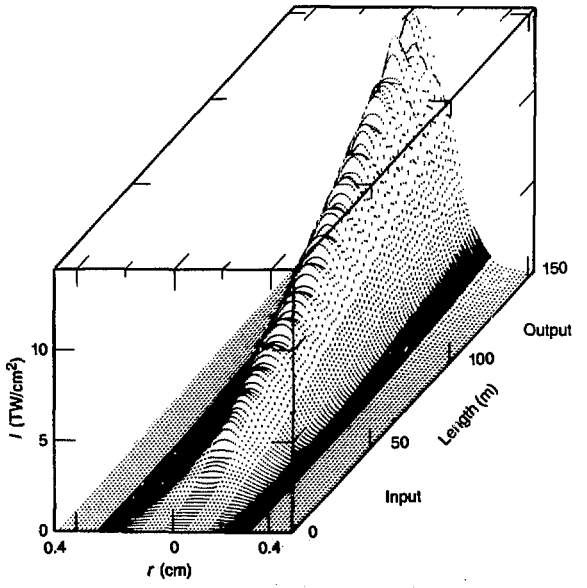

Advances in Atomic and Molecular Theory

Vibrational Excitation of HF by Electron Impact. Kinetic modeling of electron-beam (e-beam) pumped rare-gas halide (RGH) lasers has revealed that the formation rates of the upper laser levels can be dominated by electron attachment to the halogen-bearing donor molecules that are present in the laser medium. For example, experiments

carried out at LLNL[139] and elsewhere[140] on the XeCl laser have shown that laser performance improves markedly when HCl is substituted for Cl_2 in the gas mixture. The improvement has been attributed to the difference in the dissociative electron attachment rates for the two molecules. Both Cl_2 (Ref. 141) and HCl have small attachment cross sections in the ground vibrational states, but the attachment rate for HCl increases dramatically with increasing vibrational temperature.[142] Hence, we now believe that the formation of Cl^- proceeds first by vibrational excitation of HCl followed by electron attachment.

Experimental investigations of vibrational excitation of the strongly polar hydrogen halide molecules by electron impact have revealed a number of unusual features. The large vibrational-excitation cross sections that have been measured for HF, HCl, and HBr (Ref. 143) are all dominated at threshold by extremely narrow (~0.1 eV) resonance peaks for which there is currently no satisfactory theoretical explanation. These molecules are important as halide donors for RGH lasers, and there is considerable theoretical uncertainty regarding the mechanisms responsible for the large vibrational-excitation cross sections. Thus, we undertook an extensive theoretical study of low-energy electron collisions with HF.

There are several aspects of low-energy electron scattering by polar molecules that make the calculation of accurate vibrational-excitation cross sections a formidable computational undertaking. Electron-exchange effects are quite important at low energies. Furthermore, the long-range nature of the electron–dipole interaction makes it essential to include a large number of partial-wave components in the expression for the integrated cross sections. To handle these problems, we developed an approach based on a separable representation of the exchange interaction between the scattered and molecular electrons.[144] The formalism uses a single center-body-frame treatment of the collision dynamics, where the electron-exchange potential is represented by a rapidly convergent sum of separable terms obtained by projection onto a set of normalizable basis functions. A numerical integral-equations method was then used to solve the resulting set of coupled equations noniteratively.

We obtained fully converged (with respect to both the number of exchange and partial-wave terms) scattering matrix elements in the fixed-nuclei static-exchange approximation for the $^2\Sigma$, $^2\Pi$, and $^2\Delta$ symmetry components of the e–HF system in the 0- to 5-eV energy range. Matrix elements that describe vibrational excitation in the adiabatic-nuclei approximation require an integration over the vibrational coordinate of the target molecule. We therefore performed calculations for five different values of the HF internuclear separation. The $^2\Sigma$ scattering matrix elements were indeed found to depend very strongly on both the electron energy and geometry and to give rise to structure in the cross sections near threshold.

For the higher-symmetry components of the scattering matrix, which are required for convergence, but are not particularly sensitive to the detailed dynamics of the collision, we used the results of an exact electron–point dipole[145] and a laboratory-frame first-Born approximation.[146]

In Fig. 7-128, we show our calculated cross sections for exciting the first four rotational levels of HF, along with simultaneous excitation of the first vibrational level. The total cross section summed over rotational levels is compared with the experimental data of Rohr and Linder[147] in Fig. 7-129. The results obtained in the first Born approximation are also shown for comparison. Note that ours are the first ab initio calculations to reproduce the sharp peak in the cross section near threshold that, as previously mentioned, can be clearly identified with the behavior of the $^2\Sigma$ components of the computed scattering matrix at energies below 0.1 eV. Between 1 and 5 eV, our results are roughly a factor of 2 smaller than the experimental data. However, there is reason to believe that the data, to which the relative cross sections of Ref. 147 were normalized, are themselves a factor of 2 too large.[148] When the HF experimental data are thus renormalized, the agreement with our calculated cross sections is quite good, both for the $v = 0 \rightarrow 1$ and $v = 0 \rightarrow 2$ (not shown) cross sections.

However, a definitive calculation of the magnitude and width of the threshold peak would require the inclusion of nonadiabatic effects beyond the fixed-nuclei approximation. This is still beyond the scope of

present computational capabilities.

Time-Dependent Hartree–Fock Theory of Charge Exchange. Charge-exchange processes play a fundamentally important role in many physical phenomena. For example, they are important in high-temperature gas dynamics, in excimer lasers, and ion-beam transport. These processes have been studied extensively, both experimentally and theoretically, over the complete range of collision energy from subthermal to millions of electron volts. Traditional theoretical studies have employed basis-set expansions in either atomic orbitals at high energies or in molecular orbitals at low energies to describe the electronic wave functions during the collision. In the intermediate-energy range (from a few eV to several keV), a very large number of electronic basis states are necessary for a converged expansion. Therefore, calculations of charge-exchange processes in this energy range become very expensive, particularly for many-electron systems. As an alternative, we studied the feasibility of solving the time-dependent Hartree–Fock (TDHF) equations on a spatial finite-difference grid, rather than using a basis expansion, to determine the time evolution of the wave function during the collision. We solve the TDHF equations

$$i\frac{\partial}{\partial t}\phi_n(r,t) = h_n(t)\,\phi_n(r,t) \quad , \qquad (132)$$

where h_n is the usual Fock–Hamiltonian, whose time dependence is due both to the time evolution of the wave function and to the motion of the nuclei. The nuclei are assumed to follow a classical Coulomb trajectory. Equation (132) is solved for each of the occupied electronic orbitals $\phi_n(r,t)$. The effect of the Hamiltonian on the orbital is determined using standard finite-difference techniques, and the time evolution is calculated using the Peaceman–Rachford alternating-direction implicit method.[149] We follow the evolution of the wave function through the collision to the asymptotic (separated atom) limit, at which point we can determine the final state of the system. We project the final wave function onto separable atomic states to obtain state-to-state transition probabilities as a function of impact parameter and collision energy.

We applied these methods to the double-symmetric charge-exchange process

$$He + He^{+2} \rightarrow He^{+2} + He$$

for a range of collision energies from 10 to 70 keV and for a fixed scattering angle of 3°. These conditions were chosen to compare our results to the results of Ref. 150. In Fig. 7-130, we show the agreement between our calculated and the measured double charge-transfer probability, P_2, of Ref. 150. Earlier basis-set expansion calculations[151] were not able to reproduce the positions and heights of the peaks in the probabilities quite as well as have our TDHF calculations. Our calculations[152] have shown that the TDHF method can be used to obtain

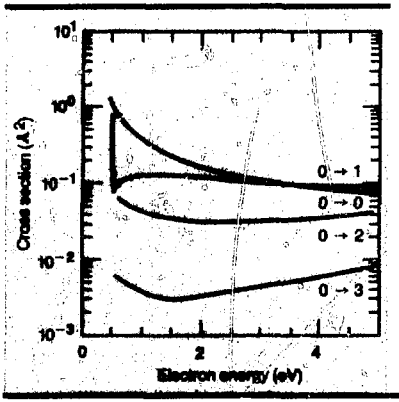

Fig. 7-128. Rotational/vibrational excitation cross section e + HF ($v = 0 \rightarrow 1$); specific rotational transitions are labeled separately.

Fig. 7-129. Vibrational excitation cross sections e + HF ($v = 0 \rightarrow 1$) (summed over rotational levels).

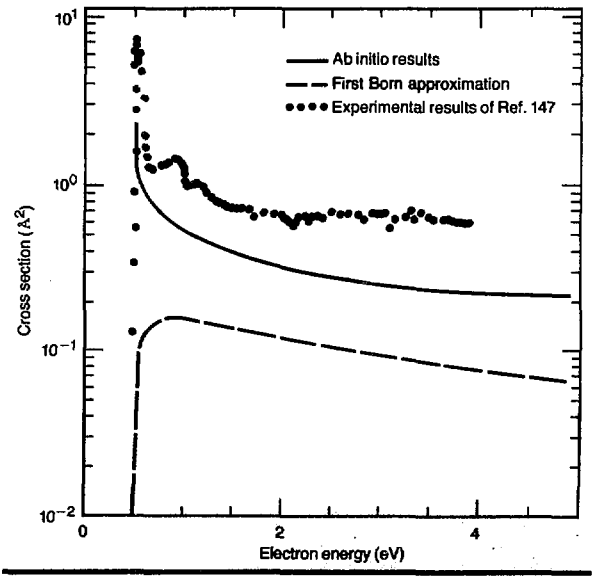

accurate results in the intermediate-energy range for atomic-collision processes.

Photodetachment Cross Sections for $He^-(^4P^o)$. With the availability of powerful tunable lasers, we can study the optical properties of unstable atomic negative ions. Very recently, two groups[153,154] have measured independently the absolute photodetachment cross sections of $He^-(^4P^o)$ at selected wavelengths. The $(1s2s2p)\ ^4P^o$ state of He^- is bound by 0.079 eV relative to $He(2^3S)$, and it is metastable against the autodetachment of the extra electron because of spin-selection rules.[155,156]

Theoretically, photoabsorption by $He^-(^4P^o)$ is intrinsically interesting for several reasons. First, very little is known about the photodetachment of electrons from unstable negative ions. Second, photoexcitation of $He^-(^4P^o)$ may lead to higher quartet autodetaching states of He^- which, in contrast to the doublet states, are not accessible in electron-scattering experiments on the ^1S ground state of He. Finally, although the experimental cross sections of Refs. 153 and 154 agree fairly well with each other, there are large energy regions (e.g., 0.2 to 1.1 eV and 1.2 to 1.6 eV) where the magnitude of the cross section is not known.

We have performed a theoretical study[157] of the photodetachment process

$$h\nu + He^- (1s2s2p\ ^4P^0) \rightarrow He\ (1s2s\ ^3S$$

or

$$1s2p\ ^3P^0) + e \quad . \tag{133}$$

We have used extensive configuration-interaction (CI) wave functions and the Stieltjes moment-theory technique[158,159] to calculate the total cross section for Eq. (133) at photon energies between 0.08 and 3 eV. We also searched the region just below the $n = 3$ thresholds to identify any possible even-parity quartet Feshbach-type autodetaching states of He^-. Figure 7-131 compares the total cross sections, calculated with the dipole-length and dipole-velocity forms of the transition operator, to the experimental data.

The present calculations are noteworthy for several reasons. At the energies where experimental data are available, we find reasonably good agreement between the measured and calculated cross sections. We predict a very large (24×10^{-16} cm^2) photodetachment cross section just above the 2^3P^o threshold at 1.23 eV due to a $(1s2p^2)\ ^4P$ autodetaching shape resonance. An independent scattering calculation fixed the resonance position at ~11 meV above $He(2^3P^o)$ and yielded a resonance width of 7 meV. In contrast, we found that the $(1s3p^2)\ ^4P$ state is a Feshbach-type resonance lying ~0.16 eV below $He(3^3P^o)$. The very sharp feature at threshold (0.079 eV) and the broad peak near 0.35-eV photon energy are due to the photoejection of the loosely bound $2p$ electron into the s-wave and d-wave continua of $He(2^3S)$, respectively.

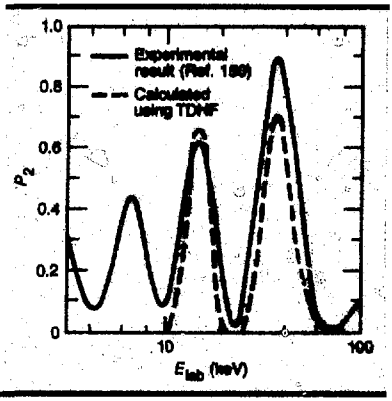

Fig. 7-130. Double symmetric charge-exchange probabilities for 3° scattering angle as function of collision energy.

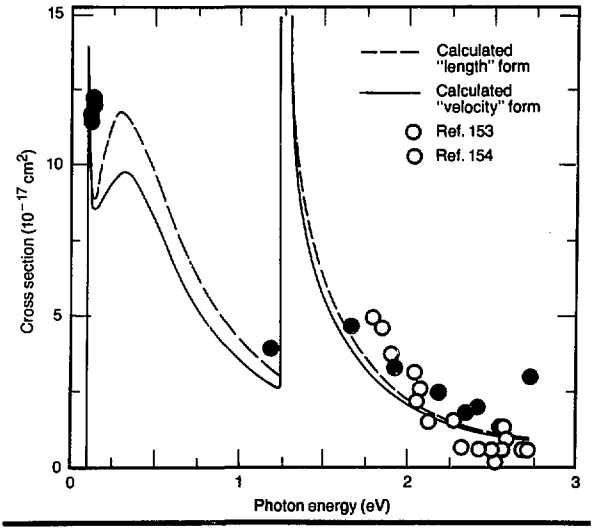

Fig. 7-131. Total photodetachment cross section of $He^-(^4P^o)$.

Currently, new experiments are under way[160,161] to verify the very large magnitude of the photodetachment cross sections in the 1.25- to 1.50-eV energy range.

Laser-Assisted Chemical Reactions. There have been many theoretical predictions and several recent experimental realizations of how a laser field can alter the course of atom–atom and atom–ion collision processes. In addition to producing changes in the final product-state distributions, laser excitation of the reactants also may give rise to interesting coherent effects. We wish to examine the consequences of laser excitation on charge-transfer processes. In particular, we are investigating the effects of coherently exciting a resonant transition in the reactants before the collision. Because of their strong *S–P* transitions and the arrangement of crossing points in the excited-state potential-energy curves, we have chosen to study the Li^+–Na system. This project is being carried out in collaboration with an experimental effort at SRI International, Menlo Park, Calif., as part of a project funded by the Air Force Weapons Laboratory, Albuquerque, N. Mex.

The accuracy of the charge-exchange cross sections is critically dependent on the quality of the potential-energy curves and the nonadiabatic matrix elements that couple them. We have, therefore, carried out extensive ab initio calculations of the potential-energy curves at several levels of approximation to ensure the accuracy of the results. We have calculated the first seven Σ and first five Π states at three increasingly accurate levels of approximation. The final results, which are shown in Figs. 7-132 and 7-133, employed ab initio wave functions with CI at the level of quadruple excitation, with the restriction that only one excitation is allowed outside the valence space. This allows for the important core polarization that occurs for alkali atoms heavier than Li.

We also have carried out calculations of the nonadiabatic coupling elements for the Li^+–Na system at several levels of approximation. Although the results were qualitatively correct, we did not feel them to be sufficiently accurate. Thus, we are calculating these coupling terms with no approximations. This, combined with our highly accurate potential-energy surfaces, will yield cross sections of the quality necessary to examine this sensitive problem.

Another interesting example of the effects of a strong laser field on atom–atom and atom–ion collision processes was observed in Ref. 162. The authors were studying laser-induced associative ionization during the collision of two Li atoms and observed a pronounced enrichment in the production

Fig. 7-132. $^2\Sigma^+$ states of Li^+-Na.

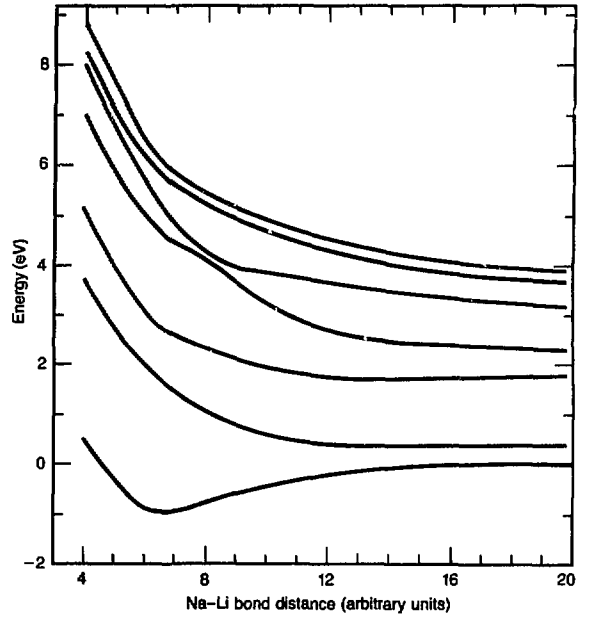

Fig. 7-133. $^2\Pi$ states of Li^+-Na.

of diatomic ions of $^{13}Li_2^+$ relative to $^{14}Li_2^+$. We have been investigating this previously unexplained isotopic selectivity.

The process involves the collision of two Li atoms, each in the excited 2*p* state, in the presence of the laser field. Therefore, we needed accurate potential-energy curves for highly excited states of the diatomic ions. Our first extensive ab initio calculation involved a moderate Slater-type orbital basis and full CI for the two valence electrons. This calculation gave very accurate results for the ground and low-lying excited states (yielding a dissociation energy for the ground state of 0.96 eV, within 0.03 eV of the best theoretical calculation). However, we found that the basis set was inadequate in its description of the Rydberg levels, which are essential for the scattering calculation. Therefore, we redid the calculation with a much larger Gaussian-type orbital basis, which included a larger number of functions to represent the excited atomic Li levels. The basis set is extensive enough to allow a description of photoionization of Li_2 from the excited levels. We then carried out full CI in the two-electron valence space. This calculation accurately reproduced the dense manifold of Rydberg levels leading to the Li_2^+ limit. These curves are shown in Figs. 7-134 and 7-135. The nonmonotonic nature of these curves is caused by ion-pair states, which asymptotically behave as $-1/R$ and cross the entire manifold of Rydberg states. We are presently studying the dynamics of this system in the presence of a strong laser field.

Fig. 7-134. Singlet states of Li_2.

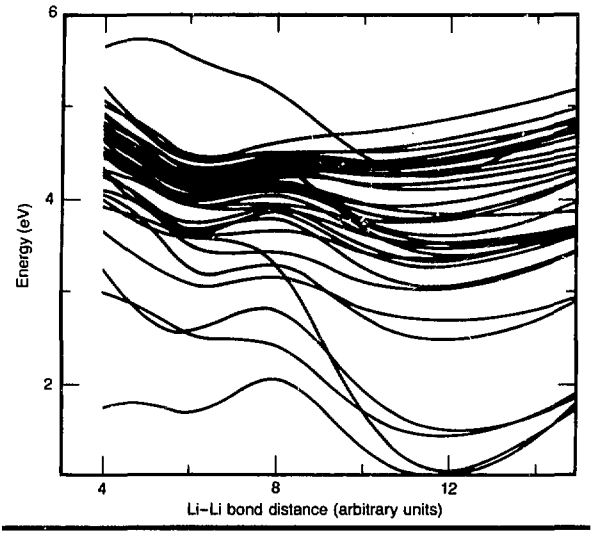

Fig. 7-135. Triplet states of Li_2.

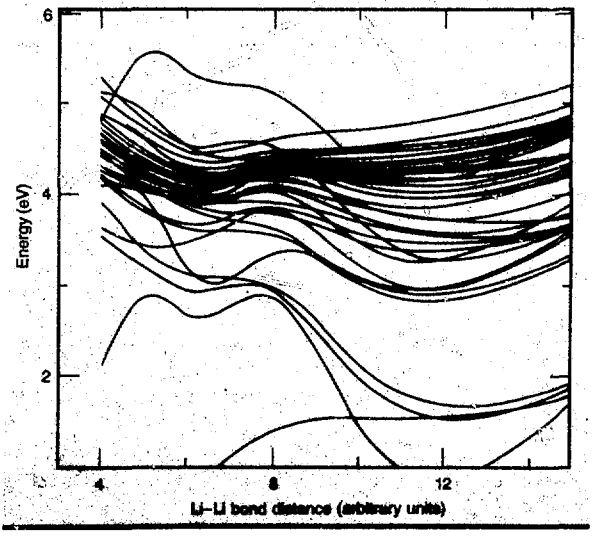

Studies of Near-Resonant Interaction of Lasers and Vapor. During 1981, we continued our studies of the basic physics governing the interaction of multiple near-monochromatic colinearly propagating plane-wave lasers with multilevel atomic or molecular vapor. As in the past, our major progress was in understanding the behavior of excitation and ionization in the presence of a given laser field. We also examined instances of optically thick vapor where the excitation-induced oscillatory dipole moments modify the propagating field.

In previous works,[163–165] we noted the existence of two-level periodicities in idealized theoretical models of monochromatic excitation of multilevel systems. We have now provided[166] a theoretical derivation of such two-level dynamics from the more general *N*-level rotating-wave-approximation Schrödinger equation. We applied the resulting formulas to two different extremes of excitation in a nondegenerate system of sequential *N*-level (ladder-like) excitation.

First, when intermediate levels have much larger cumulative detunings, Δ_i, than Rabi frequencies, Ω_i, the two-level Rabi frequency, Ω, satisfies the well-known formula for multiphoton resonance[164]

$$\left|\frac{1}{2}\Omega\right| = \frac{1}{2^{N-1}}\frac{\Omega_1\,\Omega_2 \ldots \Omega_{N-1}}{\Delta_2\,\Delta_3 \ldots \Delta_{N-1}} \quad . \tag{134}$$

Second, when intermediate Rabi frequencies are much larger than cumulative detunings, we find that two-level behavior occurs when all lasers are tuned to the appropriate Bohr frequencies of an even-N sequence so that no detuning occurs in any step. Two-level behavior also occurs when the first- and last-step Rabi frequencies, Ω_1 and Ω_{N-1}, are much smaller than all intermediate Rabi frequencies. Then, the two-level Rabi frequency (for even-integer N) is

$$|\Omega| = \frac{\Omega_1\,\Omega_3\,\Omega_5 \ldots \Omega_{N-1}}{\Omega_2\,\Omega_4 \ldots \Omega_{N-2}} \quad . \tag{135}$$

Equation (135) provides an explanation for behavior noted in an earlier publication.[163]

Two-step coherent excitation involving simultaneous irradiation by two lasers is often depicted as a three-level atom and, as such a system, has been studied extensively. When the system is nondegenerate, the population simply cycles periodically through the several levels. All of the population flows at some time through the most excited level (level 3) and, hence, is available for ionization.

With the addition of degeneracy, the system becomes more complicated and the excitation behavior can differ quite markedly with different laser polarizations. This difference is most pronounced for the angular-momentum sequence $J = 0 \rightarrow J = 1 \rightarrow J = 0$. Previous authors have shown[167-170] how the presence of hyperfine structure (HFS) can dramatically alter the excitation by circularly polarized light and, thus, permit separation of (odd) isotopes having HFS from those (even) isotopes lacking HFS. The selection rules provide a very dramatic effect. Such effects are also present with linearly polarized light.

First, consider the excitation in the absence of nuclear spin. The ground level is then a single state, with magnetic quantum number $M_J = 0$; the first excited state comprises three sublevels, with $M_J = -1$, 0, and +1, and level 3 is again a single sublevel with $M_J = 0$. Figure 7-136 shows linkage diagrams for three choices of polarization. Figure 7-136(a) shows both lasers linearly polarized along the same axis. Figure 7-136(b) shows both lasers circularly polarized in opposite sense (right, then left circularly polarized). Figure 7-136(c) shows both lasers circularly polarized in the same sense. We immediately recognize that, while (a) and (b) will eventually produce complete ionization from level 3, (c) yields absolutely no ionization. Thus, ionization is very sensitive to the choice of polarizations.

To analyze the effects of crossed linear polarization (say, first-step polarization along the X axis and second step along the Y axis), we express the polarization in a helicity basis as a combination of right- and

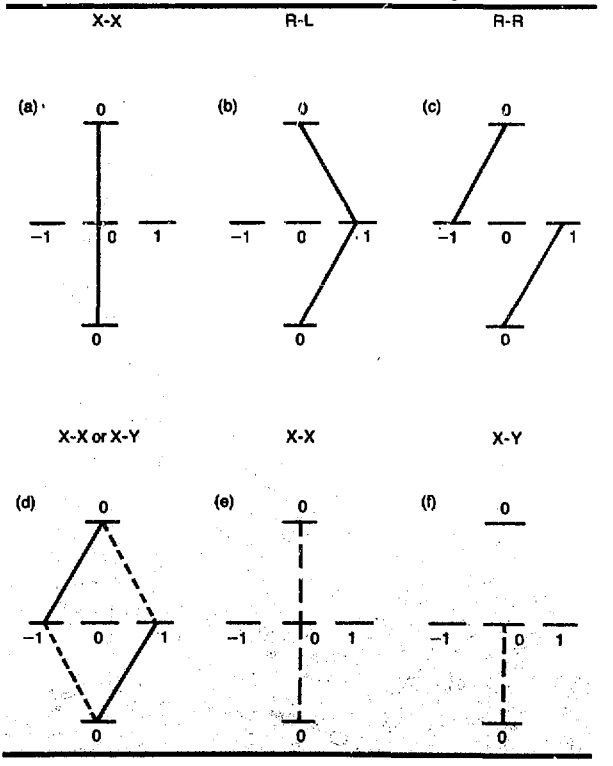

Fig. 7-136. Linkage diagrams.

left-circular polarizations. Figure 7-136(d) shows such a linkage diagram. By reversing the sign of one of the dipole matrix elements (say the linkage marked ±), we change from X–X to X–Y polarization axes. We also alter the dynamics from the equivalent to Fig. 7-136(e) (for X–X polarization) to that equivalent to Fig. 7-136(f) (for X–Y polarization). In other words, destructive interference occurs when polarizations are crossed, and this interference prevents any population from reaching level 3. Thus, there is no ionization for crossed polarization in the sequence $J = 0 \rightarrow 1 \rightarrow 0$. (This null effect disappears for larger J values.)

How does hyperfine structure affect these results? When the hyperfine splitting frequency is much weaker than the Rabi frequencies, we can neglect the hyperfine splitting and can account for nuclear spin, I, by simply increasing the degeneracy of the sublevels. That is, we label states with quantum numbers M_I and $M_I = -I, \ldots, +I$. For the simple case $I = 1/2$, the inclusion of nuclear spin doubles each sublevel of Fig. 7-136. Because M_I remains unchanged by a transition, we simply have $2I + 1$ independent linkage diagrams, just like those of Fig. 7-136. Figure 7-137(a) shows the alteration of Fig. 7-136(d) for $I = 1/2$. In this limit (weak HFS), we conclude that there is complete ionization for R–R (or L–L) circular and X–X (or Y–Y) linear polarization, no ionization for R–L (or L–R) circular, and X–Y (or Y–X) linear polarization.

When HFS is much greater than the Rabi frequency, we obtain a better description of the atom by employing a basis of states labeled F and M_F. When $I = 1/2$, the ground level has $F = 1/2$, the first excited states are $F = 1/2$ and $F = 3/2$, and the second excited state has $F = 1/2$. Using this basis, we can see that the linkage patterns of Figs. 7-137(a), 7-136(b), and 7-136(c) remain unaffected by HFS. For example, Fig. 7-137(b) shows the generalization of Fig. 7-136(a) when $I = 1/2$. In Fig. 7-137(b), the lasers are tuned to resonance with the $F = 1/2$ intermediate level, while, in Fig. 7-137(c), the intermediate level has $F = 3/2$.

However, the situation with crossed polarization is more interesting. Figure 7-137(d) shows the complete linkage diagram for the $I = 1/2$ generalization of Fig. 7-136(d). When the $F = 1/2$ and 3/2 levels are degenerate (weak HFS), then constructive and destructive interference are possible, with the results noted above. But, when the HFS becomes large, we can tune to one of the intermediate F values and thereby eliminate one of the interference paths. The results, shown in Fig. 7-137(e) (for $F = 1/2$ as intermediate level) or Fig. 7-137(f) (for $F = 3/2$), are insensitive to the sign of the dipole moments, and complete ionization can occur.

We conclude[171] that, when the hyperfine splitting is large enough to permit unambiguous tuning to a single intermediate hyperfine component, then, in due time, complete excitation (and ionization) occurs with linear polarization, independent of whether the polarization planes are parallel or perpendicular. In the absence of HFS, no ionization occurs for crossed polarization.

Studies of saturation curves provide a means of identifying J values of the levels involved. By varying the laser polarization, we can gain information useful for

Fig. 7-137. Linkage diagrams.

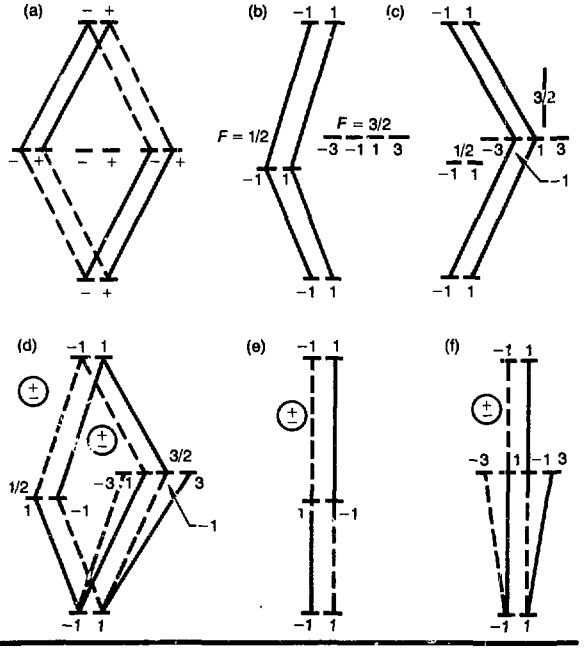

identifying J values. We find, for example, a qualitative difference between the behavior of the sequence $J \rightarrow J + 1 \rightarrow J + 2$ and that of the sequence $J \rightarrow J + 1 \rightarrow J$.

We computed the time history of excitation and ionization for three J-value sequences $J = 6 \rightarrow 7 \rightarrow 8$, $J = 6 \rightarrow 7 \rightarrow 7$, and $J = 6 \rightarrow 7 \rightarrow 6$, and for four polarization combinations, $R_{circ} + L_{circ}$ (R-L), $R_{circ} + R_{circ}$ (R-R), $X_{lin} + X_{lin}$ (X-X), and $X_{lin} + Y_{lin}$ (X-Y).

We found the ionization behavior was sensitive to the combination of polarization and J. The fastest and most complete ionization occurs with parallel linear polarization (X-X) and the sequences $J \rightarrow J + 1 \rightarrow J + 2$ or $J \rightarrow J + 1 \rightarrow J$. Slowest and least complete ionization occurs with same-sense circular polarization (R-R) and the sequence $J \rightarrow J + 1 \rightarrow J$.

Thus, any given J-value sequence has an optimum polarization choice to maximize ionization. The best and worst choices are given in Table 7-20. We see that crossed polarization (X-Y) can, at times, be desirable.

Suppose that we do not know the J sequence, but that we can vary the relative polarization of the two lasers. Then, when we change from R-R polarization to R-L polarization, the ionization increases in the $6 \rightarrow 7 \rightarrow 6$ sequence, whereas it decreases in the $6 \rightarrow 7 \rightarrow 8$ sequence.

This qualitative difference still persists when we have hyperfine structure. Although hyperfine structure diminishes the effect of polarization, there remains a pronounced dependence of ionization on polarization.

Traditional descriptions of radiation transport in vapors assume that absorption of radiation occurs in accordance with a linear Einstein rate equation. That is, the rate of change in molecular-level population is assumed to be directly proportional to the molecular-population inversion. By the same token, the absorption process is assumed to deplete the radiant intensity in accordance with the linear Beer-Lambert law of attenuation: the rate of depletion of intensity with distance is locally proportional to the intensity.

As is now well known, such traditional descriptions are valid as limiting cases, applicable to long-duration incoherent molecule-field interactions. Phenomena associated with short, intense pulses of resonantly tuned and nearly monochromatic light require a more elaborate and nonlinear theoretical description. In the absence of relaxation phenomena (such as collisions), the molecular excitation is determined by the time-dependent Schrödinger equation. The propagating laser fields, in turn, satisfy Maxwell's equations. Thus, the basic equations appropriate to coherent pulse propagation are the coupled nonlinear Maxwell-Schrödinger equations (or, with the inclusion of relaxation, the Maxwell-Bloch equations).

The Maxwell-Schrödinger equations predict a variety of well-studied propagation phenomena, including self-induced transparency, pulse reshaping, and pulse breakup into solitons.[172,173] These effects are associated with the simplest (two-level) model of the molecular absorber. We believe that further unusual behavior will be discovered as we extend our experience from the elementary two-level model to more complicated multilevel models of molecules.

In many discussions of laser-induced molecular excitation,[174] it is recognized that, in polyatomic molecules, the energy levels become increasingly dense, even for low energies. Thus, the molecule can behave toward photon absorption as though the molecular energy levels formed a nearly continuous distribution—the so-called quasi-continuum

Sequence	Best	Worst
$J \rightarrow J+1 \rightarrow J+2$	X-X	R-L
$J \rightarrow J+1 \rightarrow J$	X-Y	X-X
$J \rightarrow J+1 \rightarrow J$	X-X	R-R

Table 7-20. Best and worst choices for J-value sequences.

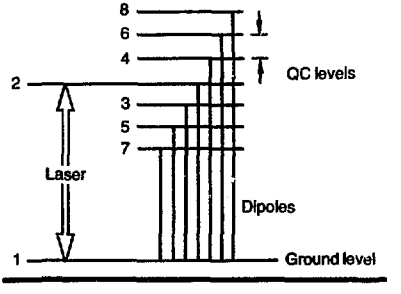

Fig. 7-138. Linkage pattern for QC model.

(QC). Because the QC is so often invoked to explain features of laser-induced molecular excitation, it is important to understand both the underlying physics of optically thin excitation of QC as well as the QC effect on propagation. Here, we describe numerical studies aimed at clarifying the nature of optically thin excitation of QC.

Figure 7-138 shows the simplified QC model we considered[175]: an N-level QC ($N = 7$) whose nondegenerate equally spaced levels are all linked by equal dipole moments to the ground level. A pulsed laser with its carrier frequency tuned to the central level of the QC (level 2) excites the molecule.

Fig. 7-139. Weak-field QC ($N = 26$).

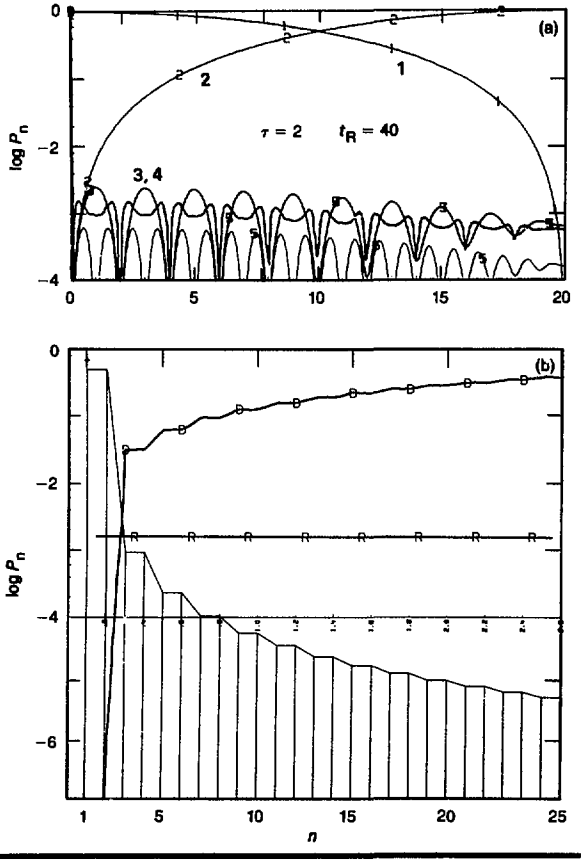

We let the QC levels be evenly spaced with angular-frequency separation, δ, and we let the dipole moments, d_{ln}, between ground and QC levels all be equal, so the rotating-wave approximation (RWA) Hamiltonian has the off-diagonal elements $H_{ln} = v$.

When the field is sufficiently weak, then only level 2 ever receives appreciable excitation. The population oscillates sinusoidally between level 1 and level 2 with the two-level Rabi period $t_T = \pi/v$. The remaining levels, being far off resonance, do not noticeably participate in the excitation. We can, therefore, as a first approximation, treat these virtual levels as undergoing independent low-amplitude off-resonant sinusoidal population modulations. Thus, the levels nearest to resonance (levels 3 and 4 in Fig. 7-138) oscillate at the detuned period $\tau = 2\pi/\delta$, the next-nearest levels (5 and 6 in Fig. 7-138) oscillate with period $\tau/2$, and subsequent levels oscillate at $\tau/3$, $\tau/4$, ..., etc.

We see that τ constitutes a basic recurrence time.[175] For weak fields the recurrence time is much shorter than the Rabi period. Figure 7-139, showing plots of level-occupation probability, P_n, for an $N = 25$-level QC, illustrates this situation. In Fig. 7-139(a), we see the sinusoidal Rabi oscillations between levels 1 and 2, as well as the higher-frequency, lower-amplitude oscillations into virtual levels 3 and 4. The long-term (infinite time) population averages, $\bar{P}_n$, show that the virtual levels $n > 2$ have populations some 10^{-3} smaller than the resonant levels 1 and 2 [see Fig. 7-139(b)].

At the opposite extreme, when the field is sufficiently strong, we can neglect the presence of detuning and treat the system as a degenerate two-level system, and the system exhibits periodic depletion of level 1 at the band Rabi period $T_R = t_R/(N)^{1/2}$. For such two-level behavior to appear, the bandwidth of the QC levels must be much less than the interaction strength. Figure 7-140(a), showing the behavior of populations under this condition, exhibits the expected oscillatory pattern of level-1 populations.

In neither of these two extremes is there any obvious behavior indicative of a QC distribution of energy levels. The QC

becomes evident for intermediate situations, which we next examine.

The condition for weak-field excitation is equivalent to the requirement that the recurrence time be much shorter than the two-level Rabi period, t_R. Although the population in level 1 gives the appearance of sinusoidal Rabi oscillations, Yeh et al.[176] have shown that the apparent sinusoid actually consists of a piecewise continuous sequence of exponential decays—or linear segments on a semilogarithmic plot of population vs time. The initial decay occurs during the first recurrence time interval $0 < t < \tau$, when the time bandwidth $2\pi/t$ *greatly exceeds the detuning. This linear decay* occurs according to the traditional Fermi Golden Rule at rate

$$R = 2\pi\rho V^2 = \pi^2 \tau / t_R^2 = \pi\tau / \left(NT_R^2\right) \quad , \tag{136}$$

where $\rho = 1/\delta$ is the density of the energy levels, and V^2 is the sum of the individual interaction squares; as above, t_R is the two-level Rabi period, and T_R is the Rabi period appropriate to the full band of levels.

The population cannot continue to decay exponentially at rate R indefinitely, if for no other reason than the initial population becomes exhausted. What actually occurs is rather curious. During the interval $0 < t < \tau$, the population decays at rate R; during interval $\tau < t < 2\tau$, it decays at rate $3R$, and so forth.[176] Figure 7-141 illustrates the behavior. We see here that the piecewise exponential behavior ceases for a time exceeding half the two-particle Rabi period $t > t_R/2$. This terminus applies so long as $\tau < t_R/2$. The exponential decay can be prolonged to longer times, up to one Rabi period $t = t_R$, by increasing τ to the value t_R.

As τ ranges over values from $\tau \ll t_R$ to $\tau \gg t_R$, the population histories, P_n, exhibit a variety of behavior, as shown in Fig. 7-141. When $\tau < t_R$, as is the case for Fig. 7-141(a) where $\tau = 2$ and $t_R = 10$, the history of level 1 consists of a very large number of exponential decays. In the limit of $\tau \ll t_R$, the curve becomes indistinguishable from a sinusoid. When τ and t_R are approximately equal [Fig. 7-141(d)], the exponential decay persists until the time $t = t_R$, after which time the population undergoes near-periodic variation. When the recurrence period τ exceeds t_R [Fig. 7-141(e) and (f)], then the exponential decay curve becomes sinusoidally modulated. Finally, when τ greatly exceeds the band Rabi period, T_R [Fig. 7-141(h)], the behavior shows no sign of exponential decay. Thus, for fixed laser power (i.e., fixed t_R), QC behavior is most pronounced for level spacings such that $\tau \cong t_R$, (or $\delta = v/2$) and for times $t < \tau$.

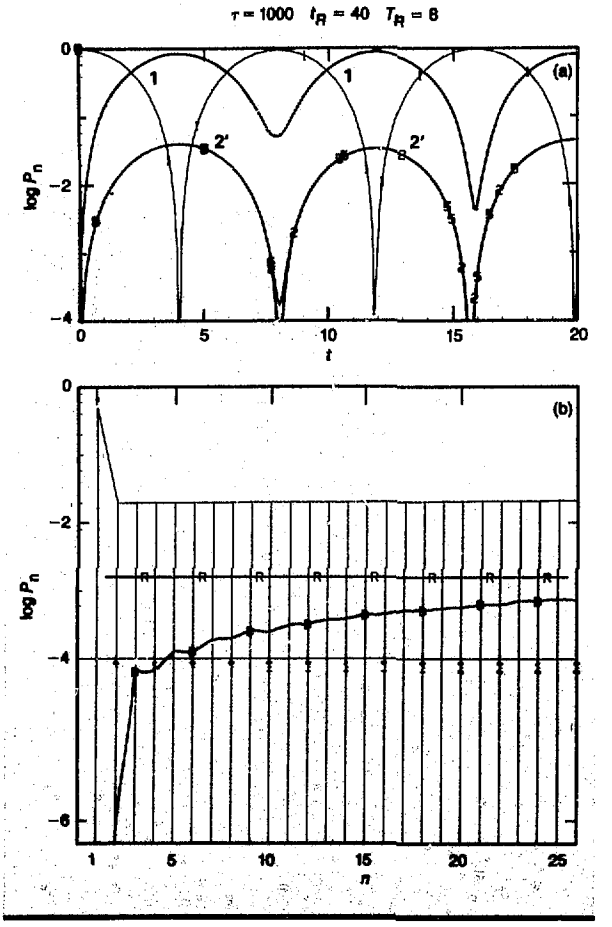

Fig. 7-140. Quasi-continuum ($N = 26$, $t_R = 40$).

In the present article, we extend the previous treatment of optically thin excitation to the treatment of pulse propagation.[177] We show the appearance of Beer's law attenuation, and we exhibit pulse echoes. The same two elementary parameters characterize our study of propagation: the two-level Rabi frequency, $2v$ (i.e., the dipole coupling between level 1 and any one of the QC levels), and the QC-level spacing, δ. These parameters enter most naturally when regarded as a (two-level) Rabi period $t_R = \pi/v$ and a recurrence time $\tau = 2\pi/\delta$.

We have already mentioned that QC behavior, as manifested by the exponential decay of the ground-level population, occurs most prominently when these two times are roughly comparable. To exhibit QC behavior most distinctly, we chose values $\tau = 1$ and $t_R = 2$, so that one Rabi period encompassed two recurrence times. Figure 7-142 shows the population behavior

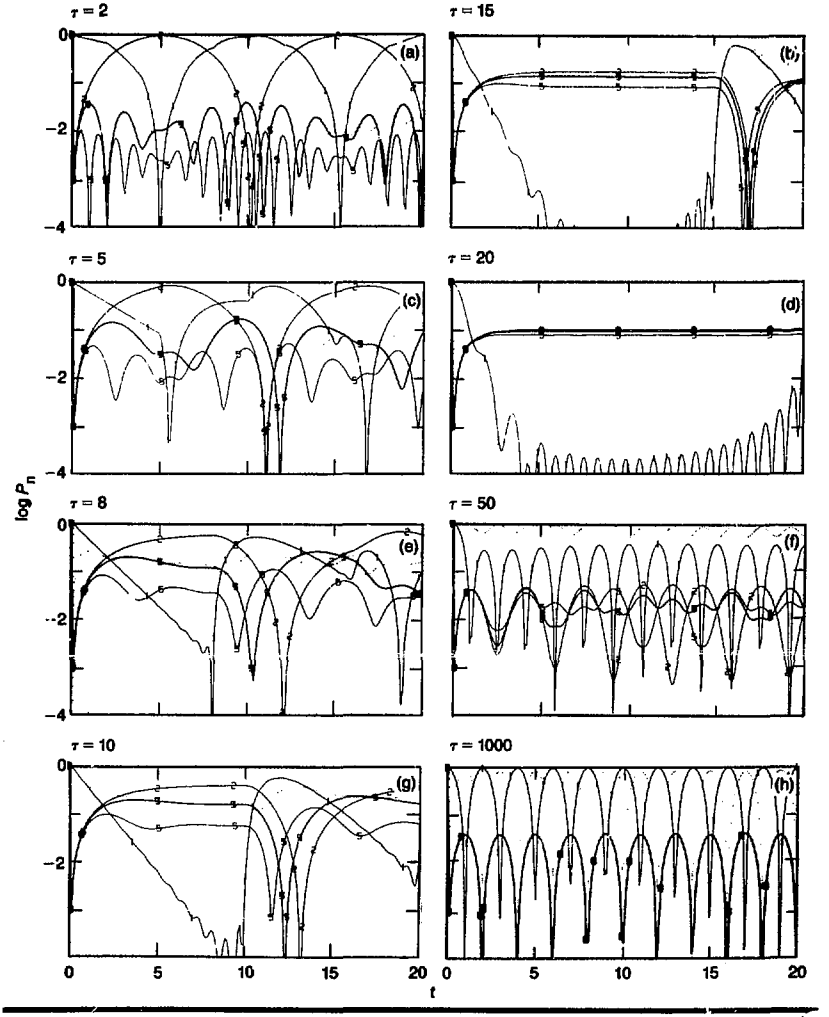

Fig. 7-141. Plots of populations $P_n(t)$ vs time t for optically thin $N = 25$ level QC with fixed Rabi period $t_R = 10$ and various recurrence times, t, with monochromatic excitation.

for this choice of parameters, under the assumption of monochromatic excitation starting at $t = 0$. Figure 7-142 shows quite clearly the exponential decay of level 1 up to time $t = 1 = \tau$. As discussed above, the decay rate for conditions of monochromatic excitation is, according to Fermi's Golden Rule, given by Eq. (136), and the population in level 1 follows approximately the decay law

$$P_1(t) = P_1(0) \exp(-Rt)$$

$$= \exp(-Rt) \qquad (137)$$

during the interval $0 < t < 1$.

To examine propagation, we assumed a short pulse, of duration much briefer than the repetition time, τ, so that, during the excitation time interval, the conditions produce exponential population decay. Figure 7-142 shows the resulting population variations subject to this pulse.

As Fig. 7-142 shows, once the pulse has passed the molecules at the entry face of the vapor, they remain in a distribution of excited states and, hence, give rise to a superposition of oscillating dipole moments. In turn, these moments act as sources for an electromagnetic field. Each of the QC dipole moments has a different phase and a frequency fixed by the detuning. At $t = 0$, the moments are in phase, but, after a short time, the different phases cancel, so that the total molecular dipole moment vanishes. After one recurrence time, the dipoles will be in phase and, hence, can produce a total dipole moment. The result is a pulse echo. A second echo occurs after an additional recurrence time. Each such echo produces an impulsive diminution of the excited population by stimulating emission. Figure 7-142(c) shows these impulsive changes. They occur cyclically at multiples of the repetition rate.

Figure 7-143, showing the pulse intensity vs time, t, and propagation depth, x, reveals two recurrence echoes. The initial pulse fluence falls monotonically and satisfies Beer's law of exponential attenuation.

Authors: A. U. Hazi, K. C. Kulander, A. E. Orel, T. N. Rescigno, and B. W. Shore

Major Contributors: K. Reed, K. R. Sandhya Devi, and S. E. Koonin, California Institute of Technology, Pasadena, Calif.

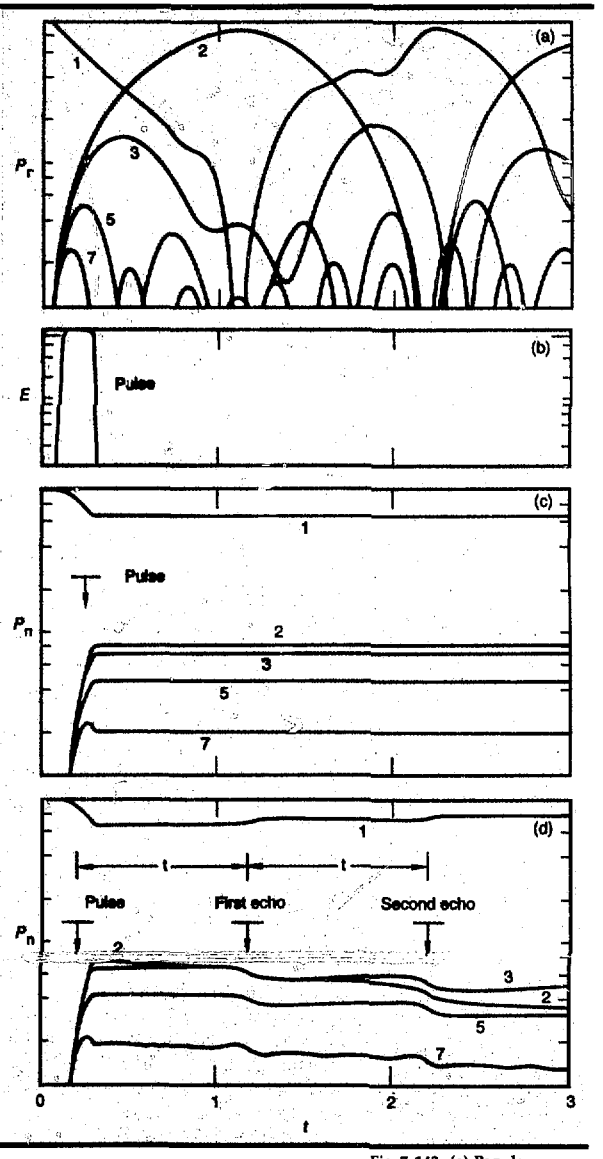

Fig. 7-142. (a) Populations $P_n(t)$ vs t for optically thin level QC excited by monochromatic light, (b) pulse envelope. (c) Excitation $P_n(t)$ produced by optically thin pulse. (d) After propagation.

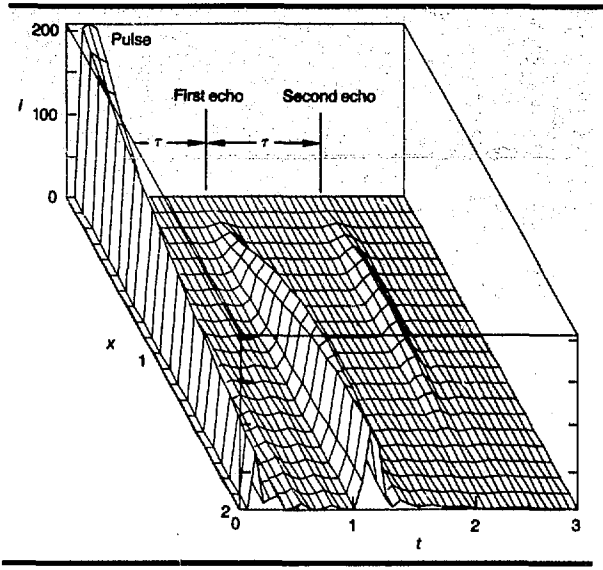

Fig. 7-143. Pulse amplitude vs time, t, and distance, x, showing echoes.

Pulsed Power

Rotary Flux Compressors

Current Programs. We have been pursuing methods to convert inertial (rotational) energy to high-power electricity because of the inherent low cost of storing energy in a rotating mass. A large rotating machine could cost-effectively drive flashlamps in large lasers if the conversion of rotational to electrical energy could be made at a very high power level. That is, we require a high enough level to transform a large percentage of the mechanical energy to electrical energy in less than 1 ms. In an effort to solve this problem, a new family of rotary flux-compression devices was invented by, and is being developed at, the Center for Electromechanics, University of Texas, Austin, Tex. The new flux compressors have produced millisecond pulses at the requisite power levels for the first time from any rotating machine.

This year, we have been evaluating the merits of the active rotary flux-compressor (ARFC) concept. Earlier studies of flux compressors included the compensated pulsed alternator (compulsator) and, briefly, the brushless rotary flux compressor (BRFC). Any of these new rotary machines can deliver very high-power electrical pulses. In all three machines, laminated sheet steel provides the necessary magnetic circuit for high flux compression.

Compulsator. The compulsator shown in Fig. 7-144(a) is a three-winding rotary flux compressor. Voltage is produced across the armature winding as it rotates through a magnetic field created by the field winding. When the circuit is closed, current is generated that is forced to flow back through the compensating winding. The latter winding is as nearly identical to the armature winding as possible, but it is wound on the member containing the field winding (i.e., the stator if the armature rotates, or the rotor if the armature is stationary). The armature, compensating winding, and load are all in series, connected via brushes and slip-rings, and have an external switch. The switch is closed when the inductance in the armature/compensating circuit is high. The generated voltage starts current flowing that is amplified by flux compression as the two windings rotate into their lowest inductance position.

The compulsator generates its own start-up current, but it provides much improved output if the start-up current is boosted with an external source. It requires a fast-recovering output switch to avoid multiple pulsing. A large sustaining motor is also needed to make up iron-core losses while the field is on. These losses also cause undesirable heating of the windings.

Active Rotary Flux Compressor. The active rotary flux compressor, shown in Fig. 7-144(b), has two windings. The field winding is omitted, so the machine cannot generate its own current. Start-up current is supplied from an external capacitor bank when the rotor is in the high-inductance position. Flux compression provides a high-current output pulse as the machine rotates to the low-inductance position. The stator and rotor windings are connected in series via brushes and slip rings to the external circuit, comprising a start-up current source and the load.

The ARFC is a smaller machine than the compulsator for a given power output because no space is required for a field winding. It does not require sophisticated switching. In fact, with commutation, it can be operated without a high-current output switch. There is also no core loss caused by

repeated rotation through a dc field as there is with the compulsator. This means that the sustaining motor can be smaller and that core heating will not be a problem. The principal disadvantage with the ARFC is that it requires a rather large capacitor to provide start-up current (5 to 15% of the total energy output).

Brushless Rotary Flux Compressor. The brushless rotary flux compressor, shown in Fig. 7-144(c), has only one winding, and that winding is on the stator. Start-up current is also required in this machine; however, the start-up and load circuits are only connected to the stator winding, and no slip rings or brushes are used. The rotor surface is effectively a shorted winding. Current is induced in this winding when the start-up circuit is pulsed. As the rotor turns, the induced current in the rotor opposes the current in the stator and flux is compressed, generating a high-current output pulse.

The BRFC is an interesting machine because it is the simplest of the rotary flux compressors. It can only be used for fast-pulse operation because of current diffusion in the rotor. It also suffers from inefficiency that reduces the available power output. Because of its limitations, the BRFC machine is not currently being considered as a candidate to drive flashlamps.

In view of the above arguments, the ARFC is expected to be the most cost-effective rotary flux compressor for providing a 1-ms pulse to a large array of flashlamps. New switching technology is not needed with the ARFC machine, and it is small and relatively simple. We have, *therefore, concentrated our efforts on an* evaluation of the ARFC because we judge it to have a good potential to reduce the future power-conditioning cost for driving flashlamps in very large solid-state lasers.

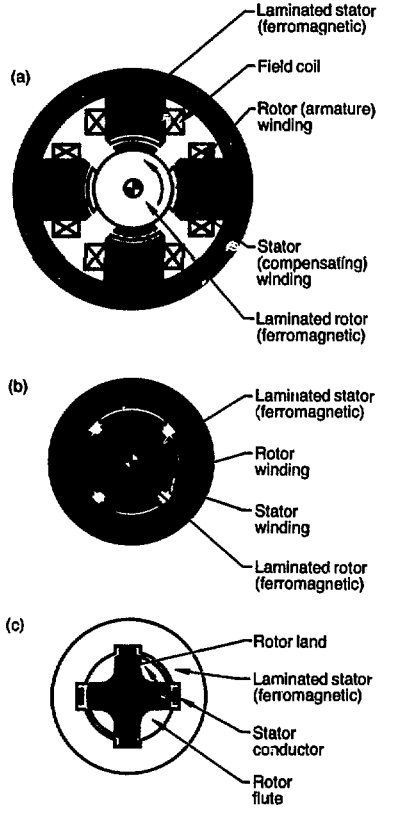

Fig. 7-144. Family of rotary flux compressors. (a) Compulsator. (b) Active rotary flux compressor. (c) Brushless rotary flux compressor.

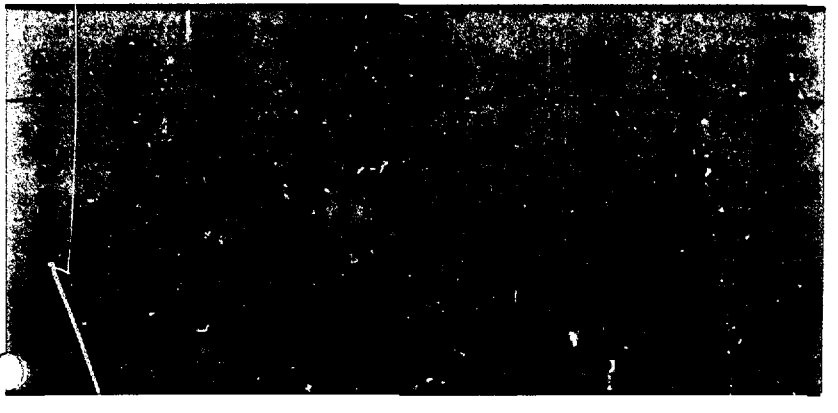

Table 7-21. Summary of test results with 20-cm ARFC.

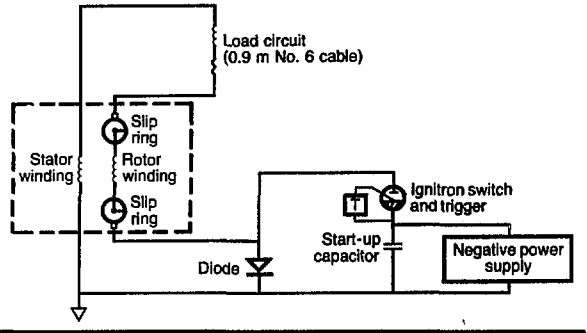

Fig. 7-145. Test circuit for ARFC; start-up capacitor provides initial seed current and internal flux. When discharged, diode permits high-current compressed pulse to bypass start-up circuit.

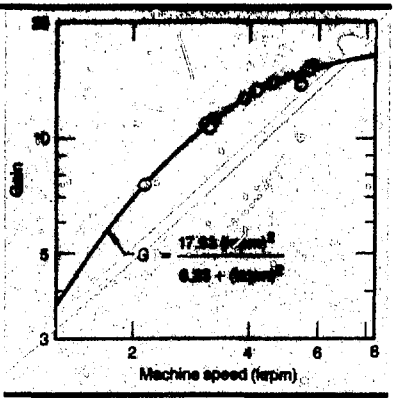

Fig. 7-146. Energy gain vs machine speed for 20-cm ARFC.

20-cm-Model ARFC. The rotary flux-compression concept was demonstrated with an ARFC that had a 61-cm-long, 20-cm-diam rotor.[178-180] The rotor mass and inertia were 98 kg and 0.488 kg m^2, respectively. It, therefore, mechanically stored 86 kJ at the maximum test speed of 5680 rpm. At this speed, an energy gain of 15 was recorded, and a maximum of 23 kJ was delivered to the electrical circuit. A series of tests on the machine culminated in 12 discharges that are summarized in Table 7-21. Figure 7-145 shows a schematic of the circuit used for these runs.

The stored energy in the rotor is given in Table 7-21 for each of the runs, together with the initial energy in the start-up capacitor. Also given for each run is the energy out of the machine that was delivered to the circuit. This energy was calculated using the measured speed of the rotor before and after the electrical pulse. The energy gain is simply the energy out of the machine plus the energy in the start-up capacitor divided by the initial energy in the start-up capacitor.

The peak current, the current gain (i.e., the ratio of peak current to start-up current), and the full width at half maximum (FWHM) of the current pulse are also presented in Table 7-21. Note that pulse widths well below 1 ms were recorded, with a minimum of 590 μs.

The energy gain was found to be independent of the energy in the start-up capacitor over a range of at least 4 in the start-up capacitor energy. However, this gain factor, G, is dependent on machine speed. A good fit to the data is given by

$$G = 17.92\ (\text{krpm})^2/[6.23 + (\text{krpm})^2] \quad . \tag{138}$$

This curve is plotted in Fig. 7-146, and the comparisons to the energy-gain data are shown in the last columns of Table 7-21.

Since the inertially stored energy, W_s, is dependent on the speed squared, i.e., $W_s = 2676\ (\text{krpm})^2$, and since the gain is independent of the start-up capacitor energy, we can extrapolate to estimate a maximum start-up energy, $W_{c\,max}$. For the test circuit used, if the start-up capacitor energy $W_c = W_{c\,max}$, then all of the inertial energy would be delivered to the load, and the rotor would stop. This projected maximum start-up energy is given by

$$W_c\ (\text{max}) = W_s/(G - 1) \tag{139}$$

For example, at 5600 rpm, the stored energy is 84 kJ, and the gain is 15, so that 6 kJ in the start-up capacitor would extract virtually all of the energy from the machine.

Summary. During 1981, a series of test runs with a four-pole 20-cm-diam rotor ARFC has conclusively proven that rotary flux compression is feasible. Performance exceeded expectations on this ARFC. Ratios of peak current to start-up current of 17 have been generated, with pulse widths as short as 590 μs (FWHM) and energy gains of 15.

Our computer codes were upgraded and now provide an accurate reproduction of the output current from existing machines. In addition, an optimization feature of the codes allows new machine designs to be studied that are optimized to provide the best return for the dollar. For example, optimizing return per dollar incorporates the pumping and decay-rate parameters of the

laser glass into the codes, together with machine cost parameters. The result is a machine design that provides the highest number of pumped centers in the laser glass per dollar of power-conditioning system.

With present computerized designs, we estimate that an ARFC system of about 15-MJ output (in <1 ms) could be constructed for about one-half of the cost of the present equivalent capacitive energy-storage system. Also, because machines should be cheaper as the size increases, we are exploring sizes of 100-MJ output and even larger. The impetus behind our research is the possibility that gigajoule or larger energy-storage systems will be needed in the near future.

Author: B. M. Carder

Major Contributors: W. L. Bird, M. L. Spann, W. F. Weldon, and H. H. Woodson (University of Texas, Austin, Tex.); R. J. Foley, D. Eimerl, and E. J. Goodwin (LLNL)

Plasma Shutter

Introduction. The plasma shutter is a new laser component developed for Nova to prevent light from entering a chain of laser amplifiers from the wrong direction—the direction away from the fusion target. A high-intensity pulse of light can be propagated in the inverse direction by several mechanisms. One mechanism results from missing the target at the center of the target chamber, thus propagating an unattenuated pulse backwards into an opposing laser chain. Another is reflection from the target. Target reflection can amount to as much as 30% of the incident energy.

The reason for blocking backward-propagating light is to avoid the remaining gain in the laser amplifiers after the laser pulse has passed through them on its way to the target. Any reflected 1ω light entering a disk amplifier from either direction potentially can be amplified to the damage threshold of the optical components. The consequence could be substantial damage to expensive optics in the laser chains.

The current method for blocking reflected light is to use a Faraday isolator incorporating a Faraday rotator–polarizer combination. This relatively expensive component uses the planar polarization of the light and diverts the beam into an absorbing medium. Cost estimates for a Nova-size Faraday isolator are as high as $500 000 per chain, plus additional components necessary to account for losses caused by the isolator. For this reason, the plasma shutter was developed as a relatively inexpensive replacement for the large-aperture Faraday isolators and was estimated to cost $80 000 to $90 000 in production quantities.

The plasma shutter operates by using the optically opaque nature of a dense plasma, the same phenomenon that causes light to be reflected back from the fusion target. A dense plasma can be generated by passing a very high electrical current through a metallic foil, causing it to vaporize explosively. The metallic foil is initially located adjacent to the path of the laser pulse near the pinhole of a spatial filter.

The distance from the plasma shutter to the target is only 60 m and, at the speed of light, the reflected pulse will return to the shutter in less than 400 ns. The plasma must not be allowed to interfere with the outgoing pulse and yet must fill the beam path with dense plasma less than 400 ns later. This is accomplished by passing 600 kA from a 35-kV power supply through a small metallic foil, thus forming the plasma. The compact high-voltage rail-gap switch that accomplishes the task was developed at LLNL.

A prototype of the plasma shutter was tested on Shiva in 1981 to verify the generation of a plasma of sufficient density to either block the intense laser pulse outright or refract the light out of the aperture of the spatial-filter lens.[181] The Shiva laser was used instead of the Argus laser because of its capability of high output energy and the relative ease with which the plasma shutter could be mounted into one of the output spatial filters. The shutter was configured to block outward-propagating pulses rather than pulses reflected from the target so the entire laser-arm output could be focused onto the plasma. The focused intensity exceeded 1000 TW/cm^2 over a 100-μm-diam spot. This is the same intensity that Nova will impose on the plasma, but over a much larger diameter than could be simulated with Shiva.

During the Shiva testing of the plasma shutter, two questions were of primary concern

- When, after the pulser circuit is triggered, does any attenuating plasma emanate from the foil and potentially interfere with the outgoing pulse?
- How much pulse attenuation can be expected 300 ns after the plasma starts obscuring the beam path?

A direct measurement of the plasma density was obtained on a second, identical plasma-shutter pulser using x-ray backlighting and streak-camera photographic diagnostics. The x-ray backlight data indicate that the foil initially produces a subcritically dense plasma for the 1ω light, but the laser pulse induces electron stripping of the plasma, which raises the plasma density to critical density. This abruptly reduces the optical transmission through the plasma. The laboratory diagnostics also indicated that a diffuse hydrogen precursor plasma precedes the more dense metallic plasma. The outgoing laser pulse will therefore be synchronized to precede the precursor plasma, which might disrupt the beam before it reached the target chamber.

Chip and Foil Design. A replaceable chip containing the exploding foil is positioned 4 cm downstream from the pinhole in the output spatial filter. An electrical current from the pulser vaporizes the foil, superheats it to 15 eV, and drives the resulting plasma across the optical beam path. The electrodes that carry the current to the plasma also concentrate a magnetic field behind the foil, which increases the plasma velocity above the thermal-expansion velocity.

Experimental Configuration on Shiva. Two identical plasma-shutter pulsers were used to demonstrate the operation of the plasma shutter. One was configured with a prototype thyratron trigger and computer controls and was installed in the output spatial filter of arm 16 on Shiva. The other, with a preprototype Marx trigger, was located in a laboratory and contained more detailed plasma diagnostics,

On Shiva, a beam splitter located after the last delta rotator directed a portion of the light incident on and reflected from the shutter into a calorimeter and photodiode. The normal Shiva incident-beam diagnostic (IBD) package, photographic film plates, and full-aperture calorimeters were used to monitor the light transmitted through the shutter.

Initial beam attenuation was determined by probing the area above the exploding foil with 1-ns rod energy pulses (2 to 3 J) and watching for initial signs of plasma leaving the heated foil. A typical sequence of shadowgraphs is shown in Fig. 7-147. In Fig. 7-147(a), the initial beam attenuation was determined by imaging the area above the exploding foil and watching for initial

Fig. 7-147. Typical sequence of shadowgraphs.

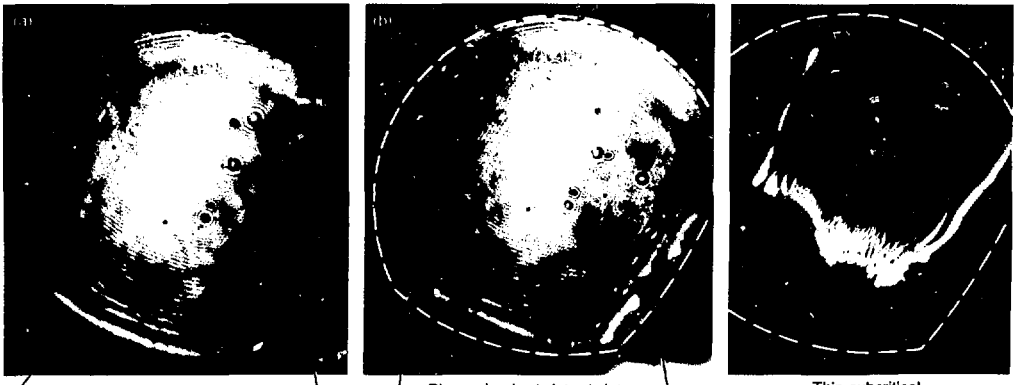

signs of plasma leaving the heated foil. In Fig. 7-147(b), plasma does not leave the foil until at least 75 ns after triggering the high-voltage pulser. Figure 7-147(c) shows that, 450 ns after the shutter is triggered, plasma has moved across nearly half the optical aperture. Note that the image of contaminants apparent in Fig. 7-147(a) remains undisturbed even in the 150-ns photo, verifying the lack of any plasma in that portion of the aperture.

To measure attenuation on a full-system shot (300 to 400 J), one calorimeter was mounted looking through a beam splitter at the input beam, and another full-aperture calorimeter was mounted looking at the exit of the spatial filter. The ratio of these two calorimeters was used as a measure of plasma attenuation.

Optical Transmission of the Plasma Shutter. The optical transmission of the evolving plasma, as measured by the low-power rod amplifier and with full-system shots (10^{15} W/cm^2), is shown in Fig. 7-148. The data are plotted vs the delay time after triggering the plasma shutter. Data for times shorter than 450 ns were taken using wide foils; data after 450 ns were taken with narrow preformed foils. Although the latter delays are longer than the round-trip time of the laser pulse, they were included to demonstrate that the optical transmission does continue to decrease at longer delay times.

The first signs of beam disruption commenced 75 ns after triggering the plasma shutter; after an additional 325 ns, the transmission was 2×10^{-3}. At times greater than 450 ns, the optical transmission was $<5 \times 10^{-4}$ and was at the limit of detectability as the diagnostics were configured.

By timing the outgoing laser pulse to pass the plasma shutter 50 ns after it has been triggered, no plasma will obscure the aperture. Attenuation commences 75 ns after triggering with a hydrogen plasma front moving across the aperture, as shown in Fig. 7-147. At delay times of interest to Nova (415-ns round-trip time), the attenuation will be more than 1000 to 1.

Laboratory Measurement of Plasma-Density Profile. In the laboratory-mounted pulser, a pulsed x-ray source (20 ns FWHM, K_α line of titanium at 4.5 keV) was used to record the plasma areal density profile (i.e., g/cm^2) on film. This monitor was calibrated using a thin-foil step wedge. A streak camera was substituted on some shots to monitor the spatial distribution of the plasma fluorescence.

The areal atomic density distribution (in mg/cm^2), as measured by x-ray backlighting, is a directly observable parameter that may be used to compare the performance of different foils. This diagnostic was used extensively, since we had access to the soft x-ray source, but only limited access to Shiva for full-system testing.

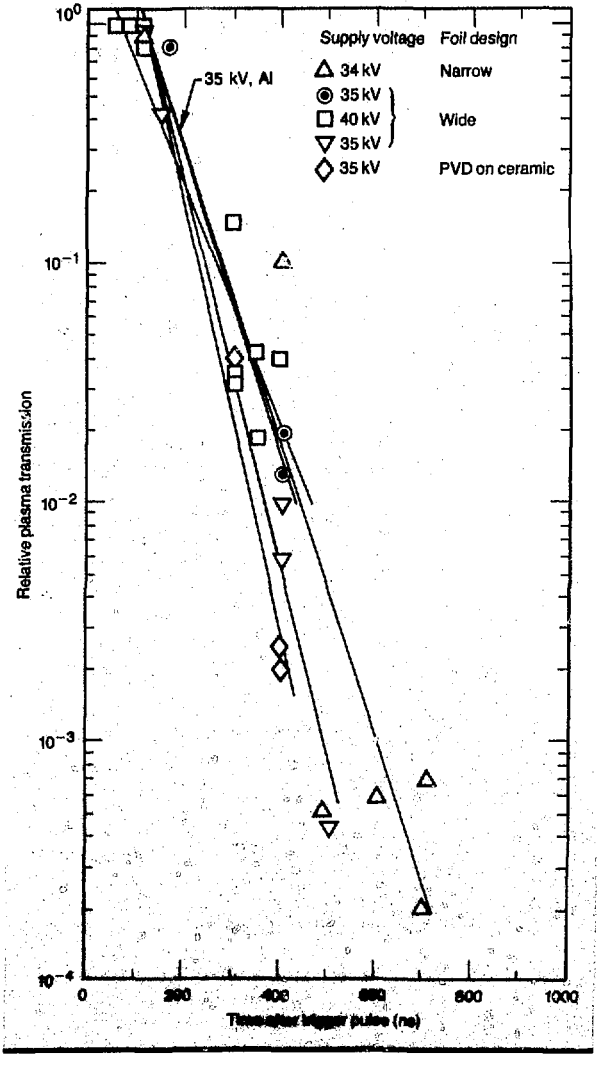

Fig. 7-148. Relative transmission of evolving plasma vs delay time after triggering plasma shutter.

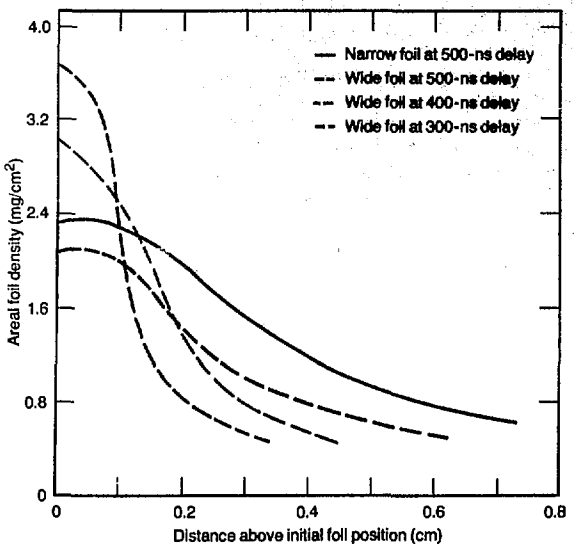

Fig. 7-149. A real-density distribution obtained from soft x-ray backlight diagnostic for two chip and foil designs.

The areal density distribution, as obtained from the soft x-ray backlight diagnostic, is shown in Fig. 7-149 for two different chip designs. The plasma density is shown for the Nova wide physically vapor-deposited (PVD) foil (with delay times of 300, 400, and 500 ns) and for the narrow preformed foil (at a delay time of 500 ns). Figure 7-149 clearly shows the benefit of closely spaced electrodes. At any given instant, the more closely spaced electrodes produced a plasma that had both advanced farther across the aperture and had a higher density. This behavior occurs because the magnetic field is higher and because the foil impedance is better matched to the pulser. However, the narrow electrode spacing was not chosen for Nova because it intrudes on the beam diameter at the location selected for the plasma shutter within the spatial filter.

The SLAP code[182] has been used to guide the modeling of the plasma shutter from the earliest experiments to the present design. For the pulser parameters and foil dimensions used in the Shiva experiments, the code predicts the plasma temperature and degree of ionization. The predicted plasma temperature is 15 eV, and the mean degree of ionization is 3.5; i.e., some atoms are triply ionized, and some are quadruply ionized.

Operating Voltage. The operating voltage for the shutter has been fixed at 35 kV, a voltage that drives the plasma sufficiently to meet all Nova and Novette requirement This operating voltage is well below the upper limit of 50 kV for the pulser. Such a conservative operating point will ensure long component lifetime and freedom from flashover around the chip.

The fill gas for the rail-gap switch has been selected as a mixture of SF_6 and Ar. The rail-gap switch has been designed to operate for the life of Nova at one setting of voltage and gas pressure. Once the first production shutter is acquired, we can carefully select the gas pressure to minimize both jitter and prefiring.

Conclusions. Optical-transmission measurements taken on Shiva, when coupled with x-ray opacity and streak-photography data taken in the laboratory, give a clear picture of the laser attenuation and the plasma behavior. The initial plasma density is 60% of the critical density for 1ω light. However, the laser beam causes additional stripping, which quickly brings the plasma to critical density. The optical transmission through the plasma, as measured 400 ns after triggering the shutter, is 2×10^{-3}, more than sufficient to protect the components on Novette or Nova. The operating voltage has been selected to permit conservative operation of the pulser with minimal maintenance.

Authors: I. F. Stowers, L. P. Bradley, and J. A. Oicles

Fast-Pulse Research

Thyratron Pulser Development. A thyratron-based trigger unit for the plasma-shutter rail-gap switches has been developed. Output greater than 35 kV is required for four parallel 100-Ω transmission lines with a rise time of less than 15 ns. However, the prime requirement is reliability. Failure to trigger a plasma shutter could result in tens of thousands of dollars damage to a Nova beamline. Thus, the trigger was designed to be redundant, i.e., two identical units in each shutter module.

Each trigger unit consists of capacitive energy storage, a thyratron switch to

discharge the energy, and an output transformer to step up the resultant voltage pulse by a factor of 4. Also included are several low-level circuits to provide the required operating voltages from 117-V ac line power and a high-level trigger to the thyratron. These circuits accept fiber-optic trigger inputs from the master oscillator room (MOR). The unit delivers anode currents in excess of 50 kA and a current rate of charge in excess of 10^{12} A/s. The unit has a shorter lifetime compared to conventional thyratrons, but is still more than adequate (10^8 shots) for Nova.

Testing to date has been quite successful, with the prototype providing approximately 45 kV into a 25-Ω resistive load. Forthcoming changes in the transformer ferrite material are expected to improve pulse rise time from 22 to under 15 ns. The unit has been mated to a plasma-shutter rail-gap switch, and robust, reliable triggering action has been achieved.

Planar Triode Pockels-Cell Drivers. Two types of Pockels-cell drivers will be used on Nova: fast devices based on planar triodes; and a slower thyratron-based unit capable of driving 20 50-Ω loads. The planar triode driver is composed of a two-tube preamplifier driven by an avalanche transistor stack and a six-tube amplifier. The tubes used are planar triodes from Varian Associates, Salt Lake City, Utah, that are typically used as radar modulators. The driver design has evolved over the past three years to the current operational driver.

Development work has continued this year to improve the maintainability and reliability of the basic design. The transistor avalanche stack was changed from a three-high stack using type MMT 2222 transistors to a two-high stack using MMT 2484 transistors. This change improved the preamplifier rise time and increased the reliability of the stack by decreasing the number of components. Redesign of the power supply has resulted in using two separate power supplies in each chassis. Bias voltages are now supplied by a source that is independent of the high-voltage plate supply. This was necessary to eliminate the bias variations that accompanied high-voltage capacitor charging following a shot. We also added triode warm-up for 90 s before the application of high voltage to promote tube longevity.

Figure 7-150 illustrates the current performance of a driver that is used for pulse slicing on the Shiva system. The three waveforms shown represent three different tube bias-voltage settings on the preamplifier. Waveform (a) is a 3.5-ns, 29.5-μJ pulse resulting from a 290-V negative bias; (b) is a 3.0-ns, 22-μJ pulse at −325 V; and (c) is a 2.5-ns, 15-μJ pulse at −360 V. Using bias control to select the pulse width yielded a straightforward solution to the short-pulse requirements for the backlighter series of Shiva experiments.

Driver performance satisfies present requirements, but short tube life presents an operational problem. Tube lifetime is currently being addressed by improved isolation of incoming tubes and by increased buffering in the preamplifier.

***N*-Way Pockels-Cell Drivers.** The Shiva laser used a spark gap to drive the 20 Pockels cells in the laser chains. On Nova, the spark gap will be driven by a hydrogen thyratron, that will decrease the maintenance load presented by the Shiva design. Rise time will degrade from the range of 3 to 5 ns to 15 ns, but, for chain Pockels cells, the increase in reliability is much more important. The thyratrons that will be evaluated in the *N*-way are types HY8 and HY1102 from EG&G, Electronic Components, Salem, Mass. Previous operational experience with these devices was derived during development of the plasma shutter.

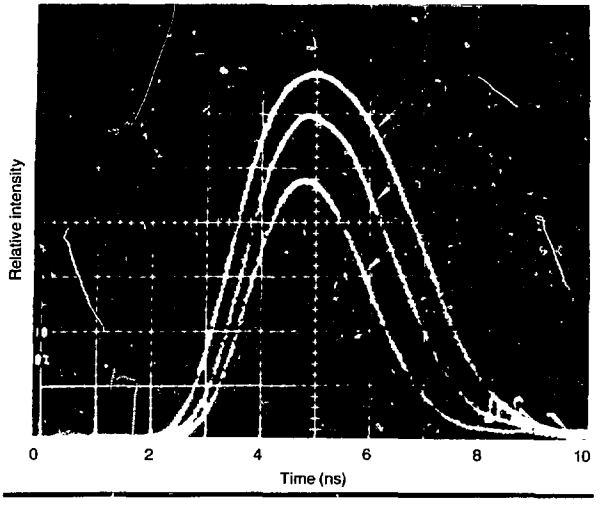

Fig. 7-150. Current output of planar-triode Pockels-cell driver used in Shiva.

The HY1102 is rated at 20 kV and 120 kA, with a rise time of 7 ns and a demonstrated jitter of ±200 ps. The low thyratron jitter helps compensate for the degraded rise time. The Nova unit will be tested on Novette as a two-way driver.

Large-Area Planar-Triode Development. We are presently exploring ways to reduce the complexity of planar triode-based Pockels-cell drivers. Available microwave triodes suitable for our application have a limited cathode area of 2 cm^2. Six output tubes in parallel are presently used on our driver. Tubes with a larger cathode area and similar bandwidth could increase reliability by reducing both complexity and cathode current density.

Thus, we contracted with the Eimac Division of Varian, Salt Lake City, Utah, to develop prototype tubes of 3 cm^2 cathode area as an interim step to 4-cm^2 or, preferably, 5-cm^2 devices. The planar structure was abandoned for a structurally stronger domed configuration. Two tubes were delivered and are under evaluation at LLNL. We are presently negotiating a follow-on contract that would yield prototype 4- or 5-cm^2 tubes.

Bulk Silicon-Switch Development. A bulk semiconductor switch (Auston switch) is a fast photoconductive switch made of high-resistivity semiconductor material. When illuminated with a short laser pulse, high-voltage devices can switch many kilovolts in tens or picoseconds,[183] and we are currently developing such switches as fast Pockels-cell drivers. One application is a driver designed to deliver a 4.5-kV, 1- to 10-ns square pulse into a 50-Ω load. The driver will be used with a Pockels-cell pulse slicer to divert short light pulses out of a Q-switched pulse from the long-pulse oscillator in the Novette MOR.[184]

Part of the energy from a 0.1- to 1-ns pulse from the short-pulse oscillator is split off to illuminate the silicon switch. The switch becomes conductive and discharges a charge line, generating a pulse that drives the slicer. The slicer then passes a light pulse that enters the preamplifier. The temporal jitter between this light pulse and the one from the short-pulse oscillator is within a few tens of picoseconds, thus providing the synchronization required when both pulses are used to illuminate a fusion target, such as in backlighting experiments.[185]

Prototype switches hold off charge-line voltages of 10 kV (charge voltages are maintained for about 200 ns to avoid thermal runaway) and can switch 5 kV into 50 Ω in less than 0.5 ns. For future applications, it may be possible to vary the switch illumination to produce more complex pulse shapes.

Authors: G. R. Dreifuerst, J. A. Oicles, I. F. Stowers, and R. B. Wilcox

References

1. *Laser Program Annual Report—1980*, Lawrence Livermore National Laboratory, Livermore, Calif., UCRL-50021-80 (1981), pp. 2-254 to 2-286.
2. H. Schroeder, "Thin Film Formation on Glass Surfaces in Chemical Coating Processes," *Proc. Intern. Cong. Glass, 10th, Kyoto, 1974* (The Ceramic Society of Japan, Kyoto, Japan, 1974), pp. 8-118.
3. L. M. Cook and K. Mader, "Integral AR Coated Glasses for High Energy Laser Applications," *Proc. Electro-Optic Laser* (Laser Institute of America, Anaheim, Calif., 1981), published by Cahners Exposition Group, Chicago, Ill. (1981), pp. 211-220.
4. L. M. Cook, W. H. Lowdermilk, D. Milam, and J. E. Swain, "Antireflecting Surfaces for High Energy Laser Optics Formed by Neutral-Solution Processing," *Appl. Opt.* **21**, 1482 (1982).
5. H. Schroeder, "Properties and Applications of Oxide Layers Deposited on Glass from Organic Solutions," *Opt. Acta* **9**, 249 (1962).
6. H. Dislich, "New Routes to Multicomponent Oxide Glasses," *Angew. Chem. Int.* **10**, 363 (1971).
7. S. P. Mukherjee, J. Zarzycki, and J. P. Traverese, "A Comparative Study of Gels and Oxide Mixtures as Starting Materials for the Nucleation and Crystallization of Silicate Glasses," *J. Mat. Sci.* **11**, 341 (1976).
8. S. P. Mukherjee, "Sol-Gel Processes in Glass Science and Technology," *J. Non-Cryst. Solids* **42**, 477 (1980).
9. H. Schroeder, "Oxide Layers Deposited from Organic Solutions," *Physics of Thin Films*, Vol. 5, G. Hass and R. E. Thun, Eds. (Academic Press, New York, 1969), p. 87.
10. S. P. Mukherjee and W. H. Lowdermilk, "Gradient-Index AR Films Deposited by the Sol-Gel Process," *Appl. Opt.* **21**, 293 (1982).
11. *Laser Program Annual Report—1980*, Lawrence Livermore National Laboratory, Livermore, Calif., UCRL-50021-80 (1981), p. 2-226.
12. J. Swain, S. Stokowski, D. Milam, and F. Rainer, *Improving the Bulk Laser Damage Resistance of KDP by Pulsed Laser Irradiation*, Lawrence Livermore National Laboratory, Livermore, Calif., UCRL-86537 (1981); *Appl. Phys. Lett.* (in press).
13. *Laser Program Annual Report—1980*, Lawrence Livermore National Laboratory, Livermore, Calif., UCRL-50021-80 (1981), p. 2-229.
14. F. Rainer, D. Milam, and W. H. Lowdermilk, "Laser Damage Thresholds of Thin Film Optical Coatings at 248 nm," *Proc. Boulder Damage Conf., 1981* (National Bureau of Standards, Boulder, Colo., in press).
15. T. T. Hart, T. L. Lichtenstein, C. K. Carniglia, and F. Rainer, "Effects of Undercoats and Overcoats on Damage Thresholds of 248-nm Coatings," *Proc. Boulder Damage Conf., 1981* (National Bureau of Standards, Boulder, Colo., in press).
16. S. F. Stokowski, R. A. Saroyan, and M. J. Weber, *Laser Class: Nd-Doped Glass Spectroscopic and Physical Properties*, Lawrence Livermore National Laboratory, Livermore, Calif., M-095, 2nd Rev. (1981).
17. M. J. Weber, *Faraday Rotator Materials*, Lawrence Livermore National Laboratory, Livermore, Calif., M-103 (1982).
18. P. Liu, W. L. Smith, H. Lotem, J. H. Bechtel, N. Bloembergen, and R. S. Adhav, *Phys. Rev. B* **17**, 4620 (1978).
19. *Laser Program Annual Report—1980*, Lawrence Livermore National Laboratory, Livermore, Calif., UCRL-50021-80 (1981), p. 2-219.
20. P. V. Avizonis and R. L. Grotbeck, *J. Appl. Phys.* **37**, 307 (1966).
21. W. E. Martin and D. Milam, "Gain Saturation in Nd:doped Laser Materials," *IEEE J. Quantum Electron.* **18**, 1155 (1982).
22. *Laser Program Annual Report—1977*, Lawrence Livermore National Laboratory, Livermore, Calif., UCRL-50021-77 (1978), p. 2-180.
23. *Laser Program Annual Report—1978*, Lawrence Livermore National Laboratory, Livermore, Calif., *UCRL-50021-78 (1979)*, p. 7-76.
24. W. L. Smith, "High-Intensity Transmission Properties of Index-Matching Fluids for Laser Fusion Applications," *Tech. Dig. CLEO, D.C., 1981* (IEEE, Washington, D.C., 1981), p. 32.
25. W. T. White and W. L. Smith, Lawrence Livermore National Laboratory, Livermore, Calif., internal memorandum ELR 81-136 (1981).
26. A. P. Veduta and B. P. Kirsanov, "Variation of the Refractive Index of Liquids and Glasses in a High Intensity Field of A Ruby Laser," *Sov. Phys.—JETP* **27**, 736 (1968).
27. E. S. Bliss, D. R. Speck, and W. W. Simmons, "Direct Interferometric Measurements of the Nonlinear Refractive Index Coefficient n_2 in Laser Materials," *Appl. Phys. Lett.* **25**, 728 (1974).
28. D. Milam and M. J. Weber, "Measurement of Nonlinear Refractive Index Coefficients Using Time-Resolved Interferometry," *J. Appl. Phys.* **47**, 2497 (1976).
29. M. J. Moran, C. Y. She, and R. L. Carman, "Interferometric Measurements of the Nonlinear Refractive-Index Coefficient Relative to CS_2 in Laser-System-Related Materials," *IEEE J. Quantum Electron.* **11**, 259 (1975).
30. K. J. Witte, M. Galanti, R. Volk, "n_2 Measurements at 1.32 μm of Some Organic Compounds Usable as Solvents in a Saturable Absorber for an Atomic Iodine Laser," *Opt. Commun.* **34**, 278 (1980).
31. G. B. Al'tschuler, A. I. Barbaskev, V. B. Karasev, K. I. Krylov, V. M. Orchinnikov, and S. F. Sharlai, "Direct Measurement of the Tensor Elements of the Nonlinear Optical Susceptibility of Optical Materials," *Sov. Tech. Phys. Lett.* **3**, 213 (1977).
32. N. L. Boling, A. J. Glass, and A. Owyoung, "Empirical Relationships for Predicting Nonlinear Refractive Index Changes in Optical Solids," *IEEE J. Quantum Electron.* **14**, 601 (1978).
33. A. J. Tavarowski and D. S. Kliger, *Chem. Phys.* **20**, 253 (1977).
34. W. B. Jackson, N. M. Amer, A. C. Boccara, and D. Fournier, *J. Appl. Phys.* **20**, 1333 (1981).
35. M. J. Weber, D. Milam, and W. L. Smith, *Opt. Eng.* **17**, 463 (1978).

References

36. P. H. Sarkies, J. N. Sandoe, and S. Parke, *J. Phys. D* **4**, 1642 (1971); R. R. Jacobs and M. J. Weber, *IEEE J. Quantum Electron.* **12**, 102 (1976); N. B. Brachkovskaya, A. A. Grubin, S. G. Lunter, A. K. Przhevuskii, E. L. Raaben, and M. N. Tolstoi, *Sov. J. Quantum Electron.* **6**, 534 (1976).
37. W. D. Krupke, *IEEE J. Quantum Electron.* **10**, 450 (1974).
38. J. M. Pellegrino, W. M. Yen, and M. J. Weber, *J. Appl. Phys.* **51**, 6332 (1980).
39. M. J. Weber, D. C. Ziegler, and C. A. Angell, *J. Appl. Phys.* **53**, 4344 (1982).
40. *The Rare Earths in Modern Science and Technology*, Vol. 2, G. J. McCarthy, J. J. Rhyme, and H. B. Silber, Eds. (Plenum Press, New York, 1979), p. 463.
41. D. J. Newman, *Adv. Phys.* **20**, 197 (1971).
42. S. A. Brawer and M. J. Weber, *Phys. Rev. Lett.* **45**, 460 (1980).
43. S. A. Brawer and M. J. Weber, *J. Chem. Phys.* **75**, 3522 (1981).
44. *Laser Program Annual Report—1980*, Lawrence Livermore National Laboratory, Livermore, Calif., UCRL-50021-80 (1981), p. 2-321.
45. D. W. Hall, S. A. Brawer, and M. J. Weber, *Phys. Rev. B* **25**, 2828 (1982).
46. S. A. Brawer and M. J. Weber, *Appl. Phys. Lett.* **35**, 31 (1979).
47. V. P. Lebedev and A. K. Przhevuskii, *Sov. Phys. Solid State* **19**, 1389 (1979).
48. J. Hegarty and W. M. Yen, *Phys. Rev. Lett.* **43**, 1126 (1979).
49. P. M. Selzer, D. L. Huber, D. S. Hamilton, W. M. Yen, and M. J. Weber, *Phys. Rev. Lett.* **36**, 813 (1976).
50. D. E. McCumber and M. D. Sturge, *J. Appl. Phys.* **34**, 1682 (1963).
51. S. Hunklinger and W. Arnold, "Ultrasonic Properties of Glasses at Low Temperature," *Physical Acoustics*, Vol. 12, W. P. Mason, Ed. (Academic Press, New York, 1976). W. A. Phillips, *J. Non-Cryst. Solids* **31**, 267 (1978).
52. P. W. Anderson, B. I. Halperin, and C. M. Varma, *Philos. Mag.* **25**, 1 (1972).
53. W. A. Phillips, *J. Low Temp. Phys.* **7**, 351 (1972).
54. R. Vacher, H. Sussner, and S. Hunklinger, *Phys. Rev. B* **21**, 5850 (1980).
55. S. K. Lyo and R. Orbach, *Phys. Rev. B* **22**, 4223 (1980).
56. T. L. Reinecke, *Solid State Commun.* **32**, 1103 (1979).
57. *Laser Spectroscopy of Solids*, W. M. Yen and P. M. Selzer, Eds. (Springer-Verlag, Berlin, 1981).
58. *Laser Spectroscopy of Solids*, W. M. Yen and P. M. Selzer, Eds. (Springer-Verlag, Berlin, 1981), p. 189; S. A. Brawer and M. J. Weber, *Phys. Rev. Lett.* **45**, 460 (1980); S. A. Brawer and M. J. Weber, *J. Chem. Phys.* **75**, 3516 (1981).
59. M. Svoronos, C.N.R.S., Meudon, France, private communication (1981).
60. *Physical Acoustics*, Vol. 12, W. P. Mason, Ed. (Academic Press, New York, 1976).
61. S. A. Brawer, "Interaction of Rare Earth Ions with Two Level Systems in Glasses," *Phys. Rev.* (To be published.)
62. S. K. Lyo and R. Orbach, *Phys. Rev. B* **22**, 4223 (1980); T. L. Reinecke, *Solid State Commun.* **32**, 1103 (1979); J. Hegarty and W. M. Yen, *Phys. Rev. Lett.* **43**, 1126 (1979); P. M. Selzer, D. L. Huber, D. S. Hamilton, W. M. Yen, and M. J. Weber, *Phys. Rev. Lett.* **36**, 813 (1976).
63. *Laser Program Annual Report—1980*, Lawrence Livermore National Laboratory, Livermore, Calif., UCRL-50021-80 (1981), p. 2-304.
64. *Physical Acoustics*, Vol. 12, W. P. Mason, Ed. (Academic Press, New York, 1976).
65. W. A. Phillips, *J. Low Temp. Phys.* **7**, 351 (1972).
66. P. M. Selzer, D. L. Huber, D. S. Hamilton, W. M. Yen, and M. J. Weber, *Phys. Rev. Lett.* **36**, 813 (1976).
67. S. A. Brawer and M. J. Weber, *J. Chem. Phys.* **75**, 3522 (1981).
68. L. V. Woodcock, C. A. Angell, and P. Cheeseman, *J. Chem. Phys.* **64**, 1565 (1976).
69. S. A. Brawer, *Phys. Rev. Lett.* **46**, 778 (1981).
70. *Laser Program Annual Report—1973*, Lawrence Livermore National Laboratory, Livermore, Calif., UCRL-50021-73 (1974), p. 44.
71. P. B. Newell, *Performance of Large Xenon Flashtubes For Nd:Glass Disk Lasers*, EG&G, Salem, Mass., B-4420 (1975).
72. J. B. Trenholme and J. L. Emmett, *Proc. Int. Cong. High-Speed Photog., 9th, New York, 1970* (Society of Motion Picture and Television Engineers, New York, 1970), p. 289.
73. J. Markiewicz and J. L. Emmett, *IEEE J. Quantum Electron.* **2**, 707 (1966).
74. L. M. Frantz and J. S. Nodvik, *J. Appl. Phys.* **34**, 2346 (1963).
75. *Laser Program Annual Report—1977*, Lawrence Livermore National Laboratory, Livermore, Calif., UCRL-50021-77 (1978), pp. 2-224 to 2-235.
76. *Laser Program Annual Report—1980*, Lawrence Livermore National Laboratory, Livermore, Calif., UCRL-50021-80 (1981), p. 8-32.
77. W. L. Morgan, B. L. Whitten, and J. N. Bardsley, *Phys. Rev. Lett.* **45**, 2021 (1980).
78. A. U. Hazi, A. E. Orel, and T. N. Rescigno, *Phys. Rev. Lett.* **46**, 918 (1981).
79. W. R. Wadt and P. J. Hay, *J. Chem. Phys.* **15**, 3850 (1978).
80. C. B. Edwards, F. O'Neill, and M. J. Shaw, *Appl. Phys. Lett.* **38**, 843 (1981).
81. J. H. Jacob, D. W. Trainor, M. Rokni, and J. C. Hsia, *Appl. Phys. Lett.* **37**, 522 (1980).
82. M. Rokni, J. H. Jacob, and J. A. Mangano, *Phys. Rev. A* **16**, 2216 (1977).
83. International Mathematical and Statistical Libraries, Inc., Houston, Tex.
84. C. H. Chen and M. G. Payne, *IEEE J. Quant. Electron.* **15**, 149 (1979).
85. G. P. Quigley and W. M. Hughes, *Appl. Phys. Lett.* **32**, 649 (1978).
86. W. L. Morgan and A. Szoke, *Phys. Rev. A* **23**, 1256 (1981).
87. G. P. Quigley and W. M. Hughes, *Appl. Phys. Lett.* **32**, 627 (1978).
88. N. J. Berger and S. M. Seltzer, "Studies in Penetration of Charged Particles in Matter," Nuclear Science Series Rept. No. 10, NAS-NRC Pub. 1133 (Natl. Acad. Sci., Washington, D.C., 1964).

89. D. W. Trainor and J. H. Jacob, *Appl. Phys. Lett.* **37**, 675 (1980).
90. A. M. Hawryluk, J. A. Mangano, and J. H. Jacob, *Appl. Phys. Lett.* **31**, 164 (1977).
91. T. N. Rescigno, A. U. Hazi, and A. E. Orel, *J. Chem. Phys.* **68**, 5283 (1978).
92. W. J. Stevens, M. Gardner, A. Karo, and P. Julienne, *J. Chem. Phys.* **67**, 2860 (1977).
93. H. H. Michaels, R. H. Hobbs, and L. A. Wright *J. Chem. Phys.* **71**, 5053 (1979).
94. W. R. Wadt, *J. Chem. Phys.* **73**, 3915 (1980).
95. A. Mandl, *Phys. Rev. A* **3**, 251 (1971).
96. K. J. McCann and M. R. Flannery, *Appl. Phys. Lett.* **31**, 599 (1977).
97. H. A. Hyman, *Appl. Phys. Lett.* **31**, 14 (1977).
98. P. J. Hay and T. H. Dunning, Jr., *J. Chem. Phys.* **66**, 1306 (1977).
99. *Laser Program Annual Report—1975*, Lawrence Livermore National Laboratory, Livermore, Calif., UCRL-50021-75 (1976), p. 500.
100. J. R. Murray, J. Goldhar, D. Eimerl, and A. Szoke, *IEEE J. Quant. Electron.* QE **15**, 368 (1979).
101. R. R. Jacobs, J. Goldhar, D. Eimerl, S. B. Brown, and J. R. Murray, *Appl. Phys. Lett.* **37**, 264 (1980).
102. M. A. A. Clyne and I. S. McDermid, *Trans. Faraday Soc.* **75**, 905 (1979).
103. R. Colin, *Can. J. Phys.* **47**, 979 (1969).
104. M. A. A. Clyne and M. C. Heaven, *Chem. Phys.* **51**, 299 (1980).
105. D. H. Parker and P. Avouris, *Chem. Phys. Lett.* **53**, 515 (1978).
106. A. M. Halpern, *Chem. Phys. Lett.* **6**, 296 (1970); A. M. Halpern and R. M. Danziger, *Chem. Phys. Lett.* **16**, 72 (1972); A. M. Halpern, *Mol. Photochem.* **5**, 517 (1973).
107. E. Heilbronner and K. A. Muszkat, *J. Am. Chem. Soc.* **92**, 3818 (1970); S. K. Nelson and J. M. Buschek, *J. Am. Chem. Soc.* **96**, 7930 (1974).
108. D. H. Parker and P. Avouris, *J. Chem. Phys.* **71**, 1241 (1979).
109. T. Wada, E. Kishida, Y. Tomiie, H. Suga, S. Seki, and I. Nitta, *Bull. Chem. Soc. Japan* **33**, 1317 (1960).
110. T. N. Rescigno, A. U. Hazi, and A. E. Orel, *J. Chem. Phys.* **68**, 5283 (1978).
111. *Laser Program Annual Report—1977*, Lawrence Livermore National Laboratory, Livermore, Calif., UCRL-50021-77 (1978), pp. 7-28 to 7-30.
112. *Laser Program Annual Report—1980*, Lawrence Livermore National Laboratory, Livermore, Calif., UCRL-50021-80 (1981), pp. 8-40 to 8-44.
113. T. H. Dunning and P. J. Hay, *Appl. Phys. Lett.* **28**, 649 (1976).
114. P. J. Hay and T. H. Dunning, *J. Chem. Phys.* **66**, 1306 (1977).
115. M. Shimauchi, S. Karasawa, and T. Miura, *J. Chem. Phys.* **68**, 5657 (1978).
116. G. Herzberg, *Spectra of Diatomic Molecules* (Van Nostrand Reinhold, New York, 1950), Ch. III.
117. J. Goldhar and J. R. Murray, *Opt. Lett.* **1**, 199 (1977).
118. *Laser Program Annual Report—1977*, Lawrence Livermore National Laboratory, Livermore, Calif., UCRL-50021-77 (1978); *Laser Program Annual Report 1978*, Lawrence Livermore National Laboratory, Livermore, Calif., UCRL-50021-78 (1979); *Laser Program Annual Report 1979*, Lawrence Livermore National Laboratory, Livermore, Calif., UCRL-50021-79 (1980); *Laser Program Annual Report 1980*, Lawrence Livermore National Laboratory, Livermore, Calif., UCRL-50021-80 (1981).
119. J. Goldhar and J. R. Murray, "Intensity Averaging and Four Wave Mixing in Raman Amplifiers," *IEEE J. Quant. Electron.* QE **18**, 399 (1982).
120. L. G. Schlitt, J. C. Swingle, W. R. Rapoport, J. Goldhar, and J. J. Ewing, "An Efficient Narrowband Electron Beam Pumped KrF Laser for Pulse Compression Studies," *J. Appl. Phys.* **52**, 91 (1981).
121. W. R. Rapoport, J. Goldhar, and J. R. Murray, "KrF Laser-Triggered SF_6 Spark Gap for Low Jitter Timing," *IEEE Trans. Plasma Sci.* PS **8**, 167 (1980).
122. M. W. Taylor, J. Goldhar, and J. R. Murray, "An Instant Photographic Material Suitable for Ultraviolet Laser Beam Intensity Diagnostics," *Appl. Opt.* **21**, 4 (1982).
123. *Laser Program Annual Report—1980*, Lawrence Livermore National Laboratory, Livermore, Calif., UCRL-50021-80 (1981), p. 8-17.
124. *Laser Program Annual Report—1979*, Lawrence Livermore National Laboratory, Livermore, Calif., UCRL-50021-79 (1980), p. 7-53.
125. M. D. Sturge, E. T. Merritts, L. F. Johnson, H. J. Guggenheim, and J. P. Van der Ziel, "Optical and Microwave Studies of Divalent Vanadium in Octahedral Fluoride Coordination," *J. Chem. Phys.* **54**, 405 (1971).
126. L. F. Johnson and J. H. Guggenheim, "Phonon Terminated Coherent Emission from V^{2+} Ions in MgF_2," *J. Appl. Phys.* **38**, 4837 (1967).
127. *Laser Program Annual Report—1980*, Lawrence Livermore National Laboratory, Livermore, Calif., UCRL-50021-80 (1981), pp. 8-60 to 8-67.
128. P. F. Moulton, "Research V:MgF_2 Crystals for Laser Fusion Applications," Lincoln Laboratory, Lexington, Mass., Progress Report, June 1979–March 1981, SAN-L Contract 806-013 (1981).
129. *Laser Program Annual Report—1980*, Lawrence Livermore National Laboratory, Livermore, Calif., UCRL-50021-80 (1981), p. 8-55.
130. D. Prosnitz, A. Szoke, and V. K. Neil, *Phys. Rev. A* **24**, 1436 (1981).
131. N. M. Kroll, P. L. Morton, and M. N. Rosenbluth, *IEEE J. Quant. Electron.* QE **17**, 1436 (1981).
132. J. H. Mauburger, *Progr. Quant. Electron.* **4**, 35 (1975).
133. J. A. Fleck, Jr., J. R. Morris, and E. S. Bliss, *IEEE J. Quant. Electron.* QE **14**, 353 (1978).
134. W. W. Simmons, J. T. Hunt, and W. E. Warren, *IEEE J. Quant. Electron.* QE **17**, 1727 (1982).
135. R. J. Gelinas, S. K. Doss, and K. Miller, *J. Comput. Phys.* **40**, 202 (1981).
136. A. J. Campillo, J. E. Pearson, S. L. Shapiro, and W. J. Terrell, Jr., *Appl. Phys. Lett.* **23**, 85 (1973).

References

137. J. M. Slater, *IEEE J. Quant. Electron.* QE **17**, 1476 (1981); J. M. Slater and D. D. Lowenthal, *J. Appl. Phys.* **52**, 44 (1981).
138. C. A. Brau and R. K. Cooper, "Variable Wiggler Optimization," in *Free Electron Generators of Coherent Radiation*, S. F. Jacobs, H. S. Pilloff, M. Sargent III, M. O. Scully, and R. Spitzer, Eds. (Addison-Wesley, Reading, Mass., 1980), pp. 647-664.
139. *Laser Program Annual Report—1979*, Lawrence Livermore National Laboratory, Livermore, Calif., UCRL-50021-79 (1980), p. 7-72.
140. L. F. Champagne, *Appl. Phys. Lett.* **33**, 523 (1978).
141. W. V. Kurepa and D. S. Belic, *J. Phys. B* **11**, 3719 (1978).
142. M. Allan and S. F. Wong, *J. Chem. Phys.* **74**, 1687 (1981).
143. K. Rohr, in *Symposium on Electron-Molecule Collisions*, I. Shimamura and M. Matsuzawa, Eds. (University of Tokyo, Tokyo, Japan, 1979), p. 67.
144. T. N. Rescigno and A. E. Orel, *Phys. Rev. A* **24**, 1267 (1981).
145. C. W. Clark and J. Siegel, *J. Phys. B* **13**, L31 (1980).
146. L. A. Collins and D. W. Norcross, *Phys. Rev. A* **18**, 467 (1978).
147. K. Rohr and F. Linder, *J. Phys. B* **9**, 2521 (1976).
148. L. A Collins, R. J. W. Henry, and D. W. Norcross, *J. Phys. B* **13**, 2299 (1980).
149. D. W. Peaceman and H. H. Rachford, *J. Soc. Indust. Appl. Math.* **3**, 28 (1955).
150. W. C. Keever and E. Everhart, *Phys. Rev.* **150**, 43 (1966).
151. C. Harel and A. Salin, *J. Phys. B* **13**, 785 (1980); V. Lopez, A. Macias, R. D. Piacentini, A. Riera, and M. Yanez, *J. Phys. B* **11**, 2880 (1978).
152. K. C. Kulander, K. R. Sandhya Devi, and S. E. Koonin, *Phys. Rev. A* **5**, 2968 (1982).
153. R. N. Compton, G. D. Alton, and D. J. Pegg, *J. Phys. B* **13**, L651 (1980).
154. R. V. Hodges, M. J. Coggiola, and J. R. Peterson, *Phys. Rev. A* **23**, 59 (1981).
155. B. Brehm, M. A. Gusinow, and J. L. Hall, *Phys. Rev. Lett.* **19**, 737 (1967).
156. A. V. Bunge and C. F. Bunge, *Phys. Rev. A* **19**, 452 (1979).
157. A. U. Hazi and K. Reed, *Phys. Rev. A* **24**, 2269 (1981).
158. P. W. Langhoff, J. S. Sims, and C. T. Corcoran, *Phys. Rev. A* **10**, 829 (1974).
159. P. W. Langhoff, in *Electron-Molecule and Photon-Molecule Collisions*, T. Rescigno, V. McKoy, and B. Schneider, Eds. (Plenum, New York, 1979), p. 183.
160. R. N. Compton, Oak Ridge National Laboratory, Oak Ridge, Tenn., private communication (1981).
161. J. R. Peterson, SRI International, Menlo Park, Calif., private communication (1981).
162. A. V. Hellfeld, J. Caddick, and J. Weiner, *Phys. Rev. Lett.* **40**, 1369 (1978).
163. B. W. Shore and R. J. Cook, *Phys. Rev. A* **20**, 1958 (1979).
164. A. Bernhardt and B. W. Shore, *Phys. Rev.* **23**, 1290 (1981).
165. B. W. Shore and R. J. Cook, *Phys Rev. A* **20**, 1958 (1979).
166. B. W. Shore, *Phys. Rev. A* **24**, 1413 (1981).
167. T. W. Ducas, M. G. Littman, and M. L. Zimmerman, *Phys. Rev. Lett.* **35**, 1752 (1975).
168. L. C. Balling and J. J. Wright, *Appl. Phys. Lett.* **29**, 411 (1976).
169. *Laser Program Annual Report—1980*, Lawrence Livermore National Laboratory, Livermore, Calif., UCRL-50021-80 (1981), p. 10-52.
170. G. I. Bekov, A. N. Zherikhin, V. S. Letokhov, V. I. Mishin, and V. N. Fedoseev, *Pis'ma Zh. Eksp. Teor. Fiz. (JETP Lett.)* **33**, 450 (1981).
171. B. W. Shore and M. A. Johnson, *Phys. Rev. A* **23**, 1608 (1981).
172. S. L. McCall and E. L. Hahn, *Phys. Rev.* **183**, 451 (1969).
173. G. L. Lamb, Jr., *Rev. Mod. Phys.* **43**, 99 (1971).
174. M. Quack, *J. Chem. Phys.* **69**, 1282 (1978); A. A. Makarov, V. T. Platonenko, and V. V. Tyakht, *Sov. Phys. JETP* **48**, 1044 (1978); C. D. Cantrell, V. S. Letokhov, and A. A. Makarov, in *Coherent Nonlinear Optics*, M. S. Feld and V. S. Letokhov, Eds. (Springer Verlag, Heidelberg, Fed. Republic of Germany, 1980), Ch. 5.
175. J. J. Yeh and J. H. Eberly, *Phys. Rev. A* **22**, 1124 (1980).
176. J. J. Yeh, C. M. Bowden, and J. H. Eberly. (Submitted to *J. Chem. Phys.*)
177. B. W. Shore and J. H. Eberly, *Physica*. (In press.)
178. M. L. Spann et al., "The Design, Assembly, and Testing of an Active Rotary Flux Compressor," *3rd IEEE Pulsed Power Conference, Digest of Technical Papers, June 1981* (IEEE, New York, 1981), pp. 300-303.
179. W. L. Bird, *The Continued Testing and Evaluation of the Engineering Prototype Compulsator*, Center for Electromechanics, University of Texas, Austin, Tex. (1981).
180. B. Carder et al., "Testing and Optimizing Active Rotary Flux Compressors," *3rd IEEE Pulsed Power Conference, Digest of Technical Papers, June 1981* (IEEE, New York, 1981), pp. 304-307.
181. I. F. Stowers, "Conclusion of Plasma Shutter Testing on Shiva," Lawrence Livermore National Laboratory, Livermore, Calif., Internal Memo CD 81-49 (1981).
182. L. P. Bradley, E. L. Orham, I. F. Stowers, and P. Koert, *Development of a Plasma Retropulse Shutter for Shiva and Nova*, Lawrence Livermore National Laboratory, Livermore, Calif., UCRL-52830 (1979).
183. G. Mourou and W. Knox, "High-Power Switching with Picosecond Precision," *Appl. Phys. Lett.* **35**, 492 (1979).
184. *Laser Program Annual Report—1980*, Lawrence Livermore National Laboratory, Livermore, Calif., UCRL-50021-80 (1981), p. 2-48.
185. *Laser Program Annual Report—1980*, Lawrence Livermore National Laboratory, Livermore, Calif., UCRL-50021-80 (1981), p. 2-20.

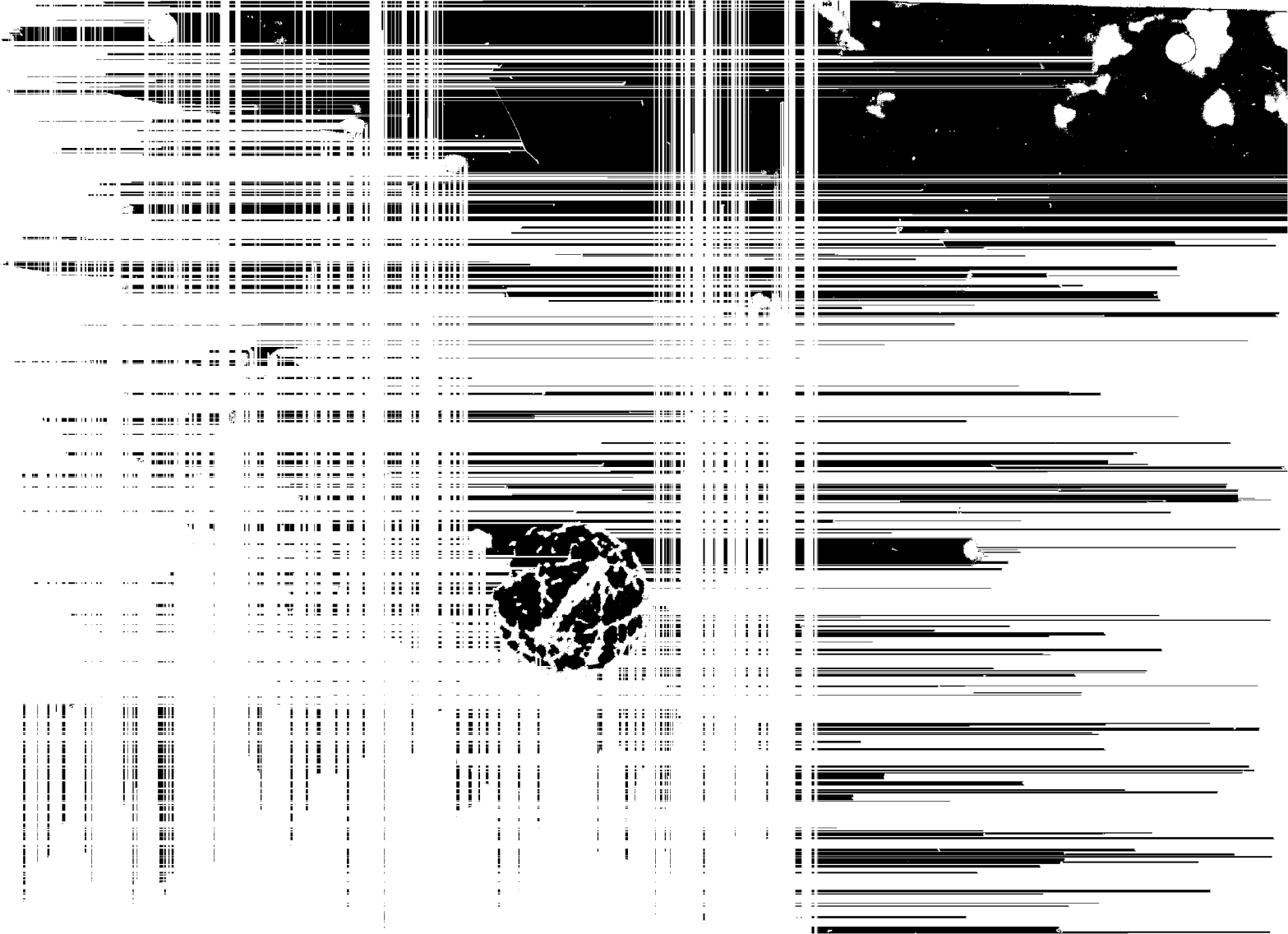

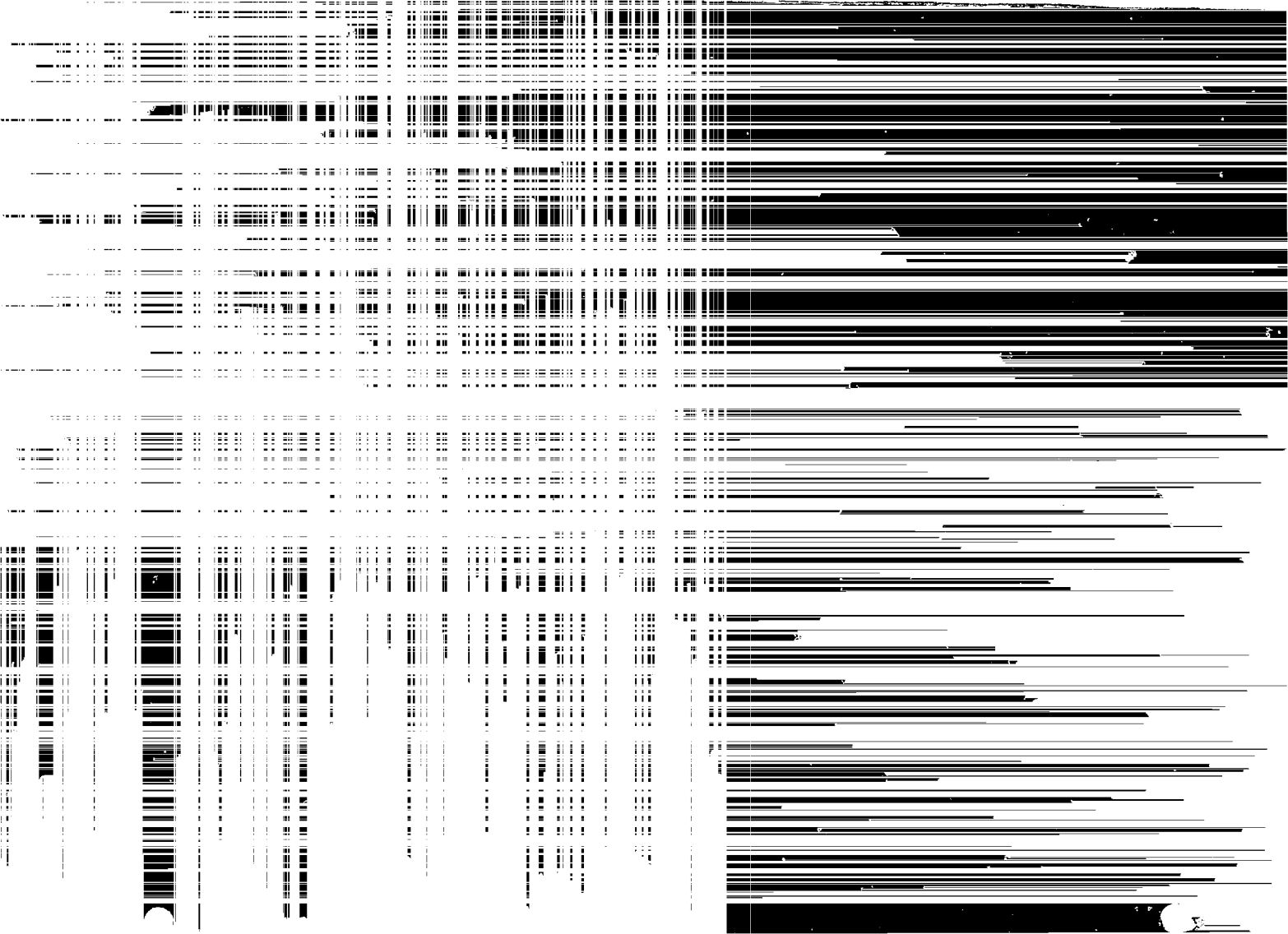

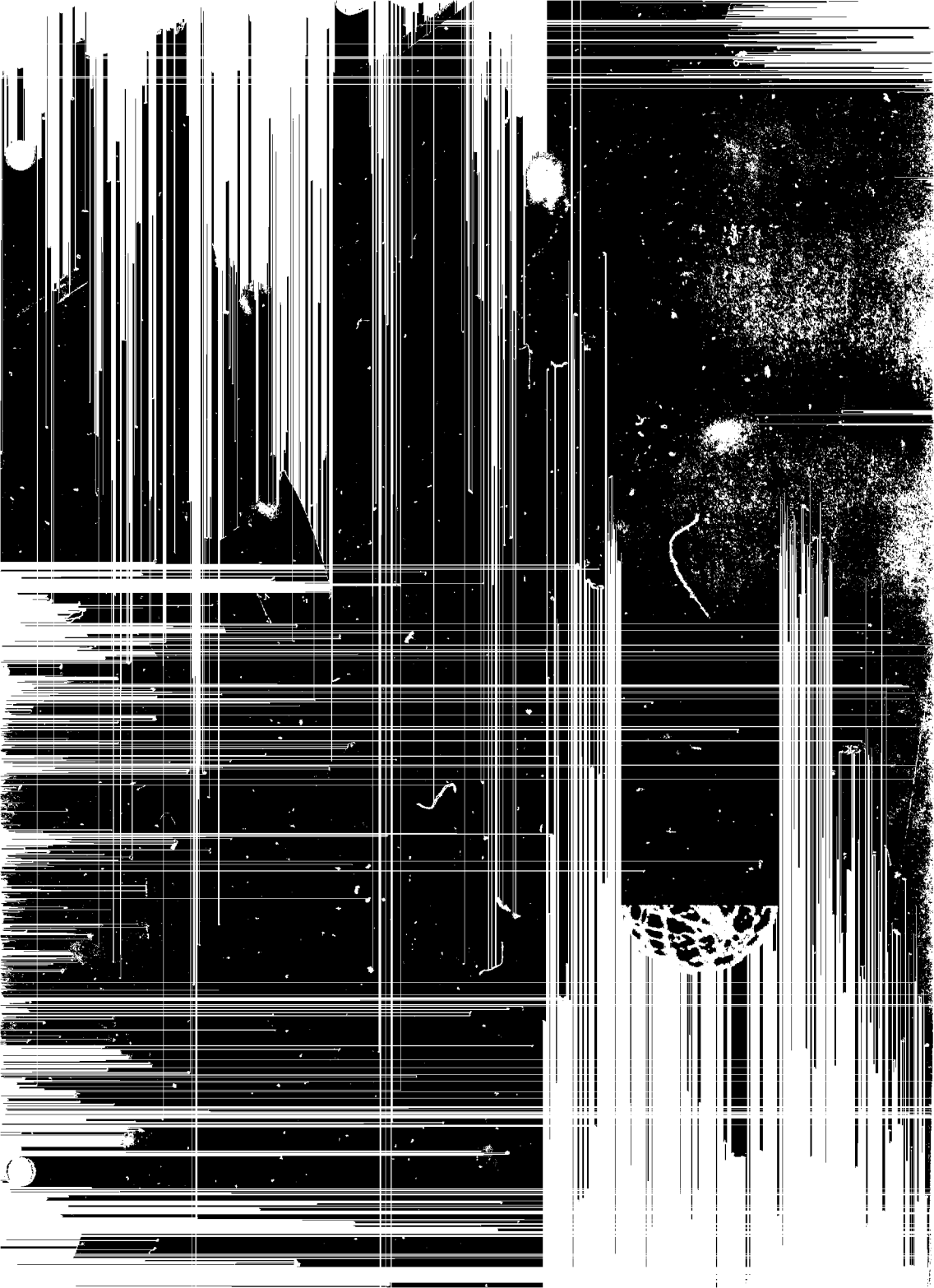

Energy and Military Applications

Contents

Section Editor: J. Hovingh

Energy and Military Applications

Introduction

M. J. Monsler

The primary objective of current research in inertial confinement fusion (ICF) is to provide a cost-effective approach to the understanding of nuclear weapon physics that is complementary to underground testing. We use concentrated laser or particle beams to study the behavior of matter at very high temperatures and pressures, and to implode targets containing deuterium and tritium to study thermonuclear physics. This research has an immediate payoff for our nation's defense program. Yet we realize that the most compelling application of inertial fusion for the long term is commercial power production: the production of electricity, transportable chemical fuels, and fissile fuel.

It is not unusual for an important new technology to be first developed for the military: commercial jet airliners evolved from military aircraft, fission reactors from submarine power plants, and computers from trajectory-calculating machines. Inertial-fusion technology is likewise fortunate to have a military champion at this early stage of its development. But major new technologies take a long time to mature, even with military support. For example, it took 16 years for jet aircraft to make the transition from the first military jet to the first commercial jetliner in 1958 (Ref. 1). Only five more years were needed to penetrate 25% of the commercial market, because the capital investment required was modest.

Nuclear power took longer to achieve a substantial penetration, because the electric utility system is so large, complex, and capital-intensive. Indeed, it took 18 years to go from the Fermi pile in 1942 to the first commercial plants (Dresden-1 and Yankee Rowe) in 1960, and another 15 years to achieve a 10% market penetration in the US.[1] It takes even longer to penetrate world markets and affect the global energy-supply picture. Remarkably, it took coal, oil, and natural gas each approximately 100 years to rise from 1% market shares to capture a significant portion (>30%) of the market.[2] The supply of fossil fuels will be essentially exhausted within this century-long time scale.[2] If we are to realize the long-term benefits of inertial fusion through commercial energy production, we must begin design and technology development now, even though funding dedicated to civilian power is still unavailable.

Toward this end, we have undertaken conceptual design studies of future ICF power plants, working with experts from industry and universities. This design process is our most valuable tool for assessing the potential benefits of fusion energy and discovering the development problems associated with fusion-energy technology. Most importantly, we seek key innovations which can dramatically increase the attractiveness of the commercial application of fusion, either by reducing costs or significantly reducing development time.

The crucial link between the scientific demonstration of ICF and the realization of economically viable energy production is the invention of a reactor cavity in which the pulses of fusion energy, produced at the rate of 1 to 10 per second, can be converted to a useful form of energy. The reactor must collect the energy from intense pulses of x rays, atomic particles, and neutrons without significant damage to its structure. In a surrounding blanket, it must breed sufficient tritium fuel. Finally, the reactor cost, safety, and environmental impact must be acceptable in comparison to conventional energy sources.

For the past several years, we have concentrated on a simple reactor design for electricity production which shows great promise. The HYLIFE (high-yield lithium-injected fusion energy) reactor shown in Fig. 8-1 features an array of free jets of liquid lithium between the fusion microexplosion and the reactor structure. The x-ray and hot-particle energy is deposited in the first row of liquid jets, causing some evaporation of the liquid. The high-energy neutrons are deposited throughout the array of jets, breeding tritium and causing the jets to disassemble into droplets. The droplets then cool the hot lithium vapor, which condenses out in time for the next microexplosion.

By converting most of the neutron kinetic energy to thermal energy, and through tritium breeding, the liquid lithium reduces the number and energy of the neutrons prior to their interaction with the reactor structure. Thus, the radiation damage in the structural material will be reduced to the point where the reactor structure will maintain its integrity for the life of the power plant.

While continuing to research and refine HYLIFE, in the last year we have also broadened our studies to include other applications and concepts. The following are highlights of the systems studies and experiments that are described in detail in this section.

- In a fast-track development scenario, a demonstration power reactor can be operational in approximately the year 2020.
- Cryogenic pellets can be stored for several minutes or more in liquid helium, but the transit time in the reactor chamber is limited to about 18 ms for symmetrically illuminated pellets.
- Corrosion studies show that the intergranular penetration rate of 2-1/4 Cr-1 Mo steel by liquid lithium and lead-lithium alloys at 300 to 600°C is acceptably small, indicating that proper design of liquid-lithium fusion reactors will assure safe operation.
- The two most promising techniques for tritium recovery are molten-salt extraction and yttrium gettering; either technique can remove tritium to <1 ppm by weight.
- The difference in cost between two- and eight-sided illumination of radiation-driven pellets, using high f/number mirrors, is insignificant when compared on the basis of total capital cost.
- We have developed a computer code and quick-look analytical technique to calculate the activity of radionuclides produced in a fusion reactor.

In our continuing studies of the HYLIFE reactor concept, we found that:

- A new design point for a 1000-MW(e) power plant, with a yield of 1800 MJ(t) at 1.5 Hz and a reduction of the effective lithium thickness, results in a 60% decrease in the required lithium inventory without compromising plant lifetime.
- Performing a two-dimensional analysis of the interaction of the chamber plasma with the lithium jets results in a substantial reduction of the first-structural-wall (FSW) stress from that suggested by one-dimensional calculations.
- Based on water simulations, the HYLIFE jets can be reestablished after each microexplosion, and will not break up due to instabilities, even in the presence of structural vibrations.
- A helical-rotor electromagnetic pump is a promising candidate for circulating lithium in the HYLIFE reactor concept.
- The radioactivity, biological hazard potential, and thermal decay power in the HYLIFE reactor are less than 10, 1, and 5%, respectively, of the figures for the STARFIRE tokamak.

In studies of new reactor concepts and the applications of inertial fusion to hydrogen production, we found that:

- Our JADE reactor concept, featuring a thick, porous, wick-like metal-fiber FSW saturated with liquid metal, provides a high-repetition-rate alternative to HYLIFE and has a lower flow rate by a factor of 6.
- For hydrogen production, an ICF energy source can potentially outperform a proposed tandem-mirror energy source if both systems use the General Atomic sulfur-iodine production scheme.
- The selection of a given hydrogen production system is premature at this time; instead we should concentrate on the design of a high-temperature ICF reactor.
- The SEBREZ concept, utilizing a segregated tritium-breeding zone comprising only 30 to 40% of the blanket, may be a promising way to keep a major fraction of the blanket free of tritium.
- SCEPTRE, a second-generation high-temperature reactor concept, looks promising. It incorporates a helium-cooled blanket, a lead-cooled JADE first-wall structure, and small pellets of Li_2O coated with graphite and silicon carbide for breeding and isolation of tritium. Capable of output temperatures of 850 to 1000°C, this reactor can be used either for hydrogen production or the generation of electricity at 50% efficiency with a combined Brayton and Rankine cycle. In the SCEPTRE design, there is no mechanism for a liquid-metal fire, breach of containment from internal cause, or the subsequent release of tritium or activated structural isotopes.

At this embryonic stage in the development of fusion, it is difficult to see far into the future. Scientific progress is difficult. Our concepts for using fusion energy are rather primitive and are inevitably based on conventional power technology. Nevertheless, we must not forget that we are at the stage of the Wright brothers: perhaps able to conceive of a WWI biplane, but unable to foresee a Boeing 747. This is not because the fusion community is unimaginative; instead, it reflects a natural conservatism due to the great remaining uncertainties in the underlying physics and technology.

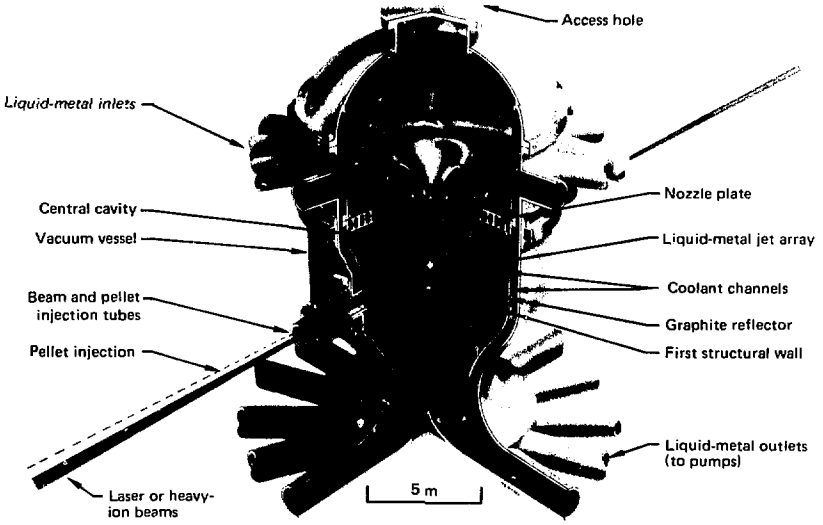

As difficult as it may be to foresee a technological path, it is even more difficult to see the impact on society. It is entirely possible that the long-term benefits of fusion energy will far surpass our modest expectations. Such truly momentous inventions in human civilization as the horse-drawn plow and the power loom were not so merely because they provided competitive alternatives, but because they fundamentally changed the way society works.[3] The plow and the power loom provided such a surplus of foods and textiles that revolutionary changes occurred in patterns of feeding and clothing people. The same may be possible with fusion energy, if we continue to have the courage to create.

Commercialization of Fusion Electrical Power

Commercial Laser-Fusion Development Strategy

Although inertial confinement fusion (ICF) is currently funded primarily for its military applications, most ICF research applies equally well to commercial power production. The military applications are likely to be realized by the year 2000, while cost-effective commercial electric power from ICF will require continuing experiments and additional facilities. In this article and the next, we summarize two studies that address the expeditious development of commercial ICF power. The first study, summarized here, has been prepared in cooperation with Bechtel Group, Inc.; it proposes a development plan that minimizes the facilities and development time to commercialization.

If inertial fusion is to be used for civilian energy production, a major milestone will be the construction and operation of a demonstration power reactor (DEMO) that performs well enough to convince utilities to order fusion reactors with individual capacities ≥ 1 GW(e). Our objective is to devise a development schedule to achieve this goal with a minimum expenditure of time and funds and with few large, separate facilities. We intend to rely heavily on small, inexpensive, nonintegrated experiments, and to borrow extensively from the more mature and heavily funded programs for magnetic fusion and breeder reactors.

The first major step toward the DEMO is the construction of a single-pulse high-gain test facility (HGTF) that demonstrates high target gain and limited qualification of power-reactor concepts along with driving military-applications experiments. The second facility, an experimental power reactor (EPR), couples a pulsed laser driver and an automated target factory to targets the same size as those used in the HGTF, but at a low power of 500 MW(t). The final facility, the DEMO, includes a balance of plant to demonstrate safe and reliable operation at the 450-MW(e) level—the same power level as the Clinch River liquid-metal fast-breeder reactor (LMFBR). Once in operation, the DEMO must convince utilities that a full-scale plant, with a capacity of 1 GW(e) or more, will produce cost-effective electric power.

Design and Construction Schedule. The exigencies of design and construction limit how much any development schedule can be compressed. We expect it will take three or four years of design and four or five years of construction for each large first-of-a-kind facility. A commitment to build a given facility will probably not be made until its predecessor has operated for one to two years. These constraints give us the time line shown in Fig. 8-2. We have assumed the use of a laser driver in this schedule, but the plan could be easily modified to use a heavy-ion-beam driver in the later stages.

As presently envisioned, our commercial laser-fusion development strategy would unfold as follows. The preconceptual design phase (see Fig. 8-2) for the HGTF would end as early as late 1986. The conceptual design would be pursued for two more years, after which the Congress would commit to funding the design and construction of the facility. After two more years of design effort, requests for bids would go out to vendors, jobs would be let, and equipment would be manufactured so that construction could begin in 1992. A four-year construction effort would allow the HGTF to operate by 1996.

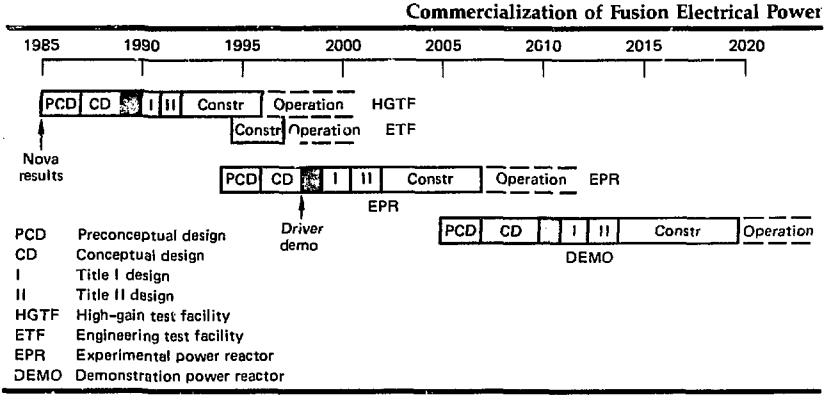

Fig. 8-2. Time line for commercial laser-fusion development strategy.

Preconceptual design of the EPR would commence while the HGTF was under construction. Because detailed design work for the EPR would not be funded until the HGTF had produced results for about two years, it would not be necessary to begin the EPR preconceptual design effort before 1994. Construction would commence in 2002 and take approximately five years.

The scenario for the DEMO would be similar, although of longer duration; detailed design on the DEMO would begin after the EPR had been operating for three years. Construction would start in 2014 and, due to the size of the project, last for six years. Operation of the complete DEMO facility could then begin in 2020.

Although this schedule is not fixed, it cannot be arbitrarily shortened, especially in terms of the relative development times of the successive facilities. Without scientific breakthroughs or a crash program, in fact, no more than three to five years can reasonably be cut from our proposed schedule, because of

- The requirement for three separate facilities.
- The need to operate each facility for a short period before committing to the next one.
- Normal design and construction time.

Adding a fourth or even a fifth facility to minimize program risk would extend the schedule by 10 or more years.

Engineering Objectives for the Three Facilities. We define "engineering breakeven" as the gain required to produce enough fusion power to drive a reactor-quality laser, given a laser efficiency η_ℓ and thermal-to-electrical conversion efficiency η_t. If the EPR laser has an efficiency of 3 to 5% and $\eta_t = 35\%$, engineering breakeven requires gains between 57 and 95. However, the production of net electrical power requires even larger demonstrated gains. For engineering feasibility the gain must exceed $1/\eta_\ell\eta_t f$, where f is the minimum acceptable recirculating power fraction. If f is in the range of 50 to 70%, the gain for engineering feasibility ranges between 75 and 200. The HGTF will demonstrate gains on this order for the EPR.

Another criterion that must be met in the HGTF is the repeatability of the target yield. Targets must be manufactured and lasers must be controlled to tolerances that allow yields to vary no more than ~10% by the time the EPR design and construction plan is funded (~1998). This and the other engineering objectives are displayed in Table 3-1. The purpose of the table is to show relationships among facilities, not precise specifications, since the parameters will change with time and additional information.

The HGTF will not generate electrical power, since it is a single-shot device. The HGTF laser may be operated so that the laser pulse arrives at the target as several small pulses rather than as one large pulse. This additional capability of the HGTF, called an engineering test facility (ETF), is included in Fig. 8-2 and discussed in detail in the following article. In that article, we show that this additional capability can serve to prequalify the EPR reactor design concept.

The purpose of the EPR is to demonstrate the integrated engineering of a power-producing fusion reactor on a scale that makes the next step a precommercial-sized, 450-MW(e), demonstration power

Parameter	HGTF	EPR	DEMO
Laser type	Single pulse	Pulsed	Pulsed
Energy (MJ)	3	3	3
Efficiency (%)	1	4	6
Repetition rate (Hz)	10^{-4}	1.5	3
Target gain	100	100	180
Yield (MJ)	300	300	540
Repeatability	0.9	0.90	0.95
Blanket multiplication	—	1.1	1.15
Thermal efficiency (%)	—	0.35	0.35
Power			
Thermal [MW(t)]	—	500	1860
Gross electrical [MW(e)]	—	175[a]	650
Net electrical [MW(e)]	—	45[a]	455
Recirculating power fraction			
Total	—	0.74[a]	0.30
Laser	—	0.64	0.23
Auxiliaries	—	0.10	0.07
Availability	—	0.3	0.6
Shot life	10^4	10^8	10^9
Capital allotment (billions of 1981 dollars)	0.5	2	3.5
Initial operation date	1996	2007	2020

[a]The EPR will generate electricity only if the capital cost of the steam generator and turbine is balanced by the savings in purchased electricity during the limited time the facility is operated.

Table 8-1. ICF engineering objectives.

reactor (DEMO). There is no EPR task associated with the target, since the required gain of 100 will have been demonstrated in the HGTF. The key subsystems for the EPR will be the pulsed driver, the target production factory, and the blanket heat removal system. A relatively low availability of 30% is acceptable for most runs. We would like to raise that percentage considerably by the year 2010 to be certain that an acceptable availability can be reached in the DEMO. A shot life of 10^8 for a device firing at 1.5 Hz and with an availability of 0.3 translates into an operating lifetime of about 10 years. We assume that three years would yield enough data for a decision to be made on the DEMO.

The EPR would be designed with changeout flexibility to accommodate new reactor concepts that may supplant present thinking. If this reactor-concept changeout option were in fact utilized, the commercialization schedule would slip the few years necessary to install and adequately test the new system. The EPR could continue to run after the DEMO decision point to test materials and refine reactor designs.

The final step in the commercialization of laser fusion is the safe and reliable operation of a medium-size power plant (DEMO) of approximately 450 MW(e) (net). Because the DEMO will be the first of its kind, and will use a full-size pulsed laser, it will be expensive on a cost-per-unit-power basis. It should, however, assure utilities and reactor vendors that a full-scale plant will be cost-effective. The DEMO might be able to use the same driver as the EPR, depending on that driver's efficiency and reliability. The DEMO facility itself will be designed for a 20-year life.

If the ICF program is funded at current levels (~$200 million per year) in constant 1981 dollars during the period of the development plan outlined here, the majority of the ICF budget would be allocated to the three primary facilities: HGTF, EPR, and DEMO. Program successes that allow positive decisions to be made on the construction of each facility may generate significantly more funds, in which case the major facilities would require a smaller portion of the overall ICF budget. Current spending for the liquid-metal fast-breeder reactor program is ~$700 million per year—about three times the level of ICF funding. An ICF budget the size of the LMFBR budget would reduce considerably the impact of the proposed facilities on ICF resources.

Supporting Technology. Most technology issues in the commercialization of fusion power can be resolved in the three sequential facilities described here. Each of these facilities requires demonstration of a number of subsystems during the facility's formal design phase (see Fig. 8-2). Therefore our commercialization strategy implies substantial demonstration of supporting technologies in two narrow time windows which occur around 1998 and 2010.

Conclusions. The schedule presented here minimizes costs in the 1980s and defers the demonstration of a high-pulse-rate laser and automated target factory until as late as 1998. The schedule allows pretesting of reactor concepts in the HGTF and ETF at only a 10% increase in the HGTF cost. Our strategy also minimizes the thermal power of each facility to reduce capital and fuel costs and to increase reliability. If followed as outlined here, the plan could result in operation of a demonstration power plant as early as 2020.

Any particular date in the schedule should not be viewed as invariant. Rather, the whole schedule can be translated into the future, maintaining the development

time of each facility and its relationships to the others. Or, the overall schedule can be stretched, with the HGTF commitment occurring as now planned around 1989, but the operation of each facility delayed by limited funding. Without a science breakthrough that changes the plan of attack significantly, however, it is hard to envision a contraction of more than three to five years, based on industry's experience in the design and construction of large facilities.

Fundamental logic intrinsic to the ICF program implies that ICF targets must display significant gain before there will be support for the construction of a fully integrated facility with a pulsed laser driver and an automated target factory. The need to demonstrate high gain is so fundamental to the ICF program that it is imperative that work on the HGTF begin as soon as possible.

Authors: J. A. Blink (LLNL); W. O. Allen, J. E. Simpson, and J. Caird (Bechtel Group, Inc.)

Major Contributor: M. J. Monsler

Engineering Test Facility for the HGTF

The goals for the ICF physics program, for both energy and military applications, are to achieve fuel ignition in the Nova facility and to demonstrate high-gain targets in a high-gain test facility (HGTF). The HGTF can achieve its goal using a single-pulse, 3- to 5-MJ solid-state or gas laser. Yet, with the addition of an engineering test facility (ETF), the laser can also be used in a pulsed mode to economically obtain reactor design information for the experimental power reactor described in the previous article. In this article, we summarize the ETF study prepared in cooperation with the Energy Technology Engineering Center (ETEC).[4]

Suppose the HGTF produces target yields in the range of 300 to 400 MJ. A multiarm HGTF laser can be fired with appropriate delays between the arms, such that each of two or three subpulses (of 1 to 2 MJ each) drives a separate 55-MJ fusion target. Each target would produce full-scale neutron-energy density profiles in a HYLIFE chamber of scaled-down dimensions.[5] Other ICF concepts have even lower yield requirements for full-scale energy-density testing. Therefore, for two or three pulses, the HGTF can produce full-scale energy densities in a reactor concept at any desired repetition rate.

Several ICF concepts utilize flowing liquid lithium. Development of a pump to meet the requirements of a full-scale power plant will require an extensive program lasting 10 years or more. Fortunately, the limited capacity and facility life of the ETF will permit use of unmodified sodium pumps.[6] We have identified two such liquid-sodium pumps. The Clinch River Breeder Reactor prototype pump, manufactured by Byron Jackson, was tested in water in 1980 and will also be tested in sodium. The pump internals will not be used at Clinch River and thus would be available for use after tests are completed in 1982. This prototype pump has a flow rate of 1.8 m^3/s at a head of 27.4 m of Li. The Hallam sodium-graphite reactor facility pump is in storage at ETEC. The pump has a flow rate of 0.85 m^3/s at a head of 27.4 m of Li.

To determine the effectiveness of an ETF and the cost of adding it to the HGTF, we must

- Specify potential experiments.
- Scale the reactor concept to ETF size.
- Design the liquid-metal and heat-removal systems.

ETEC has completed these tasks for the HYLIFE reactor concept,[4] and we discuss their results below. Although other reactor concepts remain to be evaluated, we expect similar results.

There are many potential experiments we can conduct with the ETF, including

- The response of liquids to fusion pulses.
- Fluid flow.
- Vibrational stability.
- Vacuum-system effectiveness.
- Tritium extraction.
- Impurity removal.
- Beam propagation.
- Target injection.

However, some of these experiments are not a requirement for each run. For example, vacuum, tritium impurity, and vibrational equilibrium will not be reached in a three-pulse experiment and will not interfere with the experiments. Conversely, the

Table 8-2. Lithium circulation system descriptions and costs.

Generic Inertial-Fusion Studies

Parameter	Case 1	Case 2	Case 3	Case 4
HYLIFE array effective thickness (cm)	16	16	8	8
Flow description	Steady	Pulsed	Steady	Pulsed
Heat dump [MW(t)]	25	none	25	None
Lithium temperature (°C)	400	400	400	400
Temperature rise from 105 MJ(f) (°C)	1.9	1.8	3.2	4.6
Pump power input [MW(e)]	0.34	—	0.15	—
Argon drive pressure	—	207	—	207
Chamber pressure drop (gravity only) (kPa)	14.8	14.8	14.8	14.8
Friction pressure drop (kPa)	55.4	114	67.7	118
Flow rate (m^3/s)	1.58	1.58	0.63	0.63
Li circulation system volume (excluding tanks, chamber, and heat exchanger) (m^3)	20.6	15	12	6.1
Li facility volume (m^3)	29	30	17	12
Fraction of total Li in the experiment array (%)	1.3	1.2	0.9	1.2
Cost (millions of dollars)	14	6	8	4

reaction chamber can be deliberately vibrated or injected with hot gas, and the liquid metal can be deliberately contaminated with tritium and impurities, to test equilibrium situations.

For energy-deposition calculations, the HYLIFE lithium jet array was scaled down, maintaining the ratio of jet length to diameter, the ratio of array radius to jet radius, and other geometric parameters. The scaled-down array has an effective thickness of 16 cm, compared to 74 cm in the full-scale HYLIFE. Four ETF geometries were studied for the scaled-down HYLIFE concept (see Table 8-2). The 16-cm array was designed both for steady flow and for pulsed flow maintained for ~5 s. A thinner (8 cm) array was also designed for both steady and pulsed flow. Pulsed flow can be produced by opening a valve between a high-pressure argon tank and the low-pressure lithium storage tank. The two steady-flow geometries can be supported by the Na pumps described above.

HYLIFE's liquid-metal loops have been sized for the four ETF cases; all liquid-metal tanks, pumps, and pipes have been laid out, and their costs have been estimated. The steady-flow designs include a 25-MW(t) lithium-to-air heat exchanger to reject the fusion heat if the driver is later upgraded to steady operation at the reactor pulse rate. The cost estimates in Table 8-2 include the liquid-metal components, mechanical support structures, and the building foundation and structure; the final optics and outer building walls are not included, however. All estimates are in 1981 dollars and include a contingency allowance of 30% plus an escalation of 1% per month during a 30-month construction period beginning in October 1981.

The low cost of adding an ETF to the HGTF provides an opportunity for us to study commercial laser-fusion power applications at a small fraction of the cost of the HGTF or of comparable magnetic-fusion facilities, such as the fusion engineering device (FED). The gains demonstrated in the HGTF, coupled with the reactor experiments performed in the ETF, can provide much of the data required to build a 500-MW(t) experimental power reactor.

Authors: J. A. Blink (LLNL); N. J. Hoffman, N. M. Jeanmougin, and K. A. Curlander (Energy Technology Engineering Center)

Generic Inertial-Fusion Studies

Introduction

We have performed or sponsored work on several aspects of inertial fusion that are generic to virtually all ICF reactor concepts:

- We have investigated the heat-transfer limits on cryogenic pellets for laser-driven fusion reactors.
- We have sponsored a study concerning the corrosion of ferritic steels by liquid lithium and lead lithium and a study of safety considerations in using lithium in fusion reactors. These studies were conducted at the Colorado School of Mines

and the Energy Technology Engineering Center (ETEC), respectively.

- We have sponsored work at Bechtel National to study the feasibility of using heat pipes to cool a stagnant lithium blanket and to eliminate the secondary sodium heat-transfer loop by transferring the circulating blanket energy directly to the steam cycle.
- We sponsored ETEC's evaluation of the various proposed methods for removing tritium from lithium and engaged Bechtel to study the design considerations for an ICF power plant, with plant layouts and cost estimates.
- We also developed computer codes and estimation techniques for activation analysis of materials in an ICF reactor.

These generic studies are summarized in the next nine articles; they should be of value to anyone designing or analyzing ICF power plants.

Author: J. Hovingh

Heat-Transfer Limits on Pellets

During 1981, we conducted a spherically symmetric, transient heat-transfer analysis on a cryogenic multiple-shelled laser-driven pellet to determine heat-transfer limitations during pellet manufacture, storage, acceleration, and injection.[7] Our analysis included heat generation, conduction, convection, boiling, condensation, and thermal radiation as appropriate. It is necessary to include the effects of variable material properties, because they vary drastically near absolute zero.

Limitations on pellets during injection are particularly important, because not all of the interpulse time between fusion reactions is available for the injection process. Material inside the chamber following a fusion reaction must be cleared from the injection path before the next pellet is injected. If the material is mostly lithium, as in several ICF reactor concepts, the next pellet injection cannot occur until the lithium vapor condenses and any droplets resulting from splashing lithium fall out of the injection path. Alternatively, a prepellet may be injected to clear a pathway through the material, with the reaction pellet injected immediately afterward through the cleared space. In either case, some portion of the interpulse time is unavailable for pellet injection. The time actually available for injection varies with the design of the reaction chamber; some designs allow as much as 75% of the interpulse time.

Another constraint results from the fact that most high-gain reactor-pellet designs are cryogenic and contain frozen deuterium–tritium (D–T) fuel, which has a triple point of 19.8 K. The D–T must be maintained below the triple point for the pellet to function correctly; otherwise gaseous D–T will form and, as it expands, the desired symmetry and other properties of the pellet will be destroyed. In addition, the exposed surfaces of D–T pellets must be kept below about 14 K to reduce surface migration in which D–T from one region of the surface sublimates and deposits on another region, again destroying the symmetry of the pellet. The rate at which surface migration occurs decreases with decreasing temperature[8]; hence, the lower the D–T surface temperature, the better. These maximum permissible D–T temperatures result in further restrictions on pellet-injection velocity. If the injection velocity is too low, the pellets are exposed too long to the hot (770 K) walls of the reaction chamber, and the maximum permissible D–T temperatures will be exceeded. On the other hand, high injection velocity may also be a problem. During acceleration, the concentricity of the inner shells must be maintained by mechanical supports from the outer shells, by magnetic levitation, or by other means.

Just prior to use, the pellet will be placed in a sabot for mechanical and thermal protection during acceleration to the desired injection velocity. The sabot itself will initially be at liquid-helium temperature and will have enough thermal capacity to prevent excessive heating of the pellet during the acceleration process. The sabot may be removed prior to injection into the reaction chamber; conceptually, however, the sabot can be manufactured of solid lithium and injected along with the pellet into the HYLIFE reaction chamber, where it melts and forms part of the main lithium flow. If the sabot is injected into the chamber, it will effectively clear a pathway through material remaining in the reaction chamber.

All material external to the innermost layer of frozen D–T must have reasonably good heat-transfer characteristics. Heat generated in the frozen D–T fuel needs to be dissipated with a total temperature differential across the pellet of only a few degrees. Otherwise, the frozen D–T will exceed its maximum temperature limits. This limit on total temperature differential provides restrictions on the design and manufacture of pellets; any enclosed spaces must be filled with a suitable gas and perhaps contain superconducting mechanical supports. Contact resistance between layers must be carefully monitored during manufacture.

Heat transfer at the outer surface of the pellet depends on the external environment. In all cases, our analysis includes the effects of thermal radiation, which is important when the environment is at high temperature. All surfaces are considered to have an emissivity of unity, and all gas is taken to be nonabsorbing.

Analysis. We considered two cases for gas surrounding the pellet. In the first case, we analyzed a pellet traveling at insignificant velocity through helium gas at 4.2 K. This corresponds to the phase of pellet life when it is surrounded by a cryogenic sabot during the acceleration phase. Conduction dominates the heat transfer at the outer surface. There is no condensation, and radiation heat-transfer is negligible.

In the second case, we analyzed a pellet traveling at 300 m/s through saturated lithium vapor surrounded by a vessel, both at a temperature of 770 K. This second case corresponds to the injection period when the pellet is exposed to the hot walls of the reaction chamber. No gases other than the lithium vapor were considered to be present in the surroundings. Here, thermal radiation dominates, and, although the maximum spatial values of both convection and condensation heat transfer are included over the entire outer surface of the pellet, their effect on heat flux across the pellet outer surface is less than 20%. Although we might have considered a different pellet velocity, such a change would have a small effect because of the dominance of thermal radiation.

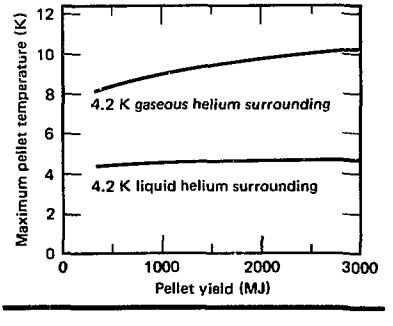

Fig. 8-3. Effect of pellet yield on the maximum pellet temperature when the surroundings are liquid or gaseous helium at 4.2 K.

Figure 8-3 shows the maximum steady-state temperatures of pellets of various yield when they are immersed in liquid helium and in gaseous helium at 4.2 K. The time needed to reach this steady state is short. If all material in a pellet starts at 4.2 K, a steady state will be reached after ~1 s in a liquid-helium environment and after ~50 s in a gaseous-helium environment.

The maximum calculated pellet temperature increases with pellet yield, because both the pellet radius and mass of fuel also increase with yield. The change in maximum pellet temperature is smaller than would normally be expected, however, because the thermal conductivity of all pellet materials increases with temperature. If the pellet is immersed in liquid helium at 4.2 K, the maximum pellet temperature remains practically constant at 4.5 K for all pellet yields. This temperature is well below both the D–T surface-migration limit of 14 K and the D–T triple point of 19.8 K.

If a cryogenic sabot filled with helium gas at 4.2 K surrounds the pellet, the major thermal resistance is between the pellet and the helium gas. Hence, the pellet is nearly isothermal at the temperature shown in Fig. 8-3. While it may take only a few seconds to place the pellet in a cryogenic sabot and to complete the acceleration process, the steady-state temperature represents an upper bound. The sabot must have enough thermal capacity so that during the acceleration phase the pellet sees only a wall at 4.2 K or slightly higher temperature. Since the maximum steady-state temperature is less than the allowable D–T limits for all yields, gaseous helium can be used as a storage medium if desired.

During injection, the pellet is exposed to a chamber at 770 K filled with saturated lithium vapor at 770 K. For this analysis, no other gases are considered to be present. The initial temperature of the pellet is taken to be the same as the temperature in Fig. 8-

with helium gas surroundings. This corresponds to the maximum pellet temperature reached after the acceleration phase is complete and the sabot is separated from the pellet. The pellet rapidly increases in temperature during injection, with the outer portion of the frozen D–T fuel reaching its triple point in only 18 ms. At this time, the fuel starts to vaporize, destroying the pellet.

The allowable injection time of 18 ms is essentially independent of pellet yield. Two opposing phenomena are present: the size of the pellet increases with yield, and, for identical initial conditions, the D–T fuel in a larger-yield pellet will take longer to reach its maximum allowable temperature. As Fig. 8-3 shows, however, the initial temperature increases with pellet yield as well, which reduces the allowable injection time. The two effects nearly cancel each other, resulting in the constant injection time of 18 ms.

If we use this result with a 5-m-radius chamber, the pellet must be injected with a minimum velocity of about 300 m/s. Heat transfer during the injection period is dominated by thermal radiation. Changes in condensation or convection heat transfer have only small effects.

Conclusions. Four conclusions emerge from the foregoing analysis. First, a transient heat-transfer analysis conducted on a cryogenic multiple-shelled, spherically symmetric, laser-illuminated pellet shows that injection times of 18 ms or less are required. Otherwise, frozen D–T fuel in the pellet vaporizes and destroys its cryogenic nature. If the reaction chamber is 5 m in radius, the minimum injection velocity is about 300 m/s. The length of the accelerator necessary to obtain this velocity depends on the maximum allowable pellet acceleration. For example, if a uniform maximum acceleration of 1000 m/s^2 is permitted, the accelerator must be 45 m long.

Second, there are no heat-transfer limitations during storage if the pellet is submersed in liquid helium at 4.2 K. The temperature difference across the pellet under this condition is about 0.25 K. Any mechanism used to support the inner layers must be able to withstand the maximum pellet acceleration and to dissipate the heat generated in the frozen D–T fuel.

Third, the cryogenic sabot surrounding the pellet during the acceleration process must have enough thermal capacity to keep its surface adjacent to the pellet at 4.2 K or slightly above until the pellet is injected into the chamber. Otherwise, required pellet injection velocities increase significantly.

Finally, during the critical injection period, the dominant mechanism at the pellet's outer surface is thermal radiation. Conduction from the outer surface is the dominant heat-transfer mechanism during acceleration.

Author: J. H. Pitts

Major Contributors: M. J. Monsler, J. D. Lindl, and D. H. Darling

Corrosion of 2-1/4 Cr-1 Mo Ferritic Steel in Liquid-Lithium and Lead-Lithium Solutions

Engineering alloys for containing lithium in fusion power plants must meet criteria of availability, fabricability, and code acceptance, in addition to being resistant to corrosion from liquid lithium. A potential candidate alloy is either regular-grade (unstabilized) or niobium-stabilized 2-1/4 Cr-1 Mo steel. Niobium-stabilized 2-1/4 Cr-1 Mo steel provides good corrosion resistance to a lead–lithium liquid at 500°C. Moderately good lithium corrosion resistance can be achieved with regular-grade 2-1/4 Cr-1 Mo steel by using a careful heat treatment that stabilizes the carbides. In terms of availability, fabricability, and code acceptance, regular-grade 2-1/4 Cr-1 Mo is more desirable than the niobium-stabilized grade, and preliminary data on lithium corrosion are sufficiently encouraging to warrant further investigation of this commonly utilized pressure-vessel steel.[9,10]

Workers at the Colorado School of Mines (CSM) experimentally investigated the effects of corrosion on unstabilized 2-1/4 Cr-1 Mo steel disks spinning in liquid lead–lithium baths. They also studied the effect of the lead content in static liquid lead–lithium on the corrosion of unstabilized 2-1/4 Cr-1 Mo steel.[11] The unstabilized steel used in these experiments was austenitized at 927°C, cooled at 50°C/h to 700°C, held there for 2 h, cooled at 50°C/h to 500°C, then furnace-cooled to ambient temperature. Two heat treatments were investigated. To simulate a welded

microstructure, the heat treatment consisted of austenitizing the steel at 1300°C, followed by an oil quench. To simulate a weld after stress relief, some of the above specimens were given a postweld heat treatment for 10 h at 760°C.

Effect of Velocity. The effect of velocity on the susceptibility to lithium corrosion of 2-1/4 Cr-1 Mo steel at 500°C for 400 h is shown in Fig. 8-4. For angular velocities from 0 to 268 rpm (0 to 0.33 m/s), 2-1/4 Cr-1 Mo steel was quite insensitive to the velocity, and the postweld heat treatment was very effective in preventing penetration by a 17.6 wt% lead–lithium liquid. Previous work on dynamic corrosion,[12] similar to that reported here, suggests that lead–lithium penetration should be independent of velocity when the observed attack is of intergranular nature.

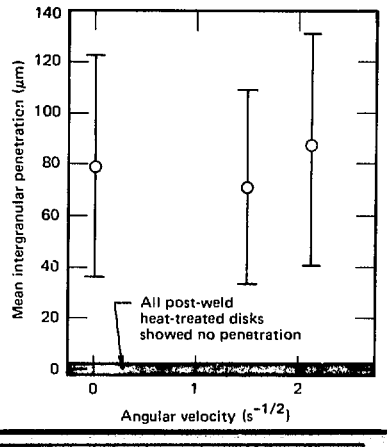

Fig. 8-4. The effect of postweld heat treatment and angular velocity on the intergranular corrosion of a 24-mm-diam 2-1/4 Cr-1 Mo steel disk spun in 17.6 wt% lead-lithium liquid at 500°C for 400 h.

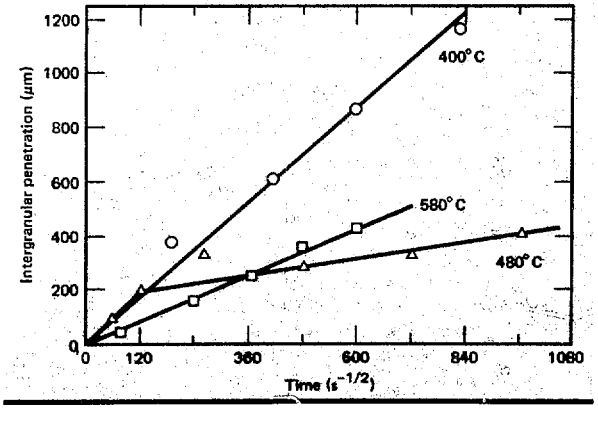

Fig. 8-5. The intergranular penetration of 2-1/4 Cr-1 Mo steel by a 17.6 wt% lead-lithium static liquid.

Effect of Lead. In the static corrosion experiment, CSM workers obtained penetration data at temperatures between 300 and 600°C. The lead–lithium liquids investigated contained lead concentrations of 0, 17.6, 53, and 99.3 wt%. Results showed that the postweld heat treatment was extremely effective in preventing penetration by the various liquid alloys. Also, the 99.3 wt% lead–lithium liquid did not penetrate either the corrosion-susceptible steel or the postweld heat-treated 2-1/4 Cr-1 Mo steel specimens for exposure times up to 1000 h.

Analysis. Previous data have shown that the lithium penetration of 2-1/4 Cr-1 Mo steel is adequately described as parabolic in time.[9,10] Consequently, we analyze the data of the present study by first plotting the penetration against the square root of the exposed time. Figure 8-5 shows a typical result for corrosion temperatures of 400, 480, and 580°C. Note that penetration data at the high (580°C) and low (400°C) temperatures are linearly related to the square root of exposure time. Previous research indicates that the penetration is classically parabolic at low temperatures, because the transformation of the most unstable carbide, epsilon carbide, is sufficiently slow to be available for lithium attack during the entire exposure.[9] A similar result occurs at high temperature, because epsilon carbide is almost immediately converted to cementite, which is more stable and consequently less susceptible to lithium corrosion. At intermediate temperatures (~440 to ~530°C), we observe the dual-slope behavior depicted in Fig. 8-5, which indicates a series mechanism.

We can obtain important information about corrosion mechanism(s) from penetration data by analyzing the temperature dependence. For parabolic time dependence, which occurs when the corrosion rate is controlled by steady-state diffusion, the apparent activation energy for the corrosion process can be calculated from the slope of the penetration vs plots of $\sqrt{t}$ obtained from the various temperatures. When series mechanisms occur, however, this analysis is only correct for the initial mechanism. This is because the time at which the subsequent mechanism initiates does not occur at zero, and the penetration is not zero at the time of initiation. An accurate rate constant for the secondary mechanism will be the slop(

obtained from a plot of penetration squared vs time (P^2 vs t).

Anderson's penetration data for the corrosion of 2-1/4 Cr-1 Mo steel[9,10] were reexamined for both the initial and secondary mechanisms. The analysis using P^2 vs t yields a significantly lower activation energy for the secondary mechanism than does the earlier analysis using P vs $\sqrt{t}$. The activation energy obtained for the initial mechanism was not significantly changed by reanalysis.

Reduction of the apparent activation energy for the secondary mechanism by more correct data analysis allows the same mechanistic interpretation for both the initial and the secondary penetrations. Thus, the current interpretation of the intergranular penetration of 2-1/4 Cr-1 Mo steel by liquid lithium is that both the initial and secondary rates of penetration are controlled by the diffusion of carbon through liquid lithium. The change in penetration rate at intermediate times and temperatures (~440 to ~530°C) represents only a decrease in the chemical potential gradient (i.e., when epsilon carbide is converted to more stable cementite).

Activation energies for the initial and secondary liquid-lithium penetration of 2-1/4 Cr-1 Mo steel were found to be 32 and 30 kJ/mole, respectively. Corresponding values for a 53 wt% lead–lithium liquid were found to be 24 and 69 kJ/mole. The activation energies for the penetration by liquid lithium and 53 wt% lead–lithium were not significantly different from those calculated for penetration by a 17.6 wt% lead–lithium liquid. Therefore, we conclude that the presence of up to 53 wt% (~3.6 at.%) of lead in the liquid does not markedly affect the mechanism by which the liquid lithium attacks the steel.

The rates at which the various lead–lithium liquids corrode 2-1/4 Cr-1 Mo steel can compared using Fig. 8-6. Note that the initial and secondary rates of attack decrease as more lead is added to the liquid lithium. These data suggest that lead must inhibit the diffusion of the carbon through the lithium in the corroded grain boundaries.

The Anomalous Behavior at 500°C. If we make an Arrhenius plot of the rate constants calculated from exposure of 2-1/4 Cr-1 Mo steel to lead–lithium liquids at 500°C, we observe that the measured corrosion rates fall well below the values estimated for that temperature using values measured at the other temperatures. This observed anomaly is not an isolated case; Anderson also observed the anomaly but believed it to be caused by slight microstructural differences in the steel samples.[9] Great care was taken in the CSM experiments to assure uniformity of specimen microstructure. Nevertheless, the anomalously low corrosion rates at 500°C were observed again; this observation is shown in Fig. 8-7, which is constructed from Fig. 8-6.

We have now constructed a model that consistently explains the apparent anomaly at 500°C. If a protective corrosion product holds the penetration of 2-1/4 Cr-1 Mo steel by lead–lithium liquids to a minimum at 500°C, then the accumulation rate of that product can be assumed to be dependent on temperature. The corrosion-product accumulation rate decreases at temperatures

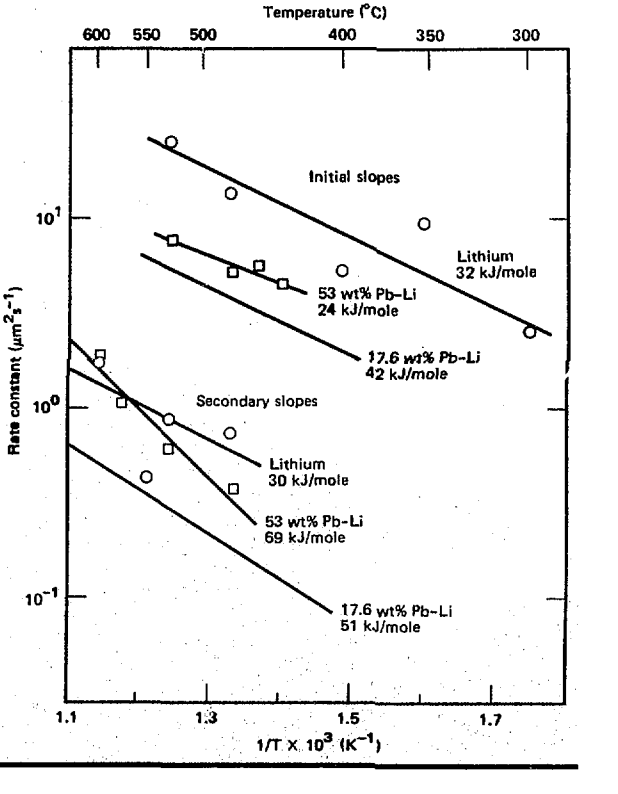

Fig. 8-6. The temperature dependence of the intergranular corrosion of 2-1/4 Cr-1 Mo steel by lead-lithium liquids.

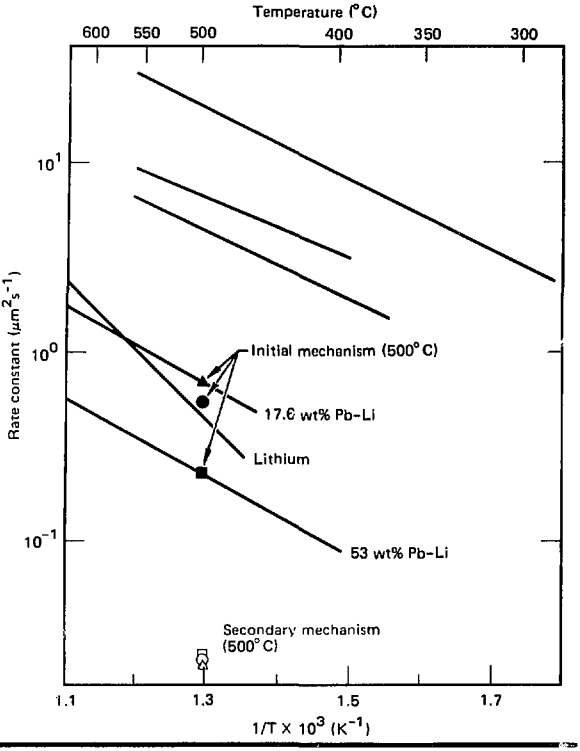

Fig. 8-7. The anomalously low corrosion of 2-1/4 Cr-1 Mo steel by lead-lithium liquids at 500°C.

greater than 500°C, because the solubility of that product in the liquid metal increases rapidly with increasing temperature, dissolving away the product as it forms. On the other hand, the corrosion-product accumulation rate decreases at temperatures lower than 500°C, because the formation rate is a typical thermally activated chemical reaction, and the reaction rate rapidly decreases with decreasing temperature.

Summary. The intergranular penetration of corrosion-susceptible 2-1/4 Cr-1 Mo steel by 17.6 wt% lead–lithium liquid is not increased by increasing the velocity of the liquid (up to 0.33 m/s). A previous Arrhenius analysis of lithium-corrosion data yielded an erroneously high activation energy for long exposure times. A corrected analysis yields an activation energy similar to that obtained for short exposure times. The penetration of 2-1/4 Cr-1 Mo steel by lead–lithium liquids can be explained as a process controlled by the diffusion of carbon in liquid lithium over all exposure times. The intergranular penetration of 2-1/4 Cr-1 Mo steel by liquid lithium is reduced by additions of lead at temperatures from 300 to 600°C. Anomalously low corrosion of the steel by lead–lithium liquids occurs at 500°C. This behavior may be related to the formation of a corrosion product.

Authors: B. Wilkinson and G. R. Edwards (Colorado School of Mines)

Major Contributors: J. Hovingh (LLNL) and N. J. Hoffman (Energy Technology Engineering Center)

Feasibility of Using Heat Pipes in ICF Reaction Chambers

Heat pipes offer the possibility of passive cooling in ICF reactors. We examined two possible applications of heat pipes: to eliminate the secondary sodium loop, and to cool the blanket.[13] Heat pipes are composed of an evaporator section, an adiabatic section, and a condenser portion. Heat flows through the walls of the evaporator and vaporizes a working fluid that coats the inner wall. The vapor then expands through the adiabatic section, where no heat is lost, to the lower-pressure condenser, where it condenses on the walls and gives up its heat. The heat travels radially through the wall of the condenser section and is carried away by another fluid. The working fluid in the pipes is then transported back to the evaporator by gravity or by capillary action in a wick structure lining the pipe. Grooves are sometimes made in the wall of the pipes behind the wick to provide a quick return for the fluid and to ensure that the wick is wet everywhere.

One requirement of ICF heat pipes is that the working fluid be able to withstand elevated temperatures in the range from 350 to 500°C. Blanket pipes also have to survive neutron fluxes of 10^{14} to 10^{15} n/cm^2·s for years. Furthermore, the fluid must have a high latent heat of vaporization, since the amount of energy it must transport is large.

The temperature criterion rules out using all organic and most inorganic compounds as a working fluid, so we decided to consider only the chemical elements as possible working fluids. After taking into account the natural abundance, radioactive stability, melting points, critical temperatures, and

extreme toxicity of each element, we reduced the number of candidates to the 12 elements listed in Table 8-3. Radionuclide production was not considered. Lithium was eliminated because its latent heat of vaporization is low. Mercury has the highest flux limit (much higher than sodium or potassium) and appears to be the best choice as a working fluid despite its wetting problems and possible biological hazards.[13]

Elimination of the Secondary Sodium Loop. The first potential application of heat pipes for passive cooling is in replacing the secondary sodium loop in ICF reactors. According to the schematic diagram in Fig. 8-8, liquid lithium from the blanket passes over the evaporators of the heat pipes. The blanket energy is transferred by the working fluid in the heat pipes to the condenser region, which is cooled by the evaporation of water to steam. Calculations indicate, however, that this application is not feasible at present.

Consider, for example, a square array of heat pipes. Let d be the length of each side, f the total packing fraction of heat pipes, P_t the thermal power needing transport, and r_0 the outer radius of each pipe with internal vapor column of radius r. Then the energy flux Φ that the pipes must manage is

$$\Phi = \frac{P_t}{(r/r_0)^2 f d^2} \quad . \tag{1}$$

If there is a limit $\overline{\Phi}$ on the flux the pipes can carry, then the array must have sides larger than a minimal value,

$$d \geq \frac{r_0}{r}\left[\frac{P_t}{f\overline{\Phi}}\right]^{1/2} \quad . \tag{2}$$

Typically, the maximum flux that heat pipes carry is in the neighborhood of 10 MW/m^2. Since we expect r_0/r to be relatively close to 1, a 3.8-GW(t) reactor requires $d \geq 28$ m for a pipe array of packing fraction 1/2. Since a

Table 8-3. Possible heat-pipe working fluids.

Element	Melting point[a] (K)	Critical temperature[b] (K)	Theoretical sonic flux limit[c] (MW/m^2)
Bismuth	544		
Cesium	301		
Gallium	303		
Indium	430		
Iodine	387	808	
Lead	601		
Lithium	454		
Mercury	234	1173	400
Potassium	337		5.4
Sodium	371	1313	3.6
Sulfur	386		
Tin	505		

[a]The reactor operating temperature is assumed to be 623 to 773 K (350 to 500°C).

[b]Critical temperature is the temperature above which the vapor will not condense; many critical temperatures were unavailable.

[c]The theoretical sonic flux limit is the maximum flux which can be carried along the length of the heat pipe when vapor is traveling at sonic speed.

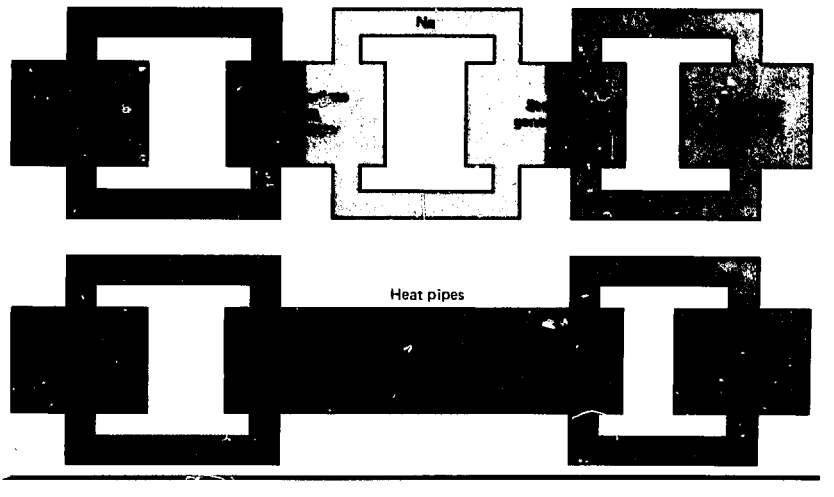

Fig. 8-8. Schematic showing replacement of the secondary Na loop in an ICF reactor (the upper figure) with heat pipes (the lower figure).

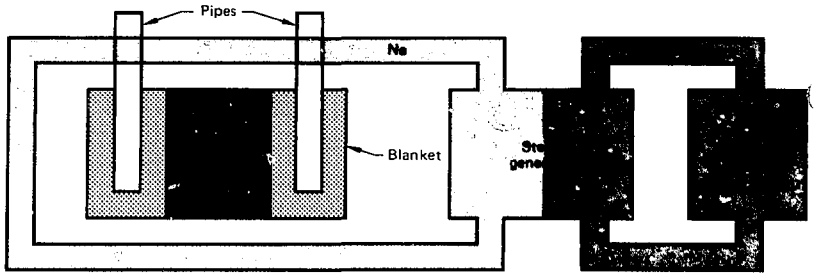

Fig. 8-9. Schematic showing vertical heat pipes used to cool the lithium blanket in an ICF reactor.

Requirement	Orientation: Vertical	Orientation: Horizontal
Flux	145 MW/m^2	24 MW/m^2
Number	3337	20 000
Length	>10 m	>2 m
Wicks	Perhaps unnecessary due to gravity	Necessary
Neutron streaming	Not a problem	Doglegs and a thicker blanket required
Na condenser region	Covers the top of the blanket	Surrounds the outer wall of the blanket completely
Blanket segmentation	Top	Inner and outer walls

Table 8-4. Relative merits of vertical and horizontal heat pipes for cooling a lithium blanket 10 m high, with inner radius of 5 m and outer radius of 7 m, at a reactor power of 3.8 GW(t).

reasonable maximum magnitude for d is perhaps 10 m, the results of the above calculation indicate that pipes must be designed that can carry at least 10 times the flux value used in the calculation. Hence, the use of heat pipes to replace the secondary sodium loop is not feasible at present.

Heat-Pipe Cooling of the Lithium Blanket. Heat pipes might also be placed in the liquid-metal blanket to serve as intermediate heat exchangers (IHXs). As Fig. 8-9 illustrates, the primary Li loop is eliminated (the Li is static), while Na in the secondary loop, which passes over the condenser region of the pipes, carries the heat away to the steam generator. Although the figure shows the heat pipes in a vertical position, we considered a horizontal orientation as well. Relative merits of the horizontal and vertical orientations for cooling of the blanket are listed in Table 8-4.

Compared to the vertical orientation, the horizontal orientation makes necessary the use of a larger number of heat pipes, with a resulting lower heat-flux requirement. Because of neutron streaming, however, horizontal heat pipes would require doglegs and a thicker blanket. In either orientation, the pipes would have a required flux that exceeds the upper limit for present-day heat pipes of 10 MW/m^2.

Problems. Using heat pipes in ICF reactors presents a number of problems. The first difficulty involves materials compatibility. Pipes in a Li bath might be made of 2-1/4 Cr-1 Mo steel; alternatively, they might be made of a compound wall if 2-1/4 Cr-1 Mo steel is not compatible with the heat pipes' working fluid. The possibility of pipe breaks will necessitate looking at the chemical interaction of hot Li and the working fluid.

Heat transfer in the condenser section of the heat pipes may be hampered by generation of noncondensible gases by corrosion, by thermal decomposition of a compound working fluid, or by neutron fluxes. These factors would all have to be prevented. Heat pipes must also have a high reliability and long life. Current heat-pipe designs for environments different from ICF systems have lifetimes of two to five years. Thus the cost of replacing the pipes every few years would have to be weighed against their advantages.

Conclusion. Based on the studies summarized here, we conclude that utilizing heat pipes for blanket cooling does not appear advantageous compared to normal convective cooling.

Author: Bechtel Group, Inc. (Research & Engineering, Advanced Physical Processes Group)

Major Contributors: J. H. Pitts and M. J. Monsler

Tritium Extraction from Liquid Lithium

One of the key chemical problems associated with lithium in fusion reactors is extraction of the tritium generated in or trapped by lithium.[14] An important figure of merit for tritium extraction is the tritium inventory in the lithium blanket. Very large

inventories require large, expensive start-up purchases and are a potentially large radioactive effluent in the event of a catastrophic accident.

Tritium extraction presents different problems depending on whether the tritium must be extracted from solid Li compounds, from liquid Li, or from a gas medium. In many fusion concepts, the tritium breeding medium is not in direct contact with the plasma exhaust, and unburned tritium must be extracted directly from the plasma exhaust. Similarly, in solid breeders and some liquid breeders, a gas removes tritium from the breeding blanket; the gas is then processed to release the tritium.

For solid blankets using Li_2O or $LiAlO_2$, retention of tritium in the solid is the limiting factor. The STARFIRE tokamak solid-lithium-blanket concept has an estimated tritium inventory of 0.7 to 8.2 kg (Ref. 15). However, radiation could cause stoichiometric changes, grain growth, tritium trapping, and sintering. These tritium-retention effects could increase the required blanket tritium inventory to hundreds of kilograms.

Several methods have been proposed to extract tritium from molten Li or molten Li alloys. These include

- Fractional distillation.
- Cold trapping.
- Gettering.
- Diffusion through a large permeable window.
- Diffusion into heat pipes.
- Molten salt extraction.

In all of these methods, concurrent removal of corrosion products from the liquid lithium could increase the corrosiveness of the liquid metal downstream from the extraction equipment due to an increase in the solid-to-liquid concentration gradient. This factor has not been evaluated for most schemes, but it has caused problems in some lithium loops that use getters.

Liquid lead–lithium ($Li_{17}Pb_{83}$) has been proposed as a liquid-metal coolant in several reactor concepts. Recent work indicates that tritium is very insoluble in $Li_{17}Pb_{83}$ and can be effectively recovered from the vapor phase.[16,17]

Distillation. An azeotrope has been reported in the lithium-tritium phase diagram at ~1000°C (Fig. 8-10). Reference 18 estimates the azeotrope concentration at 2000 weight parts per million (wppm) of tritium, while Ref. 19 estimates 3 wppm of deuterium (corresponding to ~4 wppm of tritium). If the high value is correct, a dilute tritium solution will have a vapor that is less rich in tritium than is the melt. As the vapor is removed, both the vapor and the melt would increase in tritium concentration until a constant boiling-point mixture at the azeotrope concentration is achieved. If the lower azeotrope concentration is correct, fractional distillation could be effective.

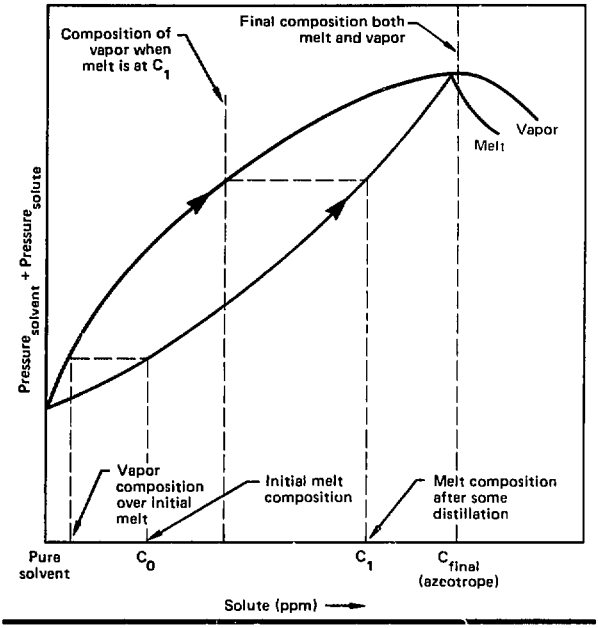

Fig. 8-10. This phase diagram for a dilute solution with an azeotrope can be used qualitatively to predict the distillation behavior of tritium (the solute) in lithium (the solvent).

Ihle and Wu[19] estimate that the concentration ratio of tritium in the gas phase to tritium in the liquid phase should exceed 1.0 at temperatures above ~1200 K, reaching a value of ~6 at 1600 K. However, this argument is complicated by the presence of other tritium vapor phases such as LiT. For example, when Ihle and Wu's work is extrapolated to 850°C and applied to tritium at 10^{-5} atom fraction, the LiT and Li_2T pressures are of comparable magnitude at 2.6 mPa (2×10^{-5} Torr), and exceed the T_2 partial pressure by a factor of 40.

Cold-Trapping. There is considerable uncertainty about the concentration to which tritium can be cold-trapped from Li (Fig. 8-11). The work of Natesan and Smith (Ref. 20) can be used to estimate concentrations of 1800 wppm of protium and 2700

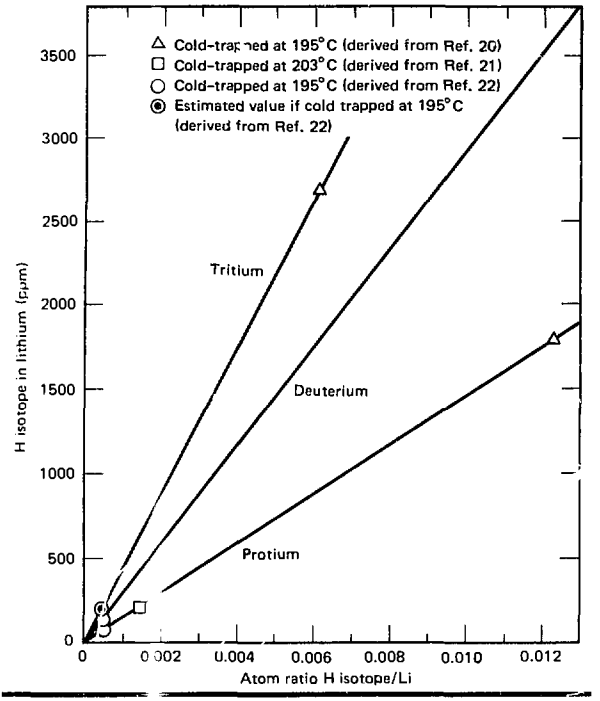

Fig. 8-11. Concentrations to which hydrogen isotopes can be cold-trapped from lithium.

wppm of tritium at a cold-trap temperature of 195°C. Katsuta estimates a protium concentration of 200 wppm at a cold-trap temperature of 203°C (Ref. 21). Veleckis estimates protium and deuterium concentrations of 75 and 135 wppm, respectively, at a cold-trap temperature of 195°C (Ref. 22). The corresponding tritium concentration would be ~ 200 wppm. Thus, Veleckis (200 wppm) and Natesan (2700 wppm) bracket the available estimates of tritium concentration at cold-trap temperatures. In a 1630-m^3 Li blanket, such as that planned for HYLIFE, these tritium concentrations would result in blanket tritium inventories of 160 and 2200 kg, respectively. The actual tritium inventory may be reduced by about 25% due to the presence of deuterium, but this effect has been ignored in this article.

Gettering. The gettering approach to tritium extraction applies to processing of either liquid metals or gas streams containing tritium. The stream is passed through a bed of porous metal that serves as the getter. After sufficient exposure, the getter bed is regenerated by heating under vacuum or in a carrier flow stream to recover the tritium. Yttrium and cerium have shown a limited degree of success as getters at relatively low temperatures (i.e., below 350°C).[23,24] To achieve acceptable performance with an yttrium sorber,[25] surface areas greater than about 0.4 m^2/g and porosities >30% are required. These conditions have been met by pressing and sintering pellets of yttrium powder. Yttrium has demonstrated the ability to remove tritium from lithium to below 1 wppm; engineering scale-up is still required. A tritium concentration of 1 wppm corresponds to a HYLIFE inventory of less than 1 kg.

Diffusion Through the Primary Heat-Transfer Loop. Permeation of a gas through a metal is given by

$$F = C A \Delta \sqrt{P/t} \quad , \tag{3}$$

where F is the gas flux, C is the permeability constant, and $\Delta\sqrt{P}$ is the difference of the square roots of the tritium pressures on the high-pressure and low-pressure sides of a diffusing medium that has area A and thickness t.

For a 30% tritium burn fraction and a 1.75 tritium breeding ratio, 19.5 mg/s of tritium are added to a 1-GW(e) HYLIFE plant's liquid-metal wall. The permeability constant for tritium diffusing through 2-1/4 Cr-1 Mo steel at 500°C is 4.68×10^{-7} mg/(s·m·$\sqrt{\text{Pa}}$) (Ref. 26). For lithium temperatures of ~500°C, a liquid-metal heat exchanger requires ~3.3 to 8.0 m^2 of area per MW(t). The wall thickness will be about 0.65 to 1.3 mm for a 2-1/4 Cr-1 Mo heat exchanger.

If the low-pressure side of the heat exchanger is considered to have essentially a zero tritium pressure, the high-pressure side ranges from 1.1 to 27 Pa (0.0084 to 0.20 Torr) for the above conditions. Using the pressure-concentration relationship[20] shown in Fig. 8-12 gives tritium concentrations of 2900 and 14 000 wppm, or a HYLIFE tritium inventory of 2300 to 11 000 kg. If the low-pressure side is liquid sodium cold-trapped to 4 mPa (3×10^{-5} Torr), the high-pressure side ranges from 1.3 to 27 Pa (3100 to 14 000 wppm). Therefore, using a secondary fluid that [illegible] a lower pressure [illegible] such as NaK, which can be cold-trapped to 30 nPa or 2×10^{-10} Torr) does not significantly improve the situation.

Considerable improvement is possible, however, using a heat exchanger with a much larger area. For example, if the tubes of the 25 600-m^2 HYLIFE heat exchanger are reduced in radius and coiled, perhaps 100 times more area could result. Using 0.65-mm-thick 2-1/4 Cr-1 Mo steel and cold-trapped NaK on the secondary side would then result in a primary tritium pressure of 0.12 mPa (29 wppm or 23 kg of tritium in the HYLIFE lithium-blanket inventory).

An alternative method of reducing the blanket tritium inventory is to use a more permeable heat-exchanger material such as niobium, which has a permeability constant of 2.6×10^{-4} mg/(s·m·$\sqrt{Pa}$) at 500°C (Ref. 27). For the original heat-exchanger areas and thicknesses and for a cold-trapped NaK secondary, tritium pressure ranges from 4.4 to 89 μPa. This range gives a result of 6 to 26 wppm, or 5 to 20 kg of tritium in the HYLIFE lithium-blanket inventory. These calculations are uncertain, however. For example, the rate-controlling factor may not be diffusion, which is proportional to root pressure as in Eq. (3), but rather the rate at which tritium atoms on the low-pressure surface recombine into gaseous molecules.

Heat Pipes. The principle involved in tritium removal with heat pipes has been described by Lee and Werner.[28,29] Tritium in the liquid-metal breeder enters the heat pipe through a permeation membrane such as niobium or vanadium. The tritium is then picked up by the rapid sweeping action of the sodium or potassium vapor in the heat pipe and carried to the heat-rejection end of the heat pipe. There, the tritium is entrapped and compressed by the condensing heat-pipe vapor. With a tritium concentration of a few wppm in the liquid-metal blanket (corresponding to ~1 μPa or 10^{-8} Torr in 500°C Li), tritium concentrations up to ~130 Pa (1 Torr) are expected in the heat-rejection end of the heat pipe, where the tritium is extracted through a metal permeation membrane. Because of the selective sweeping and concentrating action of heat pipes for the noncondensible hydrogen isotope gases, heat pipes have significant potential as a tritium recovery method. Development of further designs and materials for this application would be very useful.

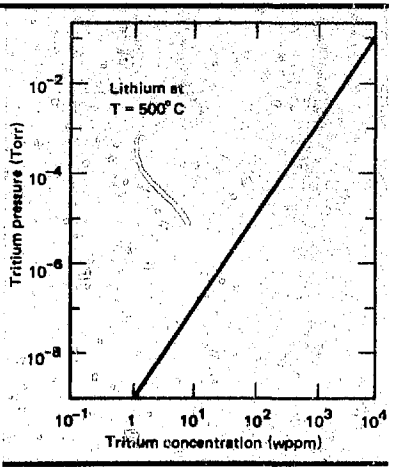

Fig. 8-12. Relationship of tritium pressure to tritium concentration in 500°C Li.

Molten Salt Extraction. The final tritium extraction process we examine is molten salt extraction.[30] In this process, molten lithium or lithium alloy is placed in contact with a molten salt solution (22 mole % LiF—31 mole % LiCl—47 mole % LiBr) that melts at 445°C. Tritium (present as ions) is more soluble in the molten salt than in the molten lithium, and when the immiscible salt and liquid-lithium phases are separated, most of the tritium remains with the salt. The metallic liquid carries less than 1 wppm total hydrogen isotope as it returns to the liquid-metal circuits of the fusion reactor. The salt is processed to remove tritium ions by electrochemical evolution. The hydrogen isotopes released are swept away in molecular form by argon gas emerging from the porous anode. This technique could remove tritium to 0.5 wppm, corresponding to a 0.4-kg inventory in the HYLIFE lithium blanket.

Conclusion. The two most promising techniques for tritium recovery are molten salt extraction and yttrium gettering. Both processes can remove tritium to <1 wppm, which results in <1 kg of tritium in the HYLIFE lithium, and both processes have been demonstrated at small scale. These two processes should be given priority in future development efforts.

All of the other methods discussed either require small-scale demonstration or result in excessive tritium inventories. Diffusion through the heat exchanger results in excessive inventories even if expensive materials or geometries are used. Use of heat pipes

might require excessive heat-pipe area in the lithium. Cold-trapping requires excessive tritium inventory. Finally, fractional distillation requires high temperatures and is based on uncertain data.

Authors: J. A. Blink (LLNL) and N. J. Hoffman (Energy Technology Engineering Center)

Major Contributor: O. H. Krikorian

Conceptual Design Considerations for an ICF Power Plant

In this article, we present a preliminary conceptual design and economic analysis of an inertial confinement fusion (ICF) power plant.[1] The major systems of a generic fusion power plant (shown in Fig. 8-13) determine the structures and buildings required in our design. The baseline facility design outlined here is for a twin-unit electric generating station. Each unit has an electrical output of 1000 MW(e). The concept provides for two separate reactor-turbine-generator plants driven by a single 4.4-MJ short wavelength laser system operating at a repetition rate of 10 Hz (5 Hz to each reactor). The site also contains all appropriate auxiliary and waste-handling facilities. With the exception of the laser, optics, and target systems, the plant is comparable in size and function to a liquid-metal fast-breeder reactor (LMFBR) plant.

A key issue in the design of a laser-fusion power plant is the degree of symmetry in the illumination of the target that will be required for a proper burn. In this study, we outline the effect of symmetry requirements on the total plant size, layout, and cost. Two alternative beam-transport systems are examined. The first provides two-sided illumination of the target as used in the HYLIFE design; the second provides symmetrical eight-sided illumination of the target. We assumed that the target gain is the same for both the two- and eight-sided examples. We have also kept the mirror distance and f/number unchanged; given present uncertainties about the effects of

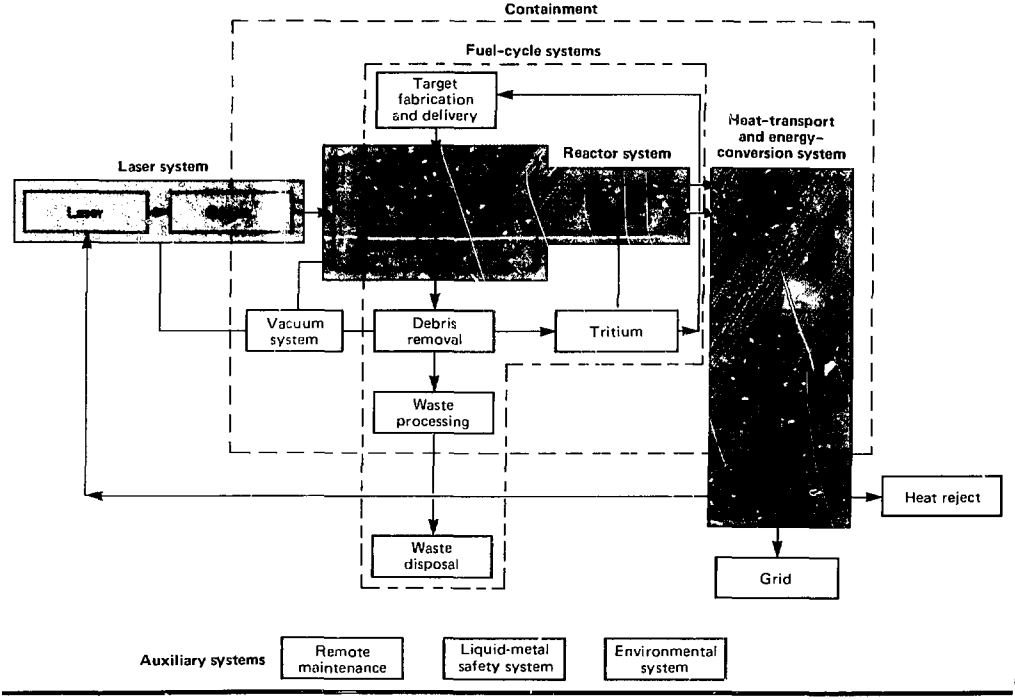

Fig. 8-13. Generic laser-fusion power plant systems.

illumination uniformity on target gain, this is the only prudent assumption. It should be understood, however, that the plant layout and cost estimates may be quite different if a larger number of small-f/number mirrors, placed closer to the target, are required. We have not examined this case.

The other primary design areas addressed in this study are the reactor concept, the heat-transfer system, the balance of plant, and capital cost. The balance of plant is modeled as much as possible after the current LMFBR design.[32]

Power Plant Design. The heart of an ICF plant, the nuclear steam-supply system, is comprised of the reactor vessel and internals, primary coolant pumps, intermediate heat exchangers, secondary coolant pumps, steam generators, and all other secondary equipment necessary to operate the nuclear steam-supply system in an efficient and safe manner. A schematic of this system is shown in Fig. 8-14. There are two primary lithium loops and four intermediate heat exchangers (IHXs). Each IHX has a secondary sodium loop that delivers the power to two separate steam-generator/superheater pairs.

At the core of the nuclear steam-supply system is a 3800-MW(t) [1000 MW(e)] reactor in which the fusion events occur. The reactor is a cylindrical vacuum vessel that is 15 m high and 7 m in radius. The walls are protected by a primary coolant that flows inside the reactor at a rate slow enough that only two loops are required. Specifically, we chose a reactor inlet temperature of 573 K, an outlet temperature of 723 K, and a total primary lithium flow rate of 12.4 m^3/s (6.2 m^3/s for each pump). The pumps (similar to those in the breeder program) are centrifugal vertical-shaft units equipped with a variable-speed drive to provide balanced heat delivery to each loop. Pump outlet pressure is determined by the pressure losses in pipes and the IHX and by the pressure drop developed across the reactor. The piping throughout the loop and the internal surfaces of the components are specified as 2-1/4 Cr-1 Mo low-alloy ferritic steel, which resists lithium corrosion (see "Corrosion of 2-1/4 Cr-1 Mo Ferritic Steel in Liquid–Lithium and Lead–Lithium Solutions" earlier in this section).

Each IHX delivers hot sodium at 713 K to superheater, where steam from the steam generator is raised to a temperature of 703 K; the steam exits the superheater at a pressure of 17.2 MPa. After superheating the steam, the sodium moves down to the steam generator, where it develops steam from feed water coming in at 503 K. A sodium pump returns the cold (563 K) sodium to the IHX. The sodium flows at 5.7 m^3/s through each loop.

The purpose of the secondary loop is to isolate the primary coolant (which carries radioactive target debris) from the steam generator and turbine which would become contaminated if there were a rupture in the steam generator. This requires that the Na in the secondary loop be kept at a slightly higher pressure than the Li in the primary loop, so that a break in the IHX would result in the Na flowing into the Li.

The turbine-generator is an axial-flow, 1800-rpm, tandem-compound, six-flow unit with 1.1-m final blades. We use a multicylinder turbine that has a double-flow high-pressure cylinder, a double-flow intermediate-pressure cylinder, and three double-flow low-pressure cylinders. The turbine is provided with two moisture-separator/reheaters, with two stages of reheat in each moisture-separator/reheater unit. The generator is a liquid-cooled stator type with a gross capability of 1300 to 1400 MW(e) at rated turbine conditions of inlet steam.

We assume the laser driver to be a rare-gas-halide (RGH) laser system servicing two colocated reactors. The laser drives two amplifiers for each reactor. The amplifiers are rated with an output of 2.2 MJ at 5 Hz, together delivering 4.4 MJ on target five times a second. The laser itself is fired at 10 Hz to service both reactors. The amplifier output beams are transported to the reactor building through evacuated tunnels. Turning mirrors direct the beams to the final focusing mirrors located 30 m from the target.

Arrangement of Buildings. The site for a fusion power plant requires a number of separate, but interrelated, facilities:

- Equipment and buildings for manufacturing the 3×10^8 targets per year consumed by a twin-reactor fusion plant.
- Target-delivery and debris-removal systems.
- Systems to remove the debris from the lithium coolant and to recover unburned tritium.

- Facilities to recondition the debris for recycling as target material and to purify the tritium for reuse.

Finally, radioactive waste material must be separated and processed to some degree on site before it can be shipped to a final waste repository.

Auxiliary systems that an ICF power plant requires include such things as

- Safety systems against fires—especially liquid-metal fires (see "Lithium Safety Considerations" later in this section).
- Radiation monitoring systems.
- Service systems (including some remote systems) for the reactor.
- Intermediate heat exchangers.
- Pumps.
- Steam-generator/superheater units and other major related equipment.
- Security systems.
- Emergency power systems.
- Receiving and storage facilities for liquid metals.
- Cover-gas storage systems.
- Water-treatment facilities.

All the major and auxiliary systems described above require buildings of various specifications to support and house them; we describe these structures below. Figure 8-15 shows the building arrangements for a typical ICF power plant. These and other systems must be included in an overall plant design and cost estimate.

The reactor-containment building is tied to the nuclear island base mat, which has a common foundation. The building itself is tornado hardened and rated in seismic category I; thus the building is designed to withstand the largest possible earthquake or tornado that is credible for the site and to withstand the impact of projectiles generated by such a tornado. The building extends 10 m below ground and rises 78 m above the surface. The reactor-containment building has an area 70 × 42 m for the two-sided illumination case and 65 × 48 m for the eight-sided illumination case (see Fig. 8-16).

The major systems housed in the reactor-containment building are the fusion reactor, the laser-transport tunnels, the final turning and focusing mirrors, the target-injection system, the primary Li heat-transport system, the IHXs, and portions of the secondary Na heat-transport system.

The reactor-containment building serves to structurally support its internal systems, to protect them from the environment, and to contain them and their working fluids and materials in the case of an accident. The building also provides radiation shielding for protection of equipment and personnel during operation and maintenance; space for maintenance and removal of equipment; and separation and fire protection for the systems. Although the internal structures are designed to withstand all design loads, including those from design-basis accidents, vibrations of operating equipment, and earthquakes, their thickness is generally dictated by shielding requirements. Typically the internal structures are 2 m thick and made of normal-density reinforced concrete.

The reactor-containment building must also provide compartments for running electrical cable, piping, and gas ducts and space for equipment-transfer, elevators, stairwells, and redundant control panels. Piping runs must loop the liquid lithium to a separate reactor service building (discussed below), where processing equipment removes target debris from the lithium and recovers usable target-shell material and tritium. This separation is necessary to prevent fouling of the primary heat-transport pumps and the IHXs. Portions of the reactor-containment building are also set aside for vacuum systems for the reactor and beam tunnels. Cells must be dedicated to cleanup of liquid-metal spills and to fire-control equipment such as pumps and fire-extinguishment stores.

As we mentioned above, the reactor-containment building houses a number of large mirrors for delivering the laser beams on target. For two-sided illumination, each of the two turning mirrors is an 8- × 8-m array of 64 planar 1- × 1-m mirror segments. Each of the two final-focusing mirrors is a parabolic array of 64 1- × 1-m segments. Thus two-sided illumination requires 256 1- × 1-m mirror segments in the reactor-containment building. Three or four times this many mirror segments will be needed to transport the beams from the amplifier to the reactor. In the eight-sided illumination case, for each beam there is a 4- × 4-m planar turning-mirror composed of 16 1- × 1-m segments. The final focusing

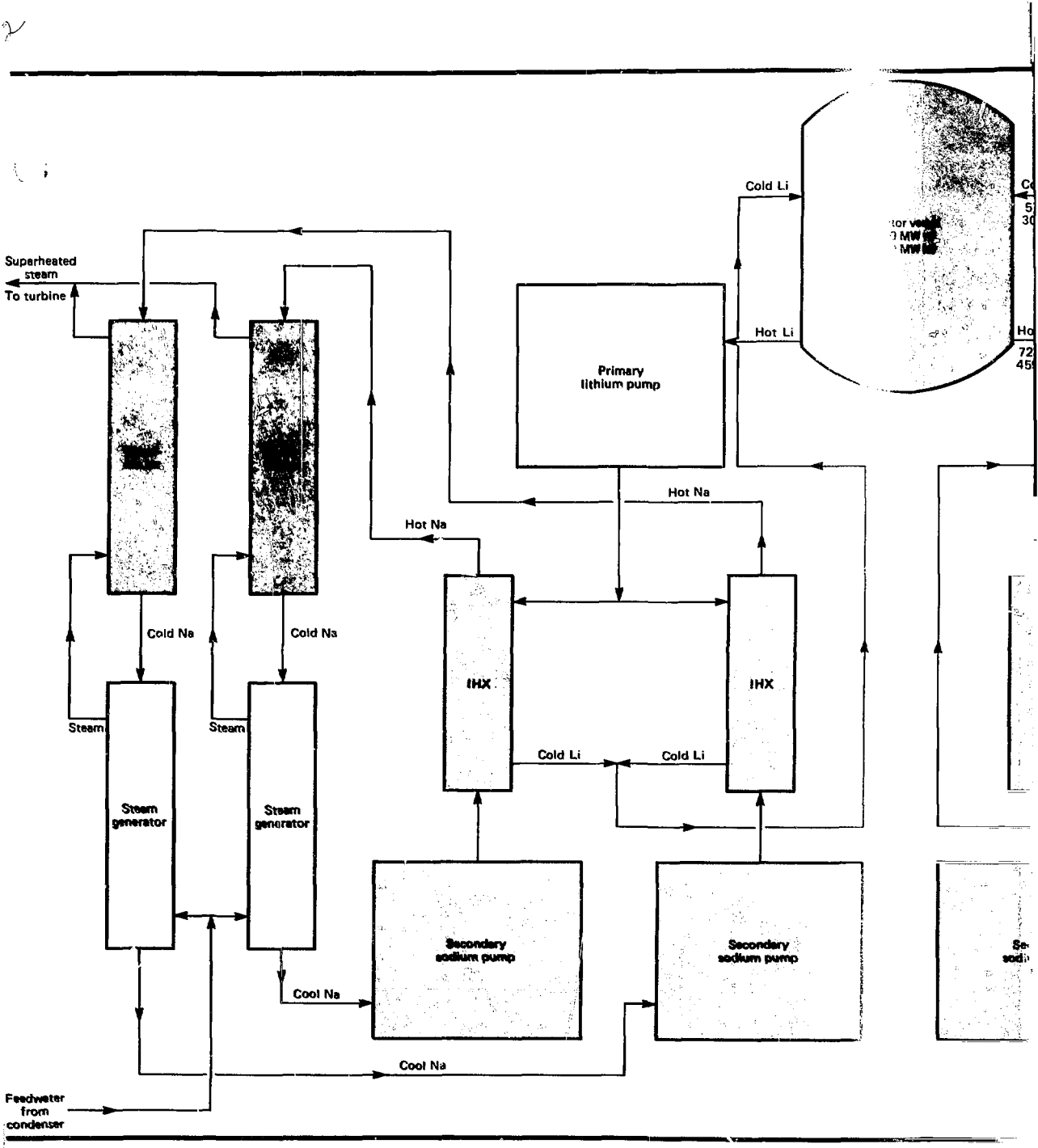
Superheated steam
To turbine
Cold Li
Hot Li
Primary lithium pump
Hot Na
Hot Na
Cold Na
Cold Na
IHX
IHX
Steam
Steam
Steam generator
Steam generator
Cold Li
Cold Li
Secondary sodium pump
Secondary sodium pump
Cool Na
Cool Na
Feedwater from condenser

Fig. 8-14. Schematic of the nuclear steam-supply system.

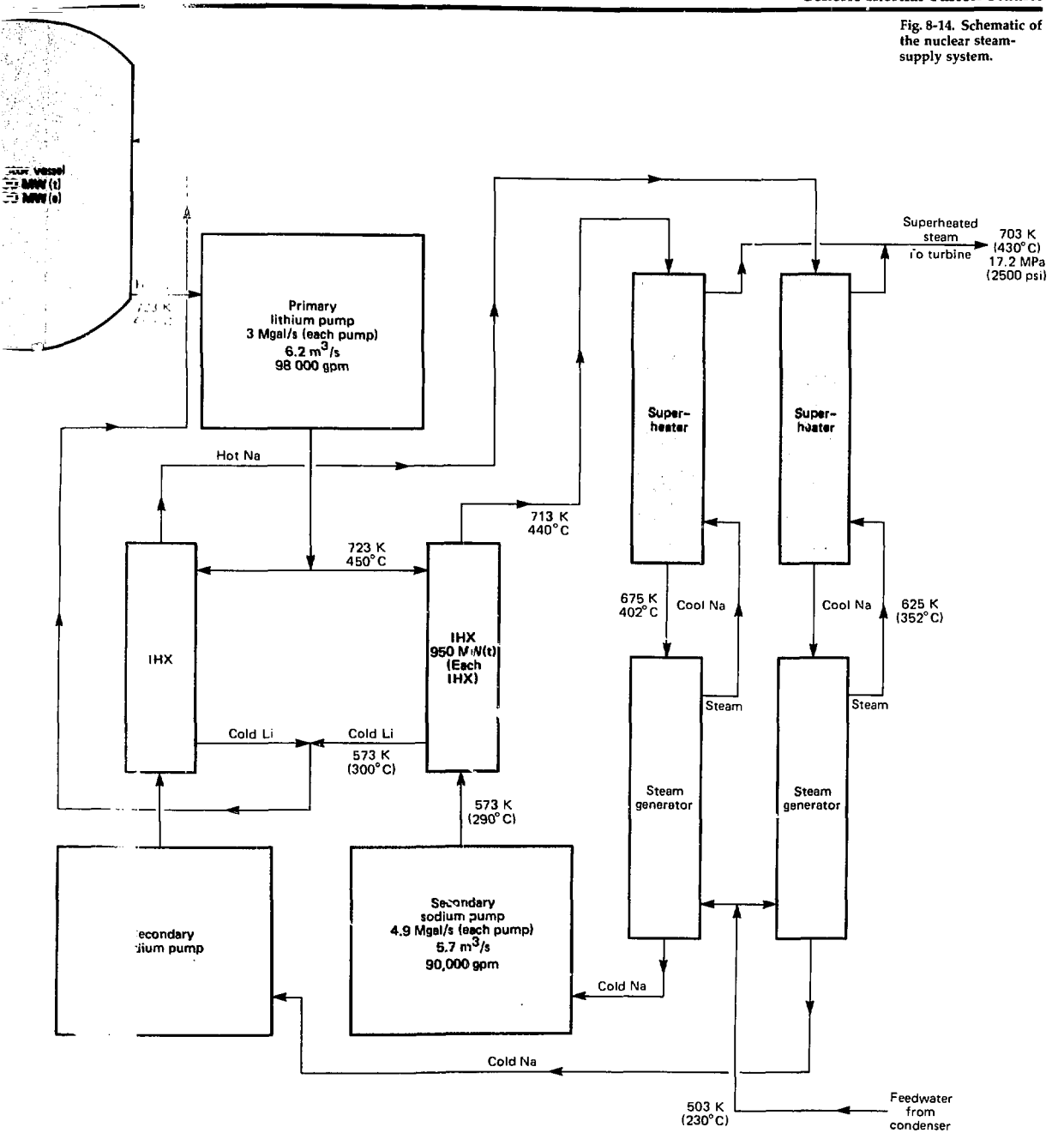

mirrors are 4- × 4-m parabolic segmented reflectors. Thus, eight-sided illumination requires that the reactor-containment building house 128 turning and 128 focusing mirror segments, for a total of 256 mirror segments (the same as for two-sided illumination). Mirrors in the reactor are actively cooled with flowing sodium, if necessary.

Also included in the reactor-containment building are portions of the recirculating-gas cooling system. Typically, a well-insulated 3800-MW(t) reactor and heat-transport system will leak 10 to 15 MW(t). Since the temperature of the concrete everywhere in the containment building must be maintained below 340 K to prevent the

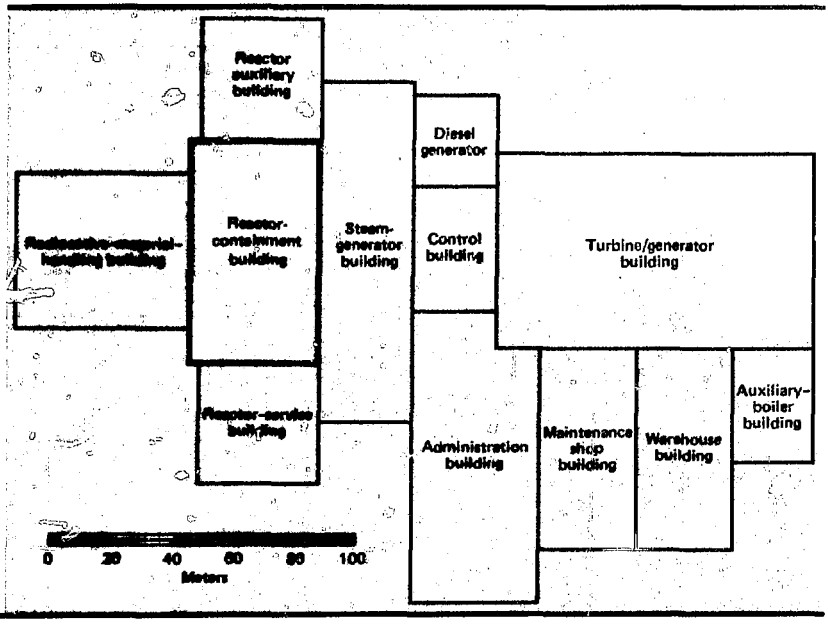

Fig. 8-15. Power-plant building arrangement.

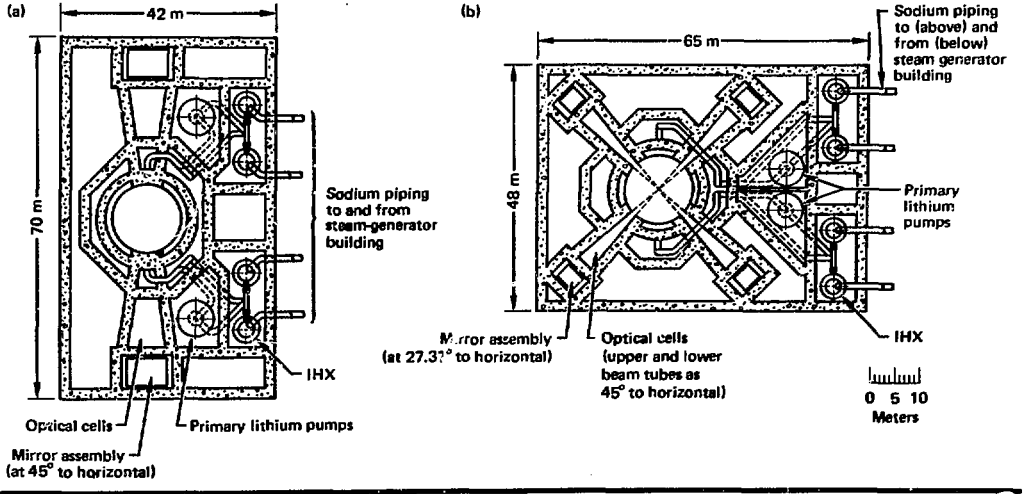

Fig. 8-16. Reactor-containment building layout for (a) two-sided illumination and (b) eight-sided illumination.

evaporation of its water, and so maintain structural integrity, the cover gas in the containment building must be actively cooled.

Adjacent to the reactor-containment building is the steam-generator building, a 30- × 105-m reinforced-concrete structure 60 m in height. The steam-generator building, too, is a tornado-hardened structure in seismic category I. In addition to equipment support requirements, the steam-generator building must also have the integrity to withstand internally and externally generated projectiles. The building's outer walls, roof, and floors are 1.5-m-thick reinforced concrete (see Fig. 8-17).

The building is partitioned into four steam-generator cells. Each cell contains a steam generator, a steam separator, a superheater, a sodium pump, sodium dump tanks for use during a sodium-water reaction, and sodium expansion tanks. Each cell has two internal walls separating each of the three main pieces of equipment (the steam generator, superheater, and sodium pump) to isolate sodium systems from water systems as much as possible. Walls of the cells are steel-lined and have a catch pan covering the floor for sodium containment in case of a spill. The atmosphere of the steam generator building is inert and maintained at 340 K.

The reactor-service building attached to the reactor containment building is 38 × 38 m and 50 m high. The reactor-service building houses major portions of the cover-gas processing system (gas coolers, water chillers, gas storage) and the equipment for debris removal and the tritium recovery process. It provides storage, transfer, and lay-down space for new equipment and components for the reactor-containment building. The reactor-service building also houses environmental-control systems needed for the safety of personnel on the nuclear island. Portions of the service building are set aside for liquid-metal storage. Tritium and recovered target material are piped from the service building to an on-site target-fabrication building (not shown in Fig. 8-15) where they are recycled into new targets.

The reactor auxiliary building houses a variety of ancillary systems such as low-level waste-handling systems; heating, ventilation, and air conditioning; and Li-pump and Na-pump motor controls. The auxiliary building is about the same size as the service building.

The radioactive-material-handling building, 48 × 58 m and 88 m high, is the remote maintenance and radiation-waste-handling facility servicing the reactor-containment and reactor-service buildings. It provides space and equipment to retrieve radioactively hot reactor internals; canyons in which to cut up, package, and store such components; and packaging and storage areas for materials received from the

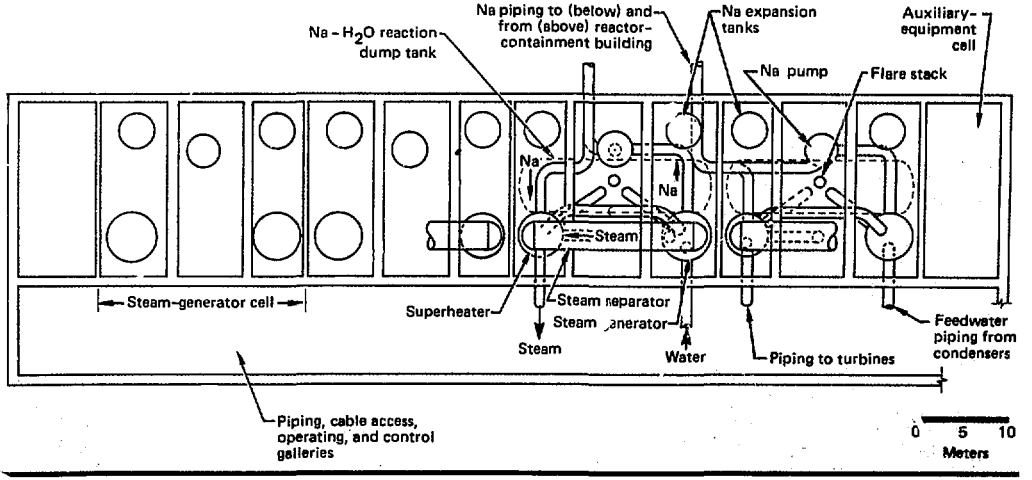

Fig. 8-17. Steam-generator building plan for two- or eight-sided illumination.

reactor-service building, such as process fluids and solids used in the target-debris and tritium-recovery systems.

The control building is 40 × 28 m and 40 m high and is located between the steam-generator building and the turbine-generator building to minimize expensive cable runs. On the main operational floor, the control building houses the main control room, technical support center, and auxiliary control and computer systems not in the main room. The floors above and below are dedicated to the main cable spreads. The floor above the upper cable spread accommodates the control-building maintenance systems (HVAC and power). The floor below the lower cable spread contains the onsite operational support center. The control building, along with the technical support center, is used to assist in the administration and control of the plant during accidents, as well as during routine operation.

The turbine-generator building supports and environmentally protects the turbine-generator and the support equipment needed for power conversion (steam condensers, condensate pumps, and feedwater pumps). The turbine-generator building is located adjacent to the control building and is 102 × 62 m and 50 m high. The turbine generator building is supported by its own concrete base mat.

The 28- × 28-m diesel generator building houses and protects two redundant diesel generators used to provide emergency power in the event that both the offsite source of auxiliary power and the reactor power-recycle system fail. The building provides separate cells for the generators to preserve their redundancy.

The administration building is a 90- × 42-m two-story structure housing the many support services required by the plant. The structure provides offices for administrative, engineering, and plant-operation personnel. There are laboratories for chemical and radiological analyses and a shop for calibration and storage of plant instrumentation. Also included are health-physics facilities, a whole-body counter room, protective-clothing stores, a personnel locker room, showers, and personnel decontamination facilities. The plant cafeteria and other personnel-related services are located in the administrative building, which also provides controlled access to the nuclear island.

Other balance-of-plant buildings and structures include a maintenance shop, a warehouse, an auxiliary-boilers building, switchyards, water pumps for cooling towers, and security facilities.

Capital-Cost Analyses. We completed capital-cost analyses for a total of six plant designs. For both two- and eight-sided illumination, we considered three options: a single-unit first-of-a-kind plant, a single-unit fifth-of-a-kind plant, and a twin-unit fifth-of-a-kind plant. Our analyses are based on extrapolated LMFBR costs where feasible. However, it is difficult to make an accurate comparison of the capital costs computed here with the capital costs of a light-water reactor (LWR), an LMFBR, or even another fusion plant, because of the different computing methods used in various analyses. The value of our cost analysis is for internal comparison: between one building and another, between two- and eight-sided illumination, between first-of-a-kind and fifth-of-a-kind facilities, etc. We

Table 8-5. Summary of normalized costs for ICF designs.

	Single unit				Twin units[a]	
	First-of-a-kind		Fifth-of-a-kind		Fifth-of-a-kind	
	2-sided	8-sided	2-sided	8-sided	2-sided	8-sided
Direct cost	0.423	0.427	0.282	0.285	0.247	0.250
Field-distributable costs	0.085	0.085	0.057	0.057	0.049	0.050
Engineering and home-office costs	0.101	0.103	0.068	0.069	0.059	0.060
Owner's cost	0.043	0.043	0.028	0.029	0.025	0.025
Contingency	0.130	0.132	0.087	0.088	0.076	0.076
Interest and escalation during construction	0.218	0.220	0.146	0.147	0.127	0.129
Total capital cost	1.000	1.010	0.668	0.675	0.583	0.590

[a] Twin-unit costs are given per unit; hence they can be compared directly with single-unit costs.

have, therefore, normalized these costs for a single-unit first-of-a-kind plant with two-sided illumination.

A summary of these normalized costs is shown in Table 8-5, and a breakdown of direct costs is given in Table 8-6. These tables show that a single-unit fifth-of-a-kind facility saves 33% over a single-unit first-of-a-kind plant. A cost savings of 42% is realized for a twin-unit fifth-of-a-kind plant. Further, the difference in cost between two- and eight-sided illumination is insignificant when compared on a total capital-cost basis.

The costs shown in Tables 8-5 and 8-6 do not include the cost of land, the laser, optics, and targets. If all these items are included, the capital cost of an ICF power plant is roughly double the capital cost of an LWR power plant in 1981 dollars. It is most likely that conventional fuel-cycle costs will escalate faster than the rate of inflation, however, so that in time the total cost of ICF electrical power will become cost-competitive with electricity from other sources.

Author: Bechtel Group, Inc. (Research & Engineering, Advanced Physical Processes Group)

Major Contributors: J. H. Pitts and M. J. Monsler

Table 8-6. Breakdown of normalized direct costs for ICF designs.

	Single unit[a]		Twin unit[a,b]
	First-of-a-kind	Fifth-of-a-kind	Fifth-of-a-kind
Structures and site facilities			
Site improvements	0.014	0.014	0.010
Reactor building	0.094 (0.099)	0.069 (0.073)	0.070 (0.073)
Turbine building	0.023	0.023	0.018
Cooling-system structures	0.007	0.007	0.007
Steam-generator building	0.031	0.024	0.024
Miscellaneous buildings	0.091	0.091	0.060
Subtotal	0.260 (0.265)	0.228 (0.232)	0.189 (0.192)
Reactor-plant equipment			
Reactor equipment	0.092	0.040	0.036
Main heat-transfer system	0.046	0.026	0.024
Secondary heat-transfer system	0.186	0.103	0.099
In-containment optical system	0.005 (0.010)	0.003 (0.006)	0.003 (0.007)
Radioactive waste systems	0.058	0.029	0.023
Other reactor plant equipment	0.151	0.066	0.053
Instrumentation, plant control, and protection	0.031	0.014	0.011
Miscellaneous reactor equipment	0.004	0.002	0.001
Subtotal	0.573 (0.578)	0.283 (0.286)	0.252 (0.256)
Turbine-plant equipment			
Turbine-generator	0.040	0.040	0.039
Heat-rejection system	0.003	0.003	0.003
Heating and condensing system	0.023	0.023	0.023
Other turbine plant equipment	0.024	0.024	0.021
Subtotal	0.090	0.090	0.086
Electric plant equipment	0.047	0.047	0.042
Miscellaneous plant equipment	0.030	0.020	0.014
Total direct cost	1.000 (1.010)	0.668 (0.675)	0.583 (0.590)

[a]Single numbers in a column show normalized costs for either two- or eight-sided illumination. A double number shows normalized costs for two- illumination without parenthesis and eight-sided illumination with parenthesis.

[b]Twin-unit costs are given per unit; hence, they can be compared directly with single-unit costs.

Numerical Calculation of Fusion-Reactor Activation

Fusion has the potential to provide virtually unlimited energy at a reasonable cost with a high degree of safety and minimal environmental impact. One of the key issues in determining the safety and environmental impact of fusion is the buildup of radionuclides. The quantity of neutron-activated nuclides present during and after reactor operation provides the time-dependent heat source for afterheat calculations and the radioactivity source for dose-rate calculations. In this article, we describe a method of calculating the population of neutron-activated nuclides as a function of time after start-up and time after shutdown of the reactor.

To calculate the quantities of radioactive nuclides within the reactor as a function of time, we require

- Neutron fluxes as a function of time, energy, and location.
- A library of energy-dependent activation cross sections.
- A mathematical method to solve the coupled activation and decay equations.

We obtain neutron fluxes as a function of energy and location using TARTNP, a Monte Carlo neutronics transport code.[33] In pure fusion problems, the time variation of the flux is usually negligible; however, TARTNP can be used to recalculate the flux as a function of time, if required, by changing material compositions. Neutron-activation cross sections assembled for fission-reactor problems are inadequate for fusion problems due to the high energy of fusion neutrons. At our request, R. Howerton has used experimental data, theoretical calculations, and nuclear systematics to add over 200 cross sections to the ACTL library, which represents about a 20% increase in that library.[34,35] Howerton has also eliminated over 400 reactions with thresholds above 15 MeV.

The ORIGEN2 activation/depletion computer code[36] is widely used to mathematically model neutron activation of fission-reactor fuel and structure. ORIGEN2 is a single-region, single-energy code that requires single-energy cross sections. Thus, the energy-dependent cross sections must first be collapsed (or energy-averaged) using the energy-dependent flux as a weighting function. To collapse the cross sections, we wrote the ORLIB code[37] to run on the LLNL Cray network. In addition to energy collapsing, ORLIB can spatially average the cross sections by using the spatial distribution of the TARTNP neutron fluxes in conjunction with material composition as a function of location. Spatial averaging is valid only for activation of parents to daughters; activation of daughters to granddaughters requires knowledge of the spatial distribution of the daughters prior to collapse of the cross-section library. If activation of daughters is significant, the problem must be rerun with a separate cross-section library for each region.

Once spatial and energy-averaged cross sections are available from ORLIB, we can use ORIGEN2 to solve the time-dependent activation and decay equations. We have modified ORIGEN2 to accept the more extensive (and hence differently formatted) ORLIB cross sections and to handle up to 15 activation or decay removal paths for each parent (ORIGEN2 can handle seven paths). The modified code, called FORIG, is available on the LLNL Cray network.[38]

The collapsed cross-section library can also be used for abbreviated hand calculations if the nuclide list is not overly extensive. This method is described in the next article.

Author: J. A. Blink

Major Contributors: R. E. Dye, R. J. Howerton, J. R. Kimlinger, G. P. Lasche, and W. E. Warren (LLNL); A. Croff (Oak Ridge National Laboratory)

Analytical Radioactivity Estimation Technique

We have developed a method to perform "back-of-the-envelope" activity calculations which accounts for ongoing impurity removal, burnup, and both the equilibrium and nonequilibrium states for each nuclide in a neutron-irradiated material.[39] Our calculation method provides an upper-bounded estimate of activity, thermal decay power, and biological hazard potential. The method accounts for any number of transmutations of a nuclide. In addition, the method we have developed can be used to

place an upper bound on the error that results from assumptions involved in the analytic equations describing the buildup and decay of radionuclides. In this article, we first describe an order-of-magnitude scaling rule for radioactivity in fusion reactors and then the uniform treatment of induced-radioactivity calculations based on reaction rates.

Reaction Rate and Proportionality to Thickness. For a material with uniform density, n, for which the energy-averaged product of neutron-reaction cross section and path length per source neutron is $\langle\sigma\ell\rangle$, and total source neutron rate is Φ, the reaction rate is $n\Phi\langle\sigma\ell\rangle$. Consider a closed shell with negligible far-side neutron reflection. If this shell is sufficiently thin and far away from a source of 14-MeV neutrons such that ℓ is approximately the thickness, t, and such that only collisions with 14-MeV neutrons need be considered, the reaction rate becomes $n\Phi t\sigma_{14}$, where σ_{14} is the reaction cross section at 14 MeV (Ref. 40).

If any nuclide is produced at a constant rate, its activity at any time is directly proportional to the rate with which it is produced, whether or not equilibrium has been achieved. Therefore, for fusion reactors of comparable power that also have essentially similar first-structural-wall (FSW) composition, the total radioactivity, biological hazard potential, and thermal decay power in the FSW at similar times after startup are roughly proportional only to the FSW thickness.

The proportionality of radioactivity to thickness is a good approximation for the reaction rate in the radiation case of an ICF target. However, the proportionality of radioactivity to thickness underestimates the activation rate for the FSW of a magnetic-confinement fusion reactor chamber. This is due to three factors:

- Averaged path lengths are longer for cylinders and toroids than for spheres.
- Averaged path lengths are longer for a distributed source of neutrons than for a central point source.
- Neutron reflections are much more important if the radius of the FSW material is comparable with that of the reflecting material.

Reaction, Removal, and Decay Probability Rates. If the reaction $X \rightarrow Y$ has cross section $\sigma_{X,Y}$, the reaction probability, $\lambda_{X,Y}$, per nucleus located in volume V per unit time is

$$\lambda_{X,Y} = \Phi\langle\sigma_{X,Y}\ell\rangle/V \quad .$$

In addition, if an impurity cleansing system removes a fraction, F, of the total nuclide population number, N, from the volume per unit time, each nucleus' probability of removal, λ_R, per unit time is F.

We can now define a "total loss constant," Λ, such that

$$\Lambda_i = \lambda_R + \sum_u \lambda_{i,u} + \lambda_D \quad ,$$

where $\lambda_D = (\ln 2)/T_{1/2}$ is the radioactive decay constant.

Taking early time and equilibrium limits of the resulting population-rate equations, we see that if the total production rate from decays, reactions, and deposition, Q, of a nuclide not initially present does not increase in time, the nuclide's population is absolutely upper-bounded at time T by

$$N \sim Q/\Lambda \text{ for } \Lambda T \gg 1$$

and

$$N \sim QT \text{ for } \Lambda T \ll 1 \quad .$$

These approximations simply assume no decays for long-lived radionuclides and the maximum equilibrium population for short-lived radionuclides.

A General-Case Estimate for the Absolute Upper Bound. Applying the above approximations to a sequence of transmutations leads to a convenient upper-bounded analytical method for estimating the populations of all nuclides, whether or not they are initially present, with or without a constant parent population, and whether or not they are in equilibrium. Consider the production of a nuclide by any arbitrary sequence of neutron reactions and decays, beginning with a nuclide member of population N_1. We could be concerned, for example, with estimating the importance of the production of nuclide n by the sequence $1 \rightarrow 2 \rightarrow \ldots \rightarrow n$. The population N_1 represents the original parent population of nuclide 1, and δN_1 represents population changes resulting only from reactions with N_1 in this particular sequence. Because we

treat other sequences for nuclide n separately, N_1 never increases for any particular sequence under consideration. Then, because Q_{i+1} equals $\lambda_{i,i+1}N_i$,

$$\delta N_n < \frac{N_1}{m!}\prod_{i=1}^{n-1}\xi_i \quad ,$$

where

$$\xi_i = \lambda_{i,i+1}T \text{ if } \Lambda_{i+1}T < 1 \quad ,$$

$$\xi_i = \lambda_{i,i+1}/\Lambda_{i+1} \text{ if } \Lambda_{i+1}T > 1 \quad ,$$

and m is the number of times T appears after the expressions for ξ_i have been substituted.

Refining the Upper-Bound Estimates for the Case of High Burnup. The above equations neglect burnup of parents. In the case of high burnup, a second procedure may be more appropriate. The absolute upper bound of the increase in population of a sequence member j can also be written as the product of N_1 and the branching ratios of preceding members,

$$\delta N_j < N_1 \prod_{i=1}^{j-1}\frac{\lambda_{i,i+1}}{\Lambda_i}$$

which assumes that none of the N_i have been lost and that reactions or decays have occurred with every preceding member.

Combining the two bounding methods, a population change is least upper-bounded by the choice of j yielding the smallest value,

$$\delta N_j < \frac{N_1}{m!}\left[\prod_{i=1}^{j-1}\frac{\lambda_{i,i+1}}{\Lambda_i}\right]\left[\prod_{k=j}^{n-1}\xi_k\right] \quad .$$

Decay Activity, Biological Hazard Potential, Waste Production Rate, and Decay Thermal Power. When a nuclide may be produced in more than one way, the population will equal a sum of terms corresponding to all possible sequences, plus one for the original number present, if any. Because the populations are sums of upper bounds, the results themselves are upper bounds.

The decay activity for the nuclide is the product of the population and the radioactive decay constant. Similarly, the waste production rate is the product of the population and λ_R, which represents the probability (per unit time per nucleus) of removal from the system. The biological hazard potential of the nuclide is calculated by dividing its activity by the smallest maximum permissible concentration for that nuclide found in 10 CFR 20 (Ref. 41). The decay thermal power for the nuclide can be found from its decay activity and deposited energy per decay.

Precision of Estimates. For each sequence $1 \rightarrow 2$, the exact contribution to the population of the daughter nuclide is given by[42]

$$\delta N_2 = \frac{\lambda_{12}N_1}{\Lambda_2 - \Lambda_1}\left(e^{-\Lambda_1 T} - e^{-\Lambda_2 T}\right) \quad .$$

The precision of the result is limited by the assumption that we can neglect contributions to nuclide population due to higher-order sequences (such as $1 \rightarrow 2 \rightarrow 3 \rightarrow 2$ or $1 \rightarrow 2 \rightarrow 1 \rightarrow 2$). The error resulting from this assumption can be quantitatively upper-bounded with the method described in this article.

Summary of the Technique. The foregoing method is always valid as an upper bound if the flux-averaged microscopic cross sections do not change appreciably in time or over the volume considered. (The code described in the previous article is subject to the same limitation.) The analytic method does not require evaluation in a series of time steps; the calculation is done only for the time of interest. It gives an upper-bounded estimate of population by nuclide; hence it also gives estimates of radioactivity, biological hazard potential, waste-production rate, and decay thermal power. Calculations using the technique described here require, except in cases where the $\sigma_{(14)}t$ approximation is valid, the energy-averaged values of $\langle\sigma\ell\rangle$ as a base data. The technique is especially useful in providing a quantitative upper bound on errors arising in analytical or computational techniques which neglect multiple-neutron reaction sequences.

Author: G. P. Lasche

Lithium Safety Considerations

Molten lithium and lead-lithium ($Li_{17}Pb_{83}$) have been proposed for several fusion-reactor designs. The possibility of Li combustion is greatly minimized by passive design measures, such as intermediate sodium loops, steel-lined concrete, inerted containments, minimum-surface-area catch basins, and prepositioned low-density graphite.[43] Nevertheless, the large quantity of potential chemical energy in lithium prompts us to further examine the consequences of lithium-air-water interactions. This examination is also important for present and future lithium experimental loops, since these facilities are often located in buildings containing air atmospheres and standard plumbing systems. Since the reactions of sodium with water and air have been studied extensively during the engineering development of the liquid-metal fast-breeder reactor (LMFBR), we will compare lithium behavior with sodium behavior whenever possible.

Reactions with Water. Solid (cold) Li is considerably easier to handle than solid Na. If a chunk of solid Li is dropped in water, it fizzes like a selzer tablet and skitters around on the surface until it is consumed. Molten (500°C) lead-lithium dropped through air into 95°C water in a closed vessel exhibits a very modest reaction, producing only a very slow evolution of H_2 bubbles.[44] But molten (500°C) Li injected *under* 95°C water results in an explosion, with a pressure rise of ~2 MPa at a time 513 ms after injection.[44]

One possible explanation for these explosion is rapid vaporization of water into steam. A second hypothesis involves the immediate release of hydrogen, transport of the hydrogen to the surface, and a hydrogen-oxygen explosion. A third hypothesis involves high-temperature dissociation of LiH, which is formed by reaction of liquid lithium and water. The heat released by the Li-water reaction raises the temperature of the mixture to above the 997°C LiH dissociation temperature. The resulting free H_2 has a pressure of 600 MPa if there is no available expansion volume.[45] At a free liquid surface, the H_2 may bubble out before it dissolves, and free H_2 above the liquid can react with any free oxygen there. This third explanation is also used by Muhlestein to explain the sudden rise in pressure and free hydrogen concentration in experiments in which molten lithium interacted with concrete[46]; the sudden increases coincided with a liquid temperature near 1000°C.

The mechanism of heating followed by LiH dissociation suggests a passive safety feature not listed in the beginning of this article: placing marble-sized steel balls in catch basins to provide heat absorption capacity in the event of Li spills.[47]

Interaction of a large quantity of lithium with a relatively small amount of water could be fairly quiescent, due to the high heat capacity of the extra lithium. However, if the local temperature reaches 1000°C, the sudden production of hydrogen pressure can be destructive to a closed system. For this reason, lithium-to-water heat exchangers are not recommended. The same is not true of sodium-to-water heat exchangers, in which high-pressure water leaking into sodium continuously evolves hydrogen that forms a gas barrier and minimizes further contact between the sodium and water.

Reactions with Air. The interaction of cool (230°C) and hot (510 to 540°C) molten lithium with nitrogen, dry air, and moist air have also been studied by Muhlestein.[47] The nitrogen interaction was very mild, and the lithium-pool temperatures immediately started to decrease. A crust of Li_3N formed on the surface. Although such a crust over a catch basin is helpful because it separates the Li and air reactants, nitrogen leakage *into* a Li system is undesirable because nitrogen concentrations above 2000 wppm greatly enhance the corrosion attack of lithium on steels. At very high nitrogen concentrations (1800 wppm at 200°C or 66 000 wppm at 500°C), the Li_3N precipitate can clog pipes.

In Muhlestein's experiments with dry air, the initial lithium temperatures (230 and 510°C) did not have a significant effect. In both cases, an immediate reaction drove the temperature up to a peak of 1050°C in only a few minutes. The pool temperature oscillated around 1000°C for about an hour, and then steadily cooled to 500°C in 5 h. For moist air, the hot (540°C) lithium reacted immediately, but the cool lithium did not begin to react for 30 min. Once the

reactions began, both hot and cool lithium pools reached the same 1050° peak, but the cooling rate was slower (down to 800°C in 5 h) than for dry air.

Since Muhlestein's experiments reached temperatures above the LiH dissociation temperature without releasing a pulse of hydrogen pressure, it appears that the water vapor in air is not a major energy contributor to the reactions observed. With cool lithium, however, the water vapor appears to cause a delay before the reaction begins. If the delay is long enough, the lithium temperature could decrease to a level that will not permit violent reaction.

Molten Lithium Reactions with Concrete. The lithium-concrete experiments[46] at Hanford Engineering Development Laboratory (HEDL) released more energy and reached higher temperatures than similar sodium-concrete experiments. The lithium initially reacted with water near the concrete surface, producing heat which drove more water to the surface. In time, enough heat was generated to drive more energetic lithium reactions with SiO_2 and Fe_3O_4 in the aggregate of the basalt-and-magnetite concrete, producing elemental Si and Fe, respectively. In some cases 1000°C was reached, and the LiH dissociated, producing a pressure and hydrogen concentration pulse. If free oxygen was also present, the hydrogen burned.

The time needed to generate enough heat to initiate the more energetic reactions of lithium with concrete aggregate depends on the geometry. In the cases in which energetic reactions occurred, the heating rate suddenly increased about 7 h after the experiment began and at about 300°C. The Li temperature then increased to ~900°C in the next hour, and it reached the 997°C LiH dissociation temperature ~10 h after the experiment began.

The lengthy time before the heating rate became large indicates that if a spill on steel-lined concrete is quickly drained away, the small amount of residual lithium in steel cracks could be insufficient to heat the concrete aggregate to the threshold of energetic reactions. Alternatively, if the concrete is designed with aggregate that is nonreactive with hot lithium, the temperature would not reach the LiH dissociation temperature.

Firefighting Considerations. Under contract to LLNL, the Energy Technology Engineering Center (ETEC) completed a series of experiments with lithium, water, and air in 1981. In one experiment, solid (encrusted) lithium was heated with a torch in dry open air. Ignition did not occur until the temperature was well above the melting point. The lithium burned with a very short, intense flame a few millimetres high; a bare hand held ~20 cm above the flame was not burned. Therefore, if a lithium spill somehow ignites in a fusion-reactor building, and the flame is not in direct contact with activated reactor components, an extremely large fire will be required to heat the entire containment atmosphere before activated components could be vaporized.

In a second ETEC experiment, water droplets at 20°C were sprayed at the burning lithium, generating a white smoke. The water droplets appeared to vaporize in the lithium flame. High-speed photography revealed many brief hydrogen flares that were not visible to the naked eye.

In a third ETEC experiment, burning lithium was placed in contact with insulation and fire-fighting equipment. The results of this experiment are summarized in Table 8-7. As the table shows, carbon microspheres were most effective in starving a lithium fire of oxygen and providing heat-absorption capacity.

Both HEDL and ETEC have investigated methods of extinguishing lithium fires. If air is a reactant, the two best methods are inert-gas flooding and application of low-density carbon powder. If water or concrete are reactants, the amount of water, concrete, or lithium in contact should be limited by removing unreacted material or by adding a barrier to the interface. Addition of a nonreacting heat sink can both prevent the more energetic lithium reactions and avoid the sudden release of hydrogen that is due to high-temperature LiH dissociation.

Summary. Lithium reactions with air, water, and concrete are different from sodium reactions and can be violent. Geometrical considerations—including surface-to-volume ratio, heat capacity, temperature of the reactants, and heat-transport properties—are essential in predicting the result of an interaction.[48] If reasonable design measures are taken, however, liquid

lithium can be safely used in fusion reactors. These measures include using an intermediate heat-transfer loop, an inerted containment, steel-lined concrete, minimum-surface-area double-walled steel catch basins, and preplacement of heat-sink material and low density graphite in potential spill areas.

Authors: J. A. Blink (LLNL) and N. J. Hoffman (Energy Technology Engineering Center)

Reactor Design Studies

Many imaginative schemes have been devised for protecting the walls of an inertial-fusion reactor. Examples include dry walls of carbon and tantalum, gas-protected walls, wetted walls, magnetic protection, and thick layers of liquid metal.[49] The design freedom that makes such diverse solutions possible is a result of the separability of the fusion plasma from the reactor cavity and energy-conversion blanket. After much comparative analysis, we favor the liquid-metal-wall (LMW) concepts because of their simplicity, ease of tritium breeding and recovery, long lifetime, low induced radioactivity, and adaptability to both laser and heavy-ion-beam drivers.

The two functions of a thick region of lithium in LMW fusion-reactor concepts are to protect the structure from neutron damage and to minimize the structural shock loads from the fusion pulse. The jet array in the HYLIFE reactor concept is designed to vent and cool the hot gas produced when the short-ranged fusion product energy vaporizes the line-of-sight jet surfaces. The venting of the gas reduces the impact of the liquid on the structure.[50] This process is facilitated by the dissipation (by liquid-liquid interaction) of a substantial fraction of the kinetic energy of the liquid expansion from the neutron energy absorption. The cooling of the gas substantially reduces the gas pressure on the wall.

Injecting liquid metals directly into the chamber, however, brings new technical problems. We must understand the hydrodynamic response of liquids with free surfaces to rapid energy addition (both surface and volumetric) and subsequent liquid impact and gas pressure on the walls. We must also understand the fluid-injection stability limits, pump-design considerations, and erosion and corrosion of structural material by the liquid metal. We have made excellent progress in understanding these phenomena, and the LMW concepts exemplified by HYLIFE still look attractive.

Material	Results
Aluminum foil (four layers)	Almost immediate hole; no sparking or spalling.
Carbon steel plate	No gross degradation; several reaction-product rings noted.
Floor tile (vinyl asbestos)	Violent reaction; hole produced; sparking and spalling.
Concrete	Violent reaction; sparking and spalling.
Leather gloves	Immediate hole; sparks flew; the glove burst into flames.
PVC gloves	Almost immediate hole; black carbon smoke coated the lithium, extinguished the fire, and left 1 of the 2 g of Li under the residue.
Asbestos gloves	Burned a hole in the glove.
Goggles (full-face Jones)	Lithium poured on the face ran off; lithium placed on the inside melted a hole without violent reaction.
"Cereblanket" insulation (50% Al_2O_3-50% SiO_2	Violent reaction; hole produced; experiment repeated on oven-dried insulation was identical.
"Therme-12" calcium-silicate insulation	Violent reaction; sparks; hole usually produced; experiment repeated on oven-dried insulation was identical.
Quartz wool (SiO_2)	Reaction produced sparks and burning lithium ejecta.
NaX (a sodium fire extinguishment)	Reaction produced a fire the color of sodium flame.
Aluminized material (fire suit)	Immediate hole; a flame flared and the base material charred.
Carbon microspheres	Smothered and cooled the fire almost immediately; the microspheres swelled as they heated, increasing the coverage.

Table 8-7. Results of placing 2 to 4 g of ignited Li in contact with various materials.

During 1981, we continued our studies on fluid-mechanics issues in the HYLIFE reactor concept. We used the 1980 flow-rate-optimization results to select a new HYLIFE design point at repetition rate = 1.5 Hz, yield = 1800 MJ, and gain = 400. We expanded our analysis of the hot-gas flow in the HYLIFE chamber from the one-dimensional analysis of last year[51] to a two-dimensional analysis in the axial direction as well as in the radial direction.[52] We also sponsored an experimental study on the stability of lithium jets at the University of California at Davis.[53] We concluded our feasibility study of helical rotor electromagnetic pumps at the Energy Technology Engineering Center. We also performed new estimates of the induced radioactivity in the HYLIFE reactor.

One of the limitations of HYLIFE is that substantial flow rates are required to ensure the reestablishment of the liquid-metal blanket configuration between pulses. The

practical repetition-rate limit appears to be in the range of 1 to 2 Hz. Our JADE concept addresses this issue and offers a configuration that slows the liquid metal flow using a porous fiber-metal structure. This structure acts like a great liquid-metal saturated sponge. It holds over 10 times its own mass of liquid metal and controls the flow such that the average residence time of the fluid will be 5 to 10 shots. The JADE concept allows the system a pulse repetition rate of 5 to 10 Hz, using only 15% of the liquid-metal flow rate of HYLIFE.

In the following nine articles we describe our progress in solving some of the design problems associated with both HYLIFE and JADE.

Authors: M. J. Monsler and J. Hovingh

Table 8-8. Characteristics of the 1978 and 1981 HYLIFE designs.

Characteristics	1978 HYLIFE	1981 HYLIFE
System parameters		
Fusion power (MW)	2700	2700
Gross thermal power [MW(t)]	3215	3170
Gross electric power [MW(e)]	1255	1236
Net electric power [MW(e)]	1060	1007
Net system efficiency (%)	33	32
Tritium breeding ratio	1.7	1.0 to 1.7 (1.6 used)
Laser and pellet parameters		
Beam energy (MJ)	3	4.5
Pellet gain	900	400
Yield (MJ)	2700	1800
Repetition rate (Hz)	1	1.5
Laser efficiency (%)	3	5
Laser power consumption [MW(e)]	100	135
Fusion energy gain	27	20
Fusion chamber		
Radius (m)	5	5
Height (m)	8	8
Material	2-1/4 Cr-1 Mo	2-1/4 Cr-1 Mo
Midplane neutron flux (MW/m^2)		
without lithium	6.9	6.9
with lithium	0.32	0.74
Midplane neutron damage (dpa/21 full-power years; limit = 165 dpa)	74	164
Midplane neutron damage (appm He/21 full-power years; limit = 500 appm He)	90	269
Lithium array geometry		
Number of jets	300	175
Midplane jet diameter (m)	0.2	0.2
Midplane packing fraction	0.50	0.57
Inner array radius (m)	0.43	0.52
Outer array radius (m)	2.43	1.82
Effective array thickness (m)	1.00	0.74
Flow parameters		
Midplane jet velocity (m/s)	9.9	13.3
Injection velocity (m/s)	4.4	9.48
Injection head (m Li)	1.0	4.6
Total head (m Li)	23.5	17.6
Array flow rate (m^3/s)	93.3	72.2
Total pump flow rate (including IHXs) (m^3/s)	128.7	96.0
Total lithium pumping power [MW(e)]	23.9 (72%)	22.9 (35%)
Total lithium inventory (m^3)	2700	1630
Number of lithium loops (excluding IHXs)	16	11
Lithium outlet temperature (°C)	500	500
Lithium temperature rise per pulse (°C)	13	18

HYLIFE Design Progress

The driver and target performance criteria (for driver energy, pulse repetition rate, and target gain) are the starting points in determining the dimensions and operating parameters of the HYLIFE reactor. During 1981, we selected a new design point for HYLIFE to utilize lower fusion-gain targets and a higher-repetition-rate driver. The design point has evolved from a driver energy of 3 MJ, a gain of 900, and a pulse-repetition frequency of 1 Hz in 1978[54] to the current values of 4.5 MJ, 400, and 1.5 Hz, respectively. The new design requires a target performance intermediate between the conservative and optimistic target-gain predictions.[55] Note, however, that the desired HYLIFE fusion power of 2700 MW is unchanged. Table 8-8 gives a detailed comparison of the 1978 and 1981 HYLIFE designs, and Fig. 8-18 shows the power balance for our current HYLIFE design. Several of the significant design-point changes are discussed below.

Liquid-Metal-Wall (LMW) Geometry and Radiation Damage. Parametric calculations[56,57] produce values for the minimum liquid flow rate and pumping power when the lithium-array geometry has an inner radius of 0.52 m, an effective thickness of 0.74 m, a midplane packing fraction of 57%, and a midplane velocity of 13.3 m/s. For the same 0.2-m midplane jet diameter as in the 1978 HYLIFE design, the number of lithium jets decreases from ~300 to ~175.

For the new LMW geometry, liquid-impact and thermal-stress considerations require a first-structural-wall (FSW) thickness of 3.6 cm. Gas-impact calculations (discussed in the next article, "HYLIFE Chamber Phenomena") show that the FSW thickness in the range from 2.6 to 11.3 cm

when the new 1800-MJ target is used. If a 3.6-cm-thick FSW is inadequate, a thicker, internally cooled wall can be used, or the gas impact can be reduced by use of a vortex flow scheme.[58]

Based on one-dimensional neutronic calculations, the new LMW geometry increases the midplane FSW flux from 0.32 to 0.74 MW/m^2. In 21 full-power years (30 years at a 70% capacity factor), the radiation damage to the wall is 164 displacements per atom (dpa) and 269 atomic parts per million (appm) He using the new LMW geometry. Thus, the 1981 HYLIFE first structural wall will operate up to its damage limit from both radiation-damage and mechanical-load considerations.

Flow Rate and Temperature Rise. The parametric calculations yield a jet-array flow rate of 72.2 m^3/s, an injection velocity of 9.5 m/s at the top of the 0.5-m-thick nozzle plate, and an injection head of 4.6 m. For 20-mm-thick lithium flows on both sides of the FSW, the flow rate is 7.5 m^3/s at a velocity of 6 m/s to provide the same bulk-liquid temperature rise. The beam-aperture protection flow is 5.4 m^3/s, as before. These two flows also contribute to the 14-m^3/s neutron reflector cooling. Therefore, the chamber flow total is 86.2 m^3/s. The flow rate in the intermediate heat exchanger (IHX) is 9.8 m^3/s, as before. Hence, the total flow through pumps is 96.0 m^3/s, or 75% of the original design, and the resultant temperature rise in the array is 18 K.

Pumping Power. The total pump head in the vessel circuit is distributed as follows: 1.5 m to friction, 2 m to suction (electromagnetic pumps), 8 m to the reactor chamber, 0.5 m to the nozzle, 4.6 m to the injection head, and 1 m to pipe diameter. This gives a total pump head of 17.6 m, equivalent to 82 kPa. The injection head is based on a 9.5-m/s injection velocity. For an electromagnetic pump with only 35% efficiency, the vessel pumping power is 20.6 MW(e).

The pump head for the primary lithium circuits is estimated to be 18 m (Ref. 59). This head is due to the pressure drop across the shell side of the IHX. No gravity head is included, since the primary loops begin and end at the same elevation when nonsuperconducting electromagnetic pumps are used. Because of the similar head

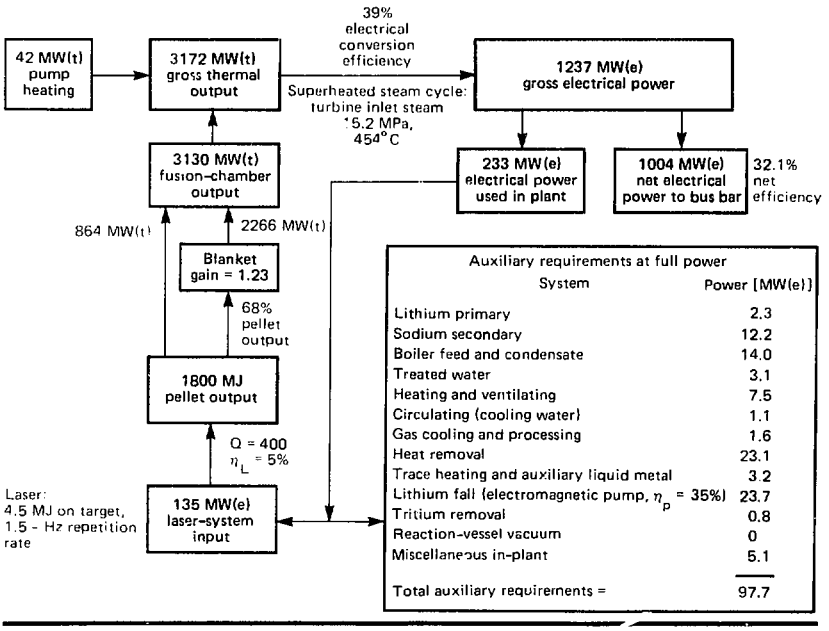

Auxiliary requirements at full power

System	Power [MW(e)]
Lithium primary	2.3
Sodium secondary	12.2
Boiler feed and condensate	14.0
Treated water	3.1
Heating and ventilating	7.5
Circulating (cooling water)	1.1
Gas cooling and processing	1.6
Heat removal	23.1
Trace heating and auxiliary liquid metal	3.2
Lithium fall (electromagnetic pump, η_p = 35%)	23.7
Tritium removal	0.8
Reaction-vessel vacuum	0
Miscellaneous in-plant	5.1
Total auxiliary requirements =	97.7

Fig. 8-18. Power balance for a laser-driven HYLIFE power plant using electromagnetic pumps.

requirements, both the vessel and the primary pumps are of similar design. The primary pumping power for 35%-efficient pumps is 2.3 MW(e).

The total lithium pumping power in the present design is 22.9 MW(e). There are 11 recirculation pumps at 7.84 m^3/s; each pump has a total head of 17.6 m. There are two primary pumps with this same pump head and with a flow rate of 4.9 m^3/s. About 82% of the lithium pump input, including the hydraulic power, is deposited as heat in the fluid. When the pump heat from the sodium and steam loops is added, the total pump heating is 40 MW(t).

Lithium Inventory. The inventory of lithium in the jet array is 48.1 m^3. The reflector inventory is 18.7 m^3 if a 6-m/s flow velocity is used. The 4.6-m injection-head pool will occupy 54 m^3 if its inner and outer radii are 0.5 and 2.0 m, respectively. Finally, if an additional 100 m^3 is added for miscellaneous regions, the chamber contains ~220 m^3 of liquid lithium.

The vessel piping inventory scales as the flow rate with a correction for the reduced vertical runs due to the lower head requirement. The resulting lithium inventory in pipes is 1190 m^3 in the present design compared with 1930 m^3 in the original design. When the IHX and tritium-processing inventories (250 m^3) are added, the total lithium inventory becomes 1660 m^3, or 61% of the original.

Author: J. A. Blink

Major Contributors: M. J. Monsler, W. R. Meier, J. H. Pitts, and J. Hovingh

HYLIFE Chamber Phenomena

During 1981, we examined the hydrodynamic response of the HYLIFE reactor concept to large ICF microexplosions. Typically, at least 65% of the energy released is in the form of high-energy neutrons (up to 14 MeV). Since the neutrons penetrate deeply into the lithium, the maximum specific energy acquired is far below the cohesive energy, and the outward-directed momentum is, to first approximation, independent of the lithium mass. Moreover, the impulse imparted to the reactor walls is delivered more or less uniformly over a time interval equal to or greater than the natural period of the wall, so that the peak wall stress derives not from the momentum itself, but from the maximum rate of arrival of the momentum.[60]

The remaining energy released by the pellet is "short-range" energy in the form of low-energy x rays and ionic debris which penetrate only a very thin layer at the exposed outer radii of the innermost jets. As a result, the specific energy of the lithium in this layer increases by several orders of magnitude, and the instantaneous pressure may exceed 100 GPa. A strong shock then moves out, but it is quickly caught and attenuated by a rarefaction centered on the free inner surface. This causes a blow-off of lithium plasma into the inner cavity (void) bounded by the innermost jets. Most of the short-range deposition then reappears as inward-directed kinetic energy. As a consequence of the energy-focusing effect of the convergent geometry, the free surface is accelerated and the leading edge may implode on the cylindrical axis with a velocity of several hundred mm/μs. The kinetic energy is then reconverted to internal energy. The substantial fraction—if not the major fraction—of this internal energy is in the form of radiation. A more detailed description of these events, and the subsequent fireball formation, has been given elsewhere.[61] Calculations have been made of the drag exerted on the jets as the plasma expands through the jet array[62] and of the impulse delivered to the wall when impact occurs.[63,64]

In all of the previous work, the fusion target was modeled as a line source, rather than as a point source, so that the flow could be treated as one-dimensional or quasi-one-dimensional, with cylindrical symmetry. Axial pressure relief was thereby ignored; the source strength was taken to be that obtaining at the plane of the fusion pellet, which makes it possible to derive an upper bound on the wall loading. But the energy deposition varies roughly inversely as the square of the distance from the pellet, and the energy and mass density at the pellet plane are at least six times the average values overall. Therefore two-dimensional calculations are necessary to provide more realistic results, as well as information on injector (nozzle plate) loading We have completed these calculations and

present our method and results in this article. All calculations were performed for the maximum conceivable yield, 2700 MJ.

Problem Formulation. Figure 8-19 shows an end view of the jet array at the plane of the fusion pellet. Neglecting the staggered jet row that protects the beam ports, there is approximate axial symmetry, which is the justification for ignoring circumferential motion in comparison with radial and axial flow components. Furthermore, we assume that the jets are everywhere parallel to the vertical axis and are stationary with respect to the motion of the plasma: the plasma is initially contained in the jet-free "chimney" region defined by $0 < r \leq R_0, 0 < z \leq Z$. We also assumed symmetry on either side of the plane that passes through the fusion pellet and perpendicular to the axis. The jets are initially surrounded by a vacuum, which is the condition of the outer, jet-free region as well. A closed nozzle plate located at Z [Fig. 8-19(b)] is specified to place an upper bound on the loads and stresses.

Our mass-conservation model includes vaporization of the material at the surface of the jets, due to convection and radiation.[65] Any mass vaporized from the jet surface is assumed to mix instantaneously with the plasma, so that local thermodynamic and mechanical equilibriums are maintained.

The radial and axial momentum-conservation models include both skin-friction effects and the material contributions to pressure and radiation pressure.[65] The impulse delivered to the jets is due partly to form (or profile) drag and partly to skin friction. Shear retardation of the plasma has been modeled and was deduced for this purpose from quasi-steady parallel-flow theory.[66] Both the skin-friction coefficient and the convective heat-transfer coefficient, h, are, in general, functions of the local Reynolds and Mach numbers; h also depends weakly on the Prandtl number.

The rate at which the specific internal energy of the plasma changes according to our two-dimensional model differs from our one-dimensional model principally in that we have neglected radiation diffusion in the plasma.[65] We did so because including radiation diffusion in the plasma substantially increases the computational cost but yields relatively little in return. This was verified by a series of one-dimensional calculations in a Eulerian coordinate frame with identical radial discretization. We found that when radiation transport in the plasma was omitted, there was an insignificant difference in the pressure on the wall as a function of time. As expected, the temperature near the wall was somewhat higher in this case, but even this discrepancy will be diminished by the vorticity developed in our two-dimensional calculations (vorticity is absent altogether in one-dimensional calculations).

In physical terms, as long as the surface temperature remains below the vaporization

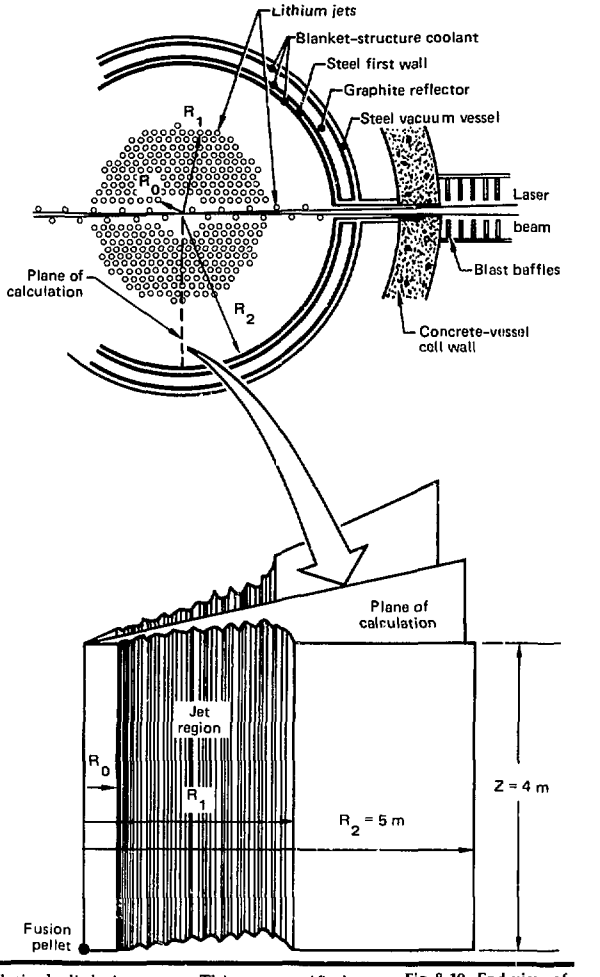

Fig. 8-19. End view of the jet array at the plane of the fusion pellet.

level at the ambient pressure, any energy transport from the plasma diffuses into the interior of the liquid. If the energy flow at the liquid surface should exceed that required to just raise or maintain the surface temperature at the local vaporization state, the excess goes towards vapor generation. We assume that such vapor mixes instantaneously with the local plasma.

The initial short-range deposition and subsequent lithium implosion from a one-dimensional solution at 60 μs (just prior to fireball contact with the jet array) was mapped onto the pellet plane. The "initial" internal and kinetic energies at any other elevation were obtained by inverse-square scaling.[65] To first approximation, the momentum generated by the plasma varies with the product of the mass density and the square root of the specific energy. Maximizing the mass-density product would seem to be indicated to maximize the wall loading and thus obtain a worst-case scenario. Our one-dimensional calculations showed, however, that when the plasma mass was increased by a factor of 4 (by jet surface vaporization), for a fixed initial plasma energy, the impulse delivered to the wall (as measured by the peak hoop stress) actually declined by almost the same amount.[63] The reason is that the added momentum was imparted to the jet array before the plasma—now very much cooled as a consequence of mixing with jet vapor—arrived at the wall. The one-dimensional calculations clearly showed that the peak hoop stress due to plasma impact resulted when the initial specific energy of the plasma was highest.

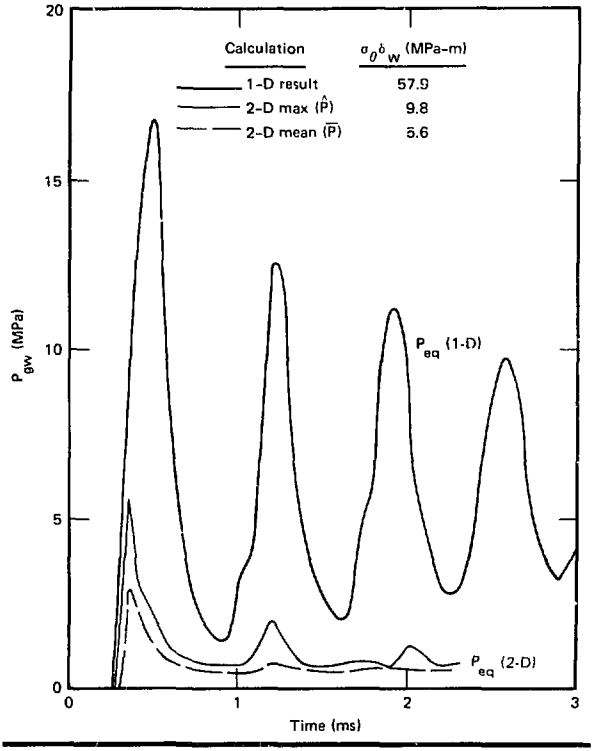

Fig. 8-20. Pressure exerted on the cavity wall as a function of time, for the case of the adiabatic plasma.

Method of Solution. A two-dimensional computer code, employing explicit finite-difference analogs of the system, was formulated and assembled on a PRIME-750 minicomputer. The program structure was based on a modification[65] of the AFTON codes.[67,68] The complete set of finite-difference equations, together with details of the minicomputer code and the performance thereof, are given in Ref. 69. The equation-of-state and opacity data for lithium are described in Ref. 70.

We employed a computational mesh of 96 × 77, and chose a Eulerian coordinate frame. The principal reason for this latter choice derives from our one-dimensional earlier calculations, which were performed in Lagrangian coordinates.[63] We found that the steep velocity gradient that developed at the free surface of the expanding plasma resulted in too coarse a spacial resolution when impact with the wall occurred, even with very fine initial spacing in the plasma. The effect was to diminish the peak pressure recorded on the wall (although the impulse itself was unaffected since momentum conservation was rigorously enforced). Eulerian coordinates were also chosen because they are more efficient.

Results of the Calculations. From the standpoint of wall loading, there are two cases of interest, each of which is discussed separately in detail below. The worst-case scenario [case (a) in Ref. 63] is that of an adiabatic plasma in which no heat or mass is exchanged with the jets, so that the impulse delivered to the wall is at a maximum. If heat transfer and mass transfer are admitted, the most optimistic situation

[case (g) in Ref. 63] is that the 200-mm-diam jets disassemble into 2-mm fragments before or during the cross-flow of plasma, so that the available jet surface is increased and the wall impulse is less. In both cases, the one-dimensional calculation resulted in peak hoop stresses in the first wall that probably exceed the allowable design limit.

The Adiabatic Plasma. At 260 μs, just prior to the first impact on the wall, the momentum density is highest near the pellet plane. The first impact occurs at the top, however, where the lithium-injector nozzle plate meets the wall. The initial axial-pressure gradient creates a strong flow up the jet-free chimney ($r < R_{fl}$) which results in the development of a downward-moving shock. The shock front moves downward at a relative velocity of $\sim$12 mm/μs. The pressure behind the shock radially accelerates the relatively low density plasma below the nozzle plate and creates a shear layer in the wake.

At 400 μs, the relative velocity of the downward-moving shock slows to $\sim$3 mm/μs, and several shocks have formed by the wall impact. The foremost of these shocks is near the intersection of the wall and the nozzle plate. At 500 μs, the original downward-moving shock is almost entirely attenuated, the several fronts that originated at the wall have expanded and coalesced, and interaction of the inward-moving plasma with the outermost jets occurs near the nozzle plate. A region of intense vorticity develops behind these fronts; this vorticity is largely responsible for bringing the plasma to overall mechanical equilibrium much more rapidly than was the case in our one-dimensional calculations.

The pressure exerted on the cavity wall is shown as a function of time in Fig. 8-20. The one-dimensional Lagrangian result is contrasted with maximum and space-averaged results from the two-dimensional calculations. Both the one-dimensional and two-dimensional calculations show the characteristic spiking that results from initial impact, followed by subsequent shocks rebounding from the jet array. Cavity equilibrium pressure, P_{eq}, is 4.2 and 0.64 MPa for the one-dimensional and two-dimensional calculations, respectively. Figure 8-20 shows that, for the two-dimensional case, both the maximum pressure, P_{gw}, and the spatially averaged pressure, $\overline{P}_{gw}$, differ little from P_{eq} after 2 ms, whereas the one-dimensional calculation has a much slower approach to equilibrium.

If the wall is to remain elastic under load, the maximum hoop stress is easily obtained by integrating the equations of motion for an internally pressurized cylinder, using the wall-pressure history as the forcing function.[60] In Fig. 8-20 we have tabulated the peak value of the product of the wall thickness times the hoop stress, $\sigma_{fl}\delta_{fw}$ for each of the three forcing functions. The two-dimensional stress is less by a factor of 2, based on the maximum two-dimensional result, and by a factor of 10 based on the mean two-dimensional result.

Figure 8-21 depicts the pressure on the nozzle plate as a function of time. The maximum and average pressures are defined in similar fashion to those at the wall. We see that the maximum pressure decreases from its initial value of 4.9 MPa (cf. Ref. 62) to 2.4 MPa at 100 μs, and then rises sharply to its peak value of 42.4 MPa at 170 μs. The motion below the nozzle plate at "start-up" is initially radial, in accordance with the mock initial conditions accounting for the initial drop in pressure. The axial pressure gradient in the chimney quickly establishes a strong vertical velocity component that stagnates at the nozzle plate. This results in

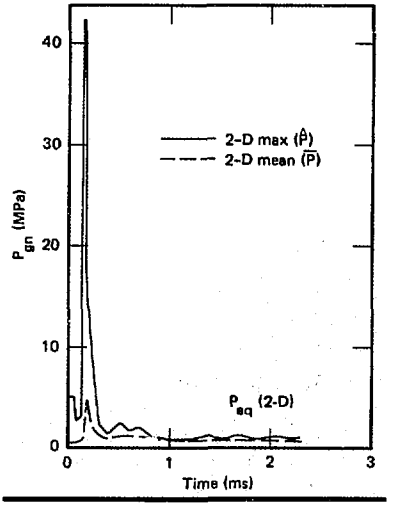

Fig. 8-21. Pressure exerted on the nozzle plate as a function of time, for the case of the adiabatic plasma.

the sharp pressure rise and a downward-moving shock. We see also in Fig. 8-21 that the peak value of the mean pressure, P_{gn}, is an order of magnitude less than the peak value of the maximum pressure, $\hat{P}_{gn}$, implying that the spike is spatially localized in the chimney region of the nozzle plate. The ratio $\overline{P}_{gn}/\hat{P}_{gn}$ would be even smaller had we defined P as an area average (which is more appropriate for determining the overall force on the plate). Moreover, the surge in pressure is short-lived, and mechanical equilibrium is rapidly established; by 1 ms there is little difference between $\overline{P}_{gn}$ and $\hat{P}_{gn}$.

Combined Heat and Mass Transfer (D = 2 mm). In the case of the adiabatic plasma, axial flow up the chimney was responsible for driving the free surface across the nozzle plate to impact the wall ahead of the main body of plasma at the pellet plane. When the jets act as an energy sink, the picture is very much changed. As the hot, low-density plasma enters the jet array, rapid cooling takes place with a corresponding drop in pressure. When the mainly radiative heat flux was too high to accommodate diffusion into the jet interiors, vaporization occurred and the excess energy was returned to the plasma in the form of increased mass.

The one-dimensional and two-dimensional relative energy transports are in remarkable agreement. The first two rows of jets lower the plasma temperature to the point where radiative transport is no longer effective. The residence time of the plasma is too short for convective cooling to make a significant contribution, although convective cooling is the controlling process for eventual condensation.[63]

The cooling effect near the nozzle plate very much weakens the shock in the chimney and the shear layer virtually disappears. The free surface near the nozzle plate substantially lags that at the pellet plane, where contact with the wall first occurs.

Figure 8-22 shows the pressure exerted on the cavity wall, again contrasting the one-dimensional and two-dimensional results, and tabulates the peak values of the hoop stress. Note that the one-dimensional results displayed in Figs. 8-22 and 8-23 are from a Eulerian calculation with the same radial mesh spacing as for the two-dimensional calculation, not from the Lagrangian calculation of Ref. 63. The Lagrangian calculation is considered less accurate, especially when heat transfer to the jets was allowed, since the spatial increments defining the plasma were not congruent with those defining the jets.

The effect of plasma cooling in reducing the average pressure on the wall is about the same in two dimensions as in one, but the maximum pressure is diminished to a lesser relative extent. Nevertheless, Fig. 8-22 shows that, compared with the adiabatic plasma, the peak hoop stress with plasma cooling has been reduced by about 30% when the basis is $\hat{P}_{gw}$ and about 60% when the basis is $\overline{P}_{gw}$. As in the case of the

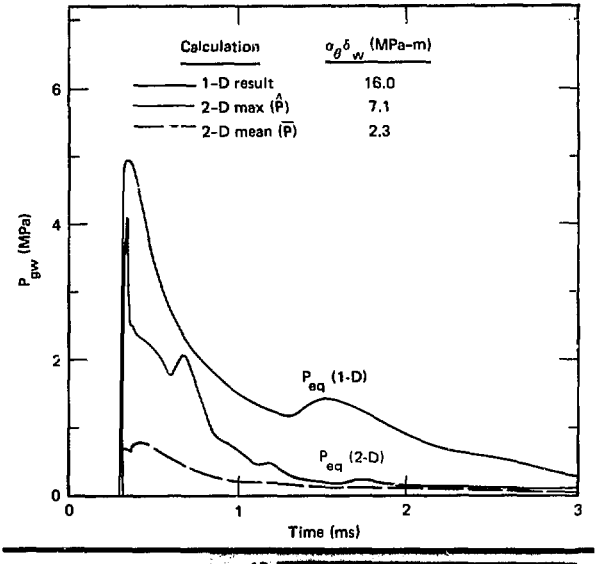

Fig. 8-22. Pressure exerted on the cavity wall as a function of time, for the case of combined heat and mass transfer (D = 2 mm).

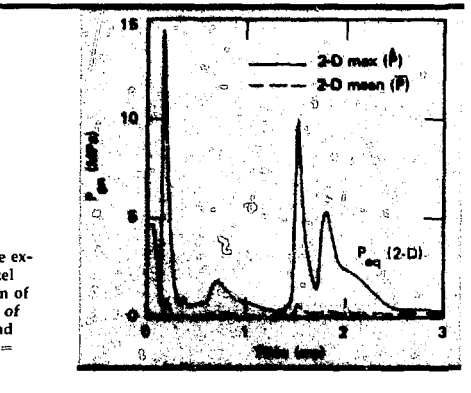

Fig. 8-23. Pressure exerted on the nozzel plate as a function of time, for the case of combined heat and mass transfer (D = 2 mm).

adiabatic plasma, the two-dimensional calculation displays a rapid approach to mechanical equilibrium.

The pressure on the nozzle plate as a function of time is shown in Fig. 8-23. The initial behavior is the same as in the case of the adiabatic plasma, although the peak amplitude of the chimney spike at 170 μs is less by a factor of 3. The surge in pressure at 700 μs ($\hat{P}_{gn}$ = 2.2 MPa) derives from the region near the reactor wall. Its counterpart in Fig. 8-21 begins earlier, at about 500 μs. Both result from the conversion of radial to axial momentum via plasma impact with the wall.

The subsequent pressure spikes in Fig. 8-23, at 1500 and 1800 μs, have no counterpart in Fig. 8-21. For the case of combined heat and mass transfer, contact of the plasma with the wall occurs first at the pellet plane. In addition to the several smaller vortices formed, a large counter-clockwise vortex is created which then sweeps upward along the wall and is reinforced by the arrival of the free surface near the nozzle plate. The flow then sweeps radially inward and collapses on the nozzle plate in the vicinity of the jet-free chimney.

Conclusion. In our one-dimensional calculations, we found that $\sigma_i \delta_{\alpha}$ varied from 58 MPa-m, when heat and mass exchange between plasma and jets were entirely ignored, to 16 MPa-m for the most optimistic situation. Taking account of two-dimensional effects, the present work has demonstrated that, even in the worst case, the value of 58 MPa-m is reduced to between 6 and 10 MPa-m. If the beneficial effects of plasma-jet interaction are fully realized, the equivalent numbers are 2 and 7 MPa-m. We note here that the expected loading from liquid impact, due mainly to isochoric neutron heating, was estimated at ~7 MPa-m.[70] While these loadings are additive, the liquid impact will most likely occur well after the plasma has cooled and condensed, so present design concepts appear sound.

The two-dimensional model has also illuminated a potential trouble spot on the closed nozzle plate near the axis of symmetry, in the "chimney" region. Since the HYLIFE concept has an open nozzle plate in the chimney region, the stresses are probably well within design specifications.

We conclude by emphasizing once again that all of the above results rest on many assumptions, some of which cannot be verified without experiment. In our opinion, more elaborate computational models are not justified without concomitant experiments.

Author: L. A. Glenn

Jet Stability Experiments

A potential problem arises in the use of liquid jets in the HYLIFE reaction chamber. The pulsed nature of laser-fusion microexplosions subjects the reactor vacuum vessel and jet nozzles to sustained vibrations. If the amplitude of these vibrations is large enough, the "ringing" of the entire structure may cause jet breakup, allowing neutrons, ions, and x rays to stream directly onto the structure and thereby drastically shorten the useful life of the chamber. As part of our HYLIFE design study, workers at the University of California, Davis (UCD) theoretically and experimentally analyzed the stability of both cylindrical and sheet water jets under forced vibrations.[71-77]

Cylindrical Jets. Using a water-jet test apparatus (pictured in the *1980 Laser Program Annual Report* in Fig. 9-52), we investigated the breakup of cylindrical jets of 12.7 mm diameter issuing vertically downward from long cylindrical nozzles. Studies were conducted at both 1 atm ambient pressure and at a reduced pressure of about 0.2 atm (Ref. 72); jet velocities were from 1.25 to 5.0 m/s. The nozzles were vibrated transversely using an electromagnetic shaker at frequencies in the range of 20 to 320 Hz and amplitudes from about 0.2 to 5 mm. This vibration produced maximum wave amplitudes in the jet of 100 mm for a fall distance of about 0.9 m.

The range of parameters for our experiments is shown on the nondimensional plot of Fig. 8-24 (Refs. 78-83). The upper boundary is at a ratio of fall distance to water-jet diameter, L/D_0, of about 70. This was fixed by the maximum fall distance available in our apparatus. The range of Weber numbers (We) available was fixed by the range of velocities we could obtain.

In all but three of the approximately 100 photographs analyzed, the jets showed no signs of breakup. This implies breakup lengths in excess of about 70 diameters, even with forced transverse vibration. This is in general agreement with the smoothed data of others, as indicated by the solid curves in Fig. 8-24 which show that breakup L/D_0 ratios in the range of 60 to 100 were measured with no forced vibration. We can conclude that even in the presence of large transverse vibrations, the breakup length of our turbulent cylindrical jets was not reduced over the values found without forced vibrations. These conclusions only hold for the relatively low vibration-forcing frequencies and transverse accelerations employed in our experiments. At higher frequencies and accelerations, the vibrations can induce a jet-"bunching" phenomenon, which can lead to earlier breakup.[84]

The few runs in which jet breakup was observed at our test L/D_0 ratios occurred at very large nozzle forcing amplitudes (~4 mm) and at the reduced pressure of about 0.2 atm. In these runs, the breakup was probably induced by air bubbles, which tended to come out of solution and grow rapidly at the reduced pressure. This is a potential problem area for any fusion reactor employing liquid jets (or liquid film flows) if there are significant amounts of helium or other gases in the liquid.

HYLIFE cylindrical jets are expected to have ratios of fall distance to jet diameter occurring in the region marked "HYLIFE" in Fig. 8-24. This region lies below all the breakup data in the figure except those of Miesse and of Vitman, who employed special nozzles to induce early breakup for fuel atomization studies. We can therefore conclude that the HYLIFE jets are unlikely to experience breakup due to transverse vibrations in the fall lengths in the reactor, provided that gas bubbles are unimportant.

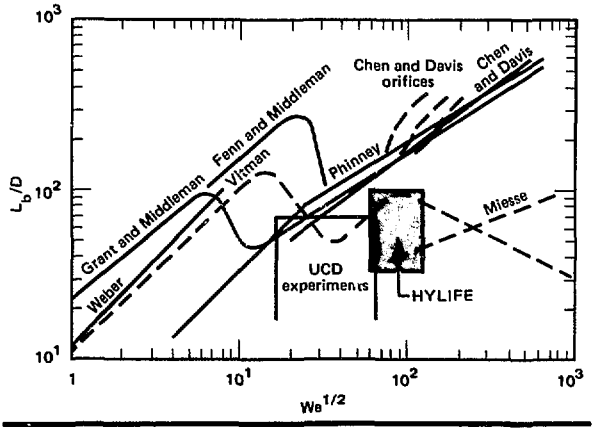

Fig. 8-24. A summary of data on cylindrical-jet breakup.

The cylindrical-jet breakup data (the solid curves) in Fig. 8-24 were all taken using nozzles (usually hypodermic needles) with large ratios of nozzle length to diameter. For ease of comparison with these data, all our experiments were run using long cylindrical nozzles with $L/D_0 \simeq 50$. For our runs where the Reynolds numbers were greater than ~2300, the flow issuing from these long nozzles was a fully developed turbulent flow. McCarthy and Malloy[85] have shown that these turbulent jets tend to break up sooner than laminar jets do at the same Reynolds numbers. In the flow from a well-rounded short nozzle or orifice, the turbulence has no time to develop and the flow will be nearly laminar, resulting in longer breakup lengths. This result is supported by the very long lengths to breakup measured by Chen and Davis[78] (shown in Fig. 8-24) for high-velocity, high-Reynolds-number flows from orifices. This suggests that to minimize the possibility of jet breakup the nozzles in the HYLIFE reactor nozzle plate should be designed with small L/D_0 ratios.

A few experiments were run to see the effect of a collision between two adjacent cylindrical jets of different initial velocities due to transverse vibration.[72] As the wave amplitudes of the jets increased with fall distance, they would eventually collide as they grew more and more out of phase with one another. However, no jet breakup was observed even for jet-velocity differences of up to a factor of 3. Consequently, velocity differences in the jet array, such as might occur in HYLIFE due to a nonuniform liquid head above the nozzle plate, should not cause serious jet-breakup problems.

Rectangular (Sheet) Jets. Several instabilities associated with rectangular jets could cause neutron streaming to the walls of the HYLIFE reactor. One of the instabilities is the breakup of the rectangular jet caused by

horizontal vibrations of the nozzle plate. Another instability is the jet-edge convergence due to surface tension. Rectangular jet breakup was studied at UCD and reported earlier.[73-77] From these experiments and theoretical predictions we can tentatively conclude that the sheet jets in the HYLIFE reactor are unlikely to break up due to transverse vibrations.

Edge convergence, however, may present a problem. As a rectangular jet falls, it not only accelerates but also tends to change in cross section from a rectangular shape toward a round shape because of surface-tension forces. For a sheet jet with a width much larger than the thickness, edge convergence can be modeled as an accumulation of fluid in the two edges of the sheet as the edge fluid is accelerated toward the center by surface-tension forces. In other words, the two edges grow in radius and also tend to converge toward the center of the sheet. This tends to produce a dumbbell-shaped cross section (Fig. 8-25).

The key question is how large the rectangular sheet jets must be so that the edge convergence will have a negligible effect in reducing the total lithium thickness at the midplane. Monson ran a series of small-scale sheet-jet edge-convergence experiments using three different nozzles.[72] These produced sheet jets with an initial thickness of 1.6 mm and initial widths of 5, 10, and 15 mm. The distance to the first convergence point, L_{c1}, was measured, converted to the time to convergence, t_{c1}, and plotted vs the initial sheet-jet velocity.

We then developed a simplified theory to predict the time to edge convergence. We identified three significant times as shown on Fig. 8-25:

- The time when the round edges first touch (*C-C*).
- The time when the two edges have merged (*D-D*), which we defined as the edge convergence time.
- The time when the centers of the two edges would be at the same point, or collocated (*E-E*), if the two round edges simply merged together.

In actuality, as the two round edges make contact, the conservation of mass and momentum causes the liquid to squirt out in a plane perpendicular to the original sheet jet; this is known as the Weber effect. The predictions of our theoretical model bracket the experimental data.

Using this theoretical model, we calculated L_{c1} for a wide variety of rectangular jets with initial widths and thicknesses which might be used in HYLIFE. Our predictions (shown in Fig. 8-26) indicate that the rectangular jets proposed for the HYLIFE design will not converge significantly due to surface tension forces either in the 5-m fall distance to the midplane or in the 10-m fall distance to the bottom of the reactor.

Conclusion. Extrapolating the results of our small-scale water experiments to the large-scale HYLIFE lithium jets, we tentatively conclude that the HYLIFE jets can be reestablished after laser-fusion microexplosions. With careful design the jets should not break up due to instabilities during the relatively quiescent period between

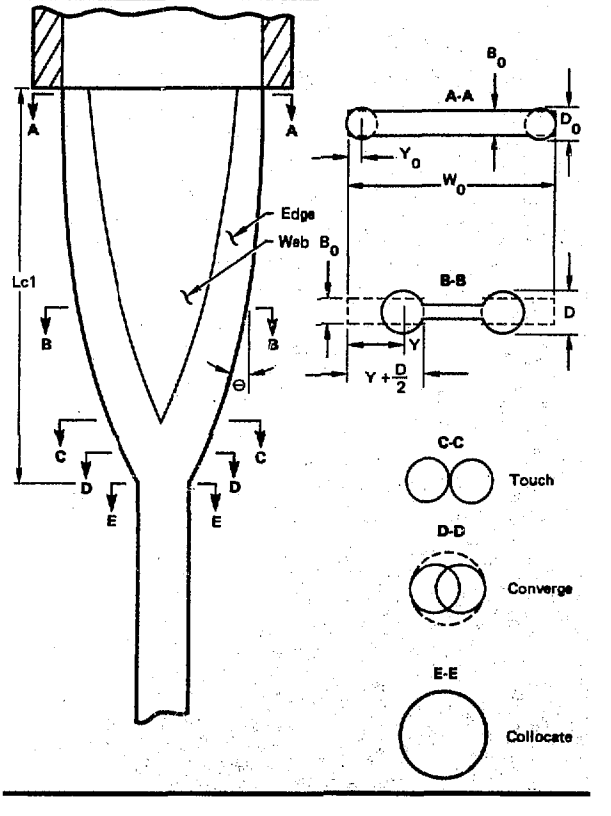

Fig. 8-25. Predicted edge-convergence behavior for lithium sheet jets.

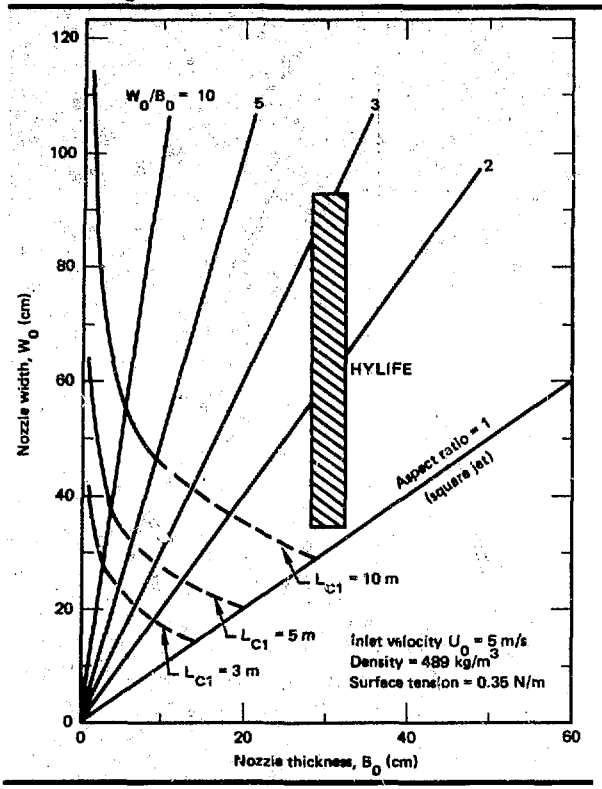

Fig. 8-26. Theoretical model of sheet-jet edge convergence.

microexplosions, even in the presence of structural vibrations.

Authors: M. A. Hoffman and R. D. Monson (University of California, Davis)

Major Contributor: J. Hovingh

Radioactivity in the HYLIFE Reactor

We have applied the techniques described in "Analytical Radioactivity Estimation Technique" (earlier in this section) to the ferritic steel proposed for the HYLIFE reactor vessel, assuming 30 years' irradiation. Using the upper-bounding technique cited in that article, the error in neglecting sequences of third order and higher was estimated to be <0.1%. The exact analytical equation for second-order sequences was then used to calculate radioactivities, biological hazard potential (BHP), and decay thermal powers for the HYLIFE reactor vessel. These results were then compared to computational calculations using the ORIGEN2 code[86] based on an independently determined set of initial densities and compositions. Our comparison detected an error in the data base of the ORIGEN2 library, which included the decay energy of the electron-captured neutrino from ^{55}Fe in the decay heat calculations. Otherwise, the results are in close agreement.

We have also compared the radioactivity of HYLIFE to that of the STARFIRE tokamak,[87] employing the more likely lead-zircate neutron-multiplier option. The comparison showed that the total radioactivity, BHP, and decay thermal power of HYLIFE are impressively small in comparison to the STARFIRE tokamak. This can be attributed to the thick liquid-lithium wall between the fusion neutrons and steel structure in HYLIFE, and to STARFIRE's use of a lead-zircate neutron multiplier and steels with high nickel content (^{59}Ni directly produces ^{60}Co by way of the (n,p) reaction, and ^{58}Ni is largely responsible for helium embrittlement in the steel by way of the (n,γ) and (n,α) reactions).

All D–T fusion-reactor concepts having unprotected stainless steel first walls will have roughly the same radioactivities, BHP, and decay thermal power in their steel walls as the STARFIRE tokamak, adjusted in proportion to wall thickness (as indicated by the argument presented at the beginning of "Analytic Radioactivity Estimation Technique").

The estimated radioactivity, BHP, and decay thermal power for HYLIFE's 2-1/4 Cr-1 Mo steel vessel at shutdown after 30 years' operation are given in Table 8-9 (Refs. 88 and 89). From the figures in this table alone, we can construct decay curves for radioactivity, BHP, and decay thermal power as a function of time after shutdown. Activation of minor assay impurities and of the exterior shielding, structure, and atmosphere are expected to make only a small contribution to the totals, as is the case in STARFIRE. These refinements are currently in progress.

Radioactive waste from activated fusion-target debris will be of negligible concern if (in addition to hydrogen, lithium, carbon, and oxygen) lead alone can be used in target fabrication,[89] such as for the pusher

material in a direct-illumination target. Lead can be kept to 1 at.% in liquid lithium by an efficient eutectic separation process. This amount gives rise to an equilibrium level of 8.18 MCi of ^{203}Pb and 7.66 MCi of ^{209}Pb in the liquid lithium, with half-lives of 52.1 and 3.28 h, respectively. Also, 0.0053 MCi of ^{204}Tl and 0.023 MCi of ^{203}Hg would be present, with half-lives of 3.77 years and 46.6 days, respectively. Secondary activation of these activation products is expected to be of negligible concern.

If we assume that the activated target debris is removed at the same rate at which it is added, then, if all the waste from removing activated debris from the liquid lithium for 30 years' operation were to be gathered together with no reprocessing, there would be a sum total radioactivity of only 0.021 MCi—less than 0.01% of total plant activity. After 3.77 years, there would remain 0.0027 MCi, decreased by half every 3.77 years thereafter.

Because of its low level of activity and short decay time, most of the lead removed from the reactor could probably be recycled directly at the plant in the manufacture of fusion targets.

Radioactive waste from activated target debris can be eliminated entirely (after a nine-day holding period) if, in addition to being able to use only lead in target fabrication, the lead were composed only of its principal isotope, ^{208}Pb. In this case, there would be an equilibrium activity in the lithium of 15.73 MCi of ^{209}Pb alone, which decays with a 3.28-h half-life. ^{209}Pb emits no gamma ray, emitting only a 0.6446-MeV beta particle. The maximum (equilibrium) waste from plant activity would be 0.00154 MCi of ^{209}Pb. Every four days, its activity would decrease a billionfold, which means that after nine days there would be only a 1.4% probability that one single radioactive nucleus remains in the stockpile of radioactive waste from activated target debris in the HYLIFE reactor.

Figure 8-27 shows a comparison of the radioactivity of the HYLIFE steel chamber for 30 years' irradiation and the STARFIRE blanket modules for 5 years' irradiation (the STARFIRE data are taken from Tables 12-5 and 12-6 and page 12-41 of Ref. 90). The values in the figure are normalized for a 1000-MW(e) plant capacity. The irradiation times of 30 and 5 years are appropriate for comparing accident-release potential because the STARFIRE blanket modules must be replaced every 6 years,[87] while the HYLIFE chamber is designed for the full lifetime of the plant (~30 years). For radioactive-material-handling and waste-disposal considerations, however, the higher frequency of transport and introduction into the environment of the quantities in Fig. 8-27 for STARFIRE must be kept in mind.

Isotope	Half-life	Activity (MCi)	Biological hazard potential (Mkm^3-air)	Decay thermal power (kW)
^{55}Fe	2.7 yr	170.00	5.96	0.089
^{59}Fe	44.6 d	5.00	2.75	0.095
^{56}Mn	2.58 h	100.00	8.20	2.128
^{54}Mn	312.3 d	35.97	26.97	0.124
^{51}Cr	27.71 d	16.50	0.33	0.001
^{101}Tc	14.3 min	6.24	0.21	0.036
^{101}Mo	14.6 min	6.24	0.21	0.063
^{99}Mo	66.02 h	12.50	2.57	0.011
^{93}Mo	3500 yr	0.00	0.50	—
^{95}Nb	3.50 d	0.01	—	—
^{94}Nb	20 000 yr	0.01	0.10	—
^{92}Nb	10.13 d	0.04	0.40	—
^{89}Zr	78.5 h	0.005	0.05	—
Total		422.97	49.02	2.45

Table 8-9. Radioactivity per GW(e) of HYLIFE's 2-1/4 Cr-1 Mo steel vessel at shutdown after 30 years' irradiation.

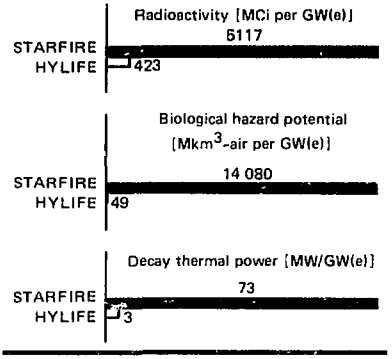

Fig. 8-27. Comparison of radioactivity, biological hazard potential, and decay thermal power at shutdown for the HYLIFE reactor after 30 years and the STARFIRE reactor after five years' irradiation.

Although activity, BHP (air), and decay thermal power do not form a complete comparison, these simple, reproducible figures are fundamental quantities for environmental, reliability, and safety concerns and are relatively insensitive to subjective interpretation.

The potential for either the HYLIFE or STARFIRE reactor to accidentally release the contaminants of Fig. 8-27 into the environment could be much different for the two reactors. In STARFIRE, for example, there is a large amount of decay-heat energy available in addition to magnetic-field energy. In HYLIFE, a large amount of heat energy is potentially available from

liquid-lithium fire, whereas STARFIRE employs an inert lithium-aluminate tritium breeding blanket.

The BHP for other reactor designs could be significantly less than that for STARFIRE, as 95% of the STARFIRE BHP is associated with the lead-zircate neutron multiplier and not with the steel wall.[91] Nevertheless, the BHP of other reactor concepts would be greater than that of HYLIFE by about the ratio of the activities. In addition to a lead-zircate neutron multiplier, STARFIRE requires isotopic enrichment of lithium to 60% ^{6}Li (Ref. 87) to breed sufficient tritium, whereas HYLIFE requires no lithium enrichment at all. (Enrichment in STARFIRE would not be required if the lead zircate is replaced with beryllium, but this option for a full fusion-power economy is probably resource-limited; also beryllium is highly toxic.)

HYLIFE's circulating liquid-lithium concept permits constant removal of tritium to low levels with salt-extraction techniques. Diffusion loss of tritium from the liquid lithium is low because of the low partial pressure of tritium in liquid lithium. At 1 wppm in 1630 m^3, HYLIFE would have about 0.87 kg of tritium, corresponding to about 8.42 MCi, 0.042 Mkm^3-air, and 0.00046 MW. STARFIRE assumes about 10 kg of tritium in its inert lithium-aluminate breeder medium.[92]

To perform a complete safety analysis for fusion reactors, the mechanisms for potential radioactivity release and their associated probabilities must be considered together with hazard potential. Such a full analysis requires a detailed (final) reactor design, more complete failure-rate data, and proper evaluation using reliability-engineering techniques.

Author: G. P. Lasche

JADE

In an attempt to overcome limitations in the repetition rate and wall loadings of other ICF reaction-chamber concepts, Monsler conceived of the JADE chamber.[93,94] The JADE concept uses a porous fiber-metal structure having a very high surface area (Fig. 8-28); this structure is placed inside the chamber's first structural wall (FSW). The JADE chamber provides an increased residence time for liquid metal in the reaction chamber, with reduced recondensation times for the liquid metal ablated during energy deposition. JADE would allow repetition rates of up to 10 Hz, and reduced forces on structural components would prolong the life of the chamber materials.

The JADE chamber wall has an inner section of fiber-metal wedges canted at an angle from the point where fusion reactions occur. The wedges, saturated with liquid metal that slowly flows between the metal fibers, are spaced far enough apart so that liquid metal ablated from the fiber-metal regions by x rays can expand, interact, and recondense without building up excessive pressure. Outside the inner-wedge region is a blanket region that absorbs neutron energy and breeds tritium. Void spaces are included to allow the liquid metal to expand without building up excessive pressure. Surrounding the outer fiber-metal structure are a solid FSW, a reflector, and a containment vessel.

The next two articles describe some of the JADE design considerations and the response of liquid metal to the JADE fusion environment.

Author: J. H. Pitts

JADE Design Considerations. The JADE reaction-chamber concept[95] utilizes a thick, porous, wicklike fiber-metal wall formed as a cylindrical or spherical shell with a 5-m radius. Liquid metal migrates from top to bottom through the porous structure, increasing in temperature by as much as 160 K. The liquid metal contained in the porous wall will, in principle, recoat all surfaces exposed directly to the fusion reactions prior to the next fusion reaction.

The porous structure in a cylindrical chamber consists of vertical porous plates canted at an angle with the radius vector in the horizontal plane and attached to the FSW. Approximately horizontal porous ribs support the vertical plates. As Fig. 8-28 shows, these ribs are canted with respect to the radius vector in the vertical plane. Space between the ribs and vertical plates in the porous structure allows for a lower average flux and provides a region for expansion of the fluid. The ribs and vertical plates are made of metal fibers bound in a

matrix containing a void fraction of up to 90%. Metal-fiber materials for the porous structure are presently manufactured for use in filters, sound-absorbing structures, and other applications. For JADE, the metal-fiber material may be manufactured as either a flexible or rigid structure.

The JADE reaction chamber is designed to convert the kinetic energy of the fluid to thermal energy before the fluid reaches the FSW. The particular geometric shape of the JADE thick porous wall is used

- To minimize reaction forces on the FSW due to blow-off caused by the deposition of x-ray energy.
- To provide space for the droplets formed from the isochoric neutron-energy deposition in the liquid to undergo liquid-liquid interactions and reduce their kinetic energies.
- To provide large surface areas for rapid condensation of the vaporized liquid.

There are a number of design considerations associated with such a porous structure.[96] First, flow relationships need to be determined to establish the residence time for the fluid in the reaction chamber. A solution of the Napier-Stokes equation in such a complex domain is not feasible, so we have used simplified models to describe the flow. They fall into two groups: continuum models, such as ones treating the actual tortuous path followed by a fluid element in a pipe, and statistical models, such as those used in diffusion theory. Nevertheless, the lack of simple fundamental principles for deriving flows in porous media makes it necessary to rely heavily on experimental correlations.

A number of disciplines deal with porous media, and the phenomenological laws found in one area usually apply to other areas. Studies in hydrology, petroleum production, packed beds, filtration, and even the movement of fluids in the human lung have led to a body of theory useful for an analysis of the JADE reaction chamber.

Darcy's law (which says that the volume of flux per unit area, q, is proportional to the gradient of the pressure across the medium, Δp) is commonly used to described the flow in porous media. Thus

$$q = -\frac{k}{\mu}\nabla p \quad , \tag{4}$$

where k is the permeability and μ is the fluid viscosity. For inhomogeneous media, k varies with position; for anisotropic media, k becomes the permeability tensor, **k**.

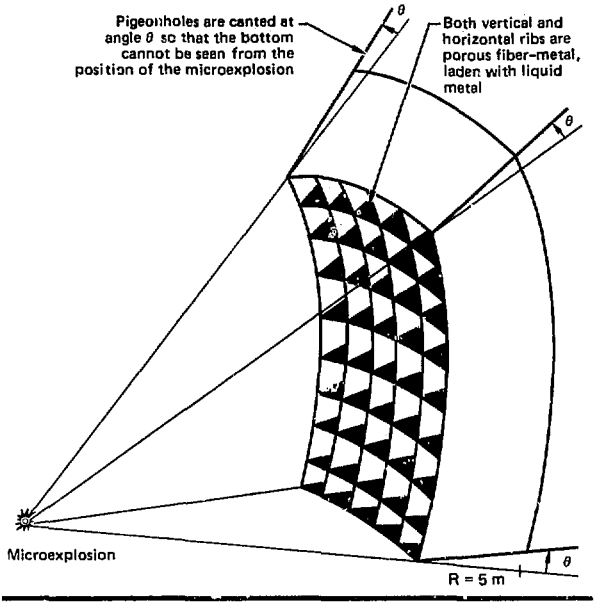

Fig. 8-28. Schematic cross section of cylindrical JADE reaction chamber.

Darcy's law is applicable for Reynolds numbers up to about unity, based on a characteristic length associated with the microgeometry. There is some uncertainty as to the meaning and measurement of the characteristic length that leads to uncertainty in Reynolds number. Extensions of Darcy's law have been developed by Forchheimer[97] and Ergun[98] to accommodate flows with higher Reynolds numbers.

A flow pattern which might be typically encountered in the porous wall is shown in Fig. 8-29. Actual streamlines depend on the permeability and porosity of the wall, the applied fluid pressure, and gravity. For a large enough porosity and fiber size, a wall can be designed that would require only moderate applied fluid pressure. Alternatively, a number of arteries running from top to bottom can be used to feed the porous sections with liquid metal, thus reducing the distances the liquid metal must travel to saturate the medium.

A primary task in more detailed design will be tailoring the permeability of the porous wall. This will be necessary

- To reduce the thermal gradient across the porous structure.

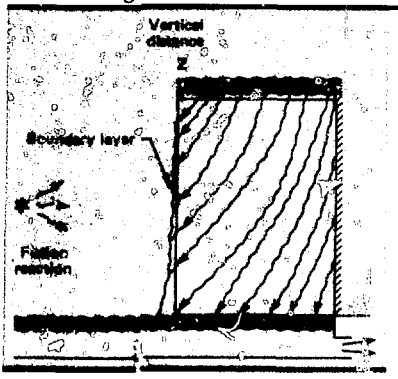

Fig. 8-29. Possible flow pattern in an annular JADE porous fiber-metal wall.

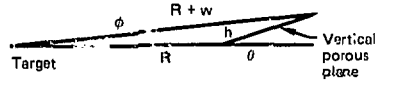

Relations	Approximations for small θ
$h = -R\cos\theta + [(R+w)^2 - R^2\sin^2\theta]^{1/2}$,	$h \sim w$
$0 \leq \theta \leq \pi/2$	$\phi \sim \frac{w}{R+w}\,\theta$
$\sin\phi = \frac{h}{R+w}\sin\theta$	
$n = 2\pi/\phi$	$n \sim \frac{2\pi}{\theta}\left[1+\frac{R}{w}\right]$
$\frac{A^T}{A_0^T} = \frac{1}{\phi}\frac{h}{R}$	$\frac{A^T}{A_0^T} \sim \frac{1}{\theta}\left[1+\frac{w}{R}\right]$
$\frac{A^T}{A_0^T} = \frac{1}{\phi}\frac{h}{R+w}$	$\frac{A^T}{A_0^T} \sim \frac{1}{\theta}$

Fig. 8-30. Surface-area relationships for the JADE vertical porous planes.

- To examine the effects of changes in pore size due to shock propagation in the medium.
- To avoid stagnation of the fluid in the lower portions of the metal-fiber structure. Stagnation might result if there is a tendency for the fluid to flow out of the top and down the side of the structure rather than through the pores.

A second major design consideration involves the surface area of the JADE porous wall. Figure 8-30 is a top view of the surface-area relationships for the JADE chamber's vertical porous planes, having inner radius R and outer radius $R_O = R + w$. The vertical plates (also called fins or inserts) have a width h, height H, and a cant angle θ with the horizontal radius vector from the target (thickness is neglected here to simplify calculations). There will be n such fins, each subtending an angle ϕ at the target. In the list of relationships among these parameters shown in the figure, the total area A^T which is exposed to the soft x rays and debris is compared both to the surface area A_0^T of a cylinder of radius R and to one of radius $R + w$ having area A_0^T. Finally, for small cant angle θ, the formulas in Fig. 8-31 have simple approximations that are useful in making design trade-offs

It should be noted that the gain in area of the porous wall over its cylindrical outer envelope is dependent only on the cant angle θ, and for $\theta = \pi/18$ (= 10°) the gain is 5.7, while for $\theta = \pi/36$ (= 5°) it is 3. . . . there is a lower limit on θ, perhaps due to some reactor-based design constraint there is then an upper bound on the area gain that JADE offers over the outer cylinder. Of course, absolute area increases with increasing radius. The inclusion of fin thickness in the calculation will reduce somewhat the number of inserts in the chamber and, therefore, reduce the surface area.

A third design consideration is the corrosion and erosion associated with the large surface area in the thick porous wall. For a fiber radius, r, and a porosity of ϵ, the surface-to-volume ratio, s, is

$$s = 2\frac{(1-\epsilon)}{r} \quad , \tag{5}$$

which, for a porosity of 0.8 and fiber radius of 100 μm, implies that $s = 4000\ m^2/m^3$.

If a metal has a corrosion rate of v (in units of μm/yr) for a fiber operating at reactor temperatures, then the time, t, it takes the fibers of initial radius r_0 to lose a fraction λ of their mass (and volume) is

$$t = \left|1-(1-\lambda)^{1/2}\right|\frac{r_0}{v} \cong \frac{\lambda}{2}\frac{r_0}{v} \quad . \tag{6}$$

Rearranging the terms of this equation, we see that for a given corrosion rate, v, desired JADE lifetime, t, and tolerable mass loss, λ, the initial fiber radius must be

$$r_0 = \frac{2}{\lambda}vt \quad . \tag{7}$$

The Colorado School of Mines studied the effects of lithium at 450°C flowing across 304 L stainless steel and found that the lithium first leached out the nickel and then attacked the iron at a rate of 5 μm/yr. Figure 8-31 shows the required initial fiber

radius vs this corrosion rate for 304 L stainless steel, for various chamber lifetimes, assuming that a mass loss above 25% is not permitted. The lifetime of the thick porous wall must be a considerable fraction of the plant lifetime, or one of the main purposes of the concept is defeated. For a reasonable lifetime, the required fiber radius lies within the range of 0.1 to 1 mm (Fig. 8-31). Other alloys and metals (such as Ti-V or Nb) that have lower corrosion rates are good alternatives and would result in an extended range for the required fiber radius, but mechanical properties, neutron activation, and compatibility in a liquid-metal environment limit their use.

From a structural point of view, mass loss due to corrosion appears to be acceptable. As long as the mass loss remains in solution with the primary fluid, there is no difficulty with the porous walls in the JADE concept. It may be necessary, however, to separate out the corroded or eroded structural material from the porous wall. Otherwise, undesirable amounts of plating could occur in the primary loops, causing damage to pumps and intermediate heat exchangers. We believe that some of these problems may be eliminated if we use fibers several millimetres in radius that are tightly bound and long enough to be woven.

Although the JADE porous wall presents some new difficulties, it also offers the promise of solutions to major liquid-metal-wall problems. This promise provides sufficient incentive for further study.

Author: Bechtel Group, Inc. (Research & Engineering, Advanced Physical Processes Group)
Major Contributors: J. H. Pitts and M. J. Monsler

Response to the Fusion Environment. The design of the JADE reactor geometry must tailor the liquid-metal flow to produce a relatively uniform temperature rise, since localized higher temperatures will increase material-damage rates. Also, the kinetic velocity imparted to the liquid by the volumetric fusion-energy deposition must not greatly exceed the flow velocity; this is necessary to prevent voids and damage to the matrix. Flow and disassembly velocities can be estimated using the energy-deposition profile.

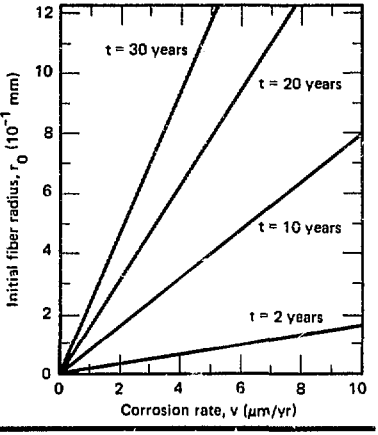

Fig. 8-31. Required initial fiber radius vs corrosion rate.

The inner region of the spherical JADE reactor is 50 cm thick, with a 28% packing fraction. The material is 90 vol% lithium or lead-lithium and 10 vol% steel or SiC fibers. The inner region is arranged as a set of wedges pointing at the fusion source. X rays and pellet debris are absorbed along one side of the wedges, and the resulting ablated material from each wedge crosses the gap and hits the rear of the adjacent wedge. The outer region of the JADE chamber is 0.8 m thick, with a 90% packing fraction. As in the inner region, the material is 90% liquid and 10% solid. The JADE chamber's outer region is protected from x rays and debris, and its primary function is to absorb neutron energy. In this article, we consider the flow and disassembly velocities of only the outer region, using pure lithium as our liquid metal.

We first fit[99] an empirical equation to the energy-deposition profile from the results of several two-dimensional Monte Carlo neutronics calculations:

$$\frac{E}{m}\left(\frac{\mathrm{J}}{\mathrm{Kg}}\right) = 166\left(\frac{P_{\mathrm{TN}}(\mathrm{MW})}{\phi(\mathrm{H_r})}\right) \times (R_i + 0.25\ \mathrm{m})^{-2} \exp\left\{\left[3.5\left(\frac{\rho}{\rho_0}\right)^{0.6} - 0.37R_i\right](0.25\ \mathrm{m} - x)\right\}, \quad (8)$$

where x is the depth into the array, and R_i is the array inner radius. The equation was fit too midplane energy-deposition results for pure lithium arrays with packing fractions between 41 and 100% and with array

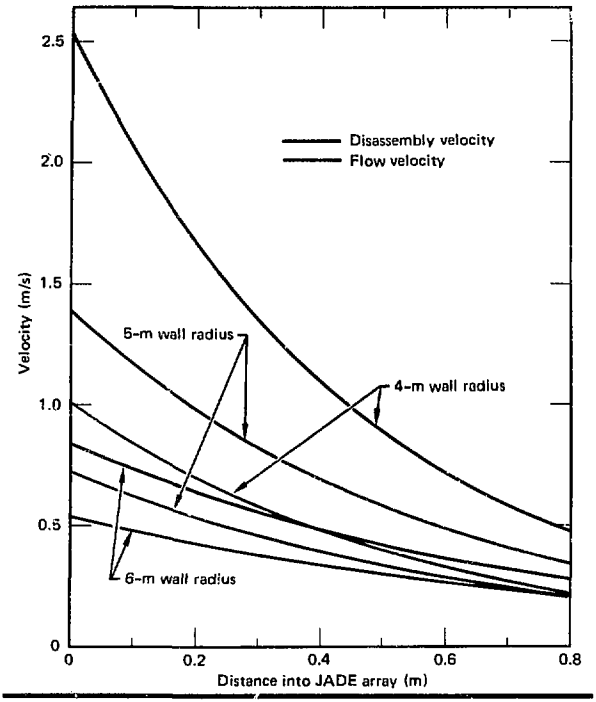

Fig. 8-32. Disassembly and flow velocities in the outer region of the JADE array.

inner radii between 0.44 and 1.94 m. We used Eq. (8) to analyze the outer region of JADE. However, the inner region will perturb the result, and the array radii used are larger than those used to derive the equation. Thus, the results given here are only a preliminary estimate.

We assume the thermal power is 3200 MW (based on a fusion power of 2700 MW and a system multiplication power of 1.185). For a temperature rise of 150°C in the liquid during passage through the chamber, the total flow rate is $P_t/\rho_0 \cdot c \cdot \Delta T$, where ρ_0 is the liquid density (485 kg/m^3) and c is the specific heat (4220 J/kg·K). Hence, the total flow rate is ~10.4 m^3/s, or ~15% of the HYLIFE flow rate (based on a pulse repetition rate of 1.5 Hz and total power of 1800 MJ).

For a JADE reactor with a 5-m wall radius, the reactor size and power density are identical to those of HYLIFE, but the flow rate and pumping power are reduced by a factor of 6. Further, JADE's lower pellet yield relaxes the driver size and cost. These advantages must be compared to JADE's decreased revenue due to the increased recirculated power to the driver. (Recirculated power is inversely proportional to pellet gain, which decreases with pellet yield.)

The disassembly velocity of the liquid metal, neglecting surface tension effects, is

$$v = \Gamma(E/m)/c_s \quad , \tag{9}$$

where Γ and c_s are the Gruneisen constant (0.9) and liquid sound speed (4500 m/s), respectively. The flow velocity at a point within the JADE array is

$$v = \frac{\text{dist}}{\text{time}} = \frac{\pi(R_w - 0.8\text{ m} + x)}{150\,^\circ\text{C}\left/\frac{\phi}{c}\frac{E}{m}\right.}$$

$$= \frac{\pi(R_w - 0.8 + x)\,\phi\,(E/m)}{(150^\circ\text{C})} \quad . \tag{10}$$

Equations (9) and (10) are plotted in Fig. 8-32 for wall radii of 4, 5, and 6 m. The disassembly velocities range between 1.5 and 2.5 times the flow velocities. The absolute magnitudes of both velocities are in the range of 0.5 to 2.5 m/s, where erosion and corrosion problems are not significant. For comparison, lithium flow in pipes is usually limited to about 6 m/s, and the HYLIFE liquid is moving at about 30 m/s when it strikes the chamber wall.

Author: J. A. Blink

New Directions for ICF

We are exploring new directions for inertial fusion. These directions include new energy applications as well as new reactor concepts.

Currently more than 70% of the energy consumed in the US is used in nonelectrical applications.[100] Thus, there is a high leverage potential for fusion to make a significant contribution to nonelectrical energy applications. This opportunity led us to study using ICF as an energy source for the production of hydrogen to be used as a clean fuel.[101]

High heat is required for many thermochemical processes, and high temperatures will also increase the efficiency of electricity-generating power plants. We have investigated a reactor concept, called

SEBREZ, which utilizes a high-temperature blanket with segregated tritium breeding zones to minimize the migration of tritium to the coolant cycle.[102] We are applying the knowledge gained from the SEBREZ study to design a high-temperature, gas-cooled inertial-fusion reactor.

In the next five articles, we detail the studies that represent new directions and concepts for our inertial fusion program.

Author: J. Hovingh

Hydrogen Production

The production of hydrogen as a relatively nonpolluting fuel may be necessary in the long-term future. A hydrogen economy based on fusion energy may ensure a self-sufficient energy future for the United States.

Of the various processes for producing hydrogen, the best developed is electrolysis; work is also proceeding on thermochemical and hybrid thermochemical-electrochemical cycles. Since neither advanced electrolysis nor thermochemical processes have been demonstrated on a power-plant scale, the costs and efficiencies of both systems are uncertain.

The US Department of Energy is currently sponsoring two studies of magnetically-confined fusion-energy sources for hydrogen production.[103] Exploring thermochemical cycles is the joint project of LLNL and the University of Washington (UW). The high-temperature electrolysis project is being performed at Brookhaven National Laboratory (BNL). The BNL study employs a tokamak fusion-energy source and emphasizes the design of high-temperature fusion blankets.[104,105] The LLNL/UW study of hydrogen production using fusion energy utilizes the General Atomic (GA) sulfur-iodine cycle[106] with a tandem-mirror fusion reactor.[107-110]

Systematics of a Fusion-Energy Source for the Production of Hydrogen. Figure 8-33 shows a power-flow diagram for a fusion-energy-driven hydrogen-production source. The fusion energy is furnished to the hydrogen-production plant as heat and electricity. The high temperatures required in the hydrogen-production process can be generated by Joule heating. The performance of a fusion plant that produces a ratio, ξ, of hydrogen to net electricity can be estimated from

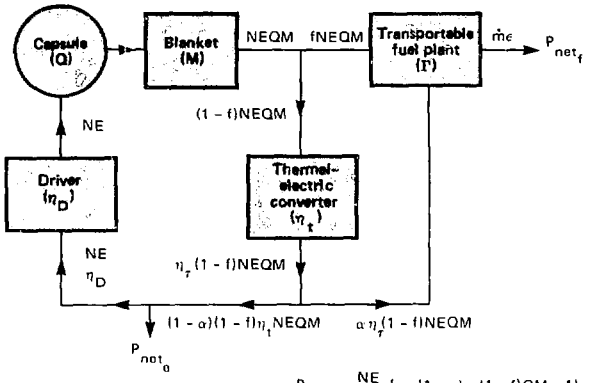

Fig. 8-33. Power-flow diagram for hydrogen-production plant using fusion energy in a low-temperature cycle.

$$\zeta = \frac{P_{net}}{P_{net}} = \frac{\Gamma QM\eta_D\left[f + \alpha\eta_t(1-f)\right]}{\eta_D\eta_t(1-\alpha)(1-f)QM - 1} ,$$

where α is the fraction of the electric power produced that is circulated to the hydrogen-production plant, and f is the fraction of the fusion power that is utilized as heat by the hydrogen-production plant. An additional constraint on this analysis is that the hydrogen-production plant will require a given ratio, ξ, of the thermal power to the electric power for the process,

$$\xi = \frac{f}{\alpha\eta_t(1-f)} .$$

Combining these equations yields

$$f = \frac{\zeta\xi\left[\eta_D QM\eta_t - 1\right]}{\eta_D QM\left[\zeta(\xi\eta_t + 1) + \Gamma(\xi + 1)\right]} .$$

There are three important figures of merit for a fusion-driven hydrogen producer: the system gain, G, the production fraction, x, and the electric consumption ratio, y. For a system producing no net electric power ($\zeta \to \infty$), the system gain, G, is defined as

the ratio of the heat rate of hydrogen production to the fusion-reactor circulating electric power requirements; G is thus a rough ratio of the revenues from the hydrogen produced to the operating cost of the fusion-energy source. The production fraction, x, is the ratio of the heat rate of hydrogen production to the fusion power. The ratio is roughly proportional to the ratio of the revenues from the hydrogen produced to the capital cost of the plant. The electricity-consumption ratio, y, is the ratio of the reactor circulating power to the gross electric power produced by the system. This ratio is a relative comparison of the cost of electricity for running the fusion plant with the cost of electricity to run the total system.

In 1981, we compared an ICF-driven system for producing hydrogen to the LLNL tandem-mirror hydrogen producer.[110] Both systems use the GA sulfur-iodine hydrogen production cycle, consisting of the following three reactions:

$$2H_2O(\ell) + SO_2(g) = I_2(\ell) \rightarrow H_2SO_4(aq) + 2HI(aq) \quad (300\ K)$$

$$2HI(aq) \rightarrow H_2(g) + I_2(\ell) \quad (400\ K)$$

$$H_2SO_4(aq) \rightarrow H_2O(g) + SO_2(g) + 1/2\ O_2(g) \quad (1200\ K)$$

Neither system produced net electric power to the grid. The performance of the tandem-mirror and ICF hydrogen-production systems are compared in Table 8-10. The blanket neutron-energy multiplication factor listed in the table is applied to 80% of the fusion energy for the tandem mirror reactor system, and to 68% of the fusion energy in the inertial fusion reactor. The auxiliary heating fraction is applied to the total plasma power for the tandem mirror system and to the fusion power for the ICF reactor system. The plasma gain for the tandem-mirror reactor system is 11.6 which does not include the heating power to the plasma.

Table 8-10. Performance comparison for *tandem-mirror-driven* and fusion-driven hydrogen-production systems.

Component	System: Tandem mirror	Fusion
Thermoelectric conversion efficiency, η_t (%)	40	40
Heat-to-electricity ratio for hydrogen plant, ξ	4.0	4.0
Auxiliary heat fraction	0.03	0.03
Blanket neutron-energy multiplier, M	1.12	1.12
Plasma heating efficiency, η_D (%)	55	—
Direct converter efficiency, η_{DC} (%)	55	—
Plasma gain	11.6	—
Net electric power	0.0	0.0
System gain, G	1.89	—
Hydrogen production fraction, x	0.33	—
Electric consumption ratio, y	0.57	—

The system gain for the ICF-driven hydrogen-production plant are shown in Fig. 8-34 as a function of fusion gain. For very large fusion gains, the maximum system gain becomes 12.0, the maximum production fraction becomes 0.39, and the minimum electric consumption ratio becomes 0.075.

An ICF-driven hydrogen producer will have higher system gains and lower electrical-consumption ratios than the design point for the tandem-mirror system if the inertial-fusion energy gain $\eta_D Q > 8.8$. However, for the ICF system to have a higher production fraction than the tandem-mirror system requires that $\eta_D Q > 17$. The advantage of the tandem-mirror system, in terms of the hydrogen-production fraction for $9 < \eta_D Q < 17$, is due to the direct converter (see Table 8-11) which supplies all the tandem-mirror injection power requirements.

A design curve for an ICF-driven hydrogen-production plant using the same hydrogen-production plant as the tandem-mirror system is shown in Fig. 8-35; the figure shows system gain, Q (*as currently*

Fig. 8-34. Performance characteristics of an ICF-driven hydrogen-production plant.

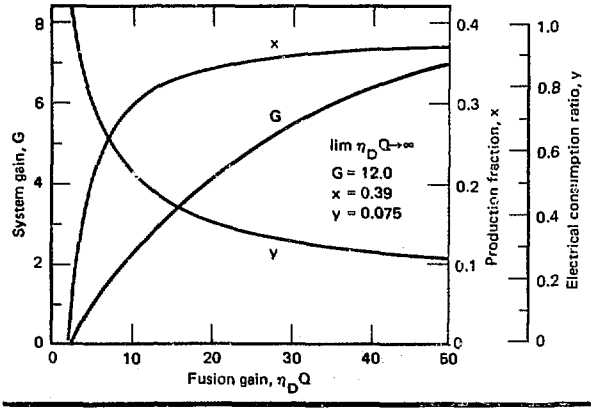

estimated for several types of pellets), for various driver energies, E_D. For a given $\eta_D Q$ = 8.8, and a given laser efficiency of 7%, the required pellet gain is 126. The lowest driver energy that falls in the "best-estimate" gain area on the figure for a gain of 126 is 4 MJ using pellet B. For a production rate of 5.8 kg-moles/s of H_2, the required pulse-repetition frequency is 11 Hz. This case is given as Example 2 in Table 8-11.

The inertial-fusion reactor system in Fig. 8-35 will have the same system gain and hydrogen-production rate as the tandem-mirror system, but a lower hydrogen-production fraction. Reducing the driver efficiency to 4.4% will require a pellet gain of 220 (Example 1 in Table 8-11). The lowest driver energy for this gain in the "best-estimate" gain curve is 10 MJ for pellet B. For a fusion-energy gain of 17 and a driver efficiency of 7%, the required pellet gain is 240 (Example 3 in Table 8-11). Using a 10-MJ driver will require that the performance of pellet B slightly exceed the "best-estimate" gain.

Fusion-Reactor Design Considerations. For a given $\eta_D Q$, a low-efficiency driver will need to deliver more energy to the pellet to achieve the required larger pellet gain. This will result in high-yield fusion microexplosions that reduce the variety of first-wall protection schemes available for the reactor compared to those available for lower-yield

Table 8-11. Performance comparison for the LLNL fusion-driven tandem-mirror hydrogen-production plant for several pellet gains and driver energies.

Performance parameter	Example 1	Example 2	Example 3
Fusion-energy gain, $\eta_D Q$	8.8	8.8	17
Driver efficiency, η_D (%)	4.4	7.0	7.0
Fusion gain, Q	220	126	240
Driver energy (MJ)	10	4	10
Fusion yield (MJ)	2200	500	2400
Pulse repetition rate (H_2)	3	11	<3
System gain, G	1.89	1.89	3.6
Hydrogen-production fraction, x	0.28	0.28	0.33
Electric-consumption ratio, y	0.57	0.57	0.41

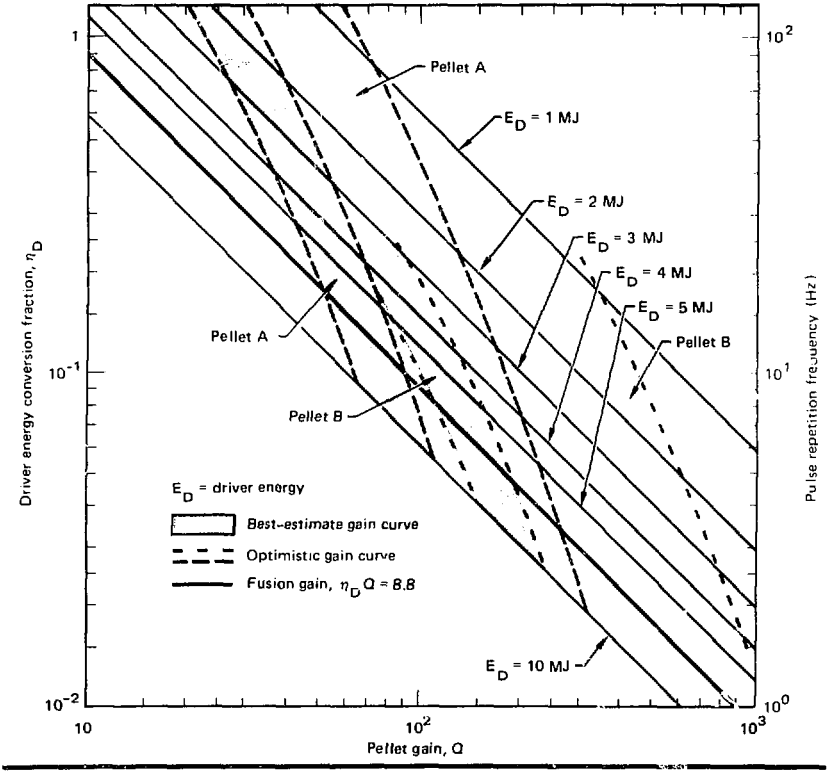

Fig. 8-35. Fusion-driver parameter space for the hydrogen-production plant in Fig. 8-34, producing 5.8 kg-mole/s of H_2.

microexplosions. According to Table 8-11, for example, a system with $\eta_D Q = 8.8$ will have a required yield of 2200 MJ for a 4.4%-efficient driver. This high required yield may limit effective reaction-chamber options to thick liquid-metal-wall chambers.[111] If the driver efficiency is 7%, the required 500-MJ fusion yield may allow, in addition to thick liquid-metal-wall chambers, both dry-wall and wetted-wall chambers.

The most efficient method of producing hydrogen requires temperatures in the range of 1200 to 1500 K. These temperatures restrict the material options available and require cooled structures that are well insulated from the high-temperature blanket. The use of high-temperature alloys will increase the cost of the fusion-reactor system. The higher capital cost of the high-temperature systems may be overcome, however, by the increased revenues from the hydrogen (or electricity) produced by the more efficient system.

ICF reactors can tolerate flowing conducting fluids, high vapor pressures in the fusion cavity, and large reactor geometries more readily than can magnetic-confinement fusion reactors. These freedoms associated with ICF should be exploited. For example, the gas heated by the short-range fusion products in a gas-protected first-wall concept, such as SOLASE,[111] is unable to radiate its energy to the reactor structure in reasonable times. This hot gas could be circulated through an intermediate heat exchanger and the extracted energy used in a hydrogen-production plant. Blanket options could include high-temperature circulating lithium or lead–lithium mixtures in a Nb-1% Zr structure, since the Nb-1% Zr corrosion rate by lithium is acceptable up to temperatures as high as about 1300 K. Other acceptable high-temperature blankets can be made up of a solid-lithium compound, such as Li_2O, with graphite moderators and boron carbide absorbers.

In addition to the fusion-system performance requirements for economically producing hydrogen, there are additional practical constraints. These constraints on the fusion-driven hydrogen-production plant system are as follows:

- The system must be self-sufficient as a tritium producer.
- The thermal energy produced must be of a form that matches the requirement of the hydrogen plant processes.
- The primary coolant systems of the fusion reactor must be physically decoupled from the energy-transport media into the hydrogen plant.
- The energy-transport media entering the hydrogen plant must be inert with respect to the ingredients of the hydrogen-plant process materials at the process temperature.

These constraints have several effects, including

- Requiring a heat exchanger in the primary reactor coolant loop.
- Requiring either the use of an inert-gas energy-transport media or the use of Joule heating for the high-temperature leg of a thermochemical hydrogen-production process.
- Effectively eliminating neutron radiolysis from consideration as a hydrogen-production process.

Conclusions. An inertial-fusion energy source can potentially outperform the proposed LLNL tandem-mirror energy source for the GA sulfur-iodine hydrogen-production system. The selection of a given hydrogen-production method is, however, premature at this time. Therefore, we should monitor the development of thermochemical, electrolytic, and hybrid processes for the production of hydrogen. We should meanwhile marshall our efforts and concentrate on the design of a high-temperature ICF reactor.

Author: J. Hovingh

SEBREZ: An Inertial-Fusion Reactor Concept

We have studied the neutronic aspects of an inertial-fusion reactor concept that relies on asymmetrical neutronic effects to enhance the tritium production in the breeding zones. We find that it is possible to obtain a tritium breeding ratio greater than 1.0 with a chamber configuration in which the breeding zones subtend only a fraction of the total solid angle. This concept is called SEBREZ (SEgregated BREeding

Zones). The two primary objectives of SEBREZ are

- To confine tritium breeding to a small fraction of the blanket by means of neutron scattering from lithium-free regions into breeding regions.
- To leave the major fraction of the blanket free of tritium, thus eliminating concerns about the release of tritium through the heat-transfer system.

Neutronic studies indicate that the neutron leakage through a hole in an ICF chamber can be considerably higher than we would estimate based only on the solid angle of the hole.[112-114] Leakage beyond the direct loss of fusion neutrons is due to the neutrons from the blanket reentering the fusion chamber and escaping through the hole. The origin of the SEBREZ concept was an effort to use these effects to channel neutrons from blanket regions with low neutron absorption into tritium breeding zones which are physically segregated from the low-absorption regions.

Neutronics Model for Scoping Calculations. The spherical blanket geometry shown in Fig. 8-36 forms the basis of scoping calculations for the SEBREZ concept. Centered along the axis of symmetry are two tritium breeding zones containing natural lithium. Each zone is the intersection of a cone with the spherical shell; the vertices of the cones coincide with the center of the sphere. The remaining two portions of the blanket each consist of two zones. The inner zone contains a neutron multiplier of either Be or Pb. The outer zone, backing the multiplier, is a graphite moderator/reflector.

The total thickness of the blanket is held constant at 1 m while the thickness of the neutron multiplier and the solid-angle fraction of the breeding zones are varied. A 14.1-MeV point source is located at the center of the chamber, which has a 6-m inner radius. TARTNP,[115] a coupled neutron-photon Monte Carlo code, and ENDL,[116] the 175-group LLNL nuclear data library, were used in all calculations.

The measure of performance for the various blanket configurations is their tritium breeding ratio. Clearly, the simple model shown in Fig. 8-36 will give optimistic results for several reasons. First, there is no protective first wall, which would reduce the neutron multiplication and increase the number of parasitic neutron captures at the expense of tritium breeding. Second, there is no structural material within the blanket, which, if included, would increase the rate of parasitic capture. Third, there are no beam ports, which, if included, could result in additional neutron losses.

Tritium Breeding Ratio vs Multiplier Thickness. In the first set of scoping calculations, the total solid-angle fraction of the breeding zones was held constant at 30% while the thickness of the neutron multiplier was varied. We chose the 30% value because it corresponds to the solid-angle fraction of the top plus bottom of a right circular cylinder with a height-to-diameter ratio of unity.

Figure 8-37 shows the tritium breeding performance as a function of the Pb multiplier thickness. The contribution to the breeding ratio from ^{7}Li(n,n'T)α reactions is labeled T_7. This contribution is unaffected by the neutron multiplier, since the energy of the secondary neutrons from Pb(n,2n) reactions is below the threshold energy for tritium breeding reactions with ^{7}Li.

The contribution from ^{6}Li(n,T)α reactions (labeled T_6), on the other hand, increases with increasing multiplier thickness up to ~10 cm. Beyond that point, it is relatively constant over the range shown. As the Pb thickness is increased further, T_6 is expected to drop off, since neutrons produced deep within the multiplier or reflected back from the graphite region will have a higher probability of parasitic capture in Pb before they find their way to the Li zones.

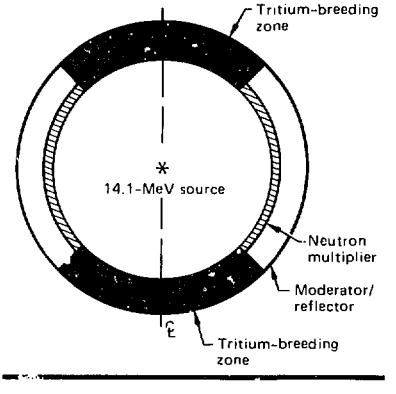

Fig. 8-36. Spherical blanket model for SEBREZ scoping calculations.

The total tritium breeding ratio, T_t, follows the same trends as T_6. Unfortunately, the maximum breeding ratio is 0.96. Therefore, it is not possible to confine the tritium breeding zones to as little as 30% of the blanket with a Pb multiplier.

Fig. 8-37. Tritium breeding performance vs thickness of a lead multiplier.

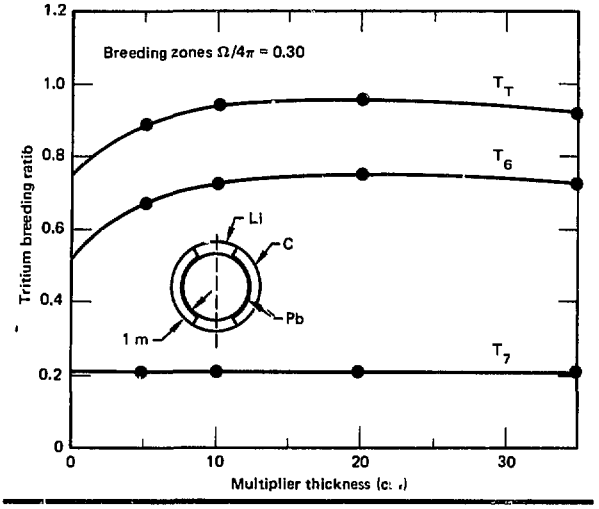

Fig. 8-38. Tritium breeding performance vs thickness of a beryllium multiplier.

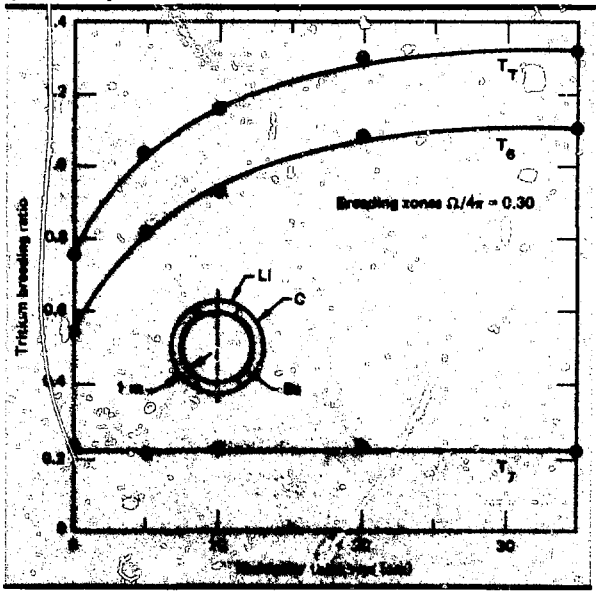

Figure 8-38 shows the tritium breeding performance using a Be multiplier. Again, the contribution from ^{7}Li is unaffected by the presence of the multiplier. The contribution from ^{6}Li increases rapidly with increasing multiplier thickness up to ~20 cm. The total tritium breeding ratio reaches a maximum of ~1.3 in this range of Be thicknesses. For this simple model, only 5 cm of Be is needed to boost the tritium breeding ratio above 1.0.

The advantage of Be over Pb as a neutron multiplier in this application is primarily the result of two factors. First, Be has a lower threshold (1.9 vs 7.4 MeV) and a comparable macroscopic cross section (Σ = 0.067 vs 0.073 cm^{-1} at 14.1 MeV) for (n,2n) reactions. This leads to a higher neutron-production rate for Be. Secondly, Be has a lower macroscopic capture cross section for reflected neutrons (Σ = 0.0012 cm^{-1} vs 0.0051 cm^{-1} at 0.025 eV), resulting in less parasitic capture.

Tritium Breeding Ratio vs Subtended Solid Angle. In the second set of scoping calculations, the size of the breeding zones is varied by changing the size of the included angle of the intersecting cones. A base case without a neutron multiplier illustrates how the tritium breeding ratio can be enhanced by neutron scattering alone. In the other two cases, the multiplier thickness is held constant at 10 cm. This thickness is chosen based on the performance of the Pb multiplier shown in Fig. 8-37.

Figure 8-39 gives the tritium breeding performance as a function of the solid-angle fraction subtended by the breeding zones for the three cases of the second set of scoping calculations. For a complete 1-m-thick shell of Li ($\Omega/4\pi$ = 1.0), the tritium breeding ratio is 1.49 with T_6 = 0.75 and T_7 = 0.74. As indicated, T_7 is proportional to Ω, whereas T_6 (and thus T_T) drop off less rapidly as Ω decreases. For the base case (without a neutron multiplier), the T_6 enhancement is due entirely to neutrons scattered from the graphite zone into the Li zones. The energy of these neutrons, however, is below the threshold for ^{7}Li(n,n'T)α reactions, and therefore T_7 is unaffected. The net effect on T_T is significant. With $\Omega/4\pi$ = 0.3, for example, the tritium breeding ratio is 0.75 compared to a geometrically predicted value of T_T = 0.3 × 1.49 = 0.45 based on a linear scaling with Ω. The

tritium breeding ratio is >1.0 for $\Omega/4\pi$ > 50% with this blanket configuration.

Figure 8-39 also shows the tritium breeding performance as a function of Ω with a 10-cm-thick Pb multiplier. In this case, T_6 actually increases as $\Omega/4\pi$ decreases from 1.0. This indicates that the increase in the $^6Li(n,T)\alpha$ reaction rate due to the additional neutrons generated in the system by the multiplier outweighs the decrease in reaction rate due to reducing the breeding-zone coverage. Compared to the case without a multiplier, T_6 and T_1 are greater for all intermediate values of $\Omega/4\pi$. The maximum difference of ~0.2 occurs at $\Omega/4\pi = 0.35$. This is also the minimum breeding-zone fraction for a tritium breeding ratio >1.0.

With a 10-cm-thick Be multiplier, the increase in T_6 is quite dramatic. The tritium breeding ratio is >1.0 for $\Omega/4\pi > 0.18$. The maximum difference in T_1 with and without the Be multiplier is 0.45 at $\Omega/4\pi = 0.2$.

Two-Dimensional Cylindrical Chamber Model. A more detailed model of the SEBREZ chamber was made based on the results of the scoping calculations. The two-dimensional cylindrical chamber with a horizontal axis to facilitate beam entry is illustrated in Fig. 8-40. This model includes

- Target effects, with a D–T fuel ρR of 3.0 g/cm^2 and a pusher $\rho\Delta R$ of 0.8 g/cm^2.
- A first wall consisting of 0.5 cm of graphite on 1.0 cm of Zr. The zirconium was used because of its low neutron-capture cross section.
- A 10-cm-thick neutron multiplier followed by 90 cm of graphite in the radial blanket.
- Tritium breeding only in the axial blankets.
- A 30-cm-thick graphite reflector for the breeding zones.
- An 8-cm-thick vessel wall on the outside of the graphite zones in both the radial and axial blankets.
- Use of 1.4-m-diam holes in the axial blankets for beam ports (total $\Omega/4\pi$ for the two holes = ~5%).

Three cases were run with the cylindrical chamber model: one with a Pb multiplier and a Li breeder, one with a Be multiplier and a Li breeder, and one with a Be multiplier and a Li_2O breeder. With the Pb multiplier, the inside diameter of the chamber was 16.0 m and the height was 12.0 m. This gives a value of $\Omega/4\pi$ = 40% for the breeding zones. In the two cases with the Be multiplier, the inside diameter and height were equal at 12.0 m, giving a solid-angle fraction of 30% for the breeding zones.

The tritium breeding results are tabulated in Table 8-12. All cases show a tritium breeding ratio >1.0. The increase in T_6

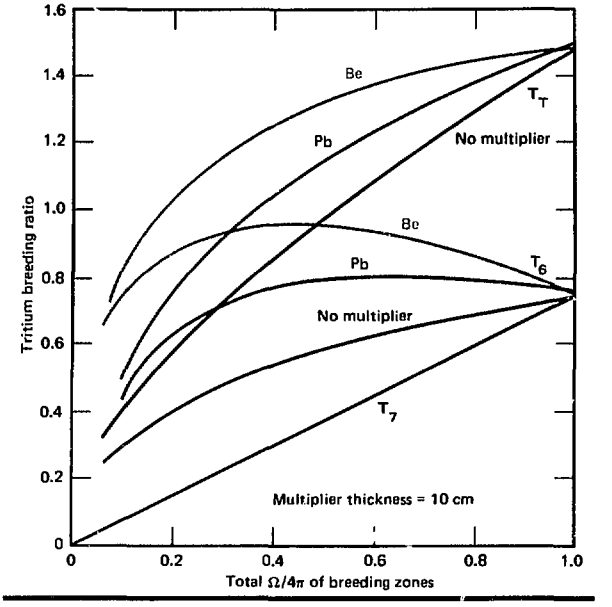

Fig. 8-39. Comparison of tritium breeding performance for different neutron multipliers.

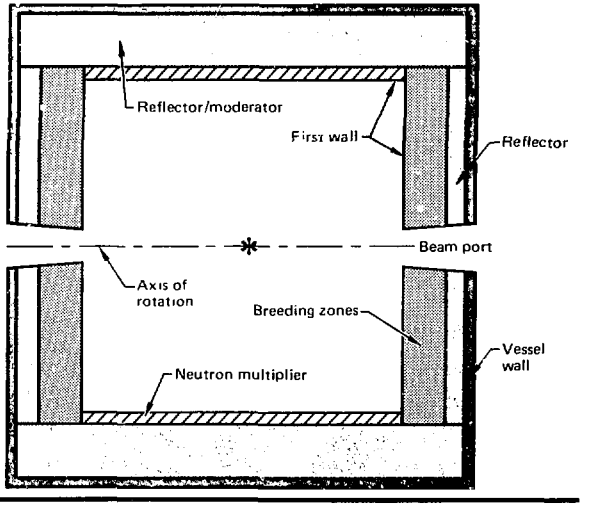

Fig. 8-40. Schematic of the SEBREZ cylindrical chamber.

Table 8-12. Tritium-breeding results for a cylindrical chamber.

Contribution	Multiplier/Breeder (Ω/4π) Pb/Li (0.4)	Be/Li (0.3)	Be/Li_2O (0.3)
T_6	0.8	0.98	0.97
T_7	0.2	0.14	0.09
T_T	1.05	1.12	1.06

Zone	Multiplier/Breeder (Ω/4π) Pb/Li (0.4)	Be/Li (0.3)	Be/Li_2O (0.3)
Axial			
First wall[a]	2.70	2.08	2.08
Breeder	7.29	6.93	6.99
Graphite	0.16	0.11	—
Vessel	0.23	0.16	0.03
	10.38 (49%)	9.28 (41%)	9.10 (41%)
Radial			
First wall[a]	4.08	5.08	5.09
Multiplier	2.86	3.54	3.56
Graphite	2.89	3.42	3.33
Vessel	0.92	1.25	1.11
	10.75 (51%)	13.29 (59%)	13.09 (59%)
Total	21.13	22.57	22.19

[a]Includes fraction of x-ray and debris energy (~5.7 MeV per D–T reaction) equal to solid angle fraction.

Table 8-13. Total energy deposition by zone (MeV/D-T reaction).

compared to the results of the scoping calculations (see Fig. 8-40) is primarily the result of adding a graphite reflector behind the Li zones. The reduction in neutron leakage more than offsets the additional neutron losses in the first wall. Note, however, that the combined moderating effects of the compressed target material and the first wall reduces T_7 by ~35%.

The distribution of energy deposition within the chamber for the three cases is given in Table 8-13. The neutron energy deposited in the compressed target materials is ~2.2 MeV. This energy plus the 3.5 MeV alpha-particle energy will appear as x rays and debris, most of which will be deposited in the first wall. In Table 8-13, the x-ray and debris energy is divided according to the solid-angle fractions of the radial and axial first walls and added to the neutron energy deposited in those structures. For example, in the Be/Li case, the neutron energy deposited in the axial first walls is 0.37 MeV, while the total energy deposited is $0.37 + 0.3(5.7) = 2.08$ MeV.

The total energy deposited per D–T reaction varies from 21.13 MeV for the Pb/Li system to 22.57 MeV for the Be/Li case. The chamber with a Be multiplier and Li_2O breeder has an energy deposition of 22.19 MeV.

The division in energy deposition between the axial and radial blankets is important, since one of the objectives of SEBREZ is to recover the majority of the system energy from the nontritium-breeding radial blanket. The Pb/Li system, in which the breeding zones subtend a solid-angle fraction of 40%, has a radial/axial energy split of 51 to 49%. The energy split for both Be systems, in which $\Omega/4\pi = 0.3$, is 59% in the radial blanket and 41% in the axial blankets. The energy share of the axial blankets is higher than their solid-angle fraction, primarily because of the exoergic $^6Li(n,T)\alpha$ reactions which release 4.8 MeV. This energy appears as kinetic energy carried by the T and α particles and is deposited locally.

Tritium Production in Beryllium. Although Be is much more effective than Pb in minimizing the required size of the breeding zones, it has one serious disadvantage: Be produces tritium both directly and indirectly. Direct production is via the $^9Be(n,T)^7Li$ reaction, which occurs at a rate of $\sim 7 \times 10^{-3}$ per D–T reaction in the cylindrical-chamber model. The ^7Li produced is then available for additional tritium production. Another source of tritium production in Be is the result of the $^9Be(n,\alpha)^6He$ reaction, which occurs at a rate of 0.062 per D–T reaction. ^6He beta-decays with a half-life of 0.85 s to ^6Li. The moderated neutrons reflected back through the Be multiplier can then convert the ^6Li to tritium.

To illustrate the magnitude of this production, consider a 3000-MW(t) reactor which produces 5.6×10^4 moles of D–T neutrons per full-power year. The direct tritium production rate in Be would therefore be 1.2 kg/yr. If all the ^6Li and ^7Li produced in the Be zone were also converted to tritium, an additional 11.6 kg/yr would be produced.

Conclusions. We find that it is possible to segregate the tritium breeding regions in a small fraction of the blanket solid angle by means of neutron multiplication and scattering. With a Be multiplier the required solid-angle fraction is <30% for either Li or Li_2O breeders, and nearly 60% of the system energy is deposited in the lithium-free portion of the blanket. Unfortunately, tritium is produced in Be; this unwanted production conflicts with our objective of having the major fraction of the blanket free of tritum. Using a Pb multiplier requires a greater solid-angle fraction for the

breeding zones (~40%); as a result, nearly half of the energy must be recovered from these regions. It is not clear with this energy split that a tritium-free blanket has a compelling advantage.

While the tritium-free blanket may not be a practical design goal, the SEBREZ concept demonstrates that the tritium breeding regions can be confined to a much smaller fraction of the blanket than one would predict by scaling one-dimensional neutronics results. Taking advantage of the asymmetric neutronic effects is a design technique that gives us significant latitude in chamber configuration.

Author: W. R. Meier

SCEPTRE: A High-Temperature ICF Reactor

The first generation of fusion reactors will most likely use such conventional technology as steel construction and a steam power-generation cycle. If the fusion source for these reactors costs more than a combustion chamber, and the balances of plant are equivalent, then first-generation fusion reactors are not likely to demonstrate a great advantage over conventional fossil and fission sources, beyond the promise of an unlimited fuel supply and reduced environmental impact.

Second-generation fusion reactors, however, are likely to offer greater performance and safety with less environmental impact and a lower power cost than for first-generation reactors, because of the longer time available for materials and technology development. Creating such an advanced second-generation inertial fusion reactor is the goal of our SCEPTRE project. SCEPTRE offers the potential for

- Generating electricity at 50% efficiency.
- Providing high-temperature (850°C) heat for hydrogen production.
- Producing fissile fuel for light-water reactors, with a chamber configuration that is intrinsically free of the hazards of catastrophic fire or tritium release.

Although SCEPTRE incorporates several speculative ideas that may require decades of development, it is more likely to lead to power plants that can deliver the ultimate benefits of fusion. The fundamental SCEPTRE concept is for an ICF high-temperature gas-cooled reactor (HTGR) that borrows heavily from fission HTGR technology.[117] The spherical reactor cavity for SCEPTRE consists of a porous first-wall structure, heavily laden with flowing liquid lead, which can withstand many years of x-ray and debris energy deposition before replacement (see "JADE Design Considerations" earlier in this section). The reactor cavity is enclosed by a neutron blanket consisting of vertical pipes filled with graphite-coated, helium-cooled lithium oxide particles, used for tritium breeding. The SCEPTRE reactor is illustrated in Fig. 8-41.

SCEPTRE's extremely large number of individual tritium-breeding particles provides insurance against significant releases of tritium in an accident. Each tritium-breeding particle is coated in a multilayer process to prevent tritium migration (in the same way fission-product gases are contained in an HTGR fuel particle). Tritium recovery is accomplished by slowly circulating the particles through the blanket to allow continuous refueling without reactor shutdown and to solve the difficult problem of in-situ tritium recovery from solid-lithium compounds.[118] This concept is the origin of SCEPTRE's name (Small Capsules Effectively Prevent Tritium RElease). The blanket configuration appears to be immune to a liquid-metal fire hazard involving the release of tritium or activated materials, because

- The lithium is in the form of a high-temperature ceramic.
- The tritium inventory is encapsulated in 10^7 independent ceramic particles.
- The liquid-lead first-wall coolant has a negligible affinity for dissolved tritium.

The geometry of the reactor is that of a sphere within a cylinder. A spherical shell is a minimum-mass shape for a first-wall structure which must absorb directed x-ray and debris energy from a point source. The space just outside the spherical shell is filled with a spray of liquid lead to cool and condense hot vaporized lead. The shell is surrounded by a neutron blanket consisting of a dense array of vertical 20-cm-diam pipes headed by toroidal inlet and outlet manifolds for the helium coolant. The pipe array forms the cylindrical portion of a right circular cylinder, as shown in Fig. 8-41. This is a convenient geometry for easily replacing

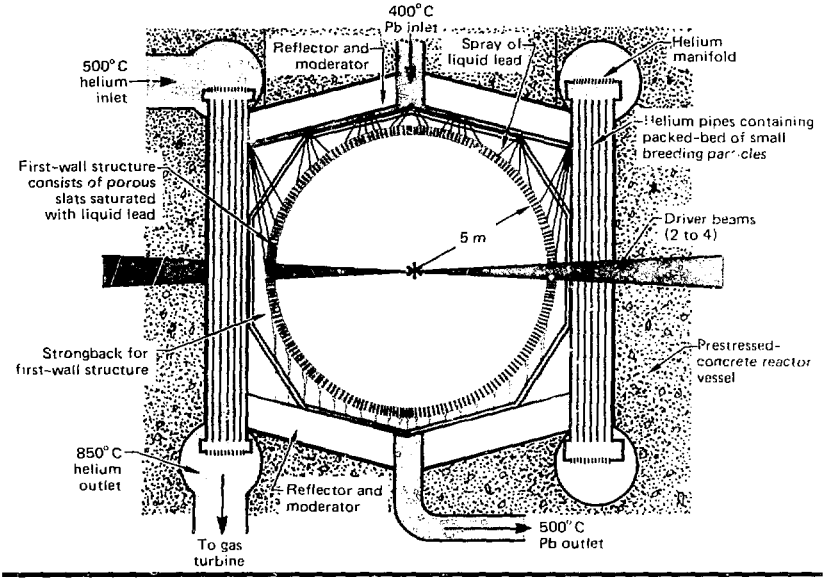

Fig. 8-41. Schematic drawing of SCEPTRE high-temperature gas-cooled reactor.

the inner JADE structure without disassembling the neutron blanket. Automatic devices for continuous supply and removal of breeding particles are located in the upper and lower helium manifolds; they assure a very slow, but steady, gravitational flow of coated spheres through the helium pipes.

The top and bottom of the reactor consist of only a lead neutron reflector and multiplier. The feasibility of segregating the breeding zone in this fashion has been demonstrated in the two-dimensional neutronic calculations of the SEBREZ study described in the previous article.

To assure that SCEPTRE's tritium-breeding performance will exceed unity, two kinds of calculations were required. First, we performed a stress analysis to determine the wall thickness and diameter of the helium pipes. This determination of the volume fraction of steel required in the blanket, an important source of parasitic neutron loss, is described in the next article, "SCEPTRE Mechanical Design." Second, we performed a two-dimensional neutronics calculation to demonstrate that tritium breeding in only the radial zones was sufficient. This is described in "SCEPTRE Neutronics Design" at the end of this section. More detailed calculations await the specification of a feasible coated breeding particle.

The JADE first-wall structure, the liquid lead, the outer helium pipes, and the outer-chamber vacuum vessel all operate between 400 and 500°C. The resulting background pressure in the chamber, $<10^{-4}$ Torr, is adequate for propagation of either laser or heavy-ion beams. A continuous shower of liquid lead is sprayed into the reactor from the top to wet the JADE structure, cool the outside of the helium pipes and outer wall, and provide a large number of spray droplets for cooling and condensing the lead plasma created on each shot by the energy deposition of x rays and debris.

The entire reaction chamber is housed in a prestressed-concrete reactor vessel (PCRV), similar to that housing an HTGR. Figure 8-42 shows a PCRV poured in place to enclose the entire primary cooling system of an HTGR. The SCEPTRE chamber of Fig. 8-41 could simply replace the fission core of the HTGR, with the size of the PCRV remaining unchanged. Of course the SCEPTRE PCRV would have horizontal apertures to let in the laser beams; there would also be a liquid-lead heat-exchanger loop.

The PCRV forms the third layer of protection against pipe failure and tritium diffusion. Because of the strength of the PCRV, the thickness of the containment building can be significantly reduced. In

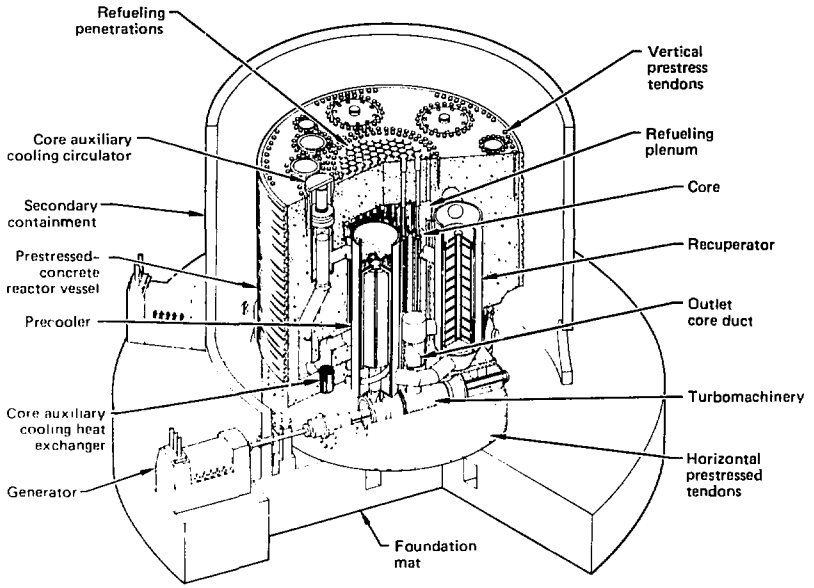

Fig. 8-42. Arrangement of reactor, turbine generator, and heat exchangers in the SCEPTRE prestressed-concrete reactor vessel.

addition, since ICF reactors carry no danger of energy release as do fission-reactor cores, and since SCEPTRE contains no liquid lithium, a relatively inexpensive containment building strong enough to resist only external shocks (such as from tornados and earthquakes) is all that is required to form the fourth level of protection.

SCEPTRE will operate at a fusion power of 3 GW with driver energy in the range of 3 to 4 MJ, target gains of 150 to 200, and pulse repetition rates of ~5 Hz. We presently envision a power-conversion cycle (described below) that includes an advanced Brayton cycle plus a steam bottoming cycle, with a combined effective efficiency of 50%. This would yield a net output power near 1400 MW(e).

Coated Particles. The key to the SCEPTRE concept is the individual encapsulation of a lithium-bearing compound in small particles,[119] similar to the coated fissile fuel particles (~0.03 cm diam) now currently used in gas-cooled reactors in the US and Britain. The coating of uranium carbides and oxides with layers of pyrolytic carbon (PyC) and silicon carbide (SiC) is now a mature technology,[120,121] capable of producing particles to contain all fission-product gases. As Fig. 8-43 shows, layers of carbon and silicon carbide are built up over a kernal of fission fuel or tritium-breeding material. These small ceramic spheres are extremely strong and, due to the PyC, get stronger with temperature. PyC coatings, for example, are applied in fluidized bed furnaces at 1500 to 1800°C by chemical vapor deposition.

The coatings on the particles serve in a dual capacity as diffusion barriers and pressure vessels, to provide protection against the release of fission-product gases, in the case of fission, or the release of tritium, in the case of fusion. Typically, particle coatings are composed of four layers:[117,122]

- An innermost porous PyC layer, which provides void space to accommodate gas-pressure buildup.
- A very dense inner PyC layer, which acts as a diffusion barrier to fission-product gases and also protects the overlying SiC from chemical attack.
- An SiC layer, for high strength under large irradiation doses.
- An outer PyC layer, also for high-temperature strength.

There has been no significant analysis of the feasibility of such an approach for a tritium-breeding fusion blanket, yet many of the advantages of coated fuel-bearing particles carry over from fission to fusion. Layers of a suitable oxide, such as BeO,

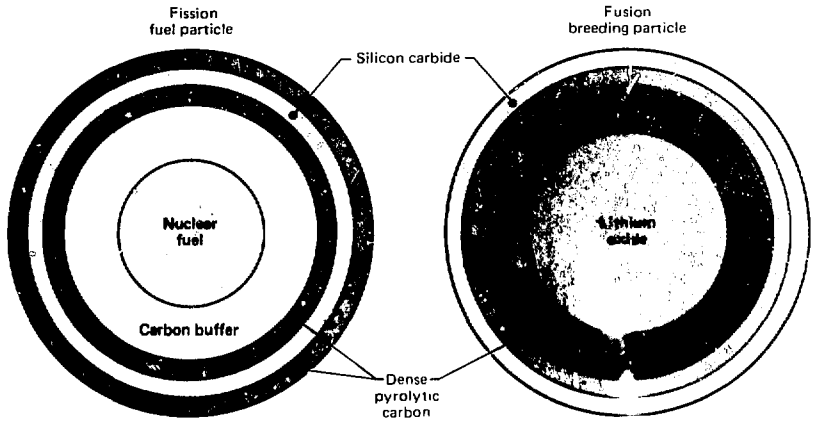

Fig. 8-43. Composition of fission fuel particles and fusion tritium-bredding particle.

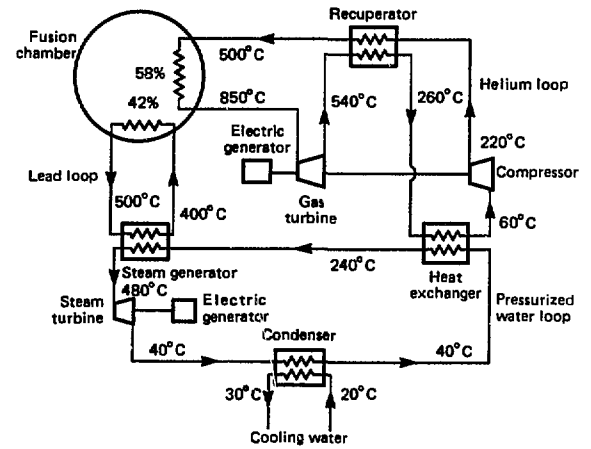

Fig. 8-44. Power-conversion cycle for an ICF reactor using liquid lead as first wall protection and coolant and helium as the neutron-blanket coolant.

may be a valuable tritium barrier. An unburnable outside layer of SiC will insure fire safety in an externally-caused catastrophic accident. The design of a particle with suitable tritium-migration barriers is the crucial issue that still must be worked out. We envision that removal of the tritium from the particles will be accomplished by simply raising the temperature, or, if necessary, by crushing the particles.

The concept of using individually coated particles for either tritium breeding or fission suggests that the SCEPTRE reactor can be used as a fusion-fission hybrid simply by using a mixture of coated particles in the blanket at any one time: tritium-breeding particles of one size, and fertile particles of another size bearing breeding fissile material. The different particle sizes assure easy separation at the end of the irradiation period. Brief irradiation times would lead to a fission-suppressed mode of operation wherein the production rate of fissile material can be maximized and afterheat minimized.

Power Conversion. In our SCEPTRE study, we have included a balance of plant having a very high combined-cycle efficiency of 50% when generating electricity. To achieve this efficiency, we incorporated a closed helium-driven Brayton cycle to effectively use SCEPTRE's high (850°C) temperatures. We also use a steam Rankine cycle to employ the lower-quality heat and minimize its rejection into the environment. Although there are not many large helium-driven Brayton cycles currently in operation, there are many air-driven cycles that operate at the same temperature with uncooled cast turbine blades of a standard high-nickel alloy.[123]

Figure 8-44 illustrates the SCEPTRE power-conversion cycle; the cycle shown in the figure has been adapted from HTGR work at General Atomic.[123, 125] The fraction of the thermal power removed by the helium coolant, f_H, is 58%, while the lead coolant removes the remaining 42%. The helium turns the gas turbine generator and then rejects heat to both the recuperator and the pressurized water loop before being compressed back up to ~4 MPa. In the steam cycle, the water heated by the helium is superheated to 480°C at 3.45 MPa by the lead loop before entering the steam turbine

The efficiencies of the helium Brayton and the steam Rankine cycle are approximately $\eta_B = 40$ and $\eta_R = 35\%$, respectively. The combined cycle efficiency is $\eta = \eta_B f_H + \eta_R [(1 - f_H) + f_H(1 - \eta_B)]$. For the parameters given above, the combined cycle efficiency is $\eta = 50\%$.

Although the power-conversion cycle shown in Fig. 8-44 is designed for electricity generation, it is clear that using the high-temperature heat for synfuel production and the low-temperature heat for cogeneration or domestic steam heating are equally viable.

The complexity of SCEPTRE's balance of plant will increase plant cost, but it is likely that the fusion-specific components will be sufficiently costly that a highly efficient balance of plant will be economically justified to convert the very largest possible fraction of fusion energy released. Striving for a high capacity factor will be similarly important. Today's LWRs have efficiencies of 33% and capacity factors of 60%. If these parameters for fusion can be raised to 50 and 80%, respectively, the capital costs can be a factor of 2 higher than for a LWR without affecting the cost of electricity.

Authors: M. J. Monsler and W. R. Meier

SCEPTRE Mechanical Design. To evaluate the neutronic characteristics of SCEPTRE, it is necessary to have a reasonable estimate of the amount of steel in the neutron blanket. This value is important because parasitic neutron captures can significantly degrade the tritium-breeding performance. We have performed calculations of the stresses in SCEPTRE's steel pipes to determine the pipe dimensions and, thus, the fraction of steel in the blanket.

The stresses in the steel pipes will consist of a cyclic thermal stress due to neutron heating and a steady stress due to internal pressure. We have previously demonstrated that the temperature rise during heating is negligible compared to the temperature profile in the HYLIFE FSW (Ref. 126); therefore, a steady-state analysis of the thermal stress is valid. As a first cut, we assumed this is also true for the helium flow pipes. This assumption will be evaluated for the resulting pipe dimensions and heat loads.

The thermal stresses in an unconstrained hollow cylinder are as follows:[127]

$$\sigma_{rr}(r) = \frac{\alpha E}{(1-\nu)r^2} \times \left[\frac{r^2 - a^2}{b^2 - a^2}\int_a^b T(r)rdr - \int_a^r T(r)rdr\right] \quad (11)$$

$$\sigma_{\theta\theta}(r) = \frac{\alpha E}{(1-\nu)} \times \left[\frac{2}{b^2 - a^2}\int_a^b T(r)rdr - T(r)\right] \quad (12)$$

and

$$\sigma_{zz}(r) = \sigma_{zz}(r) - \sigma_{rr}(r) = \frac{\alpha E}{(1-\nu)r^2}\left[\frac{r^2 + a^2}{b^2 - a^2}\int_a^b T(r)rdr + \int_a^r T(r)rdr - T(r)r^2\right], \quad (13)$$

where α is the coefficient of thermal expansion, E is Young's modulus, ν is Poisson's ratio, and a and b are the inner and outer radii, respectively.

We calculated the temperature distribution assuming a uniform heat source in the pipe wall with cooling only on the inside surface. The thermal conductivity is taken as constant, and the temperature at the inner surface of the pipe is specified. Thus, we have

$$T(r) = \frac{Q}{2K}\left[b^2\ln(r/a) - (r^2 - a^2)/2\right], \quad (14)$$

where Q is the heat rate and K is the thermal conductivity. Note that $T(r)$ is the difference between the local temperature and the known inner-surface temperature.

The resulting thermal stresses are

$$\sigma_{zz}(r) = -\frac{\alpha EQ}{16K(1-\nu)}\cdot\frac{1}{r^2} \times \left\{\frac{r^2 - a^2}{b^2 - a^2}\left[4b^4\ln(b/a) - 3b^4 + 4a^2b^2 - a^4 + 2b^2r^2[1 - 2\ln(r/a)] - 2a^2[b^2 + r^2] + r^4 + a^4\right]\right\}, \quad (15)$$

$$\sigma_{zz} = \frac{\alpha EQ}{16K(1-\nu)} \left\{ \frac{2}{b^2 - a^2} \times \left[4b^4 \ln(b/a) - 3b^4 + 4a^2b^2 - a^4 \right] - 8b^2 \ln(r/a) + 4r^2 - 4a^2 \right\} , \quad (16)$$

and

$$\sigma_{\theta\theta} = \frac{\alpha EQ}{16K(1-\nu)} \cdot \frac{1}{r^2} \times \left\{ \frac{r^2 + a^2}{b^2 - a^2} \left[4b^4 \ln(b/a) - 3b^4 + 4a^2b^2 \right] - 2b^2r^2[1 + 2\ln(r/a)] + 2a^2(b^2 - r^2) + 3r^4 - a^4 \right\} . \quad (17)$$

The stresses can each be expressed in terms of a common factor,

$$\sigma_0 \equiv \frac{\alpha EQb^2}{16K(1-\nu)} , \quad (18)$$

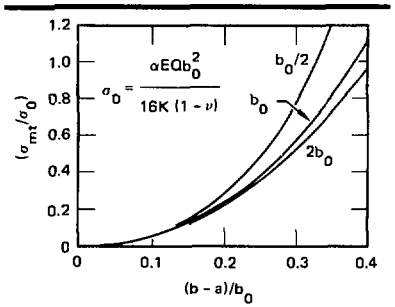

Fig. 8-45. Maximum thermal tensile stress vs wall thickness.

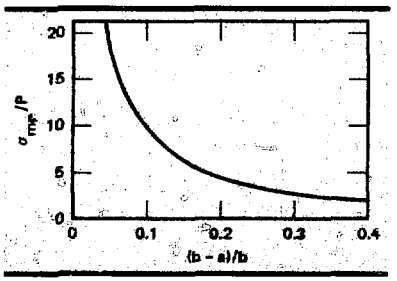

Fig. 8-46. Maximum pressure-induced tensile stress vs wall thickness.

and functions of (r/b) and (a/b). The maximum thermal tensile stress, σ_{mt}, occurs at $r = a$ and is given by

$$\sigma_{mt} = \sigma_{zz}(a) = \sigma_{\theta\theta}(a) = \sigma_0 \left\{ \frac{2}{1 - (a/b)^2} [4\ln(b/a) - 3 + 4(a/b)^2 - (a/b)^4 \right\} . \quad (19)$$

For a fixed (a/b), the maximum stress is proportional to σ_0, which goes as b^2. The maximum stress as a function of the pipe thickness, $(b - a)$, for a fixed pipe radius, b, is shown in Fig. 8-45, which gives curves for pipes of radii $b_0/2$, b_0 and $2b_0$. From the standpoint of thermal stresses, the advantages of thin-walled pipes are clear in the figure. Note that, for thin-walled pipes, the maximum stress is independent of the radius.

The stresses in an unconstrained hollow cylinder resulting from an internal hydrostatic pressure, P, with zero external pressure, are given by[127]

$$\sigma_{rr}(r) = \frac{-Pa^2}{(b^2 - a^2)} \cdot \frac{(b^2 - r^2)}{r^2} , \quad (20)$$

$$\sigma_{zz}(r) = \frac{2Pa^2}{(b^2 - a^2)} = \text{constant} , \quad (21)$$

and

$$\sigma_{\theta\theta}(r) = \frac{Pa^2}{(b^2 - a^2)} \cdot \frac{(b^2 + r^2)}{r^2} . \quad (22)$$

As with the thermal stress, the maximum pressure-induced tensile stress, σ_{mp}, occurs at $r = a$. It is given by

$$\sigma_{mp} = \sigma_{\theta\theta}(a) = \frac{P(b^2 + a^2)}{(b^2 - a^2)} . \quad (23)$$

In contrast to the thermal stress, the maximum pressure-induced stress decreases with increasing wall thickness (Fig. 8-46).

The sum of the maximum tensile stresses due to the neutron heating of the pipe wall

and the internal coolant pressure is

$$\sigma_m = \sigma_{mt} + \sigma_{mp} = \frac{\alpha E Q b^2}{16K(1-\nu)} \times \left\{ \frac{2}{1-(a/b)^2} \left[4\ln(b/a) - 3 + 4(a/b)^2 - (a/b)^4 \right] + P \left[\frac{1+(a/b)^2}{1-(a/b)^2} \right] \right\} .$$

To calculate σ_m for a given pipe, we need appropriate values of the heating rate, Q, and the coolant pressure, P. To estimate Q, we note that the neutron heating in an unprotected steel wall is on the order of 1 MeV per cm of wall thickness per D-T reaction.[125] Therefore,

$$Q \sim \frac{(I/t)}{14.1\ \text{MeV}} \cdot \Gamma_w \cdot \frac{(100\ \text{W/cm}^2)}{(\text{MW/m}^2)} ,$$

where I/t is neutron heating per unit wall thickness ($\simeq$1 MeV/cm) and Γ_w is the neutron wall loading in MW/m^2 ($= 0.8\ P_f/4\pi R_w^2$). In this latter term, P_f is the fusion power (in MW) and R_w is the chamber-wall radius (in m). Using a thin JADE-type chamber structure[125] to absorb the soft x rays and debris allows us to achieve a high neutron wall loading. For $\Gamma_w > 5$ MW/m^2, Q will be > 35 W/cm^3.

The coolant pressure will depend on the characteristics of the blanket and the desired thermodynamic cycle. In general, high pressures are required to improve the heat-transfer and heat-transport characteristics of the gas. Typical values cited for He-cooled reactors range from less than 2 MPa (20 atm) to greater than 6 MPa (60 atm) (Ref. 130).

Figure 8-47 is a plot of σ_{mt}, σ_{mp}, and σ_m as a function of (a/b) for a 2-1/4 Cr-1 Mo steel pipe of radius $b = 10$ cm with a heat load of 40 W/cm^3 and an internal pressure of 4.05 MPa. The material properties (assumed to be constant) used for the steel are listed in Table 8-14 (Ref. 126). To correctly select a design point, these stresses must be compared to the allowable design constraints[131,132] to determine the range of values of (a/b) that meet the various criteria. For simplicity, however, assume that (a/b) is selected to minimize σ_m. For the case shown in Fig. 8-47, the sum of the maximum tensile stresses reaches a minimum at $(a/b) \simeq 0.95$.

For heat rates ranging from 20 to 60 W/cm^3 and coolant pressures ranging from 2 to 6 MPa in a 10-cm-radius pipe, the value of (a/b) at which σ_m is minimized ranges from 0.925 to 0.964. For pipe radii ranging from 5 to 20 cm, and with $Q = 40$ W/cm^3 and $P = 4.05$ MPa, the value of (a/b) at which σ_m is minimized ranges from 0.918 to 0.967. Based on these results and typical stress limits for 2-1/4 Cr-1 Mo steel at reasonable temperatures, $(a/b) = 0.95$ and $b = 10$ cm are selected as typical dimensions to be used in the neutronics calculation. Using larger pipes will lower the volume fraction of steel in the blanket, which is roughly proportional to $[1 - (a/b)]$. However, using larger pipes will also result in higher total stresses.

We can now evaluate the assumption that a steady-state analysis is suitable for calculating the thermal stress. From Eq. (15), the temperature difference across the wall of a 10-cm-radius pipe with $(a/b) = 0.95$ and $Q = 40$ W/cm^3 is 14.5°C. The temperature rise per pulse depends on the pulse repetition rate as well as Q, such that[126]

$$\Delta T \simeq Q\tau/\rho C_v ,$$

where τ is the interpulse time in seconds, ρ is the density of the steel in g/cm^3, and C_v

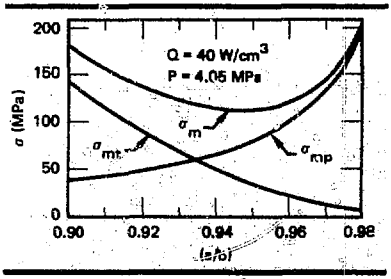

Fig. 8-47. Combination of maximum tensile stresses.

α	$= 1.19 \times 10^{-5}$/°C
E	$= 2.04 \times 10^5$ MPa
ν	$= 0.318$
K	$= 0.35$ W/cm·°C
C_v	$= 0.66$ J/g·°C

Table 8-14. Properties of 2-1/4 Cr-1 Mo steel used for SCEPTRE steel-pipe stress calculations.

is the specific heat capacity in J/g·°C. A repetition rate of 6 Hz is taken as typical for a chamber with a JADE-type first wall.[129] Using $\tau = 1/6$ s, $\rho = 7.86$ g/cm^3, and $C_v = 0.66$ J/gm·°C, we obtain $\Delta T = 1.3$°C for $Q = 40$ W/cm^3. Since this is $<1/10$ of the temperature difference across the wall, it is assumed that the steady-state analysis is adequate for these preliminary calculations.

Increasing (a/b) or τ increases the temperature-difference ratio $\Delta T/[T(b) - T(a)]$. For example, with $(a/b) = 0.97$ and $\tau = 2/3$ s, $\Delta T \simeq T(b) - T(a) = 5.2$°C, and a time-dependent thermal-stress analysis would be required.

Based on our steady-state stress analysis, a radius of 10 cm and a wall thickness of 0.5 cm are selected as the dimensions of the helium-coolant pipes in the blanket of the SCEPTRE gas-cooled ICF reactor for the purpose of neutronic modeling. The neutronics calculations are described in the following article.

Author: W. R. Meier

SCEPTRE Neutronics Design. We have completed initial one-dimensional and two-dimensional neutronics calculations for SCEPTRE. Based on the favorable tritium-breeding performance for the one-dimensional geometry ($T_T = 1.275$), we propose a cylindrical chamber with tritium breeding only in the radial zones. In this configuration, breeding in the radial zones is enhanced by neutrons scattered from the top and bottom blankets.[133] For the specific two-dimensional and blanket composition evaluated, we obtained a tritium-breeding ratio slightly greater than 1.0, which demonstrates the neutronic feasibility of the SCEPTRE concept.

The SCEPTRE first wall is a lead-cooled honeycomb structure made of porous fiber-metal.[134] The Pb-saturated fiber-metal is 90 vol% Pb and 10 vol% 2-1/4 Cr-1 Mo steel. The first wall is modeled as a 10-cm-thick zone of this material with a density multiplication factor of 0.28. This reduced density accounts for both the honeycomb construction and triangular configuration of the first wall, which has an inner radius of 6 m.

The tritium-breeding blanket is made up of an array of steel pipes containing coated Li_2O balls and high-pressure He coolant. Based on preliminary stress calculations, we chose 20-cm-diam pipes with 0.5-cm-thick walls as the base case.[135]

To reduce the pressure drop as the coolant flows through the breeding balls, we propose a configuration with concentric coolant channels. This configuration reduces the pressure drop by reducing the distance the coolant must flow through the packed bed of balls. A cross section of a single pipe is shown in Fig. 8-48. The tritium-breeding balls are contained within an annular region by thin, fine-mesh metal screens. An open, annular region between the inside surface of the pipe wall and the outer edge of the breeding material forms a channel for the coolant inlet. The coolant flows radially inward to the center of the breeding material, where it is exhausted through the central channel.

The coated Li_2O balls comprise 60 vol% of the annular breeding region; He comprises the remaining 40 vol%. The packing fraction of 60 vol% is typical for a bed of spheres.[136] Assuming the outer coolant channel is 0.5 cm wide and the central channel is 2 cm in diameter, the volume fractions for a single pipe are

- Breeding balls = 0.4800
- He coolant = 0.4225
- Steel pipe = 0.0975

The breeding balls themselves are Li_2O spheres coated with layers of BeO, C, and SiC, which provide barriers to tritium diffusion and allow high-temperature operation (see the previous article). For these initial calculations, we assume the following volume fractions for the breeding balls:

- Li_2O = 0.50
- BeO = 0.20
- C = 0.20
- SiC = 0.10

We used a relative-density multiplier of 0.907 in our neutronics calculations; this value corresponds to a close-packed hexagonal array of cylindrical pipes. Note that the total coating thickness, which is 26% of the Li_2O radius, is relatively much thinner than fission HTGR fuel-particle coatings. We have not yet specified the actual dimensions of the breeding balls, which will depend on the materials selected, on heat-transfer and heat-transport considerations, and on the effectiveness of the

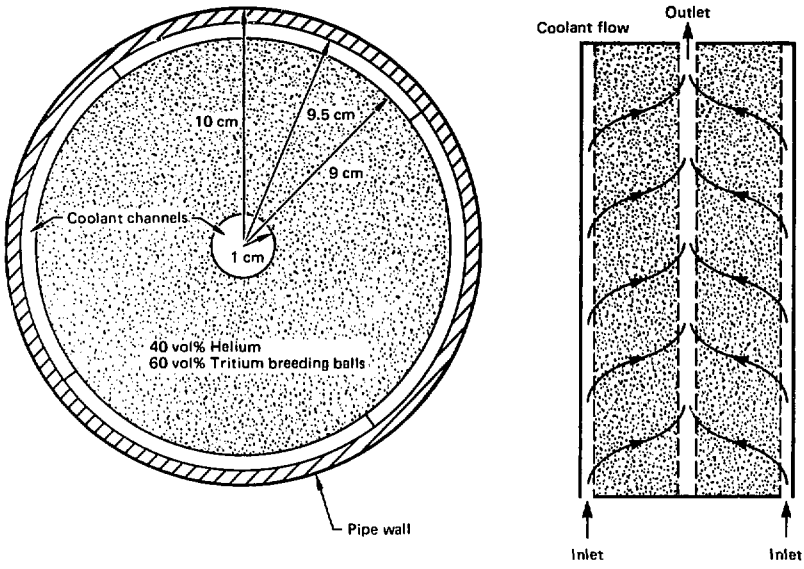

Fig. 8-48. Cross section of a SCEPTRE breeding-blanket pipe.

coatings in preventing tritium diffusion.

The neutronics model for the one-dimensional calculation is summarized in Table 8-15. The target is modeled as a D–T region with $\rho R = 3.0$ g/cm^2, surrounded by a pusher with $\rho \Delta R = 0.8$ g/cm^2. The neutron source is uniformly distributed throughout the D–T region. The breeding blanket is modeled as a 0.5-cm-thick steel shell followed by a 1-m-thick region containing a homogeneous mixture of breeding balls, He, and steel, as described above. The 0.5-cm-thick steel shell represents the steel walls of the innermost row of pipes; it is included so that the resulting neutron heating rate can be compared to the 40 W/cm^3 assumed in the thermal stress calculations (see the previous article). The breeding blanket is backed by a 30-cm-thick graphite reflector and an 8-cm-thick steel vessel wall. Beam penetrations are not included in this model.

For the one-dimensional calculations, the total energy deposited per 14.1-MeV source neutron is 17.44 MeV. Including the alpha-particle energy, a total of ~21 MeV is deposited per D–T reaction, which gives an energy-multiplication factor for the system of 1.19. Besides the direct heating from neutrons, the first wall also absorbs the alpha-particle energy and neutron energy deposited in the target; these combine for a total of 7.03 MeV. The Pb coolant must therefore remove ~33% of the total system energy. The neutron energy deposited in the 0.5-cm-thick pipe wall is 0.52 MeV, giving a heating rate of 38 W/cm^3 for a typical chamber fusion power of 3000 MW. The tritium breeding ratio is 1.275, comprised of ^{6}Li$(n,T)\alpha$ reactions (1.162) and ^{7}Li$(n,n'T)\alpha$ reactions (0.113).

Table 8-15. One-dimensional SCEPTRE neutronics model.

Zone description	Material	Inner radius (cm)	Thickness (cm)	Density multiplier
First wall	Pb and steel	600	10.0	0.280
Pipe wall	Steel	610	0.5	1.000
Breeding blanket	Breeding balls, steel, and helium	610.5	99.5	0.907
Reflector	Graphite	710	30.0	1.000
Vessel wall	Steel	740	8.0	1.000

The two-dimensional SCEPTRE neutronics model, illustrated in Fig. 8-49, is a right circular cylinder having a height-to-diameter ratio of unity, with the breeding-blanket pipes running parallel to the chamber axis. This configuration allows the use of straight pipes with access at the ends for coolant manifolds. It also simplifies access to the breeding balls, which must be removed and processed periodically to recover the bred tritium. The radial blanket has the same dimensions and composition as used in the one-dimensional calculation

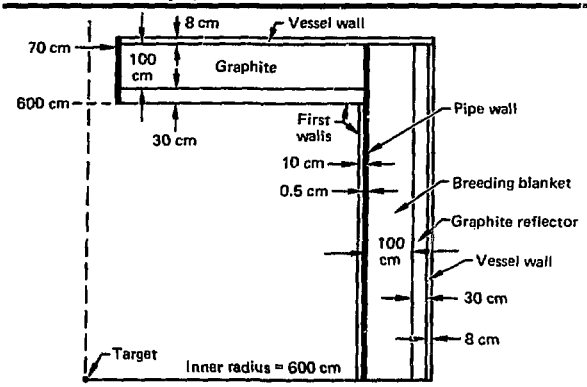

Fig. 8-49. Two-dimensional neutrons model for the SCEPTRE gas-cooled ICF reactor.

Zone	Energy deposited (MeV)
Fuel	1.93
Pusher	0.26
Radial zones	
First wall	1.14
Pipe wall	0.50
Breeding blanket	10.01
Reflector	0.01
Vessel wall	0.02
Axial zones[a]	
First wall	2.10
Graphite	1.47
Vessel wall	0.31
Beam-port liner	0.05
Total	17.80

[a] Half of the indicated energy is deposited in each end of the axial zones.

Table 8-16. Results of SCEPTRE two-dimensional neutron-energy deposition calculations.

(see Table 8-15). The axial blankets are 1-m-thick regions of He-cooled graphite. A thicker first wall (30 cm at $\rho/\rho_0 = 0.28$) is used in front of the axial blankets to increase the neutron multiplication via (n,2n) reactions with Pb. An 8-cm-thick vessel wall lies outside the graphite zones. There is no tritium breeding in the axial blankets.

Two beam penetrations, one through each axial blanket, are included in this model. Each hole is 1.4 m in diameter, which corresponds to a 2-MJ beam with 4 J/cm^2 on a mirror located ~40 m from the center of the chamber.

For the two-dimensional calculations, the total energy deposited per 14.1-MeV source neutron is 17.80 MeV, which is slightly higher than the one-dimensional result of 17.44 MeV. Table 8-16 gives the energy deposition by zone. Adding the alpha-particle energy gives 21.3 MeV per D–T reaction for a system energy-multiplication factor of 1.21. In this case, the total energy deposited in the first walls (including the alpha-particle energy and neutron energy deposited in the target) is 8.93 MeV. Assuming there is no heat transfer between the first walls and the He-cooled blankets, the Pb coolant must remove 42% of the chamber energy. The 0.50 MeV deposited in the 0.5-cm-thick pipe wall gives an average heating rate of 30 W/cm^3 for a fusion power of 3000 MW.

The tritium-breeding ratio for the two-dimensional calculation is 1.02, with $T_6 = 0.942$ and $T_7 = 0.078$. The contribution from ^{7}Li reactions scales with the fractional breeding blanket coverage ($0.7 \times 0.113 = 0.79$), as expected.

The beam ports have a total solid angle of 0.45% at the outer edge of the vessel wall. The neutron leakage out the ports is 0.015 neutrons per D–T neutron, 3 times greater than the solid-angle fraction of the ports. The neutron-energy leakage out of the ports, ~0.6 MeV, is dominated by the direct loss of 14.1-MeV neutrons.

Using the cylindrical-chamber model described above, with tritium breeding only in the radial zones, we have performed two-dimensional calculations of the neutronic aspects of SCEPTRE. The breeding blanket consists of an array of thin-walled steel pipes that contain coated Li_2O balls and high-pressure He coolant. Even though lithium comprises only 30 at.% of the breeding blanket, which subtends only ~70% of the chamber solid angle, our calculations yield a tritium-breeding ratio of 1.02. The total energy deposited in the chamber per D–T reaction is 21.3 MeV.

An interesting result is that 42% of the total energy must be removed by the Pb coolant flowing through the porous first-wall structure. The Pb temperature will be limited by corrosion and vapor-pressure considerations. As we suggest in the previous article, one possibility is to use the heat from the Pb coolant to drive a superheated steam Rankine cycle, which also serves as a bottoming cycle for a high-temperature, helium-driven Brayton cycle.

It should be emphasized that this is only one possible configuration for the SCEPTRE chamber. A plethora of design options needs to be investigated. Coated metallic lithium spheres may be better in terms of tritium containment. A carbonized fibrous

material may be an attractive alternative to the porous fiber-metal first wall. Finally, there may be little advantage in using a pure Pb coolant instead of the more commonly chosen $Pb_{83}Li_{17}$ eutectic in terms of maintaining a low tritium concentration. It is worth noting that, if all other factors are held constant, each of these latter three options is expected to increase the tritium-breeding ratio.

Author: W. R. Meier

References

1. R. L. Rudman and C. G. Whipple, "Time Lag of Energy Innovation," in *EPRI Journal*, Electrical Power Research Institute, Palo Alto, Calif. (1958), p. 14.
2. W. Hafele, Ed., *Energy in a Finite World: Paths to a Sustainable Future, Vol. 1* (Ballinger Publishing Co., Cambridge, Mass., 1981), p. 102.
3. J. Burke, *Connections* (Little, Brown & Co., Boston, 1978).
4. N. J. Hoffman, N. M. Jeanmougin, and K. A. Curlander, *Conceptual Design for a Laser Fusion Engineering Test Facility*, Final Report by Energy Technology Engineering Center, Canoga Park, Calif., to Lawrence Livermore National Laboratory, Livermore, Calif. (1981).
5. *Laser Program Annual Report—1980*, Lawrence Livermore National Laboratory, Livermore, Calif., UCRL-50021-80 (1981), pp. 9-88 to 9-90.
6. M. McDowell, Energy Technology Engineering Center, Canoga Park, Calif., private communication (September 1981).
7. J. H. Pitts, "Heat-Transfer Limitations on Pellets Used in ICF Reaction Chambers," *Proc. 9th Symp. Eng. Problems of Fusion Research*, Chicago, Ill., October 26-29, 1981 (IEEE, New York, 1981), pp. 676-679.
8. T. M. Henderson, R. J. Simms, and R. B. Jacobs, "Cryogenic Pellets for Laser-Fusion Research—Theoretical and Practical Considerations," *Advances in Cryogenic Engineering* **23**, J. D. Timmerhaus, ed. (Plenum Press, New York, 1978), p. 683.
9. *Laser Program Annual Report—1980*, Lawrence Livermore National Laboratory, Livermore, Calif., UCRL-50021-80 (1981), p. 9-26.
10. T. L. Anderson, *An Evaluation of the Corrosion Resistance of 2.25 Cr-1 Mo Steel in a Lithium-Lead Liquid*, M.S. thesis, Colorado School of Mines, Golden, Colo., T-2372 (May 1980).
11. B. Wilkinson, *The Corrosion Susceptibility of 2.25 Cr-1 Mo Steel in Lead Lithium Liquids*, M.S. thesis, Colorado School of Mines, Golden, Colo. (January 1982).
12. T. F. Kassner, "Rate of Solution of Tantalum Disks in Liquid Tin," *J. Electrochem. Soc.* **114**, 689-694 (1967).
13. Bechtel Group, Inc., *Conceptual Design of a Laser Fusion Power Plant—Part II. Two Technical Options: 1) The JADE Reactor, 2) Heat Transfer by Heat Pipes*, Final Report to Lawrence Livermore National Laboratory, Livermore, Calif., UCRL-15467 (1981).
14. J. A. Blink, O. H. Krikorian, and N. J. Hoffman, "The Use of Lithium in Fusion Reactors," *ACS Symposium Series* **179** (American Chemical Society, 1981), pp. 517-524.
15. D. L. Smith et al., "Analysis of In Situ Tritium Recovery from Solid Fusion-Reactor Blankets," *Proc. 4th Top. Mtg. Tech. Controlled Nucl. Fusion* (King of Prussia, Pa., October 14-17, 1980), ANS Pub. No. CONF-801011 (1981).
16. F. Cafasso and E. Veleckis, Argonne National Laboratory, Argonne, Ill., private communication (August 1980).
17. E. M. Larsen, M. S. Ortman, and K. E. Plute, *Comments on the Hydrogen Solubility Data for Liquid Lead, Lithium and Lithium-Lead Alloys and Review of a Tritium Solubility Model for Lithium Lead Alloys*, University of Wisconsin, Madison, Wis. UWFDM-415 (1981).
18. J. S. Watson, *Evaluation of Methods for Recovering Tritium from the Blankets or Coolant Systems of Fusion Reactors*, Oak Ridge National Laboratory, Oak Ridge, Tenn., ORNL TM 3794 (1972).
19. H. R. Ihle and C. H. Wu, "Experimental Determination of the Partial Pressures of D_2, HD and H_2D in Equilibrium With Dilute Solutions of Deuterium in Liquid Lithium," *Proc. 8th Symp. Fusion Tech.* [Leeuwenhorst Congress Centre Noordwijkerhout (The Netherlands), 1974], published by Commission of European Communities Directorate General, Scientific and Technical Information and Information Management, Luxembourg (1974).
20. K. Natesen and D. Smith, "Effectiveness of Tritium Removal from a Lithium Blanket by Cold Trapping Secondary Liquids, Na, K, and NaK," *Nucl. Tech.* **22**, 138 (1974). Figures 8 and 9 of this reference are used to estimate the hydrogen isotope concentrations.
21. H. Katsuta, T. Ishigai, and K. Furukuwa, "Equilibrium Pressure and Solubility of Hydrogen in Liquid Lithium," *Nucl. Tech.* **32**, 297 (1977).
22. E. Veleckis, R. M. Yonco, and V. A. Maroni, "Solubility of Lithium Deuteride in Liquid Lithium," *J. Less Common Metals* **55**, 85 (1977).
23. R. E. Buxbaum and E. F. Johnson, *The Use of Yttrium for the Recovery of Tritium from Lithium at Low Concentrations*, Princeton Plasma Physics Laboratory (Princeton University), Princeton, N.J., PPPL-1548 (1979).
24. M. E. Singleton, C. I. Folkers, and C. M. Griffith, "Assessment of Uranium and Cerium as Hydriding Materials for Hydrogen Isotopes in Flowing Argon," *Transactions of the ANS* **26** (American Nuclear Society, New York, 1977), pp. 74-75.
25. P. W. Fisher, J. B. Talbot, S. D. Clinton, E. L. Rogers, and J. S. Watson, "Properties of Yttrium Sorbers Which Improve Tritium Sorption Rate from Liquid Lithium," *9th Symp. Eng. Problems of Fusion Research* (Chicago, Ill., 1981), pp. 2094-2097.
26. J. E. Selle, Oak Ridge National Laboratory, Oak Ridge, Tenn., private communication (October 1977).
27. R. W. Webb, *Permeation of Hydrogen Through Metals*, Atomics International, Canoga Park, Calif., NAA-SR-10462 (1965).
28. J. D. Lee and R. W. Werner, *Concept for a Gas-Buffered Annular Heat Pipe Fuel Irradiation Capsule*, Lawrence Livermore National Laboratory, Livermore, Calif., UCRL-50510 (1968).
29. R. W. Werner, *The Generation and Recovery of Tritium in Thermonuclear Reactor Blankets*, Lawrence Livermore National Laboratory, Livermore, Calif., UCID-15390 (1968).

30. W. E. Calaway, "Electrochemical Extraction of Hydrogen from Molten LiF-LiCl-LiBr and Its Application to Liquid-Lithium Fusion Reactor Blanket Processing," *Nucl. Tech.* **39**, 63 (1978).
31. Bechtel Group, Inc., *Conceptual Design of a Laser Fusion Power Plant—Part I: An Integrated Facility*, Final Report to Lawrence Livermore National Laboratory, Livermore, Calif., UCRL-51467 (1981).
32. U. S. Department of Energy, Office of Reactor Research and Technology, *Demonstration Plant Conceptual Design Final Report*, U.S. Government Printing Office, Washington, D.C., CDS-400-8 (1981).
33. E. T. Plechaty and J. R. Kimlinger, *TARTNP: A Coupled Neutron Photon Monte Carlo Transport Code*, Lawrence Livermore National Laboratory, Livermore, Calif., UCRL-50400, Vol. 14 (1976).
34. R. J. Howerton, Lawrence Livermore National Laboratory, Livermore, Calif., private communication (August 1981).
35. M. A. Gardner and R. J. Howerton, *ACTL Evaluated Neutron Activation Cross Section Library—Evaluation Techniques and Reaction Index*, Lawrence Livermore National Laboratory, Livermore, Calif., UCRL-50400, Vol. 18 (October 17, 1978).
36. A. G. Croff, *A User's Manual for the ORIGEN2 Computer Code*, Oak Ridge National Laboratory, Oak Ridge, Tenn., ORNL/TM-7175 (1980). Also published as *Radiation Shielding Information Center Report CCC-371*, Radiation Shielding Information Center, Oak Ridge, Tenn. (1981).
37. J. A. Blink, R. E. Dye, and J. R. Kimlinger, *ORIB: A Computer Code That Produces One Energy Group, Time, and Spatially Averaged Neutron Cross Sections*, Lawrence Livermore National Laboratory, Livermore, Calif., UCRL-53262 (1981).
38. J. A. Blink, *FORIG: A Modification of the ORIGEN2 Isotope Generation and Depletion Code for Fusion Problems*, Lawrence Livermore National Laboratory, Livermore, Calif., UCRL-53263 (in press).
39. G. Lasche, *Activity Calculations—A Methodology*, internal memorandum E&MA 81-145, Lawrence Livermore National Laboratory, Livermore, Calif. (1981).
40. G. Lasche, *Primary Parameters Affecting Induced Activity of Radiation Case Material in an Inertial Confinement Fusion Reactor*, internal memorandum E&MA 81-007, Lawrence Livermore National Laboratory, Livermore, Calif. (February 1981).
41. "Standards for Protection Against Radiation," *U.S. Nuclear Regulatory Commission: Rules and Regulations*, 10 CFR 20, Part 20 (November 1978).
42. G. Lasche, *Radioactivity Estimates in HYLIFE*, internal memorandum E&MA 81-161, Lawrence Livermore National Laboratory, Livermore, Calif. (October 1981).
43. *Laser Program Annual Report—1980*, Lawrence Livermore National Laboratory, Livermore, Calif., UCRL-50021-80 (1981), pp. 9-61 to 9-63.
44. P. A. Finn, R. G. Clemmer, D. R. Armstrong, N. E. Parker, and T. Bova, "The Reactions of Li-Pb Alloys With Water," *Trans. Am. Nucl. Soc.* **34**, 55 (1980).
45. H. Migge, "Thermochemistry in the Systems Li-O-H, Li-O-C, Li-N-C," given at the 2nd Intl. Conf. on Liquid Metal Tech., Richland, Wash., April, 1980 (Conf. 800401, p. 18-9). Sponsored by the American Nuclear Society and the U.S. Department of Energy.
46. L. D. Muhlestein, "Liquid Metal Reactions Under Postulated Accident Conditions for Fission and Fusion Reactors," given at the 2nd Intl. Conf. on Liquid Metal Tech., Richland, Wash., April, 1980 (Conf. 800401, p. 5-1). Sponsored by the American Nuclear Society and the U.S. Department of Energy.
47. D. Matlock, Colorado School of Mines, Golden, Colo., private communication (November 1981).
48. R. G. Clemmer, D. R. Armstrong, and N. E. Parker, "An Experimental Study of the Reaction of Li-Pb, With Water," *Trans. Am. Nucl. Soc.* **32**, 71 (1979).
49. M. J. Monsler, J. Hovingh, D. L. Cook, J. G. Frank, and G. A. Moses, "An Overview of Inertial Fusion Reactor Design," *Nucl. Tech./Fusion* **1**, 302 (1981).
50. *Laser Program Annual Report—1979*, Lawrence Livermore National Laboratory, Livermore, Calif., UCRL-50021-79 (1980), p. 8-46.
51. *Laser Program Annual Report—1980*, Lawrence Livermore National Laboratory, Livermore, Calif., UCRL-50021-80 (1981), p. 9-30.
52. L. A. Glenn, *A 2-D Model of Plasma Jet Interaction in the HYLIFE Inertial Confinement Fusion Reactor*, Lawrence Livermore National Laboratory, Livermore, Calif., UCRL-86646 (1981).
53. M. A. Hoffman, *Liquid Jet Experiments: Relevance to Inertial Confinement Fusion Reactors*, Lawrence Livermore National Laboratory, Livermore, Calif., UCRL-15367 (1981).
54. *Laser Program Annual Report—1978*, Lawrence Livermore National Laboratory, Livermore, Calif., UCRL-50021-78 (1979), p. 9-6.
55. *Laser Program Annual Report—1980*, Lawrence Livermore National Laboratory, Livermore, Calif., UCRL-50021-80 (1981), p. 3-1.
56. *Laser Program Annual Report—1980*, Lawrence Livermore National Laboratory, Livermore, Calif., UCRL-50021-80 (1981), pp. 9-9 to 9-15.
57. J. Hovingh and J. Blink, "Parametric Analysis of Stress in the ICF HYLIFE Convertor Structure," *Proc. 4th Top. Mtg. Tech. Controlled Nucl. Fusion* (King of Prussia, Pa., October 1980), ANS Pub. No. *CONF-801011* (1981).
58. *Laser Program Annual Report—1980*, Lawrence Livermore National Laboratory, Livermore, Calif., UCRL-50021-80 (1981), pp. 9-42 to 9-43.
59. M. McDowell, Energy Technology Engineering Center, Canoga Park, Calif., private communication (January 1981).
60. L. A. Glenn and D. A. Young, "Dynamic Loading of the Structural Wall in a Lithium Fall Fusion Reactor," *Nucl. Eng. Des.* **54**, 1 (1979).
61. L. A. Glenn, *The Influence of Radiation Transport on Lithium Fall Motion in an ICF Reactor*, Lawrence Livermore National Laboratory, Livermore, Calif., UCID-18573 (1980).

References

62. L. A. Glenn, "Divergent Impulsive Crossflow Over Packed Columnar Arrays," *Nucl. Eng. Des.* **56**, 429 (1980). [See also erratum, *Nucl. Eng. Des.* **58**, 141 (1980).]
63. L. A. Glenn, "Transport Processes in an Inertial Confinement Fusion Reactor," *Nucl. Eng. Des.* **64**, 375 (1981).
64. *Laser Program Annual Report—1980*, Lawrence Livermore National Laboratory, Livermore, Calif., UCRL-50021-80, (1981), p. 9-30
65. L. A. Glenn, *A 2-D Model of Plasma-Jet Interaction in the HYLIFE Inertial Confinement Fusion Reactor*, Lawrence Livermore National Laboratory, Livermore, Calif., UCRL-86646 (1981).
66. J. G. Trulio and L. A. Glenn, *Pressure Equilibration Around Ejecta in a Nuclear Surface Burst*, Defense Nuclear Agency, Alexandria, Va., DASA 2457 (1970).
67. J. G. Trulio, *Theory and Structure of the AFTON Codes*, Air Force Weapons Laboratory, Kirtland Air Force Base, Albuquerque, N. Mex., AFWL TR 66-19 (1966).
68. L. A. Glenn, *AFTON Revisited: An Improvement Algorithm for Numerical Solutions of Initial Value Problems in Continuum Mechanics: Part I—The One Dimensional Equations*, Lawrence Livermore National Laboratory, Livermore, Calif., UCRL-52512 (1978).
69. L. A. Glenn, to be published.
70. L. A. Glenn, "On the Motion Following Isochoric Heating of Concentric Liquid Annuli," *Nucl. Eng. Des.* **60**, 327 (1980).
71. M. A. Hoffman, *Liquid Jet Experiments: Relevance to Inertial Confinement Fusion Reactors*, Lawrence Livermore National Laboratory, Livermore, Calif., UCRL-15367 (1981).
72. R. D. Monson, *Experimental Studies of Round and Sheet Jets With and Without Forced Nozzle Vibrations*, M.S. thesis, Dept. of Mech. Engr., University of California, Davis, Calif. (December 1980).
73. *Laser Program Annual Report—1980*, Lawrence Livermore National Laboratory, Livermore, Calif. UCRL-50021-80 (1981). p. 9-51.
74. R. Takahashi, *Experimental Investigation of the Stability of Liquid Sheet Jets*, M.S. thesis, Dept. of Mech. Engr., University of Calif., Davis, Calif. (December 1978).
75. H. R. Asare, *Theoretical and Experimental Investigation of Water Sheet Jets Under Forced Vibration*, Ph.D. thesis, Dept. of Mech. Engr., University of California, Davis, Calif. (November 1980).
76. H. R. Asare, R. K. Takahashi, and M. A. Hoffman, "Liquid Sheet Jet Experiments: Comparison With Linear Theory," *J. Fluids Eng.* (accepted for publication).
77. H. R. Asare and M. A. Hoffman, *Liquid Sheet Jet Experiments: Comparison With a Nonlinear Theory*, Lawrence Livermore National Laboratory, Livermore, Calif., UCRL-15367 (December 1980).
78. T. F. Chen and J. R. Davis, "Disintegration of a Turbulent Water Jet," *J. Hydraulics Division, A.S.C.E.* **90**, 197–206 (1964).
79. R. W. Fenn and S. Middleman, "Newtonian Jet Stability: The Role of Air Resistance," *A. I. Ch. E. J.* **15**, 379 (1969).
80. R. P. Grant and S. Middleman, "Newtonian Jet Stability," *A. I. Ch. E. J.* **12**, 669 (1966).
81. C. C. Miesse, "Correlation of Experimental Data on the Disintegration of Liquid Jets," *Ind. Eng. Chem.* **47**, 1690-1701 (1955).
82. R. F. Phinney, "Breakup of a Turbulent Liquid Jet in a Low-Pressure Atmosphere," *A. I. Ch. E. J.* **21** 996 (1975).
83. L. A. Vitman, *Problems of Heat Transfer and Hydraulics of Two Phase Media* (Pergamon Press, Oxford, 1961), pp. 414-429
84. P. D. McCormack, H. Crane, and S. Buch, "Experimental and Theoretical Analyses of Cylindrical Liquid Jets Subjected to Vibration," *J. Appl. Phys.* **16**, 395-408 (1965)
85. M. J. McCarthy and N. A. Mallov, "Review of Stability of Liquid Jets and the Influence of Nozzle Design," *Chem. Engr. J.* **7**, 1-20 (1964)
86. J. A. Blink, *ORIG: A Modification of the ORIGEN Isotope Generation and Depletion Code for Fusion Problems*, Lawrence Livermore National Laboratory, Livermore, Calif., UCRL-53263 (in press).
87. J. B. Katter et al., *STARFIRE—A Commercial Tokamak Fusion Power Plant Study*, Argonne National Laboratory, Argonne, Ill., ANL/FPP-80-1 (1980).
88. G. Lasche, *Radioactivity Estimates in HYLIFE*, internal memorandum E&MA 81-161 Lawrence Livermore National Laboratory, Livermore, Calif. (October 1981).
89. G. Lasche, *Refinements to Radioactivity Estimates in HYLIFE*, internal memorandum E&MA 81-185, Lawrence Livermore National Laboratory, Livermore, Calif. (December 1981).
90. C. C. Baker and M. A. Abdou, "An Overview of the STARFIRE Reference Commercial Tokamak Fusion Power Reactor Design," *Proc. 4th Top. Mtg. Tech. of Controlled Nucl. Fusion* (King of Prussia, Pa., October 14-17, 1980), ANS Pub. No. CONF-801011 (1981).
91. G. Lasche, *Refinements to Radioactivity Estimates in HYLIFE*, internal memorandum E&MA 81-185, Lawrence Livermore National Laboratory, Livermore, Calif. (December 1981), p. 12-5.
92. G. Lasche, *Refinements to Radioactivity Estimates in HYLIFE*, internal memorandum E&MA 81-185, Lawrence Livermore National Laboratory, Livermore, Calif. (December 1981), p. 10-104.
93. *Laser Program Annual Report—1980*, Lawrence Livermore National Laboratory, Livermore, Calif., UCRL-50021-80 (1981), pp. 9-91 to 9-99.
94. M. J. Monsler, "A New Concept for a High-Repetition-Rate Reactor for Inertial Confinement Fusion," *Proc. 4th ANS Top. Mtg. Tech. Controlled Nucl. Fusion* (King of Prussia, Pa., October 14-17, 1980), ANS Pub. No. CONF-801011 (1981).
95. *Laser Program Annual Report—1980*, Lawrence Livermore National Laboratory, Livermore, Calif., UCRL-50021-80 (1981), pp. 9-91 to 9-99.
96. Bechtel Group, Inc., *Conceptual Design of a Laser Fusion Power Plant—Part II. Two Technical Options: 1) The JADF Reactor, 2) Heat Transfer by Heat Pipes*, Final Report to Lawrence Livermore National Laboratory, Livermore, Calif., UCRL-51467 (1981).

97. A. E. Scheiddeger, *The Physics of Flow Through Porous Media* (University of Toronto Press, Toronto, 1974).
98. I. F. McDonald et al., "Flow Through Porous Media—The Ergun Equation Revisited," *Ind. Eng. Chem. Fund* **18** (3), 199–208 (1979).
99. *Laser Program Annual Report—1979*, Lawrence Livermore National Laboratory, Livermore, Calif., UCRL-50021-79 (1980), p. 8-38. See also internal memorandum E&MA 81-088, Lawrence Livermore National Laboratory, Livermore, Calif. (1981).
100. C. K. Briggs and I. Y. Borg, *U.S. Energy Flow—1980*, Lawrence Livermore National Laboratory, Livermore, Calif., UCID-19227-80 (1981).
101. J. Hovingh, "Review of Hydrogen Production and a Strategy for the Development of an Inertial Fusion Reactor as an Energy Source for Hydrogen Production," internal memorandum E&MA 81-167, Lawrence Livermore National Laboratory, Livermore, Calif. (1981).
102. W. R. Meier, "SEBREZ: An Inertial Fusion Chamber Concept," *Trans. ANS Winter Mtg.*, San Francisco, Calif., November 1981 (American Nuclear Society, 1981).
103. R. N. Ng, "Perspective on the DOE Fusion Synthetic Fuels Program," *Proc. 15th Intersociety Energy Conversion Eng. Conf.* (Seattle, Wash., 1980), published by AIAA (1980), p. 1658.
104. J. A. Fillo et al., "HYFIRE: Fusion-High Temperature Electrolysis System," *Proc. 15th Intersociety Energy Conversion Eng. Conf* (Seattle, Wash., 1980), published by AIAA (1980), p. 1938.
105. J. R. Powell, J. A. Fillo, and M. Reich, "Thermal and Structural Design Aspects of High Temperature Blankets for Fusion Synfuel Production," *Trans. 6th Int. Conf. Structural Mechanics in Reactor Tech.* N, N2/4, Paris, France, August, 1981 (North Holland Publishing Co., Amsterdam, 1981).
106. G. E. Besenbruch et al., "Hydrogen Production by the GA Sulfur-Iodine Process: A Progress Report," *Hydrogen Energy Progress*, T. N. Veziroglu, K. Fueki, and T. Ohta, eds. (Pergamon Press, Oxford, 1980), vol. 1, p. 243.
107. R. W. Werner, "The Tandem Mirror Reactor as a Synthetic Fuel Producer," *Proc. 4th Top. Mtg. Tech. Controlled Nucl. Fusion* (King of Prussia, Pa., October 14-17 1980) ANS Pub. No. CONF-801011 (1981), p. 1802.
108. T. R. Galloway, "Some Process Aspects of Hydrogen Production Using the Tandem Mirror Reactor," *Proc. 4th Top. Mtg. Tech. Controlled Nucl. Fusion* (King of Prussia, Pa., October 14–17, 1980) ANS Pub. No. CONF-801011 (1981), p. 1630.
109. M. A. Hoffman, R. W. Werner, and G. L. Johnson, "The Heat-Pipe Liquid-Pool-Blanket Concept for the Tandem Mirror Reactor," to be published in *Proc. 9th Symp. Eng. Problems of Fusion Research* (Chicago, Ill., 1981), published by IEEE.
110. R. W. Werner et al., *Synfuels From Fusion Producing Hydrogen With Tandem Mirror Reactor and Thermochemical Cycles*, Lawrence Livermore National Laboratory, Livermore, Calif., UCID-18909, Vols. I and II (1981).
111. M. J. Monsler, J. Hovingh, D. L. Cook, T. G. Frank, and G. A. Moses, "An Overview of Inertial Fusion Reactor Design," *Nucl. Tech. Fusion* **1**, 302 (1981).
112. *Laser Program Annual Report—1980*, Lawrence Livermore National Laboratory, Livermore, Calif., UCRL-50021-80 (1981), p. 9-21.
113. M. M. H. Ragheb, A. C. Klein, and C. W. Maynard, "Neutronic Shielding Analysis of the Last Mirror-Beam Duct System for a Laser Fusion Power Reactor," *Nucl. Tech. Fusion* **1**, 99 (1981).
114. H. Omura et al., "Conceptual Design of Laser Fusion Reactor, SENRI-I: Tritium Breeding Ratio, Neutron Streaming to Laser Beam Ports and Final Mirrors," IEEE Pub. No. 81CH 1715-2 NPS (1981), p. 1188.
115. E. F. Plechaty and J. R. Kimliner, *TARTNP: A Coupled Neutron-Photon Monte Carlo Transport Code*, Lawrence Livermore National Laboratory, Livermore, Calif., UCRL-50400, Vol. 14 (1975).
116. E. F. Plechaty, D. E. Cullen, R. J. Howerton, and J. R. Kimlinger, *Tabular and Graphical Presentation of 175 Neutron-Group Constants Derived from the LLL Evaluated-Nuclear-Date Library (ENDL)*, Lawrence Livermore National Laboratory, Livermore, Calif., UCRL-50400, Vol. 16, Rev. 2 (1978).
117. H. M. Agnew, "Gas-Cooled Nuclear Power Reactors," *Scientific American* **244**(6), 55 (1981).
118. *STARFIRE—A Commercial Tokamak Fusion Power Plant Study*, Argonne National Laboratory, Argonne, Ill., ANL/FPP-80-1 (1980).
119. Briefing to the Energy and Military Applications Group, Laser Fusion Program, Lawrence Livermore National Laboratory, Livermore, Calif (July 31, 1981). Also, Patent Disclosure, "Gas-Cooled Inertial Fusion Reactor," M. Monsler (September 16, 1981).
120. K. S. B. Rose, "Coated Particle Fuels," *J. Inst. Nucl. Eng.*, Great Britain (July/August 1971), p. 95.
121. W. V. Goeddel and J. N. Siltanen, "Materials for High Temperature Nuclear Reactors," *Annual Review of Nuclear Science* **17**, Annual Reviews, Inc., Palo Alto, Calif. (1967).
122. L. R. Shepherd, "Development of Coated Particle Fuels for High Temperature Reactors," *J. British Nucl. Energy Soc.* 9(3), 173–186 (1970).
123. C. F. McDonald and C.P.C. Wong, *Closed-Cycle Gas Turbine Applications for Fusion Reactors*," Paper 81-GT-17, Gas Turbine Conference & Products Show, Amer. Soc. Mech. Engs. (Houston, Tex., March 9-12, 1981).
124. C. F. McDonald and C. R. Boland, "The Nuclear Closed-Cycle Gas Turbine (HTGR-GT)—Dry Cooled Commercial Power Plant Studies," *Eng. for Power* **103**(1), 89 (1981).
125. C. O. Peinado, J. W. Read, and C. R. Boland, "Design of the 800-MW(e) HTGR Gas Turbine Power Plant," presented at Am. Power Conf. (Chicago, Ill., April 21-23, 1980).
126. J. Hovingh and J. Blink, *Thermal Stress in the HYLIFE First Structural Wall*, internal memorandum SS&A 78-154, Lawrence Livermore National Laboratory, Livermore, Calif. (1978).
127. C. F. Bonilla, *Nuclear Engineering* (McGraw-Hill Inc., New York, 1957), Ch. 11.

References

128. W. R. Meier and W. B. Thomson, "Conceptual Design Considerations and Neutronics of Lithium Fall Laser Fusion Target Chambers," *Proc. 3rd Top. Mtg. Tech. Controlled Nucl. Fusion* (Santa Fe, N. Mex., May 9–11, 1978), published by the American Nuclear Society (1978).

129. M. J. Monsler, "A New Concept for a High-Repetition-Rate Reactor for Inertial Confinement Fusion," *Proc. 4th Top. Mtg. Tech. Controlled Nucl. Fusion* (King of Prussia, Pa., October 14–17, 1980), ANS Pub. No. CONF-801011 (1981).

130. M. M. El-Wakil, *Nuclear Energy Conversion* (Intext Educational Publishers, Scranton, 1971), Ch. 7 and 8.

131. J. Pitts, *A Design Method for Thermal Stress*, internal memorandum E&MA 79-102, Lawrence Livermore National Laboratory, Livermore, Calif. (1979).

132. J. Hovingh, *Parametric Analysis of the First Structural Wall for a Liquid Wall Inertially Confined Fusion Energy Converter*, internal memorandum E&MA 80-004, Lawrence Livermore National Laboratory, Livermore, Calif. (1980).

133. W. R. Meier, "SEBREZ: An Inertial Fusion Chamber Concept," to appear in *Trans. ANS Winter Mtg.* (San Francisco, Calif., November 29–December 4, 1981).

134. M. J. Monsler, "A New Concept for a High-Repetition-Rate Reactor for Inertial Confinement Fusion," *Proc. 4th ANS Top. Mtg. Tech. Controlled Nucl. Fusion* (King of Prussia, Pa., October 14–17 1980), ANS Pub. No. CONF-801011 (1981), p. 1162.

135. W. R. Meier, *Preliminary Sizing of the Helium Pipes in the Gas-Cooled Fusion Reactor Blanket*, internal memorandum E&MA 81-156, Lawrence Livermore National Laboratory, Livermore, Calif. (1981).

136. M. M. El-Wakil, *Nuclear Energy Conversion*, (Intext Educational Publishers, 1971), Ch. 7 and 8.

Subject Index

Italic listings are article titles; section numbers appear in boldface and precede page numbers.

D

E

F

G

H

I

J

K

L

M

N

O

P

Q

R

S

T

U

V

W

X

Z

Author Index

All authors and major contributors are listed. Page numbers indicate where articles begin, not where authors' names are found.

M

N

O

P

R

S

T

V

W

Y

Z

Divider Illustrations

Section 1

Thermal x-ray micrograph image of target implosion showing compression of deuterium–tritium fuel.

Section 2

Defects in a glass laser amplifier rod found during inspection.

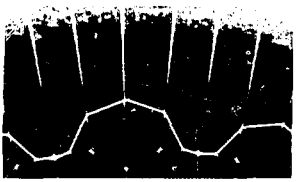

Section 3

Density contours from a two-dimensional simulation of the implosion and "burn" of a liquid deuterium–tritium pellet.

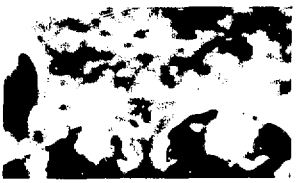

Section 4

Micrometer-sized hollow gold spheres produced by the droplet-generation technique for ICF targets.

Work performed under the auspices of the U.S. Department of Energy by the Lawrence Livermore National Laboratory under Contract W-7405-Eng-48.

U.S. Government Printing Office

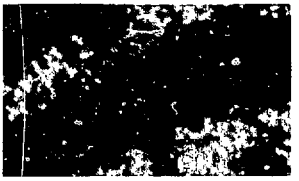

Section 5
Fresnel zone-plate imagery showing "x-ray lens" focusing for radiographic diagnostic analysis of target implosions.

Section 6
False color cathode ray tube image showing time-resolved x-ray probing of a typical colliding-disk experiment.

Section 7
Cross section of 3ω laser beam after frequency conversion.

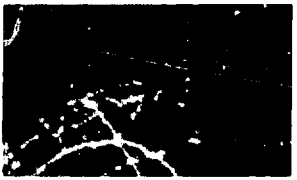

Section 8
Computer simulation of an advanced reactor design concept.

Publication Editors	John R. Strack Gerald R. Grow
Editors	Thomas C. Elkjer Robert E. Hendrickson Robert D. Kirvel
Editor and Schedule Coordinators	M. Louise Rufer Elsa A. Pressentin
Editorial Assistant	Susan J. Simecka
Art Director and Designer	William Fulmer
Designer	Richard A. Wooten
Layout and Art Coordinator	Wilma T. Leon
Compositors	Barbara L. Phillips Cathy A. Wood
Proofreader	Jill S. Silvers
Printing Coordinators	Melvin G. Moura Margaret E. Sylvester